UAB
Universitat Autònoma de Barcelona

New Molecular Systems for Biomedical Imaging and Biological Receptors Modulation

Daniel Torralba Maldonado

UAB
Universitat Autònoma de Barcelona

New Molecular Systems for Biomedical Imaging and Biological Receptors Modulation

PhD thesis

PhD programme in Chemistry

Daniel Torralba Maldonado

2025

UAB
Universitat Autònoma de Barcelona

New Molecular Systems for Biomedical Imaging and Biological Receptors Modulation

PhD thesis

PhD programme in Chemistry

Daniel Torralba Maldonado

2025

Supervisor: Dr. Ona Illa Soler

Memoria presentada para aspirar al grado
de Doctor por Daniel Torralba Maldonado

Daniel Torralba Maldonado

Con el visto bueno de,

Dr. Ona Illa Soler

Bellaterra, 9 de enero de 2025

Aquellos que afirman que no puedes lograr algo,
a menudo son los mismos que temen que
tengas éxito allí donde ellos fracasaron.

Agradecimientos

Cuando empecé el doctorado seguramente hubiese dicho que esta sección sería prescindible para mí y que podía hacerlo todo sin ayuda. Sin embargo, el resultado dice todo lo contrario, ya que no podría haberlo hecho sin algunas de estas personas, y sin otras, no hubiese sido lo mismo.

Cuando decides hacer una tesis doctoral, el consejo más repetido es “Escoge bien a tu director de tesis”, y puedo decir que no podría haber tenido a una mejor directora de tesis que Ona. Sé que siempre has hecho todo lo que has podido para ayudarme, y que siempre has estado cuando te necesitaba. Por ello, y por darme la oportunidad de hacer la tesis contigo, siempre te estaré agradecido.

Y otra persona que siempre ha estado, me ha apoyado y que más ha aguantado mis quejas, mal humor, muchas horas de trabajo… Carolina, a ti nunca te lo podré agradecer lo suficiente la paciencia que has tenido y lo comprensiva que has sido siempre durante mi tesis. Fue una suerte conocerte al principio y un regalo que sigas al final de esta, y además ahora como una familia, siendo uno más. Espero que me sigas acompañando en el futuro y sigas teniendo la misma paciencia conmigo.

En cuanto a mis compañeros, no puedo empezar por otro grupo que no sea el de “Los fijos”. Alba, aunque no hemos compartido laboratorio, hemos pasado buenos momentos juntos en los viajes, algunos con más éxito que otros, y varias casas rurales (6 o 7, deberíamos volver a repasarlas). Espero que podamos volver a coincidir en unos años otra vez en la universidad, como profesores y, quien sabe, montar un grupo juntos (TorraAlba puede ser un buen nombre, ya tenemos las camisetas por lo menos). Marc, o DJDeet, esa persona que parece el resultado de un catalán que ha sido adoctrinado por el español más patriota, que tan pronto te baila una sardana como te canta una canción de Fondo Flamenco. El catalán más aficionado del Getafe (y probablemente el único). Estos contrastes son los que te hacen único y que merezca la pena conocerte; no cambies nunca. Marc-Ricard Batten, la inocencia personificada. Un niño grande con tus canciones de Disney, y el más inclusivo de todos, permitiendo que vivan con él personas de todas las nacionalidades y todas las razas. Ya nos conocíamos, aunque no mucho, antes de que empezase el doctorado, y espero que nos sigamos viendo ahora que se acaba esta etapa. Cristina, la otra víctima (aparte de mí) de las malas influencias de este grupo. No hemos podido compartir mucho tiempo en la uni, por estar en diferentes grupos y horarios de comedor totalmente distintos, pero te aprecio mucho. Te doy mucho ánimo en esta etapa final, en la que también estás tú, y que después disfrutes de aquello que hagas y podamos seguir siendo vecinos para vernos a menudo con cualquier excusa, aunque sea ver un partido del Getafe (impuesto por tu marido). Albert, el más joven del grupo, aunque que puede que el más jodido. El fichaje revelación de este grupo, con el que me alegro de haber compartido tantas cosas y con quien me hubiese gustado compartir aún más. No sé cuáles son tus planes para el futuro, aparte de acabar la tesis, pero sea lo que sea espero poder estar ahí

para verlo y apoyarte. Aleix, esa persona polifacética, que lo mismo te pone una reacción que te hace un cálculo. Ese semidios griego, que bien podría ser modelo de ropa interior, que de vez en cuando decide honrarnos con su presencia apareciendo por el lab y codeándose con simples mortales como nosotros. Eres una gran persona y espero que encuentres aquello que te hace feliz y lo disfrutes. Por último, en este párrafo me gustaría mencionar a la antítesis de “Los fijos”, Amanda. Esa persona que necesita que el plan se le comunique con un mes de antelación para hacerse a la idea de ello, y aún así es probable que no venga. Eres la persona con la que más horas de laboratorio he compartido y eso que al principio te parecía un huraño encerrado a oscuras en el laboratorio haciendo vaya a saber qué (algo que no se alejaba mucho de la realidad). Espero que no haya sido muy terrible compartir laboratorio conmigo. Yo me alegro de haberte podido conocer más y ver como has evolucionado, desde ser un TFG a casi doctora que ya eres (cosa que espero poder ver el año que viene). Nos hemos reído mucho con los niños, también los hemos aguantado mucho, y te aprecio mucho por todo el tiempo que hemos pasado juntos.

En cuanto al grupo de los Moreno, en primer lugar, quiero mencionar a Ferran, una de sus incorporaciones más recientes (aunque ya no tan reciente, que ya va siendo hora también de que salgas de ahí). Eres esa persona que me hace sentir joven en esta planta. No hemos compartido tanto tiempo juntos, pero te he cogido mucho cariño y espero que también contigo volvamos a encontrarnos por el departamento en un futuro. Como contraste, Oriol, la persona que me hace sentir más viejo. El futuro del departamento está en buenas manos. David, marido de Amanda, un hombre cargado de paciencia (por el tema de investigación que le ha tocado). Ha sido un placer conocerte y si algún día no va bien con Amanda, ya sabes, tienes mi número. Arnau, aquella persona en la que todo el mundo confía cuando hay algún problema en la planta o cuando tienes alguna duda burocrática. Axel, aquella persona a la que todo el mundo acude cuando suena la alarma en la planta (por si ha sido él) o cuando quieres hacer una pausa y tener una conversación “random”. Por último, los dos postdocs, Pau y Marta, excelentes fichajes, ya que uno proporcionaba bebida y el otro siempre estaba dispuesto a tomársela contigo, respectivamente.

También quería agradecer a los tres TFGs a los que he dirigido y que han aportado también a esta tesis. A todos ellos quiero darle las gracias y que sepas que, si necesitan cualquier cosa, siempre estaré dispuesto a ayudarles en lo que pueda. Laura, mi primera TFG, quiero agradecerte todo lo que te esforzaste y trabajaste durante los meses en el lab. Espero que no fuese muy duro y pudieses aprender algo. Y recuerda que, hagas lo que hagas, estoy seguro de que se te dará bien. Oriol, paisano de Terrassa, nos echamos unas buenas risas en el lab, compartimos conversaciones sobre Fórmula 1 y, aunque intenté adaptarme a tu música, hubo que bajar el nivel de gritos. Tienes un gran futuro por delante y la elección que hiciste te abrirá muchas puertas en el futuro. Y Marina, mi última TFG, espero que disfrutases de tu tiempo en el lab y, sobre todo, te lo pasases bien. Te deseo mucha suerte en el futuro.

Como TFGs honoríficos, personas que hubiese adoptado encantado para ayudarles en sus primeros pasos en un laboratorio de química orgánica. Oriol, el niño, pase lo que pase, si no funciona algo, siempre encontrará la excusa, y si funciona, siempre habrá sido su idea. Un tanto cabezón, pero la persona de todas las que han pasado por el lab en la que más confié que podría haber seguido el camino del doctorado si se lo hubiese propuesto. Raül, Raulillo, el que pudo haber sido el futuro del lab, pero tomó otro camino, y Judith, la que espero que lo sea y tenga toda la suerte del mundo. Las niñas, María y Carla, que está claro que mal no lo pasasteis porque habéis decidido volver para el TFM, veremos que decidís hacer en un futuro, vosotras ya sabéis lo que pienso. Y espero que os acordéis esta vez cuando organicéis un sushi. Por última, también mencionar a Yingmin y Kate, que si bien no estaban en mi grupo, siempre tuve tiempo para escuchar alguna de sus quejas sobre cómo la química no funciona.

Otras personas que me han acompañado en el laboratorio son Romain, durante los primeros meses haciendo equipo para sacar los primeros compuestos, Roger, con nuestras conversaciones filosóficas fuiste una gran compañía durante uno de esos “contratillos”, Fátima, una buena amiga, y Marie, que, si bien no compartimos mucho tiempo en el lab, ha sido un placer conocerte, eres una gran persona, y te esperamos con los brazos abiertos si decides volver.

Los doctorandos de la antigua generación, y ya hace tiempo doctores: Adri, siempre dispuesto a darte una visión de veterano en el lab, Marc Villabona, fuente de todos los datos y conocimientos que necesites (y de los que no, también), Laura Parejo, con quien compartí ese concierto de Fondo Flamenco y una Feria de Abril descafeinada, y Kevin Reyes, con quién quizás no coincidimos tanto, pero del que estoy seguro nos hubiésemos llevado bien de compartir generación.

También agradecer a Félix y Ramon, por acogerme y ayudarme también a poder hacer esta tesis, dándome la oportunidad colaborando en los proyectos con ellos. A Yeray, doctorando en el CiQUS, contestando siempre a todas mis dudas sobre sus resultados bio. A Carlos y David, en el CICA, por acogerme tan bien durante las 3 semanas que estuve en su laboratorio, y a Saray, Antía y Charlene por hacerme participe de su grupo.

A todos vosotros, muchas gracias, porque sin vosotros no hubiese sido lo mismo.

Some of the results of this thesis have been submitted for publication or have been published in the following articles:

- Folgar-Cameán, Y.; **Torralba-Maldonado, D.**; Fulias-Guzmán, P.; Pazo, M.; Lostalé-Seijo, I.; Royo, M.; Illa Soler, O.; Montenegro, J. *A non-hydrolysable peptidomimetic for mitochondrial targeting*, Journals of Materials Chemistry B.
  Status: Submitted

- **Torralba-Maldonado, D.**; Marlin, A.; Lucio-Martinez, F.; Freire-Garcia, A.; Whetter, J.; Brandariz, I.; Iglesias, E.; Pérez-Lourido, P.; Ortuño, R.; Boros, E.; Illa, O.; Esteban-Gómez, D.; Platas-Iglesias, C. *Tuning the Properties of Rigidified Acyclic DEDPA^{2-} Derivatives for Application in PET using copper-64*, *Inorg. Chem*. **2024**, 63, 46, 22297–22307. https://doi.org/10.1021/acs.inorgchem.4c04050.
  Status: Published November 2024

Table of contents

Chapter III. Innovative Bitopic Ligands Targeting Allosteric and Metastable CB_2R Binding Sites

Chapter IV. Halogen- and Thioether-Containing Ligands Targeting the Allosteric CB_2R Binding Site

PART III. EXPERIMENTAL METHODOLOGIES

Abbreviations and Acronyms

2-AG: 2-Arachidonoylglycerol

2-AGE: 2-Arachidonoylglycerol ether

AA: Arachidonic acid

ABA: 4-Acetamidobenzoic acid

abn-CBD: Abnormal cannabidiol

AC: Adenylyl cyclase

ACN: Acetonitrile

AEA: Arachidonoylethanolamide

AEMPS: Agencia Española de Medicamentos y Productos Sanitarios

Alloc: Allyloxycarbonyl

AMA: Apparent molar activity

APCI: Atmospheric pressure chemical ionization

ATCUN: Amino-terminal Cu(II)- and Ni(II)-binding

ATP: Adenosine triphosphate

BAM: Biased allosteric modulator

BFC: Bifunctional chelator

B_L: Lewis base

Boc: *tert*-Butoxycarbonyl

Boc_2O: Di-*tert*-butyl dicarbonate

BRET: Bimolecular resonance energy transfer

BRSM: Based on recovered starting material

cAMP: Cyclic adenosine monophosphate

CBAA: Cyclobutane amino acid

CBC: Cannabichromene

CBC: Cyclobutane-containing

CBD: Cannabidiol

CBCA: Cannabichromenic acid

CBDA: Cannabidiolic acid

CBDV: Cannabidivarin

CBG: Cannabigerol

CBGA: Cannabiogerolic acid

CBN: Cannabinol

CBR: Cannabinoid receptor

Cbz: Benzyloxycarbonyl

CCCP: Carbonyl cyanide 3-chlorophenylhydrazone

CF: Carboxyfluorescein

Ch: Chalcogen

ChB: Chalcogen bond

CICA: Centro Intersciplinar de Química e Bioloxía

CiQUS: Centro Singular de Investigación en Química Biológica y Materiales Moleculares

CNS: Central nervous system

COSY: Correlation spectroscopy

***m*-CPBA:** 3-Chloroperbenzoic acid

CPP: Cell penetrating peptides

CPZ: Chlorpromazine

CRC: Concentration-response curves

CT: Computed tomography

CV: Column volumes

Cy: Cyclohexane

DCC: *N*,*N*-Dicyclohexylcarbodiimide

DCM: Dichloromethane

d.e.: Diastereomeric excess

d.r.: Diastereomeric ratio

DIBAL: Diisobutylaluminium hydride

DIC: *N*,*N*'-Diisopropylcarbodiimide

DIAD: Diisopropyl azodicarboxylate

$DIOC_6$: 3,3'-Dihexyloxacarbocyanine iodide

DIPA: Diisopropylamine

DIPEA: *N,N*-Diisopropylethylamine

DLC: Delocalised lipophilic cations

DMAP: 4-Dimethylaminopyridine

DMEM: Dubelco's Modified Eagle's Medium

DMF: *N,N*-Dimethylformamide

DMSO: Dimethyl sulfoxide

DNA: Desoxyribonucleic acid

DOG: 2-Deoxy-D-glucose

DOTA: Dodecane tetraacetic acid

Dox: Doxorubicin

DPBS: Dulbecco's phosphate-buffered saline

DPPA: Diphenylphosphoryl azide

DTPA: Diethylenetriaminepentaacetic acid

Dyn: Dynasore

EC: Electron capture

EC_{50}: Half-maximal effective concentration

ECS: Endocannabinoid system

EDC: 1-Ethyl-3-(3-dimethylaminopropyl)carbodiimide

EIPA: 5-(*N*-Ethyl-*N*-isopropyl)-amiloride

EM: Energy minimisation

EMA: European Medicines Agency

ESI: Electrospray ionisation

EtOAc: Ethyl acetate

ETPB: Ethyltriphenylphosphonium bromide

EWG: Electro-withdrawing group

FBS: Fetal bovine serum

FDA: Food and Drug Administration

^{18}F-FDG: ^{18}F-Fluorodeoxyglucose

Fmoc: 9-Fluorenylmethyl carbamate

Fmoc-O-Su: *N*-(9-Fluorenylmethoxycarbonyloxy)succinimide

FSK: Forskolin

GFP: Green fluorescent protein

GPCRs: G-protein-coupled receptors

GPP: Geranyl pyrophosphate

GPR55: G-protein-coupled receptor 55

HATU: *O*-(7-Azabenzotriazol-1-yl)-*N*,*N*,*N'*,*N'*-tetramethyluronium hexafluorophosphate

HBTU: *O*-(Benzotriazol-1-yl)-N,N,N',N'-tetramethyluronium hexafluorophosphate

HBSS: Hanks' balanced salt solution

HFIP: Hexafluoroisopropanol

HIV: Human immunodeficiency viruses

HMBC: Heteronuclear multiple-bond correlation

HMDS: Hexamethyldisiloxane

HPLC-MS: High-performance liquid chromatography-mass spectrometry

HRMS: High-resolution mass spectrometry

HTRF: Homogeneous time-resolved fluorescence

HSQC: Heteronuclear single quantum correlation

HSV-1: Herpes simplex virus type 1

IMM: Inner mitochondrial membrane

IPA: Isopropanol

IQAC: Institut de Química Avançada de Catalunya

ISC: Intersystem crossing

IR: Infrared spectroscopy

LHMDS: Lithium bis(trimethylsilyl)amide

Log*P*: Logarithm of the octanol-water partition coefficient

MAPK: Mitogen-activated protein kinase

mBu: miliBRET units

MCPs: Metallocarboxypeptidases

MD: Molecular dynamics

MM: Mitochondrial matrix

MOC: Mander's overlap coefficient

MOM: Methoxymethyl

MPP: Mitochondria-penetrating peptide

MTS: Mitochondrial targeting sequence

MTT: 3-(4,5-Dimethylthiazol-2-yl)-2,5-diphenyltetrazolium bromide

MRI: Magnetic resonance imaging

MS: Mass spectrometry

NADPH: Nicotinamide adenine dinucleotide phosphate

NAM: Negative allosteric modulator

NC: Neocuproine

NETs: Neuroendocrine tumours

NHS: *N*-Hydroxysuccinimide

NMR: Nuclear magnetic resonance

NOE: Nuclear Overhauser effect

NOESY: Nuclear Overhauser enhancement spectroscopy

OA: Orthosteric agonist

OMM: Outer mitochondrial membrane

pAntp: Penetratin

PAM: Positive allosteric modulator

PBL: Protected bitopic ligand

PBS: Phosphate-buffered saline

PCC: Pearson's overlap coefficient

pEC50: Negative algorithm of the half-maximal effective concentration

PEI: Polyethyleneimine

PET: Positron emission tomography

PG: Protecting group

Phe: Phenylalanine

PhMen: (-)-8-Phenylmenthol

PIFA: (Bis(trifluoroacetoxy)iodo)benzene

Piv: Pivaloyl

PKA: Protein kinase A

PLE: Pig liver esterases

PP: Polyproline

PPAR: Peroxisome proliferator-activated receptor

***n*-PrSH**: 1-Propanethiol

PSMA: Prostate-specific membrane antigen

PyAOP: 7-Azabenzotriazol-1-yloxy)tripyrrolidinophosphonium hexafluorophosphate

PyBOP: Benzotriazol-1-yloxytripyrrolidinophosphonium hexafluorophosphate

QSAR: Quantitative structure-activity relationship

RCY: Radiochemical yield

R_f: Retention factor

Rluc: Renilla luciferase

RNA: Ribonucleic acid

ROS: Reactive oxygen species

RP-HPLC: Reverse-phase high-performance liquid chromatography

RP-HPLC-MS: Reverse-phase high-performance liquid chromatography coupled to a mass spectrometer

RP-MPLC: Reverse-phase medium-pressure liquid chromatography

RSE: Ring strain energies

R_t: Retention time

r.t.: Room temperature

SEM: Standard error of the mean

SEMCl: 2-(Trimethylsilyl)ethoxymethyl chloride

Semiprep-RP-HPLC-MS: Semipreparative reverse-phase high-performance liquid chromatography coupled to a mass spectrometer

siRNA: Small interfering ribonucleic acid

S_N2: Bimolecular nucleophilic substitution

SNARF: Seminaphtharhodafluor

SPECT: Single photon emission computed tomography

SPPS: Solid-phase peptide synthesis

SS: Szeto-Schiller peptide

SST: Somatostatin

Tat: Trans-activator of transcription

TBAF: Tetrabutylammonium fluoride

TBDMS: *tert*-Butyldimethylsilyl

TBDPS: *tert*-Butyldiphenylsilyl

TFA: Trifluoroacetic acid

TFP: Tetrafluorophenyl

THC: Tetrahydrocannabinol

Δ^9-THCA: Δ^9-Tetrahydrocannabinolic acid

THF: Tetrahydrofuran

TIS: Triisopropylsilane

TLC: Thin layer chromatography

TM: Transmembrane helix

TMRE: Tetramethylrhodamine ethyl ester

TMSI: Trimethylsilyl iodide

TPP: Triphenylphosphonium

Trp: Tryptophan

TRPV: Transient receptor potential cation channel subfamily V

US: Ultrasound

UV: Ultraviolet

XB: Halogen bond

PART I

Cyclobutane Scaffold for Imaging Applications

General Introduction

Cyclobutane was first synthesised in 1907 as a colourless gas with no biological properties as such. Since then, synthetic efforts towards the preparation of cyclobutane derivatives have progressed, improving their usefulness in areas like medicinal chemistry. A large and growing body of literature, composed of more than 10.000 patents and papers, can be found, as cyclobutane derivatives can be used as starting materials for the synthesis of both acyclic and cyclic structures.

In this introduction, cyclobutane-containing (CBC) molecules will be presented, highlighting some of their most important applications, and how several synthetic methods have been developed for their obtention.

1. Synthesis of Cyclobutane Structures

The introduction of small-ring systems as molecular building blocks has gained importance over the last decades. Strained cycloalkanes have proven to be highly useful in synthesis thanks to their unique reactivity. Cyclobutanes are one of the most used moieties, as they are accessible by several reliable preparative methods in excellent yields.[1]

Cyclobutane is a four-membered cycloalkane that adopts a puckered conformation (**Scheme I-1**). This conformation avoids the torsion strain from eclipsed hydrogens, although it also reduces the C-C-C bond angles (88º) further from ideal and increases the angle strain of the C(sp^3)-C(sp^3) bonds (109.5º). Due to their inherent ring strain, the selective modification of their structures can be strategically used in organic synthesis.[2] Facile C-C bond breakage has given a vast array of ring-expansion or ring-cleavage reactions that can be carried out to provide a variety of carbocycles, heterocycles, and ring-opened products.[3,4]

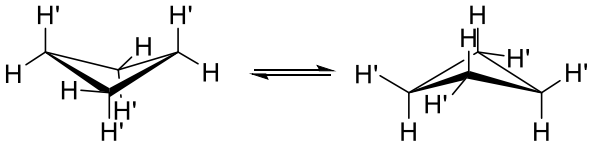

Scheme I-1. Cyclobutane geometry.

Studies have been conducted on how substituents or heteroatoms could reduce the striking ring strain of the cyclobutane motif. One of the most studied effects is the Thorpe-Ingold effect or ***gem*-dimethyl effect**. The literature indicates that there is a greater facility in the synthesis of small rings that have a *gem*-dimethyl substitution over the unsubstituted ones. This phenomenon was attributed to the kinetic effect caused by the substituents compressing the angle at that carbon that bears the two methyl groups, bringing them closer together.[5] However, other researchers have proposed an alternative approach, suggesting an increase of *gauche* conformers (over the *anti*) due to the steric hindrance introduced by the demethylation, favouring the cyclisation reaction when compared to unsubstituted systems.[6,7]

Continuing with the investigation of the *gem*-dimethyl effect, Ringer and Magers[8] also estimated the ring strain energies (RSE) by computational methods (**Figure I-1**). These reflected a trend where the RSE decreases when methyl groups are added. This was interpreted as an inherent enthalpic stability associated with the *gem*-dimethyl substitution of strained rings. However, Bachrach[9] reported results that, despite indicating the same tendency, showed a lower RSE difference (less than 2 kcal mol^{-1}). This would consider the *gem*-dimethyl-substituted small rings just slightly less strained, and no enthalpic stabilisation, by means of reduction in ring strain energy, would be shown. What it is certain is that the *gem*-dimethyl substitution is stabilising relative to unbranched acyclic alkanes.[10]

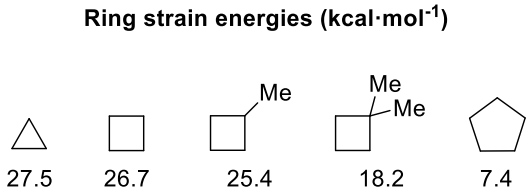

Figure I-1. RSE of different cyclic derivatives.[8]

Despite being readily reactive species when it comes to their modification, construction of these structural motifs represents a significant challenge in synthetic chemistry, especially in terms of stereoselectivity. To furnish cyclobutane scaffolds, a variety of methods have been developed (**Figure I-2**), such as [2+2] cycloadditions,[11] 1,4-cyclisations of acyclic precursors,[12] ring contractions, such as the Wolff rearrangement type,[13] or ring expansions of cyclopropanes.[14]

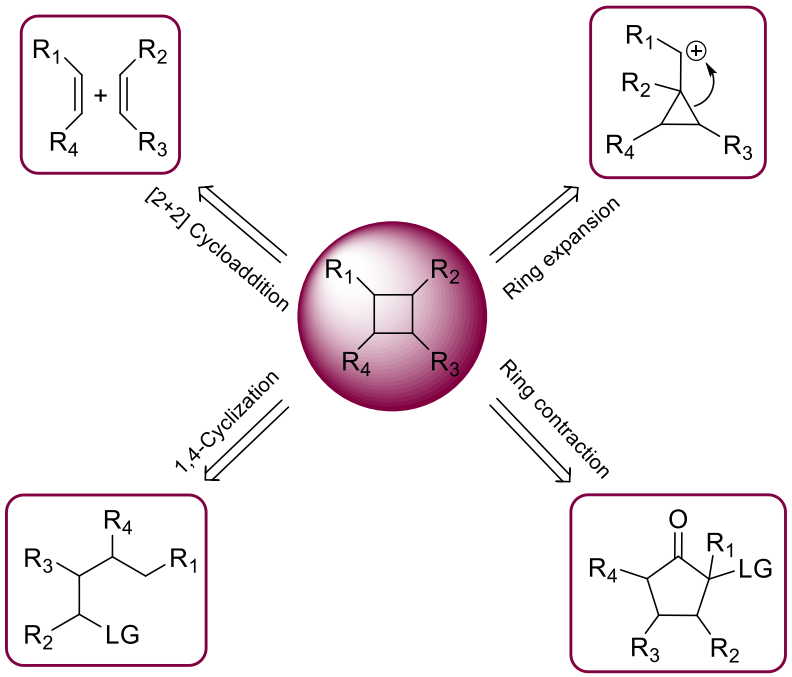

Figure I-2. Routes for the synthesis of cyclobutanes.

All these synthetic methodologies will be briefly reviewed in this **General Introduction**, giving special attention to the photochemical [2+2] cycloadditions, as this method is employed for the synthesis of compounds used in **Chapter II**. **Novel Bifunctional Ligands for PET Imaging with ^{64}Cu and ^{68}Ga Radioisotopes.**

1.1. [2+2] Cycloadditions

The [2+2] cycloaddition between two alkenes represents the most popular method for the construction of four-membered rings. This reaction involves the formation of two new σ-bonds through the interaction of two unsaturated molecules, typically alkenes or alkynes, leading to cyclobutanes and cyclobutadienes, respectively. An attractive feature of these reactions is their ability to form multiple C-C bonds in a single step, so simple precursors can build up easily more complex molecules. There are several types of [2+2] cycloadditions broadly categorised, based on the substrates and conditions used, such as **[2+2] photocycloadditions**, **thermal [2+2] cycloadditions** and **metal-catalysed [2+2] cycloadditions**.

1.1.1. [2+2] Photocycloadditions

The photochemically induced cycloaddition is a well-established and the most commonly used method for accessing cyclobutanes.[15] This light-driven photochemical process enables transformations that are otherwise forbidden under thermal conditions. The use of light to promote the [2+2] photocycloaddition circumvents the constraints imposed by Woodward-Hofmann's rules and Fukui's frontier orbital theory, which typically disfavour thermal [2+2] cycloadditions due to symmetry considerations.[16] In addition, the reaction can be tuned by selecting appropriate wavelengths of light, using sensitisers, or modifying the reaction environment, such as employing solid-state or micellar systems.

The reaction proceeds when one alkene or alkyne absorbs a photon, typically using ultraviolet (UV) light, leading to the excitation of electrons from the ground state (S_0) to the excited singlet state (S_1), enabling the formation of two new σ-bonds between the interacting alkenes or alkynes, forming the cyclobutane ring and up to four stereogenic centres in a single step (**Scheme I-2**, **A**).[17] But not all alkenes are suitable, as chromophores accessible through excitation by conventional light sources are needed. The substrate must undergo direct absorption to an excited state, but high lying S_1 requires high energy ($\lambda \leq 250$ nm) light sources. Then, this mechanistic pathway through the single state has restricted applications in the formation of the cyclobutane structure. As a result, strained non-conjugated alkenes, which have low-lying excited single and triplet states of π-π^* character, are the only type of substrate often found in examples of [2+2] photocycloadditions through this mechanism (*e.g.*, **Scheme I-2**, **B**).

A) Mechanism of [2+2] photocycloaddition *via* first excited singlet state (S_1)

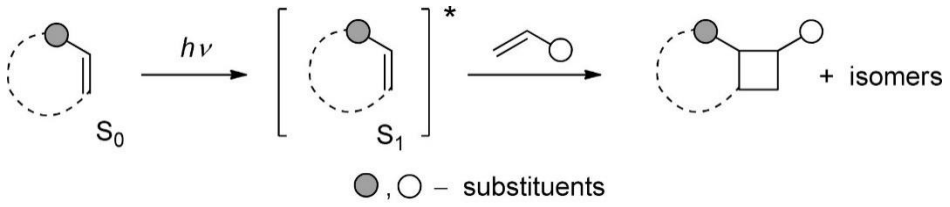

B) Example of a [2+2] photocycloaddtion through singlet state (S_1) pathway

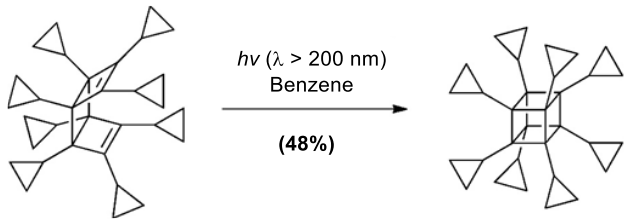

Scheme I-2. A) Representation of the mechanism of a [2+2] photocycloaddition of an olefin (S_0) *via* its first excited singlet state (S_1);[11] B) Synthesis of octacyclopropylcubane (**2**) by direct excitation of diene **1**.[18]

The number of examples of [2+2] photocycloaddition increases when olefinic substrates with double bonds conjugated to a carbonyl group are employed, typically α,β-unsaturated ketones (enones) or α,β-unsaturated carboxylic acid derivatives, which have relatively long-lived excited state, allowing the interaction with the other olefin. These can be directly excited to their respective S_1, which undergoes rapid intersystem crossing (ISC) to the corresponding triplet state (T_1). Photochemical reactions proceed from the lowest-energy T_1, which often exhibits a *π-π** character (**Scheme I-3**, **A**).

A) Mechanism of [2+2] photocycloaddition *via* first excited triplet state (T_1)

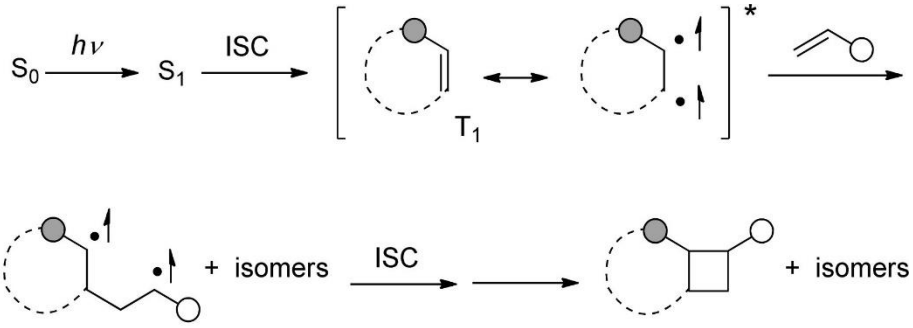

B) Example of a [2+2] photocycloaddtion through triplet state (T_1) pathway

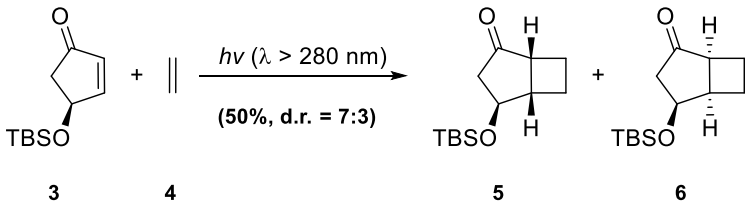

Scheme I-3. A) Representation of the mechanism of a [2+2] photocycloaddition of an olefin (S_0) *via* its first excited triplet state (T_1);[11] B) Intermolecular [2+2] photocycloaddition of a 2-cyclopentanone (**3**).[19]

In certain cases, the functional groups present in the precursors impose limitations on the reaction, as these substrates may have high-energy S_1 states, requiring high-energy light sources, which can result in unspecific reactions, less stereoselective reactions or even cause the decomposition of sensitive substrates. To surpass this drawback, the employment of photosensitisers is a very common practice in this methodology.

Photosensitisers are molecules characterised by a low-lying S_1 and a high-lying T_1, which facilitates the energy transfer process from their excited state to a substrate. Moreover, the sensitiser should exhibit a high ISC rate to ensure that the quantum yield for T_1 formation reaches unity. Once in the triplet state, the sensitiser transfers its energy to the olefin through an electron exchange mechanism. For this process to occur, the triplet energy of the olefin must be lower than that of the sensitiser (**Scheme I-4**). A key advantage of sensitisation over direct excitation is the ability to use longer wavelengths, whereas direct excitation typically requires shorter wavelengths. Acetone, with a high triplet energy (E_T = 332 kJ·mol^{-1}) and excellent solvent properties, is one of the most commonly used triplet sensitisers.

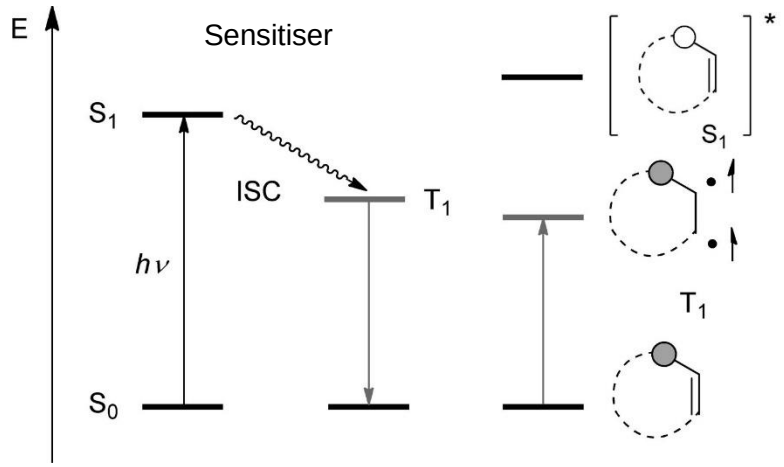

Scheme I-4. Sensitisation *via* triplet energy transfer from a sensitiser (left) to an olefin (right).

Other limitations involve challenges with regioselectivity, particularly related to head-to-head and head-to-tail coupling in unsymmetrical olefins, as well as *E/Z* isomerisation, which can occur under commonly employed reaction conditions. The problem of obtaining mixtures of regioisomers may be overcome using ketene as one of the reagents, as in many cases a single regioisomer is obtained.[20] In addition, [2+2] photodimerisation can sometimes interfere with a desired [2+2] photocycloaddition reaction by leading to the formation of unintended dimers.[21]

Overall, the [2+2] photocycloaddition remains a powerful and versatile tool in the synthesis of CBC molecules. Despite the challenges posed by issues such as regioselectivity and potential side reactions, advancements in new photochemical methodologies have significantly enhanced the versatility and applicability of this reaction. As research continues to address these challenges, the [2+2] photocycloaddition is poised to remain an indispensable tool in the synthesis of complex molecules, driving innovation in organic synthesis, materials science, and pharmaceutical chemistry.

1.1.2. Thermal [2+2] Cycloadditions

As previously discussed, concerted thermal [2+2] cycloadditions are forbidden by the Woodward-Hofmann's rules and Fukui's frontier orbital theory. However, certain alkenes can stabilise 1,4-biradical or zwitterionic intermediates, enabling [2+2] cycloadditions through non-concerted pathways. Among these, tetrafluoroethylene stands out as highly reactive in cycloadditions with other alkenes, facilitating the formation of fluorinated cyclobutanes (*e.g.*, **Scheme I-5**).[22]

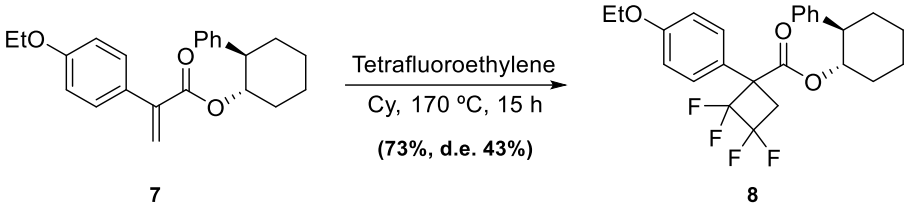

Scheme I-5. [2+2] cycloaddition of acrylate **7** employing thermal conditions in the presence of tetrafluoroethylene.[23]

Other noteworthy examples of thermally driven [2+2] cycloadditions include reactions between enamines[24] or ketenes[25] with electrophilic acetylenes. In particular, thermal [2+2] cycloadditions involving ketenes are one of the most valuable reactions for cyclobutane synthesis due to the numerous methods available for generating ketenes *in situ* and the high regio- and stereoselectivity of these reactions (*e.g.*, **Scheme I-6**). Additionally, allenes have also been identified as useful substrates for these cycloadditions.[26] Overall, thermal [2+2] cycloadditions are not applied often, as they require elevated temperatures and extended reaction times, which can limit their applications.

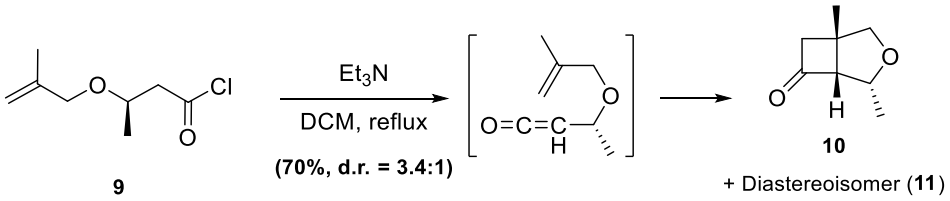

Scheme I-6. Ketene cycloaddition to obtain bicyclic cyclobutanones intermediates **10** and **11** for the synthesis of (±)-grandisol.[27]

1.1.3. Catalysed [2+2] Cycloadditions

Harsh reaction conditions are generally required for the [2+2] cycloaddition of two electron-rich olefins. An alternative approach involves the use of transition metal catalysts, such as rhodium, titanium, and nickel, which can coordinate with olefin or alkyne substrates, facilitating the formation of reactive intermediates that undergo cycloaddition (*e.g.*, **Scheme I-7**). The metal centre often stabilises the transition state, lowering the activation energy required for the reaction and allowing it to proceed under milder conditions.[28]

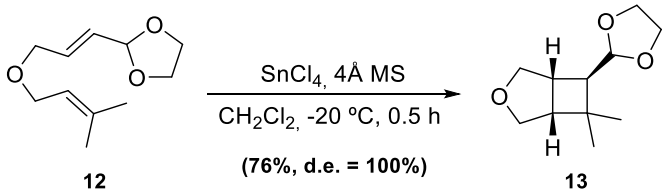

Scheme I-7. $SnCl_4$-catalysed intramolecular [2+2] cycloaddition.[29]

Photoredox systems are also employed, where the oxidation of one of the substrates generates a radical cation. This reactive species adds to a second unsaturated molecule, forming a new radical intermediate, which undergoes a second radical addition or a cyclisation step, leading to the formation of a four-membered ring under mild conditions. This method is commonly employed to dimerise unactivated olefins, for instance. Furthermore, the use of radical intermediates enables unique regio- and stereochemical outcomes that are difficult to achieve with traditional cycloaddition methods. For example, the ability to control the site of radical generation and propagation can lead to highly selective formation of specific cyclobutane isomers.[30] Unfortunately, this method requires an aryl enone or an electron-rich styrene for productive cyclisation and strictly provides head-to-head adducts (*e.g.*, **Scheme I-8**).

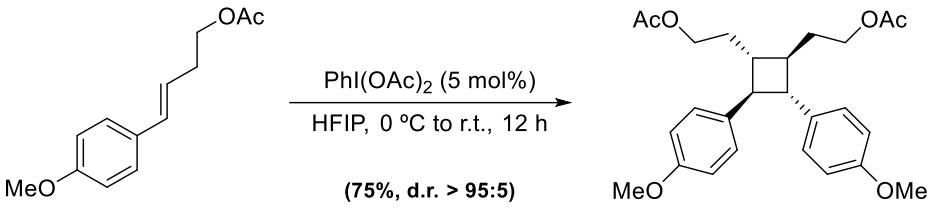

Scheme I-8. Example of an oxidative radical dimerisation of styrene **14** to form tetrasubstituted cyclobutane structure **15**.[31]

1.2. Intramolecular Cyclisation

Intramolecular direct ring-closure strategies provide an efficient method for constructing the strained cyclobutane frameworks, despite the fact that these processes are entropically unfavourable. The intramolecular cyclisation, also referred as 1,4-cyclisation, of acyclic precursors can take place through non-photochemical or photochemical methods, that can proceed through ionic or radical mechanisms. When it comes to the stereochemical outcome of the reactions, those can be performed in a highly stereospecific manner, as acyclic precursors with stereogenic centres at C-2 and C-3 retain their stereochemistry during cyclisation.[28] Also, a better regioselectivity is displayed for this reaction because it avoids the formation of head-to-head and head-to-tail products, unlike in intermolecular cycloadditions of unsymmetrical alkenes.

One possible cyclisation mechanism is the **intramolecular S_N2 reaction**, which involves a carbanion as an intermediate. A clear instance in the literature for this type of mechanism is the intramolecular cyclisation of epoxynitriles (*e.g.*, **Scheme I-9**). Usually, these reactions are facilitated by acid or base catalysis, which activates the electrophilic centre. The efficiency of this approach is further enhanced by the fact that the nucleophilic attack is often faster in an intramolecular setting compared to intermolecular reactions, due to the proximity of the reactive sites.

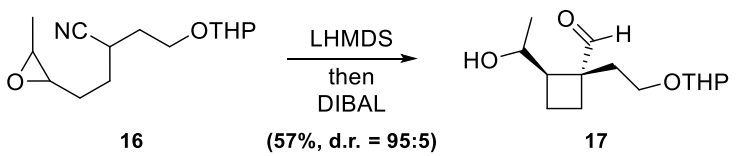

Scheme I-9. Intramolecular epoxynitrile cyclisation to form the cyclobutane core *en route* to the synthesis of (±)-grandisol.[32]

Another interesting method to easily access cyclobutanes, that also involves the formation of a carbanion (or an enolate), is the **intramolecular Michael-aldol** reaction (*e.g.*, **Scheme I-10**). The reaction combines two steps: the Michael addition, where an enolate or a carbanion attack the α,β-unsaturated carbonyl compound forming a new C-C bond, and the aldol reaction, in which the resulting enolate can react with a nearby carbonyl group within the same molecule, forming the second C-C bond.[33]

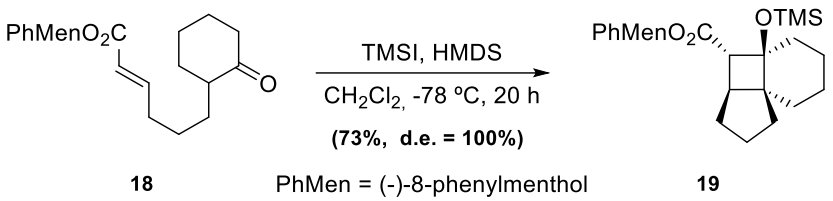

Scheme I-10. Chiral auxiliary-induced diastereoselective Michael-aldol reaction of α-substituted cyclohexanone **18**.[34]

Radical cyclisation is a method that has not been much used, probably because of the reversibility of the reaction to the corresponding acyclic form due to the ring strain of the generated cyclobutane. This approach involves the generation of an alkenyl radical, which then adds to a π-system within the same molecule to form a new C-C bond (*e.g.*, **Scheme I-11**). To enhance the stability of the radical intermediate, electron-withdrawing groups such as sulfones or esters can be introduced. Also, *gem*-substituents could favour the reaction. The advantage of radical cyclisation lies in its tolerance to a wide range of functional groups, although its application to form enantiopure cyclobutanes is rare.[28]

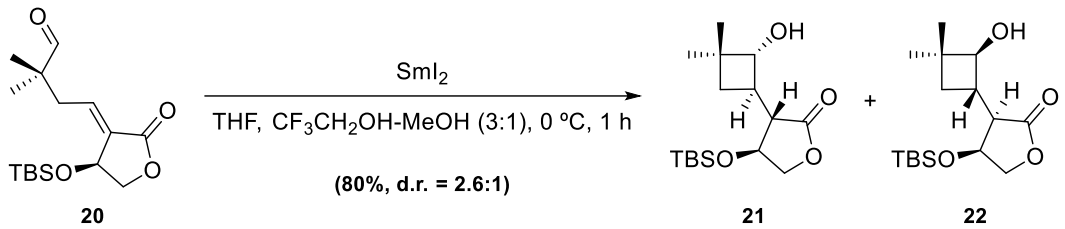

Scheme I-11. The chiral radical precursor **20** reacts with samarium diiode (SmI_2) to cyclise by a 4-*exo*-trig mechanism.[35]

Lastly, an example of an intramolecular photocyclisation is the **Norrish-Yang** reaction, in which a γ-substituted ketone is employed. The irradiation of the ketone by UV light generates a 1,4-biradical intermediate, to finally obtain a cyclobutanol ring structure (*e.g.*, **Scheme I-12**). However, due the planar conformation of the intermediate, the γ-carbon loses the stereochemistry information of the starting compound. Also, depending on the nature of the substituents, this reaction can undergo fragmentation (Norrish type II reaction).[36]

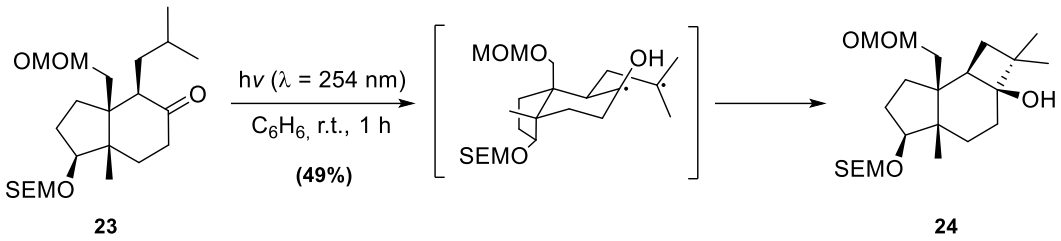

Scheme I-12. Norrish-Yang cyclisation of cyclohexanone **23** to cyclobutane **24** in the synthesis of (-)-punctaporonin A.[37]

1.3. Ring Expansion

The release of the strain generated in the expansion of cyclopropanes makes this methodology a possible route to be examined for the obtention of cyclobutane scaffolds. However, such strategy is not as common as expected, as it usually gives rise to a number of quite unstable products under the strain-releasing conditions and it is not very useful as a method for cyclobutane synthesis. Otherwise, the presence of a donor group at C-1 of the cyclopropane ring increases the selectivity for cyclobutane formation.[28] One of the most common starting materials are hydroxycyclopropyl carbinols, that can be ring-expanded by treatment with Brönsted or Lewis acids. However, using these compounds as starting material would result in cyclobutanones as a product (*e.g.*, **Scheme I-13**).

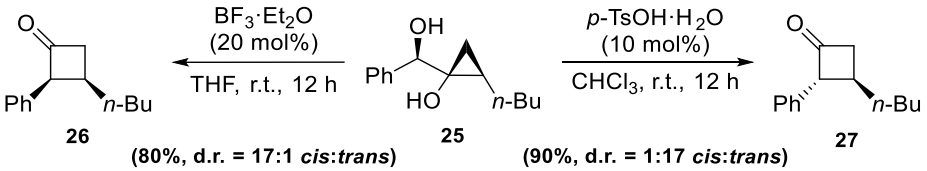

Scheme I-13. Ring expansion of α-hydroxycyclopropyl carbinol **25** *via* pinacol-type rearrangements.[14]

1.4. Ring Contraction

Although such reactions would appear unfavourable because of the increase in the ring strains, ring contraction has demonstrated to be quite useful in the obtention of four-membered cyclic scaffolds. Through the appropriate reactive intermediates, these reactions can be triggered towards the desired product, affording highly substituted cyclic compounds possessing an array of stereocentres and/or sterically hindered quaternary carbon centres. Some of the most common mechanisms involve **Wolff rearrangement** of α-diazocyclopentanones, **Favorskii rearrangement** of α-halocyclopentanones, and **Zr-catalysed ring contractions** (*e.g.*, **Scheme I-14**). However, despite the effort that has been done, as the many different methodologies developed demonstrate, there is a limitation in the obtention of the desired products due to the generation of by-products that lead to low-yielding reactions.[38]

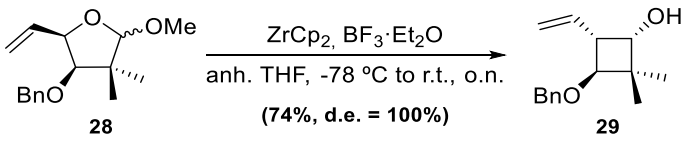

Scheme I-14. Zr-catalysed ring contraction of 4-vinylfuranoside derivative **28**.[39]

1.5. Cyclobutane-containing (CBC) Molecules and Applications

The chiral pool of natural products represents a source from which enantiomerically pure cyclobutanes can be obtained. These substrates include materials which have the cyclobutane ring incorporated in an asymmetric carbon framework or others from which cyclobutanes can be readily prepared by any of the methods described above. The former include dehydro sugars, steroids, and terpenes. **(-)-Verbenone** (**30**) (**Figure I-3**), a terpene, is used as starting material of cyclobutane-containing structure in **Chapter I. Hybrid γ,γ-Peptidomimetics as Mitochondria-Penetrating Peptides**. As will be further explained in subsequent sections of the thesis, the easy oxidative cleavage of the C-C double bond in **(-)-verbenone** (**30**) and **α-pinene** (**31**), leads to *gem*-dimethyl-substituted cyclobutanes functionalised in positions 1 and 3.

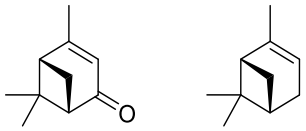

Figure I-3. (-)-Verbenone (**30**), as well as **α-pinene** (**31**), represent inexpensive chiral starting materials for the preparation of highly substituted cyclobutanes through oxidative cleavage.[40]

Alongside of its importance in organic synthesis, the cyclobutane unit is found as a basic structural element in a diverse array of naturally occurring compounds. Known since 1890s with the isolation of α- and β-pinenes, a large number of cyclobutane derivatives has been found and isolated in many life forms. Besides, some of them showed intrinsic biological activity, contributing to the development of promising therapeutic agents[41] or providing new insights for the study of enzyme mechanisms.[42] **Figure I-4** shows some examples of natural and biologically active compounds that contain the cyclobutane moiety, such as the antibiotic **X-1092**, produced by a *Streptomyces* species,[43] **β-caryophyllene oxide**, which has demonstrated analgesic and anticancer activities, inhibiting the growth and proliferation in several cancer cell lines,[44] and **cyclobut-A**, which has a potent anti-HIV activity *in vitro*.[45]

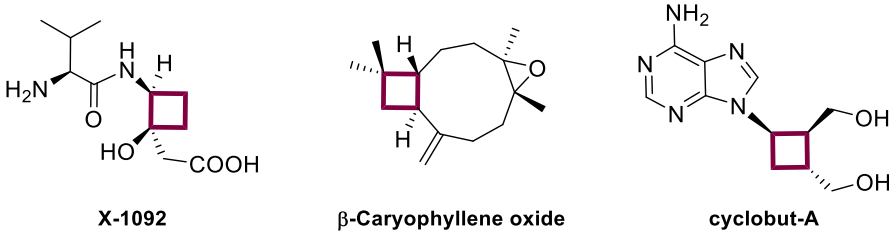

Figure I-4. Examples of naturally occurring CBC molecules with bioactive effects.

Isolated compounds have shown strong antibacterial, antimicrobial, antinociceptive, and other activities. These may be attributed to the structural rigidity of the molecules, which, in turn, allows for a well-defined spatial arrangement of their substituents, a feature that is often favourable in drug design.[46,47] As an example, ligands of certain biological receptors can benefit from the conformational restrictions present in the cyclobutane moiety, as the introduction of a 1,3-disubstituted cyclobutane as a linker limits the number of possible conformations. This could

reduce the entropic penalty, upon binding with the receptor, when compared to more flexible ligands.[48] Additionally, the substitution of planar aromatic rings by saturated cyclobutane rings is associated with stronger binding affinities, as saturated molecules complement the spatial architecture of the targeted proteins. This increase saturation also leads to enhanced water solubility and lower melting points, both of which are crucial for the successful development of a lead compound.[49] Furthermore, the cyclobutane ring can be employed to position key pharmacophore groups,[50–52] occupy hydrophobic pockets within target enzymes,[53–55] prevent *cis/trans* isomerisation,[56,57] improve metabolic stability,[58] or reduce overall planarity.[59]

The stereochemistry of the cyclobutane ring also plays an important role, as in many cases, the biological activity of two enantiomers differs substantially, and on occasions, the inactive enantiomer can interfere with or significantly reduce the activity of the active compound.[60]

As many applications have been found for CBC molecules, this section will summarise the demonstrated potential applications of the precedents in our research group, focused on 1,2- and 1,3-disubstituted cyclobutanes.

1.5.1. Precedents in Our Research Group

Over the last two decades, a part of our research group has focused on the development of several enantioselective synthetic methods with the objective of obtaining molecules that contain a disubstituted cyclobutane moiety as conformational restriction element, exploring their potential in a wide range of applications.

With these synthetic methodologies, **1,2- or β-disubstituted** (**Scheme I-15**), and **1,3- or γ-disubstituted** (**Scheme I-16**) cyclobutanes have been prepared. The β-substituted cyclobutane compounds can be obtained through a photochemical reaction between **ethylene** (**4**) and **maleic anhydride** (**32**), yielding the corresponding cycloadduct, which upon opening with an alcohol and acidic conditions, generates an achiral product. This *meso* cyclobutane derivative can be desymmetrised using a chemoenzymatic approach. Then, selective modification of the functional groups, along with the performance of epimerisation steps, enabled the synthesis of the different isomers in an enantiopure manner.[61]

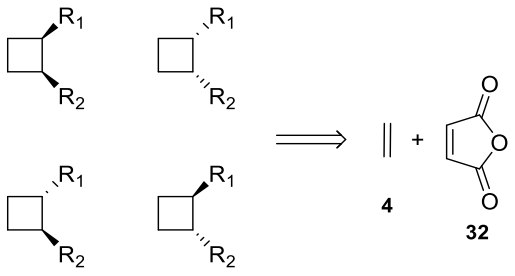

Scheme I-15. Retrosynthetic scheme of the preparation of different isomers of 1,2-disubstituted cyclobutane derivatives and their corresponding synthetic precursors.

The γ-substituted cyclobutane-based compounds can be derived from either **(-)-verbenone** (**30**) or **(-)-α-pinene** (**31**) (**Scheme I-16**), both of which are commercially available at a reasonable cost in

their enantiopure form. Oxidative cleavage of the C-C double bond of these terpenes, followed by selective functional group modifications, enables the synthesis of the targeted compounds.[62] Unlike β-disubstituted cyclobutanes, only *cis*-1,3-disubstituted cyclobutane-based compounds can be readily obtained from the chiral pool, due to the inherent stereochemistry of the starting materials.

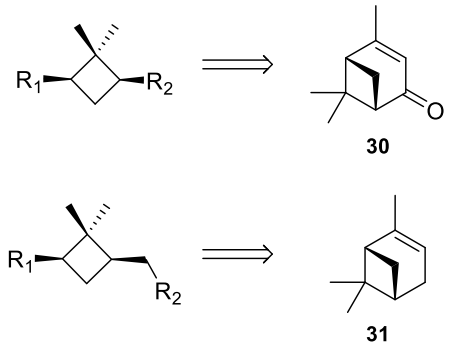

Scheme I-16. Retrosynthetic scheme of the synthesis of the different 1,3-substituted cyclobutane-based isomers and their corresponding synthetic precursors.

One of the main topics of investigation has been the synthesis of optically active cyclobutane amino acids (CBAAs) and their integration into peptides for diverse applications. The rigidity of the 1,2-substituted cyclobutane scaffold, along with its relative and absolute stereochemistry, has proven significant in stabilising well-defined secondary structures. Thus, this rigidity plays a crucial role in the properties of the derivatives that incorporate these scaffolds.[63–65]

Typically, when a 1,2-CBAA is integrated in the peptide structure, two types of hydrogen-bonded arrangements can be formed: an intra-residue 6-membered ring and inter-residue 8-membered ring (**Figure I-5**). On the other hand, for 1,3-CBAA-incorporating peptides, an intra-residue 7-membered hydrogen-bonded ring has been observed, which can also affect the conformation adopted by the peptides and, consequently, their properties.[66]

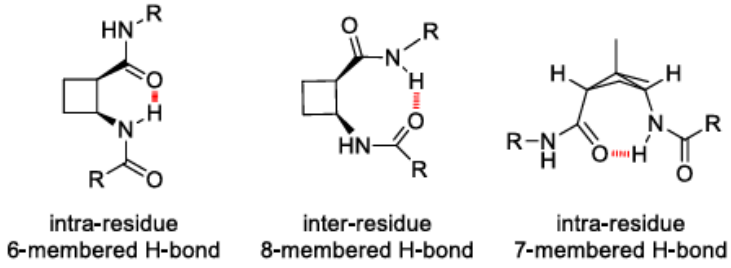

Figure I-5. Intra- and inter-residue hydrogen bonds in peptides containing *cis*-β-CBAA and *cis*-γ-CBAA.

Apart from the applications of these cyclobutane moieties in the synthesis of peptides, these structures have been also introduced in compounds in which their inherent rigidity can be beneficial for the improvement of their properties in the different fields of study. In **Figure I-6** various examples of β-disubstituted cyclobutane-based compounds are shown, such as compounds **33** or **34**, which are examples of a series of compounds that were first evaluated as ligands for metallocarboxypeptidases (MCPs).[67] These compounds demonstrated moderate selectivity in inhibiting mammalian MCPs and provided a promising alternative for developing new inhibitors

targeting disease-related MCPs. Interestingly, *trans*-cyclobutane-containing dipeptide **35**, with a similar structure to compound **34**, had a good performance as an organogelator. These opened the door to extensive studies in this field.[68–72] Additionally, based on catalysis research by Takemoto and colleagues,[73] cyclobutane-based thiourea **36** and other related derivatives were explored as organocatalysts in the Michael reaction, achieving significant yields with moderated enantioselectivity.[74] Furthermore, this cyclobutane motif was employed in novel ligand scaffolds, represented by structures **37** and **38**, to prepare stable and inert lanthanide complexes with applications as magnetic resonance imaging (MRI) contrast agents. The related Gd^{3+} and Mn^{2+} complexes provided good thermodynamic stability and relaxivity, showing compatible characteristics for clinical applications.[75,76] Lastly, the cyclobutane framework is also present in the field of materials science, including applications as supported catalysts on silica with cyclobutane diamines **39** and **40**,[77] as surfactants like compounds **41** and **42**,[78–82] and also as conductive materials such as compound **43**.[83] Furthermore, in **Chapter II. Novel Bifunctional Ligands for PET Imaging with ^{64}Cu and ^{68}Ga Radioisotopes**, compounds related to the 1,2-disubstituted cyclobutane structures will be synthesised with the aim of being used as ligands for the complexation of ^{64}Cu and ^{68}Ga.

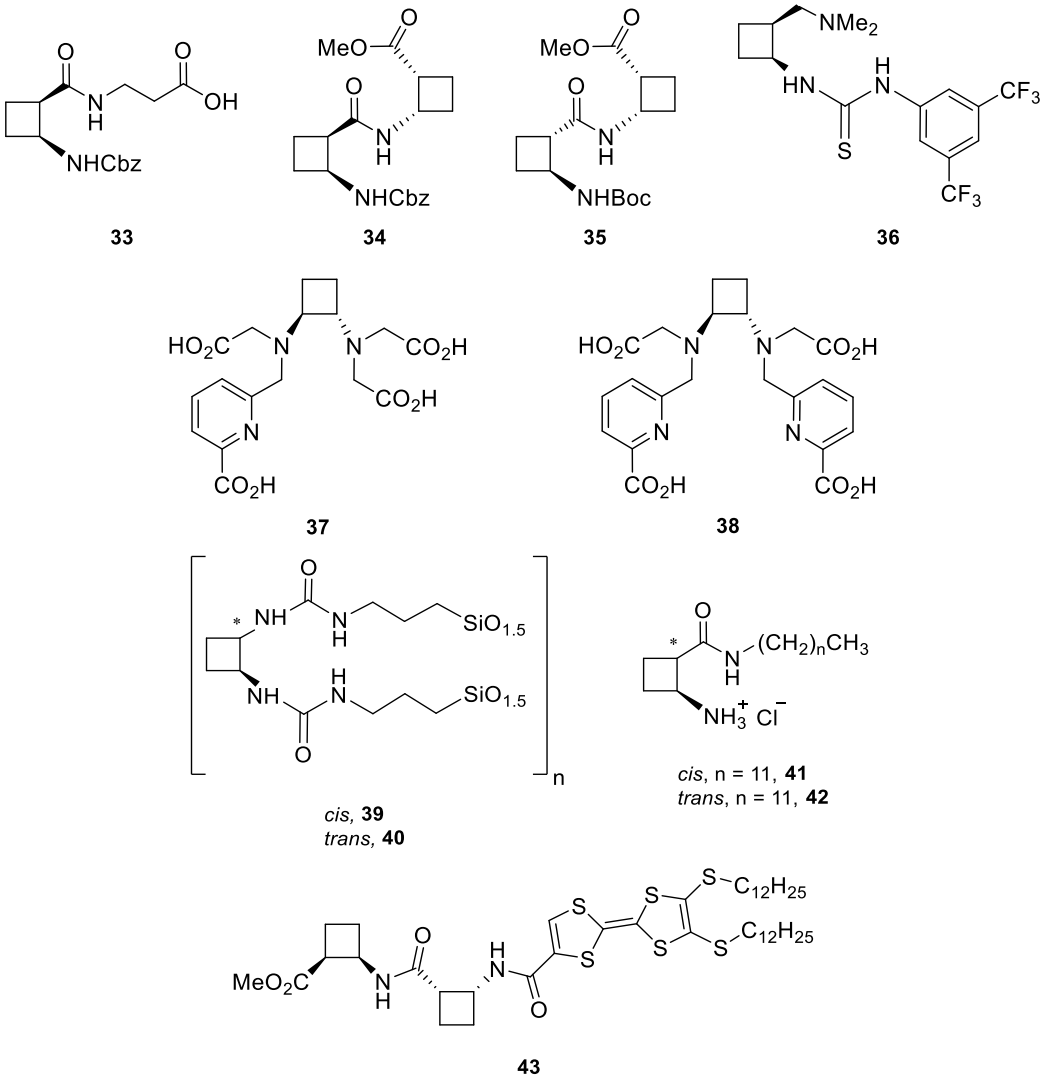

Figure I-6. β-Disubstituted CBC compounds with applications in various fields.[67-83]

1,3-Disubstituted cyclobutanes are structural motifs that are also found in a number of compounds, as depicted in **Figure I-7**, and with a wide range of applications. As an example, cyclobutane-based pyrrolidine **44** was tested as stabiliser of ruthenium nanoparticles, exhibiting excellent catalytic properties in the hydrogenation of arenes and nitrobenzenes.[84] Meanwhile, amino acid **45** was studied due to its properties as zwitterionic surfactant.[85] Organocatalysis, in particular for asymmetric aldol additions, has been also another field where these motifs have been used. Tripeptide **46**, consisting of a central γ-CBAA flanked by two D-proline residues, provided good enantioselectivity in aldol reactions, being a promising peptide catalyst.[66] As a last example, C_3-symmetric peptide dendrimer **47** offered potential for elongation and functionalisation, making it suitable for future applications in chiral materials.[86]

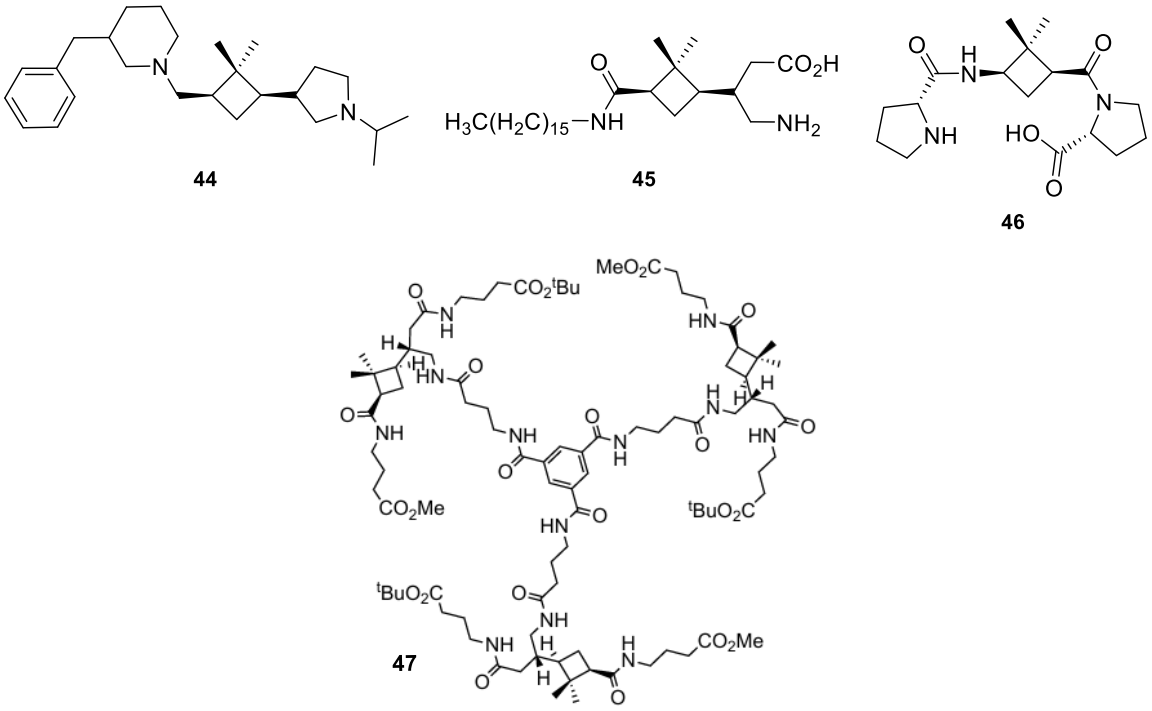

Figure I-7. γ-Disubstituted CBC compounds with applications in a diverse number of fields.[66,84-86]

In addition, the use of the γ-disubstituted cyclobutane structure in peptide synthesis will be extensively introduced in **Chapter I. Hybrid γ,γ-Peptidomimetics as Mitochondria-Penetrating Peptides**, **section 1.1.6.**, where this structure is employed in the synthesis of oligomers with cell-penetrating properties.

Chapter I

Hybrid γ,γ-Peptidomimetics as Mitochondria-Penetrating Peptides

Mitochondria, known as the powerhouse of the cell, have gained increased attention for their crucial role in cell biology, as dysfunctions in this organelle have been linked to diseases such as diabetes, cancer, and cardiovascular disorders. This has led to the development of new therapeutic treatments by targeting directly this organelle. Peptidomimetics, which mimic natural peptide activity with enhanced stability and bioavailability, have emerged as promising materials in biomedicine.

In this chapter, hybrid γ,γ-peptidomimetics, composed of alternating (1*S*,3*R*)-3-amino-2,2-dimethylcyclobutane-1-carboxylic acid and N^{α}-functionalised *cis*- or *trans*-γ-amino-L-proline residues, are synthesised. In addition, they are coupled to carboxyfluorescein and 5(6)-carboxy-SNARF-1 probes to test their properties as mitochondria-penetrating peptides and evaluate their capacity to target the mitochondria. Moreover, their potential applications in the monitoring of the mitochondrial pH and tracking mitochondria dynamics have been explored.

1. Introduction

The cell is the basic unit of life present in every living organism. It carries out all the metabolic and biochemical processes that are essential for the organism to survive. The cell has a complex structure that is organised into various components. The **cell membrane** surrounds the cell, separating the interior from its external environment. It is composed by lipids, proteins, and carbohydrates. Phospholipids, which have hydrophobic tails and hydrophilic heads, are the main components of the lipidic bilayer of the membrane. Hydrophobic tails are headed to the interior of the membrane, while the hydrophilic heads face the external environment and the cytoplasm. About the membrane proteins, these play a main role in some cell functions, such as transporting substances in and out of the cell, cell signalling, or cell adhesion (**Figure I-8**).[87]

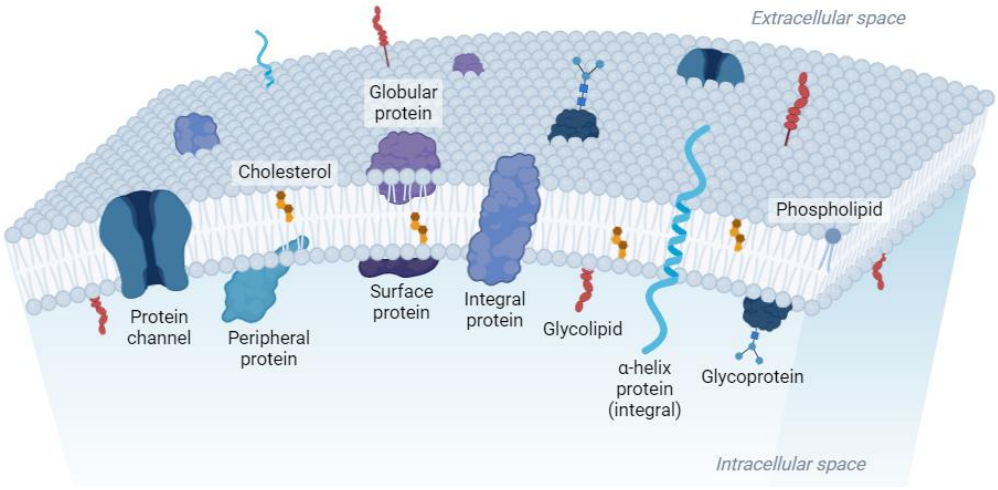

Figure I-8. Structural representation of a cell membrane. Image created with Biorender.com

This composition of the membrane makes it a selective permeable barrier, which means that it allows some substances to pass through while preventing others from entering or leaving the cell. By controlling the movement of substances, it regulates the biological processes and maintains the internal environment of the cell.

The cell membrane permeability is selective for low molecular weight hydrophobic compounds, while hydrophilic and charged molecules require assistance to translocate inside the cell.[88] The membrane achieves this through various mechanisms, including passive transport, active transport, and facilitated diffusion.

The transport of compounds through the cell membrane has been a field of study of major importance in the treatment of different therapeutic targets that are located inside the cell. One of the main drawbacks of medium or large molecular weight therapeutic molecules is their low permeability through membranes. To overcome this limitation, different strategies have been developed to introduce these biologically active molecules, such as the use of microinjection,[89] electroporation[90] or liposome- and viral-based vectors.[91] However, these methods have some disadvantages, such as low efficiency, high toxicity, deficient bioavailability or poor specificity.

In 1988, the trans-activator of transcription (Tat) protein, derived from the human immunodeficiency virus (HIV), was discovered, showing the ability to translocate the cell membrane.[92,93] Since then, short protein sequences capable of crossing the membrane, named cell-penetrating peptides (**CPPs**), have been synthesised and studied as an alternative strategy to improve the internalisation of different molecules. Their great versatility allows them to carry a wide range of compounds, covalently or non-covalently attached as a cargo, such as other peptides, antibodies, siRNAs, drugs, fluorescent compounds and quantum dots (**Figure I-9**).[94]

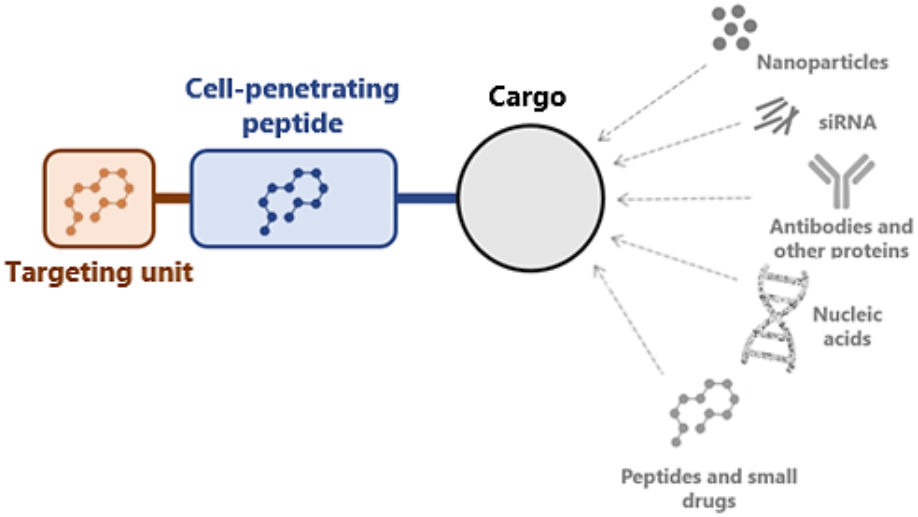

Figure I-9. CPPs can be attached to different cargoes to be carried inside the cells. In addition, the target tissue specificity can be increased by employing a targeting unit.

1.1. Peptides and Peptidomimetics

Peptides represent a valuable tool in biomedicine, as they can be used to develop biocompatible drugs or selective carriers.[95,96] Their straightforward and modular synthesis makes it easy to modify their sequence and attach them to other bioactive compounds,[97,98] with some peptides that exhibit membrane transport properties being very useful for delivering probes and cargoes inside the cell, which are described as CPPs. Furthermore, depending on their sequence and physicochemical properties, certain CPPs display affinity for specific cell types or even intracellular organelles, providing even more target specificity.[98,99]

Despite these advantages, peptides possess several limitations that may hinder their widespread use. For instance, their half-lives in biological environments are short (from minutes to hours) as they are susceptible to enzymatic hydrolysis.[100] Additionally, because of their backbone's flexibility, functional group orientation can be shifted, causing unintended interactions. To address these limitations, in the last decades there has been growing interest in **peptidomimetics** – peptide analogues with structural modifications designed to enhance stability, bioavailability or selectivity.[101–103] For example, azapeptides replace the α-carbon with a nitrogen, whereas peptoids have a peptide backbone but with side chains linked to the amide nitrogen instead of the α-carbon.[95] Furthermore, backbone alterations, such as the addition of D-amino acids, triazole rings, use of β- or γ-amino acids, or even the complete replacement of the peptide backbone with an alternative

chemical scaffold, have been explored (**Figure I-10**). Peptidomimetics are emerging as valuable tools in biomedical research as they offer significant advantages due to their ability to efficiently target intracellular organelles and their enhanced stability, which are critical goals for synthetic carriers.

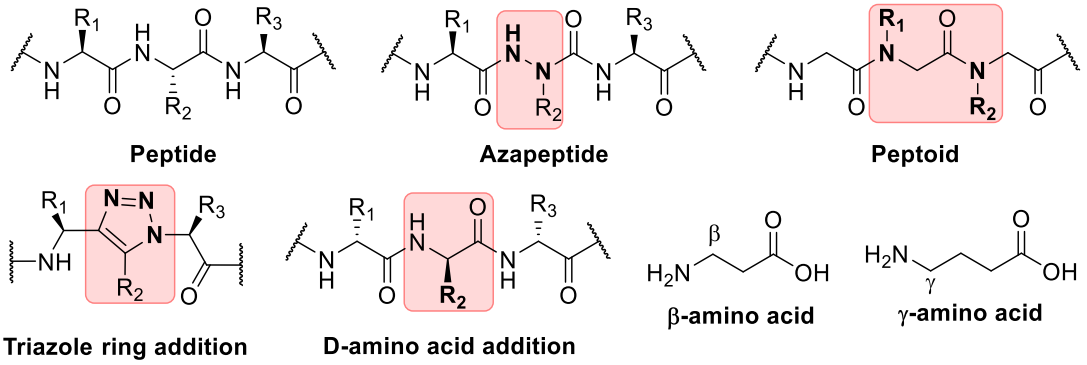

Figure I-10. Comparison between a conventional peptide structure and common modifications introduced into its backbone.

1.1.1. Cell-Penetrating Peptides (CPPs)

Cell-penetrating peptides, also called protein transductions domains, have a length of 5 to 30 amino acids, in many cases they are positively charged, and are capable of penetrating into the intracellular space. Appealing characteristics of CPPs include their high biocompatibility and the potential to fine-tune their stability and solubility in biological environments.[104] These properties make them suitable as intracellular delivery vectors for cargoes that can be covalently or non-covalently attached to them, and even target specific organelles of the cells, being potential drug delivery systems.[105,106]

The first described CPPs were reported in two articles from 1988 by Green and Loewenstein[92] and by Frankel and Pabo.[93] These studies, derived from their work with the **Tat** protein, demonstrated that Tat protein was taken up by cells *in vitro* and translocated into the nucleus. The following research with truncated versions of Tat determined that just a part of the sequence retained the penetrating ability.[107] Since then, many other CPPs have been found in biological systems such as the fusion protein **VP22** from Herpes simplex virus type 1 (HSV-1),[108] or a 16-amino acid sequence isolated from *Drosophila Antennapedia* homeodomain named **penetratin** (pAntp).[109] The isolation of sequences in the cases of the Tat and pAntp (**Figure I-11**) were especially relevant, as they highlighted the importance of the basic residues in the interaction with anionic moieties of the cell membrane for the cell penetration ability of those.

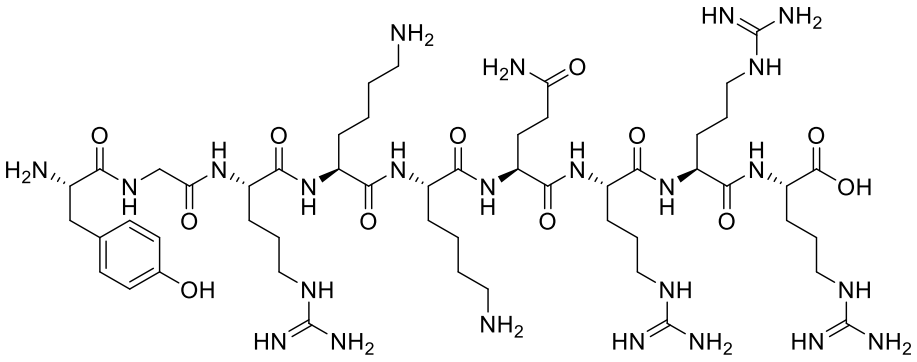

Tat protein sequence (Tat_{48-60})

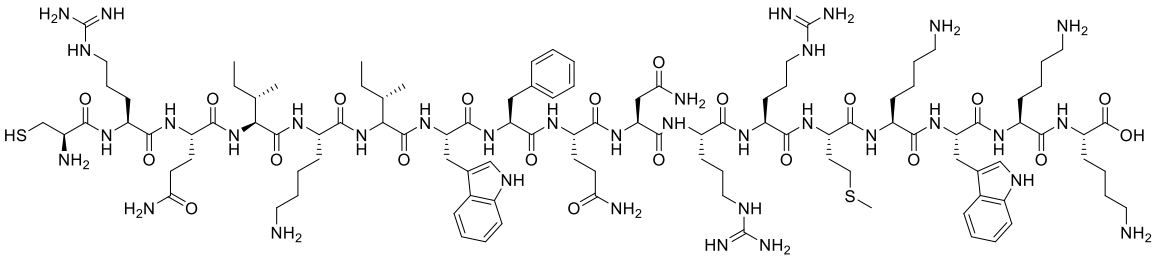

Penetratin (pAntp)

Figure I-11. Sequences of first relevant CPPs, Tat_{48-60} and pAntp.

Further research in the transport process of CPPs demonstrated that cationic residues were key for their uptake. This effect was particularly pronounced in arginine-rich peptides, attributed to the guanidinium moiety found in this residue (**Figure I-12**).[110,111]

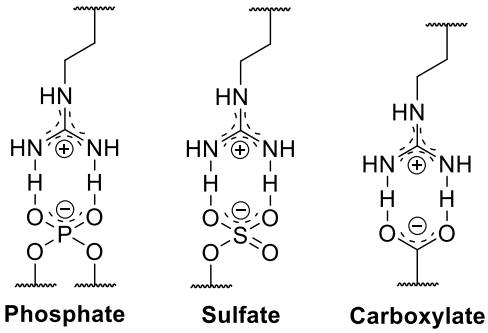

Phosphate Sulfate Carboxylate

Figure I-12. Guanidinium moieties in arginine-rich peptides can interact with phosphate, sulfate and carboxylate groups in the bilayer membrane through bivalent hydrogen bond, facilitating their penetration into the cell.

CPPs emerged as a new biological tool, many of which have been developed from synthetic sources such as **Transportan**, developed by Prof. Langel in 1998,[112] model amphipathic peptides (**MAP**),[113] or **TP2**[114] (**Table I-1**), and by 2016 there were more than 1850 CPPs in the catalogue within CPPsite 2.0 database.[115]

There are several ways to classify CPPs based on their origin, binding to lipids, interaction with the cargo, sequence,… but the most employed one is by their physicochemical properties,[116,117] in which we can find three main groups:

- **Cationic peptides:** They contain residues that, at physiological pH, present a net positive charge (*e.g.* arginine or lysine). As mentioned before, due to the positive charge of the guanidinium group (pKa > 12), arginine-rich peptides are the most efficient to penetrate into the cell. In addition, guanidine has the capacity to form bidentate hydrogen bonds with different moieties present in the cell surface (**Figure I-12**).
- **Amphipathic peptides:** Two regions, one hydrophobic and one hydrophilic, can be found in these peptides. Both naturally occurring and synthetic CPPs exploit these differences in polarity to penetrate the cell, which makes them more efficient and target-specific. They are differentiated in three subclasses, **primary** and **secondary amphipathic CPPs,** and **proline-rich sequences**. The primary ones have the domains differentiated in their primary sequence, while secondary ones have a well-defined secondary structure such as α-helixes, where the hydrophobic and hydrophilic residues are in opposite sides, or β-sheets. Finally, proline-rich peptides can also adopt a secondary structure, which is responsible for their amphiphilicity. To acquire this structure, only 50% of proline residues are required in the peptide sequence, and one of the best-known proteins in this subclass is γ-zein, which is the storage protein of maize.[118] In its enriched domain in proline, it includes the sequences $(VXLPPP)_8$, which is responsible for its penetrating properties into the endoplasmic reticulus.
- **Hydrophobic peptides:** Their structure is primarily formed by apolar and anionic amino acids, which exhibit high affinity for the hydrophobic regions of cellular membranes. This type of CPPs have been less studied, but it is thought that an energy-independent mechanism is needed for them to penetrate into the cell.[119]

Table I-1. CPPs commonly used for delivery applications.

CPP	Origin	Classification
Tat_{48-60}	HIV protein	Cationic, random coil/PPII helix
$pAntp_{43-58}$	*Drosophila melanogaster*	Cationic, α-helix
MAP	Synthetic	Amphipathic, α-helix
Transportan	Chimeric	Amphipathic, α-helix
Pep-1	Chimeric	Amphipathic, α-helix
pVEC	Vascular endothelial cadherin	Amphipathic, β-sheet
Polyarginines	Synthetic	Cationic, α-helix

Although cationic CPPs display the best cellular uptake among the three different groups, their non-specific interactions with cell membranes result in high toxicity, especially when the number of arginine residues exceeds 8 to 10. They also undergo rapid clearance from the bloodstream, further limiting their clinical use.[120–122] Furthermore, the ability to escape from the endosomes is another crucial characteristic for their effectiveness.[123,124] To address these issues, structural modifications are usually introduced by using **hydrophobic amino acids**, that show a different penetration

mechanism compared to the cationic ones, or by introducing **proline residues**, which promote the adoption of more stable secondary structures in solution due to the conformational constraints.

1.1.2. Proline-rich CPPs

Proline-rich peptides have become more common, giving rise to different CPP families that show structurally modified proline structures. The pyrrolidine ring, present in the structure of the amino acid, imparts rigidity to the peptide backbone, producing steric hindrance that results in more stable secondary structures, which are important in the penetration properties of the peptide. Despite the hydrophobic character of the proline structure, it has the advantage of being soluble in water and other organic solvents. Moreover, proline is the only natural amino acid with a secondary amino group, meaning that its conformation cannot be stabilised through hydrogen bonds due to the absence of hydrogen atoms in the amide group. Instead, interactions between adjacent amide bonds, such as n → π* interactions, contribute to the stabilisation of the secondary structure. Finally, proline is the only amino acid capable of readily isomerising between *cis* (ω = 0º) and *trans* (ω = 180º) conformers (**Figure I-13**, **left**).[125]

Proline-rich CPPs can adopt two secondary structures named polyproline I (PPI), a right-handed helix with all *cis* peptide bonds and present when aliphatic alcohols are used, and polyproline II (PPII), a left-handed helix with all *trans* peptide bonds formed in aqueous media (**Figure I-13**, **right**). Among proline-rich structures, PPII is the most abundant in proteins with α-helices and β-sheets, while no biological relevance has been found for PPI yet. However, due to proline's ability to rapidly undergo *cis*/*trans* isomerisation, both structures can be interconverted by changing the medium. Moreover, modifications in the proline structure, particularly in the γ-carbon of the pyrrolidine ring, can favour one configuration over the other.[126] Functionalisation of this γ-carbon with cationic and hydrophobic functional groups creates amphiphilic peptides that have demonstrated improved properties as CPPs.

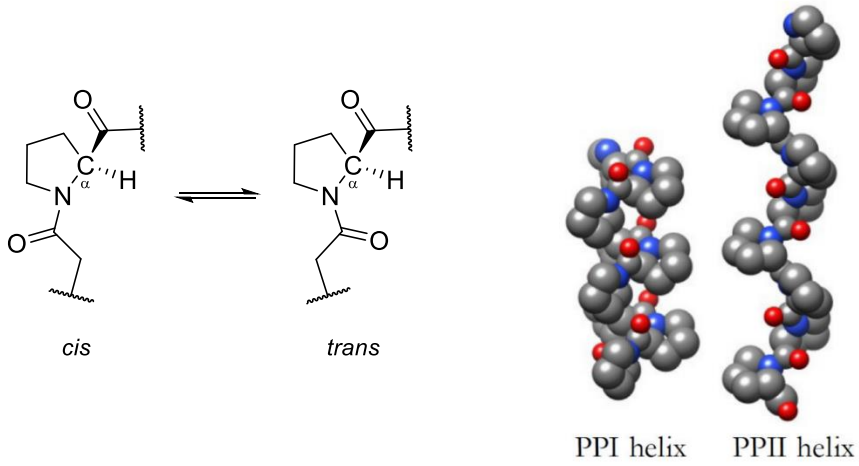

Figure I-13. Left: *Cis/trans* conformers of the proline structure. Right: Side view of PPI and PPII helices comprised of nine proline residues.[127]

From the structural modification on the proline backbone, one of the most used is the **γ-amino-L-proline** structure (**Figure I-14**), as it has demonstrated a better stability towards

degradation by proteases compared to the original proline structure.[128] Modifications on the α-amino group of the pyrrolidine ring through acylation, alkylation or guanidylation reactions are also frequently used to modulate the physicochemical properties of the peptide.[129,130]

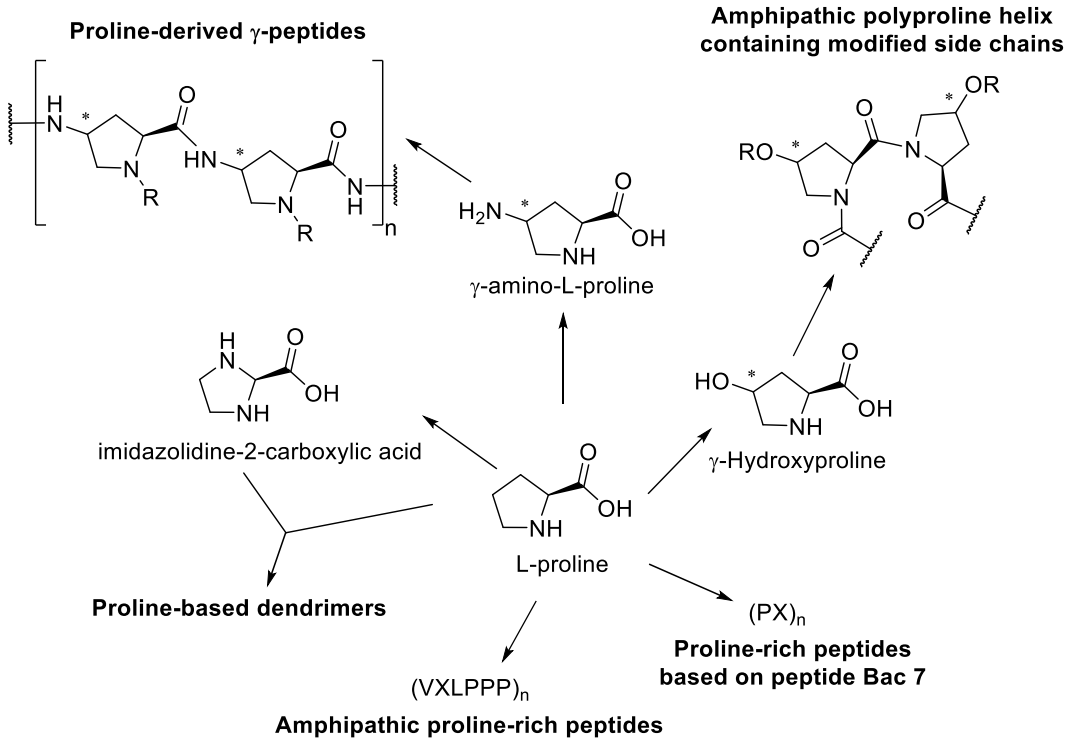

Figure I-14. Proline-derived CPPs families.

The work of Royo and co-workers, published in 2005,[128] is a compelling example of applying these modifications to enhance the properties of the peptides as CPPs. They synthesised *cis*-γ-amino-L-proline oligomers functionalised at the proline α-nitrogen with several groups that mimic the side chains of natural amino acids (**Figure I-15, 48-50**), which showed good cellular uptake into HeLa and COS-1 cells and with some advantages over the reference penetrating peptide Tat, such as less toxicity and more resistance to protease degradation. Also in 2005, Chmielewski *et al*. incorporated a guanidinium group by performing an *O*-alkylation of the γ-hydroxyproline, showing an increased uptake in MCF-7 cells when up to six guanidinium groups where introduced in the peptide, in contrast with the results of the amine-containing peptide analogue, that barely showed any increment in its penetrating properties.[131] This investigation was extended in an article by the same research group where only guanidinium-containing peptides were tested (**Figure I-15, 51 and 52**). In this case, it was demonstrated that the equilibrium between the cationic and the hydrophobic parts was key for a better performance of the CPP.[132] More recently, the group of Wennemers *et al*. used the same strategy by attaching guanidinium groups directly to the γ-carbon (**Figure I-15, 53**) to create a localised positive charge along the backbone of the PPII. This resulted in better cellular uptake into different cancer cell lines when compared to other analogues with undefined charge display.[133] Along with these examples in the literature, our research group has extended its investigation with γ-amino-L-proline based peptides, as explained in **section 1.3.** (*vide infra*).

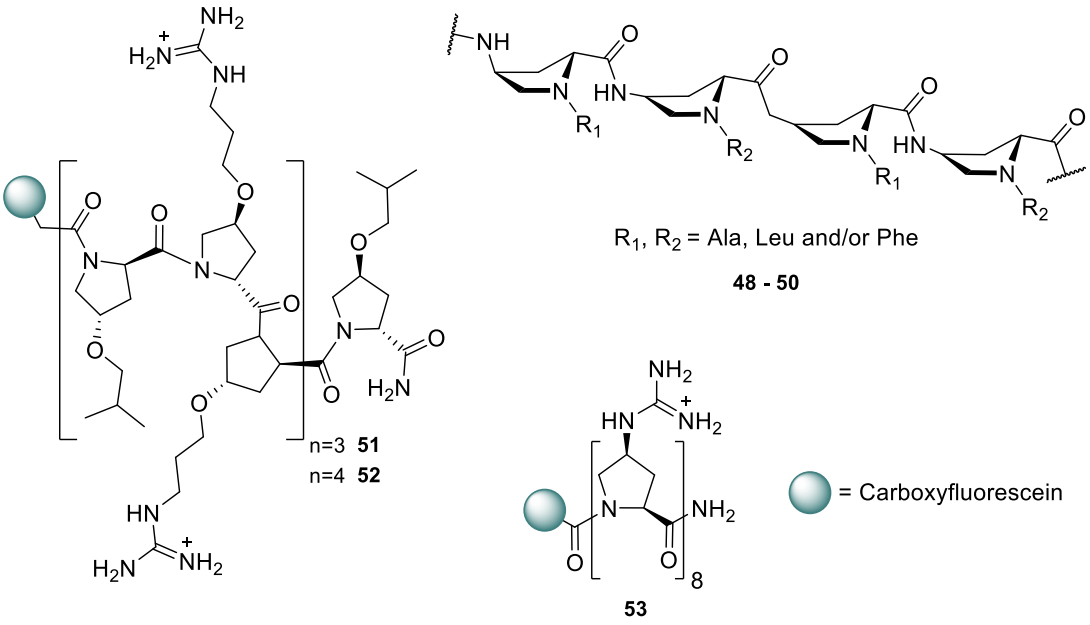

Figure I-15. Precedents of modifications in the γ-carbon of the proline residue in peptides backbone for applications as CPPs.

1.1.3. Cellular Internalisation Mechanisms of CPPs

The internalisation mechanism of CPPs is a complex process that depends on the CPP structure, concentration, cargo, experimental methodology, etc. Moreover, most CPPs penetrate into the cell through two or more uptake mechanisms depending on the specific circumstances.[121] This diversity and variability in the mechanism of internalisation makes this topic the second most common in published articles related to CPPs. However, **endocytosis** (active internalisation) and **direct translocation** (passive internalisation) through the membrane are the two most common penetration pathways into cells observed for CPPs (**Figure I-16**).[94]

Endocytosis is an energy-dependent mechanism that can occur in different ways. On one hand, the peptide can be surrounded by a clathrin coat interacting with the bilayer membrane in a mechanism that is called clathrin-mediated.[134] On the other hand, in the caveolae-mediated mechanism, a lipid-raft is formed outside the cell to engulf the peptide.[135] In both cases, the enzyme GTPase dynamin drives the invagination process of the plasma membrane. In addition, this process can be independent of these two proteins, performing the internalisation by macropynocitosis, another lipid-raft mediated and more unspecific form of endocytosis,[136] or by phagocytosis, being that last generally related to specialised cells and very uncommon for CPPs.

Unlike endocytosis, direct translocation is an energy-independent mechanism, but it is less common than endocytosis, as it requires a temporary or permanent destabilisation of the cell membrane. Different models have been proposed to explain this kind of mechanism, inverted micelles, where the negative charges of the phospholipids interact with the basic amino acids, being the most widely accepted.[137]

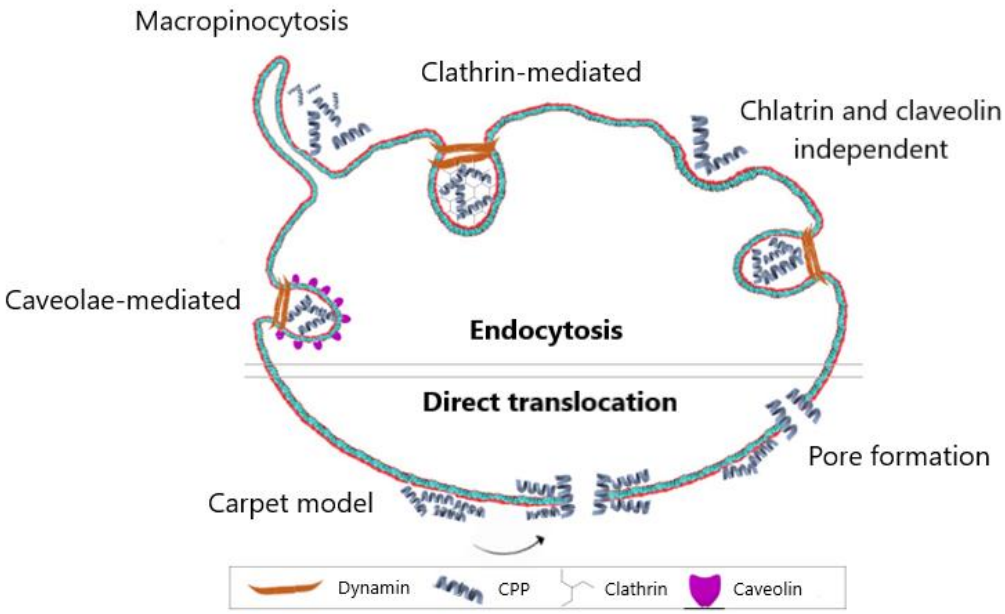

Figure I-16. Representation of the internalisation mechanisms. Adapted from *An. Quim.* **2019**, *115* (1), 9-20.

Despite the mechanism of internalisation still being a topic of discussion, there is consensus on the fact that the internalisation of CPPs is a multistep reversible process that ends up with the degradation of the CPP. For this process to happen, there must be an electrostatic interaction between the peptide and the anionic residues of the membrane, such as the proteoglycans or the phospholipids. **Proteoglycans** are a diverse group of glycoproteins constituted by a protein core bonded covalently to a type of polysaccharides named glycosaminoglycans that provide this negative charge to the cell membrane, responsible for the interaction with the positively charged residues of the peptide. This interaction causes the accumulation of the CPPs in the cell surface, which triggers a particular mechanism of internalisation depending on the characteristics of the peptide.[138] As it has been stated before, the positive charges in the CPPs are vital to have high penetration levels, but they also play a role in the endosomal escape, which is considered a crucial factor in the success rate of the CPPs function. If the mechanism of internalisation is by endocytosis, once the endosome has entered into the cell, it is important for the CPP to escape as soon as possible to avoid degradation, especially when the cargo is a drug which starts to function in the cytosol. For that purpose, it has also been observed that arginine residues interactions with the membrane of the endosome are important for an early endosomal escape.[139]

1.2. Mitochondrial Targeting

Mitochondria, the organelles also referred to as the “energy powerhouse of the cell”, have been long studied because of their essential function, not only for producing the ATP necessary for the cell metabolism, but also for being involved in other physiological processes such as autophagy, apoptosis, immunity, signal transduction, among others.[140,141] More recently, it was discover that mitochondria are not static and isolated structures. In contrast, it was observed that they have the capacity to modulate their morphology through fusion and fission events, forming a tubular network that regulates what it is known as **mitochondrial dynamics**.[142,143] This “autoregulation” of

mitochondria underpins the correct function of the cellular processes, as pathogenic mutations in the mitochondrial or nuclear DNA that affect these dynamics have been related to numerous human disorders, highlighting their important role in cell homeostasis. For this reason, mitochondria are an attractive target not only for therapeutics, such as cancer therapy,[144,145] but also for monitoring their function. This approach has been proven useful to identify neurodegenerative or pro-inflammatory events that can lead to the so-called **human mitochondrial disorders**.[141,146,147]

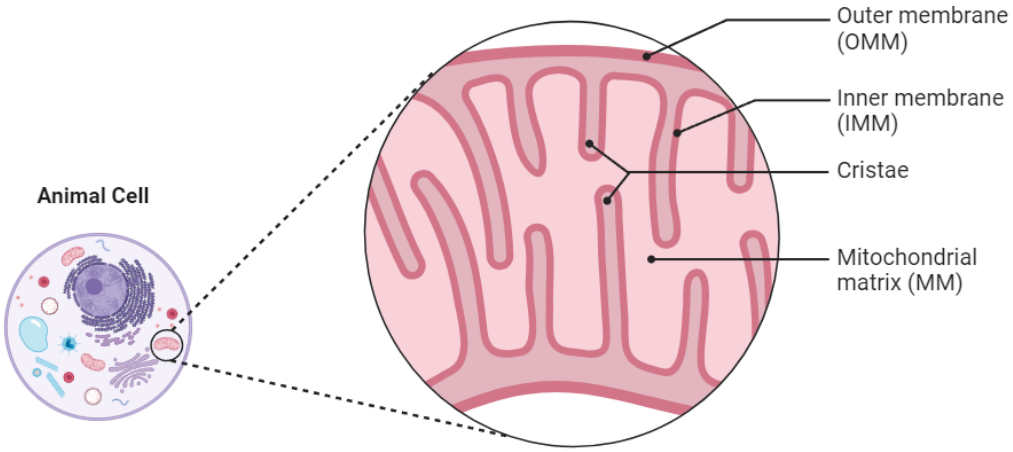

Figure I-17. Structure of a mitochondrion.

Due to their double-membrane structure (**Figure I-17**), mitochondria are organelles with low permeation, making their targeting a challenge. The structure of mitochondria includes the outer mitochondrial membrane (OMM), the inner mitochondrial membrane (IMM), and the mitochondrial matrix (MM). The OMM manages small molecule permeation, signal transduction, and material exchange with other organelles, while specific proteins like translocases facilitate protein transport. The IMM, with its folded cristae, enhances mitochondrial respiration and energy conversion and is also involved in apoptosis. While the OMM is permeable, the IMM is highly dense and saturated with phospholipids, which in combination with electron-transport chain processes that occur in it, creates an environment with a high negative membrane potential (-180 mV) and hydrophobicity. These characteristics make it difficult for macromolecules to penetrate this membrane and access the matrix. Then, the two main properties required for a substance to accumulate in a mitochondrion (also known as **mitochondriotropic**) are: To present **positive charges** ($Z > 0$) in their structure, enabling them to harness the negative membrane potential, and to have a **lipophilic character** ($\log P > -1.7$), to favour the interaction with the membranes (**Figure I-18**).[148]

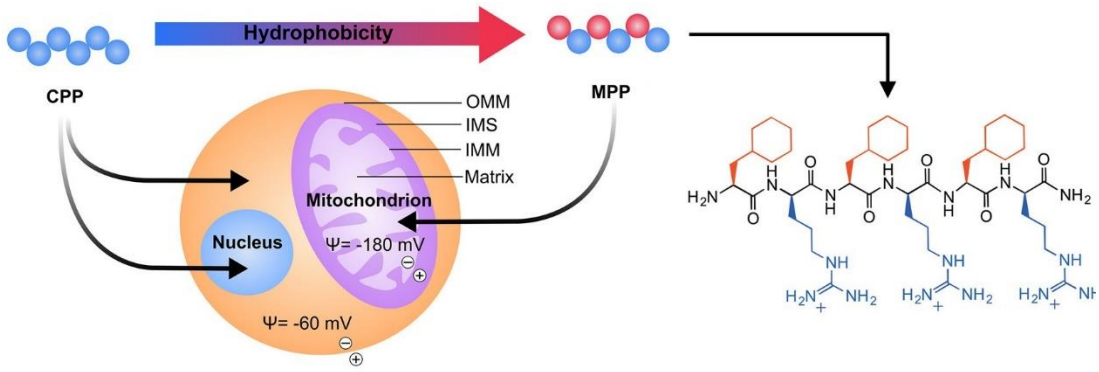

Figure I-18. Cationic charges (blue) and hydrophobicity (red) are key features for molecules to penetrate into mitochondria and to avoid them staying at the cytosol or penetrating into the nucleus. An example of MPP design based on the incorporation of hydrophobic residues is also shown. Adapted from reference 148.

As a result, different structures that accomplish these requirements have been developed to target this organelle. One of the most important classes are the **delocalised lipophilic cations (DLC)**. One example of these are the cationic mitochondria-targeting probes, like tetramethylrhodamine ethyl ester (TMRE) or Mitotracker™ (**Figure I-19**). However, these molecules cannot transport any cargo, restricting their applications to the visualisation of the organelle. To surpass this limitation, molecules like mitochondria-specific transporters, such as triphenylphosphonium (TPP) analogues[149] (**Figure I-19**, **MitoQ$_n$**) or nanocarriers,[150] have been developed. Unfortunately, their used is limited due to their toxicity and limitation to carry large polar molecules.[151]

Another method to target the mitochondria is to use **mitochondrial targeting sequences (MTS)**,[152] as they can be recognised by the mitochondrial import protein and then translocate polar molecules into the mitochondria matrix. Despite that specific recognition, this methodology limits the size of the cargo because of its dependency on the transport channels.

The first peptide sequences developed to target the mitochondria were the known as **Szeto-Schiller (SS) peptides** (**Figure I-19**, **SS-31**). These tetrapeptides were designed by alternating aromatic residues and basic amino acids, making their internalisation independent of the mitochondrial membrane potential. However, their applications are limited to their antioxidant properties, related to the delivery of the dimethyltyrosine motif.[153] In recent years, specific CPPs that target the mitochondria, called **mitochondria-penetrating peptides (MPPs)**,[154] have attracted much attention due to their good biocompatibility, modular synthesis, structural variability and excellent *in cellulo* and *in vivo* pharmacokinetic profiles, which facilitates their use as diagnostic and therapeutic agents. The internalisation of these peptides is independent of the endocytosis process, as it is driven by an electrochemical gradient (positively charged peptide and negatively charged mitochondria), which increases the chances and the speed of mitochondria targeting, avoiding multidrug resistance.[155] Moreover, the similar physicochemical properties required to penetrate mitochondria and bacteria, respectively, makes it possible to cross-target them, conferring many MPPs with antimicrobial properties, as various studies have demonstrated.[132,156–158]

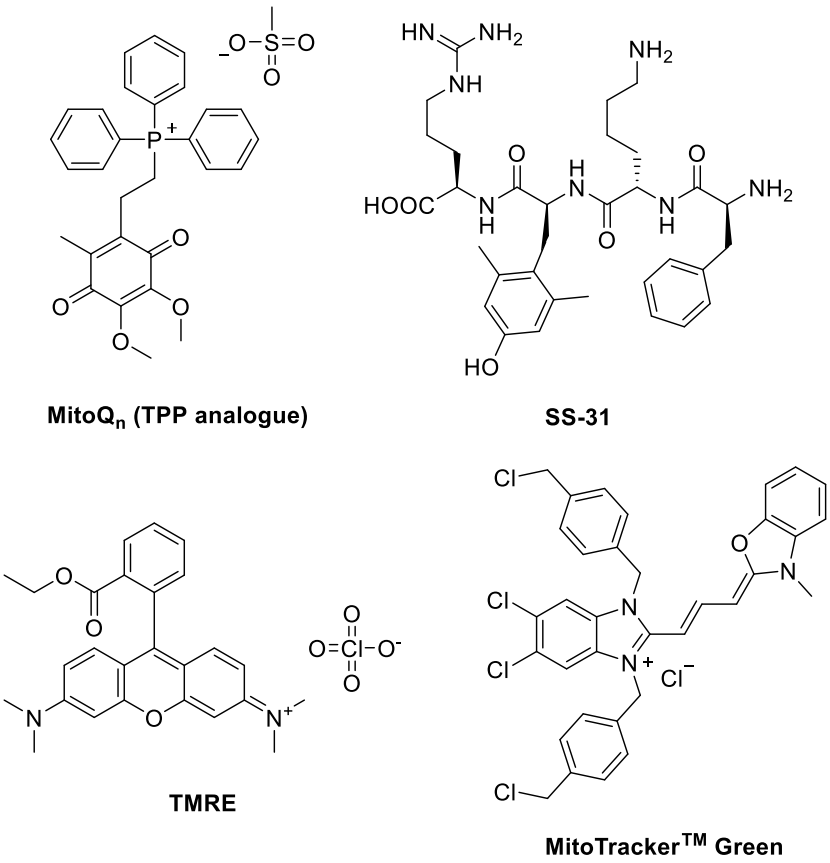

Figure I-19. Examples of structures capable of targeting mitochondria.

1.2.1. Precedents on MPPs

In 2008, Kelley *et al*. were the first investigators that, inspired by CPPs, designed a synthetic peptide that exhibited specific mitochondrial localisation in HeLa cells. These peptides alternated cationic residues, such as lysine or arginine, with lipophilic ones, like phenylalanine or cyclohexylalanine (**Figure I-20**).[154] They observed that sequences with log*P* (logarithm of the octanol-water partition coefficient) values below -1.7 had a poor internalisation in the mitochondria, with this effect being more pronounced in peptides with 3 positive charges than those with 5 cationic residues. Later, in 2009, the same research group investigated the effect of the distribution of the charge in the peptide sequences on the mitochondria targeting properties. They concluded that peptides with up to three adjacent cationic residues still displayed mitochondrial localisation. However, the sequence with four adjacent positive charges just exhibited localisation in the nucleus and the cytoplasm. The localisation of the latter peptide occurred despite its better lipophilicity compared to the other sequences, demonstrating that the distribution of the charges also plays a role in the targeting properties.[159] These studies established the physicochemical properties needed for the MPPs to penetrate efficiently in the mitochondria. But Kelley's research group not only did that, but also conjugated these peptides to several anticancer drugs such as platinum-based drugs (**55**),[160] Chlorambucil (**56**),[161] Doxorubicin (**54**),[162,163] or Luminespib[164] (**Figure I-20**). Their work illustrates the usefulness of employing these platforms for cancer therapy, as they are able to penetrate the mitochondria without being recognised by the P-glycoprotein efflux pumps, which are overexpressed in cancer cells and contribute to the degradation of the anticancer drugs.

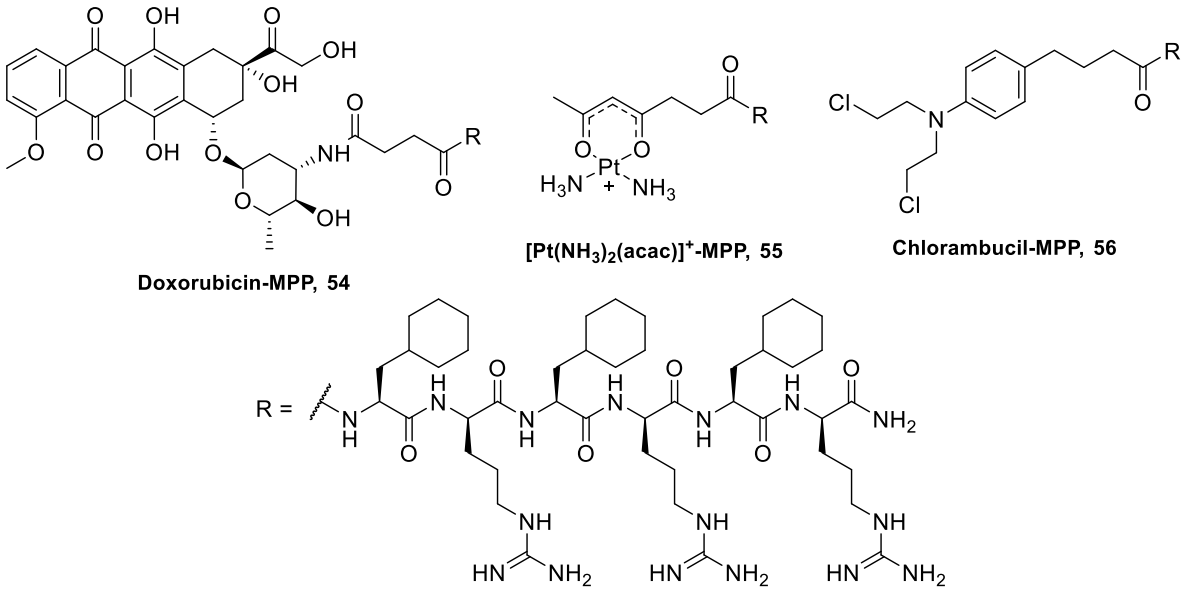

Figure I-20. Anticancer drugs coupled to an MPP developed by Kelley's research group.

Between 2010 and 2013, Chmielewski's research group published a series of papers investigating the mitochondria localisation of different amphiphilic polyproline peptides (**Figure I-15, 51 and 52,** *vide supra*).[132,165,166] These peptides demonstrated good mitochondria internalisation, but the mechanism of transport was conditioned by the concentration of peptide used and, therefore, their endosomal escape, finally influencing also their capability to target the mitochondria.

Beyond Kelley's and Chmielewski's research, other investigators have studied the applications of these MPPs, including their use in delivering metal ligands and complexes without compromising their catalytic activity. In 2018, Burke *et al*. investigated the delivery of a Ru(II) complex conjugated with an MPP (**Figure I-21**, **57**). By binding selectively to mitochondrial DNA, Ru(II) enables luminescence lifetime imaging. Furthermore, upon irradiation at 470 nm, Ru(II) complexes also exhibited photoinduced cytotoxicity, serving as a potential theragnostic agent for mitochondrial diseases.[167] Later, in 2019, Li *et al*. attached a MPP to the tripeptide **GGH**, a known amino-terminal Cu(II)- and Ni(II)-binding (ATCUN) motif (**Figure I-21**, **58**). Once it is internalised into the mitochondria, the motif binds to intracellular Cu(II) acting as a Fenton catalyst, producing hydroxyl radicals that induce apoptosis.[168]

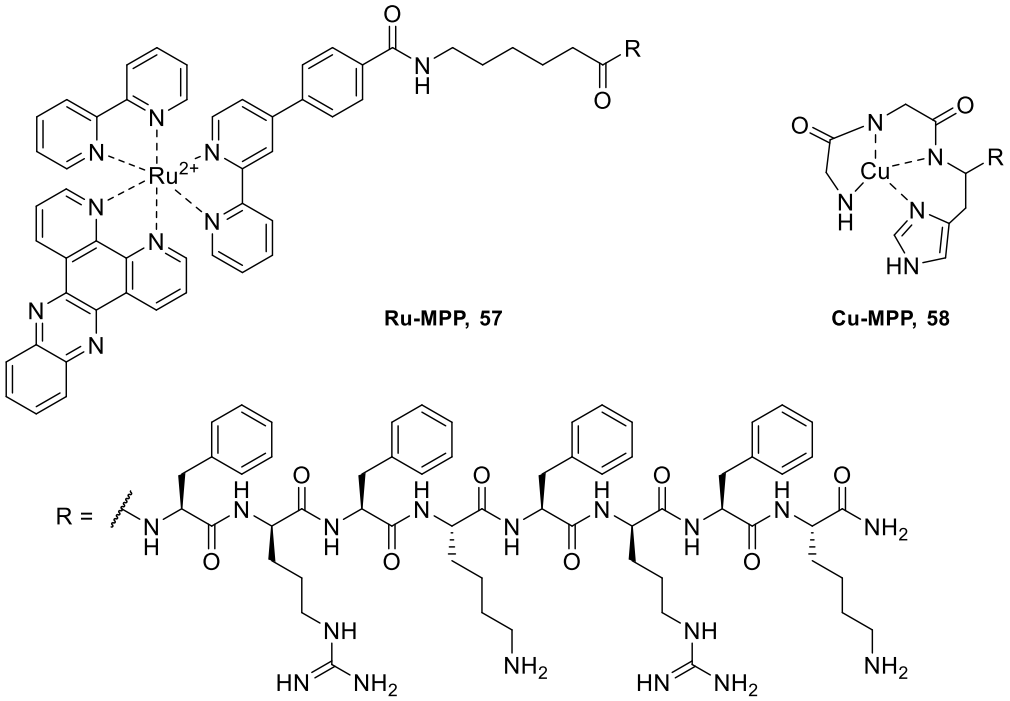

Figure I-21. MPPs conjugated with metal complexes.

1.2.2. Mitochondrial pH and SNARF Probe

A crucial aspect of mitochondrial function is maintaining an electrochemical gradient across the IMM, including the pH gradient. The MM typically exhibits a more alkaline environment (pH 7.8-8.0) compared to the slightly acidic intermembrane space (pH 7.0-7.4). This gradient is vital for adenosine triphosphate (ATP) synthesis *via* oxidative phosphorylation and for the proper functioning of various metabolic pathways. Mitochondrial pH (pH_m) influences numerous physiological processes, and deviations can indicate dysfunctions associated with pathologies such as cancer, neurodegenerative disorders, and metabolic conditions. Therefore, accurate measurement and monitoring of pH_m are essential for understanding mitochondrial physiology and pathology.

Initial techniques involved structures and probes that needed the isolation of the mitochondria to measure the pH_m,[169–171] but these methods were limited in their ability to observe and quantify spatial and temporal changes in this parameter. Alternatively, the quantification of ion concentrations, such as Ca^{2+}, where used to study the pH_m in dynamic processes.[172] However, methods developed to quantify this ion were too unspecific to obtain an accurate assessment of pH_m variations. Then, fluorescent probes, in combination with optical imaging-based approaches, have become essential tools for real-time, non-invasive measurement of intracellular pH. Among these, the xantene-derived dye 5(6)-carboxy-seminaphthorhodafluor-1, also named **5(6)-carboxy-SNARF-1 (SNARF)**, is a widely used pH-sensitive fluorescent dye that offers dual-emission properties, enabling ratiometric measurement for accurate pH assessment.[173,174] As a seminaphthofluorescein derivative, SNARF changes its emission spectrum in response to pH variations (**Figure I-22**). When excited at a specific wavelength, it emits fluorescence at two distinct wavelengths, corresponding to acidic and basic conditions. The emission ratio (typically 584 nm

and 634 nm) correlates directly with environmental pH, enabling precise quantification. The unique ratiometric properties of SNARF, in combination with its pKa of approximately 7.5, makes it particularly suitable for measuring pH_m *in situ*. Unlike single-emission probes, the ratiometric approach compensates for variations in probe concentrations, photobleaching, and instrument sensitivity, enhancing pH measurement reliability.

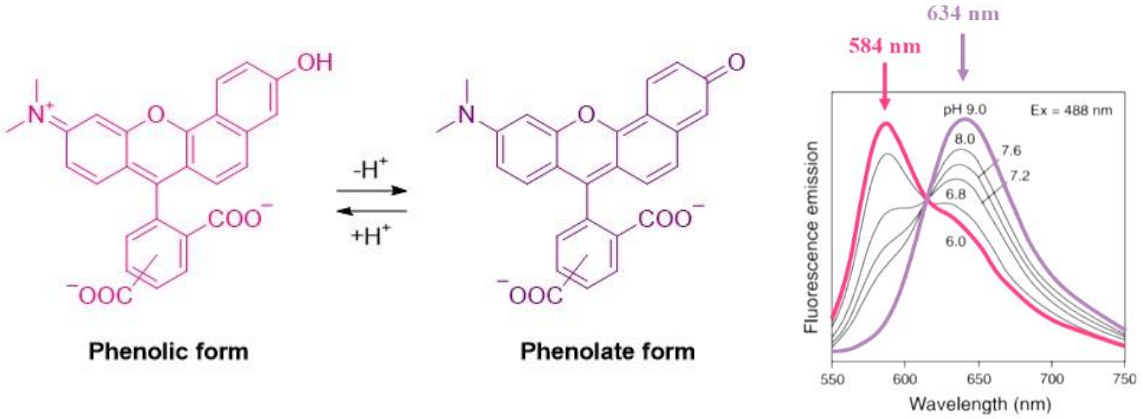

Figure I-22. Spectral changes in the fluorescence emission of the ratiometric probe SNARF-1 as a function of pH (for clarity, only the deprotonation of the phenolic group is shown). In an acidic environment (pH<pKa), the maximum emission is observed at λ=584 nm. In more alkaline media (pH>pKa), the maximum emission at λ=584 nm decreases, while a second band at λ=634 nm emerges. The ratio between these two signals, I_{634}/I_{584} provides an accurate way to measure intracellular pH.

To successfully measure the pH_m, cells are loaded with the acetoxymethyl ester of 5(6)-carboxy-SNARF. The intracellular distribution of this analogue depends on esterase activity, as it lacks intrinsic mitochondrial targeting capabilities. Its passive accumulation in mitochondria depends on the higher efflux rate of the dye in the cytosol than in the mitochondria and requires an extended incubation period to achieve ester hydrolysis and efflux equilibrium.[175] In addition, when the pH of the mitochondria and the surrounding cytosol are similar, it may be difficult to distinguish both structures based on this parameter, and the correct determinations of its locations would require simultaneous localisation and measurement of the pH_m. To avoid these drawbacks, this fluorescent probe can be conjugated to a mitochondrial targeting sequence, so it can be effectively used to investigate pH_m under various physiological and pathological conditions.

The use of SNARF has led to the study of different processes in which changes in the pH_m has been demonstrated to be significant. One example is the pH_m monitoring during apoptotic processes,[176] where a decrease in pH_m is often observed. Additionally, SNARF has facilitated studies on the impact of mitochondrial uncouplers and inhibitors of the electron transport chain, providing insights into mitochondrial dysfunction mechanisms.[177]

While SNARF is a powerful tool for measuring pH, its use in mitochondrial studies is not without challenge. Effective targeting of SNARF to mitochondria must be optimised to avoid disrupting mitochondrial function. For this reason, advances in delivery methods, including MPP carriers, are key to improve the efficiency and specificity of mitochondrial targeting.

1.3. Previous Investigations on CPPs in our Research Group

Over the past few years, our research group has developed several hybrid CPPs. The first generation of those peptides was accomplished in 2010 by Dr. Gutiérrez-Abad, by alternating a *cis*-γ-amino-L-proline residue and a cyclobutane-based γ-amino acid (γ-CBAA), using both enantiomers of this last amino acid (**Figure I-23**).[65] The incorporation of a rigid hydrophobic cyclobutane residue in combination with a functionalised γ-amino-L-proline causes conformational constraints on the peptide backbone, enhancing its stability and promoting the formation of stable secondary structures. This feature has been linked to improved uptake in various CPPs.[125,178,179]

The investigation was continued by Dr. Gorrea, who inserted different substituents in the N^{α} position of γ-amino-L-proline (**Figure I-23**). This second generation of hybrid peptides, that comprise 2, 4 or 6 alternating amino acid units, were evaluated as CPPs in HeLa cells. The hybrid CPPs showed a similar cell uptake but lower toxicity than those made exclusively of γ-amino-L-proline residues. The balance between polarity and hydrophobicity achieved by the combination of these two monomers demonstrated the importance of the cyclobutane moiety in this structure. In addition, this study looked at how peptide toxicity and penetration capabilities were affected by the peptide length, the CBAA chirality, and the N^{α} substitution.[180] From this investigation, it was concluded that i) Longer peptides facilitate the internalisation, the hexapeptide being the best candidate of the ones tested, ii) The absolute configuration of the γ-CBAA was not relevant, iii) The use of the 5-carbon spacer between the guanidium group and the N^{α} position of the proline amino acid provided the best internalisation results.[181,182]

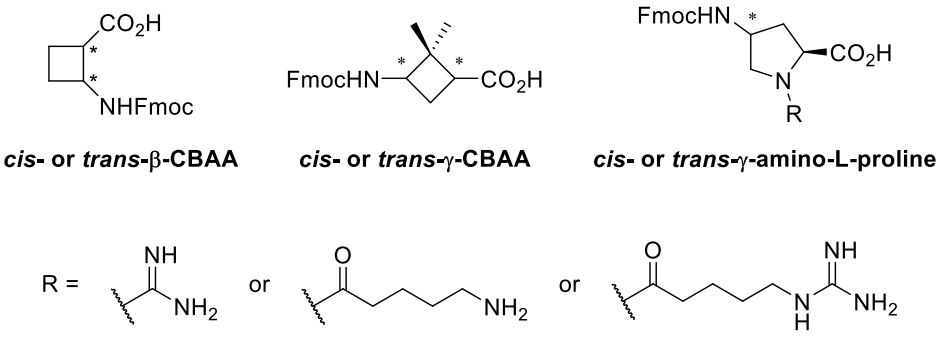

Figure I-23. Amino acids synthesised in our research group to obtain CPPs.

The conclusions extracted from Dr. Gorrea's work laid the groundwork of Dr. Ospina and Dr. Olivares investigation to synthesise a third generation of hybid γ,γ-peptides. In particular, the best peptides were extended up to 14 amino acids. In the case of Dr. Ospina, the investigation was not only focused on the synthesis of γ,γ-peptides, but also in the obtention of the β,γ-peptides, by alternating cyclobutane-based β-amino acids (β-CBAA) and γ-amino-L-proline monomers (**Figure I-23**). These oligomers were studied as drug delivery systems of doxorubicin, an anticancer drug, which has also been used to treat leishmaniasis (**Figure I-24**).[183] Biological studies demonstrated HeLa cells viability upon administration of the hybrid CPPs, showing no cytotoxicity even at a concentration of 50 μM. In terms of uptake behaviour, the peptides synthesised showed great performance in the internalisation in both HeLa cells and *Leishmania* parasites, but γ-CBAA-based

hybrid peptides demonstrated superior uptake compared to the β-CBAA-based CPPs. In addition, it was observed that the toxicity of the CPPs was not dependent either on the number of guanidinium groups in the sequence, or on the substitution of CF in the terminal amino group, with tetradecamers presenting a better uptake and microbicidal properties in assays with protozoan *Leishmania* parasites.

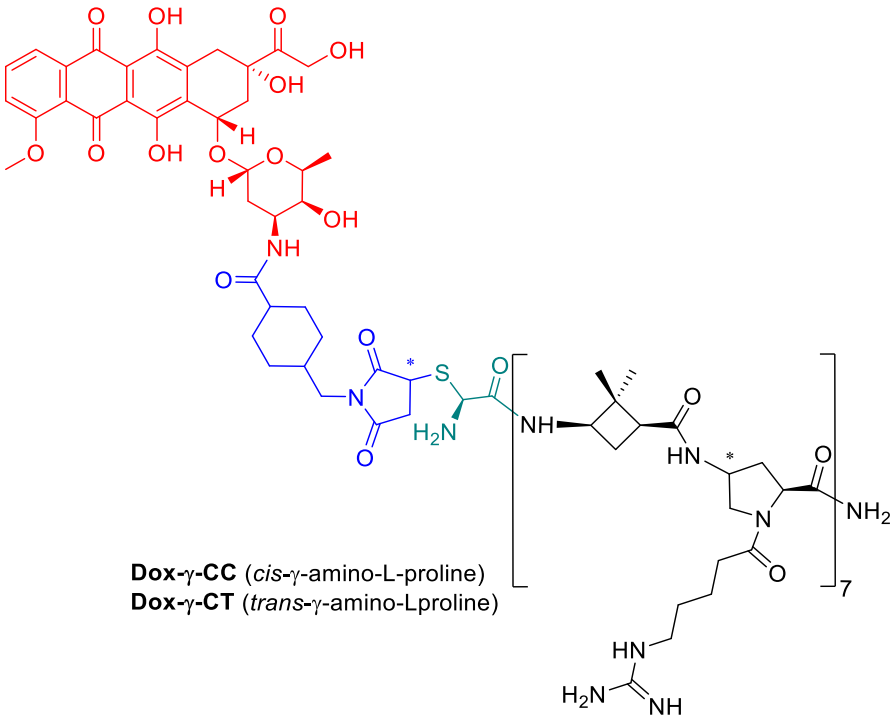

Figure I-24. Conjugation of doxorubicin (Dox) with **γ-CC** and **γ-CT** peptides. The Dox moiety is highlighted in red, the cysteine residue in green, and the linker in blue.

1.4. Solid-phase Peptide Synthesis (SPPS)

Solid-phase peptide synthesis (SPPS) is a fundamental technique in organic chemistry, particularly in the field of peptide chemistry. Developed by Dr. Merrifield in 1963,[184] SPPS revolutionised peptide synthesis by simplifying the process and enhancing efficiency. This technique has become indispensable for the synthesis of peptides and small proteins, providing a versatile platform for research and development, presenting significant synthetic advantages, such as the simplicity of removing excess of reagents and by-products through filtration and washing processes, and the efficiency and speed of the process by carrying out all the reactions in a single reaction vessel.

The core principle of SPPS involves the stepwise assembly of a peptide chain on a solid support, typically a resin, by sequential addition of protected amino acids, allowing for efficient elongation of the peptide chain without the need of constant isolation and purification at each coupling step, as for synthesis in solution. The process can be divided into several key steps (**Figure I-25**):[185]

1. **Loading the First Amino Acid**: The synthesis begins with the attachment of the first amino acid, which is typically *N*-protected, *via* its *C*-terminus to the solid support. This is achieved through a covalent bond between the carboxyl group of the amino acid and a functional group (-OH, -Cl or -NH_2) on the resin, forming an ester or an amide group.

2. **Deprotection**: The *N*-terminal protecting group (X), typically an Fmoc (9-fluorenylmethoxycarbonyl) group, is removed using a base, usually piperidine. This deprotection step exposes the amino group, rendering it available for the subsequent coupling reaction. The protecting group should be easily removed under mild conditions that maintain the integrity of the peptide and prevent epimerisation.
3. **Coupling**: The following amino acid, protected at its *N*-terminus and activated at its carboxyl group, is coupled to the growing peptide chain. This is facilitated by coupling reagents such as HATU (*O*-(7-azabenzotriazol-1-yl)-*N*,*N*,*N'*,*N'*-tetramethyluronium hexafluorophosphate) or HBTU (*O*-(benzotriazol-1-yl)-*N*,*N*,*N'*,*N'*-tetramethyluronium hexafluorophosphate), which promote the formation of the peptide bond.
4. **Repeated Cycles**: The deprotection and coupling steps are repeated iteratively to add subsequent amino acids in the desired sequence. Each cycle consists of deprotection, washing, and coupling, ensuring the elongation of the peptide chain in a controlled manner, until the desired sequence is obtained. It is important to consider that functional groups in the peptide side chains have to be orthogonally protected with motifs (Y) that are stable under the conditions used in the process. In addition, the process is monitored during these cycles by using the **ninhydrin test**, in which ninhydrin reacts with primary amines, producing a blue colour. Similarly, secondary amines in the side chains are tracked with the **chloranil test**, where a yellowish resin indicates the absence of free secondary amines, whereas a blue colour indicates their presence. Moreover, mini-cleavages of the resin can be performed in order to analyse the correct growth of the peptide by mass spectrometry.
5. **Cleavage and Final Deprotection**: Once the desired sequence has been assembled, the peptide is cleaved from the resin and the side chain protecting groups are removed. This is typically achieved using trifluoroacetic acid (TFA), obtaining peptides with a carboxylic acid or an amide in the *C*-terminus, depending on the chosen resin.

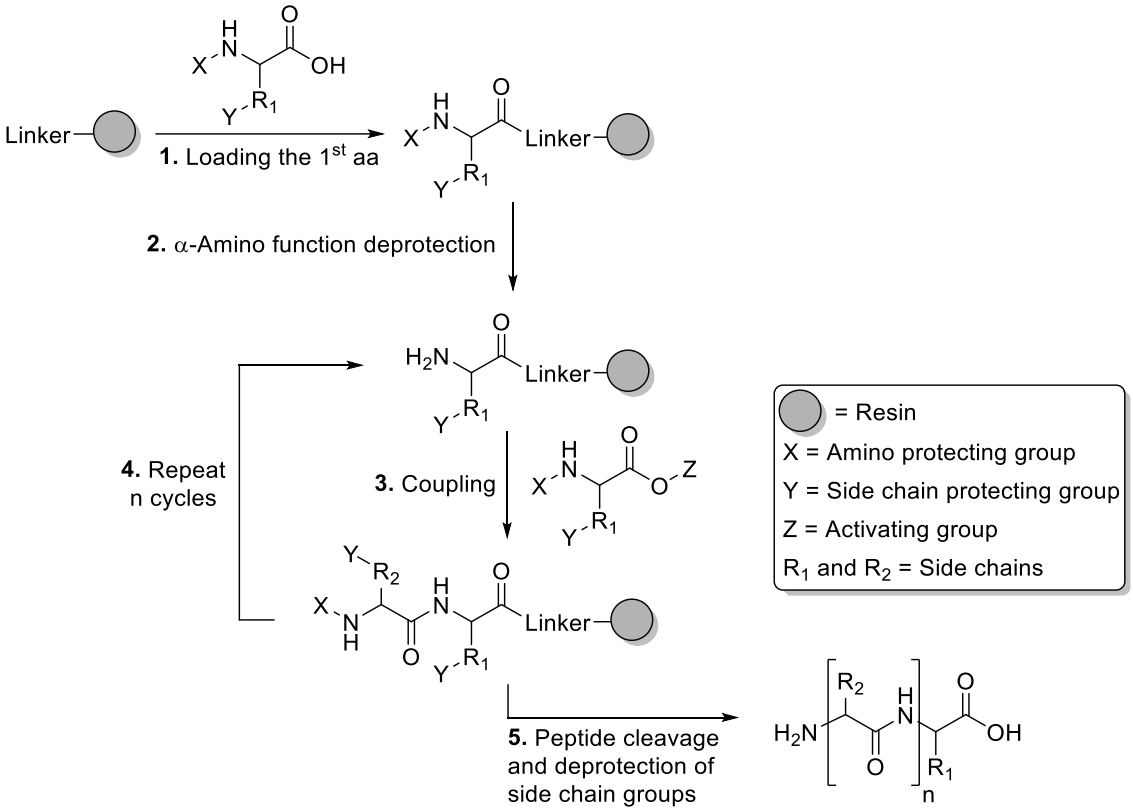

Figure I-25. General protocol for peptide building in SPPS.

2. Objectives

Owing to the promising results achieved in the previous studies, it was decided to exploit the advantageous properties of these peptidomimetic scaffolds to study their capability to penetrate into the different organelles of the cell. More specifically, their ability to act as MPPs was suspected and thus, the penetration in mitochondria, an important organelle in the metabolism of the cell and implicated in various diseases, was set as an objective.

The first biological studies to evaluate their localisation into the mitochondria would be carried out with the γ-CBAA/γ-amino-L-proline tetradecamer hybrid peptides coupled to the fluorescent probe carboxyfluorescein (CF), as they were identified as the best performing CPPs in previous studies (**Figure I-26**).

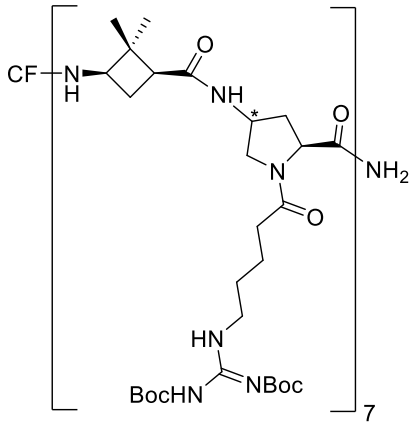

CF-γ-CBAA-*cis*-γ-amino-L-proline, **CF-γ-CC**
CF-γ-CBAA-*trans*-γ-amino-L-proline, **CF-γ-CT**

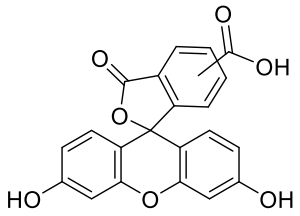

CF = 5(6)-Carboxyfluorescein
(fluorescent probe)

Figure I-26. Previously studied γ-CBAA/γ-amino-L-proline hybrid peptides coupled to CF.

In the event that penetration into the mitochondria was observed, these peptides would be coupled with the ratiometric probe 5(6)-carboxy-SNARF-1 (SNARF), and their properties as MPPs would be again tested, as well as two possible applications such as mitochondrial pH measurement and the study of the mitochondria dynamics.

To achieve these main objectives, different milestones would need to be accomplished first:

- Gram-scale synthesis of cyclobutane amino acid (1*S*,3*R*)-3-amino-2,2-dimethylcyclobutane-1-carboxylic acid **59**, replicating the synthesis published in the 2012 (**Figure I-27**).[65]
- Gram-scale synthesis of conveniently functionalised *cis*- and *trans*-γ-amino-L-proline derivatives **60** and **61** using a new strategy that inserts the side chain in the synthesis in solution (**Figure I-27**).
- Synthesis of the γ,γ-peptidomimetic tetradecameric hybrid oligomers, using a Fmoc/Boc strategy in solid-phase peptide synthesis.

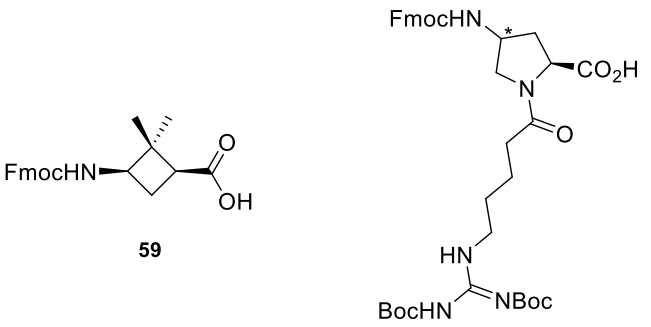

Figure I-27. Target amino acids for the synthesis of tetradecameric hybrid oligomers.

3. Results and Discussion

The results of this chapter are presented in various sections. First, the synthesis of the three monomers, γ-CBAA **59** and *cis*- or *trans*-γ-amino-L-proline **60** and **61**, used in the peptide synthesis is introduced (**section 3.1.**). Second, the SPPS of the hybrid γ-CBAA-γ-amino-L-proline peptides is discussed (**section 3.2.**). Third, the biological assays performed by Prof. Montenegro's research laboratory on the γ,γ-peptidomimetics oligomers **CF-γ-CC**, **CF-γ-CT** and **γ-SCC** will be exposed (**section 3.3.**).

3.1. Synthesis of γ-CBAA, 59 and *cis*- or *trans*-γ-amino-L-proline, 60 and 61

Hybrid γ,γ-peptides **γ-CC** and **γ-CT** were afforded using an Fmoc/Boc strategy in the SPPS. Therefore, Fmoc-*N*-protected amino acids **59**, **60**, and **61**, were needed. In addition, amino acids **60** and **61** bear a guanidinium group, pending from the N^{α} side chain, that needs to be orthogonally protected as Boc carbamates to avoid deprotection and formation of by-product during the peptide synthesis. Owing to the requirements of SPPS, gram-scale syntheses of both monomers were performed.

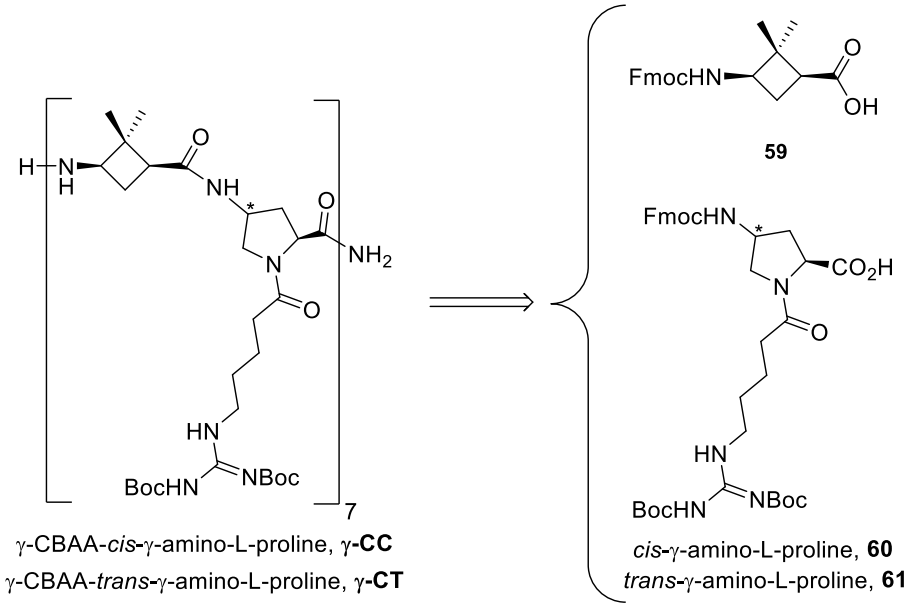

Scheme I-17. Retrosynthetic analysis of peptides **γ-CC** and **γ-CT**.

3.1.1. Synthesis of the Orthogonally Protected γ-CBAA, 59

The synthesis route shown in this section had been optimised and published by our research group.[186] It uses **(-)-verbenone (30)** as starting material, a terpenoid from the chiral pool, to obtain amino acid **59** over 9 steps, as shown in **Scheme I-18**.

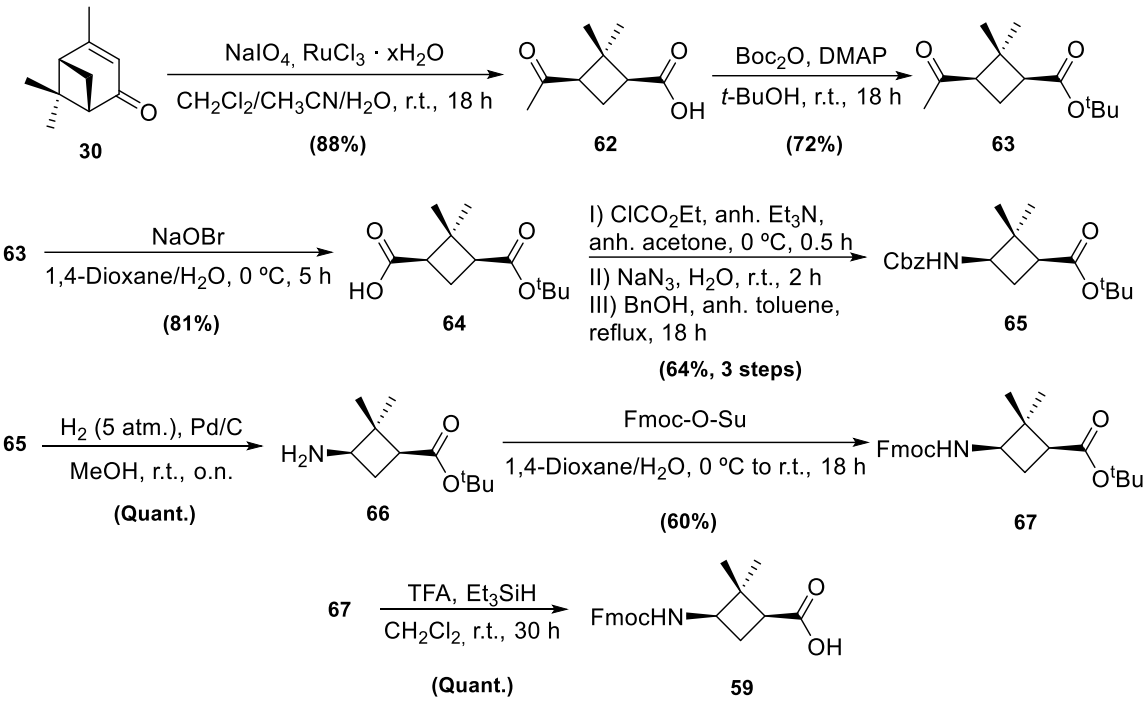

Scheme I-18. Synthetic route to prepare γ-CBAA **59** from **(-)-verbenone** (**30**).

The synthesis of the enantiopure cyclobutane amino acid was carried out using the following strategy. The synthesis started with the ruthenium-catalysed oxidative cleavage of the C-C double bond on the 6-membered ring chiral precursor **(-)-verbenone (30)**, followed by an α-carbonyl decarboxylation, obtaining **(-)-*cis*-pinononic acid (62)** without the formation of epimers. In this interphase reaction, sodium periodate ($NaIO_4$) acts as a stoichiometric oxidant, and acetonitrile plays a crucial role to prevent ruthenium catalyst inactivation, avoiding its precipitation in the form of ruthenium tetraoxide.[187] The synthesis was continued with a protection reaction, employing di-*tert*-butyl dicarbonate (Boc_2O) and catalytic amounts of 4-dimethylaminopyridine (DMAP), to afford *tert*-butyl ester **63**. Subsequently, Lieben degradation, using sodium hypobromite (NaOBr) prepared *in situ*, was performed onto the methyl ketone group to obtain carboxylic acid **64**.

Upon activation of carboxylic acid **64** by formation of a mixed anhydride through reaction with ethyl chloroformate in basic media, sodium azide (NaN_3) was added as a nucleophile to afford the acyl azide intermediate, which was manipulated carefully due to its explosive nature. Once the volume of solvent had been carefully reduced, but not until full dryness, the acyl azide was transformed through a Curtius rearrangement type reaction by heating to reflux in anhydrous toluene. The thermal decomposition of the acyl azide leads to the formation of the isocyanate along with the elimination of nitrogen. Then, the isocyanate readily reacts with the nucleophile present in the reaction medium, in this case the benzyl alcohol, to form benzyl carbamate **65**.

Thereupon, a change of protecting group was accomplished through the removal of the benzyl carbamate moiety by catalytic hydrogenation, using palladium on charcoal (Pd/C), and successive protection of the resulting amine **66** with *N*-(9-fluorenylmethoxycarbonyloxy)succinimide (Fmoc-O-Su), furnishing Fmoc-protected amine **67**. This protecting group was selected due to the requirement for orthogonal protection of the molecule for the subsequent SPPS, wherein

Boc-protected amino groups were utilised in the proline monomer. Finally, *tert*-butyl ester **67** was reacted with neat TFA, obtaining acid **59**. The overall yield of this gram-scale synthesis line to obtain the cyclobutane monomer was 20% over 9 steps.

3.1.2. Synthesis of the Guanidinium-containing Side Chain, 74 and *cis/trans*-γ-amino-L-proline, 60 and 61

In a previous work, the introduction of the side chain into the peptide structure was performed at the end of the SPPS.[183] In that case, the proline used was protected with an allyloxycarbonyl (Alloc) group at the N^{α} position. However, the deprotection reaction in presence of palladium-tetrakis(triphenylphosphine) ($Pd(PPh_3)_4$) and phenylsilane (Ph_3SiH) resulted in the obtention of the alkylated amines **72** and **73** as by-product, reducing the yields for the obtention of peptides **γ-CC** and **γ-CT** (**Scheme I-19**).

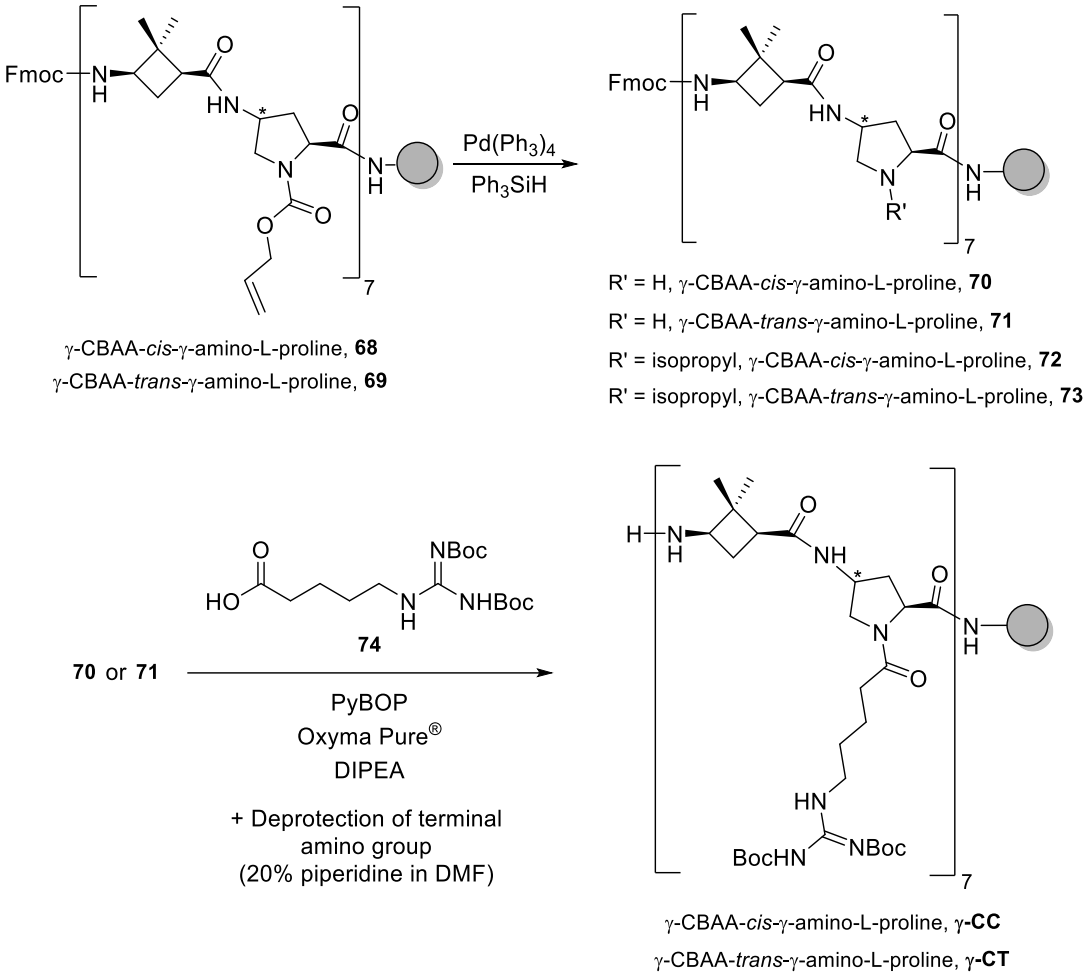

Scheme I-19. Previous synthetic route to obtain peptides **γ-CC** and **γ-CT**.[183]

To improve the yields obtained, a different approach was proposed. Initially, the chain would be introduced in the N^{α} position of the proline residue in solution. Then, the SPPS would be changed to a Fmoc/Boc strategy.

Before performing the synthesis of the conveniently functionalised γ-amino-L-prolines, the chain was prepared starting from the commercially available **aminovaleric acid (75)**. This compound was modified by introducing a terminal guanidinium group. The introduction of this substituent on the proline backbone is directed to having the same substitution as arginine, a commonly used amino acid in the fields of CPPs and MPPs. As it has been explained in the introduction, this residue plays an important role in the cell internalisation of the peptide. The use of commercial compound **76**, in the presence of triethylamine (Et_3N), facilitated the obtention of the side chain **74** in 64% yield, after purification (**Scheme I-20**).

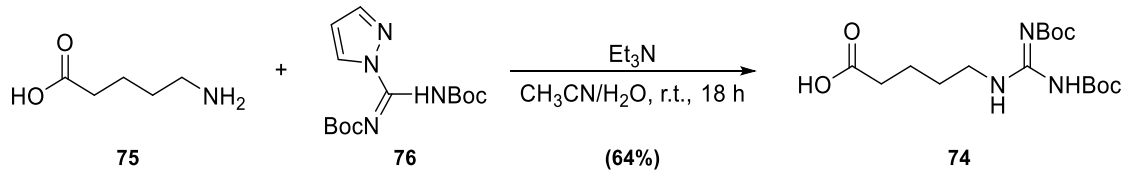

75 **76** **(64%)** **74**

Scheme I-20. Synthesis of guanidinium-containing side chain, **81**.

For the synthesis of the proline units, commercial orthogonally protected *cis*- and *trans*-γ-amino-L-prolines **77** and **78** were used as starting materials, respectively. The synthesis started with the protection of the carboxylic acid group, as it is fundamental to avoid competition between the amine and the carboxylate of the proline in the coupling reaction with the activated carboxyl group of the side chain. The protection was performed using benzyl bromide in presence of $NaHCO_3$ as a mild base to obtain products **79** and **80** in 86% and 80% yield, respectively. Then, the cleavage of the Boc protecting group was carried out under anhydrous acidic conditions to obtain salts **81** and **82** in quantitative yields (**Scheme I-21**).

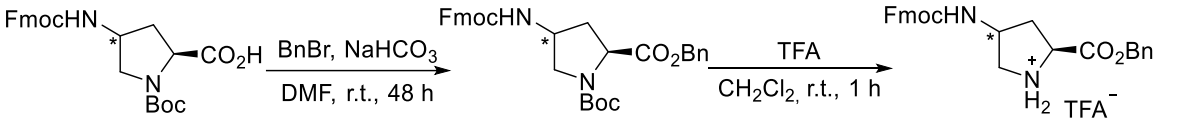

cis-γ-amino-L-proline, **77**
trans-γ-amino-L-proline, **78**

cis-γ-amino-L-proline, **79 (86%)**
trans-γ-amino-L-proline, **80 (80%)**

cis-γ-amino-L-proline, **81 (Quant.)**
trans-γ-amino-L-proline, **82 (Quant.)**

Scheme I-21. Obtention of the proline salts **81** and **82**.

Once the N^{α} position was freed, a coupling reaction between **74** and **81** was performed using PyBOP (benzotriazol-1-yloxytripyrrolidinophosphonium hexafluorophosphate) to activate the carboxylate. Surprisingly, the base used in the reaction was key to obtain the product, as when Et_3N was used with salt **81**, the free amine **83** was obtained as a by-product, as a consequence of the Fmoc cleavage (**Scheme I-22**).

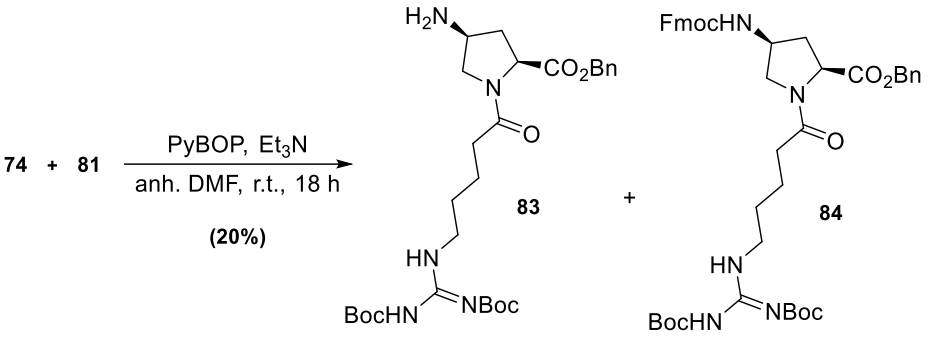

Scheme I-22. The use of Et_3N as a base caused the cleavage of the Fmoc group generating the free amine by-product **83**.

Despite Fmoc being considered a quite stable protecting group when tertiary amines are used, some examples of Fmoc cleavage in the presence Et_3N in polar medium such as DMF have been reported.[188,189] As a result, it was concluded that a more hindered base, *N,N*-diisopropylethylamine (DIPEA), was needed to perform the peptide coupling reaction for the obtention of products **84** and **85** in 61% and 55% yield, respectively. Finally, hydrogenation with Pd/C catalysis at atmospheric pressure, as Fmoc is not completely stable to catalytic hydrogenolysis,[190] was carried out to afford amino acids **60** and **61** (**Scheme I-23**) with an overall yield of 49% after 4 steps.

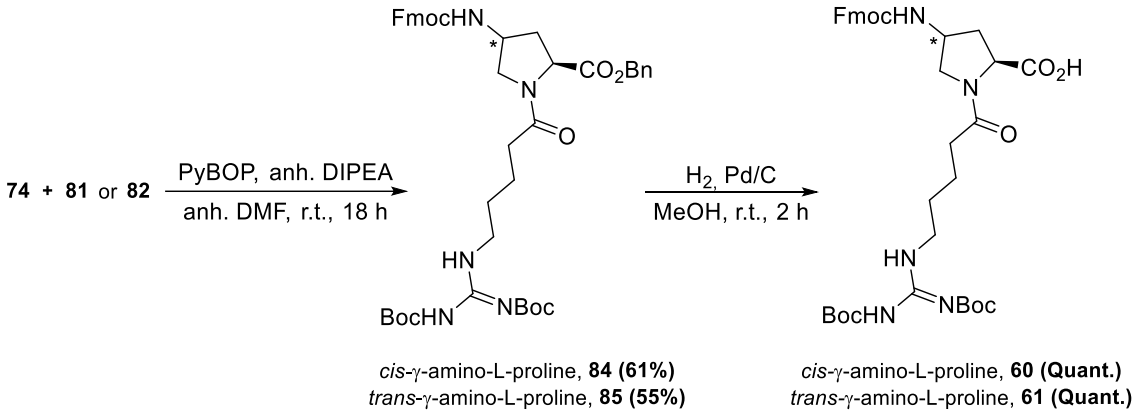

Scheme I-23. Synthetic route to prepare *cis*- and *trans*-γ-amino-L-proline **60** and **61**.

3.2. SPPS of Peptides CF-γ-CC and CF-γ-CT

Due to reasons beyond our control, created by the COVID-19 situation, the synthesis of both peptides was performed in two different research facilities. The synthesis of the peptide **γ-CT**, which employed the *trans*-proline monomer, was carried out in a laboratory of the Institut de Química Avançada de Catalunya (ICAQ) in Barcelona directed by Dr. Royo. On the other hand, the synthesis of the peptide **γ-CC**, that included the *cis*-proline monomer in its structure, was done in the group of Prof. Montenegro, by Dr. Pazo and PhD student Yeray Folgar, at the Centro Singular de Investigación en Química Biológica y Materiales Moleculares (CiQUS) research facilities in the Universidad de Santiago de Compostela (USC).

A general procedure for the SPPS is described in the following section. Both groups used the same SPPS strategy and monomers to accomplish the synthesis. The observations in the procedure

described were not necessarily made in both facilities, but they were considered important in terms of research and methodology wise.

3.2.1. SPPS of γ-CBAA-γ-amino-L-proline Hybrid Peptides CF-γ-CC and CF-γ-CT

As stated before, the solid-phase synthesis of the peptides was performed by using the Fmoc/Boc strategy. For both series of peptides, the amino acid **59** was used, and the corresponding proline derivative **60** or **61** was used depending on whether **CF-γ-CC** or **CF-γ-CT** tetradecamer peptide was synthesised.

The peptides were built onto the Rink Amide resin functionalised with terminal amino groups. Those groups were coupled with the carboxylic acid group of the proline **60** or **61**, which is the first step in the SPPS. In a first attempt, the linkage with the resin was performed in the presence of PyBOP, as coupling agent, Oxyma Pure®, as additive, and DIPEA, as base. Unfortunately, ninhydrin test revealed that most of the resin amino groups had not been functionalised by the proline amino acid. To improve the yield of this first step, an alternative methodology was tested, increasing the amino acid ratio with the amino group of the resin, and using a different coupling agent, namely *N,N'*-diisopropylcarbodiimide (DIC). In this case, ninhydrin test revealed a higher functionalisation of the resin, considering this second method the most valuable one for the synthesis (**Scheme I-24**).

Then, deprotection of the Fmoc group in presence of 20% piperidine in DMF was carried out, followed by a wash with DMF and DCM, allowing the peptide to have the *N*-terminus free to accomplish the peptide coupling with the γ-CBAA **59**, using PyAOP or PyBOP, as coupling agent, Oxyma Pure®, as additive, and DIPEA, as base, in DMF. Elongation of the peptide was continued through 6 more cycles of deprotection/coupling reaction under the same conditions previously described, intercalating the monomers **59** and **60** or **61** (**Scheme I-24**). To ensure the correct coupling of amino acids, a "mini-cleavage" of the peptide linkage with the resin was done every 5 coupling reactions, so the synthesis could be followed properly. To do so, a small amount of resin was taken and treated with acid so all the protecting groups of the side chain would be removed and the peptide cleaved from the resin. That sample was injected into a high-performance liquid chromatography-mass spectrometry (HPLC-MS) equipment to confirm that the peptide had been well-constructed at this point.

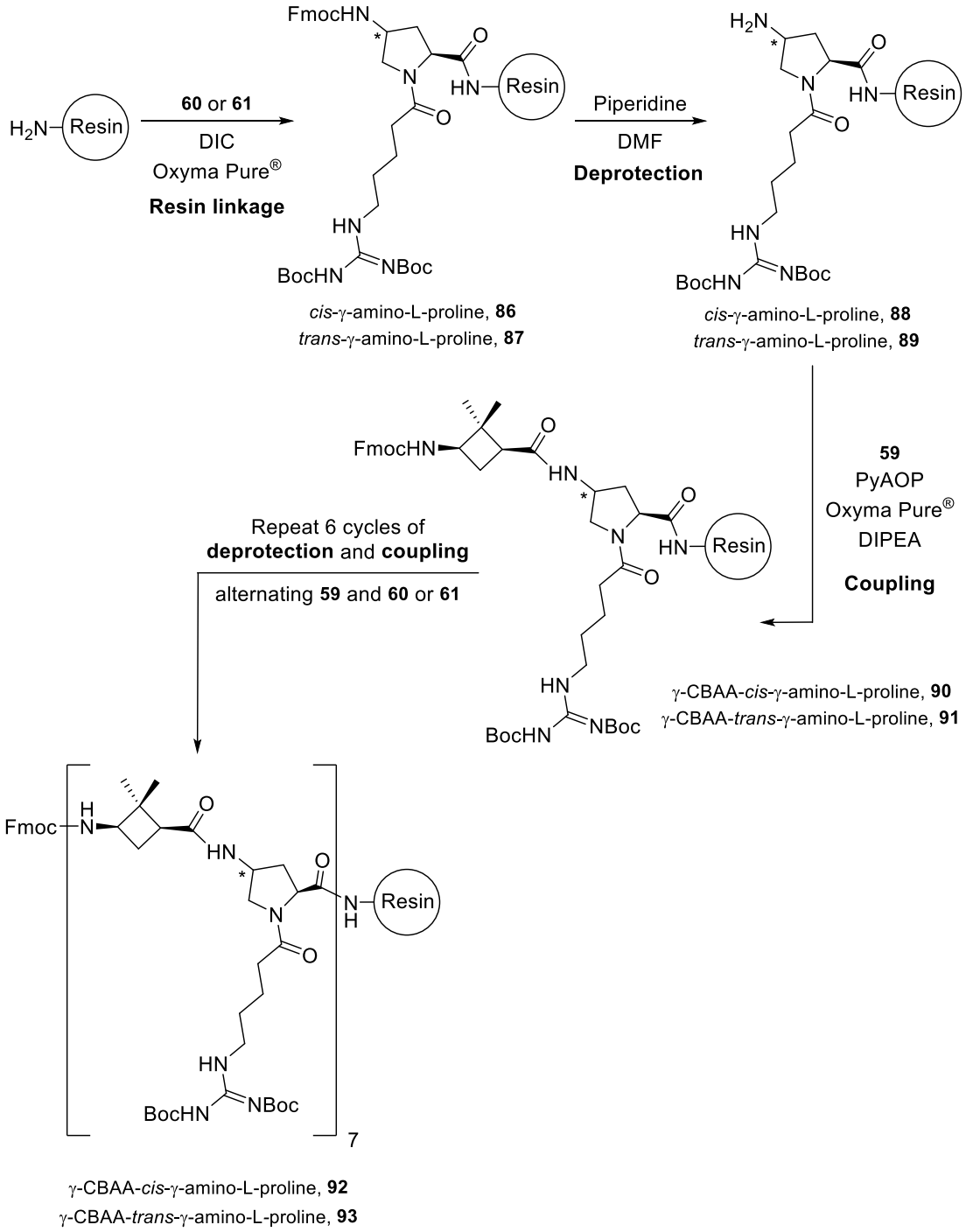

Scheme I-24. SPPS procedure for the synthesis of peptides **92** and **93**.

Once the desired peptide length was obtained, (5)6-carboxyfluorescein was coupled using PyBOP as the coupling agent, Oxyma Pure® as additive, and DIPEA as base, through the terminal amino group of the peptides **94** and **95**, which had been previously deprotected using 20% piperidine in DMF. A red colouration appeared in the medium, associated to the formation of carboxyfluorescein dimers. This by-product is generated through the acylation of the phenolic hydroxyl group, as previous studies have elucidated. To avoid its formation, a wash with 20% piperidine in DMF was performed before the cleavage from the resin, as it is known that phenolic esters are easily cleavable by nucleophiles and basic media.[191] The SPPS procedure finished with the separation of

peptides **96** and **97** from the resin by using TFA, triisopropylsilane (TIS) and H_2O. The acid hydrolysis conditions facilitated the removal of the Boc protection on the guanidine residues, yielding peptides **CF-γ-CC** and **CF-γ-CT** (**Scheme I-25**).

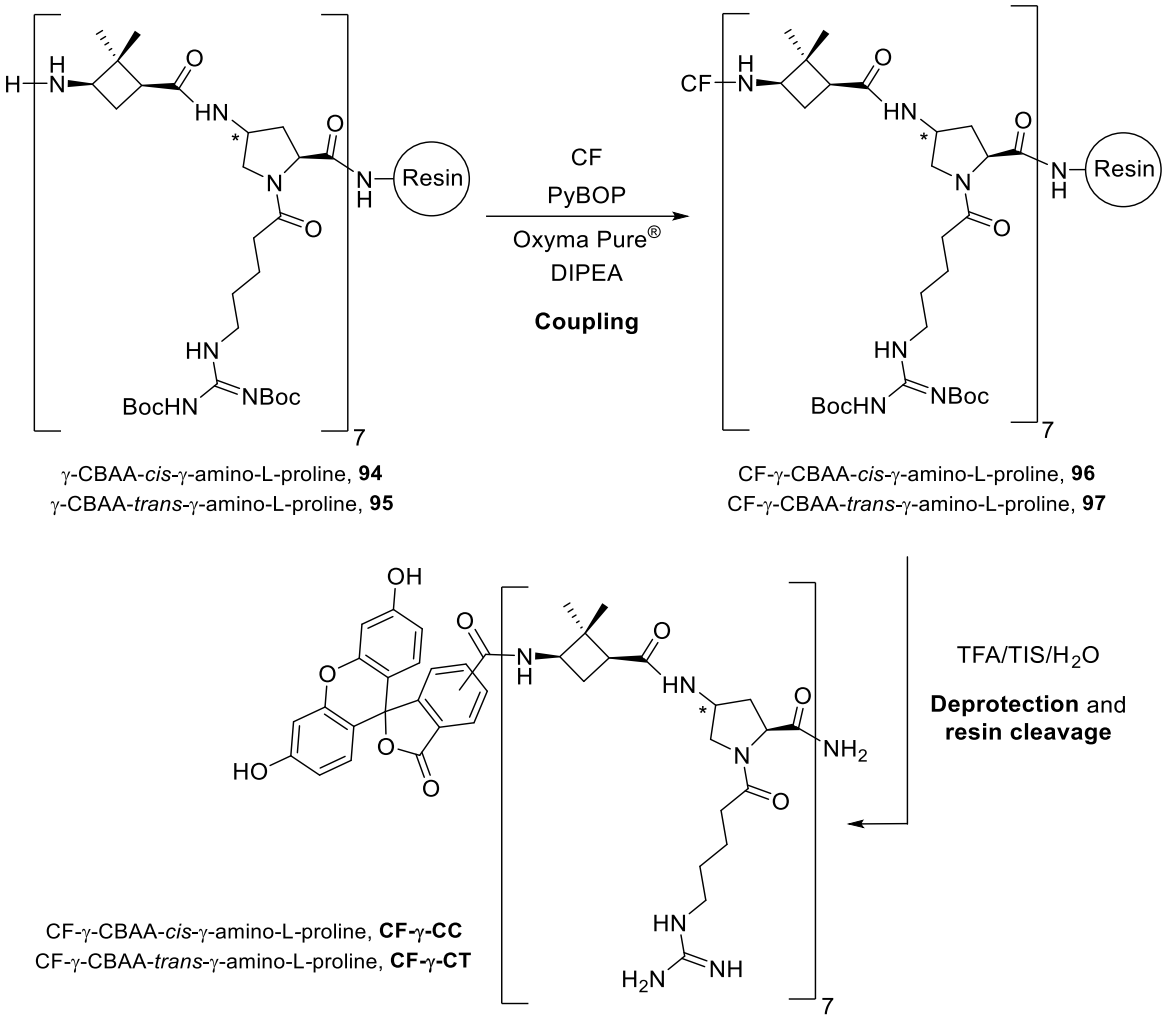

Scheme I-25. CF coupling and with concurrent deprotection and resin cleavage for the synthesis of peptides **CF-γ-CC and CF-γ-CT**.

After being lyophilised, purification of the peptides synthesised was accomplished through a semipreparative reverse-phase HPLC (Semiprep-RP-HPLC). **CF-γ-CC** and **CF-γ-CT** had low retention rates, so the gradients used had a low ratio of ACN. Characterisation was carried out by reverse-phase HPLC coupled to a mass spectrometer (RP-HPLC-MS) and fitted with the data previously reported.[179]

3.3. *In vitro* Studies

In vitro assays were carried out by Dr. Marta Pazo and Yeray Folgar, former member and PhD student, respectively, in Prof. Javier Montenegro's research group at CiQUS research centre of the Universidade de Santiago de Compostela. With these studies the capacity of **CF-γ-CC** and **CF-γ-CT** peptides to target the mitochondria was evaluated, as well as the influence of the stereochemistry of the γ-amino-L-proline residue in the properties of the peptides. Those peptides that exhibited mitochondrial localisation in HeLa cells would be coupled to the ratiometric probe

5(6)-carboxy-SNARF-1. The localisation properties of these new peptides would be again investigated in various cell lines, as well as their stability and cytotoxicity in HeLa cells. Finally, their application to monitor the mitochondrial pH and tracking mitochondria dynamics would be studied as a proof of concept for the potential biological applications of these peptides.

3.3.1. Evaluation of the Peptides CF-γ-CC and CF-γ-CT Distribution Inside HeLa cells

The distribution of the peptides in the cell was determined by confocal microscopy. For that purpose, HeLa cells were incubated in presence of the peptide at concentrations between 10 and 150 µM for 1 hour. Internalisation of peptides **CF-γ-CC** and **CF-γ-CT** was first evaluated qualitatively, studying the distribution in the cell by observing the fluorescence in the different parts of the cell. In the images obtained (**Figure I-28**), fibrillar structures could be observed starting at concentrations of 10 µM for peptide **CF-γ-CC**, indicating the internalisation in the mitochondria. However, these same structures could not be observed for peptide **CF-γ-CT**, even at the highest concentration tested, being only accumulated in the nucleus and cytosol, and pointing out that these two peptides have a different distribution in the cell.

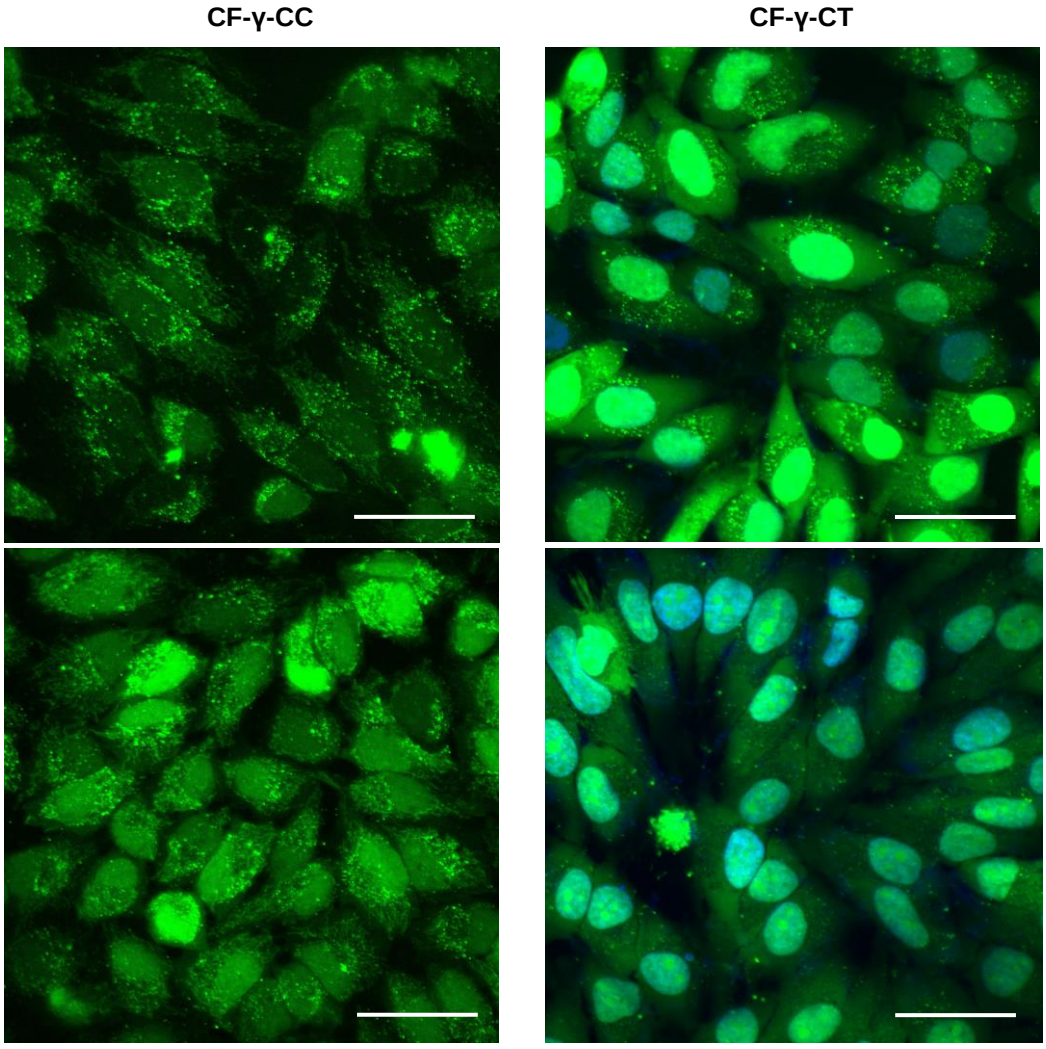

Figure I-28. Confocal microscopy images of **CF-γ-CC** and **CF-γ-CT** at concentrations of 25 µM and 50 µM, respectively. Fibrillar structures indicating mitochondria localisation are prominently observed with **CF-γ-CC**, particularly at 25 µM. In contrast, **CF-γ-CT** predominantly accumulates in the nucleus and cytosol, without mitochondrial distribution. Scale bars, 50 µm.

In these first assays, a greater toxicity for **CF-γ-CT** was also observed, especially at concentrations of 150 μM, whereas cells treated with **CF-γ-CC** remained viable under the same conditions (**Figure I-29**). However, at concentrations of 100 μM, both cell cultures showed viable cells. These data fit with those reported earlier for these peptides, where cell viability was over 90% at the highest concentration assayed (50 μM), regardless of the peptide stereochemistry.[183] Since mitochondrial internalisation happened at concentrations where cell viability had already been studied, no further studies were performed about this parameter.

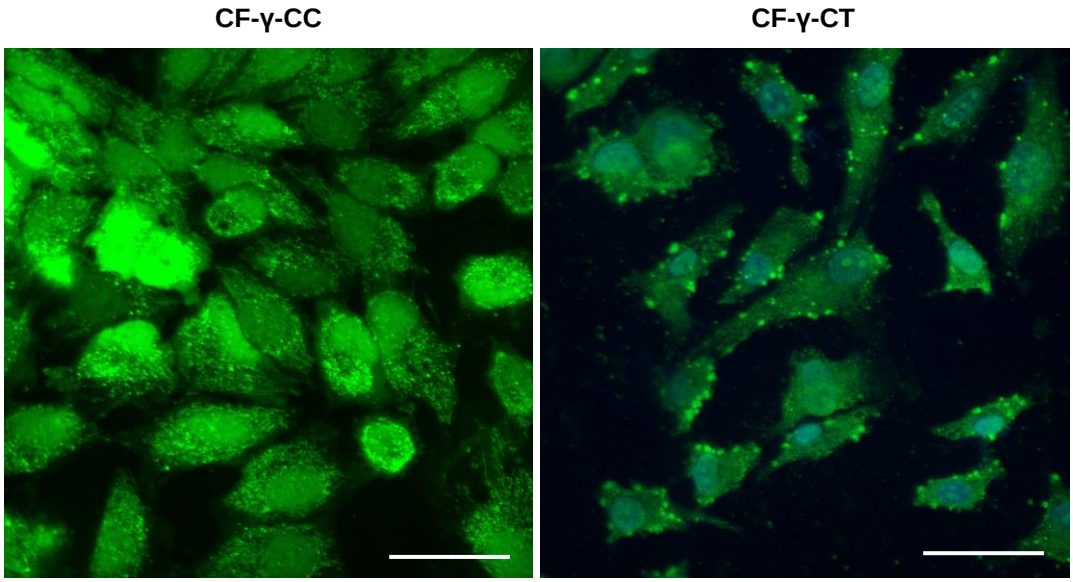

Figure I-29. Confocal microscopy images showed apoptosis for **CF-γ-CT** at the highest concentration used (150 μM), in contrast with the images obtained for **CF-γ-CC** at the same concentration. Scale bars, 30 μm.

A quantitative study was performed using MitoTracker™ Red CMXRos, a commercial fluorescent dye specifically designed for labelling mitochondria in cells. This dye enabled to perform a fluorescence colocalization analysis, which is used to determine whether two molecules associate with the same structure, in this case the mitochondria. This assay was also performed in HeLa cells incubated with the corresponding peptide at concentrations between 10 and 150 μM, and with the MitoTracker™ Red CMXRos at concentrations between 50 to 100 nM. From this set of experiments, the optimal images for analysis were obtained using a peptide concentration of 25 μM and 50 nM of MitoTracker™ Red CMXRos (**Figure I-30**).

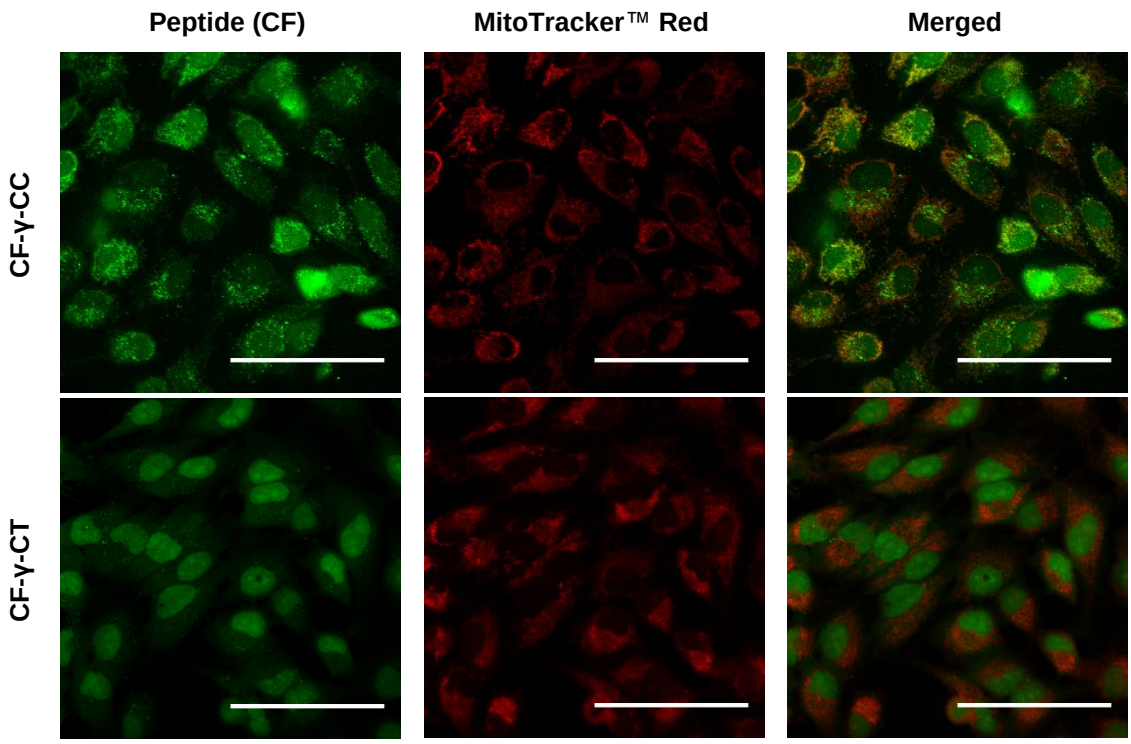

Figure I-30. Analyses of peptides **CF-γ-CC** and **CF-γ-CT** (in green, 25 μM) colocalization with mitochondria using MitoTracker™ Red CMXRos (in red, 50 nM). Scale bars, 50 μm.

The quantitative colocalization analysis was done by calculating two coefficients: **Manders' overlap coefficient (MOC)** and **Pearson's correlation coefficient (PCC)** (see more details in **section 2.2.6** of the **Part III. Experimental Methodologies**).[192] The values of MOC measured for **CF-γ-CC** (M_1 = 0.49 ± 0.04 and M_2 = 0.60 ± 0.07) and **CF-γ-CT** (M_1 = 0.26 ± 0.12 and M_2 = 0.31 ± 0.14) indicated that **CF-γ-CC** is more specific and efficient than **CF-γ-CT** at penetrating into the mitochondria (**Figure I-31**), which is aligned with the preliminary conclusions extracted with the images registered without the MitoTracker™ Red CMXRos in **Figure I-28**. On the other hand, PCC values for **CF-γ-CC** (R*r* = 0.54 ± 0.04) and **CF-γ-CT** (R*r* = 0.46 ± 0.11) did not show a significant difference between both peptides for the mitochondria localisation (**Figure I-31**). However, this might be because of a major sensitivity of this parameter on the quality of the images,[192] as PCC considers the intensity values across the image. If the intensity of the two images is not linearly related (*e.g.*, one signal is much stronger or weaker than the other), PCC might show a lower correlation, even if the signals overlap spatially, being less reliable in this case.

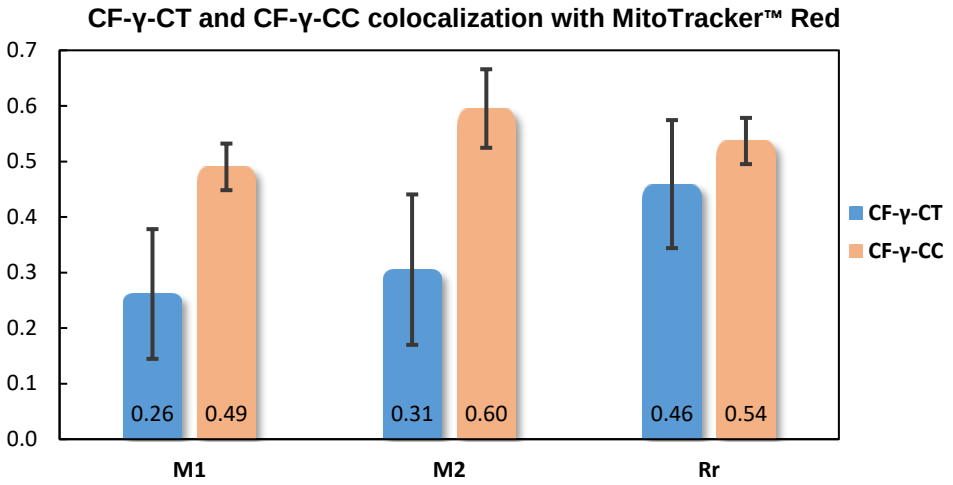

Figure I-31. Representation of the quantitative colocalization analysis. Manders' Overlap coefficients (M_1, M_2) and Pearson's coefficient (R_r) were calculated from a set of 4 independent images. Whiskers represent the total range of values with each sample.

A rational explanation for the differences in the intracellular distribution of the peptides was sought. As discussed in **section 1.2.1**, Kelley's research group identified two key parameters that peptides must exhibit for effective mitochondrial penetration: the presence of positive charges (**Z > 0**) and a lipophilic character (**log*P* > -1.7**). Since both peptides have identical charges (Z = 7), the focus shifted to their lipophilic properties.

In a previous study by our research group, molecular dynamics (MD) simulations revealed distinct secondary structures for both tetradecamers.[183] These differences were driven by the formation of intra-residue and long-range inter-residue hydrogen bonds, caused by the different stereochemistry of the γ-amino-L-proline monomer.[183] Specifically, **CF-γ-CC** predominantly adopted double harpin and laminar motifs (**Figure I-32**), where the CF moiety was buried inside the peptide, due to the hydrophobic collapse of the skeleton around the probe. In contrast, **CF-γ-CT** consistently formed a helical structure (**Figure I-33**), leaving the CF terminal moiety exposed at the peptide periphery.

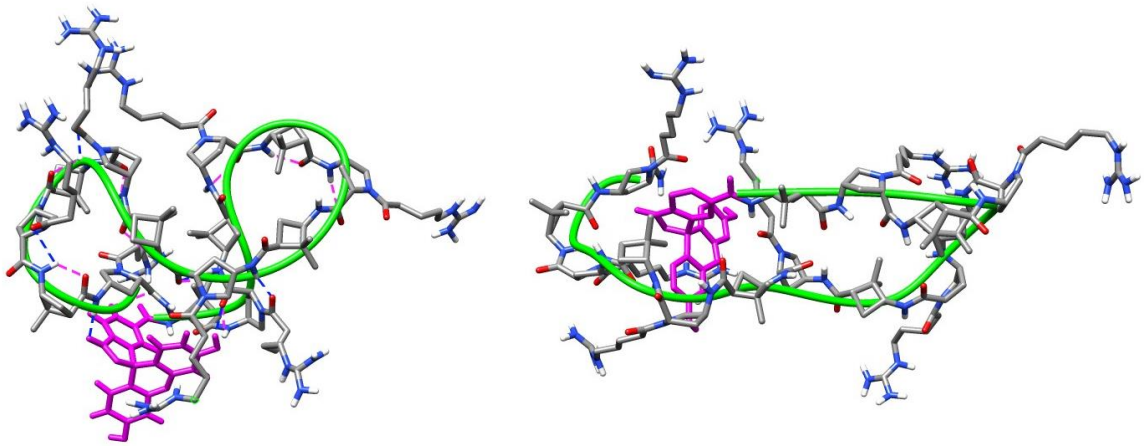

Figure I-32. Conformation predicted by MD simulations for **CF-γ-CC**, hairpin conformation (left) and laminar conformation (right). Peptide scaffold is highlighted by the green ribbon and CF is represented in magenta. Image extracted from reference 183.

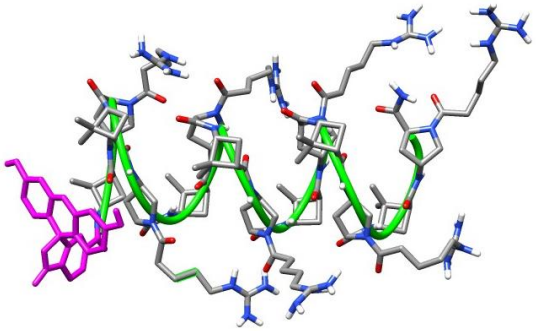

Figure I-33. Conformation predicted by MD simulations for **CF-γ-CT**, helical conformation. Peptide scaffold is highlighted by the green ribbon and CF is represented in magenta. Image extracted from reference 183.

These structural differences likely influence the peptides' lipophilicity. As experimental determination of log*P* values was not feasible, computational calculations were tried to obtain predicted values. Unfortunately, the evaluation through the available open-access tools was limited due to the size of the molecule, obtaining results only with 4 different software programmes. The predicted values obtained did not shed any light on the possible lipophilicity differences expected for the peptides, as only one resource provided different values for both peptides (**Table I-2**). This limitation likely arises from the fact that these resources are typically based on fragment-based methods or QSAR (Quantitative Structure-Activity Relationship) approaches, which calculate hydrophobicity based on the contribution from the different molecular fragments. Hence, these tools are limited when property values for more complex molecules, where secondary structures condition their properties, offering less reliable data.[193]

Table I-2. Predicted log*P* values calculated by different software and web pages.

Software / Web page	log$P_{CF\text{-}\gamma\text{-}CC}$	log$P_{CF\text{-}\gamma\text{-}CT}$
Chem3D[194]	-0.289	-0.289
ADMETlab3.0[195]	-3.104	-3.722
pKCSM[196]	-2.345	-2.345
preADMET[197]	-6.131	-6.131

A more reliable measure of lipophilicity in this case is the retention time (R_t) in RP-HPLC, which correlates with the lipophilicity of the peptides.[159] The retention time of **CF-γ-CC** was 5.127 min, while for **CF-γ-CT** was 7.959 min, indicating that **CF-γ-CT** is more lipophilic. However, this observation contrasts with the previously established trends, where higher lipophilicity was associated with improved mitochondrial uptake, as in this case, **CF-γ-CC**, the less lipophilic peptide based on the R_t, was the only one to penetrate the mitochondria.

This discrepancy may be explained by another important factor in peptide localisation, the charge distribution. As the Kelley's group noted, charge distribution plays a crucial role in mitochondrial uptake. They compared two peptides with identical number of positive charges but differing lipophilicities, and found that, opposite to what was expected, the peptide with higher log*P* and R_t values performed the worst in mitochondrial penetration studies (**Figure I-34**).[159] This was attributed to charge distribution, concluding that, despite the fact that the cluster of polar residues and

hydrophobic residues resulted in a positive outcome for the log*P* parameter, the spatial arrangement of charges was also key for the ability of the peptides to penetrate into the mitochondria.

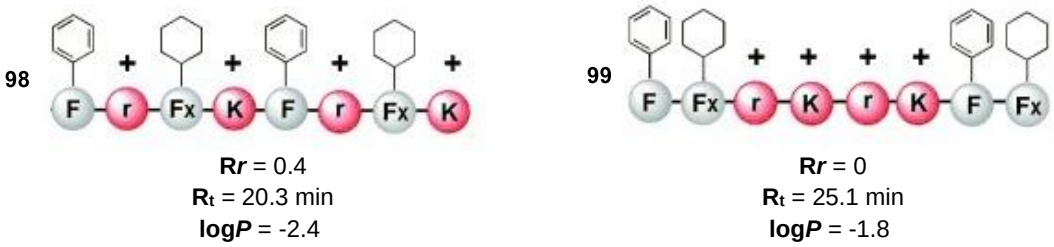

R*r* = 0.4
R_t = 20.3 min
log*P* = -2.4

R*r* = 0
R_t = 25.1 min
log*P* = -1.8

Figure I-34. Peptide sequences studied by Kelley's research group (F: phenylalanine; Fx: cyclohexylalanine; r: D-arginine; K: lysine). Despite the higher lipophilicity, as indicated by RP-HPLC retention times (R_t) and log*P* values, Pearson's correlation (R*r*) values indicated that peptide **99** had no penetration into mitochondria, while peptide **98** showed a moderate mitochondria internalisation. This difference between both peptides were attributed to the charge distribution along the peptide sequences.

Given this, the secondary structure of **CF-γ-CC** and **CF-γ-CT** were re-examined, focusing on the charge distribution. For **CF-γ-CT**, the guanidinium groups were more clustered with five of the residues with separations equal or below 11 Å, whereas **CF-γ-CC** exhibited a more balanced distribution of positive and hydrophobic residues, showing just three of the residues with distances below 11 Å in either of the conformations (**Table I-3**). This spatial arrangement, particularly the well-dispersed positive charges in **CF-γ-CC**, likely facilitated mitochondrial localisation, as has been previously demonstrated in studies of arginine-rich peptides. In these studies, an optimal spatial arrangement of guanidinium groups, determined by the secondary structures of the peptides, influenced their amphipathicity and correlated with their cellular uptake efficiency.[198–201]

Table I-3. Shortest distances between guanidinium groups across the different peptide conformations calculated by MD simulations. Distances were measured using the guanidinium quaternary carbon as the reference point. Refer to **Figures A21** to **A23** in the Annex for detailed conformational distance data.

CF-γ-CC, hairpin	**CF-γ-CC**, laminar	**CF-γ-CT**, helical
7.521 Å	7.885 Å	7.476 Å
7.626 Å	9.084 Å	9.771 Å
9.336 Å	9.900 Å	9.839 Å
14.224 Å	13.278 Å	11.313 Å
14.346 Å	13.897 Å	11.509 Å
17.883 Å	19.379 Å	14.099 Å
18.235 Å	23.117 Å	14.484 Å

Supporting this, Schepartz and colleagues demonstrated that specific arginine topologies were crucial for cellular uptake, with clustered arginine residues favouring internalisation, while a more dispersed arrangement aided endosomal escape.[202] This suggests that the clustered charges in **CF-γ-CT** may promote cell entry, performing even better than **CF-γ-CC** as observed previously,[159,183] but hinder mitochondrial penetration and endosomal escape, consistent with the observed accumulation of **CF-γ-CT** in the nucleus and cytosol (**Figure I-28**, *vide supra*).

In conclusion, **CF-γ-CC** successfully internalised into mitochondria, as confirmed by fibrillar structures and the measurement of the MOC and PCC parameters at the colocalization assays with MitoTracker™ Red CMXRos. In contrast, **CF-γ-CT** showed no mitochondrial uptake, accumulating instead in the cytosol and nucleus. Based on the literature, it appears that the distribution of charges, influenced by the secondary structure of the peptides, is the determining factor for mitochondrial localisation. Consequently, successive studies focused on the **γ-CC** peptide. For that purpose, the ratiometric probe 5(6)-carboxy-SNARF-1 was coupled to the peptide **γ-CC** following a similar procedure used to couple the carboxyfluorescein probe, described in **section 3.2.1**, yielding the peptide **γ-SCC** (**Figure I-35**).

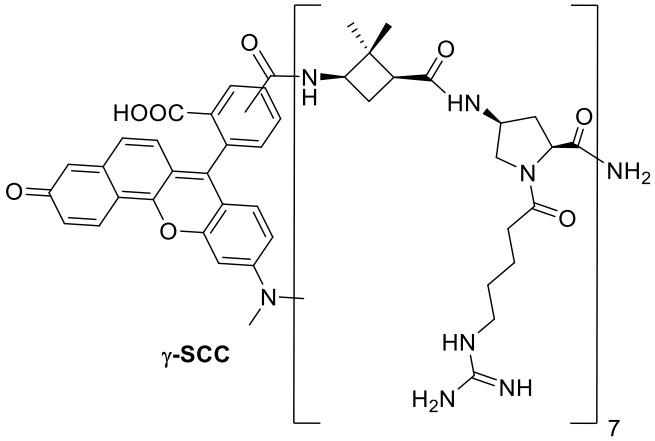

Figure I-35. Structure of the peptide **γ-SCC**.

3.3.2. γ-SCC Peptide Biocompatibility in HeLa cells

One of the most important properties to evaluate any biological application of these peptides is their cytotoxicity. The translocation of CPPs across the plasma membrane may lead to toxic effects due to membrane disruption, particularly at high peptide concentrations. Surpassing the toxic threshold can cause irreversible cellular damage, making the assessment of cytotoxicity essential. **CF-γ-CC** and **CF-γ-CT** cytotoxicity had been assessed in previous studies, showing a cell viability over 90% at the highest concentrations tested (50 μM) upon incubation of the peptides during 24 h with HeLa cells.[183]

In this case, the cytotoxicity of **γ-SCC** was evaluated using the MTT method, which is based on the ability of living cells to reduce the 3-(4,5-dimethylthiazol-2-yl)-2,5-diphenyltetrazolium bromide (MTT) to formazan salts, as a measure of their viability. HeLa cells were incubated during 1 h and 24 h with **γ-SCC** at concentrations up to 1000 μM. The MTT assay confirmed excellent cell viability for the peptide carrier within the tested concentration range, obtaining IC_{50} values of 639 μM and 133 μM for 1 h and 24 h incubation times, respectively. These are values well above the concentrations commonly used in any biological application. Furtheremore, in the same conditions than the previous studies (50 μM, 24 h), **γ-SCC** showed a cell viability over 80%, yielding results similar to those obtained for the carboxyfluorescein-labelled peptides (**Figure I-36**).

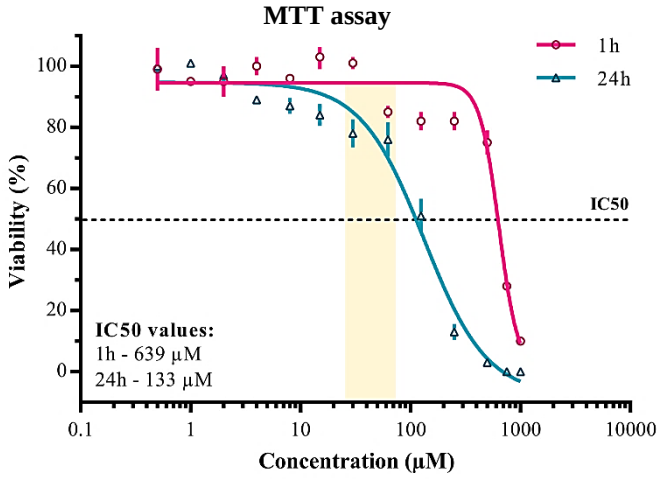

Figure I-36. Cytotoxicity profile after treating cells with increasing concentrations of **γ-SCC** at 1 h and 24 h of incubation. Curve fitting was performed with GraphPad Prism 6 software (v6.01) using a 4-parameters logistic model. In yellow, region of concentrations employed in general assays.

3.3.3. Evaluation of the γ-SCC Peptide Distribution Inside Several Cell Lines

The intracellular distribution of the **γ-SCC** peptide was evaluated using confocal microscopy across several cell lines, including A549 (human lung carcinoma), CHO (Chinese hamster ovary cells), HeLa (human cervical carcinoma), HepG2 (human hepatoblastoma), and Vero (African green monkey kidney cells). Cells were incubated with **γ-SCC** at concentrations of 25, 50 and 75 µM for 1 h. Qualitative analysis of the microscopy images revealed an effective internalisation of **γ-SCC** in all cell lines studied, observing fibrillar structures along the cytoplasm, suggesting mitochondria-penetration (**Figure I-37**).

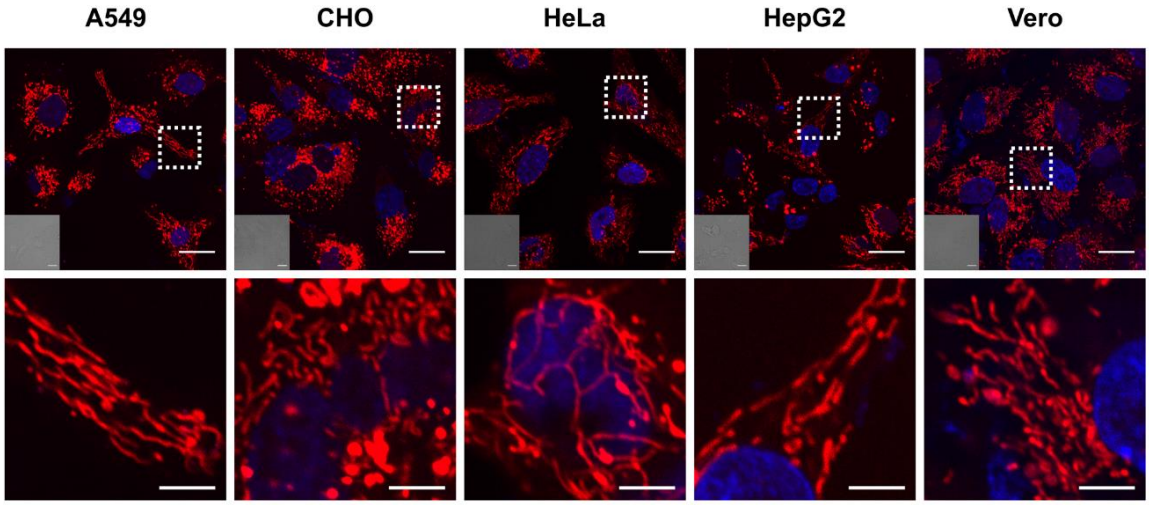

Figure I-37. Confocal microscopy images of the **γ-SCC** intracellular distribution (in red) in various cell lines with the nuclei stained with Hoechst (in blue). The images depicted correspond to cells treated with a concentration of 75 µM. The bottom row images show a representative region of a cell, where an elongated network through the cytoplasm can be observed, resembling mitochondria. Scale bars, 20 µm (5 µm for the magnified images).

To verify its distribution within the mitochondria, colocalization assays were performed using BioTracker 488 Green Mitochondria Dye, a commercial fluorescent dye specifically designed for labelling mitochondria in cells. This quantitative study was done in HeLa cells incubated with 75 µM

concentrations of **γ-SCC,** as this concentration provided the clearest images in the previous assay, and 100 nM concentration of BioTracker 488 Green Mitochondria Dye. The images obtained were analysed to calculate MOC (M_1 = 0.61 ± 0.05 and M_2 = 0.90 ± 0.05) and PCC (R_r = 0.73 ± 0.07) values (**Figure I-38**), concluding that **γ-SCC** peptide exhibits a highly specific and efficient mitochondria internalisation, with superior values than those obtained for the **CF-γ-CC**, and comparable to the best-known mitochondrial-targeting peptides reported by Kelley's research group.[154]

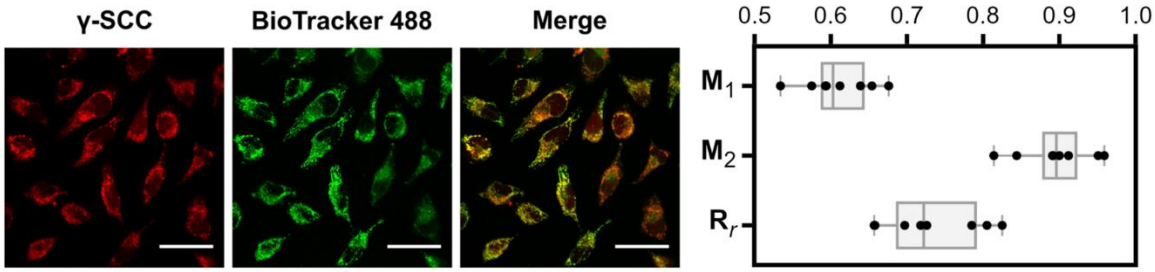

Figure I-38. γ-SCC colocalization assays. Left: Representative images of a set (n = 8) employed for evaluating **γ-SCC** (in red) mitochondria colocalization with BioTracker 488 Green (in green). The merge images of both channels are shown. Scale bars, 50 μm; Right: Representation as box plots of the MOC and PCC values calculated from a set of 8 independent images. Whiskers represent the total range of values within each sample.

To ensure that the mitochondrial localisation properties are attributed to the peptide structure and not to the attached probe, control experiments were conducted by incubating HeLa cells with the SNARF-1 probe alone at peptide test concentrations. Confocal microscopy images showed a distinct pattern compared to **γ-SCC**, showing a more punctate cytoplasmic distribution, consistent with endosomal entrapment. This confirms that the probe alone has minimal mitochondrial internalisation (**Figure I-39**).

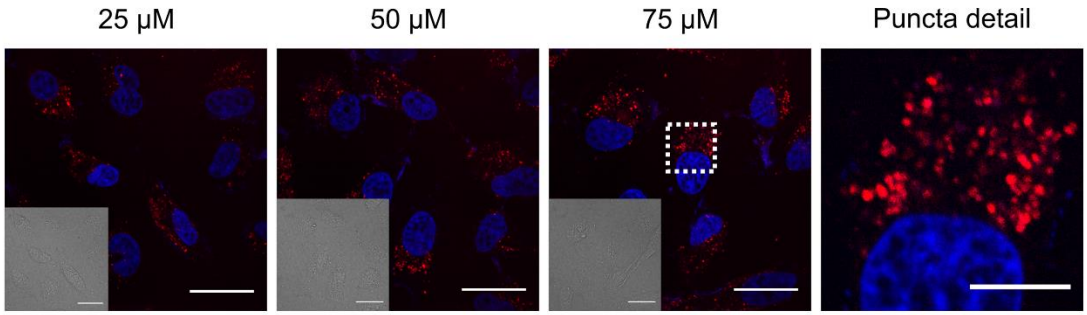

Figure I-39. Confocal microscopy images of SNARF (in red) intracellular distribution with nuclei stained with Hoechst (in blue) and differential interference contrast images provided in insets. A representative cellular region is depicted at the right, showing a punctuate pattern. Note that it was necessary to increase laser intensity and contrast to see the probe distribution, as its internalisation was much lower than the peptide conjugate. Scale bars, 30 μm (10 μm for the magnified image).

Once the ability of the **γ-SCC** to penetrate the mitochondria was confirmed through both qualitative and quantitative analyses, and control experiments supported that this property is inherent to the peptide rather than the attached probe, further investigations into the properties of the peptide were pursued.

3.3.4. Resistance to Enzymatic Hydrolysis of γ-CC and γ-SCC Peptides

One of the challenges for the use of peptides in biological applications is their sensitivity to enzymatic degradation. Biological fluids are aggressive environments for peptides due to the presence of proteases and peptidases, which significantly limit their therapeutic potential by reducing circulation half-life and bioavailability. These enzymes are particularly abundant in biobarriers that serve as defense mechanisms for the body. Consequently, assessing the metabolic stability of CPPs is essential to maximise their effectiveness and ensure successful *in vivo* applications.

First, the resistance to enzymatic degradation of the **γ-CC** peptide without any probe attached was evaluated. Its structural integrity was monitored following incubation with trypsin, a peptidase, and using 4-acetamidobenzoic acid (ABA) as an internal standard. Additionally, two peptides containing cationic residues, **R8** (CPP) and **KLAK** (cytotoxic peptide), were used as controls to verify trypsin activity. Upon enzyme addition, both control peptides rapidly degraded within 5 minutes of incubation, as indicated by the disappearance of their original peaks and the appearance of lower retention time peaks corresponding to peptide fragments. In contrast, **γ-CC** retained its original peak even after 24 hours of incubation, demonstrating a remarkable resistance of the peptide to enzymatic degradation, which is a major advantage for biological applications (**Figure I-40**).

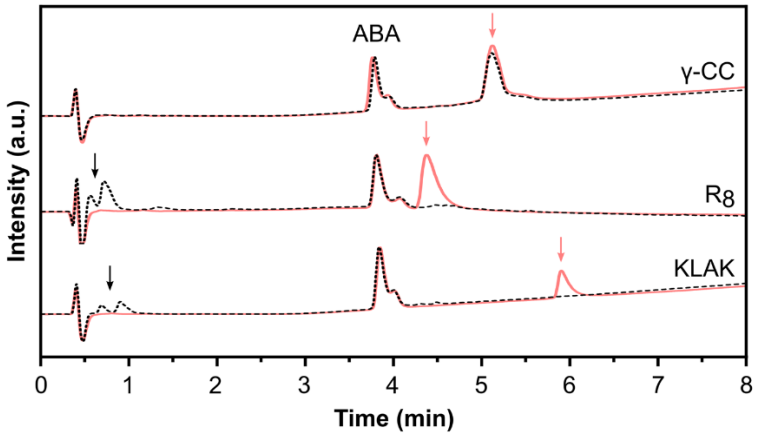

Figure I-40. Chromatograms of **γ-CC** and control peptides, **R8** and **KLAK**, before (pink lines) and after (black dotted lines) incubation with trypsin (24 h incubation for **γ-CC**, 5 min for control peptides). Pink arrows indicate intact peptide peaks; black arrows, fragmented peptides resulting from enzymatic activity. Internal standard ABA is present in all chromatograms.

Following the positive results with the **γ-CC** peptide, it was further explored whether **γ-SCC** could maintain its bioavailability and structural integrity after incubation in the presence of fetal bovine serum (FBS). Serum contains several peptidase and proteases that degrade peptides, as well as proteins that could interfere with peptide-cell interactions.[203,204] To asses this, HeLa cells were incubated with **γ-SCC** for 1 h in the presence of 10% FBS. Confocal microscopy images showed efficient mitochondrial accumulation (**Figure I-41**, **left**), similar to the results observed in serum-free conditions (**Figure I-37**), confirming the activity of the peptide in the presence of serum.

To confirm the peptide stability for longer periods of incubation, **γ-SCC** was dissolved in complete DMEM (Dubelco's Modified Eagle's Medium) containing 10% FBS and incubated at 37 ºC for 7 days, after which its mitochondrial targeting ability was re-evaluated. Impressively, even after this long period of incubation, the peptide retained its functionality and continued to accumulate in the mitochondria (**Figure I-41**, **centre-right**).

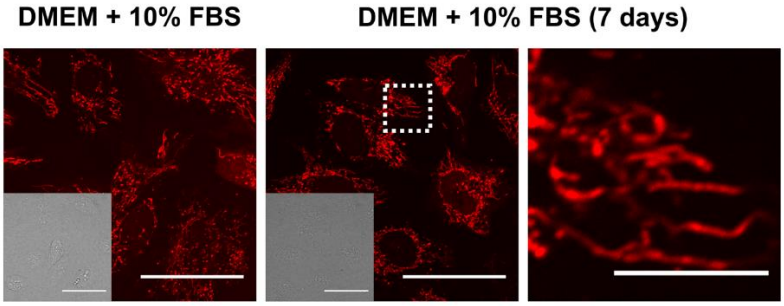

Figure I-41. γ-SCC distribution after HeLa cells incubation in the presence of 10% serum for 1 h (left) or after pre-incubation in complete DMEM (10% FBS) for 7 days (centre-right). A representative cellular region is magnified (right). Differential interference contrast images are provided in insets. Scale bars, 50 μm (10 μm for magnified image).

This prolonged stability was attributed to the presence of non-natural amino acids. Unlike conventional peptides, which typically exhibit short half-lives in serum (minutes to hours) due to rapid degradation by proteases,[100] **γ-SCC** demonstrated enhanced resistance to enzymatic hydrolysis, making it a promising candidate for applications requiring extended stability in biological environments.

3.3.5. Study of the Mechanism of Penetration of the γ-SCC Peptide

As introduced in **section 1.1.3.**, there are many mechanisms for peptides to penetrate into the cells. Understanding the mechanism of cell internalisation of peptides is crucial for the development of peptide-based therapeutics and delivery systems. The efficiency with which a peptide can cross the plasma membrane and reach its intracellular target determines its potential for therapeutic applications. Additionally, understanding the internalisation mechanism allows the optimisation of the peptide structure to improve targeting specificity.[138]

To elucidate the mechanism of internalisation of the **γ-SCC** peptide into the cell, intracellular delivery studies in HeLa cells in the presence of endocytic inhibitors were conducted (**Figure I-42**), Inhibitors of dynamin-dependent (dynasore, Dyn) and clathrin-mediated endocytosis (chlorpromazine, CPZ) resulted in a reduction of total peptide uptake, suggesting that endocytosis partially contributes to the internalisation process. On the other hand, inhibitors of micropinocytosis (5-(*N*-ethyl-*N*-isopropyl)-amiloride, EIPA) had a minor effect. The involvement of energy-dependent pathways was further supported by decreased internalisation when metabolic inhibitors capable of depleting intracellular ATP (sodium azide and 2-deoxy-D-glucose, NaN_3/DOG) were applied. However, even in the absence of this pathway, approximately half of the intracellular peptide signal persisted, indicating that **γ-SCC** can also directly translocate across the plasma membrane into the cytosol. Lastly, the reduction of uptake after membrane depolarisation induced by high potassium

buffer (K^+PBS) suggests that, like many carriers that contain cationic moieties,[205] the translocation of the peptide is driven by the membrane potential across the plasma membrane.

Altogether, these findings indicate that **γ-SCC** peptide enters into cells through a mixed mechanism involving both energy-dependent endocytosis and direct translocation facilitated by the negative membrane potential. Additionally, the excellent mitochondrial labelling and minimal punctuate fluorescent patterns observed in confocal images (**Figure I-37**, *vide supra*) indicate that **γ-SCC** efficiently escapes from potential endosomal compartments formed after the energy dependent endocytic uptake.

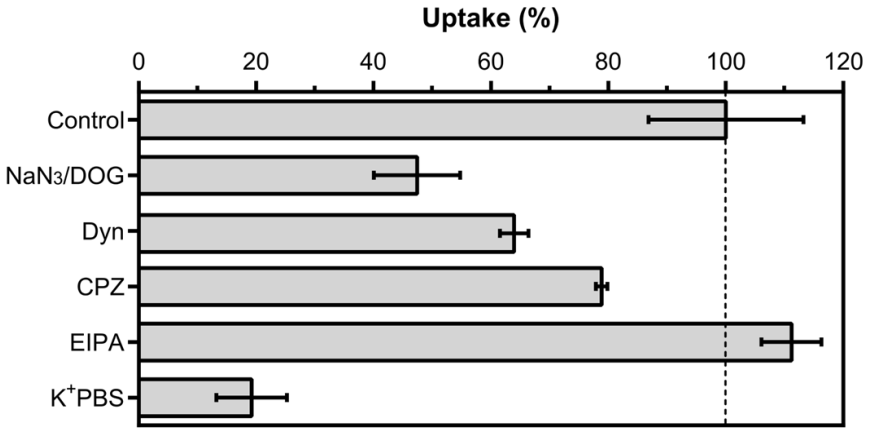

Figure I-42. Representation of the data obtained for the uptake mechanism studies with **γ-SCC** in the presence of different cellular internalisation inhibitors. Data presented as mean ± standard deviation.

3.3.6. Exploration of the Potential Applications of the γ-SCC Peptide

The straightforward labelling procedure and the reliable staining capability of the developed peptidomimetic **γ-SCC** represents an opportunity for its application in mitochondrial research. For that reason, two specific applications have been investigated, showcasing the versatility and potential of this novel mitochondria-penetrating peptide.

3.3.6.1. Monitoring of pH_m

As exposed in **section 1.2.2.**, mitochondrial pH (pH_m) is a crucial factor that influences essential cellular processes like metabolism, membrane potential, apoptosis, and reactive oxygen species (ROS) production. Therefore, measuring pH_m serves as an indicator of both mitochondrial and overall cellular function. Besides the successful FRET-based genetically encoded ratiometric pH sensors that can be selectively expressed in mitochondria,[206] small-molecule ratiometric pH sensors are particularly appealing due to their straightforward staining process, ease of reproducibility, and broader range of emission wavelengths available for imaging. The selected SNARF probe, which functions as a dual emission system, is well-suited for pH monitoring due to its significant emission shift in response to pH changes. Previous methods to measure pH_m with SNARF required additional mitochondria-specific dyes, such as $DiOC_6$ (3,3'-dihexyloxacarbocyanine iodide) or MitoTracker™ Green, or precise optimisation of dye loading based on anion transporter activity to ensure mitochondrial targeting.[177,207,208] In contrast, our system efficiently targets the ratiometric SNARF probe directly to the mitochondria, providing a

streamlined method for accurate pH_m measurement. To test this, HeLa cells treated with the labelled peptide, **γ-SCC**, were imaged at the maximum emission peak wavelength of the acidic phenol form (584 nm) and the basic phenolate form (633 nm). A calibration curve was generated by diluting **γ-SCC** in buffer and acquiring data under identical conditions. Using this calibration, the ratio of each pixel in the cell micrographs was calculated, translating it into a pH value by solving the obtained 4-parameters logistic model (**Figure I-43**). The constructed system determined a mean pH_m value of approximately 7.2, coinciding with an average between the pH values of the mitochondria matrix and the intermembrane space.[209,210] The accurate measurement of pH_m opens the possibility of applying this system to the detection of pH_m deviations in dysfunctional cells, allowing extrapolation of mitochondrial health status and insight into potential disease mechanisms.

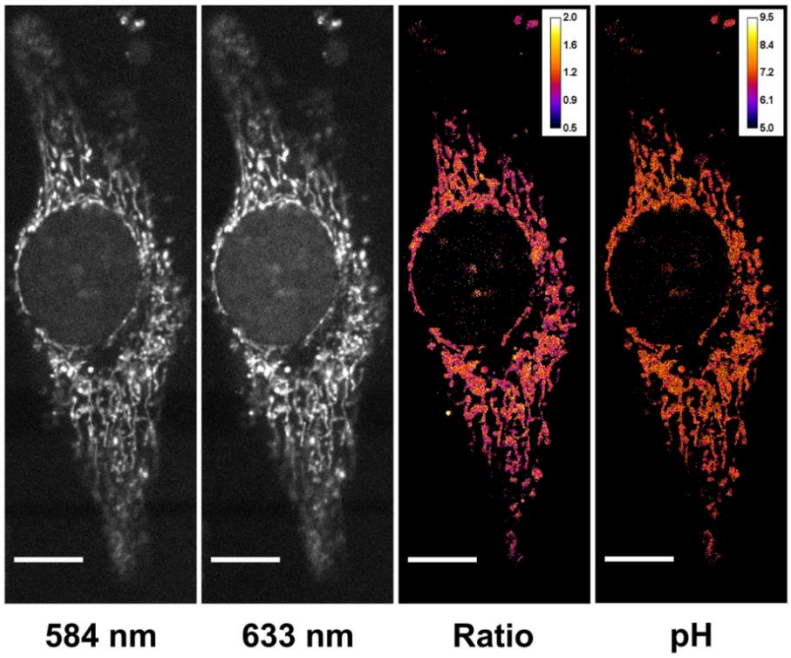

Figure I-43. Image analysis for measuring pH_m. The images at the two maximum emission peak wavelengths, their ratio, and the calculated pH image applying the calibration are shown. Scale bars, 10 μm.

I.3.3.6.2. Tracking of the mitochondria dynamics

Mitochondria are highly dynamic organelles, constantly changing their shape and size through complex fusion and fission events, while being actively transported to specific locations within the cell. These dynamic processes are essential for cellular development, apoptosis, and various diseases, highlighting the importance of real-time tracking techniques.[211]

In this regard, our labelled peptide, **γ-SCC**, enabled real-time visualisation of mitochondrial dynamics in living cells. HeLa cells were incubated with the peptide and observed over time using confocal microscopy. Mitochondrial images were captured every 5 seconds, creating videos that recorded dynamic processes, such as fission events (**Figure I-44A**) and mitochondrial movement throughout the cytoplasm (**Figure I-44B**).

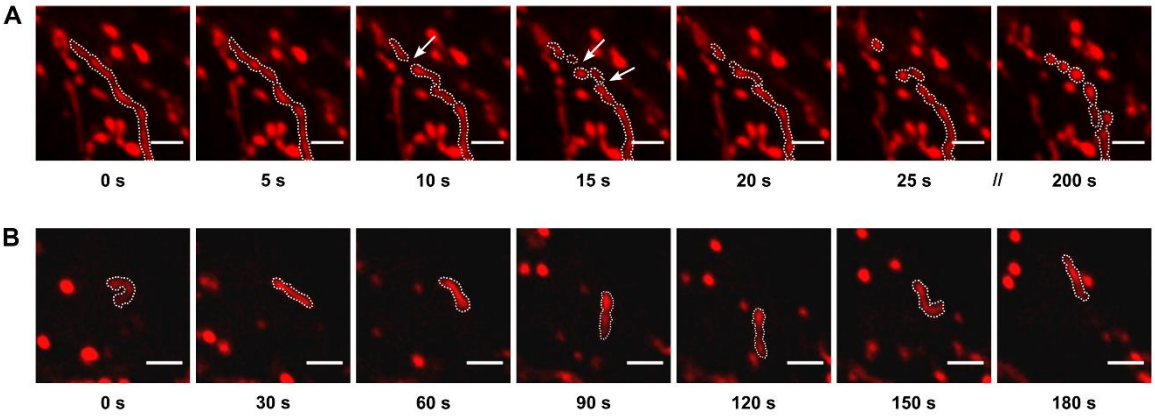

Figure I-44. Real-time tracking of mitochondria dynamics: A) Confocal microscopy images of a mitochondria fission event over a period of 200 s, with images acquired at 5 s intervals. B) Observation of mitochondria movement over a period of 180 s. Scale bars, 2 µm.

Since mitochondrial dynamics studies require frequent imaging over extended periods, **γ-SCC** demonstrated excellent mitochondrial retention and resistance to photobleaching, maintaining stable fluorescence under challenging imaging conditions, performing on par with commonly used mitochondria-targeting fluorophores. This system could then be applied to the investigation of mitochondria-related disease mechanisms through real-time monitoring of mitochondrial dynamics, offering valuable insights into how these processes are altered under pathological conditions.

4. Conclusions

The aim of the current thesis chapter has been successfully achieved, demonstrating the potential of γ-CBAA/γ-amino-L-proline tetradecamer hybrid peptides as mitochondrial penetrating peptides. These findings contribute significantly to our understanding of peptidomimetic scaffolds as versatile tools for cellular delivery, particularly targeting mitochondria, a critical organelle involved in various metabolic processes and diseases.

To accomplish it, the constituting monomers of the hybrid peptide were synthesised in gram-scale with satisfactory yields. The synthesis of the cyclobutane amino acid (1*S*,3*R*)-3-amino-2,2-dimethylcyclobutane-1-carboxylic acid (**59**), was successfully replicated based on the previously reported procedures. This was followed by the synthesis of the *cis*- and *trans*-isomers of γ-amino-L-proline derivatives, **60** and **61**, using a novel strategy to insert the side chain in solution and avoiding the inconvenience of installing this moiety during the SPPS.

Subsequently, the synthesis of γ,γ-peptidomimetic tetradecameric hybrid oligomers was accomplished using a combination of Fmoc/Boc strategies in solid-phase peptide synthesis, to which the fluorescent probe carboxyfluorescein (CF) was coupled, yielding the target structures, **CF-γ-CC** and **CF-γ-CT**, required for biological evaluations.

Biological studies confirmed, through confocal microscopy and cellular uptake assays in HeLa cells, a difference in the cell distribution for both peptides, observing an efficient mitochondrial penetration only with **CF-γ-CC** peptide, while **CF-γ-CT** was localised in the cytosol and the nucleus. These differences were attributed to their secondary structure, that influenced the distribution of the charges, which is a key factor for the interaction with the mitochondrial membrane and the endosomal scape.

The ratiometric probe 5(6)-carboxy-SNARF-1 was conjugated to the peptide **γ-CC**, yielding a novel peptidomimetic structure named **γ-SCC**. The **γ-SCC** peptide maintained excellent biocompatibility, offering a high cell viability percentage and EC_{50} values significantly exceeding the concentrations required for biological applications. In addition, cell uptake and mitochondria colocalization studies confirmed that the mitochondrial targeting properties remained unchanged, confirming that these are inherent to the peptide structure.

The integration of non-natural amino acids provided the **γ-SCC** peptide with exceptional stability, as evidenced by its resistance to enzymatic degradation and sustained bioavailability in the presence of trypsin and serum. This enhanced stability makes the peptide highly suitable for time-extended applications.

The **γ-SCC** peptide internalises *via* an energy-dependent endocytic pathway and direct translocation, ultimately accumulating in mitochondria due to their membrane potential. Preliminary studies have shown promising results in real-time mitochondrial dynamics tracking and pH monitoring, underscoring the potential of this system for advancing mitochondrial research.

Overall, the promising results obtained from these studies highlight γ,γ-peptidomimetics as valuable alternatives to conventional peptides. These finding pave the way for the development of innovative therapeutic agents and molecular tools to target mitochondria.

Chapter II

Novel Bifunctional Ligands for PET Imaging with ^{64}Cu and ^{68}Ga Radioisotopes

Positron emission tomography (PET) is a highly sensitive and quantitative imaging technique that has gained importance in the recent years, especially in dual-modal imaging. As a consequence, positron emitting isotopes research has been exploited. The archetypical PET isotope is ^{18}F, but its half-life and production characteristics limit its applications. Other radiometals such as ^{68}Ga, with an easier production system, and ^{64}Cu, with an extended half-life, offer an alternative to ^{18}F, expanding the range of situations in which PET can be used. As radiometal-based pharmaceuticals rely on bifunctional chelators (BFCs), novel ligands to chelate these metals have to be investigated. In this chapter, acyclic type cyclobutane-containing ligands are synthesised and proposed as candidates to chelate ^{64}Cu and ^{68}Ga efficiently and potentially be used as contrast agents for PET imaging.

1. Introduction

1.1. Molecular Imaging: Applications and Modalities

Over the past few decades, much research attention has been directed towards the development of *in vivo* imaging techniques. The combination of various scientific disciplines, including chemistry, physics, engineering, and biology, has led to the emergence of a new field called **molecular imaging**. This field has changed the way medicine is practiced, allowing us to visualise, characterise, and measure biological processes at the molecular and cellular levels in living systems.[212]

The imaging technique must be sensitive enough to detect biochemical events (mM to nM scale), and clinically relevant changes over time, while also having an adequate spatial resolution (µm to mm range). The development of novel contrast agents, ligands, and probes has improved molecular imaging techniques such as fluorescent imaging, magnetic resonance imaging (MRI), single photon emission computed tomography (SPECT), and positron emission tomography (PET). These techniques provide early disease detection, useful information about disease characteristics, and therapeutic efficacy.[213] Furthermore, they also offer the possibility of repetitive, uniform, non-invasive and comparative automated studies, which can help gather data for longer periods of time.

Imaging modalities can be broadly divided into morphological/anatomical and molecular imaging techniques. Molecular imaging modalities, such as optical imaging, PET, and SPECT, are able to identify disease-related molecular and cellular alterations. These techniques are characterised by their high sensitivity, but they lack spatial resolution. On the other hand, anatomical imaging techniques, such as computed tomography (CT), ultrasound (US), and MRI, provide high structural resolution and detailed information about major structures, but they have low sensitivity. Each imaging modality has certain advantages as well as limitations, being more complementary techniques than competitive (**Figure I-45**).[214] The recent rise of dual-modal or bi-modal molecular imaging techniques is evidence of this. Dual-modal imaging involves the combination of two imaging techniques, either by using both at the same time or by combining the images obtained in the post-processing stages.[215]

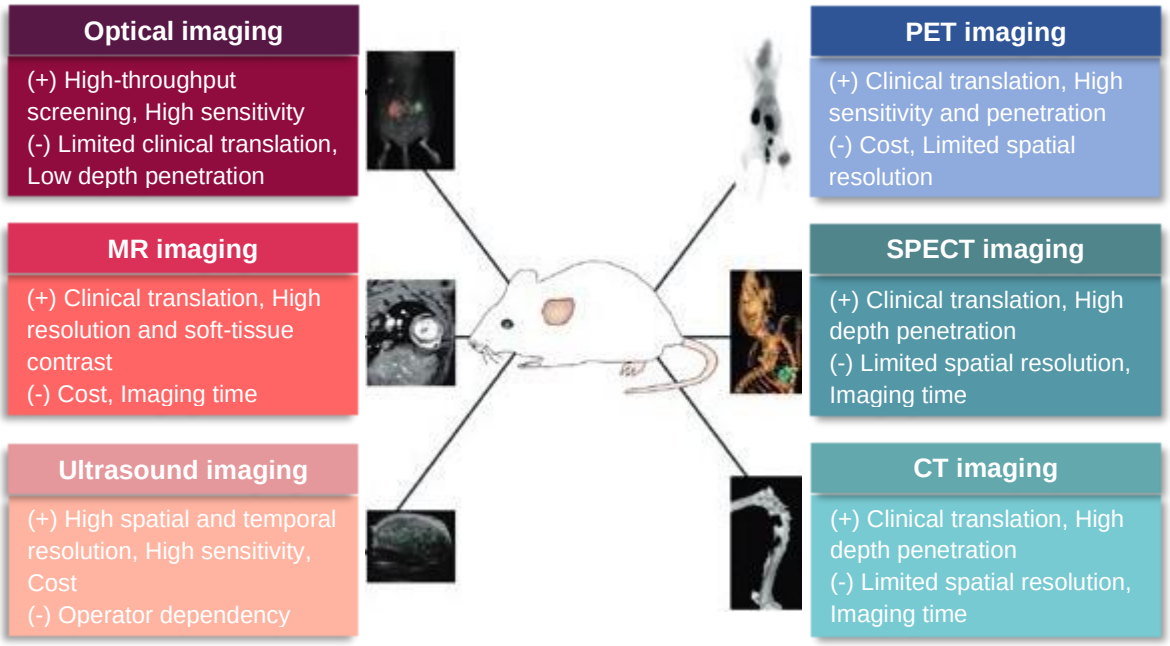

Figure I-45. Advantages and drawbacks of different molecular imaging modalities.

1.2. Positron Emission Tomography (PET)

Positron emission tomography (PET) is a non-invasive molecular imaging technique that provides three-dimensional images of functional processes *in vivo*. Originally used as a research tool, it has gained importance in medical diagnostics, especially in oncology, cardiology, and neurochemical processes. Due to its great sensitivity and resolution, PET not only allows for visualisation but also enables the measurement and quantification of physiological processes. As an example, it has been shown that quantitative uptake measurements of 2-deoxy-2-[^{18}F]fluoro-D-glucose, or ^{18}F-fluorodeoxyglucose (^{18}F-FDG), in tumours can be useful in the assessment of response to therapy.[216,217]

These characteristics are related to the use of radioactive probes. By monitoring the amount and distribution of radioactively labelled molecules, *via* the radioactive decay, high-resolution images in opaque tissues can be obtained. This is an advantage over techniques that use fluorescent probes, which are limited by the scattering of light.

The signalling molecule, which contains a **positron (β^+) emitting radionuclide** (*e.g.*, ^{15}O, ^{18}F, or ^{64}Cu), is injected into the subject of study. Subsequently, it binds to its specific targeted molecule, or it is internalised in the cells of interest, depending on the characteristics of the vector. Then, the positron particles emitted by the radionuclide encounter electrons in a process called annihilation. In this process, energy is released in the form of two gamma rays emitted in opposite directions. The PET scanner will be able to detect these gamma rays and measure the concentration of the emitting probe in a certain area. After computer processing, three-dimensional images of the targeted molecules are provided (**Figure I-46**).

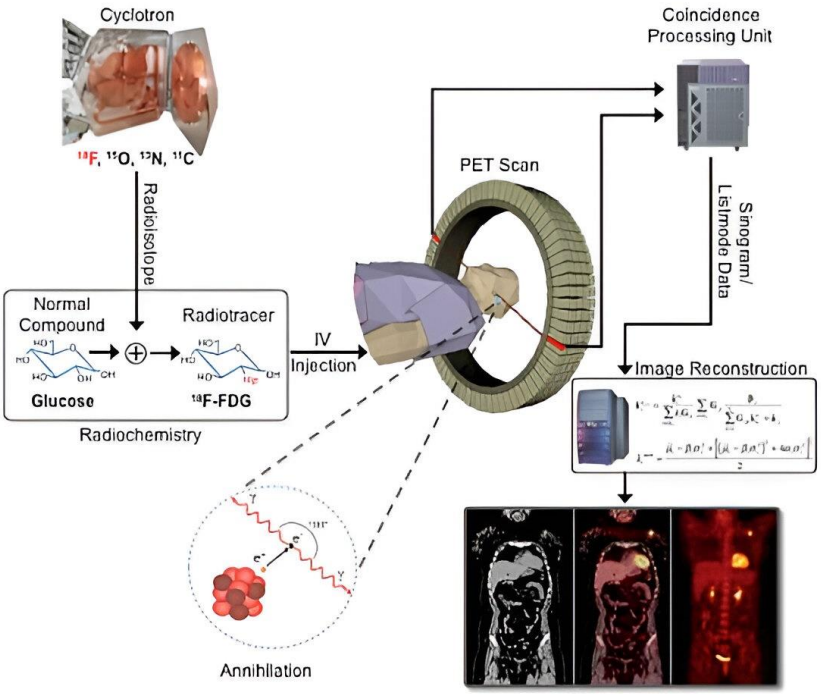

Figure I-46. PET scan process. Example with ^{18}F-FDG.[218]

As it is possible to pinpoint molecular activity within the body with this technique, there is the potential to identify a disease in its earliest stages, often long before other tests are able to reveal abnormalities. However, despite the fact that it is a sensitive technique (10^{-12} M), it has low spatial resolution (>2 mm). This means that it is not immediately clear from a PET scan which tissues are present or whether the anatomy is abnormal. Consequently, it is a more suitable technique for the study of molecular changes in a time window of minutes or longer. In addition, the resolution of the technique will be dependent on the energy decay of the particles emitted. The larger the positron energy, the greater the average distance that the particle will travel before encountering an electron, resulting in a major loss of spatial resolution. As a result, lower energy positron emission is desirable for PET, which will depend on the isotope used. Another drawback of this technique is the necessity of "on-site" cyclotrons for the obtention of the traditional isotopes, due to their short half-life, increasing the cost of the technique.

To tackle these drawbacks, in recent years research has focused on the use of new radioisotopes (*e.g.*, ^{64}Cu, ^{68}Ga, or ^{89}Zr). The properties and advantages of these metals, as well as the design and development of ligands that can chelate them efficiently, will be discussed in the following sections.

1.3. Design, Construction, and Evaluation of Radiopharmaceuticals

Molecular imaging is based on the acquisition of high-resolution images using an image contrast source. This contains different parts that depend on the requirements of each imaging technique. In the case of PET imaging, the **radionuclide**, which acts as the emitting particle, needs to be bound by a **bifunctional chelator (BFC)**. This ligand chelates the radiometal and can simultaneously attach a **vector** or **targeting moiety**, which is responsible for identifying a disease-

specific target. Peptides, antibodies, and small molecules are some examples of targeting moieties. These vectors are attached through a **linker** to the BFC. These four parts set up what is called a **contrast agent** (**Figure I-47**), and each part will be tuned depending on the characteristics of the molecular imaging modality to ensure favourable pharmacokinetics, binding specificity, and stability of these agents.[219] Factors such as the charge, polarity, denticity, donor atom type (*e.g.*, N, O, or S) and kinetics must be modular in order to optimise the *in vivo* behaviour of a radiopharmaceutical, and this requires the availability of many different bifunctional chelators. Properties such as size, mass, charge, and lipophilicity have also an impact on the biodistribution, clearance and solubility of the radioactive drug in the body. Components must be carefully chosen when designing a successful radiopharmaceutical, being mutually complementary in order to work as a unified agent. The synthetic arsenalre of the radioactive imaging agents drug components will always have space for innovation, so they can be continually improved.

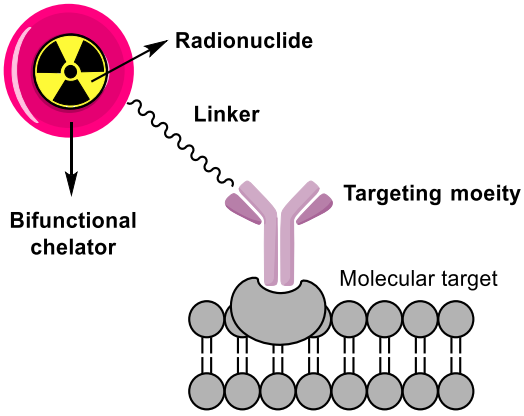

Figure I-47. General structure of the different parts of a molecular imaging contrast agent.

1.3.1. Radionuclides for PET Imaging

Dozens of radiometals have been considered for use in nuclear imaging. The radionuclide must fulfil the specific imaging needs, which will depend on the biological target, the desired imaging duration, or the radiolabelling methods. Then, an isotope with a suitable half-life, decay mode and particle energy, among other radiochemical and radiopharmacological properties, will be chosen.[220] Besides these, the ease of obtaining the isotope or the imaging facility capabilities will also determine the radiotracer used.

Nowadays, the most widely used radiotracer for PET imaging is ^{18}F. It has a 97% probability of positron decay, which is considered a high branching ratio, and one of the lowest maximum kinetic energies (E_{max} = 0.635 MeV), providing best image resolution. The most common use of ^{18}F is to couple it to a glucose analogue, ^{18}F-FDG, to visualise areas with increased glucose metabolic rates, which can be useful for cancer diagnosis.[221] However, due to ^{18}F short half-life ($t_{1/2}$ = 109 min), there is a need for an “on-site” cyclotron, increasing the cost of this technique. Additionally, ^{18}F-FDG lacks target specificity, due to its mechanism of action, so it cannot differentiate between a tumour-associated high metabolic rate and one due to infection or inflammation. When it comes to clinical applications, despite the fact that it has been proven useful for oncology diagnostics, a 2015 meta-

analysis[222] concluded that ^{18}F-FDG uptake in cancer patients shows just a moderate correlation to tumours tissue, as its uptake is also enhanced in other inflammatory and infectious diseases. Furthermore, there are tumours where the FDG uptake cannot be high enough to have a proper imaging, like early-stage prostate cancer and some types of gastric cancer.[223,224] As an alternative, ^{18}F can be coupled to proteins or antibodies, which are tracers that are more target-specific than glucose, but it might not be as straightforward as with other radionuclides. This results in multi-step syntheses that reduce the yield and prolong the synthesis time.

The study of other radioisotopes (**Table I-4**), with the aim of using them as radiotracers for PET imaging, offers the possibility of conjugating different vectors, generating a wide range of contrast agents that can target many diseases and molecular processes, thus expanding the usability of the PET imaging technique.

Table I-4. Properties of the most recent investigated radioisotopes for PET imaging compared to ^{18}F.[225,226]

Isotope	$t_{1/2}$ (h)	Method of production	Decay mode
^{18}F	1.8	Cyclotron	β^+ (97%) EC[(a)] (3%)
^{44}Sc	3.9	^{44}Ti/^{44}Sc generator	β^+ (94%) EC[(a)] (6%)
^{64}Cu	12.7	Cyclotron	β^+ (19%) EC[(a)] (43%) β^- (38%)
^{68}Ga	1.1	^{68}Ge/^{68}Ga generator	β^+ (89%) EC[(a)] (11%)
^{86}Y	14.7	Cyclotron	β^+ (34%) EC[(a)] (66%)
^{89}Zr	78.5	Cyclotron	β^+ (23%) EC[(a)] (77%)

a) EC: Electron capture

1.3.1.1. ^{64}Cu: Looking for a Longer Half-life

The presence of multiple copper isotopes, useful for diagnosis (^{64}Cu) or radioimmunotherapy (^{67}Cu), has attracted considerable interest for Cu(II). It is well-established that it is attracted to donor atoms such as nitrogen due to its borderline hard cation nature. Its coordination number (CN) ranges between 4 and 6 and its ionic radius size (57 to 73 pm) makes it more suitable for the formation of six-membered chelate rings. Cu(II) coordination allows various geometries depending on the CN, highlighting the distorted octahedral (CN = 6), that shows a tetragonal distortion due to the Jahn-Teller effect, to which Cu(II) is particularly susceptible due to is $3d^9$ electronic configuration. In such chelates, there is an uneven electron distribution in their *d* orbitals, showing axial metal-ligand bonds that differ in length from those in the equatorial positions, indicating that the octahedron is distorted, either elongated or compressed.[227] This is particularly important for determining the bond lengths and overall geometry, affecting the behaviour of the complex and the metal-ligand interaction. Moreover, Cu(II) chelates are susceptible to reduction *in vivo*, which can lead to radiocopper loss due to the lability of Cu(I), reducing image quality. Hence, kinetic inertness is a challenge in the design of Cu complexes.

The radiometal ^{64}Cu has become increasingly popular in recent years because of its favourable β^+ emission properties for PET imaging and its intermediate half-life (12.7 h), which makes it suitable to be used with peptides and antibodies. This extended half-life, compared to ^{18}F, provides logistical advantages for its production, and enables the study of slower pharmacokinetics or delayed target uptake processes. ^{64}Cu also undergoes β^- emission, making it useful for therapy, in addition to PET imaging, due to its cytotoxic potency.[228] Therefore, there has been strong interest in developing new and improved bifunctional chelators to optimise radiolabelling procedures and *in vivo* performance with copper isotopes. Nowadays, there are more than 20 clinical trials involving ^{64}Cu as a radionuclide, most of them with the objective of cancer diagnosis or the study of cancer treatment efficiency.[229]

1.3.1.2. ^{68}Ga: Easier Production, Reducing Costs

Ga(III) is an acidic metal species because of its high cation density and short ionic radius (62 pm).[230] It strongly binds to ligands featuring multiple anionic oxygen donor sites, although it has also been shown to have good affinity for thiolates and amines. With a coordination number between 4 and 6, hexadentate ligands are known for being the most thermodynamically stable and kinetically inert due to the formation of distorted octahedral complexes.[231] Unlike Cu(II), Ga(III) has a very slow water exchange, which is positive in terms of stability. However, the control of the pH in aqueous media is an important factor in the inertness of the complexes, as precipitation problems can occur when pH is raised above 4 due to the formation of $Ga(OH)_3$. Demetallation of the complexes may also happen at pH > 7, because of the formation of gallate anion $[Ga(OH)_4]^-$. About its behaviour *in vivo*, the affinity of Ga(III) for transferrin protein, which is essential for tumour localisation, is well known.[232]

Radiogallium isotopes have been extensively investigated, as they have suitable properties for their usage in radiopharmaceutical applications. ^{67}Ga is used in SPECT, while ^{68}Ga is used in the development of PET imaging agents. ^{68}Ga is, perhaps, the most promising radioisotope for PET imaging applications due to its easier production with the ^{68}Ge/^{68}Ga generator system, which has a shelf-life of up to one year. This positron-emitting radioisotope can be easily obtained on-demand through this commercialised system, avoiding the need for an “on-site” cyclotron, which reduces the cost of the PET imaging technique and enables wider availability of the radiotracer. On one hand, the high positron energy of ^{68}Ga (E_{max} = 1.88 MeV) can be seen as a negative point for this isotope, as it will provide lower resolution images when compared to other positron-emitting isotopes. But, due to its favourable branching ratio (89% β^+), shorter acquisition times can be performed to obtain the image and the interference by gamma emission is almost inexistent. With a half-life ($t_{1/2}$ = 68 min) suitable for use with antibodies fragments and peptide vectors, a wide range of ^{68}Ga chelators are under investigation to provide useful diagnostic tools to the medical community. Currently, there are more than 50 clinical trials involving ^{68}Ga as a radionuclide, with special importance in the study of prostate cancer by attaching the complex to PSMA (prostate-specific membrane antigen).[229]

1.3.2. Bifunctional Chelators (BFCs)

Radioactive isotopes need to be coupled to targeting molecules or vectors so that they can be guided to specific targets without releasing the metal in other parts of the biological system. Non-metallic isotopes (*e.g.*, ^{11}C, ^{15}O, ^{18}F) can be directly attached to biological vectors through covalent bonds (*e.g.*, ^{18}F-FDG), however, a wide variety of metal radionuclides are complexed with **bifunctional chelators (BFCs).** These ligands have the ability to form strong coordinative bonds with the metals, ensuring the stability of the complex *in vivo*, while also incorporating a functional group that enables covalent conjugation with targeting vectors. The functionalisation can be introduced in one of the pendant arms, but this could negatively impact the coordination of the metal. Therefore, it is desirable to functionalise a non-crucial position of the chelator.

Each radionuclide has unique chemical requirements, including ligand donor atom preferences (*e.g.*, N, O, S), coordination number, and coordination geometry. Therefore, it is particularly important to choose the correct chelator for the specific radiometal, fulfilling some important requirements:

- A straightforward **synthesis of the ligand** with a scalable and cost-effective process.
- The complexation of the radioisotope with the chelator (**radiolabelling**) should be fast at low temperature and concentration, and with suitable pH conditions for biological applications.
- **Thermodynamic stability** and **kinetic inertness** of the complex are important factors that will determine its stability *in vivo*.
- Versatility in the **conjugation chemistry** of vectors.

The main objective of metal complexation with a chelator is to prevent the release of free metal *in vivo*, which could result in toxicity and poor image quality. The stability of the complex can be affected by a number of unfavourable events, such as transmetallation, hydrolysis, or acid-catalysed dissociation.[233] Additionally, the overall charge of the metal complex or its polarity may affect the biodistribution of the contrast agent. Therefore, a modular design and synthesis of the ligand should allow for the modification of these characteristics to optimise the biodistribution properties.[231] In order to meet the specific requirements of the different radiometals, a large number of ligands have been developed. These ligands can be divided into two major families: macrocyclic and acyclic.

In general, macrocyclic complexes are more kinetically inert than the acyclic ones of comparable thermodynamic stability (K_{ML}).[225] This is related to the changes that the chelators experience during metal ion coordination. Acyclic chelators must undergo a more drastic change in physical orientation and geometry in solution in order to arrange donor atoms to coordinate with a metal ion. This results in a more significant decrease in entropy than in the case of macrocycles, which have a pre-organised structure. This is known as the macrocyclic effect.[234] Ruled by the same thermodynamic properties, acyclic chelators have faster metal-binding kinetics compared with their macrocyclic analogues. This affects also to the radiolabelling efficiency, which is lower for

macrocyclic ligands, requiring higher temperatures and longer times, which are crucial factors when working with heat-sensitive vectors (*e.g.*, antibodies) or short half-life isotopes (*e.g.*, ^{68}Ga). In addition, the selective functionalisation of the macrocyclic ligands can be challenging, and most research groups in need of bifunctional derivatives are supplied by a commercial source.[235]

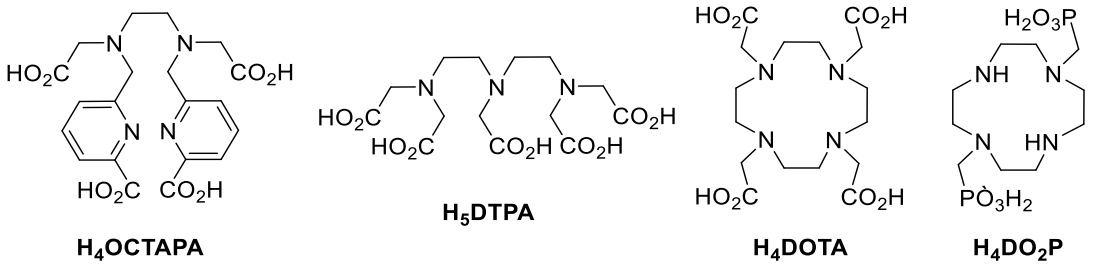

Figure I-48. Selected examples of acyclic (**H_4OCTAPA** and **H_5DTPA**) and macrocyclic (**H_4DOTA** and **H_4DO_2P**) ligands.

1.3.3. Linkers and Bioconjugation Strategies

Linkers are an important part of contrast agents. They not only bind targeting moieties, but also their properties are rather important, as they can affect imaging agents' kinetics and biodistribution.[236] It is essential that the position and binding of the linker to the BFC does not interfere with the coordination of the metal by the chelator or the affinity of the biomolecule for its intended target. Often, targeting vectors are sensitive biomolecules, so it is desirable that the conjugation strategy occurs under mild conditions to preserve the integrity of the targeting vector. Four conjugation strategies (**Figure I-49**) are mainly employed in the synthesis of radioactive imaging agents:[237]

- **Peptide bond:** This is one of the most popular conjugation strategies used in peptide-bioconjugates. It involves the coupling of a carboxylic acid to a primary amine, usually from a lysine residue. With the aid of a coupling agent or an activated ester of tetrafluorophenyl (TFP) or *N*-hydroxysuccinimide (NHS), the carboxylic acid placed in the ligand is coupled to a primary amine.[238] Due to the usual presence of various carboxylic acids in the BFCs, there is a need for selectivity for the conjugation with the primary amine. This is usually achieved by controlling the mole ratios of chelate to targeting vector, and/or using protecting groups. The peptide coupling reaction is often performed under solid-phase synthesis, followed by full deprotection of the chelate and cleavage from the resin.
- **Thioether bond:** This involves the reaction of a thiol group, present in a cysteine residue of peptides and proteins, with a maleimide moiety of the BFC. It occurs under mild conditions (pH 7.2 to 7.4) at room temperature and without a catalyst. Another advantage is that it can be accomplished on the fully deprotected ligand. However, maleimide conjugation is reversible and may result in the release of the maleimide scaffold in plasma (retro conjugate addition reaction).[239]
- **Thiourea bond:** This strategy involves the reaction between an isothiocyanate and a primary amine under slightly basic conditions (pH 8 to 9). Bond formation is slower when

compared to thioether bond formation, but it can also be performed selectively without the presence of protecting groups.

- **Azide-alkyne click reaction:** Also known as Huisgen cycloaddition, it occurs through the reaction of terminal alkynes and azides, which are very stable functional groups under coupling conditions. To be accomplished faster and with control of the regioselectivity, it is catalysed by Cu(I). It must be noticed that the 1,4-substituted triazole formed could also act as an additional donor group to the metal ion.[240] Most recently, Cu(I)-free coupling reactions, such as Diels-Alder click reaction or strain-promoted azide-alkyne cycloaddition, have garnered popularity to form these bioconjugates, as they are compatible with living systems, allowing for novel applications like *in vivo* pre-targeting.[241]

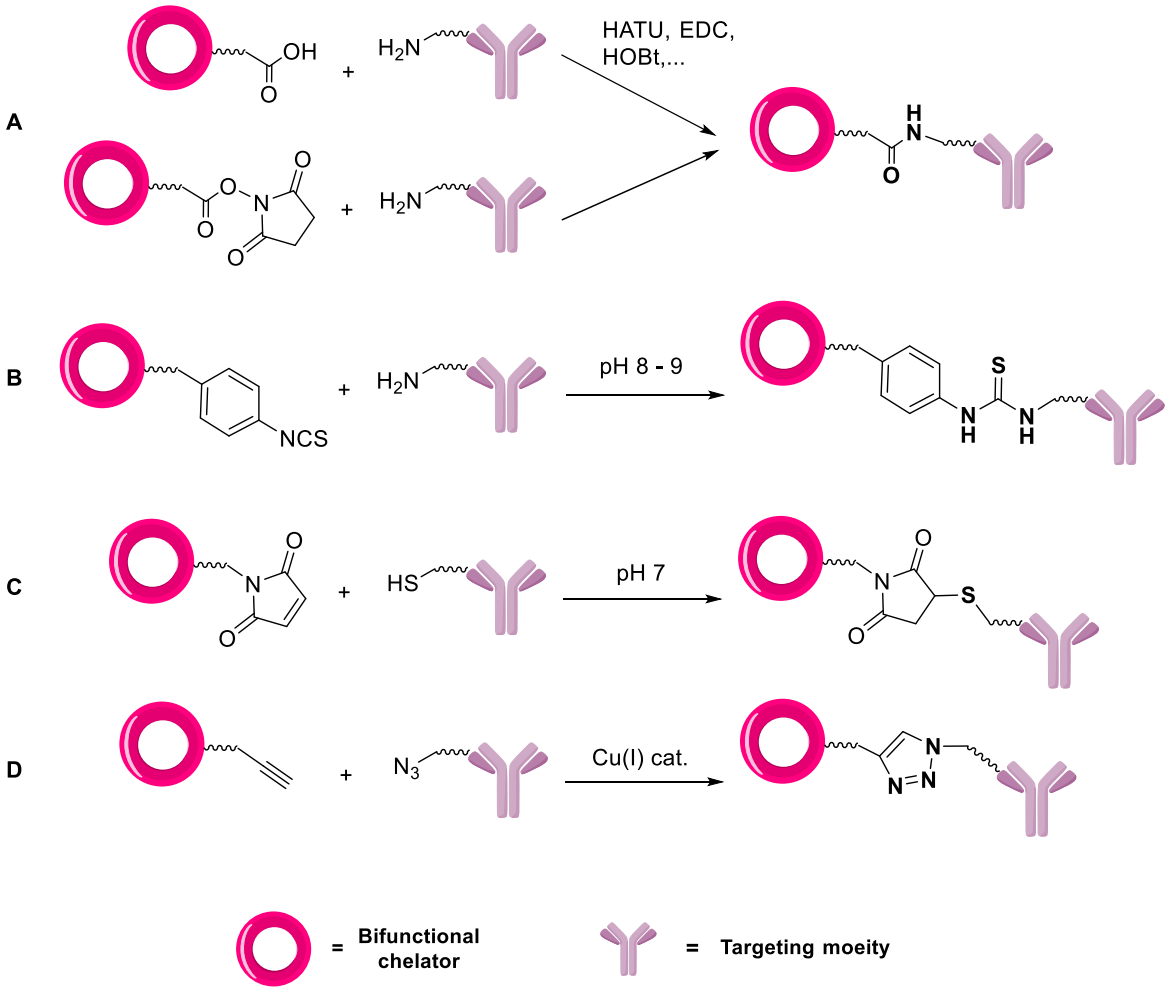

Figure I-49. Four common types of bioconjugation reactions: (A) peptide bond; (B) thiourea formation; (C) thioether by thiol-maleimide reaction; and (D) triazole-click reaction.

1.3.4. Targeting Vectors

The targeting vector is a biomolecule that exhibits strong binding affinity for a surface receptor, also called **antigen**, which is usually overexpressed due to an abnormal condition (*e.g.*, tumour). These are the vehicles that transport the radionuclide specifically to the targeted molecule, dictating the biodistribution and pharmacokinetics of the contrast agent.

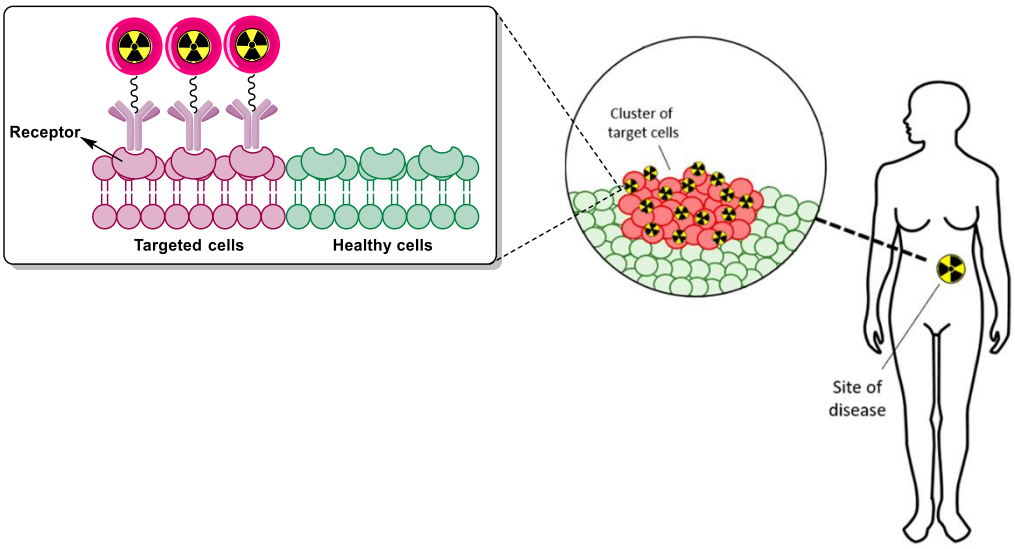

Figure I-50. Targeting vectors must exhibit high affinity for receptors in order to have a significant accumulation that allows the visualisation of the targeted structure or molecular process.[242]

Each type of targeting vector has different biological properties, which must be matched with the physical properties of the radionuclide. About their properties, size can be considered the most impactful, especially for tumour uptake. Simulations by Schmidt and Wittrup[243] predicted that small (<10 kDa) and large (>100 kDa) vectors exhibit the highest tumour uptake. Although simulations cannot replace *in vivo* experiments, this trend is confirmed by the targeting vectors used in the most recent literature. Foremost, the most popular targeting vectors are:

- **Small molecules:** These non-specific vectors can be conjugated with radionuclides to trace metabolic processes that are not specific to a particular structure, but instead allow the detection of any abnormal activity. The most well-known example is ^{18}F-FDG, which takes advantage of the increased glucose metabolism by cancerogenic cells. Despite its easy use due to the lack of complex contrast agent structures, its applications are limited due to the lack of specificity.
- **Peptides:** Peptides have grown in interest due to their size, which provides them with interesting pharmacokinetic characteristics. They have a high uptake in the targeted tissue and a quick clearance for unbound peptide radiotracers, lowering the background noise. Also, they can target a broad range of biomolecules. Moreover, peptides can be easily chemically modified or synthesised to avoid any enzymatic degradation, and they can be bioconjugated through many processes. All these characteristics suggest that they are well suited to radioisotopes of short half-life (*e.g.*, ^{68}Ga).
- **Antibodies:** Described as the natural affinity ligands of the human body, the most abundant ones are immunoglobulins (140-160 kDa). This high molecular weight makes them suffer of slow accumulation and clearance (3 to 4 weeks), which limits their applications. This long half-life also limits the number of radioisotopes that can be matched with them (*e.g.*, ^{89}Zr). Additionally, the bioconjugation can be difficult, as there are a lot of functional reacting groups due to the large surface of the antibody. This makes it difficult to control their reactivity with the BFC and the positions in which the conjugation is performed. Despite

these shortcomings, there are several contrast agents approved by the Food and Drug Administration (FDA), as well as several clinical trials that contain antibodies as targeting vectors,[229] due to their high specificity for targeting molecules.

As an alternative, antibody fragments are other possible targeting vectors, improving the pharmacokinetic properties and giving more versatility about the radionuclides used with them. With a molecular weight of 6 kDa, Affibodies are one of the most recent advances in antibody engineering, reducing clearance time below 10 hours.[231]

- **Nanoparticles:** Their use as targeting vectors, as with small molecules, does not rely on the ability of the particle to bind specifically to an overexpressed surface receptor. Instead, they take advantage of their larger size to obtain a specific biodistribution, especially in tumours. To improve the targeting ability of nanoparticles, traditional targeting vectors such as peptides or antibodies, are often introduced onto their surface.

1.4. Matching Chelators

The study of new radioisotopes also requires the development of new chelators that can bind them efficiently. Every time a new radiometal-chelator complex is synthesised, it must be evaluated to ensure that it has good complexation kinetics, high thermodynamical stability, and a suitable kinetic inertness. This is done by performing *in vitro* (*e.g.*, radiolabelling, potentiometric titration…) and *in vivo* studies, which provide objective data to compare the new complexes to the existing ones, to assess their potential as a radiopharmaceutical.

1.4.1. Radiolabelling

With this study, in which a radiometal is chelated with a ligand under certain conditions, whether the chelator shows suitable complexation kinetics or not is evaluated. These characteristics are expressed through the **radiochemical yield (RCY)**, which represents the percentage of radionuclide that has been bound to the ligand. It can also be expressed as the **specific activity (mCi/mg)**, which is the amount of activity introduced per mg of compound, or the **apparent molar activity** or **AMA (mCi/mol)**, which is the amount of activity introduced per mole of compound.[231]

The radiolabelling process can be executed manually, by semi-automated processes or by using a cold kit. Radiolabelling developed in preclinical research often starts with a manual optimisation phase (**Figure I-51**) to find suitable labelling conditions with low radioactivity, especially with new radiotracers:[244]

I. The eluted **isotope**, which is found in a stable form (*e.g.*, $^{64}CuCl_2$ or $^{68}GaCl_3$), is mixed with the **precursor**, which can be the non-bifunctional chelator, or, in more advanced stability studies, the chelator bioconjugated with a vector. These studies are usually first performed with a non-bifunctional ligand analogue because vectors, like antibodies, are often expensive. Therefore, some data that confirms the high stability and inertness of the complex is required before incorporating them. Also, depending on the characteristics of the radioisotope, a **buffer** might be required to maintain ideal radiolabelling pH conditions.

II. The reaction mixture is **incubated** for a specific reaction time and temperature to achieve the isotope chelation. Chelators are required to have fast radiolabelling kinetics, regardless of the half-life of the radioisotope. This means that the radiolabelling process ideally should be completed in less than 10 or 15 minutes. However, fast kinetics for the incorporation of the metal (on-rate) can also mean a fast radiometal release (off-rate) by the complex. This will depend on the energy barriers of each process, which should be balanced to obtain the best set of chelate properties. Also, the conditions under which the ligand is radiolabelled should be as mild as possible, which means room temperature, especially when antibodies are used as vectors, and low concentrations of the isotopes.

III. The reaction mixture is **purified** using solid-phase extraction, which allows separation of the free isotope and other impurities from the radiopharmaceutical, that gets trapped on the column.

IV. The product is eluted and passed through a **sterile filter**, so it is prepared to do the stability studies, or to be injected into the subject for the preclinical studies.

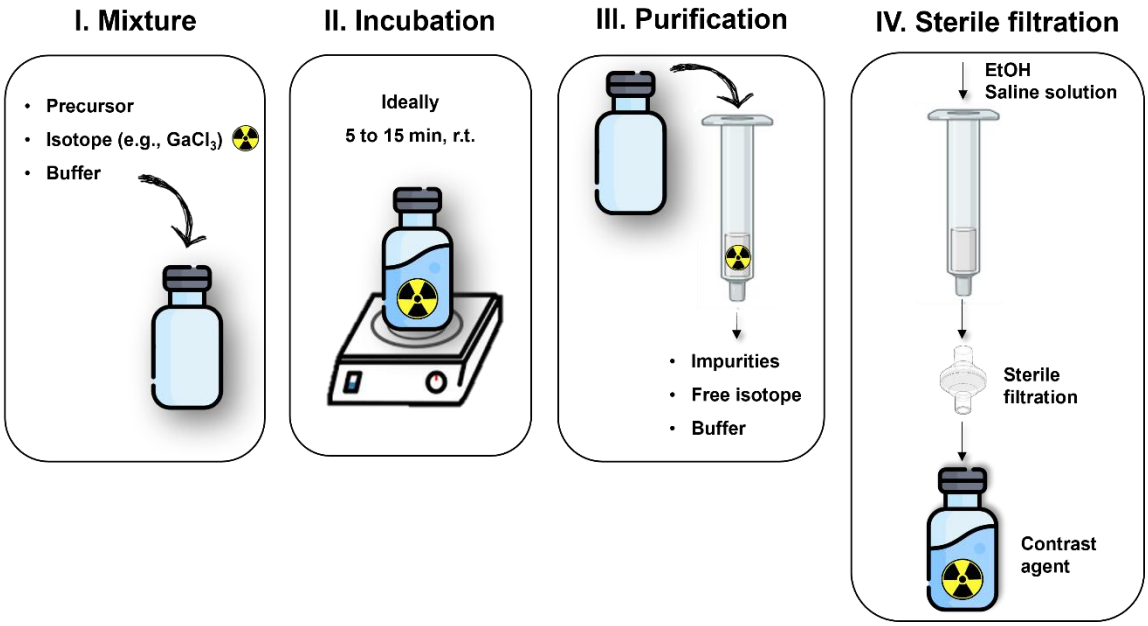

Figure I-51. Four main steps of the manual radiolabelling to produce radiopharmaceutical products.

A disadvantage of manual production is the manipulation of significant radioactivity near unshielded hands. Then, in order to improve the radiation protection of personnel and facilitate transfer for routine clinical use, automated processes are needed. They allow higher reproducibility and robustness, especially in critical stages such as elution of the generator and purification. Several semi-automated and automated systems have been developed, either in-house built or commercially available products, combining generator's elution and post-processing, ^{68}Ga-radiolabelling, and purification of the final ^{68}Ga radiotracer.

These kits enable decentralised tracer production and therefore enable the application of the radiotracer to patients who do not live in the vicinity of a centralised production site.

Although these experiments are good indicators of the stability of the complexes, they are not decisive. A case in point is the macrocyclic ligand commonly referred to as dodecane tetraacetic acid (DOTA), which requires elevated temperatures for its radiolabelling, but it has an exceptional stability *in vivo*, making it one of the most used and commercialised ligands to date.

1.4.2. Stability of the Metal Complexes

Once a chelator has been identified through early screening as having suitable radiolabelling properties for a particular radiometal ion, it must then be experimentally determined to be highly stable and inert. This is critical as complexes must remain intact inside the human body to prevent health risks, such as toxicity from the free metal, and/or to avoid a loss of image contrast in diagnostic imaging.

There are a number of factors that can affect stability of a metal complex, including the charge and size of the central metal cation. Ligand-related factors also play a significant role, such as basicity, structural type (macrocyclic or acylic) or its chelating effect (multidentate or monodentate binding). In addition, the presence of resonance stabilization or steric hindrance can significantly alter the stability of the complexes.[245] The result of a non-proper stability of the complex can lead to radiometal dissociation, potentially resulting in its accumulation within the body depending on the radiometal properties.

By using various methodologies, the **stability**, defined as thermodynamic stability, and the **inertness**, defined as kinetic inertness, can be measured. It must be understood that a thermodynamically stable complex may be kinetically labile (fast reacting complex) and, similarly, a thermodynamically unstable complex may be kinetically inert (slow reacting complex). Thermodynamic stability and kinetic inertness are two independent parameters.

Figure I-52. Thermodynamic stability and kinetic inertness are parameters measured to study in an early stage the stability and inertness of the metal complex.

1.4.2.1. Thermodynamic Stability

The tendency of a complex to remain under equilibrium is known as thermodynamic stability. In the point of equilibrium, it determines how much of the complex will be formed or converted into another complex. In other words, the thermodynamic stability of complexes is the measure of a metal ion's ability to form a certain metal complex and is directly correlated with the energies of the bonds between the metal and the ligand.

The thermodynamic stability of complexes is represented by the formation constant or stability constant (K_{ML}).

$$\boldsymbol{K_{ML}} = [ML]/[M][L] \qquad \textbf{(Equation I-1)}$$

From the equation it is observed that the higher the value of K_{ML}, the greater will be the stability of the complex formed. Thus, a large value of K_{ML} indicates that the ligand L binds to the metal ion M more strongly than H_2O (complex are usually formed in aqueous solutions) and hence L is a stronger ligand than H_2O. As a result, the complex's stability constant is employed to determine its thermodynamic stability.

It is assumed that this reaction does not occur in a single step but occurs in several steps, and each step is characterised by its individual equilibrium constant known as stepwise constant (K_n).

$$\boldsymbol{K_n} = [ML_n]/[ML_{n-1}][L] \qquad \textbf{(Equation I-2)}$$

With a few exceptions, the value of successive stability constants decreases regularly from K_1 to K_n, that is, $K_1 > K_2 > K_3 > \ldots K_{n-1} > K_n$, as it can be seen in the example of **Figure I-53**.

$$Cd^{2+} + NH_3 \rightleftharpoons [Cd(NH_3)]^{2+} \qquad K_1 = 10^{2.65}$$
$$[Cd(NH_3)]^{2+} + NH_3 \rightleftharpoons [Cd(NH_3)_2]^{2+} \qquad K_2 = 10^{2.10}$$
$$[Cd(NH_3)_2]^{2+} + NH_3 \rightleftharpoons [Cd(NH_3)_3]^{2+} \qquad K_3 = 10^{1.44}$$
$$[Cd(NH_3)_3]^{2+} + NH_3 \rightleftharpoons [Cd(NH_3)_4]^{2+} \qquad K_4 = 10^{0.93}$$

Figure I-53. Example of the $[Cd(NH_3)_4]^{2+}$ stepwise formation constants.[245]

The steady decrease in the value of stepwise formation constants from K_1 to K_n is due to:

1. An increase in the number of ligands entering the coordination sphere, which causes a decrease of the number of H_2O molecules to be replaced, and thus the probability of replacement decreases.
2. An electrostatic factor.
3. The steric hindrance, which increases with the number of ligands.
4. Statistical factors (number of replaceable positions).

Several experimental methods can be employed to evaluate the nature and degree of interaction between the metal ion and ligand,[246,247] and each method requires unique experimental conditions, leading to differences in how reaction mechanisms and stability constants are interpreted. Thermodynamic stabilities are usually experimentally determined by **potentiometric** and/or **UV-Vis spectrophotometric titrations**.

Titration experiments are carried out by fixing the concentration of one element, while one species is gradually introduced into the system, producing changes that are monitored through a physical property such as a specific chemical resonance (NMR), fluorescence or absorption band (UV-Vis).

The **UV-Vis spectroscopy** technique is suitable when the right chromophore is present in the complex. The formation, or dissociation, of the metal complex are measured by the change in the absorbance (A) and the concentration is given by Lambert-Beer's law:

$$A = \varepsilon \cdot c \cdot l \qquad \textbf{(Equation I-3)}$$

The concentration (c) of the metal complex can be determined by measuring the absorbance (A) with a spectrophotometer, along with the molar extinction coefficient (ε) at a certain wavelength (λ) and path length (l), using the equation above.

For this technique, it is recommended that concentrations of the complex are fitted to obtain absorption peaks that lie A ≤ 1 and the changes in the physical properties are noticeable, as the usual approach for the analysis of the UV-Vis titration data assumes a significant change in the molar absorption (ε) based on **Equation I-3**. Also, ideally, the species added to the solution should not have any absorption in the region of interest. As a drawback, UV-Vis titration is especially sensitive to dilution, temperature and any impurity in the species used.[248]

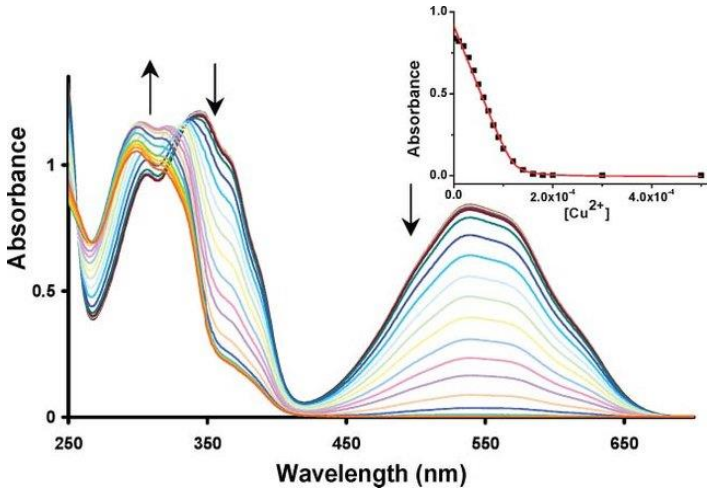

Figure I-54. Example of a K_{ML} determination. K_{ML} is obtained from the observed absorbance (A) and correlated to the concentration (c) of the complex [ML] or, in some cases, to the free metal [M] or free ligand [L].[249]

The obtained data is then plotted as a function of the species added over the fixed element, compared and correlated to binding models through commercial software, like Graphpad[250], are used to obtain information such as the formation constant (K_{ML}), thermodynamic expressions (ΔG, ΔH and ΔS) and stoichiometry.

These values can be useful as a preliminary indication of the binding affinity of a particular metal-chelator pair, but do not predict *in vivo* stability. In addition, the reliability of the data obtained in these experiments is related to several factors, such as the purity of the compounds, the precision of the measuring tools used, or the possible errors committed by the technician. It is also important to take into consideration the expected formation constants values, the technique employed, and the physical changes to decide the concentrations of the complex used and the range of addition of the species into the system.

A thermodynamic parameter that is found more useful to correlate with *in vivo* conditions is the **pM value** ($-\log[M]_{Free}$). This condition-dependent value can be calculated from the standard thermodynamic stability constants ($\log K_{ML}$), considering variables such as ligand basicity or metal ion hydrolysis. Low free metal concentrations at physiological pH are desired, which will translate into high pM values.

Stability constants and pM give a value for the direction and magnitude of the equilibrium in a metal-chelate coordination reaction. However, they give no rate information (*e.g.*, off-rates for dissociation), thus the kinetics of dissociation must be determined through other methods.

1.4.2.2. Kinetic Inertness

Even more important than complex metal-chelate thermodynamic stability is its kinetic inertness when assessing and selecting a chelator to match with a specific radiometal ion. In terms of kinetic lability or inertness, the complexes are classified according to whether substitution reactions are fast or slow. Basically, it refers to the speed at which a compound reacts rather than its stability. By using this measure, the rate at which the equilibrium is reached can be determined. Depending on their kinetic stability, metal complexes can be classified as labile, when the rate of substitution of ligands is high, or inert, when the rate of ligand exchange is very slow. In general, a metal complex is considered labile if it reacts within 1 min at 25 ºC, and inert if it takes longer.

When it comes to *in vivo* applications, evaluating kinetic inertness can be more challenging. There are many endogenous biological chelators (*e.g.*, oxide dismutase, transferrin) and competing ions in the plasma (*e.g.*, phosphate, carbonate) that can transchelate radiometals from BFC conjugates. Thus, the metal must be bound sufficiently strong to the ligand to avoid transchelation. This is an important factor because, regardless of thermodynamic stability, dissociation rate *in vivo* determines the kinetic inertness of a radiometal complex (**Figure I-55**). Moreover, the off-rate of dissociation can be greatly affected by the high dilution experienced *in vivo*, considering the small amount of radiopharmaceutical that is diluted into the blood pool.

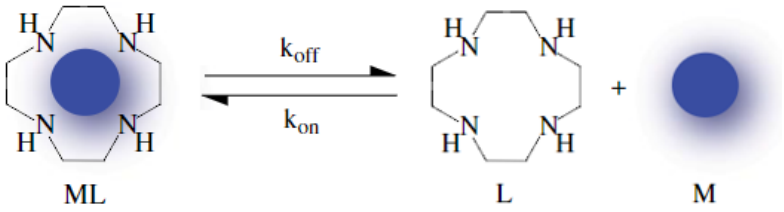

Figure I-55. Despite that both thermodynamic and kinetic properties of metal complexes are studied, the most relevant measure is the off-rate dissociation (k_{off}), representative of the kinetic inertness *in vivo*.[251]

In vitro competition experiments against an excess of free metal, proteins or blood serum are the most common way to measure the kinetic inertness of complexes in terms of transchelation. However, interpretation of these studies must be taken cautiously, as rarely the results can be extrapolated to *in vivo* situations. Also, acid-catalysed dissociation experiments can be performed, as most complexes tend to release some free metal below pH 2, but these experiments do not provide a good prediction of the *in vivo* results either.

1.5. Precedents for Rationale Design of ^{64}Cu and ^{68}Ga Ligands

In 2020, the FDA approved the first ^{64}Cu-based radiopharmaceutical for clinical use, **[^{64}Cu]Cu-DOTATATE (Detectnet™)**,[252] which provided similar results to the ^{68}Ga-based radiopharmaceutical **[^{68}Ga]Ga-DOTATATE (NETSPOT™)**, approved by the FDA in 2016[253] (**Figure I-56**). These imaging agents use a **H$_4$DOTA** derivative as a chelating unit linked to the **octreotide** peptide, an analogue of the somatostatin (SST) peptide hormone, which is overexpressed in neuroendocrine tumours (NETs). These SST-based contrast agents constitute the first-line diagnostic imaging method, as they have demonstrated a strong potential in the imaging of NETs, surpassing some of the isotope analogues in terms of sensitivity, detection rate, quantification as well as simpler production at a lower cost.[254]

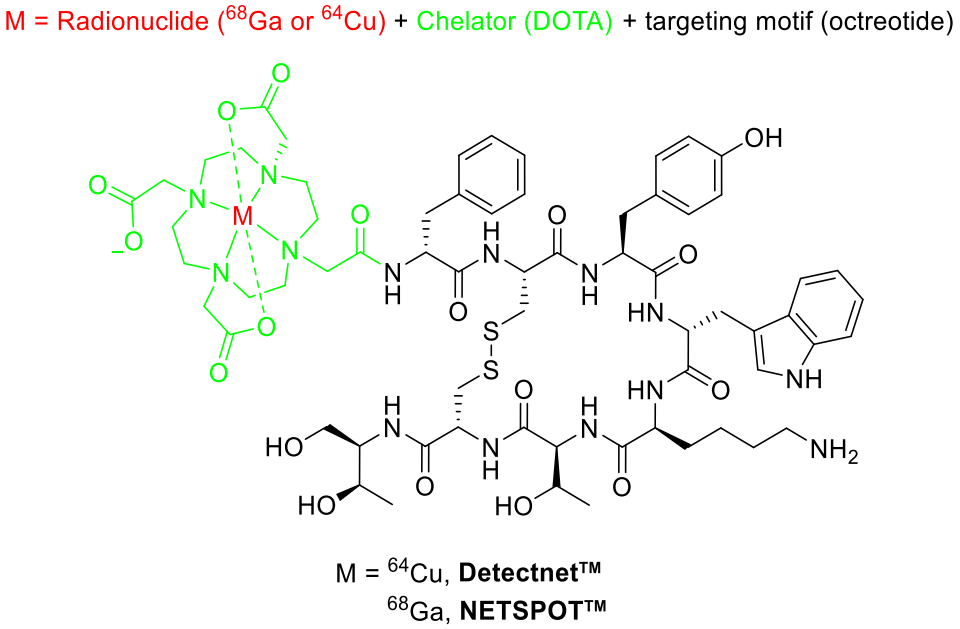

Figure I-56. Structure of ^{68}Ga and ^{64}Cu-based somatostatin analogue imaging agents.

However, while **H$_4$DOTA** derivatives are widely used, they are known to be suboptimal in terms of the stability of the chelate, especially in the case of Cu^{2+}, with **H$_3$NOTA**[255–258] or cyclam cross-bridge derivatives, such as **H$_3$CB-TEA1A1P**,[259] performing significantly better (**Figure I-57**). The influence of the chelators in the biodistribution of radioconjugates is key, which makes the investigation of novel chelators an active research area, trying to expand the range of suitable chelators.

The acyclic chelator **H$_2$DEDPA** and its rigidified analogue **H$_2$CHXDEDPA**[260] have emerged as promising candidates for the development of ^{68}Ga-based radiopharmaceuticals (**Figure I-57**).[235,261] Initial studies on **H$_2$DEDPA** derivatives showed that the **[^{64}Cu(DEDPA)]** complex exhibited low stability in serum,[262] whereas the **[^{64}Cu(CHXDEDPA)]** complex maintained 98% stability after 24 hours in human serum at 37 ºC.[263] This significant difference underscores the stabilising effect of the rigid cyclohexane group, which enhances the stability of ^{64}Cu-labeled complexes.

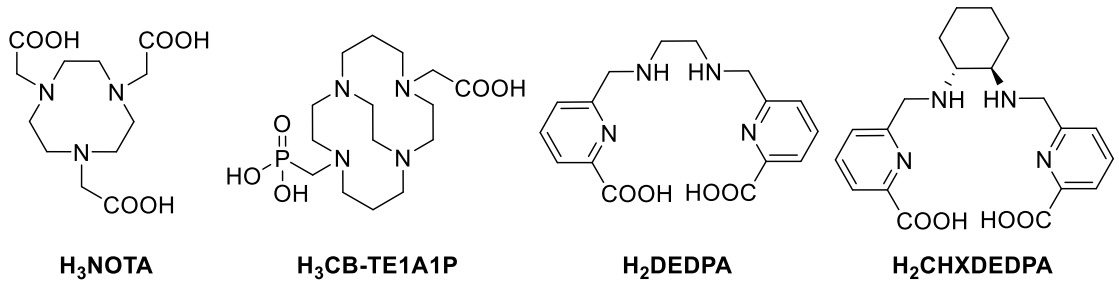

H_3NOTA **H_3CB-TE1A1P** **H_2DEDPA** **H_2CHXDEDPA**

Figure I-57. Structures of ligands used in the literature to chelate ^{64}Cu and ^{68}Ga.

Building on the promising performance of **H_2DEDPA** and its derivatives, several structural modifications have been explored to create bifunctional derivatives. Functionalisation of position 4 of the pyridyl rings of **H_2DEDPA** negatively impacted the radiolabelling efficiency and/or stability of the resulting ^{68}Ga complexes,[264] with C-functionalisation being the most promising strategy.[235] Interestingly, despite initial attempts to obtain *N*-alkylated derivatives providing unstable ^{68}Ga complexes,[265] more recent studies have demonstrated improved stability for ^{64}Cu and ^{68}Ga complexes,[266] providing an alternative for the obtention of bifunctional chelators.

Then, based on the advances made in obtaining bifunctional chelators with **H_2DEDPA** analogues, we set out to expand the range of rigid derivatives of this ligand for the development of novel ^{64}Cu- and ^{68}Ga-based radiopharmaceuticals. As part of the work of our research group, the synthesis of *trans*-1,2-cyclobutanediamine-based ligands (**Figure I-6**, *vide supra*) had been previously described for the complexation of Gd(III) and Mn(II) with applications as MRI contrast agents. Results obtained demonstrated that the modification of the **H_2DEDPA** structure by introducing the cyclobutane spacer as a rigid moiety enhanced the kinetic inertness of the resulting complexes.[75,76] However, DFT calculations indicated that this structure would not conjugate properly ^{64}Cu and ^{68}Ga radioisotopes due to the their different size and coordination numbers, proposing instead the use a *cis*-1,3-cyclobutanediamine-based ligand (**H_2CBuDEDPA**, **Figure I-58**). This ligand had already been reported for Fe(III) complexation,[267] representing a suitable candidate for the radiometals studied in this thesis.

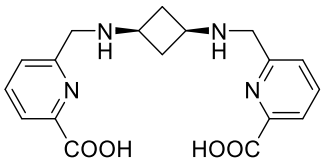

H_2CBuDEDPA

Figure I-58. Structure of the *cis*-1,3-cyclobutanediamine-based ligand used for the complexation of Fe(III).

2. Objectives

Owing to the precedents in the synthesis of ^{64}Cu- and ^{68}Ga-based radiopharmaceuticals and the advances made in the obtention of novel ligands for stable complexes formation, the obtention of H_2DEDPA derivative with a *cis*-1,3-cyclobutanediamine spacer was proposed. The rigid structure of the cyclobutane moiety is expected to increase the efficiency and stability of ^{64}Cu and ^{68}Ga complexes, making this open-chain type ligand a promising contrast agent for PET imaging.

The initial objective would be to evaluate the kinetic inertness and thermodynamic stability of Cu(II) and Ga(III) complexes formed with a *cis*-1,3-cyclobutanediamine-containing non-bifunctional ligand (**H_2CBuDEDPA**) as a chelator model. To better understand the impact of the cyclobutane ring on the coordination properties of the chelate, the study would also investigate two analogues containing a cyclopentane (**H_2CPDEDPA**) and a cyclohexane (**H_2CHXDEDPA**) rigid moiety, respectively. In addition, radiolabelling assays using ^{64}Cu and ^{68}Ga radioisotopes would be conducted to assess the chelation efficiency of these ligands.

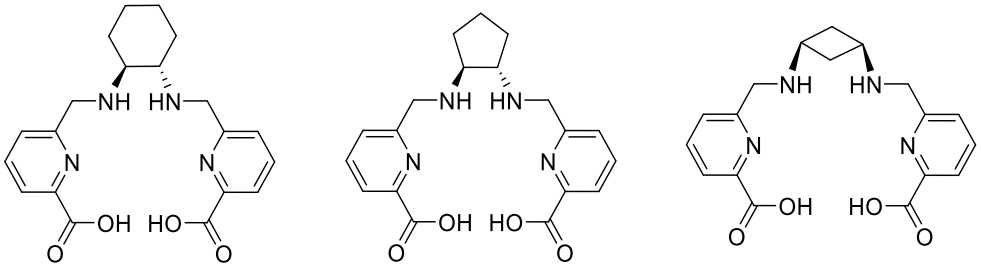

H_2CHXDEDPA **H_2CPDEDPA** **H_2CBuDEDPA**

Figure I-59. Non-bifunctional ligands employed as a chelator models.

Upon confirmation that the CBC ligand offers a sufficiently good stability and efficiency compared to its analogues due to their major rigidity, a synthetic methodology to develop a BFC, that enables the attachment of a targeting fragment, would be aimed. This involves the C-functionalisation at position 2 of the *cis*-1,3-cyclobutanediamine to introduce a functional group in either the *cis* (***cis,cis*-L1**) or *trans* (***cis*,*trans*-L2**) orientation relative to the amino groups. Finally, the performance of these bifunctional chelators in radiolabelling studies would be evaluated to understand the influence of the extra functionalisation in the coordination chemistry properties of the ligand.

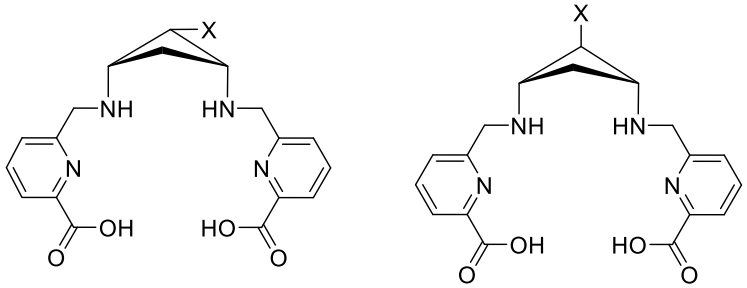

***(cis*,*cis*)-L1** **(*cis*,*trans*)-L2**

X = CH_2OH, NH_2,...

Figure I-60. Bifunctional chelators proposed based on the *cis,cis*- or *cis,trans*-1,3-cyclobutanediamine structure.

3. Results and Discussion

The results presented in this chapter are organised into several sections. First, the synthesis and characterisation of the Cu(II) and Ga(III) complexes with the non-bifunctional chelators are discussed, including the detailed synthesis of the novel ligand **H_2CPDEDPA** (**section 3.1.**). This is followed by the presentation of the ^{64}Cu and ^{68}Ga radiolabelling assays conducted with the non-bifunctional chelators (**section 3.2.**). Then, the *in vitro* stability studies performed on Cu(II) complexes are described (**section 3.3.**). Upon completion of the studies with the non-bifunctional chelators, the focus shifts to the synthesis of the cyclobutane-containing bifunctional chelators (**section 3.4.**), culminating in radiolabelling assays with these chelators (**section 3.5.**).

3.1. Synthesis of Cu(II) and Ga(III) Complexes with Non-bifunctional Chelators

The synthesis of the non-bifunctional ligands used as chelator models for the complexation of Cu(II) and Ga(III) was carried out in the research facilities of the Centro Intersciplinar de Química e Bioloxía (CICA) at the Universidade da Coruña by Dr. Lucio, a researcher in the Prof. Platas-Iglesias' group. The ligands **H_2CHXDEDPA** and **H_2CBuDEDPA** were obtained following the synthesis reported in the literature.[260,267] In the case of **H_2CPDEDPA**, that had not been reported previously, a synthesis approach similar to that of the other analogues was followed. To a solution of the commercially available (±)-*trans*-1,2-cyclopentanediamine (**(±)-100**) and DIPEA in MeOH, methyl 6-formylpyridine-2-carboxylate (**101**) was added dropwise and the mixture was refluxed. Upon cooling of the reaction to 0 ºC, the Schiff-base intermediate was reduced with sodium borohydride ($NaBH_4$). Finally, the hydrolysis of the methyl ester groups was performed in 6 M HCl and the crude was purified using reverse-phase medium-pressure liquid chromatography (RP-MPLC) affording ligand **H_2CPDEDPA** (**Scheme I-26**).

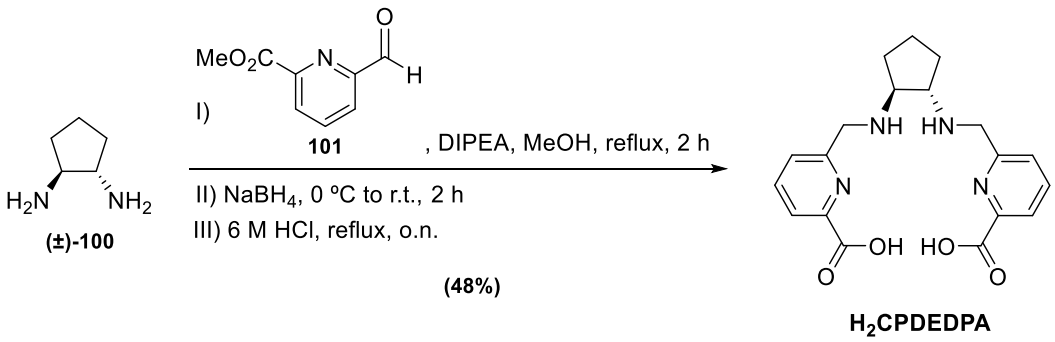

Scheme I-26. Synthesis of **H_2CPDEDPA** performed by Dr. Lucio in CICA's research facilities following an analogous procedure to those reported for the other analogues.

The complexation of the 3 chelator models with Cu(II) and Ga(III) was performed during my research stage in CICA's research facilities under Dr. Lucio's supervision.

The Cu(II) complexes were synthesised by reaction of the corresponding ligand with $Cu(OTf)_2$ in aqueous solution at pH 7 and isolated in yields between 41% and 64% after purification through reverse-phase chromatography using a C18AQ column (**Scheme I-27**).

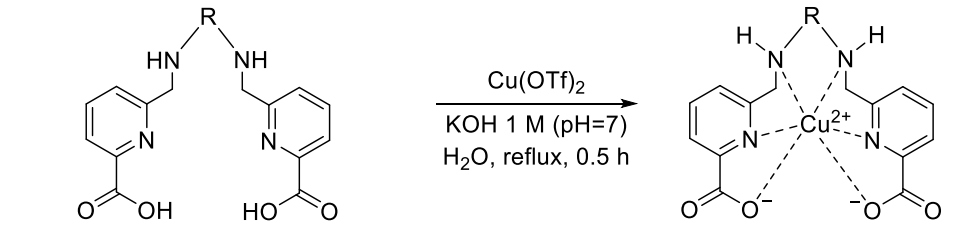

H_2CHXDEDPA, R = *trans*-1,2-cyclohexyl
H_2CPDEDPA, R = *trans*-1,2-cyclopentyl
H_2CBuDEDPA, R = *cis*-1,3-cyclobutyl

[Cu(CHXDEDPA)] (61%)
[Cu(CPDEDPA)] (41%)
[Cu(CBuDEDPA)] (64%)

Scheme I-27. General synthesis procedure of the Cu(II) complexes with the chelator models.

In the case of the Ga(III) complexes, these were synthesised by reaction of the corresponding ligand with $Ga(NO_3)_3$ in isopropanol (IPA) and isolated in yields between 56% and 70% after purification through reverse-phase chromatography using a C18AQ column (**Scheme I-28**).

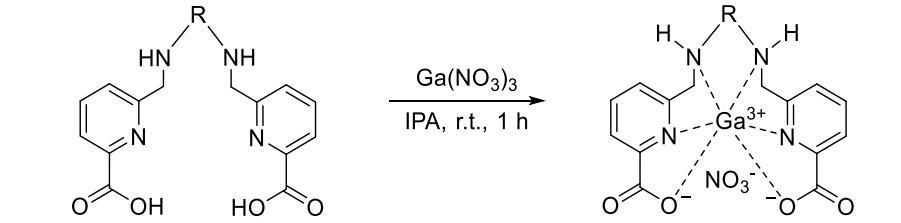

H_2CHXDEDPA, R = *trans*-1,2-cyclohexyl
H_2CPDEDPA, R = *trans*-1,2-cyclopentyl
H_2CBuDEDPA, R = *cis*-1,3-cyclobutyl

[Ga(CHXDEDPA)]NO_3 (70%)
[Ga(CPDEDPA)]NO_3 (56%)
[Ga(CBuDEDPA)]NO_3 (61%)

Scheme I-28. General synthesis of the Ga(III) complexes with the chelator models.

The UV-Vis absorption spectra of the Cu(II) complexes are very similar showing d-d absorption bands at 720 **[Cu(CHXDEDPA)]**, 732 **[Cu(CpDEDPA)]** and 728 nm **[Cu(CBuDEDPA)]**, respectively (**Figure I-61**). These absorption data are very similar to those reported for **[Cu(OCTAPA)]$^{2-}$** and **[Cu(DEDPA)]** (see **Figure I-48** for ligand structure, *vide supra*), which have distorted N_4O_2 octahedral coordination.[268] This indicates that the nature of the spacer has little impact on the structures of these complexes in solution.

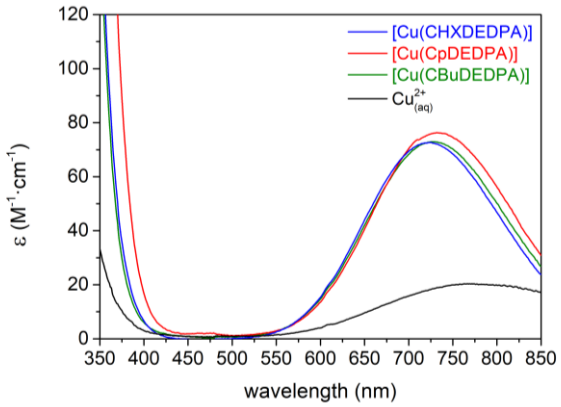

Figure I-61. UV-Vis spectra of Cu(II) complexes; **[Cu(CHXDEDPA)]** (1.4 mM, blue curve), **[Cu(CPDEDPA)]** (1.3 mM, red curve), **[Cu(CBuDEDPA)]** (1.3 mM, green curve), $CuCl_2$ (1.3 mM, black curve).

In the case of the Ga(III) complexes, in the UV-Vis absorption spectra were registered the variations in the π-π* bands of the ligand due to dissociation in acid or basic media (**Figure I-62**), except for the ligand **H_2CHXDEDPA**, which show slow dissociation kinetics in acid media. Despite being an increase in the intensity of the absorbance upon formation of the complex, suggesting a change in the electronic environment of the ligand, the differences are not very significant between the free ligand and the complex.

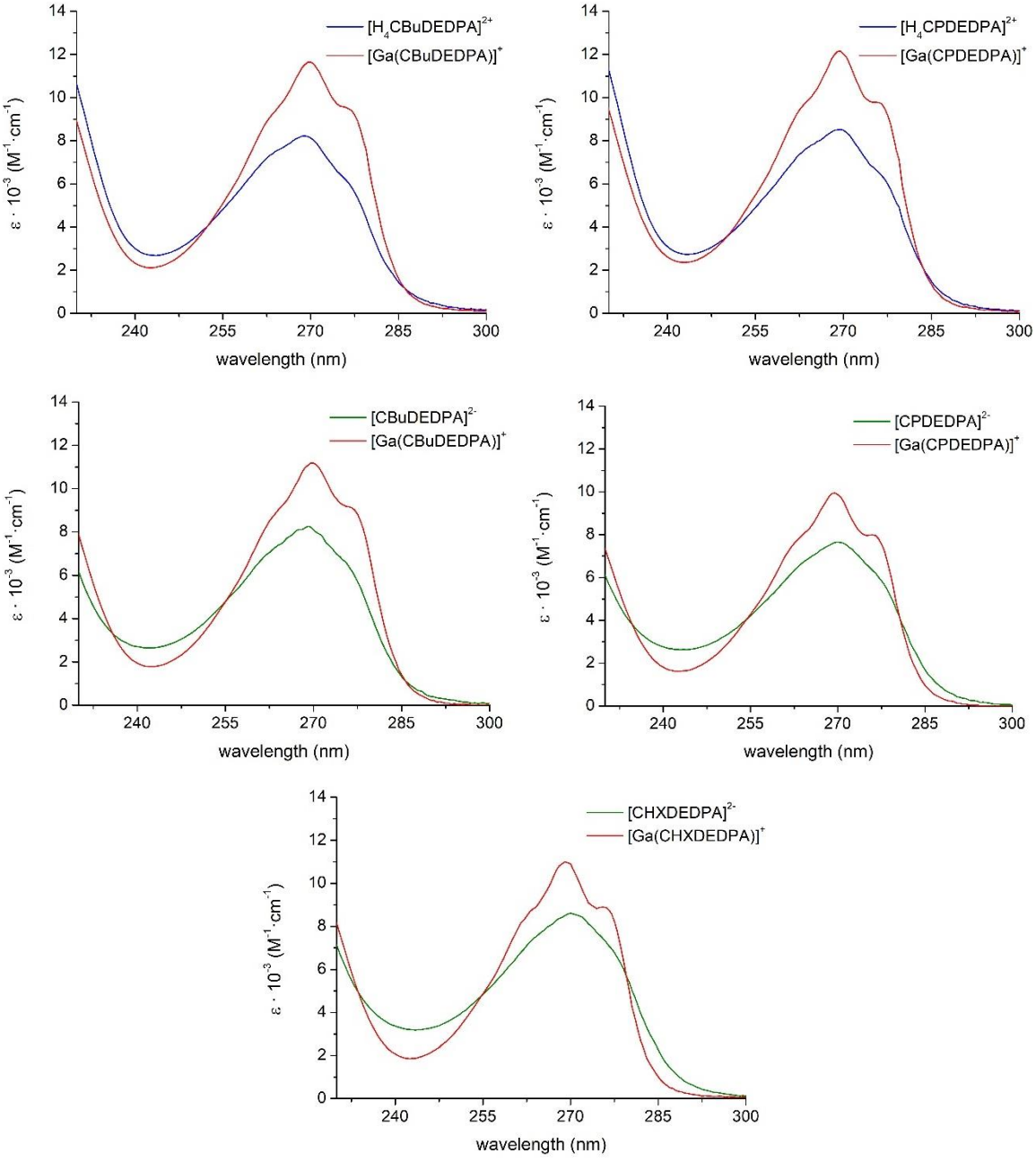

Figure I-62. UV-Vis spectra of the Ga(III) complexes (red lines) compared to the dissociated species in acid (0.1 M HCl, blue lines) or basic (0.1 M NaOH, green lines) media. **[Ga(CHXDEDPA)]**$^+$ (1.4 mM), **[Ga(CPDEDPA)]**$^+$ (1.4 mM), **[Ga(CBuDEDPA)]**$^+$ (1.4 mM). Spectra were registered in water at 298 K. Variations in the molar extinction coefficients initial point are attributed to experimental errors during solution preparations. This are considered negligible as they all fall within the same order of magnitude.

For both series of complexes, single crystals were obtained by slow diffusion of acetone into aqueous solutions of the Cu(II) and Ga(III) complexes (see **Figures A24** and **A25** in the Annex).

3.2. Radiolabelling Assays with Non-bifunctional Chelators

The ability of the ligands **H_2CHXDEDPA**, **H_2CPDEDPA** and **H_2CBuDEDPA** to coordinate ^{64}Cu and ^{68}Ga radioisotopes was determined by probing radiochelation at 25 °C in 0.5 M ammonium acetate buffer (pH 5.5) with $^{64}CuCl_2$ or $^{68}GaCl_3$, respectively. These assays, as in the case of the chelator models, were conducted by Dr. Marlin, a researcher in Dr. Boros' team at University of Wisconsin-Madison.

After the complexation with the radioisotopes, the radiochemical yield (RCY) was measured after 15, 30 and 60 min *via* radio-TLC. The degree of binding was quantified *via* autoradiography and signal integration of the bound complex versus the free ^{64}Cu or ^{68}Ga. Then, the **Apparent Molar Activity (AMA)** was determined as the ratio between the activity in the sample and the amount of ligand at 50% labelling, in which a more efficient radiolabelling shows a higher AMA value.

Figure I-63 shows the results of concentration-dependent radiolabelling with ^{64}Cu for the three tested ligands. At first sight, a more efficient radiolabelling for **H_2CBuDEDPA** is observed, with a quantitative labelling at 0.025 nmol, while for the other two complexes it is at 0.1 nmol. This indicates that the radiolabelling of the cyclobutane-containing ligand is 4 times more efficient than for the other two ligands. This conclusion is further supported by the AMA values. At 15 minutes, **H_2CBuDEDPA** produced quantitative radiolabelling at an AMA value of 4939 mCi·µmol^{-1}, while for the **H_2CHXDEDPA** and **H_2CPDEDPA** ligands produced AMA values of 631 mCi·µmol^{-1} and 565 mCi·µmol^{-1}, respectively, not observing significant differences at the different times measure except for the **H_2CBuDEDPA**, that displays its efficiency peak at 30 min (**Table I-5**).

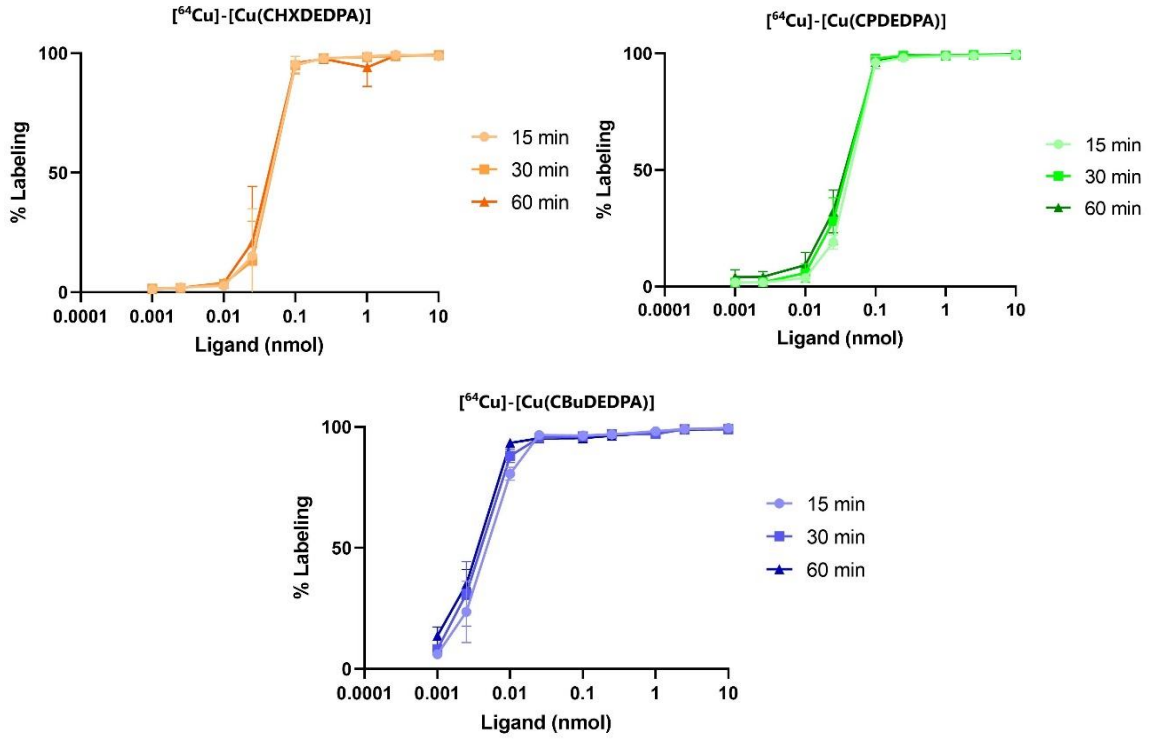

Figure I-63. AMA determination curves with ^{64}Cu for the three chelators tested. Reaction yields were analysed at three time points (15, 30 and 60 min), with n = 3 per data point. Error bars denote standard deviation.

Table I-5. Apparent Molar Activity (mCi·µmol^{-1}) for ^{64}Cu complexes.

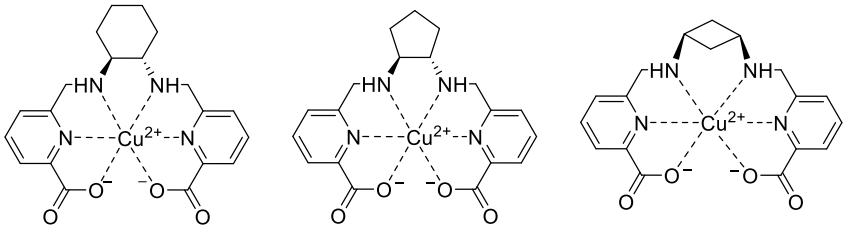

	[^{64}Cu]-[Cu(CHXDEDPA)]	[^{64}Cu]-[Cu(CPDEDPA)]	[^{64}Cu]-[Cu(CBuDEDPA)]
15 min	631	565	4939
30 min	610	647	6148
60 min	670	682	6637

Unfortunately, these positive results with the cyclobutane-containing ligand where not repeated with ^{68}Ga complexes. As depicted in **Figure I-64**, **H_2CHXDEDPA** and **H_2CPDEDPA** yielded a similar efficiency to obtain a quantitative radiolabelling, which is around 1 nmol. However, the **H_2CBuDEDPA** ligand failed to reach quantitative radiolabelling even with the highest concentrations employed. This is confirmed by AMA values of 539 mCi·µmol^{-1} for **H_2CPDEDPA** and 103 mCi·µmol^{-1} for **H_2CHXDEDPA**, while for the **H_2CBuDEDPA** ligand it could not be calculated.

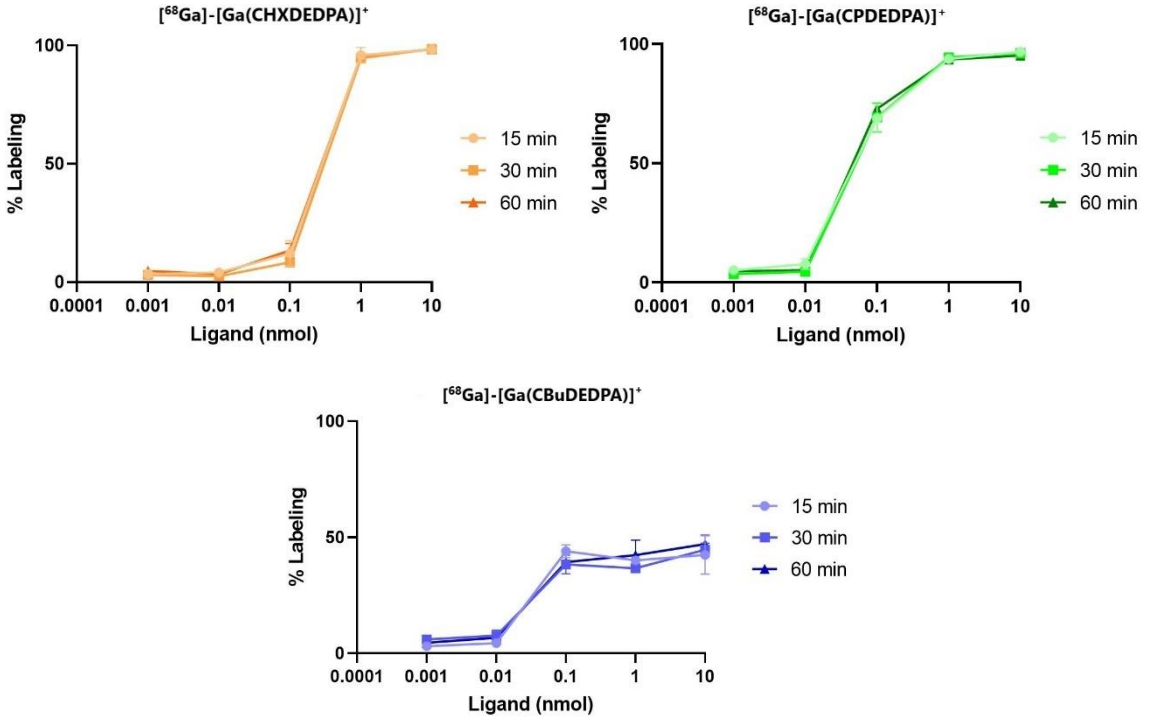

Figure I-64. AMA determination curves with ^{68}Ga for the three chelators tested. Reaction yields were analysed at three time points (15, 30 and 60 min), with n = 3 per data point. Error bars denote standard deviation.

Table I-6. Apparent Molar Activity (mCi·µmol^{-1}) for ^{68}Ga complexes.

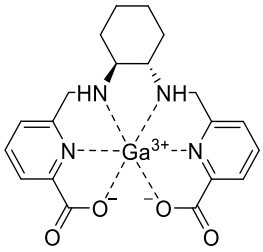

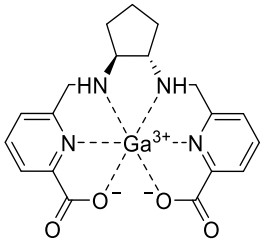

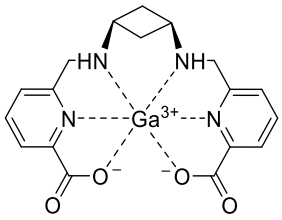

	[^{68}Ga]-[Ga(CHXDEDPA)]$^+$	[^{68}Ga]-[Ga(CPDEDPA)]$^+$	[^{68}Ga]-[Ga(CBuDEDPA)]$^+$
15 min	103	539	---
30 min	93	522	---
60 min	106	560	---

The most probable explanation for the ligand **H_2CBuDEDPA** not complexing efficiently the ^{68}Ga is that the cyclobutane spacer is too rigid to accommodate the radioisotope, having to invert its folding to bind to the metal. This, combined with slow formation kinetics for Ga(III) complexation, may favour a situation where this rigid spacer does not support convergent pre-folding to yield the mononuclear (1:1) complex. Instead, it may lead the system to an alternative stoichiometry, such as 1:2 (Ga:ligand) or a polymeric structure. Then, as the **H_2CBuDEDPA** ligand was not suitable for the complexation of ^{68}Ga, no further studies were performed on the Ga(III) complexes.

Despite these challenges with ^{68}Ga, **H_2CBuDEDPA** presented excellent radiolabelling efficiency with ^{64}Cu, outperforming the other ligands. This high efficiency, combined with rapid labelling at room temperature, highlights the potential of the ligand for PET imaging. To contextualize these results obtained with **H_2CBuDEDPA**, FDA approved **[^{64}Cu]Cu-DOTATATE** provided AMA values of 557 mCi·µmol^{-1} when radiolabelled with ^{64}Cu, which are 10 times lower.[269] However, it is important to emphasise that these values are not comparable, as **[^{64}Cu]Cu-DOTATATE** is a BFC with a targeting vector, which always reduces the efficiency of the radiolabelling.

Consequently, the inertness in physiological conditions of the ^{64}Cu complexes was evaluated in phosphate-buffered saline (PBS) solution (**Figure I-65**, **left**), evidencing no significant decomplexation of the radiocomplexes over 24 h, at the percentage of intact ^{64}Cu-complexes was over 97% in all the cases. In addition, the ^{64}Cu complexes integrity was investigated using a 100-fold excess of diethylenetriaminepentaacetic acid (DTPA) (**Figure I-48**, *vide supra*), which acts as a competing ligand. Transchelation was monitored by TLC over the course of 24 h (**Figure I-65**, **right**) revealing that **[^{64}Cu]-[Cu(CHXDEDPA)]** (96.9 ± 0.6%) and **[^{64}Cu]-[Cu(CBuDEDPA)]** (91.6 ± 1.8%) had a similar stability, while the **[^{64}Cu]-[Cu(CPDEDPA)]** (83.7 ± 1.5%) performed the worst. Considering that ^{64}Cu has a half-life of 12.7 hours, the stability values obtained at the studied time points are sufficiently robust for the medical applications of this radionuclide.

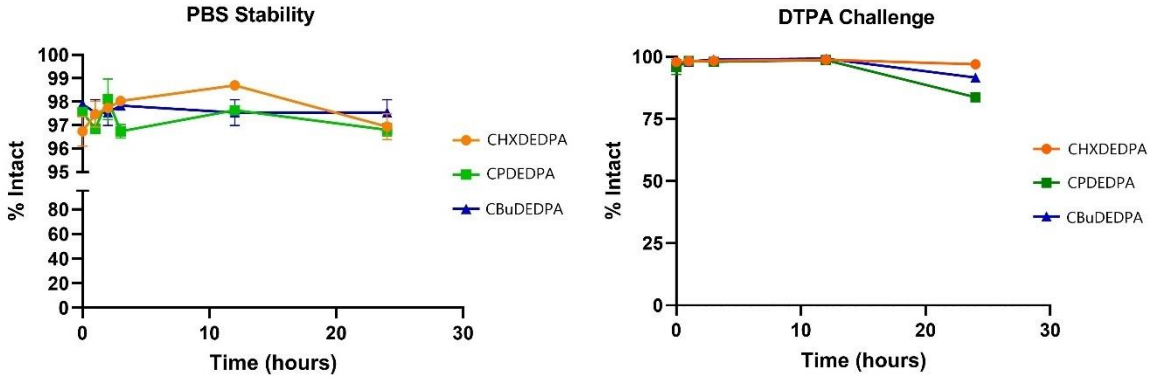

Figure I-65. Study of the kinetic stability of ^{64}Cu-complexes through PBS stability at pH 7.4 (left) and DTPA challenge (right). Solutions were monitored through TLC at six and five time points, respectively, with n = 3 per data point. Error bars denote standard deviation.

Overall, the favourable results obtained for the ^{64}Cu complexes, in terms of labelling efficiency, speed and stability, prompted further *in vitro* studies to investigate the thermodynamic stability and kinetic inertness of the Cu(II) complexes.

3.3. *In vitro* Stability Studies on Cu(II) Complexes

These studies were performed at the research laboratory of Prof. Brandariz in the Chemistry department of Universidade da Coruña. Thermodynamic stability assays were done by me, Daniel Torralba, under Prof. Brandariz's supervision during my research stage in CICA, while the cyclic voltammetry and dissociation kinetic studies were carried out by Prof. Brandariz.

3.3.1. Cyclic Voltammetry

For copper-based radiopharmaceuticals, it is crucial to consistently evaluate the redox stability of the prepared complexes, as this could limit or even prevent their use. If the Cu(II) in the radiopharmaceutical were reduced to Cu(I) due to the action of reducing agents present in the human body, such as NADPH (nicotinamide adenine dinucleotide phosphate) or ascorbic acid, the metal's coordination preferences would change completely. This would lead to a higher affinity for softer donors like sulfur, which is present in many biological molecules such as proteins. This shift would pose a serious problem for selectivity, potentially causing the release of the metal from the radiopharmaceutical and subsequent accumulation of the radioisotope in unintended areas of the body, such as organs or tissues, leading to the reduction of the quality of the images and possibly generating harmful effects for the patient.[270]

Cyclic voltammetry experiments were carried out to assess the stability of the Cu(II) complexes toward reduction. A recent study demonstrated the redox potential of Cu(II) complexes must be shifted out of the window of bioreducing agents, as even very inert Cu(II) complexes can dissociate quickly upon reduction to Cu(I).[271] The threshold of bioreducing agents was estimated to be -0.4 V versus NHE (Normal Hydrogen Electrode).[216]

The cyclic voltammograms recorded from aqueous solutions of Cu(II) complexes in 0.15 M NaCl (vs. Ag/AgCl) exhibit quasi-reversible redox behaviour, characterised by half-wave potentials ($E_{1/2}$)

and peak separation values (ΔEp) of $E_{1/2}$ = -0.695 V (ΔEp = 0.149 V), $E_{1/2}$ = -0.618 V (ΔEp = 0.073 V) and $E_{1/2}$ = -0.565 V (ΔEp = 0.120 V) for **[Cu(CHXDEDPA)]**, **[Cu(CPDEDPA)]** and **[Cu(CBuDEDPA)]**, respectively (**Figure I-66**). For all three complexes ΔEp values increase upon increasing the scan rates (10 mV/s to 500 mV/s, see **Figures A26** to **A28** in the Annex) further supporting the quasi-reversible nature of the electrochemical processes. In addition, a second irreversible oxidation wave was observed, particularly at low scan rates, most likely arising from the structural reorganisation of the reduced Cu(I) species.[272] This second oxidation wave is particularly prominent at -0.160 V for **[Cu(CHXDEDPA)]** (**Figure I-66**).

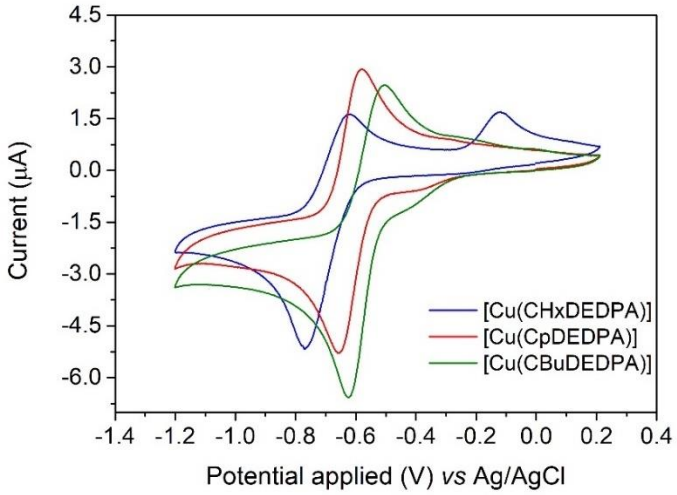

Figure I-66. Cyclic voltammograms recorded from aqueous solutions of the Cu(II) complexes (0.15 M NaCl, scan rate 50 mV/s). Conditions: **[Cu(CHXDEDPA)]**, 1.4 mM, pH 6.6; **[Cu(CPDEDPA)]**, 1.3 mM, pH 6.9; **[Cu(CBuDEDPA)]**, 1.3 mM, pH 5.0.

Furthermore, the reduction potential of **[Cu(CHXDEDPA)]** is clearly out of the threshold of common bioreductants ($E_{1/2}$ = -0.695 V versus Ag/AgCl corresponds to -0.475 V versus NHE). Otherwise, the reduction potentials for **[Cu(CPDEDPA)]** and **[Cu(CBuDEDPA)]** are right on the edge of this threshold, suggesting that these complexes may still resist the bioreduction.

Notably, when compared to the cyclic voltammogram of the acyclic analogue **[Cu(DEDPA)]**, an irreversible reduction peak can be observed at -1.12 V,[262] as well as an oxidative stripping peak of Cu(0) to Cu(II) around 0.0 V.[273] This indicates an improved stability of Cu(I) state for the derivatives **[Cu(CHXDEDPA)]**, **[Cu(CPDEDPA)]** and **[Cu(CBuDEDPA)]**, highlighting the benefit of introducing a rigid moiety to the ligand framework.

Then, from these electrochemical measurements, it can be concluded that the introduction of rigid moieties increases the stability of the complexes upon reduction when compared to **[Cu(DEDPA)]**, and that the three complexes are out of the threshold of the bioreducing agents, such as ascorbate.

3.3.2. Thermodynamic Stability

The protonation constants ($\boldsymbol{K}_n^H$) of the ligands **H_2CHXDEDPA**, **H_2CPDEDPA** and **H_2CBuDEDPA**, were determined using potentiometric titrations and compared to the reference ligand **H_2DEDPA**. The stability constant ($\boldsymbol{K}_{CuL}$) of the corresponding Cu(II) complexes were determined using

spectrophotometric titrations, as complex dissociation occurs in a pH range that is not appropriate for direct potentiometric titrations (pH<2.0), which usually employ an ionic strength (*I*) of *I* = 0.15 M NaCl. Thus, the protonation constants were determined using *I* = 1.0 M NaCl and compared with those reported in 0.15 M NaCl[261] and 0.10 M (Me_4N)(NO_3) for the ligand **H_2CHXDEDPA**.[260] The similar values obtained across different ionic strengths employed indicates that neither the nature nor the concentration of the background electrolyte significantly affects the protonation constants (**Table I-7**).

Table I-7. Ligands protonation constants and stability constants of the Cu(II) complexes determined using potentiometric and spectrophotometric titrations (*I* = 1 M NaCl, 25 ºC). The data in brackets are the standard deviations.

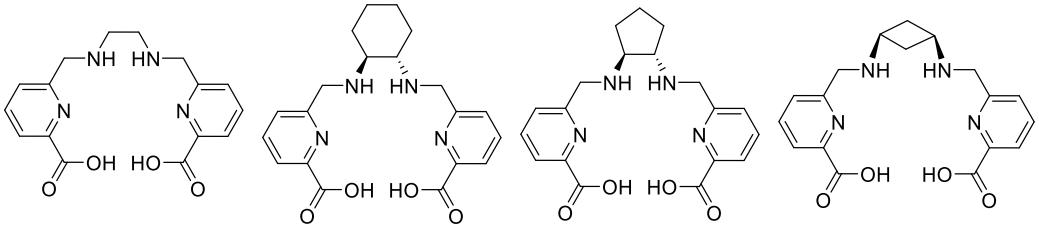

	H_2DEDPA	**H_2CHXDEDPA**	**H_2CPDEDPA**	**H_2CBuDEDPA**
logK_1^H	9.00[(a)] / 8.69[(b)]	9.41 (1) / 9.23[(d)] / 9.13[(b)]	9.05 (1)	8.95 (1)
logK_2^H	6.30[(a)] / 6.18[(b)]	6.45 (1) / 6.47[(d)] / 6.44[(b)]	6.51 (2)	6.87 (1)
logK_3^H	3.06[(a)] / 3.08[(b)]	3.35 (2) / 2.99[(d)] / 3.25[(b)]	3.28 (3)	3.32 (2)
logK_4^H	2.59[(a)] / 2.33[(b)]	2.48 (2) / 2.40[(d)] / 2.40[(b)]	2.51 (4)	2.52 (3)
Σ logK_i^H (*i* = 1-4)	20.95[(a)] / 20.28[(b)]	21.69 / 21.09[(d)] / 21.22[(b)]	22.18	20.19
logK_{CuL}	19.16[c]	25.11 (1)	22.18 (1)	20.19 (1)
pCu[e]	18.5	24.0	21.4	19.5

a) Data measured at *I* = 0.15 M NaCl from reference 235. b) Data measured at *I* = 0.1 M (Me_4N)(NO_3) from reference 260. c) Data measured at *I* = 0.15 M from reference 262. d) Data measured at *I* = 0.15 M NaCl from reference 261. e) Defined as -log[Cu(II)]free, for $[L]_{tot}$ = 10 μM and $[Cu(II)]_{tot}$ = 1 μM.

The first and second protonation constants (logK_1^H and logK_2^H) correspond to the protonation of the amine nitrogen atoms of the ligand. The value of logK_1^H increases slightly on replacing the central ethyl group of **H_2DEDPA** by a cyclohexane ring. This increment in the basicity of the amine nitrogen atoms was also observed previously for the first protonation constant of **H_4EDTA** and its cyclohexane-containing analogue **H_4CDTA** (**Figure I-69**, *vide infra*).[274] This can be attributed, at least in part, to the stronger inductive effect of the ring.[275] The value of logK_1^H decreases following the order **H_2CHXDEDPA** > **H_2CPDEDPA** > **H_2CBuDEDPA**, likely reflecting a decreased cooperation between the amine nitrogen atoms during the first protonation process.[276] However, the value of logK_2^H determined for **H_2CBuDEDPA** is the highest among this series of closely related derivatives, which likely indicates a decreased electrostatic repulsion in the deprotonated form due to the greater distance between the amine nitrogen atoms, which are placed at positions 1 and 3 of the cyclobutane unit, instead of at positions 1 and 2 as in the cyclohexane and cyclopentane derivatives.

For the data analysis of the stability constants of the Cu(II) complexes, performed through spectrophotometric titrations, the absorption spectra of the different protonated forms of the ligands were calculated using the protonation constants determined by potentiometry. The absorption spectra of the complexes display a characteristic absorption band at 270 nm, attributed to the picolinate chromophore. As pH decreases, the intensity of this band diminishes, corresponding to the complex dissociation and the formation of the LH_4^{2+} species. The fits of the spectrophotometric data (**Figure I-67** and **Figure I-69**) provided the stability constants (K_{CuL}) shown in **Table I-7**. Among the series, **[Cu(CHXDEDPA)]** exhibits the highest thermodynamic stability constant, with a remarkably high logK_{CuL} value of 25.11. This represents an increase in complex stability of six orders of magnitude compared to **[Cu(DEDPA)]**. The stability constants of the Cu(II) complexes with these ligands follow the trend **[Cu(CHXDEDPA)]** > **[Cu(CPDEDPA)]** > **[Cu(CBuDEDPA)]**, with the latter being still one order of magnitude higher than that reported for **[Cu(DEDPA)]**.[262] Thus, modification of the ligand scaffold by introducing a rigid spacer has a beneficial impact in terms of complex stability, an effect that is particularly pronounced for the cyclohexane Cu(II) complex.

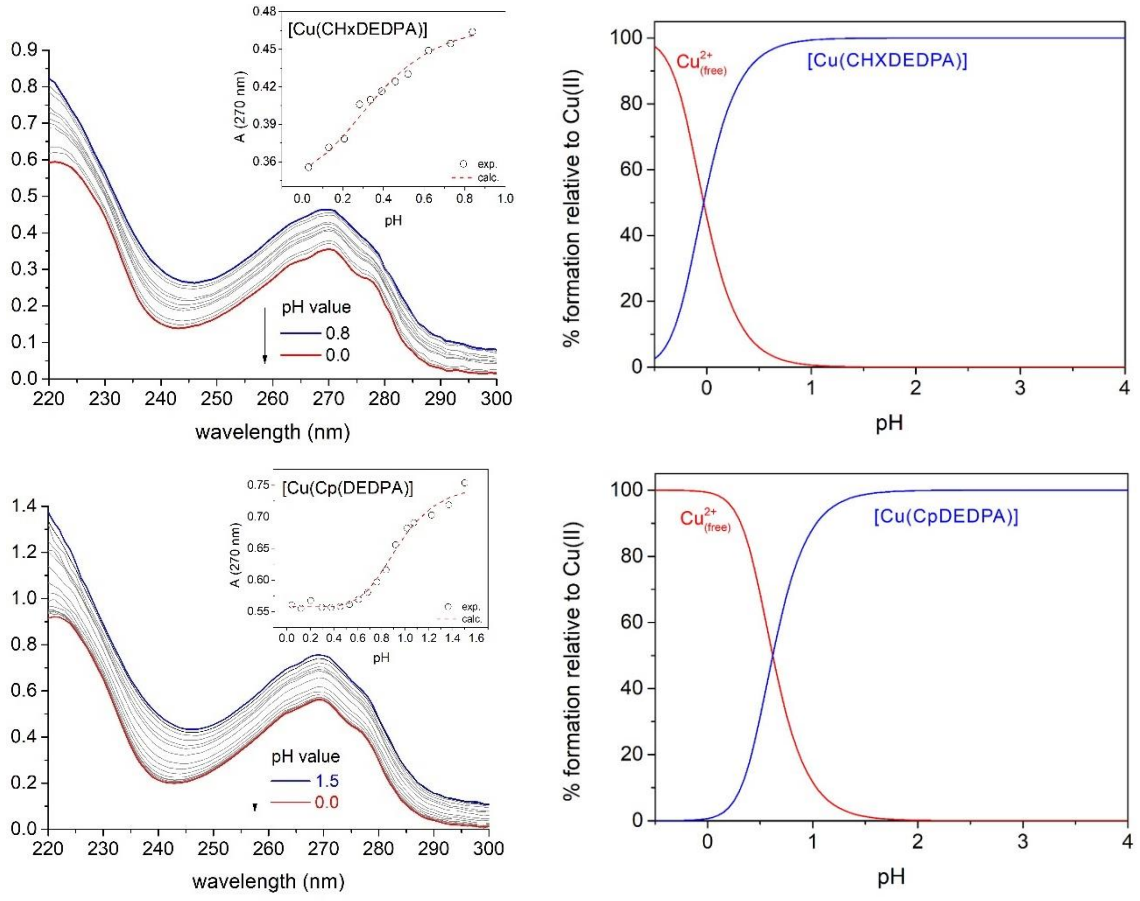

Figure I-67. Spectrophotometric titration (left column) and calculated species diagram (right column) of: **[Cu(CHXDEDPA)]** ($3.68 \cdot 10^{-5}$ M, I = 1 M NaCl) (top row), **[Cu(CPDEDPA)]** ($6.36 \cdot 10^{-5}$ M, I = 1 M NaCl) (bottom row). The inset in the spectrophotometric titration diagram shows the experimental absorbance values at 270 nm and the dashed line represents the fit of the data for stability constant determination.

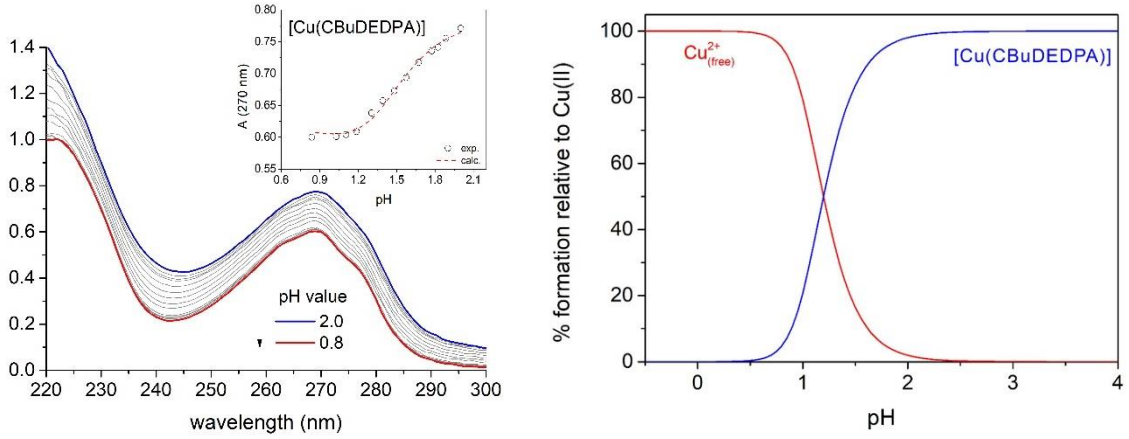

Figure I-68. Spectrophotometric titration (left column) and calculated species diagram (right column) of **[Cu(CBuDEDPA)]** ($6.68 \cdot 10^{-5}$ M, I = 1 M NaCl). The inset in the spectrophotometric titration diagram shows the experimental absorbance values at 270 nm and the dashed line represents the fit of the data for stability constant determination.

The stability of metal complexes for medical applications at physiological pH is generally assessed by their **pM** (**pCu**) values, which are often defined as $-\log[Cu(II)]_{free}$ for a total metal concentration of 1 µM and a total ligand concentration of 10 µM.[277] The pCu values calculated under these conditions follow closely the trend observed for $\log K_{CuL}$ (**Table I-7**). This is not surprising, given that **H_2DEDPA** and the three derivatives described here display similar basicities, as indicated by the $\log K_i^H$ values determined for each ligand (**Table I-7**).

The stability constants and pCu values determined are comparable to those of complexes with ligands (**Figure I-69**. See also **Figure I-48** and **Figure I-57** for ligand structures) commonly used as ^{64}Cu chelators such as **H_4DOTA** ($\log K_{CuL}$ = 22.0; pCu = 17.6, 0.1 M KCl),[278] **H_3NOTA** ($\log K_{CuL}$ = 21.6; pCu = 18.4, 1.0 M $Na(ClO_4)$)[279] or **bispa** ($\log K_{CuL}$ = 18.9; pCu = 19.3, 0.1 M KNO_3).[280] **CB-cyclam** derivatives display very high stability constants ($\log K_{CuL}$ = 27.1), though radiolabelling often requires high temperatures.[281]

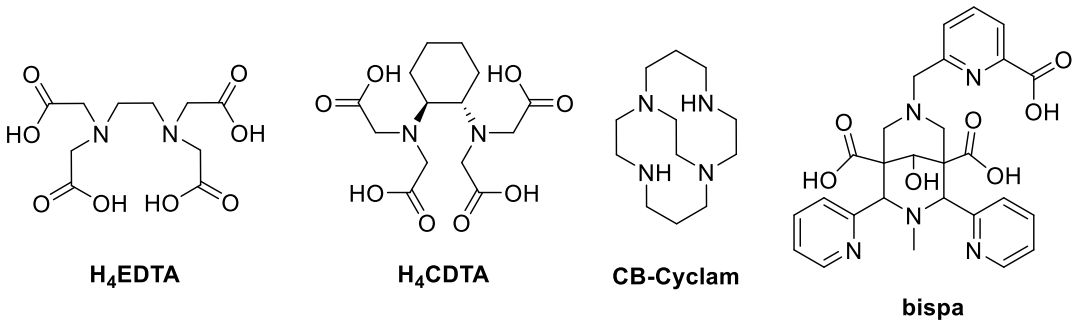

Figure I-69. Selection of relevant ligands employed for the complexation of Cu(II).

In conclusion, the thermodynamic stability of the studied Cu(II) complexes is clearly enhanced upon modification of the ligand scaffold with rigid spacers. This trend, **[Cu(CHXDEDPA)]** > **[Cu(CPDEDPA)]** > **[Cu(CBuDEDPA)]**, indicates that the introduction of rigid cyclic structures, particularly the cyclohexyl moiety, significantly strengthens the complex stability. This stabilisation effect is further supported by pCu values, which reflect the high affinity of these ligands for Cu(II) under physiological conditions, suggesting their potential for robust applications in medical and biochemical contexts, comparable to those already used for the complexation of ^{64}Cu.

3.3.3. Dissociation Kinetics

The kinetic inertness of the radio-complexes is a key property for any radiopharmaceutical candidate. In the particular case of PET agents, the release of the radioisotope decreases the uptake of the probe in the target tissue and introduces background noise that decreases the signal to noise ratio.[282] Often, the inertness of the complex is tested *in vitro* by studying the acid-catalysed dissociation under harsh acidic conditions, using acid concentrations of 1.0-6.0 M.[227,283,284] However, these conditions are far away from those found *in vivo*. As an alternative, a method within a pH range relatively close to physiological conditions was proposed to assess dissociation kinetics of Cu(II) complexes.[271] In this approach, the dissociation reaction is triggered by the presence of ascorbate using neocuproine (NC) as a scavenger. Ascorbate (AA) reduces any free Cu(II) present in the solution to Cu(I), which forms a very stable complex with NC with a characteristic absorption band at 450 nm (**Figure I-70**).[285] Thus, the dissociation of the representative **[Cu(CBuDEDPA)]** complex was investigated in the pH range of 5.4-7.5 to gain information on the pathways that can potentially lead to complex dissociation under physiological conditions. These experiments were conducted using phosphate buffer and a large excess of both NC and AA to ensure pseudo-first-order conditions.

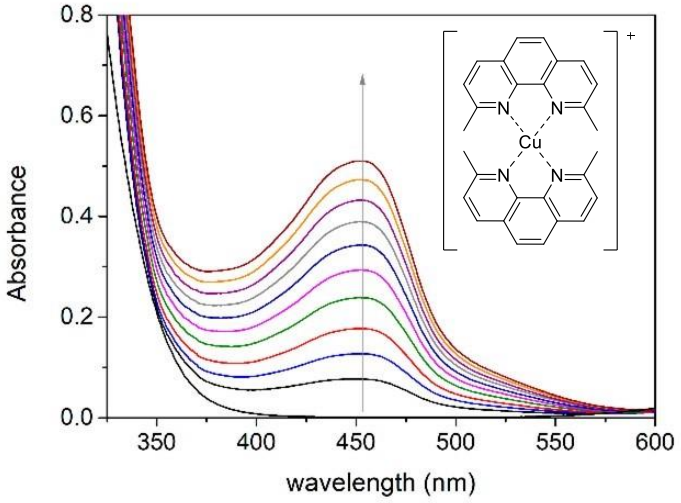

Figure I-70. Spectrophotometric variations observed along time for a solution of **[Cu(CBuDEDPA)]** = 91 μM, [NC] = 0.24 mM, [Ascorbate] = 5.4 mM, [buffer] = 0.122 M. Spectra were recorded every 6 min. The inset shows the structure of the NC complex with Cu(I).

The observed dissociation rate constants (k_{obs}), also known as off-rate dissociation constant (k_{off}), do not vary with AA concentration within experimental error (**Figure I-71**). However, an increment in the proton concentration did cause an increment in k_{obs}, showing a saturation profile that indicates the formation of a protonated complex that it is crucial for the dissociation to proceed (**Figure I-72**). Thus, the observed first-order rate constants were fitted to **Equation 4**:

$$k_{obs} = \frac{k_0 + k_1 K_1^H [\mathrm{H^+}]}{1 + K_1^H [\mathrm{H^+}]} \qquad \textbf{(Equation 4)}$$

Here, k_0 represents the rate constant for the **spontaneous dissociation**, while k_1 is the rate constant characterising the **proton-assisted dissociation** and K_1^H is the protonation constant. The least squares regression fit of the data affords $k_0 = (8.2 \pm 1.3)\cdot10^{-6}$ s^{-1}, $k_1 = (6.3 \pm 0.2)\cdot10^{-6}$ s^{-1} and $K_1^H = (1.5 \pm 0.2)\cdot10^{6}$ M^{-1}. This kinetic data provides some unexpected results. First, this protonation constant corresponds to a pK_a of 6.2 that cannot correspond to any protonation constant of the octahedral complex. This pK_a value is actually only compatible with the protonation of an uncoordinated amino group. Thus, the kinetic data suggest that the proton-assisted dissociation pathway involves a kinetically active species in which amine N atoms are not directly coordinated to the metal. Second, the spontaneous dissociation pathway provides a significant contribution to the overall dissociation of the complex in the investigated pH range. In spite of this, the **[Cu(CBuDEDPA)]** complex is remarkably inert considering its acyclic nature, with a half-life at pH 7.4 of 23.7 h. Lastly, these results confirm that kinetic experiments with concentrated acid solutions are unlikely to provide information on the spontaneous pathway, as it is likely to be negligible under those conditions.

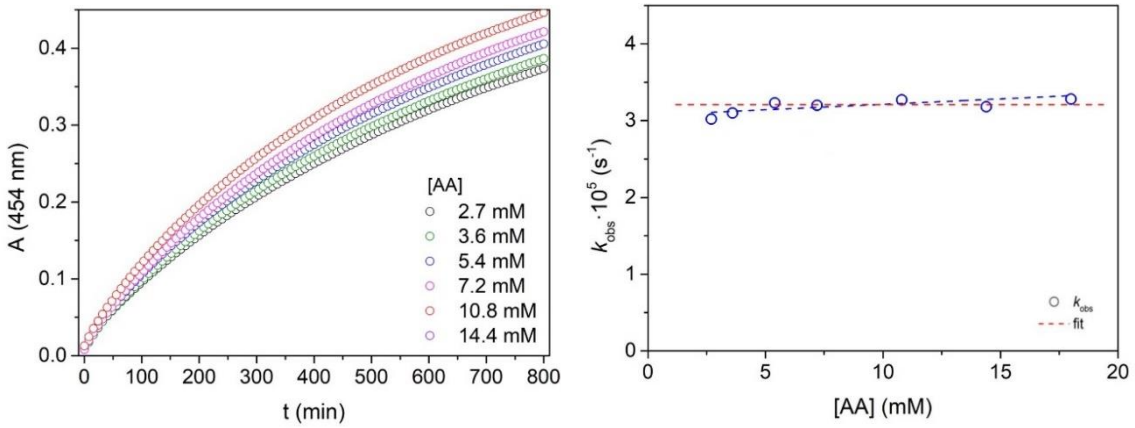

Figure I-71. Variation of the absorption along time at selected wavelength (left) and dependence of k_{obs} (right) versus: [AA] for **[Cu(CBuDEDPA)]** = 91 µM; [NC] = 0.24 mM; [buffer] = 0.12 M and pH = 6.3 recorded at 298 K.

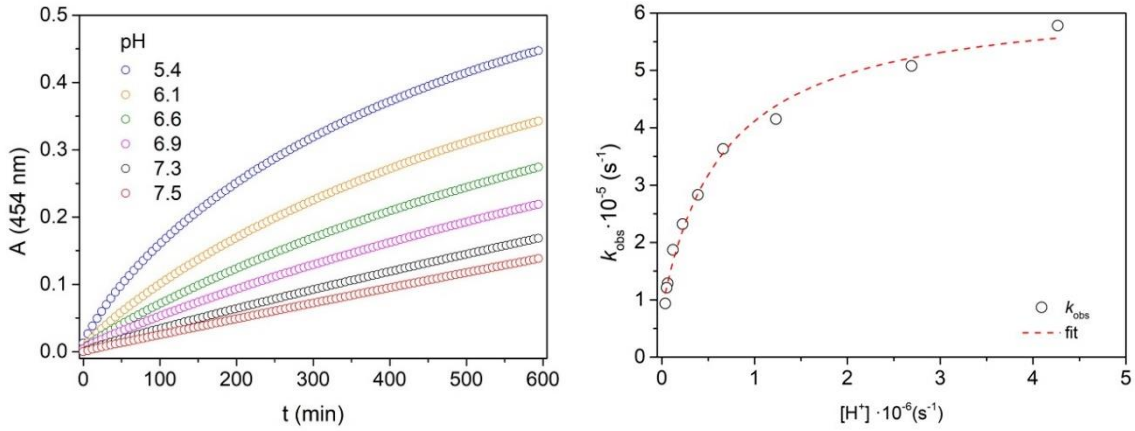

Figure I-72. Variation of the absorption along time at selected wavelength (left) and dependence of k_{obs} (right) versus: [H$^+$] for **[Cu(CBuDEDPA)]** = 91 µM; [NC] = 0.24 mM; [buffer] = 0.12 M and [AA] = 5.4 mM recorded at 298 K.

For the **[Cu(CHXDEDPA)]** and **[Cu(CPDEDPA)]** complexes, the assays showed no observable changes within the pH range in which they were performed, suggesting that no meaningful dissociation or alteration would likely occur at lower pH levels. Moreover, due to time constraints and the primary focus being the **[Cu(CBuDEDPA)]** complex, further investigations into these complexes were not pursued.

3.4. Synthesis of Cyclobutane-containing Bifunctional Chelators

The studies conducted with the chelator models confirmed that the introduction of the cyclobutane spacer into the ligand structure produces an enhancement in radiolabelling efficiency, while preserving a good thermodynamic stability and kinetic inertness. The rigid and cyclic nature of the cyclobutane ring provides an ideal platform for pre-organizing the ligand to efficiently coordinate with copper ions. These findings prompted the next step in this thesis chapter: The synthesis of a bifunctional chelator.

This section presents the synthesis of novel BFCs based on the ***cis*-1,3-cyclobutanediamine scaffold** functionalised at position 2 with a *cis*- or *trans*- relative configuration to the amino groups, making the chelator adaptable for conjugation to biomolecules. The placement of this functional group ensures that the chelator can be easily modified for the desired applications, enhancing its versatility for radiopharmaceutical applications. Based on a thorough review of the literature and prior research conducted by our group on cyclobutane derivates, the proposed structures were envisaged. Their retrosynthetic analysis is outlined in **Scheme I-29**. This scheme illustrates the strategy to synthesise two BFCs with the ability to control the *cis* or *trans* relationship between the additional functional group and the diamine substituents. This relative stereochemistry would be controlled through the epimerisation of the carbon α to the ester functional group, formed in the ring-opening reaction of the bicyclic adduct from the initial [2+2]-photocycloaddition.

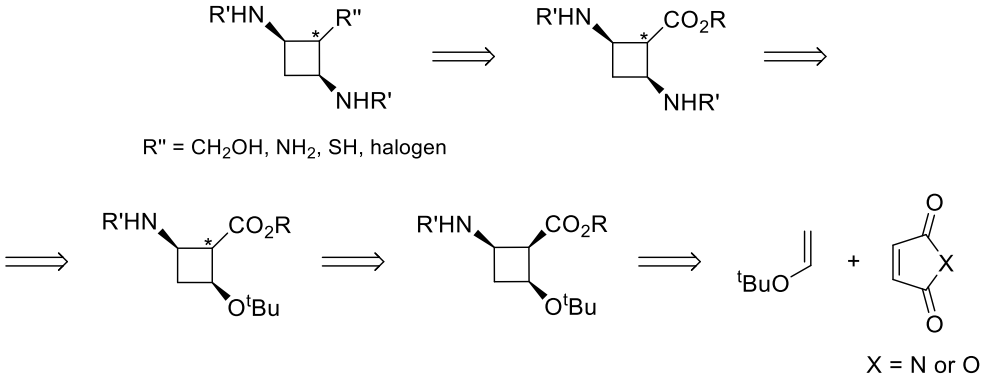

Scheme I-29. Retrosynthetic analysis for the obtention of the *cis*,*cis*- and *cis*,*trans*-1,3-cyclobutanediamines functionalised in position 2.

3.4.1. Synthesis of the Ligand *cis,cis*-L1

Three different synthetic routes were considered with the aim of synthesising the cyclobutane-containing precursor **I**, which enables access to the *cis*,*cis*-1,3-cyclobutanediamine derivative **II** (**Scheme I-30**). As a common feature, the cyclobutane structure is constructed *via* a [2+2]-photocycloaddition, using either maleimide (**102**) (synthetic route A)[286–289] or maleic anhydride

(**32**) (synthetic route B and C),[290–294] in combination with *tert*-butyl vinyl ether **103**, to afford adduct **(±)-104** or adduct **(±)-105**, respectively.

The cyclobutane-containing intermediates, **(±)-104** and **(±)-105**, would be submitted to different transformations, depending on the synthetic route, with the objective of affording the intermediate **I**. In the synthetic route A, **(±)-104** undergoes methanolysis followed by a Hofmann rearrangement. For **(±)-105**, two alternative strategies were considered. In synthetic route B, following the synthetic sequence developed by Aitken *et al*.,[295] ammonolysis of **(±)-105** is performed, followed by a Hofmann-type rearrangement. Alternatively, synthetic route C proceeds with the Fischer esterification of **(±)-105,** obtaining the diester **(±)-106**. The selective enzymatic hydrolysis of one of the ester groups could give access to a monoester, also known as hemiester, intermediate which subsequently it is transformed to an amine *via* a Curtius-type reaction.

The three different synthetic routes will be compared based on the overall yield and the number of steps required to afford intermediate **I**, choosing the most promising one to obtain the final product.

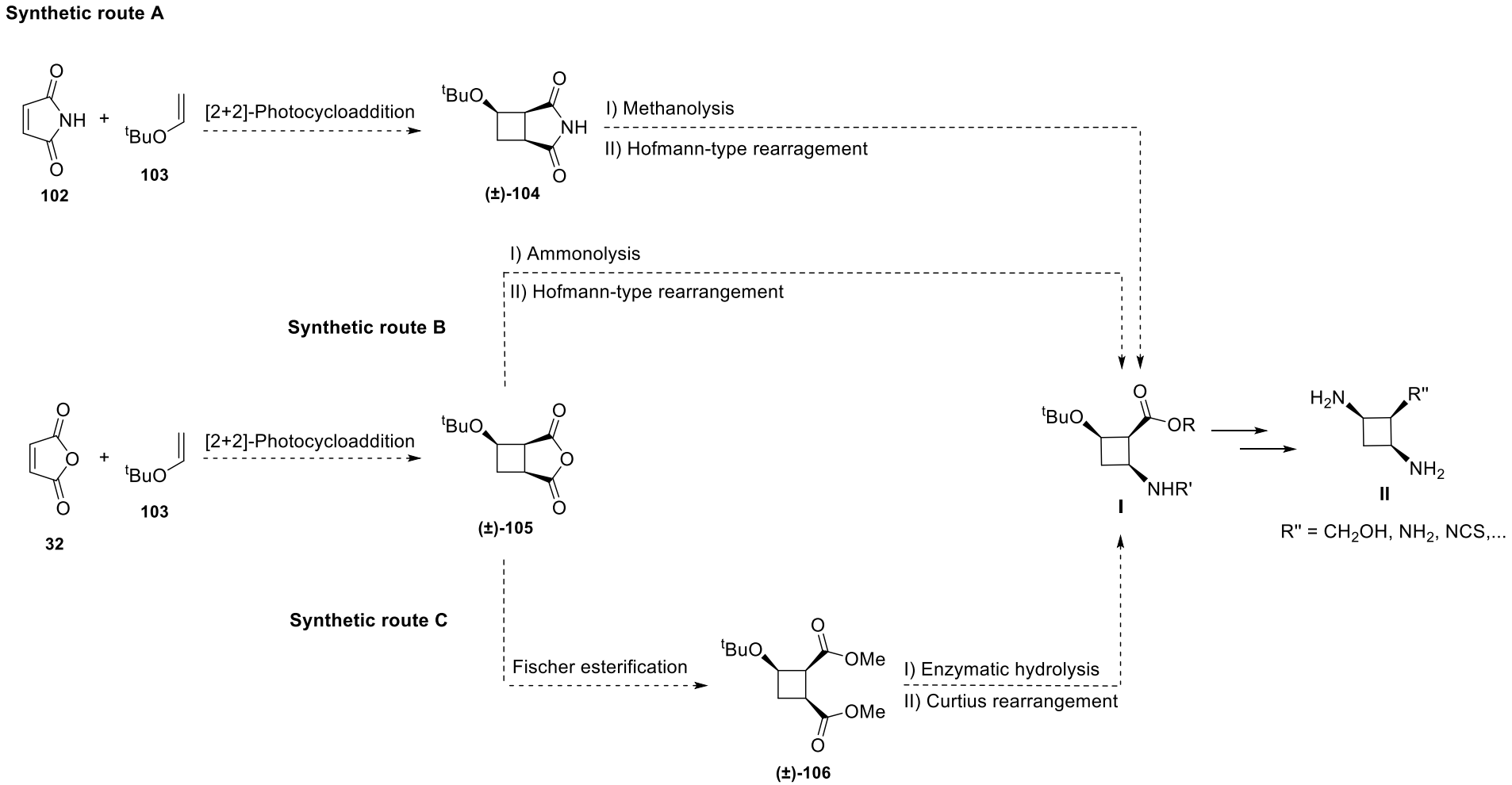

Scheme I-30. Synthetic routes foreseen to prepare the *cis*,*cis*-1,3-cyclobutanediamine functionalised in position 2, **II**.

3.4.1.1. Synthetic Route A

In this synthetic route, maleimide **102**, a versatile enone, is employed as starting material, along with an excess of the *tert*-butyl vinyl ether **103** in a [2+2]-photocycloaddition reaction. Thus, a degassed solution of both starting materials and acetophenone, as photosensitiser, in acetonitrile was irradiated using a 400 W mercury lamp in a reactor fitted with a Pyrex filter. The reaction temperature was controlled with a methanol-cooling jacket set at 20 ºC. After 1 hour, a total conversion of the maleimide was observed through ^{1}H-NMR, obtaining a mixture of *endo*-**(±)-104** and *exo*-**(±)-107** diastereoisomers (**Scheme I-31**), in a 4.2:1 proportion and a total yield of 79%, after separation by column chromatography. As expected, the product with an *endo* configuration was preferentially formed, due to the bulk of the alkyl radical of the vinyl ether.[295,296] This diastereoselectivity was favourable for the obtention of the *cis,cis*-1,3-cyclobutanediamine in the following steps. Also, there is no need for chiral resolution, as the final ligand is meso. The reaction yield, as well as the diastereomeric ratio, were consistently achieved regardless of the reaction scale (up to 12 mmol).

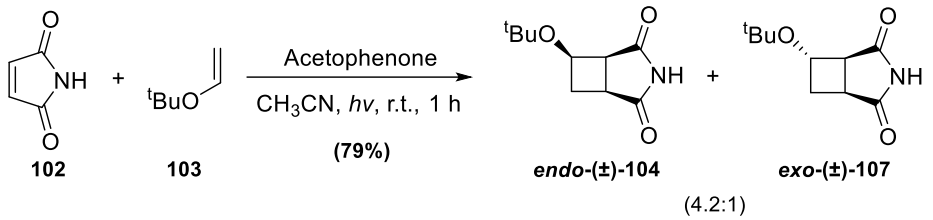

Scheme I-31. [2+2]-Photocycloaddition using maleimide for the obtention of cyclobutane-containing derivatives.

The synthesis proceeded with the *endo*-**(±)-104** diastereoisomer, with the goal of obtaining product **(±)-108**, where the ester group is held in position 2 and the carbamate in position 3*. However, opposite regioselectivity was reported by Aitken *et al.*[295] for the hydrolysis of *endo*-**(±)-104** when classic Hofmann rearrangement conditions were employed, obtaining compound **(±)-109**. As an alternative, conditions reported by Moriyama *et al.*[297] showed a different regioselectivity for the molecules studied in their research group, affording a mixture of both regioisomers **111** and **112** (**Scheme I-32**).

In an effort to obtain **(±)-108**, the opposite regioisomer from that reported by Aitken *et al.*[295], Moriyama's conditions were applied to our system. *Endo*-**(±)-104** was submitted to a tandem reaction *via* methanolysis followed by a Hofmann-type rearrangement reaction using a hypervalent iodine(III) reagent generated *in situ* from an iodoarene and an oxidant. Trivalent iodine species have been shown to directly transform carboxamides into amines[298] and, specifically, this reaction is promoted by the formation of an imide-λ^3-iodine intermediate with maleimide.

*Note that the numbering is not given according to the nomenclature.

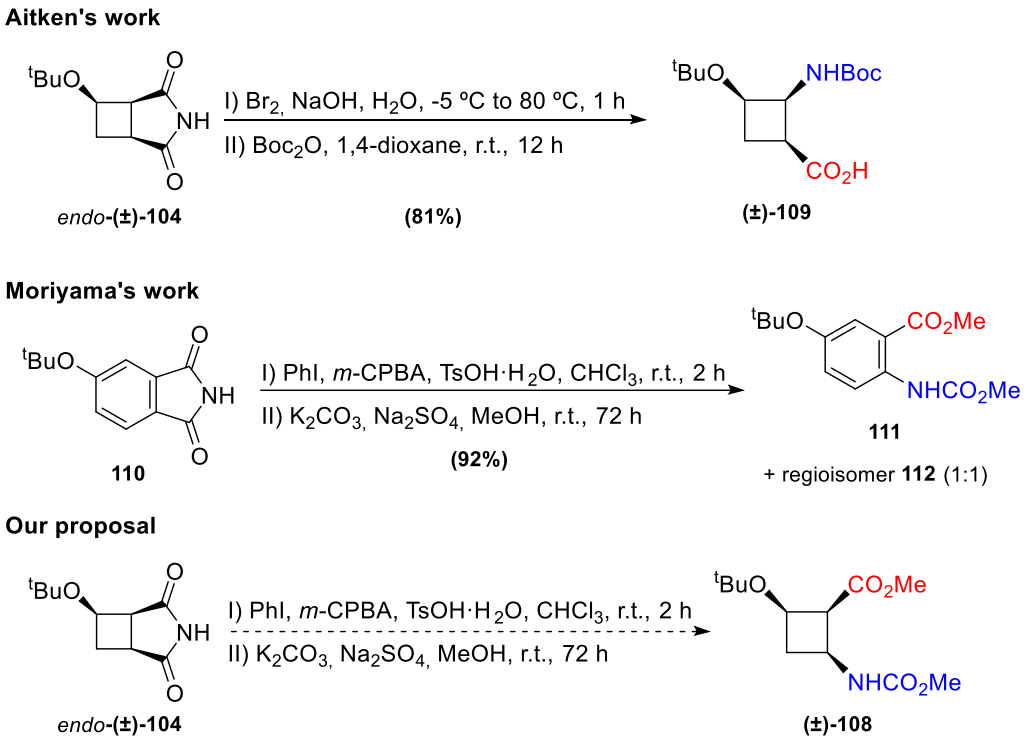

Scheme I-32. Comparison of Aitken's,[295] Moriyama's[297] and our proposal for the regioselective obtention of product **(±)-108**.

The reaction was successfully carried out, as indicated by ^{1}H-NMR and ^{13}C-NMR analysis following purification, which confirmed the presence of a cyclobutane structure substituted with a methyl carbamate, a methyl ester and *tert*-butyl ether. Notably, the NMR spectra displayed signals corresponding to a single product, but the regioisomer obtained still needed to be determined (**Figure I-73**). To elucidate the structure and stereochemistry of the product, further NMR studies were conducted, including COSY, me-HSQC, HMBC, and NOE experiments. From these experiments it could be concluded that:

- COSY spectrum (**Figure I-74**) showed correlation between H_3 and one of the H_4 protons. This could be attributed to a long-range W-type 4-bond distance coupling for structure **(±)-113**, which is quite common in cyclic compounds.[299] Instead, in structure **(±)-108**, H_3 would be expected to couple with both H_4 protons, which is not the case. In addition, H_1 and H_3 also showed correlation, indicating their vicinity, which relates to structure **(±)-113**.
- HMBC spectrum (**Figure I-75**) showed correlation between the methyl ester moiety and H_4 protons, suggesting that C_4 is vicinal to C_2, supporting the assignment of structure **(±)-113**. Instead, for structure **(±)-108**, it would be expected to see correlation between H_1 and the methyl ester moiety, which is not the case.
- NOESY and NOE experiments confirmed the stereochemistry of the molecule, particularly evident in the H_2 selective NOE (**Figure I-76**), indicating a *cis*,*cis* configuration.

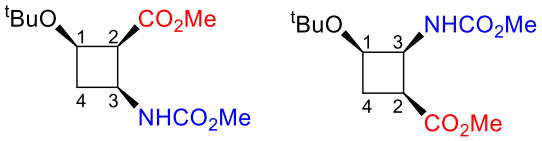

(±)-108 **(±)-113**

Figure I-73. Possible regioisomers obtained in the ring-opening of *endo*-**(±)-104**.

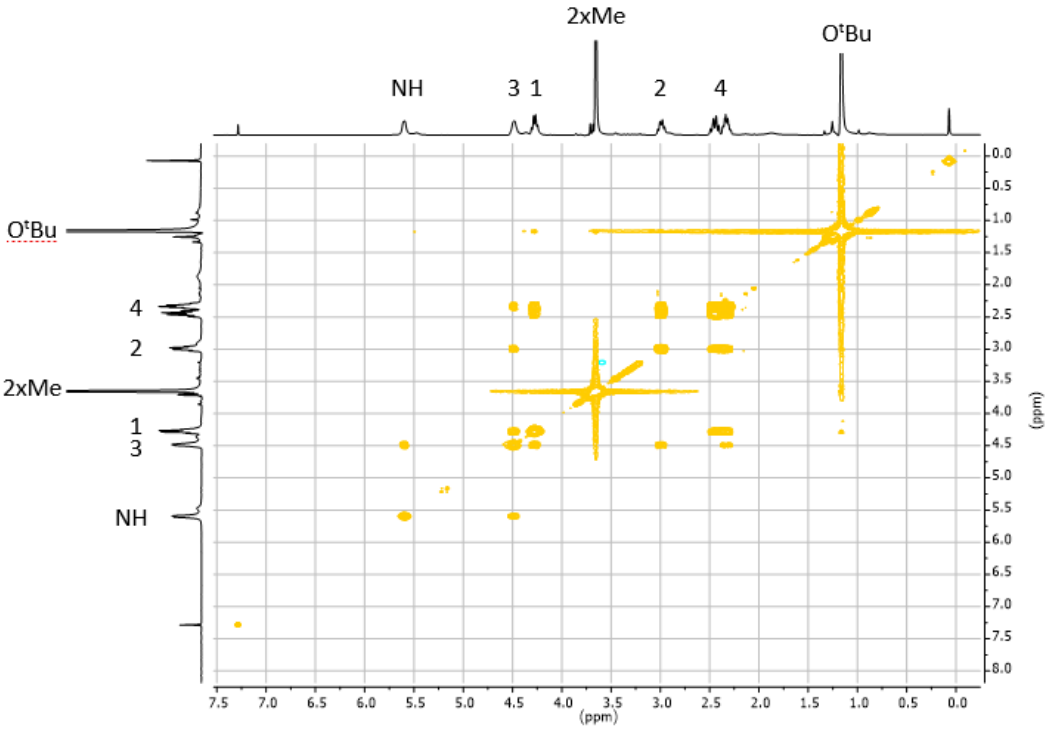

Figure I-74. COSY spectrum (400 MHz, $CDCl_3$) of the intermediate obtained in the ring-opening of *endo*-**(±)-104**.

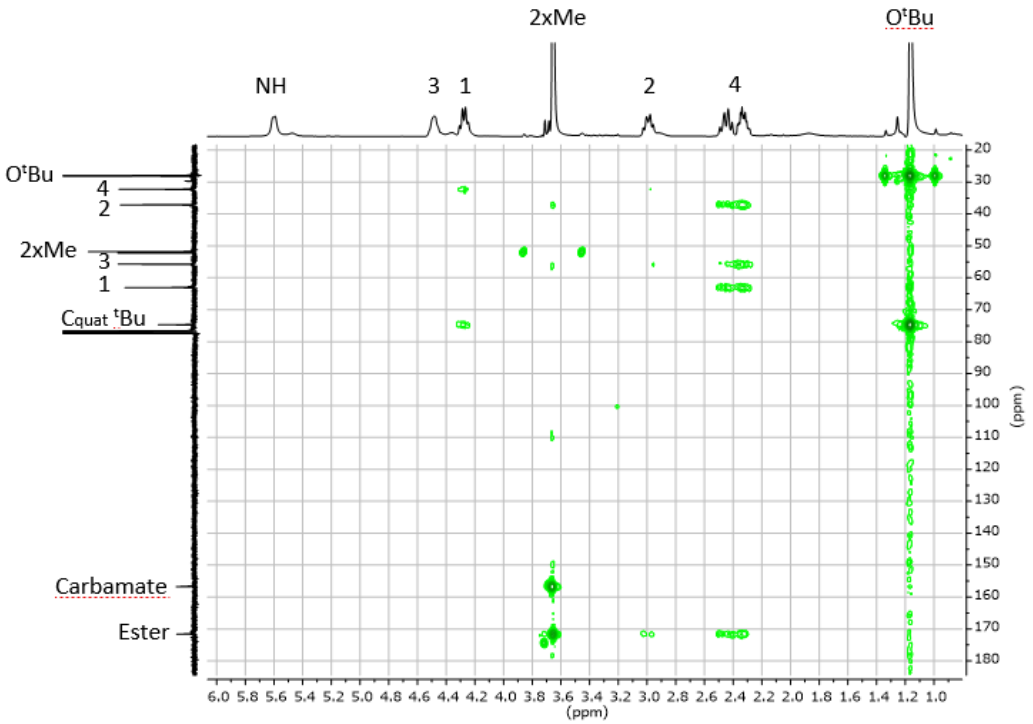

Figure I-75. HMBC spectrum (400 MHz, $CDCl_3$) of the intermediate obtained in the ring-opening of *endo*-**(±)-104**.

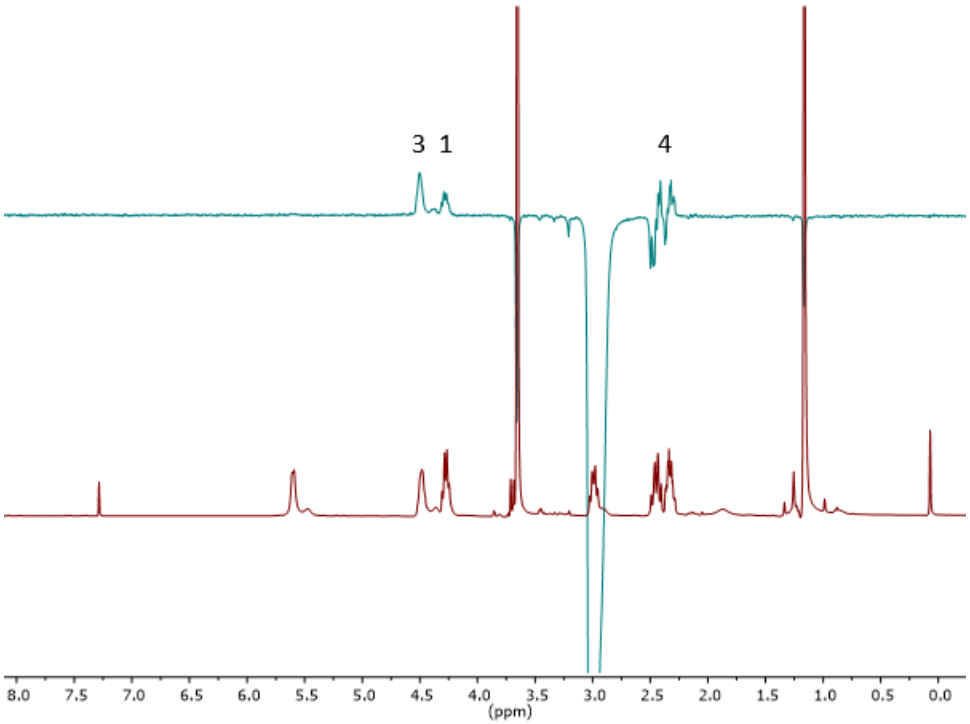

Figure I-76. Selective NOE irradiating H_2 (400 MHz, $CDCl_3$) of the intermediate obtained in the ring-opening of *endo*-**(±)-104.**

Following the NMR structural analysis, it was concluded that the regioisomer afforded in 69% yield was **(±)-113** (**Scheme I-33**), which was not the desired one. This result confirms that the regioselectivity is conditioned by the steric hindrance of the *tert*-butoxy group, rather than the methodology used in the ring-opening reaction.

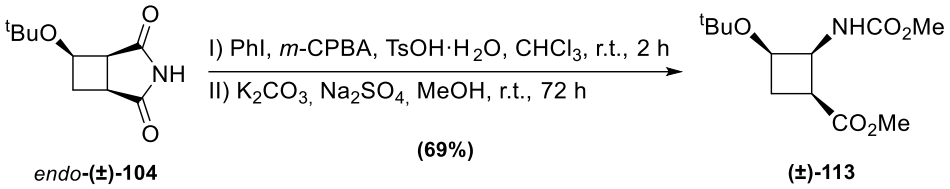

endo-**(±)-104** **(±)-113**

Scheme I-33. Hofmann-type rearrangement of maleimide derivative *endo*-**(±)-104**.

The synthetic route was dismissed due to the incompatibility of this regioisomer with the objective of obtaining a *cis,cis*-1,3-cyclobutanediamine functionalised in position 2. This is due to the need of transforming the methyl ester into an amine *via* saponification followed by a Hofmann rearrangement reaction, resulting in the formation of a cyclic urea upon the intramolecular nucleophilic attack of the methyl carbamate to the isocyanate intermediate.[300,301] The reaction is favoured due to the *cis* stereochemistry of the functional groups, requiring the double protection of the nitrogen as a dicarbamate to generate a tertiary amine in order to avoid the intramolecular cyclisation.[302] However, the discouraging yields reported for these strategies, in addition to the loss of versatility in the functional group installed in position 2, rendered these options less appealing. Consequently, further exploration of synthetic routes B and C became the most attractive alternative.

3.4.1.2. Synthetic Route B

Maleic anhydride (**32**) was used as the enone component in this synthetic route and *tert*-butyl vinyl ether **103** was retained as the alkene partner for the [2+2]-photocycloaddition. Following the protocol described by Aitken *et al*.,[295] acetone served as both the solvent and the photosensitiser. The degassed solution was irradiated for 4 h using a 400 W mercury lamp in a 700 mL reactor fitted with a Pyrex filter to afford molecule **(±)-105** as a single diastereoisomer (**Scheme I-34**). The absence of side products, as indicated by ^{1}H-NMR, along with the incompatibility of the molecule with silica gel purification, prompted the decision to use the crude material from the photochemical reaction without further purification in the subsequent step.

A one-pot ammonolysis/Hofmann rearrangement/amine protection protocol was then employed to furnish molecule **(±)-114**. Once again, the first step exhibited complete regioselectivity, due to the attack of ammonia at the least sterically hindered carbonyl group. Unfortunately, the overall yield of the methodology was only 3%, much less than the 30% reported in the literature.[295] Upon repeating the photochemical reaction, it was observed that after 1 hour, no remaining maleic anhydride was detectable by ^{1}H-NMR, suggesting that the reaction time could be shortened from the described 4 hours of reaction. However, even after adjusting this parameter, the yield of **(±)-114** remained low, achieving only 11% (**Scheme I-34**).

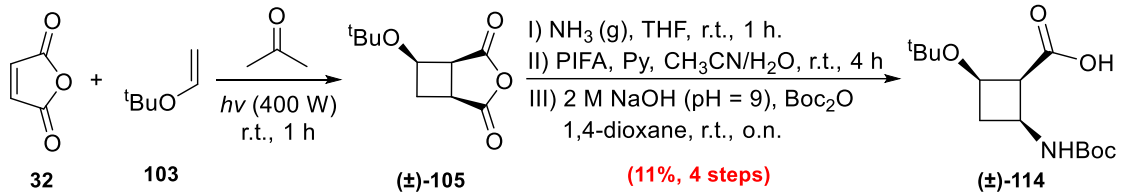

Scheme I-34. Synthesis of the cyclobutane-containing structure **(±)-114** following Aitken's research group protocol.

The low yield obtained for this early intermediate prompted the exploration of the alternative synthetic route C, expecting that this approach would improve the overall efficiency of the synthesis.

3.4.1.3. Synthetic Route C

The synthetic approach of route C was inspired by previous studies in our research group focused on cyclobutane-containing structures. The synthesis started with a Fischer esterification of the photoadduct **(±)-105**,[303] obtained through a [2+2]-photocycloaddition under identical conditions as used in synthetic route B (**Scheme I-34**). This reaction afforded a modest 25% combined yield, resulting in a 1:1 mixture of the target diester **(±)-106** and hemiester **(±)-115** (**Scheme I-35**), whose structures were confirmed by NMR analysis. This last was considered as a side product, as the desired regioisomer would position the carboxyl group at C-3, enabling subsequent conversion *via* the Curtius rearrangement to the corresponding protected amine. The obtention of this mixture of products was likely influenced by the steric hindrance exhorted by the *tert*-butyl ether group, as observed in routes A and B, favouring nucleophilic attack at the less hindered position and complicating the obtention of diester **(±)-106**.

Before performing any optimisation of the reaction, an asymmetric enzyme-catalysed hydrolysis was conducted on diester **(±)-106** to explore the reaction's selectivity for the desired regioisomer, as this substrate had not been previously examined in this context. This methodology was chosen as it had demonstrated enantioselectivity in related substrates.[294] Unfortunately, treatment with pig liver esterase (PLE) in aqueous media at pH 7[304,305] resulted in a mixture of products, as observed by ^{1}H-NMR (**Scheme I-35**). After 72 h, hemiester **(±)-115** was identified along with another product with similar signals, potentially corresponding to regioisomer **(±)-116**. This mixture of products indicates a lack of selectivity for the chemoenzymatic hydrolysis, which motivated the change in the objective in the synthetic route.

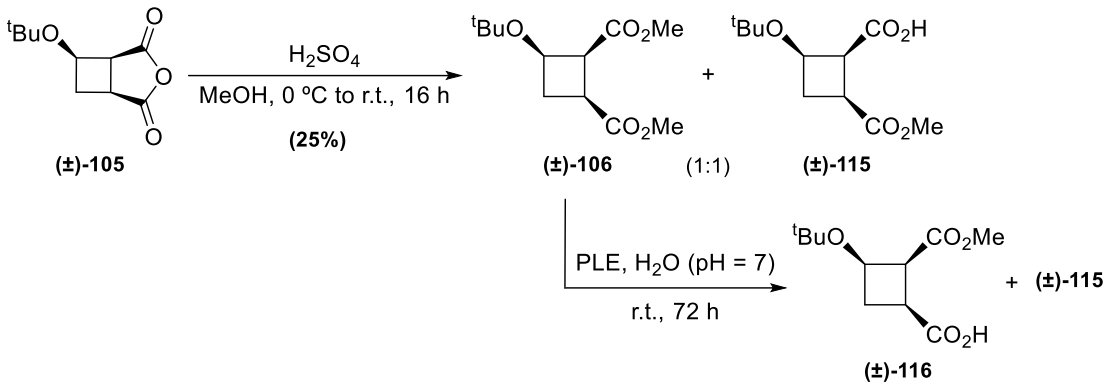

Scheme I-35. Fischer esterification of **(±)-105** and enzyme-catalysed hydrolysis of diester **(±)-106**.

Given the role of *tert*-butyl ether steric hindrance in directing the ring opening of anhydride **(±)-105**, it was decided to focus on synthesising the most favoured regioisomer, which presents the carboxylic acid at C-2 and the ester at C-3. To enhance the regioselectivity and yield a single product, *tert*-butanol (*t*-BuOH) was used in combination with DMAP,[306] anticipating that the bulky ester substituent would improve regioselectivity. The approach proved successful, as *tert*-butyl ester **(±)-117** was afforded as a single product, albeit with a low yield of 20%. This limited yield was attributed both to the low nucleophilicity of *t*-BuOH and to the formation of the diacid by-product due to the presence of water. However, attempts to improve the yield by using an anhydrous atmosphere and molecular sieves in the crude of reaction were unsuccessful. As an alternative, sodium methoxide (MeONa)[306,307] was employed to have a stochiometric control of the nucleophile used, leading to the regioselective formation of hemiester **(±)-115** in quantitative yield (**Scheme I-36**).

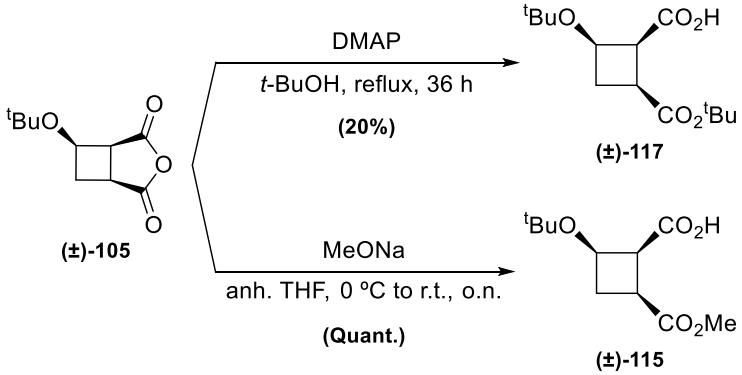

Scheme I-36. Ring opening of the anhydride **(±)-105**.

The synthesis was continued using hemiester **(±)-115**, despite the need for additional steps compared to initial synthetic plan. Direct reduction of the carboxylic acid at C-2 was not feasible, as it would result in the formation of the corresponding lactone.[308,309] Therefore, an orthogonal protecting group was installed at this position, choosing a benzyl ester due to the easy removal and the experience of the group working with it. Using benzyl bromide in presence of sodium bicarbonate ($NaHCO_3$) as a base yielded diester **(±)-118** in 42% (**Table I-8, entry 1**). This low yield was surprising for such a common protection reaction. Efforts to improve the yield by substituting $NaHCO_3$ with K_2CO_3 and increasing the equivalents of benzyl bromide and base (**Table I-8, entries 2-4**), were ineffective. Additional experiments using auxiliary reagents such as potassium iodide (KI) or a crown ether (18-crown-6) also failed to improve the yield (**Table I-8, entries 5 and 6**).

Table I-8. Reaction conditions explored for the obtention of diester **(±)-118**.

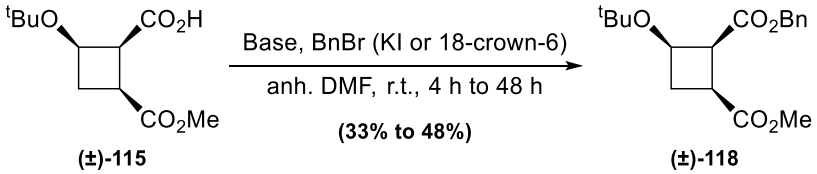

Entry	BnBr (eq.)	Base (eq.)	Additives	Reaction time	Yield (%)
1	1.3 eq.	$NaHCO_3$ (1.3 eq.)	---	48 h	42%
2	1.3 eq.	K_2CO_3 (1.3 eq.)	---	4 h	48%
3	1.5 eq.	K_2CO_3 (1.5 eq.)	---	4 h	47%
4	2 eq.	K_2CO_3 (1.5 eq.)	---	4 h	44%
5	1.5 eq.	K_2CO_3 (1.5 eq.)	KI	4 h	33%
6	1.5 eq.	K_2CO_3 (1.5 eq.)	18-crown-6	4 h	43%

Alternatively, other methodologies reported in the literature to transform a carboxylic acid into a benzyl ester were tested. Steglich esterification[309] using benzyl alcohol provided similar yields, while the employment of benzyl trichloroacetimidate[310] resulted in the degradation of the starting material (**Scheme I-37**).

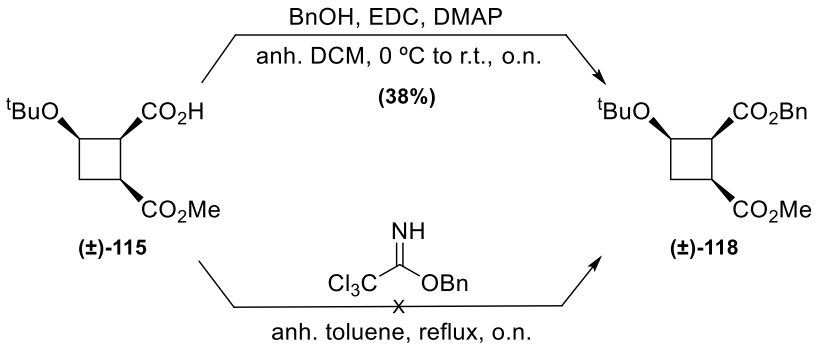

Scheme I-37. Alternative methodologies for the formation of the diester **(±)-118**.

It became obvious that the methodology employed was not the problem, neither the reactivity due to steric hindrance of the *tert*-butyl ether, as the starting material could not be observed by TLC or recovered in the column chromatography. This led to concerns about the purity of **(±)-115**, despite the fact that ^{1}H-NMR in deuterated chloroform ($CDCl_3$) showed only minor impurities under the *tert*-butyl ether signal, which slightly affected the integral value (**Figure I-77**, **B**).

To further investigate this issue, a ^{1}H-NMR spectrum was obtained in deuterated dimethyl sulfoxide (DMSO-d_6) to detect potential insoluble impurities. Only the same aliphatic impurity was observed, though it significantly affected more the *tert*-butyl peak integral (**Figure I-77**, **A**). Hexane digestions of the crude failed to remove this impurity, so as a last chance to remove any impurity that was diminishing the yields, a purification by column chromatography was performed. Surprisingly, the yield for the esterification reaction with MeONa dropped to a 32%. ^{1}H-NMR confirmed the removal of the aliphatic impurity, suggesting it was more significant than previously assumed, or the hemiester **(±)-115** may be unstable on silica gel (**Figure I-77**, **C**).

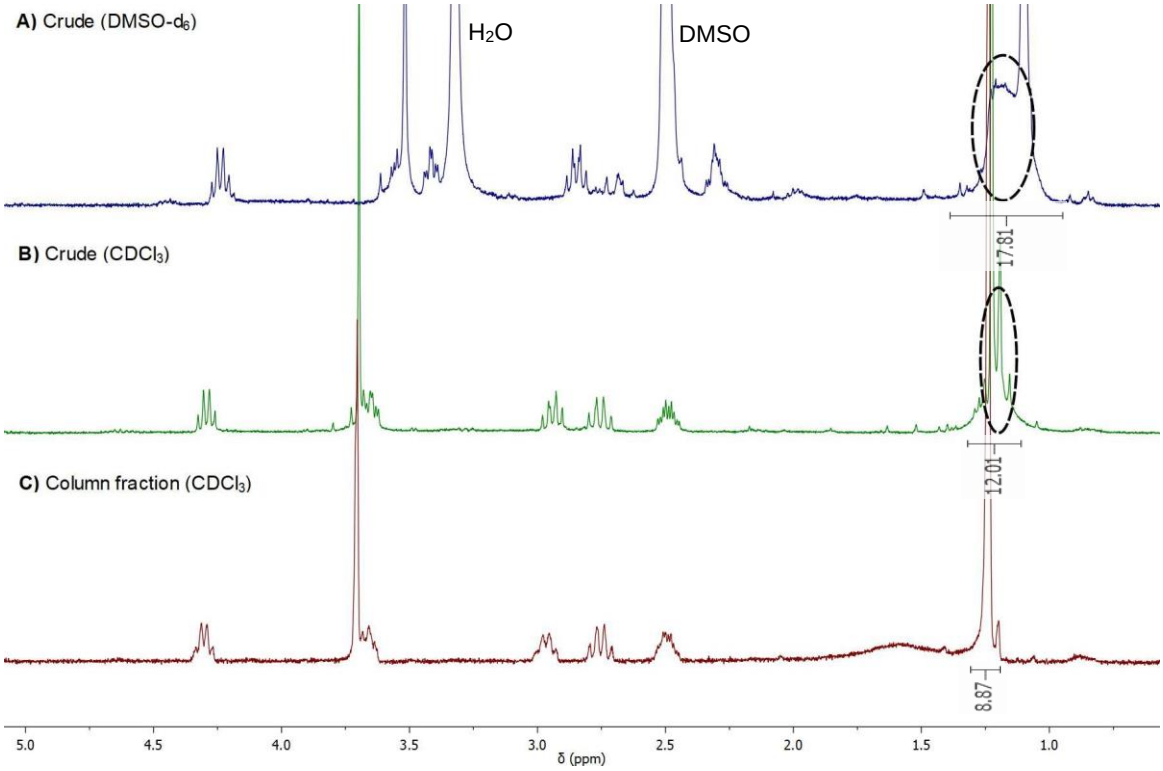

Figure I-77. Comparison of ^{1}H-NMR spectra (360 MHz) of product **(±)-115:** A) Reaction crude (DMSO-d_6); B) Reaction crude ($CDCl_3$); C) Purified fraction *via* column chromatography ($CDCl_3$).

The purified **(±)-115** was submitted to the protection reaction using the conditions that had provided the best yield (**Table I-8, entry 2**), affording diester **(±)-118** in a slightly improved yield of 64%. However, when considering the overall yield for the two-step process (**Table I-9**), it became evident that using purified **(±)-115** did not justify the added purification step. Thus, using crude **(±)-115** was determined to be the most practical choice, resulting in an overall yield of 48% for diester **(±)-118**.

Table I-9. Comparison for the synthesis of diester **(±)-118** using purified and crude of **(±)-115**.

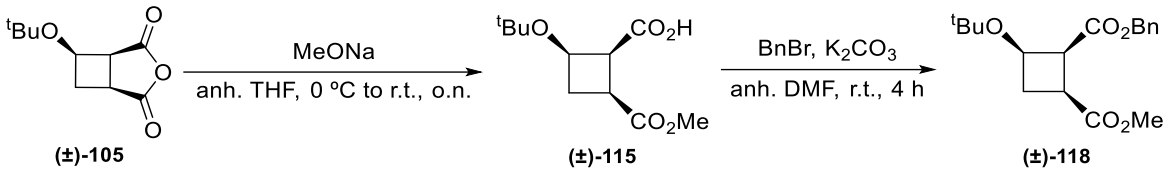

(±)-105 (±)-115 (±)-118

Starting material	Yield of (±)-105 esterification	Yield of (±)-115 esterification	2 steps overall yield
Purified fraction of **(±)-115**	32%	64%	20%
Reaction crude of **(±)-115**	Quant.	48%	48%

Selective saponification of the methyl ester was carried out under mild conditions (1 M LiOH)[311] to avoid epimerisation. The reaction led quantitatively to **(±)-119** at a 100 mg scale. However, scaling up to 700 mg reduced the yield to 72% due to a loss of selectivity, observing the formation of diacid **(±)-120** as a side product, that could be easily separated by column chromatography (**Scheme I-38**). To ensure that epimerisation had not occurred, single-crystal X-ray analysis of **(±)-119** was performed, verifying the preservation of the configuration of the stereogenic centres (**Figure I-78**).

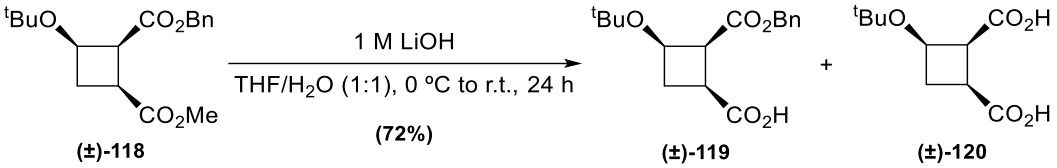

(±)-118 (±)-119 (±)-120

Scheme I-38. Hydrolysis of diester **(±)-118**.

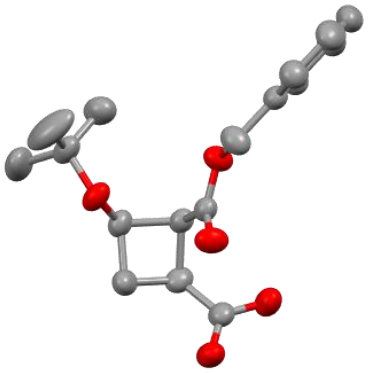

Figure I-78. X-ray structure of molecule **(±)-119**.

Compound **(±)-119** was then converted to Boc-protected amine **(±)-121** in a stepwise reaction by activating the carboxyl group of **(±)-119** with ethyl chloroformate and Et_3N, followed by treatment with sodium azide (NaN_3). The resulting acyl azide was submitted to Curtius rearrangement in the presence of *t*-BuOH (**Scheme I-39**). Unfortunately, the reaction yielded only 33%, likely due to the formation of a side product in a comparable amount to product **(±)-121**.

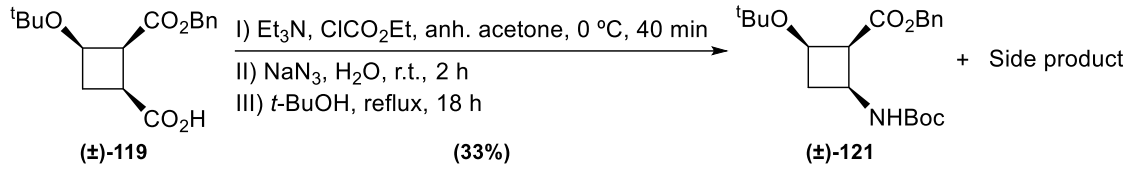

(±)-119 (33%) (±)-121

Scheme I-39. Stepwise transformation of hemiester **(±)-119** into Boc-protected amine **(±)-121**.

^{1}H-NMR analysis of the side product revealed the absence of the Boc protecting group, with bizarre multiplicities for the amine and benzyl methylene signals (**Figure I-79**). Initially, this was attributed to the formation of isomers, but ^{1}H-NMR spectrum in deuterated benzene and increased temperature experiments did not show any changes in signals multiplicity. Further NMR studies, including ^{13}C-NMR, indicated the presence of either a carbamate or a urea functionality (**Figure I-80**). In addition, the regiochemistry and relative stereochemistry of the substituents was ensured by performing HSQC, HMBC, COSY and NOESY experiments (see **Figures A50** to **A55** in the Annex), confirming the *cis*,*cis* configuration and the presence of the benzyl ester at C-2 and the carbamate or urea at C-3.

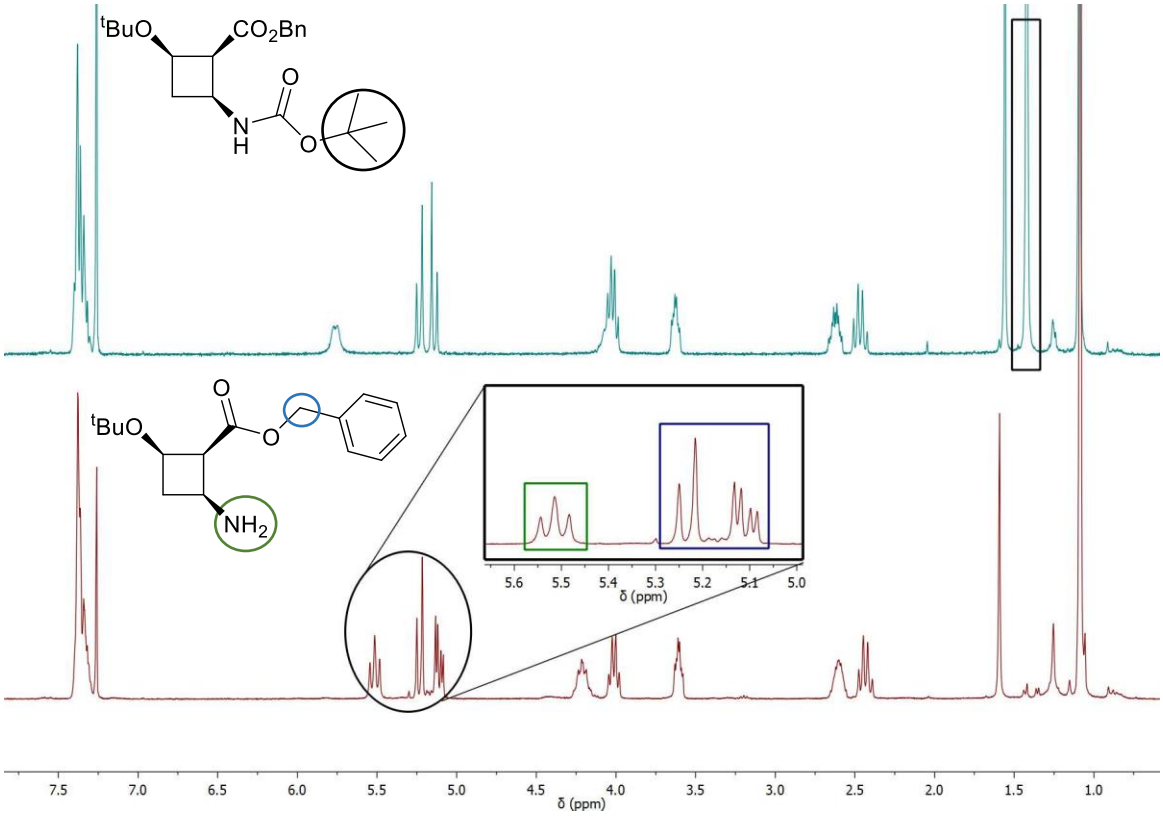

Figure I-79. ^{1}H-NMR spectra (360 MHz, $CDCl_3$) of product **(±)-121** (green) and initially proposed structure of the side product (red) generated during the Curtius rearrangement.

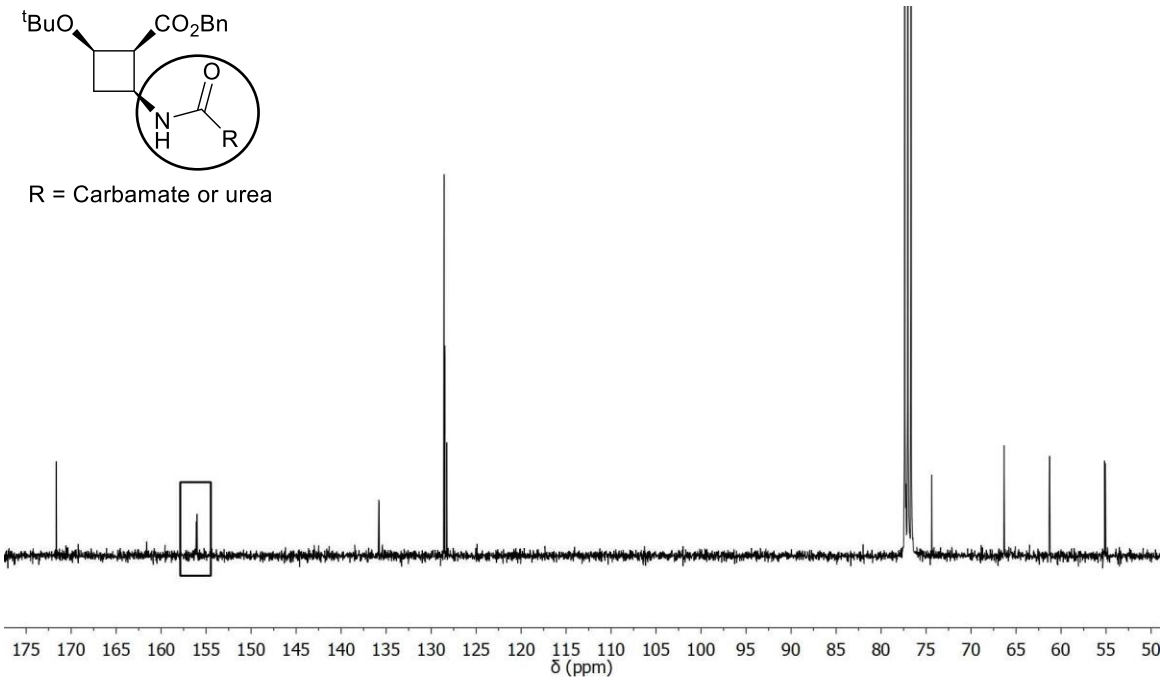

Figure I-80. ^{13}C-NMR spectrum (90 MHz, $CDCl_3$) of the side product generated during Curtius rearrangement.

Finally, HRMS analysis revealed that the major peak had a *m/z* value (M+H) of 580.011 which, in combination with the NMR analysis, fitted with the formation of urea **122** in a molar ratio of 2:1 in favour of product **(±)-121**. As depicted in **Scheme I-40**, this urea would have formed because of the presence of H_2O in the medium of reaction, which would lead to the corresponding amine. Then, this amine would react with the isocyanate intermediate, forming the urea.

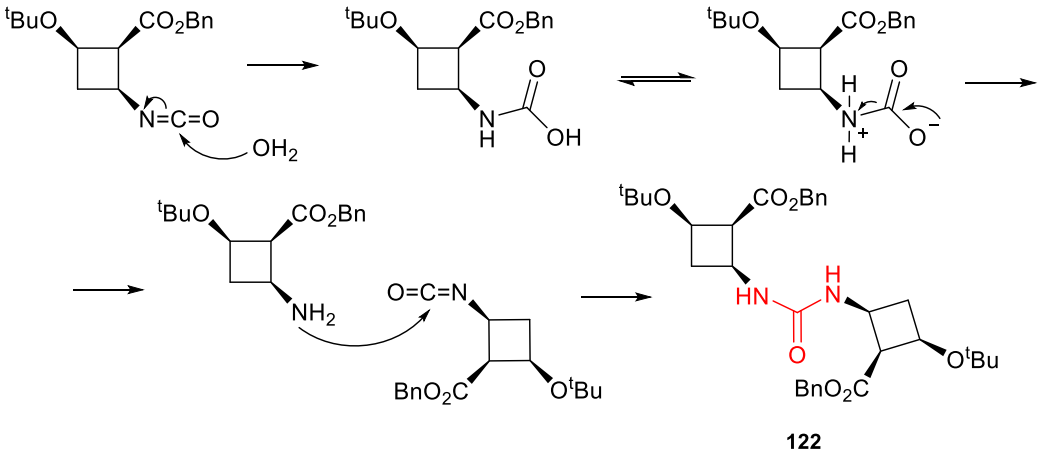

Scheme I-40. Proposed mechanism for the formation of urea **122**.

Hence, to avoid the formation of the free amine, the reaction must be carried out under strict anhydrous conditions. However, achieving this with the stepwise methodology is challenging, as the acyl azide intermediate requires extraction, which increases the likelihood of water contamination in the solvent. Additionally, the organic phase cannot be evaporated to dryness due to the explosive nature of the acyl azide. Despite these challenges, the Hofmann rearrangement step was repeated under nitrogen and with molecular sieves to further dry the reaction mixture.

While ^{1}H-NMR analysis indicated a reduction in the amount of urea **122**, the yield of the target product **(±)-121** did not improve significantly, probably due to the low nucleophilicity of the *t*-BuOH, along with the steric hindrance of the cyclobutane substituents.

Alternatively, a one-pot reaction employing diphenylphosphoryl azide (DPPA),[312] helped to avoid the formation of urea **122**, but the yield for the obtention of **(±)-121** remained low (**Scheme I-41**). Ultimately, this methodology was deemed preferable, as it achieved comparable yields with fewer manipulations and steps.

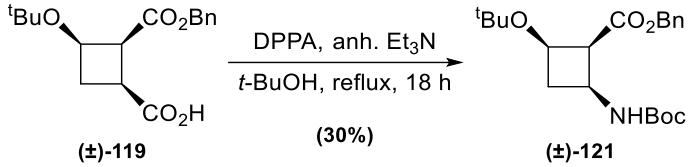

Scheme I-41. Curtius rearrangement reaction using DPPA for the obtention of protected amine **(±)-121**.

Compound **(±)-121** was then subjected to a double *N*,*O*-deprotection using TFA, followed by reprotection of the amine employing Boc_2O, but no product **(±)-123** was isolated (**Scheme I-42**). Stepwise analysis of the reaction ensured that the initial TFA treatment was successful, as indicated by *tert*-butyl groups disappearance in the ^{1}H-NMR spectrum (see **Figure A56** of the Annex), alongside peaks corresponding to the cyclobutane core. After the second step, however, the ^{1}H-NMR spectrum displayed an array of signals with unexpected chemical shifts, multiplicities and integrations (see **Figure A57** of the Annex), suggesting a ring-opening reaction due to the cyclobutane product instability under these reaction conditions.

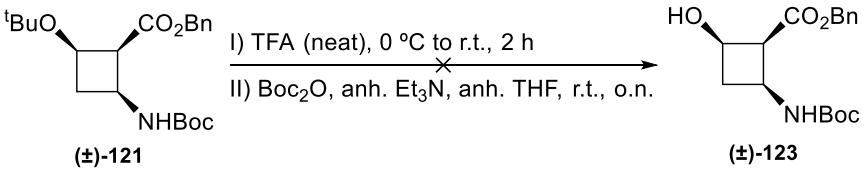

Scheme I-42. Conditions for double *N*,*O*-deprotection followed by amine reprotection to form product **(±)-123**.

The tendency of cyclobutane derivatives to undergo ring-opening under various conditions has been well-documented in the literature.[64,313–315] In this case, the amino ester is a captodative system that can evolve to an open-chain iminium salt through a push-pull mechanism (**Scheme I-43, A**), but this option was dismissed, as a stable analogue product has been reported under similar reaction conditions, having a vicinal methyl ester and a Boc-protected amino group (**Scheme I-43, B**).

A - Push-pull interaction between amine and benzyl ester

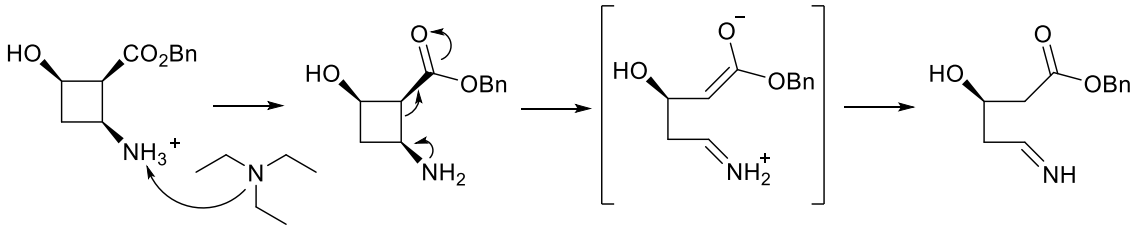

B - Reaction reported in *J. Org. Chem.* **2019**, *84*, 10518-10525

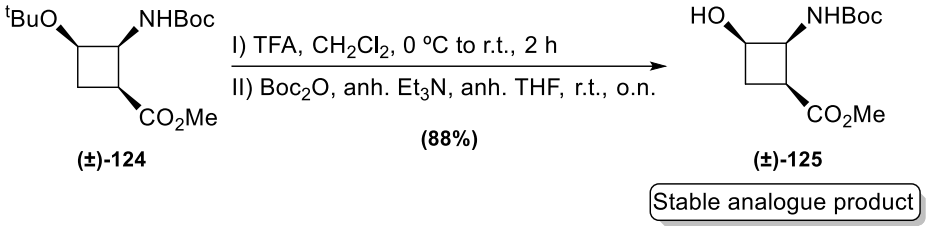

Scheme I-43. A) Proposed ring-opening mechanism driven by push-pull interactions between vicinal free amine and benzyl ester groups; B) Reported successful deprotection reaction of an analogous compound **(±)-124**, as described by Aitken *et al.*[316]

Alternatively, a ring-opening mechanism involving a push-pull interaction between the vicinal hydroxyl and benzyl ester groups was proposed. The ring-opening of the cyclobutane due to the attack of the oxygen electron pair towards the ring generates an enolate intermediate. Subsequent proton transfer would lead to the corresponding acyclic compound which rapidly tautomerises to the keto form (**Scheme I-44**). Furthermore, the structure proposed aligns with the aldehyde signal observed in ^{1}H-NMR (δ 9.72 ppm) and ^{13}C-NMR (δ 200.4 ppm) (see **Figures A57** and **A58** of the Annex).

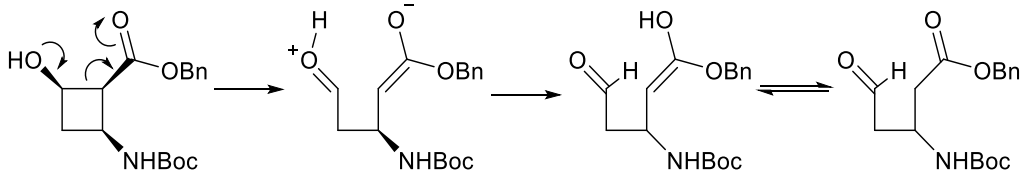

Scheme I-44. Proposed ring-opening mechanism driven by push-pull interactions between vicinal hydroxyl and benzyl ester groups.

A similar mechanism for cyclobutane ring-opening involving alkoxide formation and enolate intermediates had been proposed in the literature by Gregori *et al*.[317] Moreover, Aitken's research group had reported instability for analogous cyclobutane amino acids, suggesting irreversible ring-opening reactions.[295] To further support this proposed mechanism, Prof. Solans at the UAB conducted energy minimisation studies, pointing out that the ring-opening *via* the vicinal hydroxy and benzyl ester groups is thermodynamically favoured (E_{min} = -13.6 kcal·mol^{-1}) compared to ring-opening *via* the vicinal amine and benzyl ester groups (E_{min} = -9.8 kcal·mol^{-1}) (**Figure I-81**).

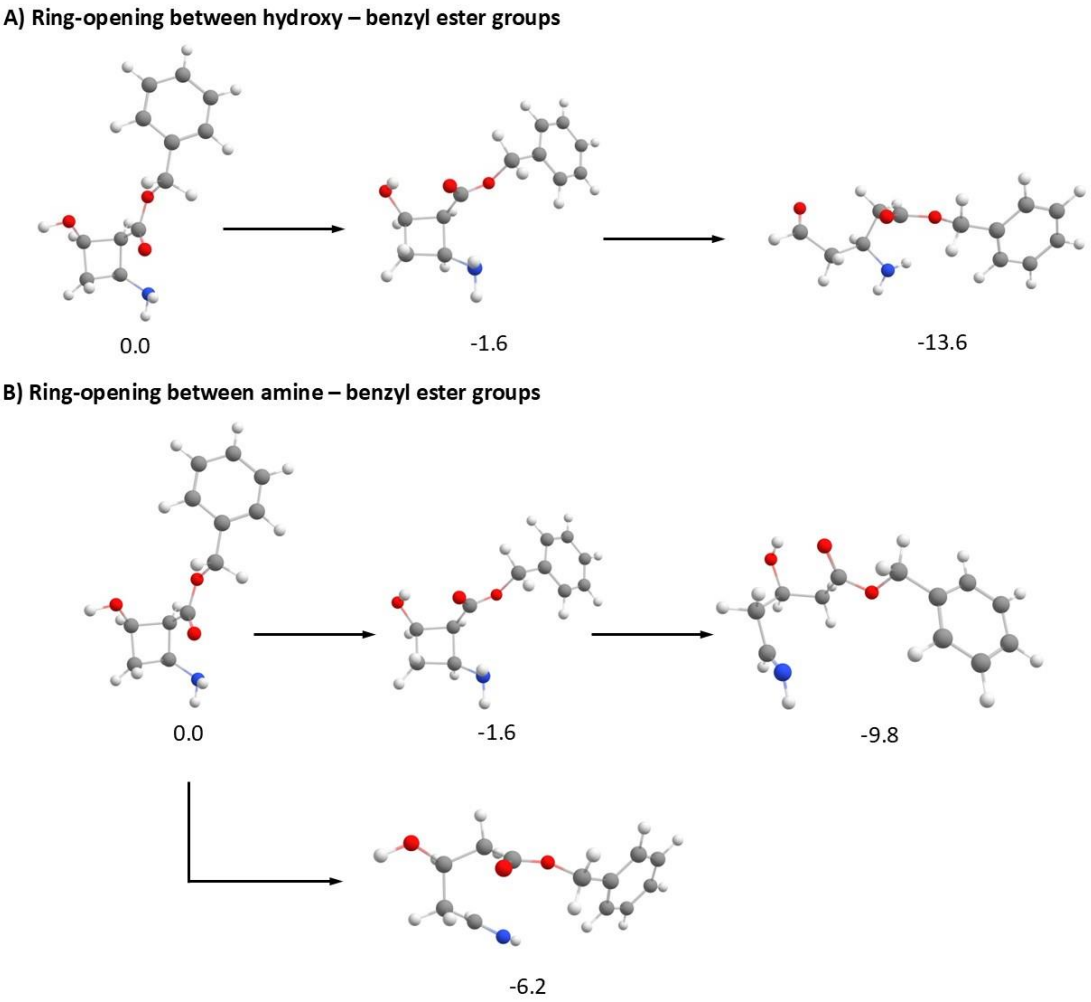

Figure I-81. Energy minimisation calculations for the two possible ring-opening mechanism. Values are expressed in kcal·mol^{-1}.

To avoid this side reaction, it is mandatory to reduce the benzyl ester prior to hydrolysing the *tert*-butyl ether. Yet before proceeding with this adjustment, a recapitulation of the yields obtained in this synthetic route was done, realizing that after the different unexpected challenges and difficulties encountered, the overall yield for the amino ester **(±)-121** resulted in 10% after 5 steps. In addition, 7 more steps would be required to obtain the amine in position 1. Then, this synthetic route did not suppose an improvement when compared to synthetic route B, in which analogue structure **(±)-114** had been afforded with an overall yield of a 10% after 4 steps (**Scheme I-45**). Therefore, instead of continuing with this synthetic route, efforts were put into improving the yields for the obtention of **(±)-114** *via* synthetic route B, continuing towards the synthesis of *cis*,*cis*-1,3-cyclobutanediamine functionalised in position 2.

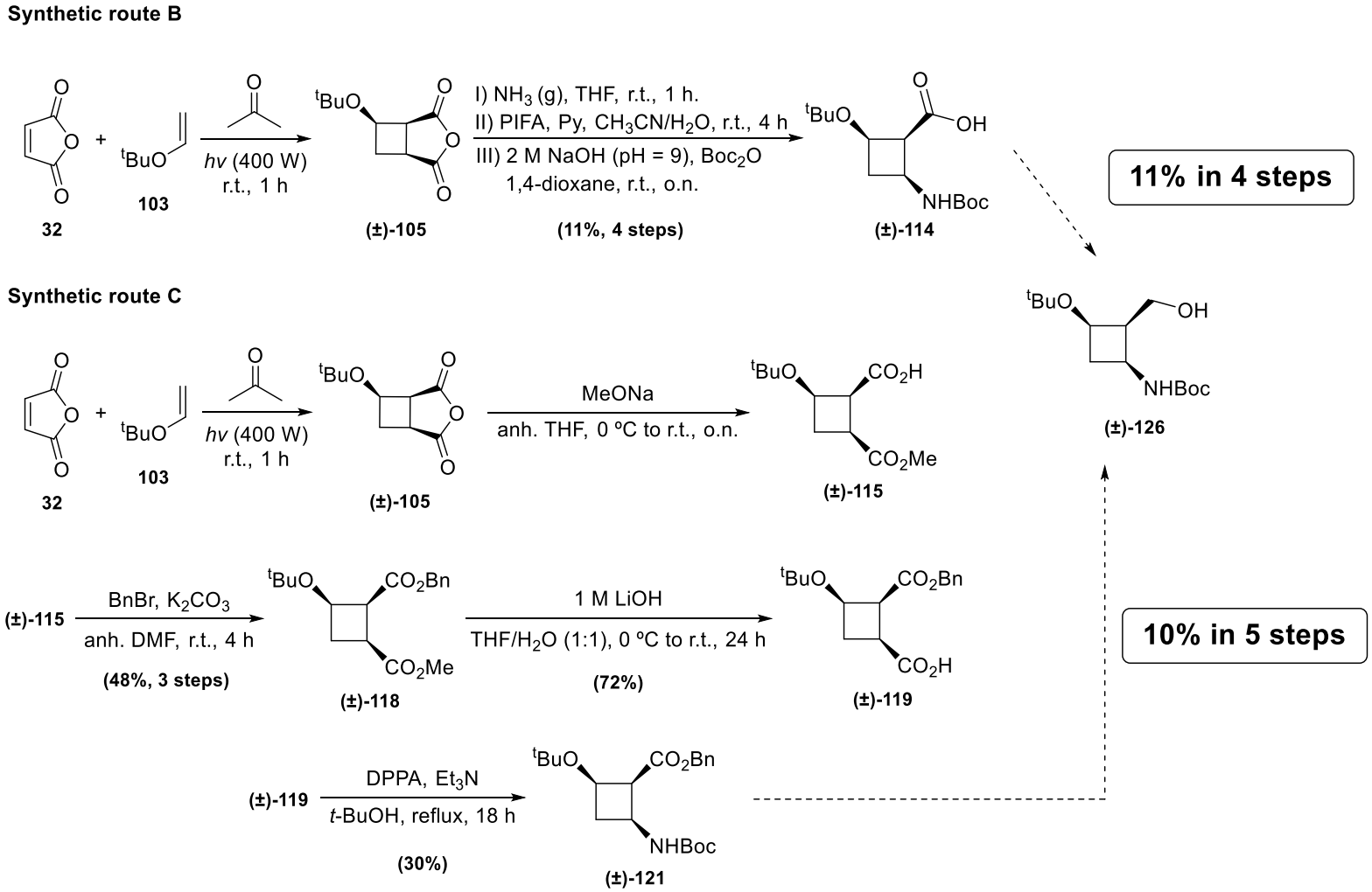

Scheme I-45. Assessment of the overall yield of both synthetic routes for the obtention of intermediate **(±)-126**.

3.4.1.4. Optimisation of Synthetic Route B

Given that synthetic route B appeared the most feasible for obtaining the target ***cis*,*cis*-L1** ligand, various optimisations were proposed to improve the yield of obtention of intermediate **(±)-114**.

The one-pot ammonolysis/Hofmann rearrangement/amine protection sequence involved numerous variables that could affect the overall yield. Consequently, after a literature review on Hofmann rearrangement-type reactions employing hypervalent iodine(III) reagents, several protocol modifications were explored to assess their influence on the yield. Some studies emphasised the use of deionised water, suggesting that ions, such as Fe(III), could negatively affect the reaction outcome.[318] In addition, the reaction was also performed in the absence of pyridine, commonly added to accelerate the reaction rate.[318,319] Also, extractions using ethyl ether were introduced to remove PIFA ((bis(trifluoroacetoxy)iodo)benzene) by-products, with the aim of simplifying purification and potentially improving the reactivity of the final protected amine.[318,320] Moreover, the addition of triethylamine as a base instead of using a 2 M aqueous solution of NaOH was also tried, to facilitate the slow formation of the amine and enhance the product formation in the presence of the excess of di-*tert*-butyl dicarbonate. Even, multiple batches of PIFA reagent were tested, and the reaction was performed protected from light, as it is known to be a photosensitive reagent that can degrade easily if it is not stored under the right conditions. Unfortunately, none of these modifications provided any improvement in the yield for the obtention of **(±)-114**.

Provided that none of the adjustments performed on the Hofmann rearrangement protocol resulted in any improvement, the focus was redirected toward optimising the preceding ammonolysis step. Ammonium salt **(±)-127** was successfully isolated and its structure verified by mass spectrometry and NMR, confirming this step proceeded reliably. Similarly, the [2+2]-photocycloaddtion yielded quantitative conversion without observable impurities. This prompted further exploration of alternative transformations on ammonium salt **(±)-127**, aiming to isolate a product with high yields and suitable for subsequent modifications to generate an analogue of **(±)-114**.

An initial approach involved methylating the carboxylate in ammonium salt **(±)-127** with methyl iodide in DMF, to further convert the amide into the amine *via* Hofmann rearrangement.[321,322] However, this reaction yielded methyl ester **(±)-128** in a poor 20%, along with several unidentified by-products. An alternative protocol was tried protonating the carboxylic acid with 0.1 M HCl prior to methylation, intending to improve the yield. Instead, the first step resulted in the formation of a slurry mixture that could not be extracted, not isolating any product (**Scheme I-46**).

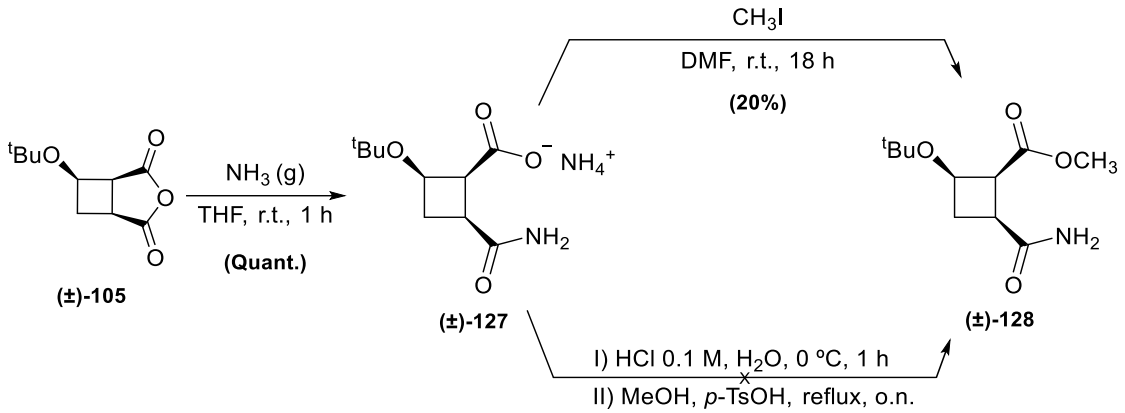

Scheme I-46. Approaches for the methylation of the isolated ammonium salt **(±)-127.**

As a last attempt to improve yields, parameters of the [2+2]-photocyclisation were revisited. Analysis by ^{1}H-NMR confirmed that no trace of the maleic anhydride photodimer had been formed in the reaction. Changing the photosensitiser was not considered, as it has been a parameter explored in previous studies.[295] Notably, reports in the literature highlighted the sensitivity of maleic anhydride derivatives to hydrolysis, which readily convert to the diacid upon exposure to water.[294,323] Although anhydrous conditions were not specified in the original protocol, this modification was deemed worthwhile to attempt. For this, the reaction was conducted with anhydrous acetone, with the volume reduced to 250 mL for manageability, instead of the 400 mL used previously. Consequently, a smaller photochemical reactor was employed, which required switching to a 125 W Hg-lamp compatible with this setup. This adjustment extended the reaction time due to slower maleic anhydride consumption.

Pleasingly, while no immediate changes were appreciated in the ^{1}H-NMR spectrum of photoadduct **(±)-105**, the yield of subsequent product **(±)-114** increased to 21% after completion of the following reaction steps (**Scheme I-47**). Although the yield did not reach the reported 30%, the result was viewed as a substantial improvement, effectively doubling the amount of obtained product.

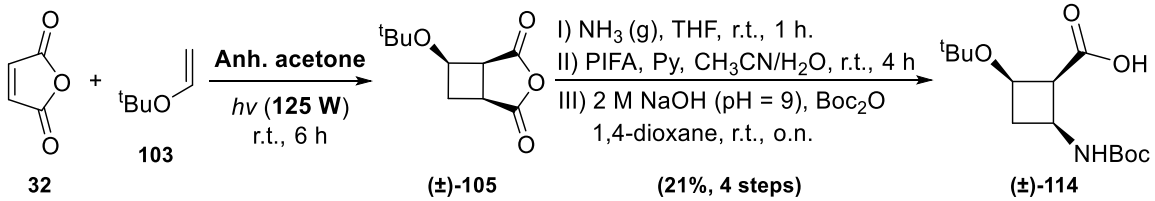

Scheme I-47. Optimisation of [2+2]-photocyclisation reaction conditions to improve yield of **(±)-114**.

To verify that this improvement was attributable to the anhydrous acetone and not to changes in lamp power or reaction volume, each parameter was independently evaluated. These experiments confirmed that anhydrous acetone was the only factor significantly impacting the yield (**Table I-10**).

Table I-10. Yields obtained with different [2+2]-photocyclisation reaction conditions.

	125 W	**400 W**
Anhydrous acetone	21%	18%
Non-anhydrous acetone	12%	11%

The synthesis was continued reducing the carboxyl group in **(±)-114** to the primary alcohol **(±)-126**. The employment of a 2 M lithium borohydride ($LiBH_4$) solution as a reducing agent resulted in a crude mixture of unidentified products that, after column chromatography, yielded **(±)-126** in a disappointing 31%. Direct reduction using borane (BH_3) was unsuccessful also, recovering the starting material. Ultimately, more satisfactory yields were achieved with $NaBH_4$ in ethanol at reflux temperatures,[324] affording alcohol **(±)-126** in 89% yield (**Scheme I-48**).

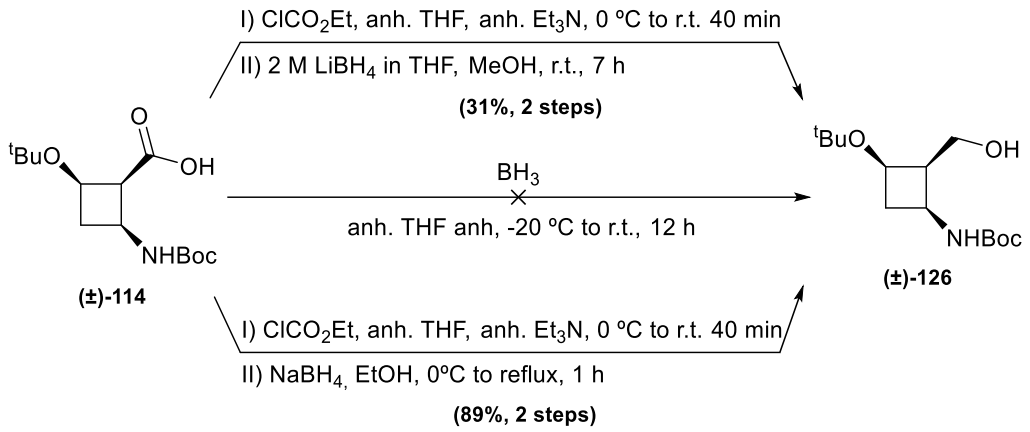

Scheme I-48. Explored reduction methods for converting carboxylic acid **(±)-114** to primary alcohol **(±)-126**.

Prior to hydrolysis of the *tert*-butyl ether, the protection of the hydroxyl group in **(±)-126** was needed to enable the selective transformation of the secondary alcohol generated upon the *tert*-butyl hydrolysis. Silyl protecting groups were selected for their reported stability under acidic conditions,[325] especially the bulky *tert*-butyldiphenylsilyl (TBDPS) protecting group. Additionally, they can be easily removed under mild conditions using fluoride sources such as tetrabutylammonium fluoride (TBAF). First, the installation of the protecting group was attempted using classical conditions,[326] employing the chloride derivative (TBDPSCl) and imidazole at room temperature. However, these conditions, along with further modifications such as the addition of DMF or heating, failed to produce the desired protected alcohol, only recovering the starting material.

As an alternative approach, silylation was performed using iodide in the presence of *N*-methylimidazole, as a nucleophile catalyst, along with TBDPSCl.[327] This methodology proved highly effective, achieving the reaction in a short time and providing silylated derivative **(±)-129** in 86% yield (**Scheme I-49**).

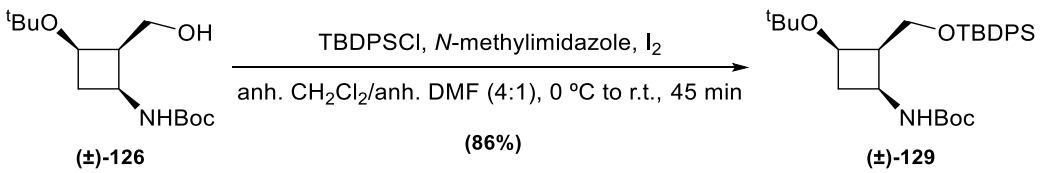

Scheme I-49. Silylation of primary alcohol **(±)-126** to yield orthogonally protected product **(±)-129**.

Subsequently, the two-step *N*,*O*-deprotection/*N*-reprotection sequence was applied to compound **(±)-129** to afford secondary alcohol **(±)-130**. An initial attempt, using the same reaction conditions as in **Scheme I-42** (*vide supra*), yielded product **(±)-130** in 40% (**Table I-11, entry 1**). However,

^{1}H-NMR analysis indicated that, alongside the target product, some diol had formed due to silyl ether removal. In addition, some free amine was also observed due to ineffective reprotection. To prevent silyl ether cleavage, different amounts of TFA were tested, while maintaining reaction concentration using DCM as a solvent. From these experiments, it could be concluded that the use of less than 40 equivalents of TFA resulted in incomplete *tert*-butyl ether hydrolysis, achieving 48% yield under optimised conditions (**Table I-11, entries 2-4**). Further exploration with acids reported in the literature to selectively remove *tert*-butyl ethers in the presence of silyl ethers, such as $TiCl_4$[328–331] or H_3PO_4 aqueous solution,[332,333], led either to product degradation or recovery of the starting material, respectively (**Table I-11, entries 5 and 6**).

Table I-11. Acids employed for the double *N*,*O*-deprotection followed by amine reprotection.

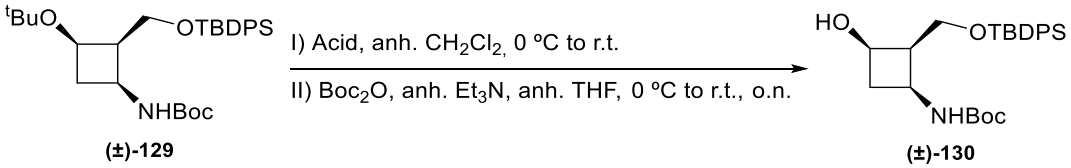

(±)-129 **(±)-130**

Entry	Acid (eq.)	Reaction time	(±)-130 (%)
1	TFA (neat)	2 h	40%
2	TFA (40 eq.)	o.n.	48%
3	TFA (20 eq.)	40 h	33%
4	TFA (5 eq.)	40 h	---[a]
5	$TiCl_4$ (1.1 eq.)	30 min	---[b]
6	H_3PO_4 (28 eq.)	o.n.	---[a]

a) No product recovered.
b) Starting material recovered.

To avoid undesired deprotection of the primary alcohol, an alternative reaction sequence was examined, beginning with the double *N*,*O*-deprotection of compound **(±)-126** using TFA, followed by amine reprotection with Boc_2O. This approach was based on the expectation that subsequent protection of the obtained diol would be selective for the primary alcohol over the secondary. The desired diol **(±)-131** was indeed obtained and isolated in 42% yield, alongside carbonate **(±)-132**, in a 3:1 ratio (**Scheme I-50**). On the basis of these investigations, the preferred two-step access to compound **(±)-130** from substrate **(±)-126** proceeds *via* intermediate **(±)-129**, as it ensured the selective primary alcohol protection.

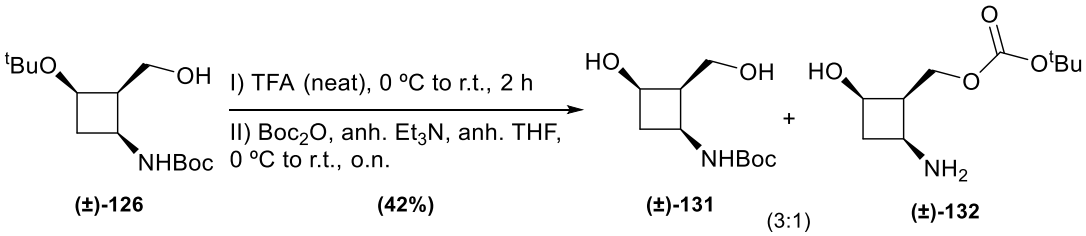

(±)-126 **(42%)** **(±)-131** (3:1) **(±)-132**

Scheme I-50. Two-step *N*,*O*-deprotection/*N*-reprotection sequence to afford diol **(±)-131**.

Focus then shifted to the stereoselective conversion of the secondary alcohol in **(±)-131** into the corresponding amine. This required two consecutive bimolecular nucleophilic substitution (S_N2)

reactions to retain the *cis*,*cis* stereochemistry. Therefore, an Appel reaction[334] was the first SN_2 carried out, employing PPh_3, imidazole, and I_2 to afford iodo derivative **(±)-133** in 64% yield (**Scheme I-51**).

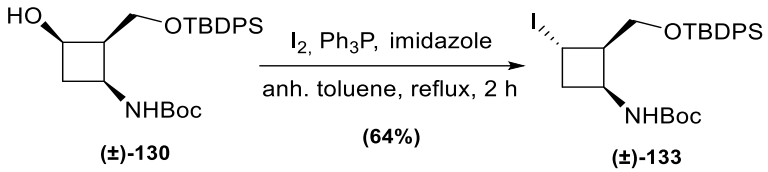

Scheme I-51. Synthesis of iodo derivative **(±)-133** through Appel reaction.

The second S_N2 consisted in the transformation of iodo derivative **(±)-133** into the corresponding azide using NaN_3 in anhydrous DMF, to subsequently be hydrogenolysed for 4 h in presence of palladium on charcoal to provide free amine **(±)-134** in 42% yield. Finally, free diamine **135**, an analogue of intermediate **II**, objective of the synthesis (**Scheme I-30,** *vide supra*), was afforded quantitatively through acidolysis followed by neutralisation with K_2CO_3 (**Scheme I-52**).

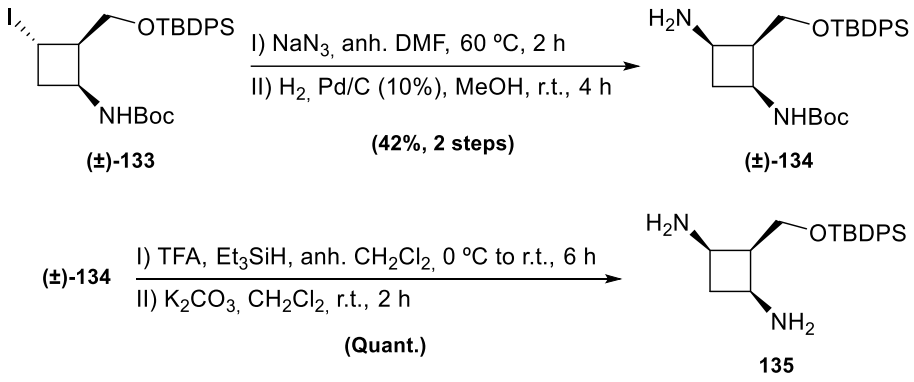

Scheme I-52. Two-step sequence for the synthesis of amine **(±)-134** followed by acidolysis and basic treatment to obtain diamine **135**.

This *cis*,*cis*-1,3-cyclobutanediamine functionalised in C-2 as a protected alcohol in the form of silyl ether could provide access to product **136**, a precursor of the desired ***cis*,*cis*-L1** ligand, through double reductive amination to introduce the picolinate pending arms. Before proceeding, aldehyde **101** was synthesised *via* partial reduction of commercially available **137** with $NaBH_4$, followed by oxidation of the intermediate alcohol with selenium oxide (SeO_2), in 68% yield (**Scheme I-53, top**). Afterwards, a first attempt to synthesise **136** was carried out on a 50 mg scale by performing a double reductive amination with diamine **135** and aldehyde **101** in MeOH, to then reduce the imine intermediate with $NaBH_4$ (**Scheme I-53, bottom**). After column chromatography, ^{1}H-NMR analysis of one of the fractions indicated the presence of some signals potentially corresponding to the expected product. However, the fraction purity and the amount obtained were insufficient for further confirmation.

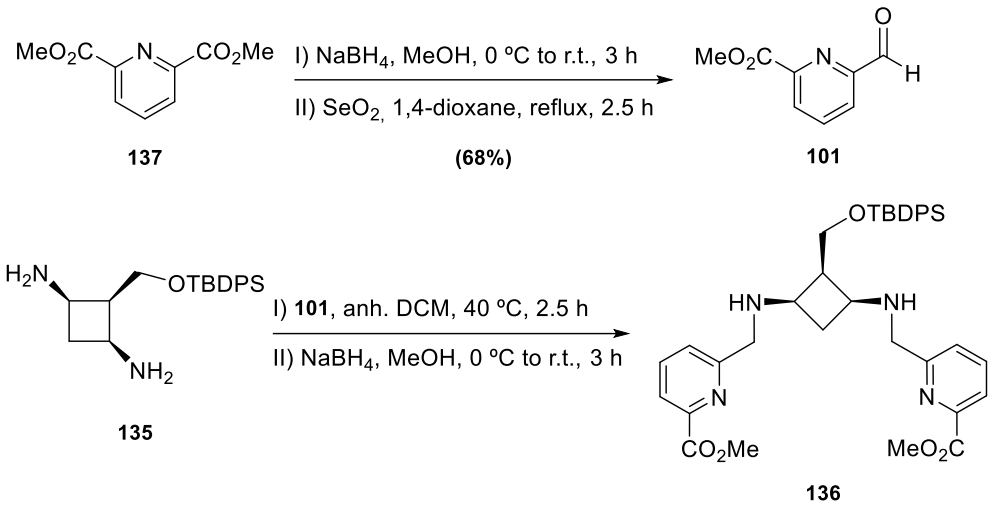

Scheme I-53. Attempt to synthesise **136** by double reductive amination reaction.

Up to this point, it was required to start the synthesis again to obtain the amount needed of ***cis*,*cis*-L1**. While it is common to repeat steps in long synthetic sequences, it was estimated that, to obtain the 300 mg to 400 mg needed to proceed with the synthesis of the complexes, it would be required to repeat the first 4 steps of the sequence between 30 and 40 times, as the overall yield to afford **135** was 2%. Therefore, despite the obtention of ***cis*,*cis*-L1** ligand was very close, it was decided to concentrate the efforts towards synthesising the ***cis,trans*-L2** ligand, which was expected to yield better results and to provide a ligand suitable for investigating its potential to chelate ^{64}Cu radioisotope.

3.4.2. Synthesis of the Ligand *cis,trans*-L2

The synthetic route proposed for the preparation of the ***cis,trans*-L2** ligand implied the esterification of acid **(±)-114** to selectively epimerise C-2 position of ester **(±)-138** affording product **(±)-139**. Afterwards, the synthesis would proceed in a similar manner as the previously followed for the ***cis*,*cis*-L1** ligand, ultimately targeting the *cis,trans*-1,3-cyclobutane diamine intermediate **III** (**Scheme I-54**).

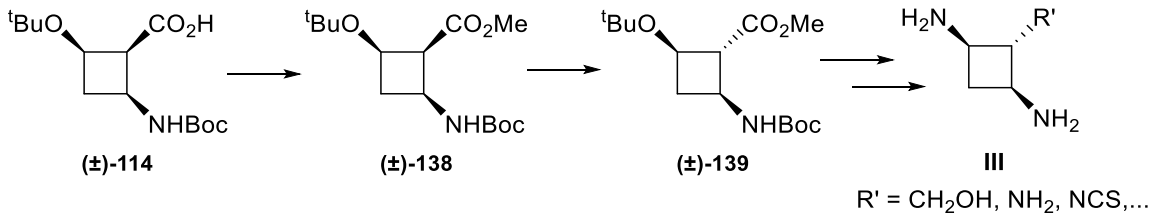

Scheme I-54. Synthetic route foreseen to prepare the *cis*,*trans*-1,3-cyclobutanediamine functionalised in position 2, **III**.

Starting acid **(±)-114** was synthesised as described in synthetic route B (**Scheme I-47**, *vide supra*). Steglich esterification conditions using MeOH, DMAP and *N*,*N*-dicyclohexylcarbodiimide (DCC)[316] provided methyl ester **(±)-138** in a moderate 40% yield (**Scheme I-55**).

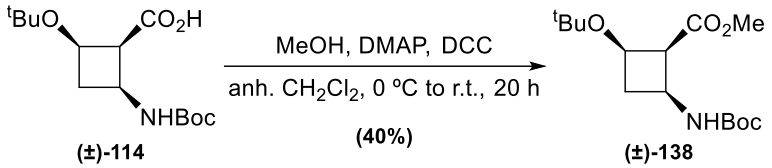

Scheme I-55. Reaction conditions for the formation of ester **(±)-138**.

This limited yield, together with the already low yield for the obtention of **(±)-114**, prompted a reevaluation of the synthetic approach. Given the anticipated challenges to afford the required amount of the ***cis,cis*-L1** ligand, priority shifted toward optimising yields in the early steps, with versatility in the functionalisation of C-2 becoming a secondary objective. Consequently, the synthetic strategy pivoted toward obtaining a triamine as outlined in the retrosynthetic analysis (**Scheme I-56**). The amine moieties in C-1 and C-3 would be introduced *via* transformations of the *tert*-butyl ether and carboxylic acid groups, respectively. This last would be previously epimerised from the *cis*,*cis*-cyclobutane-containing analogue structure, formed in the ring-opening reaction of the cyclobutane derivative from the initial [2+2]-photocycloaddition.

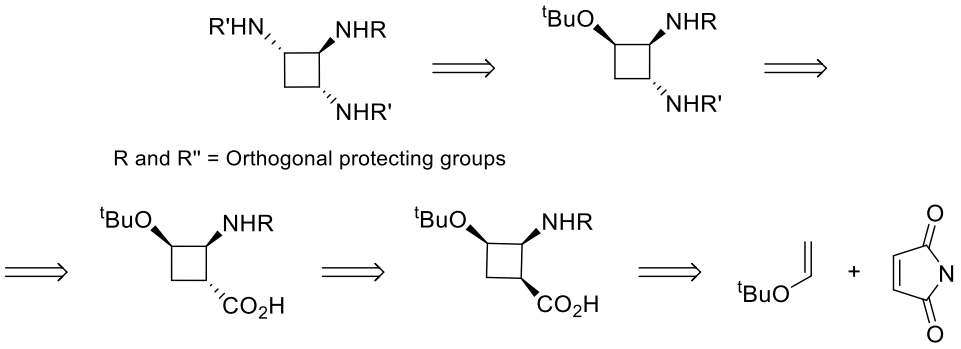

Scheme I-56. Retrosynthetic analysis for the obtention of the *cis*,*trans*-cyclobutane-based 1,2,3-triamine.

The product *endo*-**(±)-104** was obtained using the methodology discussed in **section 3.4.1.1.** through a [2+2]-photocycloaddition between maleimide **102** and *tert*-butyl vinyl ether **103** (**Scheme I-31**, *vide supra*). To install the amine and carboxylic acid functionalities, *endo*-**(±)-104** was treated with bromine in basic medium, followed by addition of Boc_2O, which facilitated selective hydrolysis/Hofmann rearrangement/amine protection reaction sequence.[295] This process provided racemic *N*,*O*-diprotected cyclobutane derivative **(±)-109** in 81% yield (**Scheme I-57**, **top**). This methodology offered improved yields over the previously employed hypervalent iodine-based approach developed by Moriyama's research group (**Scheme I-33**, *vide supra*). Therefore, this was preferred to continue the synthesis with the epimerisation of the α-position relative to the carboxyl group. The reaction proceeded through the amide intermediate which, upon basic hydrolysis, furnished the thermodynamically more stable *cis,trans*-carboxylic acid **(±)-140** in 88% combined yield, recovering an 11% of the *cis,cis*-carboxylic acid **(±)-109** (**Scheme I-57**, **middle**). To our dismay, single crystals of the product could not be obtained to ensure stereochemistry of the product through X-ray analysis. However, subsequent analyses of molecules derived from **(±)-140** along the synthesis further corroborated this assignment.

Despite one pure sample was isolated for characterisation, complete separation of diastereoisomers by column chromatography proved challenging. Therefore, the mixture of epimers was subjected to Curtius rearrangement, affording orthogonally protected *cis,trans*-diamine **(±)-141** in 81% yield after separating by-products associated with residual *cis,cis*-carboxylic acid **(±)-109** (**Scheme I-57**, **bottom**).

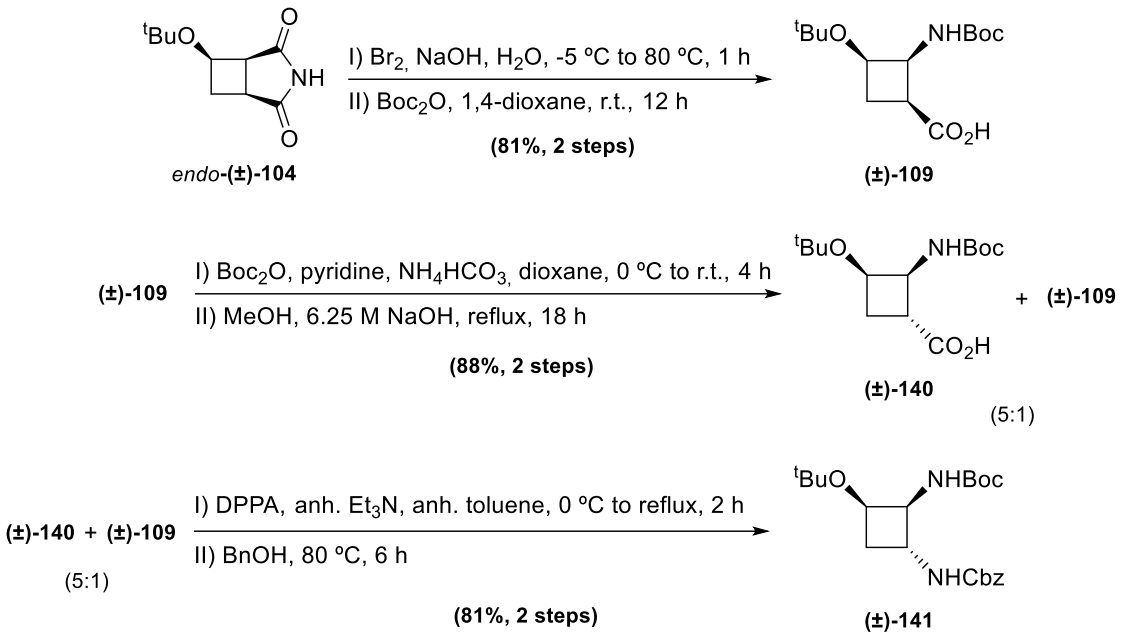

Scheme I-57. Reaction sequence for the preparation of compound **(±)-141**.

Deprotection of the hydroxyl group in **(±)-141**, along with the implied acidolysis of the *tert*-butyl carbamate, was carried out using neat TFA. The resulting amine was reprotected using Boc_2O to yield compound **(±)-142** in 87% over the two steps. Afterwards, a Mitsunobu reaction was performed in order to install an azide in place of the hydroxyl group, with inversion of configuration, employing triphenylphosphine (PPh_3), diisopropyl azodicarboxylate (DIAD) and DPPA, which afforded **(±)-143** in 79% yield. Subsequently, Pd-catalysed hydrogenolysis of benzyl carbamate and reduction of the azide group led to triamine **144** in quantitative yield (**Scheme I-58**).

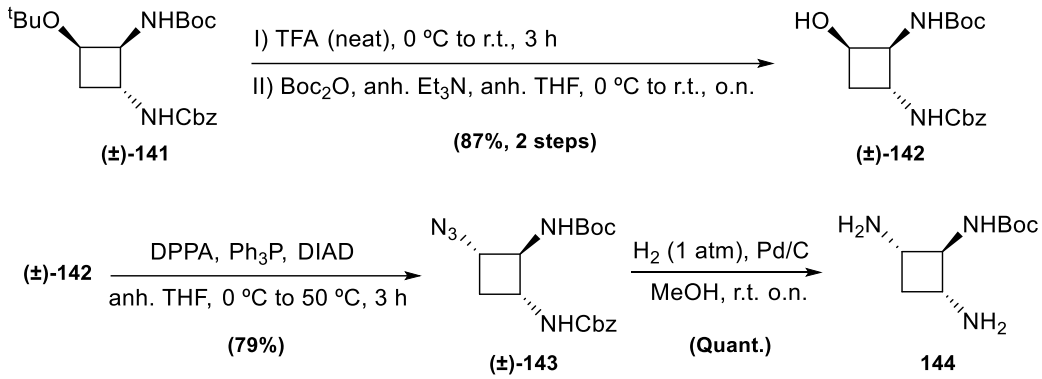

Scheme I-58. Sequence of reactions performed to afford triamine **144**.

Compound **144** was submitted to double reductive amination with aldehyde **101**, the synthesis of which had been described previously (**Scheme I-53**), to obtain orthogonally protected ligand

precursor **145**. Some experimentation was required to determine the optimal conditions, as in the first attempt using MeOH as a solvent and $NaBH_4$ as a reducing agent resulted in an unsatisfactory 25% yield (**Table I-12, entry 1**). The use of more equivalents of $NaBH_4$ decreased even more the yield, due to the reduction of the ester moiety of the picolinate arms, rendering the corresponding primary alcohol in 32% yield (**Table I-12, entry 2**). Therefore, sodium cyanoborohydride was employed as a milder reductant. However, the formation of acetal side product from reaction of aldehyde **56** with MeOH reduced the final yield to a 20% (**Table I-12, entry 3**). This could be avoided changing the solvent to anhydrous DCM in the first reaction which, upon optimisation of the time and temperature of addition of $Na[BH_3(CN)]$, yielded **145** in 57% over the two steps (**Table I-12, entry 4 and 5**).

Table I-12. Optimisation of the double reductive amination reaction conditions to render product **145**.

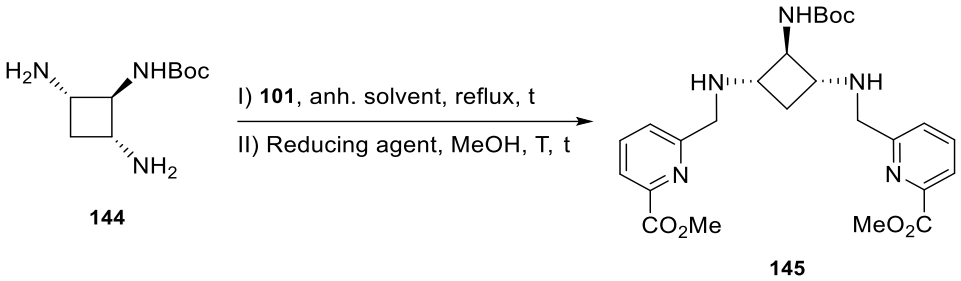

Entry	Solvents (I/II)	Reducing agent (eq.)	Reaction time (I/II)	Temp. (II)	Yield (%)
1	MeOH	$NaBH_4$ (3 eq.)	o.n / 3 h	r.t.	25%
2	MeOH	$NaBH_4$ (4 eq.)	3 h / 3 h	r.t.	3%[a]
3	MeOH	$Na[BH_3(CN)]$ (3 eq.)	3 h / 3 h	r.t.	20%[b]
4	DCM/MeOH	$Na[BH_3(CN)]$ (3 eq.)	1 h / 1 h	r.t.	40%[c]
5	DCM/MeOH	$Na[BH_3(CN)]$ (3 eq.)	1 h / 3 h	0 ºC	57%[c]

a) Formation of the primary alcohol as a by-product due to the reduction of the methyl ester.
b) Formation of the acetal side product from aldehyde **101**.
c) Yield recalculated from ^{1}H-NMR estimated quantity of unreacted aldehyde in reaction I)

Finally, saponification of the methyl esters with LiOH afforded the desired bifunctional ligand ***cis*,*trans*-L2**, which contains a spacer bearing a protected amino group suitable for conjugation, in 53% yield (**Scheme I-59**). The ligand was obtained in a 13-step synthesis in 9% overall yield.

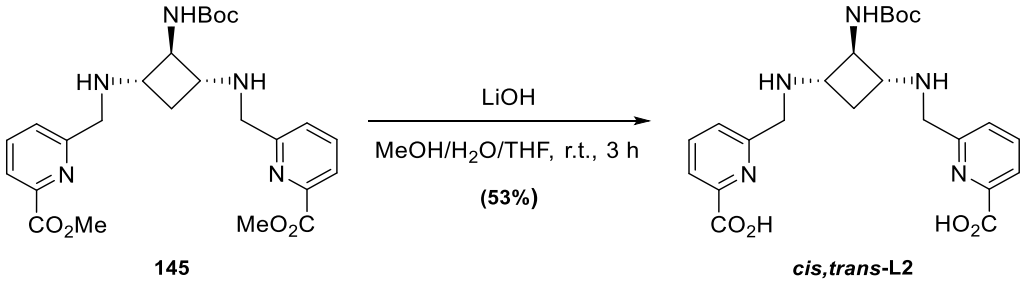

Scheme I-59. Saponification of methyl ester in **145** to obtain ***cis*,*trans*-L2** ligand.

3.5. Radiolabelling Assays with the Bifunctional Chelator *cis,trans*-L2

The ability of the bifunctional ligand (BFC) ***cis*,*trans*-L2** to coordinate ^{64}Cu nuclide was determined by probing radiochelation at 25 °C in 0.5 M ammonium acetate buffer (pH 5.5) with $^{64}CuCl_2$. These assays, as in the case of the chelator models, were conducted by Dr. Marlin, a researcher in Dr. Boros' team at University of Wisconsin-Madison.

Following the same procedure as with the chelator models, the RCY was measured after 15, 30 and 60 min *via* radio-TLC (**Figure I-82**, **top**). Quantitative labelling was observed at 1 nmol, with no significant differences at the different times measured. AMA values measured for the complexation of ***cis*,*trans*-L2** with ^{64}Cu was 3563 mCi·µmol^{-1}, thus remaining within the same order of magnitude as the parent ligand structure **H_2CBuDEDPA (Table I-13)**. On the other hand, the assessment of the inertness in physiological conditions in PBS evidenced no significant decomplexation of the radiocomplex over 24 h, offering similar stability when compared to the ^{64}Cu complexes formed with the non-bifunctional chelators (**Figure I-82**, **bottom**). However, quantitative transchelation was observed for ***cis*,*trans*-L2** at the 10 min time point, indicating that the presence of a bulky substituent at position 2 of the cyclobutane ring has a negative impact in the stability of the radiocomplex.

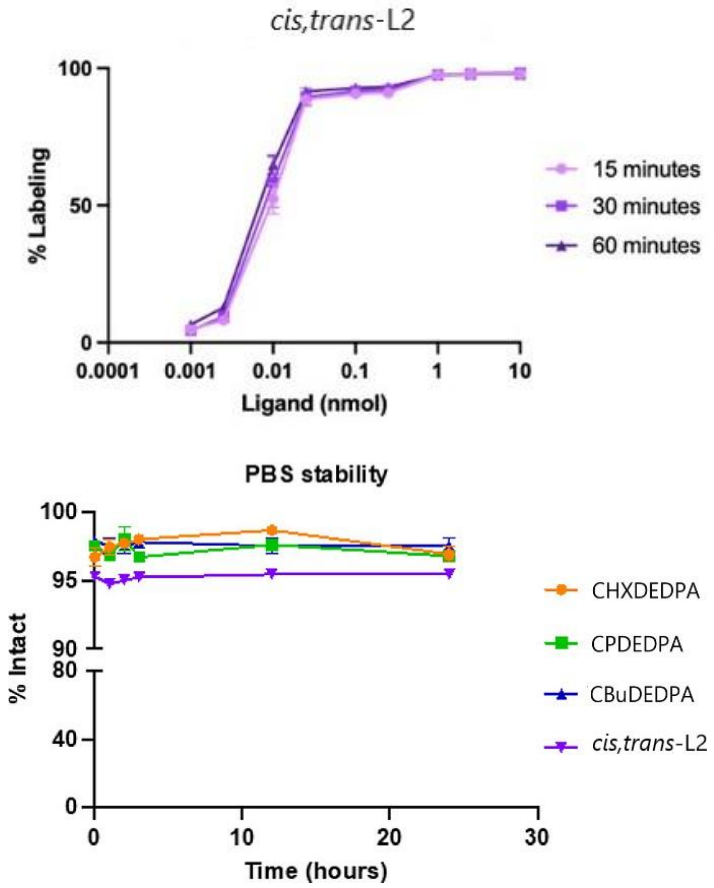

Figure I-82. Radiolabelling assays. Top: AMA determination curves with ^{64}Cu for the BFC ***cis*,*trans*-L2**. Reaction yields were analysed at 3 time points (15, 30 and 60 min), with n = 3 per data point. Error bars denote standard deviation. Bottom: Study of the kinetic stability of ^{64}Cu-complexes through PBS stability at pH 7.4. Solutions were monitored by TLC at 6 and 5 time points. Error bars denote standard deviation, with n = 3 per data point.

Table I-13. AMA (mCi·µmol^{-1}) of **[^{64}Cu]-[Cu(*cis*,*trans*-L2)]** complex compared to the parent complex **[^{64}Cu]-[Cu(CBuDEDPA)]**.

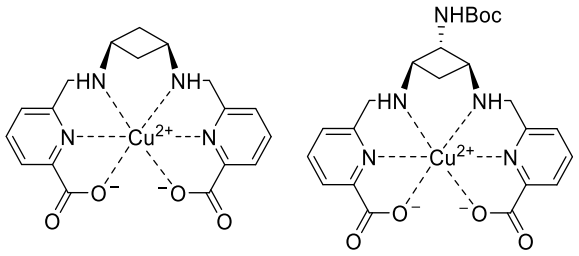

	[^{64}Cu]-[Cu(CBuDEDPA)]	[^{64}Cu]-[Cu(*cis*,*trans*-L2)]
15 min	4939	3583
30 min	6148	3981
60 min	6637	4245

From these radiolabelling assays, it can be concluded that although the bulky substituent at position 2 of the cyclobutane ring has slightly reduced the radiolabelling efficiency, the values obtained remain promising. Furthermore, the stability of the radiocom plex with the BFC in physiological conditions has not been significantly affected. However, negative results for transchelation experiments suggest that a less bulky substituent might favour the stability of the complex. Nonetheless, as a bifunctional chelator model, these encouraging findings support to continue the investigation with the *in vitro* studies of the Cu(II) complexes with the ***cis*,*trans*-L2** ligand to confirm both thermodynamic stability and kinetic inertness. If confirmed, this ligand could potentially be conjugated with a targeting moiety for evaluation as a PET imaging contrast agent in future *in vivo* studies.

4. Conclusions

This chapter of the thesis successful concludes the investigation of novel ligands as potential PET imaging contrast agents, progressing from initial studies of complexes with the chelator models to the evaluation of radiolabelling properties of the bifunctional chelator. Throughout this process, different milestones have been accomplished, with significant conclusions drawn at each stage.

Three chelators, incorporating cyclohexane, cyclopentane and cyclobutane rigid spacers, were synthesised and characterised, to obtain the corresponding Cu(II) and Ga(III) complexes, structures of which were confirmed by X-ray diffraction.

Then, the three chelators were labelled with ^{64}Cu and ^{68}Ga radionuclides. Despite the results obtained with ^{68}Ga which led to the dismissal of this line of investigation, all three chelators provided fast, quantitative and stable ^{64}Cu coordination at low concentrations, with **H_2CBuDEDPA** showing the best radiolabelling efficiency. Furthermore, the radiocomplexes of **H_2CHXDEDPA** and **H_2CBuDEDPA** show comparable stabilities in PBS and in the presence of excess DTPA.

Subsequently, the stability against bioreductants, as well as the ability to stabilise Cu(I), were assessed, revealing that the introduction of rigid moieties enhanced the complexes stability upon reduction and all three complexes are out of the threshold of the bioreducing agents. Additionally, thermodynamic stability of the Cu(II) complexes was assessed, concluding that all three chelators containing rigid spacers form complexes with higher thermodynamic stability than the parent **H_2DEDPA** ligand, with stability following the sequence **H_2CHXDEDPA** > **H_2CPDEDPA** > **H_2CBuDEDPA**. Moreover, the dissociation kinetics of the **[Cu(CBuDEDPA)]** complex was investigated close to physiological pH identifying both spontaneous and proton-assisted routes as responsible for the dissociation of the complex.

The positive results obtained with the chelator models, especially with **H_2CBuDEDPA** in terms of radiolabelling efficiency, prompted the development of a bifunctional analogue of **H_2CBuDEDPA**, functionalising position 2 of the cyclobutane ring. For the synthesis of the BFC containing a functional group in *cis* relative configuration to the amino groups (***cis*,*cis*-L1**), a precursor of the ligand (**135**) was synthesised after exploring various synthetic routes. For the BFC with a *trans* relative configuration of the functional group to the amine groups (***cis*,*trans*-L2**), a 14-step synthesis was successfully completed, introducing an amino group in position 2 of the cyclobutane ring protected as a *tert*-butyl carbamate, enabling future conjugation with a targeting moiety.

Finally, the ***cis*,*trans*-L2** bifunctional chelator was submitted to radiolabelling studies, confirming that the structural modification had a minor impact in the radiolabelling efficiency. While the stability at physiological conditions remained unchanged, transchelation experiments provided negative results.

Overall, the introduction of a rigid moiety, such as cyclobutane ring, positively influenced the stabilisation of the ^{64}Cu radiocomplexes, highlighting their potential for further exploration as PET imaging contrast agents.

Bibliography of Part I

(1) Meijere, A. de; Baird, M. S. *Carbocyclic Three- and Four-Membered Ring Compounds*, 4th Editio.; Methoden der Organischen Chemie (Houben-Weyl); Georg Thieme Verlag KG: Stuttgart, 1997. https://doi.org/10.1055/b-003-109677.

(2) Seiser, T.; Saget, T.; Tran, D. N.; Cramer, N. Cyclobutanes in Catalysis. *Angew. Chem. Int. Ed.* **2011**, *50* (34), 7740–7752. https://doi.org/10.1002/anie.201101053.

(3) Dabrowski, J. A.; Moebius, D. C.; Wommack, A. J.; Kornahrens, A. F.; Kingsbury, J. S. Catalytic and Regioselective Ring Expansion of Arylcyclobutanones with Trimethylsilyldiazomethane. Ligand-Dependent Entry to Beta-Ketosilane or Enolsilane Adducts. *Org. Lett.* **2010**, *12* (16), 3598–3601. https://doi.org/10.1021/ol101136a.

(4) Nordvik, T.; Brinker, U. H. A Novel Route to Geminal Dibromocyclobutanes: Syntheses of 2-Substituted Cyclobutanone Acetals and Their Reaction with Boron Tribromide. *J. Org. Chem.* **2003**, *68* (24), 9394–9399. https://doi.org/10.1021/jo035295o.

(5) Beesley, R. M.; Ingold, C. K.; Thorpe, J. F. CXIX.—The Formation and Stability of Spiro-Compounds. Part I. Spiro-Compounds from Cyclohexane. *J. Chem. Soc. Trans.* **1915**, *107*, 1080–1106. https://doi.org/10.1039/CT9150701080.

(6) Jung, M. E.; Gervay, J. Gem-Dialkyl Effect in the Intramolecular Diels-Alder Reaction of 2-Furfuryl Methyl Fumarates: The Reactive Rotamer Effect, the Enthalpic Basis for Acceleration, and Evidence for a Polar Transition State. *J. Am. Chem. Soc.* **1991**, *113* (1), 224–232. https://doi.org/10.1021/ja00001a032.

(7) Jung, M. E.; Piizzi, G. Gem-Disubstituent Effect: Theoretical Basis and Synthetic Applications. *Chem. Rev.* **2005**, *105* (5), 1735–1766. https://doi.org/10.1021/cr940337h.

(8) Ringer, A. L.; Magers, D. H. Conventional Strain Energy in Dimethyl-Substituted Cyclobutane and the Gem-Dimethyl Effect. *J. Org. Chem.* **2007**, *72* (7), 2533–2537. https://doi.org/10.1021/jo0624647.

(9) Bachrach, S. M. The Gem-Dimethyl Effect Revisited. *J. Org. Chem.* **2008**, *73* (6), 2466–2468. https://doi.org/10.1021/jo702665r.

(10) Bach, R. D.; Dmitrenko, O. The Effect of Substitutents on the Strain Energies of Small Ring Compounds. *J. Org. Chem.* **2002**, *67* (8), 2588–2599. https://doi.org/10.1021/jo016241m.

(11) Poplata, S.; Tröster, A.; Zou, Y.-Q.; Bach, T. Recent Advances in the Synthesis of Cyclobutanes by Olefin [2 + 2] Photocycloaddition Reactions. *Chem. Rev.* **2016**, *116* (17), 9748–9815. https://doi.org/10.1021/acs.chemrev.5b00723.

(12) Shu, C.; Noble, A.; Aggarwal, V. K. Photoredox-Catalyzed Cyclobutane Synthesis by a Deboronative Radical Addition–Polar Cyclization Cascade. *Angew. Chem. Int. Ed.* **2019**, *58* (12), 3870–3874. https://doi.org/10.1002/anie.201813917.

(13) Hui, C.; Craggs, L.; Antonchick, A. P. Ring Contraction in Synthesis of Functionalized Carbocycles. *Chem. Soc. Rev.* **2022**, *51* (20), 8652–8675. https://doi.org/10.1039/D1CS01080H.

(14) Hussain, M. M.; Li, H.; Hussain, N.; Ureña, M.; Carroll, P. J.; Walsh, P. J. Applications of 1-Alkenyl-1,1-Heterobimetallics in the Stereoselective Synthesis of Cyclopropylboronate Esters, Trisubstituted Cyclopropanols and 2,3-Disubstituted Cyclobutanones. *J. Am. Chem. Soc.* **2009**, *131* (18), 6516–6524. https://doi.org/10.1021/ja900147s.

(15) Bach, T.; Hehn, J. P. Photochemical Reactions as Key Steps in Natural Product Synthesis. *Angew. Chem. Int. Ed.* **2011**, *50* (5), 1000–1045. https://doi.org/10.1002/anie.201002845.

(16) Vollmer, J. J.; Servis, K. L. Woodward-Hoffmann Rules: Cycloaddition Reactions. *J. Chem. Educ.* **1970**, *47* (7), 491–500. https://doi.org/10.1021/ed047p491.

(17) Takeda, K.; Shimono, Y.; Yoshii, E. A Short-Step Entry to (±)-Quadrone. *J. Am. Chem. Soc.* **1983**, *105* (3), 563–568. https://doi.org/10.1021/ja00341a042.

(18) de Meijere, A.; Redlich, S.; Frank, D.; Magull, J.; Hofmeister, A.; Menzel, H.; König, B.; Svoboda, J. Octacyclopropylcubane and Some of Its Isomers. *Angew. Chem. Int. Ed.* **2007**, *46* (24), 4574–4576. https://doi.org/10.1002/anie.200605150.

(19) Le Liepvre, M.; Ollivier, J.; Aitken, D. J. Synthesis of Functionalized Bicyclo[3.2.0]Heptanes – a Study of the [2+2] Photocycloaddition Reactions of 4-Hydroxycyclopent-2-Enone Derivatives. *Eur. J. Org. Chem.* **2009**, *2009* (34), 5953–5962. https://doi.org/10.1002/ejoc.200900749.

(20) Tidwell, T. T. Structure, Bonding, and Thermochemistry of Ketenes. In *Ketenes II*; 2006; pp 5–26. https://doi.org/10.1002/0471767670.ch1.

(21) Wilsey, S.; González, L.; Robb, M. A.; Houk, K. N. Ground- and Excited-State Surfaces for the [2+2]-Photocycloaddition of α,β-Enones to Alkenes. *J. Am. Chem. Soc.* **2000**, *122* (24), 5866–5876. https://doi.org/10.1021/ja0006595.

(22) Secci, F.; Frongia, A.; Piras, P. P. Stereocontrolled Synthesis and Functionalization of Cyclobutanes and Cyclobutanones. *Molecules* **2013**, *18* (12), 15541–15572. https://doi.org/10.3390/molecules181215541.

(23) Serelis, A. K.; Simpson, G. W. Stereoselectivity in the Thermal Cycloaddition Reactions of Tetrafluoroethylene to Derivatives of α-(4-Ethoxyphenyl)Acrylic Acid. *Tetrahedron Lett.* **1997**, *38* (24), 4277–4280. https://doi.org/10.1016/S0040-4039(97)00878-2.

(24) Reinhoudt, D. N.; Verboom, W.; Visser, G. W.; Trompenaars, W. P.; Harkema, S.; Van Hummel, G. J. Reactivity of Cis-Fused 3-(Dialkylamino)Cyclobutenes in Polar and Apolar Solvents. Synthesis, x-Ray Structures, and Reactions of Cis,Cis- and Cis,Trans-1,3-Cycloalkadienes. *J. Am. Chem. Soc.* **1984**, *106* (5), 1341–1350. https://doi.org/10.1021/ja00317a029.

(25) Semmelhack, M. F.; Tomoda, S. Synthesis of (±)-Fomannosin. *J. Am. Chem. Soc.* **1981**, *103* (9), 2427–2428. https://doi.org/10.1021/ja00399a057.

(26) Alcaide, B.; Almendros, P.; Aragoncillo, C. Exploiting [2+2] Cycloaddition Chemistry: Achievements with Allenes. *Chem. Soc. Rev.* **2010**, *39* (2), 783–816. https://doi.org/10.1039/B913749A.

(27) Nori, K.; Miake, M. A New Synthesis of Both the Enantiomers of Grandisol, the Boll Weevil

Pheromon. *Tetrahedron* **1987**, *43* (10), 2229–2239. https://doi.org/10.1016/S0040-4020(01)86806-X.

(28) Lee-Ruff, E.; Mladenova, G. Enantiomerically Pure Cyclobutane Derivatives and Their Use in Organic Synthesis. *Chem. Rev.* **2003**, *103* (4), 1449–1484. https://doi.org/10.1021/cr010013a.

(29) Ko, C.; Feltenberger, J. B.; Ghosh, S. K.; Hsung, R. P. Gassman's Intramolecular [2 + 2] Cationic Cycloaddition. Formal Total Syntheses of Raikovenal and Epi-Raikovenal. *Org. Lett.* **2008**, *10* (10), 1971–1974. https://doi.org/10.1021/ol8004968.

(30) Liu, Y.; Song, R.; Li, J. The Cycloaddition Reaction Using Visible Light Photoredox Catalysis. *Sci. China Chem.* **2016**, *59* (2), 161–170. https://doi.org/10.1007/s11426-015-5516-5.

(31) Colomer, I.; Coura Barcelos, R.; Donohoe, T. J. Catalytic Hypervalent Iodine Promoters Lead to Styrene Dimerization and the Formation of Tri- and Tetrasubstituted Cyclobutanes. *Angew. Chem. Int. Ed. Engl.* **2016**, *55* (15), 4748–4752. https://doi.org/10.1002/anie.201511683.

(32) Stork, G.; Cohen, J. F. Ring Size in Epoxynitrile Cyclization. General Synthesis of Functionally Substituted Cyclobutanes. Application to (±)-Grandisol. *J. Am. Chem. Soc.* **1974**, *96* (16), 5270–5272. https://doi.org/10.1021/ja00823a053.

(33) Takasu, K.; Misawa, K.; Ihara, M. Asymmetric Synthesis of Tricyclic-Cyclobutane by Means of Enantioselective Deprotonation and Intramolecular Michael–Aldol Reaction. *Tetrahedron Lett.* **2001**, *42* (48), 8489–8491. https://doi.org/10.1016/S0040-4039(01)01817-2.

(34) Takasu, K.; Ueno, M.; Ihara, M. Auxiliary Induced Asymmetric Michael-Aldol Reaction under Kinetic and Thermodynamic Conditions. *Tetrahedron Lett.* **2000**, *41* (13), 2145–2148. https://doi.org/10.1016/S0040-4039(00)00101-5.

(35) Edmonds, D. J.; Muir, K. W.; Procter, D. J. The Remarkable Effect of Cosolvent on a Samarium(II)-Mediated 4-Exo-Trig Cyclization: Further Synthetic Studies on Pestalotiopsin A. *J. Org. Chem.* **2003**, *68* (8), 3190–3198. https://doi.org/10.1021/jo026827o.

(36) Hoffmann, N. Photochemical Reactions as Key Steps in Organic Synthesis. *Chem. Rev.* **2008**, *108* (3), 1052–1103. https://doi.org/10.1021/cr0680336.

(37) Paquette, L. A.; Sugimura, T. Enantiospecific Total Synthesis and Absolute Configurational Assignment of (-)-Punctatin A (Antibiotic M95464). *J. Am. Chem. Soc.* **1986**, *108* (13), 3841–3842. https://doi.org/10.1021/ja00273a056.

(38) de Meijere, A.; Butenschön, H.; Chow, H. F.; Fitjer, L.; Haufe, G. *Houben-Weyl Methods of Organic Chemistry Vol. E 17e, 4th Edition Supplement: Carbocyclic Four-Membered Ring Compounds, Cyclobutanes*; Thieme, 2014.

(39) Paquette, L. A.; Parker, G. D.; Tei, T.; Dong, S. Pestalotiopsin A. Enantioselective Construction of Potential Building Blocks Derived from Antipodal Cyclobutanol Intermediates. *J. Org. Chem.* **2007**, *72* (19), 7125–7134.

https://doi.org/10.1021/jo070861r.

(40) Burgess, K.; Li, S.; Rebenspies, J. Chiral 1,3-Cyclobutane Amino Acids: Syntheses and Extended Conformations. *Tetrahedron Lett.* **1997**, *38* (10), 1681–1684. https://doi.org/10.1016/S0040-4039(97)00200-1.

(41) Blakemore, D. C.; Bryans, J. S.; Carnell, P.; Carr, C. L.; Chessum, N. E. A.; Field, M. J.; Kinsella, N.; Osborne, S. A.; Warren, A. N.; Williams, S. C. Synthesis and in Vivo Evaluation of Bicyclic Gababutins. *Bioorg. Med. Chem. Lett.* **2010**, *20* (2), 461–464. https://doi.org/10.1016/j.bmcl.2009.11.118.

(42) Antonsen, S.; Østby, R. B.; Stenstrøm, Y. Naturally Occurring Cyclobutanes: Their Biological Significance and Synthesis. In *Studies in Natural Products Chemistry*; 2018; Vol. 57, pp 1–40. https://doi.org/10.1016/B978-0-444-64057-4.00001-6.

(43) Adlington, R. M.; Baldwin, J. E.; Jones, R. H.; Murphy, J. A.; Parisi, M. F. Stereospecific Synthesis of (1S,2S)-1-Hydroxy-2-[(S)-Valylamino]-Cyclobutane-1-Acetic Acid, a Novel Microbial Antimetabolite. *J. Chem. Soc. Chem. Commun.* **1983**, 1479–1481. https://doi.org/10.1039/C39830001479.

(44) Fidyt, K.; Fiedorowicz, A.; Strządała, L.; Szumny, A. β-Caryophyllene and β-Caryophyllene Oxide-Natural Compounds of Anticancer and Analgesic Properties. *Cancer Med.* **2016**, *5* (10), 3007–3017. https://doi.org/10.1002/cam4.816.

(45) Hayashi, S.; Norbeck, D. W.; Rosenbrook, W.; Fine, R. L.; Matsukura, M.; Plattner, J. J.; Broder, S.; Mitsuya, H. Cyclobut-A and Cyclobut-G, Carbocyclic Oxetanocin Analogs That Inhibit the Replication of Human Immunodeficiency Virus in T Cells and Monocytes and Macrophages in Vitro. *Antimicrob. Agents Chemother.* **1990**, *34* (2), 287–294. https://doi.org/10.1128/AAC.34.2.287.

(46) Carreira, E. M.; Fessard, T. C. Four-Membered Ring-Containing Spirocycles: Synthetic Strategies and Opportunities. *Chem. Rev.* **2014**, *114* (16), 8257–8322. https://doi.org/10.1021/cr500127b.

(47) Marson, C. M. New and Unusual Scaffolds in Medicinal Chemistry. *Chem. Soc. Rev.* **2011**, *40* (11), 5514–5533. https://doi.org/10.1039/C1CS15119C.

(48) van der Kolk, M. R.; Janssen, M. A. C. H.; Rutjes, F. P. J. T.; Blanco-Ania, D. Cyclobutanes in Small-Molecule Drug Candidates. *ChemMedChem* **2022**, *17* (9), e202200020. https://doi.org/10.1002/cmdc.202200020.

(49) Lovering, F.; Bikker, J.; Humblet, C. Escape from Flatland: Increasing Saturation as an Approach to Improving Clinical Success. *J. Med. Chem.* **2009**, *52* (21), 6752–6756. https://doi.org/10.1021/jm901241e.

(50) Anumala, U. R.; Waaler, J.; Nkizinkiko, Y.; Ignatev, A.; Lazarow, K.; Lindemann, P.; Olsen, P. A.; Murthy, S.; Obaji, E.; Majouga, A. G.; Leonov, S.; von Kries, J. P.; Lehtiö, L.; Krauss, S.; Nazaré, M. Discovery of a Novel Series of Tankyrase Inhibitors by a Hybridization Approach. *J. Med. Chem.* **2017**, *60* (24), 10013–10025. https://doi.org/10.1021/acs.jmedchem.7b00883.

(51) Quambusch, L.; Landel, I.; Depta, L.; Weisner, J.; Uhlenbrock, N.; Müller, M. P.;

Glanemann, F.; Althoff, K.; Siveke, J. T.; Rauh, D. Covalent-Allosteric Inhibitors to Achieve Akt Isoform-Selectivity. *Angew. Chem. Int. Ed. Engl.* **2019**, *58* (52), 18823–18829. https://doi.org/10.1002/anie.201909857.

(52) Macdonald, J. D.; Chacón Simon, S.; Han, C.; Wang, F.; Shaw, J. G.; Howes, J. E.; Sai, J.; Yuh, J. P.; Camper, D.; Alicie, B. M.; Alvarado, J.; Nikhar, S.; Payne, W.; Aho, E. R.; Bauer, J. A.; Zhao, B.; Phan, J.; Thomas, L. R.; Rossanese, O. W.; Tansey, W. P.; Waterson, A. G.; Stauffer, S. R.; Fesik, S. W. Discovery and Optimization of Salicylic Acid-Derived Sulfonamide Inhibitors of the WD Repeat-Containing Protein 5–MYC Protein–Protein Interaction. *J. Med. Chem.* **2019**, *62* (24), 11232–11259. https://doi.org/10.1021/acs.jmedchem.9b01411.

(53) Hu, E.; Andrews, K.; Chmait, S.; Zhao, X.; Davis, C.; Miller, S.; Hill Della Puppa, G.; Dovlatyan, M.; Chen, H.; Lester-Zeiner, D.; Able, J.; Biorn, C.; Ma, J.; Shi, J.; Treanor, J.; Allen, J. R. Discovery of Novel Imidazo[4,5-b]Pyridines as Potent and Selective Inhibitors of Phosphodiesterase 10A (PDE10A). *ACS Med. Chem. Lett.* **2014**, *5* (6), 700–705. https://doi.org/10.1021/ml5000993.

(54) Wei, B.; Gunzner-Toste, J.; Yao, H.; Wang, T.; Wang, J.; Xu, Z.; Chen, J.; Wai, J.; Nonomiya, J.; Tsai, S. P.; Chuh, J.; Kozak, K. R.; Liu, Y.; Yu, S.-F.; Lau, J.; Li, G.; Phillips, G. D.; Leipold, D.; Kamath, A.; Su, D.; Xu, K.; Eigenbrot, C.; Steinbacher, S.; Ohri, R.; Raab, H.; Staben, L. R.; Zhao, G.; Flygare, J. A.; Pillow, T. H.; Verma, V.; Masterson, L. A.; Howard, P. W.; Safina, B. Discovery of Peptidomimetic Antibody-Drug Conjugate Linkers with Enhanced Protease Specificity. *J. Med. Chem.* **2018**, *61* (3), 989–1000. https://doi.org/10.1021/acs.jmedchem.7b01430.

(55) LaPorte, M. G.; Burnett, J. C.; Colombo, R.; Bulfer, S. L.; Alverez, C.; Chou, T.-F.; Neitz, R. J.; Green, N.; Moore, W. J.; Yue, Z.; Li, S.; Arkin, M. R.; Wipf, P.; Huryn, D. M. Optimization of Phenyl Indole Inhibitors of the AAA+ ATPase P97. *ACS Med. Chem. Lett.* **2018**, *9* (11), 1075–1081. https://doi.org/10.1021/acsmedchemlett.8b00372.

(56) Liu, Y.; Laufer, R.; Patel, N. K.; Ng, G.; Sampson, P. B.; Li, S.-W.; Lang, Y.; Feher, M.; Brokx, R.; Beletskaya, I.; Hodgson, R.; Plotnikova, O.; Awrey, D. E.; Qiu, W.; Chirgadze, N. Y.; Mason, J. M.; Wei, X.; Lin, D. C.-C.; Che, Y.; Kiarash, R.; Fletcher, G. C.; Mak, T. W.; Bray, M. R.; Pauls, H. W. Discovery of Pyrazolo[1,5-a]Pyrimidine TTK Inhibitors: CFI-402257 Is a Potent, Selective, Bioavailable Anticancer Agent. *ACS Med. Chem. Lett.* **2016**, *7* (7), 671–675. https://doi.org/10.1021/acsmedchemlett.5b00485.

(57) Nowikow, C.; Fuerst, R.; Kauderer, M.; Dank, C.; Schmid, W.; Hajduch, M.; Rehulka, J.; Gurska, S.; Mokshyna, O.; Polishchuk, P.; Zupkó, I.; Dzubak, P.; Rinner, U. Synthesis and Biological Evaluation of Cis-Restrained Carbocyclic Combretastatin A-4 Analogs: Influence of the Ring Size and Saturation on Cytotoxic Properties. *Bioorg. Med. Chem.* **2019**, *27* (19), 115032. https://doi.org/10.1016/j.bmc.2019.07.048.

(58) Ahmad, S.; Washburn, W. N.; Hernandez, A. S.; Bisaha, S.; Ngu, K.; Wang, W.; Pelleymounter, M. A.; Longhi, D.; Flynn, N.; Azzara, A. V; Rohrbach, K.; Devenny, J.; Rooney, S.; Thomas, M.; Glick, S.; Godonis, H.; Harvey, S.; Zhang, H.; Gemzik, B.;

Janovitz, E. B.; Huang, C.; Zhang, L.; Robl, J. A.; Murphy, B. J. Synthesis and Antiobesity Properties of 6-(4-Chlorophenyl)-3-(4-((3,3-Difluoro-1-Hydroxycyclobutyl)Methoxy)-3-Methoxyphenyl)Thieno[3,2-d]Pyrimidin-4(3H)-One (BMS-814580): A Highly Efficacious Melanin Concentrating Hormone Receptor 1 (MCHR1) Inhibitor. *J. Med. Chem.* **2016**, *59* (19), 8848–8858. https://doi.org/10.1021/acs.jmedchem.6b00676.

(59) Deaton, D. N.; Haffner, C. D.; Henke, B. R.; Jeune, M. R.; Shearer, B. G.; Stewart, E. L.; Stuart, J. D.; Ulrich, J. C. 2,4-Diamino-8-Quinazoline Carboxamides as Novel, Potent Inhibitors of the NAD Hydrolyzing Enzyme CD38: Exploration of the 2-Position Structure-Activity Relationships. *Bioorg. Med. Chem.* **2018**, *26* (8), 2107–2150. https://doi.org/10.1016/j.bmc.2018.03.021.

(60) Yang, P.; Jia, Q.; Song, S.; Huang, X. [2 + 2]-Cycloaddition-Derived Cyclobutane Natural Products: Structural Diversity, Sources, Bioactivities, and Biomimetic Syntheses. *Nat. Prod. Rep.* **2023**, *40* (6), 1094–1129. https://doi.org/10.1039/D2NP00034B.

(61) Izquierdo, S.; Martín-Vilà, M.; Moglioni, A. G.; Branchadell, V.; Ortuño, R. M. Stereodivergent Syntheses of the First Bis(Cyclobutane) β-Dipeptides. *Tetrahedron: Asymmetry* **2002**, *13* (22), 2403–2405. https://doi.org/10.1016/S0957-4166(02)00652-3.

(62) Aguilera, J.; Moglioni, A. G.; Moltrasio, G. Y.; Ortuño, R. M. Stereodivergent Synthesis of the First Bis(Cyclobutane) γ-Dipeptides and Mixed γ-Oligomers. *Tetrahedron: Asymmetry* **2008**, *19* (3), 302–308. https://doi.org/10.1016/j.tetasy.2008.01.020.

(63) Rosa, O. M.; Albertina, M. G.; Graciela, M. Y. Cyclobutane Biomolecules: Synthetic Approaches to Amino Acids, Peptides and Nucleosides. *Curr. Org. Chem.* **2005**, *9* (3), 237–259. https://doi.org/http://dx.doi.org/10.2174/1385272053369088.

(64) Izquierdo, S.; Rúa, F.; Sbai, A.; Parella, T.; Álvarez-Larena, Á.; Branchadell, V.; Ortuño, R. M. (+)- and (−)-2-Aminocyclobutane-1-Carboxylic Acids and Their Incorporation into Highly Rigid β-Peptides: Stereoselective Synthesis and a Structural Study. *J. Org. Chem.* **2005**, *70* (20), 7963–7971. https://doi.org/10.1021/jo0510843.

(65) Gutiérrez-Abad, R.; Carbajo, D.; Nolis, P.; Acosta-Silva, C.; Cobos, J. A.; Illa, O.; Royo, M.; Ortuño, R. M. Synthesis and Structural Study of Highly Constrained Hybrid Cyclobutane-Proline γ,γ-Peptides. *Amino Acids* **2011**, *41*, 673–686. https://doi.org/10.1007/s00726-011-0912-4.

(66) Illa, O.; Porcar-Tost, O.; Robledillo, C.; Elvira, C.; Nolis, P.; Reiser, O.; Branchadell, V.; Ortuño, R. M. Stereoselectivity of Proline/Cyclobutane Amino Acid-Containing Peptide Organocatalysts for Asymmetric Aldol Additions: A Rationale. *J. Org. Chem.* **2018**, *83* (1), 350–363. https://doi.org/10.1021/acs.joc.7b02745.

(67) Fernández, D.; Torres, E.; Avilés, F. X.; Ortuño, R. M.; Vendrell, J. Cyclobutane-Containing Peptides: Evaluation as Novel Metallocarboxypeptidase Inhibitors and Modelling of Their Mode of Action. *Bioorg. Med. Chem.* **2009**, *17* (11), 3824–3828. https://doi.org/10.1016/j.bmc.2009.04.035.

(68) Gorrea, E.; Nolis, P.; Torres, E.; Da Silva, E.; Amabilino, D. B.; Branchadell, V.; Ortuño, R. M. Self-Assembly of Chiral Trans-Cyclobutane-Containing β-Dipeptides into Ordered

Aggregates. *Chem. – A Eur. J.* **2011**, *17* (16), 4588–4597. https://doi.org/10.1002/chem.201002193.

(69) Celis, S.; Nolis, P.; Illa, O.; Branchadell, V.; Ortuño, R. M. Low-Molecular-Weight Gelators Consisting of Hybrid Cyclobutane-Based Peptides. *Org. Biomol. Chem.* **2013**, *11* (17), 2839–2846. https://doi.org/10.1039/C3OB27347D.

(70) Pi-Boleda, B.; Sans, M.; Campos, M.; Nolis, P.; Illa, O.; Estévez, J. C.; Branchadell, V.; Ortuño, R. M. Studies on Cycloalkane-Based Bisamide Organogelators: A New Example of Stochastic Chiral Symmetry-Breaking Induced by Sonication. *Chem. – A Eur. J.* **2017**, *23* (14), 3357–3365. https://doi.org/10.1002/chem.201604818.

(71) Porcar-Tost, O.; Pi-Boleda, B.; García-Anton, J.; Illa, O.; Ortuño, R. M. Cyclobutane-Based Peptides/Terpyridine Conjugates: Their Use in Metal Catalysis and as Functional Organogelators. *Tetrahedron* **2018**, *74* (51), 7252–7260. https://doi.org/10.1016/j.tet.2018.10.064.

(72) Illa, O.; Serra, A.; Ardiaca, A.; Herrero, X.; Closa, G.; Ortuño, R. M. Cyclobutane-Containing Scaffolds as Useful Intermediates in the Stereoselective Synthesis of Suitable Candidates for Biomedical Purposes: Surfactants, Gelators and Metal Cation Ligands. *Int. J. Mol. Sci.* **2019**, *20* (18). https://doi.org/10.3390/ijms20184333.

(73) Okino, T.; Hoashi, Y.; Takemoto, Y. Enantioselective Michael Reaction of Malonates to Nitroolefins Catalyzed by Bifunctional Organocatalysts. *J. Am. Chem. Soc.* **2003**, *125* (42), 12672–12673. https://doi.org/10.1021/ja036972z.

(74) Mayans, E.; Gargallo, A.; Álvarez-Larena, Á.; Illa, O.; Ortuño, R. M. Diastereodivergent Synthesis of Chiral Vic-Disubstituted-Cyclobutane Scaffolds: 1,3-Amino Alcohol and 1,3-Diamine Derivatives – Preliminary Use in Organocatalysis. *Eur. J. Org. Chem.* **2013**, *2013* (8), 1425–1433. https://doi.org/10.1002/ejoc.201201307.

(75) Porcar-Tost, O.; Olivares, J. A.; Pallier, A.; Esteban-Gómez, D.; Illa, O.; Platas-Iglesias, C.; Tóth, É.; Ortuño, R. M. Gadolinium Complexes of Highly Rigid, Open-Chain Ligands Containing a Cyclobutane Ring in the Backbone: Decreasing Ligand Denticity Might Enhance Kinetic Inertness. *Inorg. Chem.* **2019**, *58* (19), 13170–13183. https://doi.org/10.1021/acs.inorgchem.9b02044.

(76) Porcar-Tost, O.; Pallier, A.; Esteban-Gómez, D.; Illa, O.; Platas-Iglesias, C.; Tóth, É.; Ortuño, R. M. Stability, Relaxometric and Computational Studies on Mn2+ Complexes with Ligands Containing a Cyclobutane Scaffold. *Dalt. Trans.* **2021**, *50* (3), 1076–1085. https://doi.org/10.1039/D0DT03402A.

(77) Sans, M.; Illa, O.; Ortuño, R. M. Organobridged Silsesquioxanes Based on Cyclobutane Diamines: Influence of the Stereochemistry on the Morphology of the Materials. *Tetrahedron* **2016**, *72* (22), 2913–2919. https://doi.org/10.1016/j.tet.2016.04.001.

(78) Sorrenti, A.; Illa, O.; Pons, R.; Ortuño, R. M. Chiral Cyclobutane β-Amino Acid-Based Amphiphiles: Influence of Cis/Trans Stereochemistry on Solution Self-Aggregation and Recognition. *Langmuir* **2015**, *31* (35), 9608–9618. https://doi.org/10.1021/acs.langmuir.5b02700.

(79) Sorrenti, A.; Illa, O.; Ortuño, R. M.; Pons, R. Chiral Cyclobutane β-Amino Acid-Based Amphiphiles: Influence of Cis/Trans Stereochemistry on Condensed Phase and Monolayer Structure. *Langmuir* **2016**, *32* (27), 6977–6984. https://doi.org/10.1021/acs.langmuir.6b01461.

(80) Pi-Boleda, B.; Sorrenti, A.; Sans, M.; Illa, O.; Pons, R.; Branchadell, V.; Ortuño, R. M. Cyclobutane Scaffold in Bolaamphiphiles: Effect of Diastereoisomerism and Regiochemistry on Their Surface Activity Aggregate Structure. *Langmuir* **2018**, *34* (38), 11424–11432. https://doi.org/10.1021/acs.langmuir.8b01462.

(81) Pi-Boleda, B.; Bouzas, M.; Gaztelumendi, N.; Illa, O.; Nogués, C.; Branchadell, V.; Pons, R.; Ortuño, R. M. Chiral PH-Sensitive Cyclobutane β-Amino Acid-Based Cationic Amphiphiles: Possible Candidates for Use in Gene Therapy. *J. Mol. Liq.* **2020**, *297*, 111856. https://doi.org/10.1016/j.molliq.2019.111856.

(82) Pi-Boleda, B.; Ramisetty, S.; Illa, O.; Branchadell, V.; Dias, R. S.; Ortuño, R. M. Efficient DNA Condensation Induced by Chiral β-Amino Acid-Based Cationic Surfactants. *ACS Appl. Bio Mater.* **2021**, *4* (9), 7034–7043. https://doi.org/10.1021/acsabm.1c00683.

(83) Torres, E.; Puigmartí-Luis, J.; Pérez del Pino, Á.; Ortuño, R. M.; Amabilino, D. B. Use of Unnatural β-Peptides as a Self-Assembling Component in Functional Organic Fibres. *Org. Biomol. Chem.* **2010**, *8* (7), 1661–1665. https://doi.org/10.1039/B922843H.

(84) Aguilera, J.; Favier, I.; Sans, M.; Mor, À.; Álvarez-Larena, Á.; Illa, O.; Gómez, M.; Ortuño, R. M. Synthesis of Chiral Functionalised Cyclobutylpyrrolidines and Cyclobutylamino Alcohols from (–)-(S)-Verbenone – Applications in the Stabilisation of Ruthenium Nanocatalysts. *Eur. J. Org. Chem.* **2015**, *2015* (4), 810–819. https://doi.org/10.1002/ejoc.201403176.

(85) Ospina, J.; Sorrenti, A.; Illa, O.; Pons, R.; Ortuño, R. M. New Chiral Polyfunctional Cyclobutane Derivatives from (−)-Verbenone: Possible Surfactant Behaviour. *Tetrahedron: Asymmetry* **2013**, *24* (12), 713–718. https://doi.org/10.1016/j.tetasy.2013.05.007.

(86) Gutiérrez-Abad, R.; Illa, O.; Ortuño, R. M. Synthesis of Chiral Cyclobutane Containing C3-Symmetric Peptide Dendrimers. *Org. Lett.* **2010**, *12* (14), 3148–3151. https://doi.org/10.1021/ol1010664.

(87) Cooper, G. M. *The Cell: A Molecular Approach. 2nd Edition*; Sinauer Associates 2000, 2000.

(88) Pereira, C. D.; Martins, F.; Wiltfang, J.; da Cruz E Silva, O. A. B.; Rebelo, S. ABC Transporters Are Key Players in Alzheimer's Disease. *J. Alzheimers. Dis.* **2018**, *61* (2), 463–485. https://doi.org/10.3233/JAD-170639.

(89) Zhang, M.; Liu, J.; Zhou, M.-M.; Wu, H.; Hou, Y.; Li, Y.-F.; Yin, Y.; Zheng, L.; Cai, J.; Liao, F.-F.; Liu, F.-Y.; Yi, M.; Wan, Y. Anxiolytic Effects of Hippocampal Neurosteroids in Normal and Neuropathic Rats with Spared Nerve Injury. *J. Neurochem.* **2017**, *141* (1), 137–150. https://doi.org/10.1111/jnc.13965.

(90) Sözer, E. B.; Pocetti, C. F.; Vernier, P. T. Asymmetric Patterns of Small Molecule Transport After Nanosecond and Microsecond Electropermeabilization. *J. Membr. Biol.*

2018, *251* (2), 197–210. https://doi.org/10.1007/s00232-017-9962-1.

(91) Majumder, S.; Garamella, J.; Wang, Y.-L.; DeNies, M.; Noireaux, V.; Liu, A. P. Cell-Sized Mechanosensitive and Biosensing Compartment Programmed with DNA. *Chem. Commun.* **2017**, *53* (53), 7349–7352. https://doi.org/10.1039/C7CC03455E.

(92) Green, M.; Loewenstein, P. M. Autonomous Functional Domains of Chemically Synthesized Human Immunodeficiency Virus Tat Trans-Activator Protein. *Cell* **1988**, *55* (6), 1179–1188. https://doi.org/10.1016/0092-8674(88)90262-0.

(93) Frankel, A. D.; Pabo, C. O. Cellular Uptake of the Tat Protein from Human Immunodeficiency Virus. *Cell* **1988**, *55* (6), 1189–1193. https://doi.org/10.1016/0092-8674(88)90263-2.

(94) Tashima, T. Intelligent Substance Delivery into Cells Using Cell-Penetrating Peptides. *Bioorg. Med. Chem. Lett.* **2017**, *27* (2), 121–130. https://doi.org/10.1016/j.bmcl.2016.11.083.

(95) Lau, J. L.; Dunn, M. K. Therapeutic Peptides: Historical Perspectives, Current Development Trends, and Future Directions. *Bioorg. Med. Chem.* **2018**, *26* (10), 2700–2707. https://doi.org/10.1016/j.bmc.2017.06.052.

(96) Muttenthaler, M.; King, G. F.; Adams, D. J.; Alewood, P. F. Trends in Peptide Drug Discovery. *Nat. Rev. Drug Discov.* **2021**, *20* (4), 309–325. https://doi.org/10.1038/s41573-020-00135-8.

(97) Wang, Y.; Cheetham, A. G.; Angacian, G.; Su, H.; Xie, L.; Cui, H. Peptide–Drug Conjugates as Effective Prodrug Strategies for Targeted Delivery. *Adv. Drug Deliv. Rev.* **2017**, *110–111*, 112–126. https://doi.org/10.1016/j.addr.2016.06.015.

(98) Cooper, B. M.; Iegre, J.; O' Donovan, D. H.; Ölwegård Halvarsson, M.; Spring, D. R. Peptides as a Platform for Targeted Therapeutics for Cancer: Peptide–Drug Conjugates (PDCs). *Chem. Soc. Rev.* **2021**, *50* (3), 1480–1494. https://doi.org/10.1039/D0CS00556H.

(99) Cerrato, C. P.; Langel, Ü. An Update on Cell-Penetrating Peptides with Intracellular Organelle Targeting. *Expert Opin. Drug Deliv.* **2022**, *19* (2), 133–146. https://doi.org/10.1080/17425247.2022.2034784.

(100) Werle, M.; Bernkop-Schnürch, A. Strategies to Improve Plasma Half Life Time of Peptide and Protein Drugs. *Amino Acids* **2006**, *30* (4), 351–367. https://doi.org/10.1007/s00726-005-0289-3.

(101) Wu, Y.-D.; Gellman, S. Peptidomimetics. *Acc. Chem. Res.* **2008**, *41* (10), 1231–1232. https://doi.org/10.1021/ar800216e.

(102) Avan, I.; Hall, C. D.; Katritzky, A. R. Peptidomimetics via Modifications of Amino Acids and Peptide Bonds. *Chem. Soc. Rev.* **2014**, *43* (10), 3575–3594. https://doi.org/10.1039/C3CS60384A.

(103) Lenci, E.; Trabocchi, A. Peptidomimetic Toolbox for Drug Discovery. *Chem. Soc. Rev.* **2020**, *49* (11), 3262–3277. https://doi.org/10.1039/D0CS00102C.

(104) Zhang, D.; Wang, J.; Xu, D. Cell-Penetrating Peptides as Noninvasive Transmembrane Vectors for the Development of Novel Multifunctional Drug-Delivery Systems. *J. Control.*

release Off. J. Control. Release Soc. **2016**, *229*, 130–139. https://doi.org/10.1016/j.jconrel.2016.03.020.

(105) Lindgren, M.; Hällbrink, M.; Prochiantz, A.; Langel, U. Cell-Penetrating Peptides. *Trends Pharmacol. Sci.* **2000**, *21* (3), 99–103. https://doi.org/10.1016/s0165-6147(00)01447-4.

(106) Lundberg, P.; Langel, U. A Brief Introduction to Cell-Penetrating Peptides. *J. Mol. Recognit.* **2003**, *16* (5), 227–233. https://doi.org/10.1002/jmr.630.

(107) Vivès, E.; Brodin, P.; Lebleu, B. A Truncated HIV-1 Tat Protein Basic Domain Rapidly Translocates through the Plasma Membrane and Accumulates in the Cell Nucleus. *J. Biol. Chem.* **1997**, *272* (25), 16010–16017. https://doi.org/10.1074/jbc.272.25.16010.

(108) Elliott, G.; O'Hare, P. Intercellular Trafficking and Protein Delivery by a Herpesvirus Structural Protein. *Cell* **1997**, *88* (2), 223–233. https://doi.org/10.1016/s0092-8674(00)81843-7.

(109) Derossi, D.; Joliot, A. H.; Chassaing, G.; Prochiantz, A. The Third Helix of the Antennapedia Homeodomain Translocates through Biological Membranes. *J. Biol. Chem.* **1994**, *269* (14), 10444–10450.

(110) Futaki, S.; Suzuki, T.; Ohashi, W.; Yagami, T.; Tanaka, S.; Ueda, K.; Sugiura, Y. Arginine-Rich Peptides. An Abundant Source of Membrane-Permeable Peptides Having Potential as Carriers for Intracellular Protein Delivery. *J. Biol. Chem.* **2001**, *276* (8), 5836–5840. https://doi.org/10.1074/jbc.M007540200.

(111) Sakai, N.; Matile, S. Anion-Mediated Transfer of Polyarginine across Liquid and Bilayer Membranes. *J. Am. Chem. Soc.* **2003**, *125* (47), 14348–14356. https://doi.org/10.1021/ja037601l.

(112) Pooga, M.; Hällbrink, M.; Zorko, M.; Langel, U. Cell Penetration by Transportan. *FASEB J. Off. Publ. Fed. Am. Soc. Exp. Biol.* **1998**, *12* (1), 67–77. https://doi.org/10.1096/fasebj.12.1.67.

(113) Oehlke, J.; Scheller, A.; Wiesner, B.; Krause, E.; Beyermann, M.; Klauschenz, E.; Melzig, M.; Bienert, M. Cellular Uptake of an Alpha-Helical Amphipathic Model Peptide with the Potential to Deliver Polar Compounds into the Cell Interior Non-Endocytically. *Biochim. Biophys. Acta* **1998**, *1414* (1–2), 127–139. https://doi.org/10.1016/s0005-2736(98)00161-8.

(114) Agrawal, P.; Bhalla, S.; Usmani, S. S.; Singh, S.; Chaudhary, K.; Raghava, G. P. S.; Gautam, A. CPPsite 2.0: A Repository of Experimentally Validated Cell-Penetrating Peptides. *Nucleic Acids Res.* **2016**, *44* (D1), D1098-103. https://doi.org/10.1093/nar/gkv1266.

(115) Raghava, G. P. S.; Gautam, A. *CPPsite 2.0. Database of Cell-Penetrating Peptides*. http://crdd.osdd.net/raghava/cppsite/ (accessed 2024-09-01).

(116) Koren, E.; Torchilin, V. P. Cell-Penetrating Peptides: Breaking through to the Other Side. *Trends Mol. Med.* **2012**, *18* (7), 385–393. https://doi.org/10.1016/j.molmed.2012.04.012.

(117) Milletti, F. Cell-Penetrating Peptides: Classes, Origin, and Current Landscape. *Drug Discov. Today* **2012**, *17* (15–16), 850–860. https://doi.org/10.1016/j.drudis.2012.03.002.

(118) Fernández-Carneado, J.; Kogan, M. J.; Castel, S.; Giralt, E. Potential Peptide Carriers: Amphipathic Proline-Rich Peptides Derived from the N-Terminal Domain of γ-Zein. *Angew. Chem. Int. Ed.* **2004**, *43* (14), 1811–1814. https://doi.org/10.1002/anie.200352540.

(119) Marks, J. R.; Placone, J.; Hristova, K.; Wimley, W. C. Spontaneous Membrane-Translocating Peptides by Orthogonal High-Throughput Screening. *J. Am. Chem. Soc.* **2011**, *133* (23), 8995–9004. https://doi.org/10.1021/ja2017416.

(120) Tünnemann, G.; Ter-Avetisyan, G.; Martin, R. M.; Stöckl, M.; Herrmann, A.; Cardoso, M. C. Live-Cell Analysis of Cell Penetration Ability and Toxicity of Oligo-Arginines. *J. Pept. Sci.* **2008**, *14* (4), 469–476. https://doi.org/10.1002/psc.968.

(121) Reissmann, S. Cell Penetration: Scope and Limitations by the Application of Cell-Penetrating Peptides. *J. Pept. Sci.* **2014**, *20* (10), 760–784. https://doi.org/10.1002/psc.2672.

(122) Szabó, I.; Yousef, M.; Soltész, D.; Bató, C.; Mező, G.; Bánóczi, Z. Redesigning of Cell-Penetrating Peptides to Improve Their Efficacy as a Drug Delivery System. *Pharmaceutics* **2022**, *14* (5), 907. https://doi.org/10.3390/pharmaceutics14050907.

(123) Shete, H. K.; Prabhu, R. H.; Patravale, V. B. Endosomal Escape: A Bottleneck in Intracellular Delivery. *J. Nanosci. Nanotechnol.* **2014**, *14* (1), 460–474. https://doi.org/10.1166/jnn.2014.9082.

(124) Brock, D. J.; Kondow-McConaghy, H. M.; Hager, E. C.; Pellois, J.-P. Endosomal Escape and Cytosolic Penetration of Macromolecules Mediated by Synthetic Delivery Agents. *Bioconjug. Chem.* **2019**, *30* (2), 293–304. https://doi.org/10.1021/acs.bioconjchem.8b00799.

(125) Pujals, S.; Giralt, E. Proline-Rich, Amphipathic Cell-Penetrating Peptides. *Adv. Drug Deliv. Rev.* **2008**, *60* (4–5), 473–484. https://doi.org/10.1016/j.addr.2007.09.012.

(126) Morgan, A. A.; Rubenstein, E. Proline: The Distribution, Frequency, Positioning, and Common Functional Roles of Proline and Polyproline Sequences in the Human Proteome. *PLoS One* **2013**, *8* (1), e53785. https://doi.org/10.1371/journal.pone.0053785.

(127) Pi, K.-S.; Sang, Y.; Straus, S. K. Viral Proteins with PxxP and PY Motifs May Play a Role in Multiple Sclerosis. *Viruses* **2022**, *14* (2), 281. https://doi.org/10.3390/v14020281.

(128) Farrera-Sinfreu, J.; Giralt, E.; Castel, S.; Albericio, F.; Royo, M. Cell-Penetrating Cis-γ-Amino-l-Proline-Derived Peptides. *J. Am. Chem. Soc.* **2005**, *127* (26), 9459–9468. https://doi.org/10.1021/ja051648k.

(129) Munyendo, W. L. L.; Lv, H.; Benza-Ingoula, H.; Baraza, L. D.; Zhou, J. Cell Penetrating Peptides in the Delivery of Biopharmaceuticals. *Biomolecules* **2012**, *2* (2), 187–202. https://doi.org/10.3390/biom2020187.

(130) Kubyshkin, V.; Rubini, M. Proline Analogues. *Chem. Rev.* **2024**, *124* (13), 8130–8232. https://doi.org/10.1021/acs.chemrev.4c00007.

(131) Fillon, Y. A.; Anderson, J. P.; Chmielewski, J. Cell Penetrating Agents Based on a Polyproline Helix Scaffold. *J. Am. Chem. Soc.* **2005**, *127* (33), 11798–11803. https://doi.org/10.1021/ja052377g.

(132) Kuriakose, J.; Hernandez-Gordillo, V.; Nepal, M.; Brezden, A.; Pozzi, V.; Seleem, M. N.; Chmielewski, J. Targeting Intracellular Pathogenic Bacteria with Unnatural Proline-Rich Peptides: Coupling Antibacterial Activity with Macrophage Penetration. *Angew. Chem. Int. Ed. Engl.* **2013**, *52* (37), 9664–9667. https://doi.org/10.1002/anie.201302693.

(133) Dobitz, S.; Aronoff, M. R.; Wennemers, H. Oligoprolines as Molecular Entities for Controlling Distance in Biological and Material Sciences. *Acc. Chem. Res.* **2017**, *50* (10), 2420–2428. https://doi.org/10.1021/acs.accounts.7b00340.

(134) Kaksonen, M.; Roux, A. Mechanisms of Clathrin-Mediated Endocytosis. *Nat. Rev. Mol. Cell Biol.* **2018**, *19* (5), 313–326. https://doi.org/10.1038/nrm.2017.132.

(135) Kiss, A. L.; Botos, E. Endocytosis via Caveolae: Alternative Pathway with Distinct Cellular Compartments to Avoid Lysosomal Degradation? *J. Cell. Mol. Med.* **2009**, *13* (7), 1228–1237. https://doi.org/10.1111/j.1582-4934.2009.00754.x.

(136) Wadia, J. S.; Stan, R. V; Dowdy, S. F. Transducible TAT-HA Fusogenic Peptide Enhances Escape of TAT-Fusion Proteins after Lipid Raft Macropinocytosis. *Nat. Med.* **2004**, *10* (3), 310–315. https://doi.org/10.1038/nm996.

(137) Herce, H. D.; Garcia, A. E. Cell Penetrating Peptides: How Do They Do It? *J. Biol. Phys.* **2007**, *33* (5–6), 345–356. https://doi.org/10.1007/s10867-008-9074-3.

(138) Ruseska, I.; Zimmer, A. Internalization Mechanisms of Cell-Penetrating Peptides. *Beilstein J. Nanotechnol.* **2020**, *11*, 101–123. https://doi.org/10.3762/bjnano.11.10.

(139) El-Sayed, A.; Khalil, I. A.; Kogure, K.; Futaki, S.; Harashima, H. Octaarginine- and Octalysine-Modified Nanoparticles Have Different Modes of Endosomal Escape. *J. Biol. Chem.* **2008**, *283* (34), 23450–23461. https://doi.org/10.1074/jbc.M709387200.

(140) Nunnari, J.; Suomalainen, A. Mitochondria: In Sickness and in Health. *Cell* **2012**, *148* (6), 1145–1159. https://doi.org/10.1016/j.cell.2012.02.035.

(141) Bock, F. J.; Tait, S. W. G. Mitochondria as Multifaceted Regulators of Cell Death. *Nat. Rev. Mol. Cell Biol.* **2020**, *21* (2), 85–100. https://doi.org/10.1038/s41580-019-0173-8.

(142) McBride, H. M.; Neuspiel, M.; Wasiak, S. Mitochondria: More than Just a Powerhouse. *Curr. Biol.* **2006**, *16* (14), R551-60. https://doi.org/10.1016/j.cub.2006.06.054.

(143) Tilokani, L.; Nagashima, S.; Paupe, V.; Prudent, J. Mitochondrial Dynamics: Overview of Molecular Mechanisms. *Essays Biochem.* **2018**, *62* (3), 341–360. https://doi.org/10.1042/EBC20170104.

(144) Wu, J.; Li, J.; Wang, H.; Liu, C.-B. Mitochondrial-Targeted Penetrating Peptide Delivery for Cancer Therapy. *Expert Opin. Drug Deliv.* **2018**, *15* (10), 951–964. https://doi.org/10.1080/17425247.2018.1517750.

(145) Yang, J.; Griffin, A.; Qiang, Z.; Ren, J. Organelle-Targeted Therapies: A Comprehensive Review on System Design for Enabling Precision Oncology. *Signal Transduct. Target. Ther.* **2022**, *7* (1), 379. https://doi.org/10.1038/s41392-022-01243-0.

(146) Ylikallio, E.; Suomalainen, A. Mechanisms of Mitochondrial Diseases. *Ann. Med.* **2012**, *44* (1), 41–59. https://doi.org/10.3109/07853890.2011.598547.

(147) Santidrian, A. F.; Matsuno-Yagi, A.; Ritland, M.; Seo, B. B.; LeBoeuf, S. E.; Gay, L. J.;

Yagi, T.; Felding-Habermann, B. Mitochondrial Complex I Activity and NAD+/NADH Balance Regulate Breast Cancer Progression. *J. Clin. Invest.* **2013**, *123* (3), 1068–1081. https://doi.org/10.1172/JCI64264.

(148) Jean, S. R.; Ahmed, M.; Lei, E. K.; Wisnovsky, S. P.; Kelley, S. O. Peptide-Mediated Delivery of Chemical Probes and Therapeutics to Mitochondria. *Acc. Chem. Res.* **2016**, *49* (9), 1893–1902. https://doi.org/10.1021/acs.accounts.6b00277.

(149) Zielonka, J.; Joseph, J.; Sikora, A.; Hardy, M.; Ouari, O.; Vasquez-Vivar, J.; Cheng, G.; Lopez, M.; Kalyanaraman, B. Mitochondria-Targeted Triphenylphosphonium-Based Compounds: Syntheses, Mechanisms of Action, and Therapeutic and Diagnostic Applications. *Chem. Rev.* **2017**, *117* (15), 10043–10120. https://doi.org/10.1021/acs.chemrev.7b00042.

(150) Liew, S. S.; Qin, X.; Zhou, J.; Li, L.; Huang, W.; Yao, S. Q. Smart Design of Nanomaterials for Mitochondria-Targeted Nanotherapeutics. *Angew. Chem. Int. Ed. Engl.* **2021**, *60* (5), 2232–2256. https://doi.org/10.1002/anie.201915826.

(151) Lu, P.; Bruno, B. J.; Rabenau, M.; Lim, C. S. Delivery of Drugs and Macromolecules to the Mitochondria for Cancer Therapy. *J. Control. release Off. J. Control. Release Soc.* **2016**, *240*, 38–51. https://doi.org/10.1016/j.jconrel.2015.10.023.

(152) Abe, Y.; Shodai, T.; Muto, T.; Mihara, K.; Torii, H.; Nishikawa, S.; Endo, T.; Kohda, D. Structural Basis of Presequence Recognition by the Mitochondrial Protein Import Receptor Tom20. *Cell* **2000**, *100* (5), 551–560. https://doi.org/10.1016/s0092-8674(00)80691-1.

(153) Zhao, K.; Zhao, G.-M.; Wu, D.; Soong, Y.; Birk, A. V; Schiller, P. W.; Szeto, H. H. Cell-Permeable Peptide Antioxidants Targeted to Inner Mitochondrial Membrane Inhibit Mitochondrial Swelling, Oxidative Cell Death, and Reperfusion Injury *. *J. Biol. Chem.* **2004**, *279* (33), 34682–34690. https://doi.org/10.1074/jbc.M402999200.

(154) Horton, K. L.; Stewart, K. M.; Fonseca, S. B.; Guo, Q.; Kelley, S. O. Mitochondria-Penetrating Peptides. *Chem. Biol.* **2008**, *15* (4), 375–382. https://doi.org/10.1016/j.chembiol.2008.03.015.

(155) Kim, S.; Nam, H. Y.; Lee, J.; Seo, J. Mitochondrion-Targeting Peptides and Peptidomimetics: Recent Progress and Design Principles. *Biochemistry* **2020**, *59* (3), 270–284. https://doi.org/10.1021/acs.biochem.9b00857.

(156) Pereira, M. P.; Kelley, S. O. Maximizing the Therapeutic Window of an Antimicrobial Drug by Imparting Mitochondrial Sequestration in Human Cells. *J. Am. Chem. Soc.* **2011**, *133* (10), 3260–3263. https://doi.org/10.1021/ja110246u.

(157) Lei, E. K.; Pereira, M. P.; Kelley, S. O. Tuning the Intracellular Bacterial Targeting of Peptidic Vectors. *Angew. Chem. Int. Ed. Engl.* **2013**, *52* (37), 9660–9663. https://doi.org/10.1002/anie.201302265.

(158) Nepal, M.; Thangamani, S.; Seleem, M. N.; Chmielewski, J. Targeting Intracellular Bacteria with an Extended Cationic Amphiphilic Polyproline Helix. *Org. Biomol. Chem.* **2015**, *13* (21), 5930–5936. https://doi.org/10.1039/C5OB00227C.

(159) Yousif, L. F.; Stewart, K. M.; Horton, K. L.; Kelley, S. O. Mitochondria-Penetrating Peptides: Sequence Effects and Model Cargo Transport. *ChemBioChem* **2009**, *10* (12), 2081–2088. https://doi.org/10.1002/cbic.200900017.

(160) Wisnovsky, S. P.; Wilson, J. J.; Radford, R. J.; Pereira, M. P.; Chan, M. R.; Laposa, R. R.; Lippard, S. J.; Kelley, S. O. Targeting Mitochondrial DNA with a Platinum-Based Anticancer Agent. *Chem. Biol.* **2013**, *20* (11), 1323–1328. https://doi.org/10.1016/j.chembiol.2013.08.010.

(161) Jean, S. R.; Pereira, M. P.; Kelley, S. O. Structural Modifications of Mitochondria-Targeted Chlorambucil Alter Cell Death Mechanism but Preserve MDR Evasion. *Mol. Pharm.* **2014**, *11* (8), 2675–2682. https://doi.org/10.1021/mp500104j.

(162) Chamberlain, G. R.; Tulumello, D. V; Kelley, S. O. Targeted Delivery of Doxorubicin to Mitochondria. *ACS Chem. Biol.* **2013**, *8* (7), 1389–1395. https://doi.org/10.1021/cb400095v.

(163) Jean, S. R.; Tulumello, D. V; Riganti, C.; Liyanage, S. U.; Schimmer, A. D.; Kelley, S. O. Mitochondrial Targeting of Doxorubicin Eliminates Nuclear Effects Associated with Cardiotoxicity. *ACS Chem. Biol.* **2015**, *10* (9), 2007–2015. https://doi.org/10.1021/acschembio.5b00268.

(164) Lei, E. K.; Kelley, S. O. Delivery and Release of Small-Molecule Probes in Mitochondria Using Traceless Linkers. *J. Am. Chem. Soc.* **2017**, *139* (28), 9455–9458. https://doi.org/10.1021/jacs.7b04415.

(165) Li, L.; Geisler, I.; Chmielewski, J.; Cheng, J.-X. Cationic Amphiphilic Polyproline Helix P11LRR Targets Intracellular Mitochondria. *J. Control. release Off. J. Control. Release Soc.* **2010**, *142* (2), 259–266. https://doi.org/10.1016/j.jconrel.2009.10.012.

(166) Kalafut, D.; Anderson, T. N.; Chmielewski, J. Mitochondrial Targeting of a Cationic Amphiphilic Polyproline Helix. *Bioorg. Med. Chem. Lett.* **2012**, *22* (1), 561–563. https://doi.org/10.1016/j.bmcl.2011.10.077.

(167) Burke, C. S.; Byrne, A.; Keyes, T. E. Highly Selective Mitochondrial Targeting by a Ruthenium(II) Peptide Conjugate: Imaging and Photoinduced Damage of Mitochondrial DNA. *Angew. Chem. Int. Ed. Engl.* **2018**, *57* (38), 12420–12424. https://doi.org/10.1002/anie.201806002.

(168) Li, X.; Hao, S.; Han, A.; Yang, Y.; Fang, G.; Liu, J.; Wang, S. Intracellular Fenton Reaction Based on Mitochondria-Targeted Copper(Ii)–Peptide Complex for Induced Apoptosis. *J. Mater. Chem. B* **2019**, *7* (25), 4008–4016. https://doi.org/10.1039/C9TB00569B.

(169) Davis, M. H.; Altschuld, R. A.; Jung, D. W.; Brierley, G. P. Estimation of Intramitochondrial PCa and PH by Fura-2 and 2,7 Biscarboxyethyl-5(6)-Carboxyfluorescein (BCECF) Fluorescence. *Biochem. Biophys. Res. Commun.* **1987**, *149* (1), 40–45. https://doi.org/10.1016/0006-291x(87)91602-0.

(170) Jung, D. W.; Davis, M. H.; Brierley, G. P. Estimation of Matrix PH in Isolated Heart Mitochondria Using a Fluorescent Probe. *Anal. Biochem.* **1989**, *178* (2), 348–354. https://doi.org/10.1016/0003-2697(89)90651-9.

(171) Shimizu, S.; Eguchi, Y.; Kamiike, W.; Funahashi, Y.; Mignon, A.; Lacronique, V.; Matsuda, H.; Tsujimoto, Y. Bcl-2 Prevents Apoptotic Mitochondrial Dysfunction by Regulating Proton Flux. *Proc. Natl. Acad. Sci. U. S. A.* **1998**, *95* (4), 1455–1459. https://doi.org/10.1073/pnas.95.4.1455.

(172) Diliberto, P. A.; Wang, X. F.; Herman, B. Confocal Imaging of Ca2+ in Cells. *Methods Cell Biol.* **1994**, *40*, 243–262. https://doi.org/10.1016/s0091-679x(08)61117-6.

(173) Liu, J.; Diwu, Z.; Leung, W. Y. Synthesis and Photophysical Properties of New Fluorinated Benzo[c]Xanthene Dyes as Intracellular PH Indicators. *Bioorg. Med. Chem. Lett.* **2001**, *11* (22), 2903–2905. https://doi.org/10.1016/s0960-894x(01)00595-9.

(174) Nakata, E.; Nazumi, Y.; Yukimachi, Y.; Uto, Y.; Maezawa, H.; Hashimoto, T.; Okamoto, Y.; Hori, H. Synthesis and Photophysical Properties of New SNARF Derivatives as Dual Emission PH Sensors. *Bioorg. Med. Chem. Lett.* **2011**, *21* (6), 1663–1666. https://doi.org/10.1016/j.bmcl.2011.01.105.

(175) Chen, Y.; Zhu, C.; Cen, J.; Bai, Y.; He, W.; Guo, Z. Ratiometric Detection of PH Fluctuation in Mitochondria with a New Fluorescein/Cyanine Hybrid Sensor. *Chem. Sci.* **2015**, *6* (5), 3187–3194. https://doi.org/10.1039/C4SC04021J.

(176) Reynolds, J. E.; Li, J.; Eastman, A. Detection of Apoptosis by Flow Cytometry of Cells Simultaneously Stained for Intracellular PH (Carboxy SNARF-1) and Membrane Permeability (Hoechst 33342). *Cytometry* **1996**, *25* (4), 349–357. https://doi.org/10.1002/(SICI)1097-0320(19961201)25:4<349::AID-CYTO6>3.0.CO;2-8.

(177) Balut, C.; vandeVen, M.; Despa, S.; Lambrichts, I.; Ameloot, M.; Steels, P.; Smets, I. Measurement of Cytosolic and Mitochondrial PH in Living Cells during Reversible Metabolic Inhibition. *Kidney Int.* **2008**, *73* (2), 226–232. https://doi.org/10.1038/sj.ki.5002632.

(178) Fominaya, J.; Bravo, J.; Rebollo, A. Strategies to Stabilize Cell Penetrating Peptides for in Vivo Applications. *Ther. Deliv.* **2015**, *6* (10), 1171–1194. https://doi.org/10.4155/tde.15.51.

(179) Illa, O.; Ospina, J.; Sánchez-Aparicio, J.-E.; Pulido, X.; Abengozar, M. Á.; Gaztelumendi, N.; Carbajo, D.; Nogués, C.; Rivas, L.; Maréchal, J.-D.; Royo, M.; Ortuño, R. M. Hybrid Cyclobutane/Proline-Containing Peptidomimetics: The Conformational Constraint Influences Their Cell-Penetration Ability. *Int. J. Mol. Sci.* **2021**, *22* (10), 5092. https://doi.org/10.3390/ijms22105092.

(180) Gorrea, E.; Carbajo, D.; Gutiérrez-Abad, R.; Illa, O.; Branchadell, V.; Royo, M.; Ortuño, R. M. Searching for New Cell-Penetrating Agents: Hybrid Cyclobutane–Proline γ,γ-Peptides. *Org. Biomol. Chem.* **2012**, *10* (20), 4050–4057. https://doi.org/10.1039/C2OB25220A.

(181) Zhou, P.; Wang, M.; Du, L.; Fisher, G. W.; Waggoner, A.; Ly, D. H. Novel Binding and Efficient Cellular Uptake of Guanidine-Based Peptide Nucleic Acids (GPNA). *J. Am. Chem. Soc.* **2003**, *125* (23), 6878–6879. https://doi.org/10.1021/ja029665m.

(182) Vazdar, M.; Heyda, J.; Mason, P. E.; Tesei, G.; Allolio, C.; Lund, M.; Jungwirth, P. Arginine "Magic": Guanidinium Like-Charge Ion Pairing from Aqueous Salts to Cell Penetrating Peptides. *Acc. Chem. Res.* **2018**, *51* (6), 1455–1464.

https://doi.org/10.1021/acs.accounts.8b00098.

(183) Illa, O.; Olivares, J.-A.; Gaztelumendi, N.; Martínez-Castro, L.; Ospina, J.; Abengozar, M.-Á.; Sciortino, G.; Maréchal, J.-D.; Nogués, C.; Royo, M.; Rivas, L.; Ortuño, R. M. Chiral Cyclobutane-Containing Cell-Penetrating Peptides as Selective Vectors for Anti-Leishmania Drug Delivery Systems. *Int. J. Mol. Sci.* **2020**, *21* (20), 7502–7526. https://doi.org/10.3390/ijms21207502.

(184) Merrifield, R. B. Solid Phase Peptide Synthesis. I. The Synthesis of a Tetrapeptide. *J. Am. Chem. Soc.* **1963**, *85* (14), 2149–2154. https://doi.org/10.1021/ja00897a025.

(185) Palomo, J. M. Solid-Phase Peptide Synthesis: An Overview Focused on the Preparation of Biologically Relevant Peptides. *RSC Adv.* **2014**, *4* (62), 32658–32672. https://doi.org/10.1039/C4RA02458C.

(186) Gorrea, E.; Carbajo, D.; Gutiérrez-Abad, R.; Illa, O.; Branchadell, V.; Royo, M.; Ortuño, R. M. Searching for New Cell-Penetrating Agents: Hybrid Cyclobutane-Proline γ,γ-Peptides. *Org. Biomol. Chem.* **2012**, *10* (20), 4050–4057. https://doi.org/10.1039/c2ob25220a.

(187) Carlsen, P. H. J.; Katsuki, T.; Martin, V. S.; Sharpless, K. B. A Greatly Improved Procedure for Ruthenium Tetroxide Catalyzed Oxidations of Organic Compounds. *J. Org. Chem.* **1981**, *46* (19), 3936–3938. https://doi.org/10.1021/jo00332a045.

(188) Protection for the Amino Group. In *Greene's Protective Groups in Organic Synthesis*; 2006; pp 696–926. https://doi.org/10.1002/9780470053485.ch7.

(189) Fields, G. Methods for Removing the Fmoc Group. *Methods Mol. Biol.* **1994**, *35*, 17–27. https://doi.org/10.1385/0-89603-273-6:17.

(190) Maegawa, T.; Fujiwara, Y.; Ikawa, T.; Hisashi, H.; Monguchi, Y.; Sajiki, H. Novel Deprotection Method of Fmoc Group under Neutral Hydrogenation Conditions. *Amino Acids* **2009**, *36* (3), 493–499. https://doi.org/10.1007/s00726-008-0109-7.

(191) Fischer, R.; Mader, O.; Jung, G.; Brock, R. Extending the Applicability of Carboxyfluorescein in Solid-Phase Synthesis. *Bioconjug. Chem.* **2003**, *14* (3), 653–660. https://doi.org/10.1021/bc025658b.

(192) Dunn, K. W.; Kamocka, M. M.; McDonald, J. H. A Practical Guide to Evaluating Colocalization in Biological Microscopy. *Am. J. Physiol. Cell Physiol.* **2011**, *300* (4), C723-42. https://doi.org/10.1152/ajpcell.00462.2010.

(193) Dulsat, J.; López-Nieto, B.; Estrada-Tejedor, R.; Borrell, J. I. Evaluation of Free Online ADMET Tools for Academic or Small Biotech Environments. *Molecules* **2023**, *28* (2), 776. https://doi.org/10.3390/molecules28020776.

(194) Chem3D, Version 17.0, PerkinElmer, Inc.: Waltham, MA, USA 2016.

(195) *ADMETlab3.0*. https://admetlab3.scbdd.com/ (accessed 2024-09-16).

(196) *pKCSM*. https://biosig.lab.uq.edu.au/pkcsm/ (accessed 2024-09-16).

(197) *PreADMET*. https://preadmet.webservice.bmdrc.org/ (accessed 2024-09-16).

(198) Potocky, T. B.; Menon, A. K.; Gellman, S. H. Effects of Conformational Stability and Geometry of Guanidinium Display on Cell Entry by β-Peptides. *J. Am. Chem. Soc.* **2005**, *127* (11), 3686–3687. https://doi.org/10.1021/ja042566j.

(199) Lättig-Tünnemann, G.; Prinz, M.; Hoffmann, D.; Behlke, J.; Palm-Apergi, C.; Morano, I.; Herce, H. D.; Cardoso, M. C. Backbone Rigidity and Static Presentation of Guanidinium Groups Increases Cellular Uptake of Arginine-Rich Cell-Penetrating Peptides. *Nat. Commun.* **2011**, *2* (1), 453. https://doi.org/10.1038/ncomms1459.

(200) Nagel, Y. A.; Raschle, P. S.; Wennemers, H. Effect of Preorganized Charge-Display on the Cell-Penetrating Properties of Cationic Peptides. *Angew. Chem. Int. Ed.* **2017**, *56* (1), 122–126. https://doi.org/10.1002/anie.201607649.

(201) Tian, Y.; Zeng, X.; Li, J.; Jiang, Y.; Zhao, H.; Wang, D.; Huang, X.; Li, Z. Achieving Enhanced Cell Penetration of Short Conformationally Constrained Peptides through Amphiphilicity Tuning. *Chem. Sci.* **2017**, *8* (11), 7576–7581. https://doi.org/10.1039/C7SC03614K.

(202) Appelbaum, J. S.; LaRochelle, J. R.; Smith, B. A.; Balkin, D. M.; Holub, J. M.; Schepartz, A. Arginine Topology Controls Escape of Minimally Cationic Proteins from Early Endosomes to the Cytoplasm. *Chem. Biol.* **2012**, *19* (7), 819–830. https://doi.org/10.1016/j.chembiol.2012.05.022.

(203) Böttger, R.; Hoffmann, R.; Knappe, D. Differential Stability of Therapeutic Peptides with Different Proteolytic Cleavage Sites in Blood, Plasma and Serum. *PLoS One* **2017**, *12* (6), e0178943. https://doi.org/10.1371/journal.pone.0178943.

(204) Lai, X.; Tang, J.; ElSayed, M. E. H. Recent Advances in Proteolytic Stability for Peptide, Protein, and Antibody Drug Discovery. *Expert Opin. Drug Discov.* **2021**, *16* (12), 1467–1482. https://doi.org/10.1080/17460441.2021.1942837.

(205) Rothbard, J. B.; Jessop, T. C.; Lewis, R. S.; Murray, B. A.; Wender, P. A. Role of Membrane Potential and Hydrogen Bonding in the Mechanism of Translocation of Guanidinium-Rich Peptides into Cells. *J. Am. Chem. Soc.* **2004**, *126* (31), 9506–9507. https://doi.org/10.1021/ja0482536.

(206) Tantama, M.; Hung, Y. P.; Yellen, G. Imaging Intracellular PH in Live Cells with a Genetically Encoded Red Fluorescent Protein Sensor. *J. Am. Chem. Soc.* **2011**, *133* (26), 10034–10037. https://doi.org/10.1021/ja202902d.

(207) Wieder, E. D.; Hang, H.; Fox, M. H. Measurement of Intracellular PH Using Flow Cytometry with Carboxy-SNARF-1. *Cytometry* **1993**, *14* (8), 916–921. https://doi.org/10.1002/cyto.990140810.

(208) Takahashi, A.; Zhang, Y.; Centonze, V. E.; Herman, B. Measurement of Mitochondrial PH In Situ. *Biotechniques* **2001**, *30* (4), 804–815. https://doi.org/10.2144/01304rv01.

(209) Porcelli, A. M.; Ghelli, A.; Zanna, C.; Pinton, P.; Rizzuto, R.; Rugolo, M. PH Difference across the Outer Mitochondrial Membrane Measured with a Green Fluorescent Protein Mutant. *Biochem. Biophys. Res. Commun.* **2005**, *326* (4), 799–804. https://doi.org/10.1016/j.bbrc.2004.11.105.

(210) Benčina, M. Illumination of the Spatial Order of Intracellular PH by Genetically Encoded PH-Sensitive Sensors. *Sensors* **2013**, *13* (12), 16736–16758. https://doi.org/10.3390/s131216736.

(211) Detmer, S. A.; Chan, D. C. Functions and Dysfunctions of Mitochondrial Dynamics. *Nat. Rev. Mol. Cell Biol.* **2007**, *8* (11), 870–879. https://doi.org/10.1038/nrm2275.

(212) Mankoff, D. A. A Definition of Molecular Imaging. *J. Nucl. Med.* **2007**, *48* (6), 18N, 21N.

(213) Massoud, T. F.; Gambhir, S. S. Molecular Imaging in Living Subjects: Seeing Fundamental Biological Processes in a New Light. *Genes Dev.* **2003**, *17* (5), 545–580. https://doi.org/10.1101/gad.1047403.

(214) Willmann, J. K.; van Bruggen, N.; Dinkelborg, L. M.; Gambhir, S. S. Molecular Imaging in Drug Development. *Nat. Rev. Drug Discov.* **2008**, *7* (7), 591–607. https://doi.org/10.1038/nrd2290.

(215) Jennings, L. E.; Long, N. J. 'Two Is Better than One' - Probes for Dual-Modality Molecular Imaging. *Chem. Commun.* **2009**, 3511–3524. https://doi.org/10.1039/b821903f.

(216) Wadas, T. J.; Wong, E. H.; Weisman, G. R.; Anderson, C. J. Coordinating Radiometals of Copper, Gallium, Indium, Yttrium, and Zirconium for PET and SPECT Imaging of Disease. *Chem. Rev.* **2010**, *110* (5), 2858–2902. https://doi.org/10.1021/cr900325h.

(217) Young, H.; Baum, R.; Cremerius, U.; Herholz, K.; Hoekstra, O.; Lammertsma, A. A.; Pruim, J.; Price, P. Measurement of Clinical and Subclinical Tumour Response Using [18F]-Fluorodeoxyglucose and Positron Emission Tomography: Review and 1999 EORTC Recommendations. European Organization for Research and Treatment of Cancer (EORTC) PET Study Group. *Eur. J. Cancer* **1999**, *35* (13), 1773–1782. https://doi.org/10.1016/s0959-8049(99)00229-4.

(218) *University of Utah Health*. https://uofuhealth.utah.edu/huntsman/cqci/clinical-patient-imaging/information-for-patients (accessed 2023-07-07).

(219) James, M. L.; Gambhir, S. S. A Molecular Imaging Primer: Modalities, Imaging Agents, and Applications. *Physiol. Rev.* **2012**, *92* (2), 897–965. https://doi.org/10.1152/physrev.00049.2010.

(220) Crișan, G.; Moldovean-cioroianu, N. S.; Timaru, D. G.; Andrieș, G.; Căinap, C.; Chiș, V. Radiopharmaceuticals for PET and SPECT Imaging: A Literature Review over the Last Decade. *Int. J. Mol. Sci.* **2022**, *23* (9), 5023. https://doi.org/10.3390/ijms23095023.

(221) Gambhir, S. S. Molecular Imaging of Cancer with Positron Emission Tomography. *Nat. Rev. Cancer* **2002**, *2* (9), 683–693. https://doi.org/10.1038/nrc882.

(222) Deng, S.-M.; Zhang, W.; Zhang, B.; Chen, Y.-Y.; Li, J.-H.; Wu, Y.-W. Correlation between the Uptake of 18F-Fluorodeoxyglucose (18F-FDG) and the Expression of Proliferation-Associated Antigen Ki-67 in Cancer Patients: A Meta-Analysis. *PLoS One* **2015**, *10* (6), e0129028. https://doi.org/10.1371/journal.pone.0129028.

(223) Kim, S. J.; Cho, Y. S.; Moon, S. H.; Bae, J. M.; Kim, S.; Choe, Y. S.; Kim, B.-T.; Lee, K.-H. Primary Tumor ¹⁸F-FDG Avidity Affects the Performance of ¹⁸F-FDG PET/CT for Detecting Gastric Cancer Recurrence. *J. Nucl. Med.* **2016**, *57* (4), 544 LP – 550. https://doi.org/10.2967/jnumed.115.163295.

(224) Shen, K.; Liu, B.; Zhou, X.; Ji, Y.; Chen, L.; Wang, Q.; Xue, W. The Evolving Role of 18F-FDG PET/CT in Diagnosis and Prognosis Prediction in Progressive Prostate Cancer.

Front. Oncol. **2021**, *11*, 683793. https://doi.org/10.3389/fonc.2021.683793.

(225) Price, E. W.; Orvig, C. Matching Chelators to Radiometals for Radiopharmaceuticals. *Chem. Soc. Rev.* **2014**, *43* (1), 260–290. https://doi.org/10.1039/c3cs60304k.

(226) *National Nuclear Data Center*. www.nndc.bnl.gov/nudat3/ (accessed 2023-07-16).

(227) Kotek, J.; Lubal, P.; Hermann, P.; Císařová, I.; Lukeš, I.; Godula, T.; Svobodová, I.; Táborský, P.; Havel, J. High Thermodynamic Stability and Extraordinary Kinetic Inertness of Copper(II) Complexes with 1,4,8,11-Tetraazacyclotetradecane-1,8-Bis(Methylphosphonic Acid): Example of a Rare Isomerism between Kinetically Inert Penta- and Hexacoordinated Copper(II) Com. *Chem. – A Eur. J.* **2003**, *9* (1), 233–248. https://doi.org/10.1002/chem.200390017.

(228) Krasnovskaya, O. O.; Abramchuck, D.; Erofeev, A.; Gorelkin, P.; Kuznetsov, A.; Shemukhin, A.; Beloglazkina, E. K. Recent Advances in 64Cu/67Cu-Based Radiopharmaceuticals. *Int. J. Mol. Sci.* **2023**, *24* (11), 9154. https://doi.org/10.3390/ijms24119154.

(229) U.S. National Library of Medicine. *ClinicalTrials.gov.* www.ClinicalTrials.gov (accessed 2023-07-02).

(230) Lepareur, N. Cold Kit Labeling: The Future of 68Ga Radiopharmaceuticals? *Front. Med.* **2022**, *9*, 812050. https://doi.org/10.3389/fmed.2022.812050.

(231) Ramogida, C. F.; Orvig, C. Tumour Targeting with Radiometals for Diagnosis and Therapy. *Chem. Commun.* **2013**, *49* (42), 4720–4739. https://doi.org/10.1039/c3cc41554f.

(232) Harris, W. R.; Pecoraro, V. L. Thermodynamic Binding Constants for Gallium Transferrin. *Biochemistry* **1983**, *22* (2), 292–299. https://doi.org/10.1021/bi00271a010.

(233) Brasse, D.; Nonat, A. Radiometals: Towards a New Success Story in Nuclear Imaging? *Dalt. Trans.* **2015**, *44* (11), 4845–4858. https://doi.org/10.1039/c4dt02911a.

(234) Hancock, R. D. Chelate Ring Size and Metal Ion Selection. The Basis of Selectivity for Metal Ions in Open-Chain Ligands and Macrocycles. *J. Chem. Educ.* **1992**, *69* (8), 615–621. https://doi.org/10.1021/ed069p615.

(235) Boros, E.; Ferreira, C. L.; Cawthray, J. F.; Price, E. W.; Patrick, B. O.; Wester, D. W.; Adam, M. J.; Orvig, C. Acyclic Chelate with Ideal Properties for (68)Ga PET Imaging Agent Elaboration. *J. Am. Chem. Soc.* **2010**, *132* (44), 15726–15733. https://doi.org/10.1021/ja106399h.

(236) Liu, S.; Edwards, D. S. Bifunctional Chelators for Therapeutic Lanthanide Radiopharmaceuticals. *Bioconjug. Chem.* **2001**, *12* (1), 7–34. https://doi.org/10.1021/bc000070v.

(237) Wangler, C.; Schirrmacher, R.; Bartenstein, P.; Wangler, B. Click-Chemistry Reactions in Radiopharmaceutical Chemistry: Fast & Easy Introduction of Radiolabels into Biomolecules for In Vivo Imaging. *Curr. Med. Chem.* **2010**, *17* (11), 1092–1116. https://doi.org/10.2174/092986710790820615.

(238) Zeglis, B. M.; Lewis, J. S. A Practical Guide to the Construction of Radiometallated Bioconjugates for Positron Emission Tomography. *Dalt. Trans.* **2011**, *40* (23), 6168–6195.

https://doi.org/10.1039/C0DT01595D.

(239) Ravasco, J. M. J. M.; Faustino, H.; Trindade, A.; Gois, P. M. P. Bioconjugation with Maleimides: A Useful Tool for Chemical Biology. *Chemistry* **2019**, *25* (1), 43–59. https://doi.org/10.1002/chem.201803174.

(240) Lebedev, A. Y.; Holland, J. P.; Lewis, J. S. Clickable Bifunctional Radiometal Chelates for Peptide Labeling. *Chem. Commun.* **2010**, *46* (10), 1706–1708. https://doi.org/10.1039/B924784J.

(241) Zeng, D.; Zeglis, B. M.; Lewis, J. S.; Anderson, C. J. The Growing Impact of Bioorthogonal Click Chemistry on the Development of Radiopharmaceuticals. *J. Nucl. Med.* **2013**, *54* (6), 829–832. https://doi.org/10.2967/jnumed.112.115550.

(242) Kostelnik, T. I.; Orvig, C. Radioactive Main Group and Rare Earth Metals for Imaging and Therapy. *Chem. Rev.* **2019**, *119* (2), 902–956. https://doi.org/10.1021/acs.chemrev.8b00294.

(243) Schmidt, M. M.; Wittrup, K. D. A Modeling Analysis of the Effects of Molecular Size and Binding Affinity on Tumor Targeting. *Mol. Cancer Ther.* **2009**, *8* (10), 2861–2871. https://doi.org/10.1158/1535-7163.MCT-09-0195.

(244) Nelson, B. J. B.; Andersson, J. D.; Wuest, F.; Spreckelmeyer, S. Good Practices for 68Ga Radiopharmaceutical Production. *EJNMMI Radiopharm. Chem.* **2022**, *7* (1), 1–26. https://doi.org/10.1186/s41181-022-00180-1.

(245) Muthaiah, S.; Bhatia, A.; Kannan, M. Stability of Metal Complexes. In *Stability of Coordination Compounds*; Srivastva, A. N., Ed.; IntechOpen: Rijeka, 2020. https://doi.org/10.5772/intechopen.90894.

(246) Martell, A. E.; Motekaitis, R. J. Potentiometry Revisited: The Determination of Thermodynamic Equilibria in Complex Multicomponent Systems. *Coord. Chem. Rev.* **1990**, *100*, 323–361. https://doi.org/10.1016/0010-8545(90)85014-J.

(247) Mohod, S. O.; Tayade, D. T. PH-Metric Study of Phenylthiocarbamidophenol with Cu (II), Co (II), Cd (II) and Ni (II) Metal Ions at 0.1 M Ionic Strength. *Int. J. Pharm. Res.* **2017**, *8* (3), 25–30.

(248) Thordarson, P. Determining Association Constants from Titration Experiments in Supramolecular Chemistry. *Chem. Soc. Rev.* **2011**, *40* (3), 1305–1323. https://doi.org/10.1039/c0cs00062k.

(249) Basurto, S.; Miguel, D.; Moreno, D.; Neo, A. G.; Quesada, R.; Torroba, T. Simple 1-Dicyanomethylene-2-Chloro-3-Aminoindene Push–Pull Chromophores: Applications in Cation and Anion Sensing. *Org. Biomol. Chem.* **2010**, *8* (3), 552–558. https://doi.org/10.1039/B916700E.

(250) Motulsky, H.; Christopoulos, A. Fitting Models to Biological Data Using Linear and Nonlinear Regression. A Practical Guide to Curve Fitting. Graphpad Software Inc: San Diego, CA 2003.

(251) Price, E. W.; Orvig, C. The Chemistry of Inorganic Nuclides (Y-86, Ga-68, Cu-64, Zr-89, I-124). In *Chemistry of Molecular Imaging*; 2015; pp 105–135.

(252) FDA, U. S. *FDA letter of approval for Detectnet*. https://www.accessdata.fda.gov/drugsatfda_docs/nda/2020/213227Orig1s000Approv.pdf (accessed 2023-08-31).

(253) Gipharma S.R.L. *FDA Letter of Approval for NETSPOTTM.* https://www.accessdata.fda.gov/drugsatfda_docs/label/2016/208547s000lbl.pdf (accessed 2023-08-31).

(254) Graham, M. M.; Gu, X.; Ginader, T.; Breheny, P.; Sunderland, J. J. 68Ga-DOTATOC Imaging of Neuroendocrine Tumors: A Systematic Review and Metaanalysis. *J. Nucl. Med.* **2017**, *58* (9), 1452–1458. https://doi.org/10.2967/jnumed.117.191197.

(255) Zhang, Y.; Hong, H.; Engle, J. W.; Bean, J.; Yang, Y.; Leigh, B. R.; Barnhart, T. E.; Cai, W. Positron Emission Tomography Imaging of CD105 Expression with a 64Cu-Labeled Monoclonal Antibody: NOTA Is Superior to DOTA. *PLoS One* **2011**, *6* (12), e28005. https://doi.org/10.1371/journal.pone.0028005.

(256) Cooper, M. S.; Ma, M. T.; Sunassee, K.; Shaw, K. P.; Williams, J. D.; Paul, R. L.; Donnelly, P. S.; Blower, P. J. Comparison of (64)Cu-Complexing Bifunctional Chelators for Radioimmunoconjugation: Labeling Efficiency, Specific Activity, and in Vitro/in Vivo Stability. *Bioconjug. Chem.* **2012**, *23* (5), 1029–1039. https://doi.org/10.1021/bc300037w.

(257) De Silva, R. A.; Jain, S.; Lears, K. A.; Chong, H.-S.; Kang, C. S.; Sun, X.; Rogers, B. E. Copper-64 Radiolabeling and Biological Evaluation of Bifunctional Chelators for Radiopharmaceutical Development. *Nucl. Med. Biol.* **2012**, *39* (8), 1099–1104. https://doi.org/10.1016/j.nucmedbio.2012.05.009.

(258) Maheshwari, V.; Dearling, J. L. J.; Treves, S. T.; Packard, A. B. Measurement of the Rate of Copper(II) Exchange for 64Cu Complexes of Bifunctional Chelators. *Inorganica Chim. Acta* **2012**, *393*, 318–323. https://doi.org/10.1016/j.ica.2012.07.012.

(259) Laforest, R.; Ghai, A.; Fraum, T. J.; Oyama, R.; Frye, J.; Kaemmerer, H.; Gaehle, G.; Voller, T.; Mpoy, C.; Rogers, B. E.; Fiala, M.; Shoghi, K. I.; Achilefu, S.; Rettig, M.; Vij, R.; DiPersio, J. F.; Schwarz, S.; Shokeen, M.; Dehdashti, F. First-in-Humans Evaluation of Safety and Dosimetry of 64Cu-LLP2A for PET Imaging. *J. Nucl. Med.* **2023**, *64* (2), 320–328. https://doi.org/10.2967/jnumed.122.264349.

(260) Ferreirós-Martínez, R.; Esteban-Gómez, D.; Platas-Iglesias, C.; de Blas, A.; Rodríguez-Blas, T. Zn(II), Cd(II) and Pb(II) Complexation with Pyridinecarboxylate Containing Ligands. *Dalt. Trans.* **2008**, 5754–5765. https://doi.org/10.1039/B808631A.

(261) Ramogida, C. F.; Cawthray, J. F.; Boros, E.; Ferreira, C. L.; Patrick, B. O.; Adam, M. J.; Orvig, C. H2CHXdedpa and H4CHXoctapa—Chiral Acyclic Chelating Ligands for 67/68Ga and 111In Radiopharmaceuticals. *Inorg. Chem.* **2015**, *54* (4), 2017–2031. https://doi.org/10.1021/ic502942a.

(262) Boros, E.; Cawthray, J. F.; Ferreira, C. L.; Patrick, B. O.; Adam, M. J.; Orvig, C. Evaluation of the H2)Dedpa Scaffold and Its CRGDyK Conjugates for Labeling with 64Cu. *Inorg. Chem.* **2012**, *51* (11), 6279–6284. https://doi.org/10.1021/ic300482x.

(263) Ramogida, C. F.; Boros, E.; Patrick, B. O.; Zeisler, S. K.; Kumlin, J.; Adam, M. J.; Schaffer,

P.; Orvig, C. Evaluation of H2CHXdedpa, H2dedpa- and H2CHXdedpa-N,N′-Propyl-2-NI Ligands for 64Cu(Ii) Radiopharmaceuticals. *Dalt. Trans.* **2016**, *45* (33), 13082–13090. https://doi.org/10.1039/C6DT00932H.

(264) Ramogida, C. F.; Murphy, L.; Cawthray, J. F.; Ross, J. D.; Adam, M. J.; Orvig, C. Novel "Bi-Modal" H2dedpa Derivatives for Radio- and Fluorescence Imaging. *J. Inorg. Biochem.* **2016**, *162*, 253–262. https://doi.org/10.1016/j.jinorgbio.2015.11.021.

(265) Ramogida, C. F.; Pan, J.; Ferreira, C. L.; Patrick, B. O.; Rebullar, K.; Yapp, D. T. T.; Lin, K.-S.; Adam, M. J.; Orvig, C. Nitroimidazole-Containing H2dedpa and H2CHXdedpa Derivatives as Potential PET Imaging Agents of Hypoxia with (68)Ga. *Inorg. Chem.* **2015**, *54* (10), 4953–4965. https://doi.org/10.1021/acs.inorgchem.5b00554.

(266) Pena-Bonhome, C.; Fiaccabrino, D.; Rama, T.; Fernández-Pavón, D.; Southcott, L.; Zhang, Z.; Lin, K.-S.; de Blas, A.; Patrick, B. O.; Schaffer, P.; Orvig, C.; Jaraquemada-Peláez, M. de G.; Rodríguez-Blas, T. Toward 68Ga and 64Cu Positron Emission Tomography Probes: Is H2dedpa-N,N′-Pram the Missing Link for Dedpa Conjugation? *Inorg. Chem.* **2023**, *62* (50), 20593–20607. https://doi.org/10.1021/acs.inorgchem.2c04123.

(267) Uzal-Varela, R.; Lucio-Martínez, F.; Nucera, A.; Botta, M.; Esteban-Gómez, D.; Valencia, L.; Rodríguez-Rodríguez, A.; Platas-Iglesias, C. A Systematic Investigation of the NMR Relaxation Properties of Fe(Iii)-EDTA Derivatives and Their Potential as MRI Contrast Agents. *Inorg. Chem. Front.* **2023**, *10* (5), 1633–1649. https://doi.org/10.1039/D2QI02665A.

(268) Kálmán, F. K.; Végh, A.; Regueiro-Figueroa, M.; Tóth, É.; Platas-Iglesias, C.; Tircsó, G. H4octapa: Highly Stable Complexation of Lanthanide(III) Ions and Copper(II). *Inorg. Chem.* **2015**, *54* (5), 2345–2356. https://doi.org/10.1021/ic502966m.

(269) Delpassand, E. S.; Ranganathan, D.; Wagh, N.; Shafie, A.; Gaber, A.; Abbasi, A.; Kjaer, A.; Tworowska, I.; Núñez, R. ⁶⁴Cu-DOTATATE PET/CT for Imaging Patients with Known or Suspected Somatostatin Receptor–Positive Neuroendocrine Tumors: Results of the First U.S. Prospective, Reader-Masked Clinical Trial. *J. Nucl. Med.* **2020**, *61* (6), 890 LP – 896. https://doi.org/10.2967/jnumed.119.236091.

(270) Anderson, C. J.; Wadas, T. J.; Wong, E. H.; Weisman, G. R. Cross-Bridged Macrocyclic Chelators for Stable Complexation of Copper Radionuclides for PET Imaging. *Q. J. Nucl. Med. Mol. imaging* **2008**, *52* (2), 185–192.

(271) Uzal-Varela, R.; Patinec, V.; Tripier, R.; Valencia, L.; Maneiro, M.; Canle, M.; Platas-Iglesias, C.; Esteban-Gómez, D.; Iglesias, E. On the Dissociation Pathways of Copper Complexes Relevant as PET Imaging Agents. *J. Inorg. Biochem.* **2022**, *236*, 111951. https://doi.org/10.1016/j.jinorgbio.2022.111951.

(272) Charette, B. J.; Griffin, P. J.; Zimmerman, C. M.; Olshansky, L. Conformationally Dynamic Copper Coordination Complexes. *Dalton Trans.* **2022**, *51* (16), 6212–6219. https://doi.org/10.1039/d2dt00312k.

(273) Salinas, G.; Ibanez, J. G.; Vásquez-Medrano, R.; Frontana-Uribe, B. A. Analysis of Cu in Mezcal Commercial Samples Using Square Wave Anodic Stripping Voltammetry. *J. Electrochem. Sci. Technol* **2018**, *9* (4), 276–281. https://doi.org/10.5229/JECST.2018.9.4.276.

(274) Kálmán, F. K.; Tircsó, G. Kinetic Inertness of the Mn2+ Complexes Formed with AAZTA and Some Open-Chain EDTA Derivatives. *Inorg. Chem.* **2012**, *51* (19), 10065–10067. https://doi.org/10.1021/ic300832e.

(275) Zhang, T.; Liu, J.-M.; Huang, X.-F.; Xia, B.; Su, C.-Y.; Luo, G.-F.; Xu, Y.-W.; Wu, Y.-X.; Mao, Z.-W.; Qiu, R.-L. Chelant Extraction of Heavy Metals from Contaminated Soils Using New Selective EDTA Derivatives. *J. Hazard. Mater.* **2013**, *262*, 464–471. https://doi.org/10.1016/j.jhazmat.2013.08.069.

(276) Vágner, A.; D'Alessandria, C.; Gambino, G.; Schwaiger, M.; Aime, S.; Maiocchi, A.; Tóth, I.; Baranyai, Z.; Tei, L. A Rigidified AAZTA-like Ligand as Efficient Chelator for 68Ga Radiopharmaceuticals. *ChemistrySelect* **2016**, *1* (2), 163–171. https://doi.org/10.1002/slct.201500051.

(277) Harris, W. R.; Raymond, K. N.; Weitl, F. L. Ferric Ion Sequestering Agents. 6. The Spectrophotometric and Potentiometric Evaluation of Sulfonated Tricatecholate Ligands. *J. Am. Chem. Soc.* **1981**, *103* (10), 2667–2675. https://doi.org/10.1021/ja00400a030.

(278) Tircsó, G.; Tircsóné Benyó, E.; Garda, Z.; Singh, J.; Trokowski, R.; Brücher, E.; Sherry, A. D.; Tóth, É.; Kovács, Z. Comparison of the Equilibrium, Kinetic and Water Exchange Properties of Some Metal Ion-DOTA and DOTA-Bis(Amide) Complexes. *J. Inorg. Biochem.* **2020**, *206*, 111042. https://doi.org/10.1016/j.jinorgbio.2020.111042.

(279) Kubíček, V.; Böhmová, Z.; Ševčíková, R.; Vaněk, J.; Lubal, P.; Poláková, Z.; Michalicová, R.; Kotek, J.; Hermann, P. NOTA Complexes with Copper(II) and Divalent Metal Ions: Kinetic and Thermodynamic Studies. *Inorg. Chem.* **2018**, *57* (6), 3061–3072. https://doi.org/10.1021/acs.inorgchem.7b02929.

(280) Comba, P.; Grimm, L.; Orvig, C.; Rück, K.; Wadepohl, H. Synthesis and Coordination Chemistry of Hexadentate Picolinic Acid Based Bispidine Ligands. *Inorg. Chem.* **2016**, *55* (24), 12531–12543. https://doi.org/10.1021/acs.inorgchem.6b01787.

(281) Sun, X.; Wuest, M.; Weisman, G. R.; Wong, E. H.; Reed, D. P.; Boswell, C. A.; Motekaitis, R.; Martell, A. E.; Welch, M. J.; Anderson, C. J. Radiolabeling and In Vivo Behavior of Copper-64-Labeled Cross-Bridged Cyclam Ligands. *J. Med. Chem.* **2002**, *45* (2), 469–477. https://doi.org/10.1021/jm0103817.

(282) Rylova, S. N.; Stoykow, C.; Del Pozzo, L.; Abiraj, K.; Tamma, M. L.; Kiefer, Y.; Fani, M.; Maecke, H. R. The Somatostatin Receptor 2 Antagonist 64Cu-NODAGA-JR11 Outperforms 64Cu-DOTA-TATE in a Mouse Xenograft Model. *PLoS One* **2018**, *13* (4), e0195802.

(283) Voráčová, I.; Vaněk, J.; Pasulka, J.; Střelcová, Z.; Lubal, P.; Hermann, P. Dissociation Kinetics Study of Copper(II) Complexes of DO3A, DOTA and Its Monosubstituted Derivatives. *Polyhedron* **2013**, *61*, 99–104. https://doi.org/10.1016/j.poly.2013.05.042.

(284) Ševčík, R.; Vaněk, J.; Michalicová, R.; Lubal, P.; Hermann, P.; Santos, I. C.; Santos, I.; Campello, M. P. C. Formation and Decomplexation Kinetics of Copper(Ii) Complexes with Cyclen Derivatives Having Mixed Carboxylate and Phosphonate Pendant Arms. *Dalt. Trans.* **2016**, *45* (32), 12723–12733. https://doi.org/10.1039/C6DT01127F.

(285) Gahler, A. R. Colorimetric Determination of Copper with Neo-Cuproine. *Anal. Chem.* **1954**, *26* (3), 577–579. https://doi.org/10.1021/ac60087a052.

(286) Booker-Milburn, K. I.; Cowell, J. K.; Delgado Jiménez, F.; Sharpe, A.; White, A. J. Stereoselective Intermolecular [2+2] Photocycloaddition Reactions of Tetrahydrophthalic Anhydride and Derivatives with Alkenols and Alkynols. *Tetrahedron* **1999**, *55* (18), 5875–5888. https://doi.org/10.1016/S0040-4020(99)00250-1.

(287) Mittendorf, J.; Kunisch, F.; Matzke, M.; Militzer, H.-C.; Schmidt, A.; Schönfeld, W. Novel Antifungal β-Amino Acids: Synthesis and Activity against Candida Albicans. *Bioorg. Med. Chem. Lett.* **2003**, *13* (3), 433–436. https://doi.org/10.1016/S0960-894X(02)00958-7.

(288) Conradi, M.; Junkers, T. Efficient [2+2] Photocycloadditions under Equimolar Conditions by Employing a Continuous UV-Flow Reactor. *J. Photochem. Photobiol. A Chem.* **2013**, *259*, 41–46. https://doi.org/10.1016/j.jphotochem.2013.02.024.

(289) Kearns Bryant K.; Warrener, Ronald N.; Margetić, Davor, P. S. . W. The Preparation of Stereoisomeric Tricyclo[4.2.1.02,5]Nona-7-Ene-3,4-Dicar-boximides and Anhydrides: Literature Corrections and New Products. *Synlett* **2014**, *25* (11), 1601–1605. https://doi.org/10.1055/s-0033-1339031.

(290) Lescop, C.; Mévellec, L.; Huet, F. A New Synthesis of 2-Azabicyclo[2.1.1]Hexanes. *J. Org. Chem.* **2001**, *66* (12), 4187–4193. https://doi.org/10.1021/jo001790y.

(291) Birman, V. B.; Jiang, X.-T. Synthesis of Sceptrin Alkaloids. *Org. Lett.* **2004**, *6* (14), 2369–2371. https://doi.org/10.1021/ol049283g.

(292) Gu, X.; Xian, M.; Roy-Faure, S.; Bolte, J.; Aitken, D. J.; Gefflaut, T. Synthesis of the Constrained Glutamate Analogues (2S,1′R,2′R)- and (2S,1′S,2′S)-2-(2′-Carboxycyclobutyl)Glycines L-CBG-II and L-CBG-I by Enzymatic Transamination. *Tetrahedron Lett.* **2006**, *47* (2), 193–196. https://doi.org/10.1016/j.tetlet.2005.10.156.

(293) Celis, S.; Gorrea, E.; Nolis, P.; Illa, O.; Ortuño, R. M. Designing Hybrid Foldamers: The Effect on the Peptide Conformational Bias of β- versus α- and γ-Linear Residues in Alternation with (1R,2S)-2-Aminocyclobutane-1-Carboxylic Acid. *Org. Biomol. Chem.* **2012**, *10* (4), 861–868. https://doi.org/10.1039/C1OB06575K.

(294) Hernvann, F.; Rasore, G.; Declerck, V.; Aitken, D. J. Stereoselective Intermolecular [2 + 2]-Photocycloaddition Reactions of Maleic Anhydride: Stereocontrolled and Regiocontrolled Access to 1,2,3-Trifunctionalized Cyclobutanes. *Org. Biomol. Chem.* **2014**, *12* (41), 8212–8222. https://doi.org/10.1039/C4OB01383B.

(295) Chang, Z.; Boyaud, F.; Guillot, R.; Boddaert, T.; Aitken, D. J. A Photochemical Route to 3- and 4-Hydroxy Derivatives of 2-Aminocyclobutane-1-Carboxylic Acid with an All-Cis Geometry. *J. Org. Chem.* **2018**, *83* (1), 527–534. https://doi.org/10.1021/acs.joc.7b02559.

(296) Griesbeck, A. G. Spin-Selectivity in Photochemistry: A Tool for Organic Synthesis. *Synlett*

2003, No. 4, 451–472. https://doi.org/10.1055/s-2003-37505.

(297) Moriyama, K.; Ishida, K.; Togo, H. Hofmann-Type Rearrangement of Imides by in Situ Generation of Imide-Hypervalent Iodines(III) from Iodoarenes. *Org. Lett.* **2012**, *14* (3), 946–949. https://doi.org/10.1021/ol300028j.

(298) Maertens, G.; Canesi, S. Rearrangements Induced by Hypervalent Iodine BT - Hypervalent Iodine Chemistry; Wirth, T., Ed.; Springer International Publishing: Cham, 2016; pp 223–241. https://doi.org/10.1007/128_2015_657.

(299) Constantino, M. G.; Lacerda, V.; da Silva, G. V. J.; Tasic, L.; Rittner, R. Principal Component Analysis of Long-Range 'W' Coupling Constants of Some Cyclic Compounds. *J. Mol. Struct.* **2001**, *597* (1), 129–136. https://doi.org/10.1016/S0022-2860(01)00591-9.

(300) Prakash Hitesh; Kaur, Harpreet; Sharma, Pawan K; Sharma, Vijay; Singh, Shiv P; Moriarty, Robert M, O. B. Hypervalent Iodine Oxidative Rearrangement of Anthranilamides, Salicylamides and Some β-Substituted Amides: A New and Convenient Synthesis of 2-Benzimidazolones, 2-Benzoxazolones and Related Compounds. *Synthesis (Stuttg).* **2001**, *2001* (4), 541–543. https://doi.org/10.1055/s-2001-12346.

(301) Landsberg Markus, D. K. Synthesis of Symmetrical Ureas by (Diacetoxyiodo)Benzene-Induced Hofmann Rearrangement. *Synlett* **2010**, *2010* (7), 1104–1106. https://doi.org/10.1055/s-0029-1219566.

(302) Sans, M.; Illa, O.; Ortuño, R. M. Stereoselective Synthesis of All Stereoisomers of Orthogonally Protected Cyclobutane-1,2-Diamine and Some Chemoselective Transformations. *Org. Lett.* **2012**, *14* (10), 2431–2433. https://doi.org/10.1021/ol300689e.

(303) Torres, E.; Gorrea, E.; Burusco, K. K.; Da Silva, E.; Nolis, P.; Rúa, F.; Boussert, S.; Díez-Pérez, I.; Dannenberg, S.; Izquierdo, S.; Giralt, E.; Jaime, C.; Branchadell, V.; Ortuño, R. M. Folding and Self-Assembling with β-Oligomers Based on (1R,2S)-2-Aminocyclobutane-1-Carboxylic Acid. *Org. Biomol. Chem.* **2010**, *8* (3), 564–575. https://doi.org/10.1039/B918755C.

(304) Sabbioni, G.; Jones, J. B. Enzymes in Organic Synthesis. 39. Preparations of Chiral Cyclic Acid-Esters and Bicyclic Lactones via Stereoselective Pig Liver Esterase Catalyzed Hydrolyses of Cyclic Meso Diesters. *J. Org. Chem.* **1987**, *52* (20), 4565–4570.

(305) Martín-Vilà, M.; Muray, E.; Aguado, G. P.; Alvarez-Larena, A.; Branchadell, V.; Minguillón, C.; Giralt, E.; Ortuño, R. M. Enantioselective Synthetic Approaches to Cyclopropane and Cyclobutane β-Amino Acids: Synthesis and Structural Study of a Conformationally Constrained β-Dipeptide. *Tetrahedron: Asymmetry* **2000**, *11* (17), 3569–3584. https://doi.org/10.1016/S0957-4166(00)00297-4.

(306) Qabaja, G.; Benavides, A. R.; Liu, S.; Petersen, K. S. Asymmetric Synthesis of Hydroxy Esters with Multiple Stereocenters via a Chiral Phosphoric Acid Catalyzed Kinetic Resolution. *J. Org. Chem.* **2015**, *80* (1), 133–140. https://doi.org/10.1021/jo5022019.

(307) Katagiri, N.; Sato, H.; Kaneko, C. Highly Stereoselective Synthesis of Carbocyclic Analogues of Oxetanocin. *Chem. Pharm. Bull. (Tokyo).* **1990**, *38* (1), 288–290. https://doi.org/10.1248/cpb.38.288.

(308) Sabbioni, G.; Shea, M. L.; Jones, J. B. Preparations of Bicyclic Chiral Lactone Synthons via Stereospecific Pig Liver Esterase-Catalysed Hyderolyses of Meso-Diesters. Ring-Size Induced Reversal of Stereospecificity. *Chem. Commun.* **1984**, 236–238. https://doi.org/10.1039/C39840000236.

(309) Archambaud, S.; Legrand, F.; Aphecetche-Julienne, K.; Collet, S.; Guingant, A.; Evain, M. Total Synthesis of (+)-Brefeldin C, (+)-nor-Me Brefeldin A and (+)-4-Epi-nor-Me Brefeldin A. *Eur. J. Org. Chem.* **2010**, *2010* (7), 1364–1380. https://doi.org/10.1002/ejoc.200901233.

(310) Mahajani, N. S.; Meador, R. I. L.; Smith, T. J.; Canarelli, S. E.; Adhikari, A. A.; Shah, J. P.; Russo, C. M.; Wallach, D. R.; Howard, K. T.; Millimaci, A. M.; Chisholm, J. D. Ester Formation via Symbiotic Activation Utilizing Trichloroacetimidate Electrophiles. *J. Org. Chem.* **2019**, *84* (12), 7871–7882. https://doi.org/10.1021/acs.joc.9b00745.

(311) Jnoff, E.; Albrecht, C.; Barker, J. J.; Barker, O.; Beaumont, E.; Bromidge, S.; Brookfield, F.; Brooks, M.; Bubert, C.; Ceska, T.; Corden, V.; Dawson, G.; Duclos, S.; Fryatt, T.; Genicot, C.; Jigorel, E.; Kwong, J.; Maghames, R.; Mushi, I.; Pike, R.; Sands, Z. A.; Smith, M. A.; Stimson, C. C.; Courade, J.-P. Binding Mode and Structure–Activity Relationships around Direct Inhibitors of the Nrf2–Keap1 Complex. *ChemMedChem* **2014**, *9* (4), 699–705. https://doi.org/10.1002/cmdc.201300525.

(312) Demchuk, O. P.; Hryshchuk, O. V; Vashchenko, B. V; Trofymchuk, S. A.; Melnykov, K. P.; Skreminskiy, A.; Volochnyuk, D. M.; Grygorenko, O. O. Fluoroalkyl-Containing 1,2-Disubstituted Cyclobutanes: Advanced Building Blocks for Medicinal Chemistry. *Eur. J. Org. Chem.* **2021**, *2021* (1), 87–95. https://doi.org/10.1002/ejoc.202001345.

(313) Aitken, D. J.; Gauzy, C.; Pereira, E. Studies on the Stability of the Cyclobutane β-Aminoacid Skeleton: A Cautionary Tale. *Tetrahedron Lett.* **2004**, *45* (11), 2359–2361. https://doi.org/10.1016/j.tetlet.2004.01.084.

(314) Roy, O.; Faure, S.; Aitken, D. J. A Solution to the Component Instability Problem in the Preparation of Peptides Containing C2-Substituted Cis-Cyclobutane β-Aminoacids: Synthesis of a Stable Rhodopeptin Analogue. *Tetrahedron Lett.* **2006**, *47* (33), 5981–5984. https://doi.org/10.1016/j.tetlet.2006.06.027.

(315) Gauzy Bertrand; Pereira, Elisabeth; Faure, Sophie; Aitken, David J, C. S. The [2+2] Photocycloaddition of Uracil Derivatives with Ethylene as a General Route to Cis-Cyclobutane β-Amino Acids. *Synlett* **2006**, *2006* (9), 1394–1398. https://doi.org/10.1055/s-2006-941571.

(316) Chang, Z.; Guillot, R.; Boddaert, T.; Aitken, D. J. Stereocontrolled Preparation of Diversely Trifunctionalized Cyclobutanes. *J. Org. Chem.* **2019**, *84* (16), 10518–10525. https://doi.org/10.1021/acs.joc.9b01463.

(317) Gregori, A.; Alibés, R.; Bourdelande, J.; Font, J. Facile and Stereoselective Synthesis of Fused γ-Butyrolactones of Carbohydrates. *Tetrahedron Lett.* **1998**, *39* (38), 6963–6966. https://doi.org/10.1016/S0040-4039(98)01477-4.

(318) Loudon, G. M.; Radhakrishna, A. S.; Almond, M. R.; Blodgett, J. K.; Boutin, R. H. Conversion of Aliphatic Amides into Amines with [I,I-Bis(Trifluoroacetoxy)Iodo]Benzene. 1.

Scope of the Reaction. *J. Org. Chem.* **1984**, *49* (22), 4272–4276. https://doi.org/10.1021/jo00196a031.

(319) Boutin, R. H.; Loudon, G. M. Conversion of Aliphatic Amides into Amines with [I,I-Bis(Trifluoroacetoxy)Iodo]Benzene. 2. Kinetics and Mechanism. *J. Org. Chem.* **1984**, *49* (22), 4277–4284. https://doi.org/10.1021/jo00196a032.

(320) Aubé, J.; Fehl, C.; Liu, R.; McLeod, M. C.; Motiwala, H. F. 6.15 Hofmann, Curtius, Schmidt, Lossen, and Related Reactions. In *Comprehensive Organic Synthesis*; Knochel, P. B. T.-C. O. S. (Second E., Ed.; Elsevier: Amsterdam, 2014; pp 598–635. https://doi.org/10.1016/B978-0-08-097742-3.00623-6.

(321) Lherbet, C.; Morin, M.; Castonguay, R.; Keillor, J. W. Synthesis of Aza and Oxaglutamyl-p-Nitroanilide Derivatives and Their Kinetic Studies with γ-Glutamyltranspeptidase. *Bioorg. Med. Chem. Lett.* **2003**, *13* (6), 997–1000. https://doi.org/10.1016/S0960-894X(03)00083-0.

(322) López-García, M.; Alfonso, I.; Gotor, V. Synthesis of (R)-3,4-Diaminobutanoic Acid by Desymmetrization of Dimethyl 3-(Benzylamino)Glutarate through Enzymatic Ammonolysis. *J. Org. Chem.* **2003**, *68* (2), 648–651. https://doi.org/10.1021/jo026254f.

(323) Somekawa, K.; Hara, R.; Kinnami, K.; Muraoka, F.; Suishu, T.; Shimo, T. Synthesis of a Carbocyclic Oxetanocin Using Photocycloaddition. *Chem. Lett.* **1995**, *24* (6), 407–408. https://doi.org/10.1246/cl.1995.407.

(324) Awada, H.; Robin, S.; Guillot, R.; Yazbeck, O.; Naoufal, D.; Jaber, N.; Hachem, A.; Aitken, D. J. Practical Syntheses of Both Enantiomers of the Conformationally Restricted GABA Analogue Cis-(2-Aminocyclobutyl)Acetic Acid. *Eur. J. Org. Chem.* **2014**, *2014* (32), 7148–7155. https://doi.org/10.1002/ejoc.201402676.

(325) Caddick, S.; Khan, S. Preparation of the A-Ring of Neocarzinostatin and Kedarcidin Chromophores via a Stereocontrolled Base Mediated Isomerisation Reaction. *J. Chem. Soc. Chem. Commun.* **1995**, No. 19, 1971–1972. https://doi.org/10.1039/C39950001971.

(326) Corey, E. J.; Venkateswarlu, A. Protection of Hydroxyl Groups as Tert-Butyldimethylsilyl Derivatives. *J. Am. Chem. Soc.* **1972**, *94* (17), 6190–6191. https://doi.org/10.1021/ja00772a043.

(327) Bartoszewicz, A.; Kalek, M.; Stawinski, J. Iodine-Promoted Silylation of Alcohols with Silyl Chlorides. Synthetic and Mechanistic Studies. *Tetrahedron* **2008**, *64* (37), 8843–8850. https://doi.org/10.1016/j.tet.2008.06.070.

(328) Caddick, S.; Delisser, V. M. Stereoselective Synthesis of a Functionalised Bicyclic Core of Neocarzinostatin and Kedarcidin Chromophores. *Tetrahedron Lett.* **1997**, *38* (13), 2355–2358. https://doi.org/10.1016/S0040-4039(97)00347-X.

(329) Etheridge, Z. C.; Caddick, S. Kinetic Resolution of 4,5-Dihydroxylated Cyclopentenones. *Tetrahedron: Asymmetry* **2004**, *15* (3), 503–507. https://doi.org/10.1016/j.tetasy.2003.11.024.

(330) Lee, S.; Kim, W.-G.; Kim, E.; Ryoo, I.-J.; Lee, H. K.; Kim, J. N.; Jung, S.-H.; Yoo, I.-D. Synthesis and Melanin Biosynthesis Inhibitory Activity of (±)-Terrein Produced by

Penicillium Sp. 20135. *Bioorg. Med. Chem. Lett.* **2005**, *15* (2), 471–473. https://doi.org/10.1016/j.bmcl.2004.10.057.

(331) Naik, S. D.; Chandra, G.; Sahu, P. K.; Kim, H.-R.; Qu, S.; Yoon, J.; Jeong, L. S. Stereo- and Regio-Selective Synthesis of 3′-C-Substituted-(N)-Methanocarba Adenosines as Potential Anticancer Agents. *Org. Chem. Front.* **2016**, *3* (11), 1472–1480. https://doi.org/10.1039/C6QO00358C.

(332) Li, B.; Berliner, M.; Buzon, R.; Chiu, C. K.-F.; Colgan, S. T.; Kaneko, T.; Keene, N.; Kissel, W.; Le, T.; Leeman, K. R.; Marquez, B.; Morris, R.; Newell, L.; Wunderwald, S.; Witt, M.; Weaver, J.; Zhang, Z.; Zhang, Z. Aqueous Phosphoric Acid as a Mild Reagent for Deprotection of Tert-Butyl Carbamates, Esters, and Ethers. *J. Org. Chem.* **2006**, *71* (24), 9045–9050. https://doi.org/10.1021/jo061377b.

(333) Mosey, R. A.; Tepe, J. J. New Synthetic Route to Access (±) Salinosporamide A via an Oxazolone-Mediated Ene-Type Reaction. *Tetrahedron Lett.* **2009**, *50* (3), 295–297. https://doi.org/10.1016/j.tetlet.2008.10.154.

(334) Andrade, V.; Mattos, M. New Reagents and Synthetic Approaches to the Appel Reaction. *Curr. Org. Synth.* **2015**, *12* (3), 309–327. https://doi.org/http://dx.doi.org/10.2174/1570179412666150305231358.

PART II

Cannabidivarin Derivatives as CB_2R Modulators

General introduction

1. *Cannabis sativa*: A Treasure Trove of Bioactive Compounds

Cannabis sativa, a member of the *Cannabaceae* family, is one of its two primary species alongside *Cannabis indica*, and it has been used for centuries for its therapeutic and psychoactive properties. Its application for medicinal purposes is documented in ancient texts dating back to the 2nd century in Asia, the original provenance of this species, and since first classified by Carl Linneaus in 1753, anaesthetic, analgesic, or anti-anorexic effects have been attributed to this plant. These properties are associated with some of its more than 500 secondary metabolites, synthesised by the glandular trichomes in feminine inflorescences as sticky resin. Terpenes, cannabinoids, flavonoids, or alkaloids are some of the multiple bioactive types of compounds found in *Cannabis sativa*. However, **cannabinoids**, also known as phytocannabinoids, are the ones that have drawn more attention. There are more than 100 of these chemical compounds, **tetrahydrocannabinol (THC)** being one of the most known, especially due to its psychoactive effects. Alongside it, and with less recreational purposes, **cannabidiol (CBD)** has also gained interest due to its potential therapeutic effects without causing any mind-altering impact (**Figure II-1**).[1]

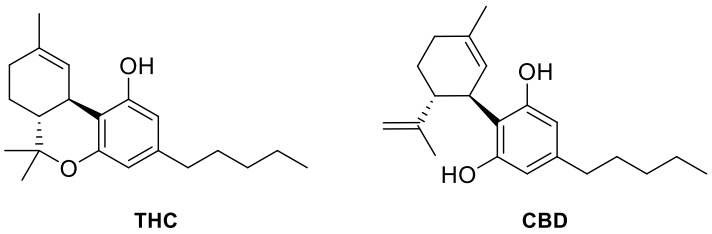

THC **CBD**

Figure II-1. Molecular structures of the two primary cannabinoids in *Cannabis sativa*.

In the early 19th century, the first attempts were made to isolate these compounds from the plant, but it was not until 1940 that CBD was successfully isolated by Adams *et al*.,[2] and later synthesised by Petrizlka *et al*.[3] in 1967. Conversely, the structure and stereochemistry of THC, the most abundant cannabinoid in the plant, were first elucidated and synthesised by Gaoni and Mechoulam in 1964.[4] The isolation of these compounds by these researchers sparked a surge of in-depth research into cannabinoids, shaping the scientific field as we know it today.

Initial studies about their structure-activity relationship were carried out in 1975, employing THC-derived small molecules, aiming to enhance affinity and selectivity for the cannabinoid receptors. In recent years, CBD, the second most abundant metabolite in *Cannabis*, has been the subject of numerous clinical trials. These studies have provided compelling evidence that CBD can protect neural cells from oxidative stress and reduce neuroinflammation, which has raised its interest as a potential active drug to treat neurological disorders such as Alzheimer's or Parkinson's diseases.[5]

2. Endocannabinoid System (ECS)

Despite the early description of cannabinoid molecular structures, the underlying molecular mechanism of the cannabinoid activity remained unresolved for decades. Initial observations attributed cannabinoids activity to their high lipophilicity,[6] without associating it with any specific receptor interaction. However, by the mid-1980's, several studies indicated that cannabinoids action was highly dependent on the stereospecificity of the compounds, suggesting interaction with an asymmetric site, such as a receptor.[7] These results prompted the research for a specific system for these compounds. Finally, during the decade of the 1990s, the endocannabinoid system (ECS) was discovered,[8] determining two G-protein-coupled receptors (GPCRs), named cannabinoid receptors 1 and 2 (**CB_1R** and **CB_2R**),[9,10] and different **endocannabinoids** as responsible for the endogenous activation of this system.

2.1. GPCRs: Cannabinoid Receptors (CBxR)

GPCRs represent one of the largest and most versatile families of cell surface receptors, playing a crucial role in human cellular function. Consequently, up to 40% of all marketed drugs target GPCRs.[11] These receptors are characterised by a transmembrane domain with seven alpha-helices, which span the cell membrane and form a binding pocket for ligands. This domain is coupled to a G protein, which is divided into three subunits: Gα, Gβ, and Gγ (**Figure II-2**). Upon ligand binding to the transmembrane domain, a conformational change in the G protein subunits catalyses downstream functions by coupling to another cellular protein (*e.g.*, adenylyl cyclase, protein kinase,…), and propagating the signalling within the cell.[12]

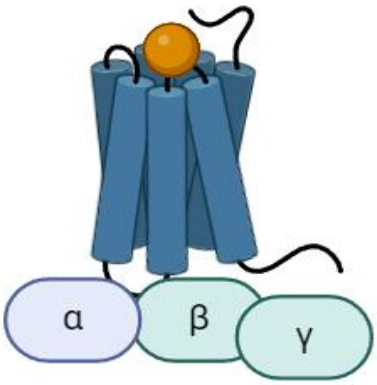

Figure II-2. Representation of a GPCR bound to a ligand and a G protein. Imaged created with Biorender.com

Of the five superfamilies into which the GPCRs are divided, cannabinoid receptors belong to the rhodopsin-like family. The first evidence for this classification was provided by Howlett *et al.*,[13] who observed that certain cannabinoids decreased cyclic adenosine monophosphate (cAMP) concentrations in cells. Further research demonstrated that when cells were exposed to a Gi protein inhibitor, a decrease in the levels of cAMP was not observed, strongly suggesting the presence of a GPCR-like receptor.[14] It was eventually confirmed that both CB_1R and CB_2R are coupled to G proteins, and they share more than 40% of their sequence. However, it has been observed that biological response in CB_1 receptors is mediated by different subfamilies of G proteins (Gi, Gs, and Go), whereas response in CB_2 receptors is associated with just one type of G protein (Gi).[15,16]

These differences extend beyond their signalling mechanisms to their locations in the human body. CB_1R is widely expressed throughout the body, but especially in the central nervous system (CNS).[10] Conversely, CB_2R was initially thought to be restricted to the immune system, being described as the peripheral CB receptor. However, more in-depth research also demonstrated its presence in brain tissue.[17–19] This discovery led to study its implication in neurodegenerative

diseases like Huntington's and Alzheimer's disorders,[20] opening a new window for their early diagnosis.[21] However, despite extensive research on these receptors, their biological functions have not yet been fully elucidated, and recent investigations suggest the presence of a third cannabinoid receptor in mammals,[22] indicating that there is a still a long way to go to fully comprehend this system.

As previously mentioned, the activation of these receptors initiates a series of downstream signalling cascades that **decrease the intracellular levels of cAMP** due to the inhibition of the adenylyl cyclase (AC), modulating the intracellular levels of Ca^{2+} and K^+ ions, and intervening different neuroreceptors like acetylcholine, dopamine, or glutamate. Additionally, other signalling pathways are associated with the activation of cannabinoid receptors, such as the **mitogen-activated protein kinase (MAPK) pathway**, which is involved in gene expression, transcription regulation, and cell differentiation (**Figure II-3**).[23]

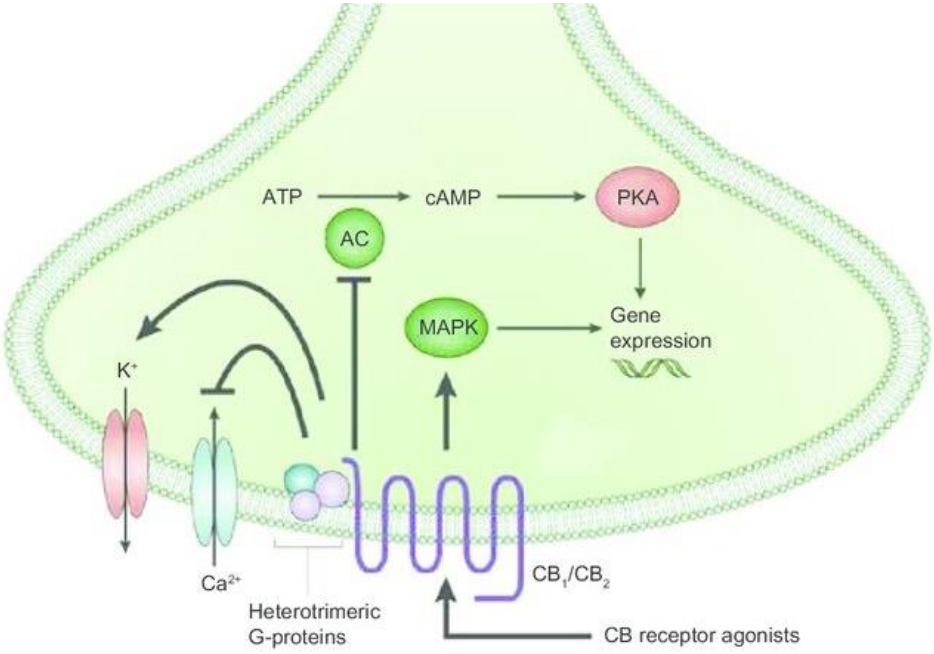

Figure II-3. Cannabinoid receptor signalling. ATP: Adenosine triphosphate, PKA: Protein kinase A.[23]

Moreover, **β-arrestin signalling pathway** also plays an important role in the regulation of GPCRs. Prolonged or repeated activation of the receptor can lead to desensitization, a mechanism that reduces receptor responsiveness. To avoid this, β-arrestins bind to the phosphorylated receptor, preventing further coupling of the receptor to G proteins. This interrupts or dampens the primary signalling pathway, thereby limiting excessive or prolonged signalling. Once β-arrestin binds to the receptor, it facilitates the recruitment of proteins involved in clathrin-mediated endocytosis, leading to receptor internalisation into the cell within vesicles to either be recycled back to the cell surface (resensitisation) or be degraded (downregulation) (**Figure II-4**).[24] But for the activation of the ECS, an agonist ligand is required, which can be either endogenous (**endocannabinoids**) or exogenous (**phytocannabinoids** or **synthetic cannabinoids**).

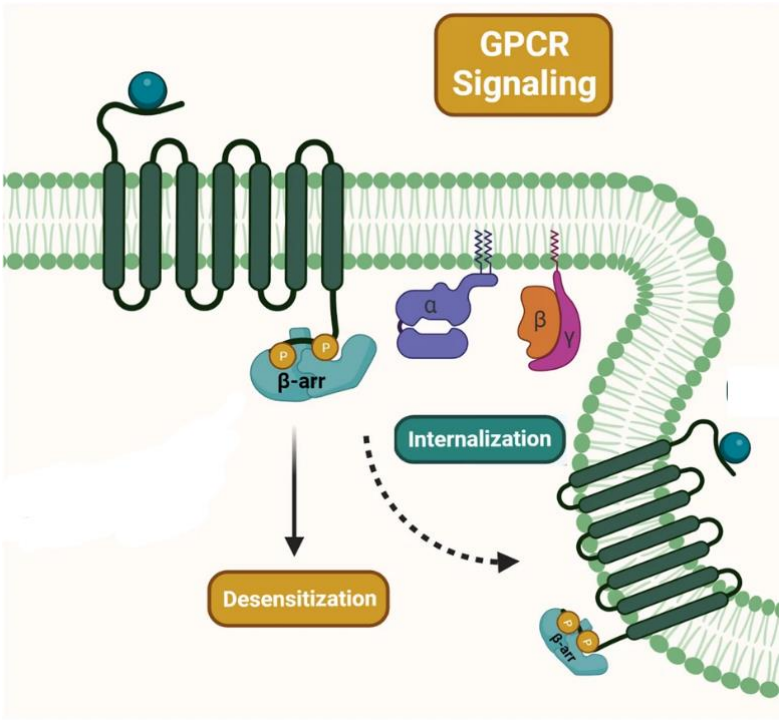

Figure II-4. Regulation functions of the β-arrestin signalling pathway. Image adapted from *Exp. Mol. Med.* **2024**, *56*, 129–141.

2.2. Endocannabinoids

In the mid-1900s, the interaction between *Cannabis* metabolites and the human body remained a mystery. Neuroscientists found that interaction of those metabolites within the human body was a hint of the presence of endogenous compounds that were able to interact equally, suggesting the involvement of an as-yet-undiscovered ligand. However, it was not until 1992 that a polyunsaturated fatty acid derivative, involved in the activation of the ECS, was isolated and its structure was elucidated as the arachidonoylethanolamide (AEA), also known as **anandamide**.[25] This compound exhibited similar effects to THC when tested in animals, producing analgesia, hypothermia, appetite stimulation, and changes in motor coordination. Its body distribution was also found to be similar to that of CB_1R.[26] From this point onwards, other endocannabinoids with structures closely related to anandamide were isolated from porcine brain samples,[27] including **2-arachidonoylglycerol (2-AG)**, *O*-arachidonoyl ethanolamine, also known as **virodhamine**, and **2-arachidonyl glyceryl ether (2-AGE) (Figure II-5**).[23]

Since their discovery, endocannabinoids have been subject of multiple studies, being possible to elucidate their interaction with the ECS. Derived from their precursor in the cellular lipid bilayer, the **arachidonic acid (AA) (Figure II-5**), endocannabinoids are synthesised and released upon demand, typically in response to GPCR activation, into the extracellular space. This “synthesis on-demand” mechanism contrasts with many other neuromodulators, which are synthesised and stored in synaptic vesicles.[28]

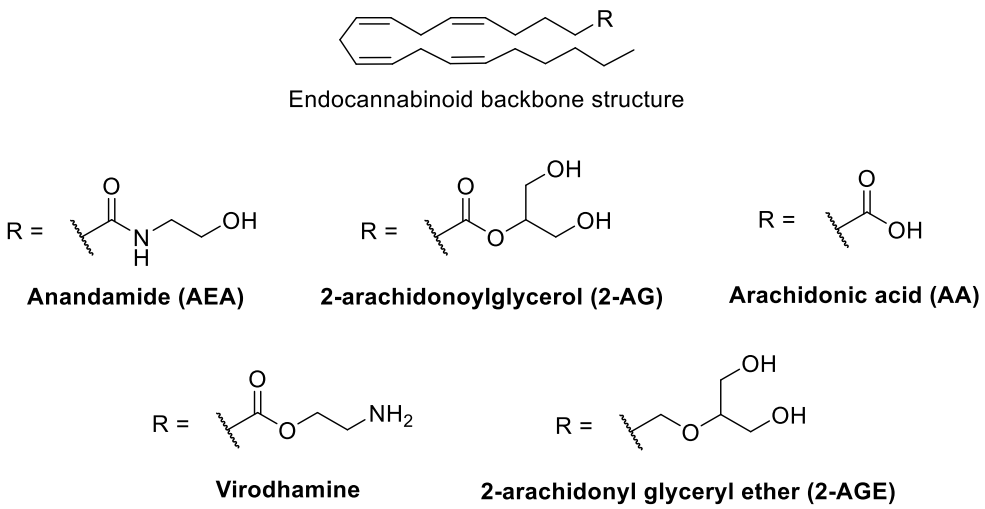

Figure II-5. Structure of major endocannabinoids.

Endocannabinoids possess diverse properties, mainly due to their uneven affinity for CB_1R and CB_2R. AEA behaves as a partial agonist of the CB_1R, while it has minimal binding to CB_2R. In contrast, 2-AG behaves as a full agonist with equal affinity for both receptors. Notably, 2-AG demonstrated significant signalling in the brain, surpassing that of anandamide, and was linked to neuroprotective effects, cell proliferation, and other significant biological processes.[29,30] This endocannabinoid also provided evidence of what is called the "entourage" effect,[7] where the activity of the endocannabinoid resulted in much higher when it was administered with other fatty acid esters of glycerol than when it was administered alone, mimicking the conditions found in the body.

2.3. Phytocannabinoids

Similarly to endocannabinoids, phytocannabinoids are able to engage with the endocannabinoid system. They are predominantly, but not exclusively, of the *Cannabis* species, and their proportions vary among different species. Phytocannabinoids are defined by a terpenophenolic structure featuring a pentyl side chain. Their biosynthetic pathway, depicted in **Figure II-6**, starts with the combination of hexanoyl-CoA and malonyl-CoA to form olivetolic acid. This intermediate is alkylated with geranyl pyrophosphate (GPP) to obtain the cannabiogerolic acid (CBGA), the precursor from which other phytocannabinoids are derived.

Primary cannabinoids, Δ^9-tetrahydrocannabinolic acid (Δ^9-THCA), cannabidiolic acid (CBDA) and cannabichromenic acid (CBCA), are synthesised through enzymatic reactions. Subsequent decarboxylation of these acids yields: tetrahydrocannabidiol (Δ^9-THC or THC), cannabidiol (CBD) and cannabichromene (CBC), respectively.[31] In addition, other phytocannabinoids such as cannabigerol (CBG), cannabinol (CBN), or cannabidivarin (CBDV), obtained through similar biosynthetic pathways, can be found in *Cannabis* species.

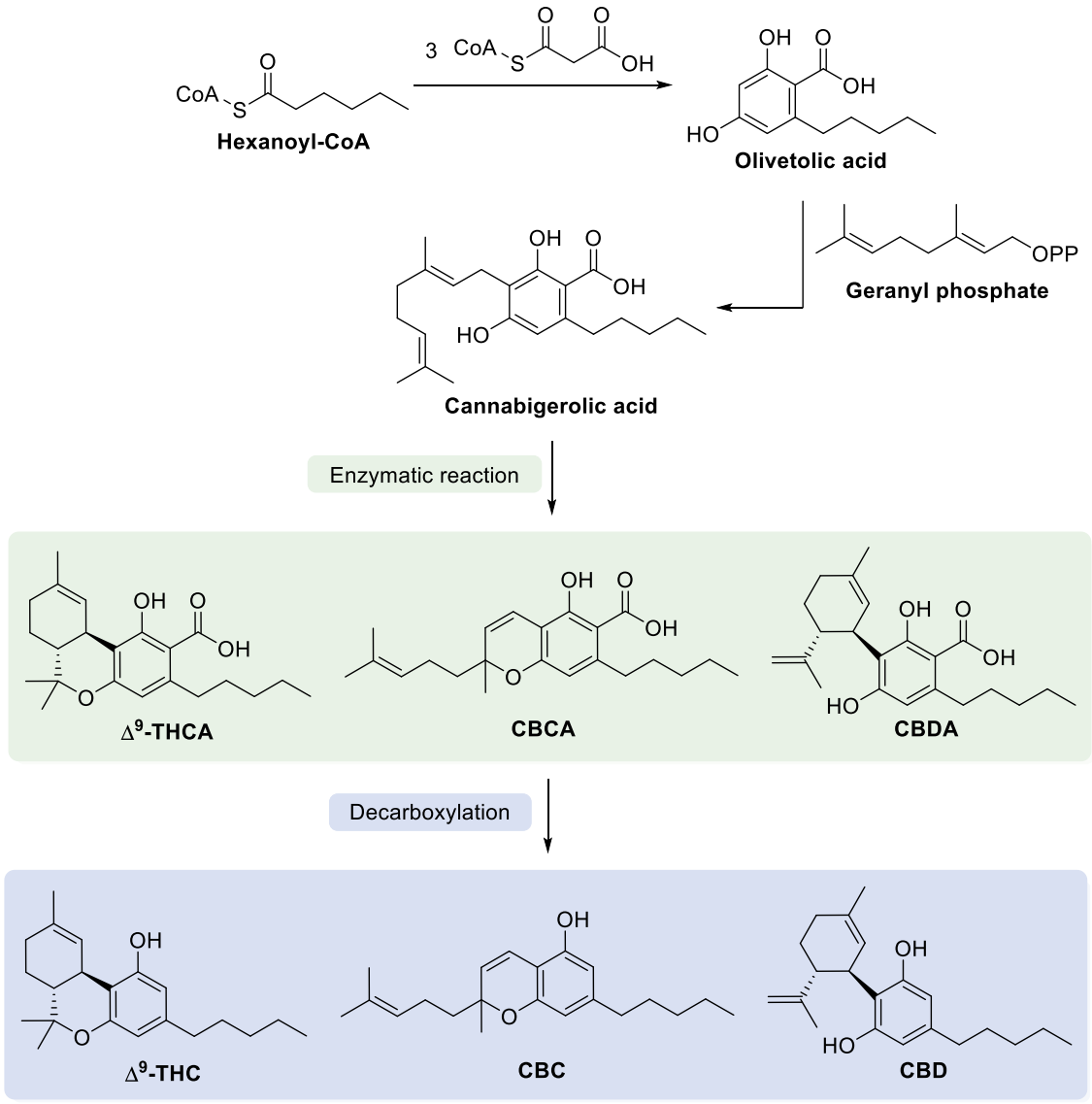

Figure II-6. Biosynthetic pathway for the obtention of different phytocannabinoids.

Phytocannabinoids bind to CB_1R and CB_2R, mimicking endocannabinoids, and can also interact with other receptors in the ECS, such as G-protein-coupled receptor 55 (GPR55), transient receptor potential cation channel subfamily V members 1 and 2 (TRPV1 and TRPV2), or peroxisome proliferator-activated receptors (PPARs). These interactions occur with different grades of affinity and roles at the receptors. One of the major phytocannabinoids, THC, is a partial agonist for both receptors, but it is commonly more related to CB_1R. It has been linked to anticarcinogen and neuroprotective properties, but also with undesired psychoactive effects, from the pharmacological point of view. On the other hand, CBD, the second most abundant phytocannabinoid in *Cannabis*, is an antagonist of CB_1R and a partial agonist of CB_2R,[32] exhibiting anxiolytic, analgesic, antiepileptic, and inflammatory properties, at the same time that psychotropic effects are avoided. These differences in the interaction with the ECS have been exploited to study different pharmacological effects that can be interesting for therapeutic purposes.

3. Therapeutic Potential of Cannabinoids

Since the mid-sixties of the 20th century, the regulation of *Cannabis* has been a controversial topic, that has been managed differently in every country. Its possible beneficial effects for medical purposes have always been weighed against its recreational use. The implementation of comprehensive medicinal *Cannabis* programmes in different countries has facilitated the introduction of cannabinoid-based drugs into the market; however, each country enforces its own legislation. In Spain, as in other European countries, CBD has not been registered on the "authorised list of supplements" of the Spanish Drug Regulatory Agency (AEMPS), meaning it cannot be commercialised for human consumption. Nonetheless, it is not classified as an illegal substance, so it can be sold for cosmetic or collectable use. This has created a legal loophole to be used for unauthorised purposes, generating further controversy.

Despite this limitation in terms of regulation, which holds back its synthesis and production, cannabinoids pharmacology has been the objective of thousands of publications over the past 40 years, leading to the approval of several cannabinoid-based drugs.

3.1. Role of the Ligand

Cannabinoids, whether endogenous or exogenous, can behave differently with every receptor and, depending on the ligand interaction, they can be classified in different ways (**Figure II-7**). This behaviour relies on how well the ligand is capable of distinguishing between the active and inactive form of the receptor.

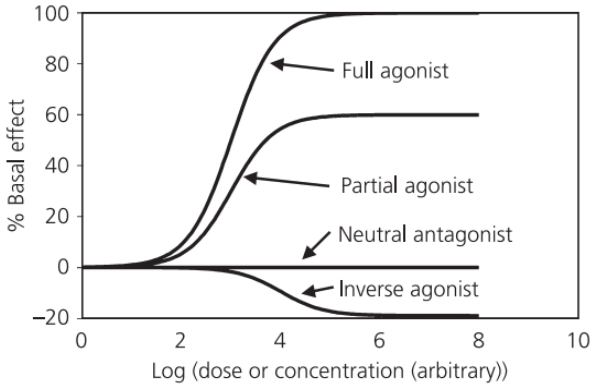

Figure II-7. Possible responses to various receptor ligands. Imaged extracted from *J. Neuroendrocinol*. **2008**, *20*, 10-14.

- **Agonist:** It stimulates the receptor to create the maximum response by causing a conformational change to the active form.
- **Partial agonist:** It is not as capable as the full agonist to distinguish between the two conformations of the receptor. In this situation, even when all the receptors are occupied by the ligand, only a fraction will be in the active conformation, producing the signalling. Depending on the density of receptors, this has implications in the response observed. If there is an excess of receptors, the response will be equal to the agonist, even if not all of them are active. However, if the receptors are limited, the biological response of the partial agonist will be lower than with the full agonist (represented in **Figure II-7**).
- **Neutral antagonist:** Despite it is able to bind to the receptor, no response is created. It does not produce any physiological response but rather blocks the response to endogenous or exogenous agonists or inverse agonists.
- **Inverse agonist:** The response to the binding of the ligand is the opposite to the one created by the agonist. This can be explained in a situation when there is a basal level of response, due

to the presence of active receptors, even in the absence of the agonist. In this case, an inverse agonist will bind preferentially to the inactive form, supressing the basal signalling.

3.2. CB_1R-Targeted Pharmacology

The fact that CB_1R was initially recognised as the sole receptor of the ECS, relegating CB_2R to a status of "peripheral receptor", focused the research on cannabinoids that specifically activated CB_1R. This led to the approval of a THC-based drug in 1985 by the US Food and Drug Administration (FDA), named as dronabinol (Marinol®), an antiemetic drug to treat chemotherapy-induced nausea and vomiting, and loss of appetite in HIV patients.[33] In the same year, nabilone (Cesamet®), a structurally related compound, was approved for similar therapeutic purposes. Years later, a 1:1 mixture of CBD and THC, named nabiximol (Sativex®), was approved in 2005 in Canada and in UK and Spain in 2010, for the treatment of symptoms of multiple sclerosis.[34]

Research has not only focused on CB_1R agonists but also on antagonists due to their potential applications in treating obesity disorders,[35] mental illness,[36] or nicotine addiction.[37] One of the first CB_1R-selective antagonists, rimonabant (Acomplia®),[38] was approved by the European Medicines Agency (EMA) in 2006 for obesity treatment. However, it was withdrawn in 2008 because of safety concerns, as it showed several adverse effects, such as anxiety, depression, and suicidal ideation.[39] This underscored the need for CB_1R antagonists that do not cross the blood-brain barrier to avoid these undesired secondary effects.

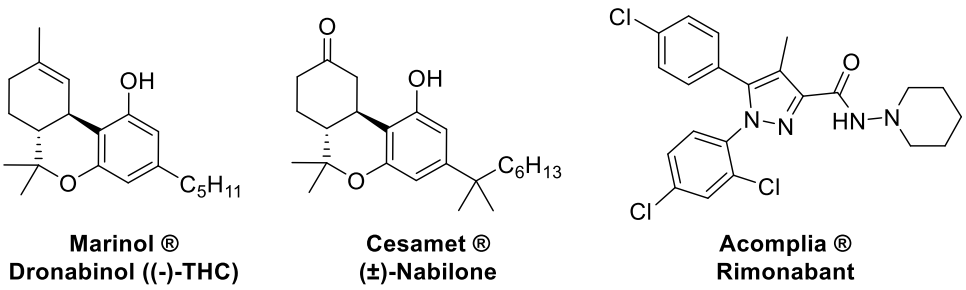

Marinol ®
Dronabinol ((-)-THC)

Cesamet ®
(±)-Nabilone

Acomplia ®
Rimonabant

Figure II-8. Commercial drugs targeting CB_1R.

3.3. CB_2R-Targeted Pharmacology

The fact that CB_2R was finally recognised as an important receptor of the ECS expanded the possibilities of treating medical disorders using this target. Significant attention is currently directed to compounds that can activate CB_2R at doses that induce little or no CB_1R activation. This has been triggered by the evidence that many of the adverse effects induced by mixed CB_1/CB_2 receptor agonists result from CB_1 rather than CB_2 receptor activation. CBD, partial agonist of CB_2R, has garnered interest in the last two decades, leading to the development of active drugs based on its structure due to its safer profile as a non-psychotropic and non-addictive substance compared to THC.[40] In 2018, cannabidiol (Epidolex®) was approved by the FDA, and later in 2019 by the EMA, as a drug to treat refractory epilepsy and patients with Dravet syndrome or Lennox-Gastaut syndrome.[41] In addition, CBD has been proven effective as a therapeutic target for immunomodulation, neuropathic pain, and neuroinflammation.[42,43]

Recently, CB_2R antagonists have also been studied, with early indications to ameliorate renal fibrosis[44] and delay tumour progression.[45] Furthermore, some CBD-based structures are currently undergoing clinical trials. HU-474, a fluorinated cannabidiol derivative, was synthesised with the objective of increasing the oral bioavailability of CBD, and it has been demonstrated to be effective for pain relief in early studies, mimicking CBD by inhibiting the fatty acid amide hydrolase enzyme.[46] Also, KLS-13019, which features a modified alkyl chain to enhance the solubility and permeability of CBD, has shown positive results for the relief of neuropathic pain derived from chemotherapy.[47]

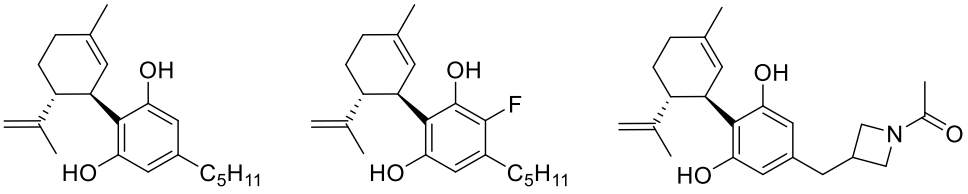

Epidolex ®
Cannabidiol ((-)-CBD)

HU-474

KLS-13019

Figure II-9. Commercial drugs and clinical trials candidates targeting CB_2R.

4. Synthetic Precedents of Cannabidiol (CBD)

Although the isolation and purification of phytocannabinoids from *Cannabis* have been extensively studied,[48–50] regulation and policies prohibiting its growth limit large-scale production. Thus, chemical synthesis has become an important alternative to obtain these active compounds. The development of new synthetic routes for the obtention of **(-)-CBD**, which can serve as a starting point for the synthesis of cannabidiol-based drugs,[51] has been ongoing for the last 60 years.

In 1965, Mechoulam and Gaomi[52] developed a bioinspired synthetic route, starting from the lithium derivative of the protected dimethyl ether of olivetol analogue **146** and **geranial** (**147**), to be the first research group to afford **(±)-CBD** with an overall yield of 2% (**Scheme II-1**, **top left**). However, this synthesis employed commercial racemic products and simple precursors, resulting in a mixture of enantiomers. In 1969, Petrizlka *et al*.[53] performed the first stereoselective synthesis of **(-)-CBD** by doing a Friedel-Crafts alkylation on **olivetol** (**148**) using **(1*S*,4*R*)-149** in the presence of oxalic acid. Unfortunately, abnormal CBD (**abn-CBD**), a regioisomer of CBD, was the main product being obtained in 34% yield, while **(-)-CBD** was obtained in 24% yield, along with 5% yield of both a dialkylated side product and (-)-Δ^9-tetrahydrocannabidiol. Years later, Mechoulam and Baek[54] used the same reagents, but this time they employed $BF_3{\cdot}Et_2O$ on alumina, instead of oxalic acid, obtaining **(-)-CBD** in 55% yield, and reducing the amount of **abn-CBD** down to 14% yield (**Scheme II-1**, **top right**). Since this first successful synthesis, many researchers have focused on achieving better selectivity in obtaining **(-)-CBD**.

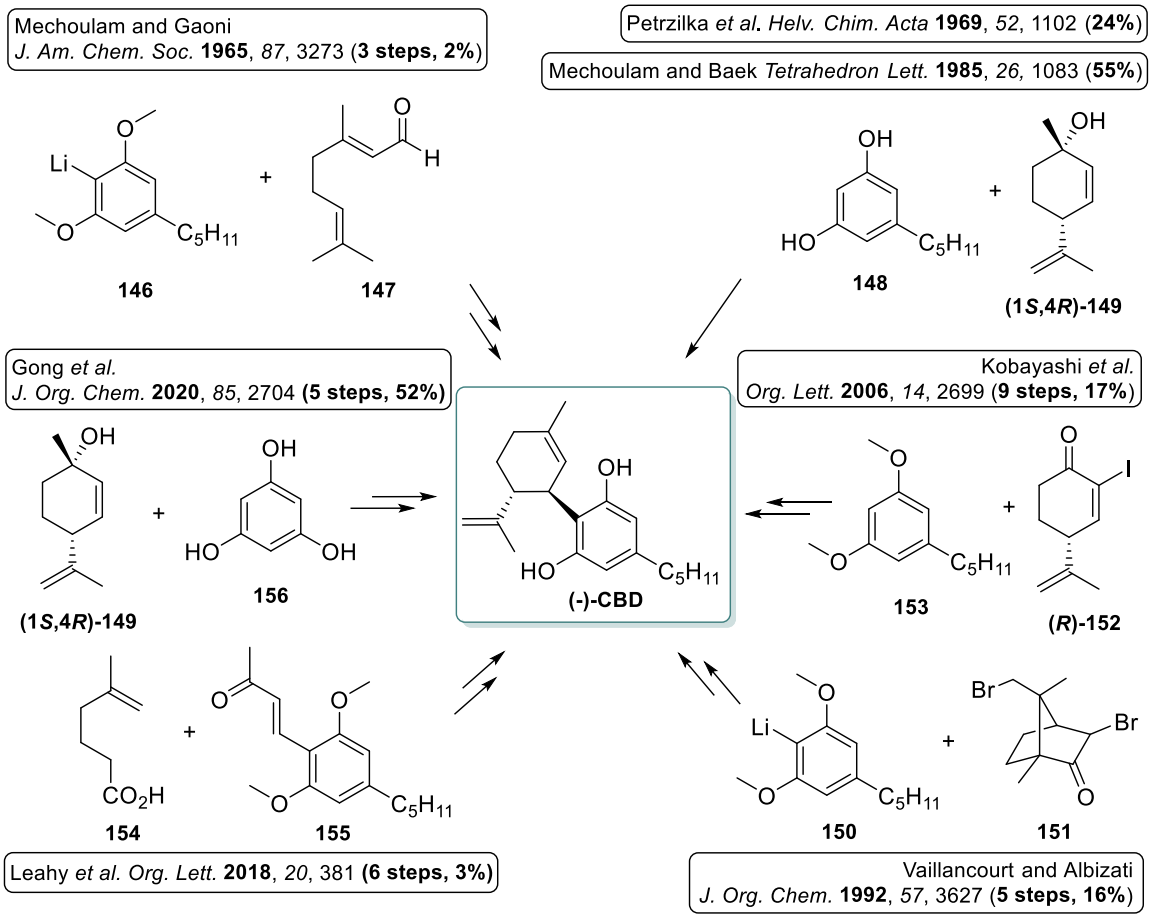

Scheme II-1. Synthetic approaches for the synthesis of **(-)-CBD**.

Common strategies in the literature to obtain **(-)-CBD** include generating stereogenic centres on the terpenoid fragment through asymmetric synthesis and modifying the olivetol fragment to reduce regioselectivity issues.

As an example of asymmetric synthesis, Vaillancourt and Albizati[55] employed the reaction of an aryllithiate (**150**) with 3,9-dibromocamphor (**151**) in presence of copper(I) iodide to obtain **(-)-CBD** in a chemo-, regio-, and stereoselective process. However, the additional steps required for the cleavage of bromide camphor derivatives, along with the corresponding purification of the intermediates, provided a low overall yield of 16% (**Scheme II-1**, **bottom right**). In 2006, Kobayashi *et al*.[56] proposed a route where they synthesised compound **(*R*)-152**, starting from 2-cyclohexene-1,4-diol, in which the key step was a nickel-catalysed allylation, to finally obtain **(-)-CBD** with an overall yield of 19% (**Scheme II-1**, **centre right**). Then, in 2018, Leahy *et al*.[57] obtained **(-)-CBD** in 3% yield, after synthesising the terpenoid fragment through an Ireland-Claisen rearrangement reaction (**Scheme II-1**, **bottom left**).

More recently, Gong *et al*.[58] published an efficient five-step linear strategy using **(1*S*,4*R*)-149** and **phloroglucinol** (**156**) as starting materials, avoiding the regioselectivity issues of the Friedel-Crafts alkylation. Then, they constructed the side chain, not only allowing them to obtain **(-)-CBD** in 52% yield but also obtaining a great number of CBDV derivatives by modifying the side chain (**Scheme II-1**, **centre left**).

A few examples of synthetic approaches to obtain **(-)-CBD** have been exposed in this section. These strategies can also be applied to obtain its derivatives, as some of these research groups have also demonstrated. However, until this point, none of these methodologies have yet enabled industrial-scale production of this phytocannabinoid. To achieve this goal, several pharmaceutical companies, such as AMRI, BioVectra, Matthey, or Noramco, among others, are working on developing industrially adapted synthesis to establish a profitable synthetic route for **(-)-CBD**.[59]

5. Allosteric Modulators on GPCRs

Therapeutic targets and strategies have evolved in parallel with the unveiling of endocannabinoid system mechanisms and receptor interactions by researchers. As outlined before, binding to CB_2R promotes therapeutic effects while reducing undesired side effects linked to CB_1R activation. However, developing molecules that bind specifically to CB_2R is challenging due to the similarity in the sequence structure of the active forms of CB_2R and CB_1R.[60]

Alternatively, targeting peripheral receptors with active compounds that do not cross the blood-brain barrier helps to avoid psychoactive effects, but it also limits the therapeutic effects of the ligands. Furthermore, relying on the role of the ligand as an agonist or antagonist has often failed to meet drug safety guidelines.[61,62] Such considerations have spurred the design of ligands known as **allosteric modulators**, which can dock with an alternative binding pocket on cannabinoid receptors and modulate the response in a different way.

It is acknowledged that numerous GPCRs, like the endocannabinoid receptors, contain distinct binding sites for the endogenous or synthetic ligands to engage, which are named **orthosteric** and **allosteric binding sites**.[63,64] The orthosteric binding pocket, also referred to as the “agonist-binding site”, is considered the primary binding site that elicits a direct response upon docking with an agonist ligand. Conversely, the allosteric binding pocket allows modulators to provide an indirect response by binding to a spatially distinct site, which is conformationally linked to the orthosteric cavity. This induces conformational changes that affects the affinity and/or efficacy of the orthosteric ligand, thereby fine-tuning the actions of the endogenous or synthetic ligands.[65]

The conformational changes produced by allosteric modulators can either enhance or inhibit the response generated by the orthosteric ligand, classifying the modulator as a **positive allosteric modulator (PAM)** or a **negative allosteric modulator (NAM)**, respectively (**Figure II-10**). An orthosteric agonist (OA) binds to the orthosteric site of a GPCR inducing a conformation change in the receptor that activates an intracellular signalling cascade. In the presence of an OA, the binding of a PAM to the allosteric site induces additional conformational changes in the receptor, leading to enhanced signalling. This enhancement can manifest as increased potency (lower concentration of OA needed for activation), affinity (stronger binding of the OA to the receptor), and/or efficacy (greater maximal response). PAMs amplify the effects of the OA without directly activating the receptor themselves.

In contrast, NAMs exert the opposite effect by binding to the same allosteric site on the GPCR and reducing the receptor's response to the orthosteric agonist (OA). This inhibition can occur through decreased affinity and/or efficacy of the OA, ultimately leading to diminished receptor signalling. Both PAMs and NAMs offer advantages over orthosteric ligands due to their allosteric site selectivity, which allows for fine-tuning of receptor activity, reduced off-target effects, and the potential to maintain physiological signalling dynamics without full receptor activation or inhibition.

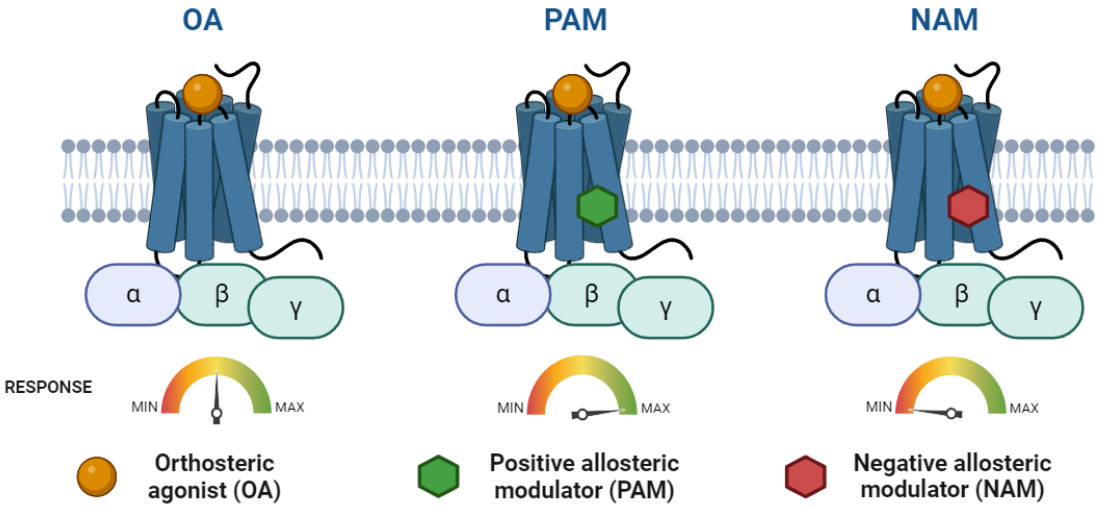

Figure II-10. Representation of the effects of GPCR allosteric modulators on the orthosteric ligand response. Image created with Biorender.com

But upon activation of the receptor, multiple signalling pathways can be activated, each affected differently by the orthosteric or the allosteric ligands, a phenomenon called **biased signalling**. As shown in **Figure II-3** (*vide supra*), the primary response of CB_2R is the decrease of intracellular cAMP levels, due to the inhibition of adenyl cyclase (AC) *via* $G\alpha_i$ protein. However, cannabinoid receptor activation also mediates other pathways, such as the β-arrestin pathway which is involved in the recycling process of the receptors and it can induce other intracellular responses. Each signalling pathway has distinct metabolites, allowing for individual measurement of the activity in each pathway. Typically, all pathways are activated equally, producing similar metabolite changes (**Figure II-11**, **reference ligand**). However, biased signalling in differential metabolite changes (**Figure II-11**, **ligands A-D**), where a ligand can be an agonist for one pathway downstream of the receptor and, at the same time, an inverse agonist for another.[66] Biased ligands are therapeutically valuable, as they can selectively modulate a response through a determined pathway, enhancing beneficial effects while minimizing the side effects.

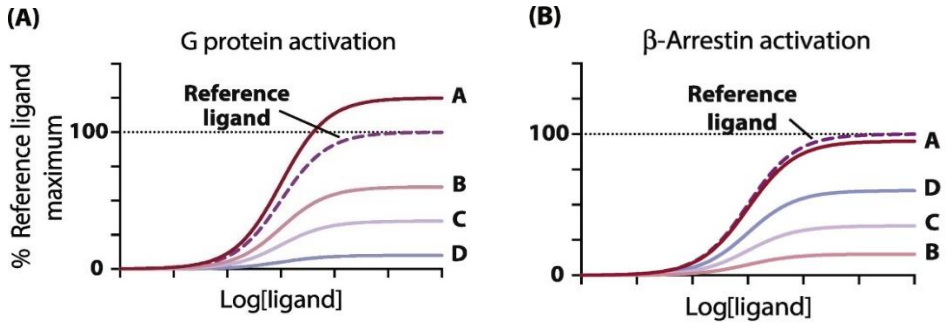

Figure II-11. Representation of the response in different signalling pathways induced by biased ligands.

The main advantage of allosterism over the direct receptor binding is that allosteric modulation only occurs in the presence of an endogenous agonist and does not compete with ligands bound to the orthosteric site. This strategy is particularly useful in pathologies where endocannabinoids levels can vary significantly "on demand", so the effect of the allosteric modulator is in consonancy with these fluctuations, thereby autoregulating the therapeutic outcome and minimising the side effects. Moreover, the allosteric site of a receptor is generally less conserved when compared to the orthosteric one. Hence, allosteric ligands can be more selective than orthosteric ligands.[67] In addition, since the effect depends on the endogenous ligands, the allosteric ligand can reach concentrations beyond saturation without increasing the magnitude of the allosteric effect, avoiding the risk of overdose (ceiling effect).[68] These advantages make allosteric modulation a promising strategy for developing safer and more effective cannabinoid-based therapies.

5.1. Interaction of CBD Analogues with CB_2R Allosteric Site

The role of CBD* in the ECS has been heavily discussed in research. It is generally accepted that CBD behaves as a partial agonist of CB_2R,[69] but its role in CB_1R remains undetermined, with some researchers suggesting it behaves as an antagonist,[32] while others have declared that it is a low-affinity agonist.[70] Regarding CBD's allosteric properties within the ECS, in 2015 it was found to be a NAM at CB_1R, linked to its antidepressant, antipsychotic, and antiepileptic effects.[71] In 2017, it was confirmed that CBD also acts as a NAM at CB_2R, as evidenced by its influence on cAMP levels upon binding to the agonist **JWH-133**.[69] Despite these studies on the interaction with the allosteric binding site of CB_2R,[69,72,73] there was still a lack of information about the allosteric binding site necessary to design potent CB_2R allosteric ligands.

In 2021, the group of Prof. Leonardo Pardo from the Universitat Autònoma de Barcelona, collaborators of our research group, conducted molecular dynamics (MD) simulations to study the interaction of CBD with the allosteric cavity of CB_2R. First MD studies were performed on the complex of the orthosteric agonist **JWH-133** with CB_2R, drawing from observations on the binding pathway of the antagonist AM6538 with CB_1R. In the CB_2R, AM6538 interacted not only with the orthosteric site, but also with a "lateral cavity", adjacent to the CB_2R agonist **JWH-133**'s binding site. By combining these MD simulations with ligand docking studies of CBD on this "lateral cavity" of the CB_2R crystal structure, a model for CBD engagement was proposed (**Figure II-12**, **left**). With this model, key residues for CBD interaction in this binding pocket were identified, and it was finally confirmed, through site-directed mutagenesis studies, that this "lateral cavity" of interaction for the CBD was in fact the allosteric binding site.[74]

Another observation during these studies was that the pentyl side chain of CBD interacts with an intracellular hydrophobic cavity, where the residue Phe3.36 (Phe = Phenylalanine) is found. This residue, along with Trp6.48 (Trp = Tryptophan), had been described to be involved in the initial activation of CB_1R[75,76], CB_2R[77] and other GPCRs[78] (**Figure II-12**, **right**). Thus, it was hypothesised

*From now on, whenever CBD is mentioned, it specifically refers to the (-)-CBD isomer.

that the interaction of the pentyl side chain of the CBD with the allosteric binding pocket near these residues modulates receptor activity.

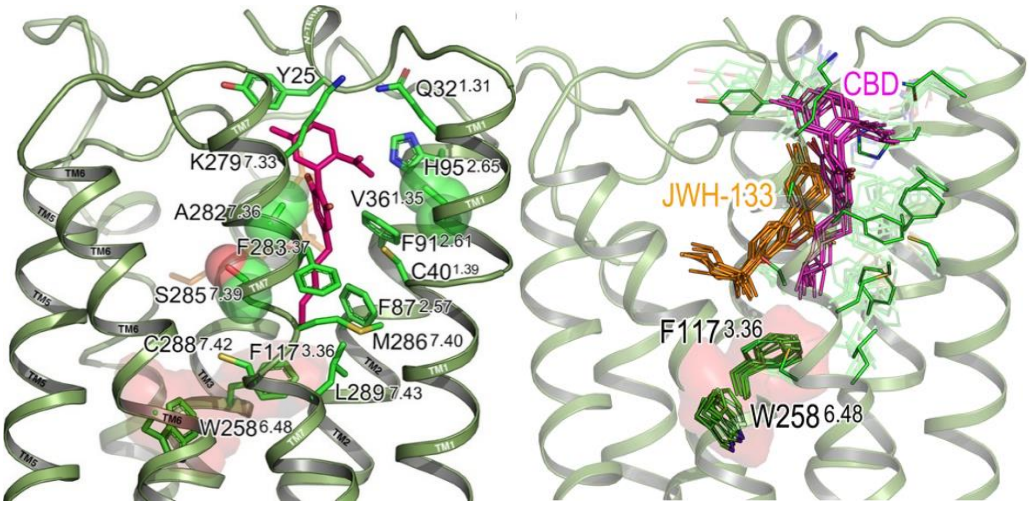

Figure II-12. Left: Detailed view of the docking model of CBD (magenta sticks) into the allosteric binding site. On this computational model, the isopropenylmethylcyclohexene moiety of the CBD of the CBD points towards the entry of the channel and the pentyl side chain towards the intracellular zone. In more detail, the isopropenyl moiety it is allocated between the Val36$^{1.35}$ (Val = Valine) and Ala282$^{7.36}$ (Ala = Alanine) residues; Right: Detailed view of the MD simulations on the complex of CBD (magenta) and **JWH-133** (orange) in the CB_2R to study the interactions with residues Phe117$^{3.36}$ (F = Phenylalanine) Trp258$^{6.48}$ (W = Tryptophan) (red transparent surfaces). Images extracted from reference 74.

To confirm this hypothesis, Dr. Adrià Sánchez, a former researcher in our group, synthesised different CBD analogues (**Figure II-13**).[79] These structure-guided design analogues presented different lengths in the pending alkyl chain of the aromatic ring. Their interaction with the CB_2R was studied by measuring the variation of cAMP levels, an important signal transmitter. The basal intracellular levels of cAMP, in the absence of the agonist **JWH-133**, were normalised to 100%. Then, upon binding of the agonist, the levels start to decrease as a response (**Figure II-13**, **green line**). This response was compared to the one generated when both the agonist and the CBD analogues were interacting with the receptor to determine the modulating effects. It was found that analogues with shorter side chains (**Figure II-13**, **n = 1** (ethyl) **or 2** (propyl)), behave as PAMs, modulating the response by enhancing the effect of the agonist, which translates into a greater decrease in the cAMP levels. In addition, the compound with the propyl chain is more active than the one with the ethyl chain, as the dose-response curve is left-shifted (0.4 log units) relative to the **n = 1** compound. On the other hand, side chains longer than 3 carbons (**Figure II-13, n = 3, 4 or 5**) decrease the response of the agonist, behaving as NAMs.[74] These studies confirmed the behaviour of CBD as NAM in the CB_2R and highlighted the importance of the side chain in the modulation of the response through the binding with allosteric binding pocket, paving the way for new PAM structures targeting CB_2R.[80]

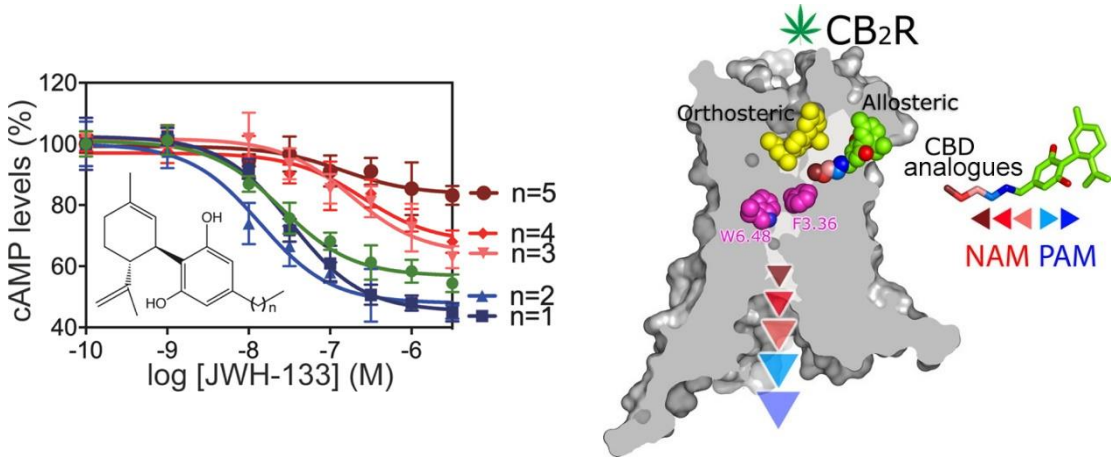

Figure II-13. Decrease of the cAMP levels upon the stimulation of the CB_2R receptor with the orthosteric agonist **JWH-133** (green line) and in conjunction with CBD analogues with a side-chain length of 2 to 6 carbon atoms (n=1 to n=5). Images extracted from reference 74.

Chapter III

Innovative Bitopic Ligands Targeting Allosteric and Metastable CB_2R Binding Sites

The cannabinoid receptor 2 (CB_2R) has gained significant interest as a therapeutic target since its crystal structure was elucidated. Its selective expression in immune cells and limited presence in the central nervous system make it an ideal candidate for developing anti-inflammatory treatments and targeting neuropathic pain without causing psychoactive effects. Among the various strategies to control CB_2R activity, the synthesis of **bitopic ligands** stands out as the most innovative. These ligands enhance affinity and selectivity by simultaneously targeting two binding pockets of a certain receptor. The detailed understanding of the CB_2R structure has led to the discovery of **metastable binding sites** or **vestibules**, which interact with ligands to induce conformational changes and modulate receptor response. By targeting both the allosteric and vestibule binding sites, several bitopic ligands were designed and synthesised to achieve enhanced positive allosteric modulation.

1. Introduction

1.1. Bitopic Ligands for GPCRs

The allosteric mechanism of GPCRs is highly complex and subject to many factors, including the dependency of an orthosteric ligand to generate the desired response. This is an important factor in neurodegenerative disorders like Parkinson's or Alzheimer's diseases, which involve a loss of neurotransmitter-releasing nerves, but their corresponding GPCR targets remain intact. As an alternative approach, **bitopic ligands**, also known as dualsteric ligands, have been developed. These compounds bear two pharmacophores connected by a linker and are capable of interacting with two cavities of a single receptor at the same time. These two binding sites are typically the orthosteric and the allosteric binding sites, but other binding sites, such as a metastable one (*vide supra*) can also participate. If the pharmacophores are identical, the ligand is classified as homobivalent, while if they are different, the ligand is defined as heterobivalent. Additionally, if the ligand binds to cavities allocated in two different receptors, then it is called a **dimeric ligand** (**Figure II-14**).[81]

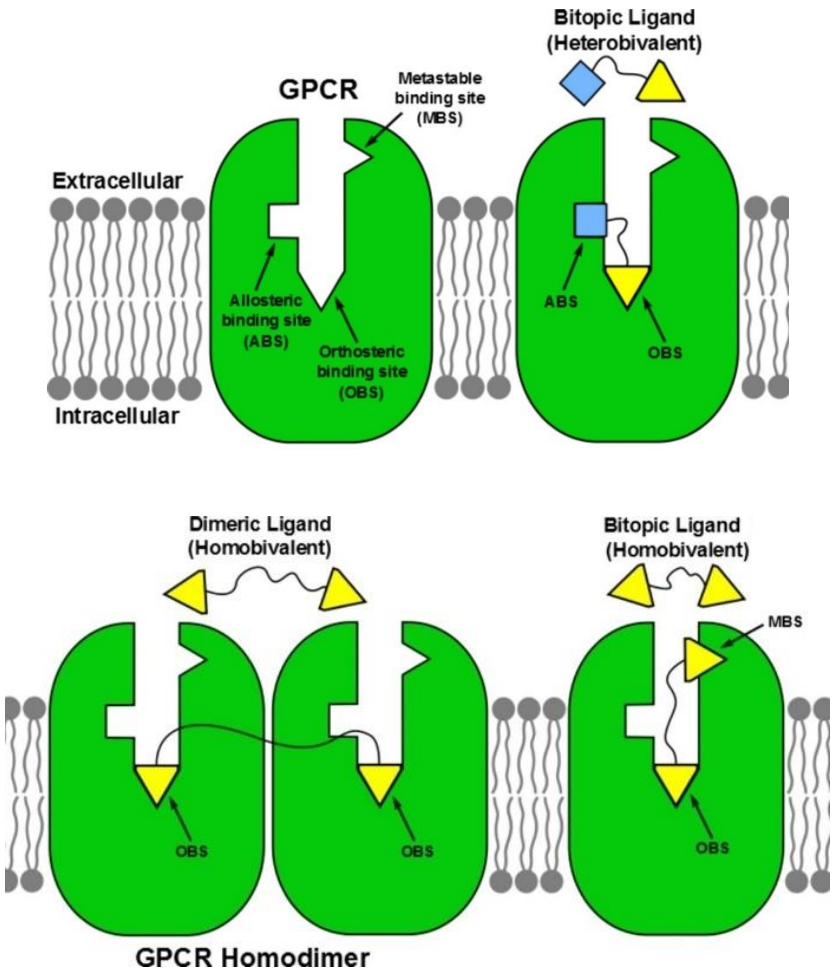

Figure II-14. Classification of the different dualsteric ligands. Image extracted from reference 81.

For the successful development of a functional bitopic ligand, the two binding sites must be accessible and in close proximity. The linker that connects both units that conform the bitopic ligand plays a crucial role in this regard. Common types of spacers include polymethylene, polyamide, and polyethylene glycol moieties. Then, for the bitopic ligand to engage with both cavities simultaneously, it is important to consider the length of the linker, its flexibility, and the proximity of relevant amino acid residues.

Bitopic ligands can be very versatile structures, as the pharmacophores that constitute them can be orthosteric agonists or antagonists connected to either a PAM or a NAM, theoretically providing a wide range of regulatory options. However, it is difficult to anticipate the outcome of such ligands. For instance, Chen *et al*.[82] coupled an orthosteric full agonist with a PAM of the M1-muscarinic acetylcholine receptor (mAChR), but instead of enhancing the potency, the bitopic ligand functioned as a partial agonist. This partial loss of affinity can arise from mismatches, such as a hybrid NAM-agonist, where each pharmacophore stabilises a different receptor conformation.[83]

Nevertheless, this is an emerging and interesting new strategy in medicinal chemistry, as these ligands can bring the qualities of both orthosteric and allosteric ligands by offering high affinity and selectivity, biased signalling pathway activation, reduced off-target activity, and therapeutic resistance. However, targeting GPCRs for lipid mediators, such as cannabinoid receptors (CBRs), is more challenging due to the more hindered pathway to the orthosteric site. As a result, just a few bitopic ligands have been reported for CBRs,[84] and they become scarcer for CB_2R. As stated by Nimczick *et al*.,[85] a careful bitopic ligand design is required since the receptor-ligand interactions within CB_2R are extremely sensitive to alterations in the monovalent structure, particularly when the intrinsic activity needs to be preserved.

Up to the moment of the deposit of this thesis, three bitopic ligands specific for CB_2R have demonstrated enhanced potency when compared to the monovalent counterparts. In 2022, Gado *et al*.[86] described several dualsteric heterobivalent ligands that combined a PAM of the CB_2R, synthesised by the same research group as the first of its kind,[87] with a structurally related orthosteric ligand of the same receptor. Among these compounds, **FD-22a** (**Figure II-15**) was the most promising, showing anti-inflammatory properties and antinociceptive activity *in vivo*. In 2023, the same researchers evaluated a series of bitopic ligands, in which the difference of those previously reported was the orthosteric agonist. On this occasion, of all the bitopic ligands tested, the one that had the most similar structure, named **JR-22a** (**Figure II-15**), was the only one that behaved as a dualsteric ligand, showing anti-inflammatory effects.[88]

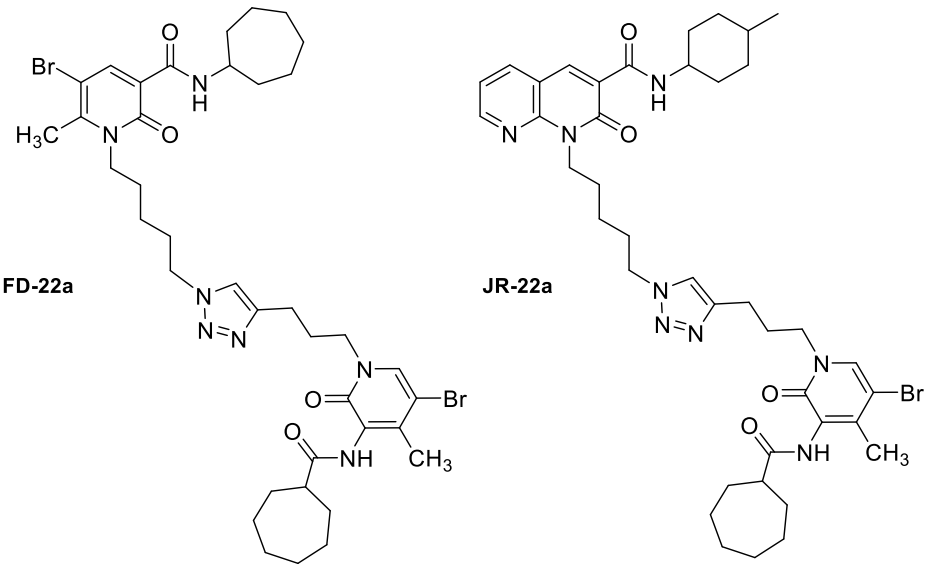

Figure II-15. Bitopic ligands that target CB_2R reported by Gado *et al*.[86,88]

Prior to the description of these structures, in 2020, the first bitopic ligand for CB_2R had been described by Morales *et al*.[89] In that case, different homobivalent ligands were synthesised using two chromenopyrazole analogues, known to be orthosteric agonist ligands of CB_2R, linked by alkyl chains of different lengths (**Figure II-16**). Unlike the bitopic ligands presented by Gado *et al*., these ligands targeted the orthosteric and metastable binding sites of the receptor, which Morales *et al*. nominated as **vestibule** or exosite.

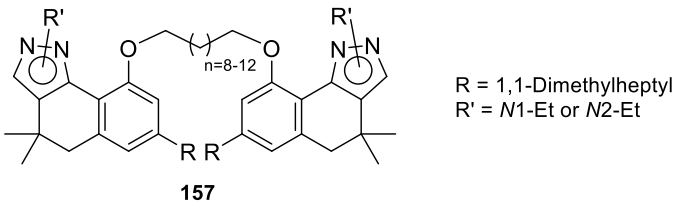

157

Figure II-16. Bitopic ligand design to target the orthosteric and vestibule binding sites of the CB_2R.[89]

1.2.GPCRs Alternative Binding Pockets: The Vestibule

With a better understanding of GPCR structures, along with the increasing computational power, more accurate molecular dynamics simulations have elucidated the binding mechanism of orthosteric ligands to receptors. Several studies have reported that various orthosteric ligands, with no related structure, developed energetically stable conformations and engaged with the entrance of the receptor before progressing towards the binding pocket or dissociating. These transitional binding sites are termed **metastable binding sites**, entrances or vestibules.[89–92] The current understanding is that these binding pockets act as filters, influencing receptor selectivity.[91] Therefore, upon engagement with a suitable ligand, the receptor undergoes a conformational change, that allows it to penetrate into the cavity and further contact the orthosteric binding pocket. If this affirmation is correct, these metastable binding sites could provide new engagement pockets to modulate receptor responses, which would entail therapeutic interest. As an example, in the study of the human 5-HT_{1B} GPCR binding to an agonist, it was observed that the orthosteric site is not accessible from the extracellular space, as the lipidic ligand binds to it through a narrow channel

located between transmembrane helixes 1 and 7. Thus, designing bitopic ligands capable of interacting with this metastable site might be a particularly useful approach due to its major accessibility compared to the orthosteric one.[93]

As exposed in the previous section, to date, just one research paper has been published where a bitopic ligand targeting this exosite is synthesised, with its biological response tested.[89] These bitopic ligands, formed by two chromenopyrazole moieties linked by an alkyl chain, were able to bind to the orthosteric site and to the exosite, as could be confirmed by performing signalling assays and induced mutation studies in the CB_2R.

Based on these results, the group of Prof. Leonardo Pardo, conducted energy minimisation (EM) studies to design a bitopic ligand capable of interacting with both the allosteric binding site and the vestibule of CB_2R (**Figure II-17**). This novel approach to designing bitopic ligands could enhance the efficacy of the positive allosteric modulators that had been described by our group.[74] Simultaneously, these drugs would prolong the residence time of the agonist in the orthosteric cavity due to the steric hindrance generated by the bitopic ligand in the cavity and at the receptor exit. This may result in longer-lasting drug efficacy after the free drug concentration has dropped, showing improved pharmacodynamic properties compared to the use of the orthosteric ligand alone.

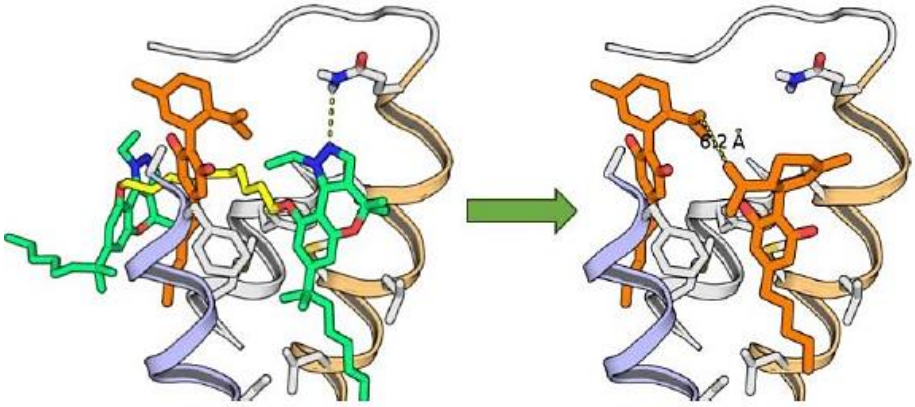

Figure II-17. Detailed views of the binding modes obtained during MD simulations of CB_2R complex with: Left) Bitopic ligand published by Morales *et al*.[89] (green-yellow) and CBD (orange) at the allosteric cavity; Right) Two CBD molecules (orange) interacting with the allosteric binding site and the vestibule. Transmembrane helices (TMs) 1 and 7 are shown in orange and blue, respectively.

2. Objectives

In this chapter of the thesis, based on the previous studies and with the purpose of continuing with the study of the modulation of the CB_2R activity, the following objective was defined:

- Synthesis of a family of bitopic ligands aiming to interact both with the allosteric site and the vestibule of the CB_2R, expecting a positive allosteric modulator behaviour.

Based on the same preliminary molecular modelling studies, the structure of the first of their kind bitopic ligands should contain the following features (**Figure II-18**):

- Homobivalent ligand.
- Based on cannabidivarin (**CBDV**) structure, which showed a positive allosteric modulator behaviour on the CB_2R,[74] as the pharmacophore.
- With an alkyl chain linker with a length of 3 to 5 carbon atoms that would be established between one of the hydroxyl groups of each pharmacophore.

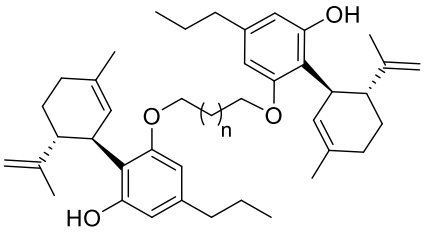

n = 1, **158**

n = 2, **159**

n = 3, **160**

Figure II-18. Molecular structure of the objective bitopic ligands of this chapter.

Once the bitopic ligands would be synthesised, their biological activity would be evaluated through *in vitro* studies. These assays focus on elucidating the ability of the ligands to behave as PAMs in different specific signalling pathways, such as:

- Adenyl cyclase inhibition assays, specific for G protein signalling pathways.
- β-arrestin recruitment assays, G protein-independent signalling pathway.

These studies aim to provide a comparative analysis of the efficacy and potency of the bitopic ligands, contributing to a deeper understanding of their potential therapeutic applications. The results will help to establish structure-activity relationship and guide the rational design of future ligands targeting specific GPCR signalling pathways.

3. Results and Discussion

The results presented in this chapter are organised into several sections. First, the rational design of the bitopic ligands is explained, along with the results of EM studies conducted to validate this design (**section 3.1.**). Next, the optimisation of the synthesis of the pharmacophore **CBDV** is detailed (**section 3.2.**), as it serves as a key intermediate for obtaining the target bitopic ligands (**section 3.3.**) Finally, the results of the *in vitro* assays are presented, evaluating the efficacy and potency of the bitopic ligands as modulators of CB_2R activity (**section 3.4.**).

3.1. Rational Design of the Bitopic Ligands

To design the bitopic ligand, the goal was to target the allosteric and vestibule binding sites to obtain an enhanced positive allosteric modulation. Therefore, a homobivalent type of bitopic ligand was chosen, as the expected response from the interaction of both units with the targeted binding pockets would be synergistic, making sense to use the same pharmacophore for both parts of the ligand.

To choose the pharmacophore, we relied on the results obtained by the group beforehand.[74] Cannabidivarin (**CBDV**) is, from the CBD analogues tested, the one with a more pronounced positive allosteric modulation, making it the ideal candidate to constitute the main structure of the bitopic ligand.

Regarding the linker, a 3 to 5 alkyl chain was determined to be the optimal choice. The spacer length was decided based on observations from MD simulations of the chromepyrazole bitopic ligand, as discussed in **section 1.2.** of the **Introduction**. Extracting that frame of the CB_2R conformation from these simulations, energy minimisation (EM) studies were performed with the CBD structure (**Figure II-17**, *vide supra*). It is important to point out that these preliminary studies used CBD instead of CBDV since the results with the CBD analogues were not available at that time. Once the spacer length was determined, different proposals on how to connect both pharmacophores were made. From a synthetic standpoint, linking both cannabinoid units *via* an ether bond through one of the hydroxyl groups of the resorcinol moiety seemed the best option (**Figure II-19**). This choice was also supported from the point of how this change in the pharmacophore unit would affect the interaction with the receptor. The previous studies included mutagenesis experiments on the CB_2R to investigate the significance of specific residues when interacting with CBD. One of the residues mutated was Ser285$^{7.39}$ to Leu, which aimed to assess the potential hydrogen bond with the hydroxyl substituents of the resorcinol moiety, demonstrating that this interaction has little effect on the capacity of CBD as a NAM.

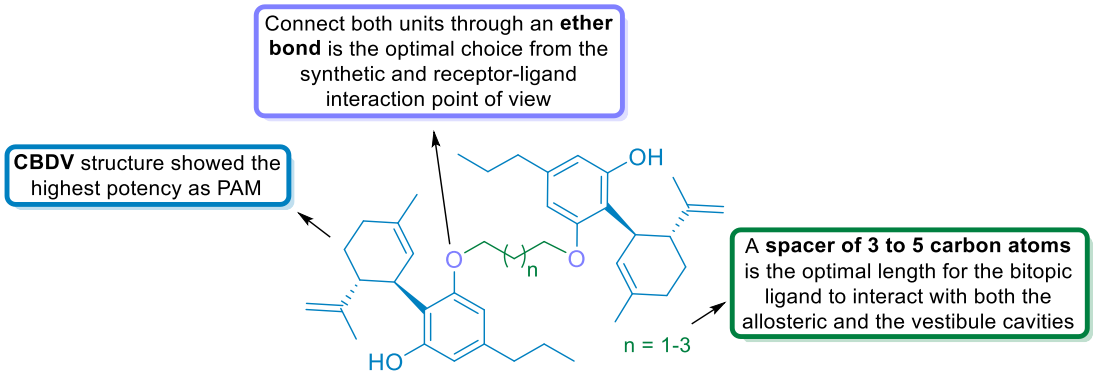

Figure II-19. Bitopic ligand structure proposed.

Once the rational design was concluded, EM studies were conducted by Aleix Quintana, a PhD student in our group and in Prof. Leonardo Pardo's research group, to evaluate the ability of the proposed structures to simultaneously interact with both the allosteric binding site and the metastable binding site. **Figure II-20** represents the modelling of the bitopic ligands **158-160** (shades of blue) interaction with the allosteric binding site and the metastable binding site, having the orthosteric binding site occupied by the agonist **JWH-133** (green). Results showed that pharmacophore units remain highly stable at the allosteric site and moderately stable at the vestibule. Visual inspection of the models confirmed that the hydroxyl groups of the aromatic moiety are a suitable attachment point to link the spacer moiety. In addition, linker lengths from three to five methylene units were ideal, enabling the bitopic ligand to span the distance between the two binding sites without disrupting the interaction of the orthosteric agonist at its binding pocket.

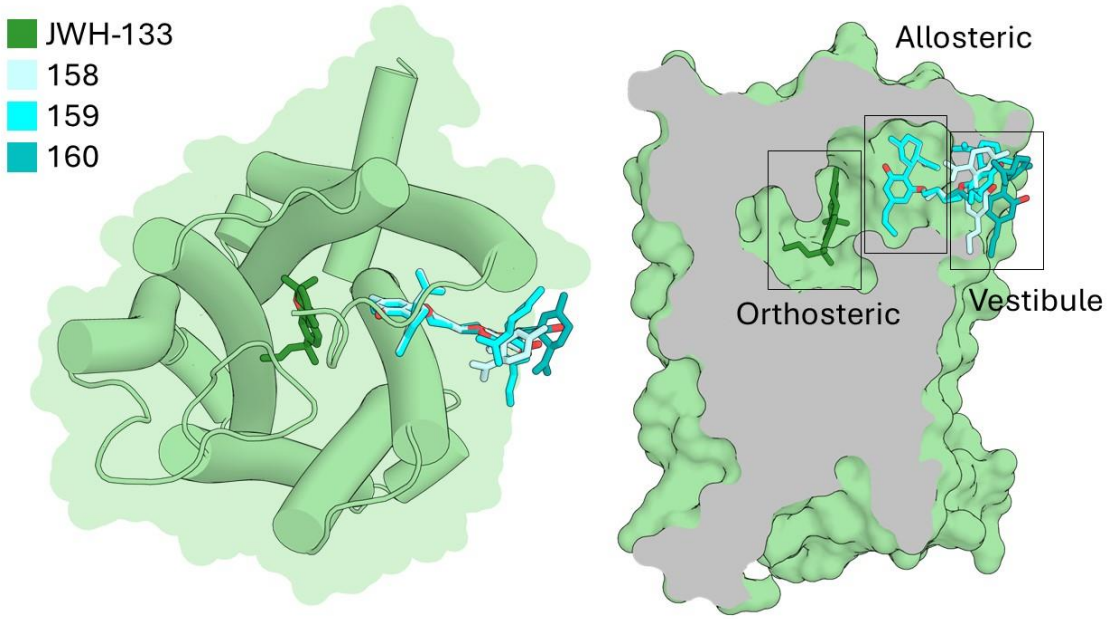

Figure II-20. Modelling of the bitopic ligands interaction in the CB_2R receptor through EM studies. Left: Top view of the CB_2R receptor; Right: Section of the CB_2R receptor highlighting the cavities.

3.2. Optimisation of the Synthesis of the Pharmacophore CBDV

As discussed in **section 4** of the **General Introduction**, the synthetic strategies to prepare CBD and its derivatives have been extensively explored, as the interest in these compounds has been growing over the last decades. Compound **CBDV**, a precursor for the synthesis of the bitopic ligand, was previously synthesised by our research group using the methodology developed by Dialer *et al*. in 2017.[50] Following this synthetic route, several CBDV derivatives were obtained and tested as allosteric modulators of the CB_2R receptor, as published in 2021 (**Scheme II-2**).[74] The synthesis begins with a Wittig reaction between **161** and the corresponding alkyl phosphonium salt, followed by hydrogenation of the obtained C-C double bond to afford compounds corresponding to structure **IV**, with an overall yield ranging from 62% to 95% for the two steps. Next, these compounds undergo bromination to produce the dibrominated derivatives (**V**), achieving yields from 70% to quantitative. Subsequently, deprotection of the hydroxyl groups yields the corresponding phenol derivatives (**VI**), with deprotection yields varying from 73% to 91%. The phenol derivatives are subjected to a Friedel-Crafts alkylation to form the key cyclised intermediates (**VII**), with yields ranging from 56% to 71%. Finally, performing reductive dehalogenation to remove the bromine atoms results in the desired cannabinoid derivatives **162, CBDV, 163, CBD, and 164**, depending on the chain length (n = 1 to 5). The total yields for the six-step sequence vary for each compound, with **CBDV** (n=2) showing a 27% yield and other derivatives, such as **CBD** (n=4), showing a 17% yield.

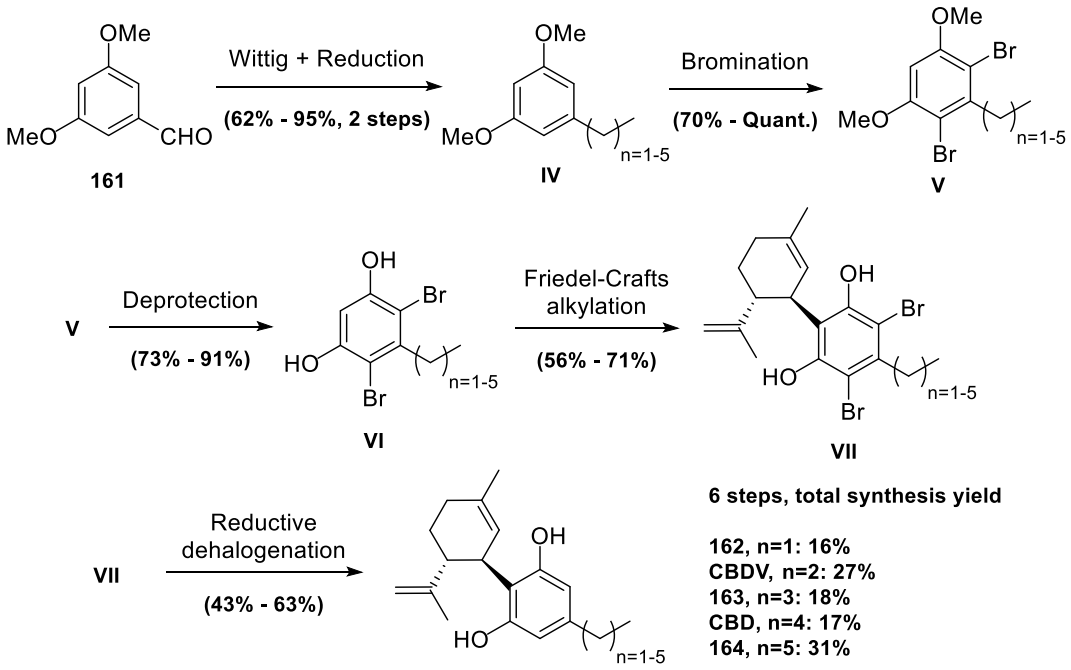

Scheme II-2. Synthetic route employed by our research group for the synthesis of cannabidiol derivatives.[74]

However, despite the good overall synthetic yield, it was considered that further optimisation of the synthesis could be achieved.

3.2.1. Optimisation of the Reductive Dehalogenation Reaction

In an initial attempt, optimisation of the dehalogenation reaction was performed, as it was the step with the lowest yield in the synthetic route (**Scheme II-3**).

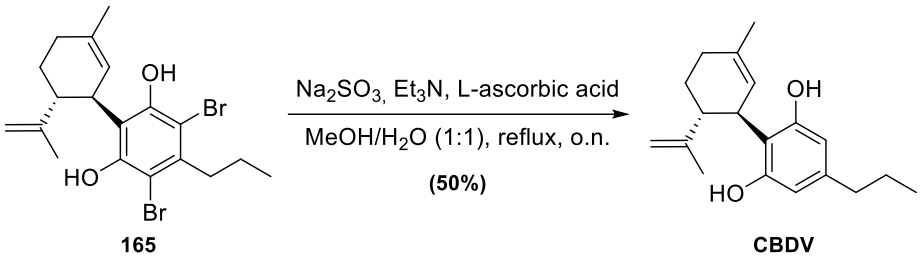

Scheme II-3. Reductive halogenation procedure employed in reference 74 for the obtention of **CBDV**.

A bibliographic review on the reductive dehalogenation reaction led to an article published by Tomanová *et al.* in 2019[94] in which several reductive dehalogenation reactions were performed on various phenols and heteroaromatics using sodium sulfite (Na_2SO_3) in an aqueous medium.[94] The article claims that Na_2SO_3 has a dual role: i) acting as a proton-transfer mediator from **165** through anion **166** to afford keto tautomer **167**; and ii) abstracting bromine from tautomer **167** to produce **169** (**Scheme II-4, path A**). In the last step, the highly reactive bromosulfonate is rapidly hydrolysed to sodium bisulfate in a fast and irreversible step. It is also suggested that the mechanism could involve the transformation of tautomer **167** into the more thermodynamically stable diketo tautomer **168** (**Scheme II-4, path B**), if the tautomerisation step is faster than the bromine abstraction from **167**. A second reductive dehalogenation would allow access to the desired product, **CBDV**.

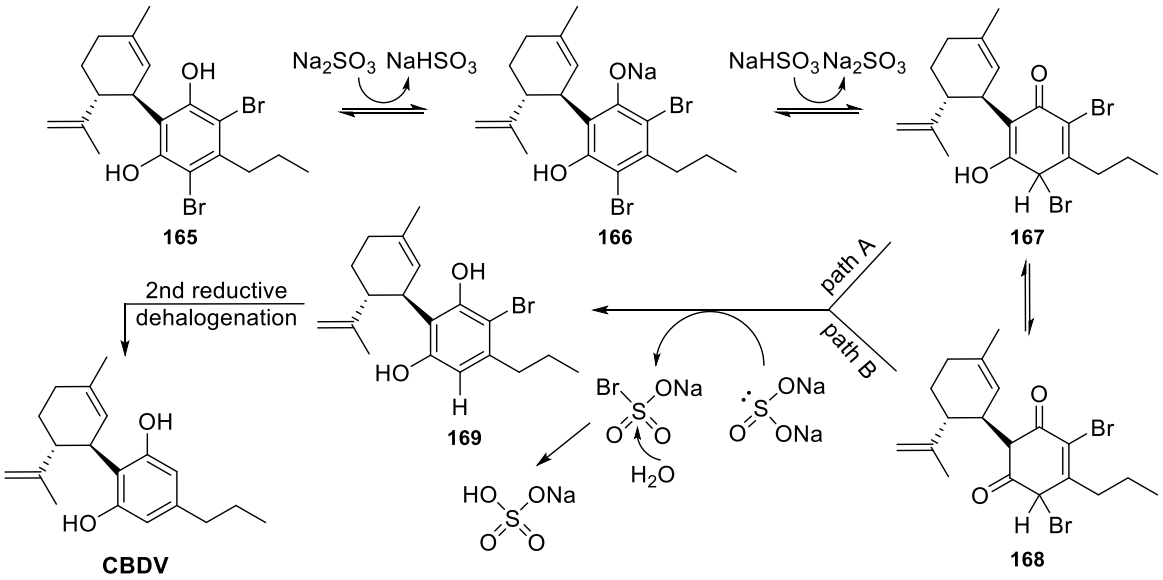

Scheme II-4. Adaptation of the mechanistic proposal for reductive dehalogenation by Tomanová *et al*.[94]

After the bibliographic search, it was observed that the use of microwave irradiation was one of the main differences in the reaction procedure compared to the one employed in our research group. However, some examples in Tomanová's article were performed under conductive heating (oil bath), so these conditions were also studied to evaluate the importance of microwave irradiation in

the outcome of the reaction. Another difference was the use of no other reagent apart from Na_2SO_3. Due to solubility issues, MeOH had to be kept as a solvent, instead of only using H_2O.

The first attempt was performed in a sealed tube under microwave irradiation (**Table II-1, entry 1**). When heated to 130 ºC, the reaction provided **CBDV** in better yields than those obtained with the previous synthetic procedure. Furthermore, the chemical shifts in the ^{1}H-NMR and ^{13}C-NMR spectra matched those reported by our research group.[74]

To further improve the yield, the reaction time was extended (**Table II-1, entry 2**). However, the yield did not improve, as more impurities formed, adversely affecting the yield. Also, using lower temperatures (**Table II-1, entry 3**) did not improve the yields either. The reaction turned out to be slower, as evidenced in the ^{1}H-NMR spectra at 30 minutes and 2.5 hours, showing a conversion of 20% and 40%, respectively. The spectrum of the best reaction also indicated an increase in the number of impurities formed.

On the other hand, using conductive heat (**Table II-1, entries 4-6**) did not yield better results, affording the product **CBDV** only when Et_3N and L-ascorbic acid were employed, demonstrating that both play a role in driving the reaction.

Table II-1. Scope of reductive dehalogenation reaction conditions on substrate **165**.

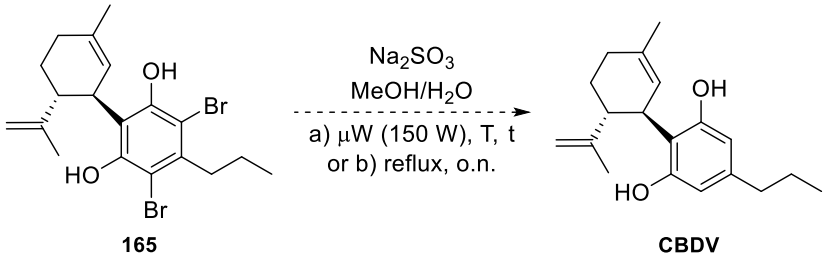

165 **CBDV**

Entry	Δ (Temperature)	Reaction time	Additives	CBDV (%)
1	μW, 150 W (130 °C)	0.5 h	None	68%
2	μW, 150 W (130 °C)	2 h	None	51%
3	μW, 150 W (110 °C)	2.5 h	None	40%
4	Sealed tube (150 °C)	2 h	None	0%
5	Reflux (75 °C)	o.n.	None	0%
6	Reflux (75 °C)	o.n.	Et_3N + L-Ascorbic acid	50%

In conclusion, the results of the optimisation of the reductive dehalogenation were positive. By employing microwave irradiation, the yield was improved compared to the previous procedure (68% vs. 50%). This translates in an improvement in the total yield of the synthesis (37% vs. 27%). Additionally, reaction times were significantly shortened from overnight to 30 minutes. However, this methodology exhibited limitations in scalability. Due to solubility issues and the size of the reactor, the reaction could not be scaled up beyond a 200 mg scale. Given that **CBDV** was needed as the starting material for the bitopic ligands synthesis, which involves several subsequent reactions, a

gram-scale synthesis would be required. Moreover, the improvement in the overall yield was not considered sufficient to overlook this limitation. Consequently, the research group started working on an alternative synthetic route with the aim of further improving the yields for the obtention of **CBDV**.

3.2.2. Alternative Synthetic Route for the Obtention of CBDV

With the same objective of improving the yields for the synthesis of **CBDV**, a thorough literature review was conducted. As a result, a synthetic route following the methodology developed by S.H. Baek and R. Mechoulam,[54] was proposed (see **Scheme II-5** for previously reported route and **Scheme II-6** for the newly proposed one). This methodology was chosen because it has been successfully exploited by several researchers for the synthesis of cannabinoid derivatives since its publication in 1985.[95–97] The main difference from the previous synthesis is that the bromination of the aromatic ring is omitted, thereby eliminating the need for the dehalogenation reaction. In this way, the number of steps is reduced, shortening the time and the costs for the obtention of the bitopic ligand scaffold **CBDV**. However, the proposed synthesis might also have caveats, as the Friedel-Crafts alkylation may lack regioselectivity on the aromatic ring, potentially increasing the number of side products obtained in this reaction.[97]

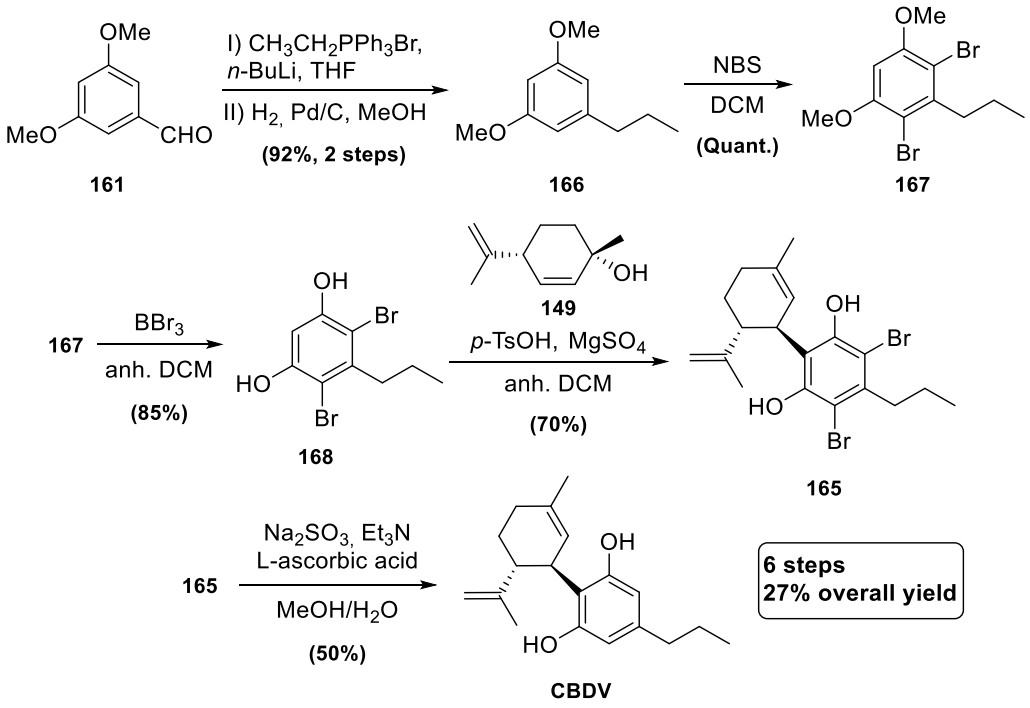

Scheme II-5. Previous synthetic route employed in our research group to obtain **CBDV**.[74]

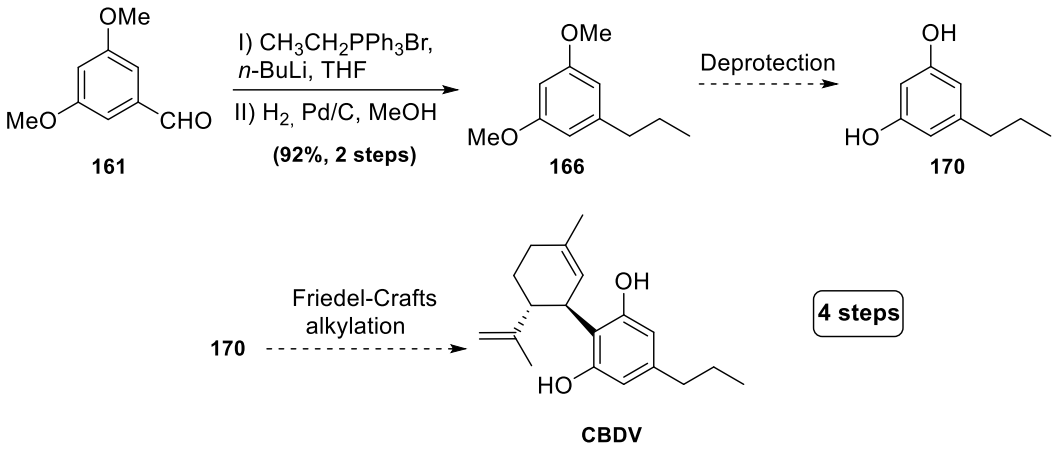

Scheme II-6. Proposed route to optimise the obtention of **CBDV**.

The first step of the synthesis was a Wittig reaction between commercially available 3,5-dimethoxybenzaldehyde (**161**) and ethyltriphenylphosphonium bromide (ETPB). The phosphonium ylide was prepared through the reaction of ETPB with a 2.5 M solution of *n*-BuLi in anhydrous THF at 0 ºC for 30 minutes. Aldehyde **161** was then added, and the mixture was stirred for 2 hours at room temperature, to obtain a mixture of *Z* and *E* olefins (**(*Z*+*E*)-169**). These olefins were reduced under a hydrogen atmosphere using Pd/C as a catalyst in MeOH to obtain product **166** (**Scheme II-7**). The success of the reduction was confirmed by the disappearance of signals between δ 6.30 and 6.40 ppm corresponding to the olefinic protons.

Both steps followed the same procedure as in the previous synthetic route. However, two significant optimisations were performed: i) For the purification of **(*Z*+*E*)-169**, precipitation of triphenylphosphine oxide in hexane was found to be equally effective as purification by column chromatography for olefins; and ii) Shorter hydrogenation times were found to be equally effective for the reduction of the double bond, reducing the reaction time from 24 hours to 6 hours. These changes resulted in time and cost savings for the procedure while maintaining the same yield.

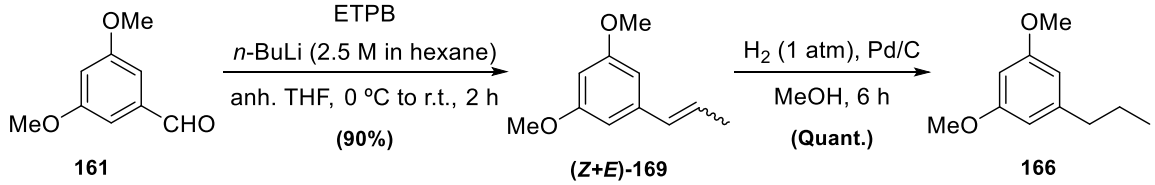

Scheme II-7. Wittig and catalytic hydrogenation reaction conditions to obtain compound **166**.

The next step in the synthetic sequence involved the deprotection of the hydroxyl groups of compound **166** employing boron tribromide (BBr_3), a highly utilised Lewis acid for ether cleavage without affecting other functional groups. BBr_3 coordinates with the oxygen of the ether function and promotes the C-O bond cleavage, obtaining an alkyl bromide and an alkoxyborane. The latter is hydrolysed to the corresponding alcohol during the work-up.

The addition of a 1.0 M solution of BBr_3 in DCM to the starting material, dissolved in anhydrous DCM, was performed at -10 ºC. Then, the reaction was allowed to reach room temperature and stirred until complete deprotection of both hydroxyl groups. It was observed that the number of

equivalents employed and the concentration of the reaction were two crucial parameters for the completion of the deprotection. The use of more diluted conditions (**Table II-2, entries 1 and 2**), as described by Navarro *et al*.[74] for an analogous compound, resulted in the incomplete deprotection of both hydroxyl groups. This issue was resolved by employing more concentrated conditions for the reaction (**Table II-2, entry 3**). Furthermore, the employment of even more concentrated solutions of the starting material resulted in a faster reaction with fewer equivalents of BBr_3 (**Table II-2, entries 4-6**), which can be considered an expensive reagent. Also, the modification of these conditions did not provide any further impurities. The well-known brominated by-products of the reaction were removed by performing an extraction, obtaining the resorcinol derivative **170** without further purification.

Table II-2. Optimisation of the parameters for the deprotection reaction of **166**.

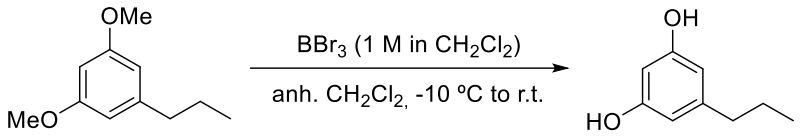

166 **170**

Entry	BBr_3 equivalents	Concentration	Time	170 (%)
1	6	0.04 M	36 h	78%[(a)]
2	8	0.03 M	28 h	81%[(a)]
3	8	0.10 M	14 h	85%[(a)]
4	6	0.15 M	12 h	94%
5	3	0.80 M	3 h	Quant.
6	2.5	0.80 M	3 h	Quant.

a) The reaction remained incomplete, with starting material detected in the ^{1}H-NMR spectrum.

The last step to obtain **CBDV** was a Friedel-Crafts alkylation using the commercially available terpenoid derivative (1*S*,4*R*)-1-methyl-4-(prop-1-en-2-yl)cyclohex-2-enol (**149**) and $BF_3{\cdot}Et_2O$ as Lewis acid. This synthetic procedure was first reported by Petrizka *et al*.[3] for the synthesis of **CBD**.

Friedel-Crafts reactions are catalysed by Brønsted or Lewis acids to generate the carbocation intermediate. However, the use of a strong Lewis acids can also lead to undesired secondary reactions, once the Friedel-Crafts reaction has occurred. The intramolecular cyclisation, driven by the addition of a hydroxyl group to the carbocation resulting from the protonation of one of the double bonds, is a well-known reaction for cannabidiol derivatives,[98–100] resulting in the formation of the Δ^9-tetrahydrocannabivarin ($\Delta^{\mathbf{9}}$**-THCV**) and the Δ^8-iso-tetrahydrocannabivarin ($\Delta^{\mathbf{8}}$**-iso-THCV**) as the main products. These can further rearrange to the more thermodynamically stable Δ^8-tetrahydrocannabivarin ($\Delta^{\mathbf{8}}$**-THCV**) and $\Delta^{4(8)}$-iso-tetrahydrocannabivarin ($\Delta^{\mathbf{4(8)}}$**-iso-THCV**) (**Scheme II-8**).

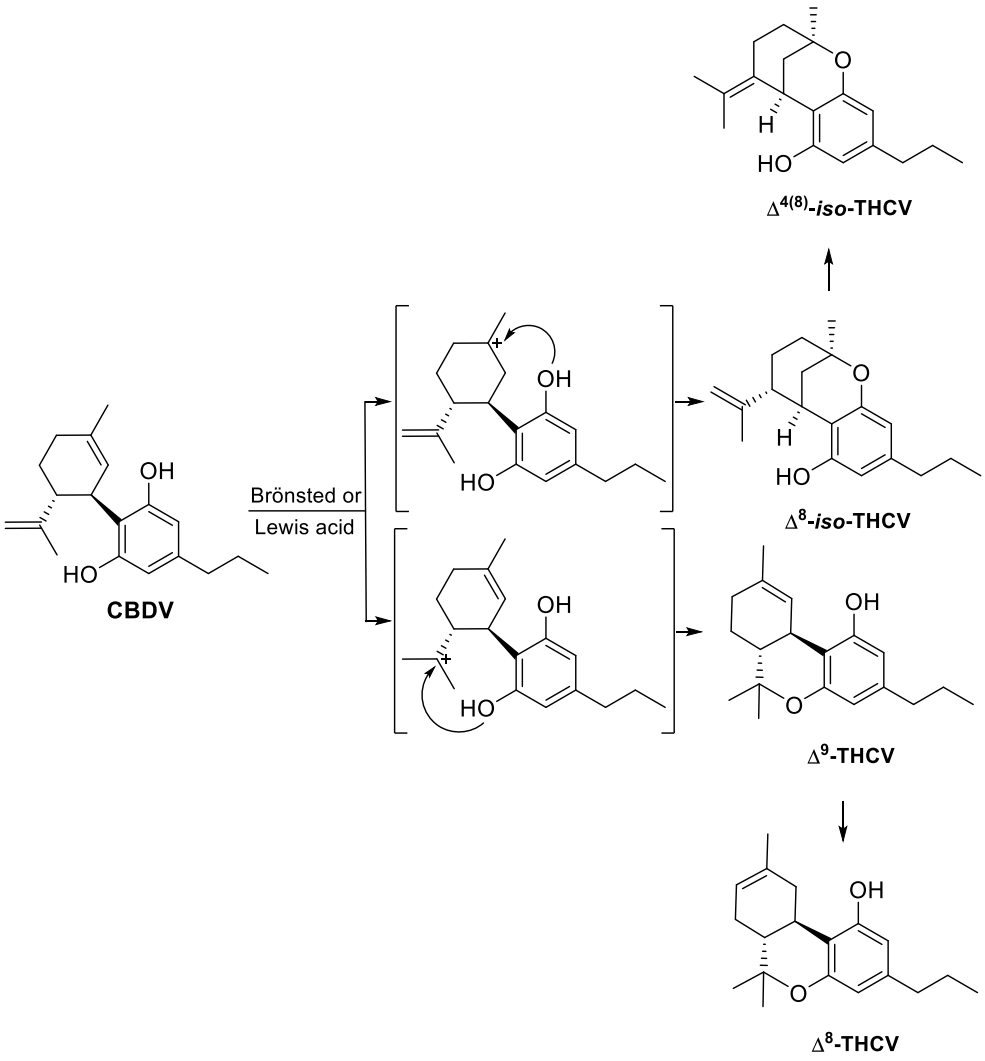

Scheme II-8. Subsequent transformations of **CBDV** in the presence of strong Brönsted or Lewis acids. Adapted from reference 98.

To modulate the reactivity of **CBDV** in the presence of BF_3, S.H. Baek and R. Mechoulam[54] proposed the use of basic aluminium oxide (Al_2O_3), as a support material for the $BF_3 \cdot Et_2O$. The hydroxyl groups on the surface of the alumina coordinate with the BF_3 (**Figure II-21**). This generates a milder Lewis acid because the boron atom has more electron density, being less electrophilic.[101] However, boron still has a strong enough electrophilic character to act as a catalyst for the reaction by forming the needed carbocation, thereby promoting a more selective formation of **CBDV**.

Figure II-21. Possible surface species for the stabilisation of BF_3 using Al_2O_3 as a support material.[102]

This Friedel-Crafts alkylation methodology applied to the reaction between resorcinol derivative **170** and the commercial terpenoid **149**, in a 25% excess, resulted in the obtention of **CBDV** as the major product in a 10-second reaction using anhydrous CH_2Cl_2 as solvent (**Scheme II-9**).

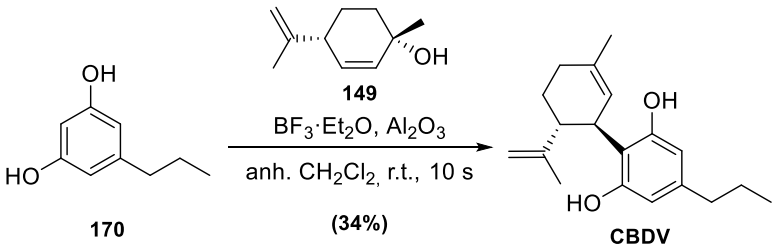

Scheme II-9. Friedel-Crafts reaction for the obtention of **CBDV** following S.H. Baek and R. Mechoulam methodology. The reported yield was obtained after the optimisation shown in the **Table II-3** (*vide infra*).

This reaction proceeded diastereoselectively, favouring the *trans* orientation relative to the isopropenyl group. This allowed the isolation of the enantiopure compound **(1'*R*,6'*R*)-CBDV**, confirming this structure by comparing the ^{1}H-NMR and ^{13}C-NMR spectra with those reported in the literature.[74] However, the reaction lacked complete regioselectivity, observing two side products, in a minor proportion: the abnormal regioisomer (***abn*-CBDV**), where the terpenoid subunit is positioned *ortho* to the *n*-propyl substituent (*para* in **CBDV**), and the disubstituted product (***bis*-CBDV**) (**Figure II-22**). Both side products were expected, as similar derivatives had been reported by researchers who have employed this methodology for the synthesis of CBDV derivatives.[4,12,96] This lack of regioselectivity is due to the unblocked positions on the aromatic ring, unlike in the previous synthesis, where the two *ortho* positions relative to the aliphatic chain were brominated. The three products generated in the reaction have substantially different R_f values (0.68 vs. 0.34 vs. 0.10, hexane:CH_2Cl_2, 1:1), making their separation by column chromatography an efficient way to isolate them. The ^{1}H-NMR spectrum of ***bis*-CBDV** was in line with the one reported by Chiurchiù *et al*.[96] (see **Figure A90** in Annex). However, the most polar product, ***abn*-CBDV**, could not be isolated due to the presence of an unidentified third side product with a similar R_f under the column chromatography conditions used.

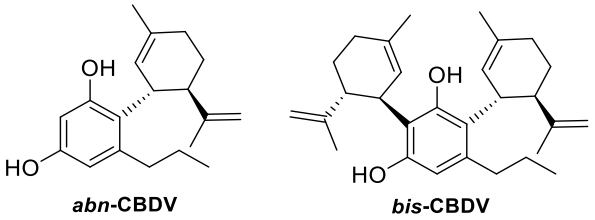

Figure II-22. Main side products observed in the Friedel-Crafts reaction.

Additionally, two other side products were identified by ^{1}H-NMR analysis: **Δ^{9}-THCV** and **Δ^{8}-*iso*-THCV**. As explained before, both products result from intramolecular cyclisation, once the Friedel-Crafts alkylation has occurred, because of the presence of the Lewis acid. Due to their similar Rf, it was not possible to isolate and characterise them individually. However, it was possible to identify each of them, due to the different chemical shift of some of their characteristic protons (**Figure II-23**). For **Δ^{9}-THCV**, deshielded olefinic proton $H_{8'}$ with δ 6.43 ppm and the proton α to the aromatic ring ($H_{7'}$) with δ 3.15 ppm could be identified. On the other hand, **Δ^{8}-*iso*-THCV** showed a characteristic signal for the isopropenyl H_{10} protons with δ 4.95 ppm, also confirmed by HSQC experiments, and the proton α to the aromatic ring (H_7) with δ 3.51 ppm. These chemical shifts were

in line with those reported in the literature.[98] With these assignments, it was possible to calculate the ratio of isomers (**Δ^9-THCV**: **Δ^8-*iso*-THCV**, 2:1) and the aromatic protons were assigned accordingly. Notably, the aromatic protons of these cyclised products appeared separate, unlike in non-cyclised products, in which the aromatic ring can rotate freely, causing both protons to be equivalent and thus to resonate at the same frequence.

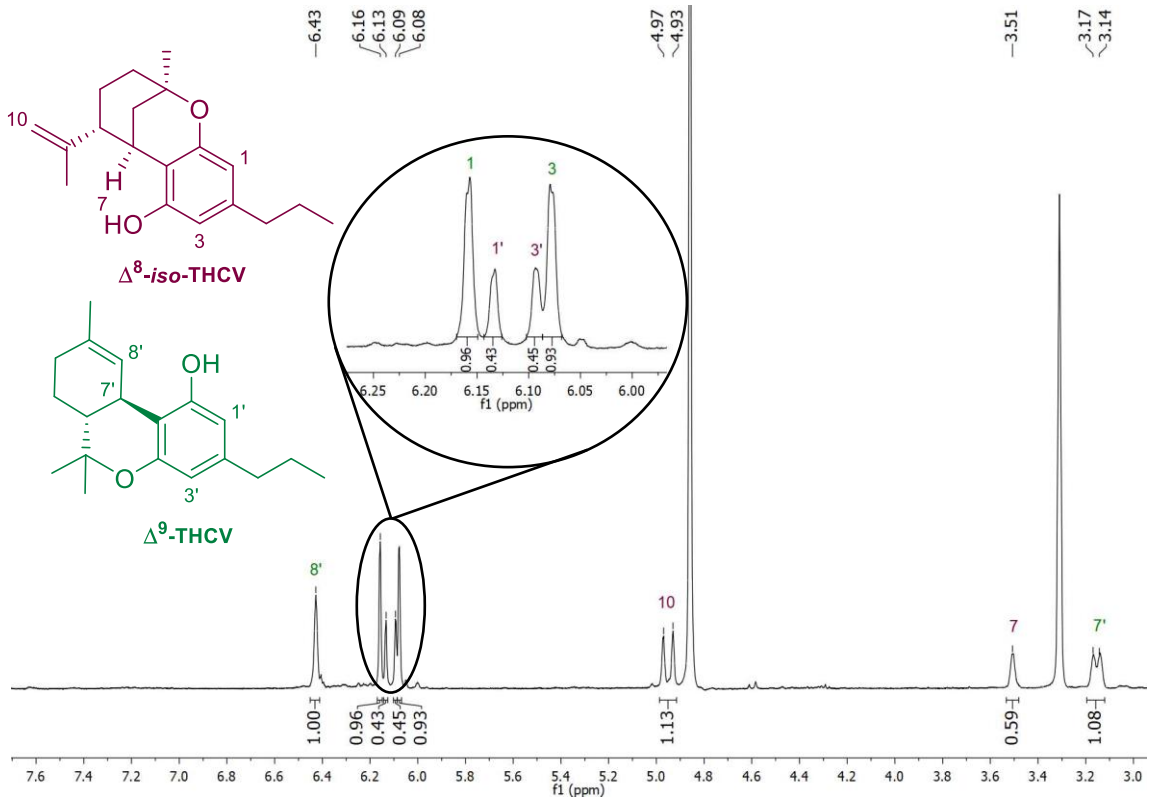

Figure II-23. Spectrum fragment of a **Δ^9-THCV** and **Δ^8-*iso*-THCV** containing fraction (400 MHz, MeOD). The atom numbers were assigned arbitrarily.

The presence of these two side products was unexpected due to the use of Al_2O_3 to generate a milder Lewis acid. In this case, these side products presented a similar R_f value to the **CBDV** product, which made the purification difficult. In order to avoid their formation and increase the yield of **CBDV**, different parameters of the reaction were tried to be improved from the original procedure described by S.H. Baek and R. Mechoulam (**Table II-3**, **entry 1**). Reducing the number of $BF_3{\cdot}Et_2O$ equivalents significantly decreased the side products, the use of 1.8 equivalents being optimal (**Table II-3**, **entry 3**). Further reduction of the equivalents just reduced the yield for **CBDV**, recovering more starting material. Scaling-up the reaction to 1.50 g of **170** (**Table II-3**, **entry 4**) not only maintained but also improved the yield, likely due to a reduction in the losses derived from the work-up and the purification by flash chromatography. This difference observed in the optimal number of $BF_3{\cdot}Et_2O$ equivalents compared to the original procedure may be related to the high sensitivity of this reagent to the presence of H_2O. Inadequate storage of the reagent can lead to an overestimation of the equivalents used. Therefore, ensuring proper preservation and storage conditions of the reagent is mandatory, especially for this reaction, which showed itself to be highly sensitive to changes in the number of Lewis acid equivalents. In addition, the fact of generating the catalyst *in situ*, or the short reaction times, could contribute to variability in the yields obtained.

Table II-3. Optimisation of the Friedel-Crafts reaction to reduce the number of side products.

Entry[a]	$BF_3{\cdot}Et_2O$ equivalents	Temperature	Reaction time	CBDV (% BRSM)	Δ^9-THCV and Δ^8-*iso*-THCV	*bis*-CBDV
1	2.5	Reflux	10 s	22% (28%)	18%	18%
2	2.0	Reflux	10 s	29% (36%)	8%	22%
3	1.8	Reflux	10 s	32% (36%)	>1%	28%
4[b]	1.8	Reflux	10 s	34% (41%)	4%	30%
5	1.6	Reflux	10 s	22% (36%)	---	14%
6[c]	1.8	0 ºC	10 s	30% (38%)	---	24%
7[c]	1.8	0 ºC	30 s	24%	10%	14%
8[c]	1.8	Reflux	30 s	26%	8%	22%
9[c]	1.8	Reflux	60 s	16%	28%	28%

a) Anhydrous CH_2Cl_2, 0.05 M **170** and 0.20 g scale were kept as fixed parameters.
b) Scale-up to 1.50 g of **170** (9.86 mmol).
c) % of the different products estimated by ^{1}H-NMR analysis.

Moreover, optimisation of other parameters was also tried. The ***bis*-CBDV** consistently maintained a similar proportion relative to **CBDV**, approximately 1:1, under all conditions tested, including when fewer equivalents of the cyclic allylic alcohol **149** were employed. When it comes to the isolated yield of **CBDV**, neither the temperature nor the reaction time adjustments (**Table II-3**, **entries 6-9**) resulted in an improvement of the yield. Additionally, the use of anhydrous $MgSO_4$ or oven-dried Al_2O_3 did not make any difference in the yield either.

Despite the formation of these side products, the overall yield of the synthesis was slightly better than the one obtained with the previous synthesis (34% vs 27%), especially when considering the yield based on the recovered starting material (41% yield BRSM). In addition, the number of steps was reduced from 6 to 4 steps, all of them scalable to gram-scale, and the number of purification procedures was also reduced. This translates into a reduction in the time required to obtain **CBDV**. For these reasons, this synthesis was the one of choice to synthesise **CBDV**, the precursor for the bitopic ligands.

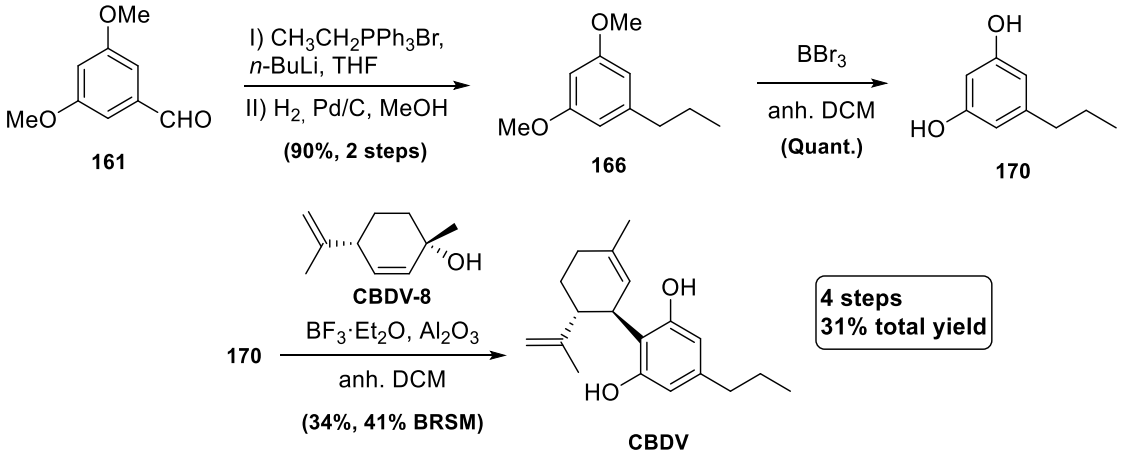

Scheme II-10. Synthesis route developed in this thesis for the more efficient obtention of **CBDV**.

3.3. Synthesis of the Bitopic Ligands

The synthetic strategy designed to afford the bitopic ligand began with the monoprotection of **CBDV** to selectively alkylate one of the alcohols (**Scheme II-11**). Otherwise, having two reactive positions in the molecule could lead to the formation of different side products, or even to the obtention of polymeric structures. Then, the alkyl chain with a length between three to five carbons would be introduced to obtain the protected bitopic ligand. In the last step, the hydroxyl groups would be deprotected to yield the bitopic ligand.

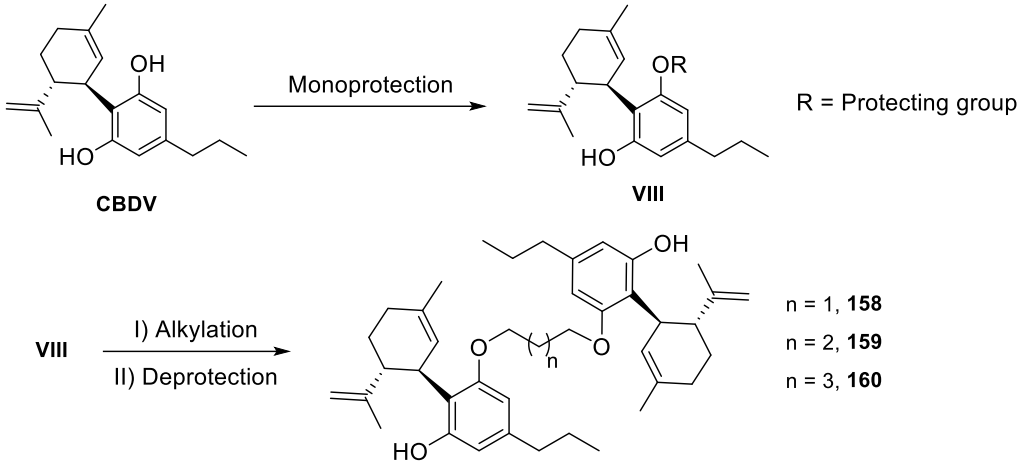

Scheme II-11. Synthetic strategy for bitopic ligands from **CBDV**.

3.3.1. Monoprotection Reaction of CBDV

The first step of the synthesis required the protection of one of the hydroxyl groups of **CBDV**. There are precedents for the protection of resorcinol scaffolds using different protecting groups with varying yields.[58] Since both hydroxyl groups are chemically equivalent, using a stoichiometric amount of the protecting group would result in a mixture of unprotected, monoprotected, and diprotected products with a 1:2:1 statistical distribution. To promote the selective formation of the monoprotected product, several methodologies that employed ion exchange resins,[103] polymer supports,[104] and cesium bases[105] have been developed. However, the substrates used for these reactions are poorly functionalised, and seemingly these strategies would not suit our diol due to possible side reactions.

Therefore, the initial approach for this reaction was to use one equivalent of the protecting group to increase the stoichiometric control of the reaction. Ideally, a large excess of starting diol is usually employed to ensure that the diprotected product is not formed, but considering that **CBDV** is not commercially available, reducing the loss of this reagent is a priority.

When selecting the protecting group, it must meet the following requirements:

- Be stable under the basic conditions used in the subsequent steps.
- Deprotection conditions must be compatible with the stability of the ether bond formed to link both units of the bitopic ligand. Also, cleavage conditions must be compatible with the double bonds present in the molecule.

Considering these requirements, and after a bibliographic review of protecting groups used in similar molecules, the possibilities were narrowed down to the following groups: Silyl ethers (R'Si-OR), a pivalate ester (Piv-OR) or a methoxymethyl ether (MOM-OR).

3.3.1.1. Silyl ethers (R'Si-OR)

Widely used in the protection of alcohols, silyl ethers are generally known to be stable under acidic and basic environments. Additionally, they can be easily removed under mild conditions using fluoride sources such as tetrabutylammonium fluoride (TBAF). Silyl ether stability can be adjusted by altering the substituent on the silicon atoms, in most cases due to steric effects, but also electronic effects. Reactivity in the installation of the protecting group is expected to change as well according to those factors. Therefore, different silyl ethers were proposed for the monoprotection of **CBDV (Table II-4)**.

Table II-4. Reaction parameters for the selective monoprotection of **CBDV** as silyl ethers.[a]

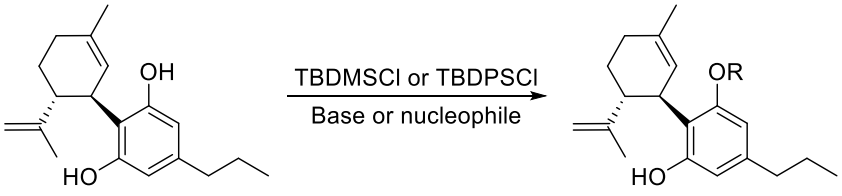

CBDV

R = TBDMS, **171**
R = TBDPS, **172**

Entry	PG	Base or Nucleophile	Solvent	Temp.	Time	Yield % (BRSM %)
1[b]	TBMSCl	Imidazole	DCM	r.t.[c]	4 h	48% (68%)
2[b]	TBMSCl	TEA	THF	Reflux	o.n.	No reaction
3[b]	TBDPSCl	Imidazole	DCM	r.t.[c]	o.n.	51% (74%)
4	TBDPSCl	*N*-methylimidazole/I_2	DCM/DMF	r.t.	4 h	Degradation
5	SEMCl	Imidazole	DCM	Reflux	o.n.	No reaction
6[b]	SEMCl[b]	DIPEA	DCM	Reflux	o.n.	No reaction
7	SEMCl + KI	DIPEA	ACN	Reflux	o.n.	No reaction
8	SEMCl	KF/Al_2O_3	DCM	Reflux	4 h	Degradation

a) These reactions were performed under anhydrous conditions, using 1 equivalent of base, 1 equivalent of the protecting group, and a concentration of 0.1 M to 0.2 M.
b) These reactions were also performed using catalytic amounts of DMAP. No changes were observed in the yield in comparison to the reactions performed in the absence of DMAP.
c) Temperature did not improve the yield.

***tert*-Butyldimethylsilyl (TBDMS)** and ***tert*-butyldiphenylsilyl (TBDPS)** ethers were the first candidates considered. Both are known for their high resistance to basic conditions, and our research group had prior experience working with them in previous projects. The first attempts to install these protecting groups used classical conditions (**Table II-4**, **entries 1 and 3**), first reported by E. J. Corey,[106] using the chloride derivative in combination with imidazole. In this context, the role of imidazole is not serving as a base only. Instead, it acts as a nucleophilic catalyst with the silyl derivate, and the reaction proceeds *via* the corresponding silyl imidazolium intermediate as a

very reactive silylating agent (**Scheme II-12**). This would explain the difference in reactivity observed when other methodologies[107,108] were employed using the same silylating reagents but a different base (**Table II-4**, **entries 2 and 4**), resulting in no reaction or degradation of the starting material.

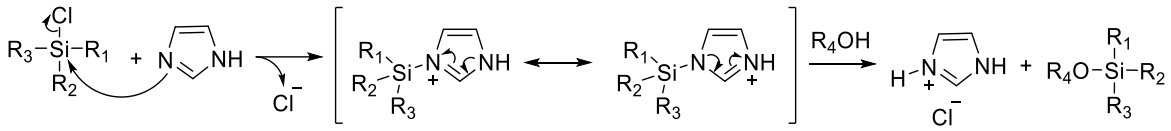

Scheme II-12. Formation of the intermediate imidazolium as a silyl transfer agent.[106]

When the reaction was performed using TBDMSCl (**Table II-4**, **entry 1**), two new aromatic signals appeared at δ 6.20 ppm and δ 6.14 ppm, respectively, along with a new alkenyl signal at δ 5.30 ppm. The splitting of the aromatic protons indicated the installation of an element into the molecule that generated asymmetry, consistent with the selective protection of one of the hydroxyl groups. Additionally, after 4 hours of reaction, a signal at δ 6.25 ppm became visible, which could indicate the beginning of the formation of the disubstituted product. For that reason, the reactions were stopped even though starting material was still observed. The **CBDV**:**171** ratio calculated through the ^{1}H-NMR spectrum at that point was 1 to 1.4.

On the other hand, when the reaction was done using TBDPSCl (**Table II-4**, **entry 3**), no aromatic signal that might correspond to the disubstituted product was observed, showing just new signals corresponding to **172**. This could be because of the greater bulkiness of the reagent, which also relates to the slower rate of reaction, requiring longer reaction times. However, presence of the disubstituted compound was also difficult to determine by ^{1}H-NMR analysis due to the complexity of the aromatic region. Neither did the TLC indicate the presence of the diprotected product. After allowing the reaction to proceed overnight, no change in the proportions of **CBDV** and **172** was observed. Neither the use of temperature nor the addition of more imidazole shifted the equilibrium. Both reactions were purified by flash column chromatography, obtaining yields of 48% (68% BRSM) and 51% (74% BRSM) for **171** and **172**, respectively (**Table II-4, entries 1 and 3**).

Regarding the formation of other silyl ethers, the **2-(trimethylsilyl)ethoxymethyl** (**SEM**) ether caught our attention because it combines the easy cleavage by employing a fluoride source with the robustness of the acetal protecting groups to bases. In the exploration of different methodologies to install the SEM protecting groups, potassium fluoride supported on alumina (KF/Al_2O_3) was employed as a base (**Table II-4, entry 8**). In this methodology, reported by B.E. Blass,[109] KF/Al_2O_3 behaves as a solid heterogeneous base catalyst, facilitating the introduction of the protecting group, and can be recycled for several runs.[110] However, the results were negative, leading to the degradation of the starting material. In fact, the reaction with SEMCl proved to be futile under different conditions, even when imidazole was employed as a base (**Table II-4, entries 5-7**).

3.3.1.2. Pivalate ester (Piv-OR)

The pivaloyl (Piv) protecting group is considered a highly sterically hindered protecting group resistant to a wide range of conditions. It can be deprotected under mild hydrolytic conditions. It drew our attention, as Xudong Gong *et al*.[58] reported the protection of the hydroxyl groups in resorcinol structures, as well as selective removal in several cannabidiol derivatives. However, they did not perform the selective protection of one hydroxyl group, which is a major challenge. The methodology employed was the classical conditions used in the literature, which use pyridine as base and solvent at the same time.

Table II-5. Reaction conditions studied for the monoprotection of **CBDV** as pivalate ester.[(a)]

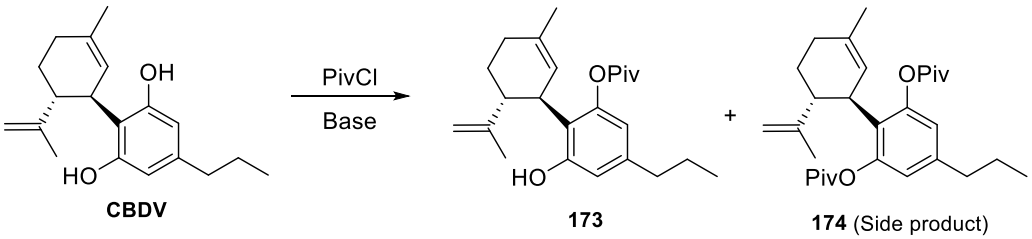

CBDV | **173** | **174** (Side product)

Entry	PG	Base	Solvent	CBDV:173:174	Yield % (BRSM %)
1[(b)]	PivCl (1.1 eq.)	---	Pyridine	0.6:1:1	26% (33%)
2[(b)]	PivCl (0.6 eq.)	DIPEA	Pyridine	5:1:0	Not isolated
3[(b)]	PivCl (0.6 eq.)	NaH	DCM	2:1:1	Not isolated

a) These reactions were performed anhydrously at a concentration of 0.15 M. They were let under stirring overnight at room temperature. Adding catalytic amounts of DMAP or refluxing showed no yield improvement compared to reactions without DMAP or heating.
b) The ratio was estimated by ^{1}H-NMR analysis.

In the first attempt, by adding 0.6 equivalent of pivaloyl chloride (PivCl), **CBDV** showed a fast reactivity, as within two hours, **173** could be observed. In spite of that, the reaction stalled, observing a proportion between **CBDV** and **173** of 5:1. Heating made no difference, so 0.5 equivalents of PivCl were added to the reaction. Unfortunately, this led to the formation of the disubstituted product (**Table II-5, entry 1**). Finally, the isolated yield was 26% for **173** and 18% **174**. Additionally, the separation of the starting material and **173** was found to be very difficult. This lack of selectivity for the monoprotected product was concerning, so different bases were used.

The use of DIPEA as a base did not result in any difference in reactivity, obtaining the same ratio for the product when 0.6 equivalents of PivCl were employed (**Table II-5, entry 2**). Also, the substitution of pyridine by NaH as base and using DCM as solvent instead did not render better results, as the reactivity was enhanced, but the formation of the disubstituted compound also increased (**Table II-5, entry 3**).

After these results for the different experiments, this protecting group was ruled out due to the difficulties in obtaining and isolating the monoprotected product **173**.

3.3.1.3. Methoxymethyl ether (MOM-OR)

The methoxymethyl (MOM) moiety is a frequently used protecting group for phenols. It is stable under basic conditions and can be selectively removed under mild acidic conditions. The standard method for its installation involves using a methoxymethyl halide in the presence of a base, typically a tertiary amine such as DIPEA.

Table II-6. Reaction conditions for the monoprotection of **CBDV** as methoxymethyl ether.[(a)]

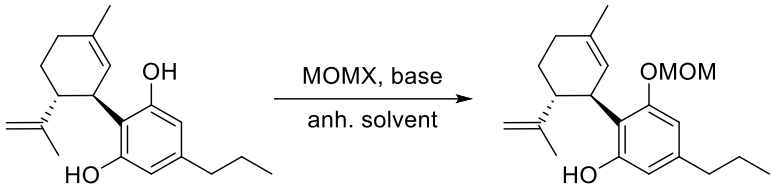

CBDV **175**

Entry	PG (eq.)	Base	Solvent	Temp.	Time	CBDV:Mono:Di[(c)]	Yield % (BRSM %)
1[(b)]	MOMBr (1 eq.)	DIPEA	DCM	r.t.	12 h	---	No reaction
2[(b)]	MOMBr (1 eq.)	DIPEA	DCM	Reflux	o.n.	0 : 1 : 1	36% (44%)
3[(b)]	MOMBr (0.6 eq.)	DIPEA	DCM	Reflux	o.n.	1 : 1.4 : 0.2	38% (58%)
4	MOMBr (0.6 eq.)	DIPEA	DCM	Reflux	4 h	1 : 1.2 : 0	42% (82%)
5	MOMCl (2 eq.)	DIPEA	DCM	Reflux	24 h	---	No reaction
6	MOMBr (0.6 eq.) + NaI	DIPEA	ACN	Reflux	o.n.	---	Degradation
7	MOMBr (0.6 eq.)	DIPEA	THF	60 ºC	4 h	1 : 0.8 : 0.1	30% (54%)
8	MOMBr (0.6 eq.)	DIPEA	ACN	60 ºC	4 h	1 : 0.8 : 0.2	Not isolated
9	MOMBr (0.6 eq.)	DIPEA	DMF	60 ºC	4 h	10 : 1 : 1	Not isolated
10	MOMBr (0.6 eq.)	DIPA	DCM	Reflux	4 h	1 : 0.8 : 0	28% (64%)
11	MOMBr (0.6 eq.)	K_2CO_3	DCM	Reflux	4 h	---	Degradation
12	MOMBr (0.6 eq.)	K_2CO_3	ACN	60 ºC	4 h	1 : 1.2 : 0.1	Not isolated

a) These reactions were performed under anhydrous conditions, a concentration of 0.10 M and using 1 equivalent of base.
b) These reactions were also performed using catalytic amounts of DMAP. No changes were observed in the yield in comparison to the reactions performed in the absence of DMAP.
c) The proportion was estimated by ^{1}H-NMR analysis.

Initially, methoxymethyl bromide (MOMBr) was employed, as it was already available in our research group database, and it is much more accessible compared to the chloride analogue. The first experiments were conducted at room temperature with different amounts of MOMBr in the presence of DIPEA as a base and using dichloromethane as a solvent. Even up to 3 equivalents were used in the reactions, but no formation of any product was observed (**Table II-6, entry 1**). In contrast, when the reaction was put to reflux in the presence of 1 equivalent of MOMBr, splitting of the aromatic signals in the ^{1}H-NMR spectrum indicated the formation of **175**. Unfortunately, a third aromatic signal, corresponding to the symmetric aromatic protons of the diprotected product, also appeared in significant amounts, affecting the overall yield and complicating the purification due to

their similar R_f compared to **175** (**Table II-6, entry 2**). Furthermore, adding MOMBr in portions did not help to avoid the formation of this side product.

Reducing the amount of MOMBr to 0.6 equivalents led to the same reaction rate, but significantly decreased the formation of the diprotected product (**Table II-6, entry 3**). The sweet spot was found when the reaction was stopped after 4 hours, avoiding the formation of the diprotected product and recovering most of the starting material (**Table II-6, entry 4**).

To test this hypothesis and potentially improve the yield, methoxymethyl chloride (MOMCl) was employed. It is the most commonly used reagent for this reaction in the literature, despite the fact that it is more expensive. This might be a hint that the hypothesis was in the right direction. However, no product formation was observed with MOMCl (**Table II-6, entry 5**). Then, the opposite approach was taken, in this case MOMBr was used in the presence of sodium iodide, looking for a halide exchange that would increase the reactivity, as a better leaving group would be generated. In this case, the reaction was performed in acetonitrile to favour the halide exchange. Nevertheless, the starting material seemed to be unstable in these reaction conditions, and no product was recovered. (**Table II-6, entry 6**).

To improve the reaction yield and extend the comprehension of the reaction, different solvents and bases were investigated. As solvents, THF, ACN and DMF were chosen, expecting that a change in polarity might favour the reactivity. In all the cases, the reaction was kept at 60 ºC to replicate the temperature used with CH_2Cl_2 (**Table II-6, entries 7-9**). With THF, it was possible to isolate **175**, but with lower yields and less starting material was recovered. On the other hand, ACN and DMF showed slower rates of reaction, and greater formation of the diprotected product. Diisopropylamine (DIPA) and K_2CO_3 were tested as bases, but neither provided better yields (**Table II-6, entries 10-12**).

After this set of experiments, it was concluded that the best conditions for the installation of the MOM protecting group into the **CBDV** structure were found to be 0.6 equivalents of MOMBr, using DIPEA as the base and CH_2Cl_2 as a solvent. 4 hours at reflux temperature were set as the compromise situation to avoid the formation of the diprotected side product while recovering most of the unreacted starting material (**Table II-6, entry 4**). Finally, the reaction was performed on gram-scale, obtaining similar yields to those reported on a smaller scale.

3.3.2. Formation of the Protected Bitopic Ligand

Once the selective protection of the phenol was achieved with reasonable yields, the synthesis was continued to the formation of the precursor, which is the protected bitopic ligand (PBL). The objective was to obtain it in one step. To achieve this, stoichiometric quantities of the alkyl chain and the monoprotected cannabidiol derivative would be used (**Scheme II-13**).

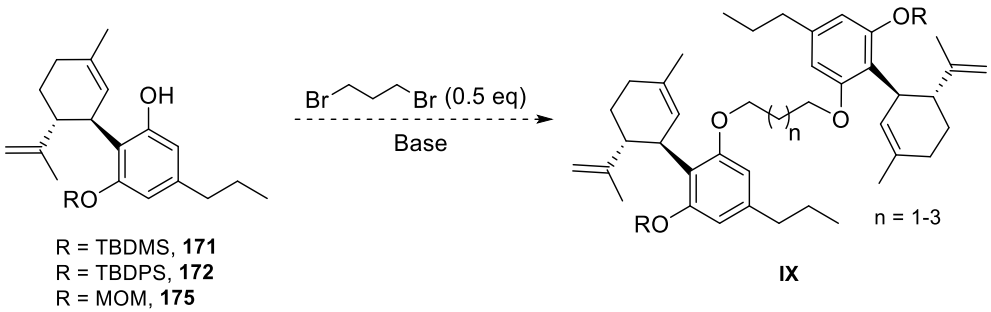

Scheme II-13. Formation of the PBL **IX** using stoichiometric reaction conditions.

3.3.2.1. Synthesis of the TBDPS-Protected Bitopic Ligand

Among all the monoprotected cannabidiol derivatives synthesised in the previous section, **172** was selected for initial experiments, due to its superior overall yield, absence of diprotected side product, and straightforward purification. For the alkyl chain, 1,3-dibromopropane was chosen, in combination with K_2CO_3 as the base and ACN as the solvent, following similar conditions to those reported in the literature for analogous compounds.[111] The first results were unexpectedly negative. Instead of the desired reaction, **172** underwent migration of the protecting group, giving the formation of unprotected **CBDV** and diprotected **176** (**Scheme II-14**).

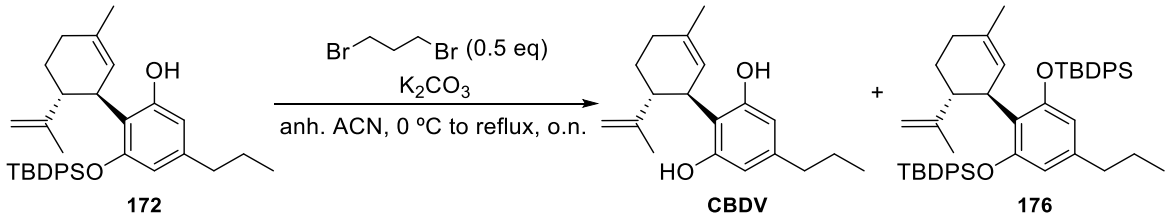

Scheme II-14. Migration of the TBDPS protecting group under basic conditions.

A review of the literature revealed examples of this side reaction under the same conditions. In some cases, these conditions are used to fully deprotect phenols. Also, the cleavage under these conditions is reported to be more pronounced in aryl silyl ethers (*e.g.*, TBDPS), allowing selective deprotection in front of other silyl ethers (*e.g.*, TBDMS).[112–114]

Undeterred by these setbacks, the literature indicated that cleavage under basic conditions only occurs when polar solvents are employed, being ineffective in solvents like benzene, toluene, or diethyl ether.[115] Moreover, there were no reported instances of deprotection or migration of aryl silyl ethers with more hindered bases like DIPEA. Having this in mind, two additional reactions were attempted to synthesise the PBL. On one hand, toluene was used as an apolar solvent in combination with NaH or K_2CO_3 as a base. On the other hand, DIPEA was employed a base in combination with a polar solvent, such as ACN. In none of the reactions the cleavage of the protecting group or migration was identified. However, neither the formation of the PBL nor the *O*-alkylation was observed (**Scheme II-15**). The explanation could be that the conditions with the apolar solvent did not favour the nucleophilic substitution, while DIPEA might be too hindered to effectively lead to the formation of the desired compound.

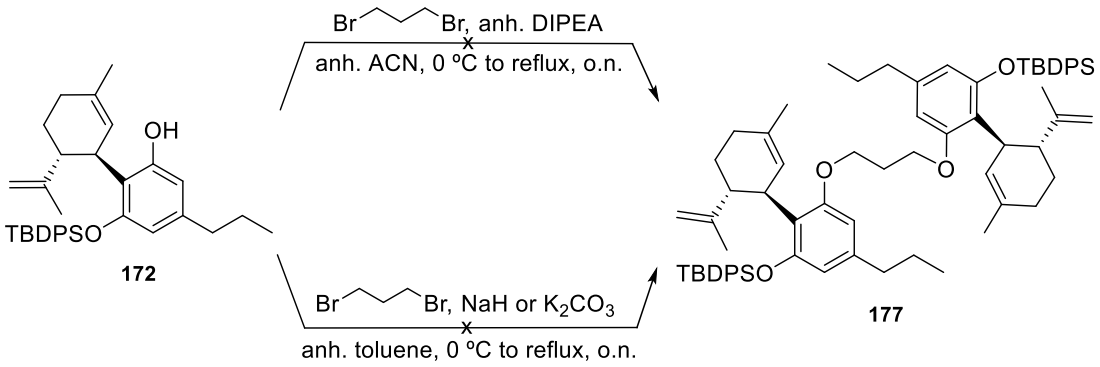

Scheme II-15. Alternative reaction conditions for formation of **177** using **172** as starting material.

Looking at the outcome of these experiments, it was concluded that none of the silyl-protected cannabidiol derivatives were suitable for the synthesis of the bitopic ligand, leaving the MOM-protected product **175** as the only viable option to continue the synthesis.

3.3.2.2. Synthesis of the MOM-Protected Bitopic Ligand

In the first attempt of the synthesis of the PBL employing **175**, the same reaction conditions as in **Scheme II-14** were used. In this case, no migration or cleavage of the protecting group was found, but neither was the formation of the desired compound. Instead, just the product of monoreaction of the dibromoalkane was identified and isolated in 27% yield. As the obtention of the PBL did not seem favourable in just one step, the approach was shifted to a two-step synthesis.

To facilitate this, the *O*-alkylation was optimised using an excess of the dibromoalkane, affording **178** in 81% yield. This same reaction was also performed with the butyl and pentyl chains, obtaining the analogous products **179** and **180**, respectively, with similar yields (**Scheme II-16**).

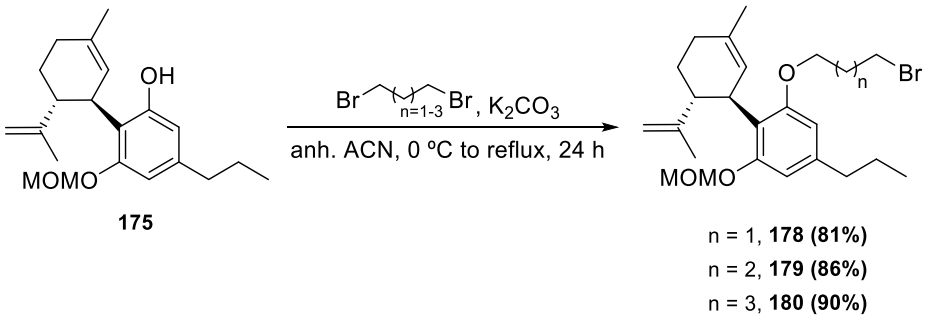

Scheme II-16. *O*-alkylation with different alkyl chain lengths of the MOM-protected **175**.

It is worth mentioning that no purification was needed to isolate the alkylated products, except when the propyl chain was employed. After the work-up of the reaction, it could be observed that vinylic protons were present, likely corresponding to the elimination product. Although it was considered a minor product, the crude mixture had to be purified by flash column chromatography, slightly diminishing the yields obtained for **178**.

To synthesise the PBL structure, the reactivity of the halogenated compound needed to be enhanced. An exchange of the halogen *via* a Finkelstein reaction was proposed. By using NaI in acetone, along with the corresponding brominated compound, the terminal bromine was substituted

by iodine, a better leaving group. Not surprisingly, most of the proton signals displayed the same chemical shift for both products. Thus, the formation of the iodinated derivative was followed by the slight shifting of the α-methylene signal from δ 3.65 ppm (brominated product) to δ 3.41 ppm (iodinated product) (**Figure II-24**).

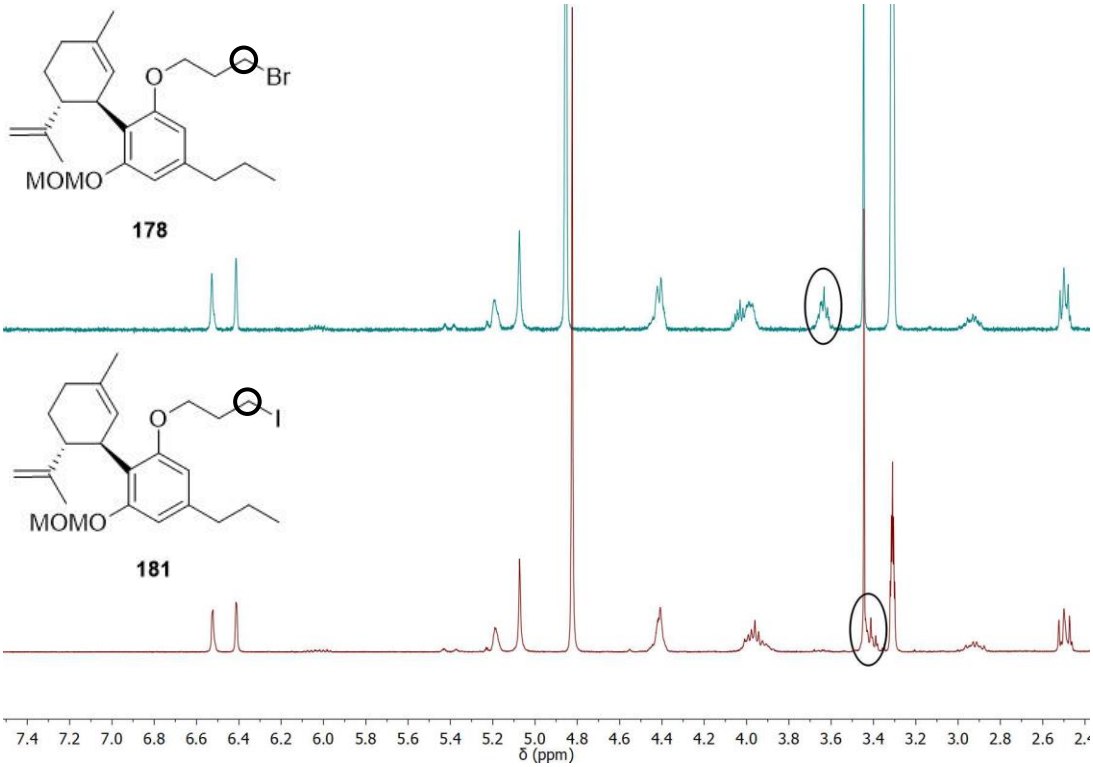

Figure II-24. Comparison of the ^{1}H-NMR (400 MHz, MeOD) spectra of the **178** and the corresponding iodinated intermediate **181**.

Once the halogen exchange was completed, stoichiometric quantities of **175** were introduced using the same Williamson's ether synthesis conditions as in the previous reaction (**Scheme II-17**).

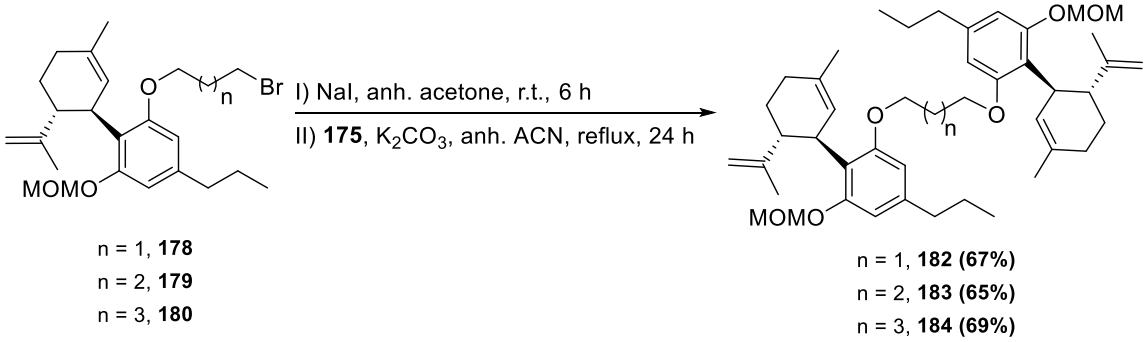

n = 1, **178**
n = 2, **179**
n = 3, **180**

n = 1, **182 (67%)**
n = 2, **183 (65%)**
n = 3, **184 (69%)**

Scheme II-17. Formation of various MOM-PBL by performing a two-step procedure.

The evolution of the reaction was monitored by the disappearance of the methylene signal α to the iodine of the intermediate in the ^{1}H-NMR spectrum, due to the symmetry of the PBLs. The three compounds were obtained with satisfactory yields after their purification by column chromatography.

Once the successful formation of the PBLs was confirmed and the effectiveness of the halogen exchange to enhance reactivity was demonstrated, an attempt was made to optimise the reaction by performing it in one-pot. This involved conducting the halogen exchange simultaneously with the *O*-alkylation. There are analogous structures that have been synthesised with this methodology.[89,116] However, in those cases, the spacer had a larger number of carbons, so the reaction would maybe face less steric hinderance. Considering this, the first attempt to perform the reaction in one-pot was carried out by using the 5-carbon linker to obtain **184** (**Scheme II-18**).

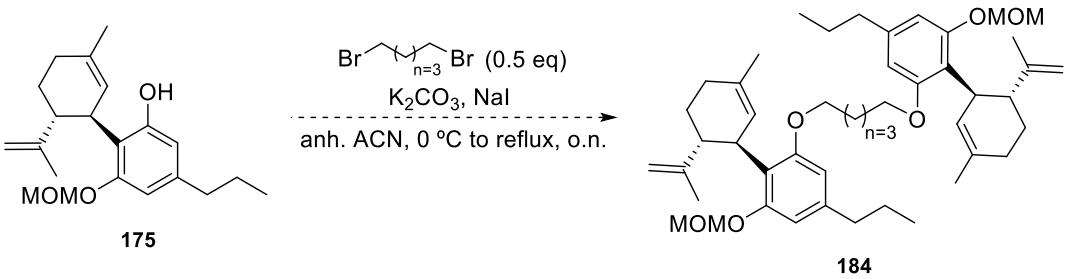

Scheme II-18. Reaction proposal for the formation of **184** in one step.

The reaction was carried out under the same conditions as in **Scheme II-14**, but this time adding NaI. After 18 hours at reflux, the iodinated intermediate of the *O*-alkylated product **180** was observed alongside the excess of **175**. The reaction was kept at reflux for another 24 hours, but instead of obtaining compound **184**, the reaction crude became extremely complex and difficult to interpret by ^{1}H-NMR analysis. It appeared that **175** had degraded, as its characteristic aromatic protons were no longer present. In addition, allylic signals could be observed, probably due to some elimination reaction. Given these results, it was concluded that the obtention of the PBL was not feasible under these conditions and would require further optimisation. However, since the yields obtained in the two-step synthesis were satisfactory, the one-pot reaction was no longer investigated, leaving it as a potential improvement in the future for this synthetic route.

3.3.2.3. Obtention of the Protected Bitopic Ligand without PG

Due to the problems encountered with the monoprotection reaction, performing the synthesis in the absence of a protecting group was suggested. This proposal was initially dismissed, as not blocking one of the hydroxyl groups could give less control over the reactivity of the molecule. One of the concerns was the formation of polymeric structures during the attempts to synthesise the bitopic ligand. However, it might be possible to isolate the bitopic ligand by carefully controlling the reaction rate. This approach could streamline the synthesis to 2 steps by eliminating the protection and the final deprotection reaction.

Before trying to obtain the bitopic ligand, the selective *O*-alkylation of one of the hydroxyl groups was tested. As seen in the previous section, performing a single reaction over **CBDV** was a challenge. To install the 5-carbon spacer, 1,5-dibromopentane was employed in combination with the starting material **CBDV** and K_2CO_3 as a base in anhydrous ACN (**Scheme II-19**).

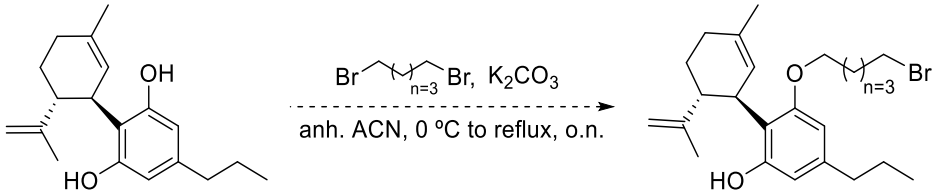

CBDV **185**

Scheme II-19. Williamson's ether synthesis performed over the unprotected resorcinol derivative **CBDV**.

As mentioned at the beginning of **section 3.3.2.2.**, the use of a restricted amount of alkyl halide resulted in poor reaction yields, that could not be solved by the use of heat or longer reaction times, as disubstituted product started to appear under these conditions. Conversely, the use of a larger number of equivalents of 1,5-dibromopentane in the reaction, provided only the disubstituted product (**Figure II-25**). This proved that the formation of alkylated product **186**, and consequently the formation of the PBL, was not possible without blocking one of the hydroxyl groups.

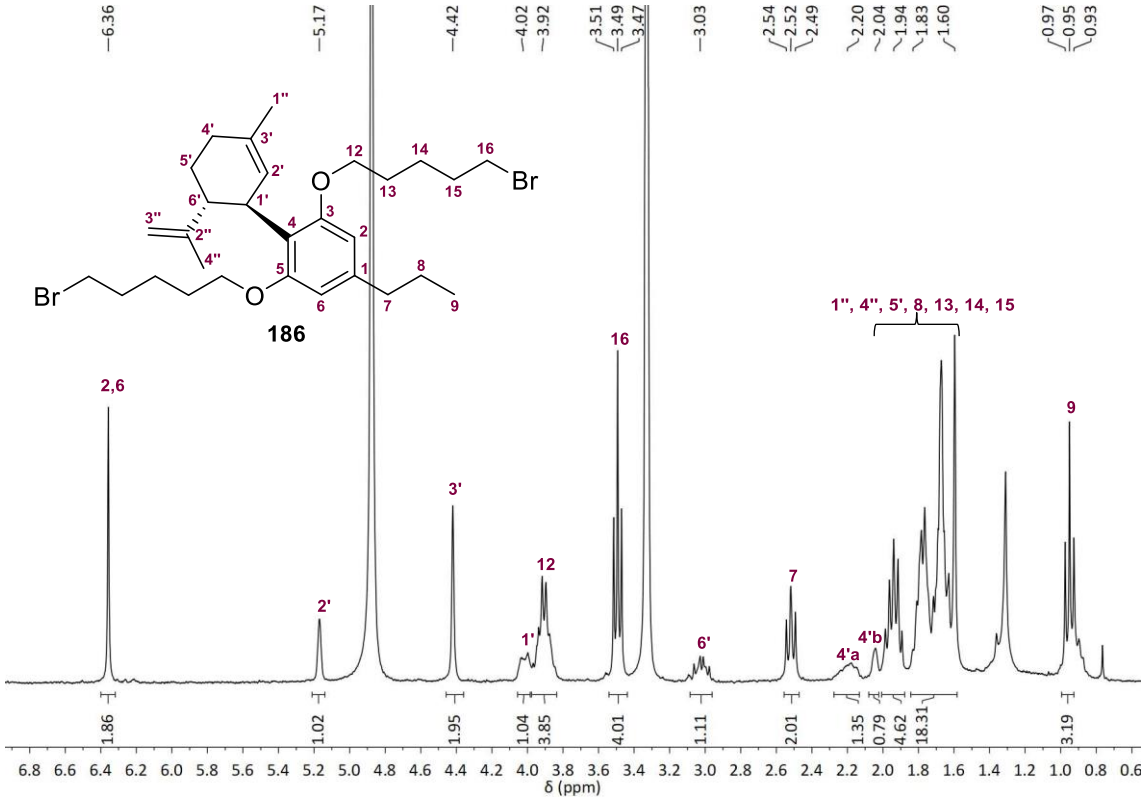

Figure II-25. ^{1}H-NMR (300 MHz, MeOD) spectrum of the dialkylated resorcinol derivative **186**.

3.3.3. Deprotection Reactions to obtain the Bitopic Ligands

In the last step, the deprotection of the hydroxyl groups was intended. The selected methodology would ideally be mild and selective for the MOM cleavage to avoid any side reactions or decomposition due to the peripheral functional groups. The most common conditions for the cleavage of the MOM protecting group are the use of HCl. As previously discussed, the presence of acid could lead to the addition of the hydroxyl group to the double bond, generating THC derivatives (*vide supra*, **Scheme II-8**). However, successful deprotection reactions of MOM ethers have been reported for similar structures,[117,118] suggesting that selective deprotection might be

achievable if the number of HCl equivalents is carefully controlled and H_2O is totally avoided in the reaction.

For that purpose, **182** was used as a substrate for the cleavage of the MOM ether, dissolved in anhydrous MeOH and in the presence of 1 equivalent of HCl, added *via* a 1 M solution in EtOAc (**Scheme II-20**). The first attempt was done at room temperature, but after 6 hours, no changes in the reaction were observed, so the reaction was set to reflux. After 2 hours, ^{1}H-NMR analysis showed no signals of the presence of the MOM protecting group, although vinylic protons could be identified. Despite these observations, the TLC indicated more spots than expected. Purification of the crude by column chromatography was attempted, isolating different side products. Unfortunately, none of them had a set of signals corresponding to the expected product. The reaction was considered unsuccessful without going more in-depth into what side products had been generated. Consequently, alternative methods for deprotecting the hydroxyl groups were explored to find a more reliable and selective approach.

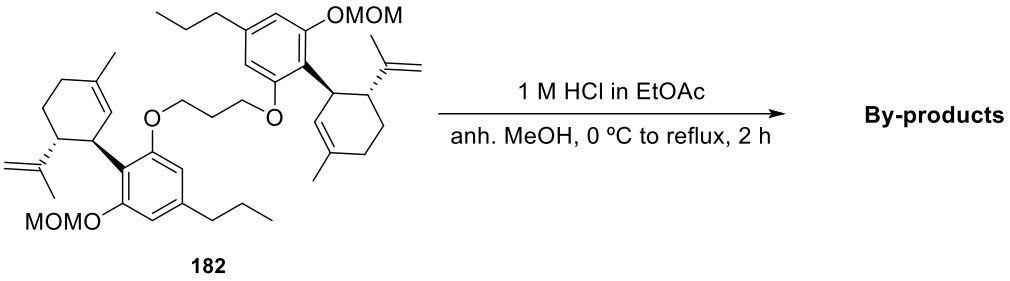

182

Scheme II-20. Unsuccessful deprotection of **182** using HCl.

After a literature review of the different methodologies developed to cleave MOM-protected alcohols, the first try was based on the employment of $ZnBr_2$, as its use for the deprotection of ethers is well-known,[119] providing remarkable results in MOM detagging. As an example, Sohn *et al.*[120] reported in 2005 an improvement in the selectivity of the deprotection when *n*-butanethiol was used alongside $ZnBr_2$. This approach was further investigated in a later publication,[121] where 1-propanethiol (*n*-PrSH) was employed. In this article, the scope of the method was reviewed, including phenol derivatives masked as MOM ethers, affording the corresponding alcohol with high yields. In addition, the use of these reagents seemed to be compatible with the presence of many different functional groups, as the methodology has been reported several times in the literature since its publication.[122,123,124]

Again, **182** was the substrate of choice to test the deprotection reaction. The methodology developed in 2010 was employed, where two equivalents of $ZnBr_2$ and *n*-PrSH in anhydrous DCM were used because the lower boiling point of *n*-PrSH allowed for easier removal after completion of the reaction (**Scheme II-21**). Despite the expectation of completion within 20 minutes, TLC analysis revealed a mixture of compounds. ^{1}H-NMR analysis of the reaction work-up revealed an unidentified set of signals, none of which could be assigned to the expected product or the starting material.

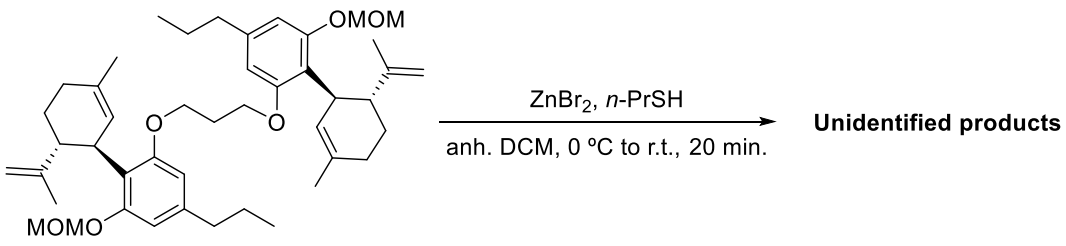

182

Scheme II-21. Unsuccessful deprotection conditions employed on **182**.

After these two unsuccessful attempts, it was thought that synthesising a model for the following studies of deprotection might be useful to avoid wasting more product, which was quite time-consuming to obtain. Thus, **187** was afforded as a framework by performing a Williamson's ether synthesis on the starting material **175** and using 1-iodobutane (**Scheme II-22**). This structure was considered representative because of the four-carbon chain, aligning with the intermediate length of the analogues that are objective of this chapter. Also, it was more representative than **179** because of the absence of the halogen atom at the end of the chain, which could induce some undesired reactivity.

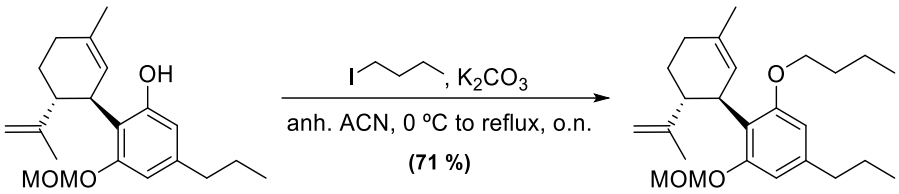

175 **187**

Scheme II-22. Synthesis of **187** as a model to study MOM deprotection methodologies.

Before exploring any other methodology, HCl and $ZnBr_2$ were tested again for the deprotection, despite prior negative results. Similar ^{1}H-NMR spectra were obtained, finally dismissing these two methodologies.

The following approach tried was the use of acetyl chloride (AcCl) in combination with MeOH aiming to generate HCl *in situ*. The formation of HCl by using these two reagents was first explored in 1998,[125] and it was conveniently used for the cleavage of MOM ethers in 2023 for the synthesis of THC derivatives.[126] In this way, the controlled formation of HCl might be beneficial if the deprotection occurs faster than the addition to the double bond, or any possible side reaction.

Table II-7. Optimisation of the reaction conditions for the deprotection of **187** by using AcCl and MeOH.

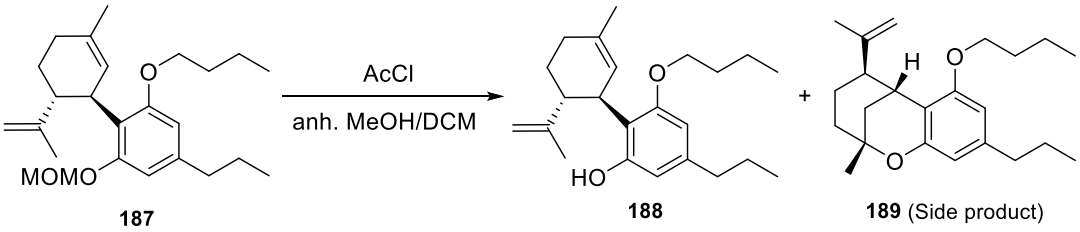

187 **188** **189** (Side product)

Entry	AcCl (eq)	T (ºC)	Time (h)	187:188:189[(a)]
1	30	-10 ºC	5 h	0 : 0 : 1
2	20	-10 ºC	5 h	0 : 0.2 : 1
3a	10	-10 ºC	4 h	1 : 0.1 : 0
3b		-10 ºC	o.n.	1 : 0.6 : 0.1
3c		0 ºC	48 h	0 : 1 : 1
4	10	0 ºC	o.n.	0 : 1 : 1

a) The ratio between the different products was estimated by ^{1}H-NMR analysis.

In the first attempt, the same reaction conditions as those reported by Schneider group were applied.[126] For that, to a solution of **187** at -10 ºC in anhydrous MeOH and DCM, were added 30 equivalents of AcCl (**Table II-7, entry 1**). The different examples of deprotection proceed between 3 hours and 2 days. Despite that, the ^{1}H-NMR spectrum showed that **187** had been totally deprotected after 5 hours, giving rise to *iso*-THCV derivative **189**, with no evidence of **188**. This confirmed that the reaction was effective for the deprotection of the hydroxyl group, but the generation of HCl was too fast to avoid the formation of cyclised products. Before giving up on this method, different optimisation attempts were made, starting by decreasing the amount of AcCl (**Table II-7, entries 2-3a-c**). The use of 10 equivalents of AcCl seemed optimal to avoid the formation of the cyclised side products, but the rate of reaction slowed down considerably, extending the reaction time up to 48 hours. Although no starting material was observed after this period, the formation of *iso*-THCV derivative **189** remained considerable. In addition, the influence of temperature was also studied by performing the reaction at 0 ºC (**Table II-7, entry 4**), resulting in an increased reaction rate, not observing any starting material after 16 hours, but with a considerably high amount of side product.

This methodology proved to be useful for the deprotection of the hydroxyl group in the model molecule, avoiding the total conversion into the cyclised side product or any other further undesired side-reactions. It was decided not to further do any optimisation with the model **187**, as reactivity might change with the PBL.

Different cleavage conditions within this methodology were tried on **182**. However, it was more difficult to determine the proportion between the different side products observed, due to the more complex structure. Despite that, it was concluded that the reaction did not happen when less than 5 equivalents of AcCl were employed or when the reaction temperature was below -10 ºC. Finally,

it was determined that the optimal reaction conditions to minimise the formation of side products while obtaining the full deprotected product were to use 5 equivalents of AcCl at 0 ºC for 48 hours (**Scheme II-23**). Under these conditions, bitopic ligands **158**, **159** and **160** could be afforded, along with mono-deprotected analogues **190**, **191** and **192** and other undesired side products. Unfortunately, the high number of side products, along with the difficulty of purification, made necessary to run several flash column chromatographies for the same reaction, providing poor yields for the fully deprotected bitopic ligands.

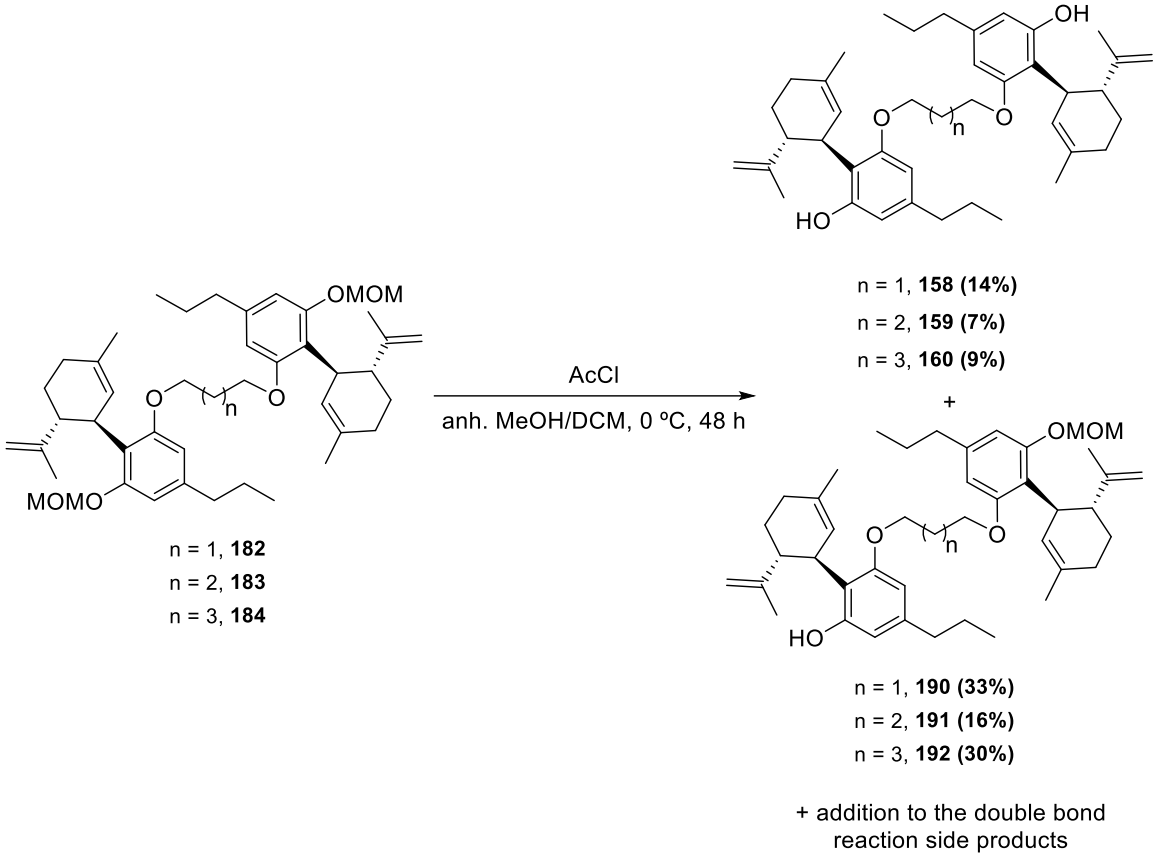

Scheme II-23. Access to bitopic ligands derivatives through deprotection reaction with AcCl and MeOH.

3.4. *In vitro* Biological Activity of Novel CB_2R Bitopic Ligands

The biological activity of the three CBDV-based bitopic ligands was assessed through *in vitro* assays carried out by Dr. Iu Raïch, researcher in Prof. Gemma Navarro's research group at the Faculty of Pharmacy and Food Science of the Universitat de Barcelona.

Inspired by previous publications,[74,89] and supported by energy minimisation (EM) studies, it was hypothesised that these bitopic ligands could interact with the allosteric cavity and the metastable binding site at the CB_2R, enhancing efficiency and potency compared to **CBDV** as positive allosteric modulators (PAMs).

To test this hypothesis and elucidate how these molecules interact with the allosteric and metastable cavities of the CB_2R, **adenyl cyclase (AC) inhibition** assays were carried out to assess changes in cAMP levels. These assays were performed on HEK-293T cells with stabilised CB_2R expression,

which had been treated with forskolin (FSK) to activate AC, generating cAMP levels that were normalised to 100% (**Figure II-26**). The agonist **JWH-133** was used to interact with the orthosteric site, with the expected outcome being a reduction in cAMP levels due to AC inhibition. Subsequently, **JWH-133** was used in the presence of 200 nM concentrations of the different bitopic ligands. The addition of these synthesised compounds is expected to modulate the response by either amplifying or attenuating the inhibitory effect of **JWH-133**, thereby decreasing or increasing the total cAMP levels compared to when **JWH-133** is used alone, acting as PAMs or NAMs, respectively. Besides the bitopic ligands, **CBD** and **CBDV**, known to behave as a NAM and a PAM, respectively, at CB_2R,[74] were also tested as reference allosteric modulators and to be compared with the bitopic ligands.

The data from these dose-response experiments are summarised in **Table II-8** and depicted in **Figure II-26**. To evaluate the behaviour of the bitopic ligands **158**, **159** and **160**, the maximum effect (E_{max}) values were analysed. A lower E_{max} indicates that the ligand behaves as a PAM, as it enhances the inhibition effect produced by **JWH-133** on the AC, whereas a higher E_{max} suggests NAM-like behaviour of the ligand as NAM, when compared to the control (absence of the allosteric ligand). In these assays, in all cases, the E_{max} values were higher than those observed with the orthosteric agonist **JWH-133** alone, suggesting a less effective AC inhibition and correspondingly higher levels of cAMP.

Another key parameter in these assays is the half-maximal effective concentration (EC_{50}), which reflects the concentrations of a compound required to inhibit 50% of AC activity (or the signalling response). For clarity, EC_{50} values are often reported as their negative logarithm (pEC_{50}). Higher pEC_{50} values (left-shifted dose-response curves) indicate higher potency, as less compound is needed to achieve the same effect. In this study, all tested compounds, except for compound **160**, displayed lower pEC_{50}, and thus higher EC_{50} values compared to the response elicited by **JWH-133** alone, indicating a decrease in potency for AC inhibition.

Table II-8. Modulation of agonist **JWH-133** downstream signalling in the cAMP levels by the different bitopic ligands **158-160**. In all the assays orthosteric ligand **JWH-133** was employed. Values were calculated using nonlinear regression analysis. Data represent mean ± SEM from n = 3 independent experiments performed in duplicate.

Ligand	pEC_{50} (nM)	E_{max} (%)	E_{max} in relation to JWH-133 alone (%)
---	8.2 ± 0.2	46 ± 2.7	---
CBD	6.7 ± 0.2	50 ± 8.0	92% NAM
158	7.8 ± 0.3	53 ± 5.0	87% NAM
159	7.2 ± 0.3	51 ± 6.0	90% NAM
160	8.6 ± 0.3	62 ± 3.2	74% NAM

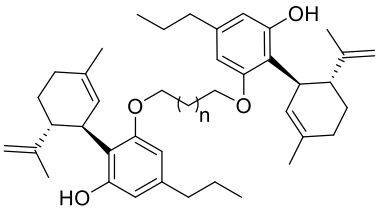

n = 1, **158**
n = 2, **159**
n = 3, **160**

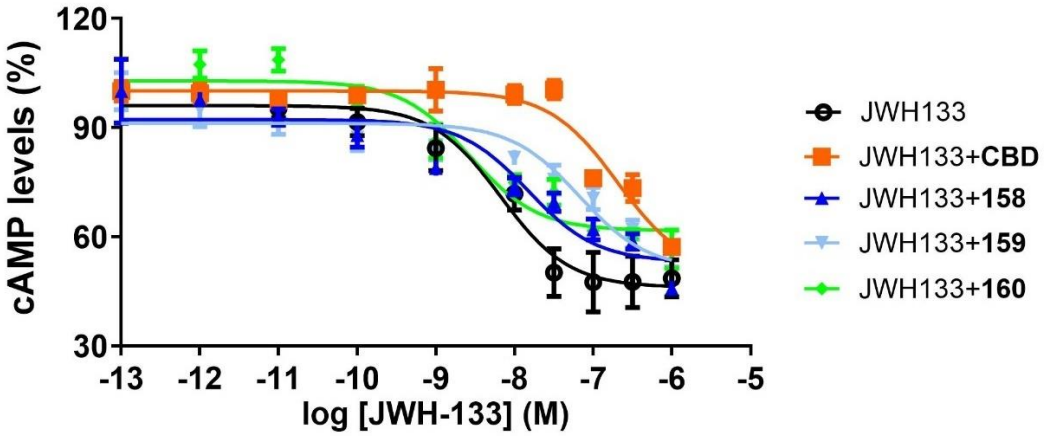

Figure II-26. Representation of the reduction of the cAMP levels in HEK-293T cells upon treatment with orthosteric agonist **JWH-133** alone and in combination with CBDV-based bitopic ligands **158-160**. Whiskers represent the total range of values within each sample.

The results obtained for the AC inhibition assays were disappointing, as our initial hypothesis posited that the bitopic ligands would behave as PAMs at CB_2R, potentially outperforming **CBDV**, but the contrary behaviour was observed, providing a NAM-like dose-response profile. However, to further explore their potential, **β-arrestin recruitment assays** were conducted, based on the hypothesis that the distinct structure compared to **CBDV** might induce a biased signalling, affecting the two CB_2R-activated pathways differently.

For these experiments, the same cell culture conditions as the AC inhibition assays were employed. β-arrestin recruitment was quantified using the orthosteric CB_2R agonist **JWH-133** as a reference. Subsequently, CBDV-based bitopic ligands **158**, **159** and **160** were assessed in the presence of **JWH-133,** and changes in β-arrestin levels were measured. For comparison, **CBD** (NAM) and **CBDV** (PAM)[74] were also tested (**Table II-9** and **Figure II-27**).

The data revealed that the three bitopic ligands had negligible effects on β-arrestin recruitment at CB_2R. Both E_{max} and pEC_{50} values showed no significant differences compared to **JWH-133** alone, suggesting that the bitopic ligands **158**, **159** and **160** do not modulate β-arrestin signalling at CB_2R. Interestingly, the curve of response of compound **160** showed has not arrived at a plateau, indicating that the E_{max} has not been reached within the tested concentration range, which might be due to its lower potency, requiring higher concentrations, or that the mechanism of interaction might follow a non-traditional pattern, further studies are required to confirm this.

Table II-9. Modulation of agonist **JWH-133** downstream signalling in the β-arrestin recruitment the different bitopic ligands **158-160**. In all the assays orthosteric ligand **JWH-133** was employed. Values were calculated using nonlinear regression analysis. Data represent mean ± SEM from n = 3 independent experiments performed in duplicate.

Bitopic ligand	pEC_{50} (nM)	E_{max} (%)	E_{max} in relation to JWH-133 alone (Fold)
---	7.7 ± 0.1	59 ± 3.6	---
CBD	7.5 ± 0.4	33 ± 4.5	0.6 (NAM)
CBDV	8.3 ± 0.2	76 ± 4.7	1.3 (PAM)
158	8.0 ± 0.2	52 ± 3.1	0.9 (NAM)
159	7.6 ± 0.3	62 ± 6.6	1 (--)
160	6.9 ± 0.3	68 ± 9.9	1.1 (PAM)

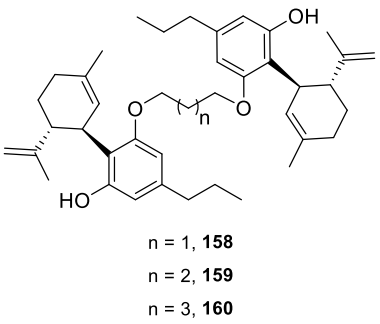

n = 1, **158**
n = 2, **159**
n = 3, **160**

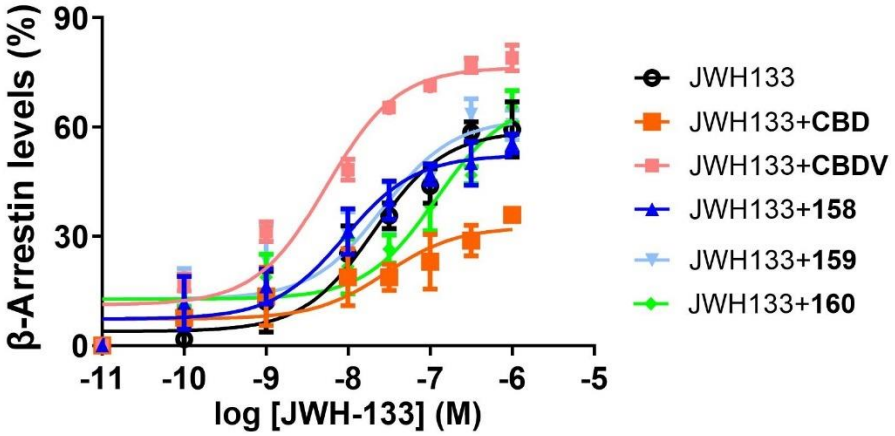

Figure II-27. CB_2R-dependent β-arrestin recruitment for HEK-293T cells upon treatment with orthosteric agonist **JWH-133** alone and in combination with CBDV-based bitopic ligands **158-160**. Whiskers represent the total range of values within each sample.

The outcome from these first assays pointed out that the CBDV-based bitopic ligands **158, 159** and **160** mainly acted as NAMs or neutral allosteric modulators for both signalling pathways. The hypothesis proposed to try to explain these results was that the interaction of both units of the bitopic ligand might not be happening in the two cavities of the same receptor, but instead it might interact with two cavities in two different receptors, acting as a homodimer.[127] To test this out **bimolecular resonance energy transfer (BRET)** assays were performed. BRET can be a powerful tool for studying the interaction of bitopic ligands with GPCR homodimers, specifically to determine whether the ligand engages with both protomers of the dimer. BRET relies on the non-radiative transfer of energy from a donor molecule (typically a bioluminescent protein) to an acceptor molecule (typically a fluorescent protein), which occurs only when the donor and acceptor are in close proximity (usually within 10 nm). This results in a measurable emission of light from the acceptor at its specific emission wavelength, instead of the donor's emission wavelength. The ratio of the light emitted by the acceptor to that emitted by the donor is measured. An increase in this ratio indicates an interaction or proximity between the donor and acceptor, while a decrease or lack of change indicates no interaction.

For this experiment, HEK-293T cells co-transfected with a constant amount of cDNA encoding for CB_2R-Rluc and CB_2R-GFP were employed. After registering the BRET baseline signal in the absence of ligand (**Figure II-28**, **black bar**), the three bitopic ligands were tested at concentrations of 100 nM. In addition, **CBD** and **CBDV** were tested as negative controls. BRET signal for the bitopic ligands showed no significant differences (**Figure II-28, yellow and orange bars**) when compared to control, as the difference was not above 20 to 30 mBU (mBU_{CBD} = 53.5, mBU_{CBDV}, = 42.8, $mBU_{Control}$ = 52.1), that would indicate a moderate or a partial interaction based on the statistical analysis. This means that these ligands did not induce any conformational change in the homodimer. Same results were obtained for the **158**, **159** and **160** (**Figure II-28**, **blue, light blue and green bars**, respectively). Despite BRET value for **158** showed the highest variation with the control (mBU_{158} = 72.7 vs. $mBU_{Control}$ = 52.1) it was not significant enough to affirm that there is an interaction with both protomers, being more likely that the interaction with one of them has promoted a conformational change that has increased the proximity between RLuc and GFP^2 tags.

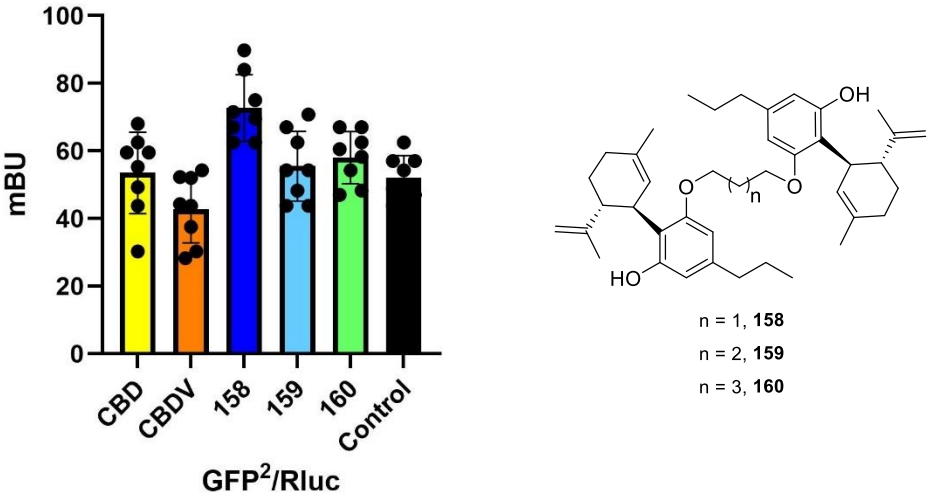

Figure II-28. $BRET_{max}$ measured in HEK-293T cells treated with CBDV-based bitopic analogues **158**, **159** and **160**. BRET data are expressed as the mean ± SEM of eight different experiments performed in triplicates. mBu: miliBret units. Whiskers represent the total range of values within each sample.

After testing the different hypothesis proposed for the biological activity of the bitopic ligands synthesised, all of them were discarded as all results indicated that our compounds provoked no significant changes in CB_2R activity. This behaviour, contrary to what was expected, might be because of several reasons. **Conformational constrains** is one of the reasons, as the structural complexity required for the dual binding with the allosteric and metastable binding sites might prevent the ligand from adopting the optimal conformation necessary for effective binding at either side. Another reason might be that CB_2R, upon interaction with the first unit of the bitopic ligand, adopts a **conformational state** that is not conductive to the desired response. In addition, the pharmacophore might require a different conformational state to adopt the active form expected.

Despite these results, it would be interesting to perform additional assays studying the **residence time** of these ligands at CB_2R, particularly in light of the observations made for compound **160** in the β-arrestin recruitment assays. Residence time, which measures the duration a ligand remains

bound to its target receptor, is a critical parameter in understanding the overall pharmacological effect of a compound. While these ligands may not elicit an enhanced effect compared to **JWH-133** when used alone, they may prolong receptor activation due to their unique conformational constraints. These conformational constraints could hinder the dissociation of the orthosteric agonist from the receptor, potentially leading to sustained receptor activation. This is because the bitopic ligand, by simultaneously occupying both the orthosteric and allosteric binding sites, might effectively block the agonist's exit from the binding cavity. This hypothesis is supported by structural data illustrated in **Figure II-20**, where the spatial overlap of the bitopic ligand with the receptor cavity suggests steric hindrance that could trap the orthosteric agonist.

Furthermore, prolonged residence time is often associated with increased therapeutic efficacy, as it can lead to sustained receptor modulation even at lower ligand concentrations. Investigating this property could provide valuable insights into the potential advantages of bitopic ligands over traditional orthosteric or allosteric modulators. Techniques such as kinetic binding assays or advanced computational modelling could be employed to quantify the residence time and confirm the proposed mechanism.

This extended analysis would not only deepen our understanding of the interaction dynamics between CB_2R and these ligands but also guide the optimisation of bitopic ligand design for enhanced pharmacological profiles.

4. Conclusions

The primary objective of this chapter was to synthesise a family of bitopic ligands designed to interact simultaneously with the allosteric site and the exosite of the CB_2R, aiming to modulate the receptor response in a manner consistent with positive allosteric modulator (PAM) behaviour.

After a rational design, based on the previous results published and supported by energy minimisation calculations, the synthesis of the bitopic ligands was initiated. A key milestone was the optimisation of the synthesis of **CBDV** as a pharmacophore, a crucial compound for the construction of the bitopic ligands. The synthesis route was streamlined, reducing the number of steps from six to four, all scalable to gram-scale. This optimisation significantly reduced both the time and cost required for obtaining **CBDV**.

Then, using **CBDV** as a starting material, the three proposed bitopic ligands **158**, **159** and **160** were successfully afforded in a five steps synthesis (**Scheme II-24**). Despite challenges arising from the high reactivity of the molecule due to the presence of multiple functional groups, the synthesis was achieved, showcasing the feasibility of this strategy.

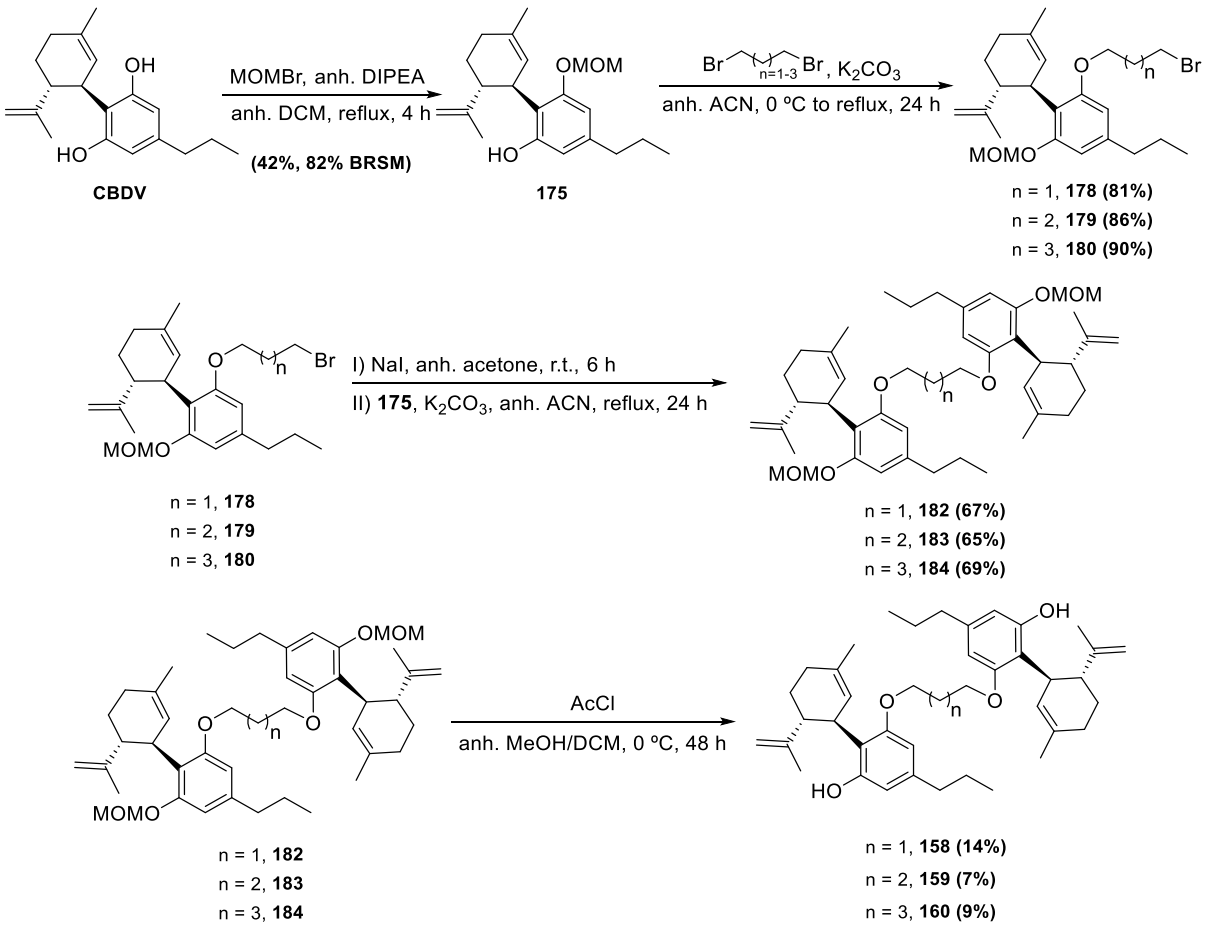

Scheme II-24. Synthetic route developed in this chapter to obtain the CBDV-based bitopic ligands **158**, **159** and **160**.

Finally, the biological activity of the CBDV-based bitopic ligands was studied, with the goal of comparing their efficacy and potency against previously reported ligands, such as **CBDV**, and using **JWH-133** as an orthosteric agonist. Unexpectedly, the data revealed that three bitopic ligands behaved as negative allosteric modulators (NAMs), contrary to the hypothesised behaviour. They did not lower the cAMP levels as much as when the orthosteric ligand **JWH-133** is used alone and produced β-arrestin pathway responses comparable to when the agonist was used alone. In addition, BRET assays did not provide any evidence suggesting that these bitopic ligands interact with two cavities of two different CB_2R acting as a homodimer. This behaviour, contrary to the one hypothesised, could be attributed to conformational constrains or specific required conformational states to induce the desired response. However, additional *in vitro* test to assess the retention time of these bitopic ligand could be interesting, as they have not increased the efficacy of the response, but they might prolong it, which is interesting from the perspective of therapeutic applications.

Allosteric modulation is complex and it can result in a range of effects. Furthermore, there is still little known about interaction of ligands with the metastable binding site of CB_2R. Also, using a bitopic ligand to interact with allosteric and metastable binding sites is an idea that has not been even explored in the literature. That is why, despite the negative results, from the perspective of the proposed hypothesis, the data obtained in the *in vitro* assays, as well as the knowledge afforded in the synthesis of these bitopic ligands, will help to create better models with MD tools to propose new bitopic ligand structures.

Chapter IV

Halogen- and Thioether-Containing Ligands Targeting the Allosteric CB_2R Binding Site

A more profound understanding of GPCRs has enabled the identification of key residues which are essential for their activation, known as toggle switches. Phe117$^{3.36}$ and Trp258$^{6.48}$, located near the allosteric site, have been identified as crucial for the activation of cannabinoid receptor 2 (CB_2R). Unlike CB_1R, the activation of CB_2R is predominantly driven by the interaction with the tryptophan residue. Therefore, ligands capable of interacting exclusively with this residue may exhibit significant selectivity for CB_2R, thereby avoiding the side effects associated with CB_1R activation. This strategy is tested in this chapter by synthesising various CBDV analogues incorporating a halogen atom or a thioether moiety. These allosteric ligands are expected to interact with the aromatic ring of the key amino acid residue through these moieties, enhancing their properties as positive allosteric modulators.

1. Introduction

1.1. Role of "Toggle Switch" Residues in CB_2R Activation

Central to the activation mechanism of GPCRs are specific amino acid residues known as **toggle switches.** These residues, typically located at key positions within the transmembrane helices of the receptor, are critical for maintaining GPCRs structural integrity and mediating the conformational changes necessary for their activation. Among these, Phe3.36 and Trp6.48 are particularly noteworthy in the activation of GPCRs, to transition between the active and inactive conformations.[78] This statement was also made for CB_2R when, in 2020, Hua *et al*.[77] unveiled the structures of an agonist-bound CB_2R in a complex with the Gi protein as well as the crystal structure of agonist-bound CB_2R. The agonist, a tricyclic tetrahydrocannabinol system named AM12033, interacts with the orthosteric binding pocket with an L-shaped conformation. In the structure of the complex, it was appreciated that the side chain of the toggle switch residue $Trp258^{6.48}$ experienced great conformational change (**Figure II-29**). When these same residues were studied in the CB_1R, it was observed that both residues, $Phe200^{3.36}$ and $Trp356^{6.48}$, suffered a change in their conformation in what is called a "twin toggle switch". This suggests a more complex activation mechanism for CB_1R compared to CB_2R. This is an important observation, as both receptors share 44% of the total sequence identity and have 68% sequence similarity, which makes it difficult to specifically modulate these receptors individually. Consequently, molecules that could interact just with the residue Trp6.48 might trigger a selective activation of CB_2R, avoiding the undesired side effects associated with CB_1R activation.

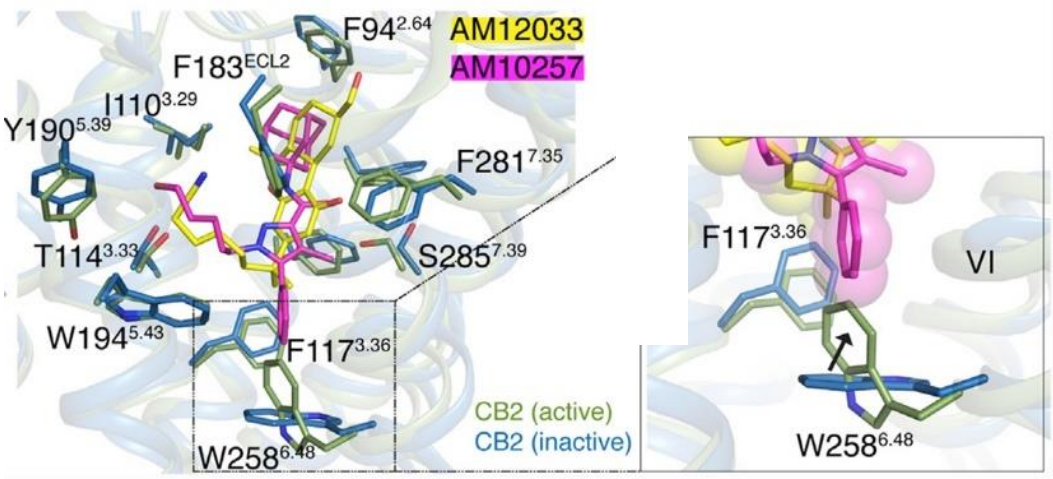

Figure II-29. Left: MD simulation of CB_2R complex with agonist AM12033 (yellow) and antagonist AM10257 (magenta); Right: Comparison of the toggle switch residue conformation in active (green) and inactive (blue) CB_2R. Image extracted from reference 77.

As stated in **section 5.1.** of the **General Introduction**, the side chain of CBD analogues interacts with an intracellular hydrophobic cavity where these two key residues are found, being able to induce conformational changes as positive or negative allosteric modulators. Inspired by the positive results obtained in the article published by our research group,[74] some modifications in the structure of the CBD analogues were proposed with the purpose of interacting with these residues

strongly, thereby stabilising a particular conformational state of the receptor. These interactions would increase the allosteric modulation effects observed, thus modulating the receptor activity.

Both residues, Phe117$^{3.36}$ and Trp258$^{6.48}$, are capable of engaging with non-covalent interactions, such as π-π stacking and hydrophobic interactions, due to their aromatic moiety. These interactions become particularly interesting in the presence of elements of group VI (chalcogens) and group VII (halogens), as they are capable of participating in non-covalent interactions named **chalcogen** and **halogen bonds**, respectively.

1.2. Halogen and Chalcogen Bond

Halogen atoms possess unique electronic properties that are often essential for molecular recognition of alkyl and aryl halides in biomolecular contexts. In the case of iodine, bromine and, to a lesser extent, chlorine, they can interact with electron donors *via* strong and complex interactions known as the **halogen bonds (XB)**. These have garnered increasing attention as a rational and reliable strategy in molecular design, aiming at improving drug-target binding affinity and providing alternatives to classical polar interactions such as hydrogen bonds.[128–130] These directional and electrostatically driven non-covalent interactions are formed between a covalently bonded halogen atom (XB donor; X = Cl, Br or I) and a nucleophile or the π electrons of an unsaturated system (*e.g.*, aromatic ring; XB acceptor). This interaction is driven by the anisotropy of the charge distribution of halogen atoms, because of a deficiency in electron density on the outer lobe that creates a positive electrostatic potential named **σ-hole**. This partial positive charge along the halogen σ-bond diminishes with the size of the halogen atom, to the point that fluorine atom interactions are considered negligible (**Figure II-30**).[131]

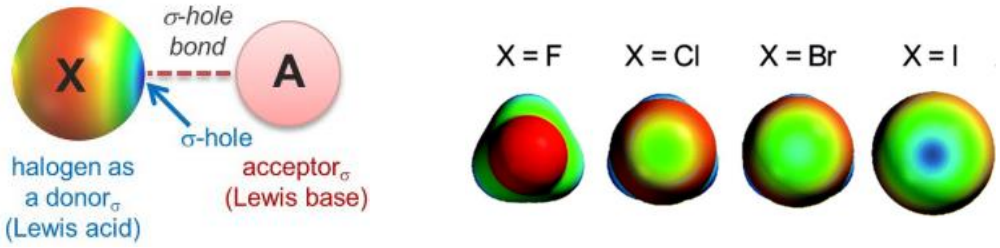

Figure II-30. Left: Schematic representation of the halogen bond (adapted from *J. Chromatogr. A* **2020**, *1616*, 460788); Right: Electrostatic potential mapped onto the surfaces of halogens. The positive σ-hole region is coloured in blue, while the most negative surface potential is coloured in red (adapted from *Chembiochem.* **2020**, *21*, 911).

Halogen bonds are prevalent in various inorganic, organic, and biological systems. One-third of drugs in clinical trials contain halogen atoms, which significantly alter the physicochemical properties of ligands, enhancing their affinity and selectivity for drug targets. Although they have a high presence in therapeutic drugs, the structural basis of their interactions with biological targets has remained poorly understood until recently. A database survey revealed an increasing trend of heavy organohalogens over organofluorines during the drug development process, which is consistent with the weaker halogen bonds from fluorine.[130]

Halogen bonds involving carbonyl oxygen atoms are the most common in the binding of ligands to their target proteins, probably due to the abundant presence of this moiety in the amino acid backbone.[129] However, there are few examples of halogen-π interactions of modulating ligands with aromatic moieties,[132,133] despite their widespread occurrence in binding pocket residues.

A less familiar σ-hole-based interaction is the **chalcogen bond (ChB)**, a non-covalent interaction between a Lewis base (B_L) or ChB acceptor, such as a carbonyl group or an aryl moiety, and an electrophilic element of the Group VI (O, S, Se, Te). Although less studied than XBs, recent years have witnessed some applications in anion binding and transportation,[134] materials and crystal engineering,[135] and catalysis.[136] The main difference with halogen bond resides in the existence of a second substituent on the chalcogen (Ch) atom. Because of its valency, two regions of positive electrostatic potential are situated on the outer part of the Ch atom, opposite to each electron-withdrawing group (EWG) at angles of 180° (**Figure II-31**).[137] Recently, an analysis of the PDB database, revealed that numerous protein-ligand complexes, where the ligand includes a chalcogen atom, adopt configurations conducive to the formation of chalcogen bonds. Of particular interest for us, are the chalcogen-π bonds, formed between the π-orbital of the σ-hole acceptor (*e.g.*, aryl moiety) and the σ* antibonding orbital of the molecule containing the chalcogen.[138]

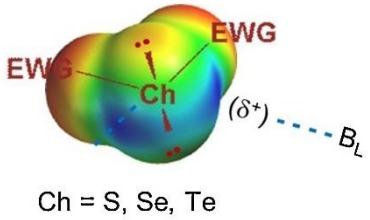

Figure II-31. Representation of the chalcogen bond (adapted from reference 137). The positive σ-hole region is coloured in blue, while the most negative surface potential is coloured in red.

Following a rational design, supported by the observation made in the computational calculations of the article published by Heroven *et al.*,[133] the strategy proposed in this chapter involves the incorporation of sulfur and heavy halogen atoms into potential ligands of the CB_2R. This may lead to active compounds with improved positive allosteric modulating properties due to the interaction of the halogen atoms with the aromatic moiety of key activation residues of the receptor (**Figure II-32**).

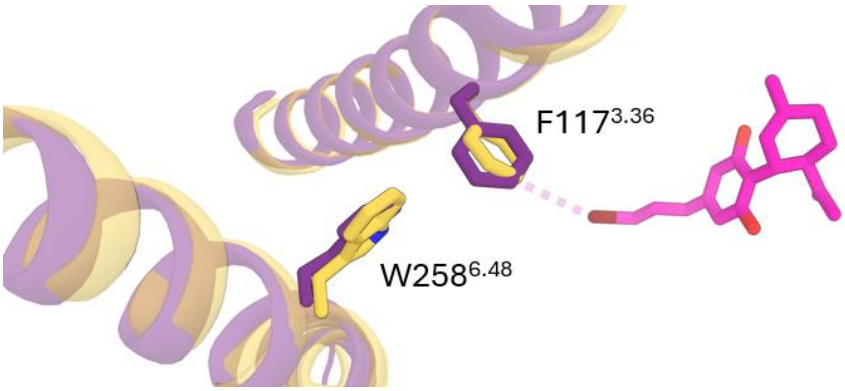

Figure II-32. Representation of a halogen-containing CBDV analogue interacting with the toggle switch residues in the cannabinoid receptor 2. F = Phenylalanine, W = Tryptophan.

2. Objectives

The positive results obtained beforehand[74] encouraged our research group to keep studying structures that can interact with the allosteric site of CB_2R as PAMs. In this chapter, different CBDV analogues were proposed based on the observations made on the residues involved in the activation of these receptors. The design of the proposed ligands was based on the following rationale (**Figure II-33**):

- To maintain a side-chain length comparable to that of CBDV, which has been demonstrated to be the most effective PAM tested. The side chain in the new target ligands would be of 2 to 3 carbon atoms.
- The structures would include a halogen atom at the side-chain terminus. In addition, an analogous structure including a thioether moiety in the same positions was also proposed. This methionine-like moiety is expected to interact similarly with the aromatic residue due to σ* antibonding orbital.

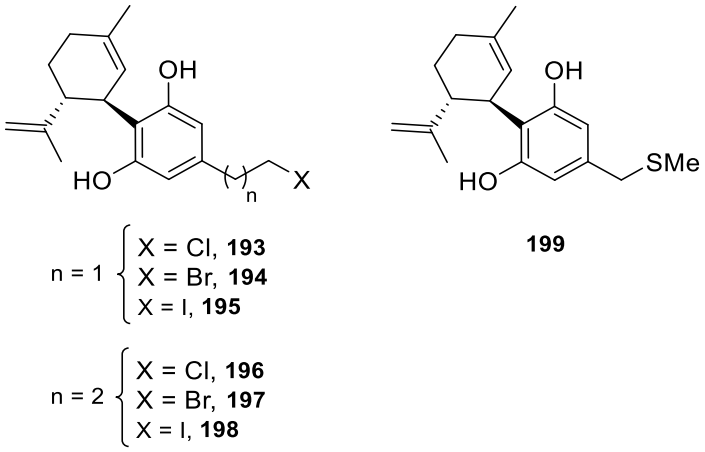

Figure II-33. Structures of halogen- and thioether-containing CBDV-based analogues targeted in this thesis chapter.

Moreover, the biological activity of these compounds would be evaluated through *in vitro* studies. These assays would study specific signalling pathways, such as adenyl cyclase inhibition assays, specific for G protein signalling pathways, or β-arrestin recruitment assays. MAPK phosphorylation assays, which are dependent on both previously mentioned signalling pathways, would also be performed.

3. Results and Discussion

The results of this chapter are organised into various sections. First, the synthetic routes to obtain the halogenated (**section 3.1.**) and thioether-containing (**section 3.2.**) CBDV-based derivatives are presented. Then, the outcomes of the *in vitro* assays are discussed, evaluating the efficacy and potency of the ligands synthesised in the previous sections with the objective of evaluate them as modulators of CB_2R activity through their interaction with the allosteric binding pocket (**section 3.3.**).

3.1. Synthesis of Halogenated CBDV-based Derivatives

To obtain the halogenated CBDV-based derivatives a similar synthetic approach to the one employed for the synthesis of CBDV in **section 3.1.** of the **Chapter III** would be followed. As illustrated in the retrosynthetic of **Scheme II-25**, the target compounds would be accessed through a Friedel-Crafts acylation reaction using the corresponding resorcinol derivatives as precursors, which would be afforded after the deprotection of the hydroxyl groups. The installation of the halogen atoms (Cl, Br, I) into the structures would be performed *via* Appel reaction performed on the corresponding primary alcohol, which would derive from the reduction of commercially available or easily accessible carboxylic acids. This sequence enables efficient modification of the CBDV core structure to generate the desired halogenated derivatives.

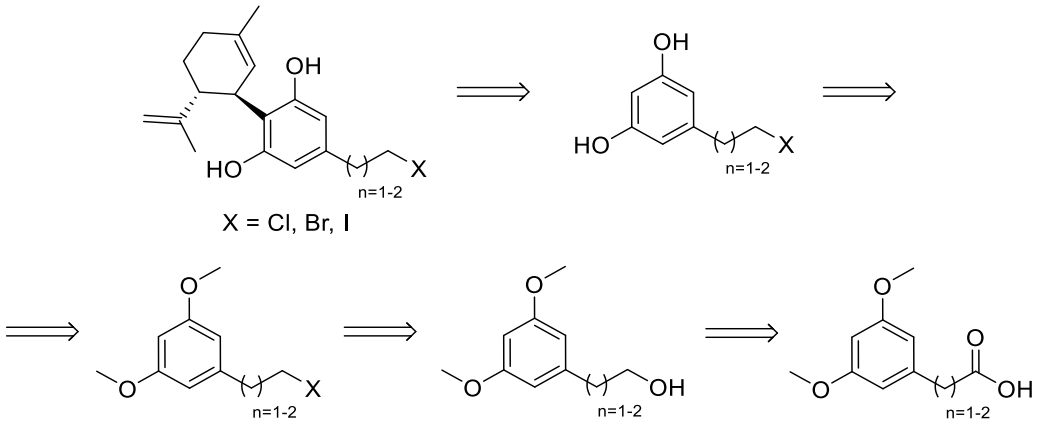

Scheme II-25. Retrosynthetic analysis for the obtention of the halogenated CBDV-based derivatives.

3.1.1. Obtention of Alcohols 203 and 204

The synthesis of the halogenated derivatives with a side-chain length of between 2 and 3 carbon atoms was run in parallel, employing the same reactions to obtain the final halogenated-side-chain CBDV derivatives, but using different starting materials. For the synthesis of the 3-carbon atom side chain, the starting material was the commercially available 3-(3,5-dimethoxyphenyl)acrylic acid (**200**), as it was less expensive than the corresponding saturated acid. 3-(3,5-Dimethoxyphenyl)-propanoic acid (**201**) was synthesised *via* Pd/C-catalysed hydrogenation of the acrylic acid **200** (**Scheme II-26 (1)**).[139]

Commercially available 2-(3,5-dimethoxyphenyl) acetic acid (**202**) and the obtained propanoic acid **201** were then reduced to the corresponding alcohols **203** and **204** using $LiAlH_4$, providing both products within 1 hour without the need of further purification (**Scheme II-26 (2)**).

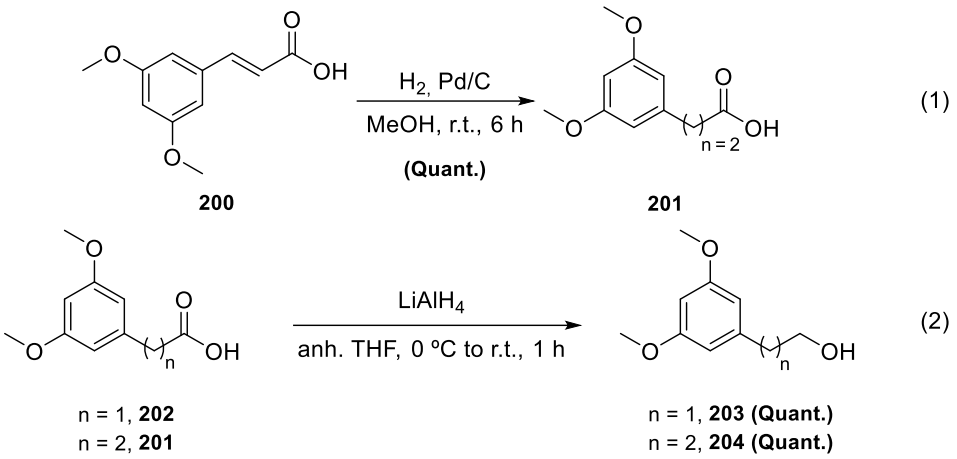

Scheme II-26. (1) Hydrogenation of acrylic acid **200**, (2) Preparation of alcohols **203** and **204** from the corresponding carboxylic acids **202** and **201**.

3.1.2. Formation of Alkyl Halides

The synthesis continued with the transformation of the alcohols into the alkyl halide analogues. Halogenation of alcohols is a fundamental reaction in organic chemistry, typically involving the conversion of the alcohol into an intermediate that can be readily displaced by a halide nucleophile through a nucleophilic substitution reaction.[140] In this case, the transformation focused on the 2-carbon atom side chain to obtain the chlorinated derivative, as the reaction was not as simple as previously anticipated (**Table II-10**).

Table II-10. Reaction conditions tested for the obtention of the alkyl halide analogues **205** and **206**.

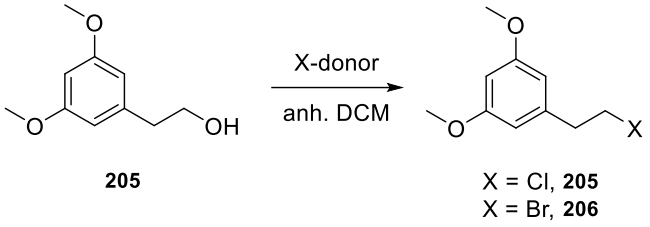

Entry	X-donor	Base	Temp.	Time	Yield %
1	$SOCl_2$	Pyridine	r.t.	0.5 h	--- (By-product)
2	$SOCl_2$	---	r.t.	0.5 h	--- (By-product)
3	PCl_3	---	r.t.	0.5 h	---
4	CCl_4	---	Reflux	36 h	94% (**205**)
5	CBr_4	---	r.t.	1 h	89% (**206**)

A common reagent to convert an alkyl alcohol into an alkyl chloride is thionyl chloride ($SOCl_2$). The reaction proceeds *via* an S_N2 mechanism for primary alcohols, as in this case, to provide the

chloroalkane. The advantage of using this reagent over other alternatives is that the by-products generated from the reaction, sulfur dioxide (SO_2) and hydrogen chloride (HCl), are both gases. This translates into a clean reaction that does not need purification. The reaction proceeded with the use of alcohol **203**, 1.5 equivalents of $SOCl_2$ and 1 equivalent of pyridine as a base. Within 30 minutes, no starting alcohol was observed by TLC, but the resulting product was not the desired one.

^{1}H-NMR analysis revealed just two aromatic protons, indicating that one of the aromatic positions had reacted. The spectrum also suggested the presence of a source of chirality in a strained system, due to large chemical shift differences and multiplicity of the methylene protons. From NMR multiplicity analysis, a chiral cyclic sulfinate ester **207** was proposed (**Figure II-34**).

Table II-11. *J*s correlation extracted from the 1H-NMR spectrum of by-product **207**.

	2a (axial)	**2b (equatorial)**	**3a (equatorial)**	**3b (axial)**
2a (axial)	---	11 Hz	3 Hz	13 Hz
2b (equatorial)	11 Hz	---	---	6 Hz
3a (equatorial)	3 Hz	---	---	18 Hz
3b (axial)	13 Hz	6 Hz	18 Hz	---

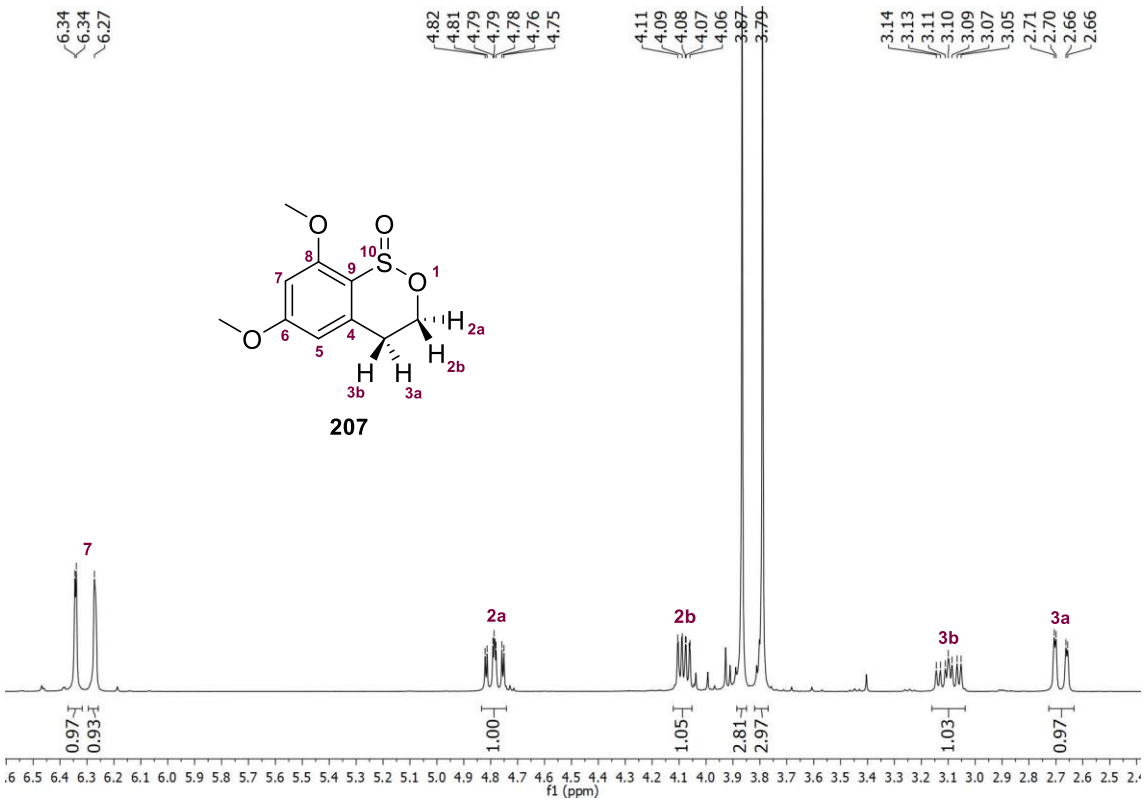

Figure II-34. ^{1}H-NMR spectrum (300 MHz, $CDCl_3$) of chiral cyclic sulfinate ester **207**.

The formation of by-product **207** would be the result of an intramolecular electrophilic aromatic substitution side reaction, which was favoured over the chloride attack due to the great stability of the six-member ring formed and the intramolecular nature of the reaction (**Scheme II-27**). The

structure is consistent with the presence of two sets of diastereotopic protons corresponding to the two methylene groups, as observed in the ^{1}H-NMR spectrum, due to the presence of a stereogenic sulfur centre. Finally, the structure was confirmed by high-resolution mass spectrometry (HRMS). It was also verified that the reaction happened independently of the presence of pyridine as a base (**Table II-10, entries 1 and 2**) obtaining the same results.

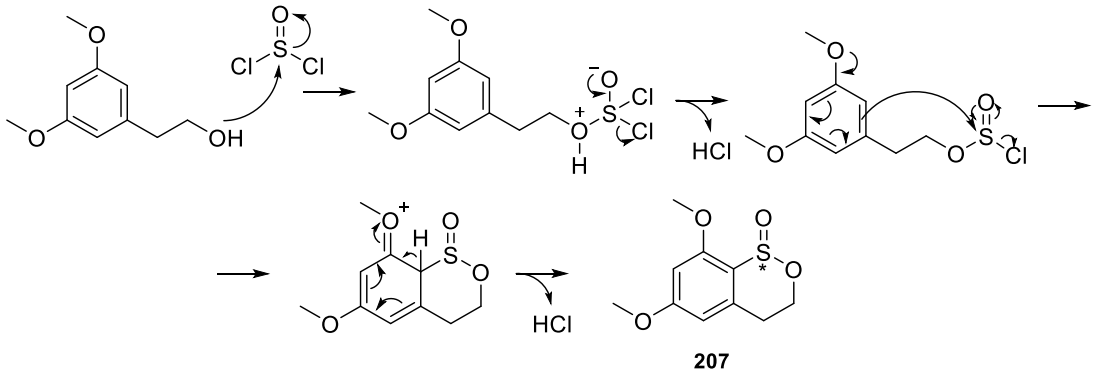

207

Scheme II-27. Proposed mechanism for the formation of chiral cyclic sulfinate ester **207**.

Phosphorus (III) chloride (PCl_3) was the subsequent reagent selected to achieve chlorinated product **205**. This reaction is typically run under mild conditions, and H_3PO_3, the main waste product generated, can be easily removed. In our case, alcohol **203**, dissolved in anhydrous DCM, was mixed with 1 equivalent of PCl_3 (**Table II-10, entry 3**). After 30 minutes, TLC analysis showed no presence of the starting alcohol, but the number of spots was far more than expected. ^{1}H-NMR analysis did not provide better results, showing a mixture of different components. In this case, it was not possible to isolate any defined product, so the reaction outcome was not resolved, ruling out PCl_3 as a possible reagent for the halogen installation reaction attempted.

Alternatively, an Appel reaction, another traditional method to transform an alcohol into the respective alkyl halide, was tested.[141] Although different variants of this reaction have been developed,[142–145] classical conditions were employed in this case, which proceed *via* reaction of CCl_4 or CBr_4 in the presence of PPh_3. Despite the methodology having some disadvantages, like the use of the phased-out CCl_4 or the need for purification due to the formation of triphenylphospine oxide (PPh_3O) as a waste product, it is still considered useful in lab scale conditions In this case, the use of CCl_4 and PPh_3, in combination with alcohol **203**, led to the first successful synthesis of the chlorinated derivative **205** in this synthetic route (**Table II-10, entry 4**). In a homologous manner, CBr_4 was employed, affording brominated derivative **206** with satisfactory yields (**Table II-10, entry 5**).

Encouraged by these results, the same reaction conditions were applied to obtain the 3-carbon atom side-chain analogues **208** and **209** (**Scheme II-28**). It is important to highlight that reflux conditions were required to furnish the chlorinated derivatives, while the brominated ones were obtained at room temperature. Also, despite reaction times being optimised to afford the chlorinated derivatives, reducing them from 36 h to 8 h by employing 2 equivalents of CCl_4, they were still more time consuming to synthesise than for the brominated derivatives, obtained within 1 h of reaction.

In all the cases, products were easily isolated by flash column chromatography with satisfactory yields between 89% and 96%.

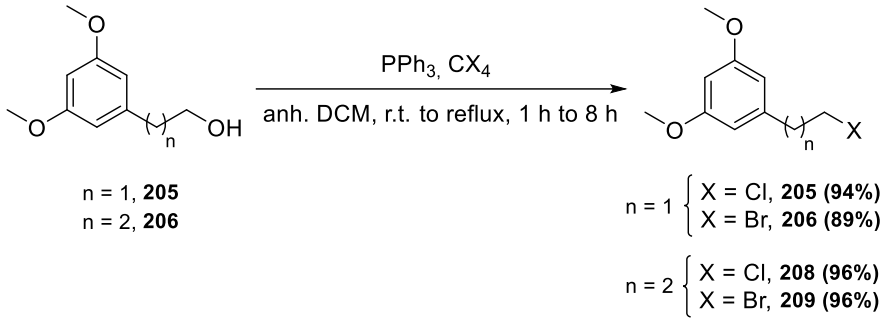

Scheme II-28. Obtention of alkyl halide analogues by applying Appel reaction methodology.

3.1.3. Obtention of Halogenated-Side-Chain Resorcinol Derivatives

The last step of the synthesis was a Friedel-Crafts reaction with terpenoid **149**. As exposed in the General Introduction**,** the synthetic routes to obtain these CBDV derivatives are diverse. In **section 3.2.2.** of the **Chapter III**, , the employment of $BF_3{\cdot}Et_2O$ with Al_2O_3 as a support proved useful to obtain **CBDV**. This proved to be an improvement compared to the previously described synthetic route employed in terms of time and cost without sacrificing the yield (**Scheme II-29**, **green line**). However, the reactivity might differ for these halogenated analogues. Therefore, in parallel, the synthetic route where regioselective Friedel-Crafts alkylation is performed by blocking the *ortho* aromatic positions of the side chain (**Scheme II-29, red line**) was also tested.

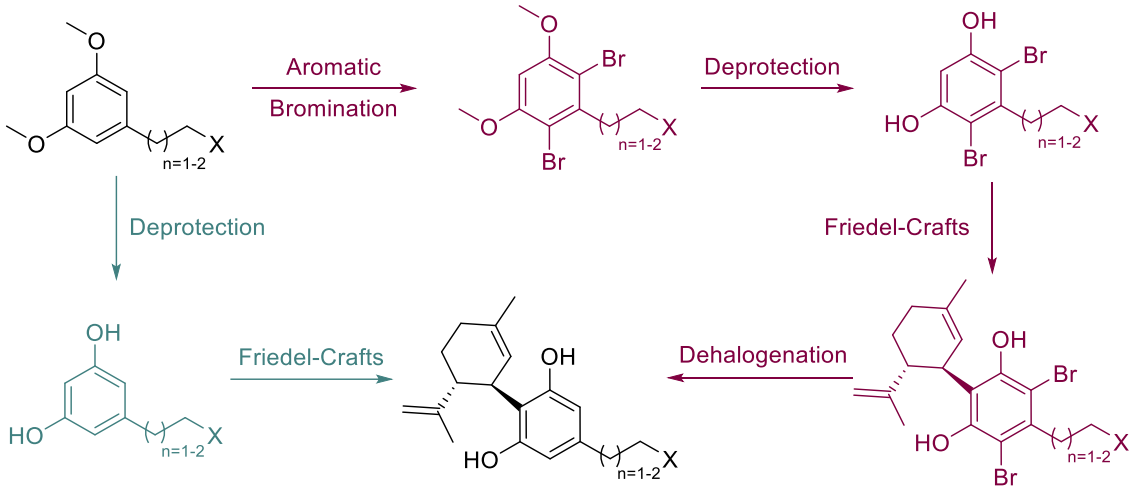

Scheme II-29. Synthetic routes proposed to afford halogenated-side-chain CBDV-based derivatives.

Following the synthetic route represented in **Scheme II-29** (**green line**), the deprotection reaction of the halogenated derivates synthesised in the previous section was carried out using the optimised conditions described in **section 3.2.2**. of the **Chapter III,** (**Table II-2**, *vide supra*) The different deprotected analogues, **210** – **213**, were afforded within 1 hour with quantitative yields and without further purification needed (**Scheme II-30**).

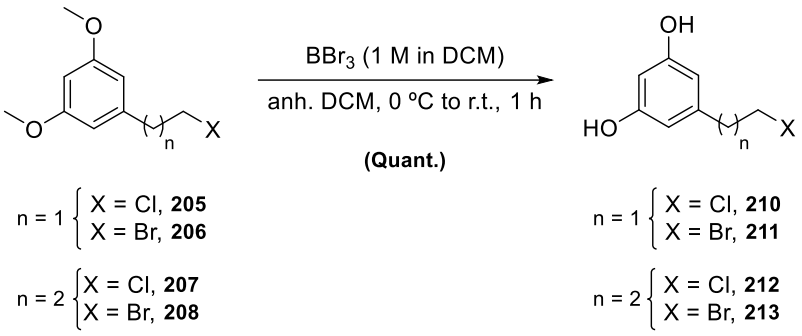

Scheme II-30. Deprotection reaction of the methyl ethers employing BBr_3.

Alternatively, halogenated derivatives **205** and **206**, were chosen as representative examples to perform the regioselective Friedel-Crafts reaction (**Scheme II-29, red line**). Then, the electrophilic aromatic bromination, employing *n*-bromosuccinimide (NBS) and anhydrous DCM, was carried out on those substrates yielding the brominated aromatic intermediates **214** and **215**. Then, the deprotection of the hydroxyl groups, protected in form of methyl ethers, was undertaken affording compounds **216** and **217** (**Scheme II-31**). It is important to highlight that this reaction had to be performed with more equivalents of BBr_3 and for a longer period of time, compared to the analogues that do not contain the halogen substituents on the aromatic ring (**Scheme II-30**).

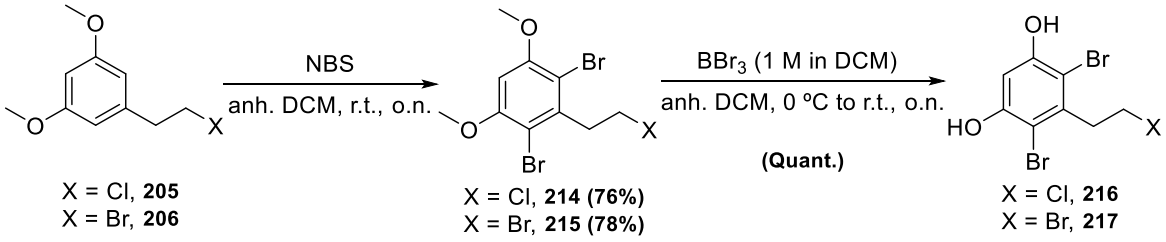

Scheme II-31. Aromatic bromination followed by methyl ether deprotection of 2-carbon halogenated-side-chain derivatives.

3.1.4. Exploration of Friedel-Crafts Reaction for Synthesising Halogenated CBDV-based derivatives

In order to explore the scope of different Friedel-Crafts methodologies and compare their efficiency to obtain halogenated-side-chain CBDV derivatives, it was deemed worthwhile to investigate the reactivity on these molecules under various reaction conditions.

The regioselective Friedel-Crafts alkylation, developed by Dialer *et al.*,[50] has proven useful in the synthesis of the different NAMs and PAMs derived from cannabidiol.[74] With this methodology, it is possible to perform a regioselective alkylation of the aromatic ring, reducing the number of possible by-products, but it requires of the aromatic bromination and posterior dehalogenation to obtain the final product. Following the procedure described in the bibliography,[74] substrates **216** and **217** were submitted to the coupling reaction with **149**, under catalytic amounts of *p*-TsOH as a Lewis acid in the presence of $MgSO_4$ (**Scheme II-32**). Surprisingly, after letting the mixture stir overnight, no reaction was observed, only recovering the starting material.

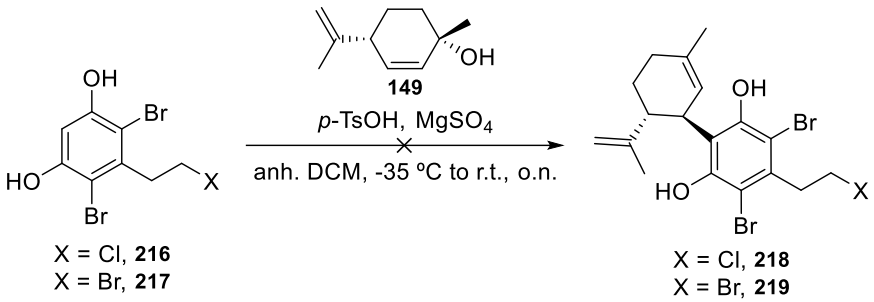

Scheme II-32. Regioselective Friedel-Crafts reaction performed on halogenated-side-chain resorcinol derivatives **216 a**nd **217** following Dialer *et al*.[50] methodology.

As the regioselective Friedel-Crafts reaction demonstrated to be ineffective for the obtention of the desired final products, an alternative methodology, developed by Gong *et al*.,[58] was investigated. In this reaction, catalytic amounts of $BF_3{\cdot}Et_2O$ (0.5 equivalents) were employed to avoid the formation of cyclised by-products. In addition, a 5-fold excess of the resorcinol derivative **211** was used relative to **149** to reduce the presence of disubstituted by-products. The reaction proceeded in the presence of $MgSO_4$, using anhydrous THF as a solvent, starting at a temperature of -10 ºC and letting the reaction attain room temperature (**Scheme II-33**). After 5 hours, ^{1}H-NMR analysis showed minimal progress, with only a few new peaks of very low intensity. To improve the reactivity, another 0.5 equivalents of $BF_3{\cdot}Et_2O$ were added and it was left to stir overnight. However, TLC analysis and posterior ^{1}H-NMR analysis revealed an slight progress, as with some new spots and signals appeared. After carrying out column chromatography of the reaction crude, it was concluded that cyclised products were formed in approximately 10% yield, along with another unidentified by-product. Resorcinol derivative **211** was the main material recovered, demonstrating that this methodology was not feasible to obtain the desired final products.

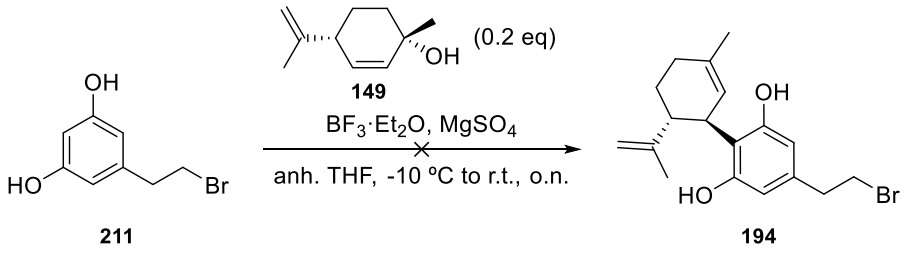

Scheme II-33. Friedel-Crafts alkylation of halogenated-side-chain resorcinol derivative **211** using catalytic amounts of $BF_3{\cdot}Et_2O$ following methodology developed by Gong *et al*.[58]

Finally, the methodology studied in **section 3.2.2**. of **Chapter III**, which used $BF_3{\cdot}Et_2O$ in combination with Al_2O_3 to generate a milder Lewis acid, was employed. Since optimisation of the conditions had already been performed for the synthesis of **CBDV**, in this case just the best conditions found were employed in all cases. The reactions of the different resorcinol derivatives **210**-**213** provided the corresponding halogenated-side-chain CBDV derivatives **193**, **194**, **196** and **197** with yields between 26% and 36%, similar to those obtained for the synthesis of **CBDV** (**Scheme II-34**). Analysis of the reaction crudes indicated the formation of disubstituted and abnormal by-products. However, as no optimisation of the reaction was intended in this case, neither of these side-products were isolated nor their yields estimated.

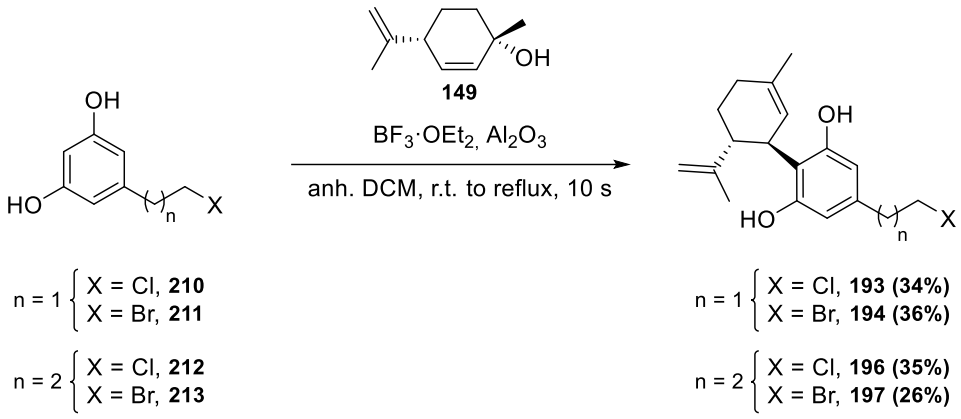

Scheme II-34. Friedel-Crafts reaction applied to the different halogenated resorcinol derivatives.

Lastly, to furnish iodinated derivatives, a Finkelstein reaction to exchange one halogen atom for another was intended. In this transformation, treatment of a primary alkyl halide with an alkali metal halide leads to the replacement of the halogen *via* an S_N2 reaction. For the transhalogenation to proceed, sodium iodide is employed, as it is soluble in acetone, and as the reaction happens, acetone-insoluble sodium halide precipitates, driving the transformation to completion.[140]

Initially, this reaction was attempted with the chlorinated derivative **193** to obtain the iodinated analogue. However, no signs of halogen exchange were appreciated by ^{1}H-NMR analysis, indicating that the reaction was not possible with this substrate. Consequently, this same reaction was attempted with the brominated derivative **194**. The use of NaI in anhydrous acetone at room temperature demonstrated to be effective, obtaining the iodinated analogue derivative **195** with a quantitative yield. Similarly, the 3-carbon chain iodinated derivative **198** was afforded using brominated analogue **197**, also with quantitative yield and without further purification (**Scheme II-35**).

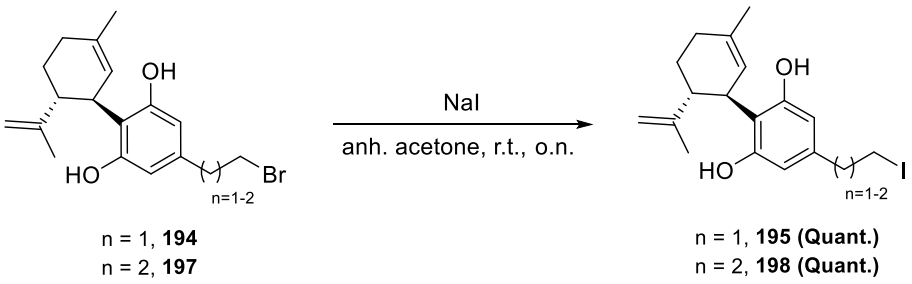

Scheme II-35. Finkelstein reaction to obtain the iodinated analogues.

3.2. Synthesis of Thioether-Containing CBDV-based Derivative

3.2.1. Installation of the Methyl Thioether Moiety

The synthesis started by reducing 3,5-dimethoxybenzaldehyde **161** to the alcohol **220** with sodium borohydride, with the idea of transforming this hydroxyl group into a better leaving group. The initial approach involved converting it into an iodide derivative, to then replace it by the methyl thioether group. In the first attempt, the transformation was tried in one step, by performing an Appel reaction

using PPh_3, I_2 and imidazole.[47] After 8 hours, the starting material was still observed by ^{1}H-NMR analysis, but, although more I_2 and PPh_3 were added, the reaction did not evolve. After purification by column chromatography, the iodinated derivative **221** was isolated in 25% yield, with most of the starting alcohol **220** recovered.

Due to the poor yield, a different approach was taken. The conversion of a similar benzyl alcohol into the chloride analogue by using an excess of methanesulfonyl chloride (MsCl) has been reported by Kuboki *et al.*[146] However, when the protocol was followed, a mixture of the mesylate and the chloride derivatives was obtained. To simplify the mixture, the reaction time with MsCl was reduced to 30 minutes, from the 4 hours of the previous attempt, ensuring complete conversion of the alcohol. NaI was then added to the mixture in anhydrous acetone to finally obtain the iodide derivative **221** in 91% yield. Once it was isolated, it was mixed with sodium methanethiolate (CH_3SNa) in anhydrous ACN, to obtain the methyl thioether-containing product **222** in 90% yield.

In an attempt to reduce the number of steps required to obtain this product, CH_3SNa was mixed with the isolated mesylate using the same reaction conditions as with product **221**. This approach yielded product **222** in 95%, thus becoming the preferred synthesis route for this intermediate (**Scheme II-36**).

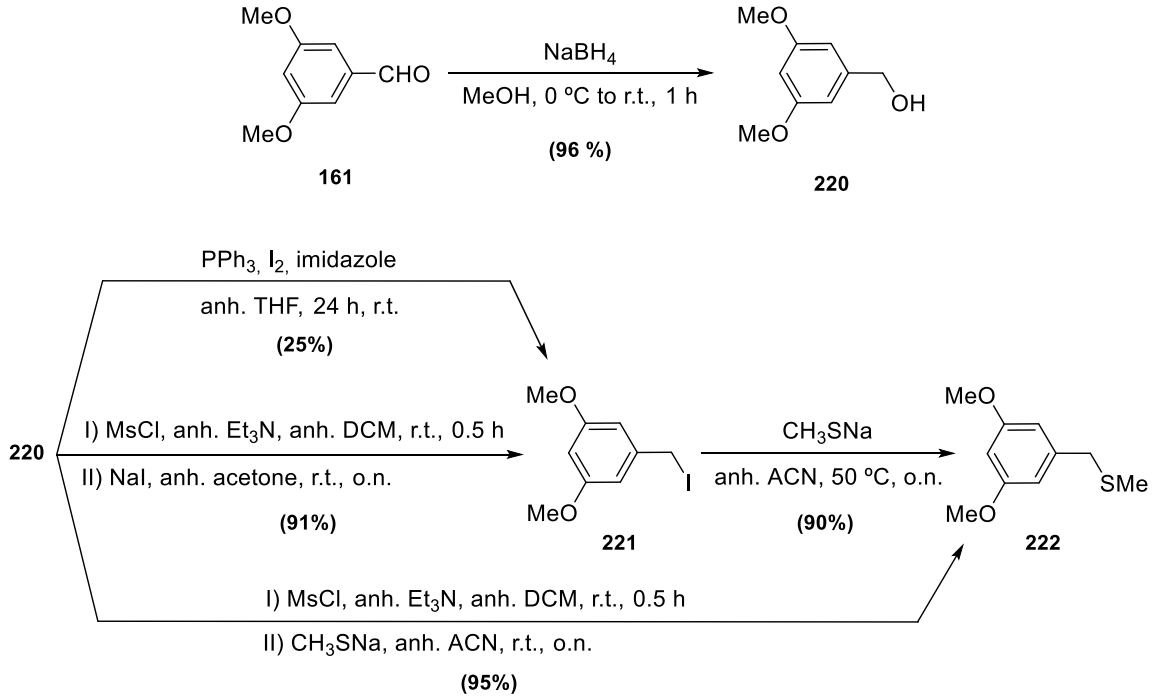

Scheme II-36. Different synthetic strategies attempted for the obtention of the thioether-containing derivative **222**.

3.2.2. Obtention of the Thioether-Containing CBDV derivative, 199

As in the previous synthesis routes presented in this thesis, the cleavage of the methyl ether protecting group was performed prior to the Friedel-Crafts alkylation reaction using a solution of BBr_3. In this case, there was concern about the selectivity of this deprotection reaction in front of the methyl thioether moiety in molecule **222**. However, this methodology has been proven to be

selective for aryl methyl ethers.[147,148] This allowed the obtention of the resorcinol derivative **223** in quantitative yields, which was used directly to perform the Friedel-Crafts alkylation reaction under the conditions optimised in **section 3.2.2.** of the **Chapter III**, affording the thioether-containing side-chain CBDV derivative **199** in 29% yield (**Scheme II-37**).

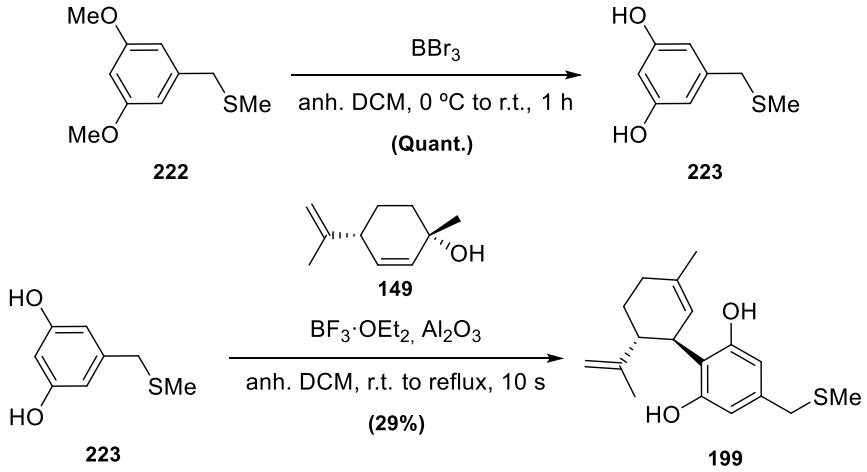

Scheme II-37. Synthesis of thioether-containing side-chain CBDV derivative **199**.

3.3. *In vitro* Biological Activity of Novel CB_2R Ligands

The biological activity of the seven different halogen- or thioether-containing CBDV analogues was evaluated through *in vitro* assays carried out by Dr. Iu Raïch, researcher in Prof. Gemma Navarro's research group at the Faculty of Pharmacy and Food Science of the Universitat de Barcelona.

Based on previous MD simulations, these analogues were hypothesised to function as positive allosteric modulators (PAMs) with enhanced efficiency and potency compared to CBDV, owing to their interactions with the toggle switch residues Phe200$^{3.36}$ and Trp356$^{6.48}$ of the CB_2R.

To test this hypothesis and elucidate how these molecules interact with the cannabinoid receptors, particularly CB_2R, **adenyl cyclase (AC) inhibition assays,** to assess changes in cAMP levels, and **mitogen-activated protein kinase (MAPK) engagement assays** were carried out. These assays were performed on HEK-293T cells with stabilised CB_2R expression. **JWH-133** was employed as a reference, as it is a known potent agonist of the CB_2R. For AC inhibition assays, cells had been treated with forskolin (FSK) to activate AC, generating cAMP levels that were normalised to 100% (**Figure II-36A** and **Figure II-37A**). In the case of MAPK phosphorylation assays, the obtained levels with **JWH-133** were normalised to 100%.

Computational calculations, performed by PhD student Aleix Quintana, studied the binding affinity in the orthosteric pocket of the CB_2R receptor and compared it with **JWH-133**, with the objective of knowing the possible activity of compounds **193** – **199** as orthosteric ligands. The molecular docking models revealed that the novel ligands synthesised exhibit a similar overall orientation to that of **JWH-133** within the binding pocket, aligning closely with its binding pose (**Figure II-35**). This suggests that the ligands maintain interactions with critical residues necessary for receptor activation.

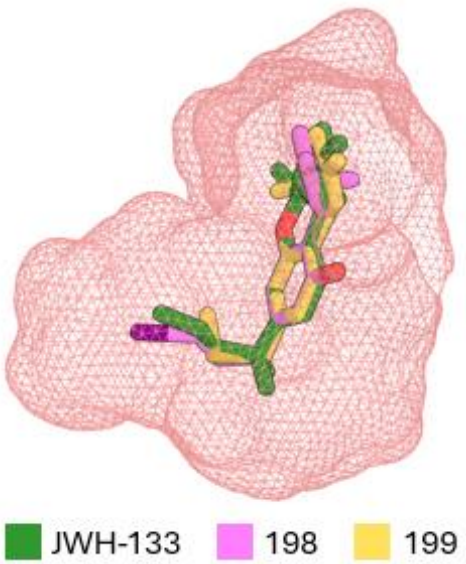

Figure II-35. Frame of the docking studies of the two novel ligands, **198** (pink) and **199** (yellow) within the orthosteric cavity of the CB_2R receptor, compared to the well-characterized orthosteric agonist **JWH-133** (green). The ligands are represented in their docked positions, overlaid on a surface representation of the receptor's orthosteric site (shown in red mesh), which highlights the steric constraints and spatial arrangement of the binding pocket.

Then, based on these findings in this preliminary docking studies, the agonist-induced signalling of the compounds **193** – **199** was assessed. In **Figure II-36A** it can be observed that increasing concentrations of reference compound, **JWH-133**, reduced the cAMP levels in a prototypical manner due to CB_2R signalling through Gi protein. However, when cells were treated with the different halogen- or thioether-containing CBDV analogues, none of the compounds displayed full agonist activity. They behave as weak partial agonists of AC inhibition at CB_2R, resulting in a weak activation of the receptor, leading to the conclusion that these compounds lack significant intrinsic agonist activity through Gi protein at submicromolar concentrations.

In the case of MAPK phosphorylation assays at the CB_2R, represented in **Figure II-36B**, MAPK levels increased in a dose-dependent manner when **JWH-133** was employed. Unlike cAMP levels, which are solely influenced by G protein signalling, MAPK activation serves as a broader marker that may be mediated by either G proteins or β-arrestin signalling pathways, making it a less specific but valuable indicator of the downstream signalling. Halogen-containing CBDV derivatives did not elicit a comparable response to **JWH-133**, as high concentrations were needed to display a partial agonist behaviour. Thus, these results show that compounds **193** – **198** cannot induce a significant CB_2R activation on their own. Notably, the thioether-containing CBDV derivative **199** achieved similar efficacy to **JWH-133** ($E_{max\text{-}JWH\text{-}133}$ = 283% ± 12% vs. $E_{max\text{-}199}$ = 274% ± 110%), although it did so with significantly lower potency ($pEC_{50\text{-}JWH\text{-}133}$ = 8.4 nM ± 0.2 nM vs. $pEC_{50\text{-}199}$ = 6.2 nM ± 0.2 nM). This finding is particularly interesting, as compound **199** appears to elicit a **biased signalling** behaviour as an agonist, which may indicate selective activation of specific downstream pathways. However, before performing any further *in vitro* test, it was suggested to perform more refined computational studies to better understand the interactions of this ligand within the orthosteric cavity

of CB_2R, providing a foundation for designing next-generation ligands with tailored pharmacological profiles based on the structure of the compound **199**.

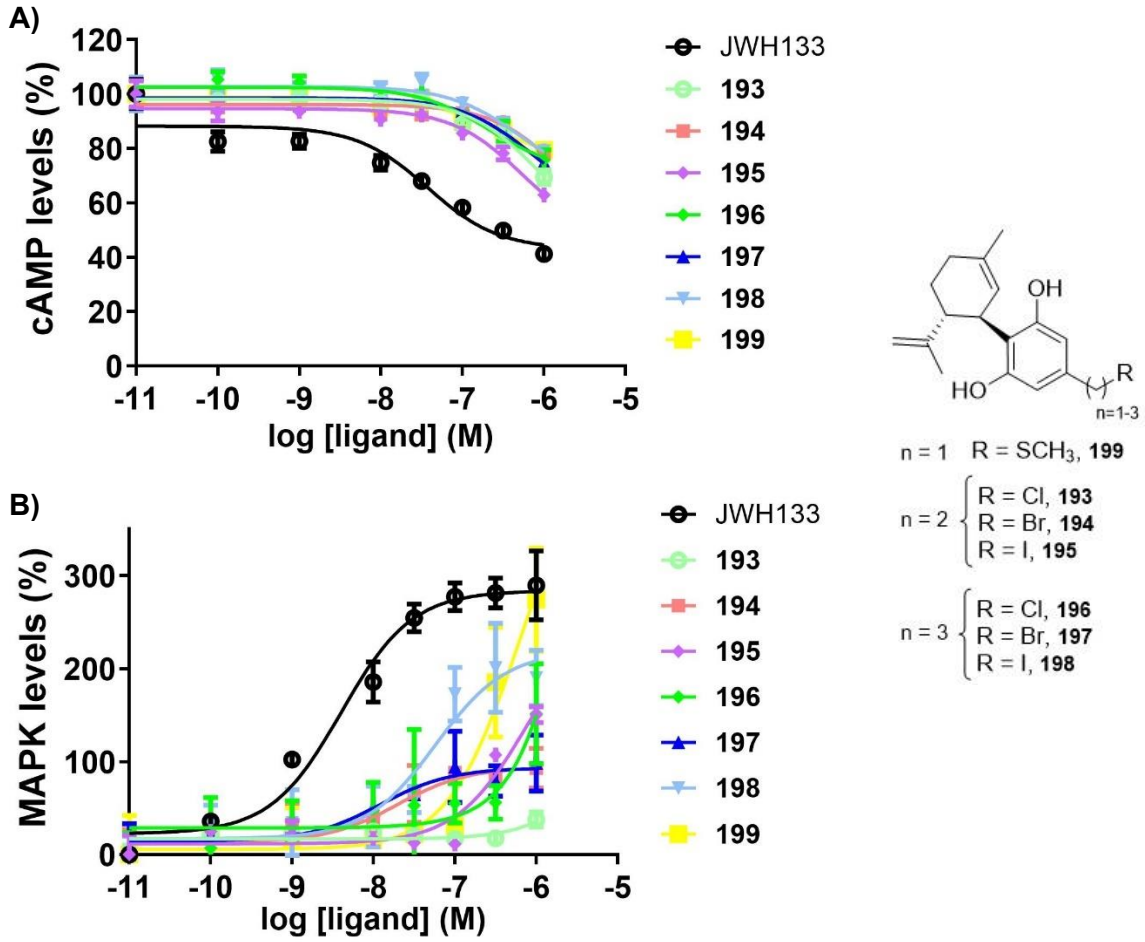

Figure II-36. Graphical comparison between orthosteric agonist **JWH-133** and halogen- or thioether-containing CBDV analogues of the: A) AC inhibition effect by measuring the reduction of the cAMP levels; B) MAPK phosphorylation levels. In both assays HEK-293T cells were employed. Data represent mean ± SEM from n = 5 independent experiments performed in triplicates. Whiskers represent the total range of values within each sample.

Once the interaction of the compounds synthesised with orthosteric site at CB_2R had been tested, their capability as allosteric modulators was assessed. In this case, **JWH-133** was used in the presence of 200 nM concentrations of compounds **193** – **199**, and the activity shown was compared to the activity of the agonist **JWH-133** alone. In the case of AC inhibition assays, the addition of the halogen- or thioether-containing CBDV analogues is expected to modulate the response by amplifying or attenuating the inhibitory effect of **JWH-133**, thereby decreasing or increasing the total cAMP levels compared to when **JWH-133** was used alone, acting as PAMs or NAMs, respectively.

The data obtained for cAMP levels, represented in **Figure II-37A** and summarised in **Table II-12**, revealed that all 3-carbon atom side-chain CBDV analogues (**196**, **197**, and **198**) exhibited PAM activity, as cAMP levels were lower than when **JWH-133** was employed alone. In contrast, only one of the 2-carbon atom side-chain CBDV analogues demonstrated a similar ability to decrease the forskolin-induced cAMP levels (**194**), while the other two (**193** and **195**), as well as the thioether-

containing analogue (**199**), reduced the inhibitory effects of the agonist, functioning as NAMs. This suggests that the side-chain length influences the allosteric modulator behaviour of the synthesised molecules. Additionally, a trend was observed concerning the halogen atom impact on the efficacy of the molecules, following the order Br > I > Cl, as shown by the E_{max} values. This is further exemplified by the fact that the only 2-carbon side-chain molecule that acted as PAM was indeed the bromine-containing derivative **194**. However, in terms of overall potency, all compounds showed worse performance when used in combination with **JWH-133** than when the agonist was used alone, as evidenced by lower pEC_{50} values.

To further assess the behaviour of these analogues as allosteric modulators at the CB_2R, the MAPK engagement was analysed. For this assay, it is expected that MAPK phosphorylation levels are increased in the presence of a PAM, while this would decrease in the presence of a NAM. **Figure II-37B** illustrates the dose-response curve of **JWH-133** for MAPK phosphorylation assays in the presence of 200 nM of any of the halogen- or thioether-containing CBDV analogues, with the data summarised in **Table II-12**. All of the novel CB_2R allosteric ligands acted as PAMs for this marker, exhibiting increased efficacy, as E_{max} values indicated when combined with the agonist **JWH-133**. Moreover, a trend in efficacy was observed concerning the halogen substitution on the moiety, following the order I > Cl ≈ Br. However, no significant difference was noted in relation to the length of the side chain among the compounds. In terms of potency, this was significantly increased in derivatives **198** (pEC_{50} = 8.9) and **199** (pEC_{50} = 8.8).

Table II-12. Modulation of agonist **JWH-133** downstream signalling in the cAMP and MAPK phosphorylation levels of the different allosteric modulators **193** – **199** ([ ] = 200 nM). In all the assays orthosteric ligand **JWH-133** was employed.

Alosteric ligand	cAMP determination assay			MAPK phosphorylation assay		
	pEC_{50} (nM)	E_{max} (%)	E_{max} in relation to **JWH-133** (%)	pEC_{50} (nM)	E_{max} (%)	E_{max} in relation to **JWH-133** (Fold)
---	7.6 ± 0.2	41 ± 1.1	---	8.3 ± 0.2	289 ± 37.1	---
193	7.3 ± 0.3	52 ± 10.0	79% **NAM**	7.7 ± 0.2	374 ± 40.8	1.3 **PAM**
194	7.2 ± 0.1	30 ± 3.4	137% **PAM**	8.1 ± 0.3	384 ± 25.0	1.3 **PAM**
195	7.6 ± 0.1	43 ± 5.9	95% **NAM**	7.3 ± 0.3	463 ± 30.3	1.6 **PAM**
196	7.2 ± 0.2	36 ± 5.6	114% **PAM**	8.0 ± 0.1	382 ± 32.8	1.3 **PAM**
197	7.0 ± 0.1	29 ± 4.1	141% **PAM**	7.8 ± 0.3	376 ± 49.6	1.3 **PAM**
198	7.1 ± 0.2	31 ± 4.1	131% **PAM**	8.9 ± 0.1	441 ± 19.0	1.5 **PAM**
199	6.8 ± 0.2	52 ± 6.6	79% **NAM**	8.8 ± 0.3	391 ± 21.5	1.4 **PAM**

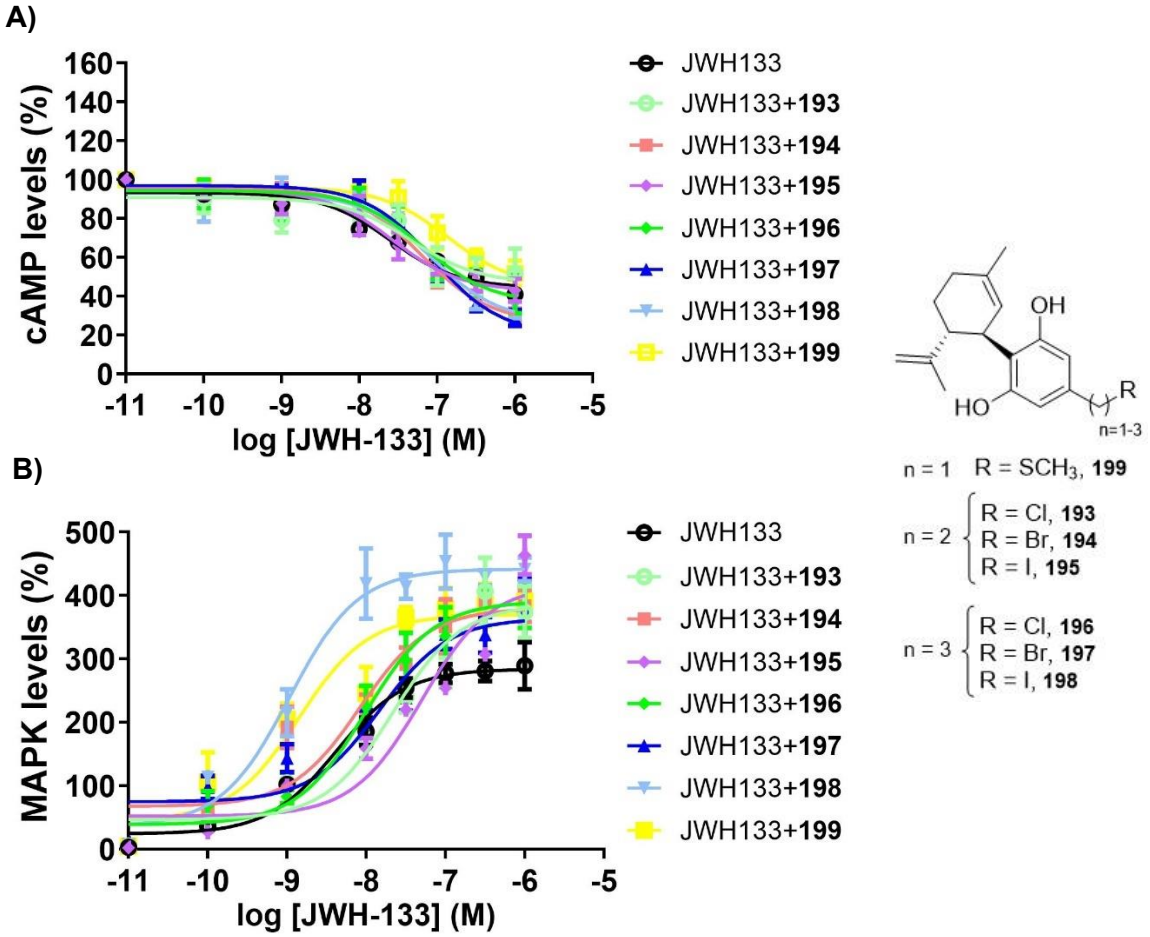

Figure II-37. Assessment of the allosteric modulation activity upon treatment with orthosteric agonist **JWH-133** alone and in combination with halogen- or thioether-containing CBDV analogues through: A) Reduction of the cAMP levels in HEK-293T cells (normalised at 100%); B) Increase of the MAPK levels in HEK-293T. Data represent mean ± SEM from n = 5 independent experiments performed in triplicates. Whiskers represent the total range of values within each sample.

Overall, *n*-haloalkyl CBDV derivatives **193** – **198** generally increased **JWH-133** signalling through CB_2R without inducing a significant activation response on their own, thus they behave as PAMs of the CB_2 receptor. However, the differences observed in their modulation patterns for cAMP and MAPK cannot be fully explained by G_i coupling alone. When the results of both markers were compared, a different behaviour could be seen, particularly influenced by the type of halogen. In the case of cAMP levels, the E_{max} values indicated that bromine-containing derivatives **194** and **197** exhibited the highest efficacy. In contrast, when MAPK levels were measured, the greatest efficacy was associated with the iodine-containing derivatives **195** and **198**, whereas the worst was obtained for bromine-containing derivatives **194** and **197**, similarly to those obtained for chlorine-containing derivatives **193** and **196**. This different behaviour depending on the signalling pathways was also observed for thioether-containing derivative **199**, performing clearly as NAM in the cAMP assay, while performing significantly as PAM for MAPK assay.

The divergent outcomes for the CBDV derivatives as allosteric modulators, depending on whether MAPK or cAMP levels were measured, suggest the presence of **biased signalling**, with the derivative potentially playing different roles in each signalling pathway. As GPCRs can also signal

through β-arrestin in a two-step process mediated by receptor phosphorylation by GPCR kinases (GRK), the hypothesis proposed is that iodine-containing derivatives have a biased response for β-arrestin signalling pathway, while the bromine-containing ones preferentially activate the G-protein signalling pathway. To explore this further, **β-arrestin recruitment assays** were conducted with the different halogen- or thioether-containing CBD analogues.

For these experiments, the same cell cultures conditions were used as in the previous assays. β-arrestin recruitment was quantified using orthosteric cannabinoid receptor agonist **JWH-133** as a reference. Subsequently, halogen- or thioether-containing CBDV analogues were assessed in presence of **JWH-133** and the modification on the levels of β-arrestin were measured (**Table II-13** and **Figure II-38**). The data showed that all of the compounds behaved as NAMs of β-arrestin recruitment at CB_2R, with just compound **195** having a similar efficacy as when **JWH-133** was used alone ($E_{max\text{-}JWH\text{-}133}$ = 63% ± 11.2% vs. $E_{max\text{-}195}$ = 62% ± 0.1%).

Table II-13. Modulation of agonist **JWH-133** downstream signalling in the β-arrestin recruitment the different allosteric modulators **193** – **199** ([ ] = 200 nM). In all the assays orthosteric ligand **JWH-133** was employed.

Allosteric ligand	pEC_{50} (nM)	E_{max} (%)	E_{max} in relation to JWH-133 alone (Fold)
---	7.6 ± 0.1	63 ± 11.2	---
193	7.4 ± 0.2	57 ± 5.2	0.9 **NAM**
194	7.0 ± 0.3	38 ± 1.7	0.6 **NAM**
195	7.4 ± 0.1	62 ± 0.1	1 (Neutral)
196	7.1 ± 0.2	52 ± 3.2	0.8 **NAM**
197	6.9 ± 0.2	39 ± 3.2	0.6 **NAM**
198	6.7 ± 0.1	37 ± 5.6	0.6 **NAM**
199	7.4 ± 0.5	41 ± 2.7	0.6 **NAM**

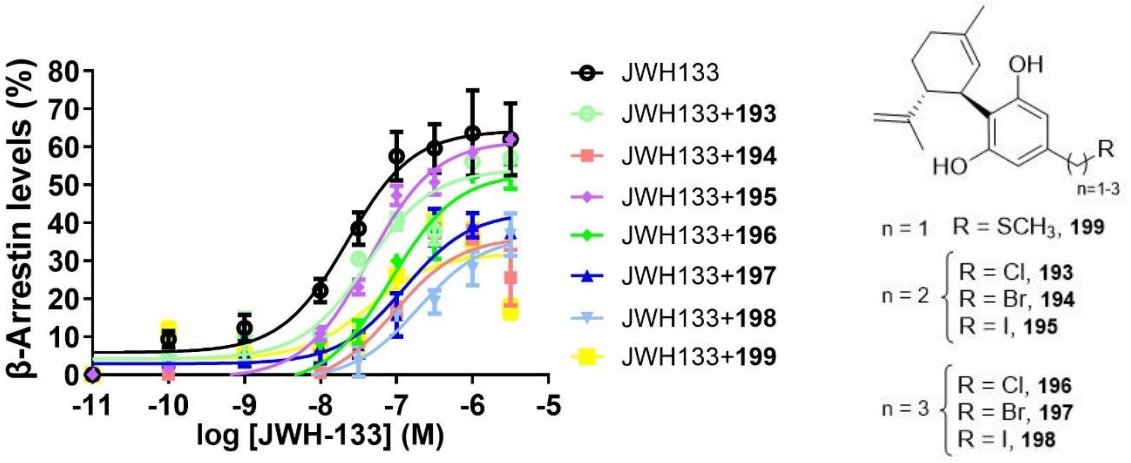

Figure II-38. CB_2R-dependent recruitment of β-arrestin for HEK-293T cells upon treatment with orthosteric agonist **JWH-133** alone and in combination with halogen- or thioether-containing CBDV analogues. Data represent mean ± SEM from n = 5 independent experiments performed in triplicates. Whiskers represent the total range of values within each sample.

Combining the results obtained in the different assays, it can be noted that compounds **194, 196, 197** and **198** act as biased modulators (BAMs) towards G protein signalling, as they behave as

PAMs in the AC inhibition assays, while they act as NAMs for β-arrestin, resulting in the increment of MAPK levels and behaving as PAMs when this marker is measured.

On the other hand, the behaviour of compounds, **193**, **195** and **199** as NAMs in both G protein and β-arrestin signalling pathways, but as PAMs when measuring MAPK phosphorylation, could be explained due to stronger affinity for the β-arrestin signalling pathway. As exposed in **section 2.1.** of the **General Introduction**, β-arrestin signalling pathway has an important regulation role for GPCRs. Then, a ligand displaying NAM activity with a strong affinity for β-arrestin recruitment could prolong the activation of other downstream pathways, such as MAPK, increasing the MAPK phosphorylation and, thus, behaving as a PAM for this pathway. This behaviour is especially pronounced in the iodinated derivatives **195** and **198,** as they exhibit the strongest response in the case of MAPK phosphorylation. This suggests that iodinated compounds may have a unique interaction profile with CB_2R, potentially enhancing MAPK signalling through mechanisms yet to be fully elucidated. Nonetheless, the variability in the duration of the response across signalling pathways and the **non-specific nature of MAPK** as a marker complicate the interpretation of these results. It is hypothesized that the PAM-like behaviour observed in MAPK phosphorylation assays may involve additional factors beyond the specific mechanisms examined in this thesis. To confirm this hypothesis, further studies investigating other markers directly related to MAPK signalling would be required.

Table II-14. Ligands behaviour as allosteric modulators in the signalling pathways studied.

Alosteric ligand	cAMP levels	β-arrestin recruitment	MAPK phosphorylation
193	NAM	NAM	PAM
194	PAM	NAM	PAM
195	NAM	Neutral	PAM
196	PAM	NAM	PAM
197	PAM	NAM	PAM
198	PAM	NAM	PAM
199	NAM	NAM	PAM

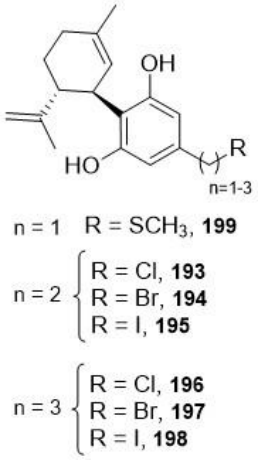

Given these promising yet inconclusive results, further MD simulations would need to be conducted with the different halogen- and thioether-containing CBDV derivatives. These simulations will model the σ-hole that promotes the halogen bond with the aromatic residues, thereby aiding in a deeper understanding of the interactions between the synthesised molecules and the allosteric cavity at the CB_2R and allowing the design of further experiments to validate the observed behaviour and guide the development of new derivatives with optimized pharmacological profiles.

4. Conclusions

With the aim of continuing studying the modulation of the CB_2R activity through the allosteric binding site, different structures capable of interacting with the toggle switch residues, key for the activation of the receptor, were proposed.

After a rational design, seven CBDV analogues, were synthesised and characterised with a side-chain length of 2 to 3 carbons. As proposed, six of them (**193** – **198**) contained a halogen atom at the end of the side chain, while one of them contained thioether moiety in the same position. A linear synthesis consisting of 4 to 6 steps resulted in the production of six halogenated compounds, with yields between 25% to 34%. Similarly, thioether-containing CBDV derivative **199** was obtained in a 4-step linear synthesis in 26% yield. All the compounds were obtained with a purity over 90%.

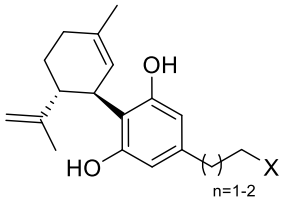

n = 1
- X = Cl, **193 (32%)**
- X = Br, **194 (32%)**
- X = I, **195 (32%)**

n = 2
- X = Cl, **196 (34%)**
- X = Br, **197 (25%)**
- X = I, **198 (25%)**

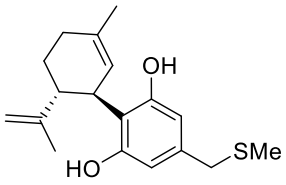

199 (26%)

The biological activity of the synthesised compounds was evaluated *in vitro* through AC inhibition, β-arrestin, and MAPK phosphorylation assays. The results illustrated that compounds **194, 196, 197** and **198** behaved a biased modulators (BAMs) towards G protein signalling, as they behave as PAMs in the AC inhibition assays, while they acted as NAMs for β-arrestin, resulting in the increment of MAPK levels, behaving as PAMs when this marker is measured.

In the case of compounds **193**, **195**, and **199**, they act as NAMs for both AC inhibition assays and β-arrestin recruitment. However, when the MAPK phosphorylation levels were measured, a PAM behaviour was observed, possibly due to a strong affinity for the β-arrestin pathway, that prolonged the activation of the signalling.

These results offered the possibility of studying a new family of compounds with possible activity as biased ligands, as they are therapeutically valuable to selectively modulate a response through a specific pathway, enhancing beneficial effects while minimizing the side effects.

Bibliography of Part II

(1) Warf, B. High Points: An Historical Geography of Cannabis. *Geogr. Rev.* **2014**, *104* (4), 414–438. https://doi.org/10.1111/j.1931-0846.2014.12038.x.

(2) Adams, R.; Baker, B. R.; Wearn, R. B. Structure of Cannabinol. III. Synthesis of Cannabinol, 1-Hydroxy-3-n-Amyl-6,6,9-Trimethyl-6-Dibenzopyran. *J. Am. Chem. Soc.* **1940**, *62* (8), 2204–2207. https://doi.org/10.1021/ja01865a083.

(3) Petrzilka, T.; Haefliger, W.; Sikemeier, C.; Ohloff, G.; Eschenmoser, A. [Synthesis and optical rotation of the (-)-cannabidiols]. *Helv. Chim. Acta* **1967**, *50* (2), 719–723. https://doi.org/10.1002/hlca.19670500235.

(4) Gaoni, Y.; Mechoulam, R. Isolation, Structure, and Partial Synthesis of an Active Constituent of Hashish. *J. Am. Chem. Soc.* **1964**, *86* (8), 1646–1647. https://doi.org/10.1021/ja01062a046.

(5) Ben-Shabat, S.; Hanuš, L. O.; Katzavian, G.; Gallily, R. New Cannabidiol Derivatives: Synthesis, Binding to Cannabinoid Receptor, and Evaluation of Their Antiinflammatory Activity. *J. Med. Chem.* **2006**, *49* (3), 1113–1117. https://doi.org/10.1021/jm050709m.

(6) Makriyannis, A.; Rapaka, R. S. The Molecular Basis of Cannabinoid Activity. *Life Sci.* **1990**, *47* (24), 2173–2184. https://doi.org/10.1016/0024-3205(90)90147-J.

(7) Mechoulam, R.; Hanus, L. A Historical Overview of Chemical Research on Cannabinoids. *Chem. Phys. Lipids* **2000**, *108* (1–2), 1–13. https://doi.org/10.1016/s0009-3084(00)00184-5.

(8) Matsuda, L. A.; Lolait, S. J.; Brownstein, M. J.; Young, A. C.; Bonner, T. I. Structure of a Cannabinoid Receptor and Functional Expression of the Cloned CDNA. *Nature* **1990**, *346* (6284), 561–564. https://doi.org/10.1038/346561a0.

(9) Hua, T.; Vemuri, K.; Pu, M.; Qu, L.; Han, G. W.; Wu, Y.; Zhao, S.; Shui, W.; Li, S.; Korde, A.; Laprairie, R. B.; Stahl, E. L.; Ho, J.-H.; Zvonok, N.; Zhou, H.; Kufareva, I.; Wu, B.; Zhao, Q.; Hanson, M. A.; Bohn, L. M.; Makriyannis, A.; Stevens, R. C.; Liu, Z.-J. Crystal Structure of the Human Cannabinoid Receptor CB_1. *Cell* **2016**, *167* (3), 750-762.e14. https://doi.org/10.1016/j.cell.2016.10.004.

(10) Li, X.; Hua, T.; Vemuri, K.; Ho, J.-H.; Wu, Y.; Wu, L.; Popov, P.; Benchama, O.; Zvonok, N.; Locke, K.; Qu, L.; Han, G. W.; Iyer, M. R.; Cinar, R.; Coffey, N. J.; Wang, J.; Wu, M.; Katritch, V.; Zhao, S.; Kunos, G.; Bohn, L. M.; Makriyannis, A.; Stevens, R. C.; Liu, Z.-J. Crystal Structure of the Human Cannabinoid Receptor CB2. *Cell* **2019**, *176* (3), 459-467.e13. https://doi.org/10.1016/j.cell.2018.12.011.

(11) Stevens, R. C.; Cherezov, V.; Katritch, V.; Abagyan, R.; Kuhn, P.; Rosen, H.; Wüthrich, K. The GPCR Network: A Large-Scale Collaboration to Determine Human GPCR Structure and Function. *Nat. Rev. Drug Discov.* **2013**, *12* (1), 25–34. https://doi.org/10.1038/nrd3859.

(12) Ghosh, E.; Kumari, P.; Jaiman, D.; Shukla, A. K. Methodological Advances: The Unsung Heroes of the GPCR Structural Revolution. *Nat. Rev. Mol. Cell Biol.* **2015**, *16* (2), 69–81. https://doi.org/10.1038/nrm3933.

(13) Howlett, A. C.; Fleming, R. M. Cannabinoid Inhibition of Adenylate Cyclase. Pharmacology of the Response in Neuroblastoma Cell Membranes. *Mol. Pharmacol.* **1984**, *26* (3), 532–538.

(14) Howlett, A. C.; Qualy, J. M.; Khachatrian, L. L. Involvement of Gi in the Inhibition of Adenylate Cyclase by Cannabimimetic Drugs. *Mol. Pharmacol.* **1986**, *29* (3), 307–313.

(15) Howlett, A. C.; Barth, F.; Bonner, T. I.; Cabral, G.; Casellas, P.; Devane, W. A.; Felder, C. C.; Herkenham, M.; Mackie, K.; Martin, B. R.; Mechoulam, R.; Pertwee, R. G. International Union of Pharmacology. XXVII. Classification of Cannabinoid Receptors. *Pharmacol. Rev.* **2002**, *54* (2), 161–202. https://doi.org/10.1124/pr.54.2.161.

(16) Howlett, A. C.; Blume, L. C.; Dalton, G. D. CB(1) Cannabinoid Receptors and Their Associated Proteins. *Curr. Med. Chem.* **2010**, *17* (14), 1382–1393. https://doi.org/10.2174/092986710790980023.

(17) Herkenham, M.; Lynn, A. B.; Little, M. D.; Johnson, M. R.; Melvin, L. S.; de Costa, B. R.; Rice, K. C. Cannabinoid Receptor Localization in Brain. *Proc. Natl. Acad. Sci. U. S. A.* **1990**, *87* (5), 1932–1936. https://doi.org/10.1073/pnas.87.5.1932.

(18) Atwood, B. K.; Mackie, K. CB2: A Cannabinoid Receptor with an Identity Crisis. *Br. J. Pharmacol.* **2010**, *160* (3), 467–479. https://doi.org/10.1111/j.1476-5381.2010.00729.x.

(19) Cabral, G. A.; Raborn, E. S.; Griffin, L.; Dennis, J.; Marciano-Cabral, F. CB2 Receptors in the Brain: Role in Central Immune Function. *Br. J. Pharmacol.* **2008**, *153* (2), 240–251. https://doi.org/10.1038/sj.bjp.0707584.

(20) Di Marzo, V.; Stella, N.; Zimmer, A. Endocannabinoid Signalling and the Deteriorating Brain. *Nat. Rev. Neurosci.* **2015**, *16* (1), 30–42. https://doi.org/10.1038/nrn3876.

(21) Savonenko, A. V; Melnikova, T.; Wang, Y.; Ravert, H.; Gao, Y.; Koppel, J.; Lee, D.; Pletnikova, O.; Cho, E.; Sayyida, N.; Hiatt, A.; Troncoso, J.; Davies, P.; Dannals, R. F.; Pomper, M. G.; Horti, A. G. Cannabinoid CB2 Receptors in a Mouse Model of Aβ Amyloidosis: Immunohistochemical Analysis and Suitability as a PET Biomarker of Neuroinflammation. *PLoS One* **2015**, *10* (6), e0129618. https://doi.org/10.1371/journal.pone.0129618.

(22) Ryberg, E.; Larsson, N.; Sjögren, S.; Hjorth, S.; Hermansson, N.-O.; Leonova, J.; Elebring, T.; Nilsson, K.; Drmota, T.; Greasley, P. J. The Orphan Receptor GPR55 Is a Novel Cannabinoid Receptor. *Br. J. Pharmacol.* **2007**, *152* (7), 1092–1101. https://doi.org/10.1038/sj.bjp.0707460.

(23) Bow, E. W.; Rimoldi, J. M. The Structure–Function Relationships of Classical Cannabinoids: CB1/CB2 Modulation. *Perspect. Medicin. Chem.* **2016**, *8*, PMC.S32171. https://doi.org/10.4137/PMC.S32171.

(24) Jean-Charles, P.-Y.; Kaur, S.; Shenoy, S. K. G Protein-Coupled Receptor Signaling Through β-Arrestin-Dependent Mechanisms. *J. Cardiovasc. Pharmacol.* **2017**, *70* (3), 142–158. https://doi.org/10.1097/FJC.0000000000000482.

(25) Devane, W. A.; Hanus, L.; Breuer, A.; Pertwee, R. G.; Stevenson, L. A.; Griffin, G.; Gibson, D.; Mandelbaum, A.; Etinger, A.; Mechoulam, R. Isolation and Structure of a Brain

Constituent That Binds to the Cannabinoid Receptor. *Science* **1992**, *258* (5090), 1946–1949. https://doi.org/10.1126/science.1470919.

(26) Fride, E.; Mechoulam, R. Pharmacological Activity of the Cannabinoid Receptor Agonist, Anandamide, a Brain Constituent. *Eur. J. Pharmacol.* **1993**, *231* (2), 313–314. https://doi.org/10.1016/0014-2999(93)90468-w.

(27) Hanus, L.; Gopher, A.; Almog, S.; Mechoulam, R. Two New Unsaturated Fatty Acid Ethanolamides in Brain That Bind to the Cannabinoid Receptor. *J. Med. Chem.* **1993**, *36* (20), 3032–3034. https://doi.org/10.1021/jm00072a026.

(28) Alexander, S. P. H.; Kendall, D. A. The Complications of Promiscuity: Endocannabinoid Action and Metabolism. *Br. J. Pharmacol.* **2007**, *152* (5), 602–623. https://doi.org/10.1038/sj.bjp.0707456.

(29) Sugiura, T.; Kondo, S.; Kishimoto, S.; Miyashita, T.; Nakane, S.; Kodaka, T.; Suhara, Y.; Takayama, H.; Waku, K. Evidence That 2-Arachidonoylglycerol but Not N-Palmitoylethanolamine or Anandamide Is the Physiological Ligand for the Cannabinoid CB2 Receptor. Comparison of the Agonistic Activities of Various Cannabinoid Receptor Ligands in HL-60 Cells. *J. Biol. Chem.* **2000**, *275* (1), 605–612. https://doi.org/10.1074/jbc.275.1.605.

(30) Kirkham, T. C.; Williams, C. M.; Fezza, F.; Di Marzo, V. Endocannabinoid Levels in Rat Limbic Forebrain and Hypothalamus in Relation to Fasting, Feeding and Satiation: Stimulation of Eating by 2-Arachidonoyl Glycerol. *Br. J. Pharmacol.* **2002**, *136* (4), 550–557. https://doi.org/10.1038/sj.bjp.0704767.

(31) Silva-Reis, R.; Silva, A. M. S.; Oliveira, P. A.; Cardoso, S. M. Antitumor Effects of Cannabis Sativa Bioactive Compounds on Colorectal Carcinogenesis. *Biomolecules* **2023**, *13* (5), 764. https://doi.org/10.3390/biom13050764.

(32) Thomas, A.; Baillie, G. L.; Phillips, A. M.; Razdan, R. K.; Ross, R. A.; Pertwee, R. G. Cannabidiol Displays Unexpectedly High Potency as an Antagonist of CB1 and CB2 Receptor Agonists in Vitro. *Br. J. Pharmacol.* **2007**, *150* (5), 613–623. https://doi.org/10.1038/sj.bjp.0707133.

(33) Badowski, M. E. A Review of Oral Cannabinoids and Medical Marijuana for the Treatment of Chemotherapy-Induced Nausea and Vomiting: A Focus on Pharmacokinetic Variability and Pharmacodynamics. *Cancer Chemother. Pharmacol.* **2017**, *80* (3), 441–449. https://doi.org/10.1007/s00280-017-3387-5.

(34) Pertwee, R. G. Cannabinoids and Multiple Sclerosis. *Mol. Neurobiol.* **2007**, *36* (1), 45–59. https://doi.org/10.1007/s12035-007-0005-2.

(35) Mazier, W.; Saucisse, N.; Gatta-Cherifi, B.; Cota, D. The Endocannabinoid System: Pivotal Orchestrator of Obesity and Metabolic Disease. *Trends Endocrinol. Metab.* **2015**, *26* (10), 524–537. https://doi.org/10.1016/j.tem.2015.07.007.

(36) Black, M. D.; Stevens, R. J.; Rogacki, N.; Featherstone, R. E.; Senyah, Y.; Giardino, O.; Borowsky, B.; Stemmelin, J.; Cohen, C.; Pichat, P.; Arad, M.; Barak, S.; De Levie, A.; Weiner, I.; Griebel, G.; Varty, G. B. AVE1625, a Cannabinoid CB1 Receptor Antagonist, as

a Co-Treatment with Antipsychotics for Schizophrenia: Improvement in Cognitive Function and Reduction of Antipsychotic-Side Effects in Rodents. *Psychopharmacology (Berl).* **2011**, *215* (1), 149–163. https://doi.org/10.1007/s00213-010-2124-0.

(37) Schindler, C. W.; Redhi, G. H.; Vemuri, K.; Makriyannis, A.; Le Foll, B.; Bergman, J.; Goldberg, S. R.; Justinova, Z. Blockade of Nicotine and Cannabinoid Reinforcement and Relapse by a Cannabinoid CB1-Receptor Neutral Antagonist AM4113 and Inverse Agonist Rimonabant in Squirrel Monkeys. *Neuropsychopharmacology* **2016**, *41* (9), 2283–2293. https://doi.org/10.1038/npp.2016.27.

(38) Rinaldi-Carmona, M.; Barth, F.; Héaulme, M.; Shire, D.; Calandra, B.; Congy, C.; Martinez, S.; Maruani, J.; Néliat, G.; Caput, D.; Ferrara, P.; Soubrié, P.; Brelière, J. C.; Le Fur, G. SR141716A, a Potent and Selective Antagonist of the Brain Cannabinoid Receptor. *FEBS Lett.* **1994**, *350* (2), 240–244. https://doi.org/10.1016/0014-5793(94)00773-X.

(39) Le Foll, B.; Gorelick, D. A.; Goldberg, S. R. The Future of Endocannabinoid-Oriented Clinical Research after CB1 Antagonists. *Psychopharmacology (Berl).* **2009**, *205* (1), 171–174. https://doi.org/10.1007/s00213-009-1506-7.

(40) Iffland, K.; Grotenhermen, F. An Update on Safety and Side Effects of Cannabidiol: A Review of Clinical Data and Relevant Animal Studies. *Cannabis Cannabinoid Res.* **2017**, *2* (1), 139–154. https://doi.org/10.1089/can.2016.0034.

(41) Abu-Sawwa, R.; Scutt, B.; Park, Y. Emerging Use of Epidiolex (Cannabidiol) in Epilepsy. *J. Pediatr. Pharmacol. Ther.* **2020**, *25* (6), 485–499. https://doi.org/10.5863/1551-6776-25.6.485.

(42) Contino, M.; Capparelli, E.; Colabufo, N. A.; Bush, A. I. Editorial: The CB2 Cannabinoid System: A New Strategy in Neurodegenerative Disorder and Neuroinflammation. *Front. Neurosci.* **2017**, *11*.

(43) Guindon, J.; Hohmann, A. G. Cannabinoid CB2 Receptors: A Therapeutic Target for the Treatment of Inflammatory and Neuropathic Pain. *Br. J. Pharmacol.* **2008**, *153* (2), 319–334. https://doi.org/10.1038/sj.bjp.0707531.

(44) Zhou, L.; Zhou, S.; Yang, P.; Tian, Y.; Feng, Z.; Xie, X.-Q.; Liu, Y. Targeted Inhibition of the Type 2 Cannabinoid Receptor Is a Novel Approach to Reduce Renal Fibrosis. *Kidney Int.* **2018**, *94* (4), 756–772. https://doi.org/10.1016/j.kint.2018.05.023.

(45) Xiang, W.; Shi, R.; Kang, X.; Zhang, X.; Chen, P.; Zhang, L.; Hou, A.; Wang, R.; Zhao, Y.; Zhao, K.; Liu, Y.; Ma, Y.; Luo, H.; Shang, S.; Zhang, J.; He, F.; Yu, S.; Gan, L.; Shi, C.; Li, Y.; Yang, W.; Liang, H.; Miao, H. Monoacylglycerol Lipase Regulates Cannabinoid Receptor 2-Dependent Macrophage Activation and Cancer Progression. *Nat. Commun.* **2018**, *9* (1), 2574. https://doi.org/10.1038/s41467-018-04999-8.

(46) Silva, N. R.; Gomes, F. V; Fonseca, M. D.; Mechoulam, R.; Breuer, A.; Cunha, T. M.; Guimarães, F. S. Antinociceptive Effects of HUF-101, a Fluorinated Cannabidiol Derivative. *Prog. Neuro-Psychopharmacology Biol. Psychiatry* **2017**, *79*, 369–377. https://doi.org/10.1016/j.pnpbp.2017.07.012.

(47) Kinney, W. A.; McDonnell, M. E.; Zhong, H. M.; Liu, C.; Yang, L.; Ling, W.; Qian, T.; Chen,

Y.; Cai, Z.; Petkanas, D.; Brenneman, D. E. Discovery of KLS-13019, a Cannabidiol-Derived Neuroprotective Agent, with Improved Potency, Safety, and Permeability. *ACS Med. Chem. Lett.* **2016**, *7* (4), 424–428. https://doi.org/10.1021/acsmedchemlett.6b00009.

(48) Reekie, T. A.; Scott, M. P.; Kassiou, M. The Evolving Science of Phytocannabinoids. *Nat. Rev. Chem.* **2017**, *2* (1), 101. https://doi.org/10.1038/s41570-017-0101.

(49) Křížek, T.; Bursová, M.; Horsley, R.; Kuchař, M.; Tůma, P.; Čabala, R.; Hložek, T. Menthol-Based Hydrophobic Deep Eutectic Solvents: Towards Greener and Efficient Extraction of Phytocannabinoids. *J. Clean. Prod.* **2018**, *193*, 391–396. https://doi.org/10.1016/j.jclepro.2018.05.080.

(50) D.Lukas; P. Denis; W.Ulrich; D. petrovic; L. Dialer; U. Weigl; D. Petrovic; U. Weig. Process for the Production of Cannabidiol and Delta-9-Tetrahydrocannabinol WO2017011210A1, 2015.

(51) Jung, B.; Lee, J. K.; Kim, J.; Kang, E. K.; Han, S. Y.; Lee, H.-Y.; Choi, I. S. Synthetic Strategies for (-)-Cannabidiol and Its Structural Analogs. *Chem. Asian J.* **2019**, *14* (21), 3749–3762. https://doi.org/10.1002/asia.201901179.

(52) MECHOULAM, R.; GAONI, Y. A TOTAL SYNTHESIS OF DL-DELTA-1-TETRAHYDROCANNABINOL, THE ACTIVE CONSTITUENT OF HASHISH. *J. Am. Chem. Soc.* **1965**, *87*, 3273–3275. https://doi.org/10.1021/ja01092a065.

(53) Petrzilka, T.; Haefliger, W.; Sikemeier, C. Synthese von Haschisch-Inhaltsstoffen. 4. Mitteilung. *Helv. Chim. Acta* **1969**, *52* (4), 1102–1134. https://doi.org/10.1002/hlca.19690520427.

(54) Baek, S. H.; Srebnik, M.; Mechoulam, R. Boron Triflouride Etherate on Alimina - a Modified Lewis Acid Reagent. An Improved Synthesis of Cannabidiol. *Tetrahedron Lett.* **1985**, *26* (8), 1083–1086. https://doi.org/10.1016/S0040-4039(00)98518-6.

(55) Vaillancourt, V.; Albizati, K. F. A One-Step Method for the .Alpha.-Arylation of Camphor. Synthesis of (-)-Cannabidiol and (-)-Cannabidiol Dimethyl Ether. *J. Org. Chem.* **1992**, *57* (13), 3627–3631. https://doi.org/10.1021/jo00039a022.

(56) Kobayashi, Y.; Takeuchi, A.; Wang, Y.-G. Synthesis of Cannabidiols via Alkenylation of Cyclohexenyl Monoacetate. *Org. Lett.* **2006**, *8* (13), 2699–2702. https://doi.org/10.1021/ol060692h.

(57) Shultz, Z. P.; Lawrence, G. A.; Jacobson, J. M.; Cruz, E. J.; Leahy, J. W. Enantioselective Total Synthesis of Cannabinoids—A Route for Analogue Development. *Org. Lett.* **2018**, *20* (2), 381–384. https://doi.org/10.1021/acs.orglett.7b03668.

(58) Gong, X.; Sun, C.; Abame, M. A.; Shi, W.; Xie, Y.; Xu, W.; Zhu, F.; Zhang, Y.; Shen, J.; Aisa, H. A. Synthesis of CBD and Its Derivatives Bearing Various C4′-Side Chains with a Late-Stage Diversification Method. *J. Org. Chem.* **2020**, *85* (4), 2704–2715. https://doi.org/10.1021/acs.joc.9b02880.

(59) Pirrung, M. C. Synthetic Access to Cannabidiol and Analogs as Active Pharmaceutical Ingredients. *J. Med. Chem.* **2020**, *63* (21), 12131–12136. https://doi.org/10.1021/acs.jmedchem.0c00095.

(60) An, D.; Peigneur, S.; Hendrickx, L. A.; Tytgat, J. Targeting Cannabinoid Receptors: Current Status and Prospects of Natural Products. *Int. J. Mol. Sci.* **2020**, *21* (14), 5064. https://doi.org/10.3390/ijms21145064.

(61) Adams, A. J.; Banister, S. D.; Irizarry, L.; Trecki, J.; Schwartz, M.; Gerona, R. 'Zombie' Outbreak Caused by the Synthetic Cannabinoid AMB-FUBINACA in New York. *N. Engl. J. Med.* **2017**, *376* (3), 235–242. https://doi.org/10.1056/NEJMoa1610300.

(62) Moreira, F. A.; Crippa, J. A. S. The Psychiatric Side-Effects of Rimonabant. *Rev. Bras. Psiquiatr.* **2009**, *31* (2), 145–153. https://doi.org/10.1590/s1516-44462009000200012.

(63) Wootten, D.; Christopoulos, A.; Sexton, P. M. Emerging Paradigms in GPCR Allostery: Implications for Drug Discovery. *Nat. Rev. Drug Discov.* **2013**, *12* (8), 630–644. https://doi.org/10.1038/nrd4052.

(64) Bartuzi, D.; Kaczor, A. A.; Matosiuk, D. Opportunities and Challenges in the Discovery of Allosteric Modulators of GPCRs. *Methods Mol. Biol.* **2018**, *1705*, 297–319. https://doi.org/10.1007/978-1-4939-7465-8_13.

(65) Ross, R. A. Allosterism and Cannabinoid CB(1) Receptors: The Shape of Things to Come. *Trends Pharmacol. Sci.* **2007**, *28* (11), 567–572. https://doi.org/10.1016/j.tips.2007.10.006.

(66) Hryhorowicz, S.; Kaczmarek-Ryś, M.; Andrzejewska, A.; Staszak, K.; Hryhorowicz, M.; Korcz, A.; Słomski, R. Allosteric Modulation of Cannabinoid Receptor 1-Current Challenges and Future Opportunities. *Int. J. Mol. Sci.* **2019**, *20* (23), 5874. https://doi.org/10.3390/ijms20235874.

(67) Scott, C. E.; Kendall, D. A. Chapter Fourteen - Assessing Allosteric Modulation of CB1 at the Receptor and Cellular Levels. In *Cannabinoids and Their Receptors*; Reggio, P. H. B. T.-M. in E., Ed.; Academic Press, 2017; Vol. 593, pp 317–342. https://doi.org/10.1016/bs.mie.2017.05.002.

(68) Gado, F.; Meini, S.; Bertini, S.; Digiacomo, M.; Macchia, M.; Manera, C. Allosteric Modulators Targeting Cannabinoid Cb1 and Cb2 Receptors: Implications for Drug Discovery. *Future Med. Chem.* **2019**, *11* (15), 2019–2037. https://doi.org/10.4155/fmc-2019-0005.

(69) Martínez-Pinilla, E.; Varani, K.; Reyes-Resina, I.; Angelats, E.; Vincenzi, F.; Ferreiro-Vera, C.; Oyarzabal, J.; Canela, E. I.; Lanciego, J. L.; Nadal, X.; Navarro, G.; Borea, P. A.; Franco, R. Binding and Signaling Studies Disclose a Potential Allosteric Site for Cannabidiol in Cannabinoid CB(2) Receptors. *Front. Pharmacol.* **2017**, *8*, 744. https://doi.org/10.3389/fphar.2017.00744.

(70) McPartland, J. M.; Duncan, M.; Di Marzo, V.; Pertwee, R. G. Are Cannabidiol and Δ(9) - Tetrahydrocannabivarin Negative Modulators of the Endocannabinoid System? A Systematic Review. *Br. J. Pharmacol.* **2015**, *172* (3), 737–753. https://doi.org/10.1111/bph.12944.

(71) Laprairie, R. B.; Bagher, A. M.; Kelly, M. E. M.; Denovan-Wright, E. M. Cannabidiol Is a Negative Allosteric Modulator of the Cannabinoid CB1 Receptor. *Br. J. Pharmacol.* **2015**, *172* (20), 4790–4805. https://doi.org/10.1111/bph.13250.

(72) Morales, P.; Goya, P.; Jagerovic, N. Emerging Strategies Targeting CB2 Cannabinoid Receptor: Biased Agonism and Allosterism. *Biochem. Pharmacol.* **2018**, *157*, 8–17. https://doi.org/10.1016/j.bcp.2018.07.031.

(73) Tham, M.; Yilmaz, O.; Alaverdashvili, M.; Kelly, M. E. M.; Denovan-Wright, E. M.; Laprairie, R. B. Allosteric and Orthosteric Pharmacology of Cannabidiol and Cannabidiol-Dimethylheptyl at the Type 1 and Type 2 Cannabinoid Receptors. *Br. J. Pharmacol.* **2019**, *176* (10), 1455–1469. https://doi.org/10.1111/bph.14440.

(74) Navarro, G.; Gonzalez, A.; Sánchez-Morales, A.; Casajuana-Martin, N.; Gómez-Ventura, M.; Cordomí, A.; Busqué, F.; Alibés, R.; Pardo, L.; Franco, R. Design of Negative and Positive Allosteric Modulators of the Cannabinoid CB2Receptor Derived from the Natural Product Cannabidiol. *J. Med. Chem.* **2021**, *64* (13), 9354–9364. https://doi.org/10.1021/acs.jmedchem.1c00561.

(75) McAllister, S. D.; Hurst, D. P.; Barnett-Norris, J.; Lynch, D.; Reggio, P. H.; Abood, M. E. Structural Mimicry in Class A G Protein-Coupled Receptor Rotamer Toggle Switches: THE IMPORTANCE OF THE F3.36(201)/W6.48(357) INTERACTION IN CANNABINOID CB_1 RECEPTOR ACTIVATION *. *J. Biol. Chem.* **2004**, *279* (46), 48024–48037. https://doi.org/10.1074/jbc.M406648200.

(76) Krishna Kumar, K.; Shalev-Benami, M.; Robertson, M. J.; Hu, H.; Banister, S. D.; Hollingsworth, S. A.; Latorraca, N. R.; Kato, H. E.; Hilger, D.; Maeda, S.; Weis, W. I.; Farrens, D. L.; Dror, R. O.; Malhotra, S. V; Kobilka, B. K.; Skiniotis, G. Structure of a Signaling Cannabinoid Receptor 1-G Protein Complex. *Cell* **2019**, *176* (3), 448-458.e12. https://doi.org/10.1016/j.cell.2018.11.040.

(77) Hua, T.; Li, X.; Wu, L.; Iliopoulos-Tsoutsouvas, C.; Wang, Y.; Wu, M.; Shen, L.; Brust, C. A.; Nikas, S. P.; Song, F.; Song, X.; Yuan, S.; Sun, Q.; Wu, Y.; Jiang, S.; Grim, T. W.; Benchama, O.; Stahl, E. L.; Zvonok, N.; Zhao, S.; Bohn, L. M.; Makriyannis, A.; Liu, Z.-J. Activation and Signaling Mechanism Revealed by Cannabinoid Receptor-G(i) Complex Structures. *Cell* **2020**, *180* (4), 655-665.e18. https://doi.org/10.1016/j.cell.2020.01.008.

(78) Pérez-Benito, L.; Doornbos, M. L. J.; Cordomí, A.; Peeters, L.; Lavreysen, H.; Pardo, L.; Tresadern, G. Molecular Switches of Allosteric Modulation of the Metabotropic Glutamate 2 Receptor. *Structure* **2017**, *25* (7), 1153-1162.e4. https://doi.org/10.1016/j.str.2017.05.021.

(79) Sánchez, A. Síntesis de Nuevos Compuestos Con Actividad Farmacológica Diseñados a Través de Simulaciones Computacionales, 2022.

(80) Polini, B.; Cervetto, C.; Carpi, S.; Pelassa, S.; Gado, F.; Ferrisi, R.; Bertini, S.; Nieri, P.; Marcoli, M.; Manera, C. Positive Allosteric Modulation of CB1 and CB2 Cannabinoid Receptors Enhances the Neuroprotective Activity of a Dual CB1R/CB2R Orthosteric Agonist. *Life (Basel, Switzerland)* **2020**, *10* (12), 333. https://doi.org/10.3390/life10120333.

(81) Fronik, P.; Gaiser, B. I.; Sejer Pedersen, D. Bitopic Ligands and Metastable Binding Sites: Opportunities for G Protein-Coupled Receptor (GPCR) Medicinal Chemistry. *J. Med. Chem.* **2017**, *60* (10), 4126–4134. https://doi.org/10.1021/acs.jmedchem.6b01601.

(82) Chen, X.; Klöckner, J.; Holze, J.; Zimmermann, C.; Seemann, W. K.; Schrage, R.; Bock, A.; Mohr, K.; Tränkle, C.; Holzgrabe, U.; Decker, M. Rational Design of Partial Agonists for the Muscarinic M1 Acetylcholine Receptor. *J. Med. Chem.* **2015**, *58* (2), 560–576. https://doi.org/10.1021/jm500860w.

(83) Kamal, M.; Jockers, R. Bitopic Ligands: All-in-One Orthosteric and Allosteric. *F1000 Biol. Rep.* **2009**, *1*, 77. https://doi.org/10.3410/B1-77.

(84) Nimczick, M.; Decker, M. New Approaches in the Design and Development of Cannabinoid Receptor Ligands: Multifunctional and Bivalent Compounds. *ChemMedChem* **2015**, *10* (5), 773–786. https://doi.org/10.1002/cmdc.201500041.

(85) Nimczick, M.; Pemp, D.; Darras, F. H.; Chen, X.; Heilmann, J.; Decker, M. Synthesis and Biological Evaluation of Bivalent Cannabinoid Receptor Ligands Based on HCB_2R Selective Benzimidazoles Reveal Unexpected Intrinsic Properties. *Bioorg. Med. Chem.* **2014**, *22* (15), 3938–3946. https://doi.org/10.1016/j.bmc.2014.06.008.

(86) Gado, F.; Ferrisi, R.; Polini, B.; Mohamed, K. A.; Ricardi, C.; Lucarini, E.; Carpi, S.; Domenichini, F.; Stevenson, L. A.; Rapposelli, S.; Saccomanni, G.; Nieri, P.; Ortore, G.; Pertwee, R. G.; Ghelardini, C.; Di Cesare Mannelli, L.; Chiellini, G.; Laprairie, R. B.; Manera, C. Design, Synthesis, and Biological Activity of New CB2 Receptor Ligands: From Orthosteric and Allosteric Modulators to Dualsteric/Bitopic Ligands. *J. Med. Chem.* **2022**, *65* (14), 9918–9938. https://doi.org/10.1021/acs.jmedchem.2c00582.

(87) Gado, F.; Di Cesare Mannelli, L.; Lucarini, E.; Bertini, S.; Cappelli, E.; Digiacomo, M.; Stevenson, L. A.; Macchia, M.; Tuccinardi, T.; Ghelardini, C.; Pertwee, R. G.; Manera, C. Identification of the First Synthetic Allosteric Modulator of the CB(2) Receptors and Evidence of Its Efficacy for Neuropathic Pain Relief. *J. Med. Chem.* **2019**, *62* (1), 276–287. https://doi.org/10.1021/acs.jmedchem.8b00368.

(88) Ferrisi, R.; Polini, B.; Ricardi, C.; Gado, F.; Mohamed, K. A.; Baron, G.; Faiella, S.; Poli, G.; Rapposelli, S.; Saccomanni, G.; Aldini, G.; Chiellini, G.; Laprairie, R. B.; Manera, C.; Ortore, G. New Insights into Bitopic Orthosteric/Allosteric Ligands of Cannabinoid Receptor Type 2. *Int. J. Mol. Sci.* **2023**, *24* (3), 2135. https://doi.org/10.3390/ijms24032135.

(89) Morales, P.; Navarro, G.; Gómez-Autet, M.; Redondo, L.; Fernández-Ruiz, J.; Pérez-Benito, L.; Cordomí, A.; Pardo, L.; Franco, R.; Jagerovic, N. Discovery of Homobivalent Bitopic Ligands of the Cannabinoid CB(2) Receptor*. *Chemistry* **2020**, *26* (68), 15839–15842. https://doi.org/10.1002/chem.202003389.

(90) Dror, R. O.; Pan, A. C.; Arlow, D. H.; Borhani, D. W.; Maragakis, P.; Shan, Y.; Xu, H.; Shaw, D. E. Pathway and Mechanism of Drug Binding to G-Protein-Coupled Receptors. *Proc. Natl. Acad. Sci. U. S. A.* **2011**, *108* (32), 13118–13123. https://doi.org/10.1073/pnas.1104614108.

(91) Medina, R. A.; Vázquez-Villa, H.; Gómez-Tamayo, J. C.; Benhamú, B.; Martín-Fontecha, M.; de la Fuente, T.; Caltabiano, G.; Hedlund, P. B.; Pardo, L.; López-Rodríguez, M. L. The Extracellular Entrance Provides Selectivity to Serotonin 5-HT7 Receptor Antagonists

with Antidepressant-like Behavior in Vivo. *J. Med. Chem.* **2014**, *57* (15), 6879–6884. https://doi.org/10.1021/jm500880c.

(92) Wang, C.; Jiang, Y.; Ma, J.; Wu, H.; Wacker, D.; Katritch, V.; Han, G. W.; Liu, W.; Huang, X.-P.; Vardy, E.; McCorvy, J. D.; Gao, X.; Zhou, X. E.; Melcher, K.; Zhang, C.; Bai, F.; Yang, H.; Yang, L.; Jiang, H.; Roth, B. L.; Cherezov, V.; Stevens, R. C.; Xu, H. E. Structural Basis for Molecular Recognition at Serotonin Receptors. *Science* **2013**, *340* (6132), 610–614. https://doi.org/10.1126/science.1232807.

(93) Franco, R.; Morales, P.; Navarro, G.; Jagerovic, N.; Reyes-Resina, I. The Binding Mode to Orthosteric Sites and/or Exosites Underlies the Therapeutic Potential of Drugs Targeting Cannabinoid CB2 Receptors. *Front. Pharmacol.* **2022**, *13*, 852631. https://doi.org/10.3389/fphar.2022.852631.

(94) Tomanová, M.; Jedinák, L.; Cankař, P. Reductive Dehalogenation and Dehalogenative Sulfonation of Phenols and Heteroaromatics with Sodium Sulfite in an Aqueous Medium. *Green Chem.* **2019**, *21* (10), 2621–2628. https://doi.org/10.1039/C9GC00467J.

(95) Activitry, A. A Simple and Convenient Method for the Synthesis of Olivetols. *Bull. Korean Chem. Soc* **1993**, *14* (2), 273. https://doi.org/10.5012/bkcs.1993.14.2.272.

(96) Chiurchiù, E.; Sampaolesi, S.; Allegrini, P.; Ciceri, D.; Ballini, R.; Palmieri, A. A Novel and Practical Continuous Flow Chemical Synthesis of Cannabidiol (CBD) and Its CBDV and CBDB Analogues. *European J. Org. Chem.* **2021**, *2021* (8), 1286–1289. https://doi.org/10.1002/ejoc.202001633.

(97) Golliher, A. E.; Tenorio, A. J.; Dimauro, N. O.; Mairata, N. R.; Holguin, F. O.; Maio, W. Using (+)-Carvone to Access Novel Derivatives of (+)-Ent-Cannabidiol: The First Asymmetric Syntheses of (+)-Ent-CBDP and (+)-Ent-CBDV. *Tetrahedron Lett.* **2021**, *67*, 152891. https://doi.org/10.1016/j.tetlet.2021.152891.

(98) Marzullo, P.; Foschi, F.; Coppini, D. A.; Fanchini, F.; Magnani, L.; Rusconi, S.; Luzzani, M.; Passarella, D. Cannabidiol as the Substrate in Acid-Catalyzed Intramolecular Cyclization. *J. Nat. Prod.* **2020**, *83* (10), 2894–2901. https://doi.org/10.1021/acs.jnatprod.0c00436.

(99) Mechoulam, R.; Hanuš, L. Cannabidiol: An Overview of Some Chemical and Pharmacological Aspects. Part I: Chemical Aspects. *Chem. Phys. Lipids* **2002**, *121* (1–2), 35–43. https://doi.org/10.1016/S0009-3084(02)00144-5.

(100) Razdan, R. K.; Dalzell, H. C.; Handrick, G. R. A Simple One-Step Synthesis of (-)-Delta9-Tetrahydrocannabinol (THC) from p-Mentha-2,8-Dien-1-Ol and Olivetol. *J. Am. Chem. Soc.* **1974**, *96* (18), 5860–5865. https://doi.org/10.1021/ja00825a026.

(101) Rhee, K. H.; Basila, M. R. Chemisorption of BF3 on Catalytic Oxide Surfaces: Infrared Spectroscopic Studies. *J. Catal.* **1968**, *10* (3), 243–251. https://doi.org/10.1016/S0021-9517(68)80005-3.

(102) Klapötke, T. M.; McMonagle, F.; Spence, R. R.; Winfield, J. M. γ-Alumina-Supported Boron Trifluoride: Catalysis, Radiotracer Studies and Computations. *J. Fluor. Chem.* **2006**, *127* (10), 1446–1453. https://doi.org/10.1016/j.jfluchem.2006.05.010.

(103) Nishiguchi, T.; Fujisaki, S.; Ishii, Y.; Yano, Y.; Nishida, A. Convenient Selective

Monoacylation of 1,n-Diols Catalyzed by Ion-Exchange Resins. *J. Org. Chem.* **1994**, *59* (5), 1191–1195. https://doi.org/10.1021/jo00084a043.

(104) Abronina, P. I.; Zinin, A. I.; Orlova, A. V; Sedinkin, S. L.; Kononov, L. O. An Easy Access to Asymmetrically Substituted Oligoethylene Glycols from 18-Crown-6. *Tetrahedron Lett.* **2013**, *54* (34), 4533–4535. https://doi.org/10.1016/j.tetlet.2013.06.065.

(105) Nagle, A. S.; Salvatore, R. N.; Cross, R. M.; Kapxhiu, E. A.; Sahab, S.; Yoon, C. H.; Jung, K. W. Selective Mono Protection of Diols, Diamines, and Amino Alcohols Using Cesium Bases. *Tetrahedron Lett.* **2003**, *44* (30), 5695–5698. https://doi.org/10.1016/S0040-4039(03)01333-9.

(106) Corey, E. J.; Venkateswarlu, A. Protection of Hydroxyl Groups as Tert-Butyldimethylsilyl Derivatives. *J. Am. Chem. Soc.* **1972**, *94* (17), 6190–6191. https://doi.org/10.1021/ja00772a043.

(107) Ashraf, M. A.; Liu, Z.; Li, C.; Zhang, D. Recent Advances in Catalytic Silylation of Hydroxyl-Bearing Compounds: A Green Technique for Protection of Alcohols Using Si–O Bond Formations. *Appl. Organomet. Chem.* **2021**, *35* (3), e6131. https://doi.org/10.1002/aoc.6131.

(108) Bartoszewicz Marcin; Nilsson, Johan; Hiresova, Renata; Stawinski, Jacek, A. K. A New Reagent System for Efficient Silylation of Alcohols: Silyl Chloride-N-Methylimidazole-Iodine. *Synlett* **2008**, *2008* (01), 37–40. https://doi.org/10.1055/s-2007-992379.

(109) Blass, B. E.; Harris, C. L.; Portlock, D. E. A Facile, Selective KF/Al2O3 Mediated Method for the Deprotection of Aryl Silyl Ethers and Preparation of Aryl SEM Ethers. *Tetrahedron Lett.* **2001**, *42* (9), 1611–1613. https://doi.org/10.1016/S0040-4039(00)02259-0.

(110) Kharbangar, I.; Rohman, R.; Mecadon, H.; Myrboh, B. KF-Al2O3 as an Efficient and Recyclable Basic Catalyst for the Synthesis of 4H-Pyran-3-Carboxylates and 5-Acetyl-4H-Pyrans. *Int. J. Org. Chem.* **2012**, *2* (3), 282–286.

(111) Pájaro, Y.; Sathicq, Á.; Puello-Polo, E.; Pérez, A.; Romanelli, G.; Trilleras, J. An Efficient K2CO3-Promoted Synthesis of 1-Bromo-2-Aryloxyethane Derivatives and Evaluation of Larval Mortality against Aedes Aegypti. *J. Chem.* **2017**, *2017* (1), 6175315. https://doi.org/10.1155/2017/6175315.

(112) Crouch, R. D. Selective Deprotection of Silyl Ethers. *Tetrahedron* **2013**, *69* (11), 2383–2417. https://doi.org/10.1016/j.tet.2013.01.017.

(113) Greene, T. W. Protection for Phenols and Catechols. In *Greene's Protective Groups in Organic Synthesis*; 2006; pp 367–430. https://doi.org/10.1002/9780470053485.ch3.

(114) Jiang, Z.-Y.; Wang, Y.-G. A Mild, Efficient and Selective Deprotection of t-Butyldimethylsilyl-Protected Phenols Using Cesium Carbonate. *Tetrahedron Lett.* **2003**, *44* (19), 3859–3861. https://doi.org/10.1016/S0040-4039(03)00736-6.

(115) Fernandes, R. A.; Gholap, S. P.; Mulay, S. V. A Facile Chemoselective Deprotection of Aryl Silyl Ethers Using Sodium Hydride/DMF and in Situ Protection of Phenol with Various Groups. *RSC Adv.* **2014**, *4* (32), 16438–16443. https://doi.org/10.1039/C4RA00842A.

(116) Battiti, F. O.; Cemaj, S. L.; Guerrero, A. M.; Shaik, A. B.; Lam, J.; Rais, R.; Slusher, B. S.;

Deschamps, J. R.; Imler, G. H.; Newman, A. H.; Bonifazi, A. The Significance of Chirality in Drug Design and Synthesis of Bitopic Ligands as D3 Receptor (D3R) Selective Agonists. *J. Med. Chem.* **2019**, *62* (13), 6287–6314. https://doi.org/10.1021/acs.jmedchem.9b00702.

(117) Agharahimi, M. R.; LeBel, N. A. Synthesis of (-)-Monoterpenylmagnolol and Magnolol. *J. Org. Chem.* **1995**, *60* (6), 1856–1863. https://doi.org/10.1021/jo00111a052.

(118) Dovhaniuk, N.; Blahun, O. P.; Sosunovych, B.; Redka, M. O.; Vashchenko, B. V; Grygorenko, O. O. Regioselective and Scalable Total Synthesis of Licochalcone C and Related Licoagrochalcones. *European J. Org. Chem.* **2023**, *26* (3), e202201226. https://doi.org/10.1002/ejoc.202201226.

(119) Greene, T. H.; Wuts, P. G. M. Protection for the Hydroxyl Group, Including 1,2- and 1,3-Diols. In *Protective Groups in Organic Synthesis*; 1999; pp 17–245. https://doi.org/10.1002/0471220574.ch2.

(120) Sohn, J.-H.; Waizumi, N.; Zhong, H. M.; Rawal, V. H. Total Synthesis of Mycalamide A. *J. Am. Chem. Soc.* **2005**, *127* (20), 7290–7291. https://doi.org/10.1021/ja050728l.

(121) Han, J. H.; Kwon, Y. E.; Sohn, J.-H.; Ryu, D. H. A Facile Method for the Rapid and Selective Deprotection of Methoxymethyl (MOM) Ethers. *Tetrahedron* **2010**, *66* (9), 1673–1677. https://doi.org/10.1016/j.tet.2010.01.007.

(122) Sulake, R. S.; Lin, H.-H.; Hsu, C.-Y.; Weng, C.-F.; Chen, C. Synthesis of (+)-Antroquinonol: An Antihyperglycemic Agent. *J. Org. Chem.* **2015**, *80* (12), 6044–6051. https://doi.org/10.1021/acs.joc.5b00345.

(123) Kaiser, M.; Schönbauer, D.; Schragl, K.; Weil, M.; Gaertner, P.; Enev, V. S. Efforts toward the Total Synthesis of Elisabethin A. *J. Org. Chem.* **2022**, *87* (22), 15333–15349. https://doi.org/10.1021/acs.joc.2c01914.

(124) Xie, J.; Zheng, Z.; Liu, X.; Zhang, N.; Choi, S.; He, C.; Dong, G. Asymmetric Total Synthesis of (+)-Phainanoid A and Biological Evaluation of the Natural Product and Its Synthetic Analogues. *J. Am. Chem. Soc.* **2023**, *145* (8), 4828–4852. https://doi.org/10.1021/jacs.2c13889.

(125) Nudelman, A.; Bechor, Y.; Falb, E.; Fischer, B.; Wexler, B. A.; Nudelman, A. Acetyl Chloride-Methanol as a Convenient Reagent for: A) Quantitative Formation of Amine Hydrochlorides B) Carboxylate Ester Formation C) Mild Removal of N-t-Boc-Protective Group. *Synth. Commun.* **1998**, *28* (3), 471–474. https://doi.org/10.1080/00397919808005101.

(126) Dorsch, C.; Schneider, C. Brønsted Acid Catalyzed Asymmetric Synthesis of Cis-Tetrahydrocannabinoids**. *Angew. Chem. Int. Ed.* **2023**, *62* (24), e202302475. https://doi.org/10.1002/anie.202302475.

(127) Navarro, G.; Gómez-Autet, M.; Morales, P.; Rebassa, J. B.; Llinas del Torrent, C.; Jagerovic, N.; Pardo, L.; Franco, R. Homodimerization of CB2 Cannabinoid Receptor Triggered by a Bivalent Ligand Enhances Cellular Signaling. *Pharmacol. Res.* **2024**, *208*, 107363. https://doi.org/10.1016/j.phrs.2024.107363.

(128) Xu, Z.; Liu, Z.; Chen, T.; Chen, T.; Wang, Z.; Tian, G.; Shi, J.; Wang, X.; Lu, Y.; Yan, X.; Wang, G.; Jiang, H.; Chen, K.; Wang, S.; Xu, Y.; Shen, J.; Zhu, W. Utilization of Halogen Bond in Lead Optimization: A Case Study of Rational Design of Potent Phosphodiesterase Type 5 (PDE5) Inhibitors. *J. Med. Chem.* **2011**, *54* (15), 5607–5611. https://doi.org/10.1021/jm200644r.

(129) Wilcken, R.; Zimmermann, M. O.; Lange, A.; Joerger, A. C.; Boeckler, F. M. Principles and Applications of Halogen Bonding in Medicinal Chemistry and Chemical Biology. *J. Med. Chem.* **2013**, *56* (4), 1363–1388. https://doi.org/10.1021/jm3012068.

(130) Xu, Z.; Yang, Z.; Liu, Y.; Lu, Y.; Chen, K.; Zhu, W. Halogen Bond: Its Role beyond Drug-Target Binding Affinity for Drug Discovery and Development. *J. Chem. Inf. Model.* **2014**, *54* (1), 69–78. https://doi.org/10.1021/ci400539q.

(131) Politzer, P.; Murray, J. S.; Clark, T. Halogen Bonding: An Electrostatically-Driven Highly Directional Noncovalent Interaction. *Phys. Chem. Chem. Phys.* **2010**, *12* (28), 7748–7757. https://doi.org/10.1039/C004189K.

(132) Tatko, C. D.; Waters, M. L. Effect of Halogenation on Edge−Face Aromatic Interactions in a β-Hairpin Peptide: Enhanced Affinity with Iodo-Substituents. *Org. Lett.* **2004**, *6* (22), 3969–3972. https://doi.org/10.1021/ol0483807.

(133) Heroven, C.; Georgi, V.; Ganotra, G. K.; Brennan, P.; Wolfreys, F.; Wade, R. C.; Fernández-Montalván, A. E.; Chaikuad, A.; Knapp, S. Halogen–Aromatic π Interactions Modulate Inhibitor Residence Times. *Angew. Chem. Int. Ed.* **2018**, *57* (24), 7220–7224. https://doi.org/10.1002/anie.201801666.

(134) Benz, S.; Macchione, M.; Verolet, Q.; Mareda, J.; Sakai, N.; Matile, S. Anion Transport with Chalcogen Bonds. *J. Am. Chem. Soc.* **2016**, *138* (29), 9093–9096. https://doi.org/10.1021/jacs.6b05779.

(135) Mahmudov, K. T.; Kopylovich, M. N.; Guedes da Silva, M. F. C.; Pombeiro, A. J. L. Chalcogen Bonding in Synthesis, Catalysis and Design of Materials. *Dalt. Trans.* **2017**, *46* (31), 10121–10138. https://doi.org/10.1039/C7DT01685A.

(136) Benz, S.; López-Andarias, J.; Mareda, J.; Sakai, N.; Matile, S. Catalysis with Chalcogen Bonds. *Angew. Chem. Int. Ed.* **2017**, *56* (3), 812–815. https://doi.org/10.1002/anie.201611019.

(137) Peluso, P.; Gatti, C.; Dessì, A.; Dallocchio, R.; Weiss, R.; Aubert, E.; Pale, P.; Cossu, S.; Mamane, V. Enantioseparation of Fluorinated 3-Arylthio-4,4'-Bipyridines: Insights into Chalcogen and π-Hole Bonds in High-Performance Liquid Chromatography. *J. Chromatogr. A* **2018**, *1567*, 119–129. https://doi.org/10.1016/j.chroma.2018.06.060.

(138) Bortoli, M.; Ahmad, S. M.; Hamlin, T. A.; Bickelhaupt, F. M.; Orian, L. Nature and Strength of Chalcogen–π Bonds. *Phys. Chem. Chem. Phys.* **2018**, *20* (43), 27592–27599. https://doi.org/10.1039/C8CP05922E.

(139) Yılmaz, S.; Göksu, S. First Synthesis of Dopamine and Rotigotin Analogue 2-Amino-6,8-Dimethoxy-1,2,3,4-Tetrahydronaphthalene. *Synth. Commun.* **2014**, *44* (8), 1058–1065. https://doi.org/10.1080/00397911.2013.841939.

(140) Clayden, J.; Greeves, N.; Warren, S. *Organic Chemistry*, 2n edition.; Oxford University Press: Oxford, 2012.

(141) Appel, R. Tertiary Phosphane/Tetrachloromethane, a Versatile Reagent for Chlorination, Dehydration, and P-N Linkage. *Angew. Chem. Int. Ed. English* **1975**, *14* (12), 801–811. https://doi.org/10.1002/anie.197508011.

(142) Denton, R. M.; An, J.; Adeniran, B. Phosphine Oxide-Catalysed Chlorination Reactions of Alcohols under Appel Conditions. *Chem. Commun.* **2010**, *46* (17), 3025–3027. https://doi.org/10.1039/C002825H.

(143) van Kalkeren, H. A.; Leenders, S. H. A. M.; Hommersom, C. R. A.; Rutjes, F. P. J. T.; van Delft, F. L. In Situ Phosphine Oxide Reduction: A Catalytic Appel Reaction. *Chemistry* **2011**, *17* (40), 11290–11295. https://doi.org/10.1002/chem.201101563.

(144) Jordan, A.; Denton, R. M.; Sneddon, H. F. Development of a More Sustainable Appel Reaction. *ACS Sustain. Chem. Eng.* **2020**, *8* (5), 2300–2309. https://doi.org/10.1021/acssuschemeng.9b07069.

(145) Fuenzalida, N. M. D. R.; Alme, E.; Lundevall, F. J.; Bjørsvik, H.-R. An Environmentally Benign and High-Rate Appel Type Reaction. *React. Chem. Eng.* **2022**, *7* (7), 1650–1659. https://doi.org/10.1039/D2RE00071G.

(146) Kuboki, A.; Yamamoto, T.; Ohira, S. Total Synthesis of (±)-Aiphanol, a Novel Cyclooxygenase-Inhibitory Stilbenolignan. *Chem. Lett.* **2003**, *32* (5), 420–421. https://doi.org/10.1246/cl.2003.420.

(147) Cheraïti, N.; Brik, M. E. Synthesis of a New Triprotonated Ligand and Selective O-Demethylation of Methyl Aryl Ether by Boron Tribromide. *Tetrahedron Lett.* **1999**, *40* (23), 4327–4330. https://doi.org/10.1016/S0040-4039(99)00786-8.

(148) Weissman, S. A.; Zewge, D. Recent Advances in Ether Dealkylation. *Tetrahedron* **2005**, *61* (33), 7833–7863. https://doi.org/10.1016/j.tet.2005.05.041.

PART III

Experimental Methodologies

1. General Procedures

1.1. Reagents and Solvents

All commercially available reagents were used as received from the suppliers (Sigma-Aldrich, CymitQuimica, TCI, BLDpharm or Iris Biotech GmbH). Solvents were dried, when needed, by distillation over the appropriate drying agents: CH_2Cl_2 (CaH_2), THF (Na), ACN (CaH_2), toluene (Na), acetone ($CaCl_2$). When required, reactions were performed avoiding moisture by standard procedures and under nitrogen or argon atmosphere. Deuterated solvents were used directly from commercial source (Eurisotop™).

1.2. Chromatography

1.2.1. Thin-layer Chromatography (TLC)

All the reactions were monitored by analytical **thin-layer chromatography (TLC)** using ALUGRAM™ SIL/UV_{254} pre-coated aluminium plates (0.25 mm thickness) covered with silica gel 60 with fluorescent indicator or using ALUGRAM™ Alox-25/UV_{254} pre-coated aluminium plates (0.25 mm thickness) covered with aluminium oxide 60 with fluorescent indicator from Scharlab. Compounds were visualized using an UV lamp at 254 nm and/or using a $KMnO_4$/KOH aqueous solution or a vanillin solution.

1.2.2. Flash Column Chromatography

Flash column chromatography was performed using silica gel (mean pore: 60 Å; particle size: 0.04-0.06 mm, 230-400 mesh ASTM) or aluminium oxide 90 (active stage I) neutral (mean pore: 9 nm; particle size: 0.063-0.200 mm; 70-230 mesh ASTM).

1.2.3. Reverse-phase Medium-pressure Liquid Chromatography (RP-MPLC)

This technique was carried out at the Centro Intersciplinar de Química e Bioloxía (CICA) to purify the ligands **H_2CHXDEDPA**, **H_2CPDEDPA** and **H_2CBuDEDPA** before performing complexation with Cu(II) and Ga(III). It was performed in a Puriflash XS 420 InterChim Chromatographer equipped with a UV-DAD detector in reverse phase, using a 20 g BGB Aquarius C18AQ reverse-phase column (100 Å, spherical, 15 µm) and H_2O (0.1% TFA) / CH_3CN (0.1% TFA) as mobile phase.

In the same equipment, the purification of the ***cis*,*trans*-L2** ligand was also carried out with a 10 mM ammonium acetate aqueous solution (phase A) and CH_3CN with 10% of phase A (phase B) as the mobile phases, operating at a flow rate of 15 mL/min. The details of the method are specified in **Table III-1**.

Table III-1. RP-MPLC method applied for the purification of ***cis*,*trans*-L2** (with mobile phases A = ammonium acetate 10 mM aqueous solution and B = CH_3CN + 10% A).

Column volumes (CV)	Time (min)	B (%)
0.00	0.00	0
6.00	8.12	0
13.50	18.28	12
16.30	22.97	12
21.00	28.43	20
24.00	32.49	100
28.00	37.91	100

1.2.4. High-performance Liquid Chromatography (HPLC)

All the HPLC related techniques were carried out at Institut de Química Avançada (IQAC), at the Centro Singular de Investigación en Química Biológica y Materiales Moleculares (CIQUS) or at the University of Wiscosin-Madison.

1.2.4.1. Reverse-phase HPLC Coupled to a Mass Spectrometer (RP-HPLC-MS)

This technique was employed to monitor coupling reaction on SPPS and for determining the molecular mass of **CF-γ-CC** and **CF-γ-CT** peptides. It was carried out in a two-system equipment consisting on a Watters Alliace 2695 with a multichannel UV-vis detector Photodiode Array Detector 2996 and a Water 2795 Separation Module coupled to a mass spectrometer Micromass ZQ with an electrospray probe. The column used was the XBridge® BEH 130 C18 (4.6 x 100 mm, 3.5 µm). Used flux was 1.6 mL/min and the eluents were A: H_2O/HCOOH (99.9:0.10, v/v) and B: CH_3CN/HCOOH (99.93:0.07, v/v). Spectra were recorded at λ = 220 nm.

1.2.4.2. Semipreparative Reverse-phase HPLC Coupled to a Mass Spectrometer (Semiprep-RP-HPLC-MS)

This technique was used to purify the synthesised peptides. This equipment was built using a binary gradient Waters 2545 integrated with two pumps, a high-pressure mixer, a Waters Aliance 2767 sample manager module and an automatic fraction collector couped to a dua UV-vis Absorbance Detector 2487 and a mass spectrometer Micromass ZQ. The column used was the XBridge® BEH C18 (19 x 100 mm, 5 µm) in the case of **CF-γ-CC** and **CF-γ-CT**, and a Phenomenex Luna C18(2) 100 Å column in the case of **γ-SCC**. The flow rate used was 16 mL/min for 10 minutes and the eluents were A: CH_3CN/HCOOH (99.93:0.07, v/v) and B: H_2O/HCOOH (99.9:0.10, v/v).

1.2.4.3. Reverse-phase HPLC (RP-HPLC)

This technique was used to measure the purity of the compounds and to make a repurification in some cases where the Semiprep-RP-HPLC-MS was not enough. This equipment consisted in a Watter Alliace 2695 with a multichannel UV-vis detector Photodiode Array Detector 2998.

The column used was the XBridge® BEH 130 C18 (4.6 x 100 mm, 3.5 µm) in the case of **CF-γ-CC** and **CF-γ-CT**, and a Phenomenex Luna C18(2) 100 Å column in the case of **γ-SCC**. The flow rate used was 1 mL/min and the eluents were A: H_2O/TFA (99.9:0.10, v/v) and B: CH_3CN/TFA (99.9:0.10, v/v). Spectra were recorded at λ = 220 nm.

1.2.4.4. Preparative HPLC

The chelator ***cis,trans*-L2** was purified by preparative HPLC before radiolabelling experiments in the facilities of the University of Wisconsin-Madison to ensure high purity. This technique was carried out using an Agilent 1260 Infinity II instrument equipped with an UV Variable Wavelenghth Detector, in manual injection and collection mode, using an Agilent InfinityLab ZORBAX 5 Eclipse Plus C18 (5 µm, 21.2 x 250 mm) and 10 mM ammonium acetate aqueous solution (phase A) and CH_3CN with 10% of phase A (phase B) as the mobile phases, operating at a flow rate of 20 mL/min. The details of the method are specified in **Table III-2**.

Table III-2. HPLC method applied for the purification of ***cis*,*trans*-L2** (with mobile phases A = ammonium acetate 10 mM aqueous solution and B = CH_3CN + 10% A).

Time (min)	B (%)
0	5
5	5
25	20
30	95
35	95

1.2.4.5. Radio-HPLC

This technique was employed with the different radiolabelled ligands in the University of Wiscosin-Madison research facilities using a Shimadzu HPLC-20AR chromatograph equipped with a binary gradient, pump, UV−vis detector, autoinjector, and Laura radiodetector on a Phenomenex Gemini C18 column (3 µm, 3 × 150 mm). For the non-bifunctional ligands radiolabelled with ^{64}Cu and ^{68}Ga, 0.1% TFA in H_2O (phase A) and 0.1% TFA in CH_3CN (phase B) were employed as mobile phase, operating with a flow rate of 0.8 mL/min. For **[^{64}Cu]-[Cu(*cis*,*trans*-L2)]** radiocomplex, 10 Mm ammonium acetate aqueous solution (phase A) and CH_3CN with 10% of phase A (phase B) were used as the mobile phases, operating at a flow rate of 0.8 mL/min. The details of the method are specified in **Table III-3**.

Table III-3. Radio-HPLC method applied for the analysis of the non-bifunctional ligands radiolabelled with ^{64}Cu and ^{68}Ga (with mobile phases A = 0.1% TFA in H_2O and B = 0.1% TFA in CH_3CN) and the **[^{64}Cu]-[Cu(*cis*,*trans*-L2)]** radiocomplex (with mobile phases A = ammonium acetate 10 mM aqueous solution and B = CH_3CN + 10% A).

Time (min)	B (%)
0	0
2	5
24	95
26	95
28	5

1.3. Spectroscopy

1.3.1. Nuclear Magnetic Resonance (NMR)

Nuclear magnetic resonance (NMR) spectra were registered at the Servei de Ressonància Magnètica Nuclear of the Universitat Autònoma de Barcelona. ^{1}H-NMR spectra were recorded in a BRUKER Avance™ DPX250 (250 MHz), BRUKER Ascend™ 300 (300 MHz), BRUKER Avance™ DPX360 (360 MHz), BRUKER AR430 (400 MHz), BRUKER Ascend™ 400 (400 MHz), BRUKER 500 UltraShield™ (500 MHz) and a BRUKER 600 UltraShield™ Avance II+ (600 MHz) spectrometers. Proton chemical shifts are reported in ppm (δ) ($CDCl_3$, 7.26 ppm; D_2O, 4.79 ppm; MeOD-d_4, 3.31 ppm; DMSO-d_6, 2.50 ppm). ^{13}C-NMR spectra were recorded with complete proton decoupling in a BRUKER Avance™ DPX250 (63 MHz), BRUKER Ascend™ 300 (75 MHz), BRUKER Avance™ DPX360 (90 MHz), BRUKER Ascend™ 400 (100 MHz), BRUKER 500 UltraShield™ (125 MHz) and a BRUKER 600 UltraShield™ Avance II+ (150 MHz) spectrometers. Carbon chemical shifts are reported in ppm ($CDCl_3$, 77.2 ppm; MeOD-d_4, 49.0 ppm; DMSO-d_6, 39.5 ppm). NMR signals were assigned with the help of COSY, me-HSQC, HMBC, NOE and NOESY experiments. All spectra were recorded at 298 K.

The abbreviations used to describe signal multiplicities are: m (multiplet), s (singlet), d (doublet), t (triplet), q (quartet), sext. (sextet), br s (broad singlet), dd (doublet of doublets), dt (doublet of triplets), dq (doublet of quartets), dquint (doublet of quintets), td (triplet of doublets), ddd (doublet of doublet of doublets), dqd (doublet of quartet of doublets), dddd (double of doublet of doublet of doublets) and *J* (coupling constant).

1.3.2. Infrared spectra (IR)

Infrared spectra (IR) were recorded on a BRUKER Tensor 27 Spectrophotometer equipped with a Golden Gate Single Refraction Diamond ATR (Attenuated Total Reflectance) or on a BRUKER Alpha II Spectrophotometer equipped with a Platinum-ATR Convenience sampling module QuickSnap, equipment provided by Servei d'Anàlisi Química of the Universitat Autònoma de Barcelona. Peaks are reported in cm^{-1}.

1.3.3. Single crystal X-ray diffraction

Single crystal X-ray diffraction was recorded on three-circle SMART APEX single crystal diffractometer from BRUKER provided with a CCD APEX area detector, molybdenum anode X-ray tube and *Krioflex* low-temperature device which allows measurements from room temperature to -180 °C. X-ray crystal structures were performed by Dr. Ángel Álvarez from the Servei Difracció Raigs X of Universitat Autónoma de Barcelona.

1.4. Mass Spectrometry (MS)

High resolution mass spectrometry (HRMS) was recorded at the Centro de I+D+I of the Parque Científico Tecnológico of the Universidad de Burgos (UBU) in an Agilent 6454 Q-TP spectrometer with an Argilent Jetstream Technology (AJT) source using electrospray ionisation (ESI); and at Servei d'Analisí Química (SAQ) of the Universitat Autònoma de Barcelona (UAB) in a ICP-MS coupled inductive plasma mass spectrometer Agilent 7500 ce, an Agilent 7900 with an autosampler SPS 4, both using Argilent Jetstream Technology (AJT) source using electrospray ionisation (ESI), and a BRUKER timsTOFPro 2 coupled to a BRUKER SCION 436GC using Atmospheric Pressure Chemical Ionisation (APCI).

1.5. Specific Optical Rotation

Specific optical rotations ($[\alpha]_D^{25}$) were measured at 25 ± 2 °C and 589.6 nm using a AUTOPOL I automatic polarimeter of RUDOLPH RESEARCH ANALYTICAL and using a 0.1 dm long cuvette at Servei d'Anàlisi Química in the Universitat Autònoma de Barcelona. Concentration values are given in g/mL.

1.6. Details on other techniques

- **Elemental analyses** were obtained using LTQ-Orbitrap Discovery Mass Spectometer coupled to a Thermo Accela HPLC in the CICA research facilities.
- **Melting points (m.p.)** were determined on a REICHERT Koffler hot stage melting point apparatus.
- **Photochemical reactions** were performed in a Pyrex T-shaped photochemical reactor from TRALLERO&SCHLEE™. Irradiation is emitted from a mercury lamp of 125 W or 400 W medium pressure ELECTRO DH™. Refrigeration of the inside of the reactor and an external bath are kept at room temperature by a C40P TERMO SCIENTIFIC™ refrigerator, Phoenix II model.
- **Hydrogenations** performed above atmospheric pressure were carried out in an autoclave hydrogenation T-reactor Swagelok™, with a pressure capacity from 1 to 20 atm (kg/cm^2).
- **Lyophilization** of samples were done using a TELSTAR™ lyophilizer, LyoQuest-85 model.
- **Micro-distillations** were carried out in a BÜCHI™ distiller, Glass Oven B-585 model.
- **pH** measurements were carried out using 20 CRINSON® pHmeter.

2. Procedures Performed in Part I

Chapter I. Hybrid γ,γ-Peptidomimetics as Mitochondria Penetrating Peptides

The procedures related to the solid phase synthesis and *in vitro* assays of the peptides **CF-γ-CC, CF-γ-CT** and **γ-SCC** were performed in Prof. Montenegro, by Dr. Pazo and PhD student Yeray Folgar, at the Centro Singular de Investigación en Química Biológica y Materiales Moleculares (CiQUS) research facilities in the Universidad de Santiago de Compostela.

2.1. Kaiser (Ninhydrin) Qualitative Test Performed in SPPS

This analytical procedure is employed to determine the presence or absence of primary amines. Also, secondary amines can be detected, but the result is not reliable. To perform this test, a sample of the peptide linked to the resin (0.5-2.0 mg) was placed into a glass tube, followed by the addition of reagent A and 2 drops of reagent B. The mixture was then heated in an oven at 100 ºC for 3 minutes. After heating, the colour of the mixture is observed: a yellow colour indicates a negative test (absence of primary amines, but presence of secondary ones), while a deep blue-purple hue implies a positive test (presence of amines). If no colour change is observed, the sample likely does not contain primary or secondary amines.

-Reagent A: A hot solution was prepared by dissolving phenol (80 g) in absolute ethanol (20 mL). Separately, 4 mL of a solution of potassium cyanide in water (0.06%, w/v) was added over pyridine (200 mL). To each of these mixtures, 8.00 g of the resin were added, and the mixtures were stirred for 45 minutes. Subsequently, the solutions were filtered and then combined.

-Reagent B: A solution was prepared by dissolving ninhydrin (5.00 g) in ethanol (100 mL). This solution was stored in a closed container, protected from light exposure.

2.2. Intracellular localisation assays

For the intracellular localisation assays of peptides, the technique employed was confocal microscopy. This technique uses a laser to scan across a specimen, with a pinhole aperture to eliminate out-of-focus light, visualising the emitted signal from a fluorophore, resulting in high-resolution, sharp images of thin optical sections. Can create images at different depths within the sample, allowing for the construction of three-dimensional structures. It is ideal for studying the fine structure of cells and tissues, including organelles, cytoskeleton, and complex cellular interactions, being able to precisely determine the localisation of the peptides within cells. In addition, this technique can also be used to observe live cells and monitor dynamic processes over time.

2.2.1. Intracellular Localisation of CF-γ-CC and CF-γ-CT in HeLa Cells

HeLa cells were seeded on a 96-well glass bottom plate at a density of 100.000 cells/mL (100 µL/well) an incubated for 24 h. **CF-γ-CC** and **CF-γ-CT** were diluted in Dubelcco's Modified Eagle's Medium (DMEM) stock at 25 µM, then added to the cells (85 µL/well) and incubated for 1 h at 37 ºC,

5% CO_2. Afterwards, cells were washed with DMEM stock and incubated in complete DMEM for 3 h. Subsequently, the samples were imaged in DMEM using Fusion software (Andor) with a Dragonfly spinning disk confocal microscope mounted on a Nikon Eclipse Ti-E and equipped with an Andor Sona sCMOS digital camera. For **CF-γ-CC** and **CF-γ-CT**, an emission of 488 nm was used while the excitation was recorded at 525/50 nm. Differential interference contrast (DIC) images were taken along with the fluorescence channel. Images were processed with ImageJ v1.52b.

2.2.2. Colocalisation of CF-γ-CC and CF-γ-CT with MitoTracker™ Red CMXRos in HeLa Cells

HeLa cells were seeded on a 96-well glass bottom plate at a density of 100.000 cells/mL (100 µL/well) an incubated for 24 h. **CF-γ-CC** and **CF-γ-CT** were diluted in DMEM stock at 25 µM, then added to the cells and incubated for 1 h at 37 ºC, 5% CO_2. Afterwards, cells were rinsed with DMEM stock and incubated during 20 minutes with a 50 nM stock solution of MitoTracker™ Red CMXRos dye in DMEM (50 µL/well) at 37 ºC and protected from light to prevent photobleaching. Then, cells were washed with DMEM and incubated in complete DMEM for 3 h. Subsequently, the samples were imaged in DMEM using Fusion software (Andor) with a Dragonfly spinning disk confocal microscope mounted on a Nikon Eclipse Ti-E and equipped with an Andor Sona sCMOS digital camera. MitoTracker™ Red CMXRos was excited with the 561 nm laser and the emission was recorded at 620/60 nm; and for the carboxyfluorescein containing peptides, **CF-γ-CC** and **CF-γ-CT**, an excitation of 488 nm was used while the emission was recorded at 525/50 nm. DIC images were taken along with the fluorescence channel. Images were processed with ImageJ v1.52b.

2.2.3. Intracellular Localisation of γ-SCC with MitoTracker™ Red CMXRos in several cell lines

A549, CHO, HeLa, HepG2 and Vero cells were seeded the day before on a 96-well glass bottom plate at a density of 100.000 cells/mL, 100 µL/well. **γ-SCC** was diluted in DMEM stock at 25, 50 and 75 µM, then added to the cells (85 µL/well) and incubated for 1 h at 37 ºC, 5% CO_2. Afterwards, cells were washed with DMEM stock and incubated in complete DMEM for 6 h. Alternatively, cells were incubated with 50 nM MitoTracker™ Red CMXRos (50 µL/well) in DMEM stock for 25 min at 37 ºC, 5% CO_2. Subsequently, nuclei were stained with 1 µM (50 µL/well) Hoechst 33342 for 20 min, and immediately imaged in DMEM without phenol red using Fusion software (Andor) with a Dragonfly spinning disk confocal microscope mounted on a Nikon Eclipse Ti-E and equipped with an Andor Sona sCMOS digital camera. Fluorescence of Hoechst was excited with the 405 nm laser and the emission was recorded at 450/50 nm; for SNARF and MitoTracker, an excitation of 561 nm was used while the emission was recorded at 620/60 nm. At least 3 representative images were taken for each condition. Images were processed with ImageJ v1.52b.

2.2.4. Colocalisation of γ-SCC with BioTracker 488 Green Mitochondria Dye in HeLa Cells

HeLa cells were seeded the day before on a 96-well glass bottom plate at a density of 100.000 cells/mL, 100 µL/well. **γ-SCC** was diluted in DMEM stock at 25 µM, then added to the cells (85 µL/well) and incubated for 1 h at 37 ºC, 5% CO_2. Afterwards, cells were washed with DMEM stock and incubated in complete DMEM for 6 h. Subsequently, mitochondria were stained with 100 nM

(50 µL/well) BioTracker 488 Green Mitochondria Dye for 20 min, and immediately imaged in DMEM without phenol red using Fusion software (Andor) with a Dragonfly spinning disk confocal microscope mounted on a Nikon Eclipse Ti-E and equipped with an Andor Sona sCMOS digital camera. BioTracker 488 Green was excited with the 488 nm laser and the emission was recorded at 525/50 nm; for γ-SCC, an excitation of 561 nm was used while the emission was recorded at 620/60 nm. DIC images were acquired alongside both fluorescence channels, and no bleedthrough was observed during colocalization studies with these parameters. A total of eight representative images were taken. Images were processed with ImageJ v1.52b.

2.2.5. Control of the SNARF Probe Cellular Internalisation

For the SNARF internalisation and targeting control, HeLa cells were seeded the day before on a 96-well glass bottom plate (Cellvis) at a density of 100.000 cells/mL, 100 µL/well. SNARF probe was diluted in DMEM stock at 25, 50 and 75 µM, then added to the cells (85 µL/well) and incubated for 1 h at 37 °C, 5% CO_2. Afterwards, cells were washed with DMEM stock and incubated in complete DMEM for 6 h. Subsequently, nuclei were stained with 1 µM, 50 µL/well, Hoechst 33342 for 20 min, and immediately imaged in DMEM without phenol red using Fusion software (Andor) with a Dragonfly spinning disk confocal microscope mounted on a Nikon Eclipse Ti-E and equipped with an Andor Sona sCMOS digital camera. Fluorescence of Hoechst was excited with the 405 nm laser and the emission was recorded at 450/50 nm; for the SNARF fluorescence, an excitation of 561 nm was used while the emission was recorded at 620/60 nm. At least 3 representative images were taken for each condition. Images were processed with ImageJ v1.52b. Notable increments were made in both laser intensity and the brightness and contrast of the image during processing compared to images obtained when using **γ-SCC** alone. This adjustment was necessary due to the difficulty in detecting the low intensity of the internalised probe alone.

2.2.6. Manders' Overlap Coefficients (MOC) and Pearson's Correlation Coefficient (PCC)

Manders' Overlap and Pearson's Correlation coefficients were calculated to assess the degree of colocalization between carboxyfluorescein containing peptides, **CF-γ-CC** and **CF-γ-CT** and MitoTracker™ Red CMXRos, and also in the colocalization experiments with **γ-SCC** and the BioTracker 488 Green Mitochondria Dye.

Manders' Overlap coefficients (MOC) provide a measure of colocalization by evaluating the overlap of pixel intensities in dual-channel images. Ranging from 0 to 1, with 0 indicating non-overlapping images and 1 reflecting 100% colocalization, M_1 and M_2 are defined as ratios of intensities in one channel coincident with the other channel's signal to the total intensity in their respective channels. In this case, M_1 refers to the fraction of the peptide (**CF-γ-CC**, **CF-γ-CT** or **γ-SCC**) overlapping the corresponding dye (MitoTracker™ Red CMXRos or BioTracker 488 Green), being related to the specificity of the peptide to the structure, in this case the mitochondria. A value of 0 indicates no specificity, whereas a value of 1 represents complete specificity for that structure. In the case of M_2, it represents the fraction of the dye overlapping the corresponding peptide, which relates to the efficiency for labelling the structure, in this case the mitochondria. An exclusive labelling of the

mitochondria translates to a value of 1, while if the peptide is distributed all over the structure of the cell, the value would be lower, down to a minimum of 0.

On the other hand, Pearson's coefficient measures the dependency of pixels in dual-channel images by plotting their grey values in a scatter plot. The coefficient ranges from 1 to −1, indicating complete positive correlation to an inverse correlation of the fluorescent intensities, with 0 representing no correlation. In our analyses, colocalization parameters were calculated from 8 representative images with ImageJ using the plugin JaCoP and the Costes method for the estimation of the threshold.

2.3. MTT Viability

Cell viability was determined via MTT assay, a colorimetric assay for assessing cell metabolic activity through the reduction of tetrazolium dye MTT (3-(4,5-dimethylthiazol-2-yl)-2,5-diphenyltetrazolium bromide) to the insoluble formazan, which has a purple colour, by the NAD(P)H-dependent cellular oxidoreductase enzymes. For these MTT assays, HeLa cells were seeded the day before on 96-well plates (Costar) at a density of 100,000 cells/mL, 100 µL/well**. γ-SCC** was diluted in DMEM stock at concentrations in the range 0–1000 µM, then added to the cells (85 µL/well) and incubated for 1 or 24 h at 37 ºC, 5% CO_2. Thereafter, cells were incubated with complete DMEM containing 0.5 mg/mL MTT for 2 h, then the medium was carefully removed, and formazan crystals were dissolved by addition of DMSO (100 µL/well). The absorbance at 570 nm was measured with a plate reader (Tecan Infinite F200Pro) and the data were normalised to the value of untreated cells (100% viability), after blank subtraction (cells previously treated with 1% Triton X-100). Each condition was measured in quadruplicate. Curve fitting was performed with GraphPad Prism 6 software (v6.01) using a 4-parameters logistic model.

2.4. Peptide Stability

2.4.1. Resistance Against Trypsin Enzymatic Activity

Resistance of **γ-CC** to enzymatic hydrolysis was investigated by incubation in the presence of the protease trypsin. As controls, two cationic peptides, $\mathbf{R_8}$ and **KLAK**, were included. **γ-CC** (50 µM), $\mathbf{R_8}$ (500 µM) and **KLAK** (100 µM) were dissolved in PBS in the presence of 100 µM 4-acetamidobenzoic acid (ABA), a compound not degraded by the enzyme, serving as an internal standard. Before addition of the protease, **γ-CC** and **KLAK** samples were analysed by RP-HPLC Agilent SB-C18 column, H_2O (0.1% TFA) / CH_3CN (0.1% TFA) 95:5→5:95 (0→12 min), while R_8 was instead analysed using H_2O (0.1% TFA) / CH_3CN (0.1% TFA) 75:25→25:75 (0→12 min). Subsequently, trypsin enzyme was added at a concentration ratio of 50:1 (peptide:enzyme), and after 5 min of incubation at 37 ºC, the control peptides $\mathbf{R_8}$ and **KLAK** were analysed by HPLC. **γ-CC** was analysed after 24 h incubation at 37 ºC. For plotting, absorbance data at 220 nm were normalised to the maximum intensity value of the internal standard peak, ABA.

2.4.2. Stability in Fetal Bovine Serum

To investigate the activity and stability of the peptide in the presence of FBS, **γ-SCC** was diluted in complete DMEM, which contains 10% FBS, at 25 µM, then added to the cells (85 µL/well) and incubated for 1 h at 37 ºC, 5% CO_2. Additionally, a peptide aliquot was incubated in complete DMEM for 7 days at 37 ºC and then incubated with the cells under the same conditions. Afterwards, cells were washed with DMEM stock and incubated in complete DMEM for another 6 h. Subsequently, cells were imaged in DMEM without phenol red using Fusion software (Andor) with a Dragonfly spinning disk confocal microscope mounted on a Nikon Eclipse Ti-E and equipped with an Andor Sona sCMOS digital camera. **γ-SCC** was excited with the 561 nm laser and the emission was recorded at 620/60 nm. At least 3 representative images were taken for each condition. Images were processed with ImageJ v1.52b.

2.5. Study of the Internalisation Mechanism into HeLa Cells

HeLa cells were seeded the day before on a 96-well plate (Costar™) at a density of 100,000 cells/mL, 100 µL/well. The next day, cells were treated with PBS (140 mM KCl, 30 mM Na_2HPO_4, 1.76 mM KH_2PO_4, 1 mM $CaCl_2$, 0.5 mM $MgCl_2$, pH 7.4) or alternatively with a mixture of sodium azide and 2-deoxy-D-glucose (10 mM each), Dynasore (80 µM), EIPA (50 µM), or chlorpromazine (30 µM) diluted in DMEM stock (50 µL/well) and incubated for 30 min at 37 ºC, 5% CO_2. Afterwards, these solutions were replaced by PBS containing 50 µM **γ-SCC** (50 µL/well) or samples in DMEM stock of 50 µM **γ-SCC** and the same amount of the corresponding inhibitor (50 µL/well), and incubated for 1 h at 37 ºC, 5% CO_2. Then, cells were washed with PBS, trypsinised, and subsequently trypsin was next neutralised with PBS containing 2% FBS and 5 mM EDTA. SNARF fluorescence was measured on a Guava easyCyte BG HT, exciting with a green laser (532 nm) and collecting the emission at 620/52 nm (Orange-G channel). Data was analysed using InCyte v.3.2. (GuavaSoft, Millipore®). Cells with typical FSC/SSC values were selected and the mean fluorescence intensity was calculated for each sample. Each condition was measured in quadruplicates.

2.6. Exploration of the Potential Applications

2.6.1. Tracking of the Mitochondria Dynamics by Confocal Microscopy

HeLa cells were seeded the day before on a 96-well glass bottom plate (Cellvis) at a density of 100,000 cells/mL, 100 µL/well. **γ-SCC** was diluted in DMEM stock at 25 µM, then added to the cells (85 µL/well) and incubated for 1 h at 37 ºC, 5% CO_2. Afterwards, cells were washed with DMEM stock and incubated in complete DMEM for 6 h. Subsequently, cells were immediately imaged in DMEM without phenol red using Fusion software (Andor) with a Dragonfly spinning disk confocal microscope mounted on a Nikon Eclipse Ti-E and equipped with an Andor Sona sCMOS digital camera. Images were recorded every 5 s until 40 photographs were obtained. Fluorescence of SNARF was excited with the 561 nm laser and the emission was recorded at 620/60 nm. Images were processed with ImageJ v1.52b. A total of 2 representative videos were recorded. The

fluorescence intensity in each frame of both recorded videos was quantified, and the average values were plotted after normalisation to the fluorescence of the first frame.

2.6.2. Measuring Mitochondrial pH by Confocal Microscopy

2.6.2.1. Calibration Curve

To assess the pH-dependent emission properties of the SNARF probe, **γ-SCC** was dissolved at 50 µM in a buffer solution (10 mM MES, 10 mM HEPES, 20 mM glucose, 1 mM $CaCl_2$, 1 mM $MgCl_2$, 135 mM KCl, and 20 mM NaCl) previously adjusted to a total of 11 pH values (from 4.6 to 9.5 pH). Samples (50 µL/well) were dispensed into a 96-well glass bottom plate (Cellvis) and imaged using a Leica Stellaris 8 FALCON. **γ-SCC** fluorescence was excited with the 561 nm laser and emission was recorded at 588/30 nm (maximum emission intensity for the acid form of the probe) and at 633/30 nm (maximum emission intensity for the basic form of the probe). Six images at different z-planes were acquired for each pH and emission wavelength. The intensity value of each pixel in the 633/30 nm images was divided by the intensity value of the corresponding pixel in the 588/30 nm images. Subsequently, six images per pH were generated, with each pixel representing the intensity ratio between 633 and 588 nm. The mean intensity value across all pixels in each image was calculated, and the average of the six ratio values obtained at each pH was determined. The calibration curve was generated by performing curve fitting with GraphPad Prism 6 software v6.01 using a 4-parameters logistic model, associating each pH value with the corresponding mean 633/588 ratio value.

2.6.2.2. Image Acquisition and Calculation of *In Vitro* Mitochondrial pH

HeLa cells were seeded the day before on a 96-well glass bottom plate (Cellvis) at a density of 100,000 cells/mL, 100 µL/well. **γ-SCC** was diluted in DMEM stock at 25 µM, then added to the cells (85 µL/well) and incubated for 1 h at 37 ºC, 5% CO_2. Afterwards, cells were washed with DMEM stock and incubated in complete DMEM for 6 h. Subsequently, cells were immediately imaged in DMEM without phenol red using a confocal microscope Leica Stellaris 8 FALCON. SNARF fluorescence was excited with the 561 nm laser and emission was recorded at 588/30 nm (maximum emission intensity for the acid form of the probe) and at 633/30 nm (maximum emission intensity for the basic form of the probe).

To obtain a pH image based on the images obtained at the two maxima, the images were processed with ImageJ v1.52b. Initially, the image acquired at 633/30 nm was divided by the image obtained at 588/30 nm, resulting in a new image where each pixel corresponds to the ratio of the two intensity values. This image was exported in text format, and the ratio value of each pixel was transformed into a pH value using the previously calculated calibration curve; these analyses were conducted using R Statistical Software v4.1.0; R Core Team 2021. The processed file was imported back into ImageJ and a thresholding mask applied to eliminate the values in the background regions. The mean intensity of pH value was then obtained for the image to determine the pH value for mitochondria in this *in vitro* living cells sample.

Chapter II. Novel Bifunctional Ligands for PET Imaging with ^{64}Cu and ^{68}Ga Radioisotopes

Radiolabelling assays (**section 2.9.**) were conducted by Dr. Marlin, a researcher in Dr. Boros' team at University of Wiscosin-Madison. In the case of the assays related to the study of kinetic inertness and thermodynamic stability of Cu(II) complexes (**section 2.10.**, **2.11.** and **2.12.**) were carried out in the research facilities of the Centro Intersciplinar de Química e Bioloxía (CICA) at the Universidade da Coruña by Dr. Lucio, a researcher in the Prof. Platas-Iglesias' group.

2.7. Microwave (MW)

Reactions carried out under microwave conditions were performed with a CEM Discover® microwave instrument, which allowed us to set the following parameters: temperature, reaction time, power, maximum pressure and PowerMAX™.

Temperature stands for the set temperature that will be maintained during the reaction time. Power corresponds to the maximum power at which the sample will be irradiated, albeit the power may change in the course of the reaction. PowerMAX™ is a technology that allows introducing more energy in the reaction (by increasing the power) while maintaining the temperature, by simultaneous cooling of the reaction with compressed gas on the outside of the reaction vessel. In all the experiments performed in the present thesis, power was set at 150 W, maximum pressure at 250 psi and the PowerMAX™ option was always enabled.

All the reactions were conducted in 10 mL glass vessels sealed with a septum. Temperature was measured with an infrared sensor placed under the reaction vessel. All experiments were performed using a stirring option whereby the contents of the vessel were stirred by means of a rotating magnetic plate located below the floor of the microwave cavity and a Teflon-coated magnetic stir bar in the vessel.

2.8. X-ray Diffraction Measurements

Single crystal X-ray diffraction data were collected at 100 K on a Bruker D8 Venture diffractometer with a Photon 100 CMOS detector and Mo-Kα radiation (λ = 0.71073 Å) generated by an Incoatec high brilliance microfocus source equipped with Incoatec Helios multilayer optics. The APEX3 software was used for collecting frames of data, indexing reflections, and the determination of lattice parameters, SAINT for integration of intensity of reflections, and SADABS for scaling and empirical absorption correction. The structures were solved by dual-space methods using the program SHELXT. All non-hydrogen atoms were refined with anisotropic thermal parameters by full-matrix least-squares calculations on F^2 using the program SHELXL-2014. For **[Cu(CBuDEDPA)]**, solvent mask command from Olex2 was used to correct the reflection data for the diffuse scattering due to the disordered molecules present in the unit cell. Hydrogen atoms of the compound were inserted at calculated positions and constrained with isotropic thermal parameters.

2.9. Radiolabelling Studies

2.9.1. ^{64}Cu and ^{68}Ga Radiolabelling

The ligands were prepared from serial dilution of stock solutions (1 mM, 0.25 mM, 0.1 mM, 0.025 mM, 0.01 mM, 0.0025 mM, 0.001 mM, 0.00025 mM, 0.0001 mM) in deionized water. A 10 µL aliquot of each chelator stock solution (10, 2.5, 1.0, 0.25, 0.1, 0.025, 0.01, 0.0025 or 0.001 nmol, respectively) was diluted with 100 µL of ammonium acetate buffer (0.5 M, pH 5.5). A 50-90 µCi aliquot of $^{64}CuCl_2$ or $^{68}GaCl_3$ was then added and the solution was mixed thoroughly. The complexation was carried out at room temperature and the radiochemical yield was measured after 15, 30 and 60 min via radio-TLC on aluminum-backed silica plates with methanol as mobile phase. The degree of binding was quantified via autoradiography and integration of the signal of the bound complex vs the free ^{64}Cu or ^{68}Ga. The AMA was determined by ratio between the activity in the sample and the amount of ligand at 50% binding. All experiments were performed in triplicate.

2.9.2. Stability in PBS

Experimental samples were prepared as previously described at a ligand concentration producing quantitative complex formation within 60 minutes (1 nmol). Once the labelling solution was prepared and quantitative formation of the desired ^{64}Cu or ^{68}Ga complex was verified, a 15 µL aliquot of the labelling solution was added to 100 µL of 1x Dulbecco's phosphate-buffered saline (DPBS). The stability of the complex was monitored by radio-TLC at 0, 1, 2, 3, 12, and 24 h following the addition of activity to DBPS.

2.9.3. DTPA Challenge

Radiolabelling stock solutions were prepared as previously described using 1 nmol of ligand. The radiolabelling solution was mixed with 100 µL of 10 mM DTPA solution. Transchelation was monitored by radio-TLC at 0, 1, 3, 12 and 24 h.

2.10. Electrochemical Measurements

Cyclic voltammetry experiments were conducted using a three-electrode setup with an Autolab PGSTAT302M potentiostat/galvanostat. The working electrode was a glassy carbon disk (Metrohm 61204600), which was polished with α-Al_2O_3 (0.3 µm) and rinsed with distilled water prior to each measurement. An Ag/AgCl reference electrode filled with 3 M KCl (Metrohm 6.0726.100) served as the reference electrode, while a platinum wire was used as the counter electrode. Prior to each measurement, the complex solutions containing 0.15 M NaCl were deoxygenated by bubbling nitrogen through them. Conditions: **[Cu(CHXDEDPA)]**, 1.4 mM, pH 6.6; **[Cu(CPDEDPA)]**, 1.3 mM, pH 6.9; **[Cu(CBuDEDPA)]**, 1.3 mM, pH 5.0.

2.11. Thermodynamic Studies

Ligand protonation constants and stability constants of the Cu(II) complexes were determined using potentiometric and spectrophotometric titrations using HYPERQUAD. All experimental data were collected at 25 ºC using NaCl as inert electrolyte to keep constant the ionic strength (*I*=1 M).

Potentiometric titrations were conducted in a dual-wall thermostated cell with recirculating water to maintain a consistent temperature. To prevent CO_2 absorption, nitrogen was bubbled over the surface of the solution, and magnetic stirring was used to ensure thorough mixing. A Crison microBu 2030 automatic burette was employed to add the titrant, and the electromotive force was measured with a Crison micropH 2000 pHmeter, which was connected to a Radiometer pHG211 glass electrode and a Radiometer REF201 reference electrode. Initially, 10 mL of a 1.5-2 mM chelator solution was added to the cell, and the pH was adjusted to 11 with NaOH. This solution was then titrated with a standard HCl solution to determine all protonation constant values within a single experiment. After reaching an acidic pH, an equimolar amount of Cu(II) was added, and the mixture was stirred for one hour to ensure complex formation. Subsequently, the solution was titrated with NaOH to determine the protonation constants of the complex. All potentiometric titrations were performed in duplicate. Due to the low pH at which dissociation occurs, the stability constants of all complexes were measured by spectrophotometry, as the glass electrode could not accurately determine these values. Spectrophotometric titrations were performed with a Uvikon-XS (Bio-Tek Instruments) double-beam spectrophotometer, utilizing 1 cm path length quartz cuvettes and recording spectra in the range of 220 to 300 nm.

2.12. Dissociation Kinetics

Kinetic reducing reactions of the **[Cu(CBuDEDPA)]** complex were studied in phosphate buffer (0.12 M) of varying pH in the presence of ascorbate, which is able to reduce Cu(II) to Cu(I), and neocuproine, an efficient Cu(I) scavenger due to 1:2 complex formation ($[Cu(NC)_2]^+$). The reactions were monitored by conventional spectroscopy following the increase in absorbance at 450 nm due to the formation of the Cu(I)-neocuproine complex ($\varepsilon \approx 7000\ M^{-1}\cdot cm^{-1}$) and keeping the ratio [neocuproine]/[CuL] higher than ca. 2.5. Neocuproine was added upon dissolution in a small amount of dioxane (%v/v dioxane/water=1.0-2% in the final solutions used for kinetics experiments). The ascorbate concentration (varying from 2 to 20 mM) was in high excess relative to complex concentration ($\sim 10^{-4}$ M). All reactions were monitored by a Kontron-Uvikon 942 UV−vis spectrophotometer at 25 °C using 1 cm path length quartz cuvettes, with the complex being the last reagent added in the reaction mixture. In every case, absorbance (A) versus time (t) curves were appropriately fitted by a first-order integrated rate law (**Equation III-1**), with A_o, A_t, and A_∞ being the absorbance values at times zero, t, and at the end of the reaction, respectively, and k_o being the calculated pseudo-first order rate constant.

$$A_t = A_\infty + (A_o - A_\infty) \cdot e^{-k_o t} \qquad \textbf{(Equation III-1)}$$

3. Procedures performed in Part II

The *in vitro* studies to assess the biological activity of the CBDV-based bitopic ligands and the halogen- and thioether-containing CBDV-based compounds was carried out by Dr. Iu Raïch, researcher in Prof. Gemma Navarro's research group at the Faculty of Pharmacy and Food Science of the Universitat de Barcelona.

3.1. HEK-293T Cell Culture

Human embryonic kidney 293T (HEK-293T) cells, were acquired from the American Type Culture Collection. Cells were amplified and frozen in liquid nitrogen in several aliquots. Cells from each aliquot were used until passage 18. HEK-293T cells were grown in 6-well plates in DMEM (15-013-CV, Corning, NY, USA) Journal Pre-proof 7 supplemented with 2 mM L-glutamine, 100 U/mL penicillin/streptomycin, MEM NonEssential Amino Acids Solution (1/100) and 5% (v/v) heat-inactivated FBS (all supplements were from Invitrogen, (Paisley, Scotland, UK)). Cells were cultured in a humid atmosphere of 5% CO_2 at 37 °C. After 24 h in culture, cells were transiently transfected with the corresponding plasmids by the polyethyleneimine (PEI) method. PEI is a commonly used cationic polymer that forms complexes with negatively charged nucleic acids and facilitates their uptake into cells. The corresponding cDNAs diluted in 150 mM NaCl were mixed for 10 min with PEI (5.5 mM in nitrogen residues, Sigma-Aldrich, St. Louis, MO, USA) prepared in 150 mM NaCl. The PEI-DNA complex mixture was added to cells dropwise in non-supplemented DMEM, and the plate was swirled gently to ensure even distribution. Cells were incubated at 37 °C in a humid atmosphere of 5% CO_2 for 4–6 h. After incubation, the transfection medium was removed and replaced with supplemented culture medium, and assays were performed after 48 h incubation at 37 °C in a 5% CO_2 humid atmosphere.

3.2. cAMP Levels Determination Assays

Determination of cAMP levels in HEK-293T cells transiently expressing CB_2R (1 µg of cDNA) was performed by using the Lance-Ultra cAMP kit (PerkinElmer). Two hours before initiating the experiment, the medium was substituted by a serum-free medium. Then, transfected cells were dispensed in white 384-well microplates at a density of 4000 cells per well and incubated for 15 min at room temperature with compounds, followed by 15 min incubation with forskolin (0.5 µM), and 1 h more with homogeneous time-resolved fluorescence (HTRF) assay reagents. Fluorescence at 665 nm was analysed on a PHERAstar Flagship microplate reader equipped with an HTRF optical module (BMG Labtech). Data analysis was made based on the fluorescence ratio emitted by the labelled cAMP probe (665 nm) over the light emitted by the europium cryptate-labelled anti-cAMP antibody (620 nm). A standard curve was used to calculate cAMP concentration. Forskolin-stimulated cAMP levels were normalized to 100%.

3.3. β-arrestin Recruitment Assays

HEK-293T cells were transiently co-transfected with cDNA coding for ß-arrestin 2-Rluc and cDNA coding for CB_2R-YFP. BRET experiments were performed 48 h after transfection. Cells were

detached using Hanks' balanced salt solution (HBSS) containing 0.1% glucose, centrifuged for 5 min at 3,200 rpm, and resuspended in the same buffer. Protein concentration was quantified using the Bradford assay kit (Bio-Rad, Munich, Germany) and adjusted to 0,2 mg/mL. Hereafter, YFP Journal Pre-proof 9 fluorescence was quantified at 530 nm in a FluoStar Optima Fluorimeter (BMG Labtech, Offenburg, Germany) to quantify receptor-YFP expression upon excitation at 488 nm. To measure β-arrestin recruitment, cells (20 µg of protein) were distributed in 96-well microplates (Corning 3600, white plates with white bottom) and were incubated for 10 min with the compounds prior addition of 5 µM coelenterazine H (Molecular Probes, Eugene, OR). BRET between β-arrestin 2-Rluc and receptor-YFP was determined and quantified 5 min after adding coelenterazine H. The readings were collected using a Mithras LB 940 (Berthold Technologies, Bad Wildbad, Germany), which allows the integration of the signals detected in the short-wavelength filter (485 nm) and the long wavelength filter (530 nm). To quantify protein-Rluc expression, luminescence readings were also collected 10 min after addition of 5 µM coelenterazine H.

3.4. Statistical Analysis of the Data

Statistical analyses were conducted using GraphPad Prism 9.0 (GraphPad Software Inc., San Diego, CA, USA). Data for ERK phosphorylation, cAMP inhibition, and βarrestin2 recruitment are represented as % of the maximal response of the reference agonist JWH-133 or fold over vehicle, as indicated in the figure descriptions. Concentration-response curves (CRCs) were fit using non-linear regression (3-parameters; Hill slope constrained to 1). Hill slope was constrained to 1 because this constraint produced the best-fit data and reduced the standard error of the regression, whereas variable slope nonlinear regression fits are often more appropriate for curves fit with more datapoints than our experiments included (GraphPad, Prism v. 9.0).

CRCs were used to estimate EC_{50} and E_{max} values. The potency of a ligand is represented by its EC_{50} value, which is the concentration of ligand required to produce 50% of its maximal response in a given signalling pathway. The efficacy of a ligand is represented by its E_{max} value, which is the maximal response of a ligand in a given signalling pathway. Based off of the CRCs and E_{max} values, ligands were defined as either full agonists, partial agonists, inactive (i.e. potential neutral antagonists) or inverse agonists.

Chapter III. Innovative Bitopic Ligands Targeting Allosteric and Metastable CB_2R Binding Sites

3.6. Bioluminescence Resonance Energy Transfer (BRET) Assays

HEK-293T cells growing in 6-well plates were transiently co-transfected with cDNA encoding for human CB_2R fused to Renilla luciferase (CB_2R-Rluc) and CB_2R fused to the green fluorescent protein GFP^2 (CB_2R-GFP^2). 48 h post-transfection cells were washed twice in quick succession in HBSS (137 mM NaCl; 5 mM KCl; 0.34 mM Na_2HPO_4; 0.44 mM KH_2PO_4; 1.26 mM $CaCl_2$; 0.4 mM $MgSO_4$; 0.5 mM $MgCl_2$ and 10 mM HEPES, pH 7.4) supplemented with 0.1% glucose (w/v), detached by gently pipetting and resuspended in the same buffer. To assess the number of cells per plate, protein concentration was determined using a Bradford assay kit (Bio-Rad, Munich, Germany) with bovine serum albumin dilutions as standards, adjusting cells to a concentration of 0.2 mg/mL. To quantify GFP^2-fluorescence expression, cells (20 µg protein) were distributed in 96-well microplates (black plates with a transparent bottom; Porvair, Leatherhead, UK). Fluorescence was read using a Mithras LB 940 (Berthold, Bad Wildbad, Germany) equipped with a high-energy xenon flash lamp, using a 10-nm bandwidth excitation and emission filters at 410 and 510 nm, respectively. GFP^2-fluorescence expression was determined as the fluorescence of the sample minus the fluorescence of cells expressing protein-Rluc alone. For the BRET measurements, the equivalent of 20 µg of cell suspension was distributed in 96-well microplates (white plates; Porvair), and 5 µM DeepBlueC (Molecular Probes, Eugene, OR) were added. Then, 30 s after DeepBlueC addition, the readings were collected using a Mithras LB 940 (Berthold, Bad Wildbad, Germany), which allowed the integration of the signals detected in the short-wavelength filter at 410 nm (400–430 nm) and the long-wavelength filter at 510 nm (500–530 nm). To quantify receptor-Rluc expression, luminescence readings were performed 10 min after addition of 5 µM coelenterazine H. The net BRET is defined as [(long-wavelength emission)/(short-wavelength emission)]-Cf where Cf corresponds to [(long-wavelength emission)/(short-wavelength emission)] for the Rluc construct expressed alone in the same experiment. BRET curves were fitted assuming a single phase by a nonlinear regression equation using the GraphPad Prism software (San Diego, CA, USA). BRET values are given as milli BRET units (mBU: 1000 × net BRET).

Chapter IV. Halogen- and Thioether-Containing Ligands Targeting the Allosteric CB_2R Binding Site

3.7. MAPK Phosphorylation Assays

To determine MAPK phosphorylation, 40,000 cells/well were plated in transparent Deltalab 96-well plates and kept at the incubator for 48 h. 2 to 4 h before the experiment, the medium was replaced by serum-free medium. Then, cells were pre-treated at 25 °C for 10 min with vehicle in serum-free DMEM medium and stimulated for an additional 7 min with compounds. Cells were then washed twice with cold PBS before addition of lysis buffer (20 min treatment). 10 µL of each supernatant were placed in white ProxiPlate 384-well plates and MAPK phosphorylation was determined using AlphaScreen® SureFire® kit (Perkin Elmer) following the instructions of the supplier and using an EnSpire® Multimode Plate Reader (PerkinElmer, Waltham, MA, USA). The value of reference was that achieved in the absence of any treatment (basal).

4. Experimental Description

For the better understanding of this section, the following clarifications are provided:

- In the General procedures described, quantities given in mL/g refer to the limiting reagent used in the procedure.
- Some of the compounds prepared were already described in the literature. Therefore, only the physical and/or spectroscopic data necessary for their identification are presented. References to the published literature are provided for these compounds.
- The numbering of atoms within the molecule has been assigned arbitrarily for NMR descriptions and is depicted in each scheme.
- The term multiplet (m) has been applied when a fine structure has been observed but the spectrum does not have enough resolution. It also includes broad singlets which corresponds to protons that couple to other protons but the resolution does not allow one to see the expected multiplicity.
- ^{1}H-NMR and ^{13}C-NMR spectra are attached in the Annex for molecules that are not reported in the literature. In case the molecules have been reported, just the ^{1}H-NMR spectrum of the final product of the synthesis is shown.

PART I. Cyclobutane Scaffold for Imaging Applications

4.1. Chapter I. Hybrid γ,γ-Peptidomimetics as Mitochondria Penetrating Peptides

4.1.1. Synthesis of the *cis*-γ-CBAA

4.1.1.1. (1*S*,3*R*)-3-Acetyl-2,2-dimethylcyclobutane-1-carboxylic acid, 62.

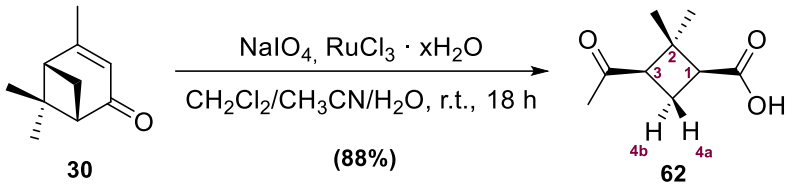

To a stirred solution of (-)-verbenone **30** (2.00 mL, 13.00 mmol) in a 2:2:3 CH_2Cl_2:CH_3CN:H_2O mixture (120 mL), catalytic $RuCl_3 \cdot xH_2O$ (0.05 g) and $NaIO_4$ (11.70 g, 54.50 mmol, 4.20 eq.) were added. The mixture was stirred at room temperature for 18 h. The crude obtained was filtered through a short pad of Celite® and the organic layer was extracted with CH_2Cl_2 (3 x 40 mL). Then, the combined organic extracts were dried over $MgSO_4$ and concentrated under vacuum to afford (-)-*cis*-pinonic acid **62** (1.95 g, 11.46 mmol, 88% yield) which was used in the next step without further purification.

Spectroscopic data for compound 62:

^{1}H-NMR (360 MHz, $CDCl_3$): δ 2.90 (dd, $^3J_{3\text{-}4a}$ = 10.5 Hz, $^3J'_{3\text{-}4b}$ = 7.8 Hz, 1H, H_3), 2.83 (dd, $^3J_{1\text{-}4a}$ = 10.5 Hz, $^3J'_{1\text{-}4b}$ = 7.8 Hz, 1H, H_1), 2.62 (ddd, $^2J_{4a\text{-}4b}$ = $^3J'_{4a\text{-}1}$ = $^3J''_{4a\text{-}3}$ = 10.5 Hz, 1H, H_{4a}), 2.07 (s, 3H, COCH_3), 1.93 (ddd, $^2J_{4b\text{-}4a}$ = 10.5 Hz, $^3J'_{4b\text{-}1}$ = $^3J''_{4b\text{-}3}$ = 7.8 Hz, 1H, H_{4b}), 1.46 (s, 3H, *pro-S*-CH_3), 0.97 (s, 3H, *pro-R*-CH_3).

Spectroscopic data are consistent with those reported in reference: Burgess, K.; Li, S, Rebenspies, J. *Tetrahedron Lett.* **1997**, *38*, 1681-1684.

4.1.1.2. *tert*-Butyl (1*S*,3*R*)-3-acetyl-2,2-dimethylcyclobutane-1-carboxylate, 63.

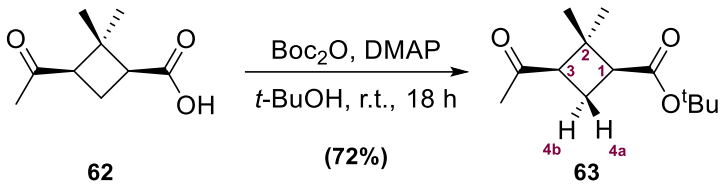

To a stirred solution of acid **62** (2.06 g, 12.11 mmol) in *tert*-butanol (20 mL), di-*tert*-butyl dicarbonate (5.50 g, 25.20 mmol, 2.10 eq.) and DMAP (0.55 g, 4.50 mmol, 0.40 eq.) were added. After stirring for 18 h at room temperature the solvent was removed at reduced pressure. The reaction crude was then purified using a flash chromatography (hexane:EtOAc, 3:1), obtaining the *tert*-butyl ester **63** (1.97 g, 8.70 mmol, 72% yield).

Spectroscopic data for compound 63:

^{1}H-NMR (360 MHz, $CDCl_3$): δ 2.83 (dd, $^3J_{3\text{-}4a}$ = 10.8 Hz, $^3J'_{3\text{-}4b}$ = 7.8 Hz, 1H, H_3), 2.66 (dd, $^3J_{1\text{-}4a}$ = 10.8 Hz, $^3J'_{1\text{-}4b}$ = 7.8 Hz, 1H, H_1), 2.62 (ddd, $^2J_{4a\text{-}4b}$ = $^3J'_{4a\text{-}1}$ = $^3J''_{4a\text{-}3}$ = 10.8 Hz, 1H, H_{4a}), 2.07 (s, 3H, CO*CH$_3$*), 1.93 (ddd, $^2J_{4b\text{-}4a}$ = 10.8 Hz, $^3J'_{4b\text{-}1}$ = $^3J''_{4b\text{-}3}$ = 7.8 Hz, 1H, H_{4b}), 1.44 (s, 9H, ^{t}Bu), 1.41 (s, 3H, *pro-S-CH$_3$*), 0.97 (s, 3H, *pro-R-CH$_3$*).

R_f (hexane:EtOAc, 3:1) = 0.45 (Vanillin stain).

Spectroscopic data are consistent with those reported in reference: Rouge, P.D.; Moglioni, A.G; Moltrasio, G.Y.; Ortuño, R.M. *Tetrahedron: Asymmetry* **2003**, *14 (2)*, 193-195.

4.1.1.3. (1*R*,3*S*)-3-(*tert*-Butoxycarbonyl)-2,2-dimethylcyclobutane-1-carboxylic acid, 64.

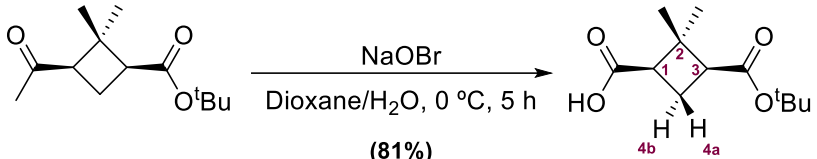

63 **64**

A solution of *tert*-butyl ester **63** (2.00 g, 8.84 mmol) was prepared using a 3:1 mixture of 1,4-dioxane:H_2O (125 mL) and cooled at 0 ºC. At the same time, a solution of sodium hypobromite was prepared using sodium hydroxide (10.00 g, 250.02 mmol, 28.30 eq.) in H_2O (240 mL) which were cooled at 0 ºC and then bromine (3.40 mL, 66.36 mmol, 7.51 eq.) was slowly added. After 10 min at 0 ºC, the sodium hypobromite solution was added to *tert*-butyl ester solution and 1,4-dioxane (80 mL) was incorporated to the mixture which was stirred for 5 h at 0 ºC. After that time, a solution of $NaHSO_3$ was added until the yellowish colour was not observed. By that time, the mixture was acidified using 6 M HCl until reaching pH 2 and then extracted with CH_2Cl_2 (4 x 70 mL). The combined organic extracts were dried over $MgSO_4$ and solvent was evaporated under reduced pressure to afford the acid **64** as a white solid (1.64 g, 7.18 mmol, 81% yield) which was used in the next step without further purification.

Spectroscopic data for compound 64:

^{1}H-NMR (360 MHz, $CDCl_3$): δ 4.54 (dd, $^3J_{1\text{-}4a}$ = 10.8 Hz, $^3J'_{1\text{-}4b}$ = 8.1 Hz, 1H, H_1), 2.71 (dd, $^3J_{3\text{-}4a}$ = 10.8 Hz, $^3J'_{3\text{-}4b}$ = 8.1 Hz, 1H, H_3), 2.53 (ddd, $^2J_{4a\text{-}4b}$ = $^3J'_{4a\text{-}1}$ = $^3J''_{4a\text{-}3}$ = 10.8 Hz, 1H, H_{4a}), 2.01 (ddd, $^2J_{4b\text{-}4a}$ = 10.8 Hz, $^3J'_{4b\text{-}1}$ = $^3J''_{4b\text{-}3}$ = 8.1 Hz, 1H, H_{4b}), 1.45 (s, 9H, ^{t}Bu), 1.35 (s, 3H, *pro-S-CH$_3$*), 1.06 (s, 3H, *pro-R-CH$_3$*).

Spectroscopic data are consistent with those reported in reference: Aguado, G.P.; Moglioni, A.G.; Ortuño, R.M. *Tetrahedron: Asymmetry* **2003**, *14* (2), 217-223.

4.1.1.4. (1*S*,3*R*)-3-Benzyloxycarbonylamino-2,2-dimethylcyclobutane-1-*(tert*-butyl)carboxylate, 65.

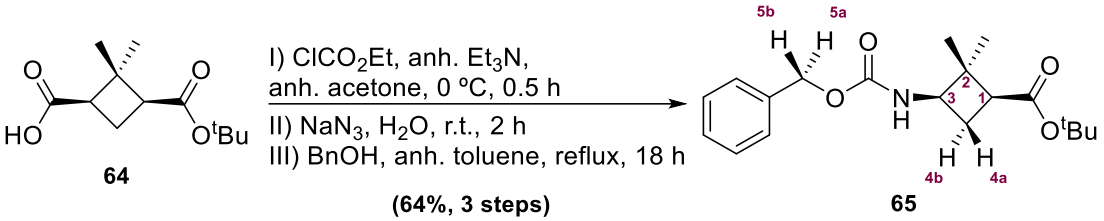

To an ice-cooled solution of acid **64** (1.50 g, 6.57 mmol) in anhydrous acetone (40 mL), anhydrous triethylamine (1.50 mL, 10.76 mmol, 1.60 eq.) and ethyl chloroformate (1.00 mL, 10.50 mmol, 1.60 eq.) were subsequently added. The mixture was stirred at 0 ºC for 40 min. Then, sodium azide (1.11 g, 17.10 mmol, 2.60 eq.) in water (10 mL) was added and the resultant solution was stirred at room temperature for 2 h. The reaction mixture was extracted with CH_2Cl_2 (4 x 20 mL), and the organic extracts were dried over $MgSO_4$. Mixture was concentrated under reduced pressure to give the corresponding acyl azide as a yellow oil, which was used in the next step without further purification. **CAUTION:** Acyl azides are instable reagents. It is very important not to heat the final product while it is being dried, and the solvent must not be removed until full dryness. The obtained acyl azide was dissolved in toluene (40 mL) and benzyl alcohol (1.45 mL, 13.80 mmol, 2.10 eq.) was added and the resulting mixture was stirred for 16 h under reflux conditions. After that time, solvents were removed under reduce pressure and residual benzyl alcohol was microdistilled under vacuum. The reaction crude was then purified using a flash chromatography (hexane:EtOAc, 3:1), obtaining orthogonally protected amino acid **65** (1.42 g, 4.21 mmol, 64% yield).

Spectroscopic data for compound 65:

^{1}H-NMR (360 MHz, $CDCl_3$): δ 7.35 (s, 5H, H_{Ar}), 5.12 (d, $^2J_{5a\text{-}5b}$ = 12.0 Hz, 1H, CH_2-Ph), 5.04 (d, $^2J_{5b\text{-}5a}$ = 12.0 Hz, 1H, CH_2-Ph), 4.86 (d, $^3J_{NH\text{-}3}$ = 7.9 Hz, 1H, NH), 3.87 (ddd, $^3J_{3\text{-}4a}$ = 10.8, $^3J'_{3\text{-}4b}$ = $^3J''_{3\text{-}NH}$ = 7.9 Hz, 1H, H_3), 2.48 (dd, $^3J_{1\text{-}4a}$ = 10.8, $^3J'_{1\text{-}4b}$ = 7.9 Hz, 1H, H_1), 2.29 (ddd, $^2J_{4b\text{-}4a}$ = 10.8 Hz, $^3J_{4b\text{-}1}$ = $^3J'_{4b\text{-}3}$ = 7.9 Hz, 1H, H_{4b}), 1.99 (ddd, $^2J_{4a\text{-}4b}$ = $^3J'_{4a\text{-}1}$ = $^3J''_{4a\text{-}3}$ = 10.8 Hz, 1H, H_{4a}), 1.44 (s, 9H, ^{t}Bu), 1.28 (s, 3H, *pro-R-CH_3*), 0.92 (s, 3H, *pro-S-CH_3*).

R_f (hexane:EtOAc, 3:1) = 0.44 (Vanillin stain).

Spectroscopic data are consistent with those reported in reference: Aguilera, J.; Moglioni, A.G.; Moltrasio, G.Y.; Ortuño. R.M. *Tetrahedron: Asymmetry* **2008**, *19* (3), 302-308.

4.1.1.5. *tert*-Butyl (1*S*,3*R*)-3-amino-2,2-dimethylcyclobutane-1-carboxylate, 66.

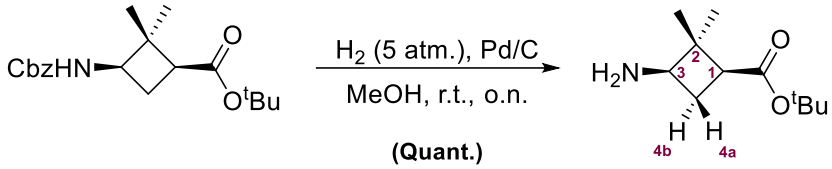

65 **66**

Diprotected amino acid **65** (3.70 g, 11.09 mmol) in MeOH (110 mL) was hydrogenated under 5 atmospheres of pressure in the presence of 10% Pd/C (10 wt%, 0.71 g, 0.66 mmol, 0.06 eq.) overnight. The reaction mixture was filtered through Celite® and washed with MeOH. The solvent was removed under vacuum affording the desired monoprotected amino acid **66** as a white solid (2.22 g, 11.13 mmol, quantitative yield) which was used in the next step without further purification.

Spectroscopic data for compound 66:

^{1}H-NMR (360 MHz, $CDCl_3$): δ 4.30 (s, 2H, NH_2), 2.95 (dd, $^3J_{3\text{-}4a}$ = 10.4 Hz, $^3J'_{3\text{-}4b}$ = 7.8 Hz, 1H, H_3), 2.38 (dd, $^3J_{1\text{-}4a}$ = 10.4, $^3J'_{1\text{-}4b}$ = 7.8 Hz, 1H, H_1), 2.22 (ddd, $^2J_{4b\text{-}4a}$ = 10.4 Hz, $^3J'_{4b\text{-}3}$ = $^3J''_{4b\text{-}1}$ = 7.8 Hz, 1H, H_{4b}), 1.91-1.81 (ddd, $^2J_{4a\text{-}4b}$ = $^3J'_{4a\text{-}3}$ = $^3J''_{4a\text{-}1}$ = 10.4 Hz, 1H, H_{4a}), 1.44 (s, 9H, ^{t}Bu), 1.16 (s, 3H, *pro-R-*CH_3), 0.93 (s, 3H, *pro-S-*CH_3).

Spectroscopic data are consistent with those reported in reference: Aguilera, J.; Moglioni, A.G.; Moltrasio, G.Y.; Ortuño. R.M. *Tetrahedron: Asymmetry* **2008**, *19* (3), 302-308.

4.1.1.6. *tert*-Butyl (1*S*,3*R*)-3-((9*H*-fluoren-9-yl)methoxycarbonylamino)-2,2-dimethylcyclobutane-1-carboxylate, 67.

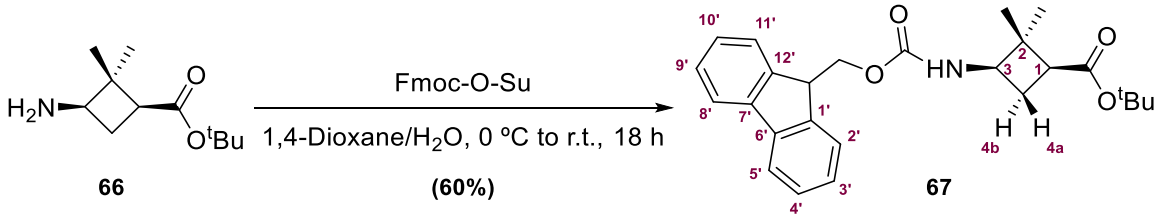

66 **67**

Protected amino acid **66** (2.03 g, 10.19 mmol) dissolved in a 1:1 mixture of 1,4-dioxane/water (80 mL) was cooled at 0 ºC for 10 min. Then, $NaHCO_3$ (1.71 g, 20.38 mmol, 2.00 eq.) and Fmoc-O-Su (4.12 g, 12.22 mmol, 1.20 eq.) were added. Reaction was then heated to room temperature, and it was stirred for 18 h. After that, NH_4Cl saturated solution (5 mL) was added and the reaction mixture was extracted with CH_2Cl_2 (4 x 30 mL), then the organic extracts were dried over $MgSO_4$. Solvents were removed under reduced pressure. The reaction crude was then purified using a flash chromatography (hexane:EtOAc, 3:1), obtaining orthogonally protected amino acid **67** (2.58 g, 6.11 mmol, 60% yield).

Spectroscopic data for compound 67:

^{1}H-NMR (360 MHz, $CDCl_3$): δ 7.77 (d, $^3J_{5'\text{-}4'/8'\text{-}9'}$ = 7.5 Hz, 2H, $H_{5',8'}$), 7.59 (d, $^3J_{2'\text{-}3'/11'\text{-}10'}$ = 7.5 Hz, 2H, $H_{2',11'}$), 7.40 (dd, $^3J_{4'\text{-}3'/9'\text{-}8'}$ = $^3J'_{4'\text{-}5'/9'\text{-}10'}$ = 7.5 Hz, 2H, $H_{4',9'}$), 7.32 (dd, $^3J_{3'\text{-}4'/10'\text{-}11'}$ = $^3J'_{3'\text{-}2'/10'\text{-}9'}$ =

7.5 Hz, 2H, $H_{3',10'}$), 4.85 (d, $^3J_{NH\text{-}3}$ = 8.7 Hz, 1H, *NH*), 4.40 (m, 2H, *CH*$_2$-Fmoc), 4.22 (dd, $^3J_{CH\text{-}ipso\text{-}CH2\text{-}Fmoc}$ = $^3J'_{CH\text{-}ipso\text{-}CH2\text{-}Fmoc}$ = 6.7 Hz, 1H, *CH-ipso*), 3.87 (ddd, $^3J_{3\text{-}4a}$ = $^3J'_{3\text{-}4b}$ = $^3J''_{3\text{-}NH}$ = 8.7 Hz, 1H, H_3), 2.49 (dd, $^3J_{1\text{-}4a}$ = $^3J'_{1\text{-}4b}$ = 8.7 Hz, 1H, H_1), 2.30 (m, 1H, H_{4b}), 1.99 (ddd, $^2J_{4a\text{-}4b}$ = $^3J'_{4a\text{-}1}$ = $^3J''_{4a\text{-}3}$ = 8.7 Hz, 1H, H_{4a}), 1.45 (s, 9H, ^{t}Bu), 1.28 (s, 3H, *pro-R-CH*$_3$), 0.92 (s, 3H, *pro-S-CH*$_3$).

^{13}C-NMR, COSY and me-HSQC experiments have been recorded.

R$_f$ (hexane:EtOAc, 3:1) = 0.48 (UV and vanillin stain).

Spectroscopic data are consistent with those reported in reference: Gorrea, E.; Carbajo, D.; Gutiérrez-Abad, R.; Illa, O.; Branchadell, V.; Royo, M.; Ortuño, R.M. *Org. Biomol. Chem.* **2012**, *10*, 4050.

4.1.1.7. (1*S*,3*R*)-3-((9*H*-Fluoren-9-yl)methoxycarbonylamino)-2,2-dimethylcyclobutane-1-carboxylic acid, 59.

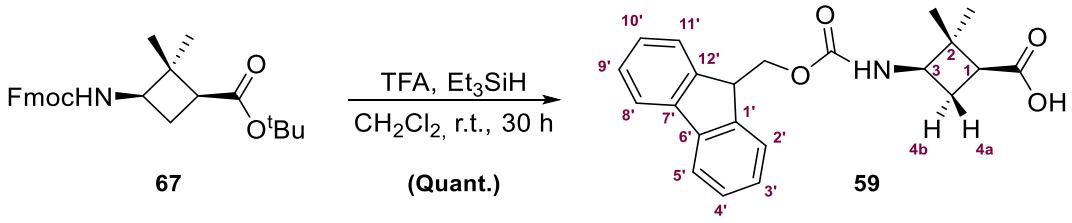

67 **(Quant.)** **59**

To a solution of orthogonally protected amino acid **67** (1.10 g, 2.60 mmol) in CH_2Cl_2 (15 mL), TFA (2.40 mL, 31.36 mmol, 12.06 eq.) and Et_3SiH (1.50 mL, 9.39 mmol, 3.61 eq.) were added and the reaction was stirred at room temperature for 30 h. Then, excess of reactants and solvent were removed under vacuum to afford protected amino acid **59** as a white solid (0.95 g, 2.59 mmol, quantitative yield) which was used for peptide synthesis without further purification.

Spectroscopic data for compound 59:

2 major conformers were observed in a 70:30 ratio in the ^{1}H-NMR spectrum.

^{1}H-NMR major conformer (600 MHz, $CDCl_3$): δ 7.77 (d, $^3J_{5'\text{-}4'/8'\text{-}9'}$ = 7.5 Hz, 2H, $H_{5',8'}$), 7.59 (d, $^3J_{2'\text{-}3'/11'\text{-}10'}$ = 7.5 Hz, 2H, $H_{2',11'}$), 7.40 (dd, $^3J_{4'\text{-}3'/9'\text{-}8'}$ = $^3J'_{4'\text{-}5'/9'\text{-}10'}$ = 7.5 Hz, 2H, $H_{4',9'}$), 7.32 (dd, $^3J_{3'\text{-}4'/10'\text{-}11'}$ = $^3J'_{3'\text{-}2'/10'\text{-}9'}$ = 7.5 Hz, 2H, $H_{3',10'}$), 4.84 (d, $^3J_{NH\text{-}3}$ = 9.1 Hz, 1H, *NH*), 4.42 (m, 2H, *CH*$_2$-Fmoc), 4.22 (dd, $^3J_{CH\text{-}ipso\text{-}CH2\text{-}Fmoc}$ = $^3J'_{CH\text{-}ipso\text{-}CH2\text{-}Fmoc}$ = 6.7 Hz, 1H, *CH-ipso*), 3.87 (ddd, $^3J_{3\text{-}4a}$ = $^3J'_{3\text{-}4b}$ = $^3J''_{3\text{-}NH}$ = 9.0 Hz, 1H, H_3), 2.65 (dd, $^3J_{1\text{-}4a}$ = $^3J'_{1\text{-}4b}$ = 9.0 Hz, 1H, H_1), 2.38 (ddd, $^2J_{4b\text{-}4a}$ = $^3J'_{4b\text{-}1}$ = $^3J''_{4b\text{-}3}$ = 9.0 Hz, 1H, H_{4b}), 2.05 (ddd, $^2J_{4a\text{-}4b}$ = $^3J'_{4a\text{-}1}$ = $^3J''_{4a\text{-}3}$ = 9.0 Hz, 1H, H_{4a}), 1.30 (s, 3H, *pro-R-CH*$_3$), 1.00 (s, 3H, *pro-S-CH*$_3$).

^{1}H-NMR minor conformer (600 MHz, $CDCl_3$): δ all signals coincide with the major conformer except for: 4.55 (m, 2H, *CH*$_2$-Fmoc), 3.56 (ddd, $^3J_{3\text{-}4a}$ = $^3J'_{3\text{-}4b}$ = $^3J''_{3\text{-}NH}$ = 9.0 Hz, 1H, H_3), 2.50 (dd, $^3J_{1\text{-}4a}$ = $^3J'_{1\text{-}4b}$ = 9.0 Hz, 1H, H_1), 2.22 (ddd, $^2J_{4b\text{-}4a}$ = $^3J'_{4b\text{-}1}$ = $^3J''_{4b\text{-}3}$ = 9.0 Hz, 1H, H_{4b}), 1.04 (s, 3H, *pro-S-CH*$_3$).

^{13}C-NMR, COSY and me-HSQC experiments have been recorded.

Spectroscopic data are consistent with those reported in reference: Berlicki, L.; Kaske, M.; Gutiérrez-Abad, R.; Bernhardt, G.; Illa, O.; Ortuño, R.M.; Cabrele, C.; Buschauer, A.; Reiser, O., *J. Med. Chem.* **2013**, *56* (21), 8422-8431.

4.1.2. Synthesis of the guanidinylated side chain

4.1.2.1. Obtention of 5-(2',3'-bis(*tert*-Butoxycarbonyl)guanidino)pentanoic acid, 74.

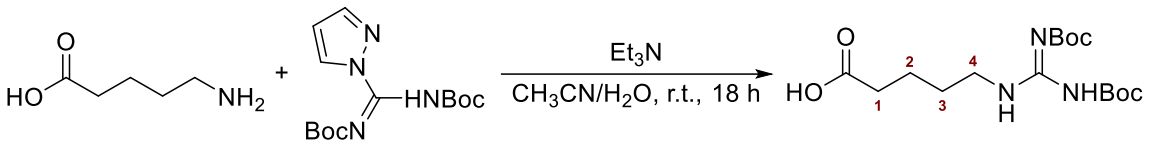

75 **76** **(64%)** **74**

Acid **75** (0.60 g, 5.12 mmol) dissolved in a 11:1 mixture of CH_3CN:H_2O (60 mL) was cooled at 0 ºC for 10 min after adding Et_3N (2.10 mL, 14.85 mmol, 2.90 eq.). Then, *N,N'*-bis(*tert*-butoxycarbonyl)-1H-pyrazole-1-carboxamidine **76** (1.75 g, 5.64 mmol, 1.10 eq.) was added and the reaction was stirred at room temperature for 18 h. After that, solvent was removed under reduced pressure. H_2O (10 mL) was added and acidified to a pH = 2 with 1 M HCl. Afterwards, EtOAc (3 x 20 mL) was added to the crude of reaction and then the organic extracts were dried over $MgSO_4$. Solvents were removed under reduced pressure. The reaction crude was purified through flash chromatography (CH_2Cl_2:MeOH, 98:2), to provide orthogonally protected amino acid **74** (1.21 g, 3.28 mmol, 64% yield).

Spectroscopic data for compound 74:

^{1}H-NMR (360 MHz, $CDCl_3$): δ 11.51 (br, 1H, CO_2H), 8.35 (br, 1H, NH), 3.44 (td, $^3J_{4\text{-}3}$ = $^3J''_{4\text{-}NH}$ = 6.3 Hz, 2H, H_4), 2.41 (t, $^3J_{1\text{-}2}$ = 7.0 Hz, 2H, H_1), 1.75-1.59 (m, 4H, H_2, H_3), 1.51 (s, 9H, NBoc), 1.49 (s, 9H, NHBoc).

Spectroscopic data are consistent with those reported in reference: Choi, S.; Clements, D. J.; Pophristic, V.; Ivanov, I.; Vemparala, S.; Bennett, J. S.; Klein, M. L.; Winkler, J. D.; DeGrado, W. F. *Angew. Chem. Int. Ed.* **2005,** *44,* 6685-6689.

4.1.3. Synthesis of the *N*-Boc-*cis*/*trans*-4-*N*-Fmoc-amino-L-proline

4.1.3.1. 2-Benzyl-1-(*tert*-butyl) (2*S*,4*S*/2*S*,4*R*)-4-((9*H*-fluoren-9-yl)methoxycarbonylamino) pyrrolidine-1,2-dicarboxylate, 79 and 80

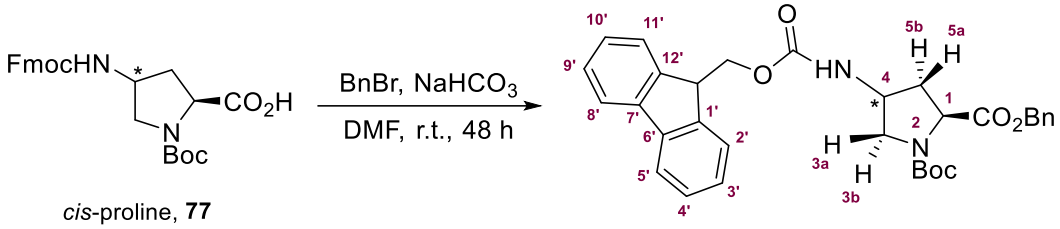

cis-proline, **77**
trans-proline, **78**

cis-proline, **79 (86%)**
trans-proline, **80 (80%)**

To a stirred solution of amino acid **77** or **78** (0.50 g, 1.10 mmol) dissolved in DMF (12 mL) was added BnBr (150 µL, 1.26 mmol, 1.10 eq.) and $NaHCO_3$ (0.118 g, 1.4 mmol, 1.27 eq.). The resulting mixture was stirred at room temperature for 48 h. The crude was concentrated under reduced pressure co-evaporating the DMF with toluene (3 x 15 mL). Afterwards, the mixture was extracted with EtOAc (4 x 20 mL) and washed with brine (15 mL). The combined organic layers were dried with anhydrous $MgSO_4$, and the solvent was removed under vacuum. To remove traces of DMF, toluene was added (4 x 15 mL) to co-evaporate it. The reaction crude was purified via flash chromatography (hexane:EtOAc, 1:3), furnishing compound **79** (0.51 g, 0.94 mmol, 86% yield) or **80** (0.44 g, 0.88 mmol, 80% yield), respectively, as white solids.

Spectroscopic and physical data for compound 79:

2 major conformers were observed in a 60:40 ratio in the ^{1}H-NMR spectrum.

^{1}H-NMR major conformer (600 MHz, $CDCl_3$): δ 7.77 (d, $^3J_{5'-4'/8'-9'}$ = 7.1 Hz, 2H, $H_{5',8'}$), 7.59 (d, $^3J_{2'-3'/11'-10'}$ = 7.1 Hz, 2H, $H_{2',11'}$), 7.40 (dd, $^3J_{4'-5'/9'-10'}$ = $^3J'_{4'-3'/9'-8'}$ = 7.1 Hz, 2H, $H_{4',9'}$), 7.39-7.28 (m, 7H, $H_{3',10'}$, *Ph*-CH_2), 5.72 (d, $^3J_{NH-4}$ = 8.5 Hz, 1H, *NH*), 5.18 (s, 2H, *CH*$_2$-Ph), 4.51-4.29 (m, 4H, H_1,H_4, *CH*$_2$ Fmoc), 4.20 (dd, $^3J_{CH-ipso-CH2-Fmoc}$ = $^3J'_{CH-ipso-CH2-Fmoc}$ = 6.9 Hz, 1H, *CH-ipso*), 3.68 (dd, $^2J_{3b-3a}$ = 11.4 Hz, $^3J'_{3b-4}$ = 5.8 Hz, 1H, H_{3b}), 3.58 (d, $^2J_{3a-3b}$ = 11.4 Hz, 1H, H_{3a}), 2.49 (m, 1H, H_{5a}), 2.01 (d, $^2J_{5b-5a}$ = 13.3 Hz, 1H, H_{5b}), 1.36 (s, 9H, ^{t}Bu).

^{1}H-NMR minor conformer (600 MHz, $CDCl_3$): δ all signals coincide with the major conformer except for: 5.31 (d, ^2J = 12.4 Hz, 1H, *CH*$_2$-Ph), 5.11 (d, ^2J = 12.4 Hz, 1H, *CH*$_2$-Ph), 3.47 (d, $^2J_{3a-3b}$ = 11.4 Hz, 1H, H_{3a}), 1.96 (d, $^2J_{5b-5a}$ = 13.3 Hz, 1H, H_{5b}), 1.48 (s, 9H, ^{t}Bu).

2 major conformers were observed in the ^{13}C-NMR spectrum.

^{13}C-NMR major conformer (125 MHz, $CDCl_3$): δ 173.9 (*C*O_2-Bn), 155.8 (CO_{Fmoc}), 153.6 (CO_{Boc}), 144.0 ($C_{1'/12'}$), 141.4 ($C_{6'/7'}$), 135.2 ($C_{quat\ Bn}$), 128.9-128.5 (C_{Ar}), 128.4 ($C_{4'/9'}$), 128.2 ($C_{3'/10'}$), 127.7 (C_{Ar}), 127.1 (C_{Ar}), 125.3 ($C_{2'/11'}$), 120.1 ($C_{5'/8'}$), 80.8 (*C*$(CH_3)_3$), 67.5 (*C*H_2-Ph), 67.1 (*C*$H_{2\ Fmoc}$), 58.1 (C_1), 53.0 (C_3), 49.8 (C_4), 47.3 (*CH-ipso*), 37.2 (C_5), 28.3 (^{t}Bu).

^{13}C-NMR minor conformer (125 MHz, $CDCl_3$): δ all signals coincide with the major conformer except for: 154.3 (CO_{Boc}), 135.4 ($C_{quat\ Bn}$), 67.4 (*C*H_2-Ph), 57.9 (C_1), 53.5 (C_3), 50.8 (C_4), 36.1 (C_5), 28.5 (^{t}Bu).

COSY, NOESY, me-HSQC and HMBC experiments have been recorded.

R_f (hexane:EtOAc, 3:1) = 0.15 (UV and vanillin stain).

IR (ATR): υ 3315, 2974, 1694, 1525, 1395, 1155, 737 cm^{-1}.

HRMS (ESI+) calcd. for $[C_{32}H_{34}N_2O_6+Na]^+$: 565.2309, Found: 565.2299.

m.p.: 55 ºC-57 ºC (from EtOAc:hexane).

$[\alpha]^{25}_D$: -10 (*c* 0.01, MeOH).

Spectroscopic data for compound 80:

2 major conformers observed in a 60:40 ratio in the ^{1}H-NMR spectrum.

^{1}H-NMR major conformer (360 MHz, $CDCl_3$): δ 7.76 (d, $^3J_{5'\text{-}4'/8'\text{-}9'}$ = 7.2 Hz, 2H, $H_{5',8'}$), 7.56 (d, $^3J_{2'\text{-}3'/11'\text{-}10'}$ = 7.2 Hz, 2H, $H_{2',11'}$), 7.43-7.28 (m, 9H, $H_{3',4',9',10'}$, *Ph*-CH_2), 5.16 (s, 2H, *CH_2*-Ph), 4.82 (br s, 1H, *NH*), 4.44 (m, 2H, *CH_2* Fmoc), 4.30 (m, 1H, H_1), 4.19 (m, 1H, *CH-ipso*), 3.76 (m, 1H, H_4), 3.39 (m, 1H, H_{3a}), 2.22 (m, 2H, H_{3b},H_{5a}), 1.84 (m, 2H, H_{5b}), 1.35 (s, 9H, ^{t}Bu).

^{1}H-NMR minor conformer (360 MHz, $CDCl_3$): δ all signals coincide with the major conformer except for: 5.22 (d, ^2J = 12.2 Hz, 1H, *CH_2*-Ph), 5.09 (d, ^2J = 12.2 Hz, 1H, *CH_2*-Ph), 3.27 (m, 1H, H_{3a}), 1.45 (s, 9H, ^{t}Bu).

R_f (hexane:EtOAc, 3:1) = 0.18 (UV and vanillin stain).

IR (ATR): υ 3318, 2970, 1689, 1543, 1387, 1167, 738 cm^{-1}.

4.1.3.2. (2*S*,4*S*/2*S*,4*R*)-4-((9*H*-fluoren-9-yl)methoxycarbonylamino)-2-(benzyloxycarbonyl)-pyrrolidin-1-ium trifluoroacetate, 81 and 82

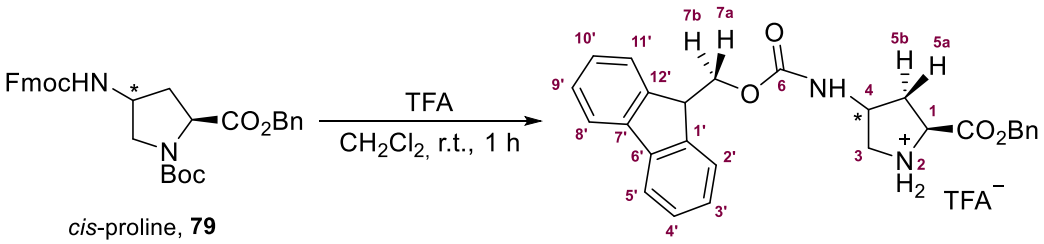

cis-proline, **79**
trans-proline, **80**

cis-proline, **81 (Quant.)**
trans-proline, **82 (Quant.)**

To a stirred solution of amino acid **79** or **80** (0.50 g, 0.92 mmol) dissolved in CH_2Cl_2 (4 mL) was added anhydrous TFA (2.50 mL, 32.67 mmol, 35.51 eq.). The resulting mixture was stirred at room temperature for 1 h. The solvent and excess of volatiles were co-evaporated under vacuum with CH_2Cl_2 (2 x 10 mL) and Et_2O (3 x 10 mL). Compound **81** (0.51 g, 0.92 mmol, quantitative yield) or **82** (0.51 g, 0.92 mmol, quantitative yield), respectively, were obtained as white solids.

Spectroscopic and physical data for compound 81:

^{1}H-NMR (360 MHz, MeOD): δ 7.78 (d, $^{3}J_{5'\text{-}4'/8'\text{-}9'}$ = 7.5 Hz, 2H, $H_{5',8'}$), 7.60 (d, $^{3}J_{2'\text{-}3'/11'\text{-}10'}$ = 7.5 Hz, 2H, $H_{2',11'}$), 7.39-7.29 (m, 9H, $H_{3',4',9',10'}$, *Ph*-CH_2), 5.28 (d, ^{2}J = 12.2 Hz, 1H, *C*H_2-Ph), 5.24 (d, ^{2}J = 12.2 Hz, 1H, *C*H_2-Ph), 4.53 (m, 1H, H_1), 4.38 (m, 2H, *C*$H_{2\ Fmoc}$), 4.25 (m, 1H, H_4), 4.16 (dd, $^{3}J_{CH\text{-}ipso\text{-}CH2\text{-}Fmoc}$ = $^{3}J'_{CH\text{-}ipso\text{-}CH2\text{-}Fmoc}$ = 6.1 Hz, 1H, *CH-ipso*), 3.54 (m, 1H, H_{3a}), 3.35 (m, 1H, H_{3b}), 2.69 (m, 1H, H_{5b}), 2.17 (m, 1H, H_{5a}).

^{13}C-NMR (90 MHz, MeOD): δ 169.5 (*C*O_2-Bn), 158.1 (CO_{Fmoc}), 145.1 ($C_{1'/12'}$), 142.6 ($C_{6'/7'}$), 136.2 ($C_{quat\ Bn}$), 129.8-129.6 (C_{Ar}), 128.8 ($C_{4'/9'}$), 128.1 ($C_{3'/10'}$), 126.0 ($C_{2'/11'}$), 121.0 ($C_{5'/8'}$), 69.5 (*C*H_2-Ph), 67.7 (*C*$H_{2\ Fmoc}$), 59.7 (C_1), 51.1 (C_3, C_4), 48.4 (*C*H-*ipso*), 34.4 (C_5).

COSY, NOESY, me-HSQC and HMBC experiments have been recorded.

IR (ATR): υ 3346, 2961, 1684, 1539, 1145, 739 cm^{-1}.

HRMS (ESI+) calcd. for $[C_{27}H_{26}N_2O_4+Na]^+$: 465.1785, Found: 465.1778.

m.p.: 87 ºC-92 ºC (from CH_2Cl_2).

$[\alpha]^{25}_D$: -10 (*c* 0.01, MeOH).

Spectroscopic data for compound 82:

^{1}H-NMR (360 MHz, MeOD): δ 7.79 (d, $^{3}J_{5'\text{-}4'/8'\text{-}9'}$ = 7.5 Hz, 2H, $H_{5',8'}$), 7.63 (d, $^{3}J_{2'\text{-}3'/11'\text{-}10'}$ = 7.5 Hz, 2H, $H_{2',11'}$), 7.43-7.28 (m, 9H, $H_{3',4',9',10'}$, *Ph*-CH_2), 5.32 (d, ^{2}J = 12.0 Hz, 1H, *C*H_2-Ph), 5.27 (d, ^{2}J = 12.0 Hz, 1H, *C*H_2-Ph), 4.60 (m, 1H, H_1), 4.47 (m, 2H, *C*$H_{2\ Fmoc}$), 4.27-4.17 (m, 2H, H_4, *CH-ipso*), 3.58 (m, 1H, H_{3a}), 3.36 (m, 1H, H_{3b}), 2.36 (m, 2H, H_5).

^{13}C-NMR (90 MHz, MeOD): δ 169.5 (*C*O_2-Bn), 158.2 (CO_{Fmoc}), 145.2 ($C_{1'/12'}$), 142.7 ($C_{6'/7'}$), 136.2 ($C_{quat\ Bn}$), 129.9-129.7 (C_{Ar}), 128.8 ($C_{4'/9'}$), 128.1 ($C_{3'/10'}$), 126.0 ($C_{2'/11'}$), 121.0 ($C_{5'/8'}$), 69.5 (*C*H_2-Ph), 67.6 (*C*$H_{2\ Fmoc}$), 59.9 (C_1), 51.7 (C_3), 51.3 (C_4), 48.4 (*C*H-*ipso*), 35.0 (C_5).

COSY and me-HSQC experiments have been recorded.

IR (ATR): υ 3348, 2964, 1676, 1537, 1155, 732 cm^{-1}.

4.1.3.3. Benzyl (2*S*,4*S/2S*,4*R*)-4-((9*H*-fluoren-9-yl)methoxycarbonylamino)-1-(2',3'-bis(*tert*-butoxycarbonyl)guanidino)pentanoyl)pyrrolidine-2-carboxylate, 84 and 85

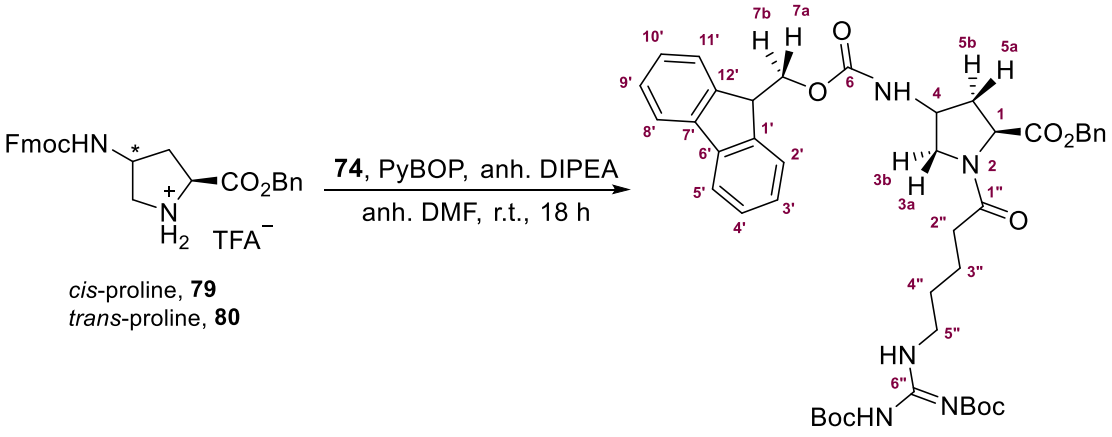

cis-proline, **79**
trans-proline, **80**

cis-proline, **84 (61%)**
trans-proline, **85 (55%)**

Amino acid **74** (0.45 g, 1.17 mmol) and PyBOP (0.61 g, 1.17 mmol, 1.00 eq.) were purged with nitrogen in a round-bottom flask before adding anhydrous DMF (4 mL) and anhydrous DIPEA (0.61 mL, 3.50 mmol, 3.00 eq.). The mixture was stirred at room temperature under a nitrogen atmosphere for 30 min to activate the acid. At this point, proline **79** or **80** (0.65 g, 1.17 mmol, 1.00 eq.) dissolved in anhydrous DMF (6 mL) was added with a syringe. The resulting mixture was stirred at room temperature for 16 h under a nitrogen atmosphere. The crude was concentrated under vacuum pressure, adding toluene (4 x 15 mL) to co-evaporate the DMF. H_2O (25 mL) and EtOAc (3 x 25 mL) were added to proceed with the extraction of the product. The organic layer was dried with $MgSO_4$, and the solvent was removed under reduced pressure. The crude was then purified by column chromatography on silica gel using a polarity gradient from EtOAc-hexane 2:1 to EtOAc-hexane 3:1, affording compound **84** (0.56 g, 0.71 mmol, 61% yield) or **85** (0.51 g, 0.64 mmol, 55% yield), respective, as white solids.

Spectroscopic and physical data for compound 84:

2 major conformers observed in a 70:30 ratio in the ^{1}H-NMR spectrum.

^{1}H-NMR major conformer (500 MHz, MeOD): δ 7.78 (d, $^3J_{5'\text{-}4'/8'\text{-}9'}$ = 7.5 Hz, 2H, $H_{5',8'}$), 7.62 (d, $^3J_{2'\text{-}3'/11'\text{-}10'}$ = 7.5 Hz, 2H, $H_{2',11'}$), 7.39-7.24 (m, 9H, $H_{3',4',9',10'}$, *Ph*-CH_2), 5.17 (d, ^2J = 12.1 Hz, 1H, *CH*$_2$-Ph), 5.07 (d, ^2J = 12.1 Hz, 1H, *CH*$_2$-Ph), 4.46 (dd, $^3J_{1\text{-}5a}$ = $^3J'_{1\text{-}5b}$ = 7.3 Hz, 1H, H_1), 4.35 (m, 2H, *CH*$_2$ Fmoc), 4.25-4.12 (m, 2H, H_4, *CH-ipso*), 3.91 (dd, $^2J_{3a\text{-}3b}$ = $^3J'_{3a\text{-}4}$ = 6.3 Hz, 1H, H_{3a}), 3.42 (dd, $^2J_{3a\text{-}3b}$ = $^3J'_{3a\text{-}4}$ = 6.3 Hz, 1H, H_{3b}), 3.34 (m, 2H, $H_{5''}$), 2.53 (m, 1H, H_{5b}), 2.39 (m, 2H, $H_{2''}$), 1.93 (m, 1H, H_{5a}), 1.63-1.56 (m, 4H, $H_{3'',4''}$), 1.51 (s, 9H, NHBoc), 1.46 (s, 9H, NBoc).

^{1}H-NMR minor conformer (500 MHz, MeOD): δ all signals coincide with the major conformer except for: 4.67 (m, 1H, H_1), 4.09 (m, 2H, *CH*$_2$ Fmoc), 3.84 (m, 1H, H_{3a}), 2.22 (m, 2H, $H_{2''}$), 2.06 (m, 1H, H_{5b}).

2 major conformers observed in the ^{13}C-NMR spectrum.

^{13}C-NMR major conformer (125 MHz, MeOD): δ 174.2 ($C_{1''}$), 173.4 (CO_2-Bn), 164.6 (CO_{Boc}), 158.1 (CO_{Fmoc}), 157.6 ($C_{6''}$) 154.2 (CO_{Boc}), 145.2 ($C_{1'/12'}$), 142.6 ($C_{6'/7'}$), 137.2 ($C_{quat\ Bn}$), 129.6-128.8 ($CH_{\ Fmoc}$, $CH_{\ Ph}$), 126.1 ($C_{2'/11'}$), 120.9 ($C_{5'/8'}$), 84.4 ($C(CH_3)_3$), 80.3 ($C(CH_3)_3$), 68.0 (CH_2-Ph), 67.8 ($CH_{2\ Fmoc}$), 59.1 (C_1), 53.0 (C_3), 51.6 (C_4), 49.5 (*CH-ipso*), 41.4 ($C_{5''}$), 35.4 (C_5), 34.6 ($C_{2''}$), 29.5 ($C_{4''}$), 28.6 (^{t}Bu), 28.2 (^{t}Bu), 22.8 ($C_{3''}$).

^{13}C-NMR minor conformer (125 MHz, $CDCl_3$): δ all signals coincide with the major conformer except for: 174.8 ($C_{1'''}$), 136.9 ($C_{quat\ Bn}$), 68.5 (CH_2-Ph), 59.5 (C_1), 52.2 (C_3), 50.3 (C_4), 22.9 ($C_{3''}$).

COSY, me-HSQC and HMBC experiments have been recorded.

R_f (hexane:EtOAc, 1:3) = 0.58 (UV and vanillin stain).

IR (ATR): υ 3329, 2975, 1717, 1154, 842, 758 cm^{-1}.

HRMS (ESI+) calcd. for $[C_{43}H_{53}N_5O_9+H]^+$: 784.3915, Found: 784.3916.

m.p.: 69 ºC-73 ºC (from hexane-EtOAc).

$[\alpha]^{25}_D$: -12 (*c* 0.01, MeOH).

Spectroscopic and physical data for compound 85:

^{1}H-NMR (360 MHz, $CDCl_3$): δ 11.49 (s, 1H, *NH*), 8.33 (s, 1H, *NH*), 7.76 (d, $^3J_{5'-4'/8'-9'}$ = 7.4 Hz, 2H, $H_{5',8'}$), 7.56 (d, $^3J_{2'-3'/11'-10'}$ = 7.4 Hz, 2H, $H_{2',11'}$), 7.42-7.29 (m, 9H, $H_{3',4',9',10'}$, *Ph*-CH_2), 5.21 (d, ^2J = 12.3 Hz, 1H, CH_2-Ph), 5.11 (d, ^2J = 12.3 Hz, 1H, CH_2-Ph), 4.94 (m, 1H, *NH*), 4.58 (m, 1H, H_1), 4.51-4.28 (m, 3H, H_4, $CH_{2\ Fmoc}$), 4.18 (m, 1H, *CH-ipso*), 3.89 (m, 1H, H_{3a}), 3.45-3.31 (m, 3H, H_{3b}, $H_{5''}$), 2.32 (m, 2H, $H_{2''}$), 2.18 (m, 1H, H_5), 1.75-1.56 (m, 4H, $H_{3'',4''}$), 1.49 (s, 9H, NHBoc), 1.48 (s, 9H, NBoc).

^{13}C-NMR (90 MHz, $CDCl_3$): δ 171.8 ($C_{1''}$), 171.6 (CO_2-Bn), 163.7 (CO_{Boc}), 156.2 (CO_{Fmoc}), 155.8 ($C_{6''}$) 153.3 (CO_{Boc}), 143.7 ($C_{1'/12'}$), 141.4 ($C_{6'/7'}$), 135.5 ($C_{quat\ Bn}$), 128.9-127.9 ($CH_{\ Fmoc}$, $CH_{\ Ph}$), 127.2 ($C_{2'/11'}$), 125.0 ($C_{4'/9'}$), 120.1 ($C_{5'/8'}$), 83.1 ($C(CH_3)_3$), 79.1 ($C(CH_3)_3$), 67.1 (CH_2-Ph), 66.8 ($CH_{2\ Fmoc}$), 57.5 (C_1), 52.6 (C_3), 50.6 (C_4), 47.2 (*CH-ipso*), 40.6 ($C_{5''}$), 34.9 (C_5), 33.8 ($C_{2''}$), 28.6 ($C_{4''}$), 28.4 (^{t}Bu), 28.1 (^{t}Bu), 21.7 ($C_{3''}$).

COSY, me-HSQC and HMBC experiments have been recorded.

R_f (hexane:EtOAc, 1:3) = 0.61 (UV and vanillin stain).

IR (ATR): υ 2926, 1718, 1636, 1366, 1249, 1131, 736 cm^{-1}.

HRMS (ESI+) calcd. for $[C_{43}H_{53}N_5O_9+H]^+$: 784.3916, Found: 784.3930.

m.p.: 60 ºC-66 ºC (from hexane-EtOAc).

$[\alpha]^{25}_D$: -4 (*c* 0.01, MeOH).

4.1.3.4. (2*S*,4*S*/2*S*,4*R*)-4-((9*H*-Fluoren-9-yl)methoxycarbonylamino)-1-(2,3-bis(*tert*-butoxycarbonyl)-guanidino)pentanoyl)pyrrolidine-2-carboxylic acid, 60 and 61

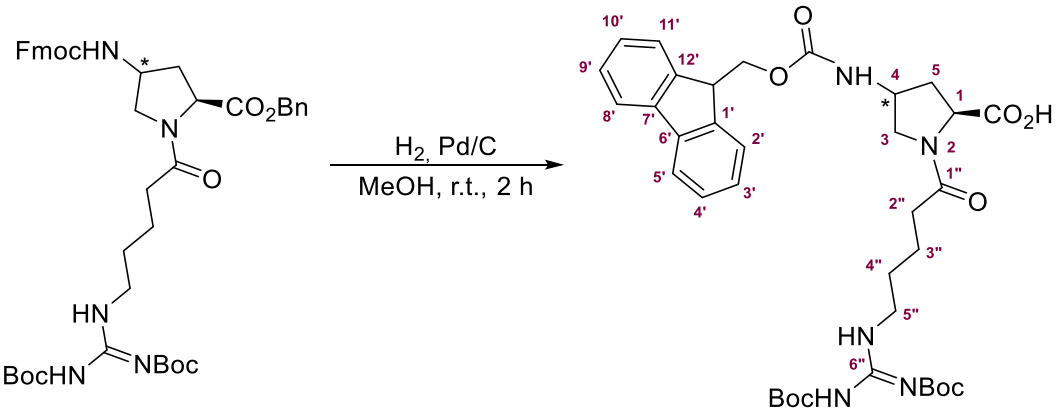

cis-proline, **84**
trans-proline, **85**

cis-proline, **60 (Quant.)**
trans-proline, **61 (Quant.)**

To a stirred solution of the orthogonally-protected amino acid **84** or **85** (0.50 g, 0.64 mmol) in previously deoxygenated MeOH (60 mL), was added 10 wt% Pd/C (0.20 g, 0.19 mmol, 0.30 eq.). Afterwards, two balloons full of hydrogen were bubbled inside the solution, and another balloon full of hydrogen was added in order to keep the hydrogen pressure, stirring the solution for 2 h. The reaction crude was filtered through Celite®, washed with MeOH and solvent was removed under reduced pressure to afford amino acid **60** (0.44 g, 0.63 mmol, quantitative yield) or **61** (0.45 g, 0.64 mmol, quantitative yield), respectively, as white solids which were used in solid phase synthesis without further purification.

Spectroscopic and physical data for compound 60:

^{1}H-NMR (600 MHz, $CDCl_3$): δ 11.47 (br s, 1H, *NH*), 8.34 (br, 1H, *NH*), 7.75 (d, $^{3}J_{5'\text{-}4'/8'\text{-}9'}$ = 7.2 Hz, 2H, $H_{5',8'}$), 7.57 (d, $^{3}J_{2'\text{-}3'/11'\text{-}10'}$ = 7.2 Hz, 2H, $H_{2',11'}$), 7.40-7.29 (m, 4H, $H_{3',4',9',10'}$), 6.19 (br, 1H, *NH*), 4.66 (m, 1H, H_1) 4.41-4.24 (m, 3H, H_4,CH_2 $_{Fmoc}$), 4.18 (dd, $^{3}J_{CH\text{-}ipso\text{-}CH2\text{-}Fmoc}$ = $^{3}J'_{CH\text{-}ipso\text{-}CH2\text{-}Fmoc}$ = 7.3 Hz, 1H, *CH-ipso*), 3.71 (m, 2H, H_3), 3.43 (m, 2H, $H_{5''}$), 2.47-2.22 (m, 4H, $H_{2'',5}$), 1.73-1.58 (m, 4H, $H_{3'',4''}$), 1.49 (s, 18H, NBoc, NHBoc).

^{13}C-NMR (125 MHz, $CDCl_3$): δ 175.2 (CO_2H), 174.1 ($C_{1''}$), 163.6 (CO_{Boc}), 156.3 (CO_{Fmoc}), 153.4 ($C_{6''}$), 149.1 (CO_{Boc}), 144.0 ($C_{1'/12'}$), 141.4 ($C_{6'/7'}$), 128.0-127.8 (CH $_{Fmoc}$), 125.4 ($C_{2'/11'}$), 120.1 ($C_{4'/9'}$), 83.3 ($C(CH_3)_3$), 79.5 ($C(CH_3)_3$), 67.2 (CH_2 $_{Fmoc}$), 60.2 (C_1), 54.7 (C_3), 51.1 (C_4), 47.3 (CH-*ipso*), 40.4 ($C_{5''}$), 34.0 ($C_{2''}$), 33.3 (C_5), 28.7 ($C_{4''}$), 28.4 (^{t}Bu), 28.2 (^{t}Bu), 21.6 ($C_{3''}$).

COSY, me-HSQC and HMBC experiments have been recorded.

IR (ATR): υ 3323, 3067, 2976, 1716, 1612, 1326, 1151, 1130, 840, 739 cm^{-1}.

HRMS (ESI+) calcd. for $[C_{36}H_{47}N_5O_9+H]^+$: 694.3447, Found: 694.3447.

m.p.: 59 ºC-63 ºC (from MeOH).

$[\alpha]^{25}_{D}$: -14 (*c* 0.01, MeOH).

Spectroscopic and physical data for compound 61:

^{1}H-NMR (600 MHz, $CDCl_3$): δ 11.47 (br s, 1H, *NH*), 8.34 (br, 1H, *NH*), 7.74 (d, $^{3}J_{5'\text{-}4'/8'\text{-}9'}$ = 7.5 Hz, 2H, $H_{5',8'}$), 7.56 (d, $^{3}J_{2'\text{-}3'/11'\text{-}10'}$ = 7.5 Hz, 2H, $H_{2',11'}$), 7.39 (dd, $^{3}J_{3'\text{-}4'/10'\text{-}9'}$ = $^{3}J'_{3'\text{-}2'/10'\text{-}11'}$ = 7.5 Hz, 2H, $H_{3',10'}$), 7.30 (m, 2H, $H_{4',9'}$), 5.47 (br, 1H, *NH*), 4.59 (m, 1H, H_1) 4.40 (m, 2H, CH_2 Fmoc), 4.30 (m, 1H, H_4), 4.16 (m, 1H, *CH-ipso*), 3.49 (m, 1H, H_{3a}), 3.36 (m, 1H, H_{3b}), 3.36 (m, 2H, $H_{5''}$), 2.27-2.02 (m, 3H, $H_{3a,2''}$), 2.52-2.09 (m, 4H, $H_{2'',5}$), 1.73-1.55 (m, 4H, $H_{3'',4''}$), 1.42 (s, 18H, NBoc, NHBoc).

^{13}C-NMR (125 MHz, $CDCl_3$): δ 175.1 (CO_2H), 173.1 ($C_{1''}$), 163.5 (CO_{Boc}), 156.3 (CO_{Fmoc}), 153.3 ($C_{6''}$), 149.1 (CO_{Boc}), 143.9 ($C_{1'/12'}$), 141.4 ($C_{6'/7'}$), 127.8-127.2 (CH Fmoc), 125.2 ($C_{2'/11'}$), 124.1 ($C_{5'/8'}$), 120.1 ($C_{4'/9'}$), 83.3 ($C(CH_3)_3$), 79.5 ($C(CH_3)_3$), 66.8 (CH_2 Fmoc), 58.8 (C_1), 53.0 (C_3), 50.7 (C_4), 47.3 (CH-*ipso*), 40.4 ($C_{5''}$), 34.4 ($C_{2''}$), 34.0 (C_5), 28.6 ($C_{4''}$), 28.4 (^{t}Bu), 28.2 (^{t}Bu), 21.8 ($C_{3''}$).

COSY, me-HSQC and HMBC experiments have been recorded.

IR (ATR): υ 3318, 2930, 1759, 1610, 1365, 1248, 1130, 737 cm^{-1}.

HRMS (ESI+) calcd. $[C_{36}H_{47}N_5O_9+H]^+$: 694.3447, Found: 694.3461.

m.p.: 60 ºC-64 ºC (from MeOH).

$[\alpha]^{25}_D$: -12 (*c* 0.01, MeOH).

4.1.4. Solid Phase Peptide Synthesis

The synthesis of the peptide **γ-CT**, which employed the *trans*-proline monomer, was carried out in the Institut de Química Avançada de Catalunya (ICAQ) laboratory in Barcelona directed by Dr. Royo. On the other hand, the synthesis of the peptide **γ-CC**, that included the *cis*-proline monomer in its structure, was done in the group of Prof. Montenegro, by Dr. Pazo and PhD student Yeray Folgar, at the Centro Singular de Investigación en Química Biológica y Materiales Moleculares (CiQUS) research facilities in the Universidad de Santiago de Compostela (USC).

As the synthesis of both peptides was performed in two different research facilities, a representative procedure for the SPPS of the different peptides has been described in the following section. Both groups used the same SPPS strategy and monomers to accomplish the synthesis.

4.1.4.1. γ-CC and γ-CT

γ-CC and **γ-CT** peptides were synthesised by using manual Fmoc/Boc strategy using Rink Amide resin (loading 0.41 mmol/g). Prior to the synthesis, the resin (0.10 mmol) was swollen in DMF (peptide synthesis grade, 2 mL) for 20 min. Coupling cycles started with the removal of the Fmoc protecting group using a solution of piperidine in DMF (20%, 3 x 2 mL, 15 min), after which the mixture was filtered, and the resin was washed with DMF (3 × 2 mL, 1 min) and DCM (3 × 3 mL, 1 min). The first orthogonally Boc-protected guanidinylated Fmoc-protected *cis*- or *trans*-γ-amino-L-proline amino acid **60** or **61** was coupled by treatment with a solution of the amino acid (2.00 eq.), Oxyma Pure® (2.00 eq.) and DIC (3.00 eq.) in DMF (2 mL), which was mixed with DIPEA (0.20 M,

3.00 eq.) 1 min before its addition. The resulting mixture was stirred by bubbling argon for 30 min. Finally, the resin was washed with DMF (3 × 2 ml, 1 min) and DCM (3 × 3 mL, 1 min). Then, correct functionalisation of the resin with the amino acid was tested through ninhydrin test. After a second round of deprotection, and the corresponding ninhydrin test, the next amino acid, (1*S*,3*R*)-γ-CBAA **59**, was coupled by adding a solution of the amino acid (3.00 eq.), Oxyma Pure® (3.00 eq.) and PyAOP (4.00 eq.) in DMF (2 mL), which was mixed with DIPEA (0.20 M, 4.00 eq.) 1 min before its addition. The resulting mixture was again stirred by bubbling argon for 30 min. These steps were repeated until the peptide scaffold was completed (**Table III-4**).

Table III-4. General protocol for the SPPS of **γ-CC** and **γ-CT** peptides.

Step	Reagents/Solvents	Aim	Cycles	Time/Cycle (min)
1	DMF	Resin conditioning	3	1
2	Piperidine in DMF (20%)	Deprotection	1	15
3	DMF	Wash	3	1
4	DCM	Wash	3	1
5	**60** or **61**/Oxyma Pure®/DIC/DIPEA (2:2:3:3) in DMF	Coupling	1	30
6	DMF	Wash	3	1
7	DCM	Wash	3	1
8	Ninhydrin test (-)[(a)]	Coupling test	1	3
9	Piperidine in DMF (20%)	Deprotection	3	15
10	DMF	Wash	3	1
11	DCM	Wash	3	1
12	Ninhydrin test (+)	Deprotection test	1	3
13	**59**/Oxyma Pure®/PyAOP/DIPEA (3:3:4:3) in DMF	Coupling	1	30
14	DMF	Wash	3	1
15	DCM	Wash	3	1
16	Ninhydrin test (-)	Coupling test	1	3
17	Piperidine in DMF (20%)	Deprotection	3	15
18	DMF	Wash	3	1
19	DCM	Wash	3	1
20	Ninhydrin test (+)	Deprotection test	1	3

a) In some cases, after performing the ninhydrin test, it was found that the amino acid did not couple to the resin or peptide properly. In that case, steps 1 to 7 were repeated. If this happened in the first coupling of the amino acid of the resin, the resin was acetylated.

4.1.4.2. Coupling with carboxyfluorescein (CF) probe to obtain CF-γ-CC and CF-γ-CT

Once the tetradecamer was properly synthesised, the resin including each peptide was used to proceed with the incorporation of the 5(6)-carboxyfluoroscein (CF) in the *N*-terminal group (**Table III-5**). The terminal Fmoc protecting group of the **γ-CC** or **γ-CT** peptide was removed by using a solution of piperidine in DMF (20%, 2 ml) for 15 min and the resin was washed with DMF (3 × 3 mL, 1 min). The coupling was carried out by the addition of a solution of CF (4.00 eq.), Oxyma Pure® (6.00 eq.), PyBOP (4.00 eq.) and DIPEA (0.20 M, 6.00 eq.) in DMF (2 mL), and the mixture was stirred by bubbling argon for 3 h. Finally, the resin was washed with DMF (3 × 3 mL, 1 min) and DCM (3 × 3 mL, 1 min).

Table III-5. General protocol for the SPPS of **γ-CC** and **γ-CT** peptides.

Step	Reagents/Solvents	Aim	Cycles	Time/Cycle (min)
1	DMF	Wash	3	1
2	Piperidine in DMF (20%)	Deprotection	1	15
3	DMF	Wash	3	1
4	DCM	Wash	3	1
5	CF/Oxyma Pure®/PyBOP/DIPEA (4:6:4:6) in DMF	Coupling	1	180
6	DMF	Wash	3	1
7	DCM	Wash	3	1
8	Ninhydrin test (-)	Coupling test	1	3

4.1.4.3. Coupling with 5(6)-carboxy SNARF-1 probe to obtain γ-SCC

To the previously synthesised **γ-CC** peptide, 5(6)-carboxy SNARF-1 probe was coupled to obtain **γ-SCC** (**Table III-6**). The terminal Fmoc protecting group of the **γ-CC** peptide was removed by using a solution of piperidine in DMF (20%, 2 ml) for 15 min and the resin was washed with DMF (3 × 3 mL, 1 min). The coupling was carried out by the addition of a solution of 5(6)-carboxy SNARF-1 (1.00 eq.), Oxyma Pure® (1.00 eq.), HATU (1.00 eq.), and DIPEA (0.20 M, 1.00 eq.) in DMF (2 mL) and the mixture was stirred by bubbling argon for 3 h. Finally, the resin was washed with DMF (3 × 3 mL, 1 min) and DCM (3 × 3 mL, 1 min).

Table III-6. General protocol for the SPPS of **γ-CC** and **γ-CT** peptides.

Step	Reagents/Solvents	Aim	Cycles	Time/Cycle (min)
1	DMF	Wash	3	1
2	Piperidine in DMF (20%)	Deprotection	1	15
3	DMF	Wash	3	1
4	DCM	Wash	3	1
5	SNARF/Oxyma Pure®/PyBOP/DIPEA (1:1:1:1) in DMF	Coupling	1	180
6	DMF	Wash	3	1
7	DCM	Wash	3	1
8	Ninhydrin test (-)	Coupling test	1	3

4.1.4.4. Cleavage from the resin and protecting groups removal

Once all amino acids and the corresponding probe were coupled, the peptide was deprotected and cleaved from the resin at room temperature following a standard TFA cleavage procedure using TFA/DCM/H_2O/TIS (90:5:2.5:2.5, 3 mL) for 2 h. Then, the mixture was filtered, washed with TFA (2 × 1 mL) and the peptide was precipitated in ice-cold Et_2O (25 mL). The precipitate was centrifuged and dissolved in H_2O (5 mL) to carry on with the purification by a C18 RP-HPLC column, with a binary gradient of H_2O (0.1% TFA) / CH_3CN (0.1% TFA) 95:5. Then, the collected fractions were lyophilised and stored at −20 °C.

4.1.4.5. Purification and characterisation of peptides CF-γ-CC, CF-γ-CT and γ-SCC

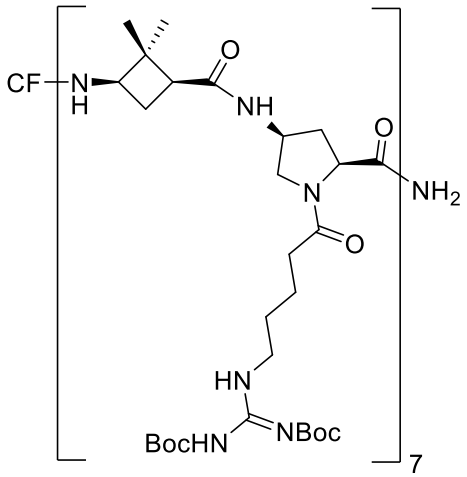

CF-γ-CBAA-*cis*-γ-amino-L-proline, **CF-γ-CC**

Characterisation of CF-γ-CC by HPLC/MS

R_t: 10.2 min [RP-HPLC Agilent SB-C18 column, H_2O (0.1% TFA) / CH_3CN (0.1% TFA) 95:5→5:95 (0→12 min)].

MS (ESI+): 1110.7 (36%, $[M+3H+2TFA]^{3+}$), 1073.1 (14%, $[M+3H+TFA]^{3+}$), 776.3 (100%, $[M+4H]^{4+}$), 621.3 (21%, $[M+5H]^{5+}$), 518.2 (34%, $[M+6H]^{6+}$).

Data are consistent with those reported in reference: O. Illa, J. A. Olivares, N. Gaztelumendi, L. Martinez-Castro, J. Ospina, M. A. Abengozar, G. Sciortino, J.-D. Marechal, C. Nogues, M. Royo, L. Rivas and R. M. Ortuno, *Int. J. Mol. Sci.,* **2020***, 21,* 7502.

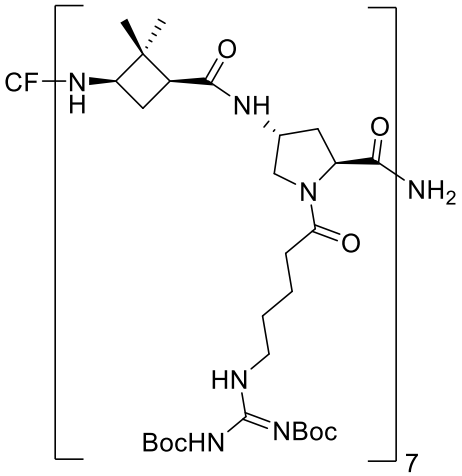

CF-γ-CBAA-*trans*-γ-amino-L-proline, **CF-γ-CT**

Characterisation of CF-γ-CT by HPLC/MS

R_t: 9.9 min [RP-HPLC Agilent SB-C18 column, H_2O (0.1% TFA) / CH_3CN (0.1% TFA) 95:5→5:95 (0→12 min)].

MS (ESI+): 1110.8 (28%, $[M+3H+2TFA]^{3+}$), 1073.4 (21%, $[M+3H+TFA]^{3+}$), 776.3 (100%, $[M+4H]^{4+}$), 621.4 (52%, $[M+5H]^{5+}$), 518.2 (43%, $[M+6H]^{6+}$).

Data are consistent with those reported in reference: O. Illa, J. A. Olivares, N. Gaztelumendi, L. Martinez-Castro, J. Ospina, M. A. Abengozar, G. Sciortino, J.-D. Marechal, C. Nogues, M. Royo, L. Rivas and R. M. Ortuno, *Int. J. Mol. Sci.,* **2020***, 21,* 7502.

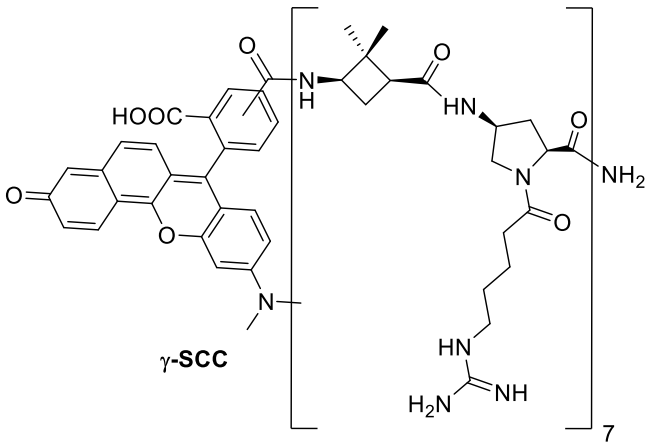

γ-**SCC**

Characterisation of γ-SCC by HPLC/MS

R_t: 6.3 min [RP-HPLC Agilent SB-C18 column, H_2O (0.1% TFA) / CH_3CN (0.1% TFA) 95:5 →5:95 (0→12 min)].

MS (ESI+): 1110.8 (41%, $[M+3H+2TFA]^{3+}$), 1073.4 (30%, $[M+3H+TFA]^{3+}$), 776.2 (100%, $[M+4H]^{4+}$), 621.6 (56%, $[M+5H]^{5+}$), 518.2 (24%, $[M+6H]^{6+}$).

4.2. Chapter II. Novel Bifunctional Ligands for PET Imaging with ^{64}Cu and ^{68}Ga Radioisotopes

4.2.1. Synthesis of the Chelator Models

4.2.1.1. 6,6'-((((1*S*,2*S*)-cyclopentane-1,2-diyl)bis(azanediyl))bis(methylene))dipicolinic acid, H_2CPDEDPA.

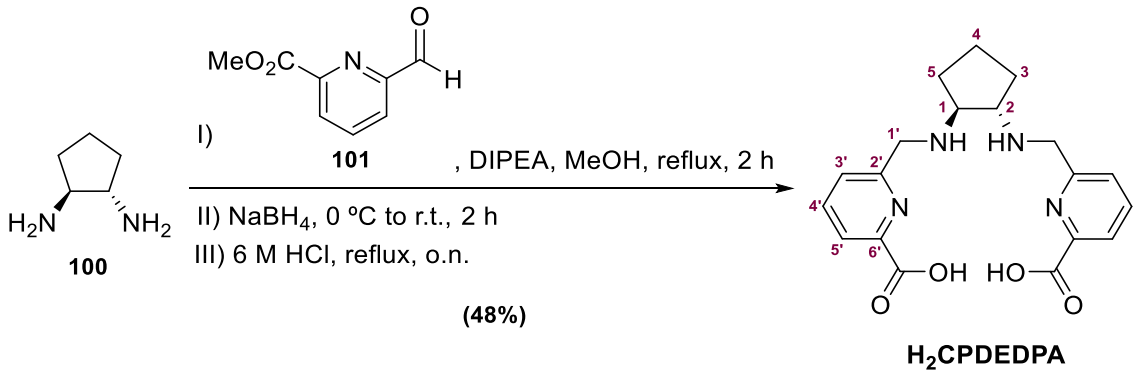

A solution of methyl 6-formylpyridine-2-carboxylate (**101**) (0.22 g, 1.35 mmol, 1.00 eq.) in MeOH (30 mL) was added dropwise to a refluxing solution of *trans*-1,2-cyclopentanediamine dihydrochloride (**100**) (0.12 g, 0.67 mmol) and DIPEA (0.23 mL, 1.34 mmol, 1.00 eq.) in MeOH (10 mL). The resulting mixture was reflux for 4 h. After this time, it was cooled to 0 ºC and $NaBH_4$ (0.04 g, 0.97 mmol) was added. The mixture was stirred at 0 ºC for additional 1.5 h, until complete reduction of the imine was confirmed by MS. Then saturated $NaHCO_3$ aqueous solution (50 mL) was added, and it was stirred for 10 min. The resulting solution was extracted with CH_2Cl_2 (3 x 50 mL). The combined organic extracts were dried over Na_2SO_4 and evaporated to give an orange oil that was hydrolysed with 20 mL of 6 M HCl upon refluxed overnight. The product was lyophilised to afford a white solid that was purified by medium performance liquid chromatography (MPLC) on reverse phase using a C18AQ (20 g) column and H_2O (0.1% TFA) / CH_3CN (0.1% TFA) as mobile phase (compound eluted at 42% CH_3CN) affording **H_2CPDEDPA** (0.20 g, 0.64 mmol, 48% yield) as a white solid.

Spectroscopic data for compound H_2CPDEDPA:

^{1}H-NMR (300 MHz, D_2O): δ 8.16 (dd, $^3J_{5'\text{-}4'}$ = 7.7 Hz, $^4J_{5'\text{-}3'}$ = 1.5 Hz, 2H, $H_{5'}$), 8.10 (dd, $^3J_{4'\text{-}5'}$ = $^3J_{4'\text{-}3'}$ = 7.7 Hz, 2H, $H_{4'}$), 7.75 (dd, $^3J_{3'\text{-}4'}$ = 7.7 Hz, $^4J_{3'\text{-}5'}$= 1.5 Hz, 2H, $H_{3'}$), 4.75 (d, $^3J_{1'a\text{-}1'b}$ = 15.5 Hz, 2H, $H_{1'a}$), 4.65 (d, $^3J_{1'b\text{-}1'a}$ = 15.5 Hz, 2H, $H_{1'b}$), 4.19 (m, 2H, H_1,H_2), 2.39 (m, 2H, H_4), 1.94 (m, 4H, H_3,H_5).

^{13}C-NMR (75 MHz, D_2O): δ 167.8 (CO_2H), 150.4 ($C_{2'}$), 147.2 ($C_{6'}$), 139.9 ($C_{4'}$), 127.3 ($C_{3'}$), 125.5 ($C_{5'}$), 60.5 (C_1, C_2), 48.9 ($C_{1'}$), 28.3 (C_3, C_5), 21.9 (C_4).

IR (ATR): υ 3064, 1716, 1667, 1577, 1181, 1122 cm^{-1}.

Elemental analysis calcd. (%) for $[C_{19}H_{22}N_4O_4]\cdot 2TFA\cdot 0.5H_2O$: C 45.26, H 3.80, N 8.44; Found: C 45.25, H 3.89, N 8.79.

4.2.2. Synthesis of Cu(II) and Ga(III) Complexes with the Chelator Models

4.2.2.1. General procedure A to obtain Cu(II) complexes derived from the ligands H_2CHXDEDPA, H_2CPDEDPA and H_2CBuDEDPA

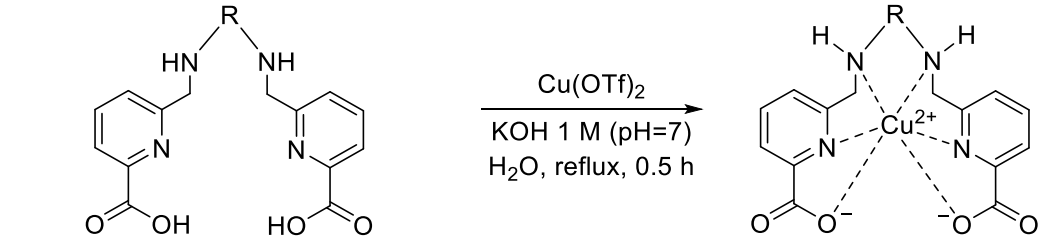

H_2CHXDEDPA, R = 1,2-*trans*-cyclohexyl
H_2CPDEDPA, R = 1,2-*trans*-cyclopentyl
H_2CBuDEDPA, R = 1,3-*cis*-cyclobutyl

[Cu(CHXDEDPA)] (61%)
[Cu(CPDEDPA)] (41%)
[Cu(CBuDEDPA)] (64%)

To a solution of the ligand in H_2O (3 mL) $Cu(OTf)_2$ was added (1.10 eq.). Additional 2 mL of H_2O were added, and the pH was adjusted to *ca* 7 with 1 M KOH. The mixture was refluxed for 30 min, and a brown precipitate appeared. Then, the pH was increased over 8 and the solution was filtered using a 0.2 µm microfilter. The solution was then lyophilised to afford a blue solid that was purified by MPLC on reverser phase using a C18AQ (20 g) column and H_2O/CH_3CN as mobile phase.

[Cu(CHXDEDPA)]: Elutes at 51% CH_3CN as a blue solid (30.8 mg, 61% yield).

Spectroscopic data for compound [Cu(CHXDEDPA)]:

IR (ATR): υ 3590, 3206, 1625, 1591, 1368 cm^{-1}.

HRMS (ESI+) calcd. for $[CuC_{20}H_{22}N_4O_4+H]^+$: 446.1007, Found: 446.1010.

Elemental analysis calcd. (%) for $[CuC_{20}H_{22}N_4O_4]\cdot 3.5H_2O$: C 47.19, H 5.74, N 11.01; Found: C 47.22, H 5.54, N 10.60.

[Cu(CPDEDPA)]: Elutes at 46% CH_3CN as a blue solid (19.8 mg, 41% yield).

Spectroscopic data for compound [Cu(CPDEDPA)]:

IR (ATR): υ 3610, 3210, 1624, 1591, 1374 cm^{-1}.

HRMS (ESI+) calcd. for $[CuC_{19}H_{20}N_4O_4+H]^+$: 432.0853, Found: 432.0853.

Elemental analysis calcd. (%) for $[CuC_{19}H_{20}N_4O_4]\cdot 3.4H_2O$: C 46.27, H 5.84, N 11.36; Found: C 46.67, H 4.95, N 10.60.

[Cu(CBuDEDPA)]: Elutes at 45% CH_3CN as a blue solid (26.0 mg, 64% yield).

Spectroscopic data for compound [Cu(CBuDEDPA)]:

IR (ATR): υ 3601, 3214, 1635, 1590, 1376 cm^{-1}.

HRMS (ESI+) calcd. for $[CuC_{18}H_{18}N_4O_4+K]^+$: 456.0256, Found: 456.0258.

Elemental analysis calcd. (%) for $[CuC_{18}H_{18}N_4O_4]\cdot 2.3H_2O$: C 47.09, H 4.96, N 12.20; Found: C 47.18, H 4.91, N 11.76.

4.2.2.2. General procedure B to obtain Ga(III) complexes

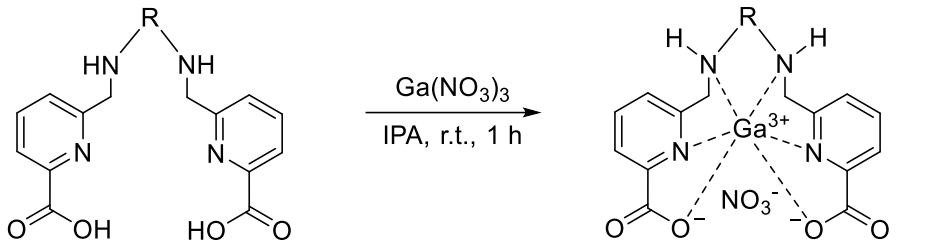

H_2CHXDEDPA, R = 1,2-*trans*-cyclohexyl
H_2CPDEDPA, R = 1,2-*trans*-cyclopentyl
H_2CBuDEDPA, R = 1,3-*cis*-cyclobutyl

[Ga(CHXDEDPA)]NO_3 (70%)
[Ga(CPDEDPA)]NO_3 (56%)
[Ga(CBuDEDPA)]NO_3 (61%)

The corresponding ligand was dissolved in IPA (5 mL) and $Ga(NO_3)_3$ (1.10 eq.) was added in one portion, appearing a white suspension. The crude is stirred at room temperature for 1 h and the reaction was followed by MS until no ligand was shown. At this point, suspension was filtered through a filter funnel. The solid was dissolved in miliQ H_2O (0.5 mL) and centrifugated. The supernatant was filtered using a 0.2 μm microfilter and purified by MPLC on reverse phase using a C18AQ (20 g) column and H_2O 100% as mobile phase.

[Ga(CHXDEDPA)]NO_3: Elutes at 100% H_2O as a white solid (28.2 mg, 70% yield).

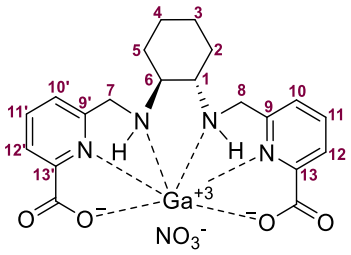

Spectroscopic data for compound [Ga(CHXDEDPA)]NO_3:

^{1}H-NMR (500 MHz, D_2O, pD = 4.3): δ 8.47 (dd, $^3J_{11\text{-}12/11'\text{-}12'}$ = $^3J'_{11\text{-}10/11'\text{-}10'}$ = 7.8 Hz, 2H, H_{11},$H_{11'}$), 8.25 (d, $^3J_{12\text{-}11/12'\text{-}11'}$ = 7.8 Hz, 2H, H_{12},$H_{12'}$), 7.99 (d, $^3J_{10\text{-}11/10'\text{-}11'}$ = 7.8 Hz, 2H, H_{10},$H_{10'}$), 4.56 (d, $^2J_{7a\text{-}7b/8a\text{-}8b}$ = 17.4 Hz, 2H, H_{7a},H_{8a}), 4.39 (d, $^2J_{7b\text{-}7a/8b\text{-}8a}$ = 17.4 Hz, 2H, H_{7b},H_{8b}), 2.29 (m, 2H, H_{2a},H_{5a}), 2.18 (m, 2H, H_1,H_6), 1.68 (m, 2H, H_{3a},H_{4a}), 1.07 (m, 4H, H_{2b},H_{5b},H_{3b},H_{4b}).

^{13}C-NMR (125 MHz, D_2O, pD = 4.3): δ 165.5 (2 CO_2^-), 150.7 ($C_{9,9'}$), 146.3 ($C_{11,11'}$), 143.1 ($C_{13,13'}$), 128.0 ($C_{10,10'}$), 123.6 ($C_{12,12'}$), 59.8 ($C_{1,6}$), 45.7 ($C_{7,8}$), 28.8 ($C_{2,5}$), 23.8 ($C_{3,4}$).

DEPT, HSQC, HMBC and COSY have been recorded.

IR (ATR): υ 3620, 3211, 1682, 1661, 1343 cm^{-1}.

HRMS (ESI+) calcd. for $[GaC_{20}H_{22}N_4O_4]^+$: 451.0897, Found: 451.0896.

Elemental analysis calcd. (%) for $[GaC_{20}H_{22}N_5O_7]\cdot 1.8H_2O$: C 43.95, H 4.72, N 12.81; found: C 44.05, H 4.47, N 12.44.

[Ga(CPDEDPA)]NO_3: Elutes at 100% H_2O as a white solid (19.8 mg, 56% yield).

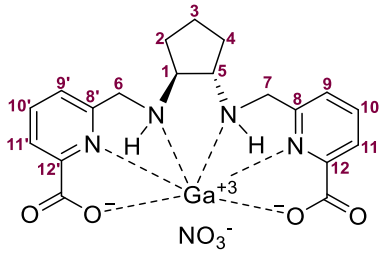

Spectroscopic data for compound [Ga(CPDEDPA)]NO_3:

^{1}H-NMR (500 MHz, D_2O, pD = 3.8): δ 8.54 (dd, $^3J_{10\text{-}11/10'\text{-}11'}$ = $^3J'_{10\text{-}9/10'\text{-}9'}$ = 7.8 Hz, 2H, H_{10},$H_{10'}$), 8.33 (d, $^3J_{11\text{-}10/11'\text{-}10'}$ = 7.8 Hz, 2H, H_{11},$H_{11'}$), 8.07 (d, $^3J_{9\text{-}10/9'\text{-}10'}$ = 7.8 Hz, 2H, H_9,$H_{9'}$), 4.54 (m, 4H, H_6,H_7), 2.62-2.55 (m, 2H, H_1,H_5), 2.18 (dddd, $^2J_{2a\text{-}2b/4a\text{-}4b}$ = 12.2 Hz, $^3J'_{2a\text{-}3a/4a\text{-}3a}$ = $^3J''_{2a\text{-}3b/4a\text{-}3b}$ = $^3J'''_{2a\text{-}1/4a\text{-}5}$ = 6.4 Hz, 2H, H_{2a},H_{4a}), 1.73 (m, 2H, H_3), 1.38 (m, 2H, H_{2b},H_{4b}).

^{13}C-NMR (125 MHz, D_2O, pD = 3.8): δ 165.4 (2 CO_2^-), 150.6 ($C_{8,8'}$), 146.3 ($C_{10,10'}$), 143.0 ($C_{12,12'}$), 128.3 ($C_{9,9'}$), 123.7 ($C_{11,11'}$), 62.4 ($C_{1,5}$), 46.8 ($C_{6,7}$), 24.1 ($C_{2,4}$), 18.1 (C_3).

DEPT, HSQC, HMBC and COSY have been recorded.

IR (ATR): υ 3593, 3214, 1673, 1609, 1344 cm^{-1}.

HRMS (ESI+) calcd. for $[GaC_{19}H_{20}N_4O_4]^+$: 437.0751, Found: 437.0585.

Elemental analysis calcd. (%) for $[GaC_{19}H_{20}N_5O_7]\cdot 1.7H_2O$: C 43.00, H 4.44, N 13.20; found: C 43.28, H 4.18, N 12.92.

[Ga(CBuDEDPA)]NO_3: Elutes at 100% H_2O as a white solid (30.1 mg, 61% yield).

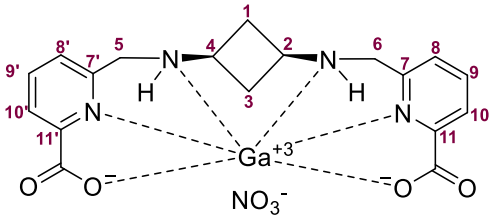

Spectroscopic data for compound [Ga(CBuDEDPA)]NO_3:

^{1}H-NMR (500 MHz, D_2O, pD = 4.1): δ 8.55 (dd, $^3J_{9\text{-}10/1'\text{-}11'}$ = $^3J'_{9\text{-}8/9'\text{-}8'}$ = 7.8 Hz, 2H, $H_{9,9'}$), 8.34 (d, $^3J_{10\text{-}9/10'\text{-}9'}$ = 7.8 Hz, 2H, $H_{10,10'}$), 8.06 (d, $^3J_{8\text{-}9/8'\text{-}9'}$ = 7.8 Hz, 2H, $H_{8,8'}$), 4.87 (d, $^2J_{5a\text{-}5b/6a\text{-}6b}$ = 18.4 Hz, 2H, H_{5a},H_{6a}), 4.43 (d, $^2J_{5b\text{-}5a/6b\text{-}6a}$ = 18.4 Hz, 2H, H_{5b},H_{6b}), 3.90 (dd, $^3J_{2\text{-}3a/4\text{-}3a}$ = $^3J_{2\text{-}1a/4\text{-}1a}$ = 6.1 Hz, 2H, H_2,H_4), 2.56 (m, 2H, H_{1a},H_{3a}), 1.34 (m, 2H, H_{1b},H_{3b}).

^{13}C-NMR (125 MHz, D_2O, pD = 4.1): δ 165.3 (2 CO_2^-), 151.8 ($C_{7,7'}$), 146.4 ($C_{9,9'}$), 142.9 ($C_{11,11'}$), 127.1 ($C_{8,8'}$), 123.5 ($C_{10,10'}$), 58.4 ($C_{2,4}$), 50.0 ($C_{5,6}$), 29.0 ($C_{1,3}$).

DEPT, HSQC, HMBC and COSY have been recorded.

IR (ATR): υ 3601, 3208, 1655, 1603, 1362 cm^{-1}.

HRMS (ESI+) calcd. for $[GaC_{18}H_{18}N_4O_4]^+$: 423.0584, Found: 423.0541.

Elemental analysis calcd (%) for $[GaC_{18}H_{18}N_5O_7]$ 1.6(H_2O): C 41.99, H 4.15, N 13.60; found: C 42.47, H 3.74, N 12.55.

4.2.3. Synthesis of *cis,cis*-L1 ligand

4.2.3.1. (1*R*,5*R*,6*S*/1*S*,5*S*,6*R*)-6-(*tert*-Butoxy)-3-azabicyclo[3.2.0]heptane-2,4-dione and (1*R*,5*R*,6*R*/1*S*,5*S*,6*S*)-6-(*tert*-butoxy)-3-azabicyclo[3.2.0]heptane-2,4-dione, *endo*-(±)-104 and *exo*-(±)-107

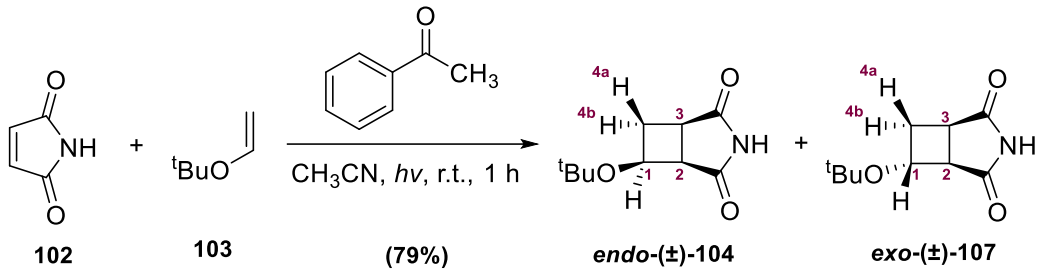

(4.2:1)

To a solution of maleimide **102** (1.18 g, 12.12 mmol) in CH_3CN (400 mL) were added *tert*-butyl vinyl ether **103** (2.39 mL, 18.18 mmol, 1.50 eq.) and acetophenone (0.14 mL, 1.21 mmol, 0.10 eq.). The mixture was stirred at room temperature, degassed with nitrogen for 30 min, and irradiated with a 400 W medium-pressure Hg lamp fitted with a Pyrex filter and a water-cooling jacket for 1 h at room temperature. The solvent was evaporated and the solid residue was purified by silica column chromatography (hexane:EtOAc, 3:2) to afford ***endo*-(±)-104** (1.63 g, 8.26 mmol, 68% yield) and ***exo*-(±)-107** (0.26 g, 1.32 mmol, 11% yield) as white solids.

Spectroscopic data for compound *endo*-(±)-104:

^{1}H-NMR (250 MHz, $CDCl_3$): δ 7.84 (br s, 1H, *NH*), 4.49 (ddd, $^3J_{1\text{-}4a} = {}^3J'_{1\text{-}4b} = {}^3J''_{1\text{-}2}$ = 8.3 Hz, 1H, H_1), 3.53 (m, 1H, H_2), 2.90-3.05 (m, 2H, H_3,H_{4a}), 2.29 (m, 1H, H_{4b}), 1.20 (s, 9H, ^{t}Bu).

^{13}C-NMR, NOE, COSY and HSQC experiments have been recorded.

R_f (hexane:EtOAc, 3:2) = 0.35 (UV and vanillin stain).

Spectroscopic data are consistent with those reported in reference: Chang, Z.; Boyaud, F.; Guillot, R.; Boddaert, T.; Aitken, D.J. *J. Org. Chem.* **2018**, *83* (1), 527-534.

Spectroscopic data for compound *exo*-(±)-107:

^{1}H-NMR (300 MHz, $CDCl_3$): δ 8.74 (br s, 1H, *NH*), 4.34 (ddd, $^3J_{1\text{-}2} = {}^3J'_{1\text{-}4}$ = 6.8 Hz, $^3J''_{1\text{-}4}$ = 3.4 Hz, 1H, H_1), 3.30 (dd, $^3J_{2\text{-}1}$ = 6.8 Hz, $^3J'_{2\text{-}3}$ = 3.4 Hz, 1H, H_2), 3.22 (m, 1H, H_3), 2.59 (m, 2H, H_{4a},H_{4b}), 1.21 (s, 9H, ^{t}Bu).

^{13}C-NMR, COSY and me-HSQC experiments have been recorded.

R_f (hexane:EtOAc, 3:2) = 0.44 (UV and vanillin stain).

Spectroscopic data are consistent with those reported in reference: Chang, Z.; Boyaud, F.; Guillot, R.; Boddaert, T.; Aitken, D.J. *J. Org. Chem.* **2018**, *83* (1), 527-534.

4.2.3.2. Methyl (1*S*,2*S*,3*R*/1*R*,2*R*,3*S*)-3-(*tert*-butoxy)-2-((methoxycarbonyl)amino)cyclobutane-1-carboxylate, (±)-108

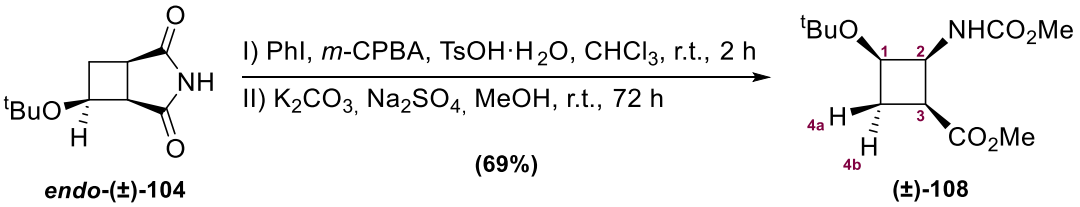

***endo*-(±)-104** **(±)-108**

To prepare the hypervalent iodine reagent, iodobenzene (0.15 mL, 1.32 mmol, 1.30 eq.), *m*-CPBA (0.25 g, 1.42 mmol, 1.40 eq.), and $TsOH·H_2O$ (0.27 g, 1.42 mmol, 1.40 eq.) were dissolved in $CHCl_3$ (3 mL), and the solution was stirred at room temperature for 2 h under a nitrogen atmosphere and protected from the light. The solvents were removed under vacuum, and the desired product was obtained *in situ* as a white solid without further purification. Then Na_2SO_4 (0.29 g, 2.03 mmol, 2.00 eq.) and MeOH (8 mL) were added, and the solution was stirred at 0 °C for 10 min. Compound **(±)-104** (0.20 g, 1.01 mmol) and K_2CO_3 (0.56 g, 4.06 mmol, 4.00 eq.) were added at 0 °C, and the obtained mixture was stirred at room temperature for 72 h. The reaction mixture was treated with a saturated $NaHCO_3$ aqueous solution (30 mL) and the product was extracted with EtOAc (3 x 45 mL). The combined extracts were washed with brine (30 mL) and dried over Na_2SO_4. The organic phase was concentrated under reduced pressure and the crude was purified by silica gel column chromatography (hexane:EtOAc, 3:2), to furnish compound **(±)-108** (0.17 g, 0.66 mmol, 69% yield). Compound **(±)-104** (0.01 g, 0.05 mmol) was also recovered.

Spectroscopic and physical data for compound (±)-108:

^{1}H-NMR (360 MHz, $CDCl_3$): δ 5.57 (br d, 1H, *NH*), 4.46 (m, 1H, H_2), 4.25 (ddd, $^3J_{1\text{-}4a} = {}^3J'_{1\text{-}4b} = {}^3J''_{1\text{-}2}$ = 7.2 Hz, 1H, H_1), 3.63 (s, 6H, 2 CO_2CH_3), 2.96 (ddd, $^3J_{3\text{-}4a} = {}^3J'_{3\text{-}4b} = {}^3J''_{3\text{-}2}$ = 7.6 Hz, 1H, H_3), 2.43 (ddd, $^2J_{4a\text{-}4b}$ = 9.9 Hz, $^3J'_{4a\text{-}3}$ = 7.6 Hz, $^3J''_{4a\text{-}1}$ = 7.2 Hz, 1H, H_{4a}), 2.31 (m, 1H, H_{4b}), 1.14 (s, 9H, ^{t}Bu).

^{13}C-NMR (90 MHz, $CDCl_3$): δ 171.6 (CO_2CH_3), 156.7 ($NHCO_2CH_3$), 74.7 ($C(CH_3)_3$), 63.1 (C_1), 55.7 (C_2), 52.2 (CO_2CH_3), 51.8 (CO_2CH_3), 37.1 (C_3), 32.3 (C_4), 28.0 ($C(CH_3)_3$).

COSY, NOE, NOESY, me-HSQC and HMBC experiments have been recorded.

R_f (hexane:EtOAc, 3:2) = 0.32 (Vanillin stain).

IR (ATR): 3351, 2956, 1712, 1516, 1366, 1156 cm^{-1}.

HRMS (ESI+) calcd. for $[C_{12}H_{21}NO_5+H]^+$: 260.1492, Found: 260.1491.

m.p.: 75 ºC-78 ºC (from hexane:EtOAc).

4.2.3.3. (1*S*,5*S*,6*R*/1*R*,5*R*,6*S*)-6-(*tert*-Butoxy)-3-azabicyclo[3.2.0]heptane-2,4-dione, (±)-105

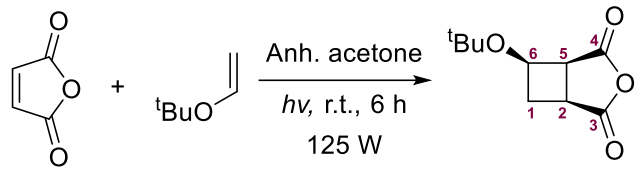

32 **103** **(±)-105**

To a solution of maleic anhydride (**32**) (0.59 g, 6.00 mmol) in anhydrous acetone (200 mL) *tert*-butyl vinyl ether (**103**) (1.18 mL, 9.00 mmol, 1.50 eq.) was added. The mixture was stirred at room temperature, degassed with nitrogen for 30 min, and irradiated with a 125 W medium-pressure Hg lamp fitted with a Pyrex filter and a methanol-cooling jacket for 6 h at room temperature. The solvent was evaporated obtaining the racemic products **(±)-105** used without further purification.

Spectroscopic data for compound (±)-105:

^{1}H-NMR (360 MHz, $CDCl_3$): δ 4.54 (ddd, $^{3}J_{6\text{-}1a} = {}^{3}J'_{6\text{-}1b} = {}^{3}J''_{6\text{-}5} = 6.7$ Hz, 1H, H_6), 3.72 (dd, $^{3}J_{5\text{-}2} = {}^{3}J'_{5\text{-}6} = 6.7$ Hz, 1H, H_5), 3.19 (ddd, $^{3}J_{2\text{-}1} = 11.4$ Hz, $^{3}J'_{2\text{-}1} = {}^{3}J''_{2\text{-}5} = 6.7$ Hz, 1H, H_2), 3.06 (m, 1H, H_1), 2.39 (ddd, $^{3}J_{1\text{-}2} = 11.4$ Hz, $^{3}J'_{1a\text{-}1b} = {}^{3}J''_{1\text{-}6} = 6.7$ Hz, 1H, H_1), 1.20 (s, 9H, ^{t}Bu).

^{13}C-NMR, COSY and HSQC experiment have been recorded.

Spectroscopic data are consistent with those reported in reference: Chang, Z.; Boyaud, F.; Guillot, R.; Boddaert, T.; Aitken, D.J. *J. Org. Chem.* **2018**, *83* (1), 527-534.

4.2.3.4. Dimethyl (1*S*,2*S*,3*R*/1*R*,2*R*,3*S*)-3-(*tert*-butoxy)cyclobutane-1,2-dicarboxylate and (1*S*,2*R*,4*S*/1*R*,2*S*,4*R*)-2-(*tert*-butoxy)-4-(methoxycarbonyl)cyclobutane-1-carboxylic acid, (±)-106 and (±)-115

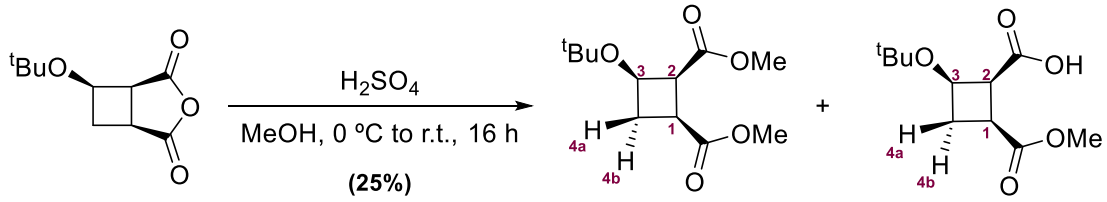

(±)-105 **(±)-106** **(±)-115**

To solution of **(±)-105** (2.38 g, 12.03 mmol) in MeOH (45 mL) at 0 ºC, concentrated H_2SO_4 (1.10 mL, 20.11 mmol, 1.67 eq.) was slowly added while the solution was stirring. The mixture was allowed to attain room temperature and was stirred for 16 h. The solvent was then removed under reduced pressure and the residue was dissolved in CH_2Cl_2 (100 mL) and it was successively washed with water (2 x 50 mL) and brine (1 x 50 mL). The organic layer was then dried over $MgSO_4$, filtered off, concentrated under reduced pressure, and products were separated and purified by flash column chromatography (CH_2Cl_2:MeOH, 97:3) to furnish product **(±)-106** (0.31 g, 1.26 mmol, 11% yield) and product **(±)-115** (0.37 g, 1.60 mmol, 14% yield).

Spectroscopic data for compound (±)-106:

^{1}H-NMR (300 MHz, $CDCl_3$): δ 4.20 (m, 1H, H_3), 3.70 (s, 3H, CO_2CH_3), 3.66 (s, 3H, CO_2CH_3), 3.61 (m, 1H, H_2), 2.84-2.73 (m, 2H, H_1,H_4), 2.47 (m, 1H, H_4), 1.14 (s, 9H, ^{t}Bu).

R_f (CH_2Cl_2:MeOH, 97:3) = 0.60 (Vanillin stain).

HRMS (ESI+) calcd. for $[C_{12}H_{20}O_5+Na]^+$: 267.1203, Found: 267.1199.

Spectroscopic data and physical for compound (±)-115:

^{1}H-NMR (360 MHz, $CDCl_3$): δ 4.30 (ddd, $^3J_{3\text{-}4a} = {}^3J'_{3\text{-}4b} = {}^3J''_{3\text{-}2}$ = 8.7 Hz, 1H, H_3), 3.70 (s, 3H, CO_2CH_3), 3.65 (ddd, $^3J_{2\text{-}3} = {}^3J'_{2\text{-}1}$ = 8.7, $^4J''_{2\text{-}4b}$ = 3.7 Hz, 1H, H_2), 2.96 (ddd, $^3J_{1\text{-}4a} = {}^3J'_{1\text{-}4b} = {}^3J''_{1\text{-}2}$ = 8.7 Hz, 1H, H_1), 2.75 (br ddd, $^2J_{4a\text{-}4b}$ = 10.7, $^3J'_{4a\text{-}1} = {}^3J''_{4a\text{-}3}$ = 8.7 Hz, 1H, H_{4a}), 2.49 (dddd, $^2J_{4b\text{-}4a}$ = 10.7, $^3J'_{4b\text{-}1} = {}^3J''_{4b\text{-}3}$ = 8.7 Hz, $^4J'''_{4b\text{-}2}$ = 3.7 Hz, 1H, H_{4b}), 1.23 (s, 9H, ^{t}Bu).

^{13}C-NMR (90 MHz, $CDCl_3$): δ 175.6 (CO_2CH_3), 172.7 (CO_2H), 75.3 ($C(CH_3)_3$), 62.9 (C_3), 52.1 (C_2), 51.9 (CO_2CH_3), 34.6 (C_4), 32.5 (C_1), 28.0 ($C(CH_3)_3$).

COSY and me-HSQC experiments have been recorded.

R_f (CH_2Cl_2:MeOH, 97:3) = 0.22 (Vanillin stain).

IR (ATR): υ 2984, 1739, 1695, 1440, 1204, 1034, 882 cm^{-1}.

HRMS (ESI-) calcd. for $[C_{11}H_{18}O_5]^-$: 229.1081, Found: 229.1080.

m.p.: 127 ºC-130 ºC (from CH_2Cl_2:MeOH).

4.2.3.5. (1*S*,2*R*,4*S*/1*R*,2*S*,4*R*)-2-(*tert*-Butoxy)-4-(*tert*-butoxycarbonyl)cyclobutane-1-carboxylic acid, (±)-117

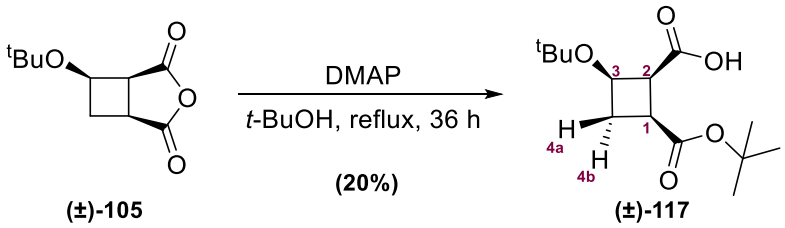

(±)-105 **(±)-117**

A mixture of compound **(±)-105** (0.51 g, 2.52 mmol), DMAP (0.31 g, 2,52 mmol, 1.00 eq.), and *t*-BuOH (4 mL) was heated at reflux for 36 h. After cooling to room temperature, the reaction mixture was diluted with Et_2O (150 mL) and washed with aqueous 1 M HCl (2 x 10 mL). The organic layer was dried over $MgSO_4$ and concentrated under vacuum. The crude obtained was washed with hexane to remove aliphatic impurities, obtaining product **(±)-117** (0.14 g, 0.51 mmol, 20% yield) as a white powder.

Spectroscopic and physical data for compound (±)-117:

^{1}H-NMR (400 MHz, $CDCl_3$): δ 4.24 (ddd, $^{3}J_{3\text{-}4a} = {}^{3}J'_{3\text{-}4b} = {}^{3}J''_{3\text{-}2}$ = 8.2 Hz, 1H, H_3), 3.59 (ddd, $^{3}J_{2\text{-}3} = {}^{3}J'_{2\text{-}1}$ = 8.2, $^{4}J''_{2\text{-}4b}$ = 3.7 Hz, 1H, H_2), 2.82 (ddd, $^{3}J_{1\text{-}4a} = {}^{3}J'_{1\text{-}4b} = {}^{3}J''_{1\text{-}2}$ = 8.2 Hz, 1H, H_1), 2.71 (ddd, $^{2}J_{4a\text{-}4b}$ = 10.3 Hz, $^{3}J'_{4a\text{-}1} = {}^{3}J''_{4a\text{-}3}$ = 8.2 Hz, 1H, H_{4a}), 2.44 (dddd, $^{2}J_{4b\text{-}4a}$ = 10.3 Hz, $^{3}J'_{4b\text{-}1} = {}^{3}J''_{4b\text{-}3}$ = 8.2 Hz, $^{4}J'''_{4b\text{-}2}$ = 3.7 Hz, 1H, H_{4b}), 1.44 (s, 9H, ^{t}Bu), 1.23 (s, 9H, ^{t}Bu).

^{13}C-NMR (100 MHz, $CDCl_3$): δ 175.6 (CO), 172.4 (CO), 81.1 ($C(CH_3)_3$), 75.3 ($C(CH_3)_3$), 62.8 (C_3), 52.0 (C_2), 34.7 (C_4), 33.5 (C_1), 28.0 (2 C(CH_3)$_3$).

COSY and me-HSQC experiments have been recorded.

IR (ATR): υ 2972, 2662, 1735, 1697, 1440, 1367, 1235, 1017, 889 cm^{-1}.

HRMS (ESI-) calcd. for $[C_{14}H_{24}O_5]^-$: 271.1551, Found: 271.1552.

m.p.: 148 ºC-152 ºC (from hexane).

4.2.3.6. (1*S*,2*R*,4*S*/1*R*,2*S*,4*R*)-2-(*tert*-Butoxy)-4-(methoxycarbonyl)cyclobutane-1-carboxylic acid, (±)-115

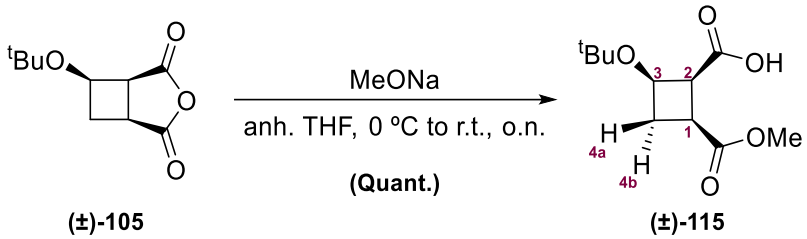

(±)-105 **(±)-115**

A solution of compound **(±)-105** (0.50 g, 2.52 mmol) in anhydrous THF (15 mL) was added over sodium methoxide (0.15 g, 2.77 mmol, 1.10 eq.) at 0 ºC and under a nitrogen atmosphere. The reaction mixture was allowed to attain room temperature and stirred overnight. Then, it was cooled down to 0 ºC and quenched by adding a 0.2 M citric acid solution until pH 4. The reaction mixture was extracted with Et_2O (150 mL) and the organic layer was washed with water (2 x 30 mL), dried over $MgSO_4$, and concentrated under vacuum to obtain product **(±)-115** (0.471 g, 2.52 mmol, quantitative yield(1)) as a white powder without further purification.

(1) As detailed in Part I, Chapter II, section 3.3.1.3, purification of the crude reaction mixture by column chromatography yielded the product in 32%. However, it was decided to proceed with the unpurified product, as this approach led to a higher overall yield with the subsequent step.

Spectroscopic and physical data for compound (±)-115:

^{1}H-NMR (360 MHz, $CDCl_3$): δ 4.30 (ddd, $^{3}J_{3\text{-}4a} = {}^{3}J'_{3\text{-}4b} = {}^{3}J''_{3\text{-}2}$ = 8.7 Hz, 1H, H_3), 3.70 (s, 3H, CO_2CH_3), 3.65 (ddd, $^{3}J_{2\text{-}3} = {}^{3}J'_{2\text{-}1}$ = 8.7 Hz, $^{4}J''_{2\text{-}4b}$ = 3.7 Hz, 1H, H_2), 2.96 (ddd, $^{3}J_{1\text{-}4a} = {}^{3}J'_{1\text{-}4b} = {}^{3}J''_{1\text{-}2}$ = 8.7 Hz, 1H, H_1), 2.75 (br ddd, $^{2}J_{4a\text{-}4b}$ = 10.7 Hz, $^{3}J'_{4a\text{-}1} = {}^{3}J''_{4a\text{-}3}$ = 8.7 Hz, 1H, H_{4a}), 2.49 (dddd, $^{2}J_{4b\text{-}4a}$ = 10.7 Hz, $^{3}J'_{4b\text{-}1} = {}^{3}J''_{4b\text{-}3}$ = 8.7 Hz, $^{4}J'''_{4b\text{-}2}$ = 3.7 Hz, 1H, H_{4b}), 1.23 (s, 9H, ^{t}Bu).

^{13}C-NMR (90 MHz, $CDCl_3$): δ 175.6 (CO_2CH_3), 172.7 (CO_2H), 75.3 ($C(CH_3)_3$), 62.9 (C_3), 52.1 (C_2), 51.9 (CO_2CH_3), 34.6 (C_4), 32.5 (C_1), 28.0 ($C(CH_3)_3$).

COSY and me-HSQC experiments have been recorded.

R_f (CH_2Cl_2:MeOH, 97:3) = 0.22 (Vanillin stain).

IR (ATR): υ 2984, 1739, 1695, 1440, 1204, 1034, 882 cm^{-1}.

HRMS (ESI-) calcd. for $[C_{11}H_{18}O_5]^-$: 229.1081, Found: 229.1080.

m.p.: 127 ºC-130 ºC (from CH_2Cl_2:MeOH).

4.2.3.7. 2-Benzyl 1-methyl (1*S*,2*S*,3*R*/1*R*,2*R*,3*S*)-3-(*tert*-butoxy)cyclobutane-1,2-dicarboxylate, (±)-118

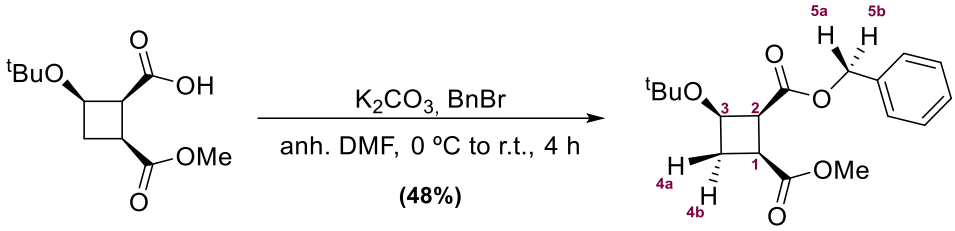

(±)-115 **(±)-118**

A solution of acid **(±)-115** (0.43 g, 1.87 mmol) in anhydrous DMF (15 mL) was cooled to 0 ºC before adding K_2CO_3 (0.34 g, 2.43 mmol, 1.30 eq.) under a nitrogen atmosphere. After 30 min of stirring at this temperature, BnBr (0.29 mL, 2.43 mmol, 1.30 eq.) was added dropwise. The resulting mixture was stirred at room temperature during 4 h. Then, the crude was concentrated under pressure co-evaporating the DMF with toluene. Afterwards, the mixture was dissolved in EtOAc (4 x 40 mL) and washed with brine (3 x 20 mL). The combined organic layers were dried with anhydrous $MgSO_4$, and the solvent was removed under vacuum. The reaction crude was purified via flash chromatography (hexane:EtOAc, 1:3), furnishing compound **(±)-118** (0.29 g, 0.90 mmol, 48% yield(1)) as a white solid.

(1) As detailed in **Part I**, **Chapter II**, **section 3.4.1.3**, purification of the starting material by column chromatography increased the yield to 64%. However, it was decided to proceed with the unpurified product, as this approach led to a higher overall yield.

Spectroscopic and physical data for compound (±)-118:

^{1}H-NMR (360 MHz, $CDCl_3$): δ 7.40-7.30 (m, 5H, H_{Ar}), 5.18 (d, $^2J_{5a\text{-}5b}$ = 13.1 Hz, 1H, CH_2-Ph), 5.14 (d, $^2J_{5b\text{-}5a}$ = 13.1 Hz, 1H, CH_2-Ph), 4.22 (ddd, $^3J_{3\text{-}4a}$ = $^3J'_{3\text{-}4b}$ = $^3J''_{3\text{-}2}$ = 7.9 Hz, 1H, H_3), 3.66 (m, 1H, H_2), 3.55 (s, 3H, CO_2CH_3), 2.88-2.76 (m, 2H, H_1, H_{4a}), 2.48 (m, 1H, H_{4b}), 1.10 (s, 9H, ^{t}Bu).

^{13}C-NMR (90 MHz, $CDCl_3$): δ 172.9 (CO), 170.6 (CO), 136.1 (C_{Ar}), 128.6-128.2 (C_{Ar}), 74.5 ($C(CH_3)_3$), 66.4 (CH_2-Ph), 62.9 (C_3), 52.9 (C_2), 51.7 (CO_2CH_3), 34.9 (C_4), 32.2 (C_1), 28.1 ($C(CH_3)_3$).

COSY and me-HSQC experiments have been recorded.

R_f (hexane:EtOAc, 3:1) = 0.31 (UV and vanillin stain).

IR (ATR): υ 3037, 2978, 1729, 1345, 1184, 1081, 1035, 750 cm^{-1}.

HRMS (ESI+) calcd. for $[C_{18}H_{24}O_5+Na]^+$: 343.1516, Found: 343.1505.

m.p.: 51 ºC-53 ºC (from hexane:EtOAc).

4.2.3.8. (1*S*,2*S*,3*R*/1*R*,2*R*,3*S*)-2-((Benzyloxy)carbonyl)-3-(*tert*-butoxy)cyclobutane-1-carboxylic acid, (±)-119

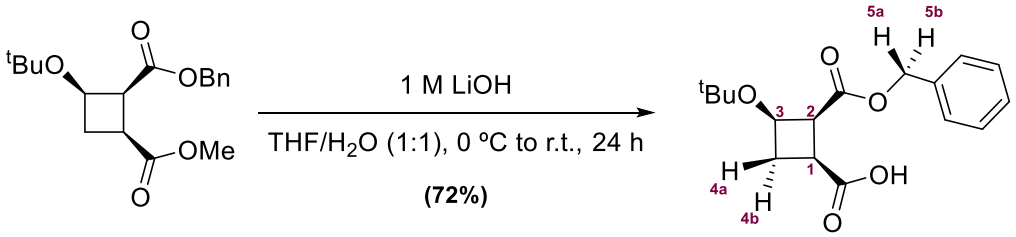

(±)-118 **(±)-119**

To a solution of diester **(±)-118** (0.67 g, 2.09 mmol) in 1:1 THF/H_2O mixture (11 mL) at 0 ºC was added an aqueous solution of 1 M LiOH (0.09 g, 2.09 mmol, 1.00 eq.) dropwise. After complete addition, the reaction mixture was allowed to warm to room temperature and stirred for 24 hours. The mixture was acidified to pH 4 by adding 0.5 M HCl and extracted with CH_2Cl_2 (3 x 30 mL). The organic layers were collected, dried over $MgSO_4$ and concentrated in vacuo. The crude residue was purified by column chromatography in silica (hexane:EtOAc, 6:1 to EtOAc 100%) to obtain compound **(±)-119** as a white solid (0.46 g, 1.50 mmol, 72% yield).

Spectroscopic and physical data for compound (±)-119:

^{1}H-NMR (360 MHz, $CDCl_3$): δ 7.39-7.27 (m, 5H, H_{Ar}), 5.19 (d, $^2J_{5a-5b}$ = 12.9 Hz, 1H, C*H*$_2$-Ph), 5.16 (d, $^2J_{5b-5a}$ = 12.9 Hz, 1H, C*H*$_2$-Ph), 4.23 (ddd, $^3J_{3-4a}$ = $^3J'_{3-4b}$ = $^3J''_{3-2}$ = 8.2 Hz, 1H, H_3), 3.68 (m, 1H, H_2), 2.91-2.78 (m, 2H, H_1, H_{4a}), 2.50 (m, 1H, H_{4b}), 1.10 (s, 9H, ^{t}Bu).

^{13}C-NMR (90 MHz, $CDCl_3$): δ 178.3 (CO_2H), 170.5 (*C*O_2-Bn), 136.0 (C_{Ar}), 128.5-128.1 (C_{Ar}), 74.6 (*C*$(CH_3)_3$), 66.6 (*C*H_2-Ph), 62.8 (C_3), 52.9 (C_2), 34.7 (C_4), 32.3 (C_1), 28.0 (C(*C*$H_3)_3$).

COSY and me-HSQC experiments have been recorded.

R_f (hexane:EtOAc, 3:1) = 0.22 (UV and vanillin stain).

IR (ATR): υ 3007, 2920, 1724, 1345, 1167, 1081, 734 cm^{-1}.

HRMS (ESI+) calcd. for $[C_{17}H_{22}O_5+Na]^+$: 329.1359, Found: 329.1358.

m.p.: 139 ºC-143 ºC (from EtOAc).

4.2.3.9. Benzyl (1*S*,2*R*,4*S*/1*R*,2*S*,4*R*)-2-(*tert*-butoxy)-4-((*tert*-butoxycarbonyl)amino)-cyclobutane-1-carboxylate, (±)-121

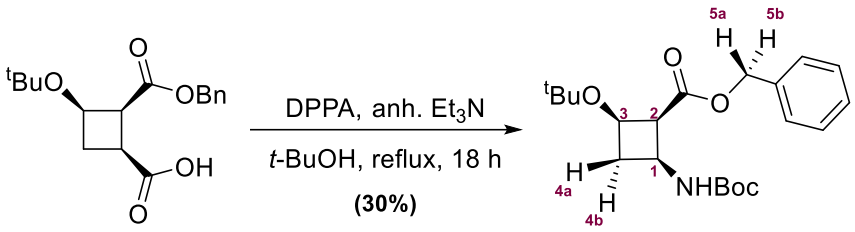

(±)-119 **(±)-121**

Carboxylic acid **(±)-119** (0.27 g, 0.88 mmol), under an inert atmosphere, was dissolved in *t*-BuOH (5 mL). Anhydrous triethylamine (0.14 mL, 0.97 mmol, 1.10 eq.) was added to the solution and the mixture was stirred at 0 ºC. Diphenylphosphoryl azide (DPPA) (0.19 mL, 0.88 mmol, 1.00 eq.) was added, and the mixture was refluxed for 18 h under a nitrogen atmosphere. Toluene was evaporated under reduced pressure. The crude obtained was dissolved in H_2O (10 mL) and extracted with CH_2Cl_2 (6 x 15 mL). The organic layers were combined, dried over $MgSO_4$ and the solvent was evaporated under reduce pressure. The residual oil was purified by column chromatography (hexane:EtOAc gradient, 8:1 to 3:1) to afford compound **(±)-121** (0.10 g, 0.26 mmol, 30% yield) as a white solid.

Spectroscopic and physical data for compound (±)-121:

^{1}H-NMR (360 MHz, $CDCl_3$): δ 7.40-7.31 (m, 5H, H_{Ar}), 5.76 (d, $^3J_{NH\text{-}1}$ = 9.0 Hz, 1H, *NH*Boc), 5.23 (d, $^2J_{5a\text{-}5b}$ = 12.3 Hz, 1H, *CH*$_2$-Ph), 5.13 (d, $^2J_{5b\text{-}5a}$ = 12.3 Hz, 1H, *CH*$_2$-Ph), 4.07-3.98 (m, 2H, H_3,H_1), 3.62 (ddd, $^3J_{2\text{-}3}$ = $^3J'_{2\text{-}1}$ = 8.3 Hz, $^4J''_{2\text{-}4b}$ = 3.6 Hz, 1H, H_2), 2.62 (dddd, $^2J_{4b\text{-}4a}$ = 11.0 Hz, $^3J'_{4b\text{-}1}$ = $^3J''_{4b\text{-}3}$ = 8.3 Hz, $^4J'''_{4b\text{-}2}$ = 3.6 Hz, 1H, H_{4b}), 2.46 (ddd, $^2J_{4a\text{-}4b}$ = 11.0 Hz, $^3J'_{4a\text{-}1}$ = $^3J''_{4a\text{-}3}$ = 8.3 Hz, 1H, H_{4a}), 1.42 (s, 9H, ^{t}Bu), 1.09 (s, 9H, ^{t}Bu).

^{13}C-NMR (90 MHz, $CDCl_3$): δ 171.4 (*C*O_2-Bn), 155.3 (NH*C*$O_2{}^t$Bu), 135.9 (C_{Ar}), 128.7 (C_{Ar}), 128.3 (C_{Ar}), 79.5 (*C*$(CH_3)_3$), 74.5 (*C*$(CH_3)_3$), 66.4 (*C*H_2-Ph), 61.4 (C_3), 55.2 (C_2), 41.0 (C_4), 38.6 (C_1), 28.5 (C(*C*$H_3)_3$), 28.0 (C(*C*$H_3)_3$).

COSY, me-HSQC and HMBC experiments have been recorded.

R$_f$ (hexane:EtOAc, 3:1) = 0.44 (UV and vanillin stain).

IR (ATR): υ 3437, 2967, 1710, 1508, 1362, 1160, 734 cm^{-1}.

HRMS (ESI+) calcd. for $[C_{21}H_{31}NO_5+Na]^+$: 400.2094, Found: 400.2089.

m.p.: 102 ºC-105 ºC (from hexane:EtOAc).

4.2.3.10. (1*S*,2*R*,4*S*/1*R*,2*S*,4*R*)-2-(*tert*-Butoxy)-4-carbamoylcyclobutane-1-carboxylate ammonium salt, (±)-127

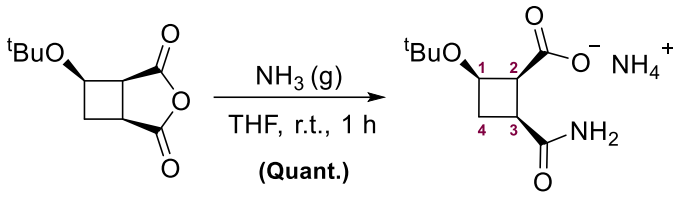

(±)-105 **(±)-127**

Compound **(±)-105** (1.21 g, 6.08 mmol) was dissolved in THF (60 mL) in a 250 mL round-bottom flask. The head space of the flask was flushed with ammonia gas for 10 min, the ammonia atmosphere was kept with 2 balloons and the mixture was stirred at room temperature for 1 h. The solution was filtered, obtaining the corresponding ammonium salt **(±)-127** (1.39 g, 5.98 mmol) as a yellowish powder, which shows sufficient purity by ^{1}H-NMR, so it was used in the following step without further purification.

Spectroscopic and physical data for compound (±)-127:

^{1}H-NMR (300 MHz, D_2O): δ 4.23 (ddd, $^{3}J_{1\text{-}4a}$ = 9.9 Hz, $^{3}J'_{1\text{-}4b}$ = $^{3}J''_{1\text{-}2}$ = 7.8 Hz, 1H, H_1), 3.40 (ddd, $^{3}J_{2\text{-}1}$ = $^{3}J'_{2\text{-}3}$ = 7.8 Hz, $^{4}J''_{2\text{-}4b}$ = 3.7 Hz, 1H, H_2), 2.74 (ddd, $^{3}J_{3\text{-}4a}$ = 9.9 Hz, $^{3}J'_{3\text{-}4b}$ = $^{3}J''_{3\text{-}2}$ = 7.8 Hz, 1H, H_3), 2.60 (ddd, $^{3}J_{4a\text{-}4b}$ = $^{3}J'_{4a\text{-}1}$ = $^{3}J''_{4a\text{-}3}$ = 9.9 Hz, 1H, H_{4a}), 2.35 (dddd, $^{3}J_{4b\text{-}4a}$ = 9.9 Hz, $^{3}J'_{4b\text{-}1}$ = $^{3}J''_{4b\text{-}3}$ = 7.8 Hz, $^{3}J'''_{4b\text{-}2}$ = 3.7 Hz, 1H, H_{4b}), 1.11 (s, 9H, ^{t}Bu).

^{13}C-NMR (90 MHz, D_2O): δ 180.5 (CO), 178.4 (CO), 75.9 ($C(CH_3)_3$), 62.6 (C_1), 57.1 (C_2), 33.9 (C_3, C_4), 27.8 ($C(CH_3)_3$).

COSY and HSQC experiments have been recorded.

IR (ATR): υ 2977, 1850, 1608, 1561, 1409, 1363, 1177, 1123 cm^{-1}.

HRMS (ESI-) calcd. for [$C_{10}H_{16}NO_4^-$]: 214.1079, Found: 214.1083.

m.p.: 148 ºC-152 ºC (from THF).

4.2.3.11. Methyl (1*S*,2*R*,4*S*/1*R*,2*S*,4*R*)-2-(*tert*-butoxy)-4-carbamoylcyclobutane-1-carboxylate, (±)-128

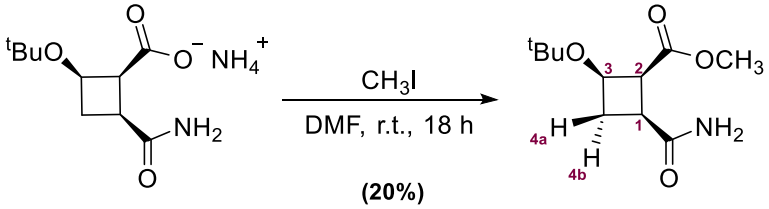

(±)-127 **(±)-128**

In a round-bottom flask that contained product **(±)-127** (1.55 g, 6.65 mmol) dissolved in DMF (40 mL) was added CH_3I (0.50 mL, 7.98 mmol, 1.20 eq.). The solution was stirred under a nitrogen atmosphere and dark conditions during 18 h at room temperature. Once the reaction was

terminated, nitrogen was flushed during 10 min to remove excess of CH_3I. EtOAc (4 x 40 mL) and H_2O (60 mL) were added to proceed to the extraction. The organic phase was dried over $MgSO_4$, filtered, and evaporated under vacuum, and the residue was purified by flash chromatography (CH_2Cl_2:MeOH, 92:8) to afford the desired ester **(±)-128** (0.30 g, 1.33 mmol, 20% yield).

Spectroscopic and physical data for compound (±)-128:

^{1}H-NMR (250 MHz, $CDCl_3$): δ 5.66 (br s, 2H, *NH_2*), 4.31 (ddd, $^3J_{3\text{-}4a} = {}^3J'_{3\text{-}4b} = {}^3J''_{3\text{-}2}$ = 7.9 Hz, 1H, H_3), 3.72 (s, 3H, CO_2CH_3), 3.68-3.60 (m, 1H, H_2), 2.83-2.64 (m, 2H, H_1,H_{4b}), 2.42 (m, 1H, H_{4a}), 1.16 (s, 9H, ^{t}Bu).

^{13}C-NMR (63 MHz, $CDCl_3$): δ 175.3 ($CONH_2$), 171.5 (CO_2CH_3), 74.6 ($C(CH_3)_3$), 62.4 (C_3), 52.9 (C_2), 51.6 (CO_2CH_3), 34.8 (C_4), 33.6 (C_1), 28.1 ($C(CH_3)_3$).

COSY and HSQC experiments have been recorded.

R_f (CH_2Cl_2:MeOH, 92:8) = 0.47 (Vanillin stain).

IR (ATR): υ 3426, 3127, 2950, 1721, 1657, 1364, 1183, 888 cm^{-1}.

HRMS (ESI+) calcd. for $[C_{11}H_{19}NO_4+Na]^+$: 252.1206, Found: 252.1202.

m.p.: 71 ºC-74 ºC (from CH_2Cl_2:MeOH).

4.2.3.12. (1*S*,2*S*,3*R*/1*R*,2*R*,3*S*)-3-(*tert*-Butoxy)-2-((*tert*-butoxycarbonyl)amino)cyclobutane-1-carboxylic acid, (±)-114

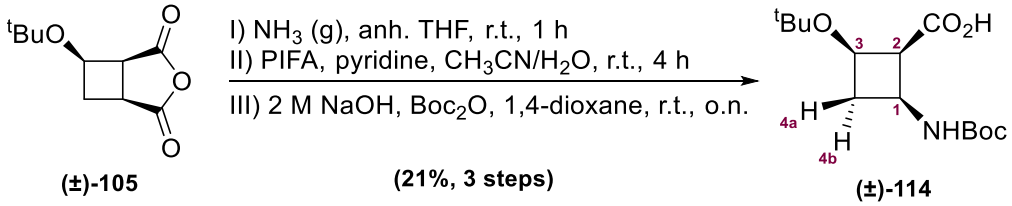

(±)-105 **(21%, 3 steps)** **(±)-114**

Compound **(±)-105** (1.21 g, 6.08 mmol) was dissolved in anhydrous THF (60 mL) in a 250 mL round-bottom flask. The head space of the flask was flushed with ammonia gas for 10 min, the ammonia atmosphere was kept with 2 balloons and the mixture was stirred at room temperature for 1 h. THF was removed under reduced pressure and the white solid obtained was dissolved in a 1:1 mixture of CH_3CN/H_2O (216 mL) and PIFA (3.87 g, 9.00 mmol, 1.50 eq.) was added. After stirring the solution for 15 min at room temperature, pyridine (1.45 mL, 18.00 mmol, 3.00 eq.) was added and the mixture was stirred for 4 h at room temperature. CH_3CN was evaporated carefully and the residual aqueous solution was basified with 2 M NaOH aqueous solution to pH 9. Boc_2O (1.70 g, 7.80 mmol, 1.40 eq.) solution in 1,4-dioxane (108 mL) was added and the mixture was stirred overnight at room temperature. Dioxane was evaporated carefully, and the residual aqueous solution was acidified with 1 M HCl aqueous solution to pH 4, followed by extraction with EtOAc (4 x 120 mL). The combined organic phases were dried over $MgSO_4$, filtered, and evaporated under

reduced pressure. The residue was purified by flash chromatography (hexane:EtOAc, 3:1) to afford compound **(±)-114** as a white solid (0.06 g, 0.21 mmol, 21% yield(1)).

(1) This yield was only achieved when anhydrous acetone was used for the obtention of **(±)-105**.

Spectroscopic data for compound (±)-114:

^{1}H-NMR (300 MHz, $CDCl_3$): δ 5.55 (d, $^3J_{NH-3}$ = 7.1 Hz, 1H, *NH*), 4.16-4.01 (m, 2H, H_3,H_1), 2.72 (m, 1H, H_{4b}), 2.34 (ddd, $^3J_{4a-3}$ = $^3J'_{4a-1}$, $^2J''_{4a-4b}$ = 9.8 Hz, 1H, H_{4a}), 1.43 (s, 9H, ^{t}Bu), 1.23 (s, 9H, ^{t}Bu).

^{13}C-NMR, COSY, NOESY and me-HSQC experiments have been recorded.

R_f (hexane:EtOAc, 1:1) **=** 0.53 (UV and vanillin stain).

Spectroscopic data are consistent with those reported in reference: Chang, Z.; Boyaud, F.; Guillot, R.; Boddaert, T.; Aitken, D.J. *J. Org. Chem.* **2018**, *83* (1), 527-534.

4.2.3.13. *tert*-Butyl ((1*S*,2*R*,3*R*/1*R*,2*S*,3*S*)-3-(*tert*-butoxy)-2-(hydroxymethyl)cyclobutyl)-carbamate, (±)-126

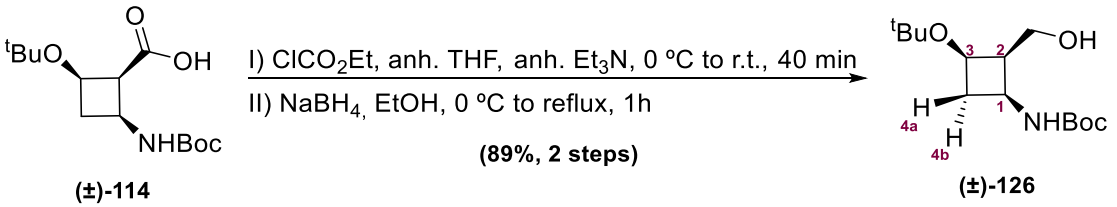

(±)-114 **(±)-126**

Amino acid **(±)-114** (0.36 g, 1.25 mmol) was dissolved in anhydrous THF (9 mL) under an inert atmosphere. Ethyl chloroformate (0.13 mL, 1.32 mmol, 1.05 eq.) and anhydrous Et_3N (0.19 mL, 1.38 mmol, 1.10 eq.) were added to the reaction mixture and stirred at room temperature for 40 min. Then, the salts were filtered, washed with THF (5 mL) and the organic phase was evaporated. The crude obtained was dissolved in EtOH (6 mL). Small portions of $NaBH_4$ (0.27 g, 12.53 mmol, 10.00 eq.) were added at 0 ºC and the reaction mixture was slowly heated to reflux for 1 h. The reaction was quenched by dropwise addition of water until no gas formation was observed. Reaction solvents were evaporated and the aqueous phase was extracted with CH_2Cl_2 (6 x 20 mL). The combined organic layers were dried with $MgSO_4$, filtered and concentrated under reduced pressure, obtaining alcohol **(±)-126** (0.30 g, 1.11 mmol, 89% yield) as a white solid without further purification.

Spectroscopic and physical data for compound (±)-126:

^{1}H-NMR (400 MHz, $CDCl_3$): δ 5.36 (d, $^3J_{NH-1}$ = 9.3 Hz, 1H, *NH*), 4.17-4.00 (m, 3H, H_3,H_1,CH_2OH), 3.83 (m, 1H, CH_2OH), 3.06 (br, 1H, OH), 2.84-2.74 (m, 2H, H_2,H_{4b}), 1.99 (ddd, $^2J_{4a-4b}$ = $^3J'_{4a-1}$ = $^3J''_{4a-3}$ = 7.9 Hz, 1H, H_{4a}), 1.43 (s, 9H, ^{t}Bu), 1.18 (s, 9H, ^{t}Bu).

^{13}C-NMR (100 MHz, $CDCl_3$): δ 155.8 (CO), 79.3 ($C(CH_3)_3$), 74.6 ($C(CH_3)_3$), 63.3 (C_3), 60.3 (CH_2OH), 48.3 (C_2), 43.5 (C_4), 40.8 (C_1), 28.5 ($C(CH_3)_3$), 28.3 ($C(CH_3)_3$).

COSY and me-HSQC experiments have been recorded.

R_f (hexane:EtOAc, 3:1) = 0.32 (UV and vanillin stain).

IR (ATR): υ 3498, 3287, 2948, 1714, 1539, 1360, 1168, 1009, 838 cm^{-1}.

HRMS (ESI+) calcd. for $[C_{14}H_{27}NO_4+Na]^+$: 296.1832, Found: 296.1827.

m.p.: 98-101 ºC (from CH_2Cl_2).

4.2.3.14. *tert*-Butyl ((1*S*,2*R*,3*R*/1*R*,2*S*,3*S*)-3-(*tert*-butoxy)-2(((*tert*butyldiphenylsilyl)-oxy)methyl)cyclobutyl) carbamate, (±)-129

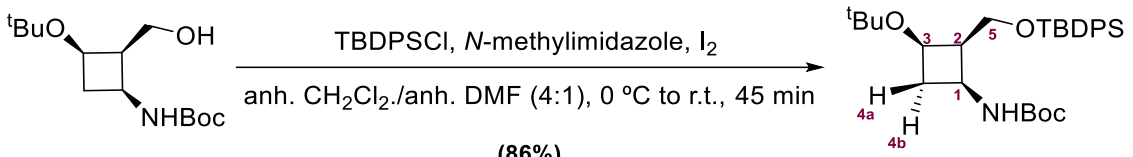

(±)-126 **(±)-129**

Alcohol **(±)-126** (0.20 g, 0.73 mmol), *N*-methylimidazole (0.18 mL, 2.20 mmol, 3.00 eq.), and iodine (0.37 g, 1.46 mmol, 2.00 eq.) were dissolved in a 4:1 mixture of anhydrous CH_2Cl_2/DMF (2.50 mL) under a nitrogen atmosphere at 0 ºC. To this mixture, *tert*-butyl diphenyl chloride (0.23 mL, 0.88 mmol, 1.20 eq.) was added and the reaction crude was warm to room temperature and stirred until complete disappearance of the starting material by TLC analysis. The solvent was then evaporated, the residue was dissolved in EtOAc and washed with a $Na_2S_2O_3$ saturated aqueous solution. The organic phase was dried over anhydrous Na_2SO_4 and evaporated. The crude obtained was purified by silica gel column chromatography (CH_2Cl_2, 100%) to obtain product **(±)-129** (0.33 g, 0.62 mmol, 86% yield) as a white solid.

Spectroscopic and physical data for compound (±)-129:

^{1}H-NMR (400 MHz, $CDCl_3$): δ 7.77 (m, 2H, H_{Ar}), 7.70 (m, 2H, H_{Ar}), 7.45-7-37 (m, 6H, H_{Ar}), 6.06 (d, $^3J_{NH-1}$ = 7.4 Hz, 1H, *NH*Boc), 4.16 (ddd, $^3J_{3-4a}$ = 10.4 Hz, $^3J'_{3-4b}$ = $^3J''_{3-2}$ = 8.0 Hz, 1H, H_3), 3.93-3.83 (m, 3H, H_1,H_5), 2.77-2.63 (m, 2H, H_2,H_{4b}), 2.17 (ddd, $^2J_{4a-4b}$ = $^3J'_{4a-1}$ = $^3J''_{4a-3}$ = 10.4 Hz, 1H, H_{4a}), 1.44 (s, 9H, ^{t}Bu), 1.08 (s, 9H, ^{t}Bu), 1.03 (s, 9H, ^{t}Bu).

^{13}C-NMR (100 MHz, $CDCl_3$): δ 155.8 (CO), 135.8 (C_{Ar}), 133.3 (C_{Ar}), 133.1 (C_{Ar}), 129.8 (C_{Ar}), 127.8 (C_{Ar}), 78.9 (*C*(CH_3)$_3$), 77.5 (*C*(CH_3)$_3$), 73.7 (*C*(CH_3)$_3$), 61.8 (C_5), 61.3 (C_3), 48.2 (C_2), 41.7 (C_4), 41.2 (C_1), 28.6 (C(*C*H_3)$_3$), 28.1 (C(*C*H_3)$_3$), 27.0 (C(*C*H_3)$_3$).

COSY and me-HSQC experiments have been recorded.

R_f (CH_2Cl_2, 100%) = 0.22 (UV and vanillin stain).

IR (ATR): υ 3428, 3394, 2969, 2931, 1702, 1510, 1363, 1168, 1089, 701 cm^{-1}.

HRMS (ESI+) calcd. for $[C_{30}H_{45}NO_4Si+Na]^+$: 534.3010, Found: 534.3013.

m.p.: 114-117 ºC (from CH_2Cl_2).

4.2.3.15. *tert*-Butyl ((1*S*,2*R*,3*R*/1*R*,2*S*,3*S*)-2-(((*tert*-butyldiphenylsilyl)oxy)methyl)-3-hydroxycyclobutyl)carbamate, (±)-130

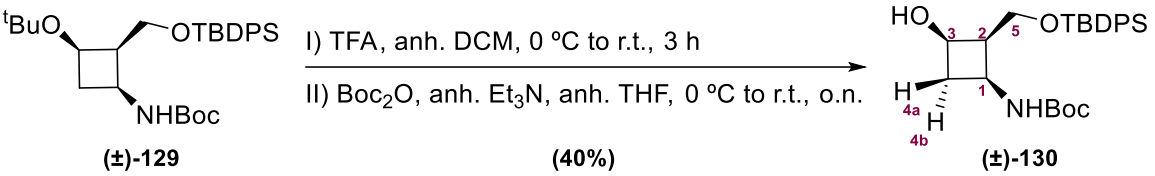

(±)-129 **(40%)** **(±)-130**

Compound **(±)-129** (0.13 g, 0.25 mmol) was dissolved in CH_2Cl_2 (2.5 mL) and TFA (0.51 mL, 6.64 mmol, 26.00 eq.) was added to the mixture under an inert atmosphere at 0 ºC. The mixture was stirred for 3 h, while the temperature slowly was increased to room temperature. After the complete evaporation of TFA under reduced pressure, the residue was diluted with anhydrous THF (2.5 mL). The mixture was cooled to 0 ºC before adding anhydrous Et_3N dropwise (0.08 mL, 0.53 mmol, 2.10 eq.) and Boc_2O (0.07 g, 0.31 mmol, 1.20 eq.) successively. The mixture was then stirred overnight at room temperature. The solvent was removed under reduced pressure and the crude obtained was dissolved in H_2O (15 mL) and extracted with EtOAc (4 x 15 mL). The combined organic phases were dried over $MgSO_4$ and the solvents were evaporated under reduced pressure, furnishing product **(±)-130** (0.05 g, 0.10 mmol, 40% yield) as a yellow oil.

Spectroscopic data for compound (±)-130:

^{1}H-NMR (400 MHz, $CDCl_3$): δ 7.72-7.67 (m, 4H, H_{Ar}), 7.49-7.39 (m, 6H, H_{Ar}), 5.33 (d, $^3J_{NH\text{-}1}$ = 8.5 Hz, 1H, *NH*), 4.23-3.96 (m, 4H, H_1,H_3,H_5), 2.96-2.80 (m, 2H, H_2,H_{4b}), 2.09 (m, 1H, H_{4a}), 1.42 (s, 9H, ^{t}Bu), 1.13 (s, 9H, ^{t}Bu).

^{13}C-NMR (100 MHz, $CDCl_3$): δ 155.5 (CO), 135.9 (C_{Ar}), 135.8 (C_{Ar}), 132.2 (C_{Ar}), 130.2 (C_{Ar}), 128.1 (C_{Ar}), 79.3 ($C(CH_3)_3$), 77.4 ($C(CH_3)_3$), 64.2 (C_3), 61.5 (C_5), 47.3 (C_2), 43.8 (C_4), 40.4 (C_1), 28.5 ($C(CH_3)_3$), 27.1 ($C(CH_3)_3$).

COSY and me-HSQC experiments have been recorded.

R_f (hexane:EtOAc, 3:1) = 0.23 (UV and $KMnO_4$).

IR (ATR): υ 3431, 3404, 2979, 1703, 1508, 1367, 1158, 1091 cm^{-1}.

HRMS (ESI+) calcd. for $[C_{26}H_{37}NO_4Si+Na]^+$: 478.2384, Found: 478.2392.

4.2.3.16. *tert*-Butyl ((1*S*,2*R*,3*S*/1*R*,2*S*,3*R*)-2-(((*tert*-butyldiphenylsilyl)oxy)methyl)-3-iodocyclobutyl)carbamate, (±)-133

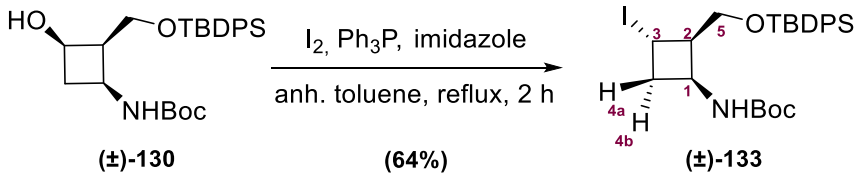

(±)-130 **(64%)** **(±)-133**

A solution of Ph_3P (0.16 g, 0.614 mmol, 2.00 eq.) and I_2 (0.12 g, 0.46 mmol, 1.50 eq.) in anhydrous toluene (2.5 mL) under an inert atmosphere at room temperature. The mixture was stirred for 40

min and then, added over a solution of secondary alcohol **(±)-130** (0.14 g, 0.31 mmol) and imidazole (0.06 g, 0.922 mmol, 3.00 eq.) in anhydrous toluene (2.5 mL). The mixture was stirred for 2 h under reflux in an oil bath. The solvent was evaporated under reduced pressure and the crude obtained was dissolved in H_2O (15 mL) and extracted with CH_2Cl_2 (4 x 15 mL). The combined organic phases were dried over $MgSO_4$ and the solvents were evaporated under reduced pressure. The residue was purified by column chromatography (CH_2Cl_2, 100%) to obtain product **(±)-133** (0.11 g, 0.20 mmol, 64% yield) as a brown oil.

Spectroscopic data for compound (±)-133:

^{1}H-NMR (300 MHz, $CDCl_3$): δ 7.70-7.66 (m, 4H, H_{Ar}), 7.49-7.39 (m, 6H, H_{Ar}), 6.35 (d, $^3J_{NH\text{-}1}$ = 6.2 Hz, 1H, *NH*), 4.76 (ddd, $^3J_{3\text{-}4a}$ = $^3J'_{3\text{-}4b}$ = $^3J''_{3\text{-}2}$ = 7.7 Hz, 1H, H_3), 4.53 (m, 1H, H_1), 3.77 (dd, $^2J_{5a\text{-}5b}$ = 11.7 Hz, $^3J'_{5a\text{-}2}$ = 3.0 Hz, 1H, H_{5a}), 3.70 (dd, $^2J_{5b\text{-}5a}$ = 11.7 Hz, $^3J'_{5b\text{-}2}$ = 3.0 Hz, 1H, H_{5b}), 2.96 (m, 1H, H_2), 2.79 (m, 1H, H_{4a}), 2.68 (m, 1H, H_{4b}), 1.44 (s, 9H, ^{t}Bu), 1.11 (s, 9H, ^{t}Bu).

^{13}C-NMR (75 MHz, $CDCl_3$): δ 155.6 (CO), 135.9 (C_{Ar}), 135.7 (C_{Ar}), 132.5 (C_{Ar}), 130.2 (C_{Ar}), 128.2 (C_{Ar}), 79.4 ($C(CH_3)_3$), 77.4 ($C(CH_3)_3$), 61.5 (C_5), 53.6 (C_2), 50.2 (C_1), 43.0 (C_4), 28.6 ($C(CH_3)_3$), 27.0 ($C(CH_3)_3$), 12.5 (C_3).

COSY and me-HSQC experiments have been recorded.

R_f (CH_2Cl_2, 100%) = 0.46 (UV and $KMnO_4$).

IR (ATR): υ 3311, 2984, 1730, 1682, 1526, 1340, 1283, 1198, 1091 cm^{-1}.

HRMS (ESI+) calcd. for $[C_{26}H_{36}NO_3ISi+Na]^+$: 588.1401, Found: 588.1392.

4.2.3.17. *tert*-Butyl ((1*S*,2*R*,3*R*/1*R*,2*S*,3*S*)-3-amino-2-(((*tert*-butyldiphenylsilyl)oxy)-methyl)cyclobutyl)carbamate, (±)-134

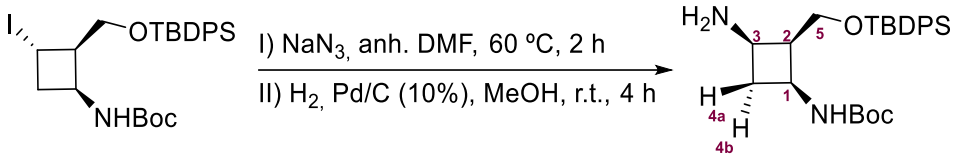

(±)-133 **(42%, 2 steps)** **(±)-134**

To a solution of compound **(±)-133** (0.13 g, 0.23 mmol) in anhydrous DMF (2.5 mL) was added NaN3 (0.06 g, 0.92 mmol, 4.00 eq.) in one portion under a nitrogen atmosphere. The mixture was heated up to 60 ºC and stirred for 2 h while following the reaction by TLC. The reaction was quenched with H_2O and extracted with CH_2Cl_2 (4 x 15 mL) and brine (3 x 10 mL). The combined organic phases were dried over $MgSO_4$ and the solvents were evaporated under reduced pressure. The residue was purified by column chromatography (CH_2Cl_2, 100%) obtaining the azide intermediate used for the hydrogenolysis reaction. Then, to a methanol solution of the intermediate was added 10 wt% Pd/C (0.03 g, 0.03 mmol, 0.10 eq.) and the mixture was stirred under hydrogen atmosphere at room temperature for 4 h. After filtration on a pad of Celite®, the filtrate was

concentrated by evaporation to afford product **(±)-134** (0.04 g, 0.10 mmol, 42% yield) as an off-white solid, which was used in the following reaction without further purification.

Spectroscopic data for compound (±)-134:

^{1}H-NMR (300 MHz, $CDCl_3$): δ 7.73-7.65 (m, 4H, H_{Ar}), 7.47-7.37 (m, 6H, H_{Ar}), 5.59 (d, $^3J_{NH-1}$ = 8.5 Hz, 1H, *NH*), 4.16-4.93 (m, 3H, H_1,H_5), 3.32 (m, 1H, H_3), 2.82-2.62 (m, 1H, H_2,H_{4a}), 1.92 (m, 1H, H_{4b}), 1.46 (s, 9H, ^{t}Bu), 1.13 (s, 9H, ^{t}Bu).

HRMS (ESI+) calcd. for $[C_{26}H_{38}N_2O_3Si+Na]^+$: 477.2544, Found: 477.2542.

4.2.3.18. (1*R*,3*S*)-2-(((*tert*-butyldiphenylsilyl)oxy)methyl)cyclobutane-1,3-diamine, 135

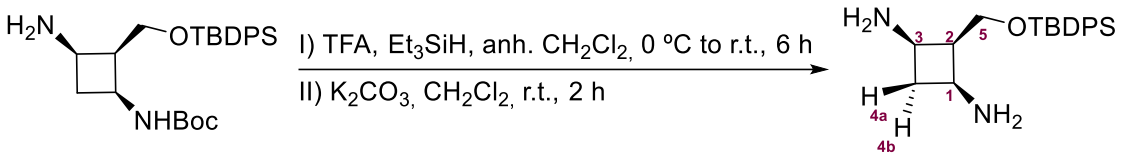

(±)-134 **(Quant.)** **135**

To a solution of half protected diamine **(±)-134** (0.08 g, 0.19 mmol), dissolved in anhydrous CH_2Cl_2 (2 mL) was added Et_3SiH (0.07 g, 0.57 mmol, 3.00 eq.) and TFA (0.17 mL, 2.28 mmol, 12.00 eq.) at 0 ºC under a nitrogen atmosphere. The mixture was stirred for 6 h while gradually increasing to room temperature. After this period, the solvent was evaporated under reduced pressure. Then, the crude product was dissolved in CH_2Cl_2 (6 mL) and stirred over an excess of K_2CO_3 (0.26 g, 1.91 mmol, 10.00 eq.). After 2 h, the solution was filtered and evaporated under reduced pressure to afford product **135** (0.07 g, 0.19 mmol, quantitative yield) as a white solid.

Spectroscopic data for compound 135:

^{1}H-NMR (300 MHz, $CDCl_3$): δ 7.72-7.64 (m, 4H, H_{Ar}), 7.47-7.38 (m, 6H, H_{Ar}), 4.08 (m, 2H), 3.35-3.29 (m, 2H), 2.65 (m, 1H), 2.52 (m, 1H), 1.78 (m, 1H), 1.11 (s, 9H, ^{t}Bu).

4.2.3.19. Methyl 6-formylpicolinate, 101

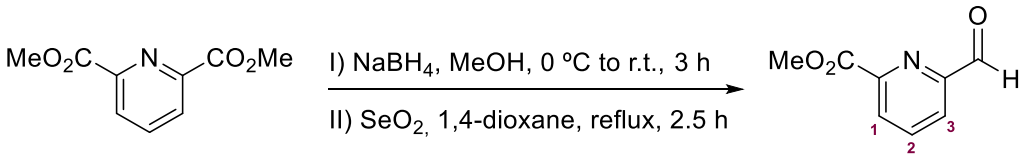

137 **(68%)** **101**

$NaBH_4$ (0.04 g, 1.10 mmol, 1.10 eq.) was added in small portions over a period of 30 min to a stirred solution of **137** (0.20 g, 1.00 mmol) in MeOH (10 mL) at 0 ºC. The mixture was heated to r.t. for 3 h and then poured into a saturated $NaHCO_3$ aqueous solution (10 mL). Methanol was evaporated under vacuum, and the resulting aqueous solution was extracted with CH_2Cl_2 (4 x 15 mL). The combined organic phases were dried over $MgSO_4$, filtered, and evaporated under reduced pressure. The solid obtained was dissolved in dioxane (20 mL) and SeO_2 (0.06 g, 0.5 mmol, 0.50

eq.) was added. The solution was heated to reflux for 2.5 h, filtered while hot, and evaporated to dryness. The crude was then purified through flash column chromatography (CH_2Cl_2:MeOH, 98:2) to isolate product **101** (0.12 g, 0.68 mmol, 68% yield) as a yellow oil.

Spectroscopic data for compound (±)-56:

^{1}H-NMR (400 MHz, $CDCl_3$): δ 10.20 (s, 1H, CHO), 8.36 (d, $^3J_{3\text{-}2}$ = 7.7 Hz, 1H, H_3), 8.15 (d, $^3J_{1\text{-}2}$ = 7.7 Hz, 1H, H_1), 8.06 (dd, $^3J_{2\text{-}3}$ = $^3J'_{2\text{-}1}$ = 7.7 Hz, 1H, H_2), 4.07 (s, 3H, CO_2CH_3).

R_f (CH_2Cl_2:MeOH, 98:2) = 0.52 (UV and $KMnO_4$).

Spectroscopic data are consistent with those reported in reference: Platas-Iglesias, C.; Mato-Iglesias, M.; Djanashvili, K.; Muller, R.N.; Vander Elst, L.; Peters, J.A.; de Blas, A.; Rodriguez-Blas, T. *Chem. Eur. J.* **2004**, *10* (14), 3579.

4.2.4. Synthesis of *cis,trans*-L2 ligand

4.2.4.1. Methyl (1*S*,2*R*,4*S*/1*R*,2*S*,4*R*)-2-(*tert*-butoxy)-4-((*tert*-butoxycarbonyl)amino)-cyclobutane-1-carboxylate, (±)-138

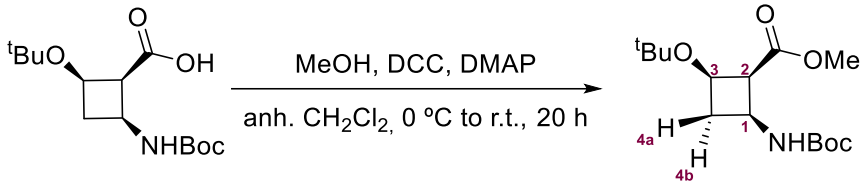

(±)-114 **(40%)** **(±)-138**

To a solution of protected *cis*-CBAA **(±)-114** (0.32 g, 1.04 mmol) and MeOH (0.13 mL, 3.15 mmol, 3.00 eq.) in CH_2Cl_2 were added DMAP (12.7 mg, 0.11 mmol, 0.10 eq.) and DCC at 0 ºC, and the mixture was stirred for 1 h at this temperature under an inert atmosphere. After being warmed to room temperature, the reaction mixture was stirred for 20 h. After filtration, the solvent was removed under reduced pressure, EtOAc was added, and the mixture was washed with 0.2 M HCl solution (15 mL), brine (15 mL), 5% $NaHCO_3$ solution (15 mL), and brine (15 mL) successively. The combined organic phases were dried over $MgSO_4$, filtered, and evaporated under reduced pressure, and the residue was purified by flash chromatography (hexane:Et_2O, 3:2) affording the desired ester **(±)-138** (0.13 g, 0.44 mmol, 40% yield).

Spectroscopic data for compound (±)-138:

^{1}H-NMR (300 MHz, $CDCl_3$): δ 5.78 (d, $^3J_{NH\text{-}1}$ = 8.8 Hz, 1H, *NH*), 4.04-3.96 (m, 2H, H_1,H_3), 3.72 (s, 3H, CO_2CH_3), 3.56 (ddd, $^3J_{2\text{-}1}$ = $^3J'_{2\text{-}3}$ = 7.3, $^4J''_{2\text{-}4b}$ = 3.9 Hz, 1H, H_2), 2.56 (dddd, $^2J_{4b\text{-}4a}$ = 10.7 Hz, $^3J'_{4b\text{-}1}$ = $^3J''_{4b\text{-}3}$ = 7.6 Hz, $^4J'''_{4b\text{-}2}$ = 3.9 Hz, 1H, H_{4b}), 2.42 (ddd, $^2J_{4a\text{-}4b}$ = $^3J'_{4a\text{-}1}$ = $^3J''_{4a\text{-}3}$ = 10.7 Hz, 1H, H_{4a}), 1.40 (s, 9H, ^{t}Bu), 1.14 (s, 9H, ^{t}Bu).

^{13}C-NMR (75 MHz, $CDCl_3$): δ 171.9 (CO_2CH_3), 155.2 ($NHCO_2CH_3$), 79.4 ($C(CH_3)_3$), 74.4 ($C(CH_3)_3$), 61.2 (C_1), 55.1 (C_2), 51.4 (CO_2CH_3), 40.7 (C_4), 38.3 (C_3), 28.4 ($C(CH_3)_3$), 27.9 ($C(CH_3)_3$).

COSY and me-HSQC experiments have been recorded.

R_f (hexane:Et_2O, 1:1) = 0.45 (Vanillin stain).

IR (ATR): υ 3437, 3345, 2974, 1745, 1688, 1527, 1363, 1162, 1013, 880 cm^{-1}.

HRMS (ESI+) calcd. for $[C_{15}H_{27}NO_5+Na]^+$: 324.1781, Found: 324.1776.

m.p.: 55 ºC-57 ºC (from hexane:Et_2O).

4.2.4.2. (1*S*,2*S*,3*R*/1*R*,2*R*,3*S*)-3-(*tert*-Butoxy)-2-(*tert*-butoxycarbonylamino)cyclobutane-1-carboxylic acid, (±)-109

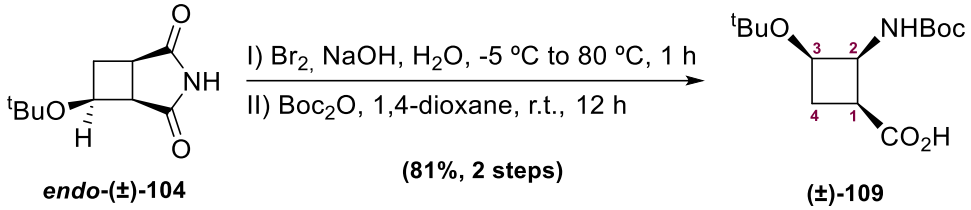

***endo*-(±)-104** **(±)-109**

Bromine (1.03 mL, 20.08 mmol, 1.10 eq.) was dissolved in a 20% w/w sodium hydroxide solution (60 mL), and the mixture was cooled to 0 °C. Compound ***endo*-(±)-104** (3.60 g, 18.25 mmol) was added in small portions to the previously prepared alkaline solution, and the mixture was stirred vigorously. The white solution was further cooled to -5 ºC, and sodium hydroxide (1.82 g, 45.62 mmol, 2.50 eq.) was added, and the mixture was stirred for 30 min. The solution was then heated to 80 °C and maintained at this temperature for 10 min. Then, 40% sodium hydrogen sulfite solution (2 mL) was added, and the mixture was cooled to 0 °C before adding concentrated HCl until pH 9. Then, a solution of Boc_2O (5.58 g, 25.60 mmol, 1.40 eq.) in dioxane (60 mL) was added and the mixture was stirred overnight at room temperature. Dioxane was evaporated under reduced pressure, 1 M HCl aqueous solution was added to the residual aqueous solution until pH 4 and extracted with EtOAc (5 x 30 mL). The combined organic layers were dried over $MgSO_4$ and the solvent was evaporated under vacuum. Traces of unreacted Boc_2O were removed by washing the resulting solid with hexane to afford **(±)-109** as a white solid (4.24 g, 14.76 mmol, 81% yield).

Spectroscopic data for compound (±)-109:

^{1}H-NMR (300 MHz, $CDCl_3$): δ 5.50 (d, $^3J_{NH-2}$ = 6.8 Hz, 1H, *NH*), 4.46 (ddd, $^3J_{2-NH}$ = $^3J'_{2-3}$ = $^3J''_{2-1}$ = 6.8 Hz, 1H, H_2), 4.26 (ddd, $^3J_{3-4a}$ = $^3J'_{3-4b}$ = $^3J''_{3-2}$ = 6.8 Hz, 1H, H_3), 3.04 (m, 1H, H_1), 2.39 (m, 2H, H_4), 1.44 (s, 9H, $NHCO_2C(CH_3)_3$), 1.17 (s, 9H, $OC(CH_3)_3$).

^{13}C-NMR, COSY and me-HSQC experiments have been recorded.

R_f (hexane:EtOAc, 1:3) = 0.57 (Vanillin stain).

Spectroscopic data are consistent with those reported in reference: Chang, Z.; Boyaud, F.; Guillot, R.; Boddaert, T.; Aitken, D.J. *J. Org. Chem.* **2018**, *83* (1), 527-534.

4.2.4.3. (1*R*,2*S*,3*R*/1*S*,2*R*,3*S*)-(*tert*-Butoxy)-2-(*tert*-butoxycarbonylamino)cyclobutane-1-carboxylic acid, (±)-140

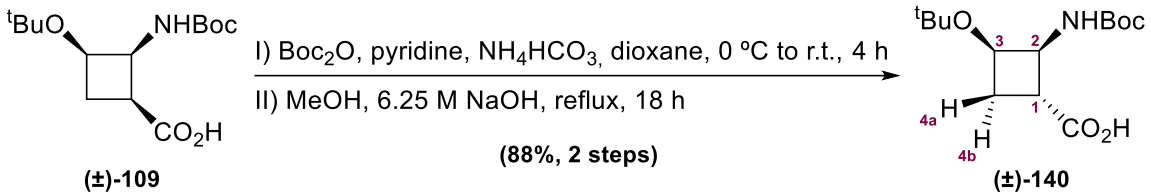

(±)-109 **(±)-140**

Carboxylic acid **(±)-109** (0.70 g, 2.44 mmol) was dissolved in 1,4-dioxane (8 mL) and the solution was cooled to 0 ºC before adding pyridine (0.49 mL, 6.09 mmol, 2.50 eq.) to the stirring crude. The solution was heated to room temperature and Boc_2O was added to the mixture, which was stirred for 30 min. Then, ammonium carbonate (0.58 g, 7.31 mmol, 3.00 eq.) was added and the crude mixture was stirred at room temperature for 4 h. Water (20 mL) was added and the solvent was removed under vacuum to dryness. The crude obtained was dissolved in EtOAc (20 mL) and the organic phase was washed with water (4 x 20 mL). The organic phase was dried over $MgSO_4$ and the solvent was evaporated under reduced pressure. The obtained solid was dissolved in MeOH (30 mL), treated with 6.25 M NaOH aqueous solution (16 mL), and the mixture was heated to reflux overnight. The methanol was then removed by careful evaporation under vacuum, and the aqueous phase was cooled to 0 °C and treated with concentrated HCl to a pH 3. The aqueous phase was extracted with CH_2Cl_2 (6 × 30 mL), the combined organic layers were dried over $MgSO_4$, and the solvent was evaporated under reduced pressure to obtain a mixture of *trans:cis* products, **(±)-140** and **(±)-109**, in a 5:1 ratio as a white powder (0.62 g, 2.36 mmol, 88% yield). Purification of diastereoisomers using column chromatography was not fully successful. As a result, both products were used in the next step and the by-products were separated by column chromatography. One pure sample of **(±)-140** was used for characterization.

Spectroscopic and physical data for compound (±)-140:

^{1}H-NMR (300 MHz, $CDCl_3$): δ 11.86 (br s, 1H, CO_2H), 5.72 (br s, 1H, *NH*), 4.31 (td, $^3J_{3\text{-}2} = {}^3J'_{3\text{-}4a} = 7.8$ Hz, $^3J''_{3\text{-}4b} = 3.0$ Hz, 1H, H_3), 4.18 (m, 1H, H_2), 3.20 (dt, $^3J_{1\text{-}4b} = 10.7$ Hz, $^3J'_{1\text{-}2} = {}^3J''_{1\text{-}4a} = 7.8$ Hz, 1H, H_1), 2.61 (dt, $^2J_{4a\text{-}4b} = 14.5$, $^3J'_{4a\text{-}1} = {}^3J''_{4a\text{-}3} = 7.8$ Hz, 1H, H_{4a}), 2.18 (m, 1H, H_{4b}), 1.48 (s, 9H, $NHCO_2C(CH_3)_3$), 1.20 (s, 9H, $OC(CH_3)_3$).

^{13}C-NMR (75 MHz, $CDCl_3$): δ 174.3 (CO_2H), 157.7 ($NHCO_2C(CH_3)_3$), 81.9 ($NHCO_2C(CH_3)_3$), 75.5 ($OC(CH_3)_3$), 63.5 (C_3), 52.1 (C_2), 46.6 (C_1), 31.5 (C_4), 28.4 (2 $C(CH_3)_3$).

COSY, NOE, me-HSQC and HMBC experiments have been recorded.

R_f (hexane:EtOAc, 1:1) = 0.37 (Vanillin stain).

IR (ATR): υ 3393, 3280, 2972, 1711, 1665, 1387, 1129 cm^{-1}.

HRMS (ESI+) calcd. for $[C_{14}H_{25}NO_5+Na]^+$: 310.1625, Found: 310.1630.

m.p.: 111 ºC-114 ºC (from CH_2Cl_2).

4.2.4.4. Benzyl *tert*-butyl ((1*R*,2*S*,3*R*/1*S*,2*R*,3*S*)-3-(*tert*-butoxy)cyclobutane-1,2-diyl)dicarbamate, (±)-141

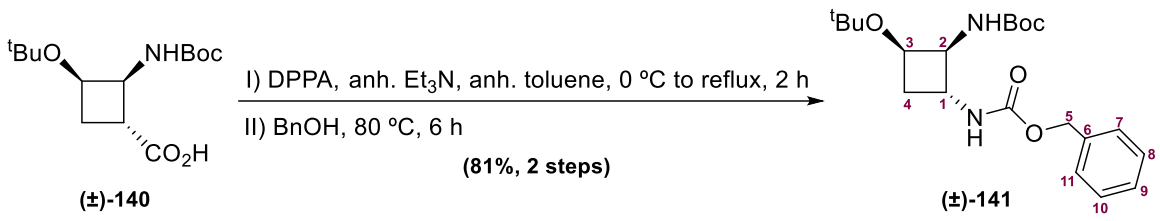

Carboxylic acid **(±)-140** (1.20 g, 4.18 mmol), under an inert atmosphere, was dissolved in anhydrous toluene (22 mL). Anhydrous triethylamine (0.64 mL, 4.60 mmol, 1.10 eq.) was added to the solution and the mixture was stirred at 0 ºC. Diphenylphosphoryl azide (DPPA) (0.99 mL, 4.60 mmol, 1.10 eq.) was added, and the mixture was refluxed for 2 h under a nitrogen atmosphere. The crude was cooled to 60 ºC, and benzyl alcohol (0.87 mL, 8.35 mmol, 2.00 eq.) was added in one portion. The mixture was then heated at 80 °C for 6 h. After this time, toluene was evaporated under reduced pressure. The crude obtained was dissolved in H_2O (30 mL) and extracted with CH_2Cl_2 (6 x 30 mL). The organic layers were combined, dried over $MgSO_4$ and the solvent was evaporated under reduced pressure. The remaining benzyl alcohol was microdistilled, and the residual oil was purified by column chromatography (hexane:EtOAc, 1:1) on silica gel to afford compound **(±)-141** (1.33 g, 3.38 mmol, 81% yield) as a white solid.

Spectroscopic and physical data for compound (±)-141:

^{1}H-NMR (400 MHz, $CDCl_3$): δ 7.36-7.28 (m, 5H, H_{Ar}), 5.31-5.21 (m, 2H, *NH*$CO_2C(CH_3)_3$, *NH*Cbz), 5.07 (m, 2H, *CH_2*-Ph), 4.22 (t, $^3J_{3\text{-}4a} = {}^3J'_{3\text{-}4b} = {}^3J''_{3\text{-}2}$ = 6.9 Hz, 1H, H_3), 4.14 (m, 1H, H_1), 4.00 (ddd, $^3J_{2\text{-}3} = {}^3J'_{2\text{-}1} = {}^3J''_{2\text{-}NH}$ = 6.9 Hz, 1H, H_2), 2.17 (m, 1H, H_{4a}), 1.83 (m, 1H, H_{4b}), 1.43 (s, 9H, $NHCO_2C(CH_3)_3$), 1.15 (s, 9H, $OC(CH_3)_3$).

^{13}C-NMR (100 MHz, $CDCl_3$): δ 155.6 (CO), 155.4 (CO), 136.5 (C_6), 128.5-128.0 (C_{Ar}), 79.5 ($NHCO_2C(CH_3)_3$), 74.6 ($OC(CH_3)_3$), 66.6 (C_5), 65.3 (C_3), 54.9 (C_2), 53.0 (C_1), 35.1 (C_4), 28.4 (2 $C(CH_3)_3$).

COSY, NOE, me-HSQC and HMBC experiments have been recorded.

R_f (hexane:EtOAc, 1:1) = 0.55 (UV and vanillin stain).

IR (ATR): υ 3377, 3262, 2943, 1708, 1653, 1384, 1122 cm^{-1}.

HRMS (ESI+) calcd. for $[C_{21}H_{32}N_2O_5+Na]^+$: 415.2203, Found: 415.2198.

m.p.: 113 ºC-116 ºC (from hexane:EtOAc).

4.2.4.5. Benzyl *tert*-butyl ((1*R*,2*S*,3*S*/1*S*,2*R*,3*R*)-3-hydroxycyclobutane-1,2-diyl)dicarbamate, (±)-142

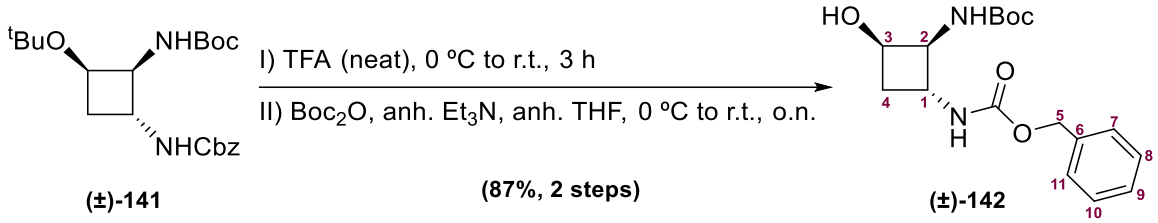

(±)-141 **(87%, 2 steps)** **(±)-142**

Compound **(±)-141** (0.80 g, 2.04 mmol) was dissolved in neat TFA (4.00 mL, 52.30 mmol, 26.00 eq.) under an inert atmosphere at 0 ºC. The mixture was stirred for 3 h while the temperature was slowly increased to room temperature. After the complete evaporation of TFA under reduced pressure, the residue was diluted with anhydrous THF (5 mL). The mixture was cooled to 0 ºC before adding anhydrous Et_3N dropwise (0.60 mL, 4.28 mmol, 2.10 eq.) and Boc_2O (0.67 g, 3.06 mmol, 1.50 eq.) successively. The mixture was then stirred overnight at room temperature. The solvent was removed under reduced pressure and the crude obtained was dissolved in H_2O (30 mL) and extracted with EtOAc (4 x 30 mL). The combined organic phases were successively washed with 2 M NaOH aqueous solution (5 mL) and brine and dried over $MgSO_4$. The solvents were evaporated under reduced pressure, furnishing product **(±)-142** (0.59 g, 1.77 mmol, 87% yield) as a white powder.

Spectroscopic and physical data for compound (±)-142:

^{1}H-NMR (400 MHz, DMSO-d_6): δ 7.60 (d, $^3J_{NH\text{-}1}$ = 8.5 Hz, 1H, *NH*Cbz), 7.38-7.29 (m, 5H, H_{Ar}), 6.63 (d, $^3J_{NH\text{-}2}$ = 8.5 Hz, 1H, *NH*Boc), 5.02-4.93 (m, 3H, *CH*$_2$-Ph, *OH*), 4.14 (dddd, $^3J_{1\text{-}NH} = {}^3J'_{1\text{-}4} = {}^3J''_{1\text{-}2}$ = 8.5 Hz, 1H, H_1), 4.06 (m, 1H, H_3), 3.91 (ddd, $^3J_{2\text{-}3} = {}^3J'_{2\text{-}1} = {}^3J''_{2\text{-}NH}$ = 8.5 Hz, 1H, H_2), 1.88-1.71 (m, 2H, H_4), 1.37 (s, 9H, ^{t}Bu).

^{13}C-NMR (100 MHz, DMSO-d_6): δ 155.1 (CO), 154.6 (CO), 137.1 (C_6), 128.3-127.8 (C_{Ar}), 77.8 ($NHCO_2C(CH_3)_3$), 65.2 (C_5), 64.5 (C_3), 54.7 (C_2), 51.2 (C_1), 33.7 (C_4), 28.2 ($C(CH_3)_3$).

COSY, HSQC and HMBC experiments have been recorded.

R_f (hexane:EtOAc, 1:4) = 0.39 (UV and $KMnO_4$).

IR (ATR): υ 3359, 2973, 1722, 1675, 1532, 1256, 1162, 1029 cm^{-1}.

HRMS (ESI+) calcd. for $[C_{17}H_{24}N_2O_5+Na]^+$: 359.1577, Found: 359.1562.

m.p.: 128 ºC-131 ºC (from EtOAc).

4.2.4.6. Benzyl *tert*-butyl ((1*R*,2*S*,3*S*/1*S*,2*R*,3*R*)-3-azidocyclobutane-1,2-diyl)dicarbamate, (±)-143

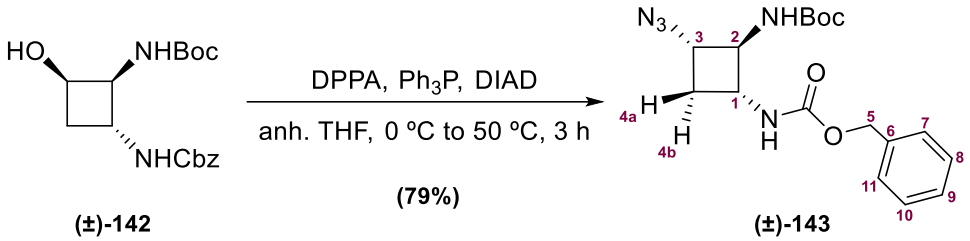

(±)-142 **(±)-143**

To an ice-cooled solution of **(±)-142** (0.58 g, 1.73 mmol) in anhydrous THF (30 mL) were added PPh_3 (1.36 g, 5.17 mmol, 3.00 eq.), DIAD (1.02 mL, 5.17 mmol, 3.00 eq.), and DPPA (1.13 mL, 5.17 mmol, 3.00 eq.) successively under nitrogen atmosphere. After 10 min, the temperature was raised to 50 ºC and the reaction was stirred for 3 h. The solvent was evaporated under vacuum, and the residue was purified by flash chromatography on silica gel (hexane:EtOAc, 3:1) to provide product **(±)-143** (0.49 g, 1.36 mmol, 79% yield) as a white solid.

Spectroscopic and physical data for compound (±)-143:

^{1}H-NMR (400 MHz, $CDCl_3$): δ 7.38-7.29 (m, 5H, H_{Ar}), 5.57 (br s, 1H, *NH*Cbz), 5.32 (br s, 1H, *NH*Boc), 5.11-5.03 (m, 2H, C*H*$_2$-Ph), 3.94-3.75 (m, 2H, H_1, H_2), 3.43 (m, 1H, H_3), 2.54 (ddd, $^3J_{4b\text{-}3}$ = $^3J'_{4b\text{-}1}$, $^2J''_{4b\text{-}4a}$ = 7.9 Hz, 1H, H_{4b}), 1.60 (ddd, $^3J_{4a\text{-}3}$ = $^3J'_{4a\text{-}1}$, $^2J''_{4a\text{-}4b}$ = 7.9 Hz, 1H, H_{4a}), 1.43 (s, 9H, ^{t}Bu).

^{13}C-NMR (100 MHz, $CDCl_3$): δ 155.9 (CO), 155.0 (CO), 136.2 (C_6), 128.5-128.1 (C_{Ar}), 80.2 (*C*$(CH_3)_3$), 66.9 (C_5), 59.4 (C_2), 55.8 (C_3), 46.7 (C_1), 30.5 (C_4), 28.3 (C(*C*$H_3)_3$).

COSY, NOESY, HSQC and HMBC experiments have been recorded.

R_f (hexane:EtOAc, 2:1) = 0.37 (UV and vanillin stain).

IR (ATR): υ 3341, 2983, 2091, 1681, 1523, 1240, 1038 cm^{-1}.

HRMS (ESI+) calcd. for $[C_{17}H_{23}N_5O_4+Na]^+$: 384.1642, Found: 384.1642.

m.p.: 139 ºC-142 ºC (from hexane:EtOAc).

4.2.4.7. *tert*-Butyl ((2*R*,4*S*)-2,4-diaminocyclobutyl)carbamate, 144

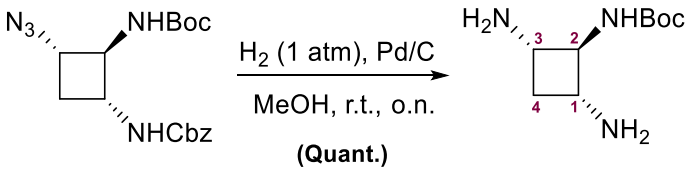

(±)-143 **144**

To a solution of compound **(±)-143** (0.22 g, 0.61 mmol) in MeOH (5 mL) was added Pd/C (10 wt%, 0.07 g, 0.06 mmol, 0.10 eq.). The mixture was stirred overnight under a hydrogen atmosphere at room temperature. After filtration on a pad of Celite®, the filtrate was concentrated by evaporation

to afford product **144** (0.12 g, 0.60 mmol, quantitative yield) as a yellow pale solid. After a ^{1}H-NMR spectrum control, this compound was used in the following reaction without further purification.

Spectroscopic data for compound 144:

^{1}H-NMR (300 MHz, MeOD): δ 3.25 (m, 1H, H_2), 2.77 (m, 2H, H_3,H_1), 2.37 (m, 1H, H_{4a}), 1.44 (s, 9H, ^{t}Bu), 1.20 (ddd, $^{2}J_{4b\text{-}4a}$ = 10.2 Hz, $J'_{4b\text{-}1}$ = $J''_{4b\text{-}3}$ = 9.2 Hz, 1H, H_{4b}).

4.2.4.8. Dimethyl 6,6'-((((1*R*,3*S*)-2-((*tert*-butoxycarbonyl)amino)cyclobutane-1,3-diyl)bis(azanediyl))bis(methylene))dipicolinate, 145

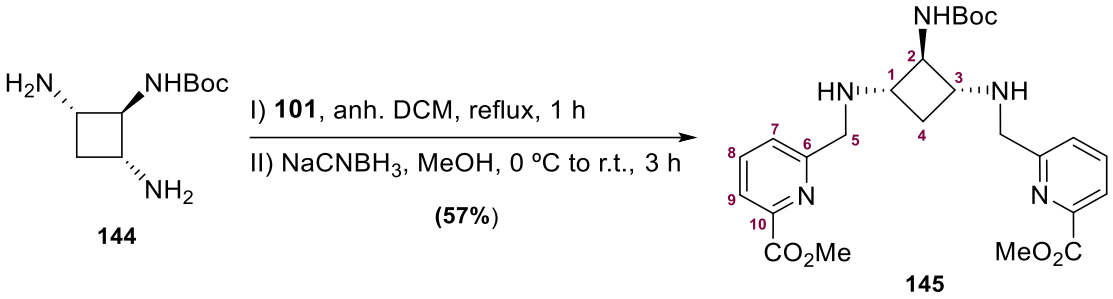

To a solution of **144** (0.12 g, 0.60 mmol) in anhydrous CH_2Cl_2 (6 mL) was added **101** (0.21 g, 1.25 mmol, 2.10 eq) under a nitrogen atmosphere and the reaction mixture was heated to 40 ºC for 2.5 h. Then, volatiles were evaporated, and the residue was dissolved in MeOH. The mixture was cooled to 0 ºC and $NaCNBH_3$ was added (0.11 g, 1.79 mmol, 3.00 eq.) in small portions along 30 min. The reaction mixture was allowed to attain room temperature and stirred for 3 h. The reaction was quenched by adding H_2O (15 mL) and MeOH was evaporated under vacuum. The aqueous phase was extracted with CH_2Cl_2 (4 x 15 mL), the organic layers were combined, dried over $MgSO_4$, and concentrated under reduced pressure. The residue was purified by column chromatography (Al_2O_3, CH_2Cl_2:MeOH, 98:2) to afford **145** (0.12 g, 0.34 mmol, 57% yield) as a yellow sticky oil.

Spectroscopic and physical data for compound 58:

^{1}H-NMR (300 MHz, MeOD): δ 8.03 (d, $^{3}J_{9\text{-}8}$ = 8.1 Hz, 2H, H_9), 7.94 (dd, $^{3}J_{8\text{-}9}$ = $^{3}J'_{8\text{-}7}$ = 8.1 Hz, 2H, H_8), 7.63 (d, $^{3}J_{7\text{-}8}$ = 8.1 Hz, 2H, H_7), 4.01-3.88 (m, 10H, 2 CO_2CH_3,H_5), 3.63 (ddd, $^{3}J_{2\text{-}1}$ = $^{3}J'_{2\text{-}3}$ = $^{3}J''_{2\text{-}NH}$ = 7.7 Hz, 1H, H_2), 2.93-2.85 (m, 2H, H_1,H_3), 2.22 (m, 1H, H_{4a}), 1.43 (s, 9H, ^{t}Bu), 1.27 (m, 1H, H_{4b}).

^{13}C-NMR (75 MHz, MeOD): δ 166.9 (CO_2CH_3), 161.4 (C_6), 157.1 ($NHCO_2C(CH_3)_3$), 148.3 (C_{10}), 139.3 (C_8), 127.4 (C_7), 124.7 (C_9), 80.0 ($NHCO_2C(CH_3)_3$), 61.2 (C_2), 55.7 (C_1,C_3), 53.2 ($NHCO_2C(CH_3)_3$, 52.8 (C_5), 31.9 (C_4), 28.8 ($C(CH_3)_3$).

COSY and HSQC experiments have been recorded.

R_f (DCM:MeOH, 98:2) = 0.23 (UV and vanillin stain).

IR (ATR): 3329, 2994, 1744, 1681, 1511, 1230, 1039 cm^{-1}.

HRMS (ESI+) calcd. for $[C_{25}H_{33}N_5O_6+H]^+$: 500.2504, Found: 500.2485.

m.p.: 157 ºC-159 ºC (from CH_2Cl_2).

4.2.4.9. 6,6'-((((1*R*,3*S*)-2-((*tert*-butoxycarbonyl)amino)cyclobutane-1,3-diyl)bis(azanediyl))bis(methylene))dipicolinic acid, *cis*,*trans*-L2

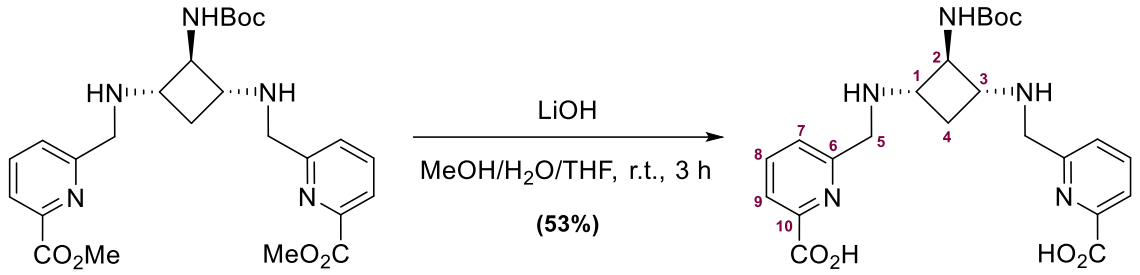

145 ***cis,trans*-L2**

To a solution of **145** (8.31 mg, 0.16 mmol) in MeOH (3 mL), a solution of LiOH (16.90 mg, 0.66 mmol, 2.00 eq) in H_2O:THF (1:1.2 mL) was added. The mixture was stirred at room temperature for 3 h and then the solvent was evaporated under reduced pressure. The resulting brown oil was dissolved in water (1.5 mL) and was purified by reverse phase MPLC with a 10 mM ammonium acetate aqueous solution (phase A) and CH_3CN with 10% of phase A (phase B) as the mobile phases. The desired product eluted at 12% phase B (retention time 20.3 min, 15.0 CV). Then, the fraction of interest was lyophilized, obtaining ***cis*,*trans*-L2** (4.20 mg, 0.08 mmol, 53% yield) as an off-white solid. The chelator was purified by preparative HPLC before radiolabelling experiments to ensure high purity.

Spectroscopic data for compound *cis*,*trans*-L2:

^{1}H-NMR (300 MHz, D_2O): δ 7.84-7.74 (m, 4H, H_8,H_9), 7.36 (m, 2H, H_7), 4.33 (m, 4H, H_5), 3.69-3.61 (m, 2H, H_1,H_3), 2.57 (m, 1H, H_2), 2.21 (m, 1H, H_{4a}), 1.83 (s, 9H, ^{t}Bu), 1.08 (m, 1H, H_{4b}).

^{13}C-NMR (75 MHz, D_2O): δ 171.9 (CO_2H), 155.6 (C_6), 152.3 ($NHCO_2C(CH_3)_3$), 149.8 (C_{10}), 139.1 (C_8), 124.7 (C_7), 123.8 (C_9), 81.6 ($NHCO_2C(CH_3)_3$), 52.8 (C_2), 51.9 (C_1,C_3), 49.3 (C_5), 27.4 (C_4), 22.5 ($C(CH_3)_3$).

COSY, me-HSQC and HMBC experiments have been recorded.

Elemental analysis calcd. (%) for $[C_{23}H_{29}N_5O_6]\cdot NH_4\cdot 2KCl$: C 43.32, H 5.19, N 13.31; Found: C 43.31, H 5.19, N 13.31.

HRMS (ESI+) calcd. for $[C_{23}H_{29}N_5O_6+Na]^+$: 494.2015, Found: 494.2012.

PART II. Cannabidivarin derivatives as CB_2R modulators

4.3. Chapter III. Innovative Bitopic Ligands Targeting Allosteric and Metastable CB_2R Binding Sites

4.3.1. Synthesis of Bitopic Ligands 158, 159 and 160

4.3.1.1. *(Z)*- and *(E)*-1,3-dimethoxy-5-(prop-1-en-1-yl)benzene, (*Z*+*E*)-169

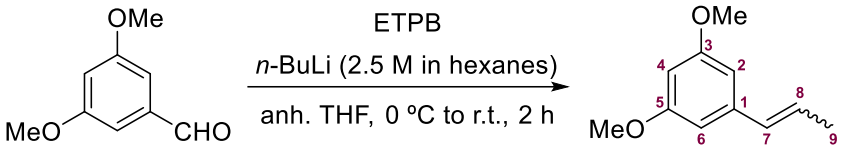

161 **(*Z*+*E*)-169**

To a suspension of ethyltriphenylphosphonium bromide (ETPB) (6.70 g, 18.05 mmol, 1.50 eq.) in anhydrous THF (25 mL) at 0 ºC under N_2 atmosphere, *n*-BuLi (2.5 M in hexane, 7.20 mL, 18.05 mmol, 1.50 eq.) was added dropwise. After continuous stirring for 20 min, a solution of **161** (2.00 g, 12.03 mmol) in dry THF (50 mL) was slowly added dropwise. Then, the reaction mixture was stirred at room temperature and monitorized by TLC (hexane:EtOAc, 4:1) until complete consumption of the starting material. The reaction was quenched with H_2O (40 mL) and extracted with EtOAc (4 x 50 mL). The combined organic layers were dried over $MgSO_4$ and concentrated under reduced pressure. The solid obtained was stirred with hexane and filtered. Hexane was evaporated to obtain a 1:1.2 mixture of (*Z*)- and (*E*)-olefins **169** (1.93 g, 10.83 mmol, 90% yield) as a colourless oil.

Spectroscopic data for compound (*E*)-169:

^{1}H-NMR (400 MHz, $CDCl_3$): δ 6.49 (d, 2H, $^4J_{2\text{-}4/6\text{-}4}$ = 2.3 Hz, H_2,H_6), 6.40-6.17 (m, 3H, H_4,H_7,H_8), 3.80 (s, 6H, 2 OCH_3), 1.87 (m, 3H, H_9).

Spectroscopic data for compound (*Z*)-169:

^{1}H-NMR (400 MHz, $CDCl_3$): δ 6.42 (d, 2H, $^4J_{2\text{-}4/6\text{-}4}$ = 2.3 Hz, H_2,H_6), 6.40-6.17 (m, 2H, H_4,H_7), 5.78 (m, 1H, H_8), 3.80 (s, 6H, 2 OCH_3), 1.90 (m, 3H, H_9).

R_f (hexane:EtOAc, 4:1) = 0.60 (UV and vanillin stain).

Spectroscopic data are consistent with those reported in reference: Navarro, G.; Gonzalez, A.; Sánchez-Morales, A.; Casajuana-Martin, N.; Gómez-Ventura, M.; Cordomí, A.; Busqué, F.; Alibés, R.; Pardo, L.; Franco, R. *J. Med. Chem.* **2021**, *64*, 9354-9364.

4.3.1.2. 1,3-Dimethoxy-5-propylbenzene, 166

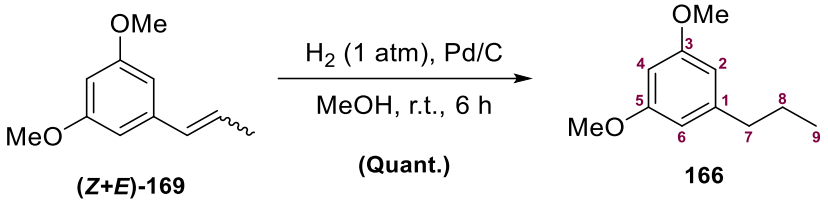

A stirred solution of **(*Z*+*E*)-169** (3.60 g, 21.66 mmol) in MeOH (60 mL) was hydrogenated over Pd/C (10 wt%, 1.00 g, 0.94 mmol, 0.04 eq.) under 1 atm of H_2 for 6 h. Then, the catalyst was removed by filtration over Celite® and the solvent was evaporated under reduced pressure to furnish compound **166** (3.62 g, 21.50 mmol, quantitative yield) as a yellow oil.

Spectroscopic data for compound 166:

^{1}H-NMR (400 MHz, $CDCl_3$): δ 6.35 (d, $^4J_{2\text{-}4/6\text{-}4}$ = 2.2 Hz, 2H, H_2,H_6), 6.30 (t, $^4J_{4\text{-}6/4\text{-}2}$ = 2.2 Hz, 1H, H_4), 3.78 (s, 6H, 2 O*CH*$_3$), 2.53 (t, $^3J_{7\text{-}8}$ = 7.4 Hz, 2H, H_7), 1.63 (sext., $^3J_{8\text{-}7}$ = $^3J'_{8\text{-}9}$ = 7.4 Hz, 2H, H_8), 0.93 (t, $^3J_{7\text{-}8}$ = 7.4 Hz, 3H, H_9).

R_f (hexane:EtOAc, 4:1) = 0.62 (UV and vanillin stain).

Spectroscopic data are consistent with those reported in reference: Navarro, G.; Gonzalez, A.; Sánchez-Morales, A.; Casajuana-Martin, N.; Gómez-Ventura, M.; Cordomí, A.; Busqué, F.; Alibés, R.; Pardo, L.; Franco, R. *J. Med. Chem.* **2021**, *64* (13), 9354-9364.

4.3.1.3. 5-Propylbenzene-1,3-diol, 170

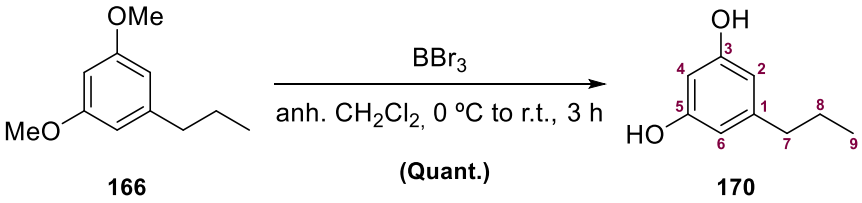

A solution of BBr_3 (1 M in CH_2Cl_2, 24.81 mL, 24.81 mmol, 2.60 eq.) was slowly added to an ice-cooled solution of compound **166** (1.72 g, 9.54 mmol) in CH_2Cl_2 (12 mL). The reaction mixture was stirred at room temperature during 3 h. Then, the reaction was quenched by slow addition of H_2O (40 mL), and the organic layer was separated. The aqueous layer was extracted with CH_2Cl_2 (3 x 40 mL), and the combine organic layers were dried over $MgSO_4$, filtered, and concentrated under vacuum. Compound **170** (1.45 g, 9.54 mmol, quantitative yield) was obtained as an orange solid without further purification.

Spectroscopic data for compound 170:

^{1}H-NMR (400 MHz, MeOD): δ 6.12 (d, $^4J_{2\text{-}4/6\text{-}4}$ = 2.2 Hz, 2H, H_2,H_6), 6.08 (t, $^4J_{4\text{-}6/4\text{-}2}$ = 2.2 Hz, 1H, H_4), 2.42 (t, $^3J_{7\text{-}8}$ = 7.4 Hz, 2H, H_7), 1.60 (sext., $^3J_{8\text{-}7}$ = $^3J'_{8\text{-}9}$ = 7.4 Hz, 2H, H_8), 0.92 (t, $^3J_{7\text{-}8}$ = 7.4 Hz, 3H, H_9).

R_f (hexane:EtOAc, 4:1) = 0.14 (UV and vanillin stain).

Spectroscopic data are consistent with those reported in reference: Villano, R.; Straker, H.; Di Marzo, V.; *New J. Chem.* **2022**, *46*, 20664-20668.

4.3.1.4. 2-[(1*R*,6*R*)-6-Isopropenyl-3-methylcyclohex-2-en-1-yl]-5-propylbenzene-1,3-diol, CBDV

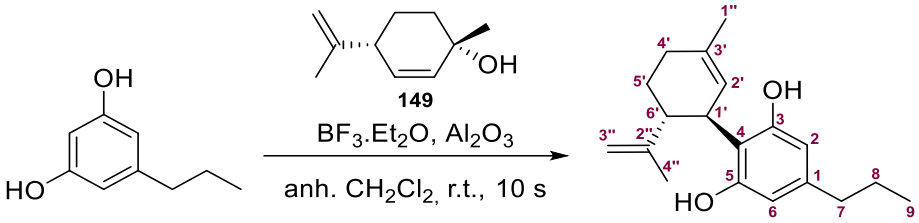

170 **(34%)** **CBDV**

$BF_3{\cdot}Et_2O$ (1.18 mL, 9.59 mmol, 1.80 eq.) was added, under an inert atmosphere, to a stirred suspension of basic aluminium oxide (9.23 g) in anhydrous CH_2Cl_2 (100 mL). The suspension was then refluxed for 15 min. Subsequently, the suspension was removed from the heat and **170** (0.80 g, 5.33 mmol) and commercially available (+)-*p*-mentha-2,8-dien-1-ol (**149**) (0.70 mL, 4.26 mmol, 0.80 eq.) in anhydrous CH_2Cl_2 (24 mL) were added to the suspension and the mixture was stirred for 10 s. The reaction was quenched with $NaHCO_3$ saturated solution (50 mL). Al_2O_3 was filtered and the aqueous phase was extracted with CH_2Cl_2 (4 x 40 mL). The organic layers were dried over $MgSO_4$, filtered, and the solvent removed under reduced pressure. The crude obtained was purified by column chromatography (hexane:CH_2Cl_2, 3:1 to 1:3) to furnish **CBDV** (0.42 g, 1.44 mmol, 34% yield) as an off-white solid.

Spectroscopic data for compound CBDV:

^{1}H-NMR (400 MHz, MeOD): δ 6.08 (s, 2H, H_2, H_6), 5.29z (m, 1H, $H_{2'}$), 4.47 (m, 1H, $H_{3"a}$), 4.43 (m, 1H, $H_{3"b}$), 3.93 (m, 1H, $H_{1'}$), 2.91 (m, 1H, $H_{6'}$), 2.36 (t, $^3J_{7\text{-}8}$ = 7.6 Hz, 2H, H_7), 2.19 (m, 1H, $H_{4'a}$), 1.98 (m, 1H, $H_{4'b}$), 1.74 (m, 2H, $H_{5'}$), 1.68 (s, 3H, $H_{1"}$), 1.64 (s, 3H, $H_{4"}$), 1.57 (sext., $^3J_{8\text{-}7}$ = $^3J'_{8\text{-}9}$ = 7.6 Hz, 2H, H_8), 0.91 (t, $^3J_{9\text{-}8}$ = 7.6 Hz, 3H, H_9).

R_f (hexane:CH_2Cl_2, 1:1) = 0.34 (UV and vanillin stain).

Spectroscopic data are consistent with those reported in reference: Navarro, G.; Gonzalez, A.; Sánchez-Morales, A.; Casajuana-Martin, N.; Gómez-Ventura, M.; Cordomí, A.; Busqué, F.; Alibés, R.; Pardo, L.; Franco, R. *J. Med. Chem.* **2021**, *64* (13), 9354-9364.

4.3.1.5. 3-((*tert*-Butyldimethylsilyl)oxy) and 3-((*tert*-butyldiphenylsilyl)oxy-2-((1*R*,6*R*)-6-isopropenyl-3-methylcyclohex-2-en-1-yl)-5-propylbenzene-1-ol, 171 and 172

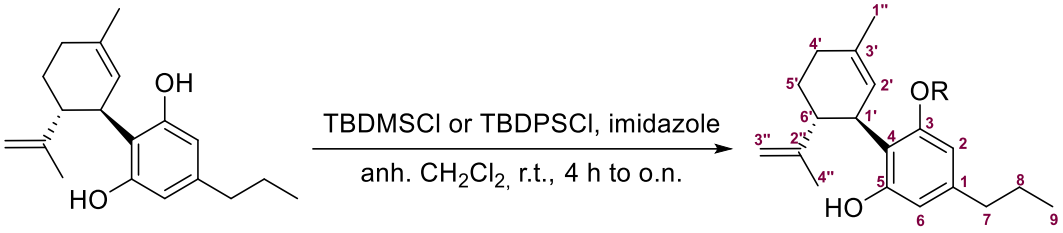

CBDV

R = TBDMS**, 171 (48%, 68% BRSM)**
R = TBDPS**, 172 (51%, 74% BRSM)**

Phenol **CBDV** (0.10 g, 0.35 mmol) was dissolved in anhydrous CH_2Cl_2 (4 mL), under an inert atmosphere. To the stirring solution was added imidazole (0.07 g, 1.05 mmol, 3.00 eq.) and the corresponding silane reagent (TBDMSCl or TBDPSCl, 0.39 mmol, 1.10 eq.) dropwise. The mixture was stirred 4 h for TBDMSCl and overnight for TBDPSCl, depending on the silylating reagent employed. The reaction diluted with CH_2Cl_2 (10 mL), washed with water (3 x 10 mL) and the water layer was extracted with CH_2Cl_2 (3 x 10 mL). The combined organic extracts were washed with brine (20 mL), dried over $MgSO_4$, and the solvent was removed under reduced pressure. The crude obtained was purified by column chromatography (hexane:CH_2Cl_2, 2:1 to 1:1) to furnish product **171** (0.07 g, 0.17 mmol, 48% yield) as or product **172** (0.09 g, 0.18 mmol, 51% yield), both as off-white solids. In both cases, starting material **CBDV** was recovered (0.03 g), obtaining a 68% BRSM and 74% BRSM yield, respectively.

Spectroscopic and physical data for compound 171:

^{1}H-NMR (400 MHz, $CDCl_3$): δ 6.29 (m, 1H, H_6), 6.19 (m, 1H, H_2), 5.87 (br s, 1H, OH), 5.52 (m, 1H, $H_{2'}$), 4.56 (m, 1H, $H_{3''a}$), 4.47 (m, 1H, $H_{3''b}$), 3.93 (m, 1H, $H_{1'}$), 2.48 (m, 1H, $H_{6'}$), 2.43 (t, $^3J_{7\text{-}8}$ = 7.5 Hz, 2H, H_7), 2.21 (m, 1H, $H_{4'a}$), 2.08 (m, 1H, $H_{4'b}$), 1.86-1.78 (m, 5H, $H_{5'}$,$H_{1''}$), 1.62 (s, 3H, $H_{4''}$), 1.58 (m, 2H, H_8), 0.98 (s, 9H, ^{t}Bu), 0.91 (t, $^3J_{9\text{-}8}$ = 7.5 Hz, 3H, H_9).

^{13}C-NMR (100 MHz, $CDCl_3$): δ 156.2 (C_5), 154.0 (C_3), 147.6 ($C_{2''}$), 142.1 (C_1), 139.6 ($C_{3'}$), 124.6 ($C_{2'}$), 117.9 (C_4), 111.7 (C_2), 111.0 ($C_{3''}$), 110.2 (C_6), 45.8 ($C_{6'}$), 37.8 (C_7), 37.0 ($C_{1'}$), 30.5 ($C_{4'}$), 28.3 ($C_{5'}$), 26.1 (C(*C*H_3)$_3$), 24.2 (C_8), 23.8 ($C_{1''}$), 20.2 ($C_{4''}$), 18.5 (*C*(CH_3)$_3$, 13.9 (C_9).

COSY, me-HSQC and HMBC experiments have been recorded.

R_f (hexane:CH_2Cl_2, 1:1) = 0.48 (UV and vanillin stain).

IR (ATR): υ 2927, 2858, 1622, 1464, 1262, 1037, 850 cm^{-1}.

HRMS (ESI+) calcd. for $[C_{25}H_{40}O_2Si+H]^+$: 401.2870, Found: 401.2856.

m.p.: 76 ºC-78 ºC (from hexane:CH_2Cl_2).

[α]$^{25}_D$: -26.7 (*c* 0.01, MeOH).

Spectroscopic and physical data for compound 172:

^{1}H-NMR (300 MHz, $CDCl_3$): δ 7.74 (m, 2H, $H_{Ar\ TBDPS}$), 7.62 (m, 2H, $H_{Ar\ TBDPS}$), 7.45-7.28 (m, 6H, $H_{Ar\ TBDPS}$), 6.19 (s, 1H, H_6), 5.91 (br s, 1H, OH), 5.78 (d, $^{4}J_{2\text{-}6}$ = 1.4 Hz, 1H, H_2), 5.59 (m, 1H, $H_{2'}$), 4.68 (m, 1H, $H_{3''a}$), 4.59 (m, 1H, $H_{3''b}$), 4.25 (m, 1H, $H_{1'}$), 2.58 (m, 1H, $H_{6'}$), 2.23 (m, 1H, $H_{4'a}$), 2.15 (m, 1H, $H_{4'b}$), 2.07 (t, $^{3}J_{7\text{-}8}$ = 7.3 Hz, 2H, H_7), 1.93-1.75 (m, 5H, $H_{5'}$,$H_{1''}$), 1.63 (s, 3H, $H_{4''}$), 1.15-1.08 (m, 11H, H_8, ^{t}Bu), 0.54 (t, $^{3}J_{9\text{-}8}$ = 7.3 Hz, 3H, H_9).

^{13}C-NMR (75 MHz, $CDCl_3$): δ 156.0 (C_5), 153.7 (C_3), 147.9 ($C_{2''}$), 141.6 (C_1), 139.4 ($C_{3'}$), 135.6 ($C_{Ar\ TBDPS}$), 133.4 ($C_{quat\ TBDPS}$), 132.81 ($C_{quat\ TBDPS}$), 129.81 ($C_{Ar\ TBDPS}$), 127.8 ($C_{Ar\ TBDPS}$), 124.8 ($C_{2'}$), 117.2 (C_4), 112.4 (C_2), 111.1 ($C_{3''}$), 110.1 (C_6), 45.5 ($C_{6'}$), 37.4 ($C_{1'}$, C_7), 30.5 ($C_{4'}$), 28.2 ($C_{5'}$), 26.9 ($C(CH_3)_3$), 23.8 (C_8), 23.7 ($C_{1''}$), 21.2 ($C_{4''}$), 19.6 ($C(CH_3)_3$, 13.4 (C_9).

COSY, me-HSQC and HMBC experiments have been recorded.

R_f (hexane:CH_2Cl_2, 1:1) = 0.53 (UV and vanillin stain).

IR (ATR): υ 3318, 2929, 2832, 1662, 1424, 1252, 1087, 827 cm^{-1}.

HRMS (ESI+) calcd. for $[C_{35}H_{44}O_2Si+H]^+$: 525.3183, Found: 525.3188.

m.p.: 84 ºC-88 ºC (from hexane:CH_2Cl_2).

$[\alpha]^{25}_D$: -38.1 (*c* 0.01, MeOH).

4.3.1.6. 2-((1*R*,6*R*)-6-isopropenyl-3-methylcyclohex-2-en-1-yl)-3-(methoxymethoxy)-5-propylbenzene-1-ol, 175

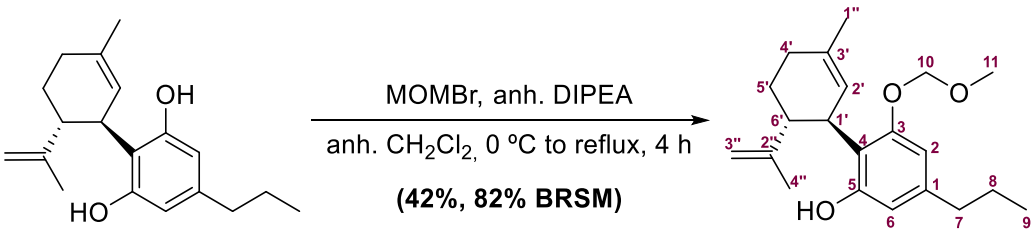

CBDV **175**

To a solution of **CBDV** (1.20 g, 4.19 mmol) in anhydrous CH_2Cl_2 (40 mL) at 0 ºC was added anhydrous DIPEA (1.17 mL, 6.70 mmol, 1.60 eq.) dropwise and it was stirred for 10 min under an inert atmosphere. Then, MOMBr (0.37 mL, 4.61 mmol, 1.10 eq.) was added dropwise to the stirring solution and the mixture was heated to reflux for 4 h. The reaction was quenched by the addition of saturated NH_4Cl solution (20 mL) and the mixture was extracted with CH_2Cl_2 (30 mL x 3). The combined organic layers were dried over $MgSO_4$, filtered, and concentrated under reduced pressure. The crude obtained was purified by column chromatography (hexane:CH_2Cl_2, 1:1) to furnish product **175** (0.58 g, 1.76 mmol, 42% yield) as a pale oil and starting material **CBDV** (0.58 g, 2.04 mmol) as a white solid.

Spectroscopic and physical data for compound 175:

^{1}H-NMR (300 MHz, MeOD): δ 6.37 (m, 1H, H_6), 6.25 (d, $^{4}J_{2\text{-}6}$ = 1.4 Hz, 1H, H_2), 5.22 (m, 1H, $H_{2'}$), 5.06 (d, 1H, $^{2}J_{10a\text{-}10b}$ = 6.6 Hz, H_{10a}), 5.03 (d, $^{2}J_{10a\text{-}10b}$ = 6.6 Hz, H_{10b}), 4.44 (m, 2H, $H_{3''}$), 3.95 (m, 1H, $H_{1'}$), 3.44 (s, 3H, H_{11}), 2.95 (m, 1H, $H_{6'}$), 2.42 (t, $^{3}J_{7\text{-}8}$ = 6.8 Hz, 2H, H_7) 2.19 (m, 1H, $H_{4'a}$), 2.00 (m, 1H, $H_{4'b}$), 1.75 (m, 2H, $H_{5'}$), 1.66 (s, 3H, $H_{1''}$), 1.62 (s, 3H, $H_{4''}$), 1.57 (m, 2H, H_8), 0.92 (t, $^{3}J_{9\text{-}8}$ = 7.3 Hz, 3H, H_9).

^{13}C-NMR (75 MHz, MeOD): δ 158.1 (C_3), 157.3 (C_5), 150.4 ($C_{2''}$), 142.7 (C_1), 127.4 ($C_{2'}$), 126.3 ($C_{3'}$), 118.7 (C_4), 110.5 (C_2,$C_{3''}$), 107.4 (C_6), 96.0 (C_{10}), 56.2 (C_{11}), 46.4 ($C_{6'}$), 39.1 (C_7), 37.8 ($C_{1'}$), 31.8 ($C_{4'}$), 30.8 ($C_{5'}$), 25.5 (C_8), 23.7 ($C_{1''}$), 19.6 ($C_{4''}$), 14.2 (C_9).

COSY, me-HSQC and HMBC experiments have been recorded.

R_f (hexane:CH_2Cl_2, 1:1) = 0.38 (UV and vanillin stain).

IR (ATR): υ 3439, 3071, 2925, 1620, 1578, 1435, 1151, 1037, 888 cm^{-1}.

HRMS (ESI+) calcd. for $[C_{21}H_{30}O_3+Na]^+$: 353.2087, Found: 353.2075.

$[\alpha]^{25}_D$: -97 (*c* 0.01, MeOH).

4.3.1.7. General procedure C to obtain the *O*-alkylation products under Williamson's ether synthesis conditions

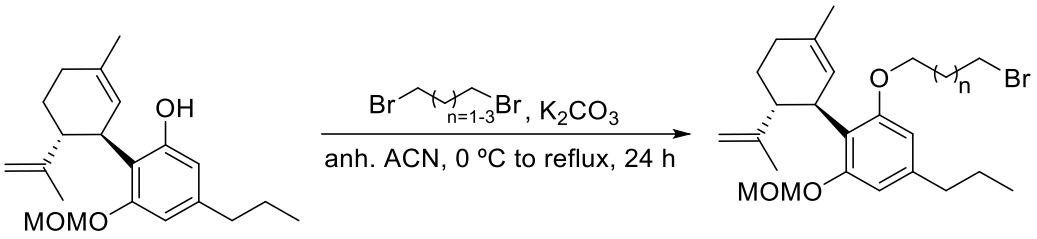

175

n = 1, **178, (81%)**
n = 2, **179, (86%)**
n = 3, **180, (90%)**

To a solution of **175** in anhydrous ACN (0.2 M) cooled to 0 ºC was added oven-dried K_2CO_3 (3.00 eq.) in small portions under a N_2 atmosphere. After 30 min stirring, the corresponding dibromoalkane (3.00 eq.) was added. The mixture was heated at reflux temperature for 24 h. Then, the reaction was cooled to room temperature before filtrating the K_2CO_3. ACN was removed under reduced pressure and the crude obtained was dissolved in CH_2Cl_2 (20 mL/g), washed with H_2O (2 x 10 mL/g) and the aqueous phase was extracted with CH_2Cl_2 (3 x 20 mL/g). The organic layers were combined and dried over $MgSO_4$, filtered and the solvent was evaporated under reduced pressure to obtain the corresponding alkylated product. If needed, the crude obtained was purified by column chromatography (hexane:CH_2Cl_2, 1:1).

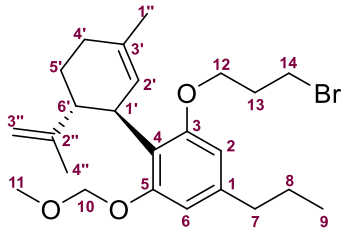

178

1-(3-Bromopropoxy)-2-((1*R*,6*R*)-6-isopropenyl-3-methylcyclohex-2-en-1-yl)-3-(methoxymethoxy)-5-propylbenzene, 178: Compound **178** was prepared as described in General procedure C by using a solution of **175** (0.37 g, 1.12 mmol) in anhydrous ACN (6 mL), K_2CO_3 (0.46 g, 3.36 mmol, 3.00 eq.) and 1,3-dibromopropane (0.34 mL, 3.36 mmol, 3.00 eq.). The crude obtained was purified by column chromatography (hexane:CH_2Cl_2, 1:1), furnishing **178** (0.41 g, 0.91 mmol, 81% yield) as a pale oil.

Spectroscopic and physical data for compound 178:

^{1}H-NMR (400 MHz, MeOD): δ 6.53 (m 1H, H_6), 6.41 (m, 1H, H_2), 5.19 (m, 1H, $H_{2'}$), 5.07 (d, 1H, $^2J_{10a\text{-}10b}$ = 6.6 Hz, H_{10a}), 5.03 (d, $^2J_{10a\text{-}10b}$ = 6.6 Hz, H_{10b}), 4.40 (m, 2H, $H_{3''}$), 4.08-3.95 (m, 3H, H_{12},$H_{1'}$), 3.65 (m, 2H, H_{14}), 3.45 (s, 3H, H_{11}), 2.95 (m, 1H, $H_{6'}$), 2.42 (t, $^3J_{7\text{-}8}$ = 6.8 Hz, 2H, H_7), 2.25 (m, 2H, H_{13}), 2.17 (m, 1H, $H_{4'a}$), 2.02 (m, 1H, $H_{4'b}$), 1.76 (m, 2H, $H_{5'}$), 1.67 (m, 8H, $H_{1''}$,$H_{4''}$,H_8), 0.93 (t, $^3J_{9\text{-}8}$ = 7.3 Hz, 3H, H_9).

^{13}C-NMR (100 MHz, MeOD): δ 159.4 (C_3), 157.5 (C_5), 150.3 ($C_{2''}$), 143.1 (C_1), 135.3 ($C_{3'}$), 127.2 ($C_{2'}$), 121.4 (C_4), 110.6 (C_2), 108.9 ($C_{3''}$), 107.1 (C_6), 95.8 (C_{10}), 66.4 (C_{12}), 56.3 (C_{11}), 46.4 ($C_{6'}$), 39.4 (C_7), 38.1 ($C_{1'}$), 34.1 (C_{14}), 31.8 ($C_{4'}$), 31.0 ($C_{5'}$), 30.8 (C_{13}), 25.6 (C_8), 23.8 ($C_{1''}$), 19.8 ($C_{4''}$), 14.2 (C_9).

COSY, me-HSQC and HMBC experiments have been recorded.

R_f (hexane:CH_2Cl_2, 3:1) = 0.31 (UV and vanillin stain).

IR (ATR): υ 3072, 2926, 1728, 1642, 1580, 1434, 1153, 1065, 796 cm^{-1}.

HRMS (ESI+) calcd. for $[C_{24}H_{35}BrO_3+Na]^+$: 473.1662 (98.8%), 475.1645 (100%), Found: 473.1648 (94.8%), 475.1639 (100%).

$[\alpha]^{25}_D$: -112 (*c* 0.01, MeOH).

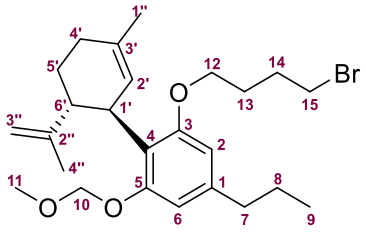

179

1-(4-Bromobutoxy)-2-((1*R*,6*R*)-6-isopropenyl-3-methylcyclohex-2-en-1-yl)-3-(methoxymethoxy)-5-propylbenzene, 179: Compound **179** was prepared as described in General procedure C by using a solution of **175** (0.42 g, 1.27 mmol) in anhydrous ACN (6 mL), K_2CO_3 (0.53 g, 3.81 mmol, 3.00 eq.) and 1,4-dibromobutane (0.46 mL, 3.81 mmol, 3.00 eq.). furnishing **179** (0.51 g, 1.09 mmol, 86% yield) as a light-yellow oil without further purification.

Spectroscopic and physical data for compound 179:

^{1}H-NMR (500 MHz, $CDCl_3$): δ 6.51 (m, 1H, H_6), 6.33 (m, 1H, H_2), 5.24 (m, 1H, $H_{2'}$), 5.07 (s, 2H, H_{10}), 4.46 (m, 1H, $H_{3''a}$), 4.42 (m, 1H, $H_{3''b}$), 4.00-3.88 (m, 3H, H_{12},$H_{1'}$), 3.49-3.46 (m, 5H, H_{11},H_{15}), 2.91 (ddd, $^3J_{6'\text{-}5'a}$ = $^3J'_{6'\text{-}1'}$ = 11.1 Hz, $^3J''_{6'\text{-}5'b}$ = 3.6 Hz, 1H, $H_{6'}$), 2.49 (t, $^3J_{7\text{-}8}$ = 7.6 Hz, 2H, H_7), 2.15 (m, 1H, $H_{4'a}$), 2.10-1.99 (m, 3H, $H_{4'b}$,H_{14}), 1.89 (tt, $^3J_{13\text{-}12}$ = $^3J'_{13\text{-}14}$ = 6.5 Hz, H_{13}), 1.76 (m, 2H, $H_{5'}$), 1.66 (s, 3H, $H_{1''}$), 1.64-1.59 (m, 5H, $H_{4''}$,H_8), 0.93 (t, $^3J_{9\text{-}8}$ = 7.3 Hz, 3H, H_9).

^{13}C-NMR (125 MHz, $CDCl_3$): δ 160.4 (C_3), 158.4 (C_5), 151.4 ($C_{2''}$), 144.0 (C_1), 133.1 ($C_{3'}$), 128.6 ($C_{2'}$), 121.5 (C_4), 112.0 (C_2), 109.8 ($C_{3''}$), 108.2 (C_6), 97.2 (C_{10}), 68.9 (C_{12}), 58.1 (C_{11}), 48.1 ($C_{6'}$), 40.5 (C_7), 38.8 ($C_{1'}$), 35.8 (C_{15}), 33.0 ($C_{4'}$), 31.7 ($C_{5'}$), 30.8 (C_{14}), 30.4 (C_{13}), 26.5 (C_8), 25.6 ($C_{1''}$), 21.6 ($C_{4''}$), 16.1 (C_9).

COSY, me-HSQC and HMBC experiments have been recorded.

R_f (hexane:CH_2Cl_2, 3:1) = 0.33 (UV and vanillin stain).

IR (ATR): υ 3067, 2921, 1713, 1647, 1575, 1429, 1178, 1069, 799 cm^{-1}.

HRMS (APCI+) calcd. for $[C_{25}H_{37}BrO_3+H]^+$: 465.1999 (98.5%), 467.1982 (100%), Found: 465.1995 (99.4%), 467.1977 (100%).

$[\alpha]^{25}_D$: -124 (*c* 0.01, MeOH).

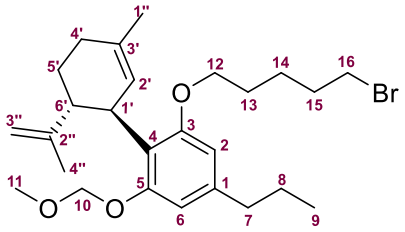

180

1-(3-Bromopentoxy)-2-((1*R*,6*R*)-6-isopropenyl-3-methylcyclohex-2-en-1-yl)-3-(methoxymethoxy)-5-propylbenzene, 180: Compound **180** was prepared as described in General procedure C by using a solution of **175** (0.40 g, 1.21 mmol) in anhydrous ACN (6 mL), K_2CO_3 (0.50 g, 3.63 mmol, 3.00 eq.) and 1,5-dibromopentane (0.49 mL, 3.63 mmol, 3.00 eq.) furnishing **180** (0.52 g, 1.09 mmol, 90% yield) as a light-yellow oil without further purification.

Spectroscopic and physical data for compound 180:

^{1}H-NMR (300 MHz, $CDCl_3$): δ 6.50 (m, 1H, H_6), 6.33 (m, 1H, H_2), 5.24 (m, 1H, $H_{2'}$), 5.07 (s, 2H, H_{10}), 4.46 (m, 1H, $H_{3''a}$), 4.43 (m, 1H, $H_{3''b}$), 3.99 (m, 1H, $H_{1'}$), 3.88 (m, 2H, H_{12}), 3.46-3.41 (m, 5H, H_{11}, H_{16}), 2.92 (ddd, $^3J_{6'\text{-}5'a} = {}^3J'_{6'\text{-}1'} = 10.6$ Hz, $^3J''_{6'\text{-}5'b} = 4.9$ Hz, 1H, $H_{6'}$), 2.49 (t, $^3J_{7\text{-}8} = 7.6$ Hz, 2H, H_7), 2.14 (m, 1H, $H_{4'a}$), 2.03 (m, 1H, $H_{4'b}$) 1.93 (tt, $^3J_{15\text{-}14} = {}^3J'_{15\text{-}16} = 7.4$ Hz, 2H, H_{15}), 1.82-1.70 (m, 4H, $H_{5'}$, H_{13}), 1.61-1.54 (m, 10H, $H_{1''}$,$H_{4''}$,H_8,H_{14}), 0.93 (t, $^3J_{9\text{-}8} = 7.3$ Hz, 3H, H_9).

^{13}C-NMR (125 MHz, $CDCl_3$): δ 158.4 (C_3), 156.4 (C_5), 149.5 ($C_{2''}$), 141.9 (C_1), 131.1 ($C_{3'}$), 126.5 ($C_{2'}$), 119.6 (C_4), 110.0 (C_2), 107.7 ($C_{3''}$), 106.4 (C_6), 95.2 (C_{10}), 67.9 (C_{12}), 56.1 (C_{11}), 45.1 ($C_{6'}$), 38.6 (C_7), 36.7 ($C_{1'}$), 33.7 (C_{16}), 32.8 (C_{15}), 31.0 ($C_{4'}$), 29.7 ($C_{5'}$), 28.9 (C_{13}), 25.1 (C_{14}), 24.5 (C_8), 23.6 ($C_{1''}$), 19.6 ($C_{4''}$), 14.1 (C_9).

COSY, me-HSQC and HMBC experiments have been recorded.

R_f (hexane:CH_2Cl_2, 3:1) = 0.37 (UV and vanillin stain).

IR (ATR): υ 3072, 2918, 1719, 1644, 1585, 1431, 1162, 1055, 791 cm^{-1}.

HRMS (APCI+) calcd. for $[C_{26}H_{39}BrO_3+H]^+$: 479.2155 (98.2%), 481.2139 (100%), Found: 479.2157 (96.2%), 481.2140 (100%).

$[\alpha]^{25}_D$: -109 (*c* 0.01, MeOH).

4.3.1.8. General procedure D to obtain the protected bitopic ligands (PBLs) through a Finkelstein reaction followed by a Williamson's ether synthesis

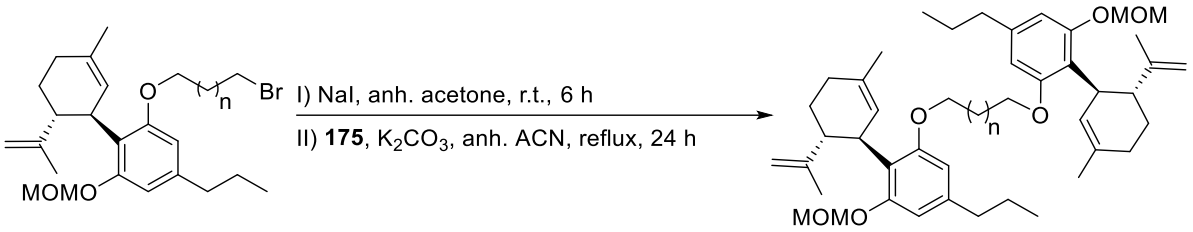

n = 1, **178**
n = 2, **179**
n = 3, **180**

n = 1, **182 (67%)**
n = 2, **183 (65%)**
n = 3, **184 (69%)**

Under a nitrogen atmosphere, the corresponding *O*-alkylated product was dissolved in anhydrous acetone (0.2 M) and NaI (2.5 eq.) was added to the flask. The reaction mixture was stirred during 6 h protected from light. The precipitate was filtered and the acetone was evaporated under reduced pressure. The crude obtained was dissolved in CH_2Cl_2 (20 mL/g) and washed with H_2O (15 mL/g). The combined organic layers were dried over anhydrous $MgSO_4$, filtered and concentrated under reduced pressure. The obtained iodinated intermediate was dissolved in anhydrous ACN (0.2 M) and added dropwise over a solution of **175** (0.90 eq.) in anhydrous ACN (0.2 M) at 0 ºC. The mixture was refluxed during 24 h under an inert atmosphere. After cooling to room temperature, the reaction mixture was filtered and the solvent was evaporated under vacuum. Then, the crude obtained was dissolved in CH_2Cl_2 (20 mL/g), washed with H_2O (2 x 10 mL/g) and the aqueous phase was extracted with CH_2Cl_2 (3 x 20 mL/g). The organic layers were combined and dried over $MgSO_4$, filtered and the solvent was evaporated under reduced pressure. The obtained oil was purified by silica column chromatography (hexane:CH_2Cl_2, 3:1) to furnish the corresponding dimeric product.

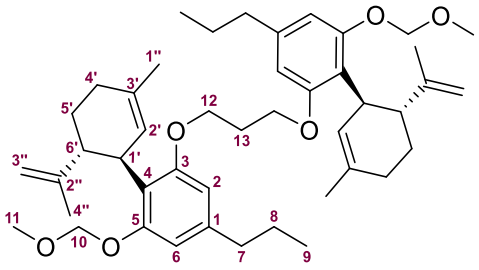

182

1,3-*Bis*(2-((1*R*,6*R*)-6-isopropenyl-3-methylcyclohex-2-en-1-yl)-3-(methoxymethoxy)-5-propylphenoxy)-propane, 182: Compound **182** was prepared as described in General procedure D by using a solution of **178** (0.43 g, 0.94 mmol) in anhydrous acetone (6 mL) and NaI (0.35 g, 2.35 mmol, 2.50 eq.). The iodinated intermediate obtained was dissolved in anhydrous ACN (3 mL) and added dropwise over a solution of **175** (0.28 g, 0.85 mmol, 0.90 eq.) in anhydrous ACN (3 mL). The crude obtained was purified by column chromatography (hexane:CH_2Cl_2, 3:1), furnishing **182** (0.40 g, 0.57 mmol, 67% yield) as a light-yellow oil.

Spectroscopic and physical data for compound 182:

^{1}H-NMR (600 MHz, $CDCl_3$): δ 6.50 (m, 2H, H_6), 6.35 (m, 2H, H_2), 5.25 (s, 2H, $H_{2'}$), 5.07 (s, 4H, H_{10}), 4.45 (m, 1H, $H_{3''a}$), 4.42 (m, 1H, $H_{3''b}$), 4.07 (m, 2H, $H_{1'}$), 4.01 (m, 4H, H_{12}), 3.46 (s, 6H, H_{11}), 2.92 (ddd, $^3J_{6'\text{-}5'a}$ = $^3J'_{6'\text{-}1'}$ = 11.1 Hz, $^3J''_{6'\text{-}5'b}$ = 3.5 Hz, 2H, $H_{6'}$), 2.47 (t, $^3J_{7\text{-}8}$ = 6.8 Hz, 4H, H_7), 2.20-2.10 (m, 4H, $H_{4'a}$,H_{13}), 1.99 (m, 2H, $H_{4'b}$), 1.75 (m, 4H, $H_{5'}$), 1.65 (s, 6H, $H_{1''}$), 1.63-1.56 (m, 10H, $H_{4''}$,H_8), 0.91 (t, $^3J_{9\text{-}8}$ = 7.3 Hz, 6H, H_9).

^{13}C-NMR (125 MHz, $CDCl_3$): δ 158.3 (C_3), 156.5 (C_5), 149.4 ($C_{2''}$), 142.0 (C_1), 131.1 ($C_{3'}$), 126.5 ($C_{2'}$), 119.4 (C_4), 110.0 ($C_{3''}$), 107.7 (C_6), 106.3 (C_2), 95.3 (C_{10}), 64.9 (C_{12}), 56.1 (C_{11}), 45.2 ($C_{6'}$), 38.5 (C_7), 36.7 ($C_{1'}$), 31.0 ($C_{4'}$), 30.0 (C_{13}), 29.7 ($C_{5'}$), 24.5 (C_8), 23.7 ($C_{1''}$), 19.6 ($C_{4''}$), 14.1 (C_9).

COSY, me-HSQC and HMBC experiments have been recorded.

R_f (hexane:CH_2Cl_2, 3:1) = 0.15 (UV and vanillin stain).

IR (ATR): υ 2938, 1609, 1581, 1419, 1215, 1169, 1038, 878 cm^{-1}.

HRMS (ESI+) calcd. for $[C_{45}H_{64}O_6+H]^+$: 701.4776, Found: 701.4778.

$[\alpha]^{25}_D$: -141 (*c* 0.01, CH_2Cl_2).

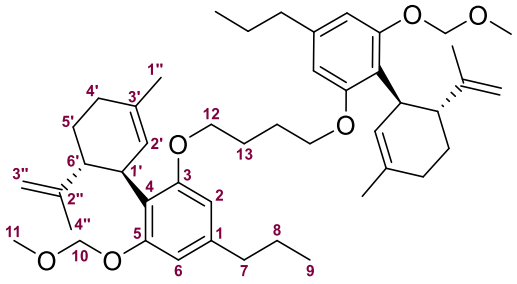

183

1,4-*Bis*(2-((1*R*,6*R*)-6-isopropenyl-3-methylcyclohex-2-en-1-yl)-3-(methoxymethoxy)-5-propylphenoxy)-butane, 183: Compound **183** was prepared as described in General procedure D by using a solution of **179** (0.41 g, 0.88 mmol) in anhydrous acetone (5 mL) and NaI (0.33 g, 2.20 mmol, 2.50 eq.). The iodinated intermediate obtained was dissolved in anhydrous ACN (2.5 mL) and added dropwise over a solution of **175** (0.26 g, 0.79 mmol, 0.90 eq.) in anhydrous ACN (2.5 mL). The crude obtained was purified by column chromatography (hexane:CH_2Cl_2, 3:1), furnishing **183** (0.37 g, 0.51 mmol, 65% yield) as a light-yellow oil.

Spectroscopic and physical data for compound 183:

^{1}H-NMR (600 MHz, $CDCl_3$): δ 6.51 (m, 2H, H_6), 6.35 (m, 2H, H_2), 5.25 (s, 2H, $H_{2'}$), 5.08 (s, 4H, H_{10}), 4.46 (m, 2H, $H_{3''a}$), 4.44 (m, 2H, $H_{3''b}$), 4.02-3.88 (m, 6H, $H_{1'}$,H_{12}), 3.46 (s, 6H, H_{11}), 2.95 (ddd, $^3J_{6'\text{-}5'a}$ = $^3J'_{6'\text{-}1'}$ = 11.2 Hz, $^3J''_{6'\text{-}5'b}$ = 2.6 Hz, 2H, $H_{6'}$), 2.50 (t, $^3J_{7\text{-}8}$ = 7.6 Hz, 4H, H_7), 2.16 (m, 2H, $H_{4'a}$), 2.01 (m, 2H, $H_{4'b}$), 1.91 (m, 4H, H_{13}), 1.75 (m, 4H, $H_{5'}$), 1.65-1.60 (m, 16H, H_8,$H_{1''}$,$H_{4''}$), 0.93 (t, $^3J_{9\text{-}8}$ = 7.3 Hz, 6H, H_9).

^{13}C-NMR (125 MHz, $CDCl_3$): δ 158.4 (C_3), 156.3 (C_5), 149.4 ($C_{2''}$), 142.0 (C_1), 131.1 ($C_{3'}$), 126.6 ($C_{2'}$), 119.5 (C_4), 110.0 ($C_{3''}$), 107.7 (C_6), 106.3 (C_2), 95.3 (C_{10}), 67.6 (C_{12}), 56.1 (C_{11}), 45.1 ($C_{6'}$), 38.6 (C_7), 36.8 ($C_{1'}$), 31.0 ($C_{4'}$), 29.7 ($C_{5'}$), 26.6 (C_{13}), 24.6 (C_8), 23.6 ($C_{1''}$), 19.6 ($C_{4''}$), 14.1 (C_9).

COSY, me-HSQC and HMBC experiments have been recorded.

R_f (hexane:CH_2Cl_2, 3:1) = 0.18 (UV and vanillin stain).

IR (ATR): υ 2954, 1619, 1593, 1417, 1225, 1167, 1041, 876 cm^{-1}.

HRMS (APCI+) calcd. for $[C_{46}H_{66}O_6+H]^+$: 715.4932, Found: 715.4929.

$[\alpha]^{25}_D$: -147 (*c* 0.01, CH_2Cl_2).

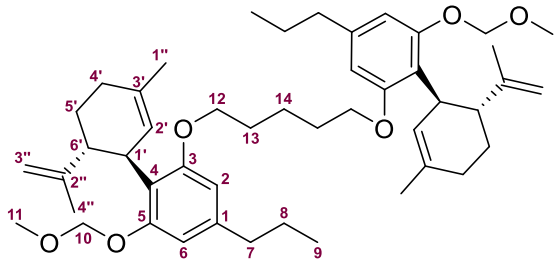

184

1,5-*Bis*(2-((1*R*,6*R*)-6-isopropenyl-3-methylcyclohex-2-en-1-yl)-3-(methoxymethoxy)-5-propylphenoxy)-pentane, 184: Compound **184** was prepared as described in General procedure D by using a solution of **180** (0.44 g, 0.92 mmol) in anhydrous acetone (5 mL) and NaI (0.34 g, 2.29 mmol, 2.50 eq.). The iodinated intermediate obtained was dissolved in anhydrous ACN (2.5 mL) and added dropwise over a solution of **175** (0.27 g, 0.83 mmol, 0.90 eq.) in anhydrous ACN (2.5 mL). The crude obtained was purified by column chromatography (hexane:CH_2Cl_2, 3:1), furnishing **182** (0.42 g, 0.57 mmol, 69% yield) as a light-yellow oil.

Spectroscopic and physical data for compound 184:

^{1}H-NMR (600 MHz, $CDCl_3$): δ 6.50 (s, 2H, H_6), 6.34 (s, 2H, H_2), 5.24 (s, 2H, $H_{2'}$), 5.07 (s, 4H, H_{10}), 4.46 (m, 2H, $H_{3''a}$), 4.43 (m, 2H, $H_{3''b}$), 4.00 (m, 2H, $H_{1'}$), 3.93-3.85 (m, 4H, H_{12}), 3.46 (s, 6H, H_{11}), 2.93 (ddd, $^3J_{6'\text{-}5'a} = {}^3J'_{6'\text{-}1'} = 11.3$ Hz, $^3J''_{6'\text{-}5'b} = 3.5$ Hz, 2H, $H_{6'}$), 2.49 (t, $^3J_{7\text{-}8} = 7.3$ Hz, 4H, H_7), 2.16 (m, 2H, $H_{4'a}$), 1.99 (m, 2H, $H_{4'b}$), 1.84-1.71 (m, 8H, H_{13},$H_{5'}$), 1.65-1.58 (m, 18H, H_8,H_{14},$H_{1''}$,$H_{4''}$), 0.93 (t, $^3J_{9\text{-}8} = 7.3$ Hz, 6H, H_9).

^{13}C-NMR (125 MHz, $CDCl_3$): δ 158.7 (C_3), 156.4 (C_5), 149.4 ($C_{2''}$), 141.9 (C_1), 131.0 ($C_{3'}$), 126.5 ($C_{2'}$), 119.6 (C_4), 110.0 ($C_{3''}$), 107.6 (C_6), 106.4 (C_2), 95.3 (C_{10}), 68.1 (C_{12}), 56.1 (C_{11}), 45.1 ($C_{6'}$), 38.6 (C_7), 36.7 ($C_{1'}$), 31.0 ($C_{4'}$), 29.7 (C_{13}), 29.5 ($C_{5'}$), 24.5 (C_8), 23.6 ($C_{1''}$), 22.8 (C_{14}), 19.6 ($C_{4''}$), 14.1 (C_9).

COSY, me-HSQC and HMBC experiments have been recorded.

R_f (hexane:CH_2Cl_2, 3:1) = 0.19 (UV and vanillin stain).

IR (ATR): υ 2922, 1607, 1579, 1430, 1235, 1151, 1040, 922 cm^{-1}.

HRMS (APCI+) calcd. for $[C_{47}H_{68}O_6+H]^+$: 729.5089, Found: 729.5083.

$[\alpha]^{25}_D$: -143 (*c* 0.01, CH_2Cl_2).

4.3.1.9. General procedure E for the MOM protecting group cleavage

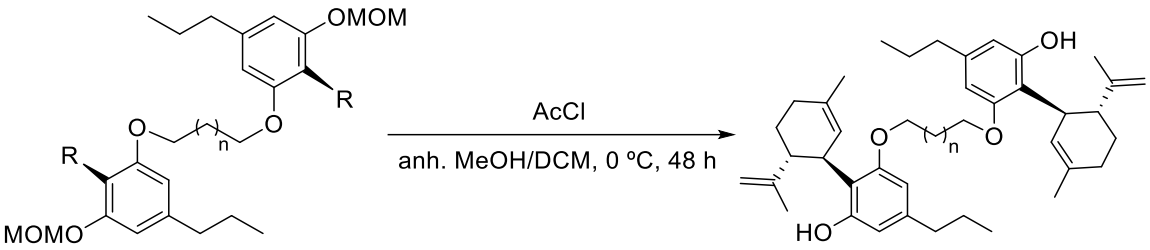

n = 1, **182**
n = 2, **183**
n = 3, **184**

n = 1, **158 (14%)**
n = 2, **159 (7%)**
n = 3, **160 (9%)**

In an oven-dried Schlenk flask was charged the corresponding PBL and it was dissolved in an anhydrous and degassed mixture of MeOH and CH_2Cl_2 (1:1, *v/v*, 0.05 M). At -20 ºC, AcCl (5 eq.) was added dropwise. The reaction was allowed to warm to 0 ºC and it was stirred for 48 h. Then, the reaction was diluted with CH_2Cl_2 (15 mL/g), quenched with a saturated $NaHCO_3$ solution, and extracted with CH_2Cl_2 (3 x 10 mL/g). The combined organic layers were dried over $MgSO_4$, filtered and evaporated under reduced pressure. The crude obtained was purified by silica flash column chromatography (hexane:Et_2O, 9:1) to furnish the corresponding bitopic ligand.

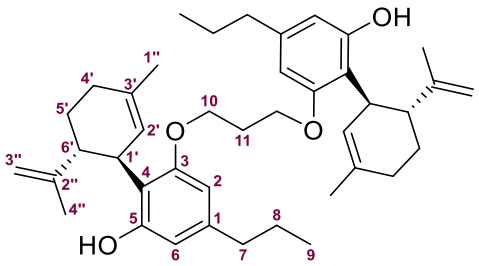

158

1,3-*Bis*(2-((1*R*,6*R*)-6-isopropenyl-3-methylcyclohex-2-en-1-yl)-3-(methoxymethoxy)-5-propylphen-1-ol)-propane, 158: Compound **158** was prepared as described in General procedure E by using a solution of **182** (0.12 g, 0.17 mmol) in an anhydrous and degassed mixture of MeOH and CH_2Cl_2 (1:1, *v/v*, 2 mL), and AcCl (0.12 mL, 1.71 mmol, 5.00 eq.). The crude obtained was purified by column chromatography (hexane:Et_2O, 9:1), furnishing **158** (14.90 mg, 0.02 mmol, 14% yield) as a light-yellow oil.

Spectroscopic data for compound 158:

^{1}H-NMR (300 MHz, $CDCl_3$): δ 6.30 (m, 2H, H_6), 6.23 (d, $^4J_{2\text{-}6}$ = 1.4 Hz, 1H, H_2), 6.01 (br s, 2H, 2 OH), 5.55 (m, 2H, $H_{2'}$), 4.52 (m, 2H, $H_{3''a}$), 4.39 (m, 2H, $H_{3''b}$), 4.07-3.95 (m, 6H, $H_{1'}$,H_{10}), 2.46 (m, 6H, H_7,$H_{6'}$), 2.21-2.13 (m, 4H, $H_{4'a}$,H_{11}), 2.06 (m, 2H, $H_{4'b}$), 1.81-1.73 (m, 10H, $H_{1''}$,$H_{5'}$), 1.64-1.53 (m, 10H, $H_{4''}$,H_8), 0.91 (t, $^3J_{9\text{-}8}$ = 7.3 Hz, 6H, H_9).

^{13}C-NMR (75 MHz, $CDCl_3$): δ 159.4 (C_3), 157.9 (C_5), 149.4 ($C_{2''}$), 144.6 (C_1), 141.7 ($C_{3'}$), 126.7 ($C_{2'}$), 117.3 (C_4), 113.0 ($C_{3''}$), 111.9 (C_6), 106.1 (C_2), 67.3 (C_{10}), 48.3 ($C_{6'}$), 40.2 (C_7), 37.9 ($C_{1'}$), 32.3 ($C_{4'}$), 31.8 (C_{11}), 30.1 ($C_{5'}$), 26.4 (C_8), 25.8 ($C_{1''}$), 21.8 ($C_{4''}$), 16.0 (C_9).

COSY, me-HSQC and HMBC experiments have been recorded.

R_f (hexane:Et_2O, 9:1) = 0.53 (UV and vanillin stain).

HRMS (ESI-) calcd. for $[C_{41}H_{56}O_4\text{-}H]^-$: 611.4106, Found: 611.4107.

Purity: 95.0% by RP-HPLC [Agilent XTerra MS C18 column, H_2O/ACN, 90:10→90:10 (0→25 min), UV-Vis detector at 280 nm].

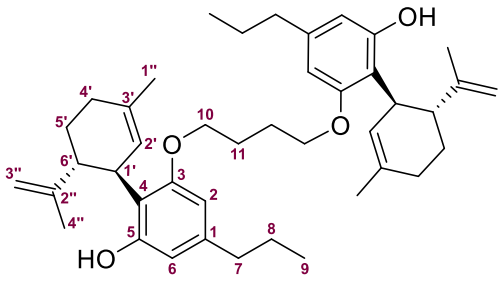

159

1,3-*Bis*(2-((1*R*,6*R*)-6-isopropenyl-3-methylcyclohex-2-en-1-yl)-3-(methoxymethoxy)-5-propylphen-1-ol)-butane, 159: Compound **159** was prepared as described in General procedure E by using a solution of **183** (0.25 g, 0.35 mmol) in an anhydrous and degassed mixture of MeOH and CH_2Cl_2 (1:1, *v/v*, 7 mL), and AcCl (0.25 mL, 3.49 mmol, 5.00 eq.). The crude obtained was purified by column chromatography (hexane:Et_2O, 9:1), furnishing **159** (15.31 mg, 0.02 mmol, 7% yield) as a light-yellow oil.

Spectroscopic data for compound 159:

^{1}H-NMR (400 MHz, $CDCl_3$): δ 6.30 (m, 2H, H_6), 6.22 (m, 2H, H_2), 6.01 (br s, 2H, 2 OH), 5.57 (m, 2H, $H_{2'}$), 4.51 (m, 2H, $H_{3''a}$), 4.37 (m, 2H, $H_{3''b}$), 4.02 (m, 2H, $H_{1'}$), 3.91 (t, $^3J_{10\text{-}11}$ = 5.6 Hz, 4H, H_{10}), 2.49-2.40 (m, 6H, H_7,$H_{6'}$), 2.22 (m, 2H, $H_{4'a}$), 2.07 (m, 2H, $H_{4'b}$), 1.90 (m, 4H, $H_{5'}$), 1.82-1.73 (m, 10H, $H_{1''}$,H_{11}), 1.64-1.58 (m, 10H, $H_{4''}$,H_8), 0.92 (t, $^3J_{9\text{-}8}$ = 7.3 Hz, 6H, H_9).

R_f (hexane:Et_2O, 9:1) = 0.58 (UV and vanillin stain).

HRMS (ESI-) calcd. for $[C_{42}H_{58}O_4\text{-}H]^-$: 625.4262, Found: 625.4263.

Purity: 92.3% by RP-HPLC [Agilent XTerra MS C18 column, H_2O/ACN, 90:10→90:10 (0→25 min), UV-Vis detector at 280 nm].

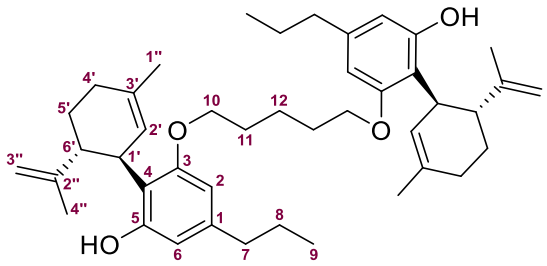

160

1,3-*Bis*(2-((1*R*,6*R*)-6-isopropenyl-3-methylcyclohex-2-en-1-yl)-3-(methoxymethoxy)-5-propylphen-1-ol)-pentane, 160: Compound **160** was prepared as described in General procedure E by using a solution of **184** (0.25 g, 0.34 mmol) in an anhydrous and degassed mixture of MeOH and CH_2Cl_2 (1:1, *v/v*, 7 mL), and AcCl (0.24 mL, 3.42 mmol, 5.00 eq.). The crude obtained was purified by column chromatography (hexane:Et_2O, 9:1), furnishing **159** (19.61 mg, 0.03 mmol, 9% yield) as a light-yellow oil.

Spectroscopic data for compound 160:

^{1}H-NMR (400 MHz, $CDCl_3$): δ 6.29 (m, 2H, H_6), 6.21 (m, 2H, H_2), 6.02 (br s, 2H, 2 OH), 5.57 (m, 2H, $H_{2'}$), 4.51 (m, 2H, $H_{3''a}$), 4.37 (m, 2H, $H_{3''b}$), 4.01 (m, 2H, $H_{1'}$), 3.91 (t, $^3J_{10\text{-}11}$ = 6.5 Hz, 4H, H_{10}), 2.49-2.39 (m, 6H, H_7,$H_{6'}$), 2.21 (m, 2H, $H_{4'a}$), 2.07 (m, 2H, $H_{4'b}$), 1.84-1.73 (m, 14H, H_{11}, $H_{1''}$,$H_{5'}$), 1.65-1.56 (m, 12H, H_8, H_{12},$H_{4''}$), 0.92 (t, $^3J_{9\text{-}8}$ = 7.3 Hz, 6H, H_9).

R_f (hexane:Et_2O, 9:1) = 0.59 (UV and vanillin stain).

HRMS (ESI-) calcd. for $[C_{43}H_{60}O_4\text{-}H]^-$: 639.4419, Found: 639.4423.

Purity: 100.0% by RP-HPLC [Agilent XTerra MS C18 column, H_2O/ACN, 90:10→90:10 (0→25 min), UV-Vis detector at 280 nm].

4.4. Chapter IV. Halogen- and Thioether-Containing Ligands Targeting the Allosteric CB_2R Binding Site

4.4.1. Synthesis of Halogen-Containing Ligands

4.4.1.1. 3-(3,5-Dimethoxyphenyl)propanoic acid, 201

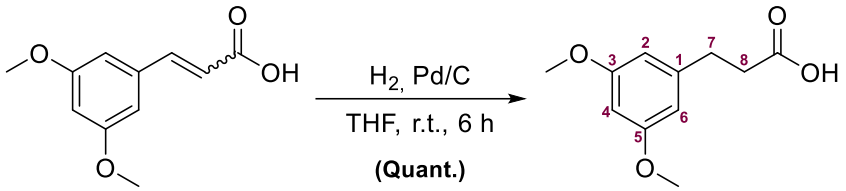

200 **201**

Carboxylic acid **200** (1.50 g, 7.20 mmol) in THF (24 mL) was hydrogenated at atmospheric pressure in the presence of 10% Pd/C (0.40 g, 0.37 mmol, 0.05 eq.) for 6 h. The reaction mixture was then filtered through Celite® and washed with THF. The solvent was removed under vacuum affording the desired acid **201** as a white solid (1.51 g, 7.18 mmol, quantitative yield) which was used in the next step without further purification.

Spectroscopic data for compound 201:

^{1}H-NMR (300 MHz, $CDCl_3$): δ 6.37 (d, $^4J_{2\text{-}4/6\text{-}4}$ = 2.1 Hz, 2H, H_2, H_6), 6.32 (t, $^4J_{4\text{-}6/2}$ = 2.1 Hz, 1H, H_4), 3.78 (s, 6H, 2 OCH_3), 2.90 (t, $^3J_{7\text{-}8}$ = 7.7 Hz, 2H, H_7), 2.67 (t, $^3J_{8\text{-}7}$ = 7.7 Hz, 2H, H_8).

Spectroscopic data are consistent with those reported in reference: Kang, B.; Wang, J.; Li, H.; Li, Y. *Med. Chem. Res.* **2014**, *23*, 1340-1349.

4.4.1.2. General procedure F for the reduction of carboxylic acids

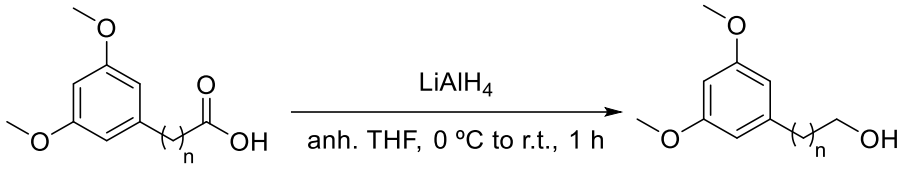

n = 1, **202**
n = 2, **201**

n = 1, **203 (Quant.)**
n = 2, **204 (Quant.)**

To a solution of carboxylic acid in anhydrous THF (0.4 M) cooled to 0 ºC was added 1.0 M lithium aluminium hydride solution in THF (2.00 eq.). The reaction mixture was allowed to warm to room temperature whilst stirring under a nitrogen atmosphere during 1 h. The reaction mixture was cooled to 0 ºC before quenching it by adding H_2O (10 mL/g) dropwise. Then a 1 M HCl solution (5 mL/g) was added, and the reaction mixture was filtered. Solvents were evaporated under reduced pressure and the aqueous phase was extracted with CH_2Cl_2 (4 x 20 mL/g). The organic layers were dried over $MgSO_4$ and concentrated under reduced pressure to obtain the corresponding alcohol.

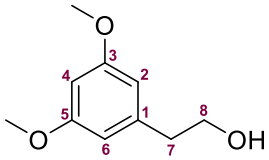

203

2-(3,5-Dimethoxyphenyl)ethan-1-ol, 203: Compound **203** was prepared as described in General procedure F by using a solution of acid **202** (1.00 g, 5.05 mmol) in anhydrous THF (14 mL) and 1.0 M lithium aluminium hydride solution in THF (10.10 mL, 10.10 mmol, 2.00 eq.), yielding alcohol **203** (0.86 g, 4.79 mmol, quantitative yield) as a yellow oil.

Spectroscopic data for compound 203:

^{1}H-NMR (300 MHz, $CDCl_3$): δ 6.39 (d, $^4J_{2/6\text{-}4}$ = 2.3 Hz, 2H, H_2, H_6), 6.32 (t, $^4J_{4\text{-}6/2}$ = 2.3 Hz, 1H, H_4), 3.85 (t, $^3J_{8\text{-}7}$ = 6.4 Hz, 2H, H_8), 3.78 (s, 6H, 2 OCH_3), 2.81 (t, $^3J_{7\text{-}8}$ = 6.4 Hz, 2H, H_7).

Spectroscopic data are consistent with those reported in reference: Racham, M.D.; Brannigan, J.A.; Rangachari, K.; Meister, S.; Wilkinson, A.J.; Holder, A.A.; Leatherbarrow R.J., Tate E.W. *Med. Chem. Res.* **2014**, *57* (6), 2773-2788.

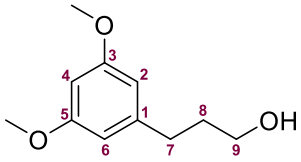

204

3-(3,5-Dimethoxyphenyl)propan-1-ol, 204: Compound **204** was prepared as described in General procedure F by using a solution of acid **201** (1.51 g, 7.18 mmol) in anhydrous THF (22 mL) and 1.0 M lithium aluminium hydride solution in THF (14.40 mL, 14.40 mmol, 2.00 eq.), yielding alcohol **204** (1.34 g, 6.82 mmol, quantitative yield) as a yellow oil.

Spectroscopic data for compound 204:

^{1}H-NMR (300 MHz, $CDCl_3$): δ 6.37 (d, $^4J_{2/6\text{-}4}$ = 2.3 Hz, 2H, H_2,H_6), 6.31 (t, $^4J_{4\text{-}6/2}$ = 2.3 Hz, 1H, H_4), 3.78 (s, 6H, 2 OCH_3), 3.68 (t, $^3J_{9\text{-}8}$ = 6.4 Hz, 2H, H_9), 2.66 (t, $^3J_{7\text{-}8}$ = 7.5 Hz, 2H, H_7), 1.89 (m, 2H, H_8).

Spectroscopic data are consistent with those reported in reference: Nikas, S.P.; Thakur, G. A.; Makriyannis, A. *Synth. Commun.* **2002**, *32* (11), 1751-1756.

4.4.1.3. General procedure G to obtain halogen-containing derivatives by Appel reaction

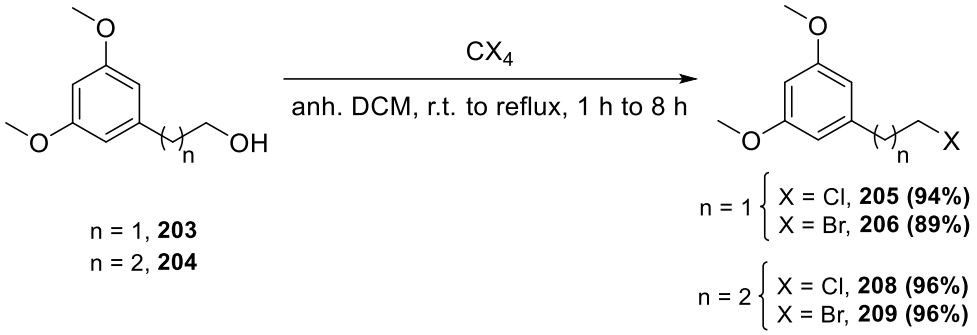

To a stirred solution of the corresponding alcohol in anhydrous CH_2Cl_2 (0.2 M) were added PPh_3 (2.10 eq. if CCl_4 used or 1.20 eq. if CBr_4 used) and CCl_4 (2.10 eq.) or CBr_4 (1.20 eq.), in portions, under a nitrogen atmosphere. After stirring for 1 to 6 h, the mixture was concentrated under reduced pressure. The residue was purified by column chromatography on silica gel (hexane:EtOAc, 3:1) to provide the corresponding halogen derivative.

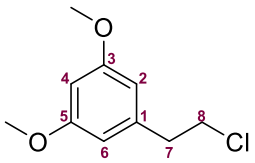

205

1-(2-Chloroethyl)-3,5-dimethoxybenzene, 205: Compound **205** was prepared as described in General procedure G by using a solution of alcohol **203** (0.74 g, 3.93 mmol) in anhydrous CH_2Cl_2 (20 mL), PPh_3 (2.16 g, 8.26 mmol, 2.10 eq.) and CCl_4 (0.80 mL, 8.26 mmol, 2.10 eq.) stirred at reflux for 6 h, yielding chlorine-containing derivative **205** (0.74 g, 3.69 mmol, 94% yield) as a yellow oil.

Spectroscopic data for compound 205:

^{1}H-NMR (500 MHz, $CDCl_3$): δ 6.37 (m, 3H, H_2,H_4,H_6), 3.79 (s, 6H, 2 O*C*H_3), 3.71 (t, $^3J_{8\text{-}7}$ = 7.5 Hz, 2H, H_8), 3.01 (t, $^3J_{7\text{-}8}$ = 7.5 Hz, 2H, H_7).

^{13}C-NMR (125 MHz, $CDCl_3$): δ 161.1 (C_3,C_5), 140.5 (C_1), 107.0 (C_2,C_6), 98.9 (C_4), 55.4 (O*C*H_3) 44.9 (C_8), 39.6 (C_7).

COSY and me-HSQC experiments have been recorded.

R_f (hexane:EtOAc, 3:1) = 0.42 (UV and vanillin stain).

IR (ATR): υ 3095, 2938, 1596, 1462, 1295, 1161, 1068, 830 cm^{-1}.

HRMS (APCI+) calcd. for $[C_{10}H_{13}ClO_2+H]^+$: 201.0677 (100%), 203.0650 (33.0%), Found: 201.0675 (100%), 203.0646 (31.4%).

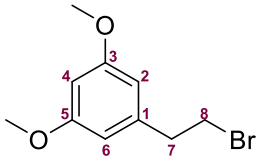

206

1-(2-Bromoethyl)-3,5-dimethoxybenzene, 206: Compound **206** was prepared as described in General procedure G by using a solution of alcohol **203** (0.74 g, 3.93 mmol) in anhydrous CH_2Cl_2 (26 mL), PPh_3 (1.34 g, 5.11 mmol, 1.30 eq.) and CBr_4 (1.57 g, 4.72 mmol, 1.20 eq.) stirred at r.t. for 1 h, yielding bromine-containing derivative **206** (0.86 g, 3.49 mmol, 89% yield) as a yellow oil.

Spectroscopic data for compound 206:

^{1}H-NMR (300 MHz, $CDCl_3$): δ 6.36 (m, 3H, H_2,H_4,H_6), 3.79 (s, 6H, 2 OCH_3), 3.56 (t, $^3J_{8\text{-}7}$ = 7.8 Hz, 2H, H_8), 2.81 (t, $^3J_{7\text{-}8}$ = 7.8 Hz, 2H, H_7).

Spectroscopic data are consistent with those reported in reference: Crombie, L.; Crombie, W.M.; Jamieson, S.V.; Tuchinda, P; Whitaker, A.J. *J. Chem. Soc. Perkin Trans. 1,* **1982**, 1485-1491.

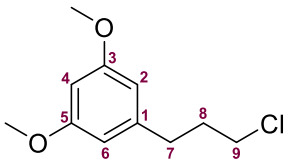

208

1-(3-Chloropropyl)-3,5-dimethoxybenzene, 208: Compound **208** was prepared as described in General procedure G by using a solution of alcohol **204** (1.15 g, 6.11 mmol) in anhydrous CH_2Cl_2 (35 mL), PPh_3 (3.37 g, 12.83 mmol, 2.10 eq.) and CCl_4 (1.24 mL, 12.83 mmol, 2.10 eq.) stirred at reflux for 6 h, yielding chlorine-containing derivative **208** (1.21 g, 5.86 mmol, 96% yield) as a yellow oil.

Spectroscopic data for compound 208:

^{1}H-NMR (300 MHz, $CDCl_3$): δ 6.36 (m, 2H, H_2,H_6), 6.32 (m, 1H, H_4), 3.78 (s, 6H, 2 OCH_3), 3.53 (t, $^3J_{9\text{-}8}$ = 6.5 Hz, 2H, H_9), 2.72 (t, $^3J_{7\text{-}8}$ = 7.4 Hz, 2H, H_7), 2.08 (tt, $^3J_{8\text{-}7}$ = 7.4 Hz, $^3J'_{8\text{-}9}$ = 6.5 Hz, 2H, H_8).

Spectroscopic data are consistent with those reported in reference: Fronza, G.; Fuganti, C.; Serra, S.; Cisero, M.; Koziet, J. *J. Agric. Food Chem*. **2002**, *50* (10), 2748-2754.

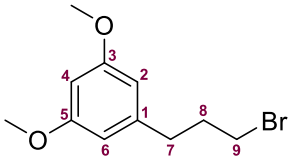

209

1-(3-Bromopropyl)-3,5-dimethoxybenzene, 209: Compound **209** was prepared as described in General procedure G by using a solution of alcohol **204** (0.72 g, 3.57 mmol) in anhydrous CH_2Cl_2 (24 mL), PPh_3 (1.22 g, 4.64 mmol, 1.30 eq.) and CBr_4 (1.42 g, 4.28 mmol, 1.20 eq.) stirred at r.t. for 1 h, yielding bromine derivative **209** (0.89 g, 3.43 mmol, 96% yield) as a yellow oil.

Spectroscopic data for compound 209:

^{1}H-NMR (300 MHz, $CDCl_3$): δ 6.39 (d, $^4J_{2/6\text{-}4}$ = 2.2 Hz, 2H, H_2,H_6), 6.32 (t, $^4J_{4\text{-}6/2}$ = 2.3 Hz, 1H, H_4), 3.78 (s, 6H, 2 OCH_3), 3.40 (t, $^3J_{9\text{-}8}$ = 6.6 Hz, 2H, H_9), 2.72 (t, $^3J_{7\text{-}8}$ = 7.3 Hz, 2H, H_7), 2.16 (tt, $^3J_{8\text{-}7}$ = 7.3 Hz, $^3J'_{8\text{-}9}$ = 6.6 Hz, 2H, H_8).

Spectroscopic data are consistent with those reported in reference: Jamie, J. F.; Rickards, R. W. *J. Chem. Soc., Perkin Trans. 1*, **1997**, 3613-3622.

4.4.1.4. General procedure H for methyl ether cleavage

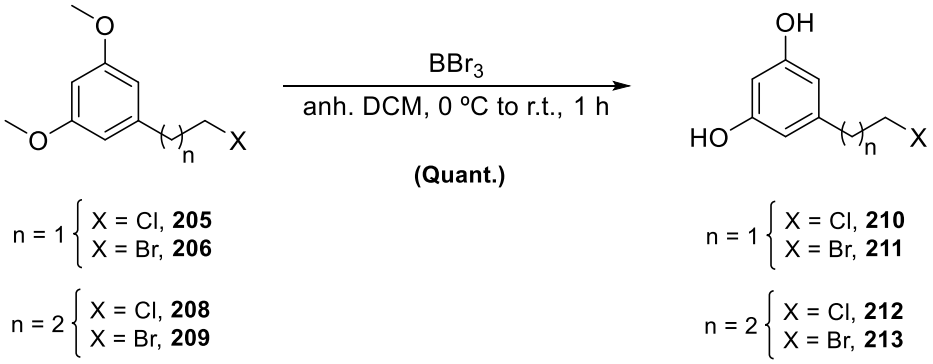

A solution of 1.0 M boron tribromide in CH_2Cl_2 (3.00 eq.) was slowly added to a solution of the halogen-containing derivative in anhydrous CH_2Cl_2 (0.6 M) at 0 ºC. The reaction mixture was warmed to r.t. and it was stirred for 1 h. The reaction mixture was then cooled to 0 °C and quenched by the addition of H_2O (30 mL/g). The product was filtered and extracted with CH_2Cl_2 (3 x 60 mL/g) to obtain the corresponding resorcinol derivative, without further purification.

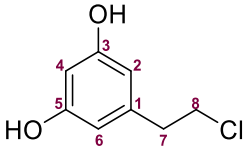

210

5-(2-Chloroethyl)benzene-1,3-diol, 210: Compound **210** was synthesised as described in General procedure H by using a solution of chlorine-containing derivative **205** (0.57 g, 2.84 mmol)

in anhydrous CH_2Cl_2 (4 mL) and 1.0 M boron tribromide in CH_2Cl_2 (8.52 mL, 8.52 mmol, 3.00 eq.) furnishing resorcinol derivative **210** (0.48 g, 2.80 mmol, quantitative yield) as a white solid.

Spectroscopic and physical data for compound 210:

^{1}H-NMR (500 MHz, $CDCl_3$): δ 6.28 (m, 2H, H_2,H_6), 6.24 (m, 1H, H_4), 3.68 (t, $^3J_{8\text{-}7}$ = 7.4 Hz, 2H, H_8), 2.95 (t, $^3J_{7\text{-}8}$ = 7.4 Hz, 2H, H_7).

^{13}C-NMR (125 MHz, $CDCl_3$): δ 157.0 (C_3,C_5), 141.2 (C_1), 108.7 (C_2,C_6), 101.6 (C_4), 44.7 (C_8), 39.1 (C_7).

COSY and me-HSQC experiments have been recorded.

IR (ATR): υ 3354, 2935, 1609, 1517, 1350, 1140, 961 cm^{-1}.

HRMS (ESI-) calcd. for $[C_8H_9ClO_2\text{-}H]^-$: 171.0218 (100%), 173.0191 (32.7%), Found: 171.0218 (100%), 173.0190 (33.7%).

m.p.: 59 ºC-62 ºC (from CH_2Cl_2).

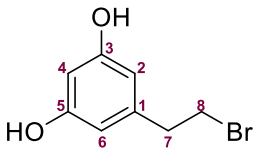

211

5-(2-Bromoethyl)benzene-1,3-diol, 211: Compound **211** was synthesised as described in General procedure H by using a solution of bromine-containing derivative **206** (0.93 g, 3.79 mmol) in anhydrous CH_2Cl_2 (6 mL) and 1.0 M boron tribromide in CH_2Cl_2 (11.37 mL, 11.37 mmol, 3.00 eq.) furnishing resorcinol derivative **211** (0.82 g, 3.77 mmol, quantitative yield) as a white solid.

Spectroscopic and physical data for compound 211:

^{1}H-NMR (600 MHz, MeOD): δ 6.17 (d, $^4J_{2/6\text{-}4}$ = 2.1 Hz, 2H, H_2,H_6), 6.14 (t, $^4J_{4\text{-}2/6}$ = 2.1 Hz, 2H, H_4), 3.54 (t, $^3J_{8\text{-}7}$ = 7.6 Hz, 2H, H_8), 2.97 (t, $^3J_{7\text{-}8}$ = 7.6 Hz, 2H, H_7).

^{13}C-NMR (75 MHz, MeOD): δ 159.6 (C_3,C_5), 142.6 (C_1), 108.1 (C_2,C_6), 102.0 (C_4), 40.6 (C_7), 33.5 (C_8).

HSQC experiment has been recorded.

IR (ATR): υ 3327, 2905, 1611, 1511, 1352, 1138, 963 cm^{-1}.

HRMS (ESI-) calcd. for $[C_8H_9BrO_2\text{-}H]^-$: 214.9713 (100%), 216.9693 (98.0%), Found: 214.9713 (100%), 216.9693 (96.5%).

m.p.: 63 ºC-67 ºC (from CH_2Cl_2).

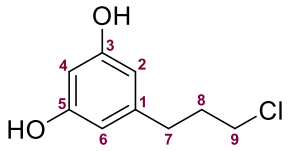

212

5-(3-Chloropropyl)benzene-1,3-diol, 212: Compound **212** was synthesised as described General procedure H by using a solution of chlorine-containing derivative **208** (0.56 g, 2.61 mmol) in anhydrous CH_2Cl_2 (4 mL) and 1.0 M boron tribromide in CH_2Cl_2 (7.83 mL, 7.83 mmol, 3.00 eq.) furnishing resorcinol derivative **212** (0.48 g, 2.60 mmol, quantitative yield) as a white solid.

Spectroscopic and physical data for compound 212:

^{1}H-NMR (600 MHz, MeOD): δ 6.15 (m, 2H, H_2,H_6), 6.11 (m, 1H, H_4), 3.52 (t, $^3J_{9\text{-}8}$ = 6.5 Hz, 2H, H_9), 2.60 (t, $^3J_{7\text{-}8}$ = 7.4 Hz, 2H, H_7), 2.00 (tt, $^3J_{8\text{-}7}$ = 7.4 Hz, $^3J'_{8\text{-}9}$ = 6.5 Hz, 2H, H_8).

^{13}C-NMR (150 MHz, MeOD): δ 159.5 (C_3,C_5), 144.4 (C_1), 108.0 (C_2,C_6), 101.4 (C_4), 45.0 (C_9), 35.2 (C_7), 33.7 (C_8).

COSY and me-HSQC experiments have been recorded.

IR (ATR): υ 3308, 2945, 1627, 1519, 1346, 1148, 977 cm^{-1}.

HRMS (ESI-) calcd. for [$C_9H_{11}ClO_2$-H]$^-$: 185.0375 (100%), 186.0409 (9.9%), 187.0348 (32.8%), 188.0381 (3.2%), Found: 185.0375 (100%), 186.0410 (9.8%), 187.0346 (31.9%), 188.0381 (3.1%).

m.p.: 57 ºC-59 ºC (from CH_2Cl_2).

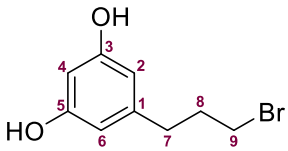

213

5-(3-Bromopropyl)benzene-1,3-diol, 213: Compound **213** was synthesised as described in General procedure H by using a solution of bromine-containing derivative **209** (0.80 g, 3.09 mmol) in anhydrous CH_2Cl_2 (6 mL) and 1.0 M boron tribromide in CH_2Cl_2 (9.27 mL, 9.27 mmol, 3.00 eq.) furnishing resorcinol derivative **213** (0.71 g, 3.06 mmol, quantitative yield) as a white solid.

Spectroscopic and physical data for compound 213:

^{1}H-NMR (600 MHz, MeOD): δ 6.16 (d, 2H, $^4J_{2/6\text{-}4}$ = 2.4 Hz, H_2,H_6), 6.11 (t, $^4J_{4\text{-}2/6}$ = 2.4 Hz, 1H, H_4), 3.39 (t, $^3J_{9\text{-}8}$ = 6.6 Hz, 2H, H_9), 2.59 (t, $^3J_{7\text{-}8}$ = 7.3 Hz, 2H, H_7), 2.07 (tt, $^3J_{8\text{-}7}$ = 7.3 Hz, $^3J'_{8\text{-}9}$ = 6.6 Hz, 2H, H_8).

^{13}C-NMR (150 MHz, MeOD): δ 159.5 (C_3,C_5), 144.3 (C_1), 108.0 (C_2,C_6), 101.4 (C_4), 35.3 (C_8), 34.9 (C_7), 33.7 (C_9).

COSY and me-HSQC experiments have been recorded.

IR (ATR): υ 3357, 2927, 1631, 1522, 1338, 1143, 961 cm^{-1}.

HRMS (ESI-) calcd. for $[C_9H_{11}BrO_2\text{-}H]^-$: 228.9870 (100%), 230.9850 (98.1%), Found: 228.9870 (100%), 230.9850 (98.0%).

m.p.: 64 ºC-66 ºC (from CH_2Cl_2).

4.4.1.5. General procedure I for aromatic bromination

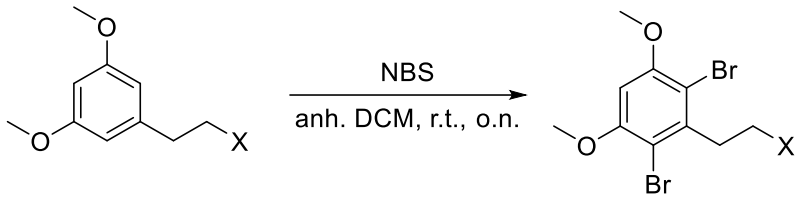

X = Cl, **205**
X = Br, **206**

X = Cl, **214 (76%)**
X = Br, **215 (78%)**

To a solution of the halogen-containing derivative in anhydrous CH_2Cl_2 (0.25 M), NBS (1.00 eq.) was added, and the reaction mixture was stirred at r.t. for 1 h. After this time, another portion of NBS (1.00 eq.) was added and the mixture was stirred for 1 h. Then, a third portion of NBS (0.50 eq.) was added and the mixture was stirred overnight at room temperature. The reaction was quenched by the slow addition of water (25 mL/g), and the aqueous layer was extracted with CH_2Cl_2 (3 x 30 mL/g). The organic layers were washed with brine, dried over $MgSO_4$, and evaporated to dryness. The resulting solid was purified by flash column chromatography (hexane:EtOAc, 1:1) to furnish the corresponding brominated aromatic derivative.

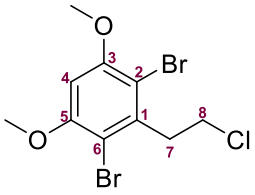

214

2,4-Dibromo-3-(2-chloroethyl)-1,5-dimethoxybenzene, 214: Compound **214** was synthesised as described in General procedure I by using a solution of chlorine-containing derivative **205** (0.10 g, 0.50 mmol) in anhydrous CH_2Cl_2 (2 mL) and NBS (0.221 g, 1.25 mmol, 2.50 eq.) furnishing brominated aromatic **214** (0.14 g, 0.38 mmol, 76% yield) as an orange solid.

Spectroscopic and physical data for compound 214:

^{1}H-NMR (300 MHz, $CDCl_3$): δ 6.46 (s, 1H, H_4), 3.91 (s, 6H, 2 O*CH_3*) 3.68 – 3.52 (m, 4H, H_7,H_8).

^{13}C-NMR (75 MHz, $CDCl_3$): δ 156.2 (C_3,C_5), 138.4 (C_1), 105.9 (C_2,C_6), 96.1 (C_4), 56.7 (OCH_3), 41.1 (C_8), 40.3 (C_7).

COSY, me-HSQC and HMBC experiments have been recorded.

IR (ATR): υ 3359, 2929, 1614, 1524, 1323, 1106, 969 cm^{-1}.

HRMS (APCI+) calcd. for $[C_{10}H_{11}Br_2ClO_2+H]^+$: 358.8866 (100%), 360.8844 (69.9%), Found: 358.8862 (100%), 360.8840 (69.0%),

m.p.: 73 ºC-78 ºC (from hexane:EtOAc).

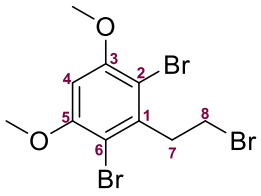

215

2,4-Dibromo-3-(2-bromoethyl)-1,5-dimethoxybenzene, 215: Compound **215** was synthesised as described in General procedure I by using a solution of chlorine-containing derivative **205** (0.11 g, 0.46 mmol) in anhydrous CH_2Cl_2 (2 mL) and NBS (0.203 g, 1.14 mmol, 2.50 eq.) furnishing brominated aromatic **215** (0.14 g, 0.36 mmol, 78% yield) as a yellow solid.

Spectroscopic and physical data for compound 215:

^{1}H-NMR (300 MHz, $CDCl_3$): δ 6.46 (s, 1H, H_4), 3.91 (s, 6H, 2 O*C*H_3) 3.66 – 3.44 (m, 4H, H_7,H_8).

^{13}C-NMR (75 MHz, $CDCl_3$): δ 156.3 (C_3,C_5), 139.5 (C_1), 105.7 (C_2,C_6), 96.1 (C_4), 56.8 (O*C*H_3), 40.7 (C_7), 28.3 (C_8).

COSY, me-HSQC and HMBC experiments have been recorded.

IR (ATR): υ 3229, 2916, 1601, 1493, 1307, 1097, 973 cm^{-1}.

HRMS (APCI+) calcd. for $[C_{10}H_{11}Br_3O_2+H]^+$: 402.8362 (100%), 404.8342 (97.9%), Found: 402.8359 (100%), 404.8339 (99.3%).

m.p.: 79 ºC-82 ºC (from hexane:EtOAc).

4.4.1.6. General procedure J for methyl ether cleavage

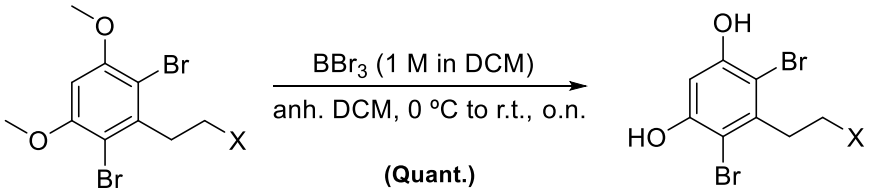

A solution of 1.0 M boron tribromide in CH_2Cl_2 (6.00 eq.) was slowly added to a solution of the halogen-containing derivative in anhydrous CH_2Cl_2 (0.6 M) at 0 ºC. The reaction mixture was

warmed to r.t. and it was stirred overnight. The reaction mixture was then cooled to 0 °C and quenched by the addition of H_2O (30 mL/g). The product was filtered and extracted with CH_2Cl_2 (3 x 60 mL/g) to obtain the corresponding resorcinol derivative, without further purification.

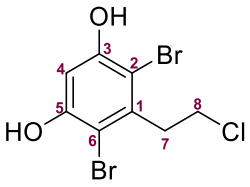

216

4,6-Dibromo-5-(2-chloroethyl)benzene-1,3-diol, 216: Compound **216** was synthesised as described in General procedure J by using a solution of chlorine-containing derivative **214** (0.13 g, 0.35 mmol) in anhydrous CH_2Cl_2 (0.6 mL) and 1.0 M boron tribromide in CH_2Cl_2 (2.10 mL, 2.10 mmol, 6.00 eq.) furnishing resorcinol derivative **216** (0.12 g, 0.35 mmol, quantitative yield) as a white solid.

Spectroscopic and physical data for compound 216:

^{1}H-NMR (300 MHz, MeOD): δ 6.52 (s, 1H, H_4), 3.64 – 3.43 (m, 4H, H_7,H_8).

HRMS (APCI-) calcd. for $[C_8H_7Br_2ClO_2\text{-}H]^-$: 328.8407 (100%), 330.8385 (69.8%), Found: 328.8405 (100%), 330.8383 (66.7%).

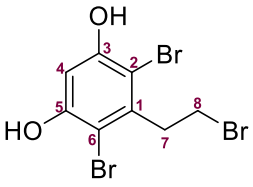

217

4,6-Dibromo-5-(2-chloroethyl)benzene-1,3-diol, 217: Compound **217** was synthesised as described in General procedure J by using a solution of chlorine-containing derivative **215** (0.13 g, 0.33 mmol) in anhydrous CH_2Cl_2 (0.6 mL) and 1.0 M boron tribromide in CH_2Cl_2 (2.00 mL, 2.00 mmol, 6.00 eq.) furnishing resorcinol derivative **217** (0.12 g, 0.33 mmol, quantitative yield) as a white solid.

Spectroscopic and physical data for compound 217:

^{1}H-NMR (300 MHz, MeOD): δ 6.53 (s, 1H, H_4), 3.57 – 3.42 (m, 4H, H_7,H_8).

HRMS (APCI-) calcd. for $[C_8H_7Br_3O_2\text{-}H]^-$: 372.7903 (100%), 374.7883 (97.8%), Found: 372.7904 (100%), 374.7884 (95.7%).

4.4.1.7. General procedure K for Friedel-Crafts alkylation

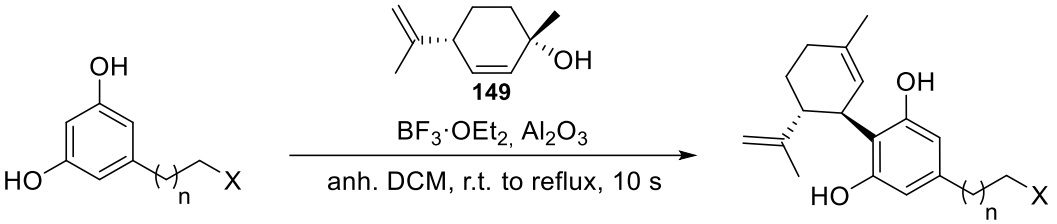

n = 1 { X = Cl, **210**; X = Br, **211** }

n = 2 { X = Cl, **212**; X = Br, **213** }

n = 1 { X = Cl, **193 (34%)**; X = Br, **194 (36%)** }

n = 2 { X = Cl, **196 (35%)**; X = Br, **197 (26%)** }

$BF_3{\cdot}Et_2O$ (1.80 eq.) was added under nitrogen to a stirred suspension of basic aluminium oxide (Woelm, grade I) in anhydrous CH_2Cl_2 (0.1 M). The mixture was stirred for 15 min at r.t. and then heated to reflux. (+)-*p*-mentha-2,8-dien-1-ol (**149**) (0.80 eq.) and the corresponding resorcinol derivative (1.00 eq.) in CH_2Cl_2 (0.2 M) were added to the boiling suspension and the reaction was quenched within 10 s with a $NaHCO_3$ saturated solution (30 mL/g). Aluminium oxide was filtered, and the crude was extracted with CH_2Cl_2 (3 x 50 mL/g). The organic layers were washed with brine, dried over $MgSO_4$, and evaporated to dryness. The obtained oil was purified by silica column chromatography (hexane:CH_2Cl_2, 3:1 to 1:3) to furnish the corresponding CBDV derivative.

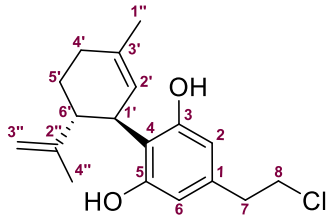

193

(1'*R*,2'*R*)-4-(2-Chloroethyl)-5'-methyl-2'-(prop-1-en-2-yl)-1',2',3',4'-tetrahydro-[1,1'-biphenyl]-2,6-diol, 193: Compound **193** was synthesised as described in General procedure K by using a solution of $BF_3{\cdot}Et_2O$ (0.63 mL, 5.00 mmol, 1.80 eq.), and Al_2O_3 (4.82 g) in anhydrous CH_2Cl_2 (50 mL). To the boiling suspension resorcinol derivative **210** (0.48 g, 2.78 mmol) and (+)-*p*-mentha-2,8-dien-1-ol (0.36 mL, 2.22 mmol, 0.80 eq.) in CH_2Cl_2 (15 mL) were added CBDV derivative **193** (0.23 g, 0.75 mmol, 34% yield) was obtained as a white solid.

Spectroscopic and physical data for compound 193:

^{1}H-NMR (500 MHz, MeOD): δ 6.13 (s, 2H, H_2,H_6), 5.26 (m, 1H, $H_{2'}$), 4.47 (m, 1H, $H_{3''a}$), 4.42 (m, 1H, $H_{3''b}$), 3.95 (m, 1H, $H_{1'}$), 3.64 (t, $^3J_{8\text{-}7}$ = 7.6 Hz, 2H, H_8), 2.94 (ddd, $^3J_{6'\text{-}5'a}$ = $^3J'_{6'\text{-}1'}$ = 10.5 Hz, $^3J''_{6'\text{-}5'b}$ = 4.9 Hz, 2H, $H_{6'}$), 2.82 (t, $^3J_{7\text{-}8}$ = 7.6 Hz, 2H, H_7), 2.20 (m, 1H, $H_{4'a}$), 2.00 (m, 1H, $H_{4'b}$), 1.74 (m, 2H, $H_{5'}$), 1.68 (s, 3H, $H_{1''}$), 1.64 (s, 3H, $H_{4''}$).

^{13}C-NMR (125 MHz, MeOD): 157.8 (C_3, C_5), 150.3 ($C_{2''}$), 138.2 (C_1), 134.1 ($C_{3'}$), 127.1 ($C_{2'}$), 117.2 (C_4), 110.5 ($C_{3''}$), 108.5 (C_2,C_6), 46.2 ($C_{6'}$), 45.6 (C_8), 40.2 (C_7), 37.5 ($C_{1'}$), 31.7 ($C_{4'}$), 30.8 ($C_{5'}$), 23.7 ($C_{1''}$), 19.4 ($C_{4''}$).

COSY, me-HSQC and HMBC experiments have been recorded.

R_f (CH_2Cl_2, 100%) = 0.58 (UV and vanillin stain).

IR (ATR): υ 3414, 2923, 1626, 1582, 1440, 1214, 1028, 889 cm^{-1}.

HRMS (ESI+) calcd. for $[C_{18}H_{23}ClO_2+Na]^+$: 329.1279 (100%), 331.1255 (34.2%), Found: 329.1276 (100%) 331.1243 (32.5%).

m.p.: 79 ºC-82 ºC (from hexane:CH_2Cl_2).

$[\alpha]^{25}_D$: -190 (c 0.01, MeOH).

Purity: 96.8% by RP-HPLC [R_t = 13.169 min, Agilent XTerra MS C18 column, H_2O/ACN, 90:10→90:10 (0→30 min), UV-Vis detector at 280 nm].

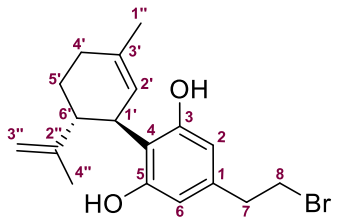

194

(1'*R*,2'*R*)-4-(2-Bromoethyl)-5'-methyl-2'-(prop-1-en-2-yl)-1',2',3',4'-tetrahydro-[1,1'-biphenyl]-2,6-diol, 194: Compound **194** was synthesised as described in General procedure K by using a solution of $BF_3{\cdot}Et_2O$ (0.29 mL, 2.32 mmol, 1.80 eq.) and Al_2O_3 (2.23 g) in anhydrous CH_2Cl_2 (26 mL). To the boiling suspension were added resorcinol derivative **211** (0.28 g, 1.29 mmol) and (+)-*p*-mentha-2,8-dien-1-ol (**149**) (0.17 mL, 1.04 mmol, 0.80 eq.) in CH_2Cl_2 (8 mL). CBDV derivative **194** (0.13 g, 0.36 mmol, 36% yield) was obtained as a yellowish solid.

Spectroscopic and physical data for compound 194:

^{1}H-NMR (300 MHz, MeOD): δ 6.13 (s, 2H, H_2,H_6), 5.27 (m, 1H, $H_{2'}$), 4.46 (m, 1H, $H_{3''a}$), 4.43 (m, 1H, $H_{3''b}$), 3.94 (m, 1H, $H_{1'}$), 3.50 (t, $^3J_{8\text{-}7}$ = 7.7 Hz, 2H, H_8), 2.91 (m, 3H, H_7,$H_{6'}$), 2.18 (m, 1H, $H_{4'a}$), 2.02 (m, 1H, $H_{4'b}$), 1.74 (m, 2H, $H_{5'}$), 1.68 (s, 3H, $H_{1''}$), 1.64 (s, 3H, $H_{4''}$).

^{13}C-NMR (75 MHz, MeOD): δ 157.7 (C_3,C_5), 150.2 ($C_{2''}$), 139.0 (C_1), 134.3 ($C_{3'}$), 126.9 ($C_{2'}$), 117.2 (C_4), 110.6 ($C_{3''}$), 108.4 (C_2,C_6), 46.2 ($C_{6'}$), 40.5 (C_7), 37.4 ($C_{1'}$), 33.4 (C_8), 31.7 ($C_{4'}$), 30.7 ($C_{5'}$), 23.7 ($C_{1''}$), 19.5 ($C_{4''}$).

HSQC and HMBC experiments have been recorded.

R_f (CH_2Cl_2, 100%) = 0.58 (UV and vanillin stain).

IR (ATR): υ 3419, 2922, 1615, 1570, 1408, 1209, 1055, 889 cm^{-1}.

HRMS (ESI+) calcd. for $[C_{18}H_{23}BrO_2+Na]^+$: 373.0774 (100%), 375.0755 (99.5%), Found: 373.0769 (100%), 375.0736 (91.6%).

m.p.: 75 ºC-78 ºC (from hexane:CH_2Cl_2).

$[\alpha]^{25}_D$: -97 (c 0.01, MeOH).

Purity: 96.9% by RP-HPLC [R_t = 13.317 min, Agilent XTerra MS C18 column, H_2O/ACN, 90:10→90:10 (0→30 min), UV-Vis detector at 280 nm].

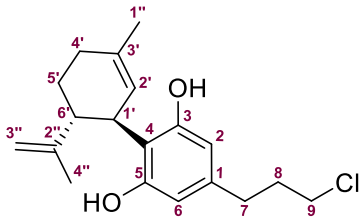

196

(1'*R*,2'*R*)-4-(3-Chloropropyl)-5'-methyl-2'-(prop-1-en-2-yl)-1',2',3',4'-tetrahydro-[1,1'-biphenyl]-2,6-diol, 196: Compound **196** was synthesised as described in General procedure K by using a solution of $BF_3{\cdot}Et_2O$ (0.54 mL, 4.33 mmol, 1.80 eq.) and Al_2O_3 (4.17 g) in anhydrous CH_2Cl_2 (45 mL). To the boiling suspension were added resorcinol derivative **212** (0.45 g, 2.41 mmol) and (+)-*p*-mentha-2,8-dien-1-ol (**149**) (0.31 mL, 1.93 mmol, 0.80 eq.) in CH_2Cl_2 (15 mL). CBDV derivative **196** (0.22 g, 0.67 mmol, 35% yield) was obtained as a white solid.

Spectroscopic and physical data for compound 196:

^{1}H-NMR (400 MHz, MeOD): δ 6.11 (s, 2H, H_2,H_6), 5.27 (m, 1H, $H_{2'}$), 4.47 (s, 1H, $H_{3''a}$) 4.43 (s, 1H, $H_{3''b}$), 3.94 (m, 1H, $H_{1'}$), 3.51 (t, $^3J_{9\text{-}8}$ = 6.5 Hz, 2H, H_9), 2.93 (m, 1H, $H_{6'}$), 2.54 (t, $^3J_{7\text{-}8}$ = 7.3 Hz, 2H, H_7), 2.21 (m, 1H, $H_{4'a}$), 2.02-1.95 (m, 3H, $H_{4'b}$,H_8), 1.74 (m, 2H, $H_{5'}$), 1.68 (s, 3H, $H_{1''}$), 1.64 (s, 3H, $H_{4''}$).

^{13}C-NMR (75 MHz, MeOD): δ 157.7 (C_3,C_5), 150.4 ($C_{2''}$), 140.7 (C_1), 134.1 ($C_{3'}$), 127.2 ($C_{2'}$), 116.5 (C_4), 110.5 ($C_{3''}$), 108.4 (C_2,C_6), 46.3 ($C_{6'}$), 45.6 (C_9), 37.5 ($C_{1'}$), 35.2 (C_8), 33.4 (C_7), 31.7 ($C_{5'}$), 30.8 ($C_{4'}$), 23.7 ($C_{1''}$), 19.5 ($C_{4''}$).

COSY, me-HSQC and HMBC experiments have been recorded.

R_f (CH_2Cl_2, 100%) = 0.58 (UV and vanillin stain).

IR (ATR): υ 3406, 2924, 1625, 1579, 1433, 1208, 1056, 889 cm^{-1}.

HRMS (ESI+) calcd. for $[C_{19}H_{25}ClO_2+Na]^+$: 343.1435 (100%), 345.1412 (34.5%), Found: 343.1425 (100%), 345.1396 (33.3%).

m.p.: 81 ºC-83 ºC (from hexane:CH_2Cl_2).

$[\alpha]^{25}_{D}$: -178 (c 0.01, MeOH).

Purity: 90.6% by RP-HPLC [R_t = 13.779 min, Agilent XTerra MS C18 column, H_2O/ACN, 90:10→90:10 (0→30 min), UV-Vis detector at 280 nm].

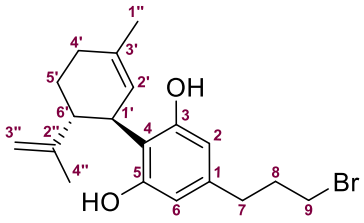

197

(1'*R*,2'*R*)-4-(3-Bromopropyl)-5'-methyl-2'-(prop-1-en-2-yl)-1',2',3',4'-tetrahydro-[1,1'-biphenyl]-2,6-diol, 197: Compound **197** was synthesised as described in General procedure K by using a solution of $BF_3{\cdot}Et_2O$ (0.69 mL, 5.63 mmol, 1.80 eq.) and Al_2O_3 (5.43 g) in anhydrous CH_2Cl_2 (60 mL). To the boiling suspension were added resorcinol derivative **213** (0.68 g, 3.13 mmol) and (+)-*p*-mentha-2,8-dien-1-ol (**149**) (0.41 mL, 2.51 mmol, 0.80 eq.) in CH_2Cl_2 (20 mL). CBDV derivative **196** (0.22 g, 0.65 mmol, 26% yield) was obtained as a yellowish solid.

Spectroscopic and physical data for compound 197:

^{1}H-NMR (300 MHz, MeOD): δ 6.11 (s, 2H, H_2,H_6), 5.28 (m, 1H, $H_{2'}$), 4.47 (dqd, $^2J_{gem}$ = 2.8 Hz, $^4J'_{3''a\text{-}4'''}$ = 0.8 Hz, $^4J'_{3''a\text{-}6'}$ = 0.8 Hz, 1H, $H_{3''a}$) 4.43 (dq, $^2J_{gem}$ = 2.8 Hz, $^4J'_{3''b\text{-}4'''}$ = 1.5 Hz, 1H, $H_{3''b}$), 3.94 (ddq, $^3J_{1'\text{-}6'}$ = 10.8 Hz, $^3J'_{1'\text{-}2'}$ = 4.4 Hz, $^3J''_{1'\text{-}1''}$ = 2.4 Hz, 1H, $H_{1'}$), 3.39 (t, $^3J_{9\text{-}8}$ = 6.6 Hz, 2H, H_9), 2.91 (m, 1H, $H_{6'}$), 2.55 (t, $^3J_{7\text{-}8}$ = 7.3 Hz, 2H, H_7) 2.20 (m, 1H, $H_{4'a}$), 2.07 (m, 3H, $H_{4'b}$,H_8), 1.75 (m, 2H, $H_{5'}$), 1.68 (m, 3H, $H_{1''}$), 1.64 (dd, $^4J_{3''b\text{-}4'''}$ = 1.5 Hz, $^4J'_{3''a\text{-}4'''}$ = 0.8 Hz, 3H, $H_{4''}$).

^{13}C-NMR (75 MHz, MeOD): δ 157.7 (C_3,C_5), 150.4 ($C_{2''}$), 140.6 (C_1), 134.1 ($C_{3'}$), 127.2 ($C_{2'}$), 116.5 (C_4), 110.5 ($C_{3''}$), 108.3 (C_2,C_6), 46.3 ($C_{6'}$), 37.5 ($C_{1'}$), 35.4 (C_8), 34.6 (C_7), 33.9 (C_9), 31.7 ($C_{4'}$), 30.8 ($C_{5'}$), 23.7 ($C_{1''}$), 19.5 ($C_{4''}$).

COSY, me-HSQC and HMBC experiments have been recorded.

R_f (CH_2Cl_2, 100%) = 0.58 (UV and vanillin stain).

IR (ATR): υ 3408, 2926, 1628, 1583, 1415, 1217, 1056, 889 cm^{-1}.

HRMS (ESI+) calcd. for $[C_{19}H_{25}BrO_2+Na]^+$: 387.0930 (100%), 389.0912 (99.7%), Found: 387.0924 (100%) 389.0901 (99.8%).

m.p.: 80 ºC-82 ºC (from hexane:CH_2Cl_2).

$[\alpha]^{25}_{D}$: -78 (c 0.01, MeOH).

Purity: 93.9% by RP-HPLC [R_t = 13.429 min, Agilent XTerra MS C18 column, H_2O/ACN, 90:10→90:10 (0→30 min), UV-Vis detector at 280 nm].

4.1.1.8. General procedure L for Finkelstein reaction

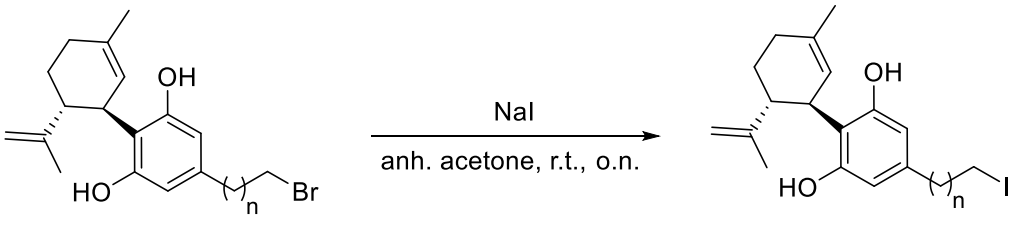

n = 1, **194**
n = 2, **197**

n = 1, **195 (96%)**
n = 2, **198 (97%)**

To a solution of brominated CBDV derivative in anhydrous acetone (0.2 M) was added NaI (2.50 eq.) in portions over 10 min. The reaction mixture was stirred at r.t. overnight. The crude was then filtered, and acetone was removed under reduced pressure. The residue was diluted in CH_2Cl_2 (40 mL/g), and the precipitate was filtered. Removal of the solvent under reduced pressure left the iodinated CBDV derivative as a yellowish solid.

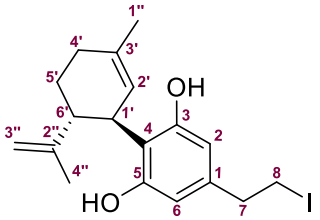

195

(1'*R*,2'*R*)-4-(2-Iodoethyl)-5'-methyl-2'-(prop-1-en-2-yl)-1',2',3',4'-tetrahydro-[1,1'-biphenyl]-2,6-diol, 195: Compound **195** was synthesised as described in General procedure L by using a solution of **194** (0.12 g, 0.39 mmol) and NaI (0.21 g, 1.42 mmol, 2.50 eq.) in anhydrous acetone (2 mL). CBDV derivative **195** (0.15 g, 0.38 mmol, 96% yield) was obtained as a yellow solid.

Spectroscopic and physical data for compound 195:

^{1}H-NMR (600 MHz, MeOD): δ 6.11 (s, 2H, H_2,H_6), 5.27 (s, 1H, $H_{2'}$), 4.47 (s, 1H, $H_{3''a}$) 4.43 (s, 1H, $H_{3''b}$), 3.96 (m, 1H, $H_{1'}$), 3.31 (m, 2H, H_8), 2.95-2.92 (m, 3H, H_7,$H_{6'}$), 2.21 (m, 1H, $H_{4'a}$), 1.99 (m, 3H, $H_{4'b}$), 1.75 (m, 2H, $H_{5'}$), 1.68 (s, 3H, $H_{1''}$), 1.64 (s, 3H, $H_{4''}$).

^{13}C-NMR (125 MHz, MeOD): δ 157.8 (C_3,C_5), 150.3 ($C_{2''}$), 140.8 (C_1), 134.2 ($C_{3'}$), 127.0 ($C_{2'}$), 117.3 (C_4), 110.5 ($C_{3''}$), 108.1 (C_2,C_6), 46.2 ($C_{6'}$), 41.6 (C_7), 37.5 ($C_{1'}$), 31.7 ($C_{4'}$), 30.7 ($C_{5'}$), 23.7 ($C_{1''}$), 19.5 ($C_{4''}$), 6.5 (C_8).

COYS, me-HSQC and HMBC experiments have been recorded.

R_f (CH_2Cl_2, 100%) = 0.58 (UV and vanillin stain).

IR (ATR): υ 3392, 2921, 1632, 1585, 1428, 1209, 1037, 889 cm^{-1}.

HRMS (ESI+) calcd. for $[C_{18}H_{23}IO_2+Na]^+$: 421.0635, Found: 421.0614.

m.p.: 85 ºC-87 ºC (from CH_2Cl_2).

$[\alpha]^{25}_D$: -92 (c 0.01, MeOH).

Purity: 95.1% by RP-HPLC [R_t = 13.834 min, Agilent XTerra MS C18 column, H_2O/ACN, 90:10→90:10 (0→30 min), UV-Vis detector at 280 nm].

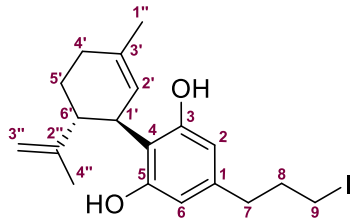

198

(1'*R*,2'R)-4-(3-Iodopropyl)-5'-methyl-2'-(prop-1-en-2-yl)-1',2',3',4'-tetrahydro-[1,1'-biphenyl]-2,6-diol, 198: Compound **198** was synthesised as described in General procedure L by using a solution of **197** (0.10 g, 0.39 mmol) and NaI (0.15 g, 0.96 mmol, 2.50 eq.) in anhydrous acetone (2 mL). CBDV derivative **198** (0.16 g, 0.38 mmol, 97% yield) was obtained as a yellowish solid.

Spectroscopic and physical data for compound 198:

^{1}H-NMR (400 MHz, MeOD): δ 6.11 (s, 2H, H_2,H_6), 5.27 (m, 1H, $H_{2'}$), 4.47 (dqd, $^2J_{gem}$ = 2.8 Hz, $^4J'_{3''a\text{-}4'''}$ = 0.8 Hz, $^4J'_{3''a\text{-}6'}$ = 0.8 Hz, 1H, $H_{3''a}$) 4.43 (dq, $^2J_{gem}$ = 2.8 Hz, $^4J'_{3''b\text{-}4'''}$ = 1.5 Hz, 1H, $H_{3''b}$), 3.93 (ddq, $^3J_{1'\text{-}6'}$ = 10.8 Hz, $^3J'_{1'\text{-}2'}$ = 4.4 Hz, $^3J''_{1'\text{-}1''}$ = 2.3 Hz, 1H, $H_{1'}$), 3.18 (t, $^3J_{9\text{-}8}$ = 6.8 Hz, 2H, H_9), 2.92 (m, 1H, $H_{6'}$), 2.55 (t, $^3J_{7\text{-}8}$ = 7.2 Hz, 2H, H_7) 2.20 (m, 1H, $H_{4'a}$), 2.06-1.97 (m, 3H, $H_{4'b}$,H_8), 1.75 (m, 2H, $H_{5'}$), 1.68 (m, 3H, $H_{1''}$), 1.64 (dd, $^4J_{3''b\text{-}4'''}$ = 1.5 Hz, $^4J'_{3''a\text{-}4'''}$ = 0.8 Hz, 3H, $H_{4''}$).

^{13}C-NMR (100 MHz, MeOD): δ 157.7 (C_3,C_5), 150.4 ($C_{2''}$), 140.4 (C_1), 134.1 ($C_{3'}$), 127.2 ($C_{2'}$), 116.6 (C_4), 110.5 ($C_{3''}$), 108.3 (C_2,C_6), 46.3 ($C_{6'}$), 37.5 ($C_{1'}$), 36.8 (C_7), 36.1 (C_8), 31.7 ($C_{4'}$), 30.8 ($C_{5'}$), 23.7 ($C_{1''}$), 19.5 ($C_{4''}$), 6.5 (C_9).

COSY, me-HSQC and HMBC experiments have been recorded.

R_f (CH_2Cl_2, 100%) = 0.58 (UV and vanillin stain).

IR (ATR): υ 3388, 2922, 1627, 1582, 1440, 1215, 1026, 889 cm^{-1}.

HRMS (ESI+) calcd. for $[C_{19}H_{25}IO_2+Na]^+$: 435.0791, Found: 435.0788.

m.p.: 80 ºC-82 ºC (from CH_2Cl_2).

$[\alpha]^{25}_D$: -107 (c 0.01, MeOH).

Purity: 94.3% by RP-HPLC [R_t = 14.405 min, Agilent XTerra MS C18 column, H_2O/ACN, 90:10→90:10 (0→30 min), UV-Vis detector at 280 nm].

4.2.2. Synthesis of Thioether-Containing CBDV analogue

4.2.2.1. 3,5-Dimethoxybenzyl alcohol, 220

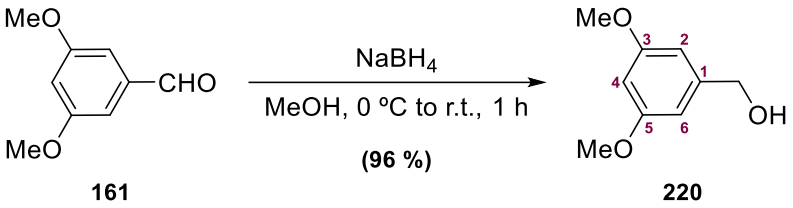

161 **220**

To an ice-cooled solution of aldehyde **161** (0.60 g, 3.61 mmol) in MeOH (15 mL), under a nitrogen atmosphere, was added $NaBH_4$ (0.16 g, 4.34 mmol, 1.20 eq.) in portions over a period of 10 min. The mixture was subsequently allowed to attain room temperature and was stirred for 1 h. The reaction was cooled to 0 °C before adding H_2O (10 mL) to quench it. MeOH was evaporated under vacuum and the residual aqueous phase was extracted with DCM (4 x 15 mL). The organic phase was dried over $MgSO_4$ and concentrated under reduced pressure affording alcohol **220** (0.58 g, 3.46 mmol, 96% yield) as a white solid.

Spectroscopic data for compound 220:

^{1}H-NMR (300 MHz, $CDCl_3$): δ 6.53 (d, $^4J_{2/6\text{-}4}$ = 2.3 Hz, 2H, H_2,H_6), 6.39 (t, $^4J_{4\text{-}6/2}$ = 2.3 Hz, 1H, H_4), 4.64 (s, 2H, CH_2OH), 3.80 (s, 6H, 2 OCH_3).

R_f (hexane:EtOAc, 1:1) = 0.33 (UV and $KMnO_4$).

Spectroscopic data are consistent with those reported in reference: Murai, N.; Yonaga, M.; Tanaka, K. *Org. Lett.* **2012**, *14* (5), 1278-1281.

4.2.2.2. 1-(Iodomethyl)-3,5-dimethoxybenzene, 221

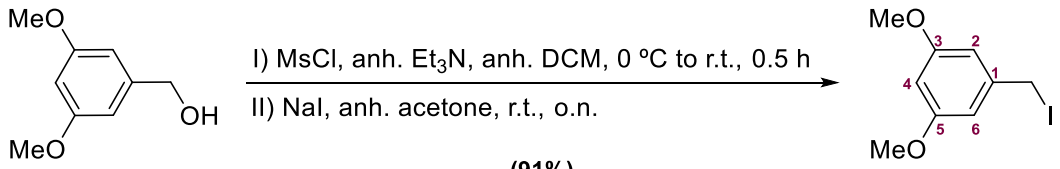

220 **221**

MsCl (0.84 mL, 10.79 mmol, 1.10 eq.) was added dropwise to a solution of alcohol **220** (1.65 g, 9.81 mmol) and anhydrous Et_3N (1.50 mL, 10.79 mmol, 1.10 eq.) in anhydrous CH_2Cl_2 (65 mL) at 0 ºC under a nitrogen atmosphere. The mixture was then stirred at room temperature for 30 min. and quenched by adding H_2O (30 mL). The reaction mixture was extracted with CH_2Cl_2 (2 x 20 mL). The combined organic layers were dried over $MgSO_4$ and concentrated under reduced pressure. The oily residue obtained was dissolved in anhydrous acetone (60 mL) and NaI (3.68 g, 24.52 mmol, 2.50 eq.) was added to the solution and stirred overnight at room temperature under nitrogen atmosphere. Solvent was evaporated, salts were precipitated in CH_2Cl_2 and filtered. CH_2Cl_2 was removed under reduced pressure, and the residue was purified by column chromatography (silica gel, hexane:EtOAc, 3:1) to afford product **221** (2.48 g, 8.93 mmol, 91% yield) as a white powder.

Spectroscopic data for compound 221:

^{1}H-NMR (300 MHz, $CDCl_3$): δ 6.52 (d, $^{4}J_{2/6\text{-}4}$ = 2.2 Hz, 2H, H_2,H_6), 6.34 (t, $^{4}J_{4\text{-}6/2}$ = 2.2 Hz, 1H, H_4), 4.38 (s, 2H, CH_2I), 3.78 (s, 6H, 2 OCH_3).

^{13}C-NMR (75 MHz, $CDCl_3$): δ 161.0 (C_3,C_5), 141.4 (C_1), 106.9 (C_2,C_6), 100.3 (C_4), 55.5 (2 OCH_3), 5.77 (CH_2I).

COSY and me-HSQC experiments have been recorded.

R_f (hexane:EtOAc, 3:1) = 0.68 (UV and $KMnO_4$).

Spectroscopic data are consistent with those reported in reference: DeCosta, D. P.; Howell, N.; Pincock, A. L.; Rifai, S. *J. Org. Chem.* **2000**, *65* (15), 4698–4705.

4.2.2.3. (3,5-Dimethoxybenzyl)(methyl)sulfane, 222

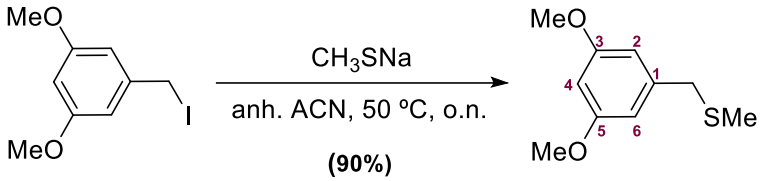

221 **222**

To a stirred solution of **221** (1.50 g, 5.39 mmol) in anhydrous ACN (18 mL) was added CH_3SNa (0.45 g, 6.47 mmol, 1.20 eq.) in portions, the reaction mixture was warmed to 50 ºC and stirred for 48 h under a nitrogen atmosphere. H_2O (15 mL) was added to the reaction, ACN was evaporated, and the aqueous phase was extracted with CH_2Cl_2 (4 x 20 mL). The organic phases were dried over $MgSO_4$, concentrated under reduced pressure, and the residue obtained was purified by column chromatography on silica gel (CH_2Cl_2, 100%) furnishing **222** (0.96 g, 4.85 mmol, 90% yield) as a white solid.

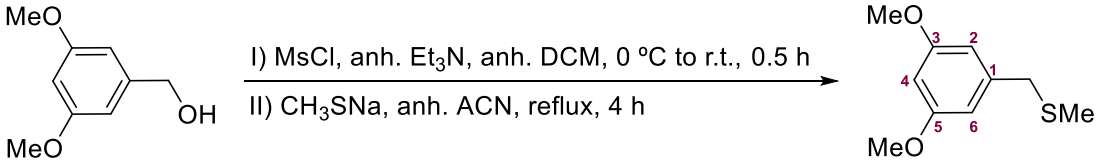

220 **222**

MsCl (0.84 mL, 10.79 mmol, 1.10 eq.) was added dropwise to a solution of alcohol **220** (1.65 g, 9.81 mmol) and anhydrous Et_3N (1.50 mL, 10.79 mmol, 1.10 eq.) in anhydrous CH_2Cl_2 (65 mL) at 0 ºC. The mixture was allowed to stir at room temperature for 30 min and then quenched by the addition of H_2O (30 mL). The reaction mixture was extracted with CH_2Cl_2 (2 x 20 mL). The combined organic layers were dried over $MgSO_4$ and concentrated under reduced pressure. The oily residue obtained was dissolved in anhydrous ACN (18 mL) and CH_3SNa was added (0.76 g, 10.79 mmol, 1.10 eq.) in portions, the reaction mixture was warmed to 50 ºC and stirred for 4 h. The crude was filtered and the solid was washed with CH_2Cl_2. The filtrate was evaporated under reduced pressure furnishing **222** (1.85 g, 9.32 mmol, 95% yield) as a white solid.

Spectroscopic and physical data for compound 222:

^{1}H-NMR (300 MHz, $CDCl_3$): δ 6.47 (d, $^{4}J_{2/6\text{-}4}$ = 2.3 Hz, 2H, H_2,H_6), 6.35 (t, $^{4}J_{4\text{-}6/2}$ = 2.3 Hz, 1H, H_4), 3.79 (s, 6H, 2 OCH_3), 3.61 (s, 2H, CH_2S), 2.01 (s, 3H, SCH_3).

^{13}C-NMR (75 MHz, $CDCl_3$): δ 160.8 (C_3,C_5), 140.6 (C_1), 106.8 (C_2,C_6), 99.0 (C_4), 55.3 (2 OCH$_3$), 38.6 (CH$_2$S), 15.0 (SCH$_3$).

COSY, me-HSQC and HMBC experiments have been recorded.

R_f (CH_2Cl_2, 100%) = 0.42 (UV and vanillin stain).

IR (ATR): 2928, 1609, 1451, 1305, 1158, 1062, 817 cm^{-1}.

HRMS (ESI+) calcd. for [$C_{10}H_{14}O_2S$+Na]$^{+}$: 221.0607, Found: 221.0595.

m.p.: 47 ºC-50 ºC (from CH_2Cl_2).

4.2.2.4. (3,5-Dimethoxybenzyl)(methyl)sulfane, 223

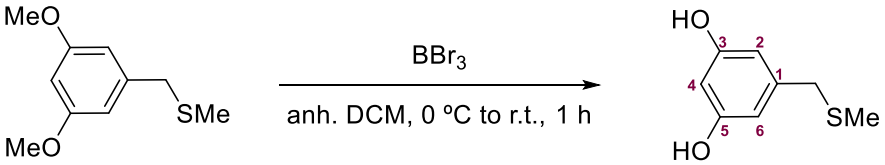

222 **223**

A solution of BBr_3 (1 M in CH_2Cl_2, 3.00 mL, 3.00 mmol, 3.00 eq.) was slowly added to a solution of compound **222** (0.20 g, 1.00 mmol) in anhydrous CH_2Cl_2 at 0 ºC and under an inert atmosphere. The reaction mixture was then warmed to room temperature and stirred for 1 h. Then, it was cooled to 0 ºC, treated with H_2O (10 mL) and the precipitate filtered. After, the solid was dissolved in EtOAc (15 mL) and washed with H_2O (10 mL x 3). The organic phase was dried over $MgSO_4$ and the solvent was removed under reduced pressure to obtain product **223** (0.16 g, 0.96 mmol, quantitative yield) as an off-white solid.

Spectroscopic and physical data for compound 223:

^{1}H-NMR (400 MHz, MeOD): δ 6.26 (d, $^{4}J_{2/6\text{-}4}$ = 2.2 Hz, 2H, H_2,H_6), 6.14 (t, $^{4}J_{4\text{-}6/2}$ = 2.2 Hz, 1H, H_4), 3.51 (s, 2H, CH_2S), 1.97 (s, 3H, SCH_3).

^{13}C-NMR (100 MHz, MeOD): δ 159.5 (C_2,C_6), 142.0 (C_4), 108.4 (C_3,C_5), 102.1 (C_1), 39.1 (CH$_2$S), 14.9 (SCH$_3$).

COSY, me-HSQC and HMBC experiments have been recorded.

R_f (hexane:EtOAc, 1:1) = 0.12 (UV and vanillin stain).

IR (ATR): 3217, 2898, 1615, 1461, 1314, 1128, 789 cm^{-1}.

HRMS (ESI-) calcd. for [$C_8H_{10}O_2$S-H]$^{-}$: 169.0329, Found: 169.0330.

m.p.: 56 ºC-58 ºC (from EtOAc).

4.2.2.5. (1'*R*,2'*R*)-5'-Methyl-4-((methylthio)methyl)-2'-(prop-1-en-2-yl)-1',2',3',4'-tetrahydro-[1,1'-biphenyl]-2,6-diol, 199

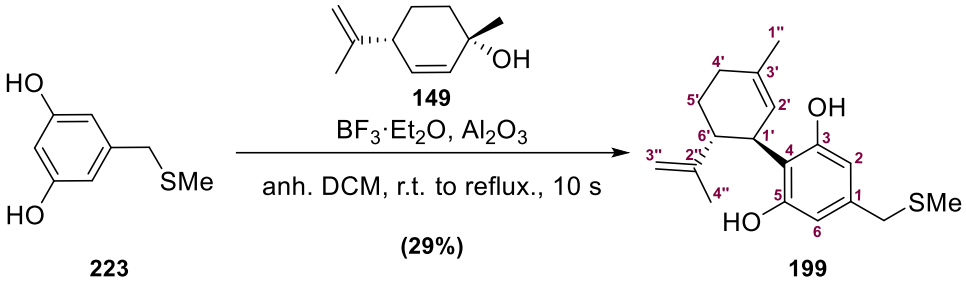

$BF_3{\cdot}Et_2O$ (0.25 mL, 2.02 mmol, 1.80 eq.) was added, under an inert atmosphere, to a stirred suspension of basic aluminium oxide (2.20 g) in anhydrous CH_2Cl_2 (22 mL). The suspension was then refluxed for 15 min. Then, the suspension was removed from the heat and thioether derivate **223** (0.19 g, 1.12 mmol) and (+)-*p*-Mentha-2,8-dien-1-ol (**149**) (0.15 mL, 0.89 mmol, 0.80 eq.) in CH_2Cl_2 (8 mL) were added to the suspension and the mixture was stirred for 10 s. The reaction was quenched with $NaHCO_3$ saturated solution (10 mL). Al_2O_3 was filtered and the aqueous phase was extracted with CH_2Cl_2 (4 x 15 mL). The organic layers were dried over $MgSO_4$, filtered, and the solvent removed under reduced pressure. The crude obtained was purified by column chromatography (hexane:CH_2Cl_2, 3:1 to 1:3) to furnish product **199** (0.08 g, 0.26 mmol, 29% yield) as a white solid.

Spectroscopic and physical data for compound 199:

^{1}H-NMR (600 MHz, MeOD): δ 6.22 (s, 2H, H_2,H_6), 5.27 (m, 1H, $H_{2'}$), 4.46 (m, 1H, $H_{3''a}$), 4.42 (m, 1H, $H_{3''b}$), 3.95 (m, 1H, $H_{1'}$), 3.46 (s, 2H, CH_2S), 2.94 (ddd, $^3J_{6'\text{-}5'a}$ = $^3J'_{6'\text{-}1'}$ = 10.5 Hz, $^3J''_{6'\text{-}5'b}$ = 5.1 Hz, 2H, $H_{6'}$), 2.20 (m, 1H, $H_{4'a}$), 2.00 (m, 1H, $H_{4'b}$), 1.94 (s, 3H, SCH_3), 1.74 (m, 2H, $H_{5'}$), 1.68 (s, 3H, $H_{1''}$), 1.64 (s, 3H, $H_{4''}$).

^{13}C-NMR (125 MHz, MeOD): δ 157.7 (C_3,C_5), 150.4 ($C_{2''}$), 138.2 ($C_{3'}$), 134.1 (C_1), 127.1 ($C_{2'}$), 117.4 (C_4), 110.5 ($C_{3''}$), 108.7 (C_2,C_6), 46.2 ($C_{6'}$), 38.9 (*C*H_2S), 37.5 ($C_{1'}$), 31.7 ($C_{4'}$), 30.7 ($C_{5'}$), 23.7 ($C_{1''}$), 19.4 ($C_{4''}$), 14.8 (S*C*H_3).

COSY, me-HSQC and HMBC experiments have been recorded.

R_f (CH_2Cl_2, 100%) = 0.40 (UV and vanillin stain).

IR (ATR): 3411, 2916, 1625, 1583, 1435, 1216, 1028, 889 cm^{-1}.

HRMS (ESI+) calcd. for $[C_{18}H_{24}O_2S+Na]^+$: 327.1389, Found: 327.1380.

m.p.: 69 ºC-73 ºC (from hexane:CH_2Cl_2).

$[\alpha]^{25}_D$: -48 (c 0.01, MeOH).

Purity: 96.6% by RP-HPLC [R_t = 12.963 min, Agilent XTerra MS C18 column, H_2O/ACN, 90:10→90:10 (0→30 min), UV-Vis detector at 280 nm].

Annex

Spectra of Selected Compounds and Supplementary Information

PART I. Cyclobutane Scaffold for Imaging Applications

Chapter I. Hybrid γ,γ-Peptidomimetics as Mitochondria Penetrating Peptides

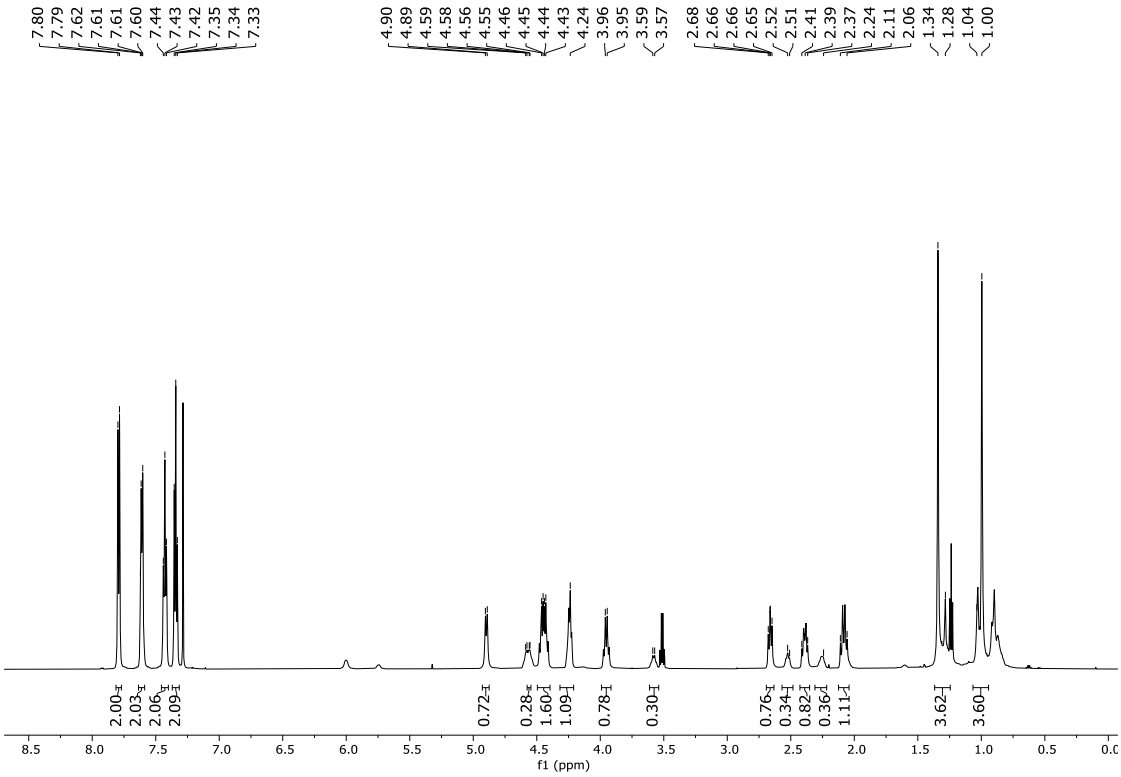

Figure A1. ^{1}H-NMR spectrum (600 MHz, $CDCl_3$) of compound **59**.

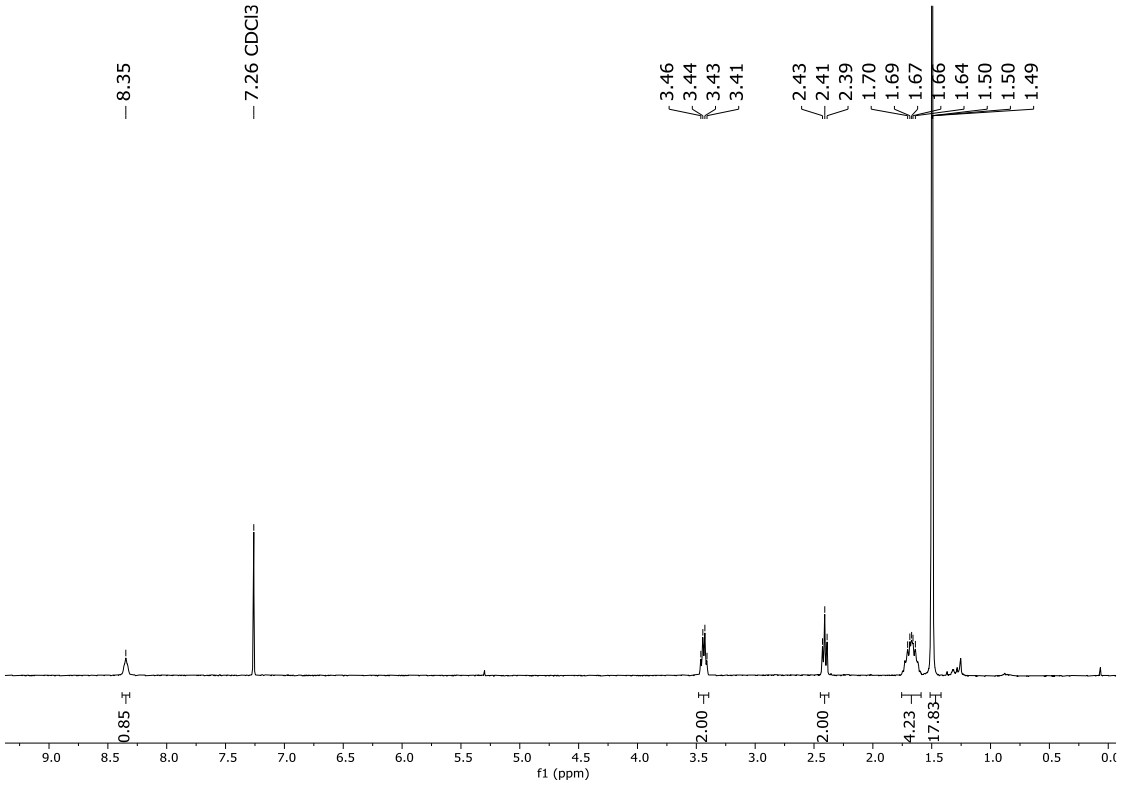

Figure A2. ^{1}H-NMR spectrum (600 MHz, $CDCl_3$) of compound **74**.

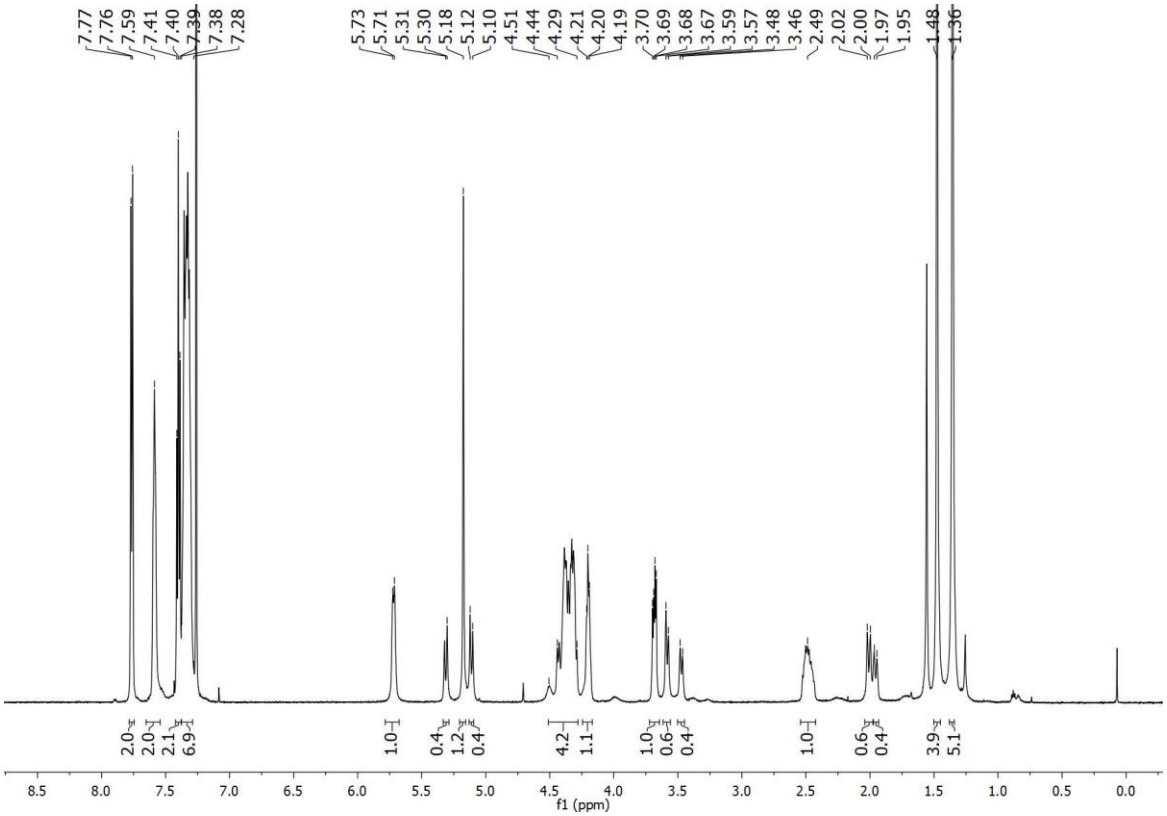

Figure A3. ^{1}H-NMR spectrum (600 MHz, $CDCl_3$) of compound **79**.

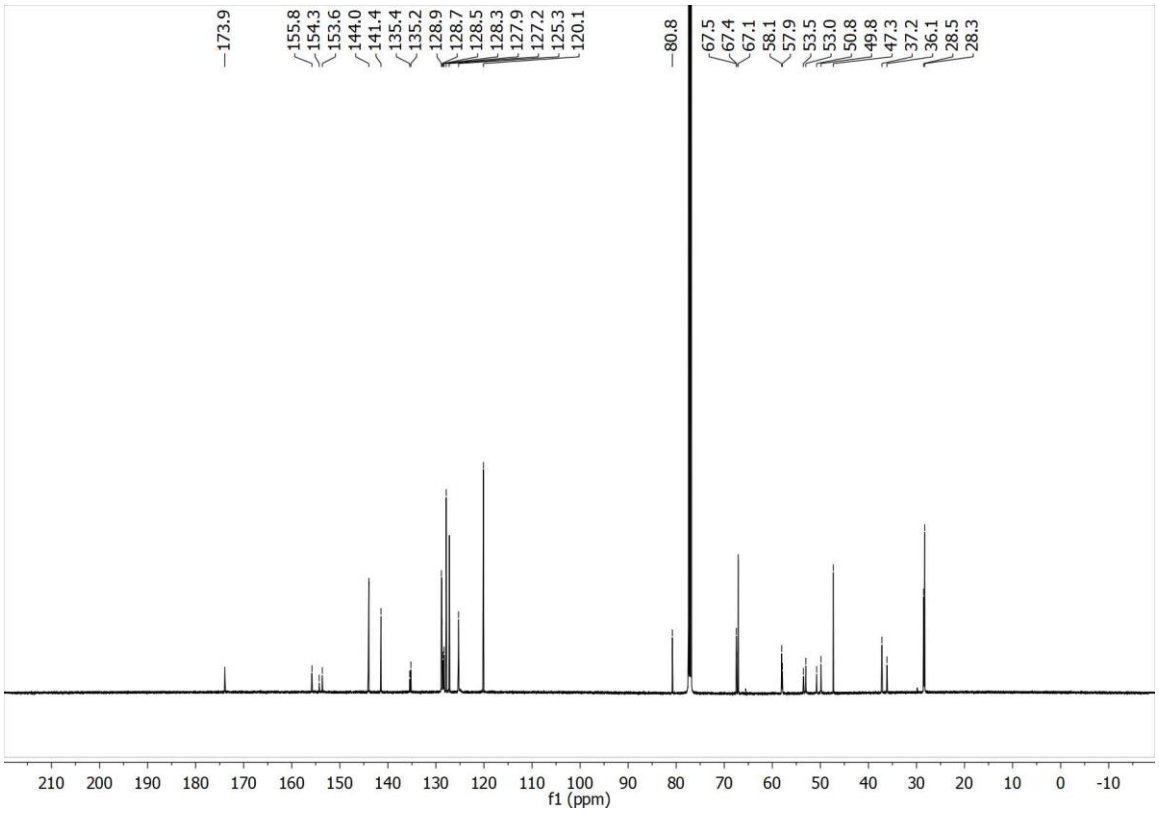

Figure A4. ^{13}C-NMR spectrum (125 MHz, $CDCl_3$) of compound **79**.

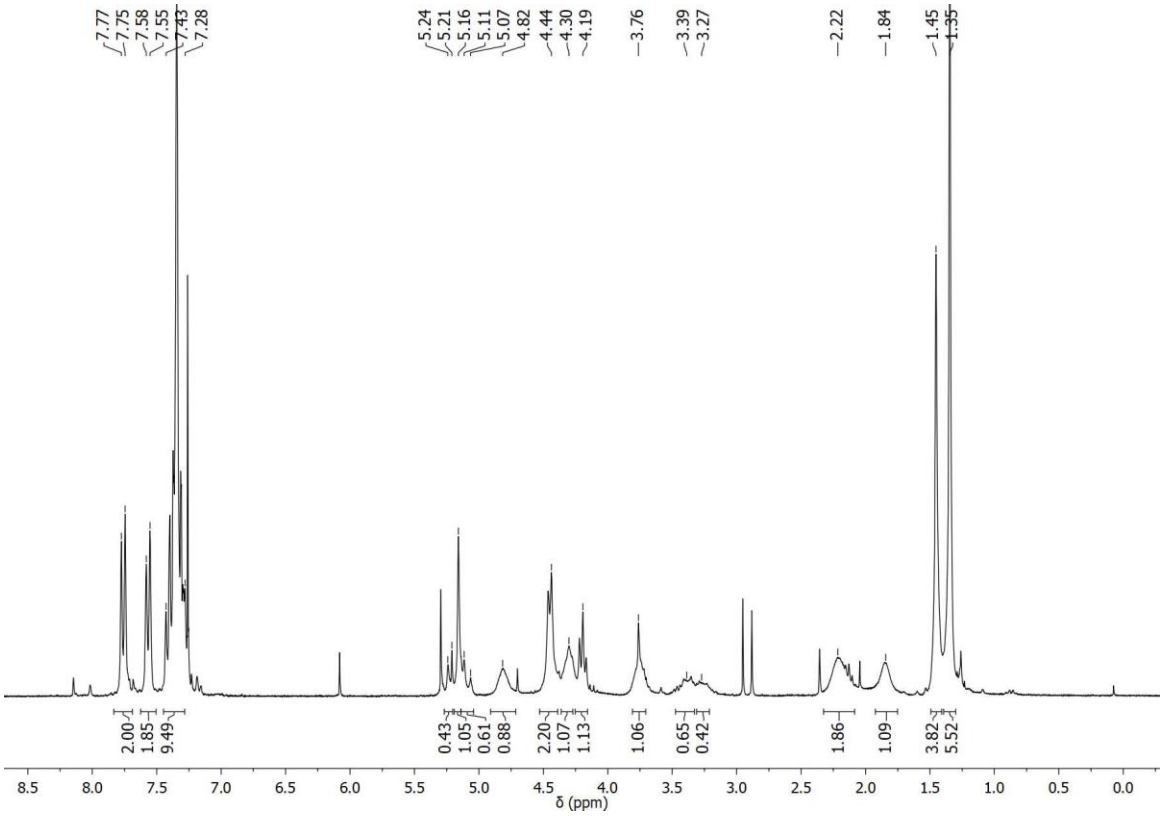

Figure A5. ^{1}H-NMR spectrum (360 MHz, $CDCl_3$) of compound **80**.

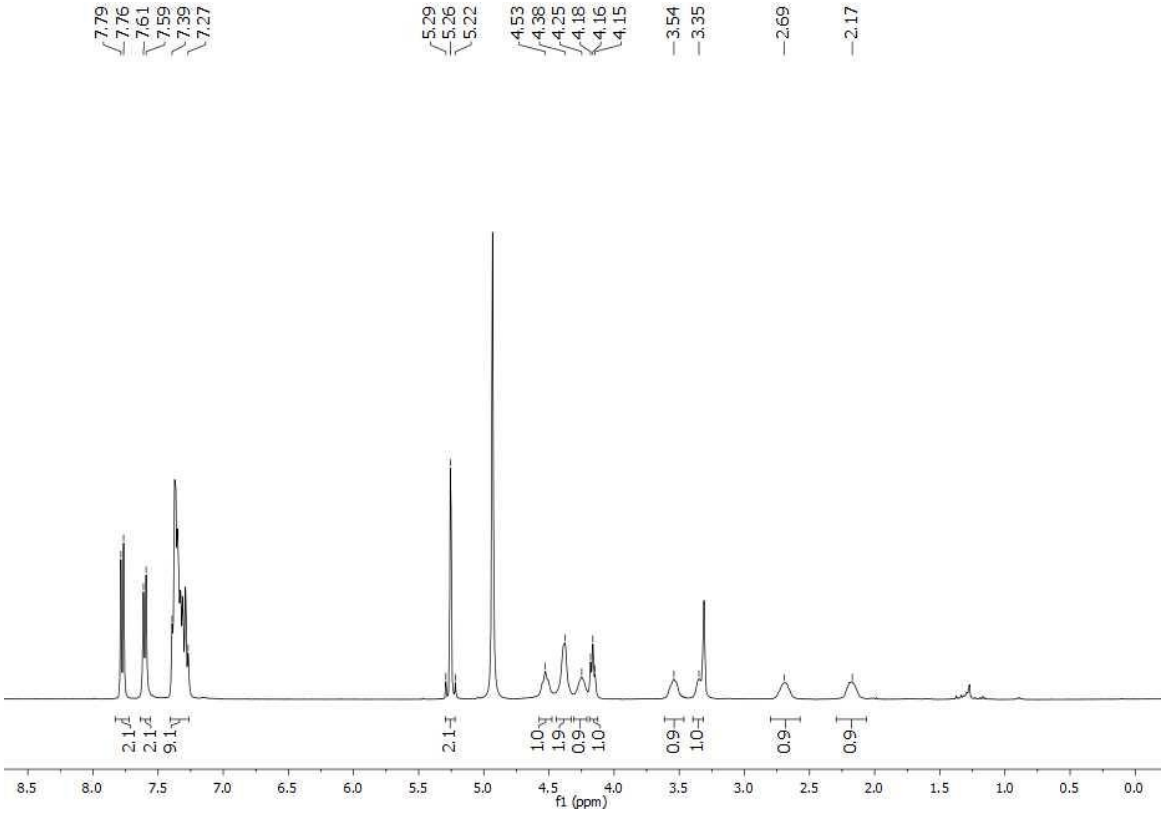

Figure A6. ^{1}H-NMR spectrum (360 MHz, MeOD) of compound **81**.

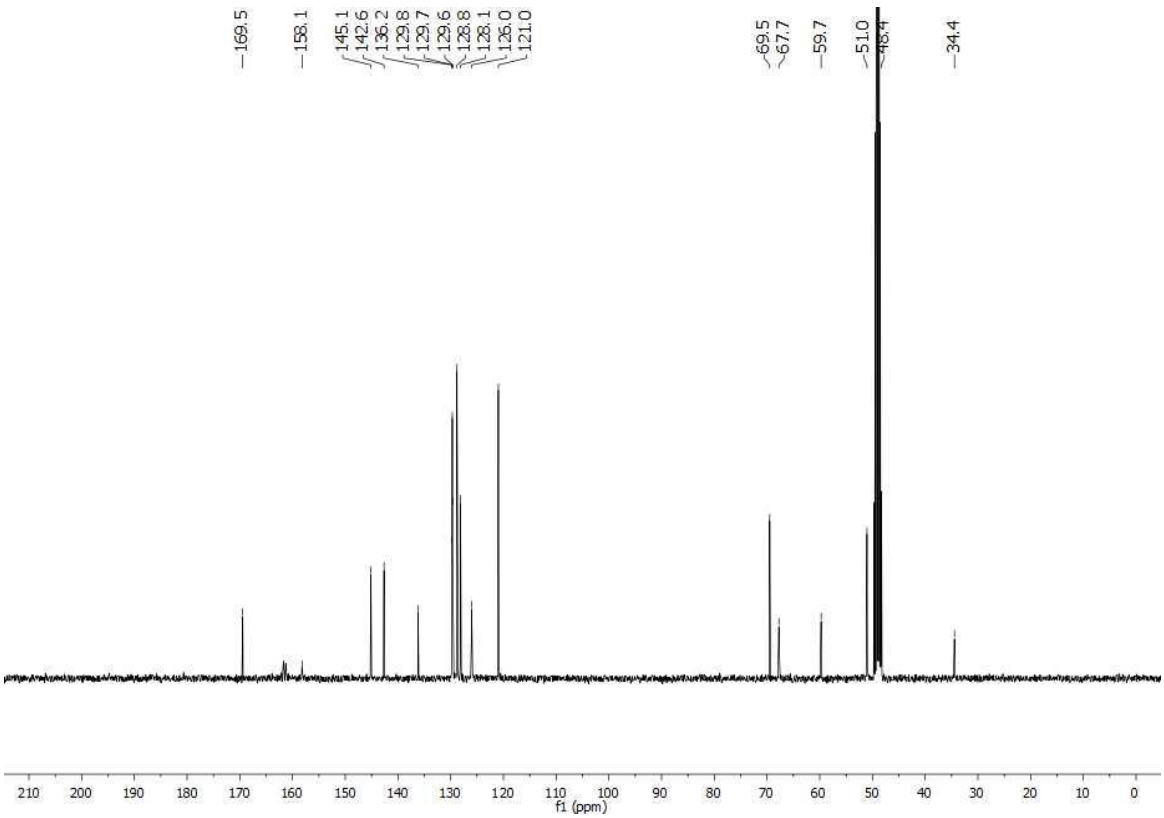

Figure A7. ^{13}C-NMR spectrum (90 MHz, MeOD) of compound **81**.

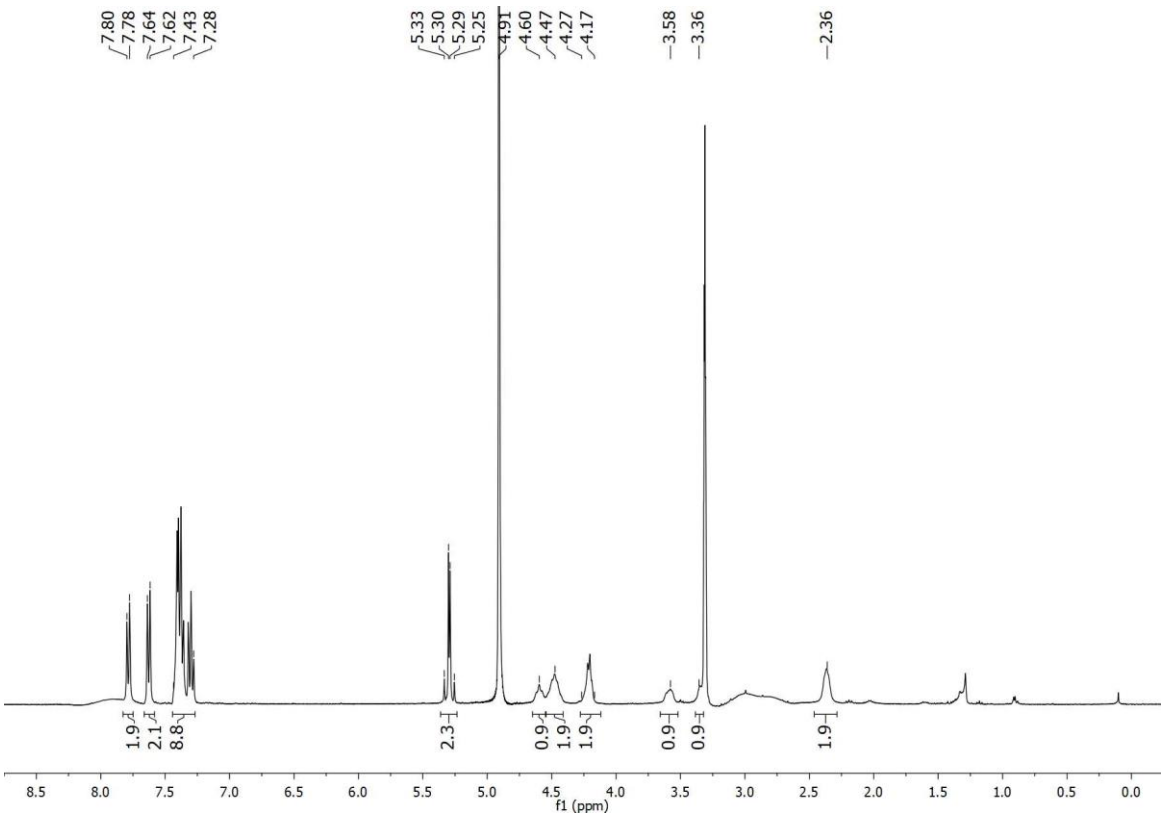

Figure A8. [1]H-NMR spectrum (360 MHz, MeOD) of compound **82**.

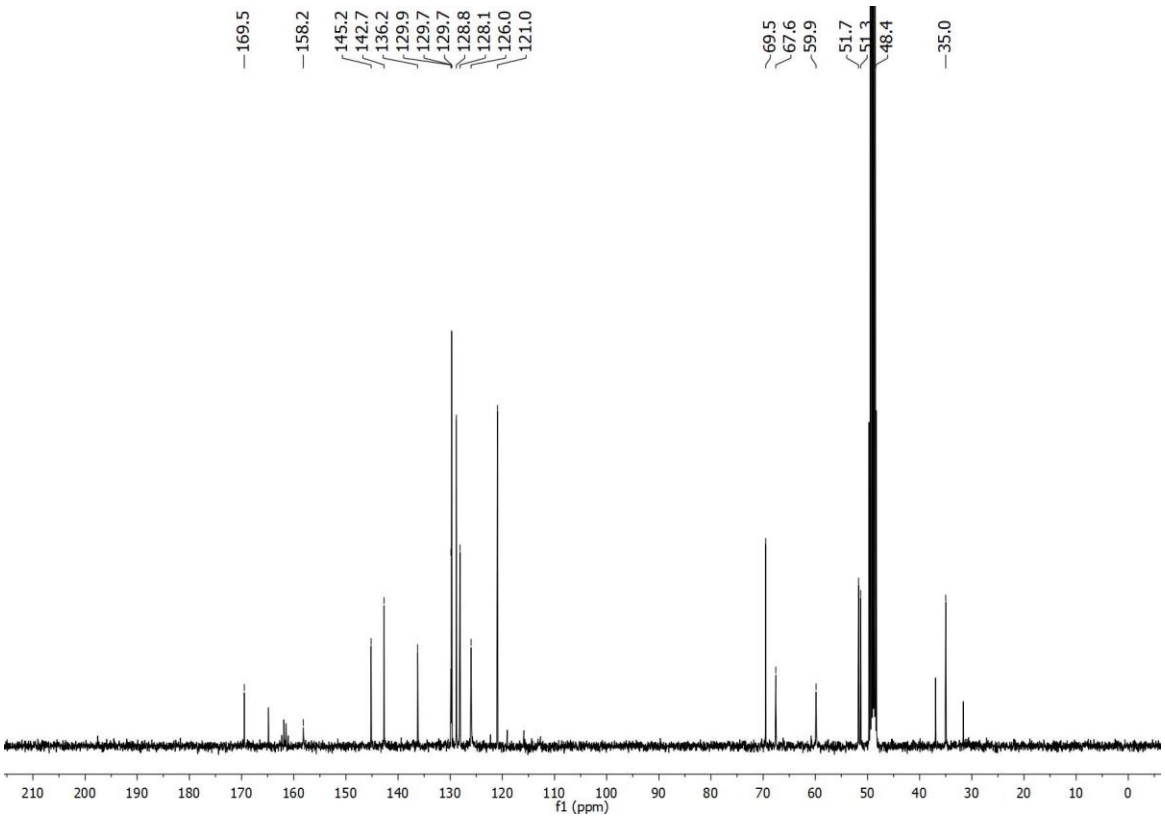

Figure A9. [13]C-NMR spectrum (90 MHz, MeOD) of compound **82**.

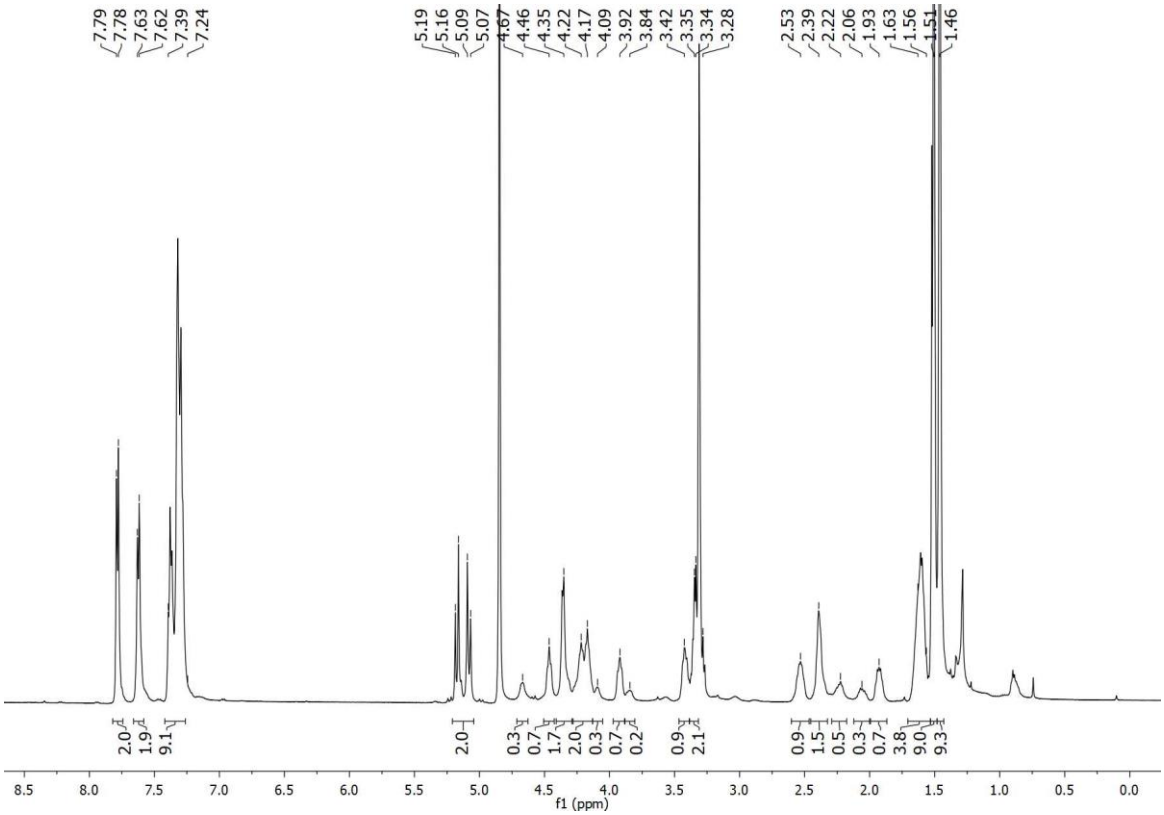

Figure A10. ^{1}H-NMR spectrum (500 MHz, MeOD) of compound **84**.

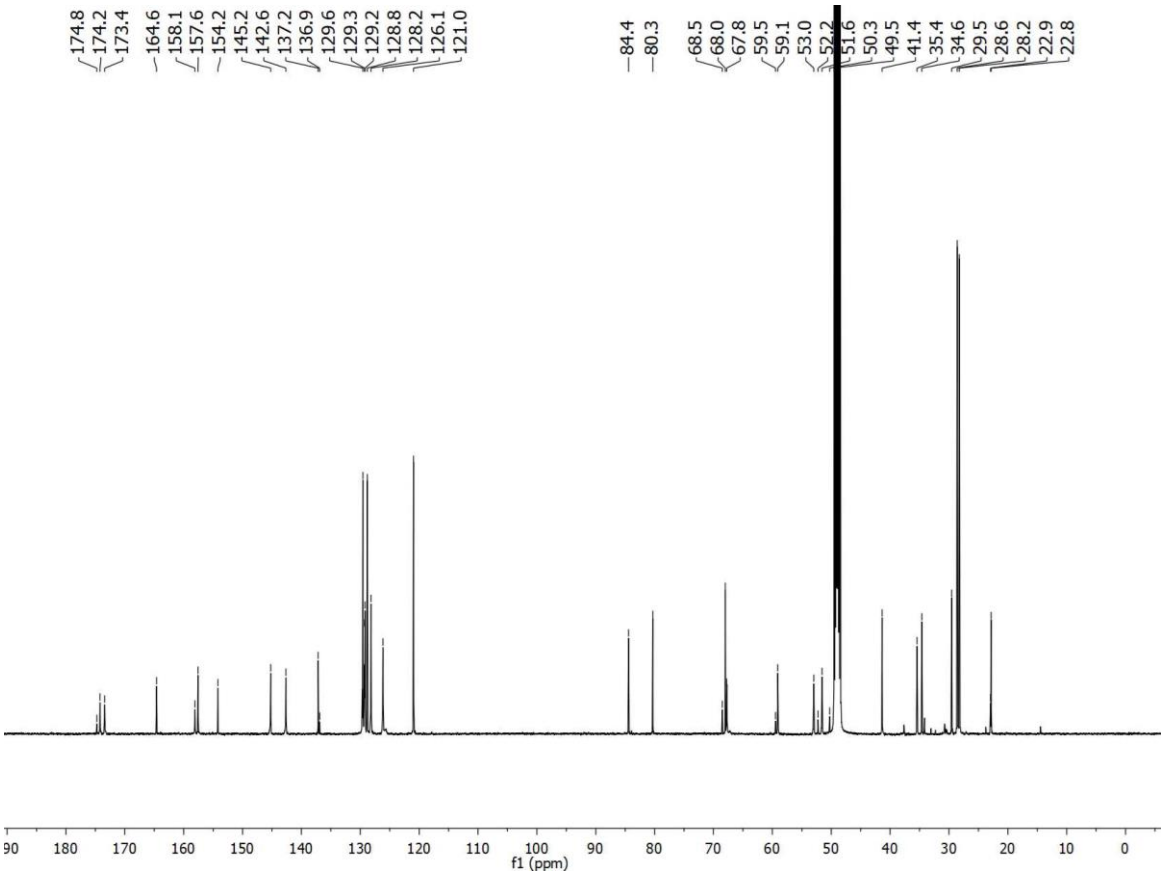

Figure A11. ^{13}C-NMR spectrum (125 MHz, MeOD) of compound **84**.

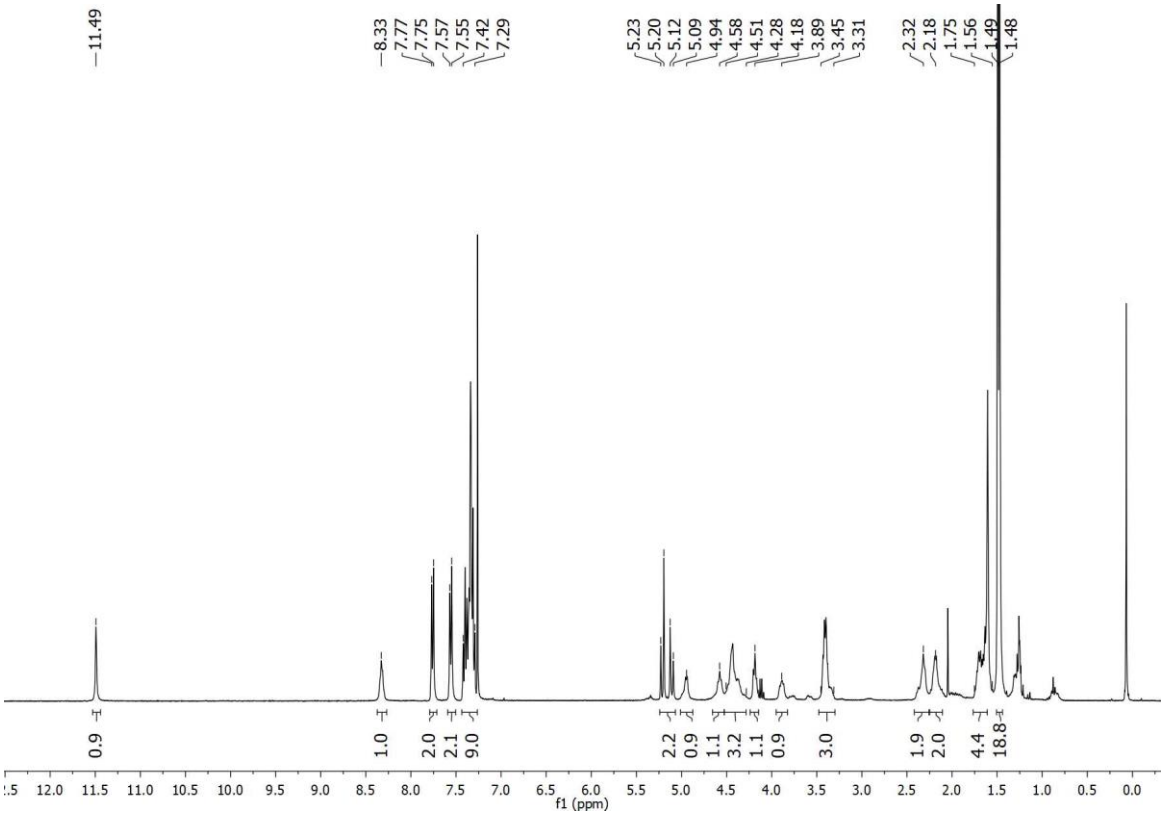

Figure A12. ^{1}H-NMR spectrum (360 MHz, $CDCl_3$) of compound **85**.

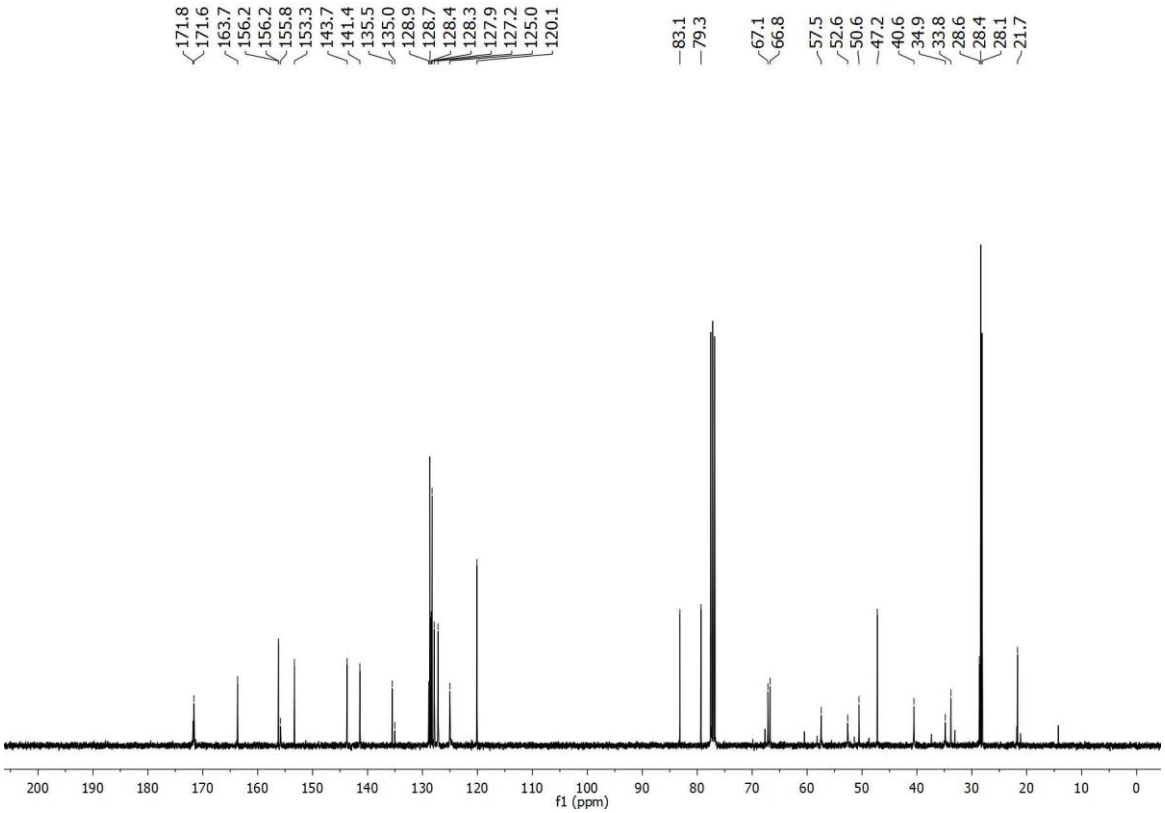

Figure A13. ^{13}C-NMR spectrum (90 MHz, $CDCl_3$) of compound **85**.

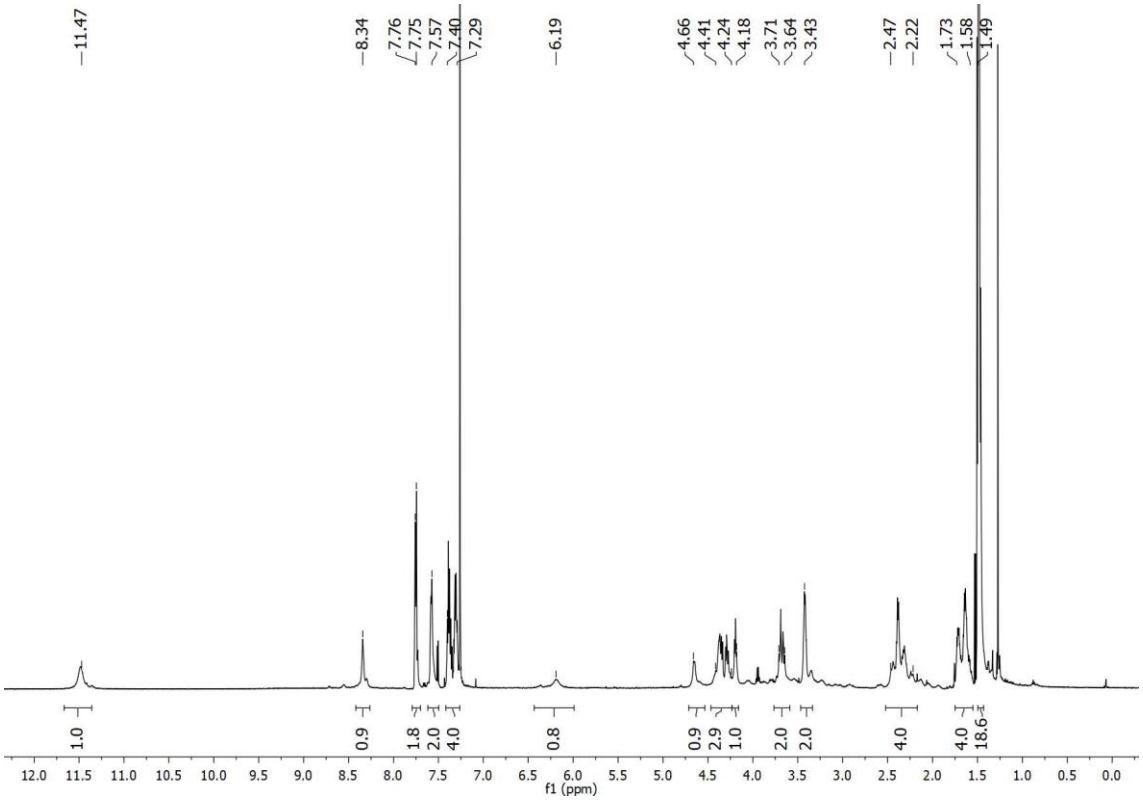

Figure A14. ^{1}H-NMR spectrum (600 MHz, $CDCl_3$) of compound **60**.

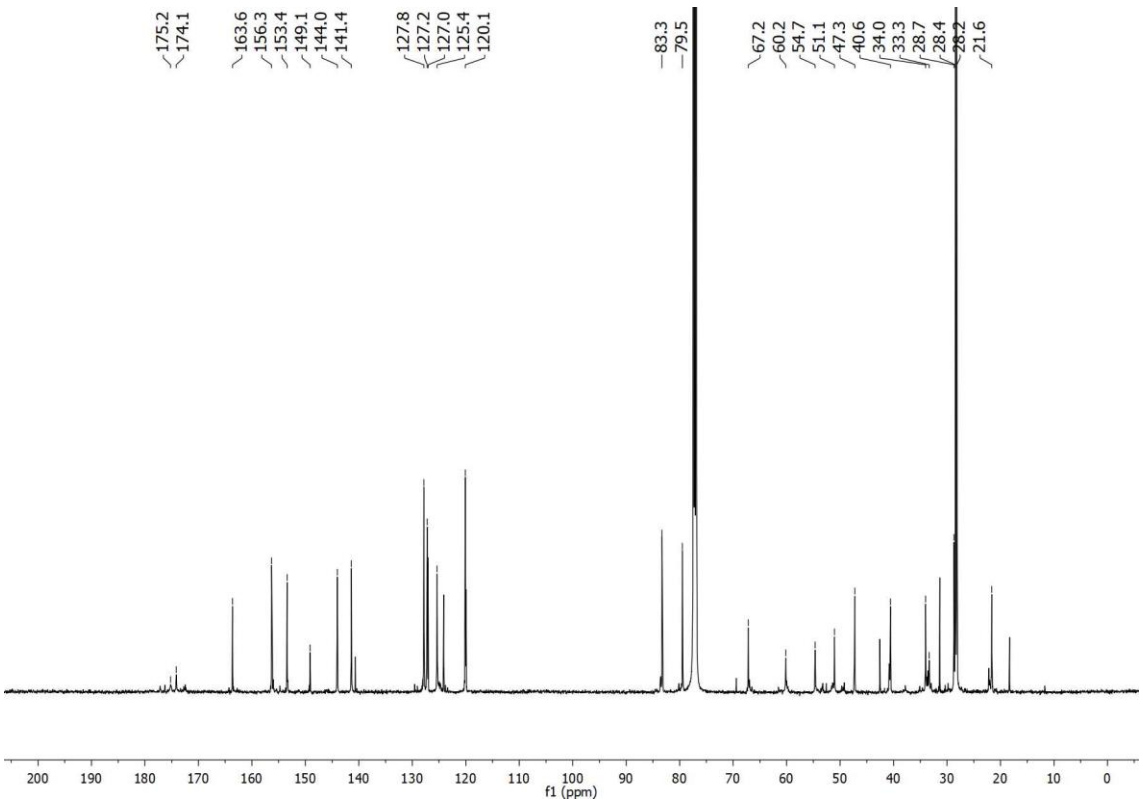

Figure A15. ^{13}C-NMR spectrum (125 MHz, $CDCl_3$) of compound **60**.

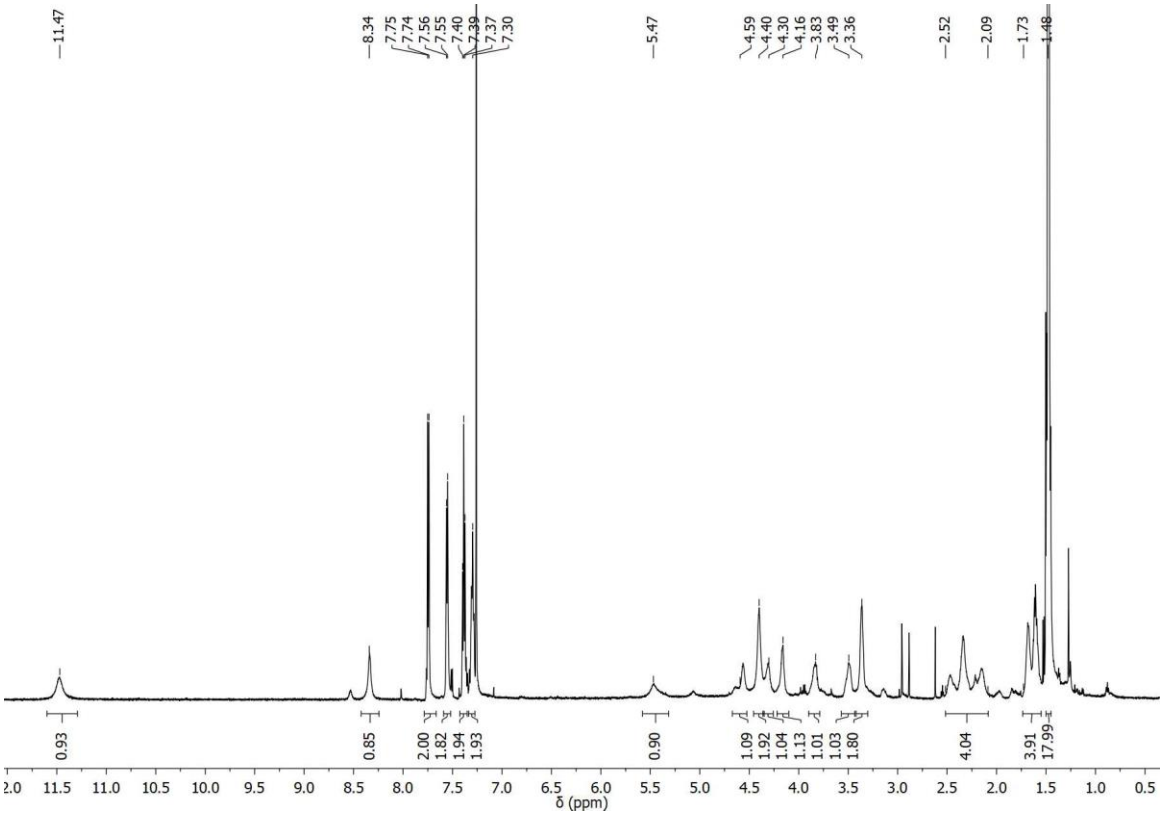

Figure A16. ^{1}H-NMR spectrum (600 MHz, $CDCl_3$) of compound **61**.

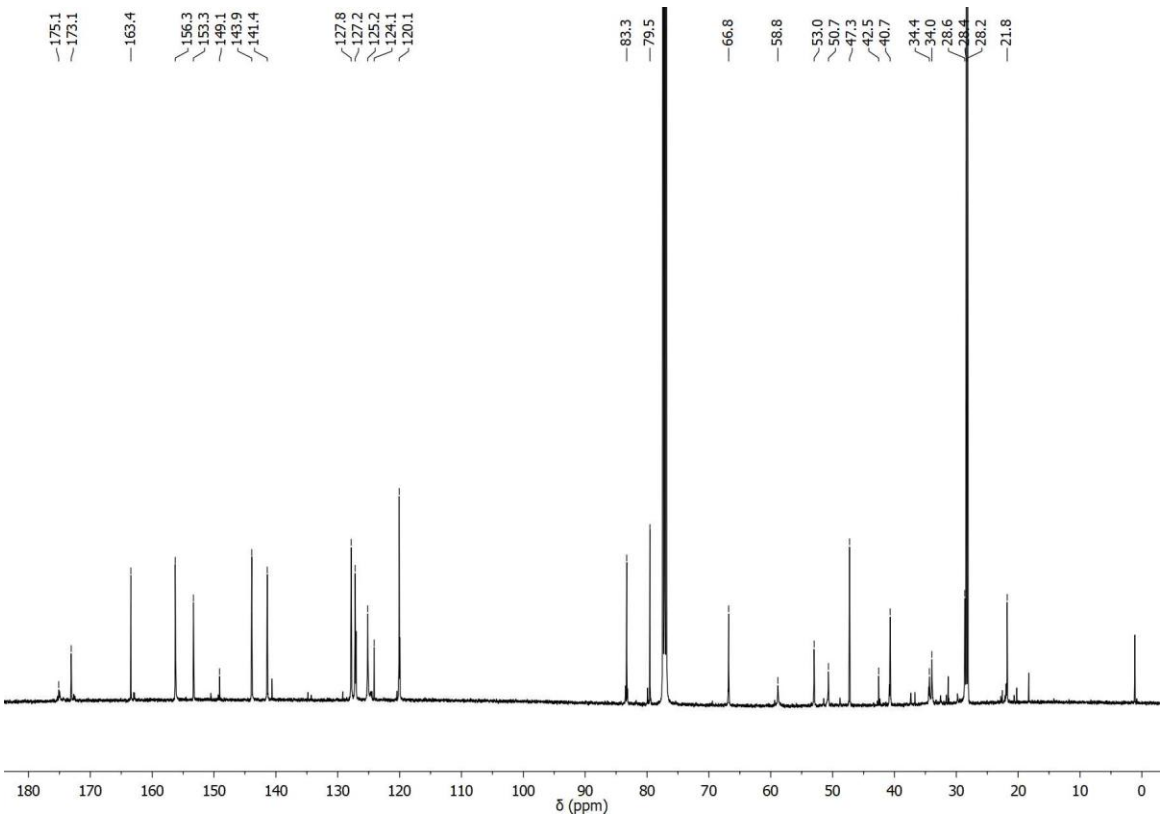

Figure A17. ^{13}C-NMR spectrum (125 MHz, $CDCl_3$) of compound **61**.

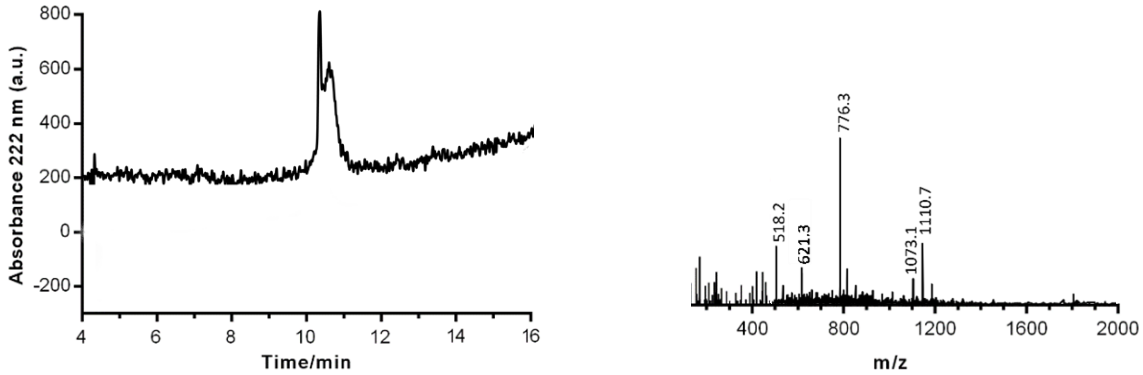

Figure A18. RP-HPLC [Agilent SB-C18 column, H_2O (0.1% TFA) / CH_3CN (0.1% TFA) 95:5→5:95 (0→12 min)] (R_t 10.2 min) and ESI-MS of the peptide **CF-γ-CC**.

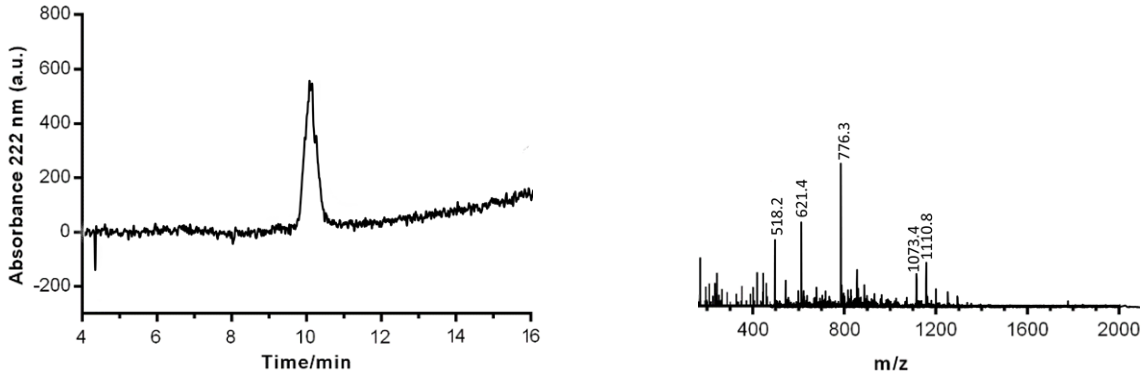

Figure A19. RP-HPLC [Agilent SB-C18 column, H_2O (0.1% TFA) / CH_3CN (0.1% TFA) 95:5→5:95 (0→12 min)] (R_t 9.9 min) and ESI-MS of the peptide **CF-γ-CT**.

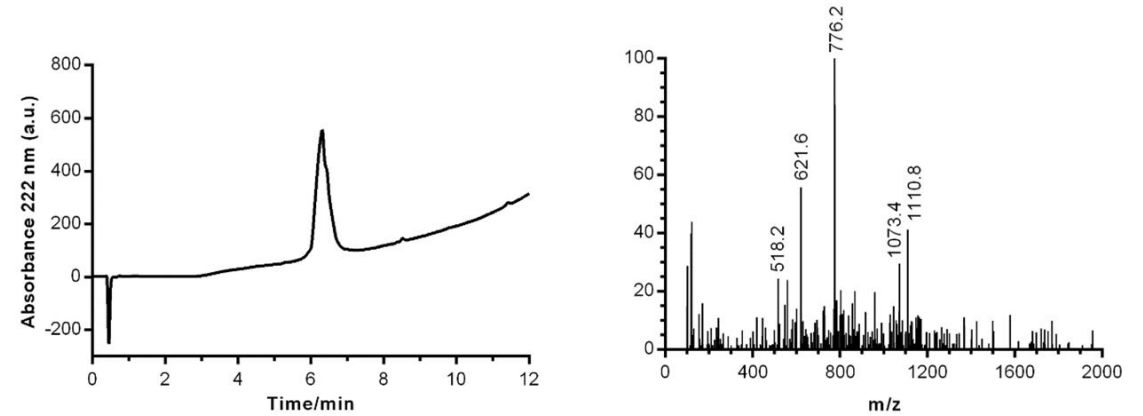

Figure A20. RP-HPLC [Agilent SB-C18 column, H_2O (0.1% TFA) / CH_3CN (0.1% TFA) 95:5→5:95 (0→12 min)] (R_t 6.3 min) and ESI-MS of the peptide **γ-SCC**.

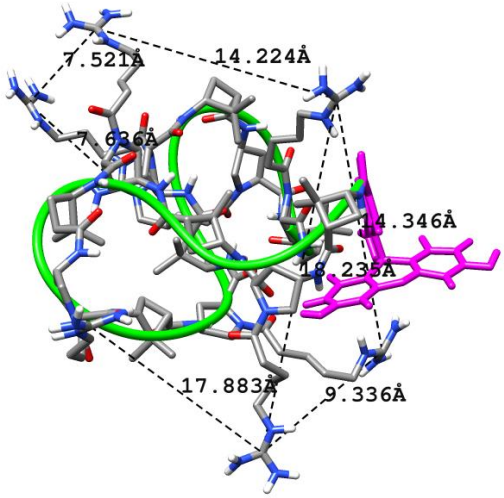

Figure A21. Shortest distances between guanidinium residues in the **CF-γ-CC** hairpin conformation predicted by MD simulations.

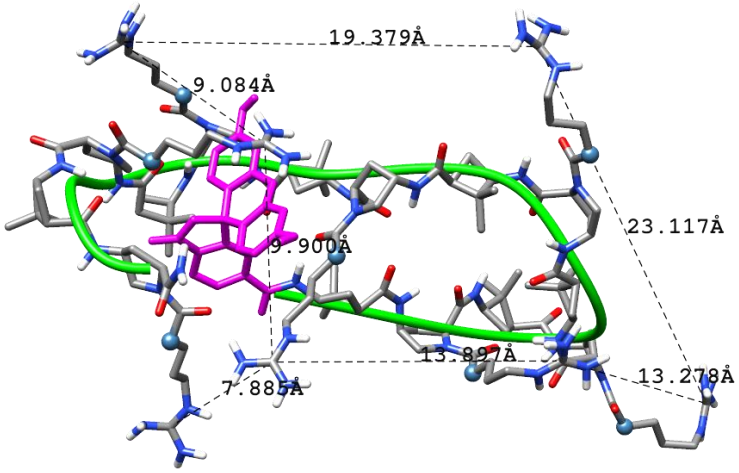

Figure A22. Shortest distances between guanidinium residues in the **CF-γ-CC** laminar conformation predicted by MD simulations.

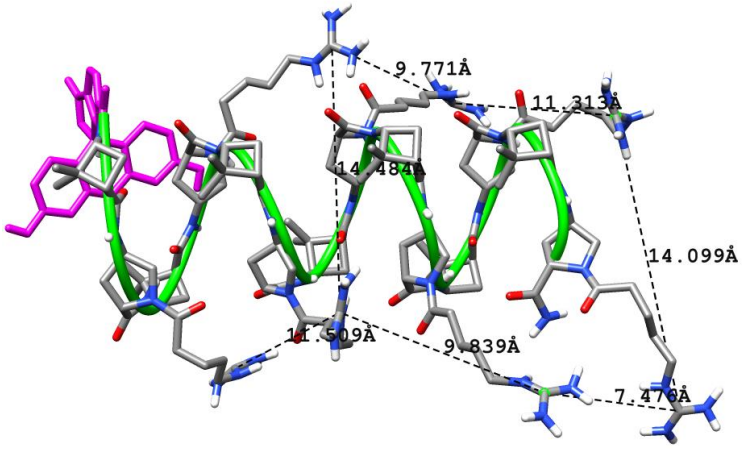

Figure A23. Shortest distances between guanidinium residues in the **CF-γ-CT** helical conformation predicted by MD simulations.

Chapter II. Novel Bifunctional Ligands for PET Imaging with ^{64}Cu and ^{68}Ga Radioisotopes

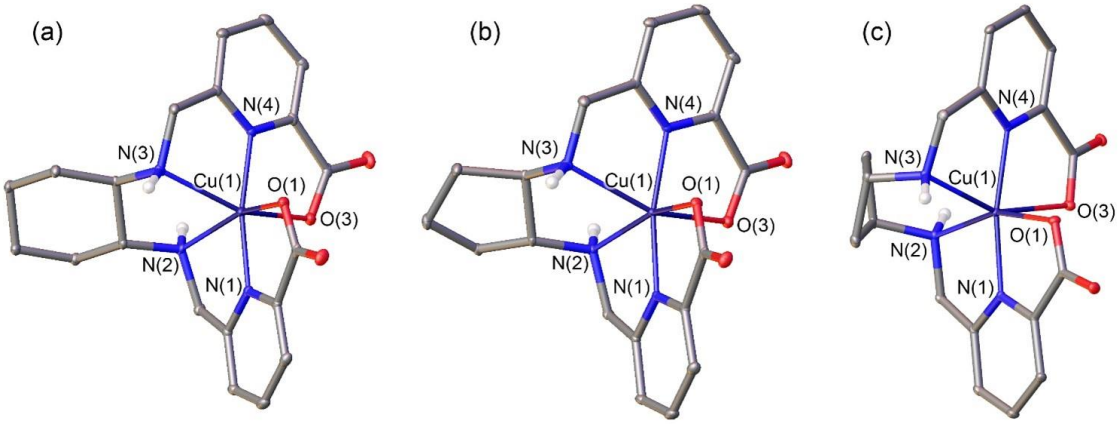

Figure A24. X-ray structures of: (a) **[Cu(CHXDEDPA)]**·$(CH_3)_2CO·H_2O$, (b) **[Cu(CPDEDPA)]**·$4H_2O$ and (c) **[Cu(CBuDEDPA)]**·H_2O with ellipsoids plotted at the 30% probability level. Solvent molecules and H atoms bonded to C atoms are omitted for simplicity.

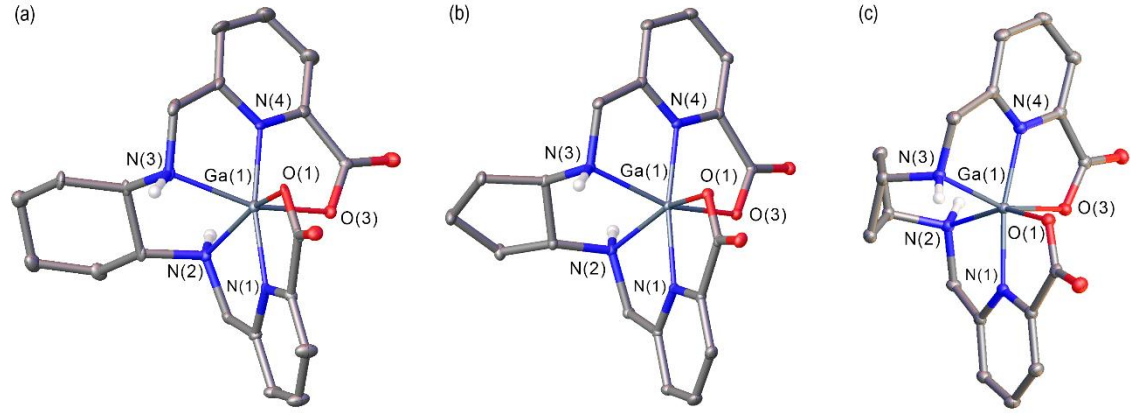

Figure A25. X-ray structures of: (a) **[Ga(CHXDEDPA)]**·NO_3·H2O, (b) **[Ga(CPDEDPA)]**·PF_6 and (c) **[Ga(CBuDEDPA)]**·NO_3 with ellipsoids plotted at the 30% probability level. Solvent molecules and H atoms bonded to C atoms are omitted for simplicity.

Accession Codes: Deposition Numbers 2382367−2382369 contain the supplementary crystallographic data for this paper. These data can be obtained free of charge via the joint Cambridge Crystallographic Data Centre (CCDC) and Fachinformationszentrum Karlsruhe Access Structures service.

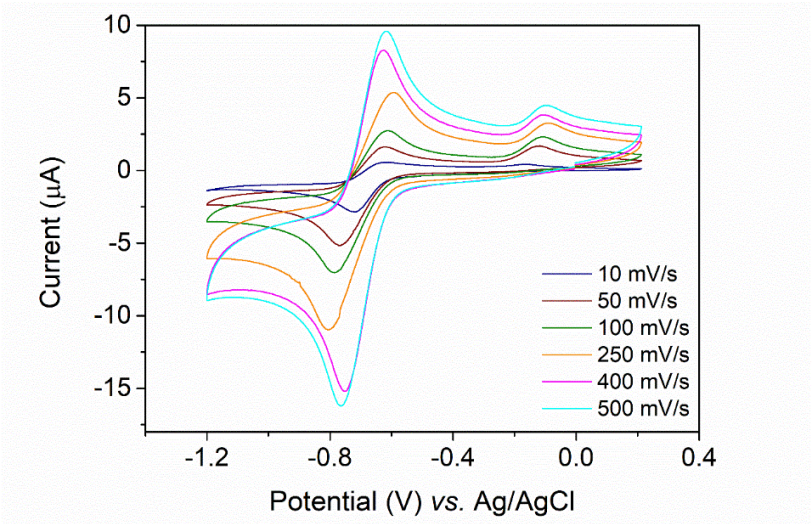

Figure A26. Cyclic voltammogram of **[Cu(CHXDEDPA)]** complex in aqueous solution in 0.15 M NaCl (1.4 mM, pH = 6.6), recorded at 10, 50, 100, 250, 400 and 500 mV·s^{-1}.

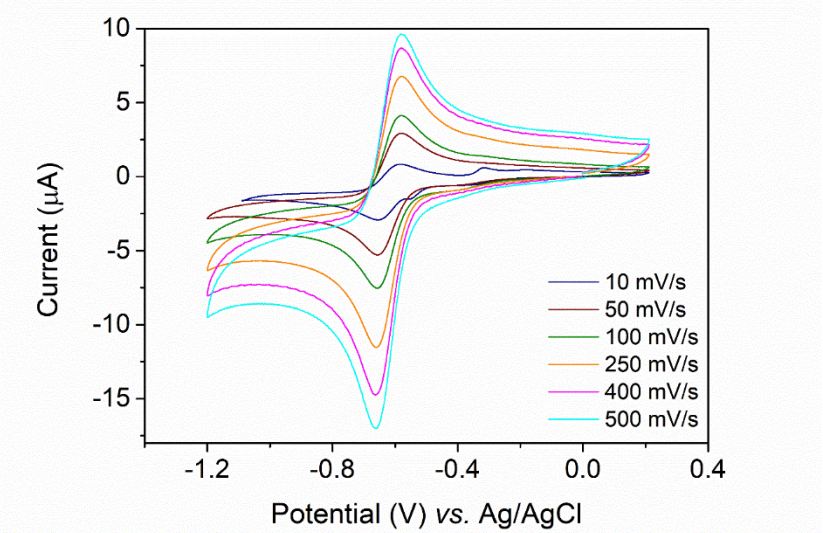

Figure A27. Cyclic voltammogram of **[Cu(CPDEDPA)]** complex in aqueous solution in 0.15 M NaCl (1.3 mM, pH = 5.9), recorded at 10, 50, 100, 250, 400 and 500 mV·s^{-1}.

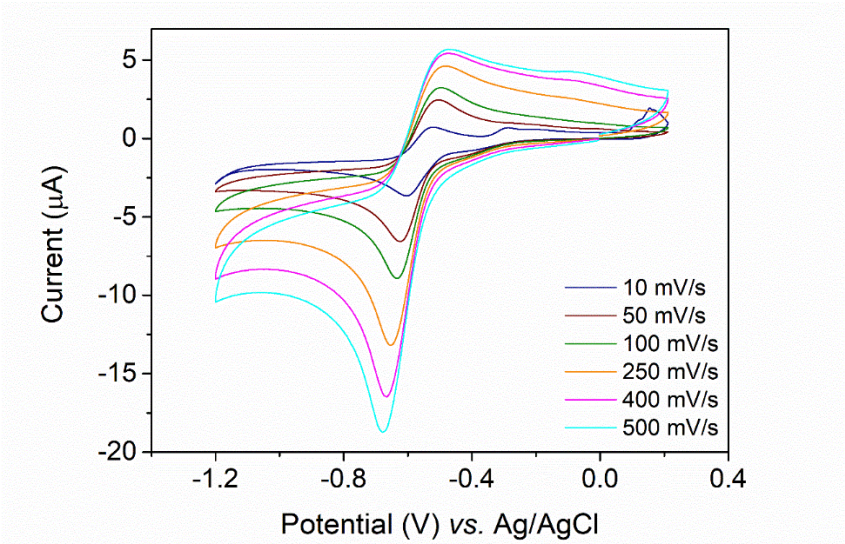

Figure A28. Cyclic voltammogram of **[Cu(CBuDEDPA)]** complex in aqueous solution in 0.15 M NaCl (1.3 mM, pH = 5.0), recorded at 10, 50, 100, 250, 400 and 500 mV·s^{-1}.

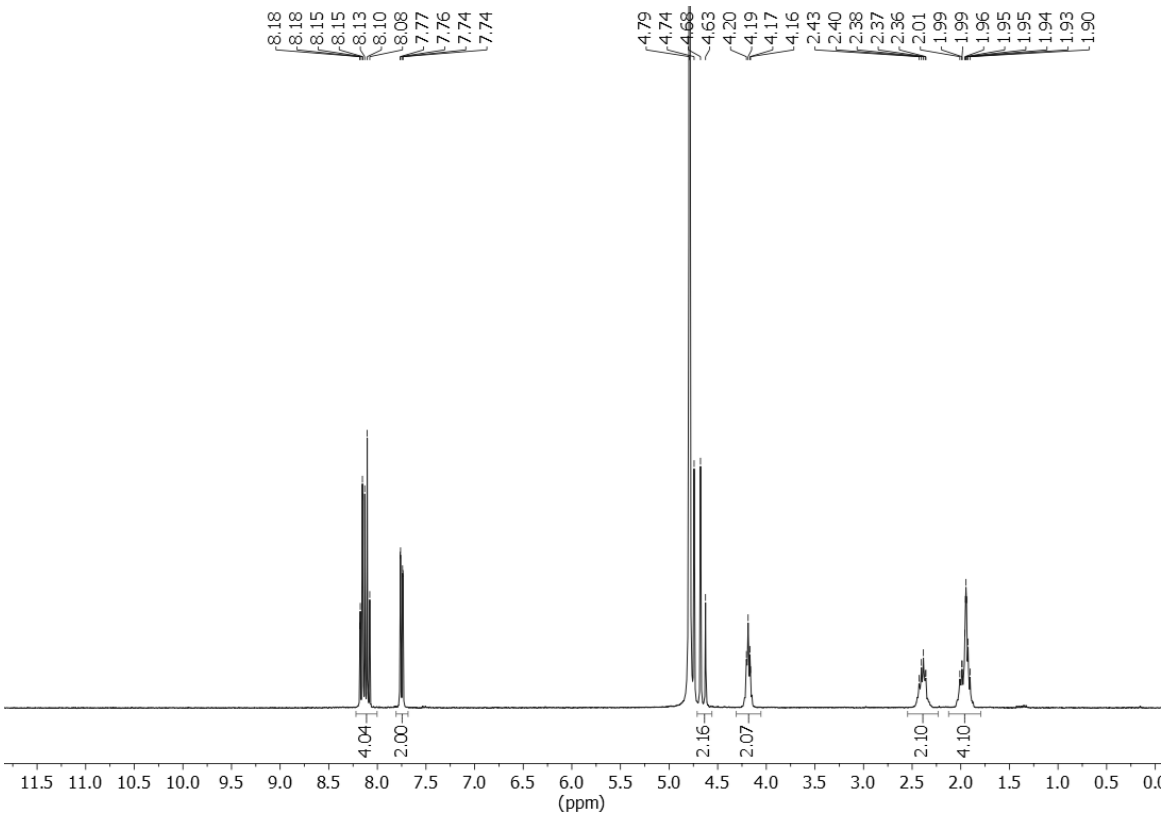

Figure A29. ^{1}H-NMR spectrum (400 MHz, D_2O) of compound **H_2CPDEDPA**.

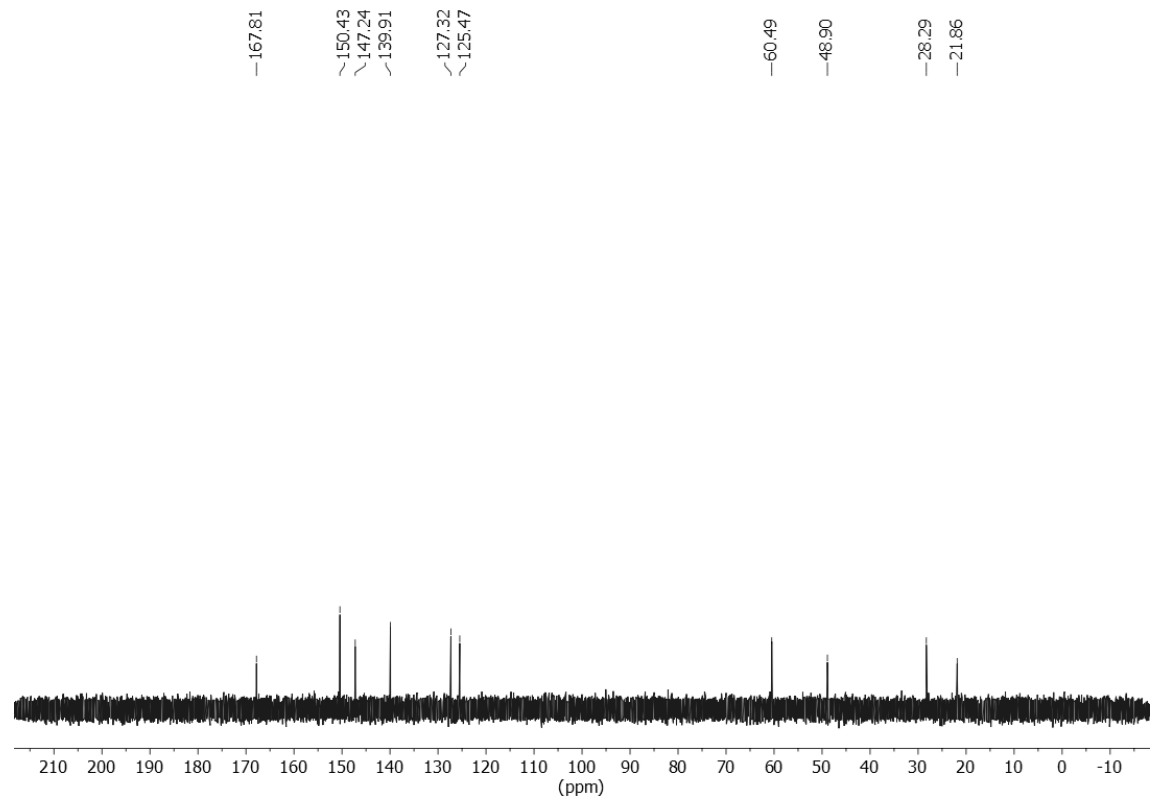

Figure A30. ^{13}C-NMR spectrum (100 MHz, D_2O) of compound **H_2CPDEDPA**.

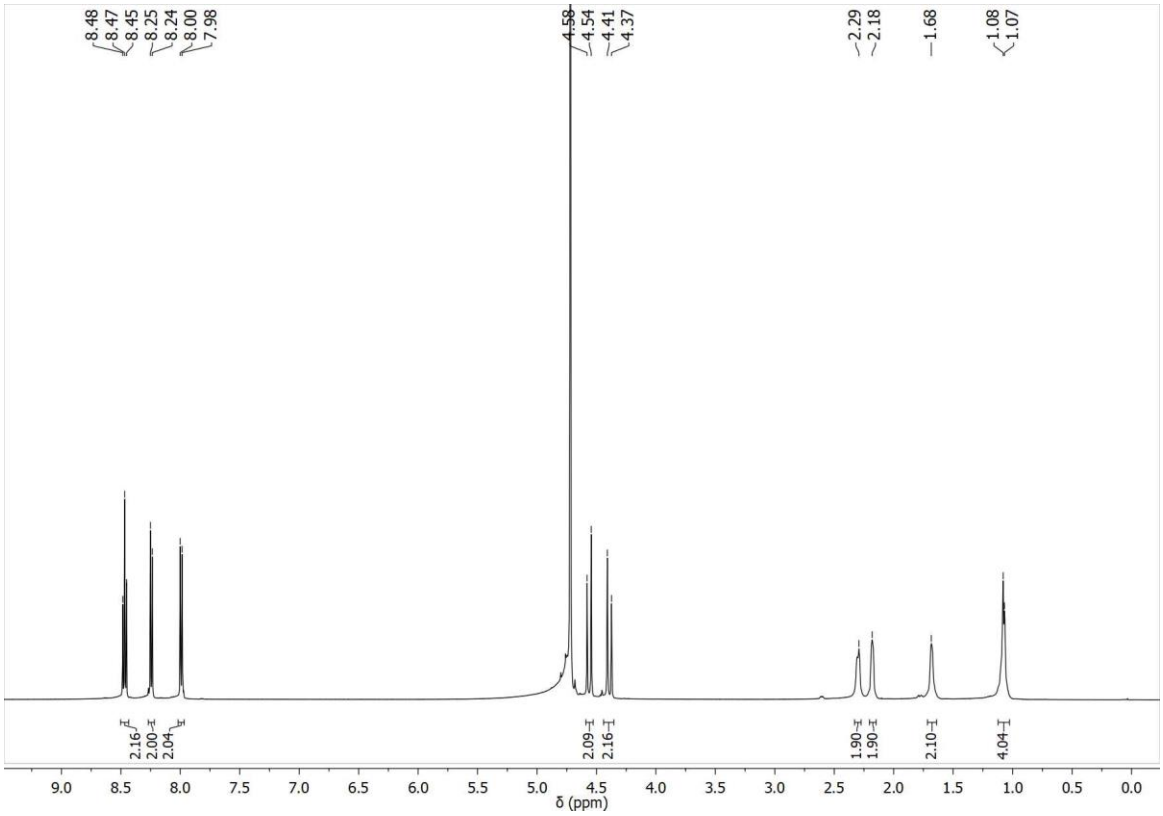

Figure A31. ^{1}H-NMR spectrum (500 MHz, D_2O) of compound **[Ga(CHXDEDPA)]NO_3**.

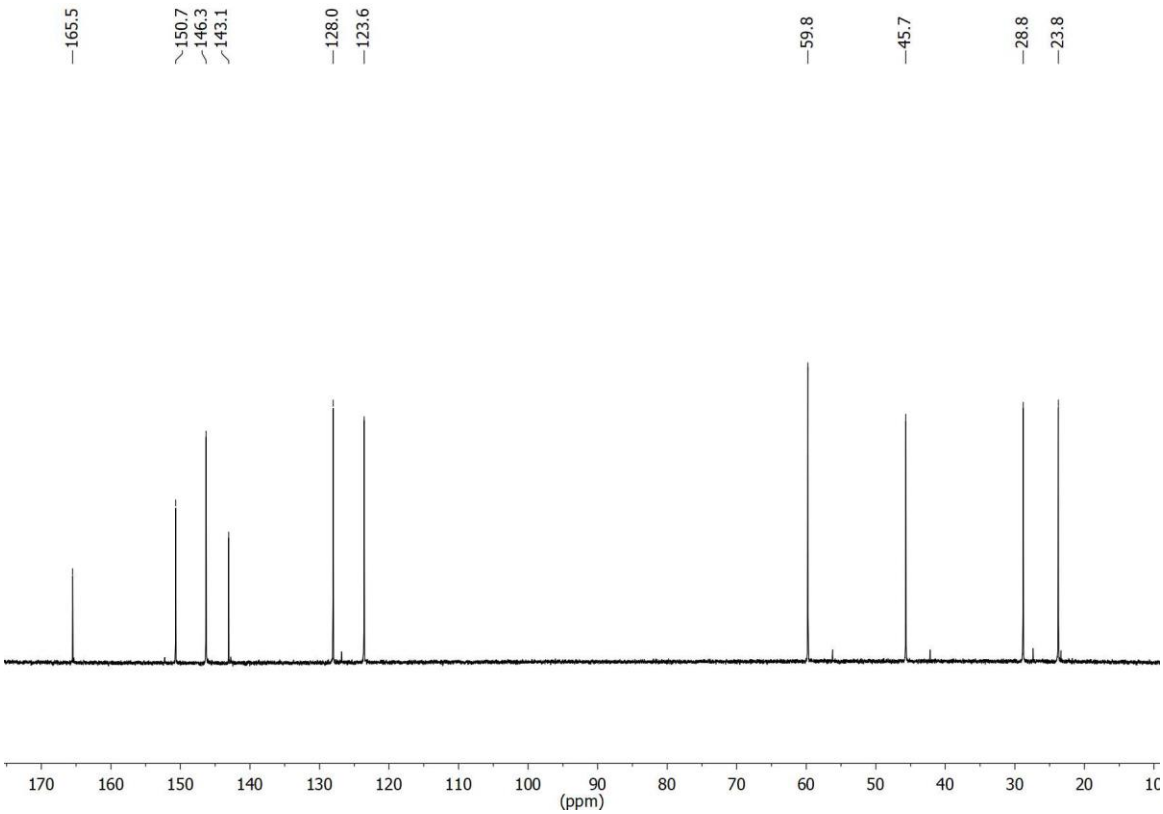

Figure A32. ^{13}C-NMR spectrum (125 MHz, D_2O) of compound **[Ga(CHXDEDPA)]NO_3**.

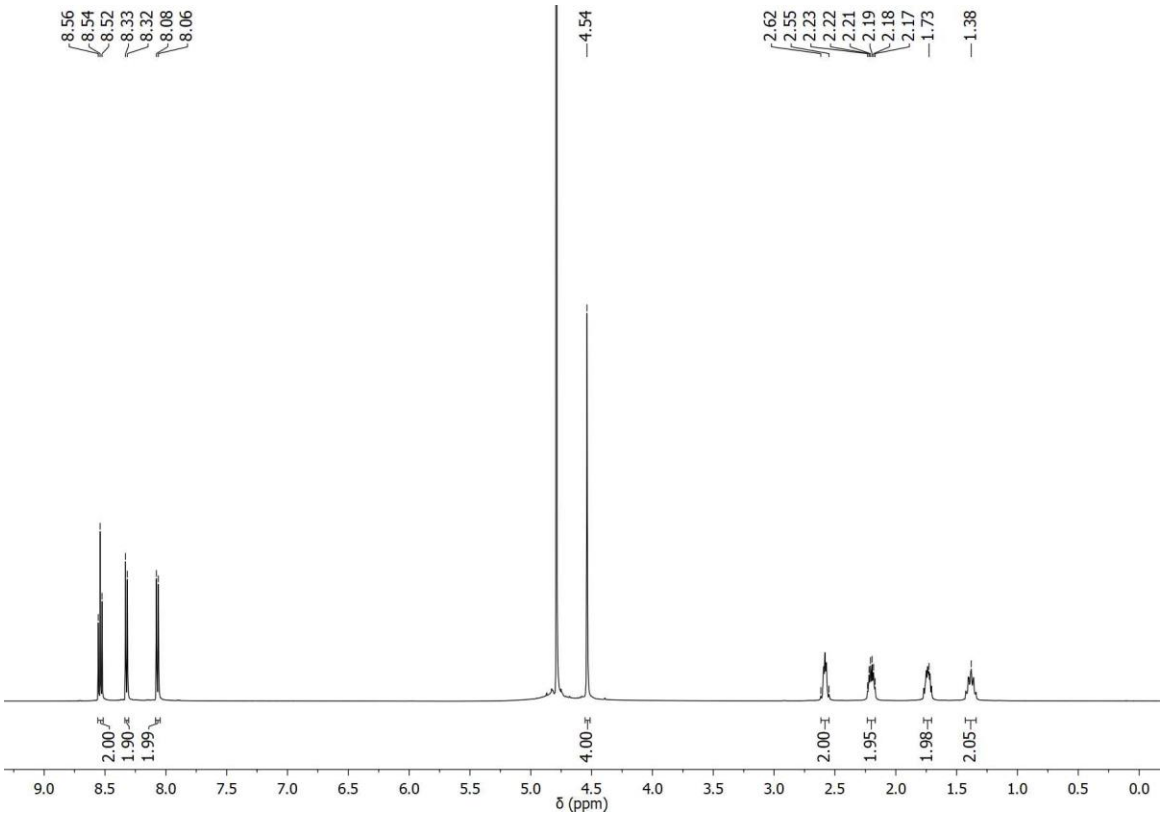

Figure A33. ^{1}H-NMR spectrum (500 MHz, D_2O) of compound **[Ga(CPDEDPA)]NO_3**.

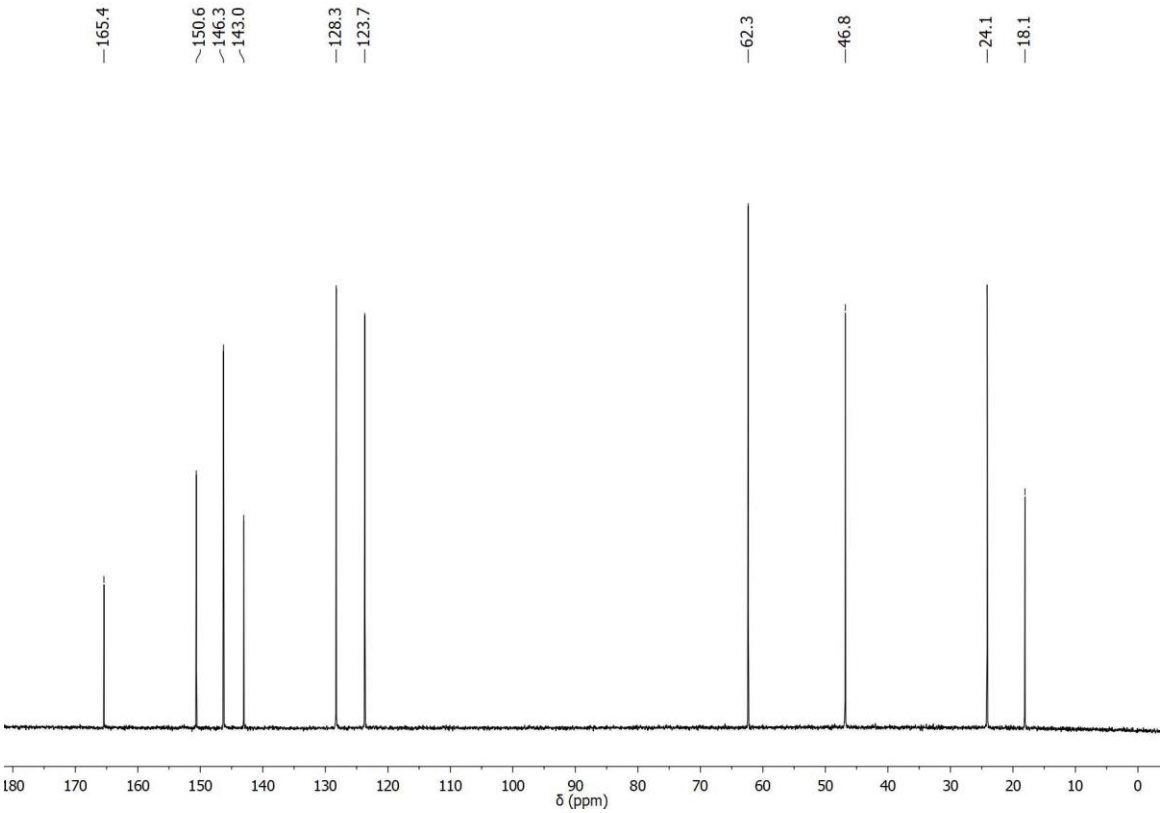

Figure A34. ^{13}C-NMR spectrum (125 MHz, D_2O) of compound **[Ga(CPDEDPA)]NO_3**.

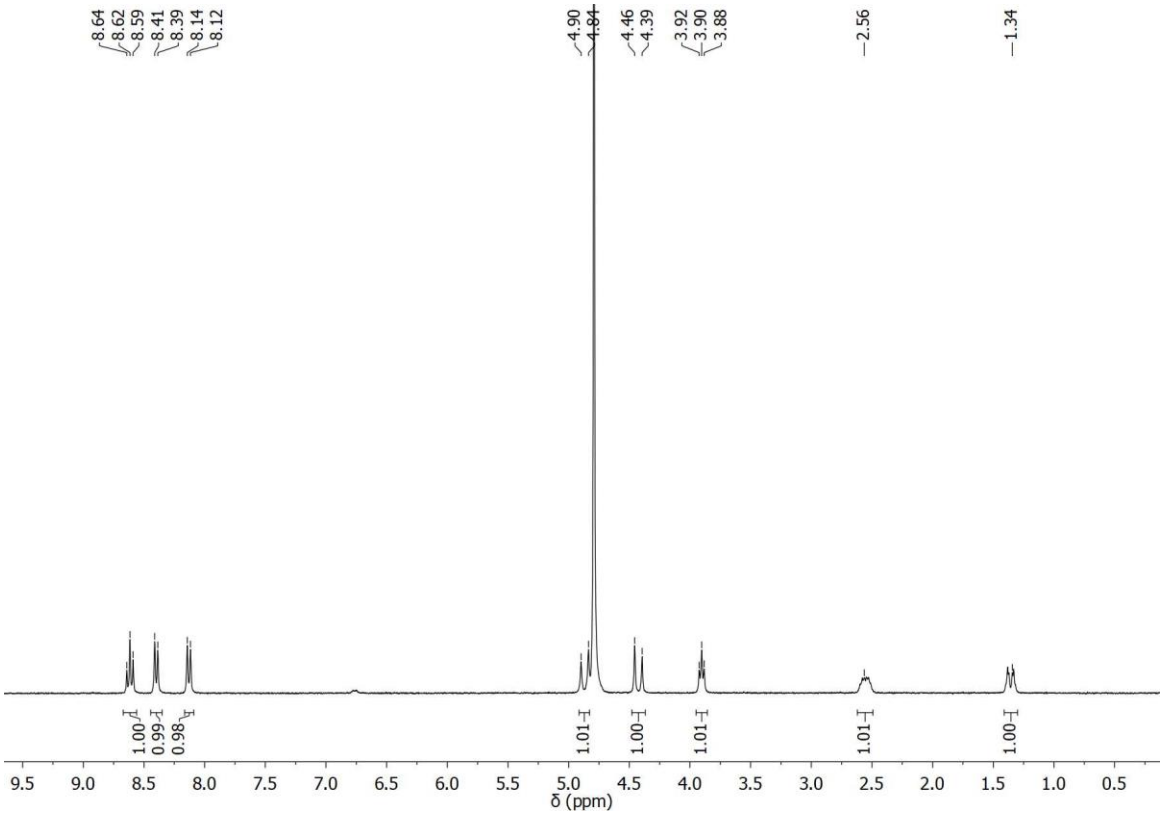

Figure A35. ^{1}H-NMR spectrum (500 MHz, D_2O) of compound **[Ga(CBuDEDPA)]NO_3**.

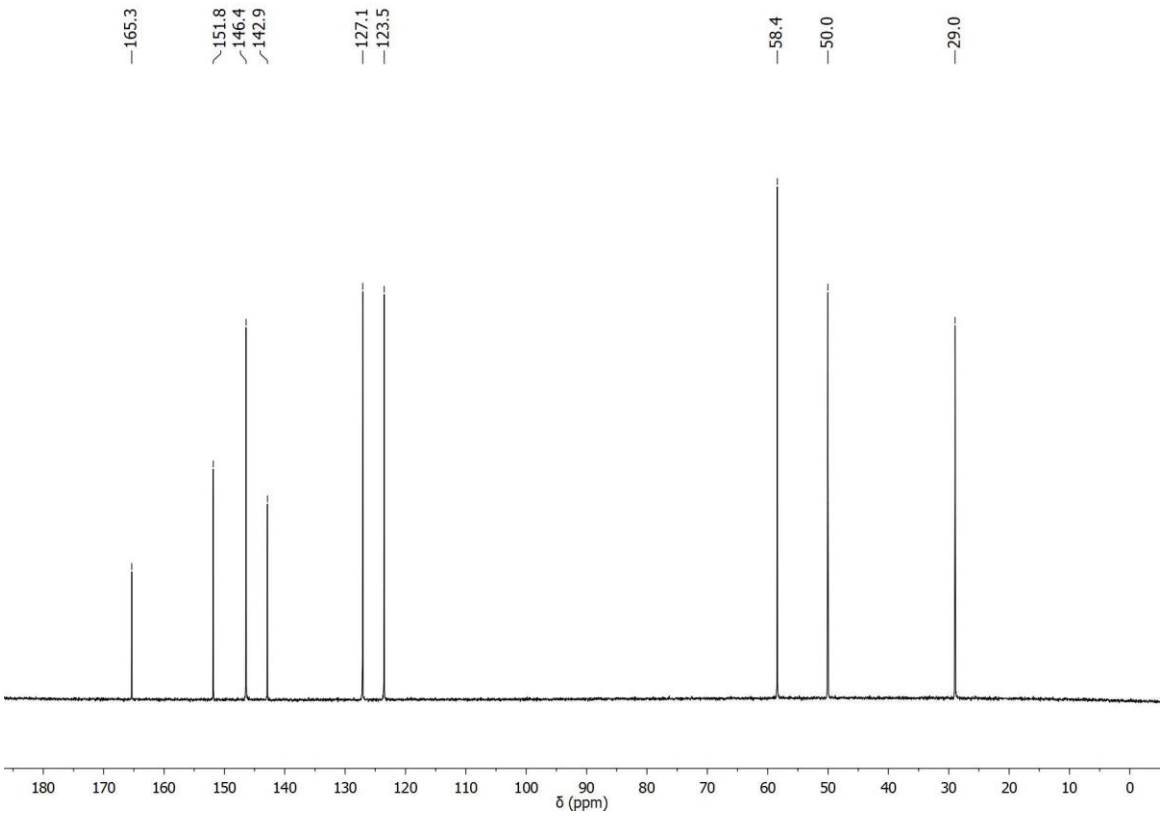

Figure A36. ^{13}C-NMR spectrum (125 MHz, D_2O) of compound **[Ga(CBuDEDPA)]NO_3**.

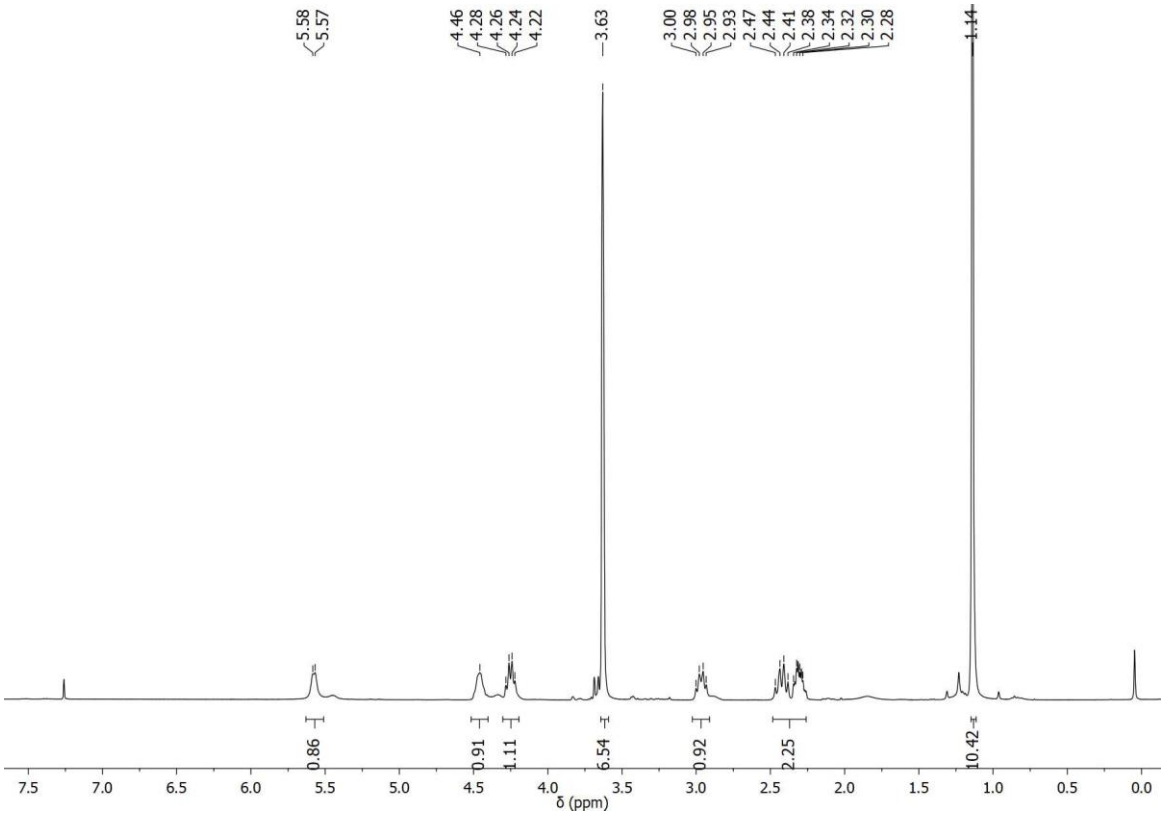

Figure A37. ^{1}H-NMR spectrum (360 MHz, $CDCl_3$) of compound **(±)-108**.

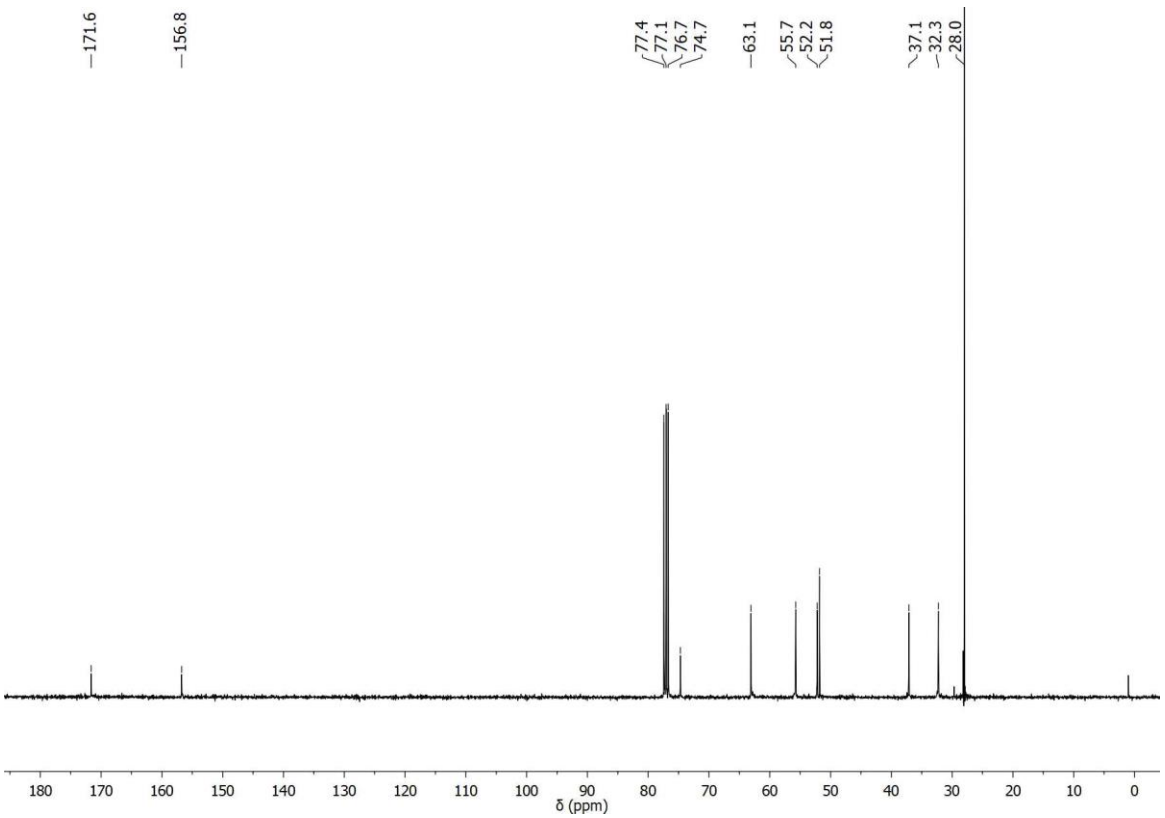

Figure A38. ^{13}C-NMR spectrum (90 MHz, $CDCl_3$) of compound **(±)-108**.

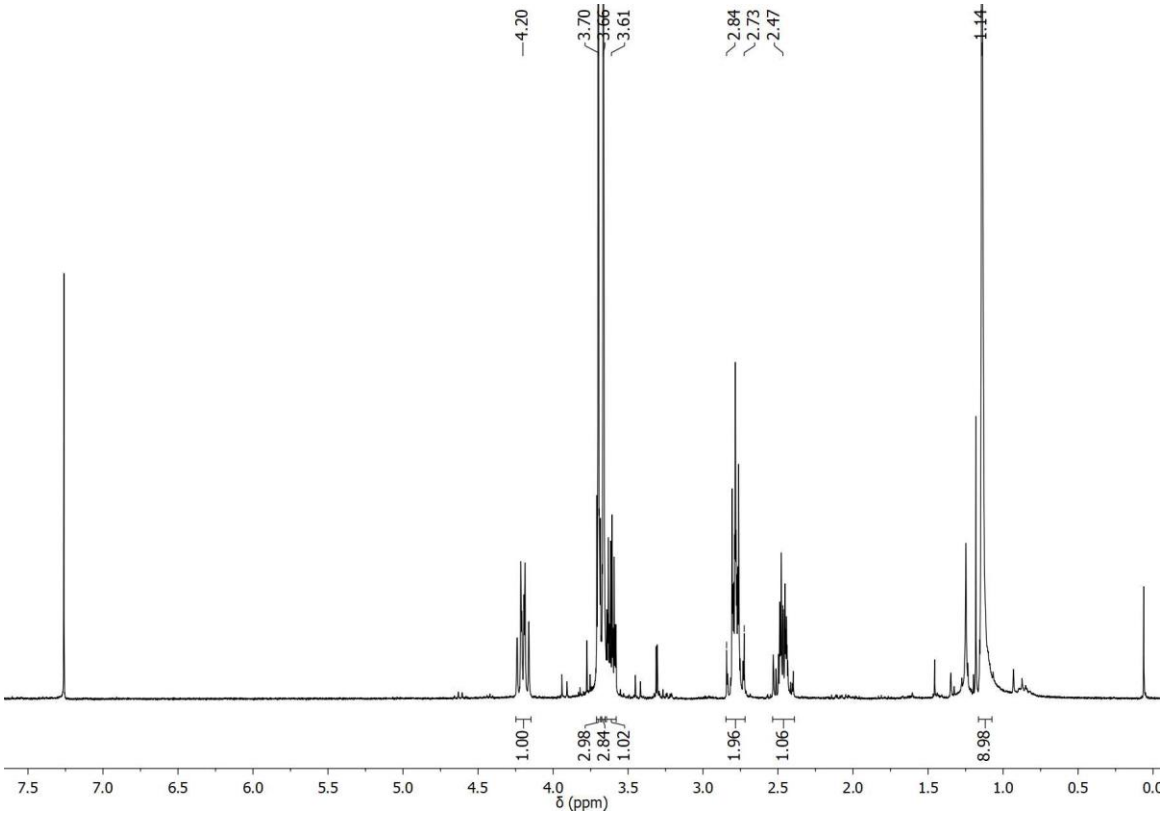

Figure A39. ^{1}H-NMR spectrum (300 MHz, $CDCl_3$) of compound **(±)-106**.

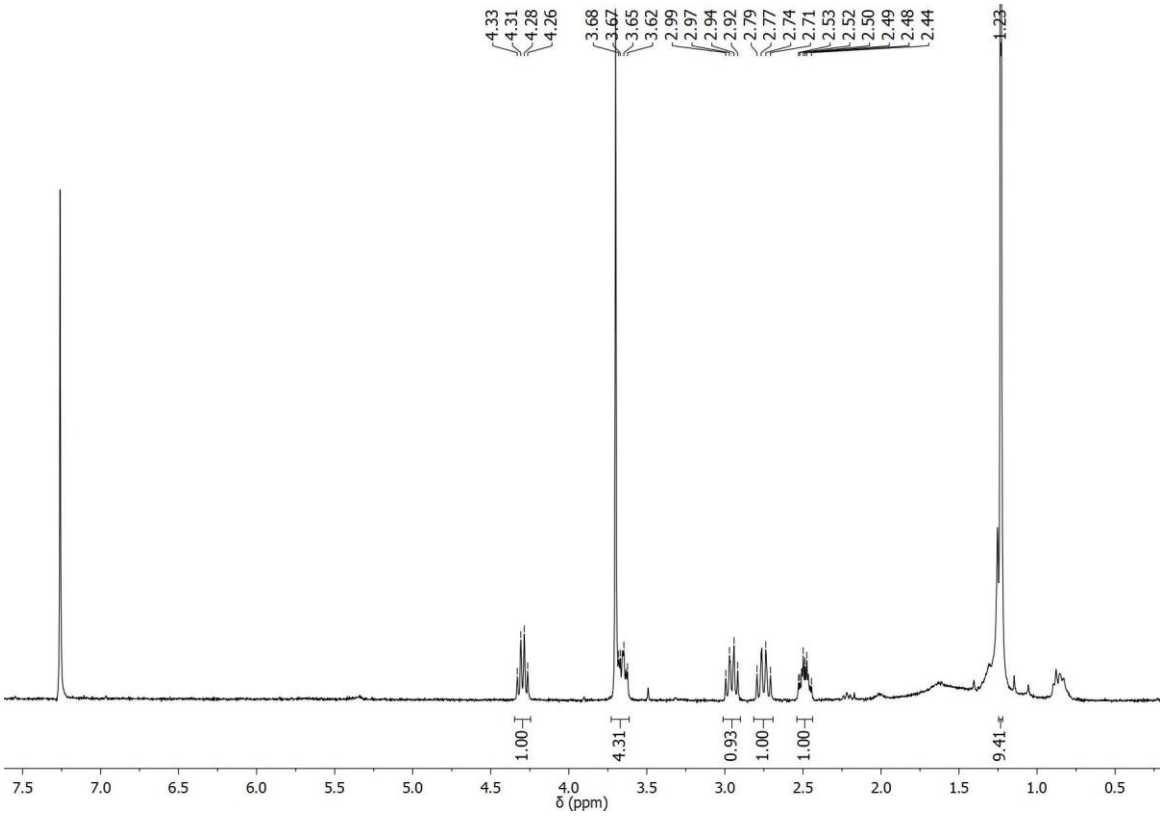

Figure A40. ^{1}H-NMR spectrum (360 MHz, $CDCl_3$) of compound **(±)-115**.

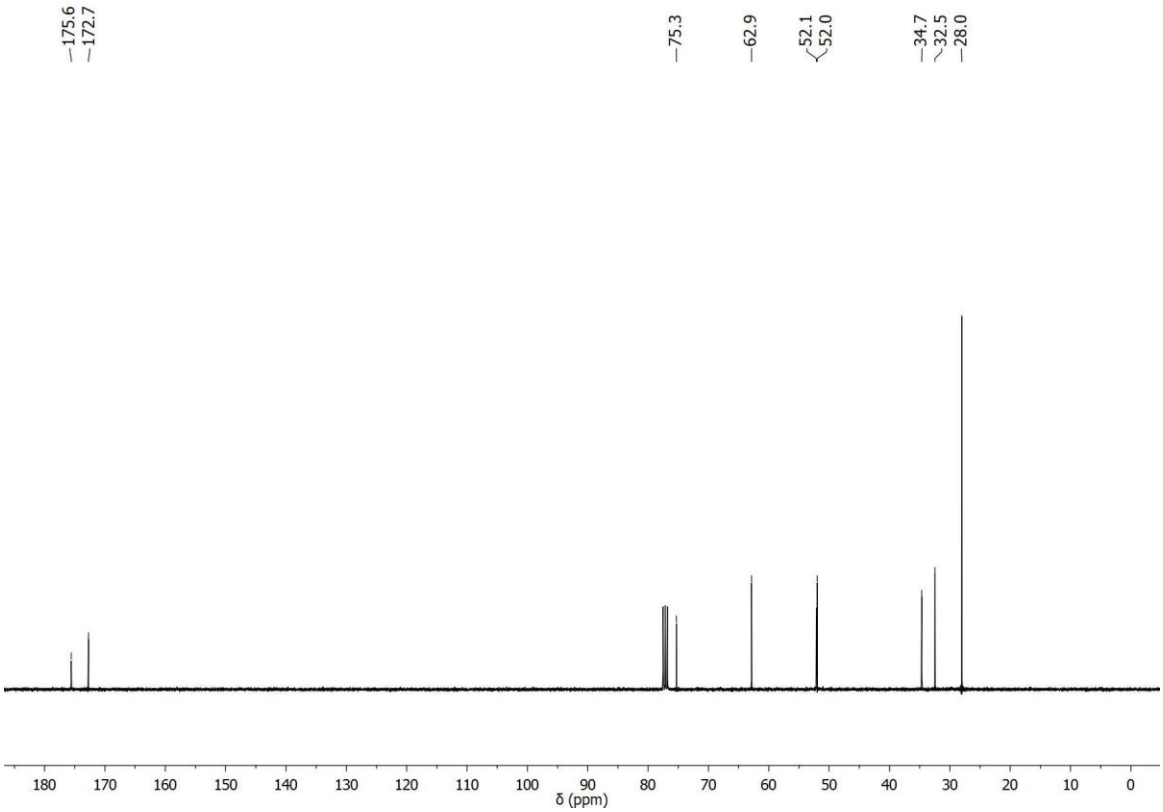

Figure A41. ^{13}C-NMR spectrum (90 MHz, $CDCl_3$) of compound **(±)-115**.

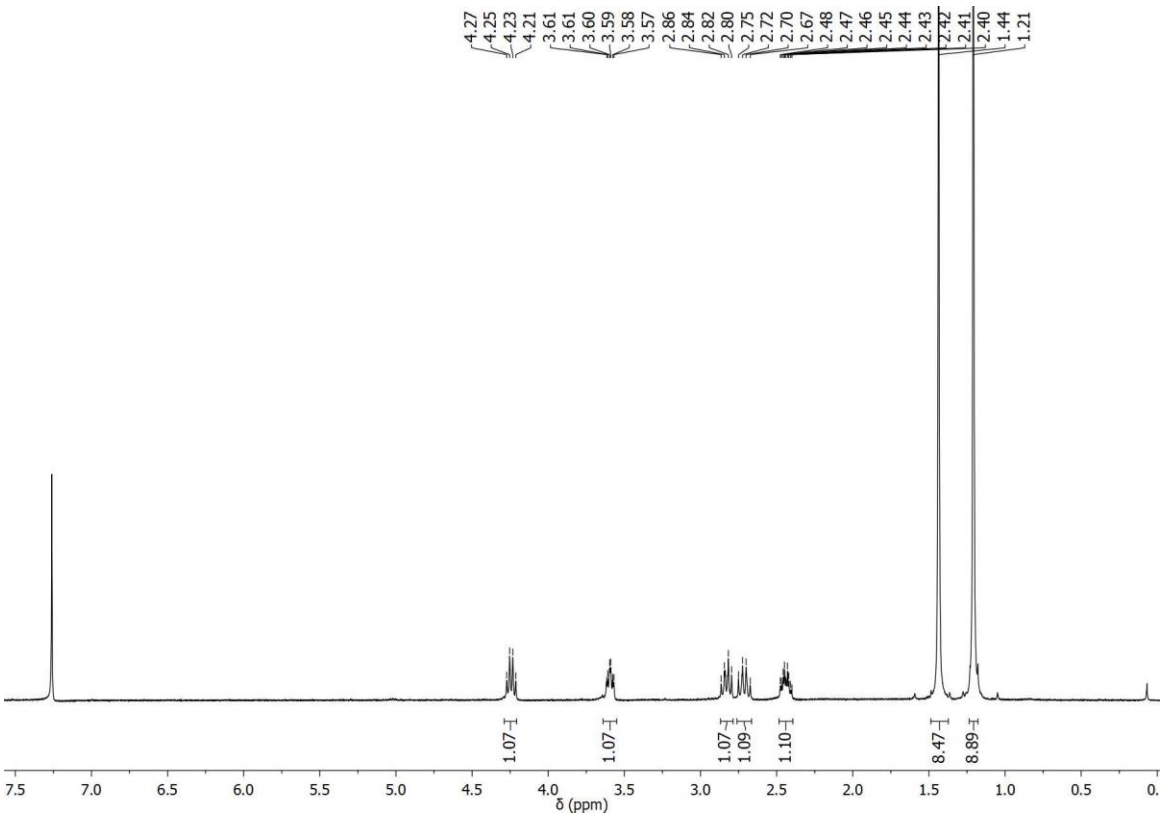

Figure A42. ^{1}H-NMR spectrum (400 MHz, $CDCl_3$) of compound **(±)-117**.

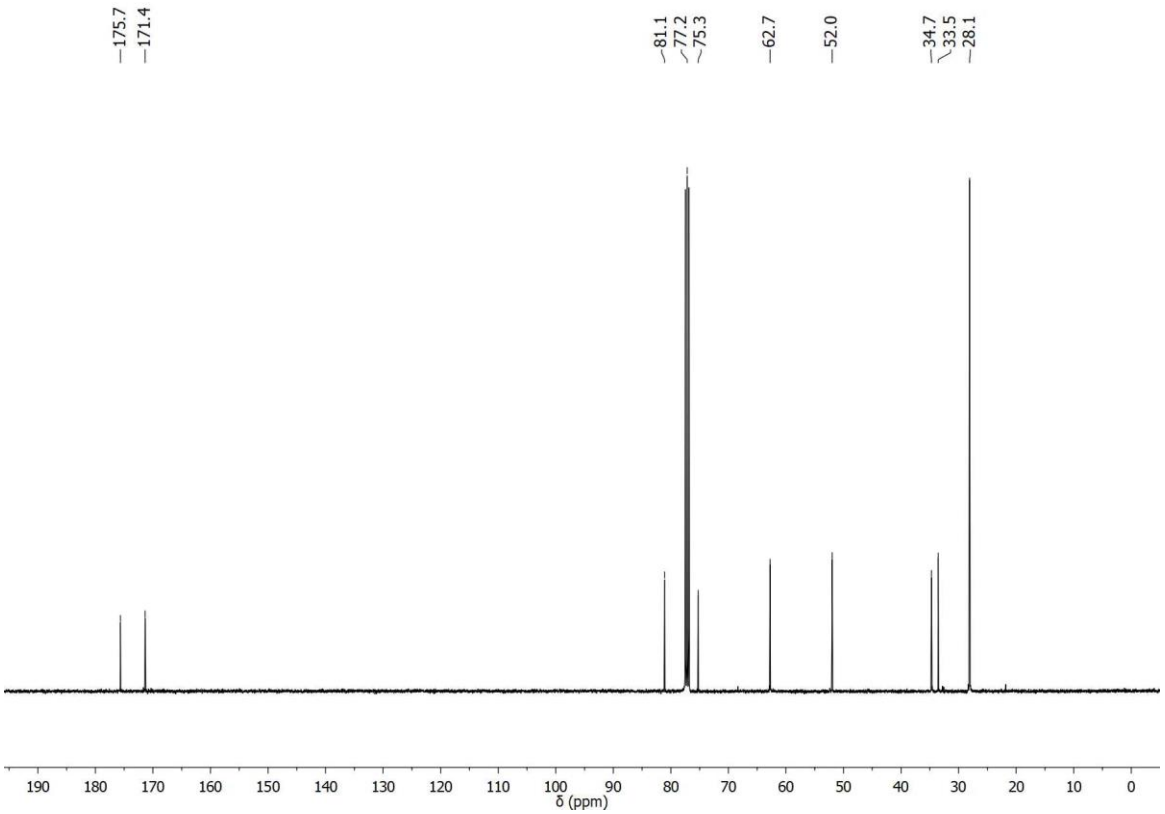

Figure A43. ^{13}C-NMR spectrum (100 MHz, $CDCl_3$) of compound **(±)-117**.

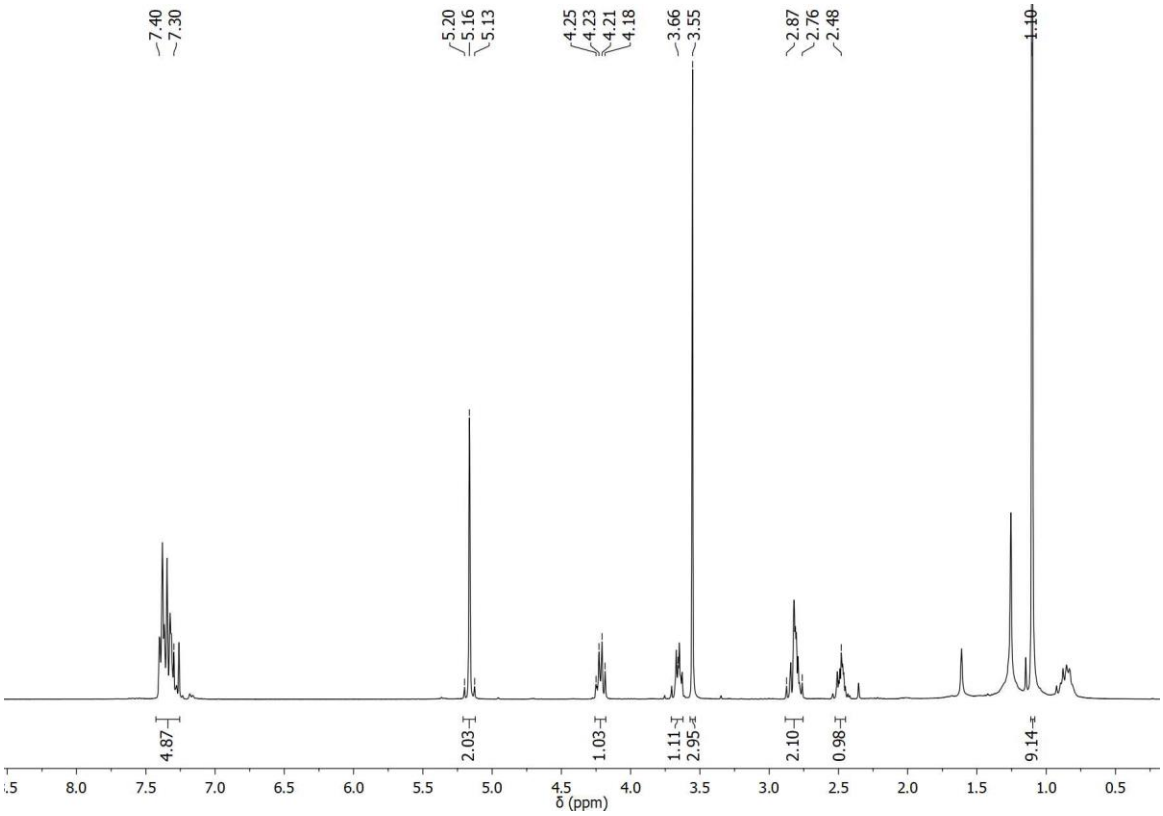

Figure A44. ^{1}H-NMR spectrum (360 MHz, $CDCl_3$) of compound **(±)-118**.

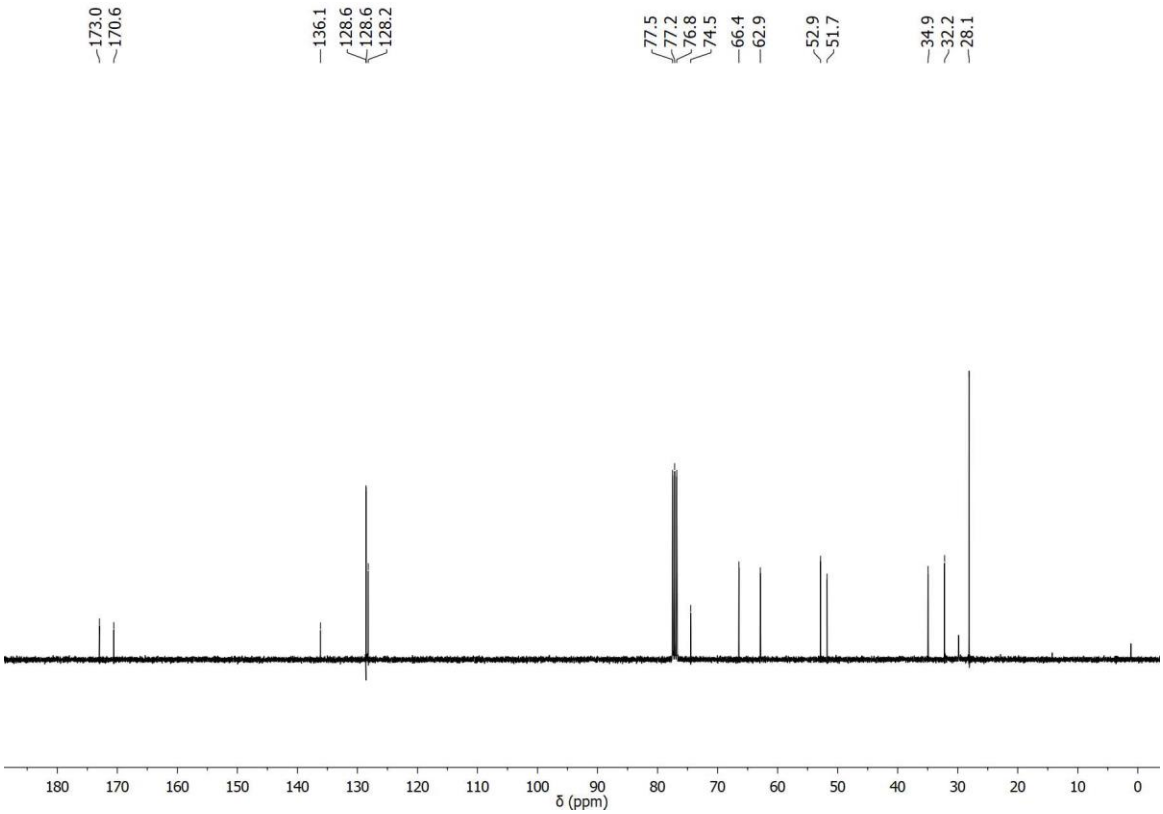

Figure A45. ^{13}C-NMR spectrum (90 MHz, $CDCl_3$) of compound **(±)-118**.

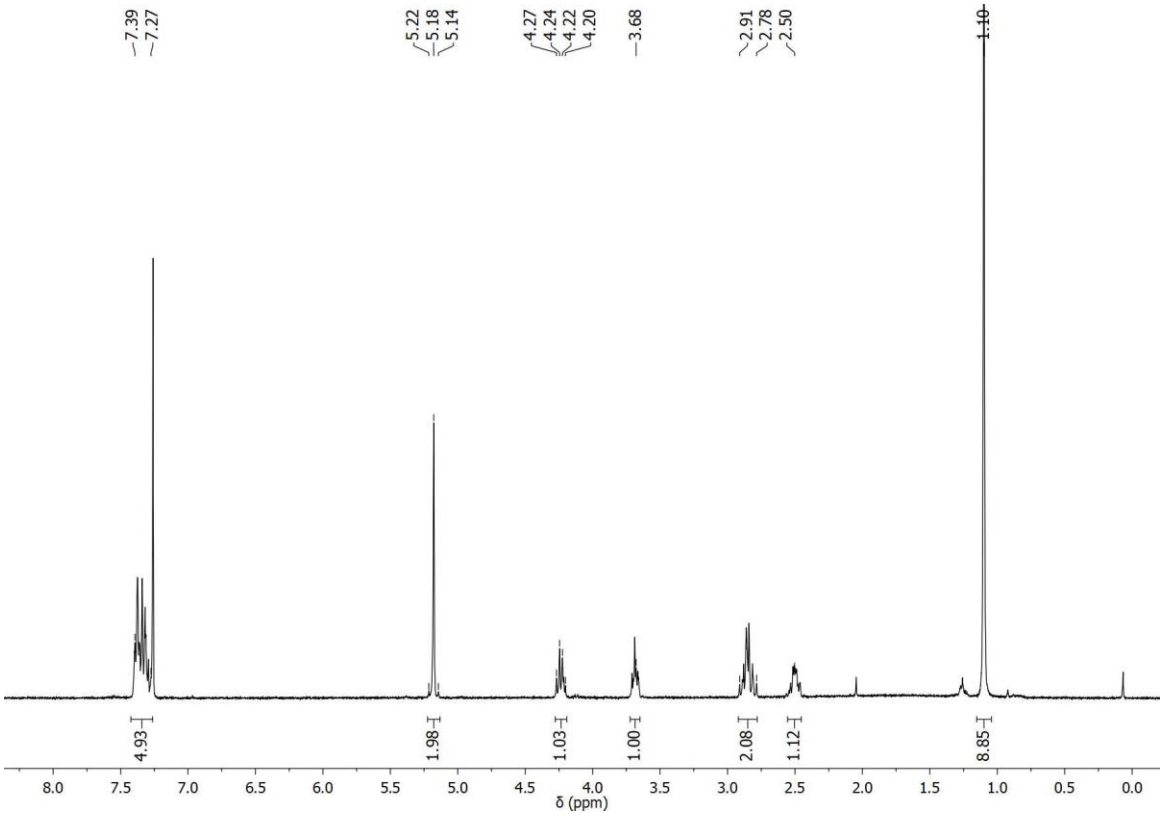

Figure A46. ^{1}H-NMR spectrum (360 MHz, $CDCl_3$) of compound **(±)-119**.

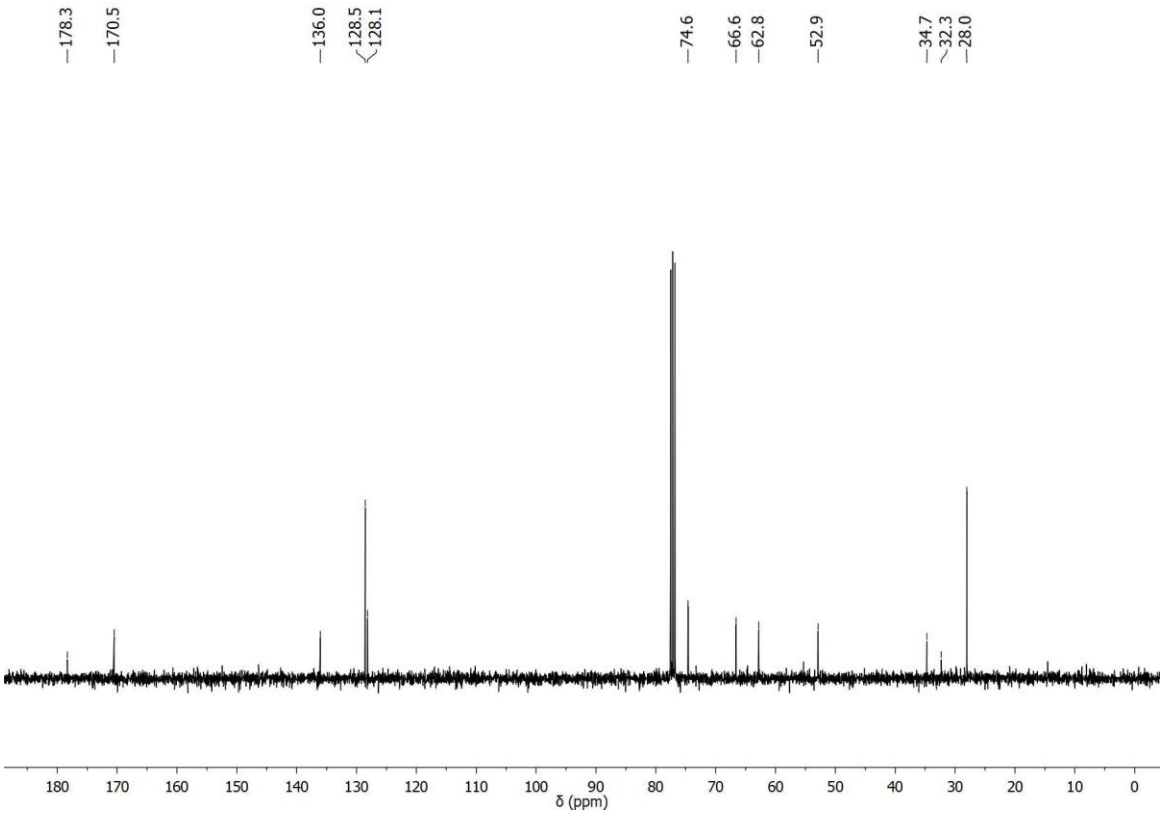

Figure A47. ^{13}C-NMR spectrum (90 MHz, $CDCl_3$) of compound **(±)-119**.

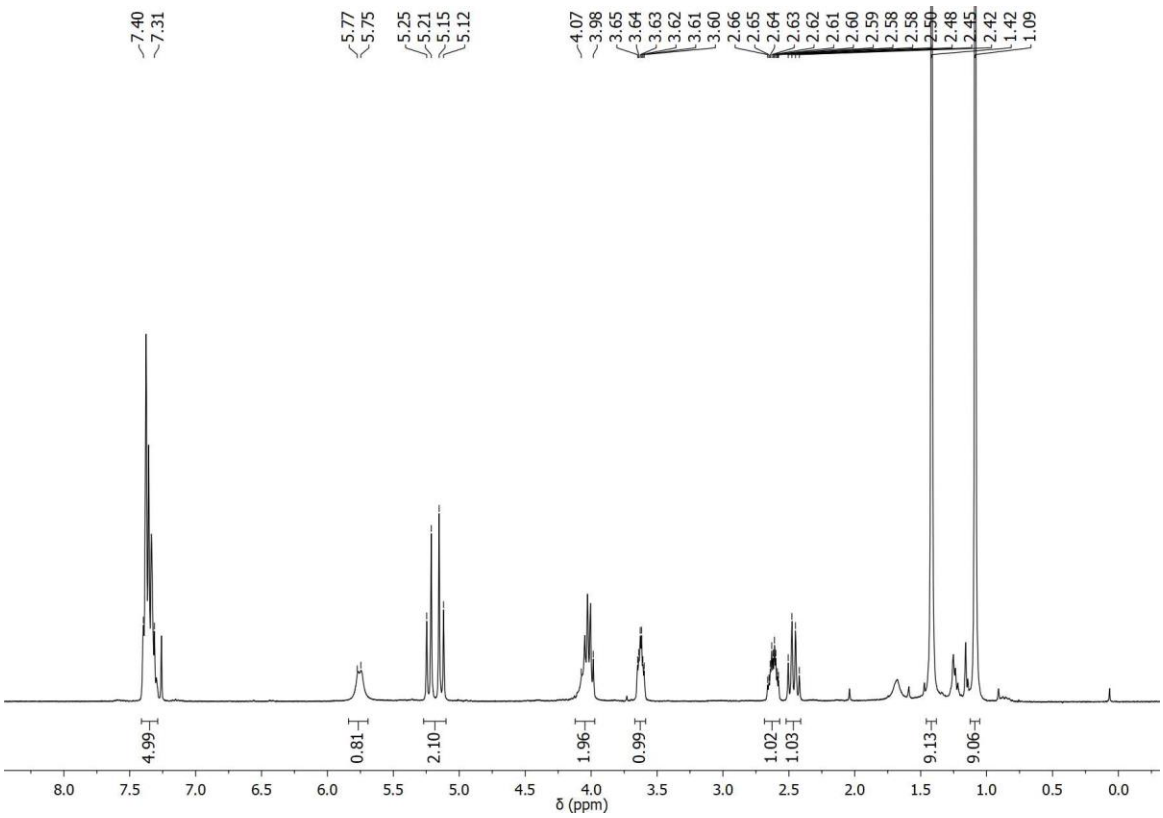

Figure A48. ^{1}H-NMR spectrum (360 MHz, $CDCl_3$) of compound **(±)-121**.

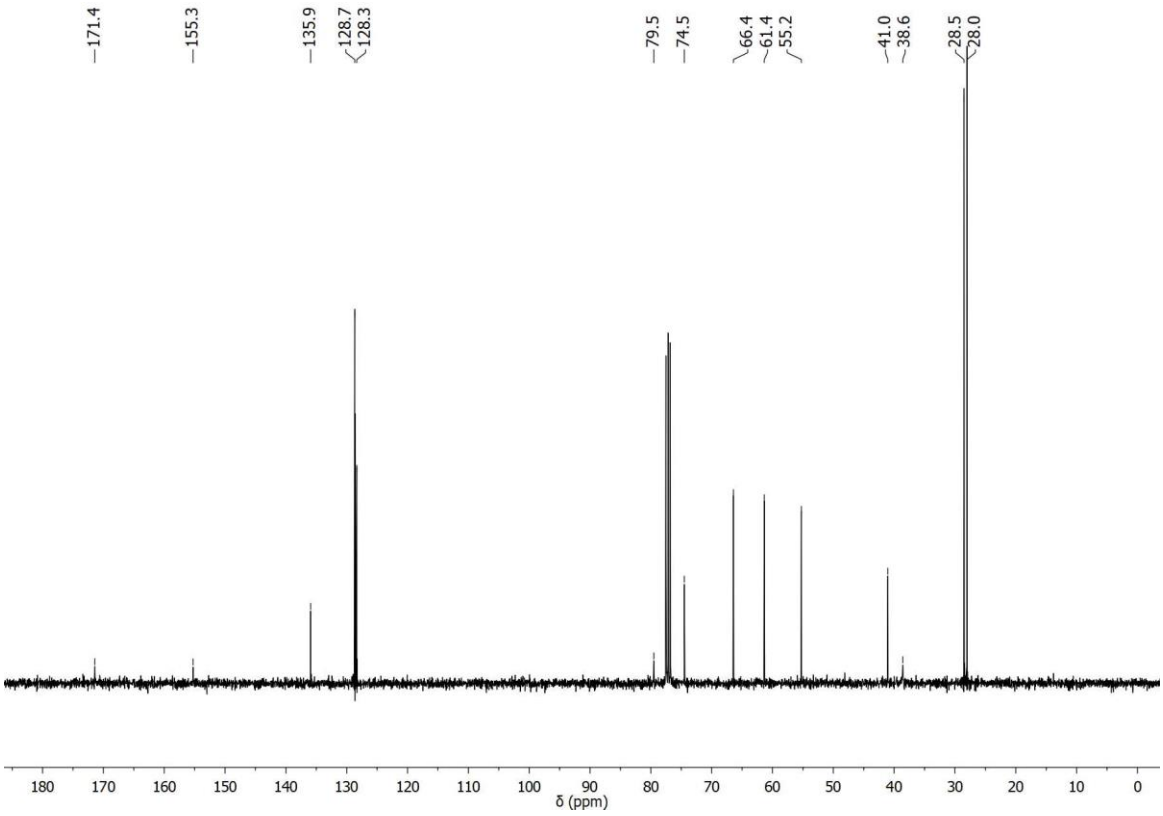

Figure A49. ^{13}C-NMR spectrum (90 MHz, $CDCl_3$) of compound **(±)-121**.

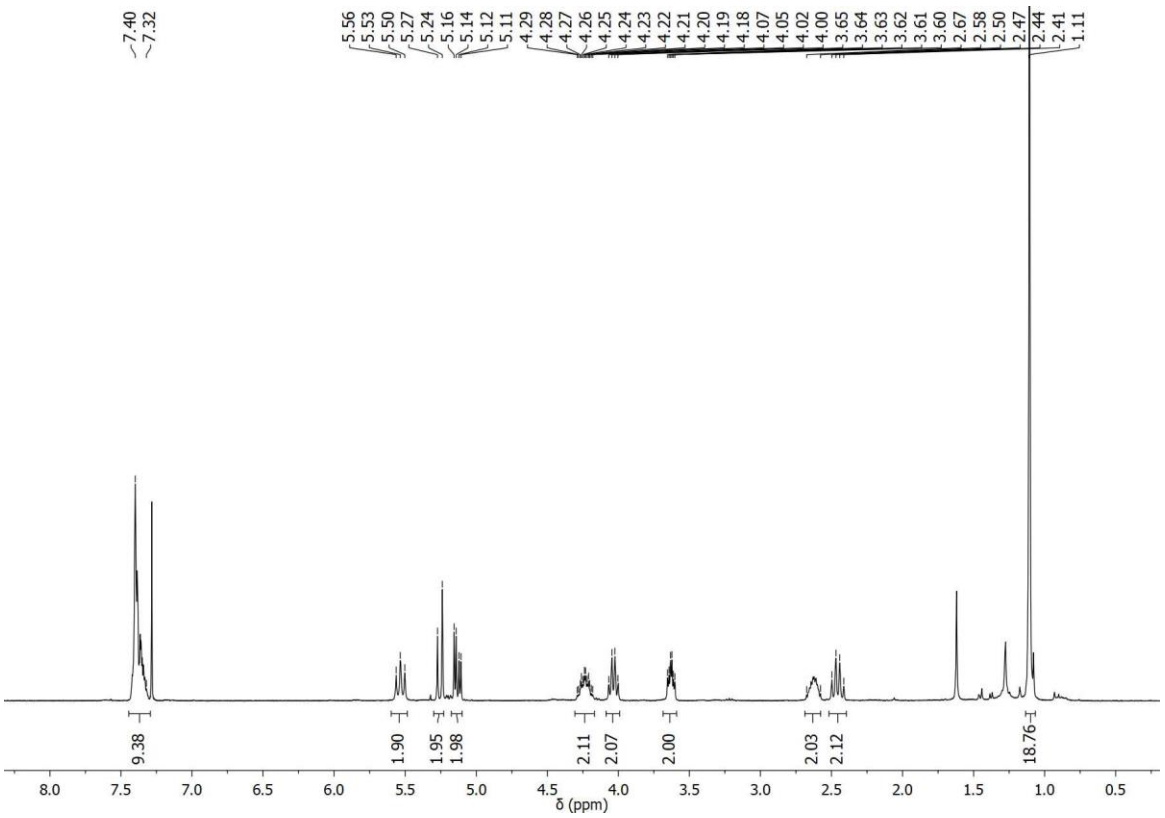

Figure A50. ^{1}H-NMR spectrum (360 MHz, $CDCl_3$) of compound **122**.

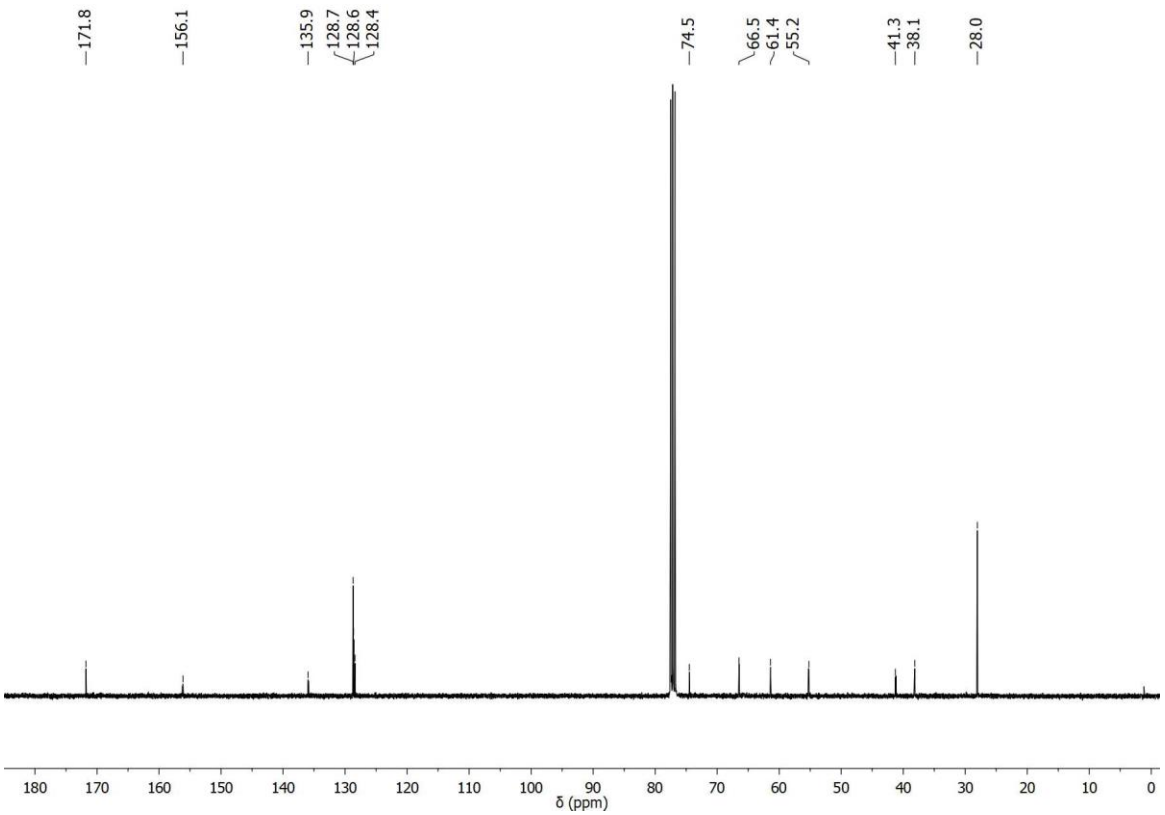

Figure A51. ^{13}C-NMR spectrum (90 MHz, $CDCl_3$) of compound **122**.

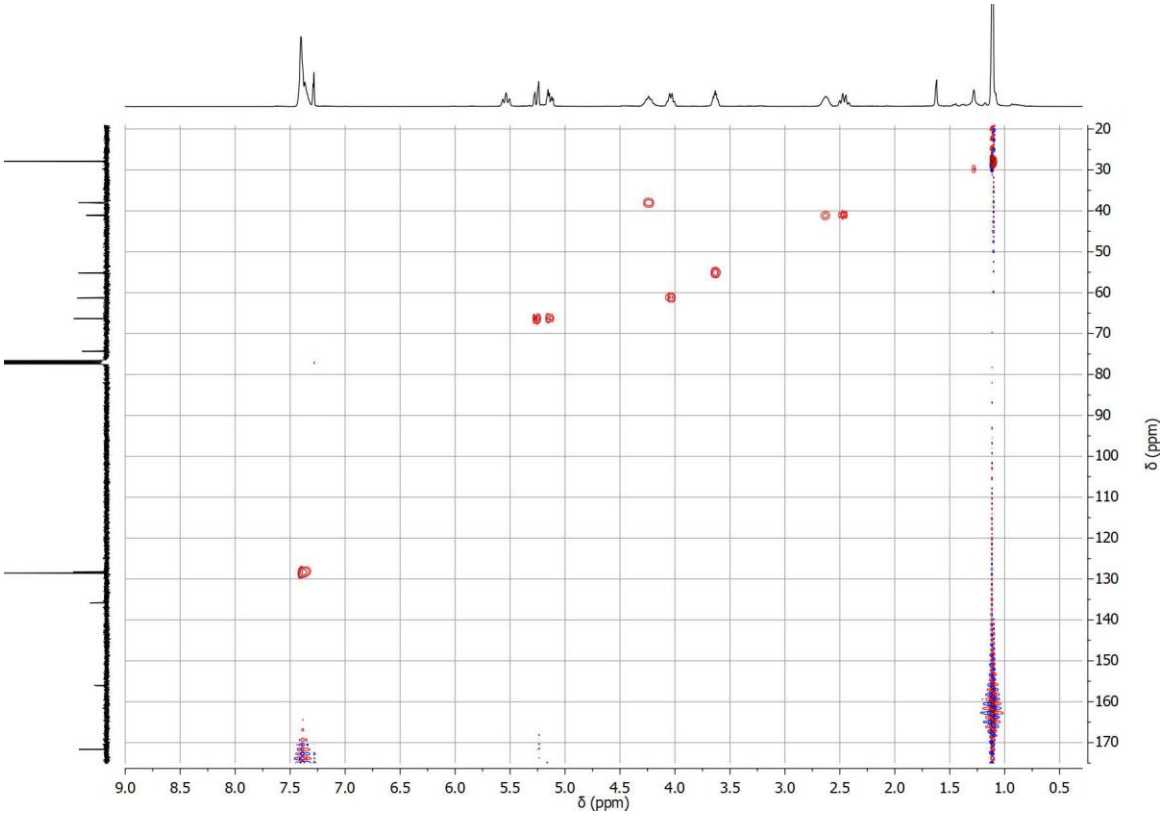

Figure A52. HSQC spectrum (360 MHz, $CDCl_3$) of compound **122**.

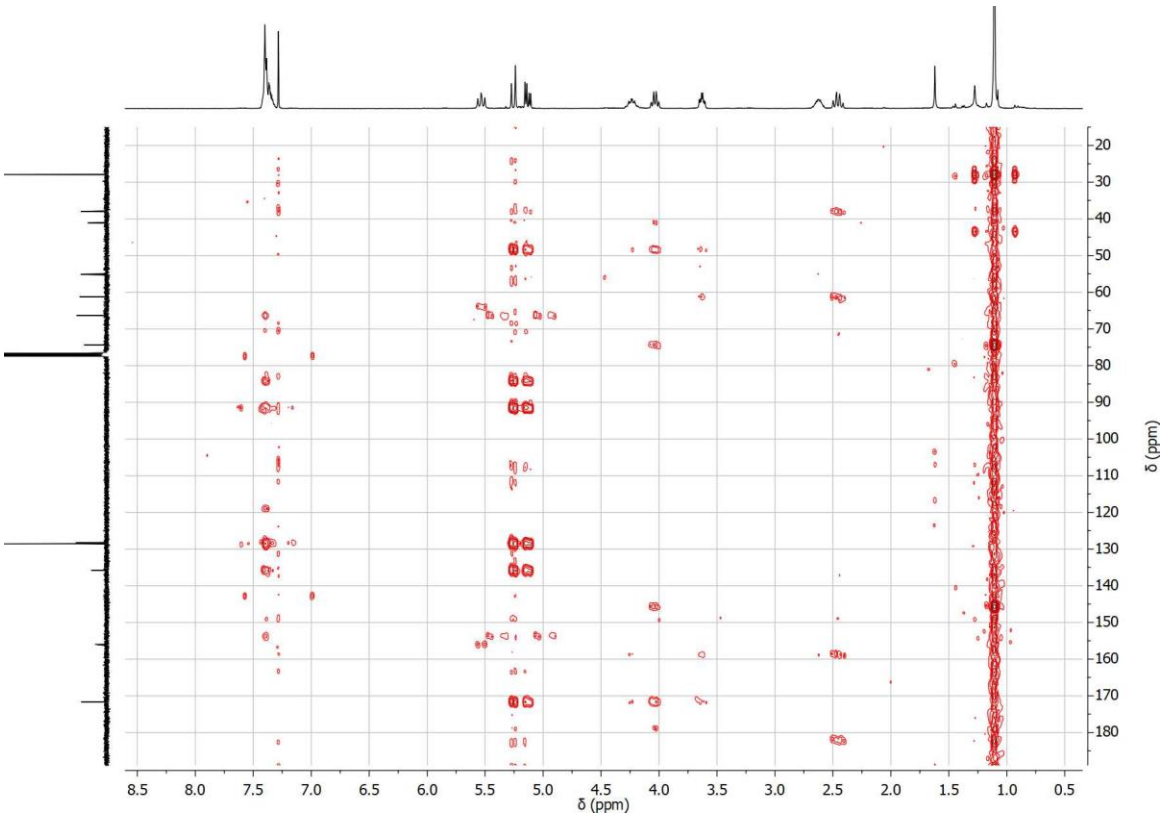

Figure A53. HSQC spectrum (400 MHz, $CDCl_3$) of compound **122**.

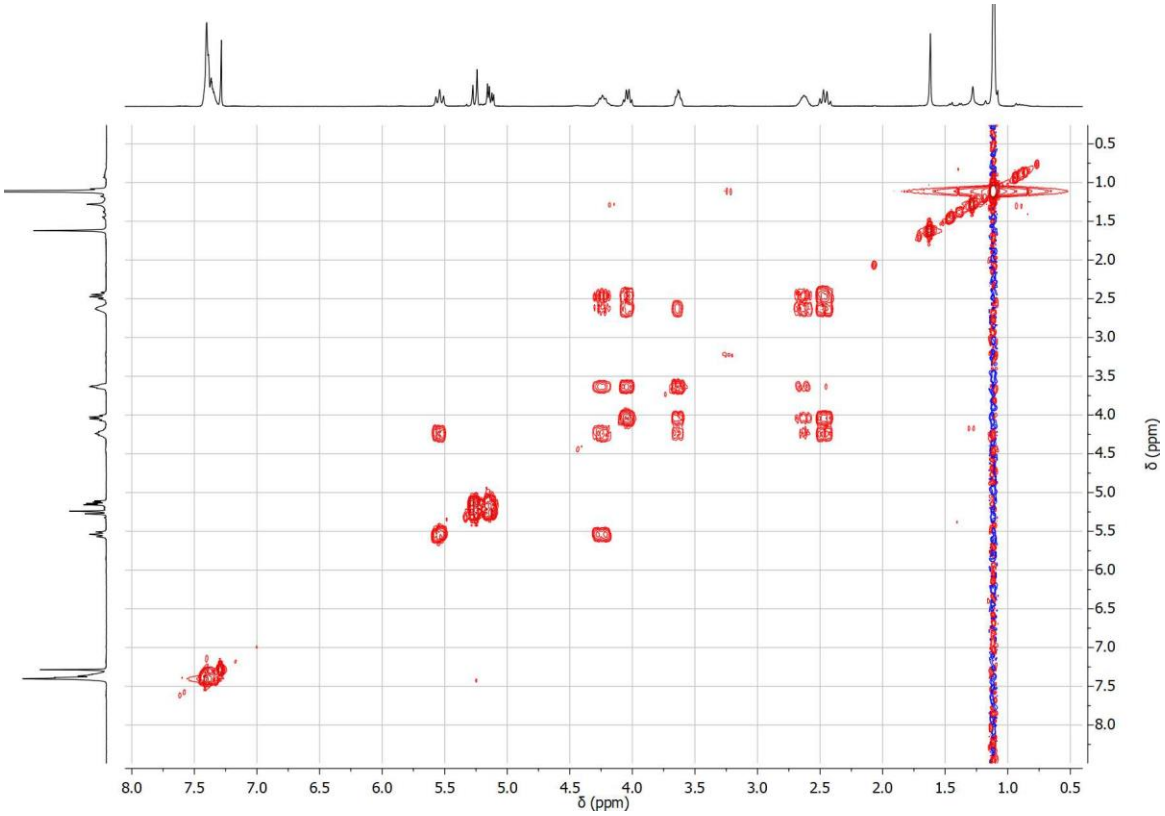

Figure A54. COSY spectrum (360 MHz, $CDCl_3$) of compound **122**.

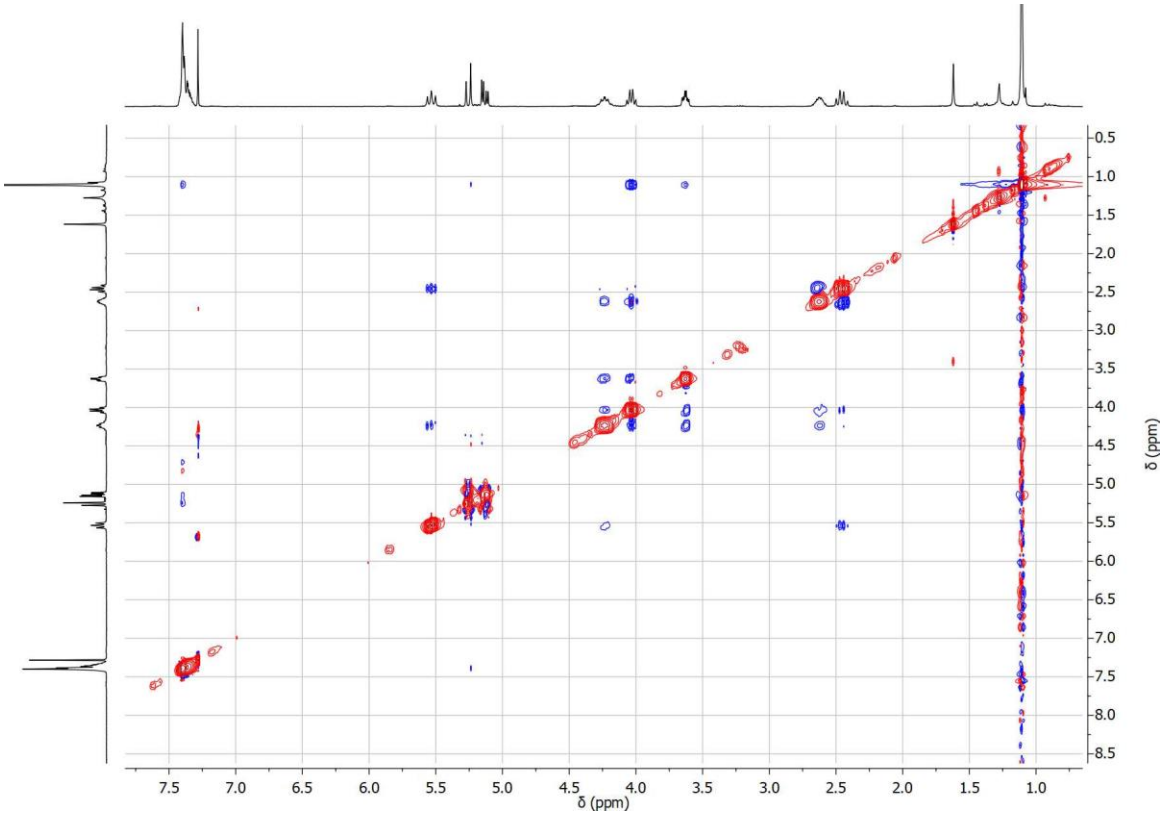

Figure A55. NOESY spectrum (400 MHz, $CDCl_3$) of compound **122**.

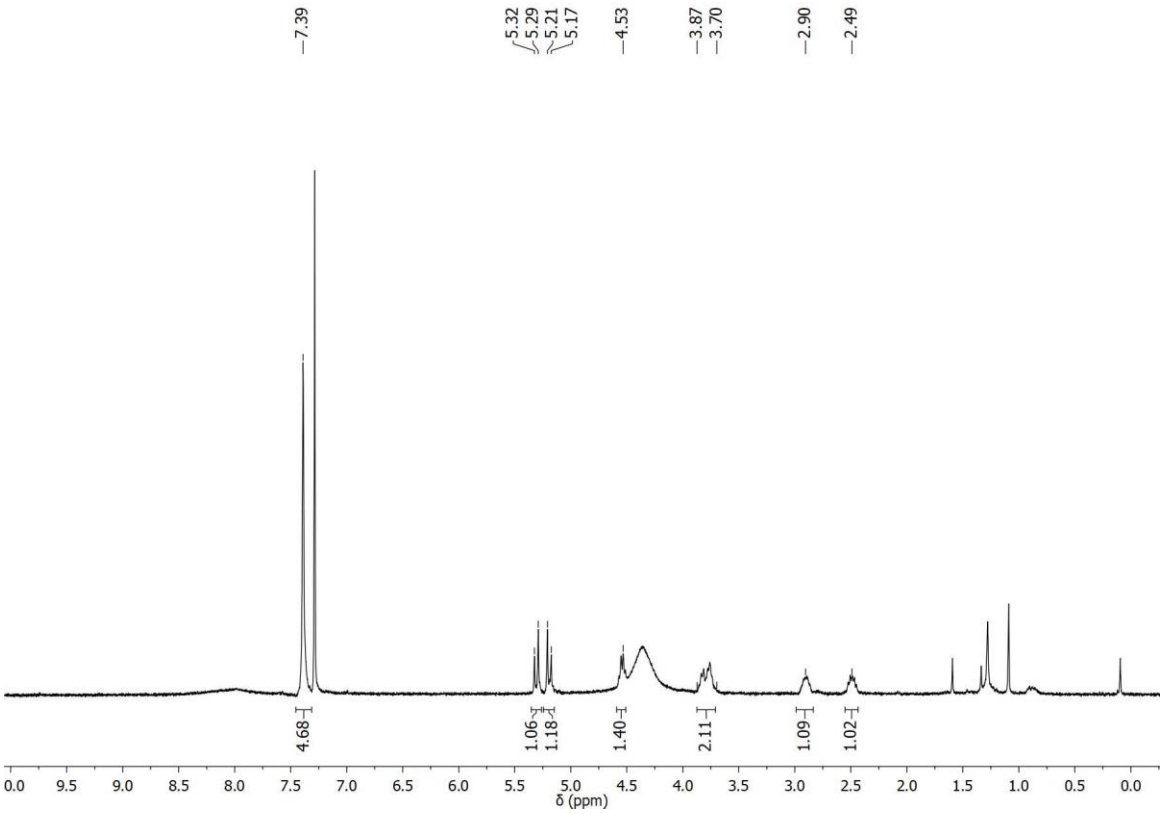

Figure A56. ^{1}H-NMR spectrum (360 MHz, $CDCl_3$) after *N*,*O*-deprotection of compound **(±)-121** with TFA.

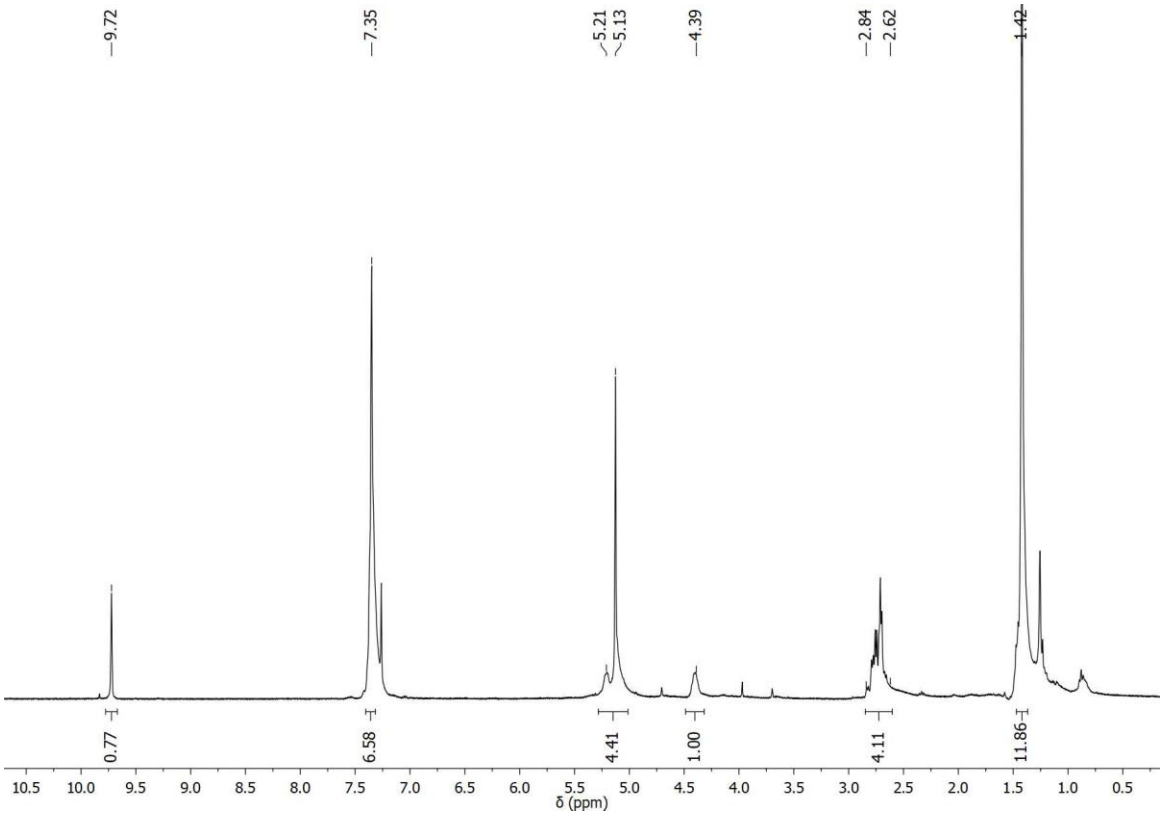

Figure A57. ^{1}H-NMR spectrum (400 MHz, $CDCl_3$) of the by-product generated in the ring-opening after reprotection of the free amine intermediate.

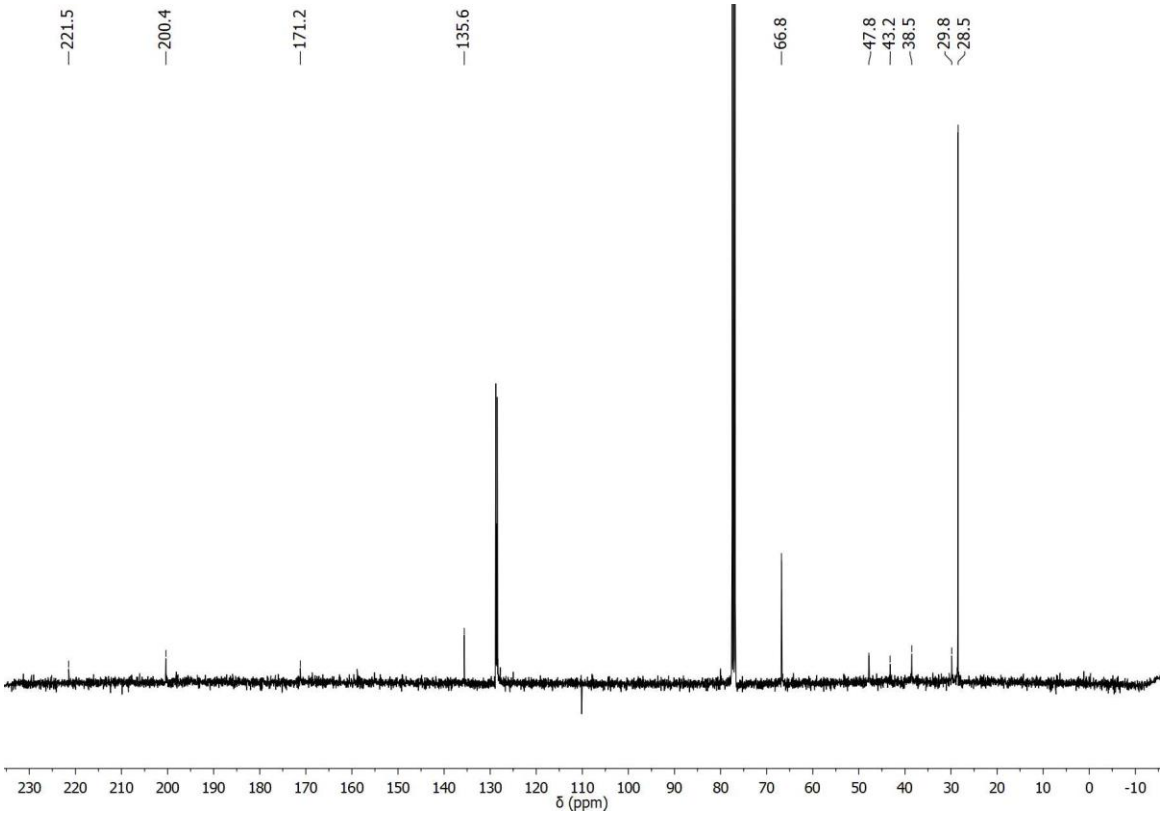

Figure A58. ^{13}C-NMR spectrum (100 MHz, $CDCl_3$) of the by-product generated in the ring-opening after reprotection of the free amine intermediate.

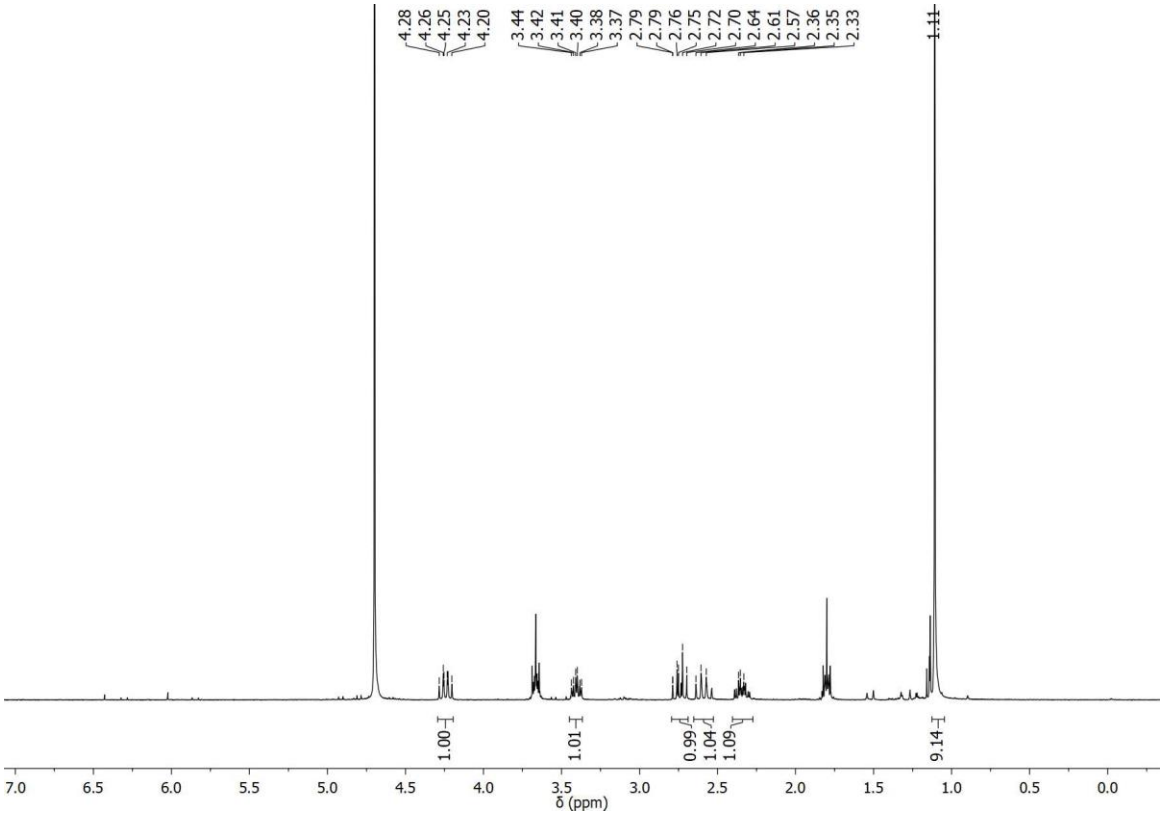

Figure A59. ^{1}H-NMR spectrum (300 MHz, D_2O) of compound **(±)-127**.

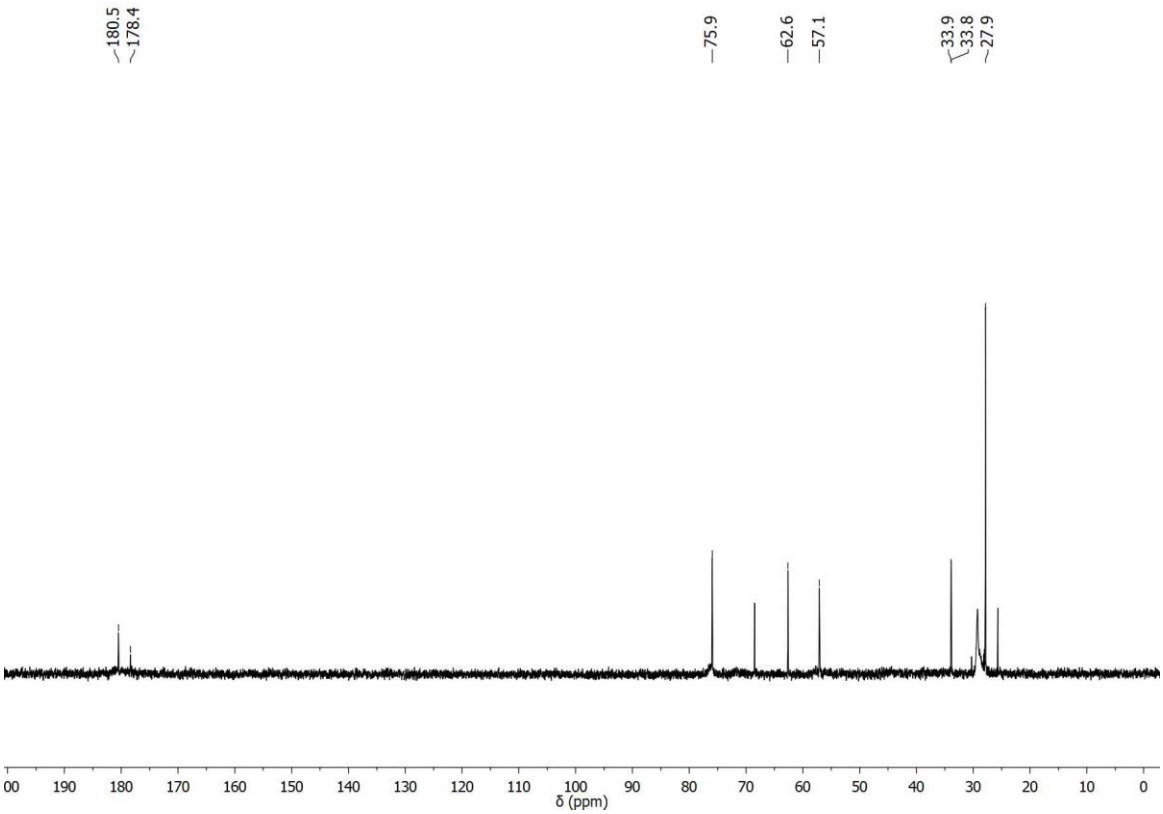

Figure A60. ^{13}C-NMR spectrum (90 MHz, D_2O) of compound **(±)-127**.

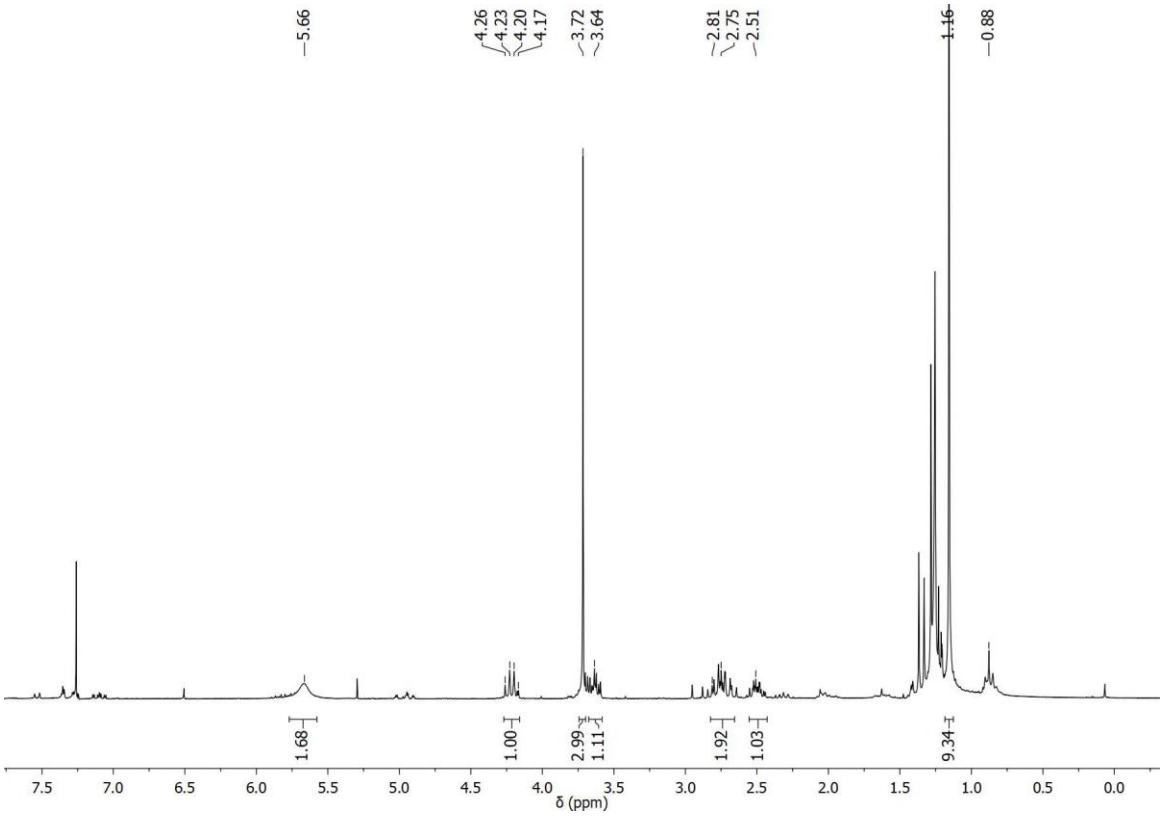

Figure A61. ^{1}H-NMR spectrum (250 MHz, $CDCl_3$) of compound **(±)-128**.

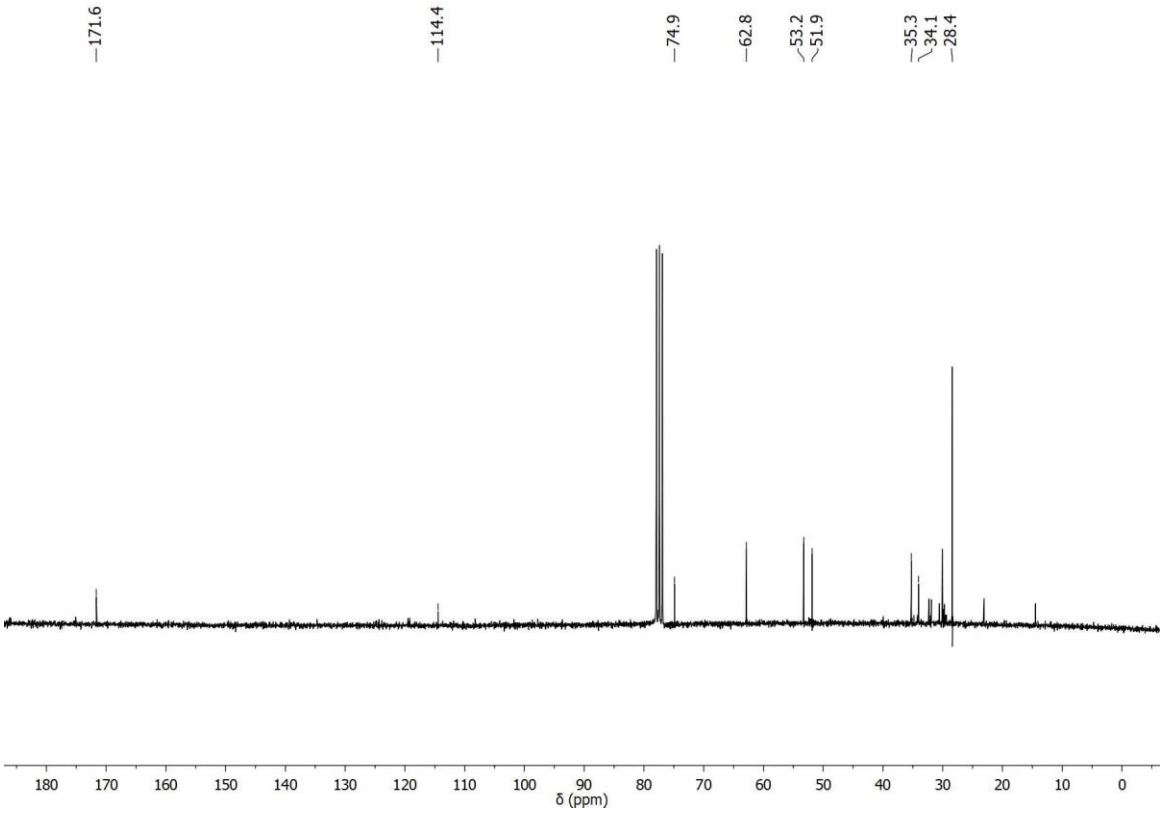

Figure A62. ^{13}C-NMR spectrum (63 MHz, $CDCl_3$) of compound **(±)-128**.

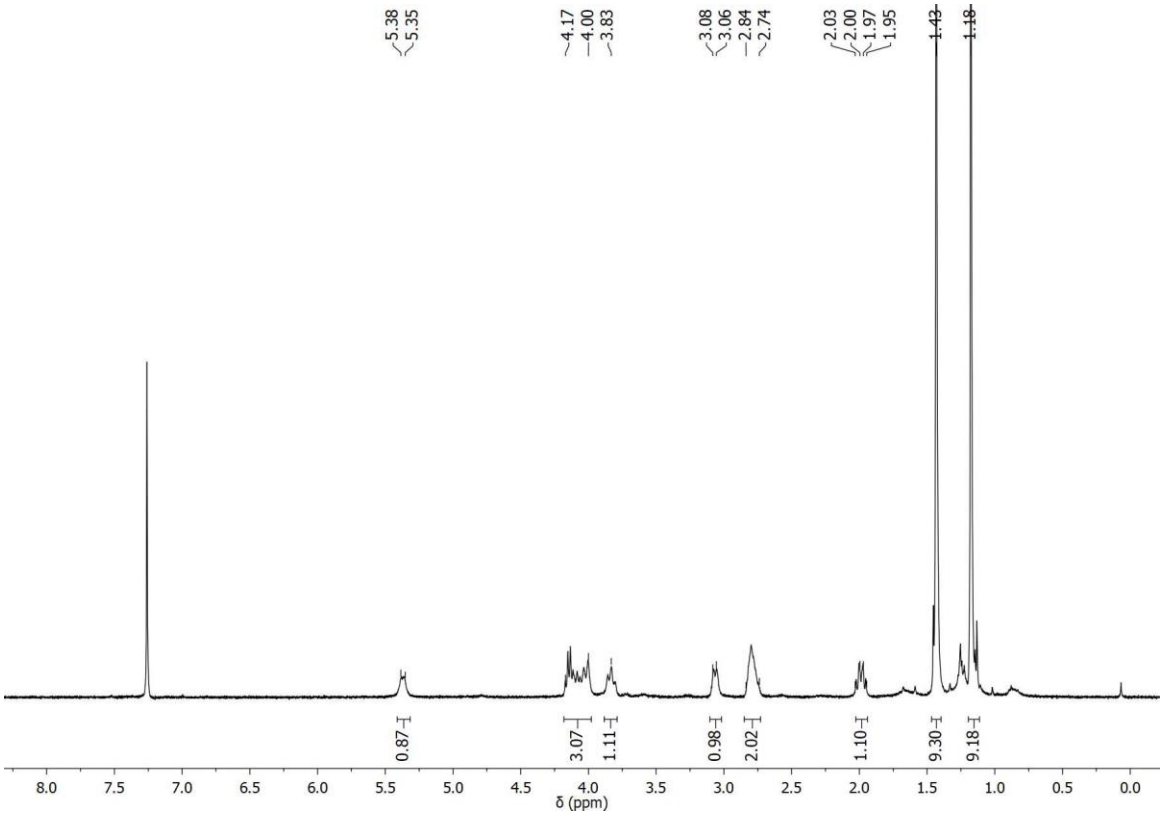

Figure A63. ^{1}H-NMR spectrum (400 MHz, $CDCl_3$) of compound **(±)-126**.

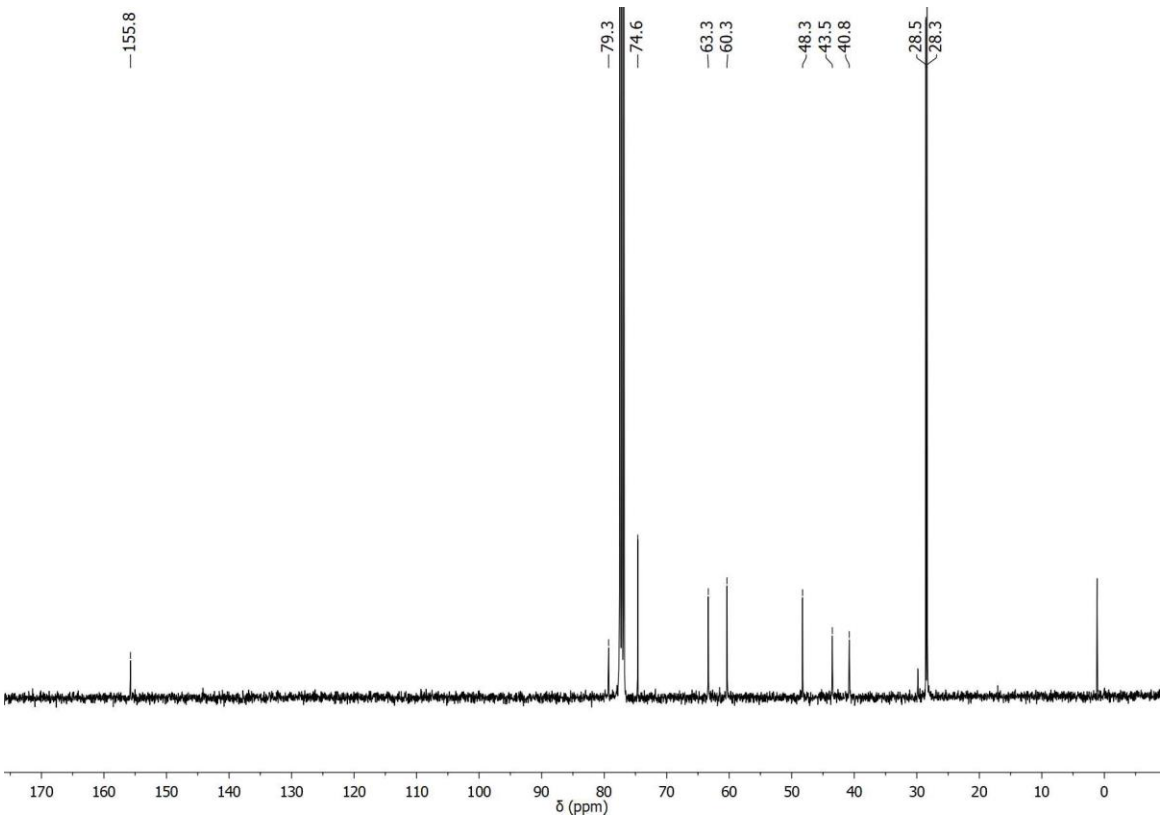

Figure A64. ^{13}C-NMR spectrum (100 MHz, $CDCl_3$) of compound **(±)-126**.

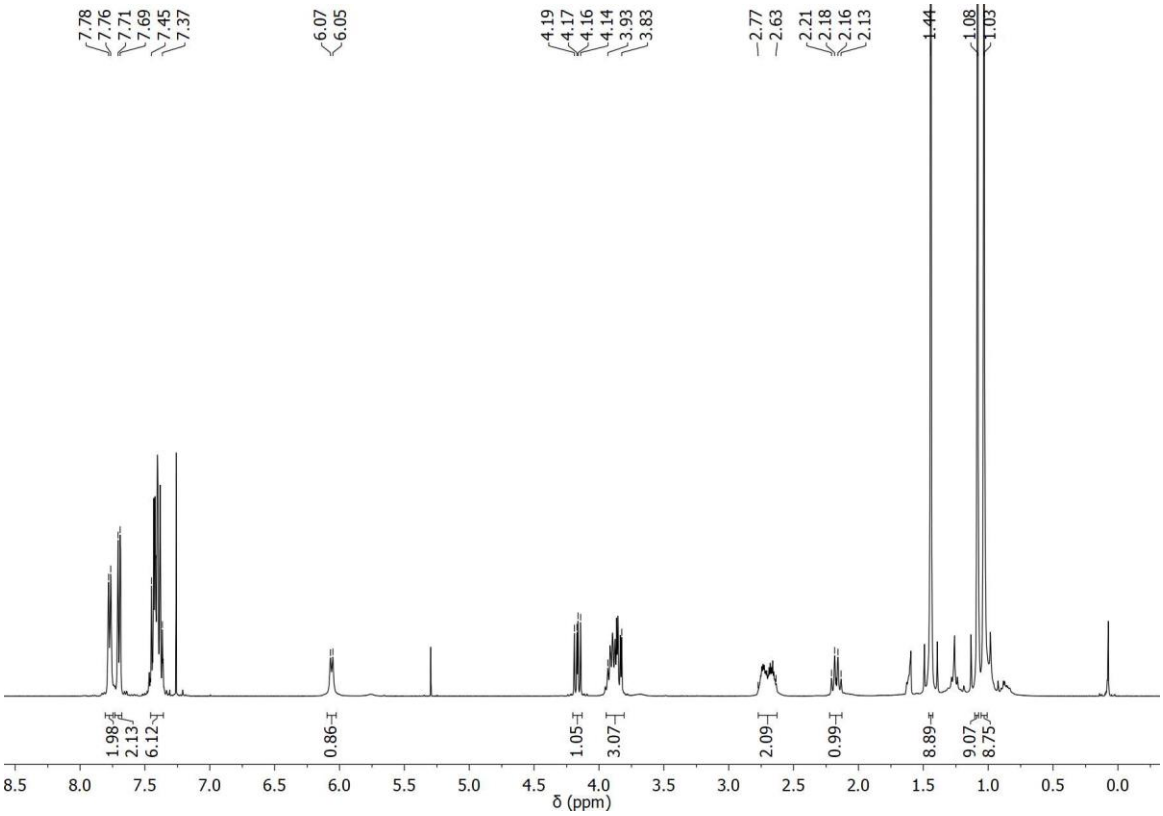

Figure A65. ^{1}H-NMR spectrum (400 MHz, $CDCl_3$) of compound **(±)-129**.

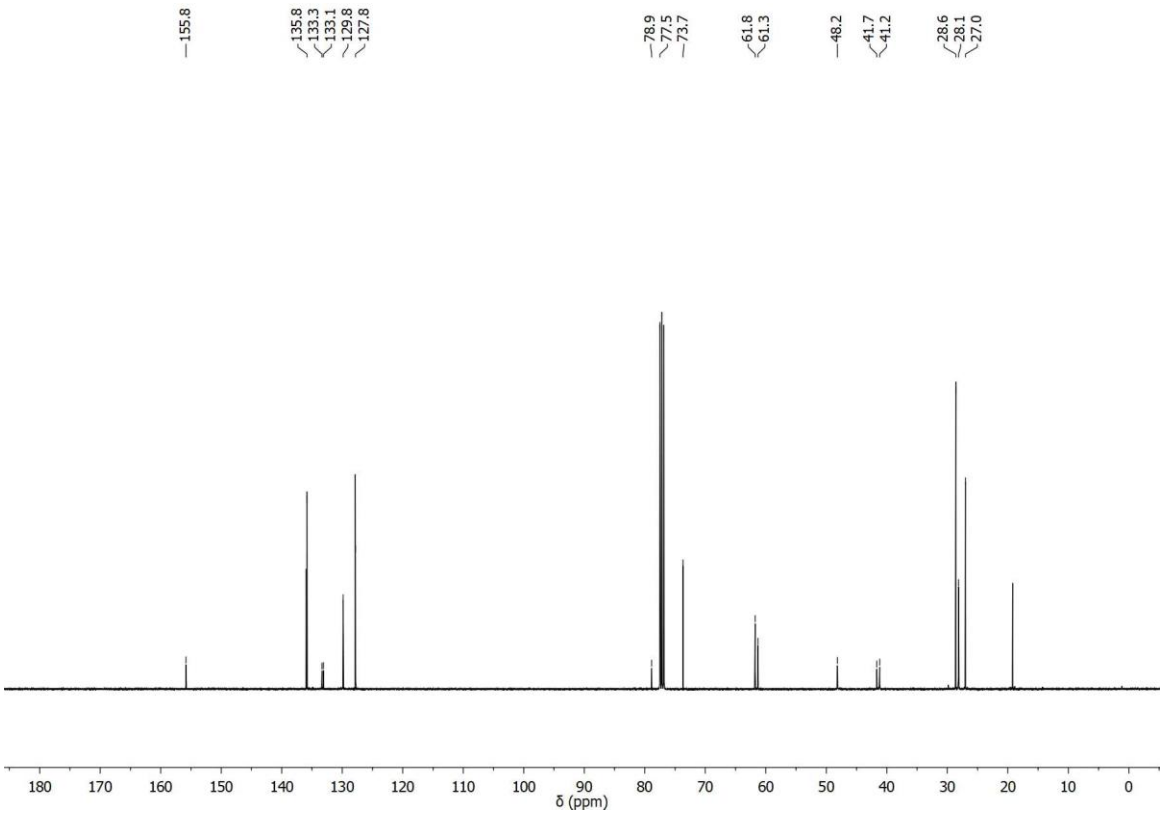

Figure A66. ^{13}C-NMR spectrum (100 MHz, $CDCl_3$) of compound **(±)-129**.

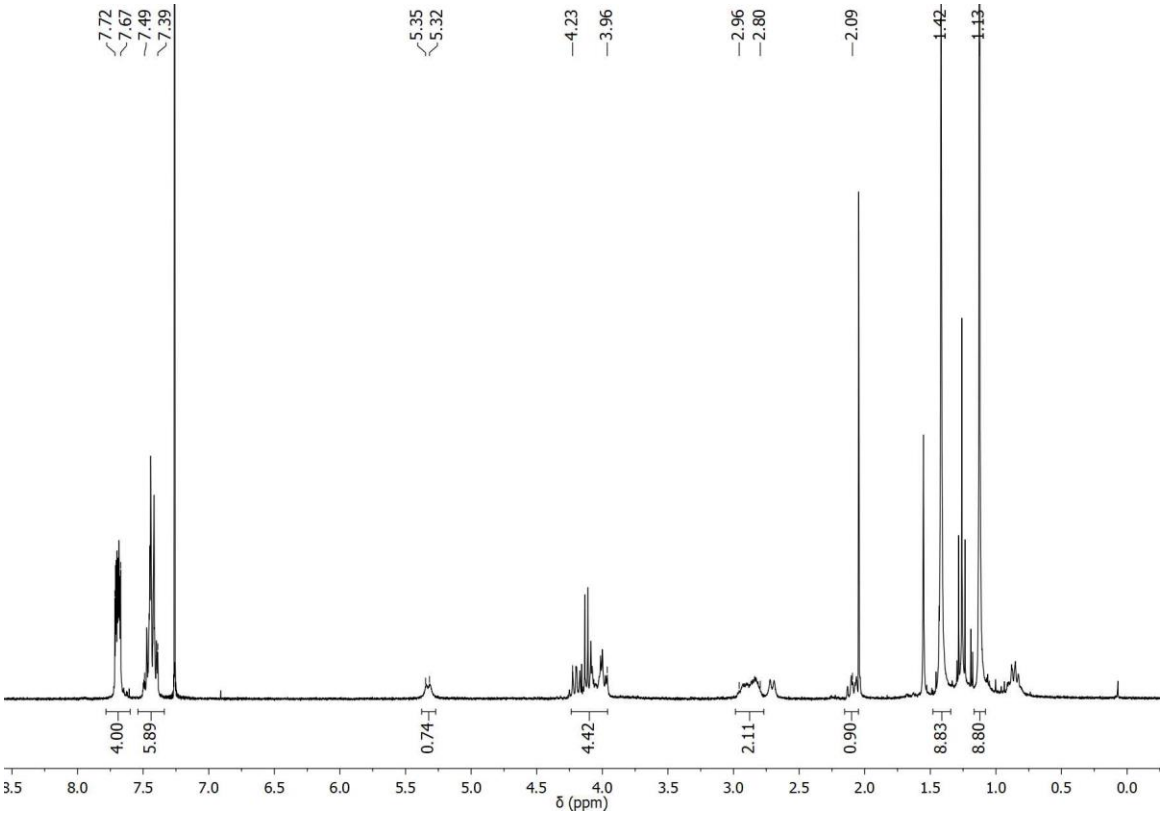

Figure A67. ^{1}H-NMR spectrum (400 MHz, $CDCl_3$) of compound **(±)-130**.

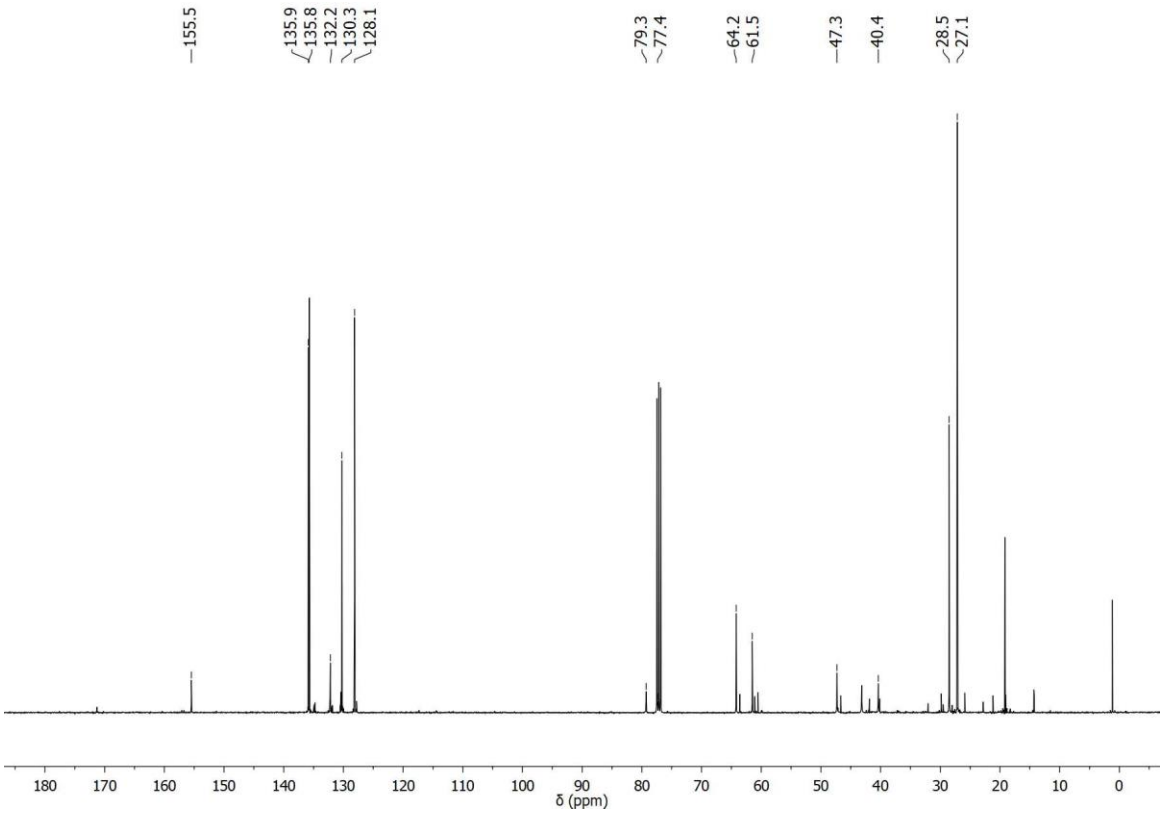

Figure A68. ^{13}C-NMR spectrum (100 MHz, $CDCl_3$) of compound **(±)-130**.

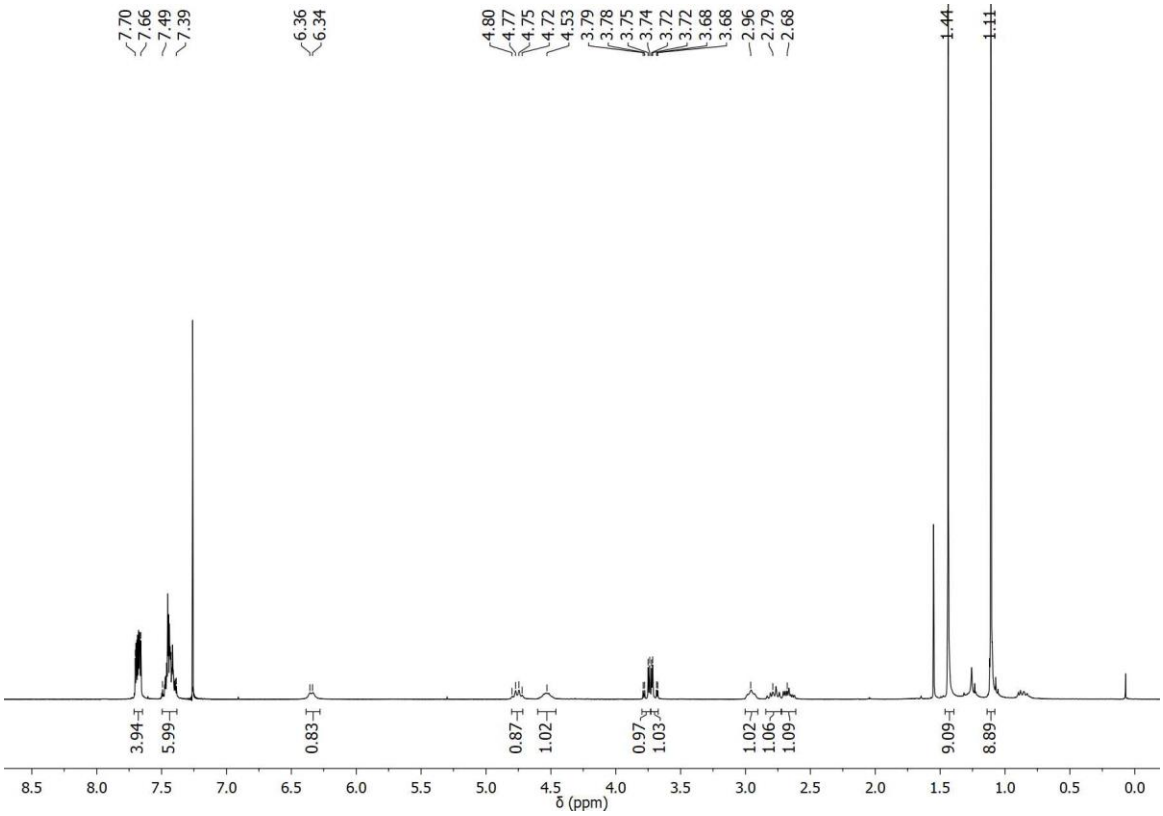

Figure A69. ^{1}H-NMR spectrum (300 MHz, $CDCl_3$) of compound **(±)-133**.

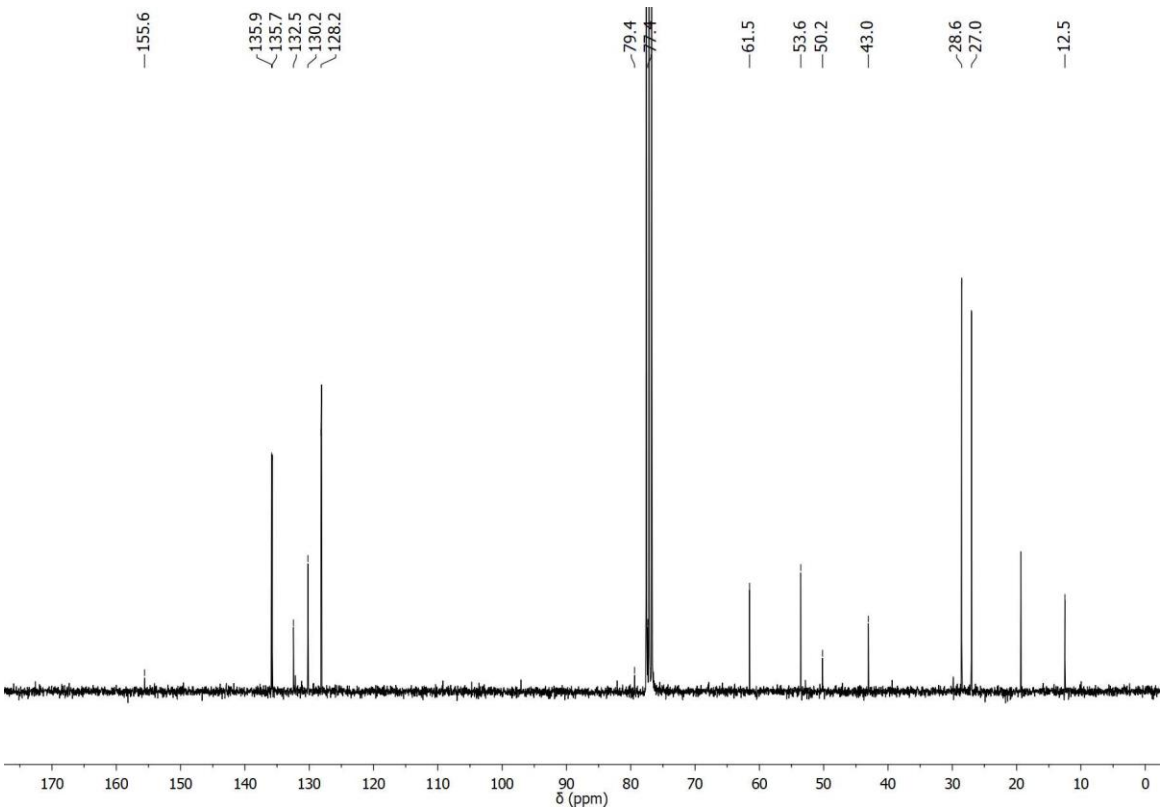

Figure A70. ^{13}C-NMR spectrum (75 MHz, $CDCl_3$) of compound **(±)-133**.

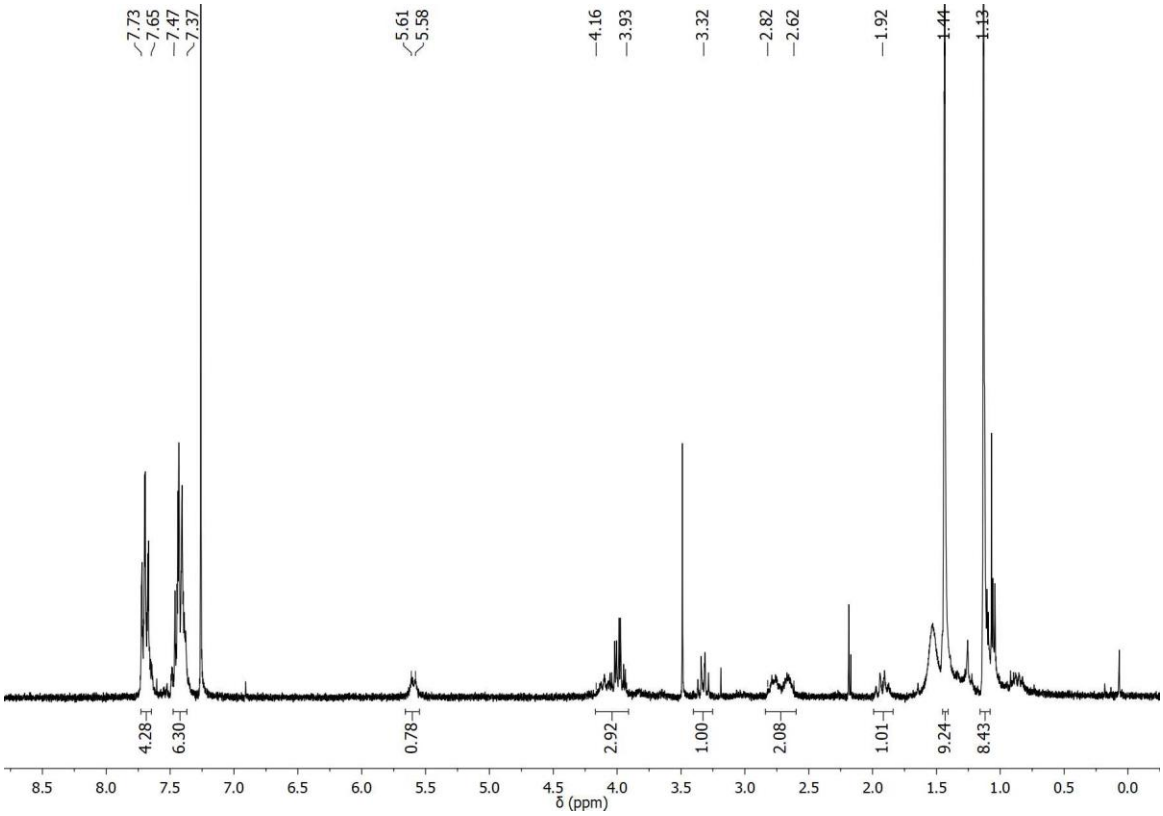

Figure A71. ^{1}H-NMR spectrum (300 MHz, $CDCl_3$) of compound **(±)-134**.

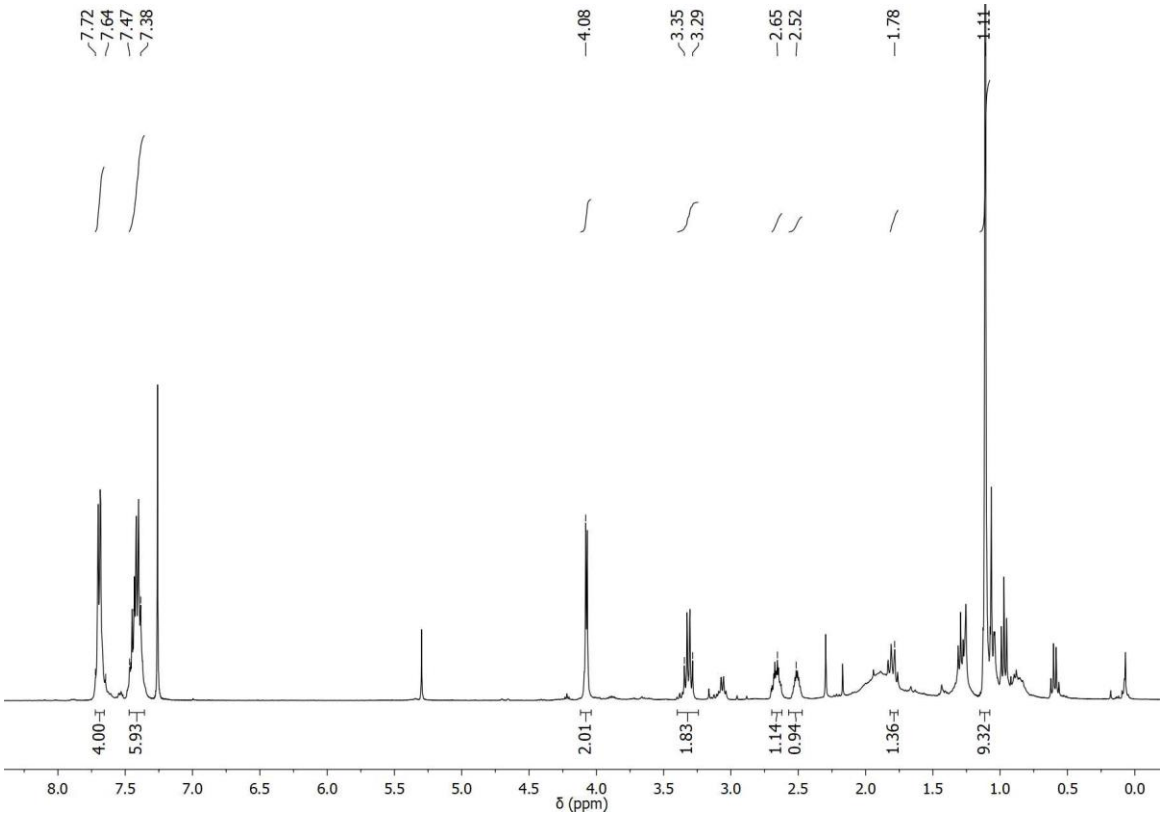

Figure A72. ^{1}H-NMR spectrum (300 MHz, $CDCl_3$) of compound **135**.

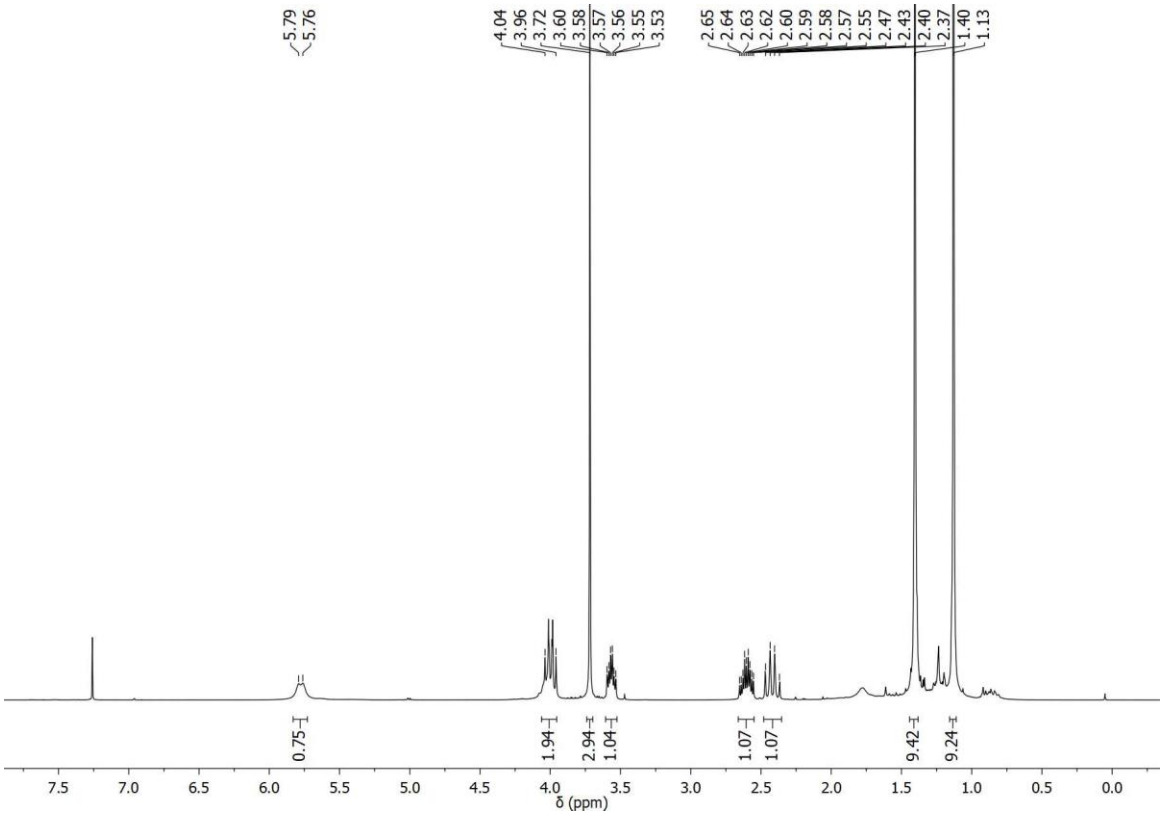

Figure A73. ^{1}H-NMR spectrum (300 MHz, $CDCl_3$) of compound **(±)-138**.

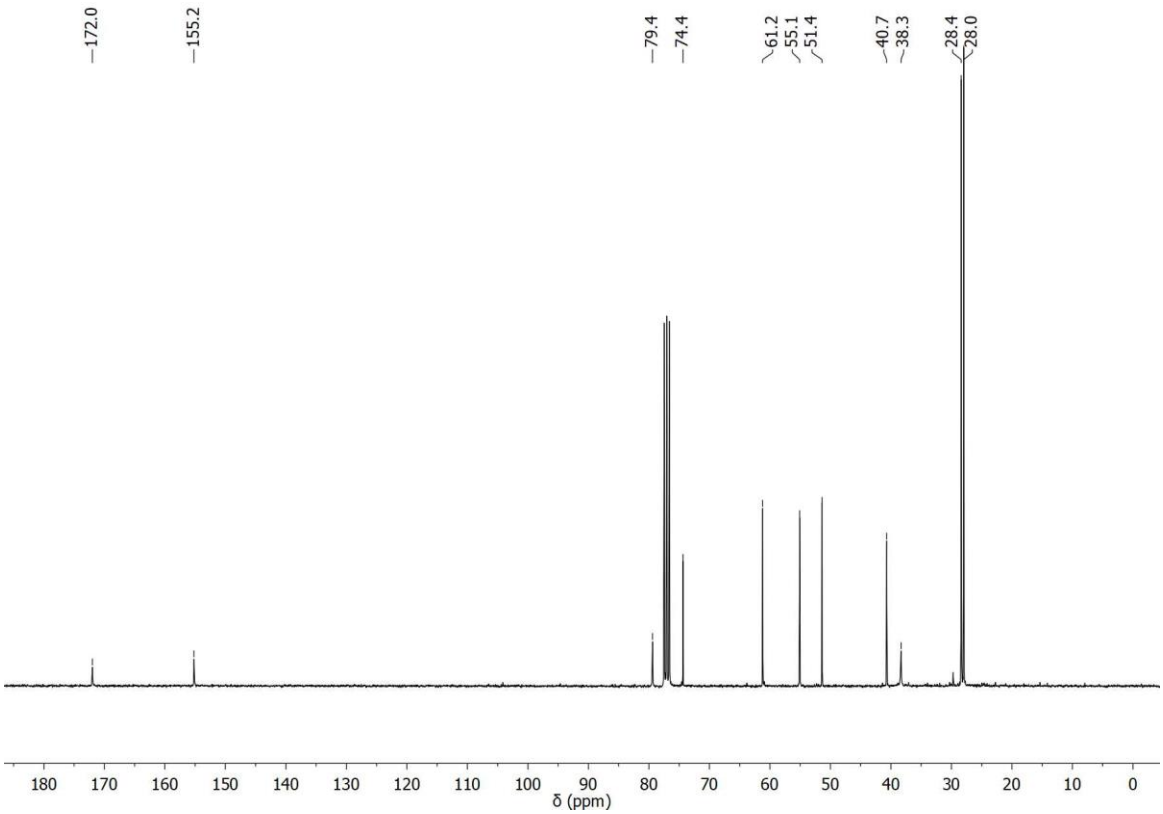

Figure A74. ^{13}C-NMR spectrum (75 MHz, $CDCl_3$) of compound **(±)-138**.

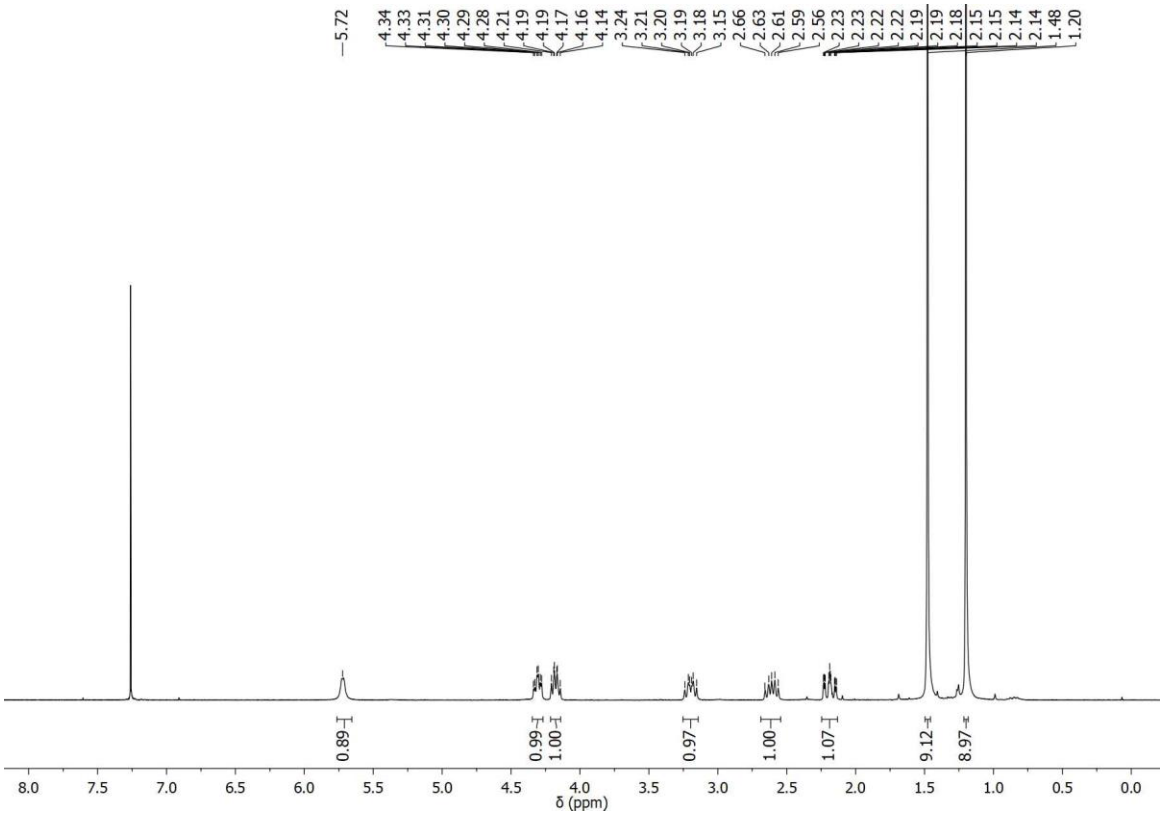

Figure A75. ^{1}H-NMR spectrum (300 MHz, $CDCl_3$) of compound **(±)-140**.

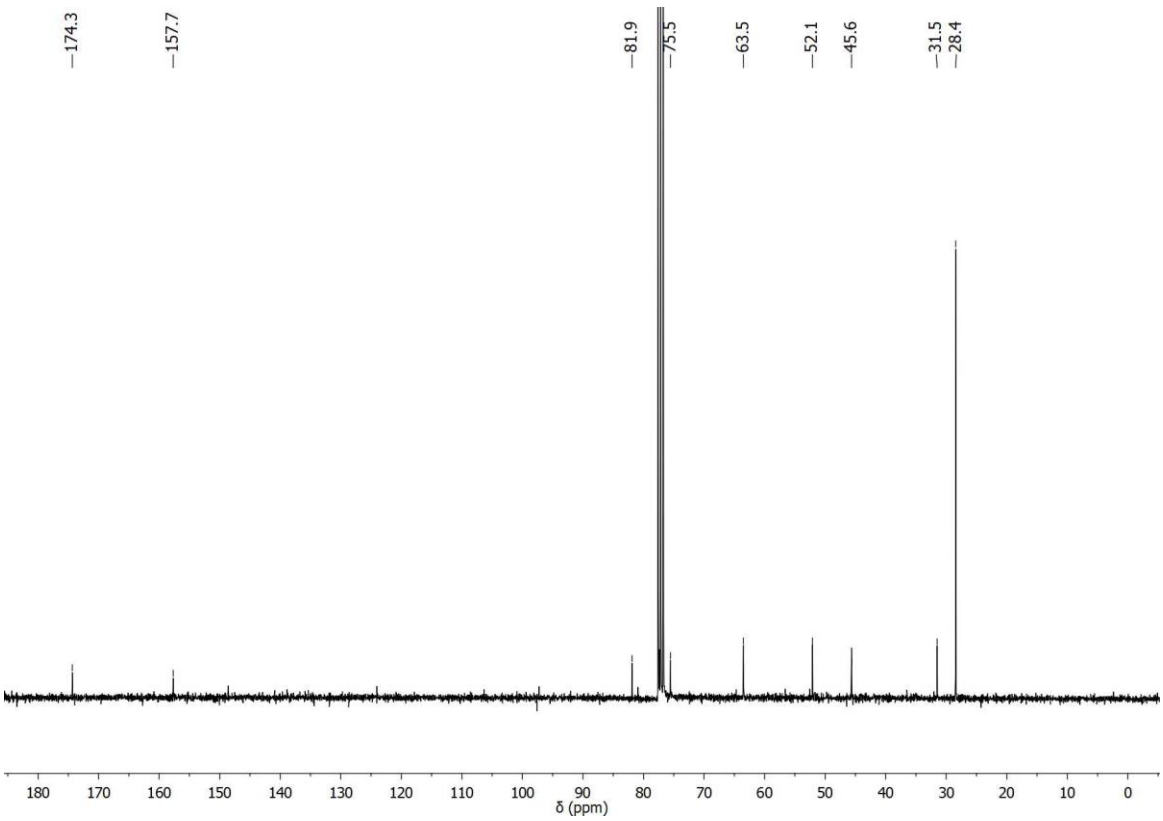

Figure A76. ^{13}C-NMR spectrum (75 MHz, $CDCl_3$) of compound **(±)-140**.

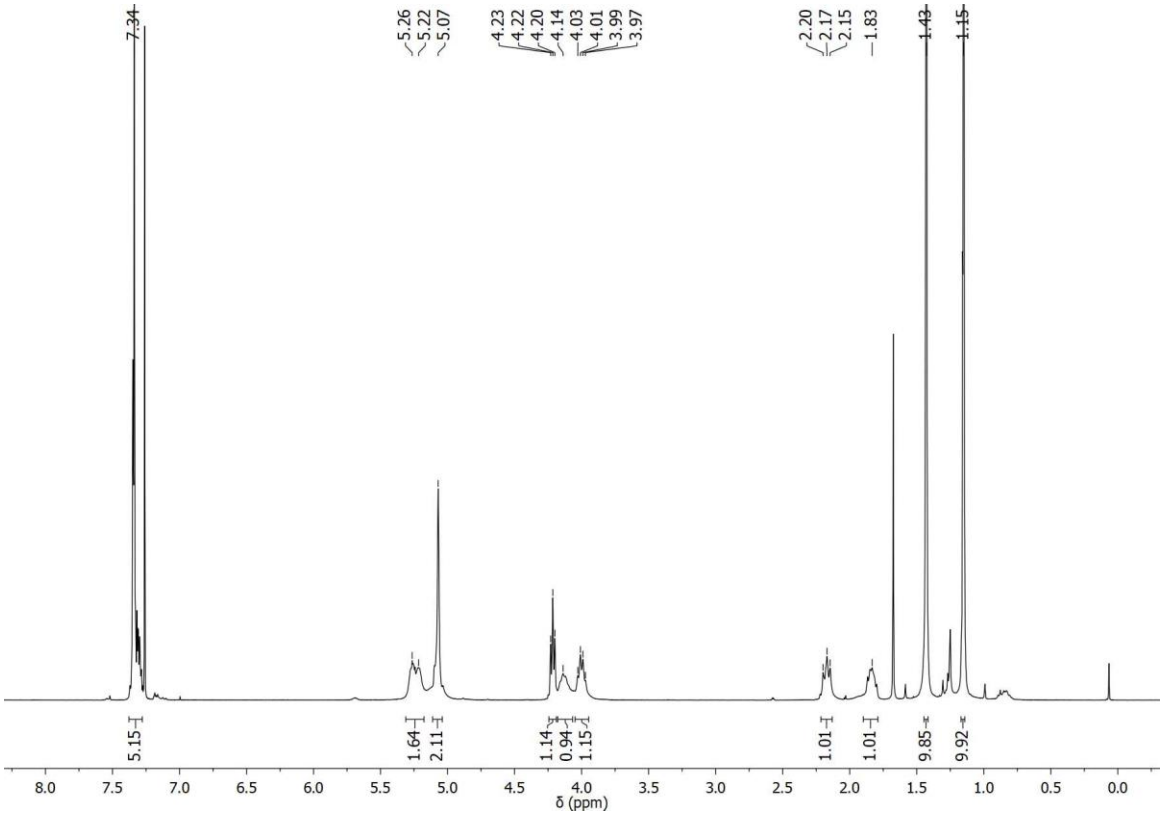

Figure A77. ^{1}H-NMR spectrum (400 MHz, $CDCl_3$) of compound **(±)-141**.

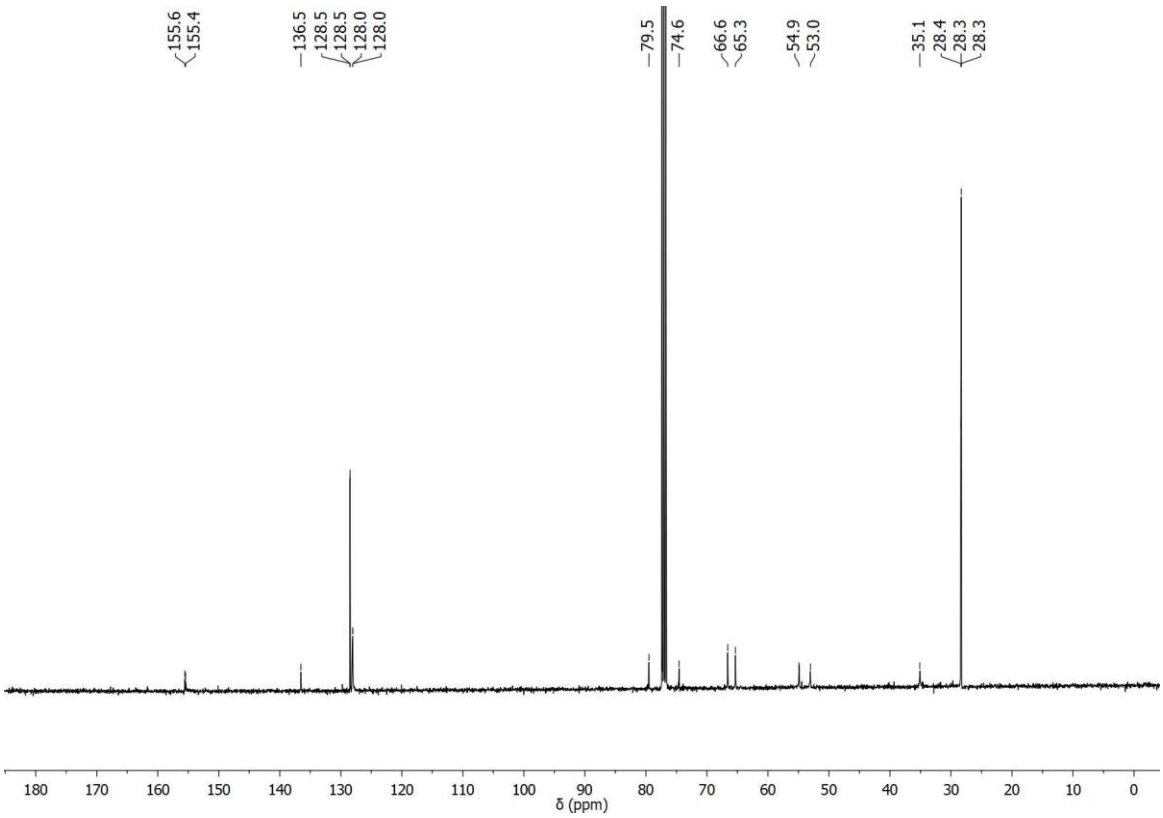

Figure A78. ^{13}C-NMR spectrum (100 MHz, $CDCl_3$) of compound **(±)-141**.

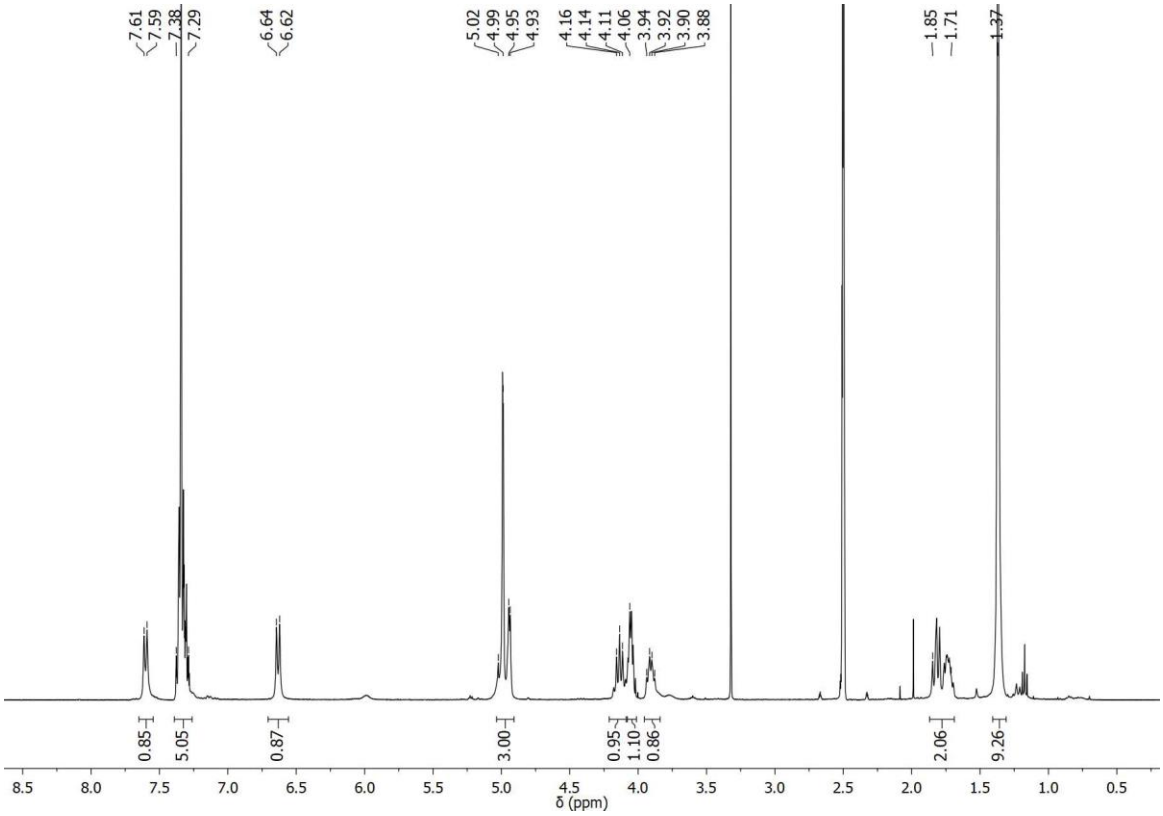

Figure A79. ^{1}H-NMR spectrum (400 MHz, DMSO-d_6) of compound **(±)-142**.

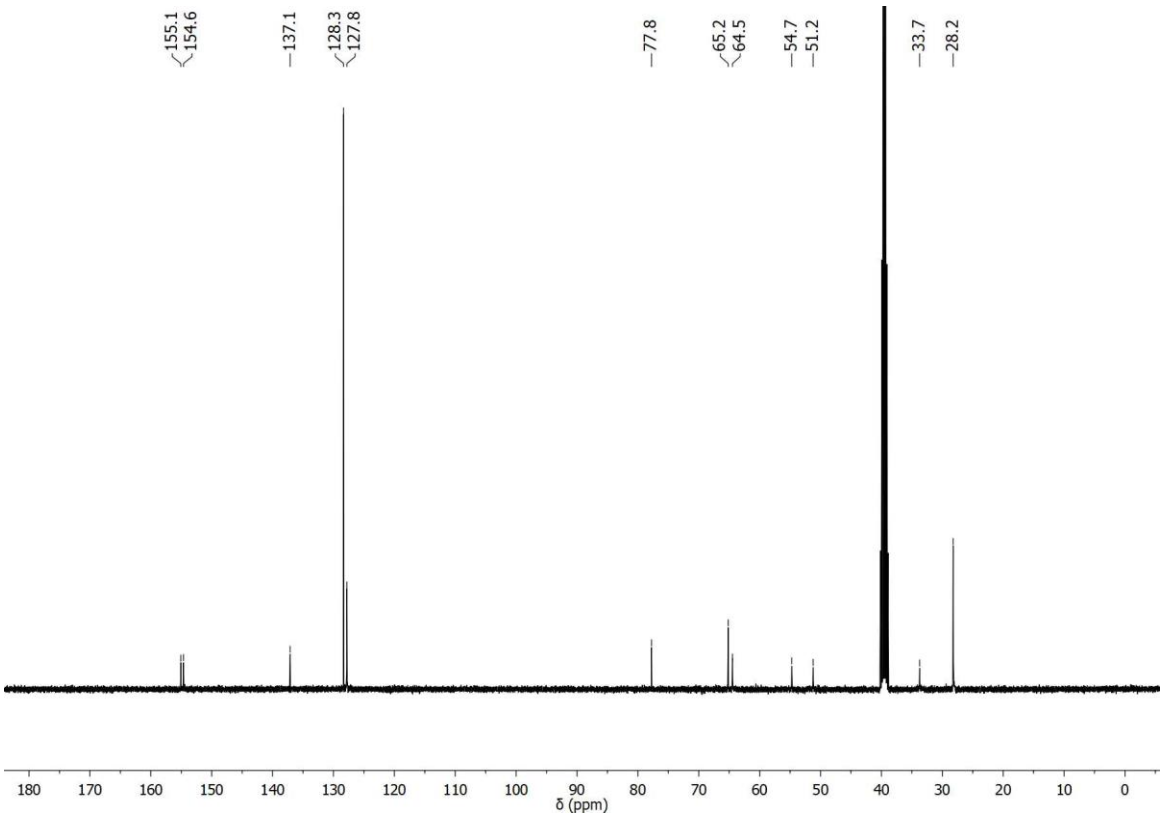

Figure A80. ^{13}C-NMR spectrum (100 MHz, DMSO-d_6) of compound **(±)-142**.

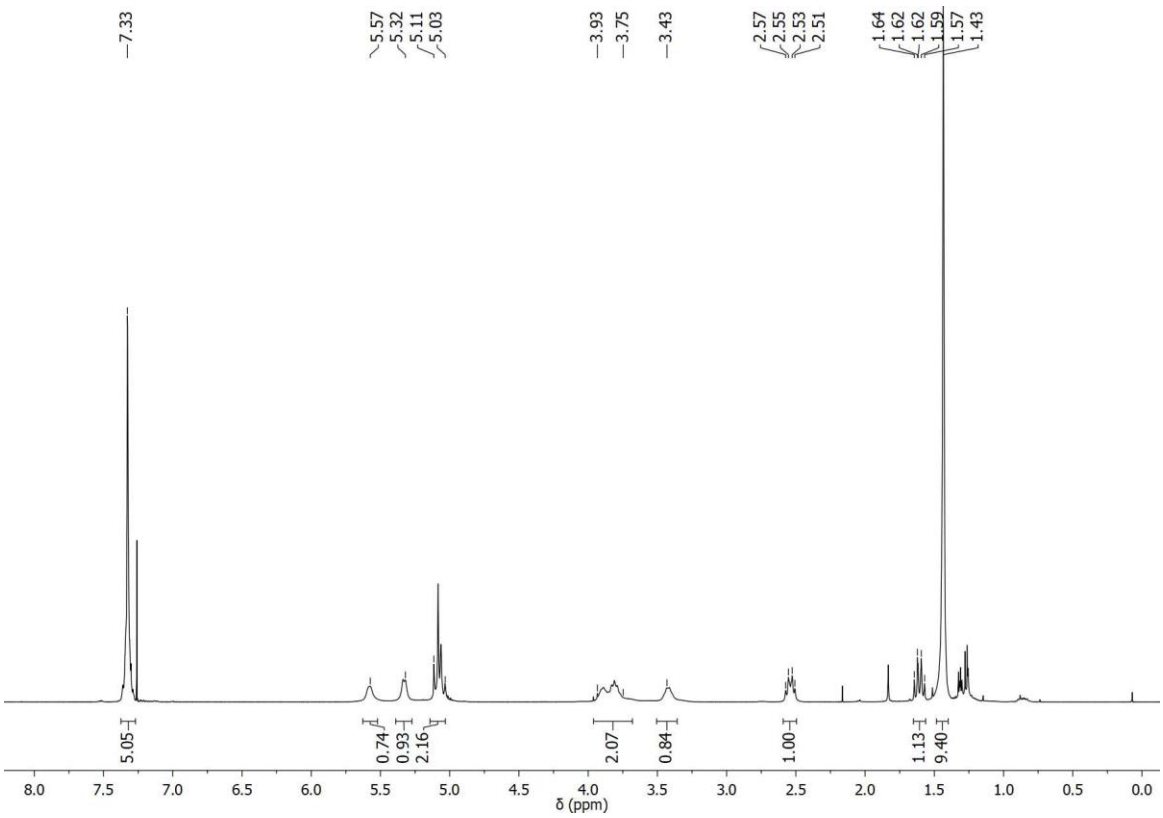

Figure A81. ^{1}H-NMR spectrum (400 MHz, $CDCl_3$) of compound **(±)-143**.

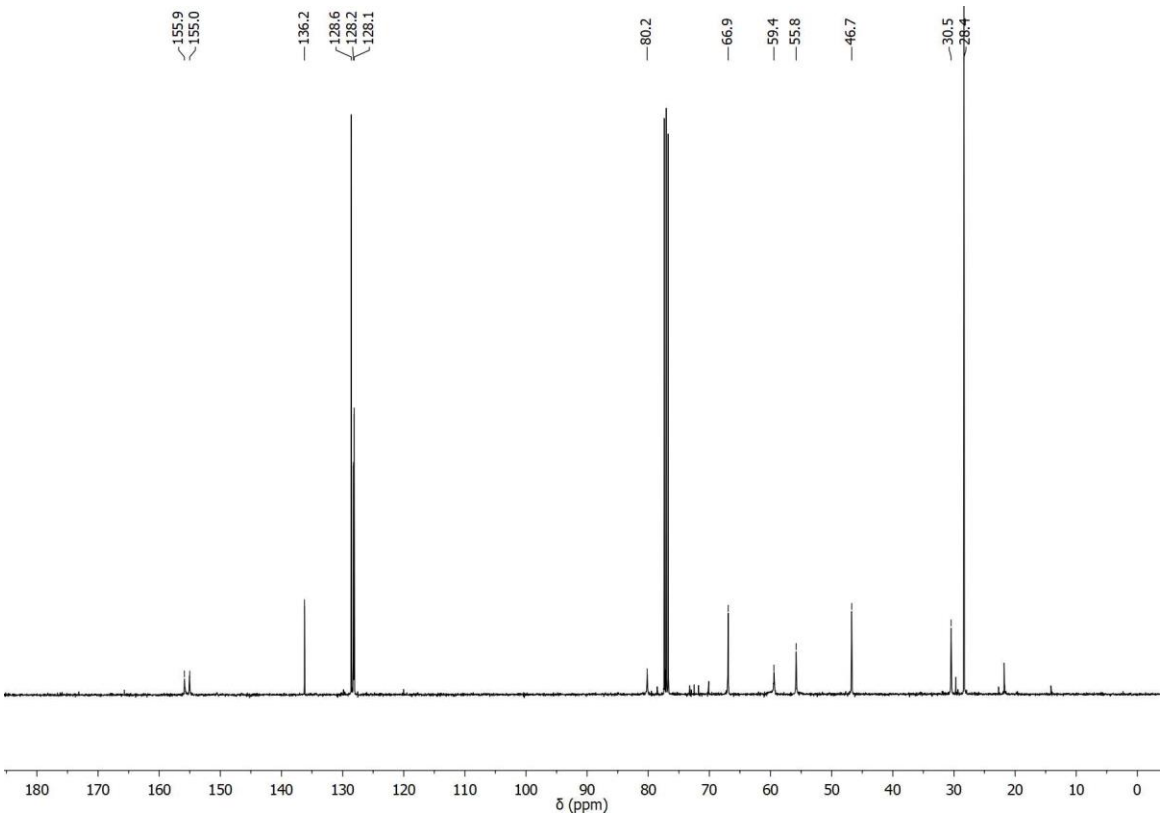

Figure A82. ^{13}C-NMR spectrum (100 MHz, $CDCl_3$) of compound **(±)-143**.

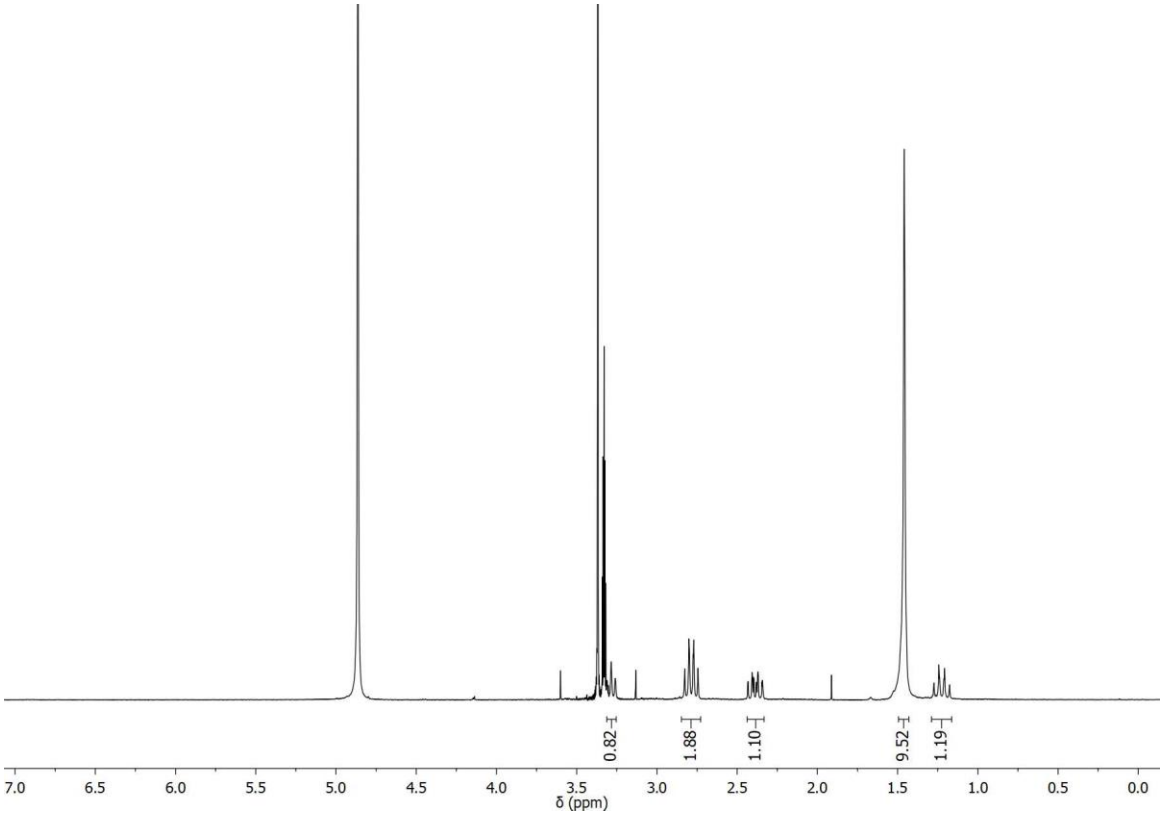

Figure A83. ^{1}H-NMR spectrum (300 MHz, MeOD) of compound **144**.

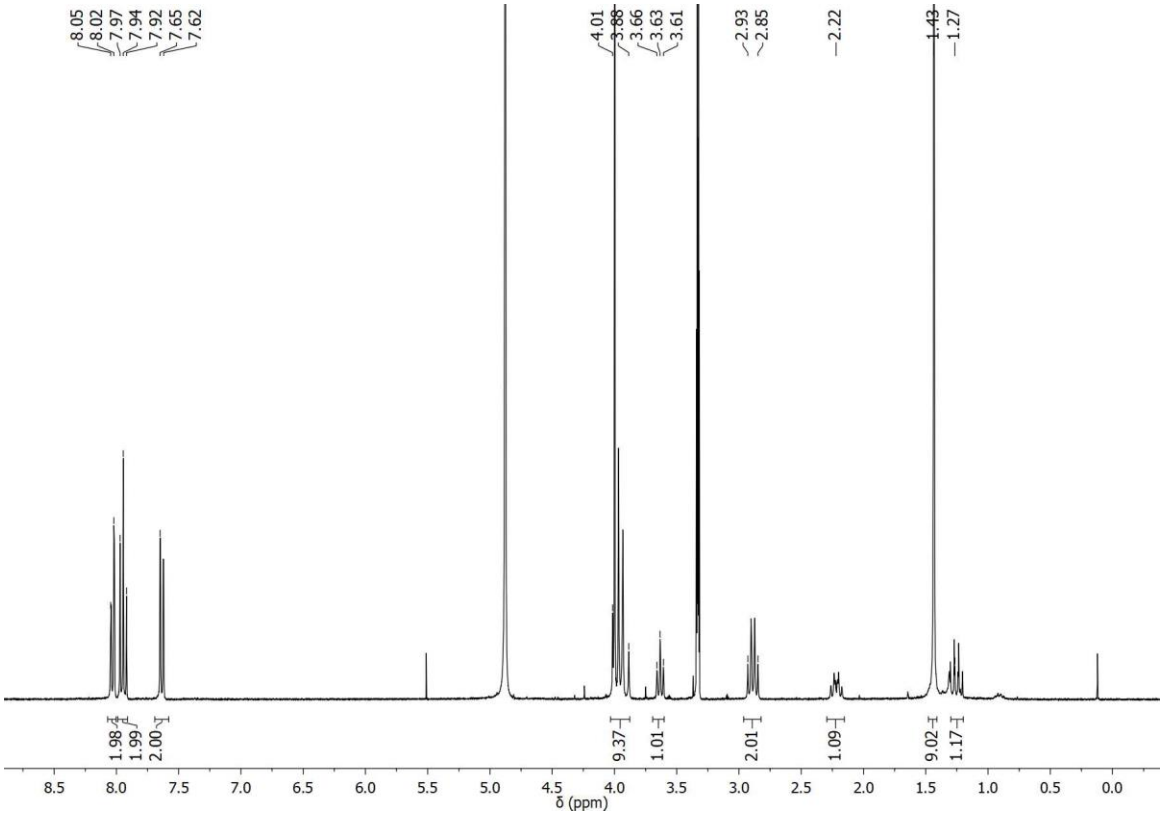

Figure A84. [1]H-NMR spectrum (300 MHz, MeOD) of compound **145**.

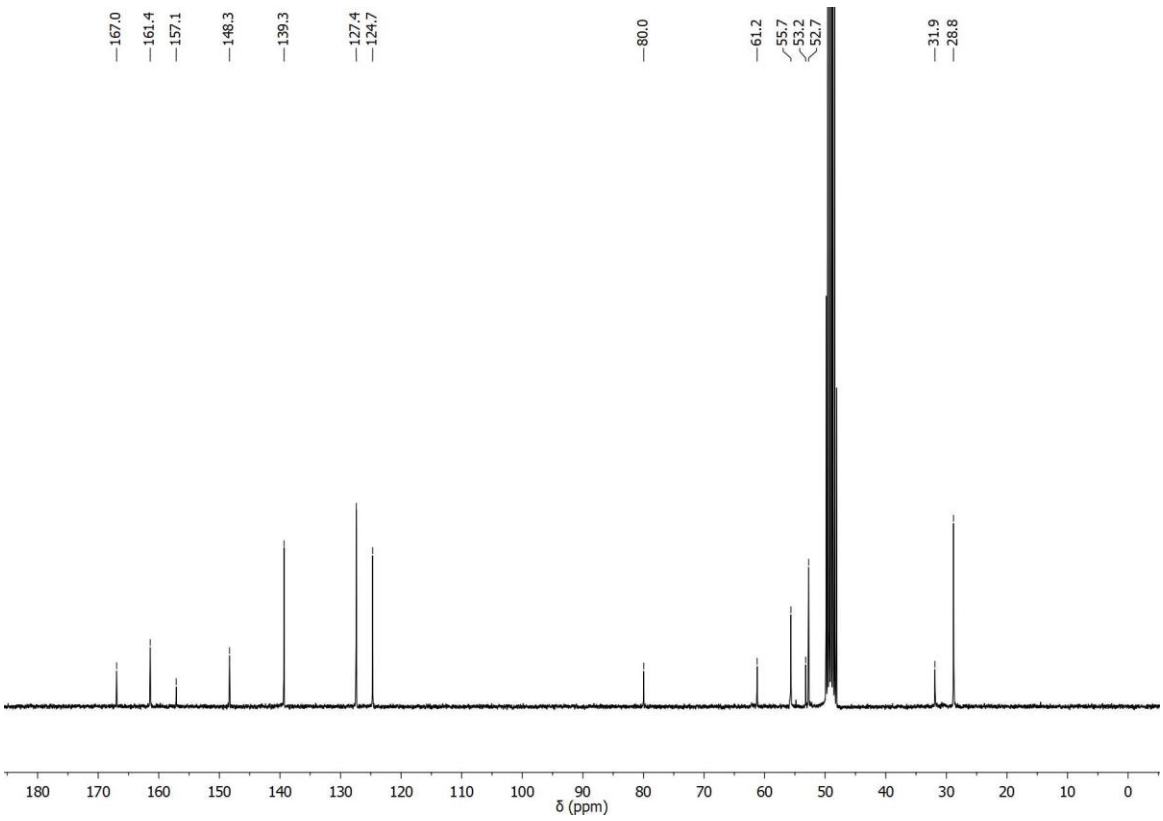

Figure A85. [13]C-NMR spectrum (75 MHz, MeOD) of compound **145**.

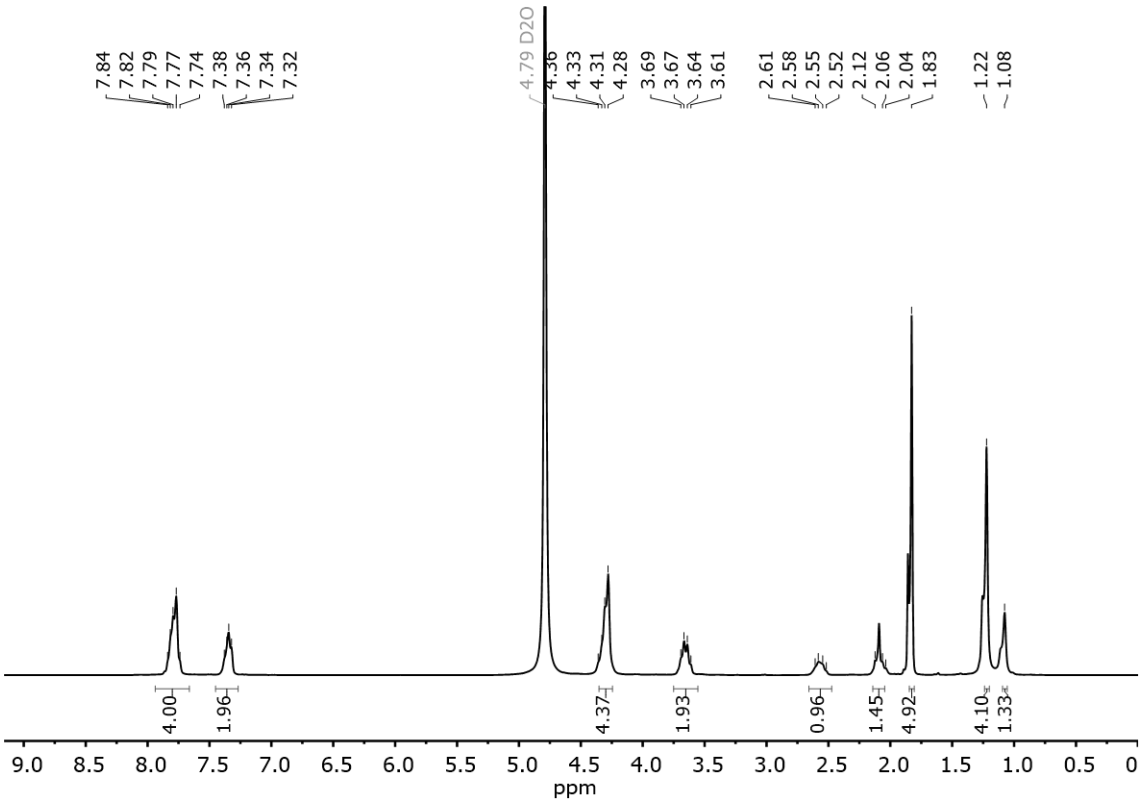

Figure A86. ^{1}H-NMR spectrum (300 MHz, D_2O, pD 6) of compound ***cis*,*trans*-L2**.

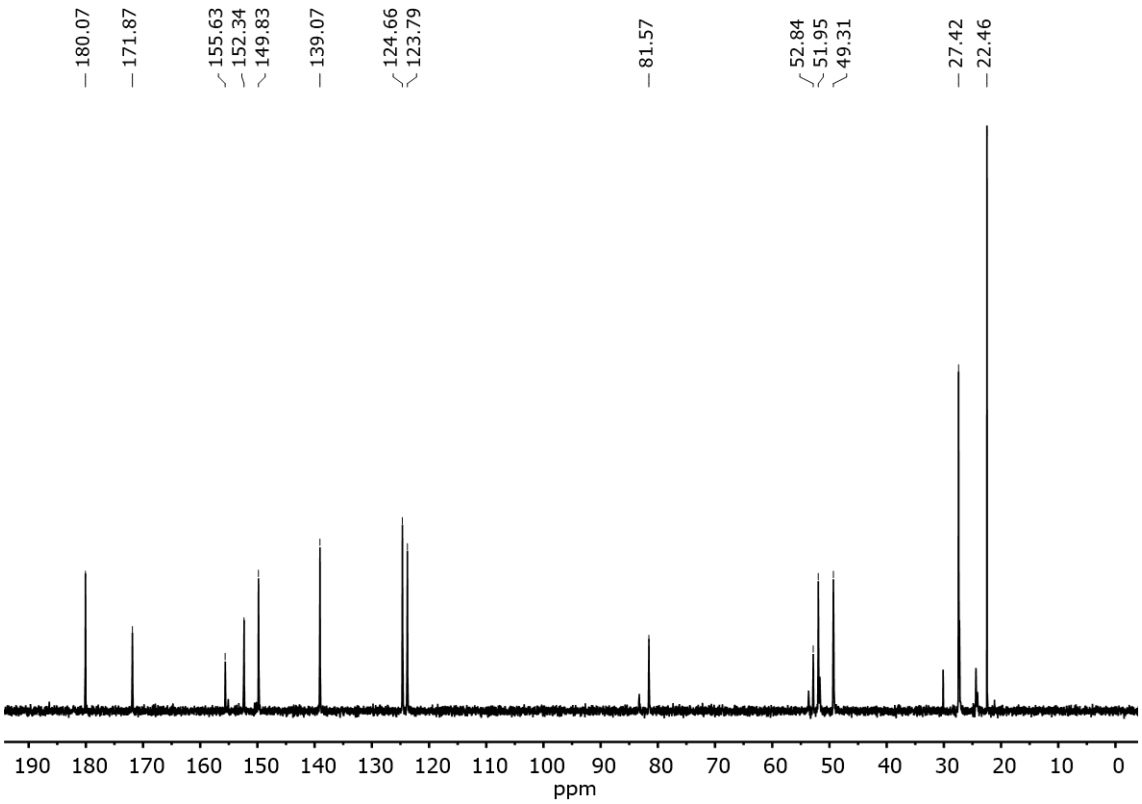

Figure A87. ^{13}C-NMR spectrum (75 MHz, D_2O, pD 6) of compound ***cis*,*trans*-L2**.

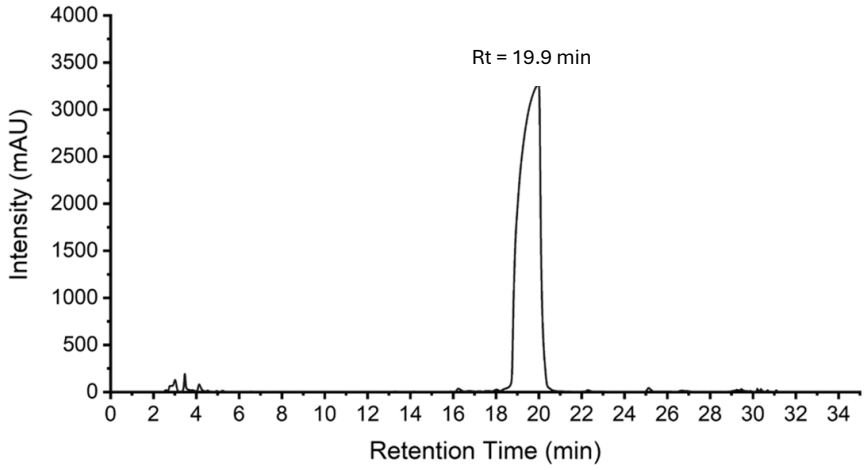

Figure A88. HPLC chromatogram (272 nm) of ***cis,trans*-L2** at Rt = 19.9 min.

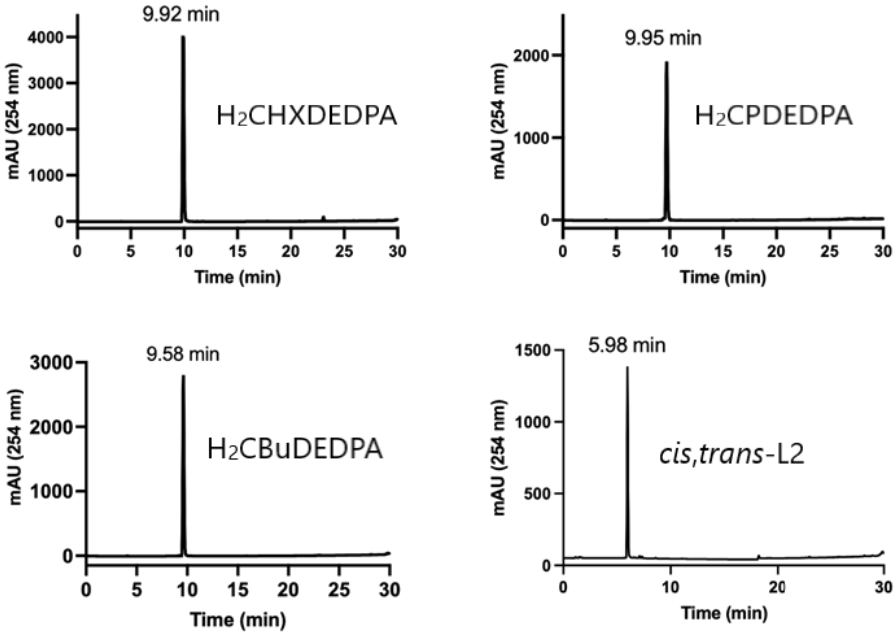

Figure A89. HPLC traces of ligands. For **H_2CHXDEDPA**, **H_2CPDEDPA** and **H_2CBuDEDPA** (Method A: (A) 0.1% TFA in H_2O and (B) 0.1% TFA in CH_3CN). For ***cis,trans*-L2** (Method B: (A) 10 mM NH_4OAc pH = 7 (B) CH_3CN). Gradient: 0-2 min: 5% B. 2-24 min: 5-95% B. 24-26 min: 95% B. 26-28 min: 95-5% B. 28-30 min: 5% B, UV detection at 220 and 254 nm.

PART II. Cannabidivarin derivatives as CB_2R modulators

Chapter III. Innovative Bitopic Ligands Targeting Allosteric and Metastable CB_2R Binding Sites

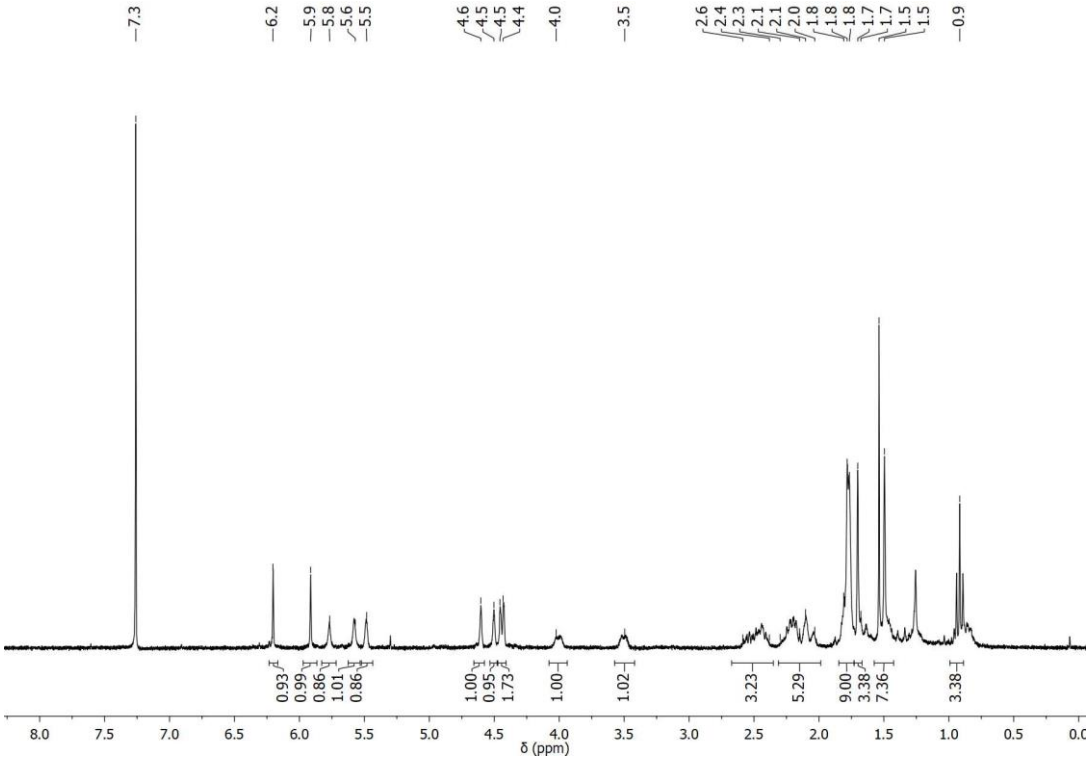

Figure A90. ^{1}H-NMR spectrum (300 MHz, $CDCl_3$) of compound ***bis*-CBDV**.

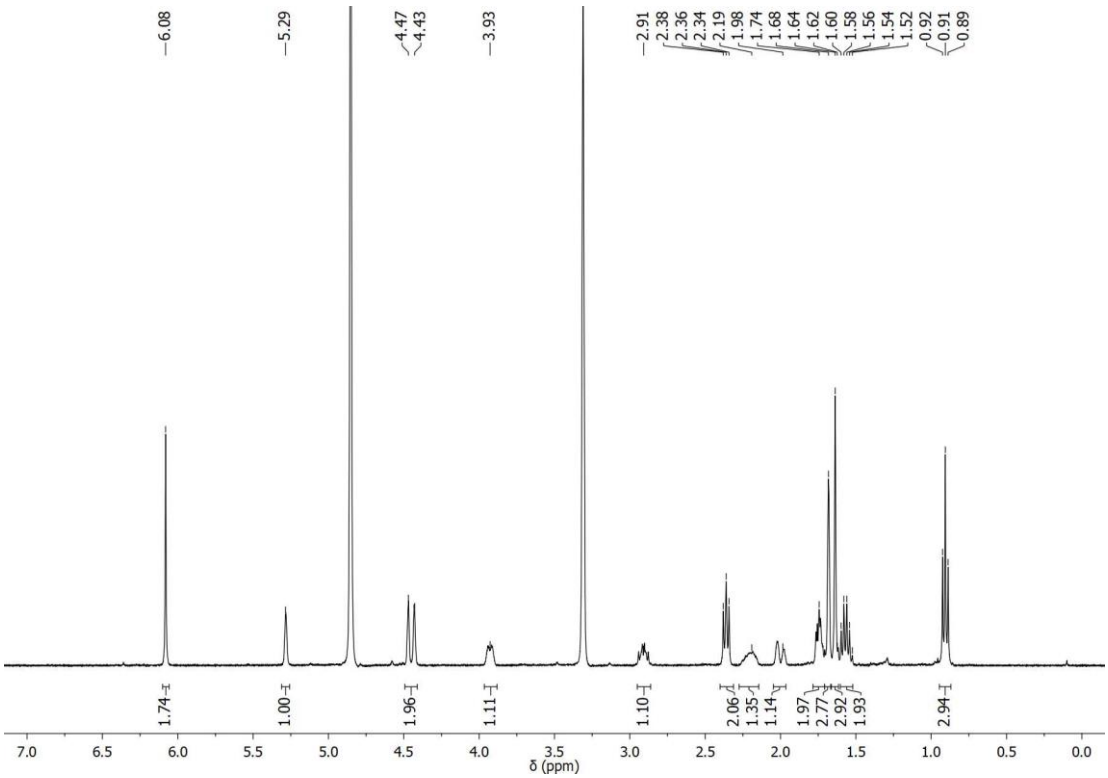

Figure A91. ^{1}H-NMR spectrum (300 MHz, $CDCl_3$) of compound **CBDV**.

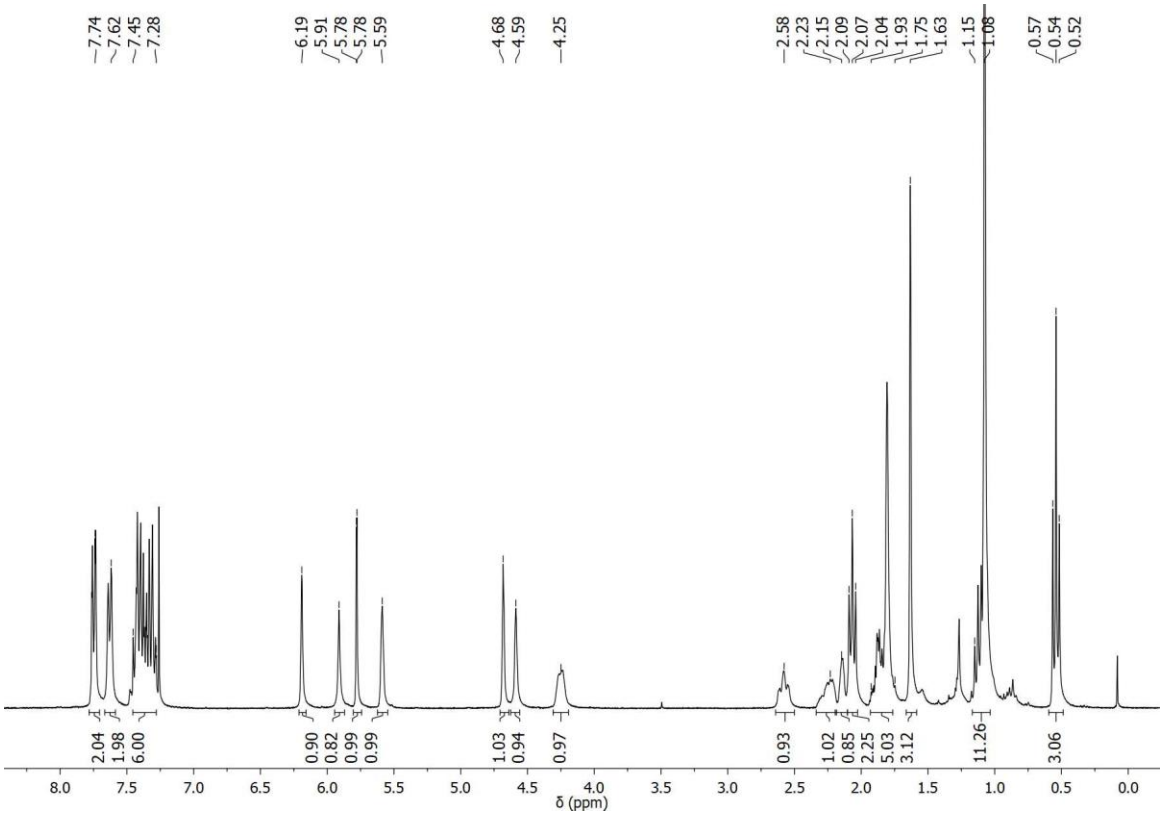

Figure A92. ^{1}H-NMR spectrum (300 MHz, $CDCl_3$) of compound **172**.

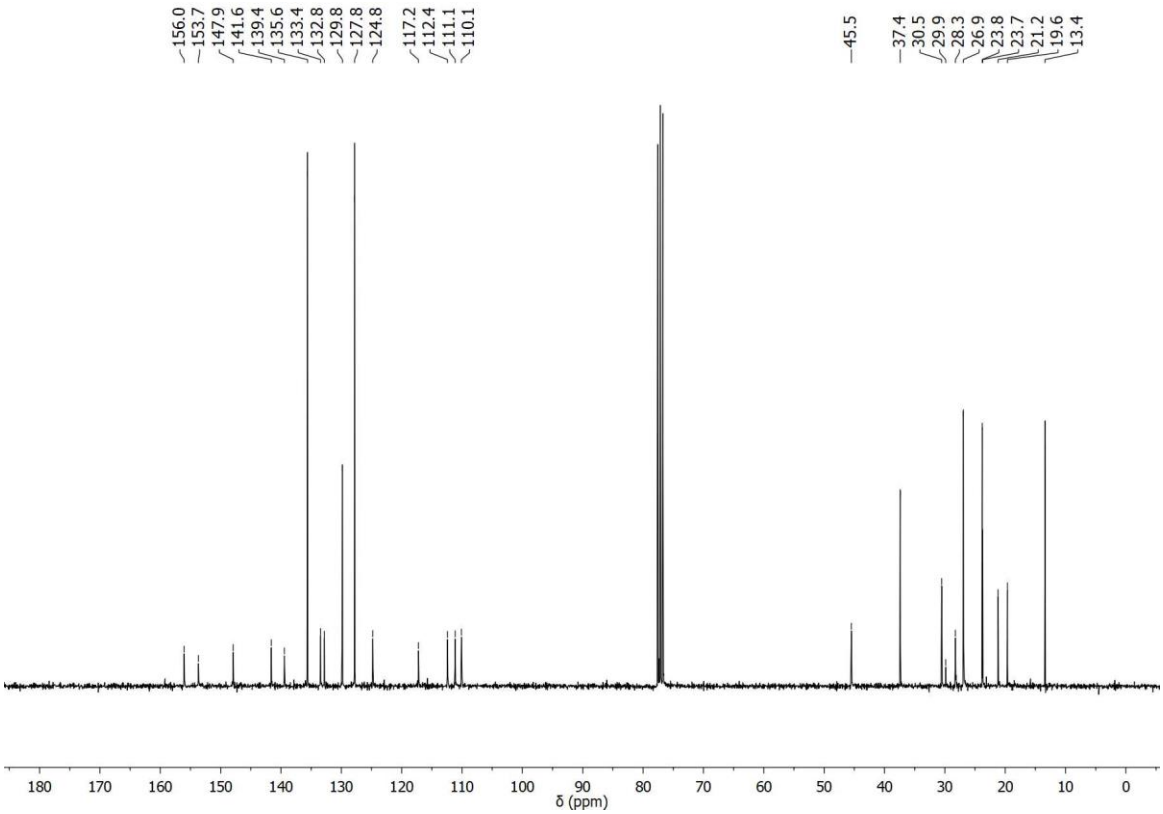

Figure A93. ^{13}C-NMR spectrum (75 MHz, $CDCl_3$) of compound **172**.

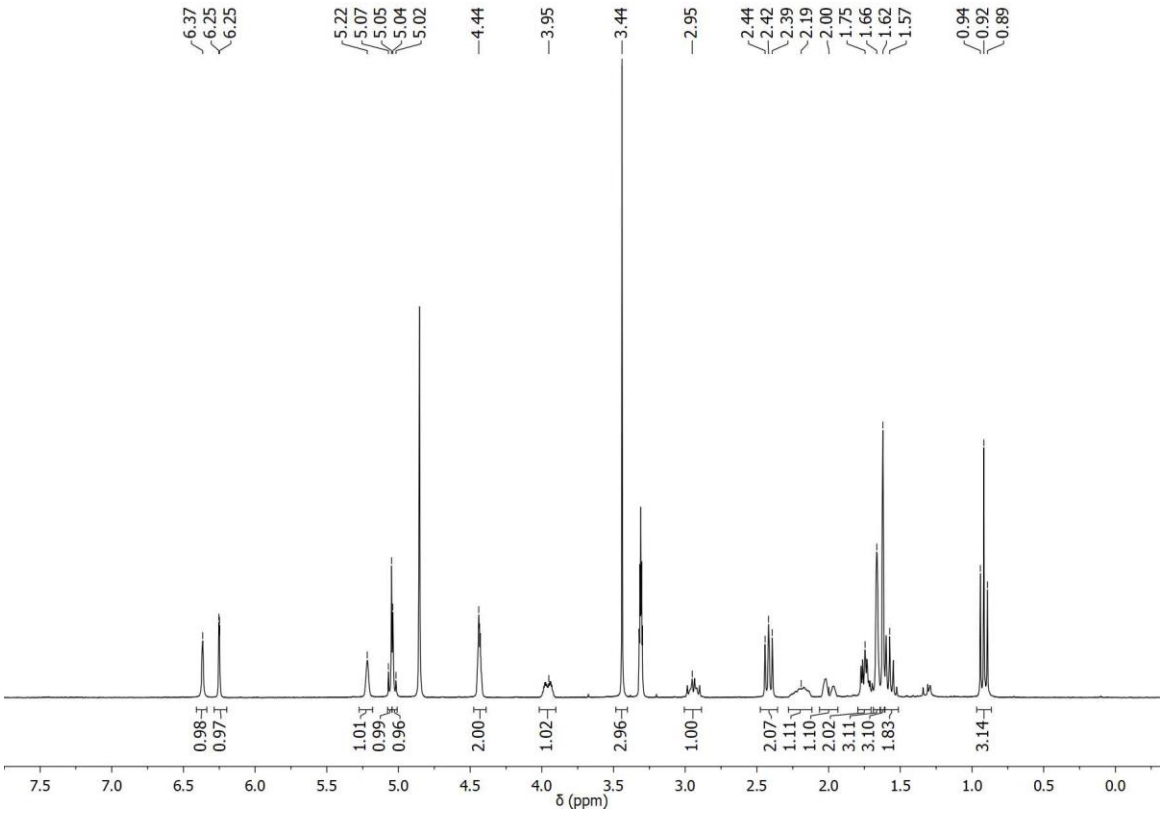

Figure A94. ^{1}H-NMR spectrum (300 MHz, MeOD) of compound **175**.

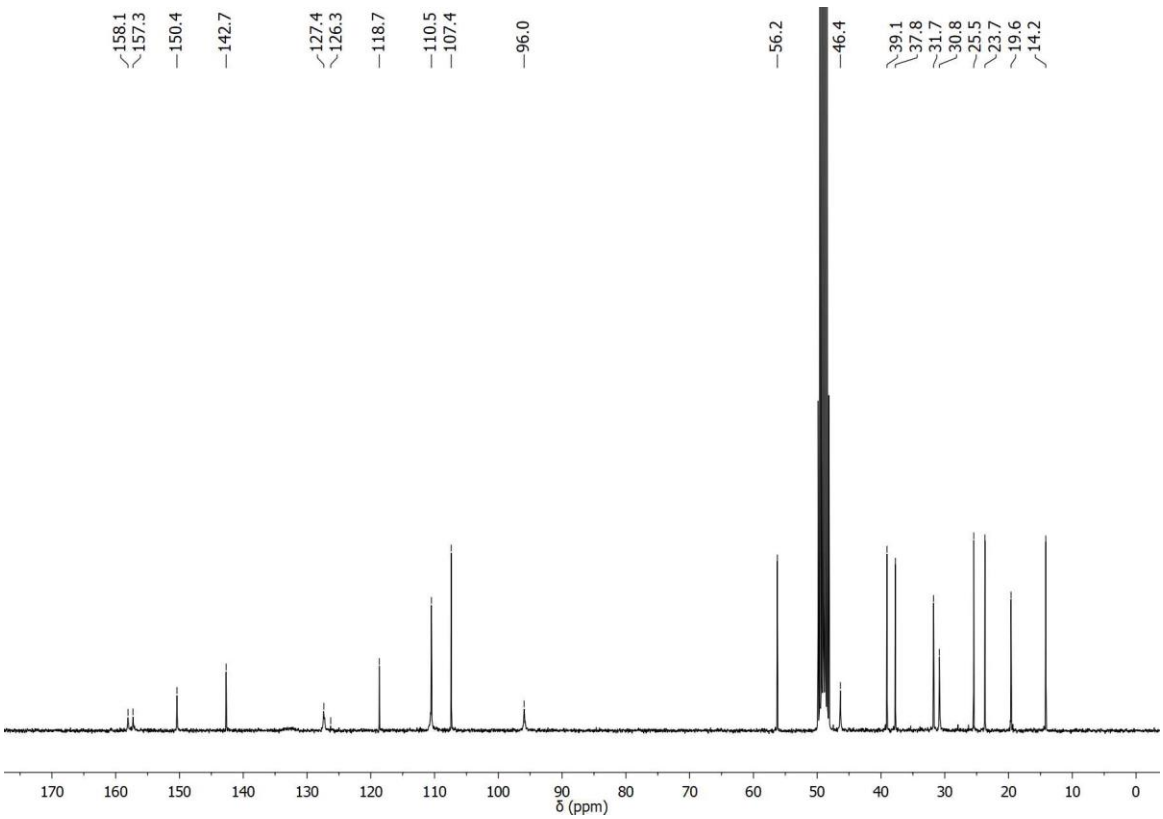

Figure A95. ^{13}C-NMR spectrum (75 MHz, MeOD) of compound **175**.

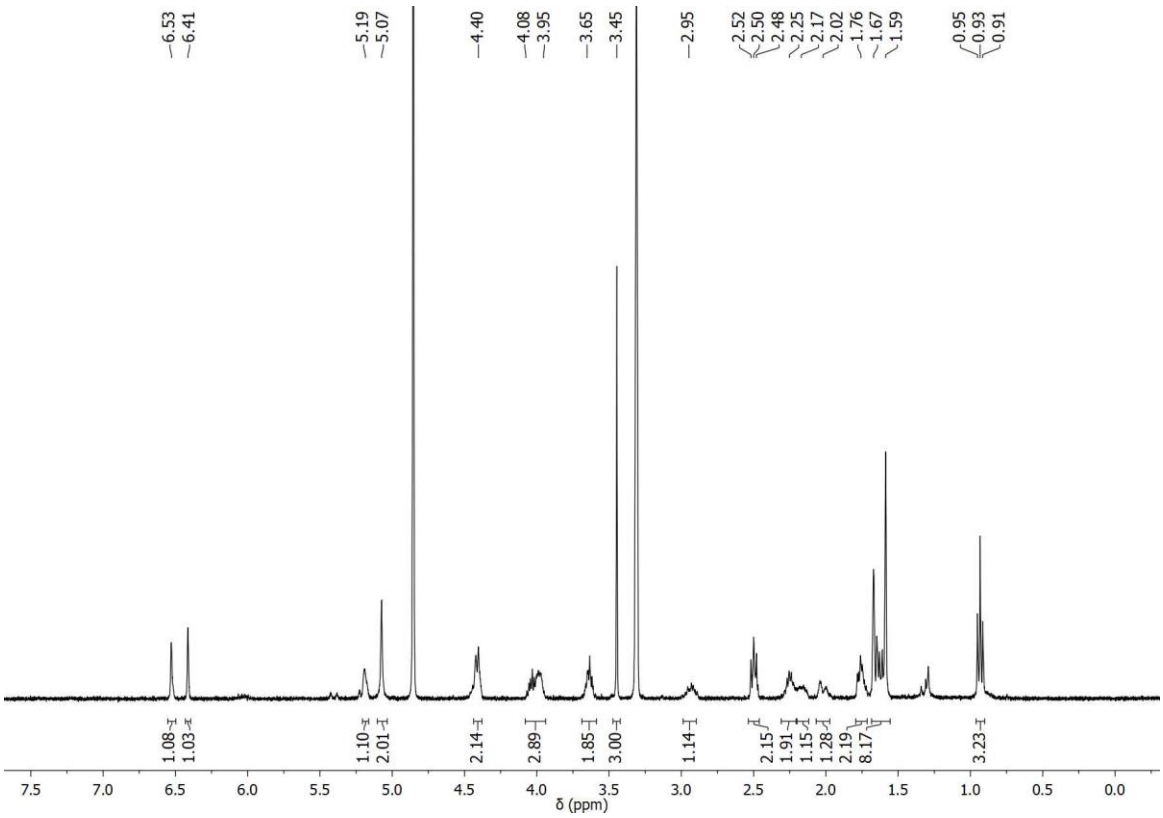

Figure A96. ^{1}H-NMR spectrum (400 MHz, MeOD) of compound **178**.

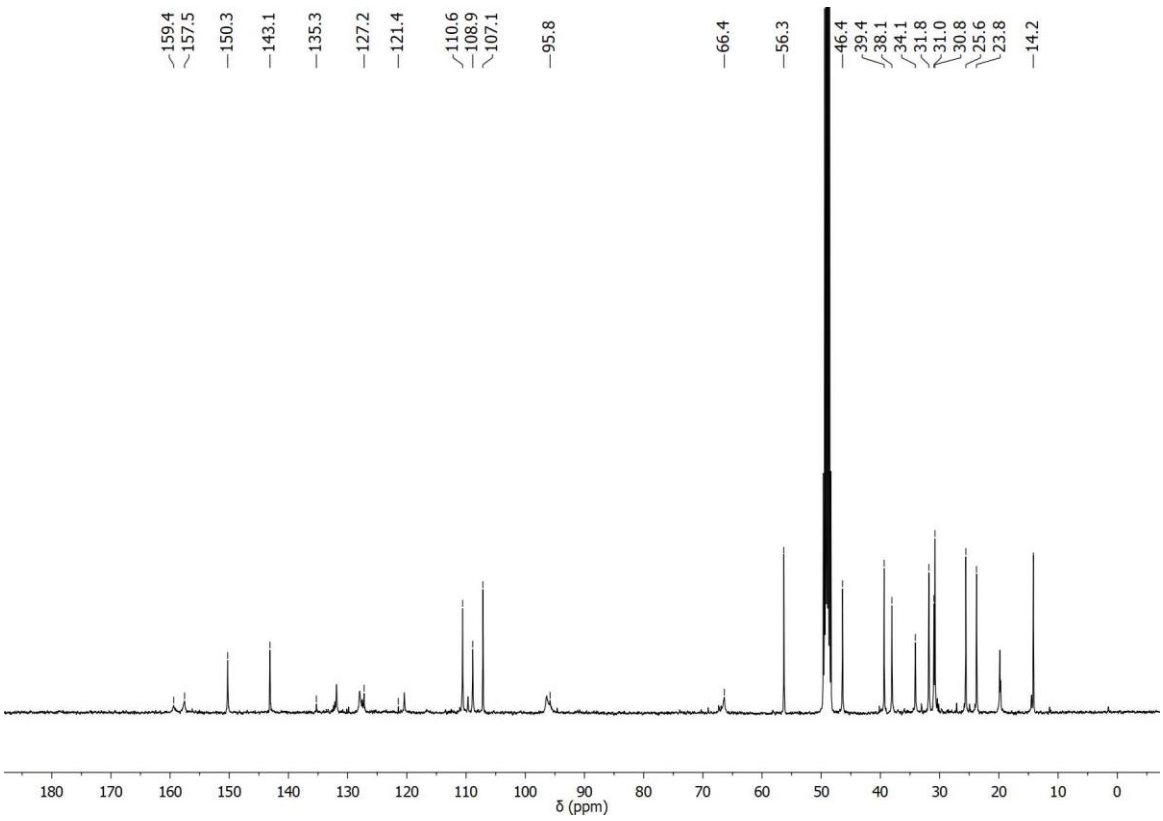

Figure A97. ^{13}C-NMR spectrum (100 MHz, MeOD) of compound **178**.

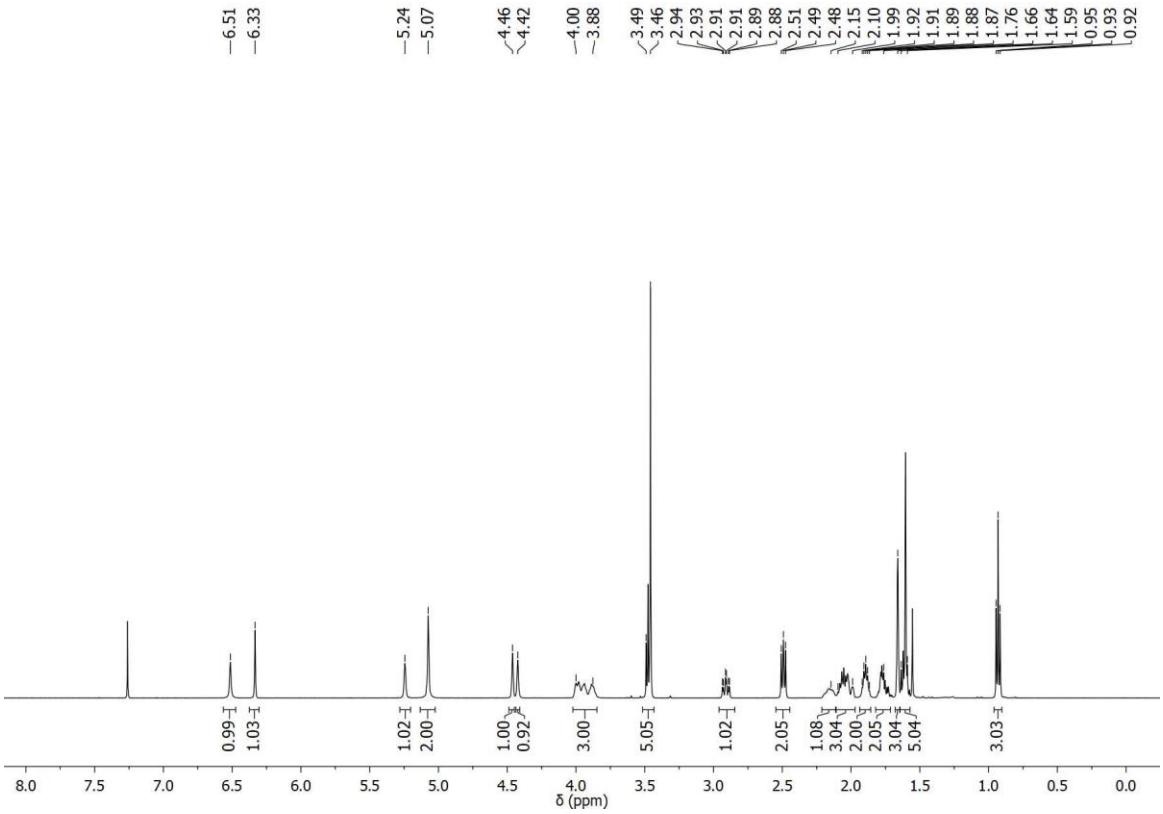

Figure A98. ^{1}H-NMR spectrum (500 MHz, $CDCl_3$) of compound **179**.

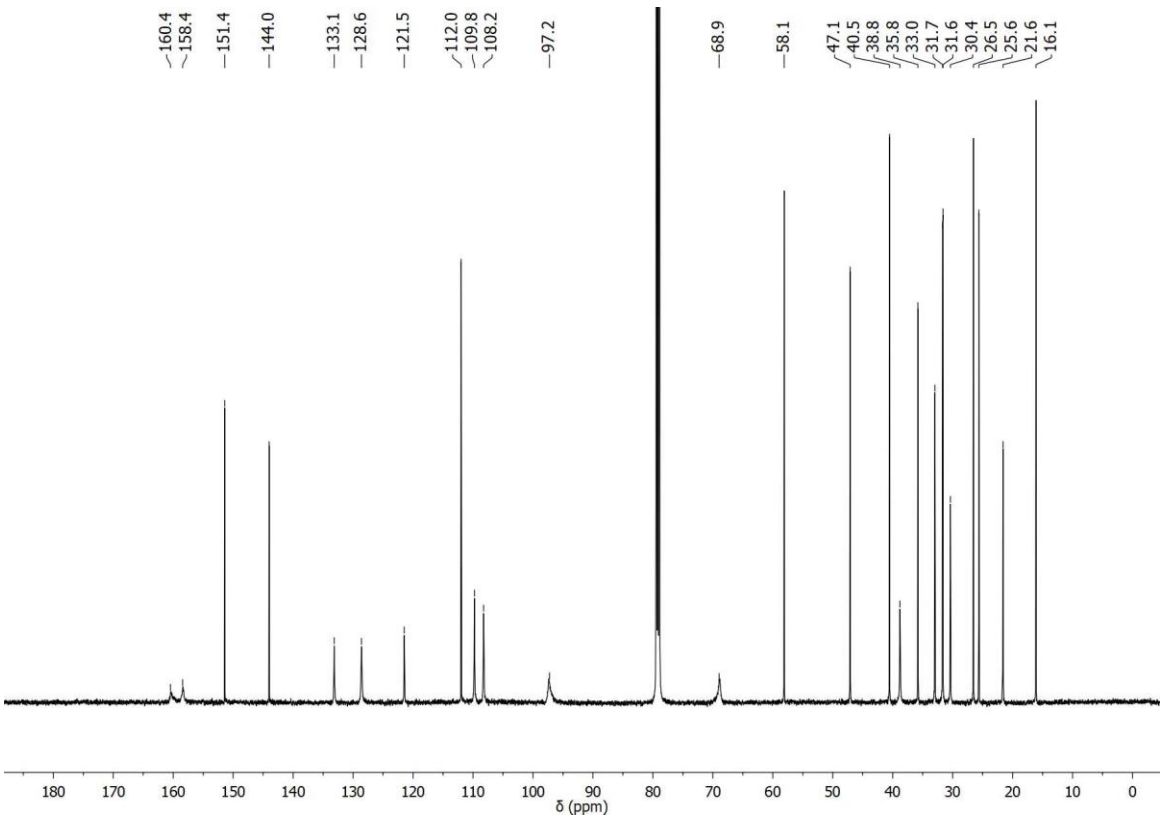

Figure A99. ^{13}C-NMR spectrum (125 MHz, $CDCl_3$) of compound **179**.

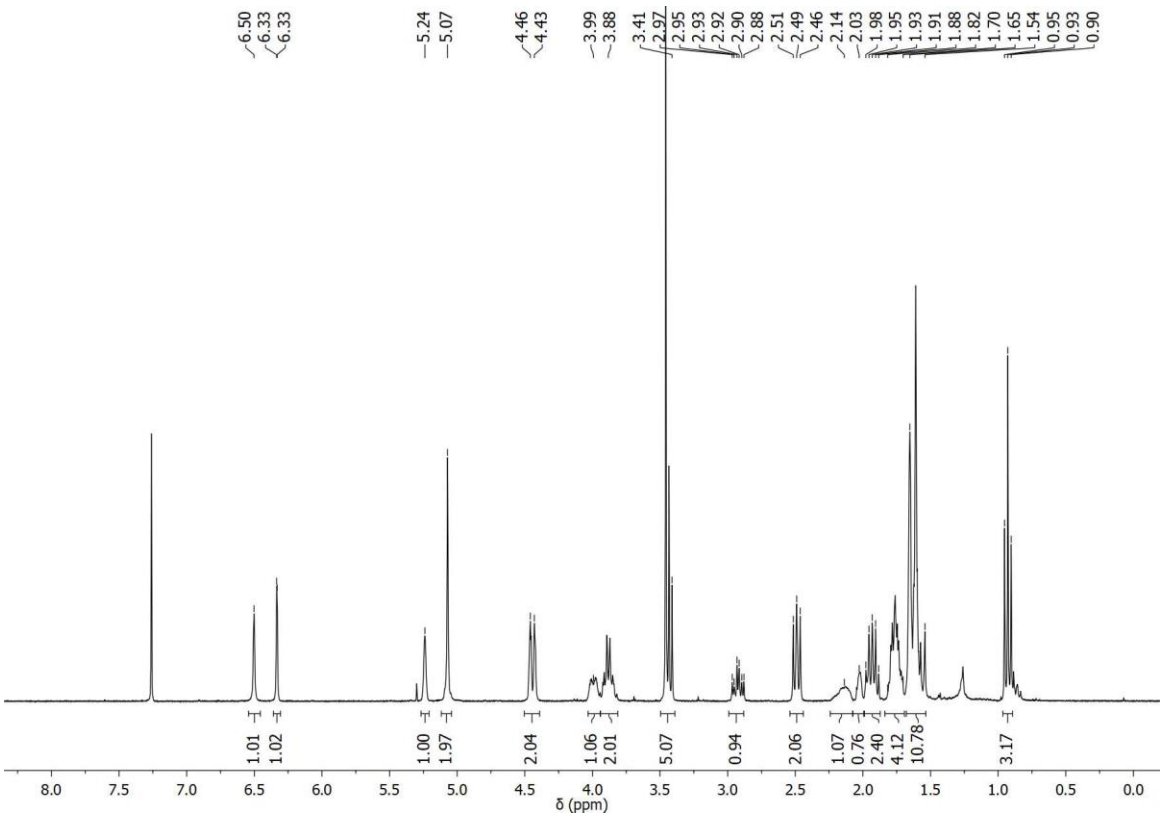

Figure A100. ^{1}H-NMR spectrum (300 MHz, $CDCl_3$) of compound **180**.

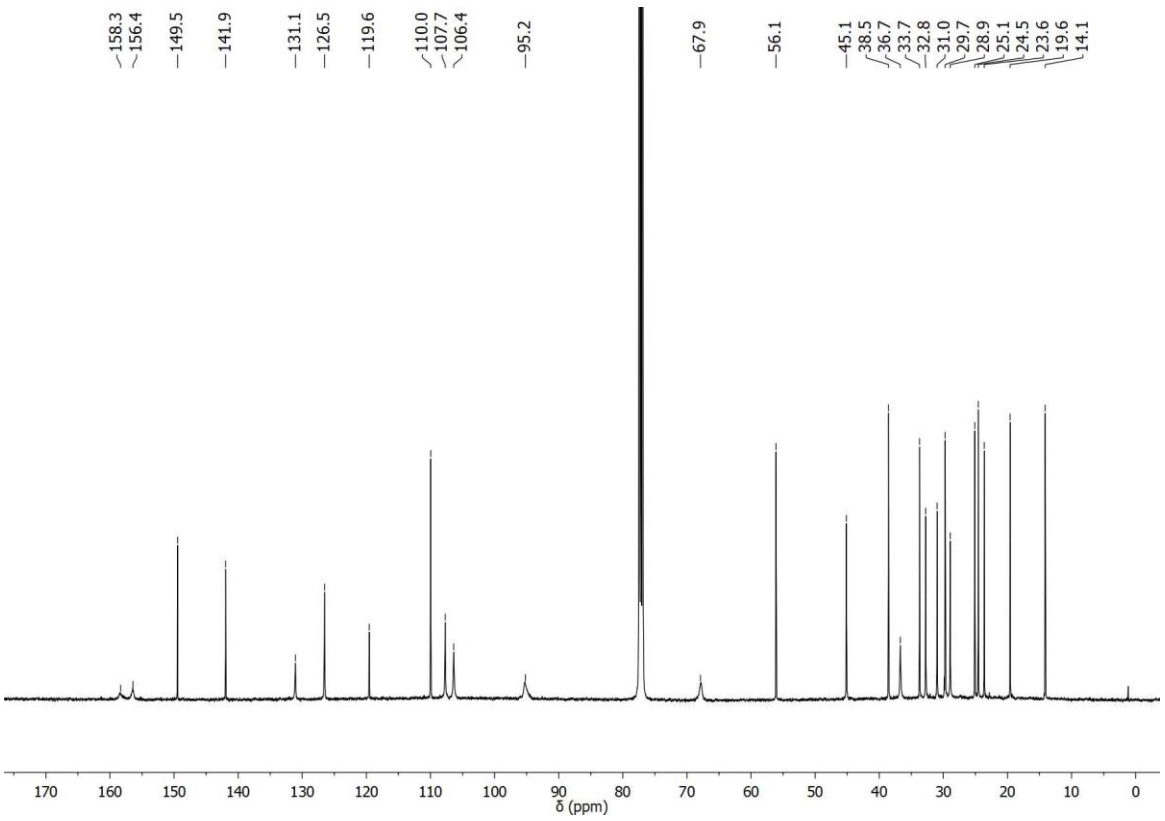

Figure A101. ^{13}C-NMR spectrum (125 MHz, $CDCl_3$) of compound **180**.

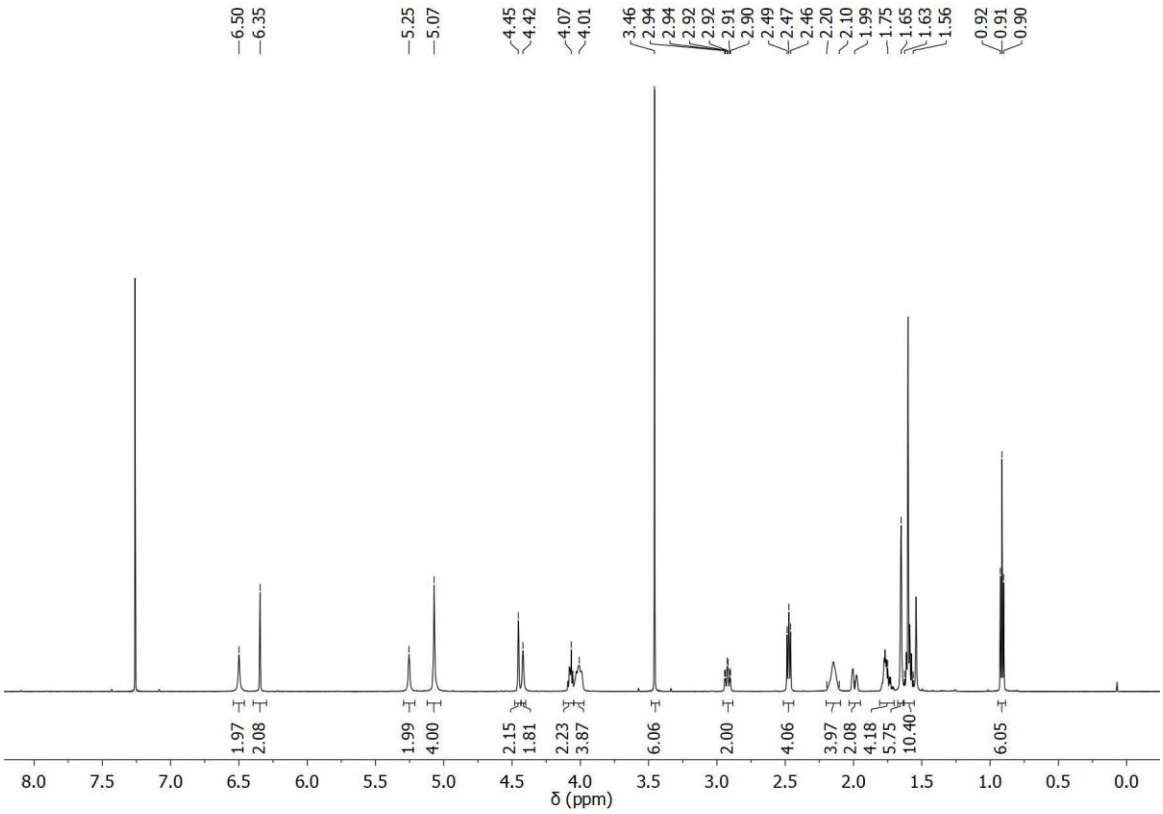

Figure A102. ^{1}H-NMR spectrum (600 MHz, $CDCl_3$) of compound **182**.

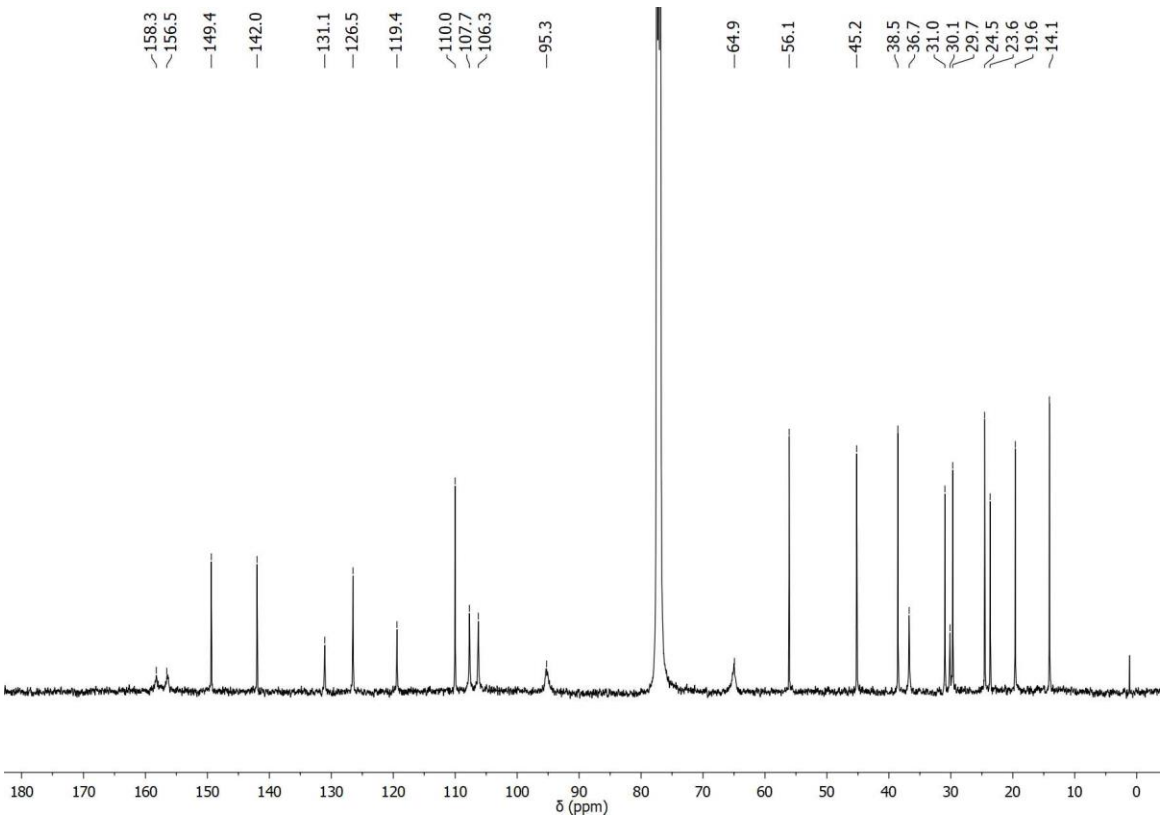

Figure A103. ^{13}C-NMR spectrum (125 MHz, $CDCl_3$) of compound **182**.

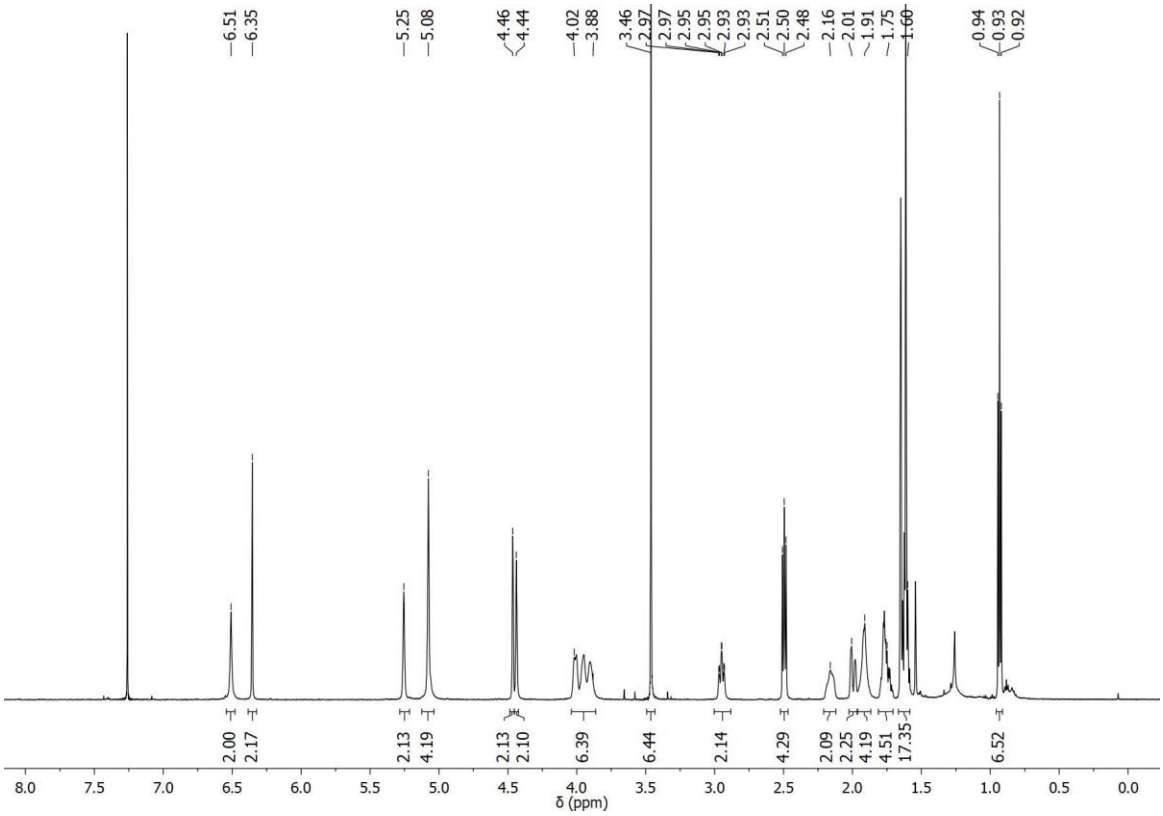

Figure A104. ^{1}H-NMR spectrum (600 MHz, $CDCl_3$) of compound **183**.

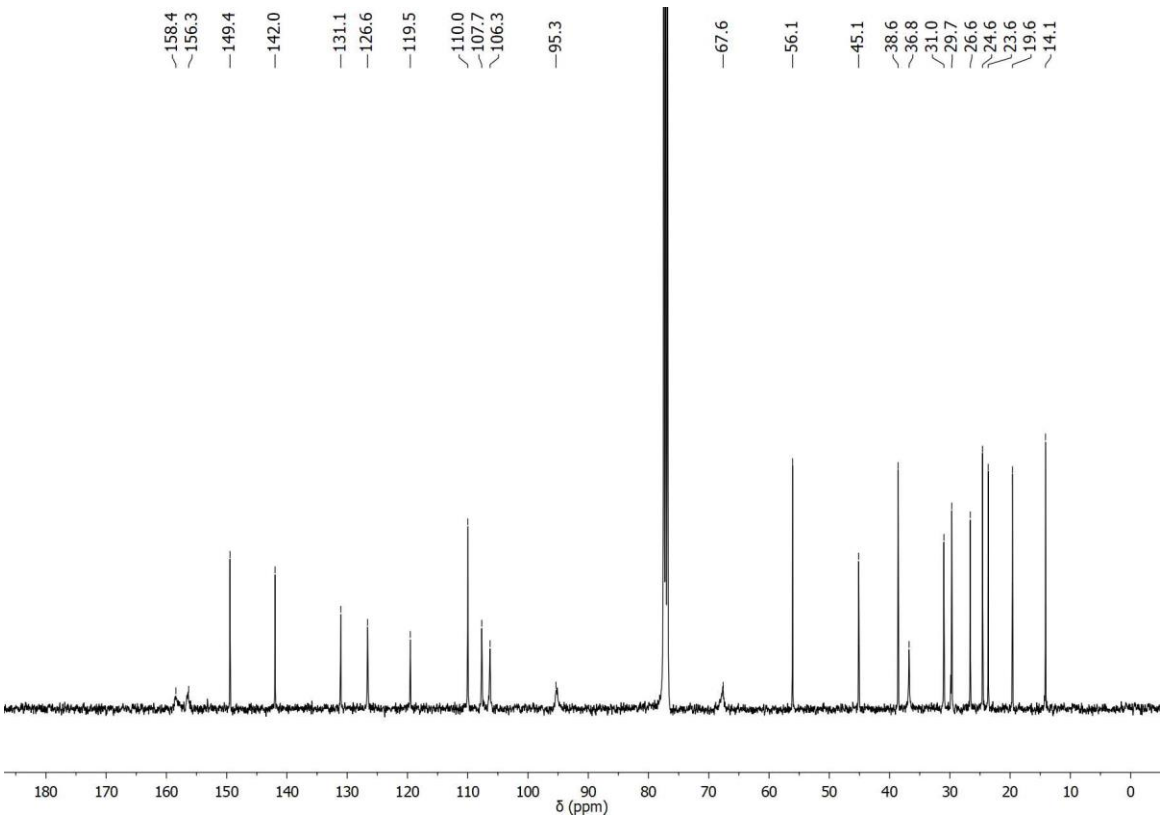

Figure A105. ^{13}C-NMR spectrum (125 MHz, $CDCl_3$) of compound **183**.

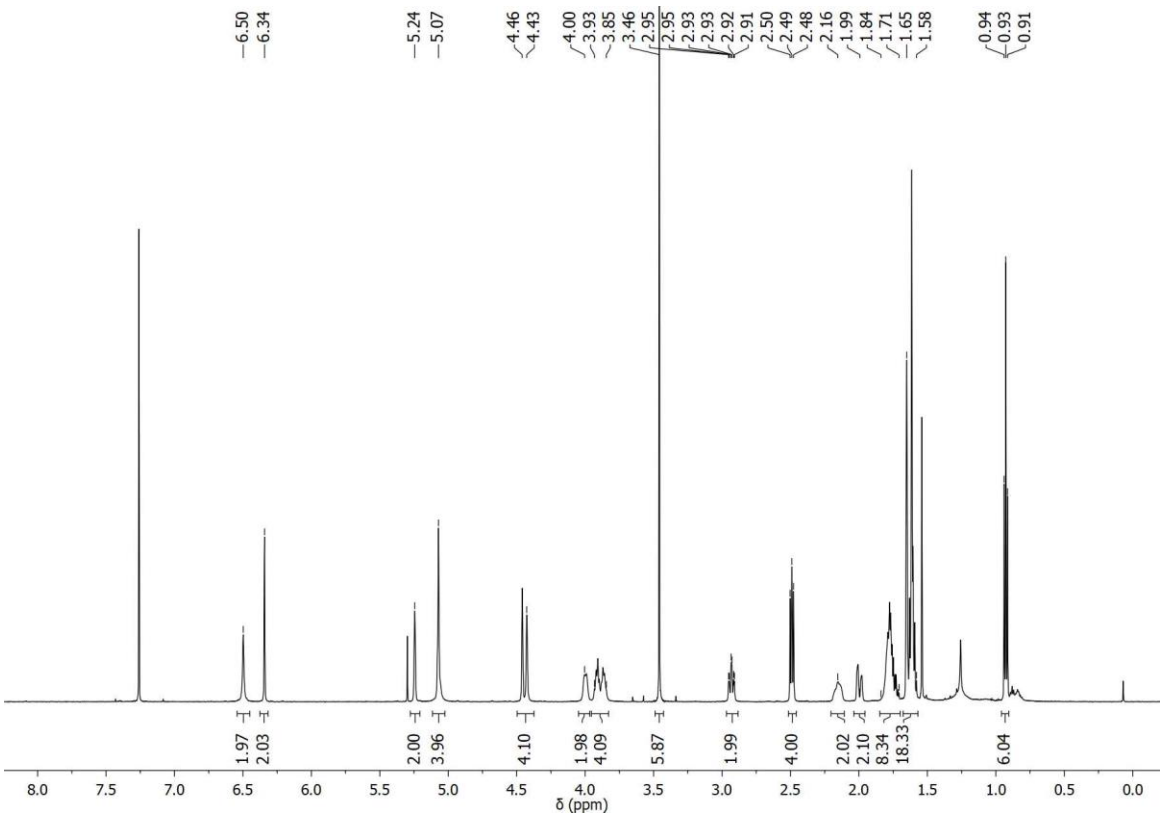

Figure A106. ^{1}H-NMR spectrum (600 MHz, $CDCl_3$) of compound **184**.

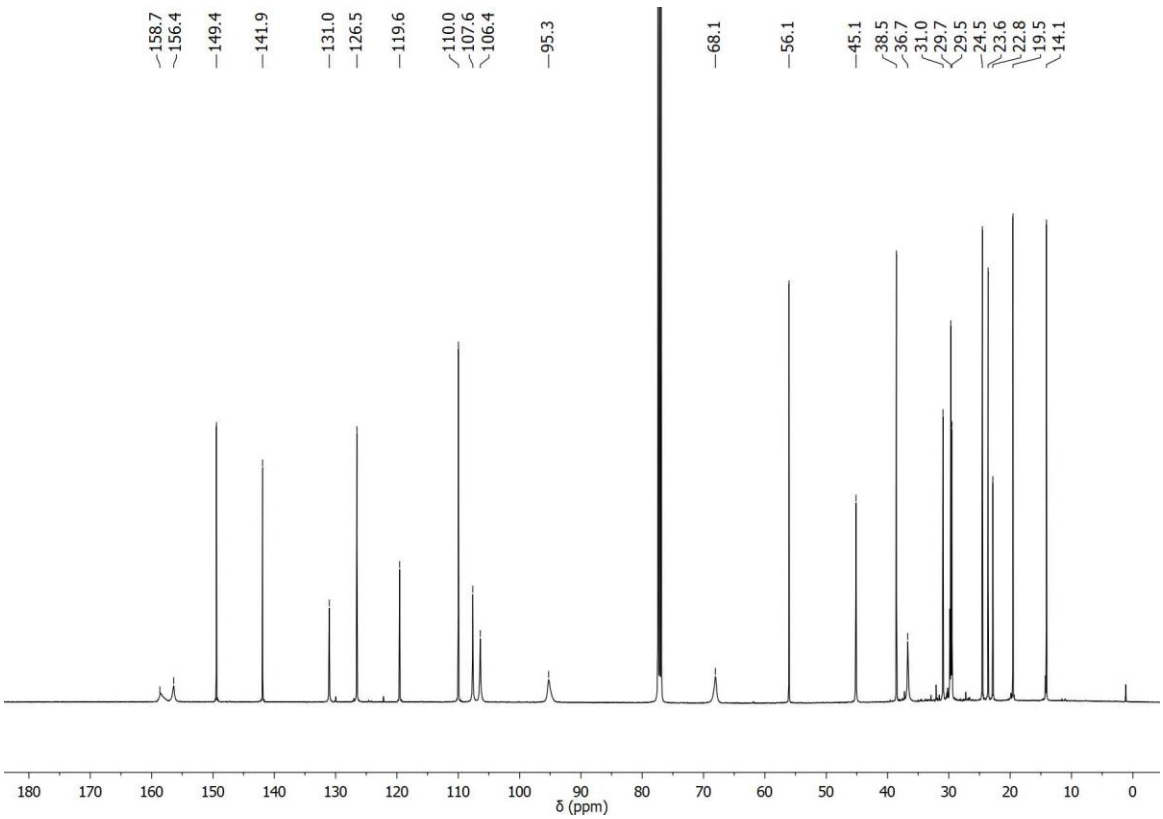

Figure A107. ^{13}C-NMR spectrum (125 MHz, $CDCl_3$) of compound **184**.

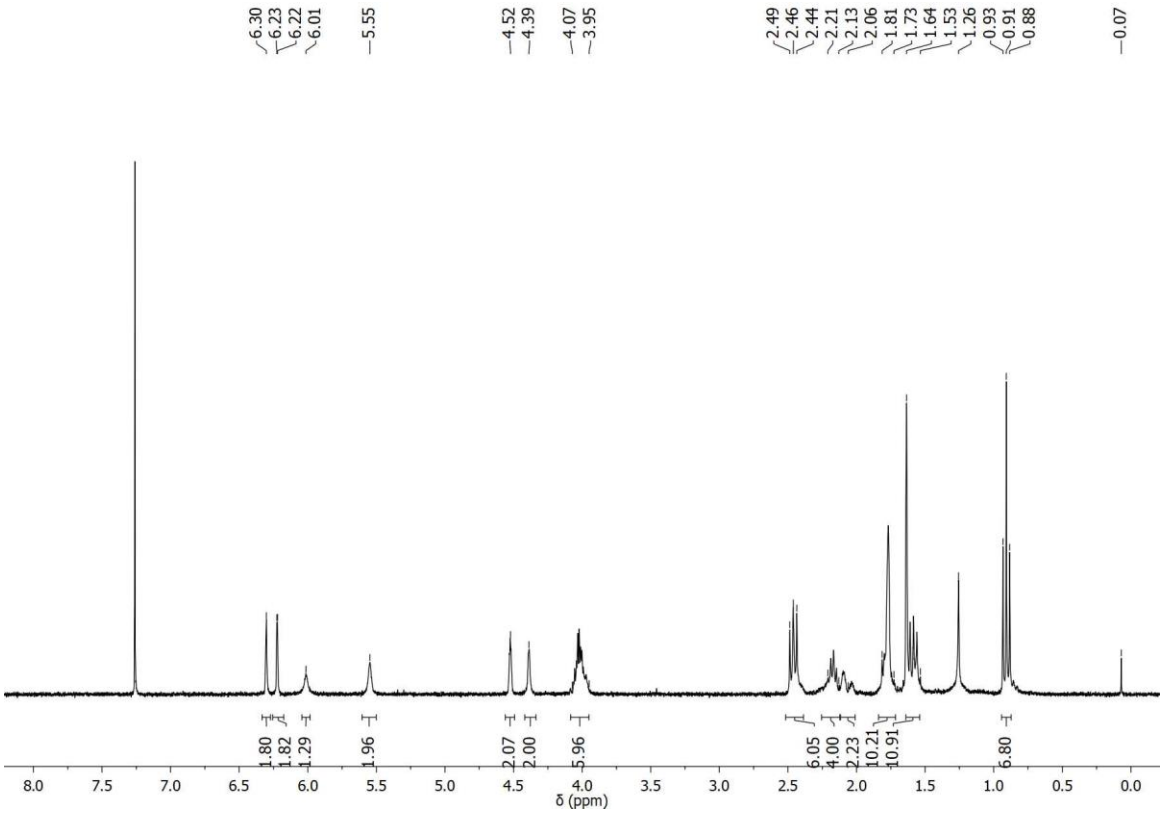

Figure A108. ^{1}H-NMR spectrum (300 MHz, $CDCl_3$) of compound **158**.

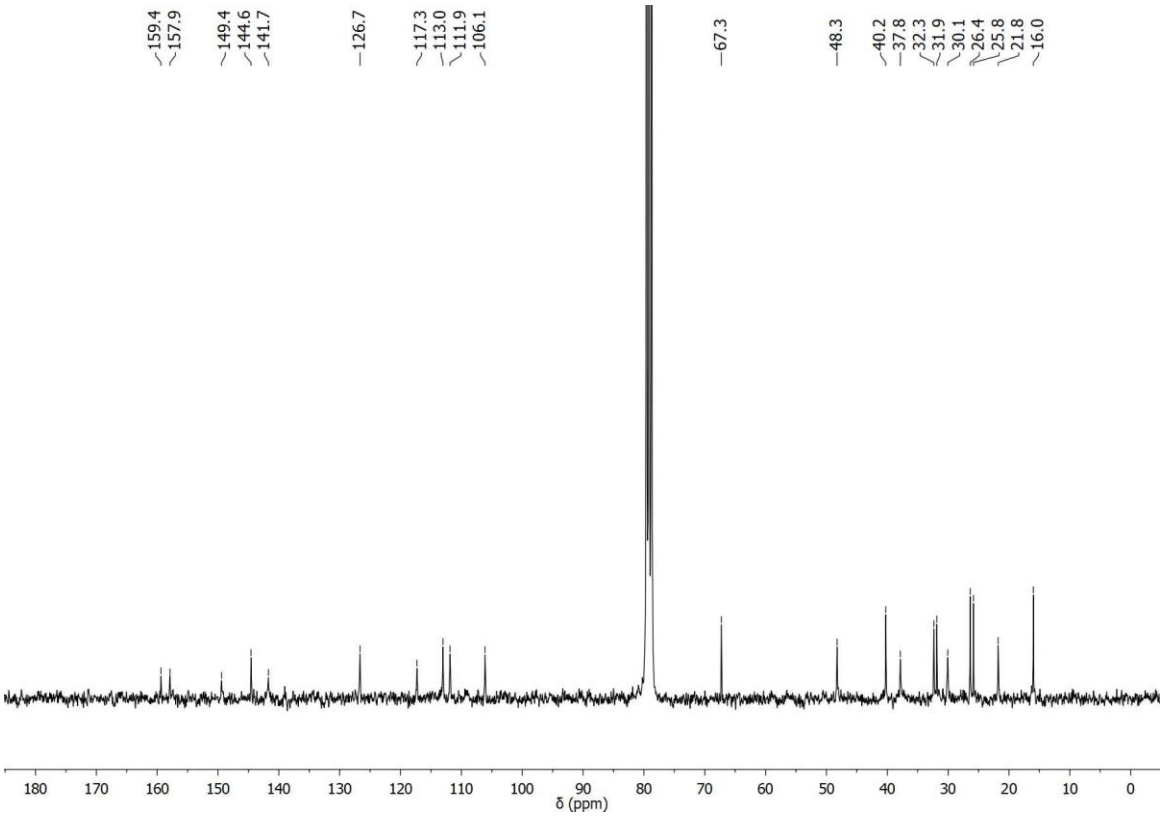

Figure A109. ^{13}C-NMR spectrum (75 MHz, $CDCl_3$) of compound **158**.

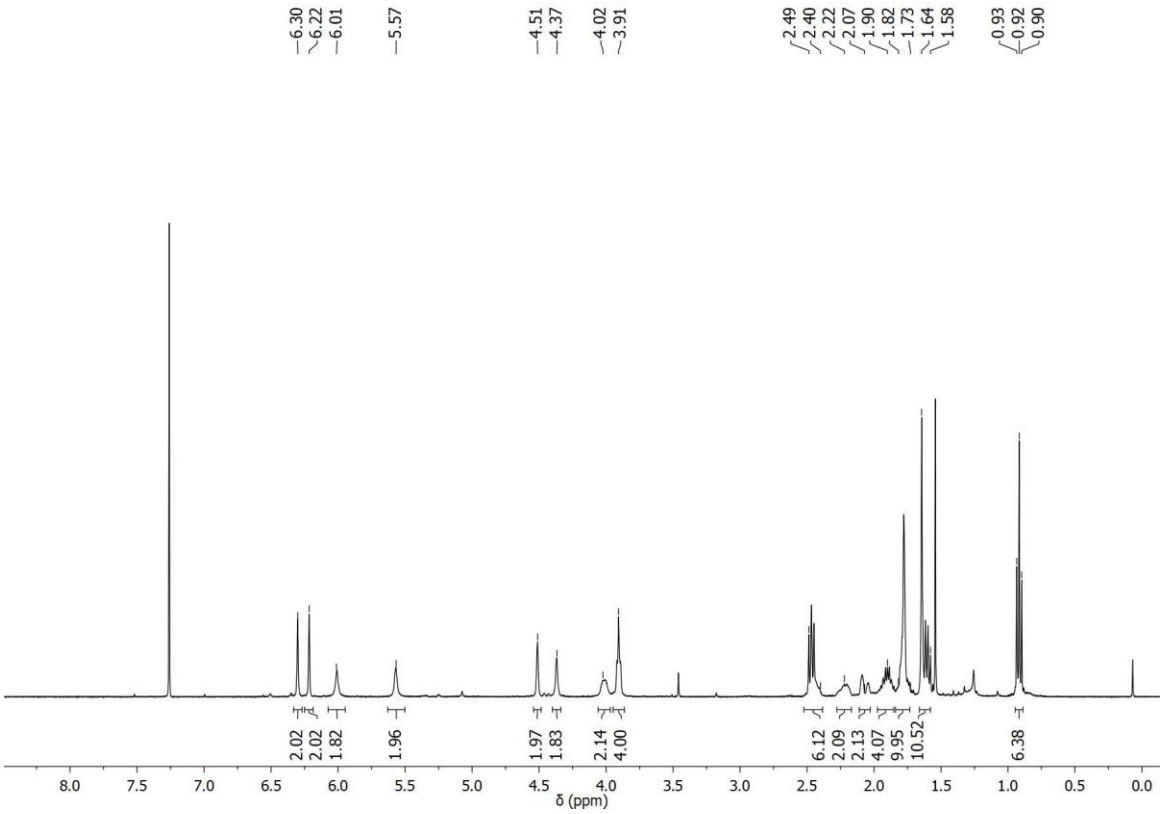

Figure A110. ^{1}H-NMR spectrum (400 MHz, $CDCl_3$) of compound **159**.

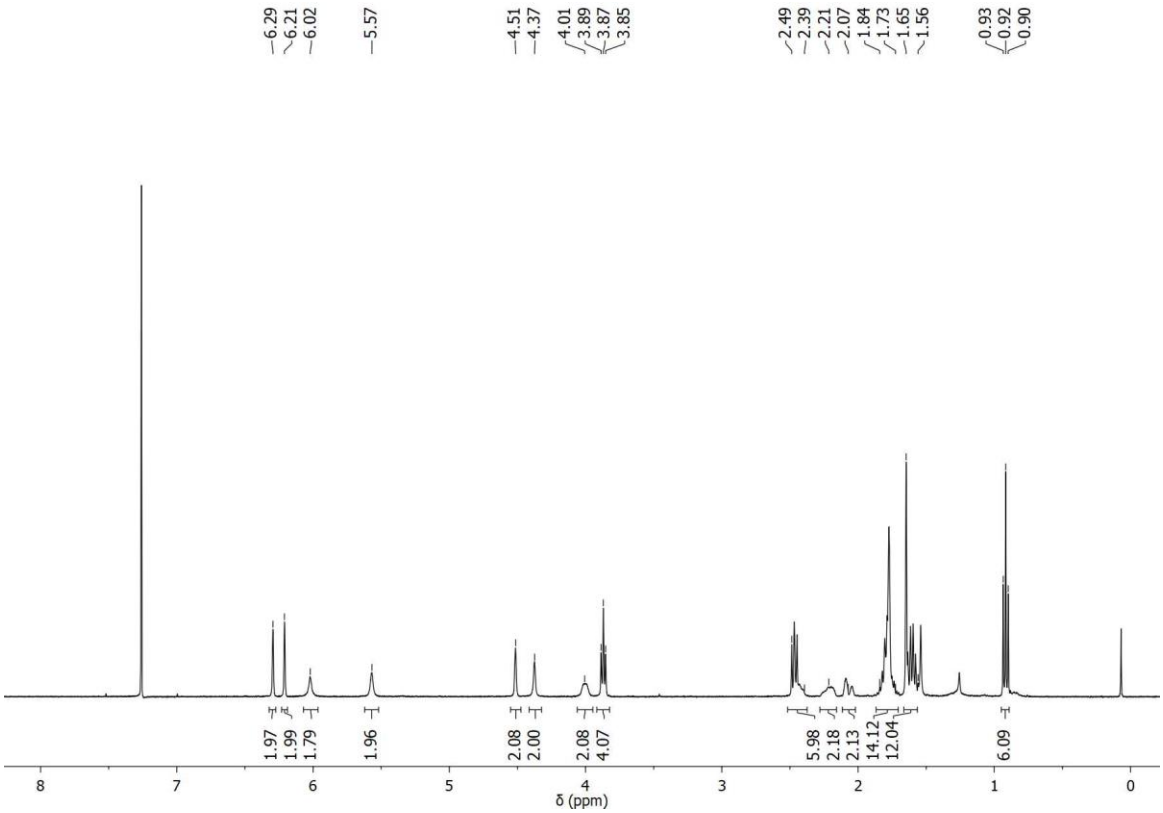

Figure A111. ^{1}H-NMR spectrum (400 MHz, $CDCl_3$) of compound **160**.

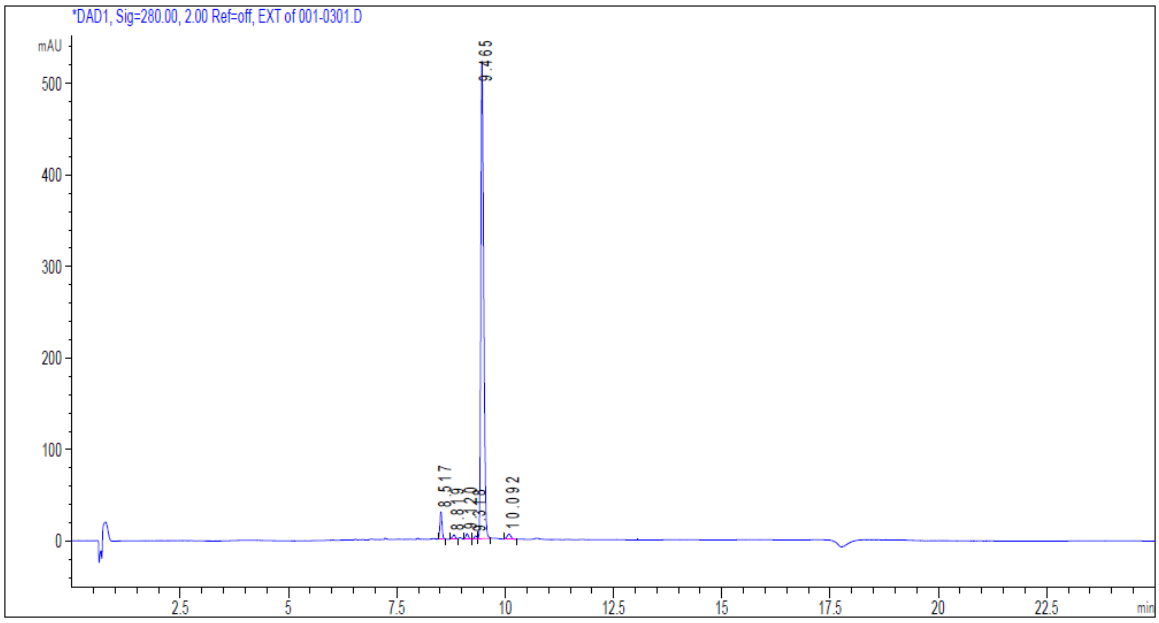

Figure A112. HPLC chromatogram for purity analysis of the compound **158**, showing a main peak at Rt = 9.465 min with a purity of 95.0%.

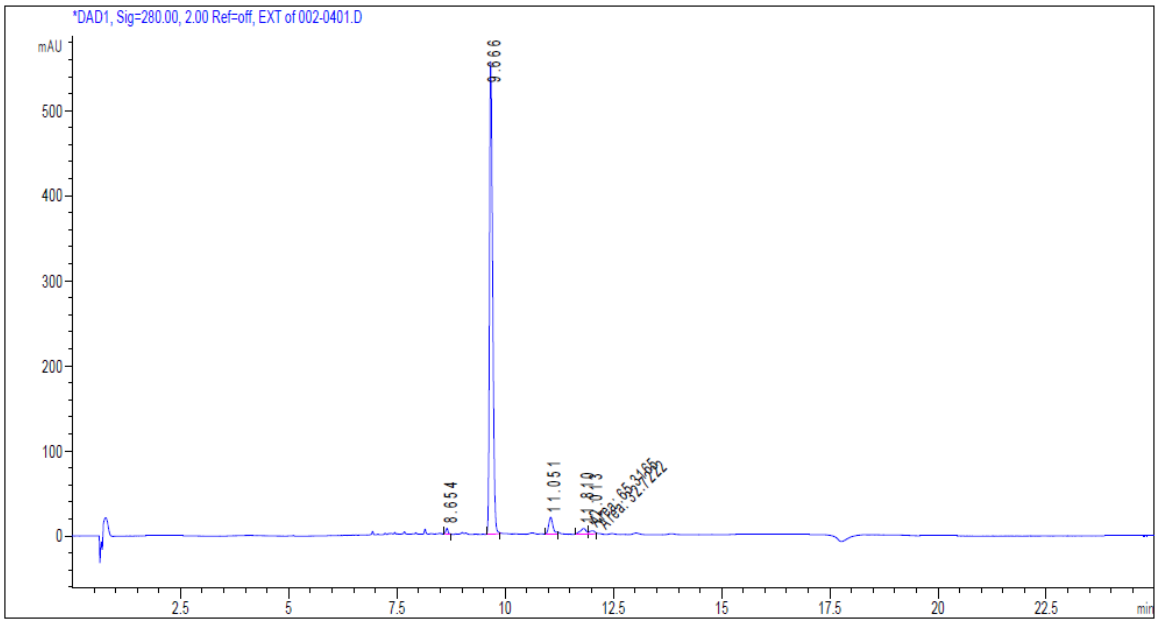

Figure A113. HPLC chromatogram for purity analysis of the compound **159**, showing a main peak at R_t = 9.666 min with a purity of 92.3%.

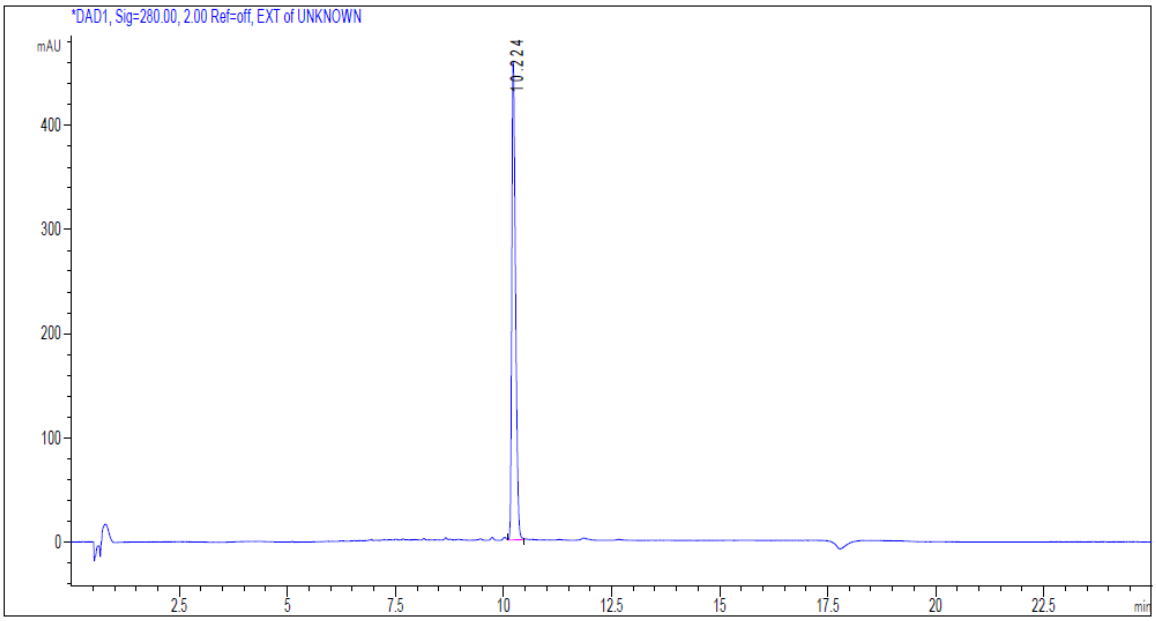

Figure A114. HPLC chromatogram for purity analysis of the compound **160**, showing a main peak at R_t = 10.224 min with a purity of 100.0%.

Chapter IV. Halogen- and Thioether-Containing Ligands Targeting the Allosteric CB_2R Binding Site

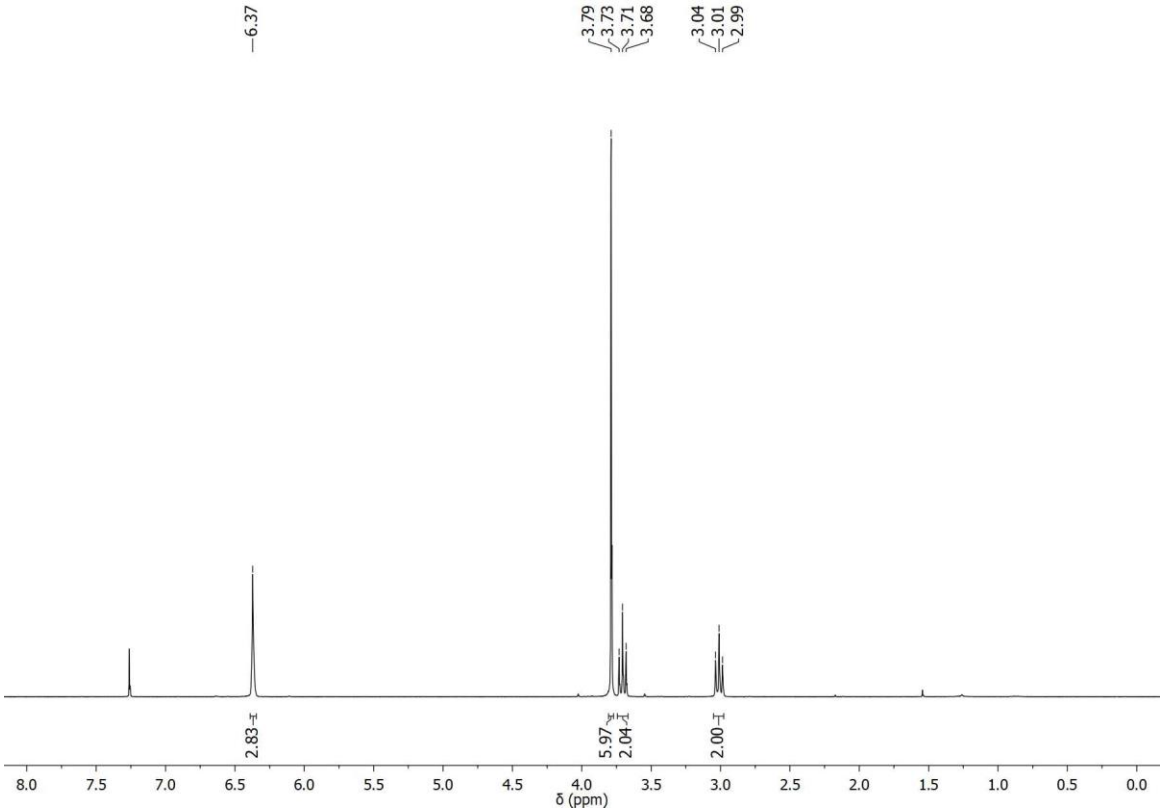

Figure A115. ^{1}H-NMR spectrum (500 MHz, $CDCl_3$) of compound **205**.

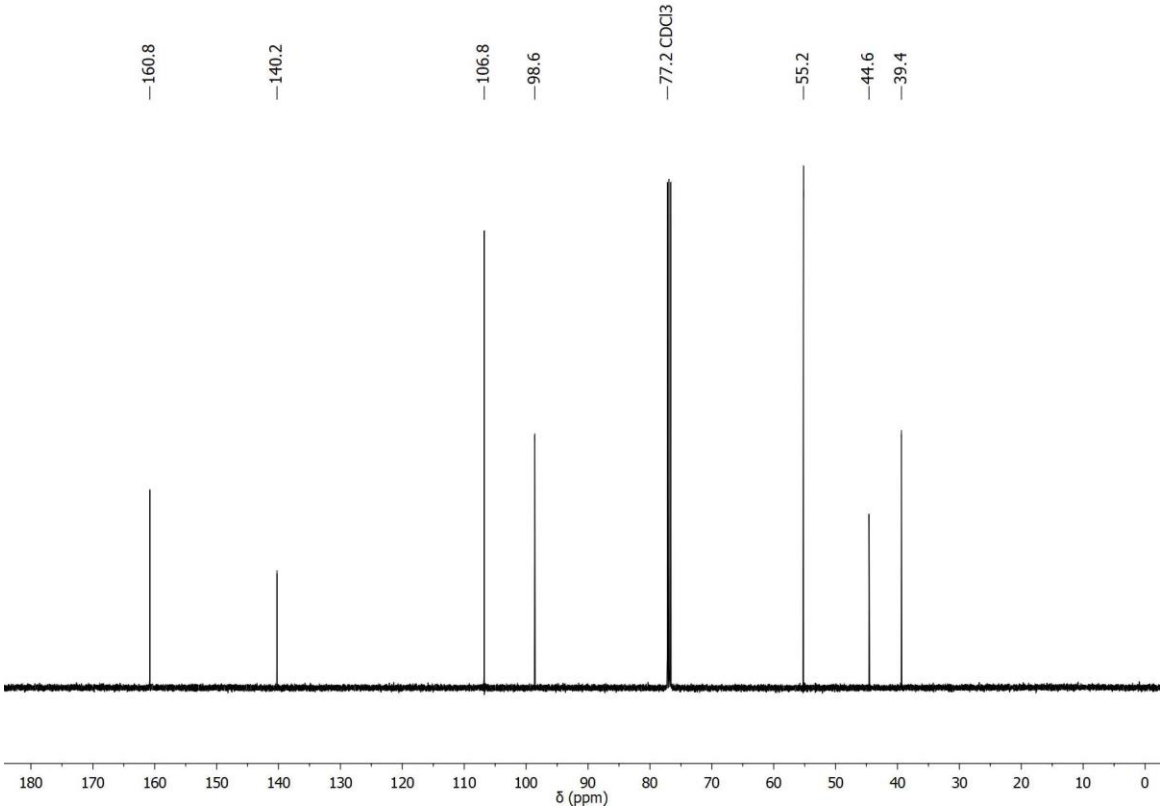

Figure A116. ^{13}C-NMR spectrum (125 MHz, $CDCl_3$) of compound **205**.

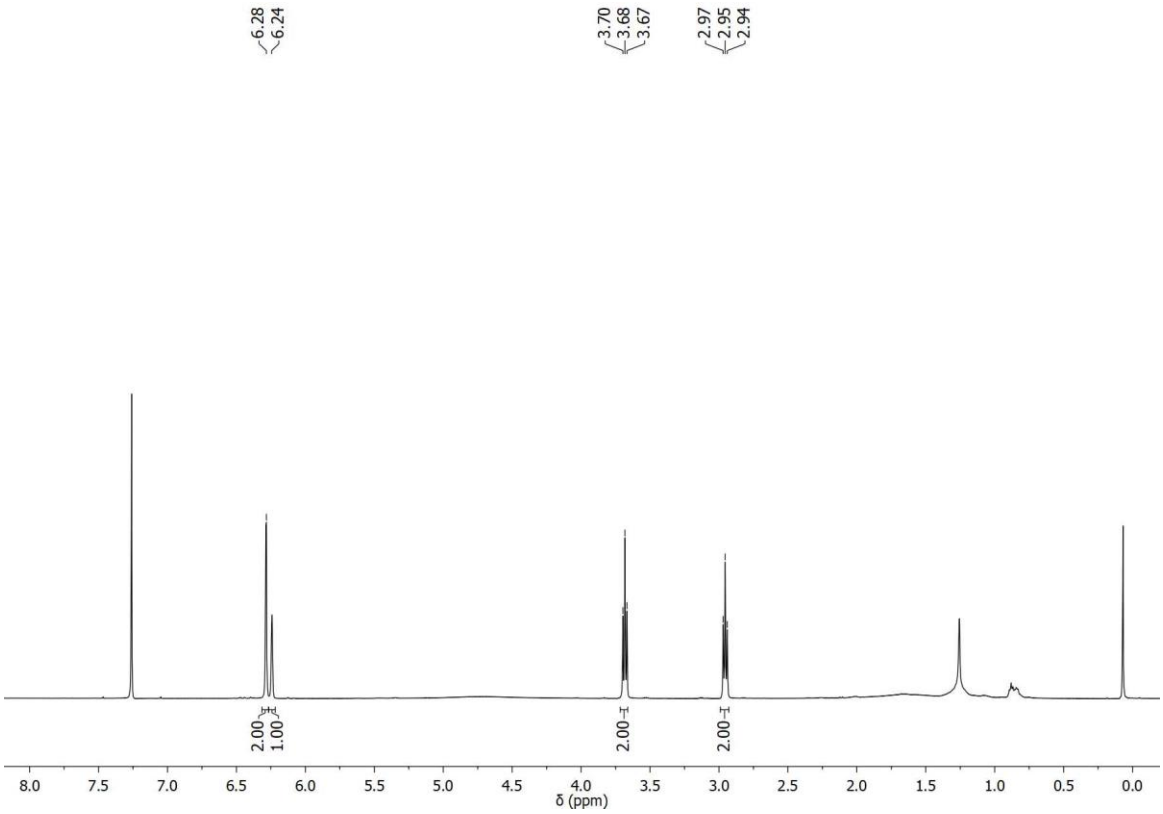

Figure A117. ^{1}H-NMR spectrum (500 MHz, $CDCl_3$) of compound **210**.

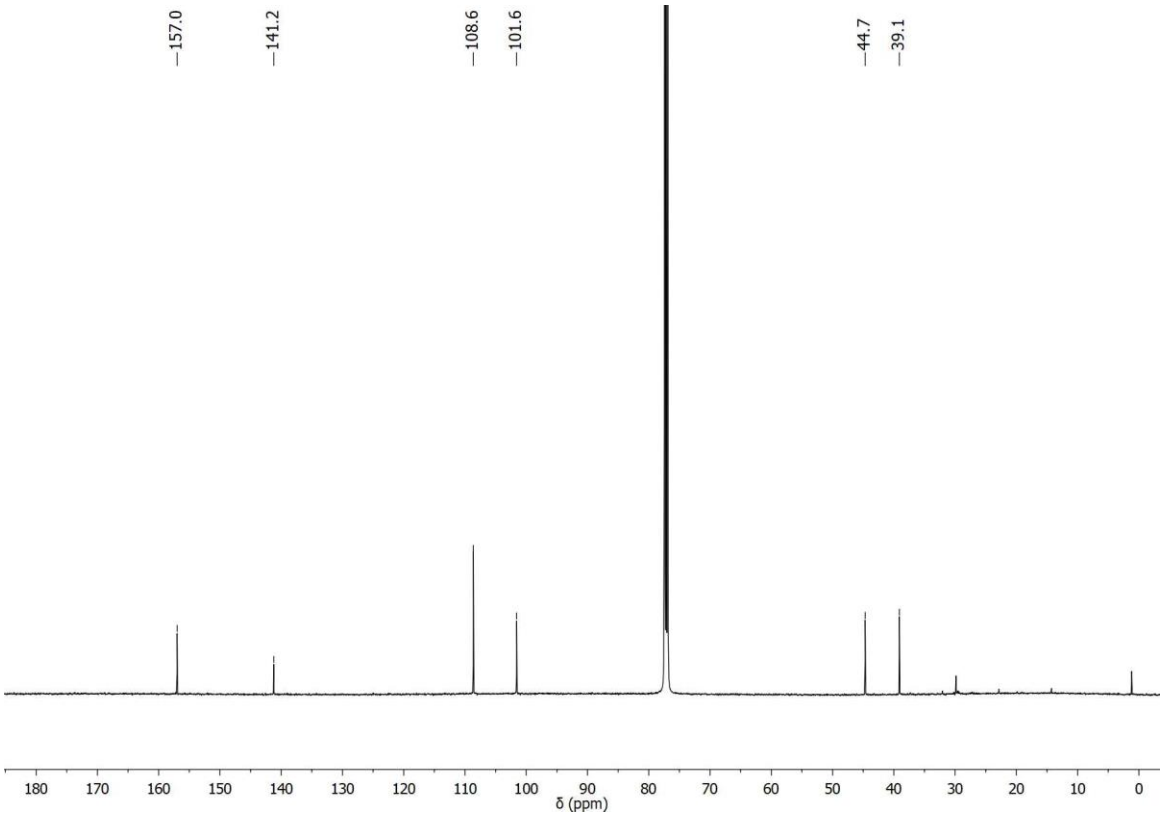

Figure A118. ^{13}C-NMR spectrum (125 MHz, $CDCl_3$) of compound **210**.

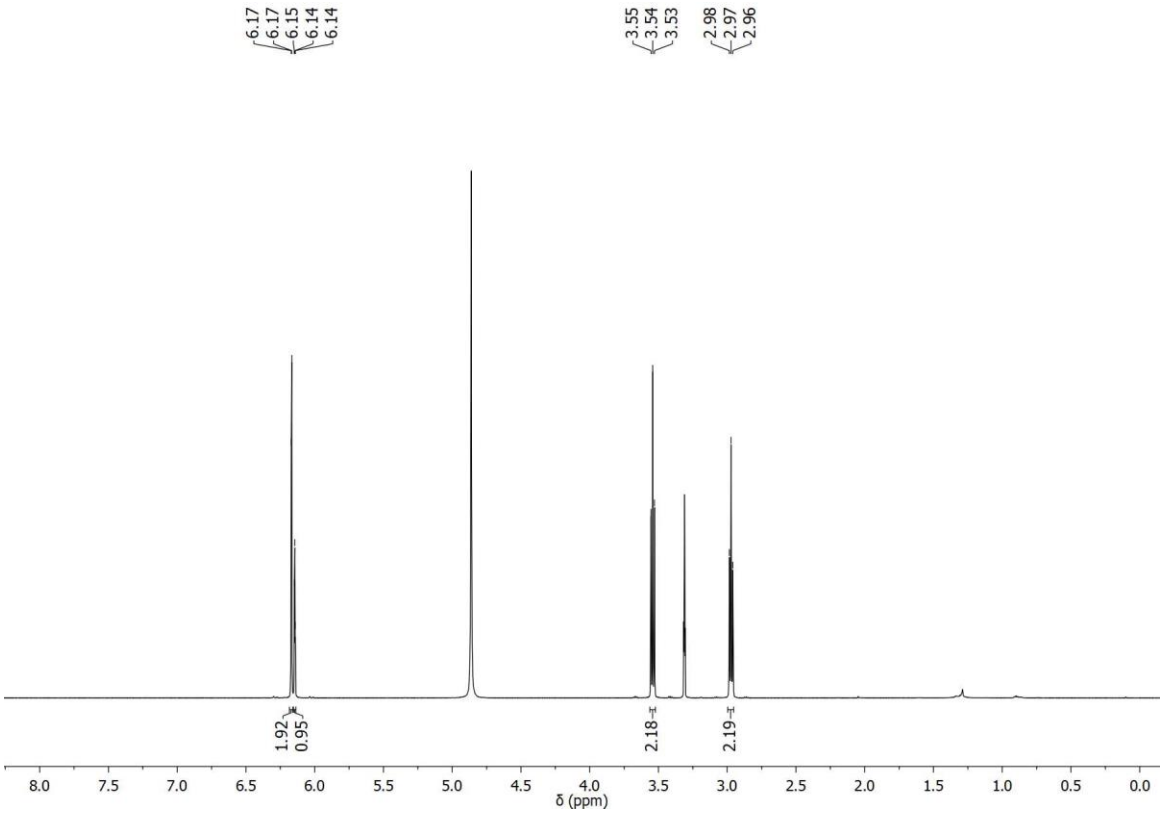

Figure A119. ^{1}H-NMR spectrum (600 MHz, MeOD) of compound **211**.

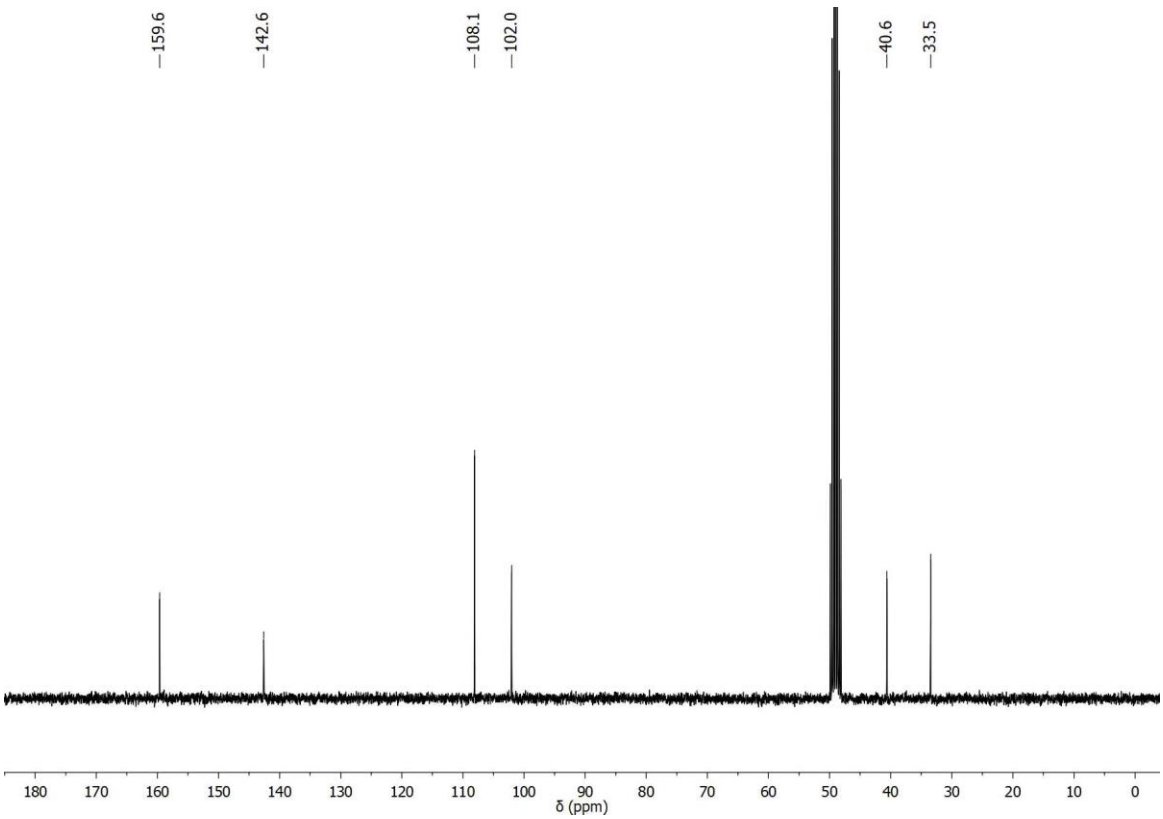

Figure A120. ^{13}C-NMR spectrum (75 MHz, MeOD) of compound **211**.

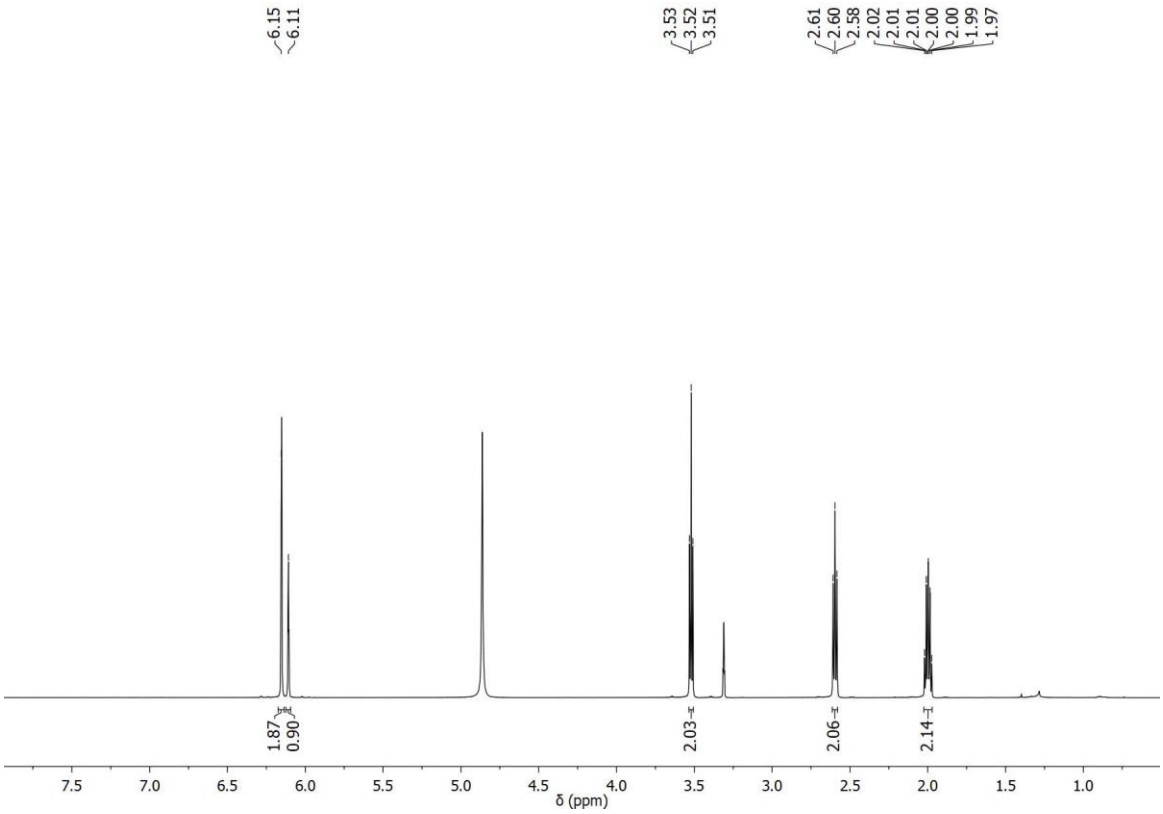

Figure A121. ^{1}H-NMR spectrum (600 MHz, MeOD) of compound **212**.

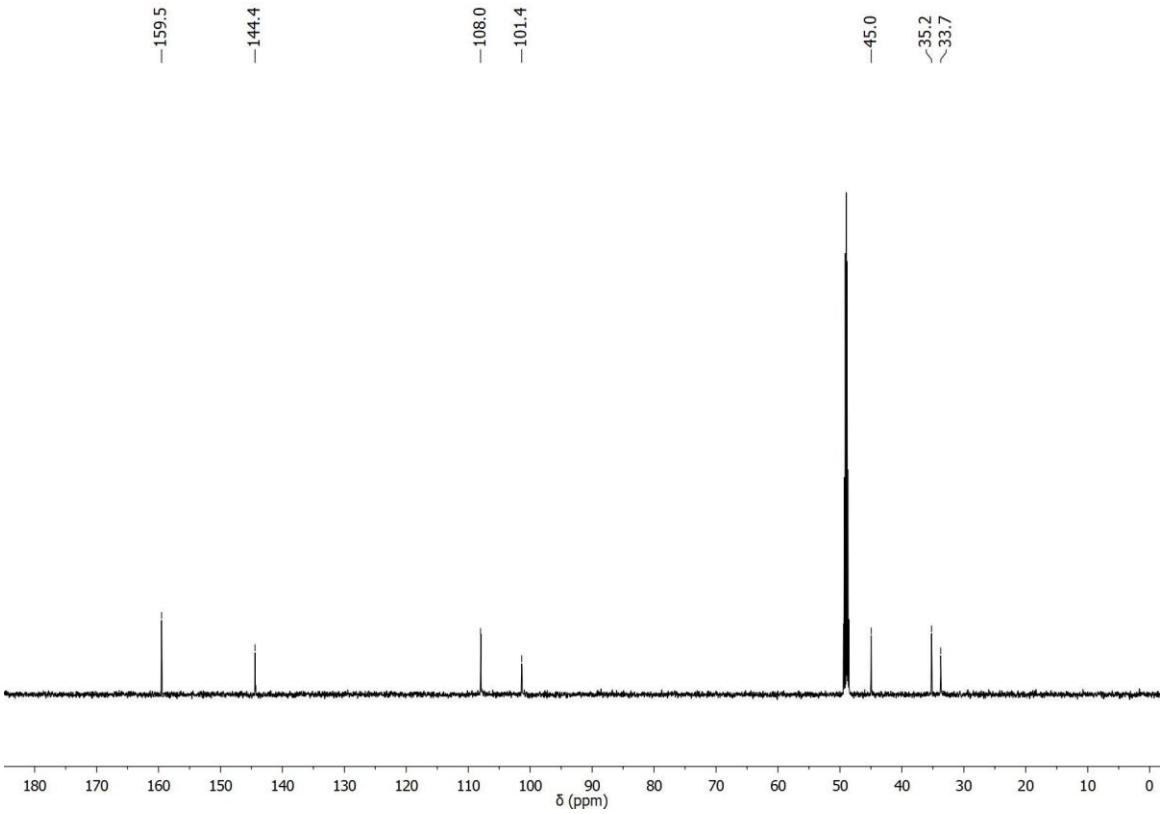

Figure A122. ^{13}C-NMR spectrum (150 MHz, MeOD) of compound **212**.

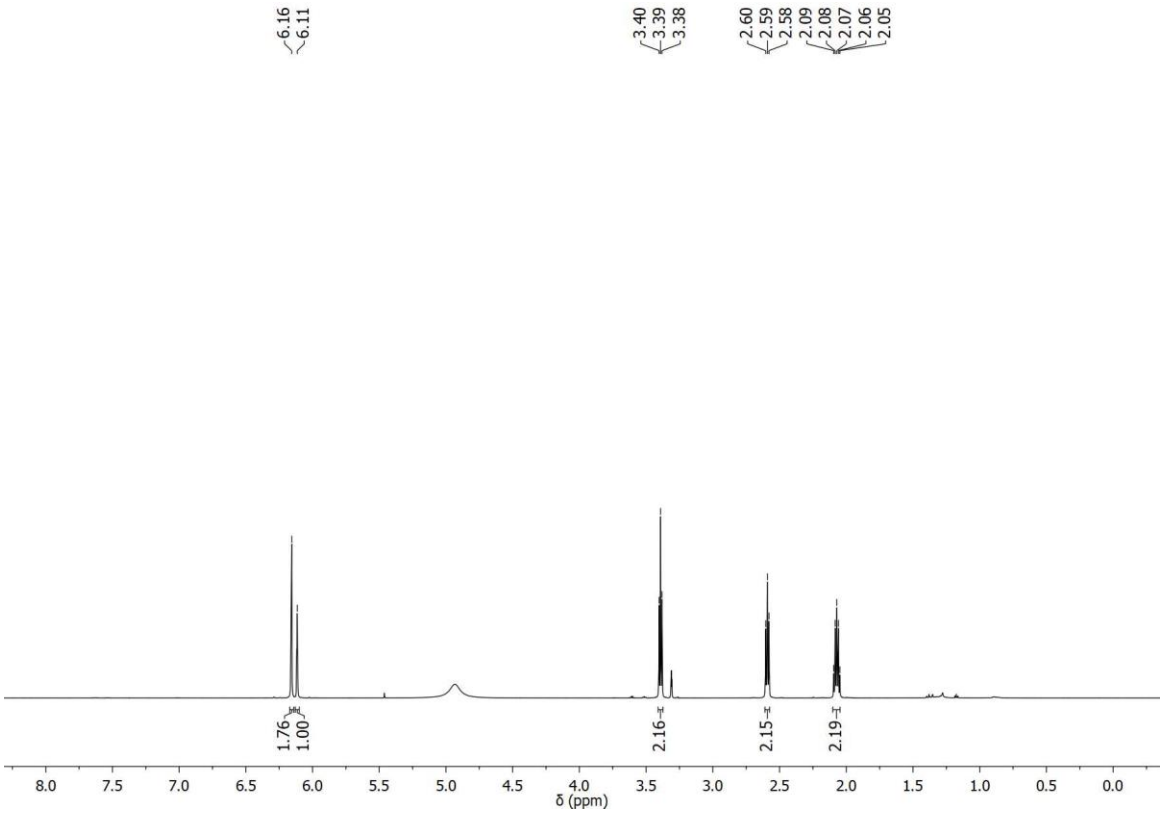

Figure A123. ^{1}H-NMR spectrum (600 MHz, MeOD) of compound **213**.

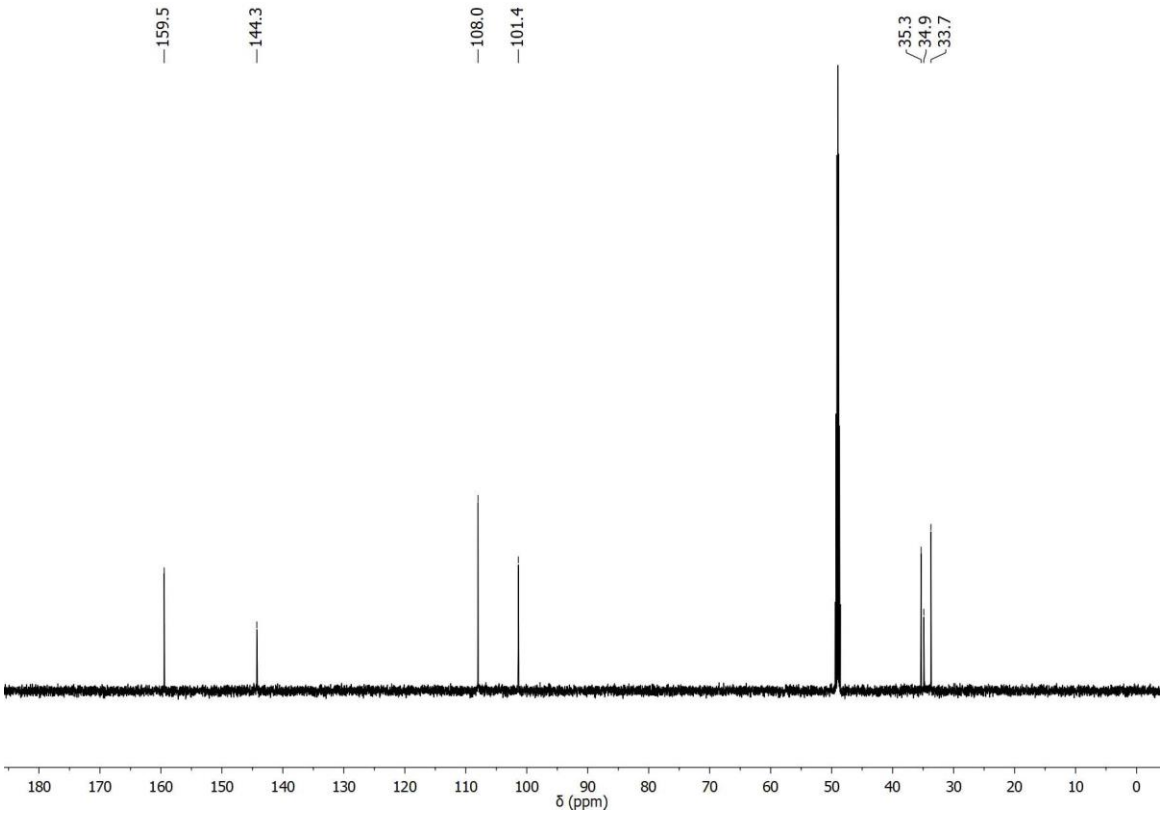

Figure A124. ^{13}C-NMR spectrum (150 MHz, MeOD) of compound **213**.

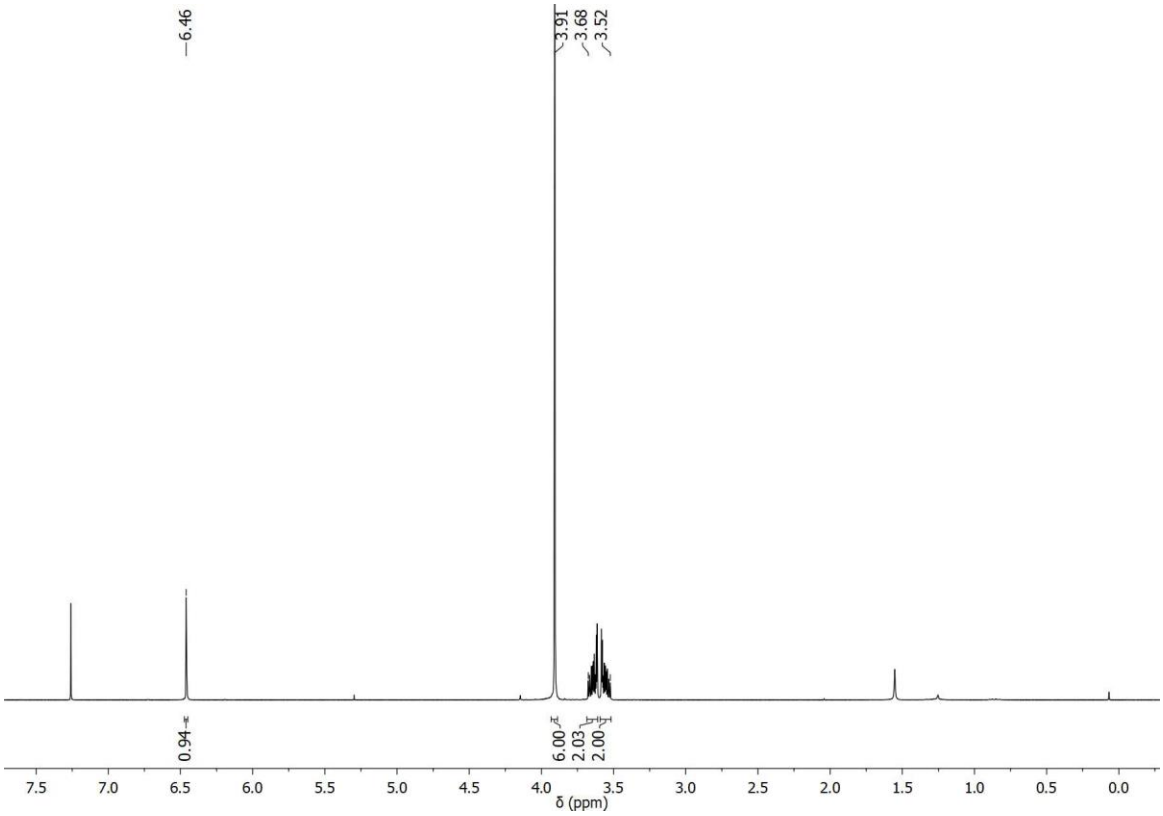

Figure A125. ^{1}H-NMR spectrum (300 MHz, $CDCl_3$) of compound **214**.

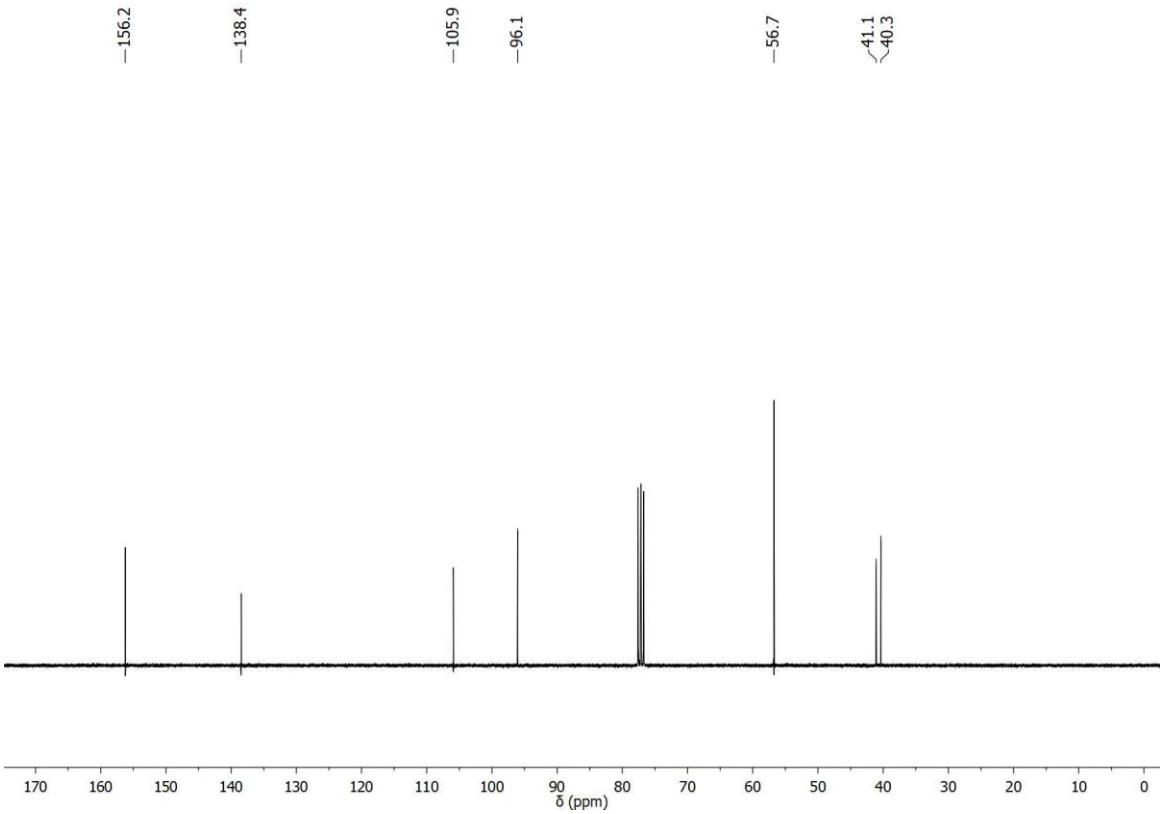

Figure A126. ^{13}C-NMR spectrum (75 MHz, $CDCl_3$) of compound **214**.

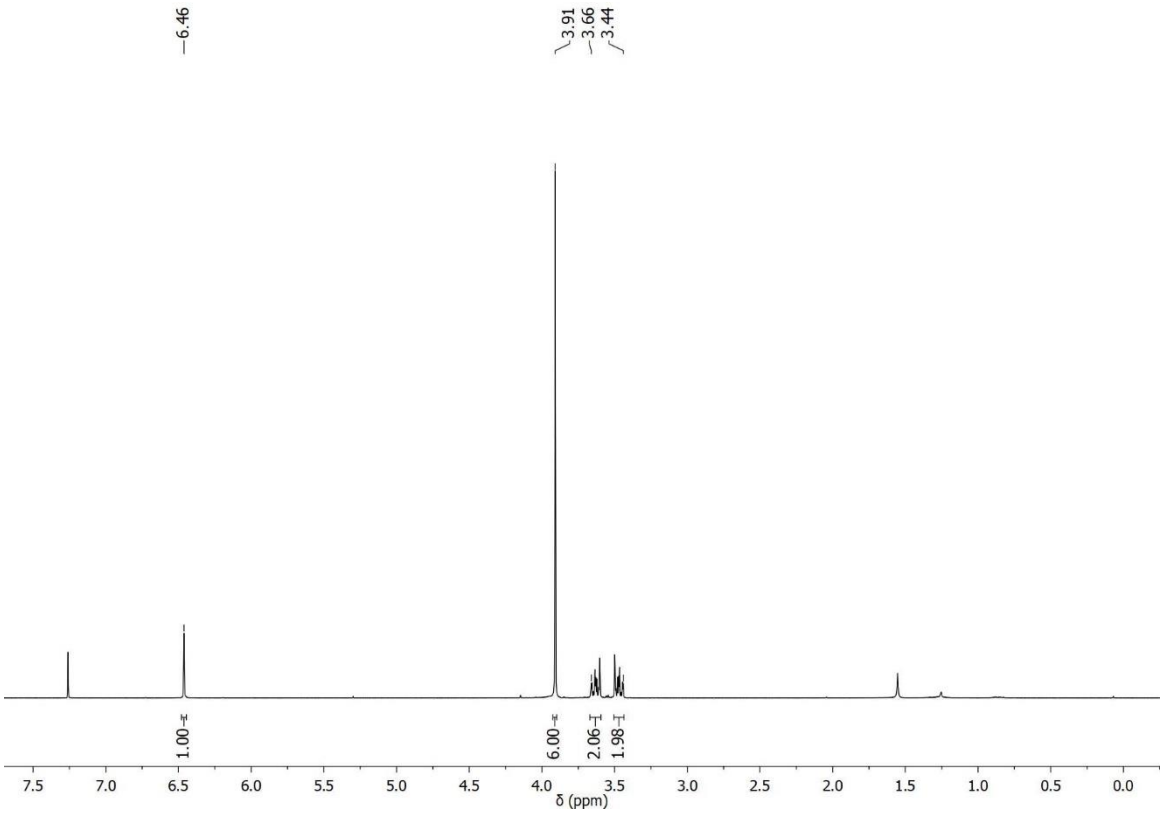

Figure A127. ^{1}H-NMR spectrum (300 MHz, $CDCl_3$) of compound **215**.

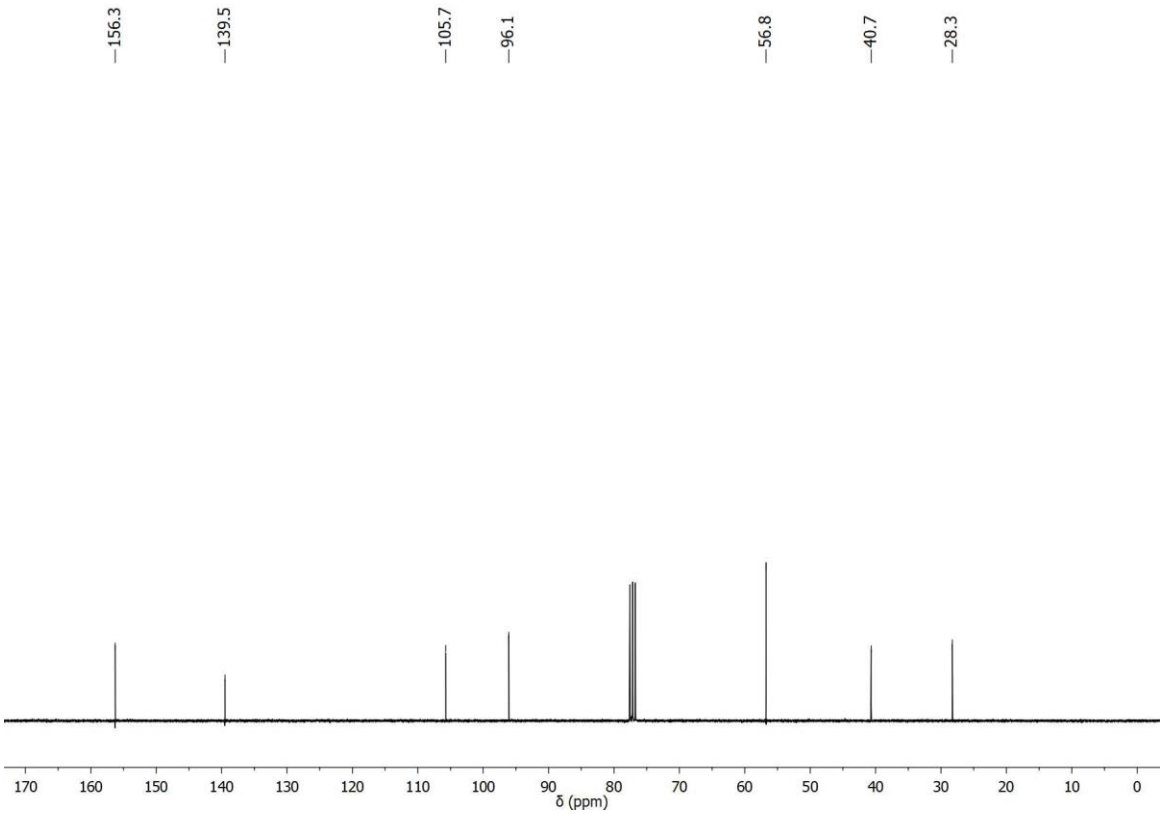

Figure A128. ^{13}C-NMR spectrum (75 MHz, $CDCl_3$) of compound **215**.

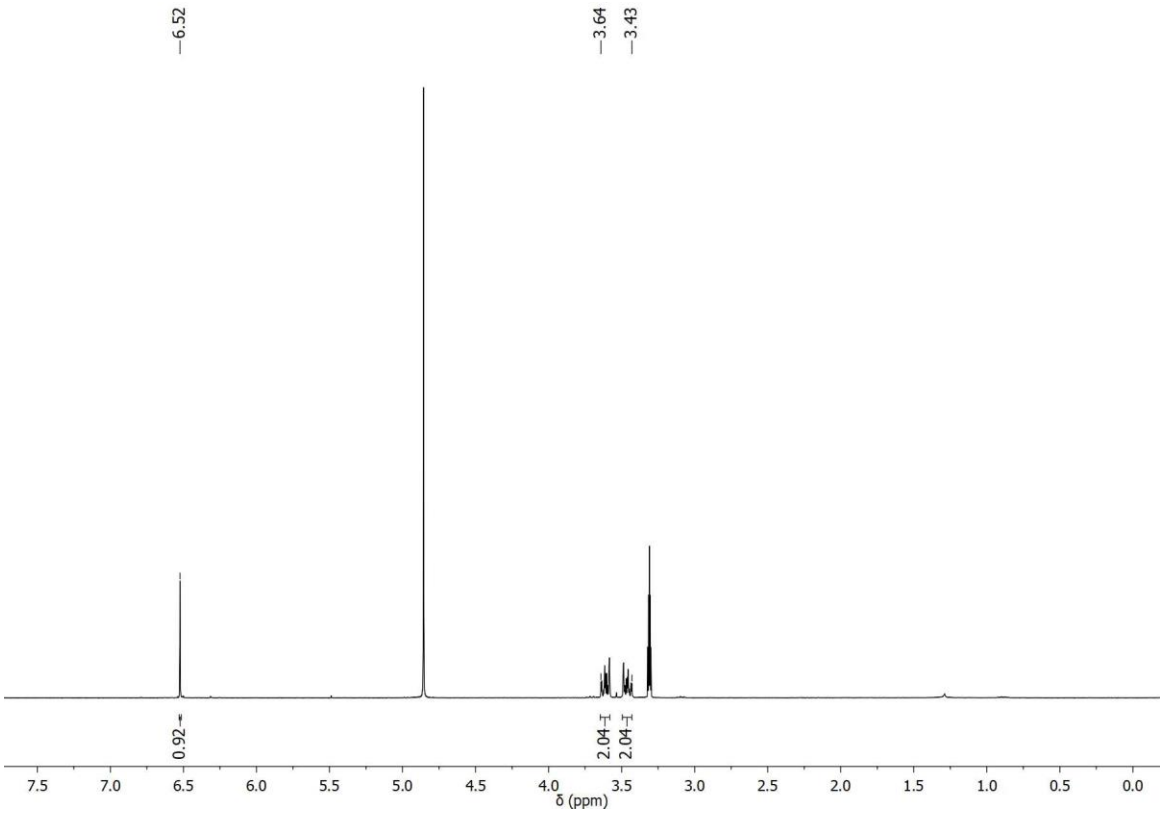

Figure A129. ^{1}H-NMR spectrum (300 MHz, $CDCl_3$) of compound **216**.

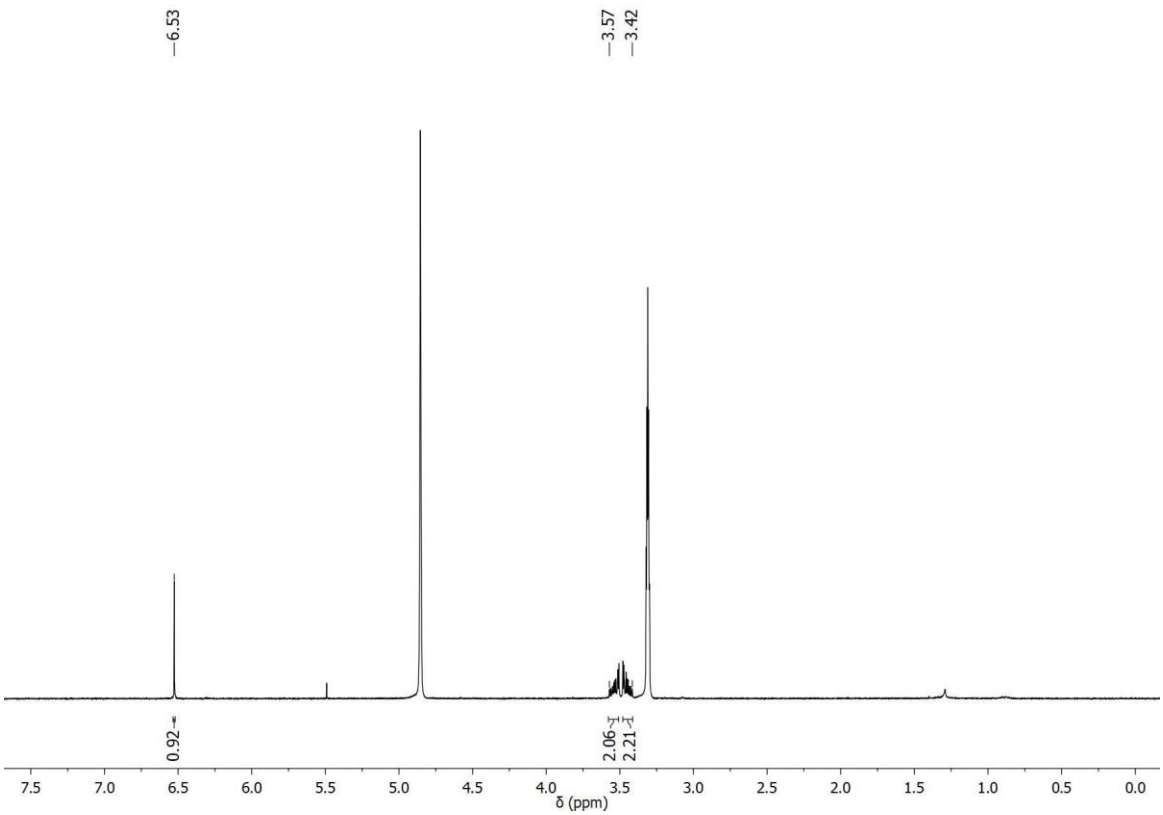

Figure A130. ^{1}H-NMR spectrum (300 MHz, $CDCl_3$) of compound **217**.

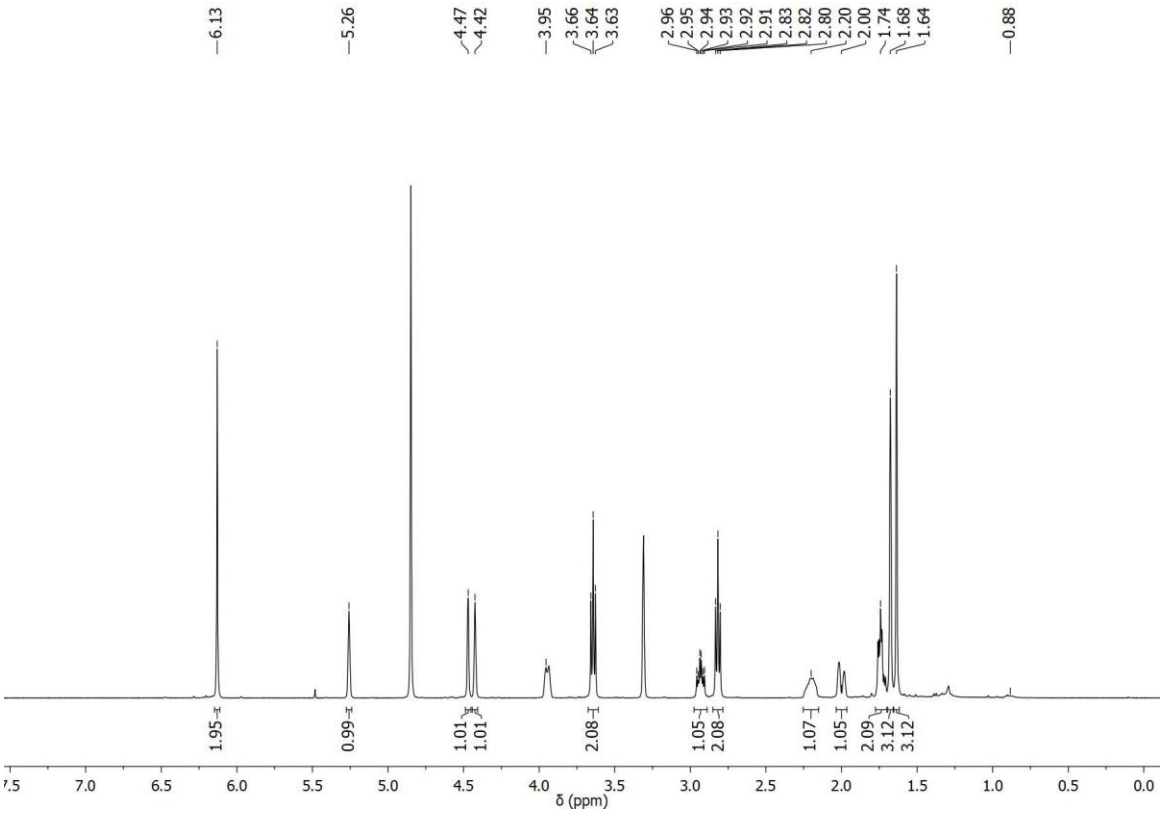

Figure A131. ^{1}H-NMR spectrum (500 MHz, MeOD) of compound **193**.

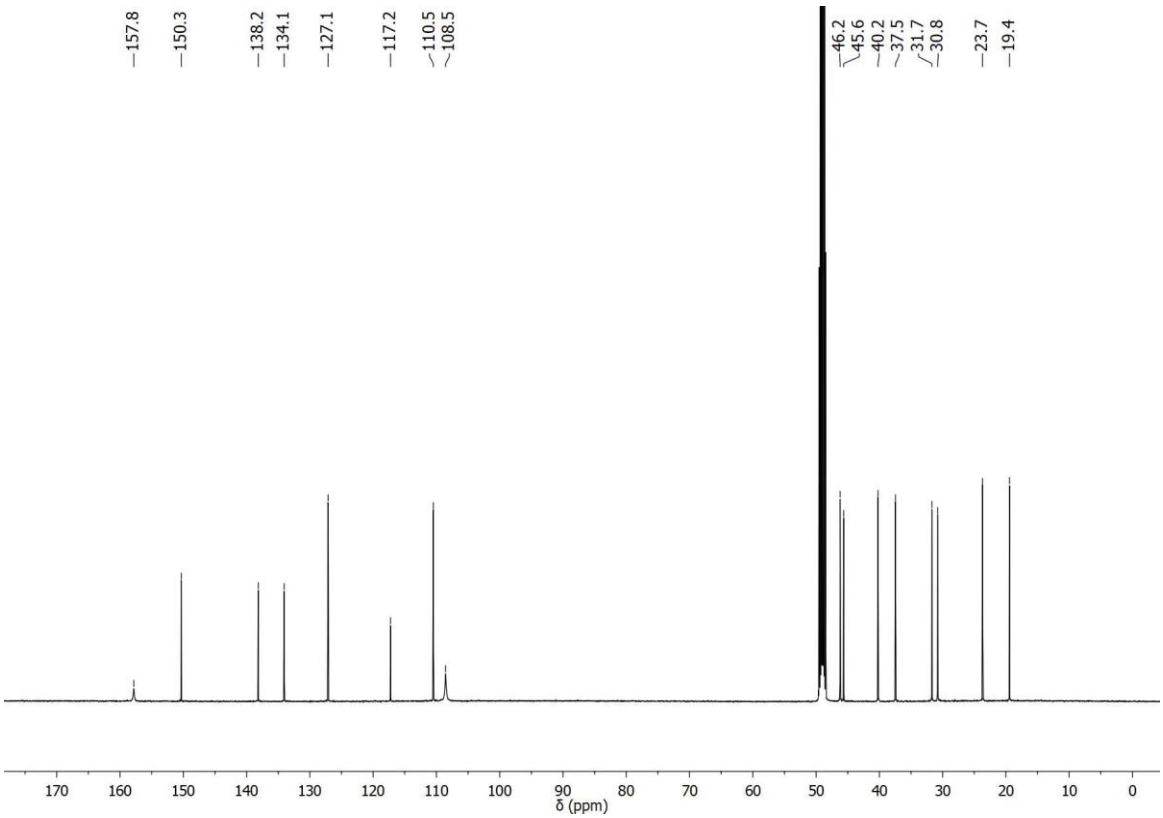

Figure A132. ^{13}C-NMR spectrum (125 MHz, MeOD) of compound **193**.

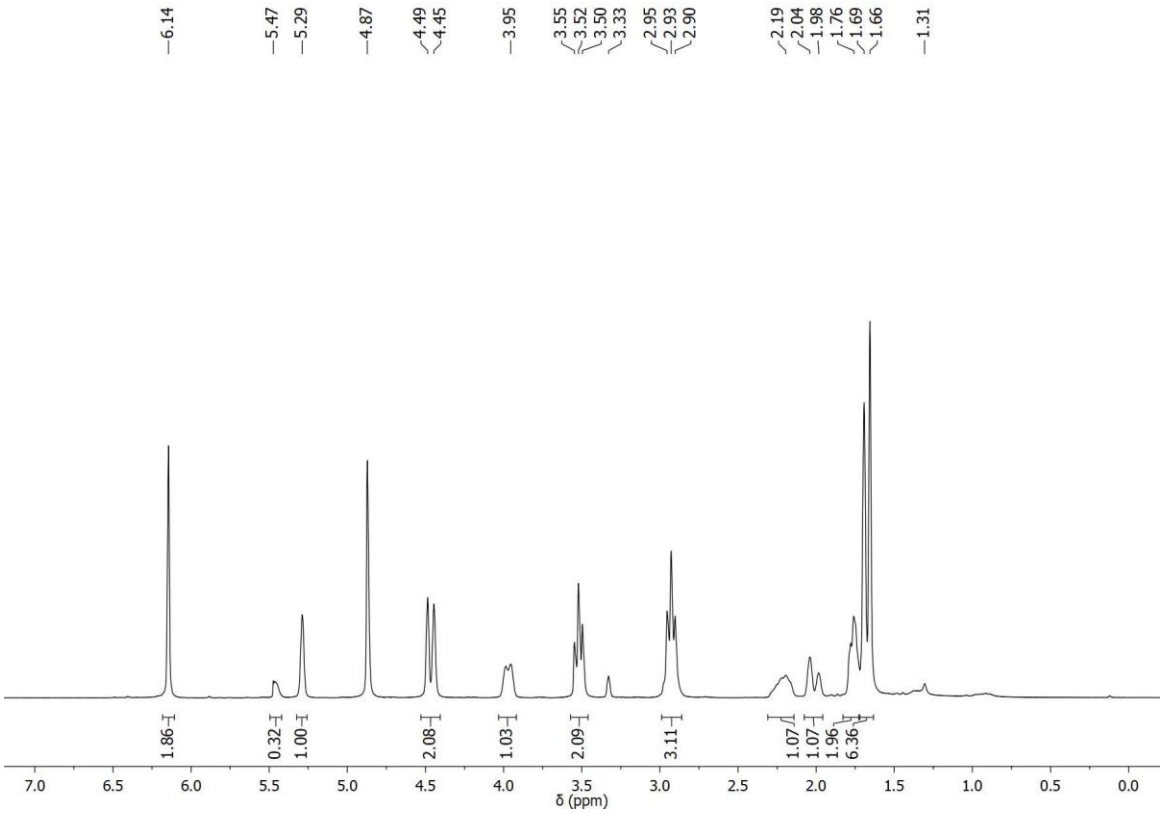

Figure A133. [1]H-NMR spectrum (300 MHz, MeOD) of compound **194**.

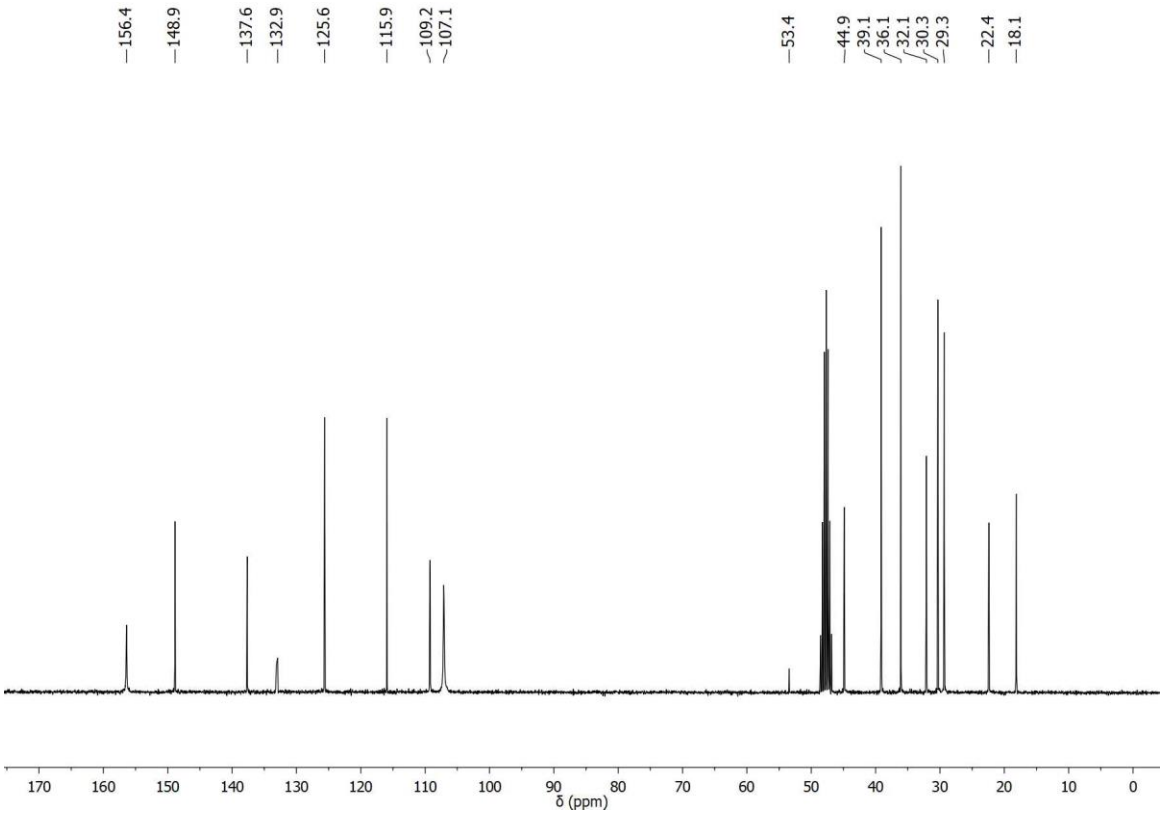

Figure A134. [13]C-NMR spectrum (75 MHz, MeOD) of compound **194**.

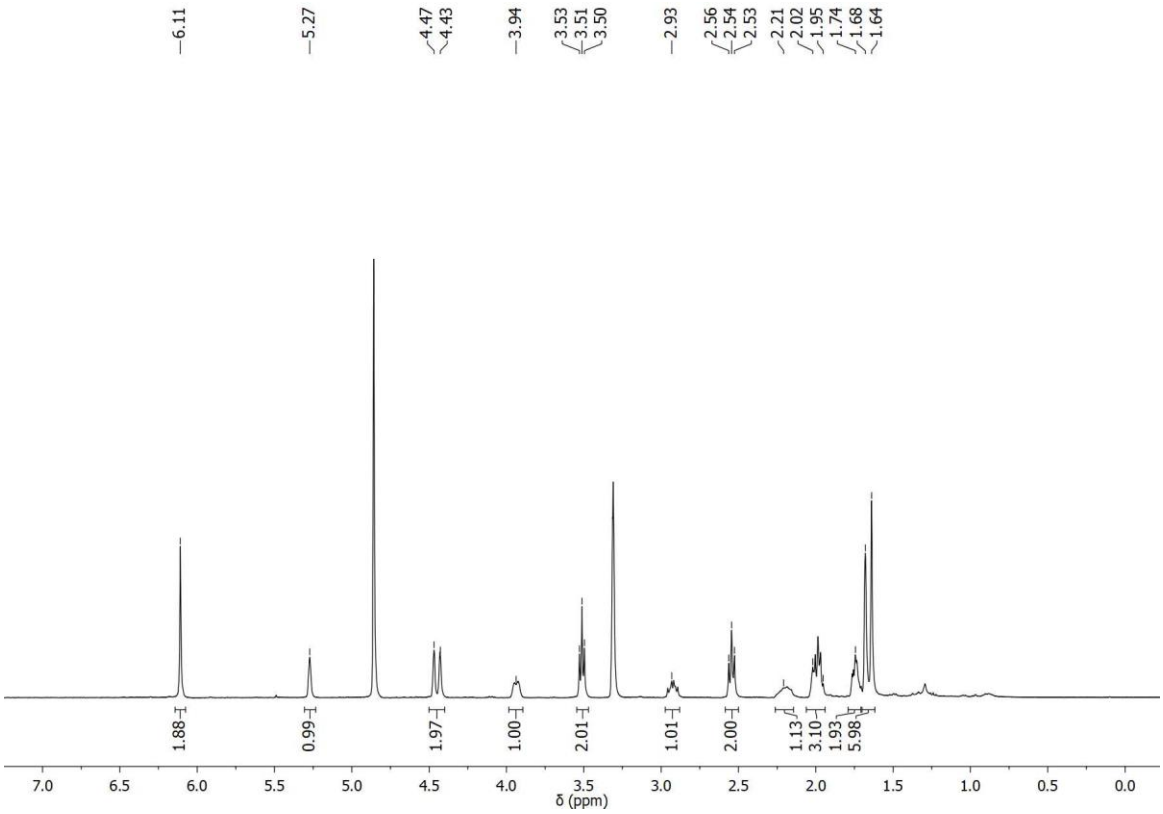

Figure A135. ^{1}H-NMR spectrum (400 MHz, MeOD) of compound **196**.

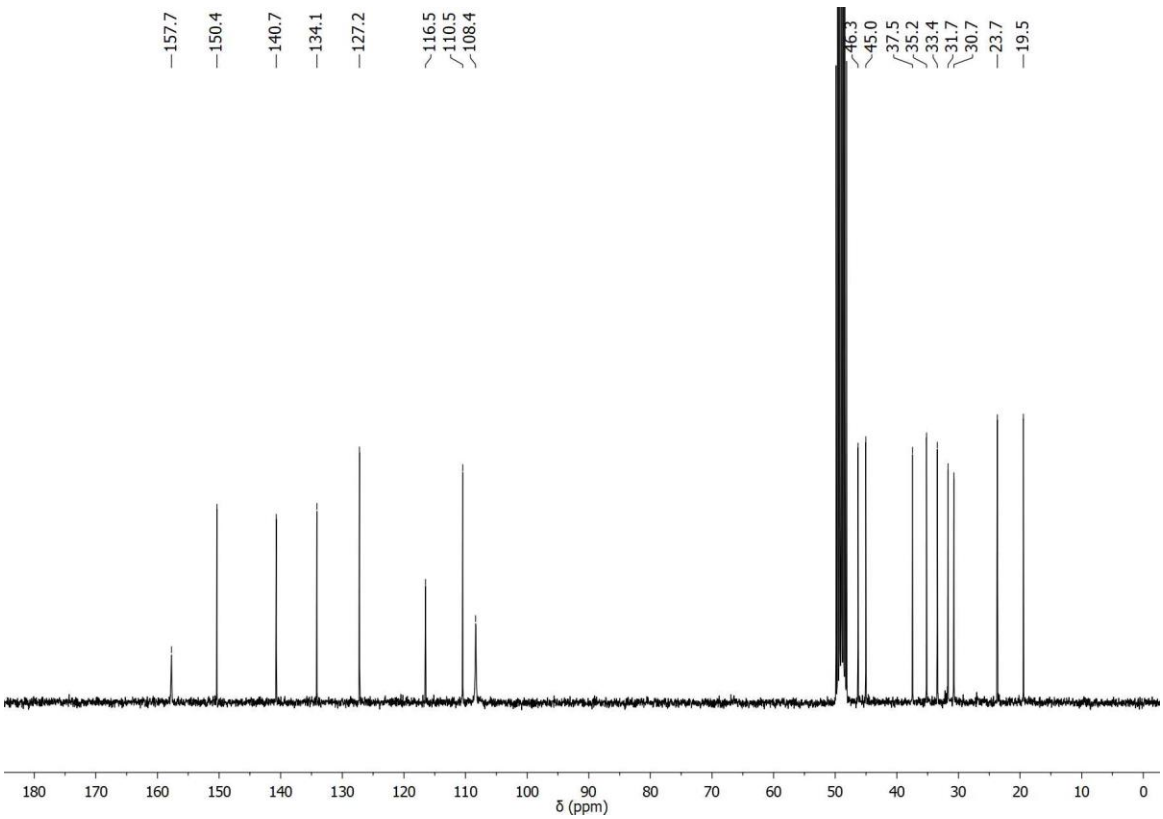

Figure A136. ^{13}C-NMR spectrum (75 MHz, MeOD) of compound **196**.

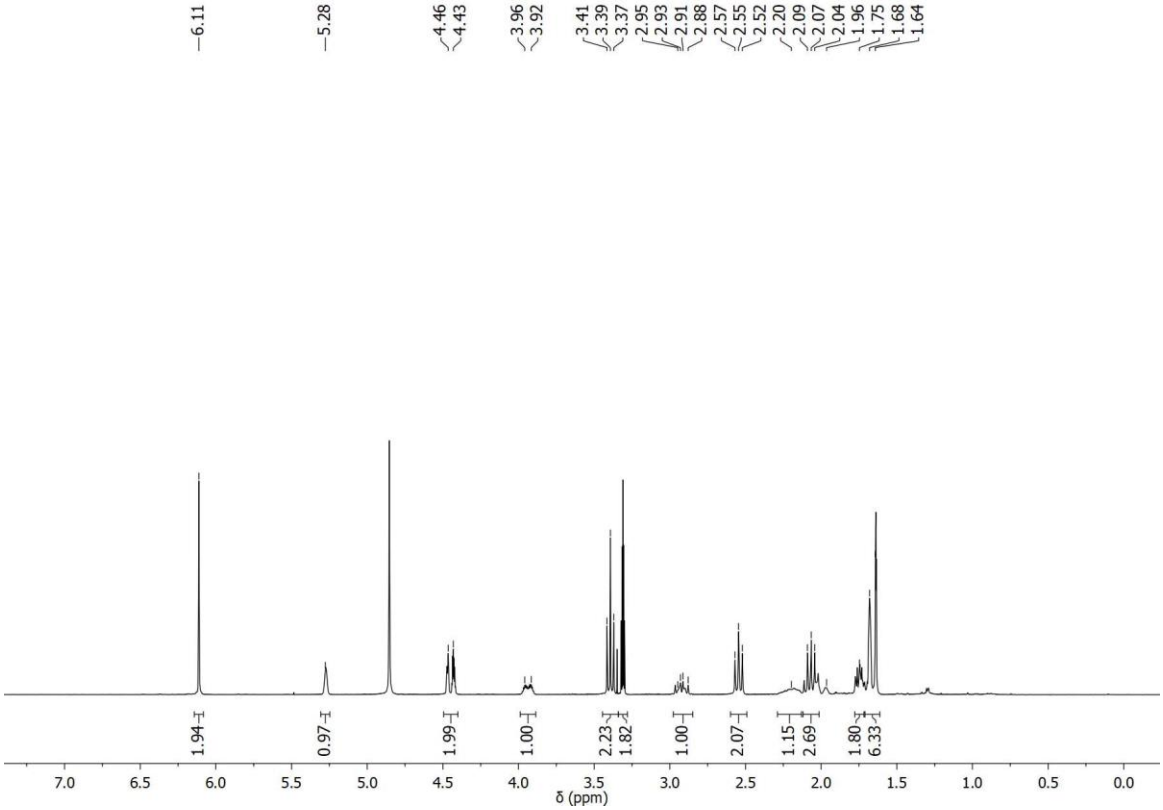

Figure A137. ^{1}H-NMR spectrum (300 MHz, MeOD) of compound **197**.

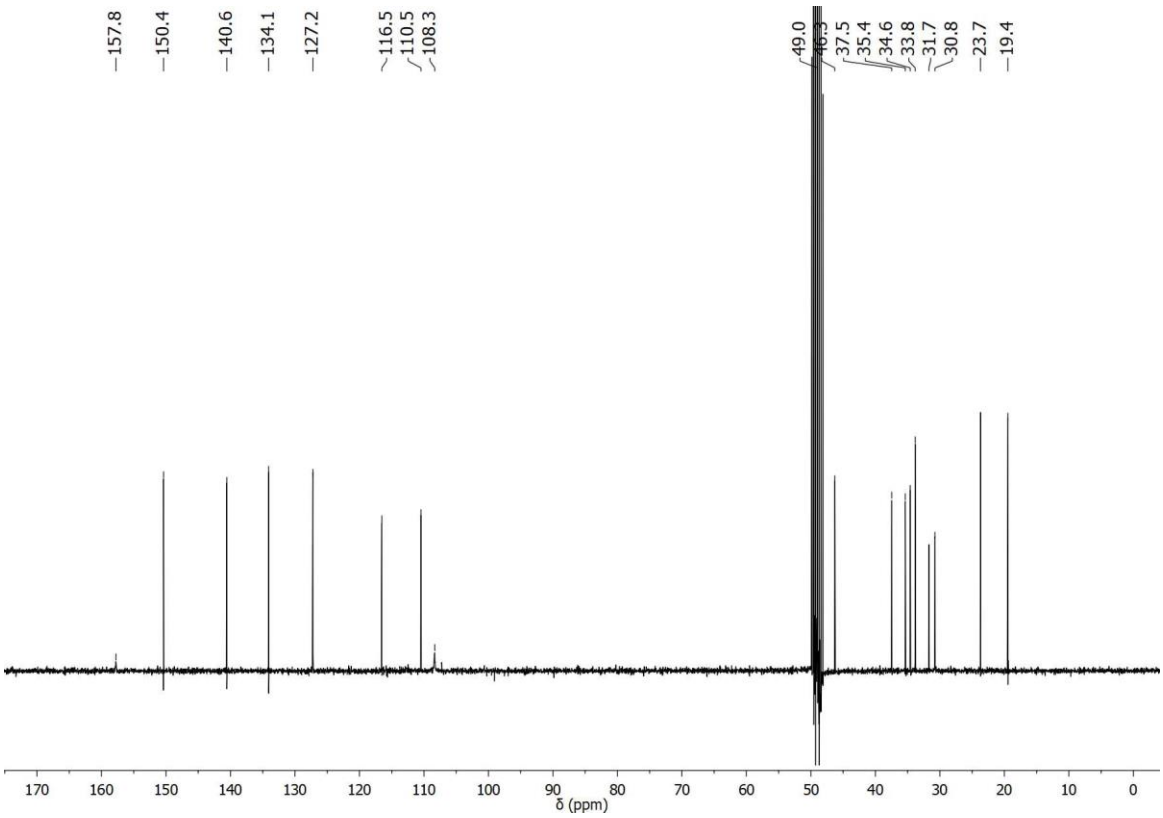

Figure A138. ^{13}C-NMR spectrum (75 MHz, MeOD) of compound **197**.

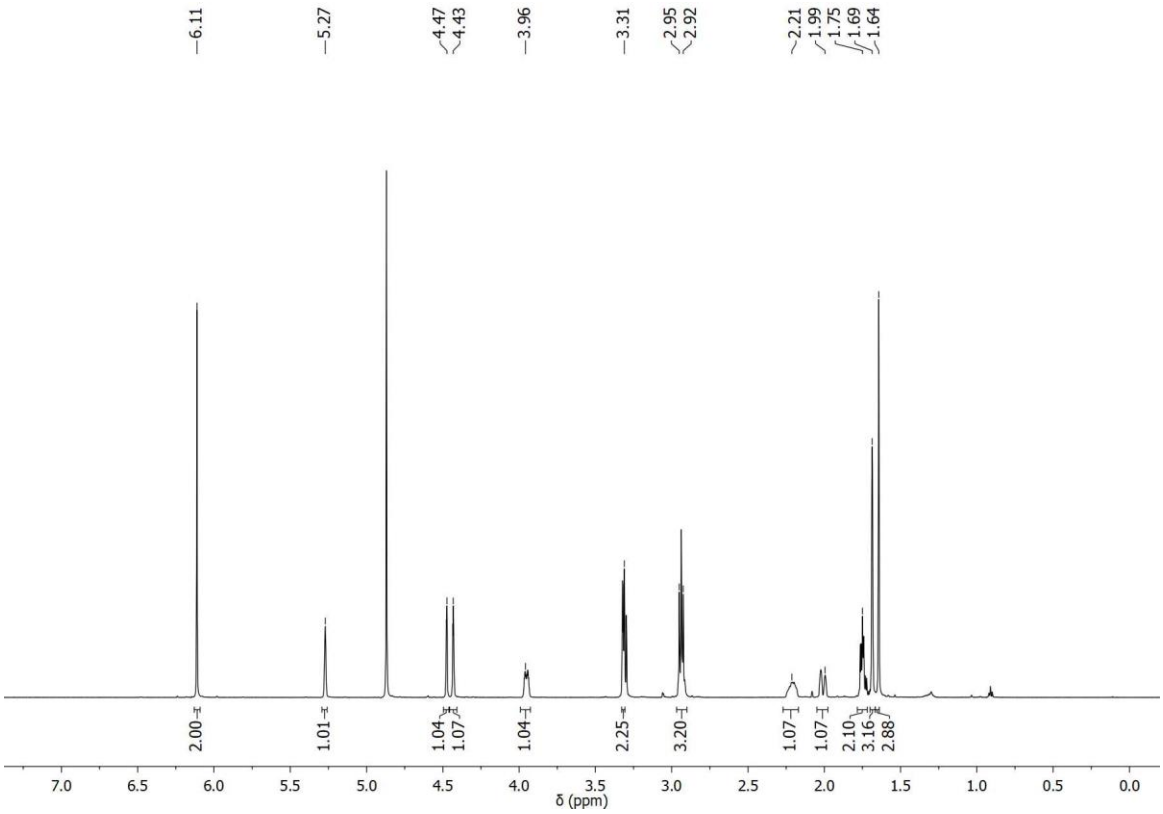

Figure A139. ^{1}H-NMR spectrum (600 MHz, MeOD) of compound **195**.

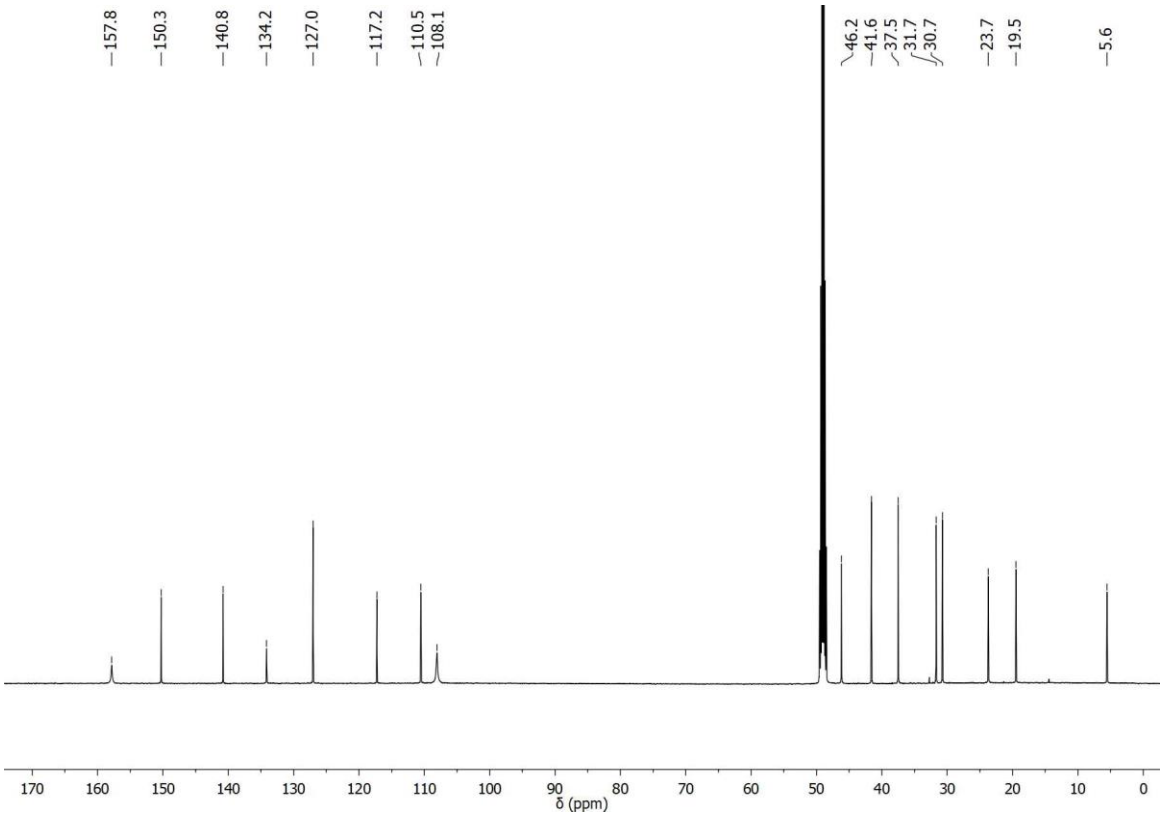

Figure A140. ^{13}C-NMR spectrum (125 MHz, MeOD) of compound **195**.

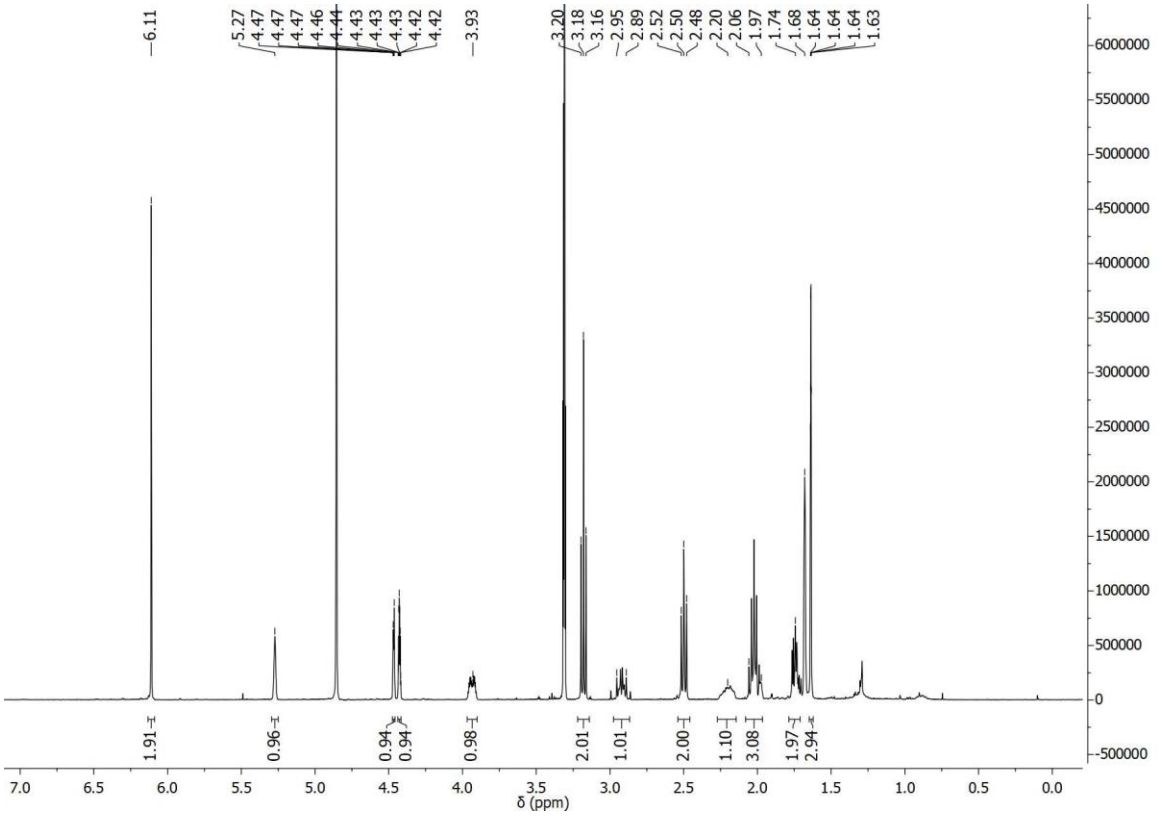

Figure A141. ^{1}H-NMR spectrum (400 MHz, MeOD) of compound **198**.

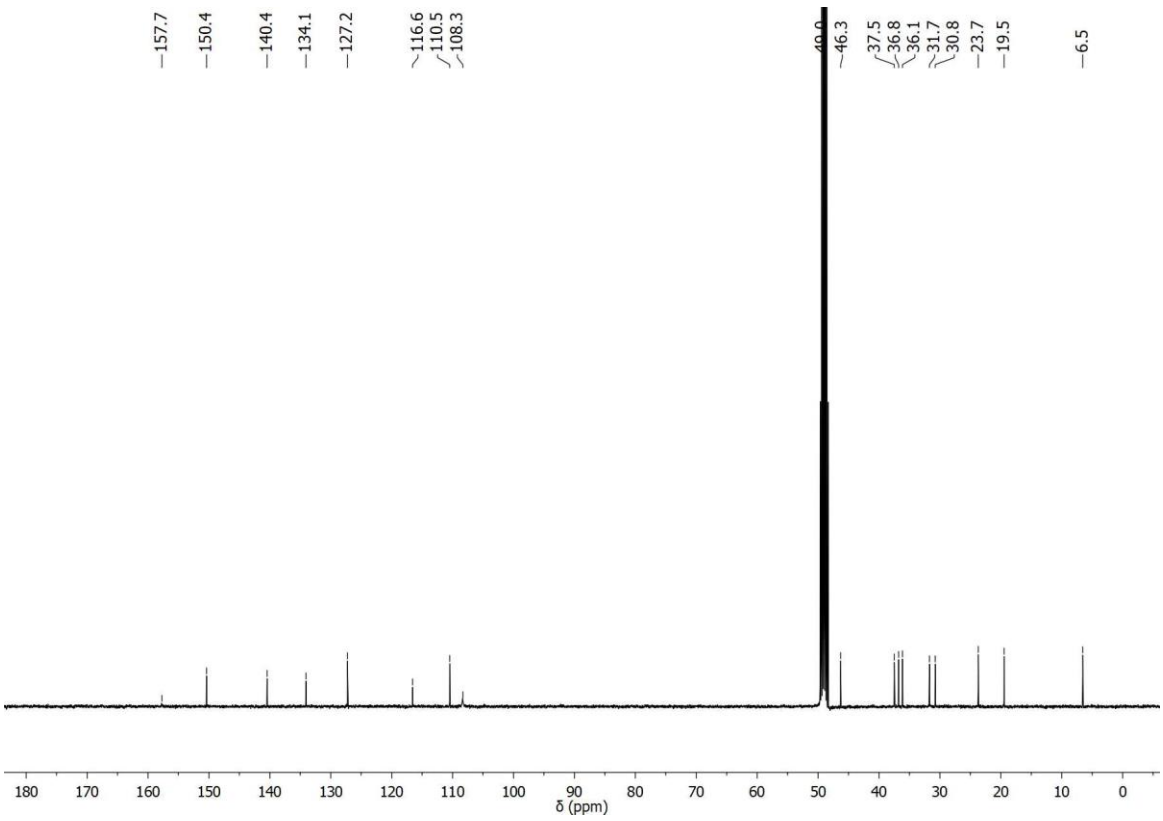

Figure A142. ^{13}C-NMR spectrum (100 MHz, MeOD) of compound **198**.

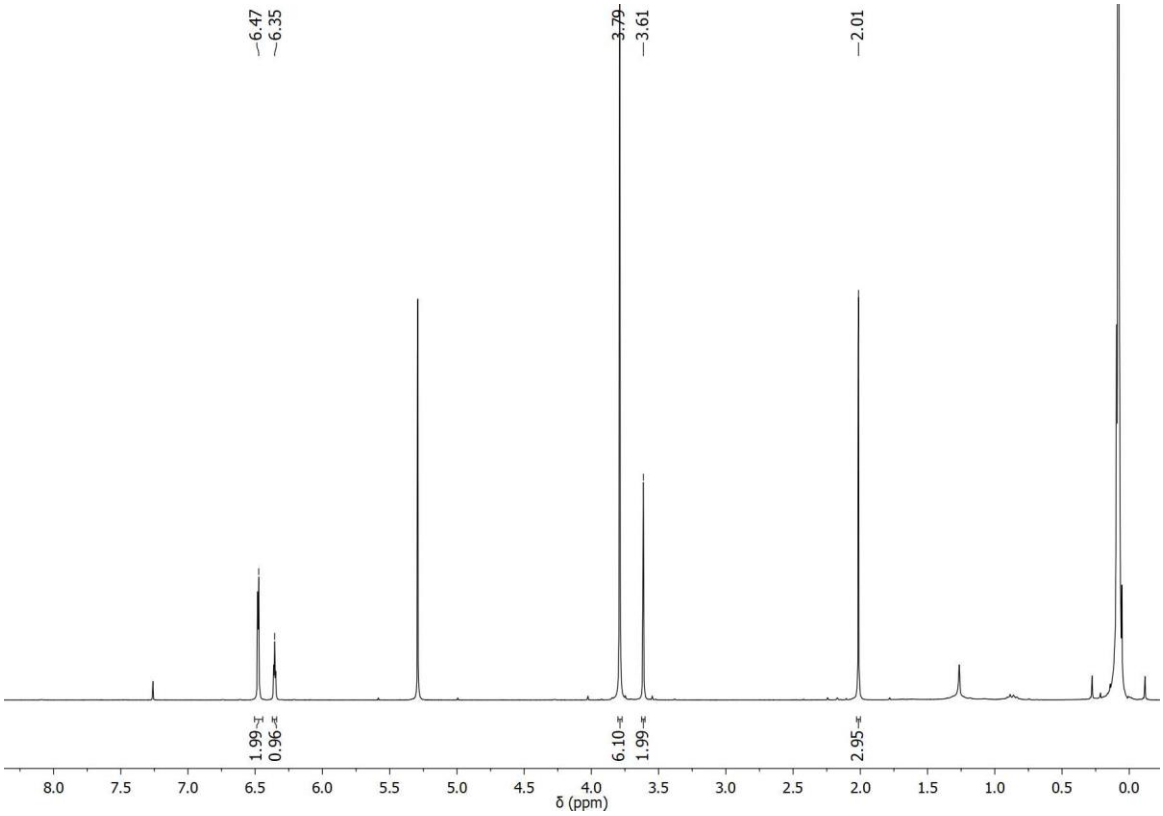

Figure A143. ^{1}H-NMR spectrum (300 MHz, $CDCl_3$) of compound **222**.

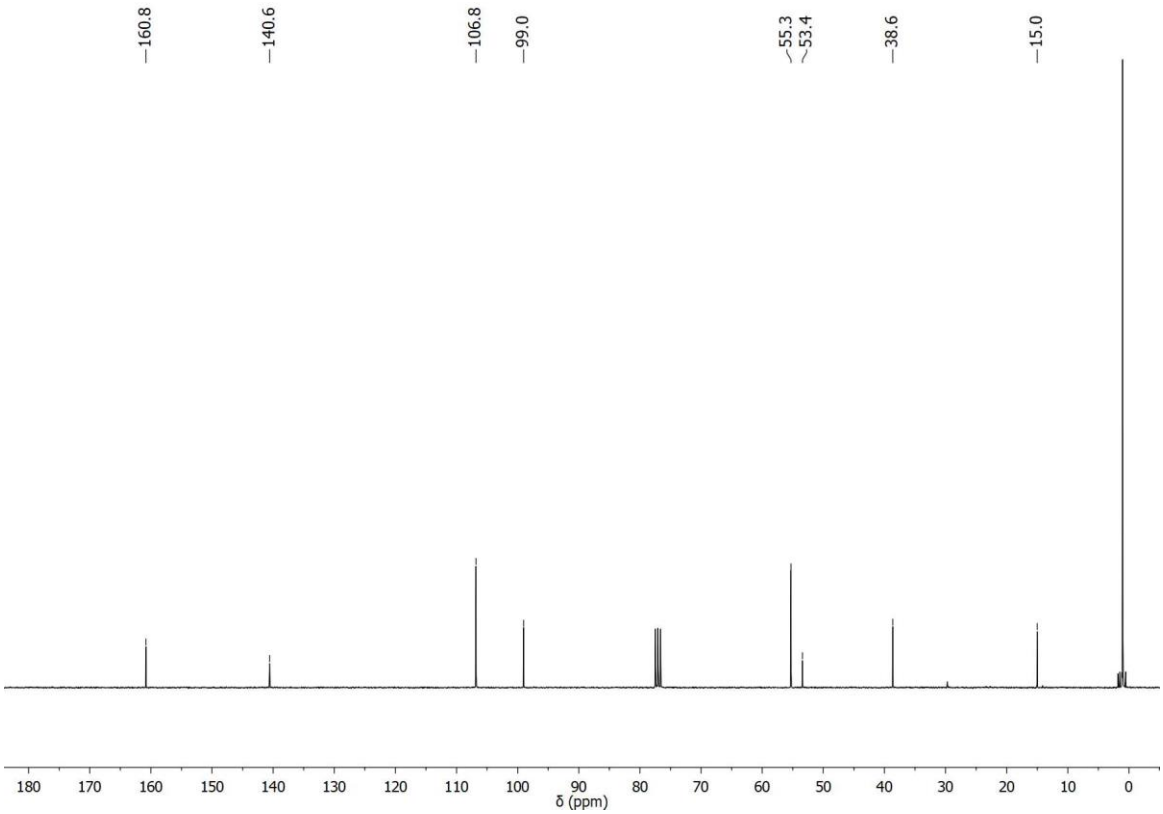

Figure A144. ^{13}C-NMR spectrum (75 MHz, $CDCl_3$) of compound **222**.

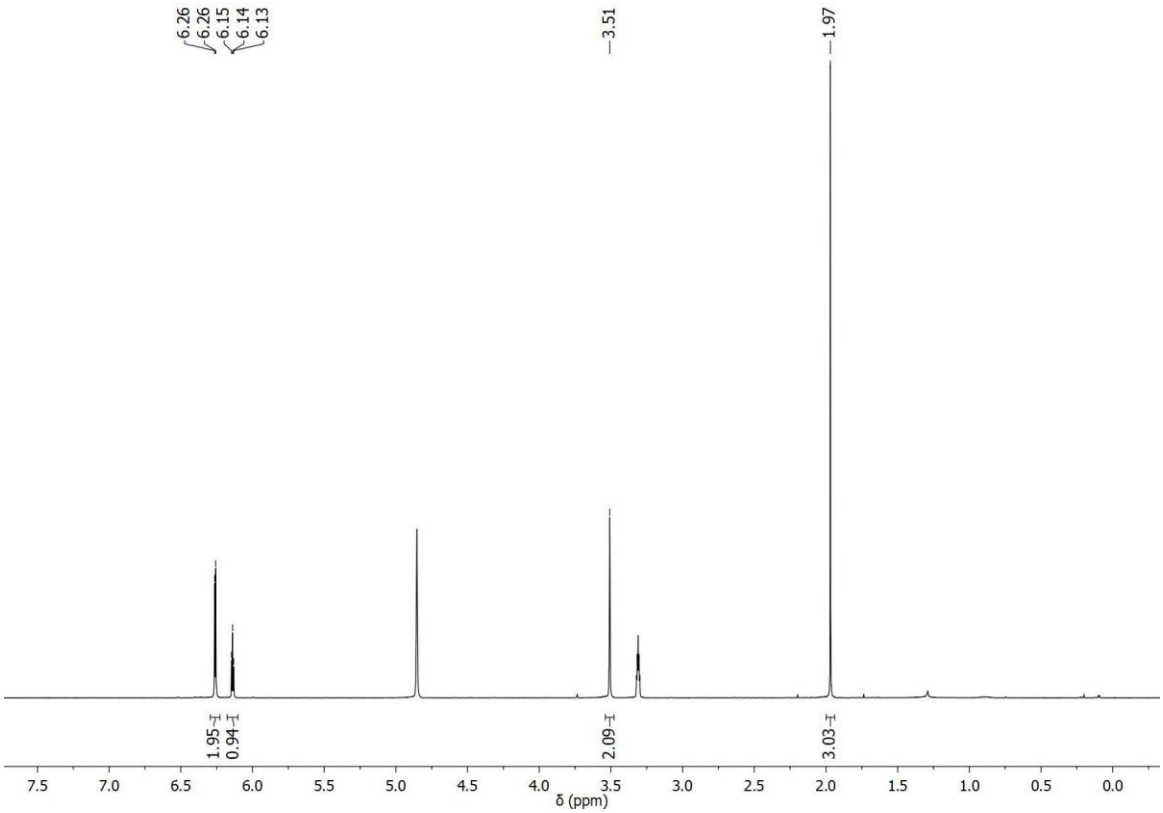

Figure A145. ^{1}H-NMR spectrum (400 MHz, MeOD) of compound **223**.

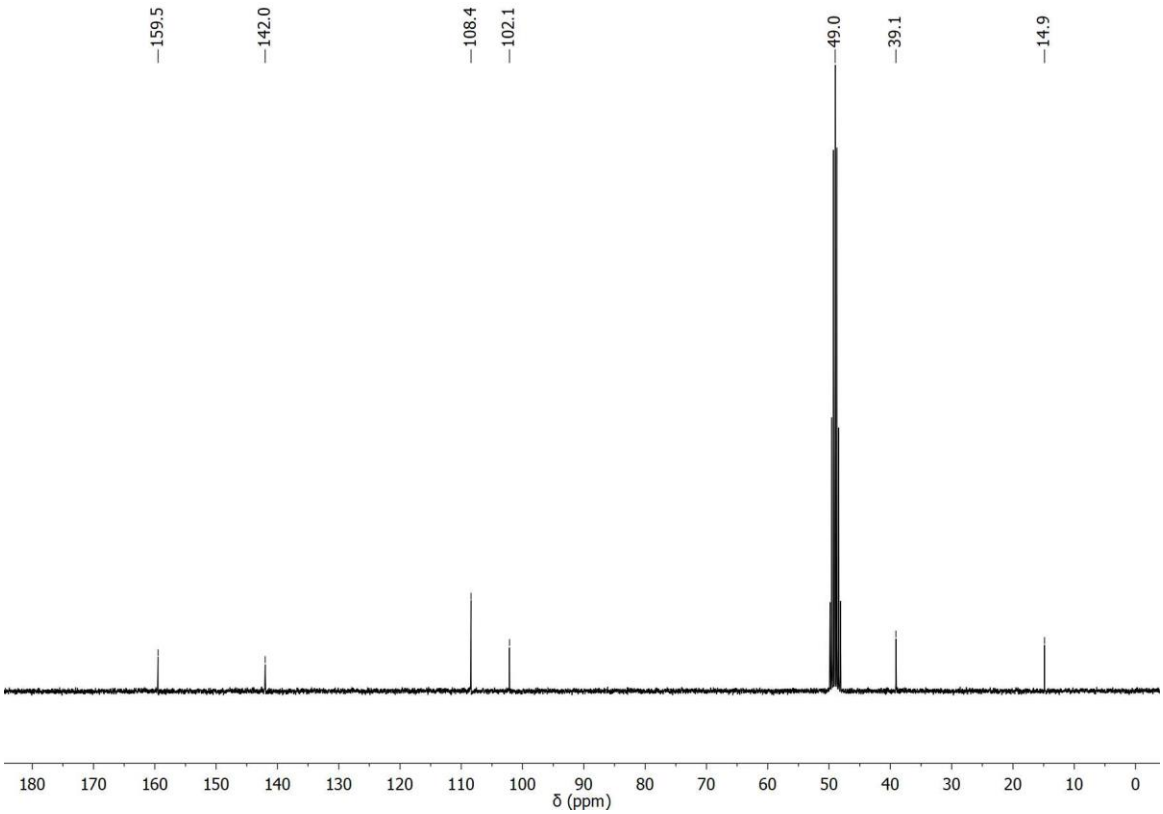

Figure A146. ^{13}C-NMR spectrum (100 MHz, MeOD) of compound **223**.

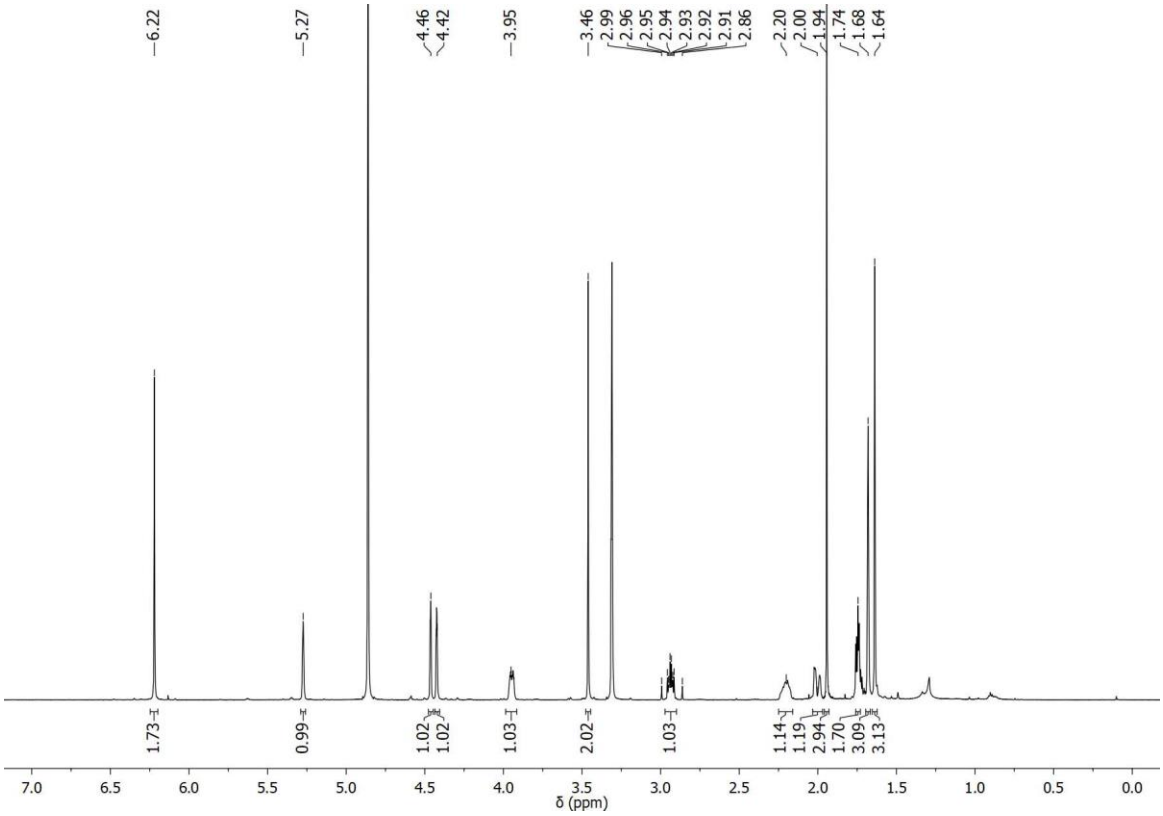

Figure A147. ^{1}H-NMR spectrum (600 MHz, MeOD) of compound **199**.

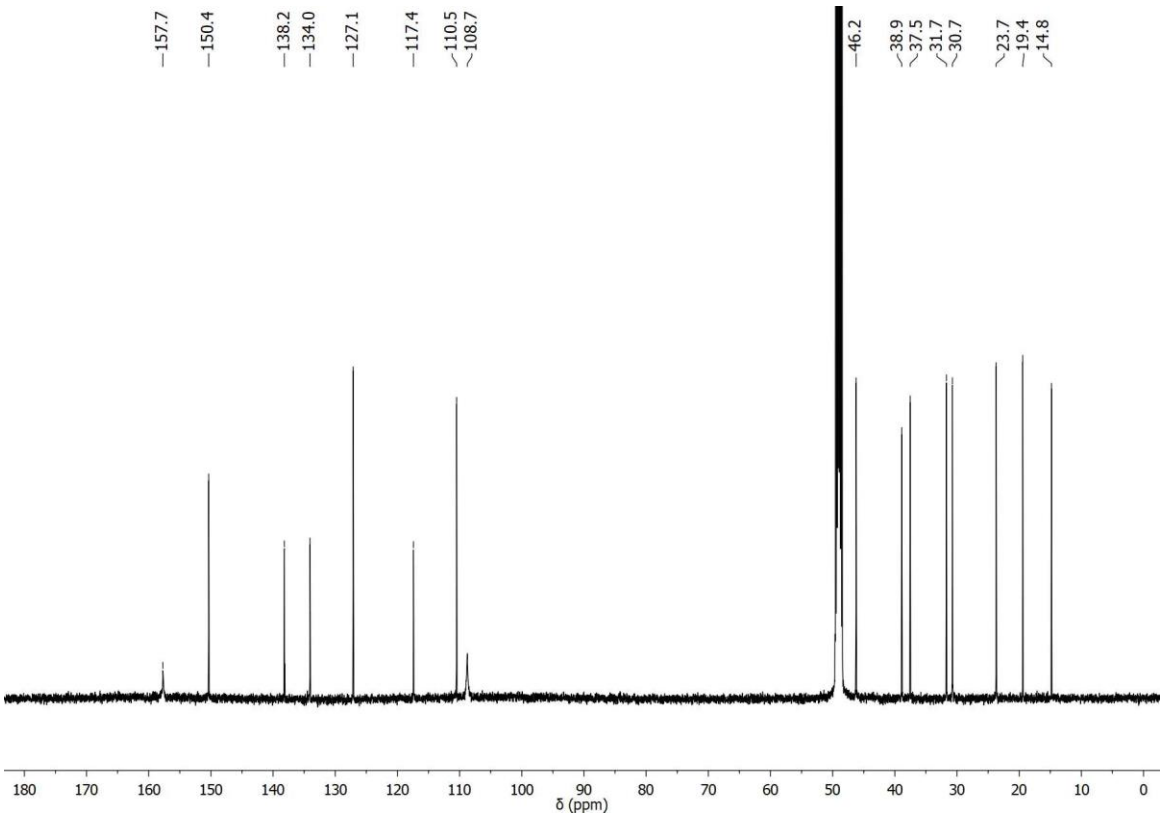

Figure A148. ^{13}C-NMR spectrum (125 MHz, MeOD) of compound **199**.

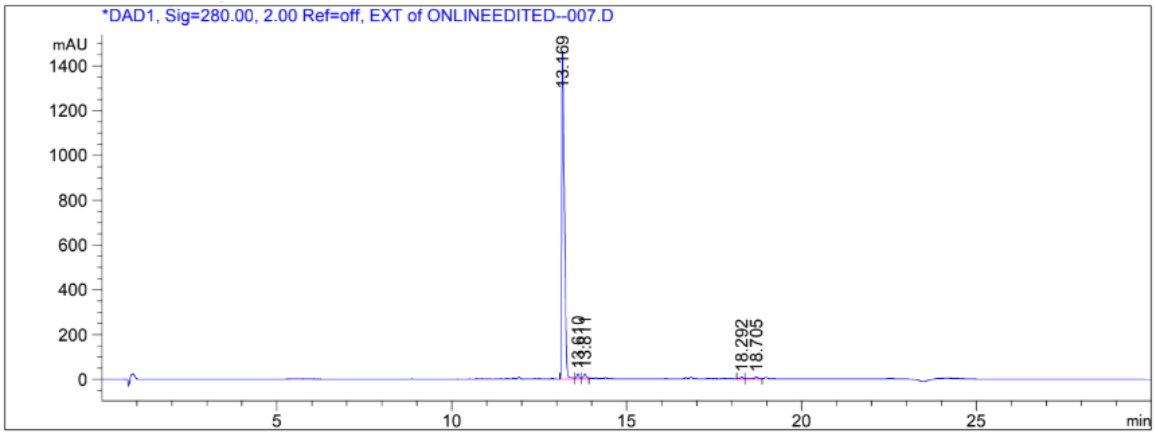

Figure A149. HPLC chromatogram for purity analysis of the compound **193**, showing a main peak at R_t = 13.169 min with a purity of 96.8%.

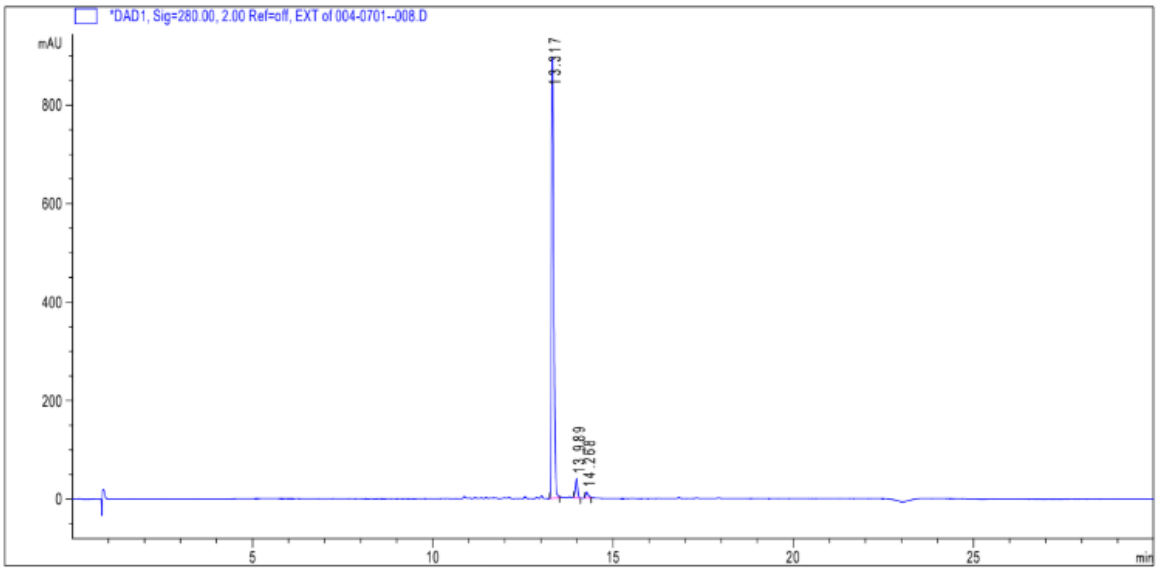

Figure A150. HPLC chromatogram for purity analysis of the compound **194**, showing a main peak at R_t = 13.317 min with a purity of 96.9%.

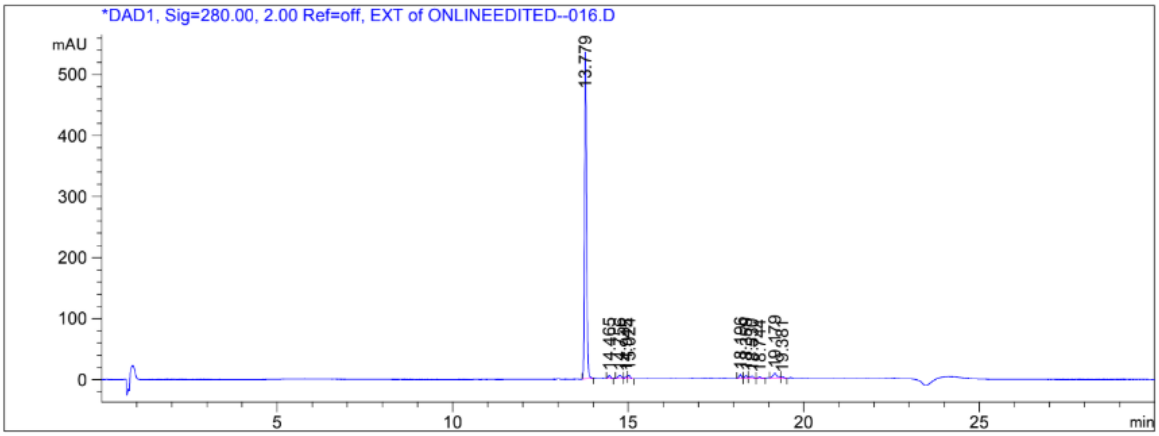

Figure A151. HPLC chromatogram for purity analysis of the compound **196**, showing a main peak at R_t = 13.779 min with a purity of 90.6%.

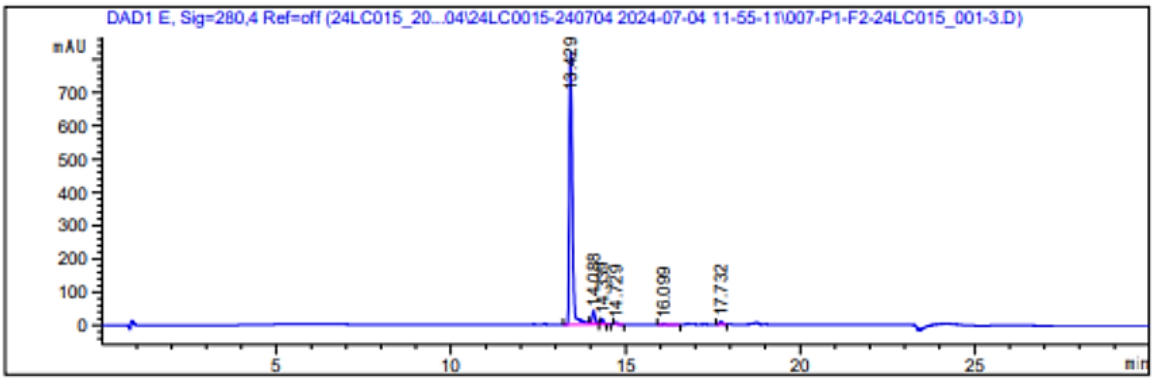

Figure A152. HPLC chromatogram for purity analysis of the compound **197**, showing a main peak at R_t = 13.429 min with a purity of 93.9%.

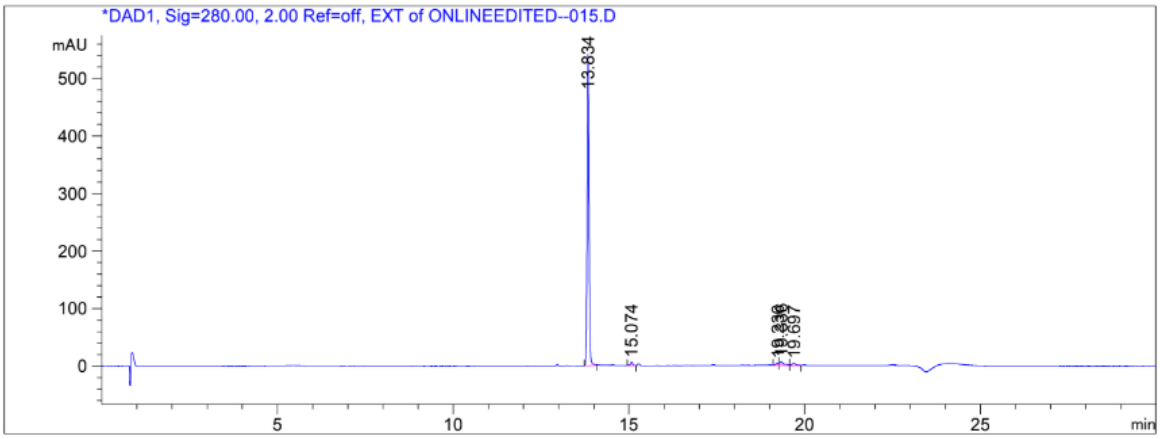

Figure A153. HPLC chromatogram for purity analysis of the compound **195**, showing a main peak at R_t = 13.834 min with a purity of 95.1%.

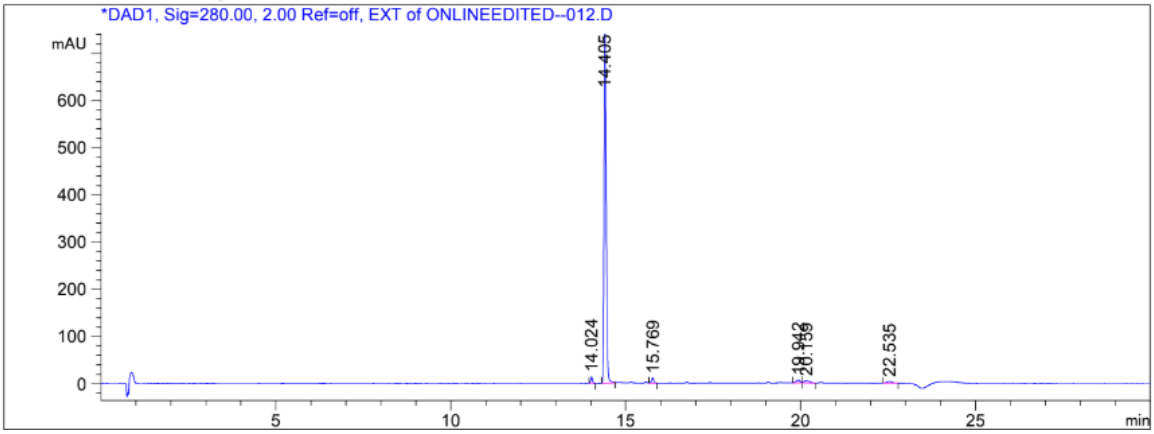

Figure A154. HPLC chromatogram for purity analysis of the compound **198**, showing a main peak at R_t = 14.405 min with a purity of 94.3%.

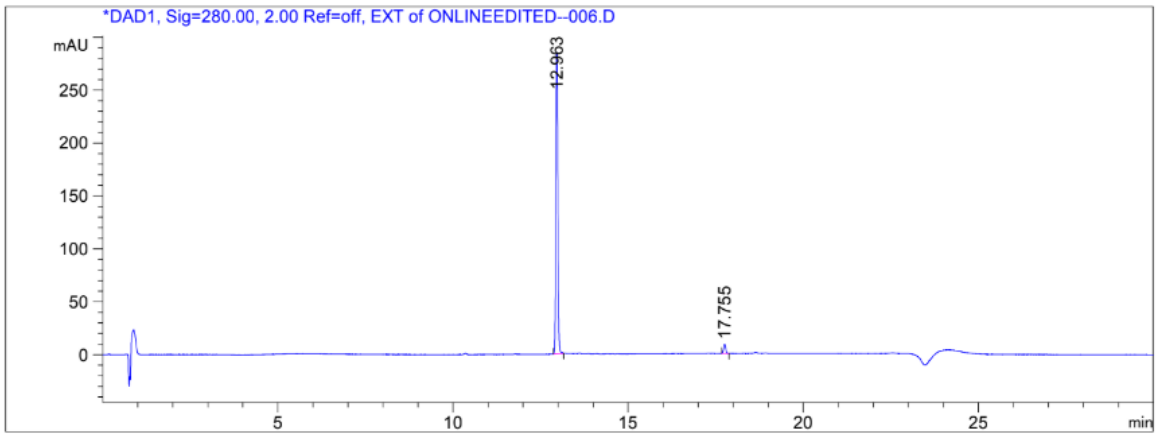

Figure A155. HPLC chromatogram for purity analysis of the compound **199**, showing a main peak at R_t = 12.963 min with a purity of 96.6%.